Handbook of Turbomachinery

Second Edition
Revised and Expanded

edited by
Earl Logan, Jr.
Ramendra Roy
Arizona State University
Tempe, Arizona, U.S.A.

MARCEL DEKKER, INC. NEW YORK • BASEL

The first edition was published as *Handbook of Turbomachinery*, edited by Earl Logan, Jr. (Marcel Dekker, Inc., 1995).

Library of Congress Cataloging-in-Publication Data
A catalog record for this book is available from the Library of Congress.

ISBN: 0-8247-0995-0

This book is printed on acid-free paper.

Headquarters
Marcel Dekker, Inc.
270 Madison Avenue, New York, NY 10016
tel: 212-696-9000; fax: 212-685-4540

Eastern Hemisphere Distribution
Marcel Dekker AG
Hutgasse 4, Postfach 812, CH-4001 Basel, Switzerland
tel: 41-61-260-6300; fax: 41-61-260-6333

World Wide Web
http://www.dekker.com

The publisher offers discounts on this book when ordered in bulk quantities. For more information, write to Special Sales/Professional Marketing at the headquarters address above.

Current printing (last digit):
10 9 8 7 6 5 4 3 2 1

PRINTED IN THE UNITED STATES OF AMERICA

MECHANICAL ENGINEERING

A Series of Textbooks and Reference Books

Founding Editor

L. L. Faulkner

Columbus Division, Battelle Memorial Institute
and Department of Mechanical Engineering
The Ohio State University
Columbus, Ohio

1. *Spring Designer's Handbook*, Harold Carlson
2. *Computer-Aided Graphics and Design*, Daniel L. Ryan
3. *Lubrication Fundamentals*, J. George Wills
4. *Solar Engineering for Domestic Buildings*, William A. Himmelman
5. *Applied Engineering Mechanics: Statics and Dynamics*, G. Boothroyd and C. Poli
6. *Centrifugal Pump Clinic*, Igor J. Karassik
7. *Computer-Aided Kinetics for Machine Design*, Daniel L. Ryan
8. *Plastics Products Design Handbook, Part A: Materials and Components; Part B: Processes and Design for Processes*, edited by Edward Miller
9. *Turbomachinery: Basic Theory and Applications*, Earl Logan, Jr.
10. *Vibrations of Shells and Plates*, Werner Soedel
11. *Flat and Corrugated Diaphragm Design Handbook*, Mario Di Giovanni
12. *Practical Stress Analysis in Engineering Design*, Alexander Blake
13. *An Introduction to the Design and Behavior of Bolted Joints*, John H. Bickford
14. *Optimal Engineering Design: Principles and Applications*, James N. Siddall
15. *Spring Manufacturing Handbook*, Harold Carlson
16. *Industrial Noise Control: Fundamentals and Applications*, edited by Lewis H. Bell
17. *Gears and Their Vibration: A Basic Approach to Understanding Gear Noise*, J. Derek Smith
18. *Chains for Power Transmission and Material Handling: Design and Applications Handbook*, American Chain Association
19. *Corrosion and Corrosion Protection Handbook*, edited by Philip A. Schweitzer
20. *Gear Drive Systems: Design and Application*, Peter Lynwander
21. *Controlling In-Plant Airborne Contaminants: Systems Design and Calculations*, John D. Constance
22. *CAD/CAM Systems Planning and Implementation*, Charles S. Knox
23. *Probabilistic Engineering Design: Principles and Applications*, James N. Siddall
24. *Traction Drives: Selection and Application*, Frederick W. Heilich III and Eugene E. Shube
25. *Finite Element Methods: An Introduction*, Ronald L. Huston and Chris E. Passerello

26 *Mechanical Fastening of Plastics An Engineering Handbook*, Brayton Lincoln, Kenneth J Gomes, and James F Braden
27 *Lubrication in Practice Second Edition*, edited by W S Robertson
28 *Principles of Automated Drafting*, Daniel L Ryan
29 *Practical Seal Design* edited by Leonard J Martini
30 *Engineering Documentation for CAD/CAM Applications*, Charles S Knox
31 *Design Dimensioning with Computer Graphics Applications*, Jerome C Lange
32 *Mechanism Analysis Simplified Graphical and Analytical Techniques*, Lyndon O Barton
33 *CAD/CAM Systems Justification, Implementation, Productivity Measurement* Edward J Preston, George W Crawford, and Mark E Coticchia
34 *Steam Plant Calculations Manual*, V Ganapathy
35 *Design Assurance for Engineers and Managers*, John A Burgess
36 *Heat Transfer Fluids and Systems for Process and Energy Applications*, Jasbir Singh
37 *Potential Flows Computer Graphic Solutions*, Robert H Kirchhoff
38 *Computer-Aided Graphics and Design Second Edition*, Daniel L Ryan
39 *Electronically Controlled Proportional Valves Selection and Application* Michael J Tonyan, edited by Tobi Goldoftas
40 *Pressure Gauge Handbook*, AMETEK, U S Gauge Division, edited by Philip W Harland
41 *Fabric Filtration for Combustion Sources Fundamentals and Basic Technology*, R P Donovan
42 *Design of Mechanical Joints*, Alexander Blake
43 *CAD/CAM Dictionary*, Edward J Preston, George W Crawford and Mark E Coticchia
44 *Machinery Adhesives for Locking, Retaining, and Sealing*, Girard S Haviland
45 *Couplings and Joints Design, Selection, and Application*, Jon R Mancuso
46 *Shaft Alignment Handbook*, John Piotrowski
47 *BASIC Programs for Steam Plant Engineers Boilers, Combustion, Fluid Flow, and Heat Transfer*, V Ganapathy
48 *Solving Mechanical Design Problems with Computer Graphics*, Jerome C Lange
49 *Plastics Gearing Selection and Application*, Clifford E Adams
50 *Clutches and Brakes Design and Selection*, William C Orthwein
51 *Transducers in Mechanical and Electronic Design*, Harry L Trietley
52 *Metallurgical Applications of Shock-Wave and High-Strain-Rate Phenomena*, edited by Lawrence E Murr, Karl P Staudhammer, and Marc A Meyers
53 *Magnesium Products Design*, Robert S Busk
54 *How to Integrate CAD/CAM Systems Management and Technology*, William D Engelke
55 *Cam Design and Manufacture Second Edition*, with cam design software for the IBM PC and compatibles, disk included, Preben W Jensen
56 *Solid-State AC Motor Controls Selection and Application*, Sylvester Campbell
57 *Fundamentals of Robotics*, David D Ardayfio
58 *Belt Selection and Application for Engineers*, edited by Wallace D Erickson
59 *Developing Three-Dimensional CAD Software with the IBM PC*, C Stan Wei
60 *Organizing Data for CIM Applications*, Charles S Knox, with contributions by Thomas C. Boos, Ross S Culverhouse, and Paul F Muchnicki

61 *Computer-Aided Simulation in Railway Dynamics*, by Rao V Dukkipati and Joseph R Amyot
62 *Fiber-Reinforced Composites Materials, Manufacturing, and Design*, P K Mallick
63 *Photoelectric Sensors and Controls Selection and Application*, Scott M Juds
64 *Finite Element Analysis with Personal Computers*, Edward R Champion, Jr and J Michael Ensminger
65 *Ultrasonics Fundamentals, Technology, Applications Second Edition, Revised and Expanded*, Dale Ensminger
66 *Applied Finite Element Modeling Practical Problem Solving for Engineers*, Jeffrey M Steele
67 *Measurement and Instrumentation in Engineering Principles and Basic Laboratory Experiments*, Francis S Tse and Ivan E Morse
68 *Centrifugal Pump Clinic Second Edition, Revised and Expanded*, Igor J Karassik
69 *Practical Stress Analysis in Engineering Design Second Edition, Revised and Expanded* Alexander Blake
70 *An Introduction to the Design and Behavior of Bolted Joints Second Edition, Revised and Expanded*, John H Bickford
71 *High Vacuum Technology A Practical Guide*, Marsbed H Hablanian
72 *Pressure Sensors Selection and Application*, Duane Tandeske
73 *Zinc Handbook Properties, Processing, and Use in Design*, Frank Porter
74 *Thermal Fatigue of Metals*, Andrzej Weronski and Tadeusz Hejwowski
75 *Classical and Modern Mechanisms for Engineers and Inventors*, Preben W Jensen
76 *Handbook of Electronic Package Design*, edited by Michael Pecht
77 *Shock-Wave and High-Strain-Rate Phenomena in Materials*, edited by Marc A Meyers, Lawrence E Murr, and Karl P Staudhammer
78 *Industrial Refrigeration Principles, Design and Applications*, P C Koelet
79 *Applied Combustion*, Eugene L Keating
80 *Engine Oils and Automotive Lubrication*, edited by Wilfried J Bartz
81 *Mechanism Analysis Simplified and Graphical Techniques, Second Edition, Revised and Expanded*, Lyndon O Barton
82 *Fundamental Fluid Mechanics for the Practicing Engineer*, James W Murdock
83 *Fiber-Reinforced Composites Materials, Manufacturing, and Design, Second Edition, Revised and Expanded*, P K Mallick
84 *Numerical Methods for Engineering Applications*, Edward R Champion, Jr
85 *Turbomachinery Basic Theory and Applications, Second Edition, Revised and Expanded*, Earl Logan, Jr
86 *Vibrations of Shells and Plates Second Edition, Revised and Expanded*, Werner Soedel
87 *Steam Plant Calculations Manual Second Edition, Revised and Expanded*, V Ganapathy
88 *Industrial Noise Control Fundamentals and Applications, Second Edition, Revised and Expanded*, Lewis H Bell and Douglas H Bell
89 *Finite Elements Their Design and Performance*, Richard H MacNeal
90 *Mechanical Properties of Polymers and Composites Second Edition, Revised and Expanded*, Lawrence E Nielsen and Robert F Landel
91 *Mechanical Wear Prediction and Prevention*, Raymond G Bayer

92. *Mechanical Power Transmission Components*, edited by David W South and Jon R. Mancuso
93 *Handbook of Turbomachinery*, edited by Earl Logan, Jr
94 *Engineering Documentation Control Practices and Procedures*, Ray E Monahan
95 *Refractory Linings Thermomechanical Design and Applications*, Charles A. Schacht
96 *Geometric Dimensioning and Tolerancing Applications and Techniques for Use in Design, Manufacturing, and Inspection*, James D. Meadows
97. *An Introduction to the Design and Behavior of Bolted Joints: Third Edition, Revised and Expanded*, John H. Bickford
98. *Shaft Alignment Handbook Second Edition, Revised and Expanded*, John Piotrowski
99. *Computer-Aided Design of Polymer-Matrix Composite Structures*, edited by Suong Van Hoa
100 *Friction Science and Technology*, Peter J. Blau
101. *Introduction to Plastics and Composites. Mechanical Properties and Engineering Applications*, Edward Miller
102. *Practical Fracture Mechanics in Design*, Alexander Blake
103. *Pump Characteristics and Applications*, Michael W Volk
104 *Optical Principles and Technology for Engineers*, James E. Stewart
105 *Optimizing the Shape of Mechanical Elements and Structures*, A A. Seireg and Jorge Rodriguez
106 *Kinematics and Dynamics of Machinery*, Vladimír Stejskal and Michael Valášek
107. *Shaft Seals for Dynamic Applications*, Les Horve
108 *Reliability-Based Mechanical Design*, edited by Thomas A Cruse
109 *Mechanical Fastening, Joining, and Assembly*, James A Speck
110 *Turbomachinery Fluid Dynamics and Heat Transfer*, edited by Chunill Hah
111. *High-Vacuum Technology. A Practical Guide, Second Edition, Revised and Expanded*, Marsbed H. Hablanian
112. *Geometric Dimensioning and Tolerancing Workbook and Answerbook*, James D. Meadows
113. *Handbook of Materials Selection for Engineering Applications*, edited by G T Murray
114. *Handbook of Thermoplastic Piping System Design*, Thomas Sixsmith and Reinhard Hanselka
115. *Practical Guide to Finite Elements. A Solid Mechanics Approach*, Steven M Lepi
116. *Applied Computational Fluid Dynamics*, edited by Vijay K. Garg
117. *Fluid Sealing Technology*, Heinz K. Muller and Bernard S. Nau
118. *Friction and Lubrication in Mechanical Design*, A. A. Seireg
119. *Influence Functions and Matrices*, Yuri A. Melnikov
120. *Mechanical Analysis of Electronic Packaging Systems*, Stephen A. McKeown
121. *Couplings and Joints Design, Selection, and Application, Second Edition, Revised and Expanded*, Jon R. Mancuso
122. *Thermodynamics: Processes and Applications*, Earl Logan, Jr.
123. *Gear Noise and Vibration*, J Derek Smith
124. *Practical Fluid Mechanics for Engineering Applications*, John J. Bloomer
125 *Handbook of Hydraulic Fluid Technology*, edited by George E. Totten
126. *Heat Exchanger Design Handbook*, T Kuppan

127 *Designing for Product Sound Quality* Richard H Lyon
128 *Probability Applications in Mechanical Design*, Franklin E Fisher and Joy R Fisher
129 *Nickel Alloys*, edited by Ulrich Heubner
130 *Rotating Machinery Vibration Problem Analysis and Troubleshooting*, Maurice L Adams Jr
131 *Formulas for Dynamic Analysis*, Ronald L Huston and C Q Liu
132 *Handbook of Machinery Dynamics*, Lynn L Faulkner and Earl Logan, Jr
133 *Rapid Prototyping Technology Selection and Application*, Kenneth G Cooper
134 *Reciprocating Machinery Dynamics Design and Analysis* Abdulla S Rangwala
135 *Maintenance Excellence Optimizing Equipment Life-Cycle Decisions*, edited by John D Campbell and Andrew K S Jardine
136 *Practical Guide to Industrial Boiler Systems*, Ralph L Vandagriff
137 *Lubrication Fundamentals Second Edition, Revised and Expanded*, D M Pirro and A A Wessol
138 *Mechanical Life Cycle Handbook Good Environmental Design and Manufacturing*, edited by Mahendra S Hundal
139 *Micromachining of Engineering Materials*, edited by Joseph McGeough
140 *Control Strategies for Dynamic Systems Design and Implementation*, John H Lumkes, Jr
141 *Practical Guide to Pressure Vessel Manufacturing*, Sunil Pullarcot
142 *Nondestructive Evaluation Theory, Techniques, and Applications*, edited by Peter J Shull
143 *Diesel Engine Engineering Thermodynamics, Dynamics, Design, and Control*, Andrei Makartchouk
144 *Handbook of Machine Tool Analysis*, Ioan D Marinescu, Constantin Ispas, and Dan Boboc
145 *Implementing Concurrent Engineering in Small Companies*, Susan Carlson Skalak
146 *Practical Guide to the Packaging of Electronics Thermal and Mechanical Design and Analysis*, Ali Jamnia
147 *Bearing Design in Machinery Engineering Tribology and Lubrication*, Avraham Harnoy
148 *Mechanical Reliability Improvement Probability and Statistics for Experimental Testing*, R E Little
149 *Industrial Boilers and Heat Recovery Steam Generators Design, Applications, and Calculations*, V Ganapathy
150 *The CAD Guidebook A Basic Manual for Understanding and Improving Computer-Aided Design*, Stephen J Schoonmaker
151 *Industrial Noise Control and Acoustics*, Randall F Barron
152 *Mechanical Properties of Engineered Materials*, Wole Soboyejo
153 *Reliability Verification, Testing, and Analysis in Engineering Design*, Gary S Wasserman
154 *Fundamental Mechanics of Fluids Third Edition*, I G Currie
155 *Intermediate Heat Transfer*, Kau-Fui Vincent Wong
156 *HVAC Water Chillers and Cooling Towers Fundamentals, Application, and Operation*, Herbert W Stanford III
157 *Gear Noise and Vibration Second Edition, Revised and Expanded*, J Derek Smith

158. *Handbook of Turbomachinery Second Edition, Revised and Expanded*, Earl Logan, Jr., and Ramendra Roy

Additional Volumes in Preparation

Progressing Cavity Pumps, Downhole Pumps, and Mudmotors, Lev Nelik

Piping and Pipeline Engineering: Design, Construction, Maintenance, Integrity, and Repair, George A. Antaki

Turbomachinery. Design and Theory, Rama S. Gorla and Aijaz Ahmed Khan

Mechanical Engineering Software

Spring Design with an IBM PC, Al Dietrich

Mechanical Design Failure Analysis: With Failure Analysis System Software for the IBM PC, David G. Ullman

Preface to the Second Edition

The original intent of this book—to serve as a reference work in turbomachinery for practicing engineers and graduate students—remains unchanged in this new edition.

In this edition the Introduction has been expanded to include new material on the mechanical and thermal design considerations for gas turbine engines. Four new chapters, written by experts in their respective subjects, have been added. The chapter on steam turbines has been completely rewritten and represents a major improvement to the book. New material has also been added to the chapter on turbomachines in rocket propulsion systems.

The original editor, Earl Logan, Jr., was joined by Ramendra Roy in the editing of this new edition. Both editors would like to express their sincere appreciation to Ms. Elizabeth Curione, the production editor at Marcel Dekker, Inc., for her help in the preparation of the manuscript.

Earl Logan, Jr.
Ramendra P. Roy

Preface to the First Edition

This book is intended as a reference work in Turbomachinery for practicing engineers and graduate students. The goal of the book is to provide rapid access to information on topics of turbomachinery that is otherwise scattered in reference texts and technical journals.

The contributors are experts in their respective fields and offer the inexperienced reader the benefit of their wide experience. The practicing engineer or student can quickly comprehend the essential principles and methods of a given area in Turbomachinery by carefully reading the appropriate chapter.

The material of this handbook comprises equations, graphs, and illustrative examples of problems that clarify the theory and demonstrate the use of basic relations in performance calculations and design. Line drawings and photographs of actual equipment are also presented to aid visual comprehension of design features.

In each chapter the authors provide an extensive list of references that have been found to be particularly useful in dealing with Turbomachinery problems in the category considered.

Earl Logan, Jr.

Contents

Contributors

Nathan G. Adams The Boeing Company, Mesa, Arizona, U.S.A.

Robert O. Bullock* Turbine Engine Division, Allied Signal Company, Phoenix, Arizona, U.S.A.

Boris Glezer Consultant, Optimized Turbine Solutions, San Diego, California, U.S.A.

L He, B.Sc., M.Sc., Ph.D. School of Engineering, University of Durham, Durham, England

Vedanth Kadambi Honeywell Engines and Systems, Phoenix, Arizona, U.S.A.

Lysbeth Lieber Honeywell Engines and Systems, Phoenix, Arizona, U.S.A.

* Deceased

Earl Logan, Jr., Ph.D.† Department of Mechanical and Aerospace Engineering, Arizona State University, Tempe, Arizona, U.S.A.

Charles MacArthur U.S. Air Force Research Laboratory, Wright-Patterson Air Force Base, Ohio, U.S.A.

David M. Mathis Honeywell Aerospace, Tempe, Arizona, U.S.A.

Thomas H. McCloskey Aptech Engineering Services, Sunnyvale, California, U.S.A.

David Mohr D&E Propulsion, Inc., Mims, Florida, U.S.A.

V. Dakshina Murty, P.E., Ph.D. Department of Mechanical Engineering, University of Portland, Portland, Oregon, U.S.A.

Harold D. Nelson Department of Mechanical and Aerospace Engineering, Arizona State University, Tempe, Arizona, U.S.A.

John N. Rajadas Department of Mechanical and Aerospace Engineering, Arizona State University East, Mesa, Arizona, U.S.A.

Warren Rice Arizona State University, Tempe, Arizona, U.S.A.

Ramendra Roy Department of Mechanical and Aerospace Engineering, Arizona State University, Tempe, Arizona, U.S.A.

William D. Siuru, Jr.‡ U.S. Air Force, Colorado Springs, Colorado, U.S.A.

Paul B. Talbert Honeywell Engines, Systems and Services, Phoenix, Arizona, U.S.A.

† Deceased

‡ Retired

1

Introduction

Earl Logan, Jr.*, and Ramendra Roy
Arizona State University, Tempe, Arizona, U.S.A.
Vedanth Kadambi
Honeywell Engines and Systems, Phoenix, Arizona, U.S.A.

Turbomachines are devices that feature the continuous flow of a fluid through one or more rotating blade rows. Energy, as work, is extracted from or transferred to the fluid by the dynamic action of the blade rows. If energy is extracted from the fluid by expanding it to a lower pressure, the devices are called *turbines* (steam, gas, or hydraulic). If energy is transferred to the fluid, thereby increasing its pressure, the devices are termed *pumps*, *compressors*, or *fans*. Stationary vanes guide the flow of fluid before and/or after the rotating blade rows.

Turbomachines can be broadly classified according to the direction of fluid flow through it. In *radial-flow* turbomachines the flow is usually toward the larger radius for pumps, compressors, or fans and radially inward for turbines. In *axial-flow* turbomachines the flow is mainly parallel to the axis of rotation of the machine so that the nominal fluid inlet and outlet radii in

* Deceased

each turbine stage is approximately the same. The Euler turbomachinery equation, which relates the work transfer between the fluid and the machine stage to the change in fluid velocity exiting the stage with respect to that entering, embodies the aforementioned characteristics. For the radial-flow turbomachines, the work transferred is determined by changes in the velocity angle as well as by changes in the radius. For the axial machines, the work transferred is determined mainly by changes in the velocity angle. The rate of energy (that is, power) transfer is the product of the torque exerted by the rotating blades on the fluid (or vice versa) and the rotor angular speed in radians per second.

A turbomachine may be without a stationary shroud (*extended* turbomachine such as aircraft and ship propeller, and wind turbine). Alternatively, it may be enclosed in a stationary casing (*enclosed* machine such as aircraft engine, steam and gas turbine for power generation, and pump).

The present chapter contains an introduction to turbomachines in two parts, each addressing a different aspect of the subject. Part 1 provides a historical background of turbomachines. Part 2 introduces the methods used in the design of gas turbines, specifically dealing with the mechanical and thermal design considerations. In addition to the introductory chapter there are 14 chapters covering various aspects of turbomachinery in this volume. Chapter 2 introduces the reader to the characteristics of the flow in turbomachinery components and the use of computational fluid dynamics in the design of compressors and turbines. Chapter 3 describes the progress made, through theory and experiment, in turbine gas-path heat transfer during the last 50 years. Chapter 4 focuses on the selection of cooling systems in gas turbines.

Chapter 5 discusses unsteady flow effects in turbomachinery. Chapter 6 presents design methods that are applied to compressors, while Chapter 7 develops design methods for turbines. The theory and design of steam turbines are elaborated in Chapter 8, and design optimization methods for turbomachinery are discussed in Chapter 9. The dynamic behavior of turbomachine rotors is detailed in Chapter 10, while Chapter 11 presents the design of turbines and pumps used in rocket propulsion systems. The methods for testing of turbomachinery components are explained in Chapter 12. Automative applications are considered in Chapter 13.

In Chapter 14, models used in the analysis and design of Tesla turbomachines are discussed. Chapter 15 treats modern hydraulic turbines.

Each chapter provides the reader with appropriate references and uses its own notation. Coordination of related material found in more than one chapter may be accomplished by the reader's use of the index.

HISTORICAL BACKGROUND

Earl Logan, Jr.

Knowledge of turbomachines has evolved slowly over centuries without the benefit of sudden and dramatic breakthroughs. Turbomachines, such as windmills and waterwheels, are centuries old. Waterwheels, which dip their vanes into moving water, were employed in ancient Egypt, China, and Assyria [1]. Waterwheels appeared in Greece in the second century B.C. and in the Roman Empire during the first century B.C. A seven-ft-diameter waterwheel at Monte Cassino was used by the Romans to grind corn at the rate of 150 kg of corn per hour, and waterwheels at Arles ground 320 kg of corn per hour [2]. The Doomsday Book, based on a survey ordered by William the Conqueror, indicates the there were 5,624 water mills in England in 1086. Besides the grinding of grain, waterwheels were used to drive water pumps and to operate machinery. Agricola (1494–1555) showed by illustrations how waterwheels were used to pump water from mines and to crush metallic ores in the 16th century [3]. In 1685 Louis XIV had 221 piston pumps installed at Marly, France, for the purpose of supplying 3,200 m^3 of Seine River water per day to the fountains of the Versailles palace. The pumps were driven by 14 waterwheels, each 12 m in diameter, that were turned by the currents of the Seine [4]. The undershot waterwheel, which had an efficiency of only 30%, was used up until the end of the 18th century. It was replaced in the 19th century by the overshot waterwheel with an efficiency of 70 to 90%. By 1850, hydraulic turbines began to replace waterwheels [1]. The first hydroelectric power plant was built in Germany in 1891 and utilized waterwheels and direct-current power generation. However, the waterwheels were soon replaced with hydraulic turbines (see Chapter 15) and alternating-current electric power [6].

Although the use of wind power in sailing vessels appeared in antiquity, the widespread use of wind power for grinding grain and pumping water was delayed until the 7th century in Persia, the 12th century in England, and the 15th century in Holland [5]. In the 17th century, Leibniz proposed using windmills and waterwheels together to pump water from mines in the Harz Mountains of Germany [4]. Dutch settlers brought Dutch mills to America in the 18th century. This led to the development of a multiblade wind turbine that was used to pump water for livestock. Wind turbines were used in Denmark in 1890 to generate electric power. Early in the 20th century American farms began to use wind turbines to drive electricity generators for charging storage batteries. These wind-electric plants were supplanted later by electricity generated by centrally located steam-electric power plants, particularly after the Rural Electric Adminis-

tration Act of 1936 [5]. Today, although a small amount of electrical power is generated by wind turbines, most electrical power is generated by large steam turbines (see Chapter 8) and gas turbines (see Part 2 of this chapter).

In the second century B.C. Hero of Alexandria invented rotors driven by steam [4] and by gas [7], but these machines produced insignificant amounts of power. During the 18th and 19th centuries the reciprocating steam engine was developed and became the predominant prime mover for manufacturing and transportation industries. In 1883 the first steam turbines were constructed by de Laval whose turbines achieved speeds of 26,000 rpm [8]. In 1884 a steam turbine, which ran at 17,000 rpm and comprised 15 wheels on the same shaft, was designed and built by Charlie Parsons. These early steam turbines are discussed in Chapter 8.

The gas turbine was conceived by John Barber in 1791, and the first gas turbine was built and tested in 1900 by Stolze [7]. Sanford Moss built a gas turbine in 1902 at Cornell University. At Brown Boveri in 1903, Armenguad and Lemale combined an axial-flow turbine and centrifugal compressor to produce a thermal efficiency of 3% [7]. In 1905 Holzwarth designed a gas turbine that utilized constant-volume combustion. This turbine was manufactured by Boveri and Thyssen until the 1930s. In 1911 the turbocharger was built and installed in diesel engines by Sulzer Brothers, and in 1918 the turbocharger was utilized to increase the power of military aircraft engines [7]. In 1939 the first combustion gas turbine was installed by Brown Boveri in Switzerland. A similar turbine was used in Swiss locomotives in 1942 [10]. The aircraft gas turbine engine (turbojet) was developed by Junkers in Germany around 1940.

References

1. R. L. Daugherty, *Hydraulic Turbines*, McGraw-Hill, New York (1920).
2. J. Gimpel, *The Medieval Machine*, Penguin, New York (1976).
3. G. Agricola (trans. by H. C. Hoover and L. H. Hoover), *De Re Metallica*, Dover, New York (1950).
4. F. Klemm, *A History of Western Technology*, Scribner, New York (1959).
5. G. L. Johnson, *Wind Energy Systems*, Prentice-Hall, New York (1945).
6. H. Thirring, *Energy for Man: Windmills to Nuclear Power*, Indiana University Press, Bloomington (1958).
7. R. T. Sawyer, *The Modern Gas Turbine*, Prentice-Hall, New York (1945).
8. A. Stodola, *Gas Turbines Vol. 1*, McGraw-Hill, New York (1927).
9. G. G. Smith, *Gas Turbines and Jet Propulsion for Aircraft*, Atmosphere, New York (1944).
10. C. Seippel, "Gas Turbines in Our Century," *Trans. of the ASME, 75*: 121–122 (1953).

MECHANICAL AND THERMAL DESIGN CONSIDERATIONS FOR GAS TURBINE ENGINES

Vedanth Kadambi

This section deals with the fundamentals of mechanical and thermal design of gas turbine engines. It lays particular emphasis on the turbine, though many of the statements are general and apply to compressor design as well. Starting from a description of thermodynamic and practical cycles used in gas turbine applications, it deals with the types of engines and their applications, the approach to design (including aerodynamic, secondary flow, thermal and stress analysis), material selection for various applications, and mechanical design considerations (turbine disk and blade design, the secondary flow circuit, and prediction of fatigue life). Finally, tests for design validation and some of the near-term developments that will improve overall performance and life are discussed.

Mechanical and Thermal Design Considerations—An Overview

The gas turbine industry is often considered as mature since new large-scale developments are few and the design process is considered to be well established. In spite of this, the mechanical/thermal design of a gas turbine is a highly complex endeavor, costing hundreds of millions of dollars and employing a team of several hundred engineers for several years. During design, advances are made through increasing levels of sophistication and detailed analyses. A full discussion of each of the design topics would easily fill a volume. A brief presentation will be given here to serve merely as an overview of the considerations involved in the mechanical design of a turbine. The topics to be discussed are (1) the gas turbine cycle, engine components, and the areas of applications of gas turbines, and (2) performance, material selection, durability, and life. The factors involved in the aerodynamic, mechanical, and thermal designs, secondary flow, stress and vibration analyses, life evaluation, etc. will be considered as well. Tests used to evaluate the performance and durability of the engine conclude the design phase. A discussion of the directions for future work to improve performance as well as life will be provided at the end. The reader should leave the chapter with a global sense of what topics the design engineer must address. For further details, individual topics should be studied in greater depth from the cited chapters in this book and literature or from comprehensive texts on specific topics.

The Thermodynamic Cycle

The thermodynamic cycle for the gas turbine engine is the Brayton cycle, which consists of four theoretical processes. The first process is one of isentropic compression where the pressure of the air drawn from the atmosphere is raised to the operating level in a compressor. This constitutes the work input part of the cycle. The second is the thermal energy input in a combustor—an isobaric (constant-pressure) process to raise the temperature of the air to the highest level permitted in the engine. The third and fourth processes are, respectively, an isentropic expansion (work output) in the turbine and an isobaric cooling process (energy rejection to the atmosphere), to complete the cycle. The ideal thermal efficiency of the cycle is given by the expression [1, 2]

$$\eta_B = 1 - [1/P_r]^{(\gamma-1)/\gamma} \tag{1}$$

It is seen that the thermal efficiency of the Brayton cycle is the same as that of the Carnot cycle with the same isentropic compression ratio. Nevertheless, its thermal efficiency for operation between the same temperature limits is lower than that of the Carnot cycle. The efficiency increases as the pressure ratio increases. For this reason, efforts are made to operate the engine at as high a pressure ratio as possible.

The work output of the theoretical Brayton cycle is a function of the maximum temperature in the cycle, the temperature of energy rejection, and the pressure ratio. There exists an optimum pressure ratio at which the work output becomes a maximum. The pressure ratio for maximum work output is given by the expression

$$(P_r)\text{opt} = (T_3/T_1)^{\gamma/[2(\gamma-1)]} = (P_r)^{1/2} \tag{2}$$

The corresponding maximum work output of the Brayton cycle is

$$W_{\max} = C_p T_1 \left[(T_3/T_1)^{1/2} - 1\right]^2 \tag{3}$$

Engines may be designed to operate close to this condition. The thermal efficiency of the Brayton cycle operating at the optimum pressure ratio is

$$(\eta_B)\text{opt} = 1 - (T_1/T_3)^{1/2} \tag{4}$$

Components of the Gas Turbine Engine

Figure 1 shows the main components of the gas turbine engine—the compressor, the combustor, and the turbine. Work input occurs in a

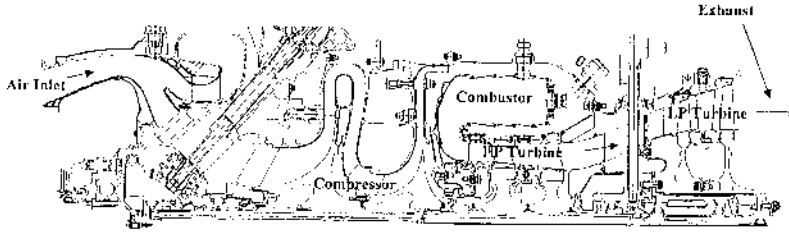

Figure 1 Cross-section showing the main components of a gas turbine engine.

compressor with several axial and/or centrifugal stages. The engine shown in Fig. 1 has only centrifugal compressors. (Figure 8 shows an engine with axial and centrifugal stages for compression.) The pressure ratio in commercial aircraft engine compressors is often in the range of 10–25, though some experimental engines have pressure ratios in the range 17–35. The turbine driving the compressor is usually an axial-flow device though in small engines (auxiliary power units, or APUs), it is often a radial inward flow device. Energy addition as heat and a slight pressure drop (3–5%) occur in a combustor where a fine spray of fuel burns in the air from the compressor. The maximum temperature of the gas is limited by material considerations, being 2200–2500 °F in most engines. The mixture of burned fuel and air at a high temperature enters the turbine. Work output is due to the expansion of the gas while flowing over the rotating turbine blades. Thermal energy rejection from the engine, as in all practical propulsion engine cycles, occurs due to the gas that is exhausted from the turbine to the atmosphere. There is no heat exchanger to reject thermal energy at constant pressure from the system.

In aircraft engines, the air flowing through a propeller or a fan driven by the turbine gives rise to the propulsive force on the aircraft. For example, in propeller-driven engines, the change in momentum of the air flowing through the propeller causes a reactive force, resulting in a forward thrust on the engine. In engines with fans, the reactive force is due to the exhaust jet at the exit of the turbine. Power generation units use the turbine output to drive a gearbox or a load compressor.

Real Gas Engine Cycle

The real engine cycle differs from the theoretical Brayton cycle in several respects. First, the processes of compression and expansion are not isentropic. So the work input needed at the compressor is higher than in

the theoretical cycle and the work output of the turbine is lower than in the theoretical cycle. (In most gas turbines used for propulsion, the adiabatic compressor efficiency ranges from 0.83 to 0.88. In turbines the adiabatic efficiency ranges from 0.85 to 0.92.) In addition, there are pressure losses associated with flow through the combustor and several other parts of the machine. These as well as other deviations from ideality reduce the net work output and the thermal efficiency as compared with that of the theoretical Brayton cycle. For engines with a pressure ratio in the range of 13–15, the typical thermal efficiency for operation at 2000 °F is about 35%. A measure of thermal efficiency is the specific fuel consumption, SFC, which is the rate of fuel consumed (lbm/hr) per unit of output. For efficient operation, it is necessary to have as low a fuel consumption and, hence, as low an SFC as possible. Reduction in SFC may require an increased inlet temperature or the use of a recuperator (a heat exchanger inserted between the compressor and the combustor). The recuperator transfers part of the thermal energy of the exhaust gases to the high-pressure air entering the combustor and reduces the fuel consumption. The engine cycle that uses a recuperator is called the regenerative Brayton cycle [2]. The thermal efficiency of the ideal regenerative cycle fitted with a recuperator where there are no pressure drops is given by the expression

$$\eta_R = 1 - (P_r)^{(\gamma-1)/\gamma}/T_r \tag{5}$$

Unlike the ideal Brayton cycle without regeneration, the thermal efficiency of this cycle diminishes with increasing pressure ratio. However, it increases with increasing temperature ratio as in the Carnot cycle.

Gas Turbine Engine Applications

The following are the areas of use of gas turbines:

1. Propulsion of aircraft as well as ground-based vehicles. There exist four types of gas turbine engines: the "turboprop," the "turbofan," the "turbojet," and the "turboshaft," based on their use in propulsion. The first three are designed for use where thrust is important. The turboprop uses a propeller to move large masses of air and has a low specific thrust. It operates at relatively low Mach numbers, usually on the order of 0.25. (There are some engines that run at higher Mach numbers, on the order of 0.6.) Figure 2 exhibits a typical turboprop engine manufactured by Honeywell Engines & Systems. Turboprops usually range in power between 600 and 6000 HP. Turboprops used in both commercial and military applications are relatively small compared with turbofans, which employ high-speed fans to move the air.

The turbofan requires large masses of air flow, though only a fraction,

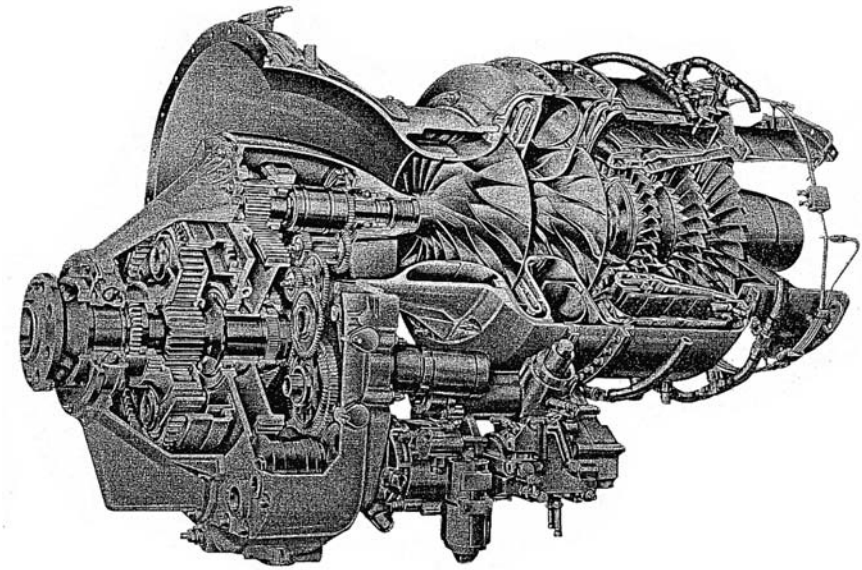

Figure 2 Turboprop engine, TPE 331-10U (Honeywell Engines & Systems).

between 15–35%, flows through the turbine. The rest of the flow passing through the fan expands in an annular nozzle to provide thrust. It operates at higher Mach numbers, 0.5–0.8. The turbofans produced by Honeywell Engines & Systems have thrusts in the range 1,300 lbf to 9,000 lbf, a typical engine being shown in Fig. 3. Such engines are used in executive jets, commercial aircraft, and military applications. Pratt & Whitney, General Electric, and Rolls Royce Plc typically produce engines with thrusts ranging to 20,000 lbf. The biggest turbofans manufactured have thrusts ranging to 100,000 lbf. For turbofans, SFC is expressed as the rate of fuel consumption per unit of engine thrust (lbm/lbf.hr). Typical values of thrust SFC range between 0.35 and 0.6 lbm/lbf.hr depending on the type of engine and its operating condition. The turbojet has a relatively low mass flow compared with turbofans. Its thrust is due to the acceleration of the fluid expanding in a nozzle at the exit of the turbine. Hence, it has a high specific thrust.

Turboshaft engines are employed in applications where it is necessary to deliver power to a low-speed shaft through a gearbox. They are used for commercial, military, rotorcraft, industrial, and marine applications and range in power from 400 to 4,600 HP. For turboshafts, SFC is expressed in flow rate per HP of output, typical values being in the range of 0.3–0.5 lbm/

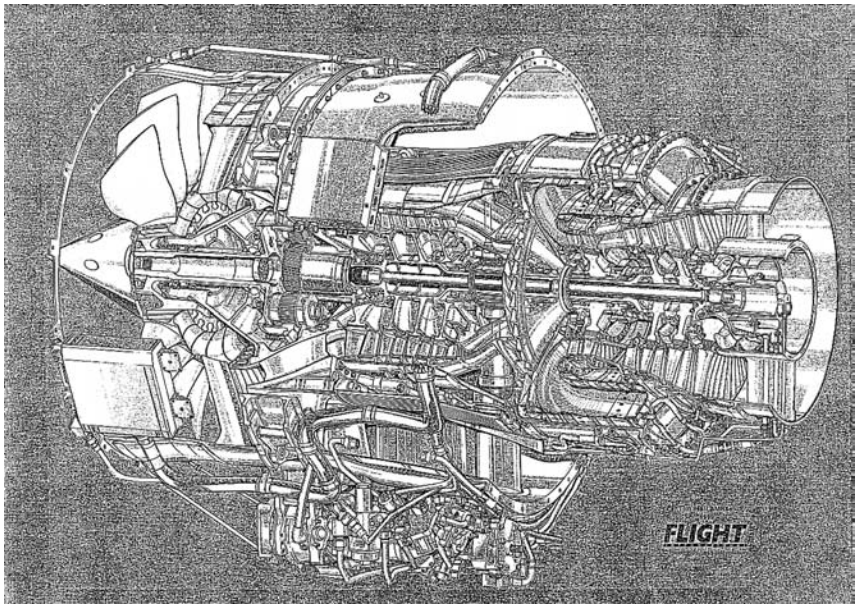

Figure 3 Turbofan engine, TFE731-60 (Honeywell Engines & Systems).

HP.hr. The U.S. army's main battle tank, Abrams M1A1, is propelled by the AGT1500 turboshaft engine, rated at 1,500 HP. It is fitted with a recuperator and operates on the regenerative Brayton cycle. Here, the wheels are directly driven through a speed-reduction gear train to reduce the rotational speed from about 22,000 rpm (power turbine) to 3,000 rpm at the wheels. A new recuperated turboshaft engine, LV100, is currently in design at Honeywell Engines and GE Aeroengines to drive future Abrams and Crusader battle tanks.

2. Auxiliary power units (APUs), Fig. 4. These are small engines (100–1,100 HP) used for air conditioning and lighting purposes in regional, executive, narrow, and wide-body commercial as well as military aircraft. They are also used to propel ground carts. As opposed to turbofan and turboprop engines that have axial compressor and axial turbine stages, these may have only centrifugal compressors and radial inflow turbines.

3. Marine applications. These include Fast Ferry transport engines, Ocean Patrol, and Hovercraft.

4. Industrial turbo-generators. These may range from small engines producing only 75 kW to 20 MW or more for power production.

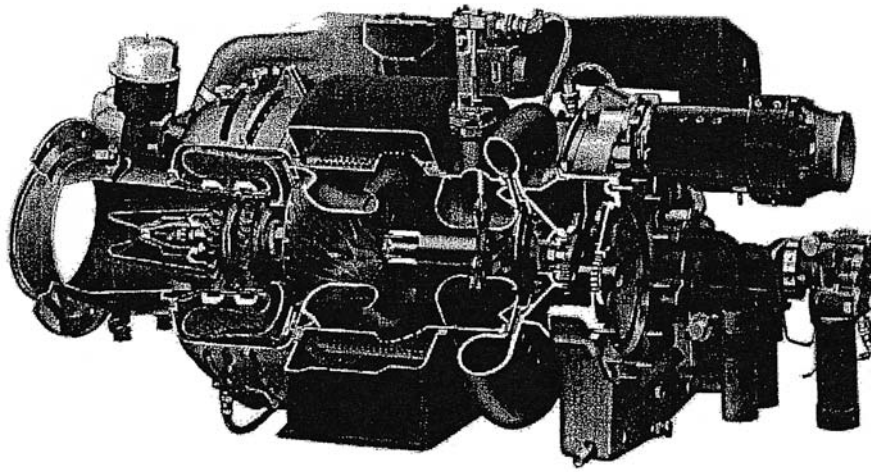

Figure 4 Auxiliary power unit, APU131-9 (Honeywell Engines & Systems).

"Microturbines," which are small industrial turbogenerators used for lighting and other applications in small buildings, workshops, and shopping complexes are produced by Honeywell Engines & Systems as well as a few others. General Electric Co. manufactures gas turbines for large power production. Siemens Westinghouse Power Corporation has built large engines with outputs in the range of 30–100 MW. In addition, the company has built some engines as large as 300 MW or more in power output.

Design Goals

Overview. In a broad sense, the design goal is to comply with all of the customer's specifications while minimizing cost. The customer specifies the minimum standards for performance (power output or thrust, fuel consumption or thermal efficiency), the maximum permissible weight, and the expected life or durability of the engine. Durability is usually specified in terms of the number of cycles of operation or the number of flight hours that the engine will experience during its expected life. Regulatory agencies impose environmental requirements relating to noise levels in aircraft applications and the permitted maximum levels of emissions (oxides of nitrogen, sulfur, etc). The importance of these individual requirements varies from application to application, as shown in Fig. 5. The regions indicated with light gray shade in the diagram are of high importance for each application. For example, in the design of commercial propulsion

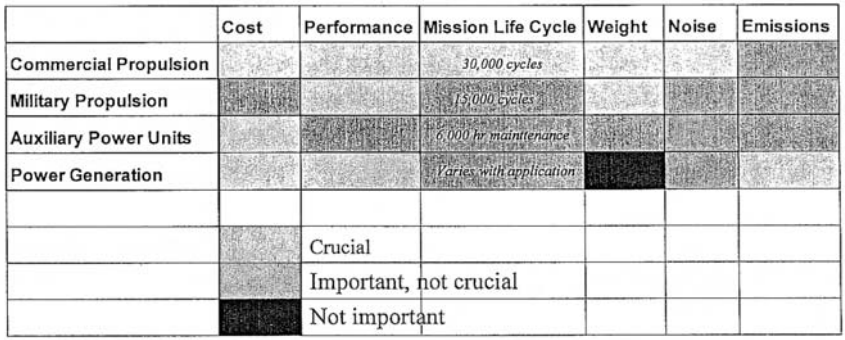

Figure 5 Design goals and their dependence on application.

engines, cost, performance, durability (expressed in mission life cycles), weight, and engine noise levels are important items to be considered. For military applications, the important items are performance and weight. The regions with medium-dark shading are of intermediate importance, while regions with dark shading indicate items of little concern. As seen from the diagram, cost is of great concern in most applications. In military applications, cost and long life are sometimes not as important as the achievement of very high levels of performance.

Since APUs have relatively small outputs and are not in continuous use, performance may not be a major consideration in their design. In all other engines, performance plays an important role. The main factors affecting performance are (1) thermodynamic cycle (maximum operating pressure, turbine inlet temperature, and ambient conditions), (2) aerodynamic efficiencies of the compressor and turbine vanes and blades (depend on airfoil loads, flow path losses, etc.), (3) losses in the combustor due to incomplete combustion, (4) losses due to installation effects, tip clearances, etc., (5) losses due to secondary flow, and (6) thermal energy losses from the turbine case to the surroundings. Of these, thermal losses are not highly significant, so that the engine is treated as an adiabatic device in most calculations.

Durability. The mechanical and thermal design of turbine components focuses on providing the least expensive unit to satisfy performance objectives without failure. Under normal operating conditions, the common failure modes of concern to the designer are low cycle fatigue, high cycle fatigue, creep, mechanical distortion, oxidation, corrosion, and erosion. For short-duration emergency conditions, one must also avoid overtemperature and overstress failures caused by speed and temperature excursions beyond the normal operating levels. Based on a study of a large number of engines, the USAF has identified the primary causes of engine failures, shown in Fig. 6.

Predicting a safe life limit requires an understanding of how the turbine is being used. The customer specifies the operating conditions and the number of cycles as well as the type of operation expected of the engine. As previously seen in Fig. 5, the operating life changes from application to application and varies with the number of cycles of operation as well as other factors. It is critical, therefore, to understand the customer's requirements before starting the design of the turbine. To illustrate this point, two types of representative operating cycles are exhibited in Figs. 7(a) and 7(b). Figure 7 (a) portrays the schematic of an operating cycle that may apply to commercial aircraft operation. Here, the engine starts at ground idle conditions and then accelerates to take-off (100% power). Usually, the speed drops about 15–20% as the aircraft reaches its cruising altitude. From here onwards, there may be only small changes in speed and turbine-inlet

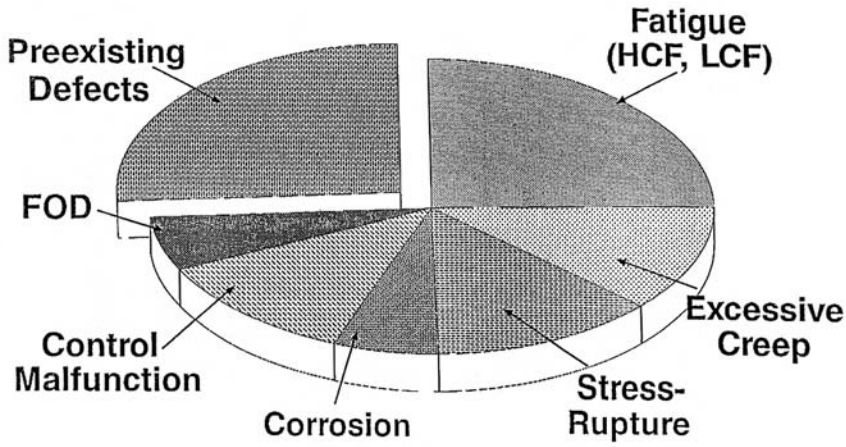

Figure 6 U.S. Air Force study of causes of engine failure.

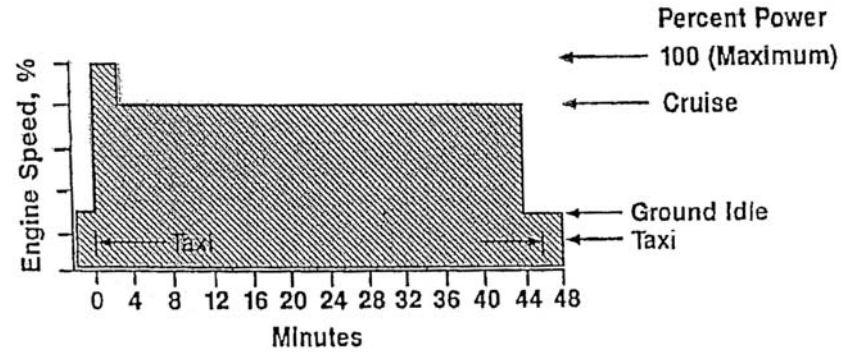

Figure 7(a) Schematic operating cycle for long-range commercial flights.

temperature for a long time, after which a quick drop in speed to idle occurs during landing. The complete operation from start to finish constitutes one mission cycle. Major variations in speed and output occur only a few times during the entire operation and only small speed changes occur during the major part of the flight. The associated temperature changes and thermal cycling during flight are thus small. Hence, the materials of the engine are not continuously subjected to cyclic temperature changes that cause thermal fatigue. Figure 7(b), on the other hand, represents an operating cycle with cyclic and sudden large variations in speed. Often, the operating conditions for a military trainer aircraft or a tank engine resemble this cycle. The initial part of the operation resembles that of Fig. 7(a) until cruising speed is reached. From here onwards, there are several cycles of rapid speed increase and decrease, so that the local material temperatures fluctuate considerably

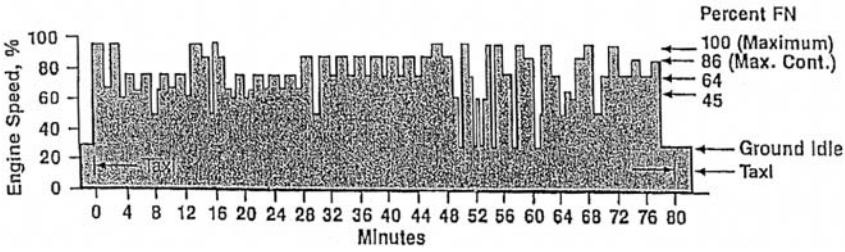

Figure 7(b) Schematic operating cycle with large speed variations.

with time during flight. Such a type of operation may result in failures due to low cycle fatigue discussed below.

Two of the main causes of failure seen in Fig. 6 are fatigue and preexisting defects, each accounting for 25% of the total. Fatigue can be of two types, low cycle fatigue (LCF) and high cycle fatigue (HCF). Low cycle fatigue occurs with the repeated stressing of a component until cracks initiate and then propagate to failure. The type of stress depends of course on the part. For example, a cooled turbine blade experiences centrifugal stresses from spool rotation, thermal stresses from temperature gradients within the blade, and stresses due to varying aerodynamic pressure distribution. An engine that undergoes many cyclic excursions in a flight, such as the application portrayed in Fig. 7(b) above, should be designed to resist LCF well. Cracks may occur in a part not only from LCF initiation, but also from preexisting defects. High cycle fatigue results from vibration at speeds close to resonance in one of the components, e.g., blades. Such stresses alternate around a mean value and are purely mechanical. They are caused by a forcing function driving the component at a frequency matching a natural frequency of the part. The forcing function could, for example, be an imbalance, or a pressure pulse. The wakes of a vane causing pressure fluctuations on the downstream rotating blade are an example of a pressure pulse. Also, a part can undergo flutter—a vibration phenomenon in which the displacement of a part due to aerodynamic loading causes a change in the load, which in turn allows the displacement to relax to its original form at which point the load starts again. Although the alternating stresses may be much lower than the background stress, the frequencies are high and a large number of cycles can be accumulated quickly. A Goodman diagram (Fig. 16; see section on thermal/stress analysis and life prediction) or one of its variants is used to assess if the combined alternating and steady-state stress levels are acceptable.

Preexisting defects are often due to small amounts of foreign material or imperfections in the disk or any other component. These imperfections act as areas of stress concentration and cause failures even when the average stress is well below the yield limit in most areas. Sometimes, small cracks exist, especially in large castings. These, too, cause local high stresses that may lead to failure. Life prediction is then a matter of calculating how rapidly such a flaw will grow until the part fails. To guard against preexisting defects, X-ray pictures may be taken to determine whether internal flaws or cracks exist in large specimens. Ultrasound and other techniques are also used. If judged as serious, parts with flaws are discarded.

Excessive creep and stress-rupture are the third and fourth major causes, each accounting for approximately 12.5% of all failures. *Creep* refers

to the continuous extension of a highly stressed material subjected to elevated temperatures for long periods of time. Creep is a function of material properties, the level of stress, the temperature, and its duration. Depending on the part, the normal design philosophy is to limit the average stress to a level such that the strain due to creep is below 1% to 2% over the expected life of the component. *Stress-rupture* [3] is the ultimate failure of a part due to creep. Different materials will undergo different amounts of creep elongation before rupture. Stress-rupture may occur with almost no noticeable creep or with considerable elongation depending on the material, the stress, and the temperature. Blades and blade roots or attachments at the disk are subject to stress-rupture. Improper design procedure and nonisotropic material properties have often been responsible for these failures. It is necessary to have a good knowledge of all the expected stresses (thermal and mechanical) and material properties if such failures are to be avoided.

Factors that are somewhat difficult to control are (1) corrosion and erosion resulting in damage to parts along the flow path, especially the leading edges of vanes and blades, (2) damage due to foreign objects like birds hitting fan or compressor blades during flight, and (3) control malfunction. Unfortunately, the effects of corrosion depend strongly on the pollutants in the atmosphere as well as on the fuel, which may contain sulfur or compounds of alkaline materials. These are hard to control and may require surface coatings that prevent contact between the hot gases and the surface (see discussion at the end of section on thermal/stress analysis and life prediction). The impact of foreign objects like birds, tire treads, gravel, and ice or hail on fan blades and the immediately following compressor stages can be severe. It is necessary to ensure that the engine can withstand such types of impact without failure. (See discussion related to bird ingestion or foreign object damage tests near the end of this chapter.) To reduce the probability of control malfunction, it is necessary to build a certain amount of redundancy in the system, so that if one of the controls fails for some reason, there is another control that will perform the required operation. Experience is the guide in determining the degree of redundancy necessary to minimize the probability of failure.

Thermal and Mechanical Design Approach

The design of a gas turbine consists of four main phases. In the first, a marketing study determines the need of the customer for a proposed engine and a conceptual study is performed to assess the feasibility that an engine can profitably be designed and developed to satisfy this need. The second is the preliminary design phase. In preliminary design, projections from

experience and existing similar designs are used to lay out the flow path, the velocity triangles at the compressor and the turbine stages and to make initial drawings of the proposed engine. The materials needed for various components are also picked on a preliminary basis. The choice of materials is based on experience and expected conditions of operation. These choices are subject to change based on the detailed analyses (thermal and stress) that occur later. Finally, first estimates of performance and secondary flow are obtained. Each company will have different criteria regarding the level of detail required before one can exit the preliminary design phase and enter the third phase, detailed design. The detailed design will perform all detailed analyses and life predictions to exit with completed component drawings. Each phase will have design reviews to ensure that the design is ready to proceed to the next level. In the fourth phase, the parts are procured, an engine is built, and qualification tests are performed. This phase is complete with certification by the regulatory agencies.

During design it is necessary to optimize the performance, the choice of materials, and the proposed manufacturing methods to satisfy life requirements and at the same time to minimize the cost. Thus, design is based on compromises affecting materials, manufacturing methods (casting as opposed to forging, welding as opposed to brazing, etc.), the levels of secondary flow, and operating temperatures. Itemized below are the main items for consideration in design.

1. Material selection and types of materials used: Different materials are used for different components of the engine, depending on the temperatures, stress levels, and expected service lives. Inexpensive and light materials are used for the front casing around the fan and the first few axial compressor stages not subjected to high temperatures. More expensive and structurally strong highly temperature-resistant materials are used in the rotating parts of the turbine. Table 1 is a partial list of the types of materials used and Table 2 lists the considerations for material selection. Many parts

Table 1 Typical Materials Used in Propulsion Gas Turbines

Component type	Fan	Compressor	Turbine
Rotating, components	Titanium Aluminum	Titanium Steel Aluminum	Nickel-based alloys
Static components	Titanium Steel	Steel Titanium Aluminum Magnesium alloy	Nickel-based alloys Cobalt-based alloys Steel

Table 2 Materials Selection Criteria

Failure modes	Cost	Manufacturing process or mode of fabrication	Weight	Others
Strength at high temperature	Material cost	Casting	Density	Containment (ductility, strength)
Low-cycle fatigue strength	Fabrication cost	Hardness and ease of machining	Strength/ weight	Thermal expansion
High-cycle fatigue strength	Vendor availability	Forging	—	Thermal conductivity
Creep strength	—	Repairability	—	Specific heat
Fast fracture, cyclic crack growth rate	—	Availability	—	—
Corrosion resistance	—	Consistency, cleanliness of product	—	—

of the turbine are made of alloys of nickel, those used commonly being Hastalloy, Inconel, and Waspalloy for compressor/turbine casings, shafts, and other areas. Blades and vanes are routinely made of single-crystal, directionally solidified, or equi-axed alloys of various compositions. Waspalloy or Inconel may be used also to make seal plates for turbine discs. In some experimental engines, turbine discs and some seal plates are made of sintered alloys of nickel. Some of them are capable of withstanding extremely high temperatures, running as high as 1,450 °F.

2. Aerodynamic design: This involves the definition of the airfoil contours, both of the compressor and of the turbine stages. The design starts with the velocity triangles laid out during preliminary design. The blade angles should match the inlet and exit angles specified by the velocity triangles. The contour of the blade is then designed to provide a smooth flow and to ensure that there is little separation at all points on the blade. Proper turning of flow over the blade and the contour design ensure that blade loading is as desired. Usually, HPT blades turn out to be somewhat thicker at the leading edge than LPT blades. In addition, they do not exhibit large radial twists. The design of compressor airfoils (refer to Chapter 6) is different from that of turbine airfoils (refer to Chapter 7). This is due to the

adverse pressure gradient against which the fluid has to move in a compressor. The adverse pressure gradient tends to cause flow separation and high levels of aerodynamic losses unless the turning angles of the blades are quite low. In the turbine blade where the pressure gradient is favorable, the flow can be turned through large angles (120°–130°), without fear of separation. Large amounts of work output can be obtained with just one or two stages in the turbine, while to compress the air through the same pressure ratio, several axial stages (each with a small pressure ratio) may be needed. For this reason, it is the common practice in several companies to use centrifugal stages that permit larger pressure ratios per stage than axial compressors. In addition, they are more durable than axial stages. It should, however, be remembered that centrifugal impellers are of large diameter and permit lower mass flow in relation to their size than axial stages and hence add considerably to the engine weight.

3. Secondary air-flow design: The search for higher and higher thermal efficiencies has led to ever-increasing temperatures at the turbine inlet, on the order of 2,600 °F in modern propulsion engines. In several military engines and in some experimental engines, this temperature is higher by several hundred degrees. The gas emerging from the combustor has both circumferentially and radially varying temperatures, the maximum of which may be 20–40% higher than the average temperature. The materials subjected to these temperatures may suffer serious deterioration in mechanical properties (yield stress, ultimate stress, fatigue limit, etc.). In addition, operation at high transient temperatures leads to thermal stresses and fatigue. It is therefore necessary to maintain metal temperatures low enough so that property deterioration and thermal fatigue do not significantly affect the life of the component. To this end, relatively cool air at the required pressure is channeled to the component where cooling is needed. Most of the cooling air is usually drawn from the plenum around the combustor (see Fig. 1), referred to as Station 3. Other lower-pressure sources such as impeller blade exit (Station 2.7) and the entry to the centrifugal compressor (Station 2.5) are employed in addition to Station 3. In some engines, for cooling shrouds and areas of low pressures, air may be drawn from still-lower pressure sources (e.g., the fan exit or an intermediate axial stage). In modern turbines, the total secondary flow may range from 8% to 22% or more of the total core flow. The cooling requirements of the HPT nozzle and blade, the HPT disk, and purge air for HPT cavities constitute a major fraction of the air drawn from the combustor plenum. Some of it may be used for thrust balancing, and sometimes to cool the LPT disk and blade as well. Air for LPT cooling and seal buffer often comes from sources such as the inlet to the impeller or an axial compressor stage. Secondary flow design therefore initially requires a decision on the

appropriate source for each of the cooling circuits, since the air drawn off the compressor does not flow over all the turbine blades. There is a greater deterioration in turbine output due to air drawn from high-pressure stages as compared with air drawn from low-pressure stages. So, every effort should be made to draw air at the lowest possible pressure to provide the required cooling effect. After these decisions are made, it is necessary to calculate the pressure drops, the clearances at labyrinth and other seals, and the sizes of orifices needed to meter the flow in each circuit.

Secondary air serves the following main purposes in the turbine.

a. Provide cooling air to critical temperature-limited components. This is indeed the main purpose of secondary flow design. The provision of cavity purge flow (to prevent hot gas ingestion) may be included in the same category, as it ensures that the disk cavities are maintained at sufficiently low temperatures for long life. Figure 8 depicts a typical turbofan engine of a low thrust class along with its secondary flow circuit, which draws air from several sources. At the front of the engine is the fan, which is a compressor stage of small pressure ratio (not shown in Fig. 8). The fan is followed by four axial compressor stages and a centrifugal stage. The first turbine stage (high-pressure turbine, HPT) drives the centrifugal compressor. The low-pressure stages of the axial compressor (low-pressure compressor, LPC), are driven by the low-pressure turbine (LPT), which may consist of two or more stages. The main secondary flow stream is drawn from the combustor plenum to cool the liner of the combustion chamber, the first HPT nozzle,

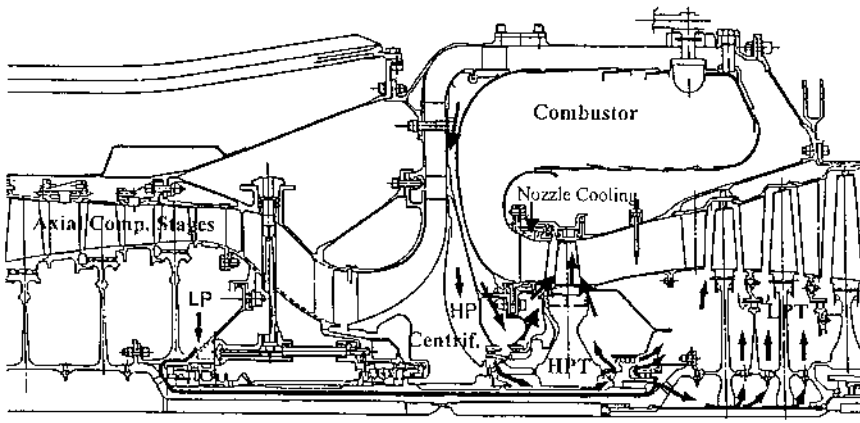

Figure 8 Cross-section of a typical turbofan engine indicating secondary flow streams.

and its attachments. A substantial fraction of the flow passes through the TOBI (tangential on-board injector). This may be a set of nozzles or an appropriately drilled set of holes designed to increase the tangential velocity of the air. The air emerging from the TOBI has a low static temperature and a tangential velocity that approximates that of the rotating disk. Hence, it cools the turbine disk and the blade and purges the HP turbine cavities as well. The second stream drawn from the impeller exit (marked HP in the diagram) flows down the back face of the impeller. It may be used to cool the bore of the turbine and for bearing cooling purposes where possible. In the illustration, it is used partly to cool the first LPT disc. Still another stream drawn from the impeller inlet flows axially through the impeller bore to purge the second and the third LPT disk cavities.

b. Provide buffer air to bearing seals. This is the second important purpose of secondary flow design. It is necessary to provide a sufficient pressure difference between bearing seal faces so that oil leakage is minimized. The air used for buffering should be at temperatures not higher than 400 °F since the oil coming in contact with the air tends to coke and form hard deposits if its temperature becomes excessive.

c. Maintain bearing thrust loads at low levels/thrust balance. The thrust on the turbine disk due to aerodynamic and other loads acts on the shaft bearing. The bearing should be designed to withstand the thrust so that the shaft is held in place. The larger the bearing load, the bigger and more expensive the bearing becomes. By using a thrust piston arrangement, secondary air at the appropriate pressure is made to exert a force on the disk to reduce the net thrust on the bearing. Thrust load calculation is a detailed bookkeeping effort to account for all the aerodynamic forces, momentum changes, and pressure forces acting on the surfaces of a control volume. Since the calculations involve differences between large numbers of similar magnitudes, there is a considerable amount of uncertainty in the estimated net thrust. It may therefore be necessary to design the bearing to withstand a larger-than-calculated load. In some cases, the calculations may lead to a very small estimate for the thrust load. Then, secondary flow may be used to ensure that the load acts in only one direction and does not reverse due to changing operating conditions. It is a good practice to check the thrust on the bearing at several operating conditions, say full power, 50% power, and idle conditions, to ensure that there is no thrust reversal in the operating range. Secondary flows have also been used to reduce the loads and thus the stresses acting on nozzles and such other components in some experimental engines. (For details regarding secondary flow design, see the chapter by Bruce Johnson.)

d. Cooled and uncooled airfoil design. Airfoils may be cooled or uncooled depending on the temperature of the gas and the material of the

airfoil. The uncooled airfoil operates at relatively low temperatures, is simpler to design, and can employ standard materials. It has a low cost, though its growth potential is limited to simple material substitutions. It is easier to manufacture and is tolerant to some manufacturing deviations. While it is possible to obtain lower temperatures with a cooled design and thus ensure a long life even with high gas temperatures, the design is more complex and takes longer to complete. The manufacturing processes are very complicated and are less tolerant to deviations. The cost of the airfoil is much higher. Nevertheless, the design provides greater flexibility and future growth potential. In addition, with the current levels of turbine inlet temperatures, it is impossible to find a material that can satisfy the cyclic life requirements with no cooling and, hence, it is quite justifiable to incur the extra cost and effort to design a cooled airfoil.

A significant fraction of the secondary flow is used for turbine airfoil cooling. The maximum operating temperature for the airfoil depends on the material used and may be as high as 1,900 °F. The cooling flow enters the passages in the blade root and passes through narrow channels in the interior of the airfoil I (see cross section, Fig. 10), designed to suit the airfoil size and shape. In turbines operating at high temperatures, even with the best heat-transfer augmentation techniques, internal convection alone cannot maintain airfoil temperatures below 1,800–1,900 °F. It is then necessary to provide a film of cool fluid on the outer surface to reduce contact between the hot gases and the metal. This film is obtained by ejecting part of the cooling air through film-holes at critical locations where high metal temperatures are expected. If shower-head film cooling is used, a fraction of the cooling flow exits through film-holes at the airfoil leading edge. Some film-holes may also be provided on the pressure and the suction surfaces. Another fraction exits at the trailing edge and a small amount may be ejected at the blade tip through nearly radial holes. The film-holes keep the leading-edge and the near-stagnation regions of the pressure and suction surfaces cool, while the air ejected along the trailing edge cools the rest of the these surfaces. Figure 9 shows a cooled blade with showerhead and pressure surface film-holes used in turbines.

Having defined the airfoil surface (the outer shape of the blade where it is exposed to gas), the next step is the cooling passage design to maintain the blade surface at temperatures commensurate with its material properties and expected life. Due to material property limitations, this temperature does not exceed 1,800–1,900°F in most designs. The cooling passages are often serpentine and may have trip-strips or fins in them for heat-transfer enhancement. Further, where shower head cooling holes are required, the cooling air is made to impinge on the inner surface of the leading edge

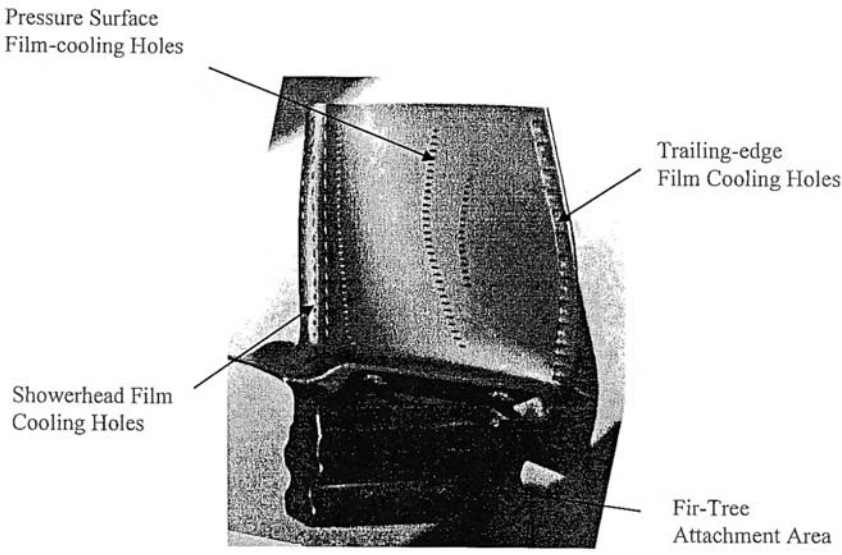

Figure 9 Typical high-pressure turbine blade with shower head and film-cooling holes.

before emerging at the surface. All these features are indicated in Fig. 10, which shows a schematic diagram of the airfoil internal passages.

The parameters affecting cooled blade design are (1) blade material characteristics and cost, (2) airfoil shape, (3) required cooling flow and the trailing-edge thickness, (4) allowable stress levels, (5) number of blades, and (6) vibratory environment. Minimizing the cooling air required for the airfoil is an important consideration in design. Cooling air flow (ejected at film-holes, trailing edge, etc.) and blade rotation generally affect (1) the aerodynamics of the blade and the overall efficiency of the system, (2) impingement heat transfer at the leading edge, and (3) the local heat transfer behind trip-strips and fins. In addition, blade-tip thickness and streamlines at the trailing edge are affected by the cooling flow issuing at the trailing edge. (For new designs, it may be necessary to use experience and extrapolate beyond the range of available data.) At present, CFD analysis does not provide accurate predictions of heat transfer and pressure drops in cooling passages with complicated internal geometry, especially where rotation is involved. Further, for complicated situations, considerable expertise and effort are needed to obtain solutions by using CFD. Hence, it is difficult to use CFD as a design tool. Improvements in CFD techniques

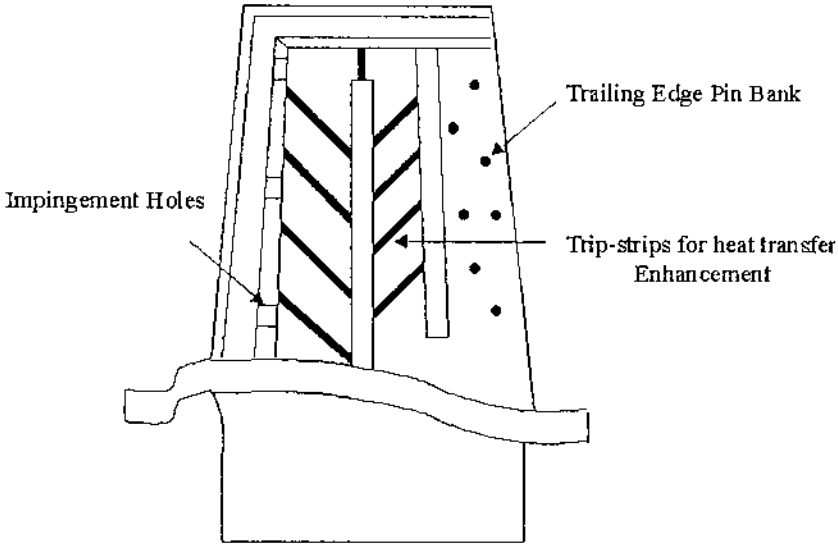

Figure 10 Schematic diagram of the interior of an airfoil with cooling passages.

and a multidisciplinary computational approach (see Chapter 9) to optimize the geometry and cooling flow requirements may help in this direction. This computation should include the external and internal surface details as well as heat transfer as variables. A good analysis therefore needs an accurate estimate of the convective heat-transfer coefficients in the airfoil passages.

Presently, the local heat-transfer coefficients inside the airfoil may be determined by using the liquid-crystal technique [4, 5], which provides reliable results for stationary internal cooling passages. The liquid crystal is a material which is sensitive to temperature and exhibits fringes of various colors (red, green, and blue), at different temperatures. A scale model of the airfoil (8 to 12 times enlarged) is made of a transparent material (plexiglass, stereo-lithography, etc.). It can be sprayed on the inside of the passage where thermal data are required. When hot air is passed through the passage, the internal surfaces become warm and the liquid crystal exhibits color fringes as a function of time. The fringes can be recorded on a video camera and the transient data analyzed by using a computer. The computer processes the data further to determine the heat-transfer coefficients on the inside of the blade. Unfortunately, the technique is difficult to use in a rotating environment. Mass transfer technique (sublimation) may be used as an alternative to liquid-crystal technique for stationary components. However, the coating of the internal passages with a sublimating material

and the measurement of local heat-transfer coefficients may pose more difficulties than for the liquid-crystal test.

1. Rotating tip shrouds. Figure 11 portrays schematically an uncooled LPT blade with a rotating tip shroud. The tip shroud is necessary due to the large radius and blade span in the low-pressure stages. The same blade-tip clearance will cause a much larger fraction of leakage at a low-pressure stage than at a high-pressure stage. The gain in power output and turbine efficiency due to the tip shroud should be balanced against the cost and complexity of design. Tip shrouds may have one or more teeth depending on the permissible leakage and the required aerodynamic efficiency. All the design parameters for a cooled blade are similar to those of the cooled blade, except the rotating tip shroud and the number of teeth on it.

2. Blade-to-disk attachment. There exist two types of attachments between the blade and the disk. The first is the integral design where the blade and the disk are made of the same material. These are cast as an integral unit and cannot be detached. This design is usually used in compressor and turbine stages in which the disk stresses are so low that the blade material can stand the temperature and the stresses. Typically in turbines, a high-strength forging that has a lower tolerance to temperature is used for the disk, whereas a material casting that can stand higher temperatures is used for the blades. In HP turbines where the blade needs cooling, the procedure is to cast the blade as a separate piece that can be inserted in the rim of the disk at the fir tree. Then the blade can be made of special alloys of nickel with high strength and tolerance to temperature. Moreover, the blade can be made with serpentine or other passages through which cooling air can be passed to maintain the surface at low temperatures to ensure long life.

3. Turbine disk design. Disk design should ensure that the stresses due to thermal transients and those induced by rotation do not become excessive at any location. The main areas of concern are the disk rim, the web, and the disk bore. At the rim, the blade-disk attachment area (fir-tree) is subjected to high stresses due to the centrifugal forces on the blades. The disk rim is heated by conduction at the blade attachment, by convection near the blade platform, and by the ingested gas in the cavities. It should therefore be cooled by providing adequate amounts of air at both faces of the disk. The flow should also be sufficient to keep the disk cavities purged such that gas ingestion is minimized. The main aspect of the design is to guard against LCF failure. It is necessary as well to guard against stress-rupture at specific points (e.g., fir-tree attachment), due to excessive creep, thermal, and bearing stresses. At the disk bore where the stresses often exceed yield limits, it is necessary to guard against the possibility of failure

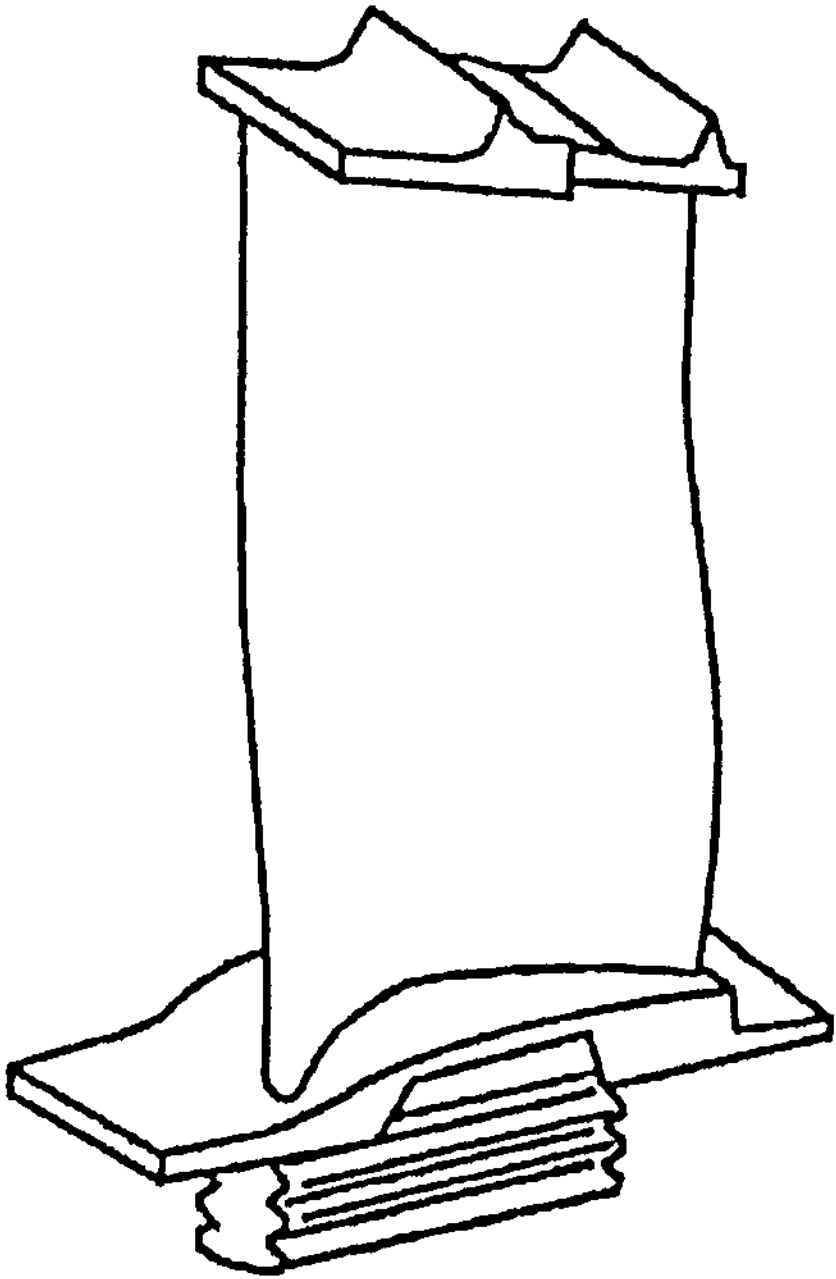

Figure 11 Low-pressure turbine blade with a tip shroud.

due to cyclic operation. In addition, disks have to be designed to operate at speeds about 20% above the engine operating speed for maximum power. Referred to as overspeed capability, this design ensures that in the event the engine needs extra power during an emergency, there is adequate margin with little risk of failure. It also provides safety against inadvertent overspeeds.

4. Turbine stage design. The design of turbine stages requires specification of the shapes of the airfoils, the rotational speeds of the rotors, the velocity triangles, aerodynamic efficiencies, and the work output. Figure 12 shows schematics of typical turbine HPT and LPT blades. Since these two blades run at different speeds, have different velocities of gas flow, and have different outputs, they are quite different in shape. The primary element of aerodynamic design is the maximization of blade efficiency. For a given stage work output, the stage efficiency increases with tip speed to reach a maximum level at a certain speed. Efforts are made to design the blade to operate close to this optimal speed. In the HP turbine stage, because of the high density and high velocity of the gas, the flow area required and the disk diameter are smaller than those of the LPT. Further, the airfoils are usually of small span compared with those of the LPT stages and turn the gas through large angles ranging to 130°. These requirements (high tip speed for maximum efficiency and small diameter) imply that they run at much higher rotational speeds than LPT blades. In gas turbines designed by Honeywell Engines & Systems, there is no attached rotating tip shroud at the HPT blade tips, since leakage across the blade is not as serious as in the LPT. (Large engines designed by Rolls-Royce Plc., for example, often have rotating tip shrouds on HPT blades as well.) As opposed to this, the LPT stages have large diameters since they are driven by low-pressure, low-density gas with large specific volumes. They tend to run at lower tip

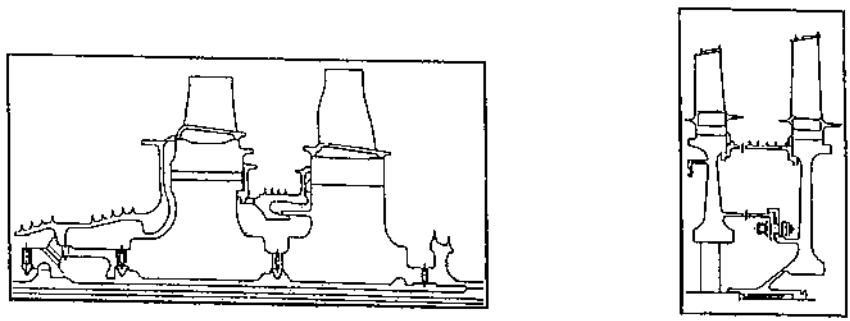

Figure 12 Schematic diagrams of typical HP turbine and LP turbine blades.

speeds as well since their work output is smaller than that of the HP stage. The span of the blade has to be sufficiently large (high aspect ratio) to pass the gas with low density. In addition, as compared with HPT blades, these blades may have more of a radial twist, to accommodate the changes in incidence angle with increasing radii. They do not need as much cooling air as the HPT stages since they deal with cooler gas. Often, LPT blades are designed with no cooling at all, since modern materials can withstand reasonably high temperatures and still have enough life to satisfy specifications. Even so, the disks require air to keep their sides cool and to purge the cavities to prevent gas ingestion. As the temperatures and speeds are lower overall, the disks may be made of materials that are generally less expensive and may still be more durable than the disks of HPT stages. The blades may be provided with rotating tip shrouds, since the problem of leakage at the airfoil tip is more serious at the LPT blades.

5. Thermal/stress analysis and life prediction. The next step in design is the determination of stresses in the disks, blades, and other critical components of the turbomachine. This starts with a finite-element thermal analysis of the component including appropriate boundary conditions. In general, a commercial code is utilized for most types of finite-element analyses. (For a nearly two-dimensional or axisymmetric geometry, in-house codes are utilized sometimes, since they facilitate the application of thermal boundary conditions. The general practice is to carry out all fully three-dimensional thermal analyses with a commercial code.) The boundary conditions specify the temperatures of the cooling fluid flowing around the component, heat-transfer coefficients, permissible surface temperatures, speed of rotation, etc. The stress analysis following the thermal analysis needs three material characteristics: the modulus of elasticity, Poisson ratio, and thermal expansion coefficient. If the material is nonisotropic, the moduli of elasticity in all three directions as well as a few other properties need to be specified. The analysis identifies areas of high stress that may limit the life of the component. Also, in areas of stress concentration, calculations are performed to determine life under operating conditions and to ensure that the component has a sufficiently long fatigue (LCF) life.

The rotating parts of turbines are subjected to both centrifugal and thermal stresses and need particular care in design. For example, turbine disks experience large temperature differences between the blade attachment area and the bore in addition to being in a centrifugal force field. In such cases, a transient thermal analysis must be performed since the highest thermal stresses often occur in the transient condition rather than at steady state. A temperature map of the interior of the disk at various time intervals is thus obtained. This is used subsequently to perform a stress analysis. To illustrate this point, Fig. 13 is a diagram of two-dimensional analyses in both

the steady and transient conditions for a disk. Schematics of isotherms and representative temperatures as well as stresses corresponding to steady-state and transient conditions are shown. Based on the indicated conditions in the diagrams, the bore thermal stress during the transient is higher than during steady-state operation at full power. This condition should be used to estimate life later.

Figure 14 portrays schematically the two-dimensional stresses due to thermal effects and centrifugal loads caused by blade and disk rotation. The stresses are expected to be low at the rim and high at the bore. Since this is a two-dimensional analysis, it will not provide the bearing surface stresses at the fir tree. A three-dimensional analysis is necessary to determine them. Blade attachment areas should be checked for excessive stresses at all root surfaces by using a three-dimensional analysis.

Fatigue Life. Fatigue life prediction at areas of high stress concentration (e.g., blade roots) may require a three-dimensional analysis. (This is because two-dimensional calculations cannot predict the variations of stress in the third direction. The local stresses at some points in that direction may exceed yield, even though the average stress remains at reasonable levels.) Tables 3(a) and 3(b) show the steps involved in this analysis. The three-dimensional analysis starts with the generation of the geometry and the corresponding solid model, which is meshed with a mesh generator. These meshes are fine compared with their two-dimensional counterparts. They are

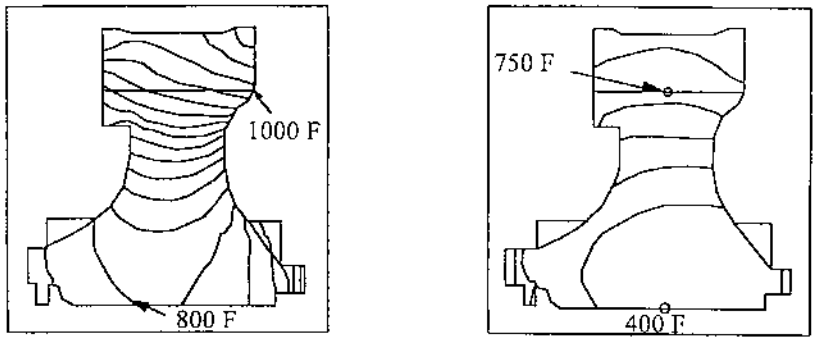

Steady-State Temp.
Rim-Bore Temp. Diff. = 200 F
Bore Stress = 150 ksi.

Transient Temps: 50 s Acceleration
Rim-Bore Temp. Diff. = 350 F
Bore Stress = 180 ksi.

Figure 13 Two-dimensional transient thermal analysis of a disk (schematic).

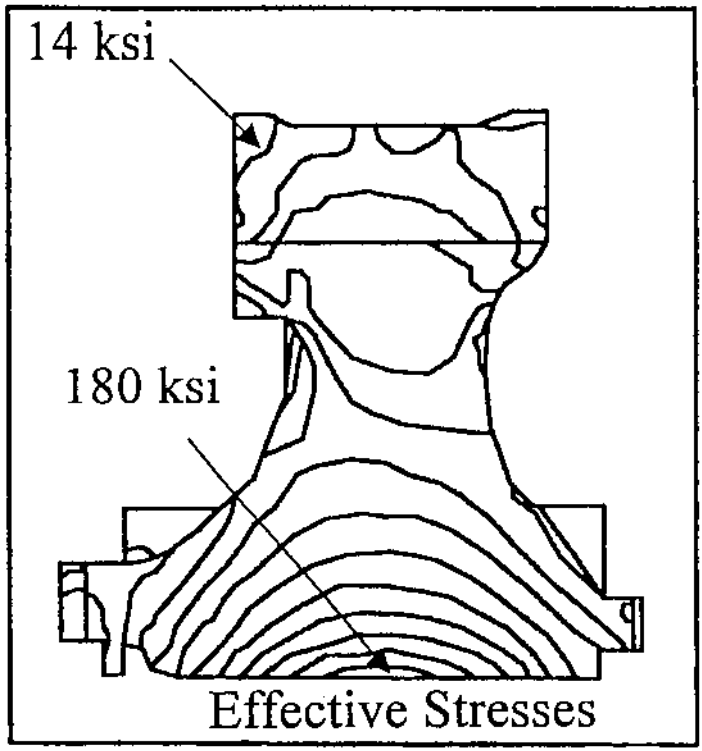

Figure 14 Two-dimensional stresses in a disk (schematic).

more difficult to create and require large amounts of storage space as well as time for computation. For these reasons, a three-dimensional analysis is carried out only in critical areas of expected high stress. After applying the appropriate boundary conditions, thermal and stress analyses are performed to determine areas of high stresses. For blades and other rotating components, the finite-element mesh used for stress analysis may also be used in vibration analysis to determine the natural frequencies, modal shapes, and associated stresses. All vibratory modes (bending, stripe, torsion, etc.) should be included in the analysis. In general, frequencies at the sixth mode and above are not significant, since aerodynamic damping will ensure low vibratory amplitudes and stresses at these frequencies. They do not contribute significantly to HCF. To avoid high stresses due to vibration, the design should ensure that there exist no sources of excitation with frequencies close to resonance (1st to 5th modes). This requirement

Table 3(a) Steps in a Three-Dimensional Thermal Analysis

Step 1	Step 2	Step 3	Step 4
Obtain CAD model	Generate 3D mesh using appropriate mesher (Note: The mesh should be fine enough to suit the requirements of stress and vibration analyses to follow.)	Apply appropriate transient boundary conditions (Use worst BCs applicable during cyclic operation)	Perform transient thermal analysis & determine worst temperature gradient and regions of max. temp. for stress analysis

may result in changing the airfoil count or the struts in the system so that excitation is avoided at critical operating speeds. The results of vibration analysis permit the generation of a Campbell diagram (Fig. 15), which portrays the natural frequencies of the blade as a function of speed (rpm or percent of maximum). Centrifugal forces tend to raise the natural frequencies while increasing temperatures tend to reduce them due to

Table 3(b) Steps in a Three-Dimensional Stress and Vibration Analysis

Step 1	Step 2	Step 3	Step 4
Refine mesh used for thermal analysis if necessary, to suit requirements for stress and vibration analyses.	Interpolate from results of thermal analysis to impose temperatures at all points on newly generated mesh.	Apply appropriate BCs applicable to stress analysis. Include body forces as necessary and perform stress analysis. Determine worst stress location.	Generate modal shapes and perform vibration analysis by using the same mesh.

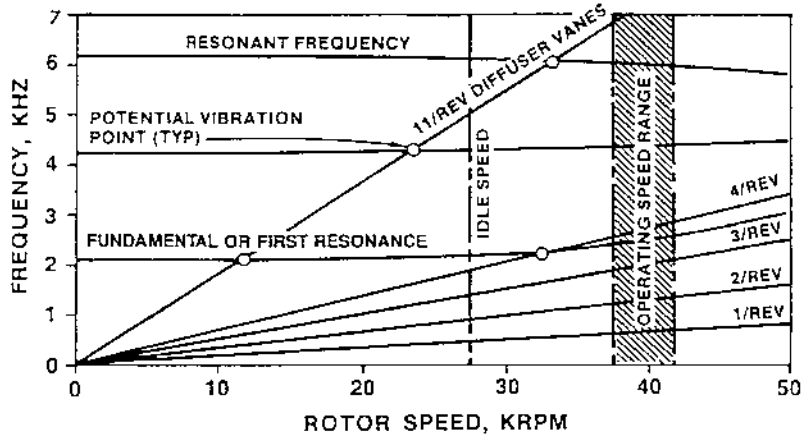

Figure 15 Schematic Campbell diagram.

attendant reductions in modulus of elasticity. The diagonal lines represent different engine excitation orders due to sources like struts, upstream nozzles, blades, etc. The points of intersections between the lines of natural frequencies of the blade and the excitations caused by the sources in the system are those that could cause resonance. Figure 15 applies to turbine blades and shows the excitation due to diffuser vanes located upstream of the blades. Steady-state operation close to the speeds ($\pm 10\%$) at which excitation may occur is to be avoided. As indicated on the diagram, no excitations to cause resonance should occur within the operating range of the engine. Engine strain-gage tests may be performed to determine the strain level (amplitude) of each excitation and determine where high vibration actually exists.

The schematic Goodman diagram portrayed in Fig. 16 is used to assess the combined effects of static and vibratory (alternating) stresses on a material. It plots the permitted alternating stress against the mean or static stress. A constant HCF lifeline corresponding to minimum properties (-3σ values) at the temperature of operation is plotted as the minimum Goodman line. The line is usually drawn with the -3σ value of the endurance limit as the ordinate intercept and the -3σ value of the ultimate tensile strength of the material as the abscissa intercept. It typically represents 10^7 cycles of HCF life. The design should ensure that the alternating and mean stresses in the material correspond to a point below the Goodman line. For airfoil design, this ordinate may range between 30% and 50% of the -3σ value, depending on the criteria used in different design groups.

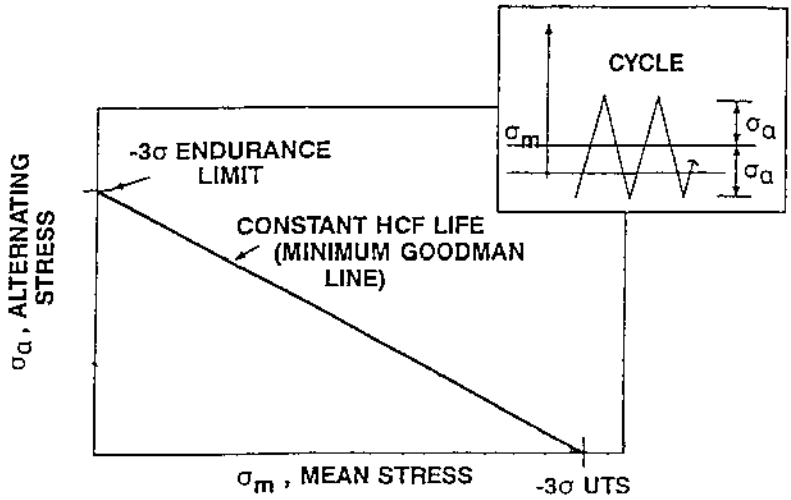

Figure 16 Schematic Goodman diagram.

Creep can cause excessive permanent deflections, unacceptably large growth of airfoils, reduced tip clearance, and increased probability of a tip rub. Further, there exists the possibility of untwist of airfoils and bending

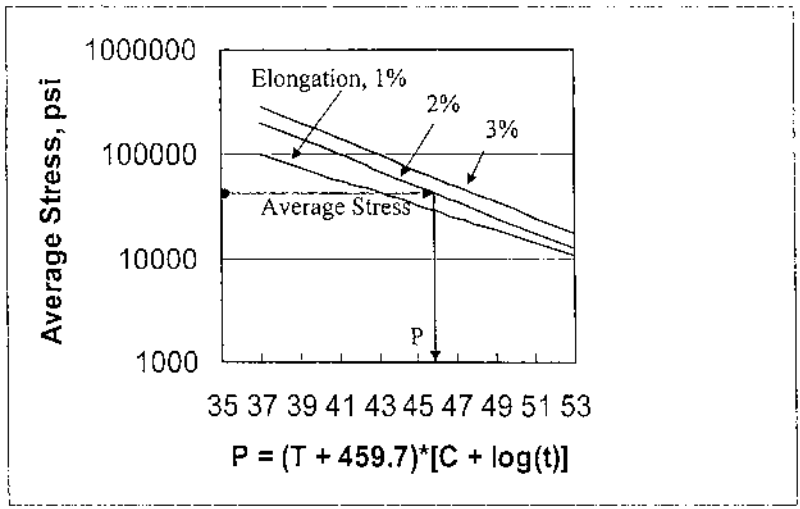

Figure 17 Schematic of a Larson–Miller plot.

overload of the blade, causing excessive stresses in critical areas. Hence, the stress-rupture life of the component must match or exceed the stipulated contract requirement. Creep and stress rupture lives are predicted by using the Larson–Miller plot [6], shown in Fig. 17. This is a plot of allowable average stress in the blade (or other components) against the Larson–Miller parameter, defined by the expression

$$P = T_m(C + \log_{10} t)/1000 \tag{6}$$

Here, C is the Larson–Miller constant, with values ranging between 15 and 25 for most metals and alloys. Usually, it is assumed to be 20 in calculations.

For a specified maximum creep (1%, 2%, etc.) and a given average stress at a cross section (determined from the finite-element analysis), the plot permits one to determine the Larson–Miller parameter, P. Since the average temperature in the specimen is also known, the parameter permits the estimation of maximum operating life. Moreover, the magnitudes of permitted creep and P permit one to calculate a short-term effect of time and temperature that is equivalent to any long-term requirement. Note that the Larson–Miller plot depends on the characteristics of the material and is different for different materials.

Corrosion And Erosion. In addition to those outlined above, the effects of oxidation, corrosion, and erosion have to be minimized to ensure long life. This is particularly true of blades and nozzles that are continuously exposed to the hot gas. The level of corrosion depends strongly on the pollutants in the atmosphere and on the composition of the fuel, which may contain sulfur or compounds of alkaline materials. These are transported by hot gases and attack the materials of the airfoils. Oxides, sulfides, and certain alkaline compounds are formed at the surfaces of the blades and vanes. To counter these effects, it is necessary to choose appropriate vane/blade materials and limit their surface temperatures to low levels. It is also appropriate to put a layer of "thermal barrier" coat (TBC, thickness, 0.003″–0.007″) over the surface of the vane/blade. The coating consists of two layers, the first being a bond-coat (platinum aluminide or similar material) followed by an outer layer of low thermal conductivity compared with the base metal. This layer may be of ceramic (e.g., yttria-stabilized zirconia) and maintains the metal surface temperature lower than for a blade without TBC. In addition, it shields the metal surface from exposure to the hot corrosive gases flowing through the turbine (e.g., oxygen, oxides of sulfur, metallic oxides). The composition of the thermal barrier coating, its thickness, and the method of application are determined by the type of metal surface, the gas temperature, and the maximum temperature the metal can withstand. These differ from application to application. Erosion may

occur due to particles of unburned carbon emerging from the combustor or dust and sand in the air in certain arid regions. The particles transported by hot gases over blades do not follow the fluid streamlines since they are more massive and the centrifugal forces tend to throw them toward the blade tips. Hence, they often damage the blade tip or the suction surface so badly that the performance is affected and the blade may need replacement. They may damage the thermal barrier coat (if present) and expose the metal surface to hot gas. While the presence of unburned carbon is determined by combustor design, the inflow of sand particles may be minimized by using an appropriate filtering medium or particle separator at the engine inlet. However, it is difficult to prevent the erosion of helicopter blades due to sand.

Corrective measures such as slight changes in geometry, introduction of an insulating layer at appropriate locations, increase in cooling flow, etc. may be initiated if the first design leads to a shorter than desired life. With the completion of stress and vibration analyses and life evaluation, drawings are prepared and released for the manufacture of the parts.

Validation and Certification Tests

It is usual to perform cold flow, spin-pit, etc. tests for items like blades and nozzles, while rig tests are performed on individual components such as the axial compressor, centrifugal compressor, HPT, or LPT. Scaled models may also be used in some of the tests. The rig tests include complete instrumentation and are used to validate the calculated performance of the components. The mass flows of air, pressures, and temperatures as well as rotational speeds are monitored at all the design points, ranging from idle to rated maximum power (usually 110% of rated power). For turboshaft engines, similar tests may be performed to determine the performance parameters of other components such as recuperators. These tests, if satisfactory, are followed by a full engine test, with operating conditions ranging from idle to maximum power conditions. The Federal Aeronautics Administration (FAA) specifies the operating cycle and the number of cycles to which the engine must be subjected without deterioration before being certified as airworthy for commercial or military use. The following is a brief list of some of the tests.

Component Tests. These are performed on individual components such as blades, vanes, shrouds, heat exchangers, etc. They may be run in laboratory rigs to verify the validity of the assumptions used in design. The components may be tested under simulated conditions close to those expected during engine operation. These consist of:

1. *Thermal tests*. These are performed in the laboratory.

Cold flow tests of actual blades, vanes, TOBI (tangential on-board injector), etc. to validate design.
Liquid-crystal tests to evaluate internal or external heat-transfer coefficients,
Scaled transparent model (e.g., stereo-lithography, plexiglass) tests, etc.

2. *Vibratory tests*. These are performed in the laboratory or in special spin-pits. They include:

Shaker-table acoustics
Component holography
Component strain gauge
Spin-pit jet impingement

3. *Stress tests*. These consist of:

Spin-pit cyclic and overspeed tests, usually of blades and disks.
Spring rate deflection

4. *Material property determination*. These tests are meant to obtain knowledge of properties of materials under development or to obtain characteristics at elevated temperatures or high stress levels. Large banks of material property data exist at most companies (Honeywell, GE, Pratt & Whitney, Rolls Royce Plc., Siemens-Westinghouse, etc.). These data banks are used in determining the elastic and thermal properties at the required design conditions. The tests may be severe enough to cause fracture or other type of failures in some of the materials.

5. *Rig tests*. They include

Cold aerodynamic tests
Seal tests
Bearing tests
Combustor tests

6. *Engine tests*. These tests comprise the following:

Performance diagnostics conducted to determine power output, specific fuel consumption, and other aspects of overall health of the engine.
Thermal survey of the whole engine to ensure that the temperatures at all points in the secondary flow system and other points are at predetermined levels. These include metal, gas path temperatures and

pressures at critical points. These data may be obtained during certification tests as well.
Engine vibration survey.
Bird ingestion or foreign object damage (FOD) tests.

Bird ingestion tests are performed to determine the robustness of the engine components to withstand the effects of ingestion of foreign objects such as a bird (1 to 4 lbm), piece of tire tread, sand, gravel or water, ice and hail. According to FAA regulations, the engine is required to demonstrate that the ingestion of a bird 4 lbm in weight, fired at the engine at a maximum climb speed of 250 knots (273 miles/hr), should cause no fire, fan or rotor burst, or loss in shutdown capability. The regulations stipulate further that a 1 lbm bird fired several times at the engine at an initial climb speed of 150 knots (173 miles/hr) should cause less than 25% thrust loss with no shutdown. (A certain minimum number of test firings proportional to the area based on the engine inlet flange diameter is required.) This test is more severe in its effects than the 4-lbm bird ingestion test. The ingestion of water, ice, or hail should cause no thrust loss or shutdown of the engine.

FAA Certification Tests and Military Quality Tests. Figure 18 shows the engine cycle for FAA accelerated mission test, which specifies variations in power level plotted against time. Each cycle shown lasts 26.4 min. The total duration of the test is 150 hr. The engine is expected to operate satisfactorily over the whole period with no deterioration in performance. At the end of the test, inspection should indicate no signs of distress at any of the components.

Future of Mechanical and Thermal Design

As seen in the foregoing, improved materials, better analytical techniques including unsteady flow prediction capability, and better experimental methods to understand the local effects of stress and heat transfer are necessary to improve the capabilities for design. These improvements may be expected to permit the design of more durable machines with improved performance. The following paragraphs provide a very limited sample of some of the areas that are showing signs of promise for future developments.

Improved Materials

Ceramics for Airfoils and Turbine Disks. Ceramics have certain characteristics that make them admirably suited for use in high-temperature applications. These are

1. High-temperature capability, about 2,200 °F, as compared with 1,900 °F for single crystals and other nickel-based superalloys. The thermal conductivity of ceramics is better than that of the alloys used in blade manufacture. These two characteristics eliminate cooling flow requirements in many vanes. The thermal efficiency of the engine and its power output improve compared with those of engines using metallic alloys for the application. The projected replacement rate of ceramic nozzles is only 10% of that of metal.

2. Very good dimensional stability, the coefficient of thermal expansion being about half that of metal. The low expansion coefficient reduces thermal stresses when compared with that of metal with the same temperature distribution. In addition, ceramic is less subject to warping, corrosion, and erosion.

3. Lower density/lower rotational inertia and reduced stresses. The density of ceramics is about 60% of that of the best nickel alloys. This leads to a reduced centrifugal load, smaller stresses at the fir-tree attachments, and a thinner container ring requirement.

4. Increased life due to reduced creep, fatigue, and erosion. Moreover, corrosive agents in the hot gases do not damage ceramics as seriously as they do metallic alloys.

As opposed to these advantages, there are certain disadvantages that need to be taken into account.

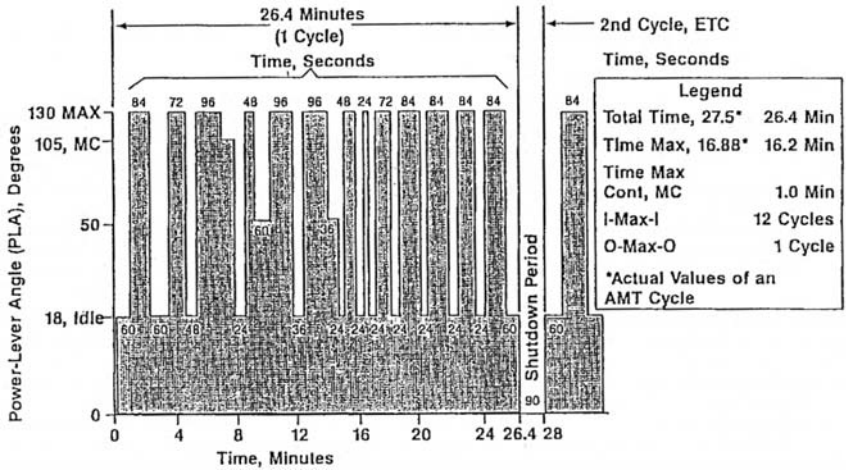

Figure 18 FAA accelerated mission test.

1. Ceramics are subject to "inclusion" and other defects. As a result, the safe design stress in ceramics is about 40,000 psi, as compared with some metal alloys, which may have safe stresses in excess of 120,000 psi.
2. Ceramics are brittle and break easily when subjected to vibration or shock. This is a serious disadvantage in turbomachines. The ceramic structure tends to shatter easily in several applications.
3. Casting large turbine wheels with uniform properties is a challenge that has not been overcome yet. The biggest ceramic disks in use are about 8" in diameter. These are currently being used on an experimental basis in APU disks.

Reduced Cooling Flow

Several items of technological improvements are needed to reduce cooling flow requirements. The main items are (1) development of erosion- and corrosion-resistant coatings, low conductivity, erosion-resistant and low-cost TBC coatings to reduce airfoil surface temperature, (2) development of inexpensive blade materials to permit higher operating temperatures, (3) better heat-transfer enhancing configurations for the blade interior as well as at film holes, and (4) better aerodynamic design of airfoil surfaces to reduce flow separation, transition to turbulence, etc. to reduce gas-side heat transfer [7].

Other Expected Improvements

Improvements in diffusion bonding technology and the development of a reliable low-inertia turbine (a small engine operating at extremely high speeds and high temperatures with fuel consumption about 25% below that of the best available commercial engines) may lead to very high efficiency engines in the near future. A few high-inertia turbines have been built on an experimental basis and are being tested. High-temperature seals and cooled ceramic airfoils for temperatures in excess of 2,500 °F could lead to improved life and durability as well as reliability. In addition, the development of computer codes capable of performing unsteady aeroelastic calculations faster and more efficiently will help considerably in the design of compressor and turbine rotors. Advanced CFD codes that predict the aerodynamic forcing functions due to struts and obstructions in the flow path as well as the effects of rotor–stator interaction will enhance the ability to predict turbine behavior under all operating conditions. These improvements and computational aids are expected to reduce the development and operating costs of engines by an estimated 20%.

Symbols

C_p = Specific heat at constant pressure for a perfect gas.
C = Larson–Miller constant ranging from 15 to 25, average = 20.
P_Y = Pressure ratio across the compressor (or turbine) in the ideal Brayton cycle.
(P_r) opt = Optimum pressure ratio for maximum work output in the Brayton cycle.
t = Expected creep life of the component or time to rupture, hr.
T_1 = Minimum (sink) absolute temperature for energy rejection in the Brayton cycle.
T_3 = Maximum (source) absolute temperature for operation in the Brayton cycle.
T_m = Mean absolute temperature of the stressed component.
$T_r = T_3/T_1$.
(T_2) avg = Average total temperature of air at the entry to the combustor.
(T_3) max = Maximum streak temperature of gas emerging from combustor.
(T_3) avg = Average or design temperature for gas emerging from combustor.
$W_{\max}$ = Work output of the cycle per unit mass flow.

Greek Symbols

η_B = Ideal Brayton cycle thermal efficiency.
η_R = Regenerative Brayton cycle thermal efficiency.
γ = Ratio of specific heats of the gas.

References

1. R. F. Huang, *Engineering Thermodynamics, Fundamentals and Applications*, McMillan Publishing Co., New York, pp. 533–535 (1988).
2. V. Kadambi and M. Prasad, *An Introduction to Energy Conversion, Vol. 2, Energy Conversion Cycles*, Wiley Eastern Limited, New York, pp. 94–106 (1974).
3. J. A. Collins, *Failure of Materials in Mechanical Design, Analysis, Prediction, Prevention*, John Wiley & Sons, New York, pp. 12–13 (1981).
4. S. V. Ekkad, H. Du, and J. C. Han, "Local Heat Transfer Coefficient and Film Effectiveness Distributions on a Cylindrical Leading Edge Model Using a Transient Liquid Crystal Imaging Method," ASME Winter Annual Meeting, San Francisco, CA (1995).
5. R. P. Vedula, W. Bickford, and D. E. Metzger, "Effects of Lateral and Anisotropic Conduction on Local Convection Heat Transfer Characteristics

with Transient Tests and Surface Coatings,'' *Collected Papers in Heat Transfer*, ASME HTD-14, pp. 21–27.
6. E. R. Larson and J. Miller, ''Time-Temperature Relationships for Rupture and Creep Stresses,'' *Trans. ASME, 74*: and 765–771 (1952).
7. V. A. Zhuralev, S. Z. Kopelev, and S. V. Gurov, ''Some Aspects of Cooled Cascade Profiling,'' *Prom. Teploteknica, 10–1*: 17–21 (1988).

2

Fluid Dynamics of Turbomachines

Lysbeth Lieber

Honeywell Engines and Systems, Phoenix, Arizona, U.S.A.

INTRODUCTION

For current turbomachinery design, and in particular for aero engine applications, a primary emphasis is being placed on improved engine performance. Perhaps the most far-reaching example of this is the Integrated High Performance Turbine Engine Technology (IHPTET) Program, sponsored by NASA and DOD [1]. The goal of IHPTET is to achieve a twofold increase in performance, for advanced military turbine engines, by the beginning of the 21st century. Depending on the application, this performance increase will be achieved in a variety of ways, including increased thrust-to-weight, increased power-to-weight, and reduced specific fuel consumption (SFC).

While the goals of IHPTET represent the extreme, in terms of performance advances, the highly competitive nature of the current business climate requires performance increases of one form or another for all new turbomachinery products. In particular, with fuel costs representing a large portion of direct operating costs for airlines, SFC is a major performance factor for commercial aero engines.

Overall engine performance goals translate directly into specific aerodynamic performance requirements for individual turbomachinery components. In order to meet demanding performance goals, such as those set by IHPTET and the competitive marketplace in general, turbomachinery components must be designed to meet the requirements of increased efficiency, increased work per stage, increased pressure ratio per stage, and increased operating temperatures.

By necessity, the dramatic improvements in performance that will be achieved will come as a result of employing components featuring advanced aerodynamic concepts. These components will have much greater complexity than those seen in the past, including a higher degree of three-dimensionality in both component and flow-path configurations. The flow fields associated with these components will be equally complex and three-dimensional. Because an understanding of this complex flow behavior is critical to the successful design of such components, more capable analysis tools employing computational fluid dynamics (CFD) are essential in the design process.

In the past, it was sufficient to design turbomachinery components using simple tools based on two-dimensional (2D) inviscid flow models. However, with the current trend toward more sophisticated designs and more complex flow fields, these earlier tools are no longer adequate to the task of analyzing and designing advanced technology components. In reality, the flows encountered in these components are highly three-dimensional (3D), viscous, turbulent, and often transonic. These complex flows will not yield to understanding or prediction without the application of equally sophisticated modeling techniques.

To address the need to design such components, advanced CFD tools are required that are capable of analyzing 3D, viscous, and transonic flows, modeling turbulence and heat transfer, and treating complex geometric configurations. In addition, unsteady flows and the interactions of multiple blade rows must be considered.

The intent of this chapter is to present a brief overview of the characteristics of the flow in various types of turbomachinery components, and also to summarize the CFD analysis capabilities required to model such flows. This should give the reader a better appreciation for the impact of flow behavior on the design of such components, and for the level of modeling capability required to properly analyze the components. The focus will be on aero engine applications, but will exclude inlets, nozzles, and combustors. In addition, an assessment of trends in both component design and CFD analysis tools is included. Due to the complexity of these subjects, only a cursory discussion will be presented. However, references are provided in order to allow the reader to explore these topics in more detail.

CHARACTERISTICS OF TURBOMACHINERY FLOW FIELDS

In this section of the chapter, the basic characteristics of turbomachinery flow fields will be examined. Although the discussion will primarily target aero engine applications, many of the flow features are common to other turbomachines as well. In addition to a brief review of general flow-field characteristics, the nature of flows specific to various component types will also be considered.

Basic Characteristics of the Flow

Turbomachinery flow fields are highly complex and three-dimensional in nature. In most cases, flows are compressible and may range from subsonic, through transonic, to supersonic. Shocks may be present in the flow path, and shock–boundary-layer interactions may occur, leading to performance losses. Substantial pressure gradients can exist in virtually any direction. Rotation is also a major factor influencing the flow behavior.

Flows are predominantly viscous and turbulent, although laminar and transitional regions may also be present. Turbulence within the flow field can occur in boundary layers and the free stream, where the level of turbulence will vary depending on upstream conditions. For example, the flow downstream of a combustor or a multistage compressor could have a much higher free-stream turbulence level than the flow entering a fan.

Complex stresses and performance losses can result from viscous flow phenomena such as three-dimensional boundary layers, interactions between blade and end-wall boundary layers, near-wall flow migration, separated flow, tip clearance vortices, trailing-edge vortices, wakes, and mixing. In addition, relative end-wall motion and the transition between rotating and stationary end walls can impact boundary layer behavior.

Unsteady flow can occur as a result of time-varying conditions upstream, vortex shedding from blade trailing edges, flow separations, or the interactions between rotating and stationary blade rows, which can impart unsteady loadings on the blades.

Thermal effects and heat transfer can be significant factors, particularly in the hot section of the engine. Hot combustor gases flow through the turbine, producing hot streaks, which are transported by the turbine flow field. To protect the components subjected to the highest temperatures, cooling flows are injected through holes in the turbine blades into the hot primary gas path, providing film cooling for the blade surfaces. Similarly, cooling flows may also be injected into the main flow stream along the end walls.

Much of the complexity of turbomachinery flow fields is directly influenced by flow-path and component geometry. Geometric considerations include the curvature and shape of the flow-path end walls, the spacing between blade rows, blade pitch, and stagger. Other aspects of flow-path geometry include the configuration of the blade rows, such as the use of tandem blades, splitter blades, midspan dampers, and tip treatments. Of equal importance are the myriad details related to blade shape, such as thickness distribution, camber, lean, bow, sweep, scallop, twist, aspect ratio, solidity, hub-to-tip radius ratio, radii of the leading and trailing edges, fillet size, and tip clearance height. Blade cooling devices are also of importance; the size and position of cooling holes in the blade surface will affect the primary gas-path flow.

Thus, the flow behavior in turbomachinery components is quite complex and is highly influenced by the flow-path geometry. A thorough understanding of the effects of component and flow-path geometry will allow the designer to use the resulting flow behavior to advantage. To achieve this understanding and to perform the analyses necessary to optimize the highly complex flow behavior requires the use of advanced flow modeling technology.

Flow in Compression System Devices

Turbomachinery compression systems for aero engine applications can employ various combinations of axial and centrifugal components. In typical turbofan engines, an axial fan is positioned upstream, followed by a flow splitter, which separates core and bypass streams. A multistage axial compressor is positioned downstream in the core and may be followed by a centrifugal compressor. Turboprop and turboshaft applications often utilize centrifugal compressors exclusively.

All configurations of compression systems are characterized by complex, three-dimensional flows, with adverse pressure gradients that can produce flow separations. In addition, rotation, relative shroud motion, tip leakage flows, shocks, shock–boundary-layer interactions, blade–end-wall interactions, and blade-row interactions all contribute to the structure of the compressor flow field. Details of flow behavior specific to both axial and centrifugal compressors will be examined in the following sections.

Flow in Axial Fans and Compressors

Axial fans and axial compressors are similar in many general respects, both being compression devices with flow paths having relatively small radius

change, and with the incoming and exiting flow primarily in the axial direction.

However, fans typically have less pressure rise per stage than axial compressors and utilize fewer stages, often only one. Fan blades have a larger span and longer chord than axial compressors. Due to mechanical considerations, fan rotors often have midspan dampers, which form a rigid ring of support, connecting all blades at a part-span location. Fan stators can be either full-span or split-span devices. Depending upon the stator configuration, a flow splitter will either be positioned immediately downstream of a full-span stator or serve as a mounting support for split-span stator blade rows in the core and bypass flow paths.

In contrast, axial compressors typically produce higher pressure rise per stage and employ multiple stages. Axial compressors have shorter blades with shorter chords than do axial fans. The flow path is uninterrupted, having no splitting devices.

Performance of axial-flow compression systems can be affected by many complex flow phenomena. A comprehensive discussion of all compressor flow characteristics would be prohibitive here. Instead, a brief review of some typical flow phenomena encountered in axial fans and compressors will be considered, in order to provide a general impression of the complex nature of the flow.

The flow field internal to the blade passage has been studied extensively for axial fans and compressors. Deutsch and Zierke [2, 3] examined in detail the behavior of boundary layers on the suction and pressure surfaces of a compressor blade in cascade, at incidence. They identified a fully turbulent boundary-layer flow on the suction surface, downstream of a small leading-edge separation bubble. Further downstream, a second region of separation was observed, followed by a fully detached flow. On the pressure surface, a laminar boundary layer was found to exist over more than 50% chord, with the ensuing transition region persisting until the trailing edge. Due to the separated flow on the suction surface, velocity profiles in the near-wake region also exhibited regions of backflow.

However, the study of boundary-layer development in an axial compressor cascade is idealized. Pouagare et al. [4] performed a comprehensive study of boundary-layer behavior on both suction and pressure surfaces for an axial compressor rotor. They concluded that the streamwise component of velocity in the boundary layer was primarily influenced by the streamwise pressure gradient. Radial velocity in the boundary layer was found to be outward at most locations, reaching a maximum value near the trailing edge. Tip leakage flow was found to significantly affect the boundary layer and near-wake behavior in the outer span region of the blade and downstream flow path.

End-wall boundary layers can also have a substantial impact on the flow through the blade passages of an axial compressor. End-wall boundary-layer thicknesses can be relatively thin in the inlet stages of a multistage compressor, but the thickness can increase to represent a significant portion of the flow field in stages further downstream. Wagner et al. [5, 6] studied the effect of end-wall boundary-layer thickness on the secondary flow in an isolated axial compressor rotor. End-wall boundary-layer thickness was found to affect both separation at midspan and the radial migration of high-loss flow from hub to tip. As a result, the radial distribution of loss was altered, depending on the thickness of the end-wall boundary layers.

For axial compressor rotors, shroud boundary-layer flow is closely coupled to the behavior of tip leakage flow. Although the leakage flow initiates within the relatively narrow tip clearance gap, the impact of this flow is felt over a substantial portion of the outer span of the rotor flow path. Based on a study by Lakshminarayana et al. [7], losses due to tip leakage appeared to dominate the shroud end-wall region, whereas losses due to secondary flow and the shroud boundary layer were of secondary importance.

Lakshminarayana and Murthy [8, 9] performed a detailed examination of flow in the tip region of an axial compressor rotor. They found that the shroud end-wall boundary layer was well behaved upstream of the rotor and far downstream; however, within the blade passage, interactions between the tip leakage flow and the shroud boundary layer became quite complicated. Beyond approximately 25% chord, the shroud boundary-layer effects were overtaken by the influence of the clearance vortex, which formed a complex mixing region in the outer 10% span of the blade. This mixing region was reinforced by further leakage along the entire chord of the blade, which served to unload the outer span region of the rotor.

Inoue et al. [10] investigated the effect of tip clearance height on shroud end-wall flow development and on the behavior of the leakage vortex. Increased tip clearance was found to negatively impact stage performance by reducing efficiency. With increased clearance, the leakage vortex became more intense, and the large vortex motion caused reversed flow in the axial direction near the shroud.

Another significant flow structure and source of losses in transonic and supersonic axial compressors is the shock system, and the resulting shock–boundary-layer interaction. Strazisar and Powell [11] mapped the shock surfaces for an axial compressor rotor with supersonic inlet relative Mach number. They observed that the flow downstream of the passage shock emanating from the leading edge was supersonic across the span; however, in the inner span region, the flow within the passage then diffused

to subsonic conditions without passing through another shock. Near the tip (with its higher inlet relative Mach number), a normal shock was present near the trailing edge. Because the rotor had a swept leading edge, the shock surface was also inclined, thereby generating an increased radial velocity component behind the shock, due to flow turning across the shock.

Dunker et al. [12, 13] also examined the shock structure within a transonic axial fan rotor. In a typical shock-wave system, they observed that a detached bow shock was followed by a subsonic bubble around the rotor leading edge. On the suction side of the blade, the flow then reaccelerated to supersonic conditions, before encountering the normal shock branch of the bow shock, running across the passage. Downstream of the passage shock, the flow exited with subsonic velocity. Within the blade passage, the normal shock interacted with the suction surface boundary layer to produce a λ shock next to the blade surface. The oblique branch of the bow shock extended upstream, interacting with expansion waves from the supersonic acceleration around the leading edge. As the inlet Mach number was increased, the bow shock attached to the leading edge and developed an oblique, rather than a normal, branch within the blade passage. Boundary-layer interaction with this passage shock triggered a separation bubble on the suction surface. Depending on the back pressure, an additional normal passage shock was present near the trailing edge.

Structure of the blade wake is another important aspect of axial compressor flow behavior. Vortices can be shed periodically from the blade trailing edge, and the velocity defect is mixed out as the flow proceeds downstream. Paterson and Weingold [14] simulated the behavior of a compressor airfoil trailing-edge flow field, by utilizing a flat-plate model with a thick, rounded trailing edge. This configuration produced trailing-edge boundary-layer separation, resulting in flow recirculation and unsteadiness. The axial extent of the reversed-flow region downstream of the trailing edge was found to be approximately 0.8 plate thicknesses. Vortex shedding from the trailing edge strongly enhanced wake mixing and also introduced unsteadiness in trailing-edge surface pressures and wake static pressures. The trailing-edge interaction region extended from approximately 10 plate thicknesses upstream of the trailing edge to 3 plate thicknesses downstream. Further downstream, the velocity defect took on the character of a far wake flow.

Prato and Lakshminarayana [15] studied the structure of an axial compressor rotor wake flow in the trailing-edge, near-wake, and far-wake regions. Asymmetric velocity profiles were observed in the trailing-edge and near-wake regions; however, the profiles tended to become symmetric in the far wake, due to mixing. Large gradients of static pressure existed across the wake in the trailing-edge and near-wake regions, with maximum static

pressure at the wake centerline. The static pressure decayed rapidly in the trailing-edge region, and much more gradually in the far wake. Wake width was found to be largest in the tip region due to mixing caused by interaction of the clearance flow, the wake, and the shroud boundary layer. Secondary flow in the hub region also produced a local increase in wake width.

Other major influences on the performance of axial compressors are unsteady flow and blade-row interaction. The effects of blade-row interaction were examined by Okiishi et al. [16]. They observed that wakes produced by an upstream rotor blade row were "chopped" into segments and transported by the downstream stator blade row. The interaction of these rotor wake segments with the stator blade boundary layers resulted in higher losses through the stator than would have been generated by the isolated wakes and boundary layers. In a follow-up study by Hathaway et al. [17], it was observed that when the rotor and stator were not too closely coupled, the transport of the rotor wakes through the stator blade row was primarily controlled by steady-state inviscid flow effects. Spreading of the rotor wake segments within the stator appeared to be minimal.

Blade-row interactions in multistage compressors become much more complex. Cherrett and Bryce [18] examined unsteady viscous flow in the first three stages of a high-speed multistage compressor. They observed that in the embedded stage rotors, strong rotor–rotor interactions occurred, which induced passage-to-passage variations in the phase-locked average (periodic) total pressure field.

This discussion provides a sampling of the flow phemonena that occur in axial fans and compressors and should give an indication of the complexity of the flow structures that are present in such devices.

Flow in Centrifugal Compressors

Centrifugal compressors may be utilized in turbofan applications as the high-pressure compressor downstream of multiple axial compressor stages. In some turboprop or turboshaft applications, a one- or two-stage centrifugal compressor will serve as the entire compression system.

Centrifugal compressors differ markedly from their axial counterparts. Pressure rise per stage is significantly higher than for axial compressors. The flow path undergoes a substantial increase in radius from inlet to exit, with the flow entering the rotor, or impeller, axially and exiting radially. In most applications, the flow then proceeds radially through a vaned diffuser.

As the flow-path radius increases, the circumferential distance between blades increases. To compensate for this, and maintain the desired flow-path area, impeller blade span decreases substantially from inlet to exit. In addition, to allow blade loadings to be maintained at desired levels, without

flow separation, splitter blades are included in the aft portion of the impeller flow path. Fillets are also present on impellers. This geometric feature can represent a significant blockage in the flow path, as the span decreases toward the impeller trailing edge.

Radial diffusers must also contend with a radius increase, and expansion of circumferential distance between blades. To compensate, the diffusers typically have increased blade thickness toward the trailing edge. The span of a radial diffuser typically remains relatively constant from leading edge to trailing edge, as radius increases.

High-performance centrifugal compressors require substantial flow diffusion, which can result in rapid growth of the boundary layers in the second half of the relatively long impeller flow passages. This behavior often initiates flow separation from the blade suction surface, causing the formation of a wake region, which shifts the through-flow (jet) toward the pressure side. This flow separation diminishes the diffusion potential for the impeller and results in a highly distorted jet/wake structure at the impeller discharge. These impeller exit conditions then contribute mixing losses and unsteady flow to the diffuser, which causes a further reduction of stage efficiency.

A comprehensive study of the flow behavior in centrifugal compressor impellers was performed by Eckardt [19, 20]. He obtained detailed measurements of flow velocities and directions at multiple locations in the flow field, from the inducer inlet to the impeller discharge.

In the first study [19], performed with a radial impeller, Eckardt observed that the flow was relatively undisturbed within the axial inducer and upstream portion of the impeller. The first significant flow distortions appeared at approximately 60% chord, with the initiation of a flow separation in the shroud/suction-side corner of the passage. After separation onset, a rapid growth of the wake area occurred in the shroud/suction-side corner, which appeared to be related to the increasing intensity of secondary flow. Vortices near both the shroud and the hub/suction-side corner "peeled" the boundary layers off the channel walls and fed the low-energy fluid into the wake. Additional low-energy fluid passed through the tip clearance into the wake region, causing the wake to increase substantially through the downstream half of the impeller flow path. The distorted flow pattern of high- and low-energy fluid (jet/wake) was sustained up to the impeller discharge, because turbulent mixing of the jet/wake shear layer was suppressed by system rotation and curvature effects. As a result, at the impeller discharge, the loss was primarily concentrated in the wake and along the passage walls.

Eckardt [20] later compared the flow behavior in two centrifugal impellers, one with a radial discharge and the other backswept. Each utilized

the same vaneless diffuser and shroud; only the blading and the hub contour were modified. He found that the flow patterns in the inducer region of the two devices developed similarly, and in both, a 3D flow separation began at the shroud in the region of maximum tip streamline curvature. However, significant differences were observed in the second half of the flow passages. In the radial discharge impeller, a strong jet/wake pattern increased in intensity approaching the exit, but much less distortion occurred for the backward-swept impeller, as a result of enhanced jet/wake mixing. The more uniform discharge flow with the backswept impeller would improve vaned diffuser performance, and therefore enhance stage efficiency.

The studies performed by Eckardt employed an unsplittered impeller. However, an impeller with splitter blades was investigated by Krain [21]. Different velocity profiles and flow patterns were observed in adjacent channels downstream of the splitter-blade leading edge. Velocity profiles indicated increased blade loading in the main-blade pressure-side channel, and a flattened velocity gradient in the suction-side channel. As the flow proceeded downstream through the split flow path, the wake showed more development in the main-blade suction-side flow path than in the pressure-side channel, particularly in the shroud/suction-side region.

Eckardt's studies were performed using a vaneless constant-area diffuser, so that the impeller flow would be unaffected by any diffuser distortion. However, in order to achieve higher efficiencies and higher pressure ratios in centrifugal compressor stages, vaned diffusers are required. The efficiency of the centrifugal compressor stage can be greatly affected by the interaction of the impeller and diffuser. Diffuser recovery is impacted by the highly distorted, unsteady flow from the impeller discharge. Also, when the impeller and diffuser are closely coupled, effects from the diffuser blades can influence the internal impeller flow, by distorting the static pressure field in the impeller exit/diffuser entrance region. This effect will also be more pronounced if supersonic Mach numbers occur at the diffuser leading edge and shocks extend into the impeller discharge region.

Krain [21] studied the flow in a centrifugal compressor stage with both a vaneless and a vaned diffuser. The stage employed a radial discharge impeller with splitter blades, and the vaned diffuser was a flat, straight-channel device. Krain observed only weak influences of the vaned diffuser on the impeller discharge flow field, relative to the flow behavior with the vaneless diffuser, due to the fairly large separation distance between the impeller and diffuser. However, within the vaned diffuser entrance region, the flow was highly distorted, with large, periodic fluctuations in local flow angle, as a result of the unsteadiness in the impeller discharge flow.

This brief examination of the flow characteristics of centrifugal compressors should serve to illustrate the complexity of such flows and to

demonstrate the necessity of understanding the flow behavior, in order to achieve optimum component and stage performance in a design.

Flow in Expansion System Devices

Expansion system devices typically consist of one or more stages of axial or radial turbines. In aero engine applications, axial turbines are almost exclusively used. Radial turbines more frequently find applications in small devices, such as auxiliary power units for aircraft, turbochargers, and small industrial gas turbines.

Flow in turbines is characterized by large, favorable pressure gradients and high heat-transfer rates, resulting from the hot gases that have exited the combustor. The composition of those gases differs from that of air, containing exhaust products from the combustion process. Because of the high-temperature environment to which turbines are exposed, film cooling flows are utilized to protect the turbine components and end walls from thermal damage. These cooling flows are injected into the primary flow path from holes in the turbine blades, and from the end walls. Interaction of the coolant jets with the primary flow results in complex flow structures with high-temperature gradients in the primary gas path.

As with compression systems, the typical turbine flow field is further affected by blade and end-wall boundary layers, blade–end-wall interaction, rotation, relative shroud motion, tip leakage flow, shocks, shock–boundary-layer interaction, unsteady flow, and blade-row interaction, resulting in a highly complex, three-dimensional flow.

In the following sections, many of these aspects of the turbine flow field will be explored in more detail, for both axial and radial components.

Flow in Axial Turbines

Axial turbines use one or more stages of stators and rotors to expand the flow that exits from the combustor. They operate at high rotational speed and can experience transonic flow. The flow paths associated with these turbines have small radius change through the blade rows, with the incoming and exiting flow primarily in the axial direction. Axial turbine blades frequently have a fairly low aspect ratio and high turning. They are typically quite thick, with blunt leading edges, to accommodate internal cooling passages.

Because the turbine operates in an environment of hot exhaust gases from the combustor, heat transfer is a major concern. The first stages of the turbine will bear the brunt of the high-temperature flow, and as a result, they typically feature some form of cooling flow. This flow can be injected

from internal cooling passages, through orifices in the blade, to provide a protective film of lower-temperature air along the airfoil surface. Cooling air can also be injected along the end walls. As a result, the primary flow will be influenced by this cooling flow. Additionally, the behavior of the hot gases from the combustor will be altered as the flow passes through each successive blade row of the turbine.

The performance of axial turbines can be affected by many complex flow phenomena. Therefore, an understanding of the structure and heat-transfer characteristics of the flow is of paramount importance to a successful design. While it is impossible to examine all these characteristics here, a representative selection of typical flow phenomena will be discussed briefly, to provide a general impression of the complex nature of axial turbine flow fields.

Significant contributors to loss in axial turbines are the end-wall boundary layer and the associated secondary flow. These flow structures have been examined by a number of investigators over the years. Langston et al. [22] performed a detailed study of three-dimensional flow within a subsonic plane turbine cascade, which concentrated on end-wall flow. Sieverding [23] compiled a comprehensive review of secondary flow phenomena in straight turbine blade passages. He described secondary vortex flow structures and their effect on end-wall boundary layers and losses. Sharma and Butler [24] provided additional insight based upon further experimentation with cascades. More recently, Detemple-Laake [25] examined end-wall flows for a transonic plane turbine cascade. Based on their descriptions, a summary of end-wall and secondary flow characteristics may be compiled.

In the region of the leading edge, the end-wall boundary layer separates and rolls up into a horseshoe vortex. This vortex has two legs, which wrap around the leading edge onto both the pressure and the suction sides of the blade. The two legs of the horseshoe vortices entering any passage of the cascade are counterrotating.

As the pressure-side leg of the horseshoe vortex enters the passage, it is convected toward the suction side of the adjacent blade, due to the blade-to-blade pressure gradient. Strong end-wall flows across the passage, from the pressure to the suction side, feed the pressure-side leg of the vortex and it grows into the passage vortex, which is the dominant feature of the flow field.

The suction-side leg of the horseshoe vortex is swept onto the suction surface behind the leading edge, due to the transverse pressure gradient in the passage. The suction-side vortex follows the contour of the airfoil suction surface, remaining near the end wall, until the passage vortex interacts with it, and the suction-side leg of the vortex is forced away from

the end wall. As the flow continues downstream, the suction-side leg of the vortex "orbits" around the outside of the passage vortex, which has the opposite sense of rotation.

A majority of the fluid from the inlet boundary layer is swept up in the horseshoe vortex; however, the fluid representing the innermost part of the original cascade inlet boundary layer does not become part of the vortex. Instead, this fluid is convected toward the suction side of the blade, where it climbs the airfoil surface, forming a narrow band of fluid on the airfoil, and exits the blade row on top of the passage vortex.

Because all the fluid from the inlet boundary layer either has become part of the horseshoe vortex or has been convected toward the suction side, a new, much thinner end-wall boundary layer is formed downstream of the horseshoe vortex system. As the pressure-side leg of the horseshoe vortex progresses across the passage, it entrains low-momentum fluid from this newly formed end-wall boundary layer and grows to become the passage vortex.

Blade boundary layers and wakes also contribute to the loss in an axial turbine. Stastny and Safarik [26] examined blade boundary-layer behavior in a straight transonic turbine cascade. They determined that on the suction side of the blade a loss of stability of the laminar boundary layer took place, in the throat region, at the location of the first supersonic compression. This was followed by a sudden transition to turbulence. A loss of stability also occurred in the laminar boundary layer on the pressure side, but transition to turbulence did not take place, due to the subsequent acceleration of the flow, following the supersonic compression.

Flow characteristics of the wake downstream of an axial turbine stator were examined by Binder and Romey [27]. Their studies focused on mixing of the wakes and the behavior of the secondary vortex flow. They investigated the losses due to wake flow at four axial stations downstream of the stator trailing edge.

Near the trailing edge, the wake was observed to be a high-loss region, somewhat skewed to the radial direction, due to the radial distribution of the stator exit flow angle. In addition to the presence of the wake, two other regions of high loss were detected, near the end walls. These structures were the result of hub and shroud passage vortices. The high-loss region due to the shroud passage vortex was shifted inward from the shroud, while that associated with the hub vortex was positioned quite close to the hub. This behavior resulted from the radial pressure gradient, produced by centrifugal forces within the blade row, which generated a flow toward the hub, causing the passage vortices to migrate radially inward. Within the wake, there was an even stronger flow toward the hub, causing the low-energy fluid from the wake to also migrate inward, increasing the loss regions near the hub.

Further downstream, the wake was even more skewed to the radial direction. Near the shroud, the wake was deformed by the shroud passage vortex. Also present within the wake were other vortices associated with both trailing-edge shed vorticity and vorticity remaining from the suction-side leg of the horseshoe vortex. Both the mixing of the wake and the radial-inward flow of the low-energy fluid tended to reduce losses in the wake. By approximately 3.3 chord lengths downstream, the discrete regions of high loss had been mixed out, and the wake itself was no longer visible.

Shocks and shock–boundary-layer interaction also represent major sources of loss in a transonic axial turbine flow field. Graham and Kost [28] and Detemple-Laake [25] examined the interactions between shocks and boundary-layer flows for high-turning transonic turbine cascades, over a range of exit Mach numbers. A summary of their findings provides some insight into the complexity of shock–boundary-layer interactions.

For subsonic exit Mach numbers, the passage flow accelerates rapidly along the suction surface, expanding down to the throat, with local regions of supersonic flow. These supersonic regions terminate downstream at a normal shock. As the exit Mach number increases through sonic conditions, the cascade becomes choked and the flow expands supersonically downstream of the throat, producing a strong normal shock at the trailing edge.

With further increases in exit Mach number, this trailing-edge shock structure becomes stronger and more oblique, eventually producing a system of deflected and reflected shocks. The suction side of the trailing-edge shock is deflected by the adjacent blade wake. The pressure-side branch of the trailing-edge shock crosses the passage to impinge on the suction surface of the adjacent blade. This impinging shock is then reflected away from the suction surface, as a sequence of compression–expansion–compression waves.

Depending on the strength of the trailing-edge shock, the pressure increase across the branch of the shock impinging on the suction surface may cause the laminar suction surface boundary layer to be lifted, developing a separation bubble. As exit Mach numbers are increased into the supersonic range, the trailing-edge shock structure becomes more oblique, such that both the impingement point and the boundary-layer separation move along the suction surface toward the trailing edge. At reattachment, the boundary layer becomes turbulent.

Unsteady flow and blade-row interaction effects can strongly influence the structure of the secondary flow field in axial turbines. Zeschky and Gallus [29] examined the effect of upstream stator wakes on the flow through a subsonic axial turbine rotor. They found that the rotor flow was significantly influenced by the periodically unsteady inlet conditions caused by the stator.

The effect of stator wakes could still be detected at the rotor outlet. Variations of the time-averaged rotor exit velocity and exit flow angle were observed that corresponded to stator wake passing. The highest fluctuations of these flow properties were detected in the hub and tip regions, where the deep stator wakes and the "chopping" of stator secondary vortices produced periodically high turbulence levels and amplified cross-flow velocity components toward the suction side.

The stator wakes impinging on the rotor blade surface also triggered early boundary-layer transition, which increased the turbulence intensity in the wake and reduced the free-stream velocity at the edge of the wake, thus leading to higher profile losses.

The flow in multistage axial turbines becomes even more complex. Arndt [30] examined the unsteady flow phenomena in a five-stage low-pressure turbine. Measurements were made downstream of each of the rotor blade rows.

Arndt found that both rotor–rotor and stator–rotor interactions had a substantial impact on the flow through the turbine, and both forms of interaction were found to be of comparable significance.

Rotor–rotor interactions resulted primarily from the wakes shed by one rotor blade row influencing the flow through the next downstream rotor. This wake-induced rotor–rotor interaction produced strong periodic velocity fluctuations for every rotor blade row downstream of the first stage.

Stator–rotor interaction resulted from the effect of the circumferentially nonuniform stator exit flow upon the next downstream rotor blade row. Circumferential variations in wake depth and turbulence level were measured downstream of each rotor. In addition, there was a strong influence on the overturning and the underturning of the rotor wakes in the end-wall regions.

The previous examples of blade-row interaction in axial turbines focused on subsonic flows. However, the unsteady passage of shock waves through a turbine stage can also have a significant impact on the flow behavior and the aerodynamic performance of the turbine blade rows.

Flows in high-pressure-ratio turbines are dominated by shock structures that pass downstream into the next blade row in an unsteady fashion. Collie et al. [31] studied the unsteady effects of shock waves passing through a cascade blade row. They observed that shock waves from the upstream blade row were repeatedly reflected across the blade passage, with continually decreasing shock strength. In addition, they found that the pressure-side branch of the trailing-edge shock moved toward the rear of the cascade, during passage of the shock from upstream, until it was almost connecting with the adjacent trailing edge, and then it began to recover back

to its original position. This unsteady behavior of the flow resulted in large fluctuations in blade lift and cascade loss.

Heat transfer is another extremely important consideration in turbine flow fields, due to the exposure of the blade rows to the hot exhaust gases from the combustion process.

Blair [32] studied the heat-transfer distribution on the blade surfaces and the hub end wall in an axial turbine rotor passage. The investigation focused on the effects of hub and tip secondary flows, tip leakage, and the leading-edge horseshoe vortex system. All of these three-dimensional flow structures were found to produce local regions of substantially enhanced heat transfer.

On the suction surface, the hub and tip secondary flows were responsible for heat-transfer rates up to 60% higher than in the midspan region of the rotor. However, the highest heat-transfer rates on the suction surface, almost double the midspan values, were observed in a highly localized region near the tip, where the tip leakage flow rolled up into a vortex.

The leading-edge horseshoe vortex caused enhanced heat transfer in the region near the intersection of the rotor leading edge and the hub end wall. Heat-transfer rates in this region were almost double the values seen on the end wall at the leading-edge midpitch.

Also of importance in a highly three-dimensional turbine flow field is the behavior of hot streaks from the combustor exit and cooling flows from upstream blade rows. Roback and Dring [33, 34] used a large-scale rotating rig with a $1\frac{1}{2}$-stage turbine model to examine the impact of a nonuniform turbine inlet temperature profile due to combustor-generated hot and cold streaks, and also to investigate the effect of "phantom cooling," which occurs when cooling air discharged from the trailing edge of the upstream stator collects in a nonuniform manner on the downstream rotor. Their investigation revealed the locations on the turbine rotor where hot and cold streak accumulation and phantom cooling were most likely to be strongest.

The experimental study revealed that the hot streaks tended to accumulate on the pressure surface of the rotor, while cold streaks accumulated on the suction surface. This difference in behavior resulted from the difference in densities of the two streams. It was also observed that the streaks could migrate to the hub and tip regions of the rotor, depending on the spanwise location at which they were introduced. Thus, the streaks could alter temperatures at both end walls and the rotor tip. However, hub and tip secondary flows on the rotor acted to minimize the accumulation of cold streaks near the end walls, by preventing them from reaching the suction surface.

The stator coolant flow behavior was strongly influenced by the coolant velocity. Under typical turbine operating conditions, where the coolant velocity was less than the free-stream velocity, the coolant flow tended to accumulate on the rotor suction surface, where hot streak accumulation was weakest. The coolant flow did not reach the pressure surface, where hot streak accumulation was the strongest, unless the coolant velocity exceeded the free-stream velocity.

Joslyn and Dring [35] examined the behavior of a simulated spanwise inlet temperature profile, as it passed through all three blade rows of a $1\frac{1}{2}$-stage axial turbine. They investigated the effect of the three-dimensional flow field on the mixing of the essentially parabolic inlet temperature profile and found that although all three blade rows contributed to the profile mixing, the impact of the rotor was greatest.

The primary sources of radial mixing within the first stator were found to be the radial flow in its wake due to the radial static pressure gradient, and the end-wall secondary flows. Additional radial mixing took place in the axial gap between the stator and the rotor.

In the rotor, radial mixing was heavily influenced by the hub and tip secondary flows, the tip-leakage flow, and the inviscid "relative eddy" associated with the rotating frame of reference. The relative eddy served to transport the hot fluid entering the rotor passage near midspan outward toward the tip along the pressure surface. This hot fluid then passed through the tip clearance gap, resulting in higher heat loads, not only at the rotor tip, but also at the second stator tip. Downstream of the second stator, mixing of the temperature profile was nearly complete.

The use of film cooling to protect turbine blade surfaces from the hot gas environment can have a significant effect on the flow behavior and can impact aerodynamic losses. Haller and Camus [36] studied the effect of film cooling on a transonic gas turbine rotor blade tested in a two-dimensional cascade. A simulated coolant flow was ejected from a row of cooling holes in the airfoil suction surface. Five different axial locations were considered for the row of cooling holes, and the results were compared with an uncooled reference airfoil.

For all of the cooled configurations examined, the impact on efficiency was minimal. Increased losses resulted, in part, from mixing of the coolant and mainstream flows and also from increased skin friction and turbulent boundary-layer mixing downstream of the injection region.

When the cooling holes were positioned very far upstream on the suction surface, in a subsonic region of rapid acceleration, the cooling film generated only small changes in blade-row efficiency. However, when the cooling holes were shifted somewhat further downstream in the accelerating region, with a free-stream Mach number only slightly below sonic, the

cooling film was found to trip the laminar boundary layer, resulting in a thick turbulent boundary layer downstream of the cooling holes.

With the cooling holes positioned just upstream of the throat, a local compression shock was produced upstream of the cooling film, and a turning shock was present downstream. The resulting disturbance to the mainstream flow was observed to extend over approximately 20% of the throat width. When the cooling holes were positioned further downstream, in the diffusing region of the suction surface, the coolant ejection generated an additional compression shock across the entire passage, as the separated film was turned back onto the blade surface.

A rapid increase in boundary-layer thickness was observed to occur across the cooling film for all cases. However, when the ejection rate was increased, the boundary layer became relatively thicker. At the higher ejection rate, the coolant jet was clearly visible, within the boundary-layer velocity profile, just downstream of the film. It gradually mixed out; however, traces of the jet were still evident near the trailing edge.

The preceding paragraphs have provided a brief survey of the complexity of the flow field in axial turbines and of the multitude of factors that can influence aerodynamic performance in turbine blade rows. Clearly, the ability to model such flow behavior is essential to the successful design of these components.

Flow in Radial Turbines

Radial turbines differ significantly from their axial counterparts. Pressure drop per stage is typically much higher than in an axial turbine. The flow undergoes a substantial radius change, passing radially inward through the stator, entering the turbine rotor radially inward, and then exiting axially.

Radial-inflow turbines offer advantages over axial configurations, in terms of simple construction, low manufacturing cost, and good performance over a wide range of operating conditions.

A typical radial turbine consists of the scroll, which directs the flow from the combustor into the stator or nozzle, the nozzle blade row, the vaneless space between the nozzle and rotor, and finally the impeller-type rotor itself. The flow is highly three-dimensional through all of these components and, in addition, is made more complex by the blade-row interaction between the nozzle and the rotor. The performance of radial turbines is strongly influenced by the losses in the nozzle and the rotor.

A brief overview of the general flow structure in each of the radial turbine components is provided next.

Malak et al. [37] investigated the flow behavior in a radial-inflow turbine scroll. They found that the flow pattern in the scroll was strongly

influenced by the geometry of the scroll cross sections and the area variation around the scroll circumference, in addition to the configuration of the scroll-to-nozzle transition. The cross-sectional geometry impacted the accumulation of low-energy flow regions, and hence contributed to the loss distribution. In the earlier scroll sections, the low-energy flow accumulation was controlled by the cross-flow velocity pattern. Through later sections the flow discharge into the nozzle became the more dominant effect, and its influence was reflected in the behavior of both through-flow and cross-flow velocity.

Details of the flow in a radial-inflow turbine nozzle were studied by Eroglu and Tabakoff [38].

Secondary flows in radial turbine nozzles were found to differ from those in axial-flow turbine cascades, because of the presence of radial pressure gradients and incidence effects. Although radial turbine nozzles produced leading-edge vortices, either the passage vortices were too weak to be detected or they did not form.

The upstream scroll geometry was found to strongly influence the flow field through the nozzle blade passages, resulting in a lack of periodicity between flow channels, and also an asymmetric distribution with respect to the two end walls. Other effects observed included significant end-wall cross flows just upstream of the trailing edge.

In addition, turbulence tended to increase as the flow proceeded downstream, which contributed to rapid mixing at the exit of the nozzle blade passages. This rapid mixing, along with high-turbulence fluctuations downstream of the trailing edge, tended to distort or smear the wakes and the free-stream regions, to the point that the wakes extended across more of the flow-path cross section than the free-stream flow.

The vaneless region downstream of the nozzle was investigated by Lakshminarasimha et al. [39]. Flow in the vaneless region was found to directly influence nozzle losses and rotor performance, through rotor–stator interaction.

The vaneless region consisted of a highly viscous, swirling flow field. The passage pressure field strongly impacted the spanwise variation of both the flow velocities and flow angles. The pitchwise variation in the velocities was most pronounced near the midchannel, in contrast to the flow angles, which were found to deviate more near the end walls.

Because of the difficulty of obtaining flow measurements within a radial turbine rotor, Zangeneh-Kazemi et al. [40] combined instantaneous measurements of shroud static pressure and exit flow distribution with numerical predictions to infer the behavior of the flow within the rotor of a low-speed radial-inflow turbine. The flow through the rotor was computed using a fully three-dimensional viscous program, and the predictions of

shroud static pressure and the exit flow distribution were compared with the actual measurements to validate the computation.

They found that the turbine exit flow showed a substantial nonuniformity, with a wake region of high loss and high absolute flow angle near the shroud, between the suction surface and the midpitch, and a jet located near the pressure surface. Comparison of measurements and numerical predictions indicated that the wake and the observed nonuniform flow at the exit of the turbine were due, in part, to secondary flows accumulating low-momentum fluid near the shroud-suction corner, but the tip-leakage flow also contributed significantly to the process by feeding low-momentum fluid on the shroud into the wake.

As with other radial and axial components, the flow structures typical of radial turbines are highly complex, three-dimensional, and viscous. To design such components to achieve minimum loss requires a thorough understanding of the behavior of the flow and the means to accurately predict it.

MODELING OF TURBOMACHINERY FLOW FIELDS

The preceding sections of this chapter have emphasized the complexity of flows that occur in typical turbomachinery components. Clearly, in order to successfully design such devices, the analysis tools used must be capable of adequately modeling those complex flow fields, in order to determine their influence on component performance.

The current section examines the requirements for flow analysis tools at different stages in the component design process and then focuses on the capabilities of state-of-the-art computational fluid dynamics (CFD) analysis tools, which can be employed in the later stages of turbomachinery component design, to model the details of complex flow fields.

Levels of Modeling as Related to the Design Process

The goal of the aerodynamic design process, for turbomachinery components, is to minimize losses and maximize aerodynamic performance, within the geometric, physical, and economic constraints placed on the component. This goal is accomplished through a process that consists of two primary phases: preliminary design and detailed design. These two phases differ, according to their specific purposes.

The preliminary design phase establishes the overall characteristics of the component, such that it will satisfy the requirements and constraints of the overall engine design. Basic flow-path configurations, blade counts,

blade-row spacings, and initial blade shapes are among the characteristics determined during preliminary design. The process is highly iterative, due to the large number of component and flow-path features that must be optimized, through the analysis of many configurations.

In contrast, the detailed design process focuses on one or a small number of design configurations that offer the optimum combination of features, and the best match with aerodynamic performance objectives, based on the analyses of the preliminary design. The objective of the detailed design process is to predict, as realistically as possible, those characteristics of the flow that are critical to the aerodynamic performance of the turbomachinery component being analyzed. Such characteristics would include tip clearance flows, shock–boundary-layer interactions, blade–end-wall interactions, flow separations, wakes, and any other regions of high loss.

The level of detail and capability required of a particular flow model will be determined by the phase of the design process to which it is applied. During the preliminary design process, simplifying assumptions are typically made that allow the flow to be modeled in less detail. Once the overall characteristics of a particular design have been established using these simple tools, then the detailed behavior of the flow for that configuration must be determined, using the full capabilities of the available CFD analysis tools.

Flow Modeling for the Preliminary Design Process

Because the preliminary design process is typically performed over many iterations, to optimize the component design, the analysis tools used must not only provide adequate insight into the flow behavior but also require a minimum of computation time. Therefore, the level of flow modeling employed during preliminary design is, to some extent, limited by the performance of the computer hardware and the modeling software.

Traditionally, simple flow models such as streamline curvature, radial equilibrium analyses, and blade-to-blade analyses, combined with appropriate loss models, have provided adequate information to perform an efficient preliminary design of flow-path shape and blade shape. However, although they offer speed of computation, such 2D design tools do not provide insight into three-dimensional flow behavior.

Because of recent rapid increases in computer speed, it is now possible to include 3D inviscid analyses in the earlier stages of the design process. Transonic Euler solutions for a single blade row can now be performed within minutes on many platforms and can therefore be utilized in a highly iterative design environment. Access to a 3D transonic Euler analysis at this

stage in the design process allows for earlier visibility into three-dimensional, compressible flow effects.

Although it is now possible to obtain considerable insight into flow path and component flow behavior during the preliminary design process by employing 3D Euler analysis tools, it has been emphasized in the earlier portion of this chapter that most turbomachinery flows are highly viscous, as well as three-dimensional. Therefore, to accurately model such flows, a more complete representation of the physics is necessary. To accomplish this, solutions of the 3D Navier–Stokes equations, with appropriate turbulence modeling, are required. However, at present, analysis tools employing 3D viscous flow modeling require considerable computation time and therefore are not well suited to preliminary design.

Flow Modeling for the Detailed Design Process

Often, during the detailed design process, design features that are specifically three-dimensional in nature are being evaluated. Characteristics that can significantly impact component performance, such as blade lean, bow, scallop, sweep, fillet radius, midspan damper position, impeller splitter blade position, and tip clearance height, must be optimized, based on their influence on a viscous flow field. To evaluate such issues in a test rig would be far too costly and time-consuming. Therefore, the analytical tools of the detailed design process must model the flow physics with sufficient accuracy to assist in the evaluation process.

To achieve the necessary level of accuracy, a 3D viscous transonic flow model must be employed in the analysis tools. The application of such a model will result in solution times several orders of magnitude longer than those for preliminary design tools. However, the expense in terms of computation time can be offset by reductions in both design/development cycle time and design risk. By employing 3D viscous flow analysis tools during the detailed design, the necessity of performing one or more redesign/retest iterations can be greatly reduced. In addition, for those components that cannot typically be redesigned, due to schedule constraints caused by long lead times for hardware acquisition, the likelihood of a successful design can be greatly enhanced by using accurate flow modeling tools.

The capabilities required in these advanced aerodynamic analysis tools are the focus of the next section of this chapter.

Critical Capabilities for Turbomachinery Flow Analysis Tools

The degree to which a CFD analysis program functions successfully as a detailed design tool depends on how closely it meets certain requirements.

Obviously, the physical model must be sufficiently accurate to represent those aspects of the flow that will impact aerodynamic performance. Governing equations that model 3D viscous transonic flow are essential to satisfy this requirement. The specification of boundary conditions for the governing equations should be general enough to accommodate all types of boundaries encountered in turbomachinery flow paths. In addition, the turbulence model should adequately account for the characteristics of typical turbomachinery flow fields, such as flow-path curvature, rotating flow, high-pressure gradients, and separated, recirculating flows. The capability to model unsteady flow and blade-row interaction is also necessary, if blade rows are to be analyzed as stages rather than as isolated components.

The selection of numerical solution techniques is also a critical issue. Discretization of the governing equations and choice of solution techniques for the resulting finite-difference or finite-volume approximations to those equations are at least partly dictated by simplifying assumptions made regarding the character of the flow. Thus, these selections must be compatible with the flow behavior anticipated in the components being analyzed.

Representation of the geometric configuration of the component, via the solution grid, must also reflect physical reality. Solution grids must be able to accurately depict blade and flow-path shapes and model complex details such as tip clearance regions. In addition, these grids must be able to resolve the details of the flow structure. Various grid types exist that will satisfy these requirements with varying degrees of success, depending on the application. The proper selection of a solution grid is essential, to ensure the accuracy of both the modeled component geometry and the flow analysis.

Program performance is also of considerable importance for detailed design flow analysis software. Because of the complex nature of the equations being solved, such software typically can require several days of computation time to obtain a solution. Therefore, optimization of the software is essential. Use of vectorization, and parallelization, where possible, are also valuable techniques for improving performance of the analysis tools.

Pre- and postprocessing also warrant consideration, due to the significant amount of time that must be invested in both preparing the input for an analysis and interpreting the results of a completed analysis. ''User-friendly'' tools are essential to assist in these processes. Most importantly, the use of an interactive graphical user interface can dramatically improve the efficiency of both of these stages of the analysis process.

Each of these areas will be discussed in detail in the following sections.

Flow Physics Modeling

Modeling of the flow physics for turbomachinery components encompasses the selection of a representative set of governing equations, the assignment of appropriate boundary conditions, and, for the case of turbulent viscous flow, the choice of a turbulence model to achieve closure of the governing equations. Special consideration may also be required for the modeling of blade-row interaction, for multiple blade-row analyses.

Governing Equations and Boundary Conditions. To accurately represent the 3D viscous transonic flows encountered in aero engine turbomachinery components, the flow model should be based on the full Reynolds-averaged Navier–Stokes equations. This set of governing equations, which is most appropriately cast in a rotating, cylindrical coordinate system, consists of equations for the conservation of time-averaged mass, momentum, and energy, along with an equation of state (the perfect gas law), the Stokes hypothesis relating the second coefficient of viscosity to the molecular viscosity, and Sutherland's law, which expresses molecular viscosity as a function of temperature. In addition, a closure must be provided for the turbulent Reynolds stress and turbulent heat-flux terms.

The primary dependent variables of the governing equations are density, the three components of velocity, total energy, pressure, total enthalpy, the nine components of the turbulent Reynolds stress tensor, and the three components of the turbulent heat-flux vector.

The governing equations are presented in most sources, including Lakshminarayana's excellent review of CFD techniques for turbomachinery design [41], which contains the differential form. Dawes [42] presents the equivalent control volume formulation.

The use of either a differential or control volume representation for the governing equations is determined by whether a finite-difference or finite-volume discretization is being used for the numerical solution. This will be discussed further in the section on numerical solution techniques later in this chapter.

Closure for the turbulent stress and heat-flux terms is achieved through the use of a turbulence model. Many turbulence models exist, of varying levels of complexity and accuracy in representing the physics of turbulent flow. A discussion of the relative merits of some of these models is provided in the next section of this chapter.

Use of the complete Reynolds-averaged Navier–Stokes equations as a governing equation set will permit the representation of the most general unsteady, 3D, viscous, transonic, turbulent flows with rotation. However, under some circumstances, a thin-layer assumption would reduce the complexity of the governing equations. In the thin-layer assumption,

streamwise diffusion terms are considered negligible. This assumption is valid for thin viscous layers, but is not appropriate for flows that contain substantial recirculation zones, or other significant viscous structures that would produce measurable streamwise diffusion.

Other levels of approximation offer even simpler representations of the governing equations; however, such flow models are not general enough to encompass many of the flows encountered in high-performance turbomachinery components. Although the use of approximations to the governing equations offers benefits in terms of equation simplicity and, therefore, solution speed, the design tool that employs such a simplified model sacrifices generality. Often, the benefits of having a more general CFD analysis tool will far outweigh the benefits of a faster tool that is only appropriate over a subset of the expected flow conditions.

The solution of the governing equations is performed over a finite space, on which a computational grid has been imposed. In order to properly model the flow physics within this space, a set of appropriate boundary conditions must be specified for the governing equations. Three different types of spatial boundaries may be identified for typical turbomachinery components: (1) wall boundaries, (2) inlet and exit boundaries, and (3) periodic boundaries.

Wall boundaries consist of blade surfaces, passage end walls, or the solid surfaces of other objects in the flow path. These boundaries may be rotating, nonrotating, or a combination of both. For solid walls, a zero-relative-velocity or no-slip condition is appropriate. Thermal boundary conditions must also be considered, through the specification of a wall temperature or a normal temperature gradient.

The most natural form of the inlet and exit boundary conditions is used to set the mass flow rate, by specifying both total pressure and temperature, along with flow angle or tangential velocity, upstream, and static pressure at the downstream boundary. Depending on the type of turbulence model selected, distributions of turbulent kinetic energy or some similar property at the inlet would also be required. The inlet and exit boundaries should be placed far enough away from the blade row that they are not influenced by its presence. Typically, this is achieved by positioning the boundaries anywhere from 50% to 100% of the blade chord upstream and downstream of the blade row. The distribution of inlet conditions may include spanwise variations, or possibly both spanwise and tangential variations, if the tangential distribution has the same period as the pitch of the solution space. Modeling of nonperiodic inlet conditions, as for inlet distortion, would essentially require that the solution space extend over the entire annulus.

Periodic boundaries upstream and downstream of the blade row are used to model the repetitive nature of the flow conditions from one blade

passage to the next, assuming that the inlet and exit conditions are also periodic. As in the case of inlet conditions, if for some reason the flow is not periodic over a single blade passage, then multiple passages would have to be modeled, representing a periodic set. Periodicity is enforced by setting the dependent flow variables equal at equivalent positions on the periodic boundaries.

Initial conditions for the dependent variables are also of concern, for both unsteady flows and steady flows, which are solved using time-marching techniques (described later in this chapter). The initial conditions differ from boundary conditions, in that they are not held fixed throughout the solution. Rather, they provide a starting point for the entire flow field, from which the solution will migrate. Although the initialization can be somewhat crude and still yield a successful solution, convergence can often be accelerated if the initialized flow distribution is reasonably realistic. Often, solutions from a preliminary design streamwise curvature program or a 3D inviscid analysis can be adapted for use as a flow-field initialization for steady flows. Similarly, unsteady flows are typically initialized using the steady flow solution.

Having established a set of governing equations for the flow, and having also identified the necessary boundary conditions that must be specified in association with those equations, it remains to deal with the turbulence closure by selecting an appropriate turbulence model. This issue will be addressed in the next section.

Turbulence and Transition Modeling. A wide variety of turbulence models is available to provide closure for the turbulent stress and heat-flux terms in the Reynolds-averaged Navier–Stokes equations. These range from relatively simple zero-equation models, which algebraically represent the turbulent stresses in terms of an empirically derived turbulent, or eddy, viscosity, through two-equation models, which utilize partial differential equations for the transport of two turbulence properties that are then related to turbulent viscosity, to more complex algebraic and full Reynolds stress models, which, as the names suggest, treat each term of the Reynolds stress tensor and turbulent heat-flux vector separately to obtain a more realistic representation of three-dimensional turbulence. Models of greater complexity, such as large eddy simulation or solutions of the full Navier–Stokes equations, are not practical at this stage for use in turbomachinery analysis tools, due to the large amounts of computation time required.

The simple zero-equation models, of which the Baldwin–Lomax model [43] is perhaps the most prevalent, require only the solution of an algebraic equation for turbulent viscosity. This type of model is adequate for the prediction of 2D boundary-layer flows, without separation; however, it

tends to be less satisfactory when three-dimensional flow, curvature, rotation, and adverse pressure gradients are present. Clearly, these conditions occur regularly in turbomachinery applications. Therefore, although the zero-equation models are desirable because of their simplicity and low impact on computation time, they are not sufficiently general to be appropriate for turbomachinery flows.

Two-equation models offer a somewhat more representative picture of the physics of turbulent flow, by utilizing two partial differential equations, which govern the transport of selected turbulence properties. Typically, those properties are turbulent kinetic energy and turbulent energy dissipation, although other properties are occasionally used. Once the turbulence properties are computed, by solving the transport equations, they are then used in an algebraic model to obtain a turbulent viscosity, in a similar manner to the zero-equation models. The two-equation model of Lam and Bremhorst [44] is frequently used for turbomachinery applications.

The advantage of the two-equation models is found in their more realistic modeling of turbulence properties, which imposes only a small penalty in terms of computation time (due to the requirement of solving two additional partial differential equations). However, the Reynolds stress terms in the Navier–Stokes equations are still being modeled using a turbulent viscosity. In addition, a set of constants must be specified in the transport equations. These constants, which are determined from experimental data for simple flows, actually vary from one flow regime to another and therefore are not always calibrated to the particular flow being analyzed. Therefore, although the two-equation models represent an improvement over the zero-equation models, many of the same shortcomings are still present, because of the basic assumption that the Reynolds stresses may be modeled through the use of a turbulent viscosity. Thus, the two-equation models, in their basic form, are still inadequate for flows with rotation, curvature, adverse pressure gradients, and a high degree of three-dimensionality.

Some researchers have attempted to compensate for the shortcomings of the turbulent-viscosity-based models by introducing modifications into the transport equations to treat the more complex flows. For example, both Hanjalic and Launder [45] and Nagano and Tagawa [46] have presented two-equation models that attempt to deal with adverse pressure gradients. Abid [47] has developed a version of the two-equation model that addresses both pressure gradients and compressibility. Another approach that offers greater accuracy is renormalization group theory [48, 49], which permits a local analytical, rather than an empirical, representation of the constants in the model. These techniques attempt to expand the range of application of the two-equation models. However, the basic assumption remains, namely, that the Reynolds stress terms may be modeled using a turbulent viscosity.

The next step in modeling accuracy is taken with the algebraic Reynolds stress model. Once again, partial differential equations are solved for the transport of two turbulence properties. However, in this type of model, these variables are not used to compute turbulent viscosity, but rather are used in individual algebraic equations for each of the Reynolds stress and turbulent heat-flux terms. In this way, more of the physics of the turbulent flow is preserved, and complex three-dimensional flows including curvature and rotation may be predicted accurately. The impact on computation time is not substantially higher than that for a two-equation model, however, because of the simplicity of the algebraic equations used to model the Reynolds stress tensor and turbulent heat-flux vector.

Examples of algebraic Reynolds stress models may be found in Rodi and Scheuerer [50] and also Zhang and Lakshminarayana [51]. The latter presents a successful application of the model to a compressor rotor flow prediction.

The next level of sophistication in turbulence modeling, the full Reynolds stress model, offers a much more realistic representation of turbulent flow. However, this accuracy comes at the price of significantly greater modeling complexity. The complete set of Reynolds stress transport equations must be solved, which approximately doubles the number of partial differential equations in the governing equation set. This imposes such a substantial computational penalty that the application of this model is presently outside the realm of practicality for turbomachinery flow analysis tools.

Therefore, based on the computing power available today, the two-equation models, with complex flow enhancements, would represent a minimum desired level of turbulence modeling capability for turbomachinery analyses, with the algebraic Reynolds stress models being preferred for additional accuracy.

The field of turbulence modeling is very active, and much current literature exists on specific models. Patel et al. [52] reviewed a variety of models for near-wall flows, and a comprehensive review paper by Lakshminarayana [53] provides many references to models being used in turbomachinery applications. In addition, Speziale [54] has produced a detailed examination of recent developments in Reynolds stress modeling.

Transition modeling, to predict the transition from laminar to turbulent flow, has received less attention for turbomachinery applications. However, a recent study by Mayle [55] provides an extensive look at the current status of this field. Among Mayle's conclusions are that transition in gas turbines is largely influenced by free-stream turbulence, pressure gradient, and the periodic, unsteady passing of wakes; in contrast, surface roughness, surface curvature, compressibility, and heat transfer have only a

secondary effect on transition. Walker [56] has offered an additional viewpoint on Mayle's work. The primary conclusion that may be drawn from these papers is that the field is not yet mature enough to provide a tested and consistently reliable model for transition in turbomachinery flows.

Unsteady Analysis and Blade-row Interaction. Most turbomachinery flows are unsteady in nature, as a result of phenomena such as vortex shedding triggered by flow separation, passage of upstream viscous wakes, or blade-row interaction in a multistage machine. In many cases, these flows are assumed to be steady, for the convenience of analysis. However, when it becomes necessary to invoke more realistic unsteady analysis techniques, special modeling considerations must be examined.

Boundary conditions for the Navier–Stokes equations must account for the unsteady nature of the flow at the inlet and exit of the computational grid. Upstream wake-passing effects, for example, must be communicated into the solution domain via unsteady boundary conditions. One approach to modeling these unsteady boundary flows involves the use of characteristic variables employing Riemann invariants [57].

Preservation of periodicity must also be considered, when the unsteady flow results from a spatially periodic forcing function, such as the passage of upstream wakes or the presence of an upstream blade row. To obtain a truly periodic solution, the ratio of upstream disturbances (wakes, blades, etc.) to downstream blades in the computational domain must match, as closely as possible, the actual ratio for the components being analyzed. When this ratio is far from 1:1, then the size of the problem becomes much larger, due to the increased number of passages that must be accommodated in the computational grid to encompass a periodic region.

Blade-row interaction presents another level of complexity in the modeling of unsteady flow, because the computational grids associated with each blade row are in motion relative to one another. A variety of approaches has been considered to treat the interface between blade rows, including the use of sliding, patched, and overlaid grids.

The analysis of unsteady turbomachinery flow fields is an active area of research. Scott and Hankey [58] have developed a technique to predict unsteady flow through a transonic compressor rotor with periodic upstream wake passing. Also, Furukawa et al. [59] have applied an unsteady technique to the analysis of a transonic turbine cascade with periodic trailing-edge vortex shedding. Rai [60] has been a major contributor in the area of viscous blade-row interaction, and recently his technique has been applied to the analysis of a $2\frac{1}{2}$-stage compressor [61].

A substantial computational overhead is imposed when performing a time-accurate analysis, particularly for blade-row interaction. Grid sizes

tend to be large, due to the necessity of modeling in three dimensions not only multiple blade rows but also multiple blade passages, in order to achieve a periodic segment of the annulus. Such computational requirements can rapidly exceed the time constraints and computer resources of most component design efforts at the present time.

One approach to avoid the massive amounts of calculation time required for an unsteady 3D blade-row interaction analysis is to perform a steady-flow solution for each individual blade row, and communicate circumferentially averaged flow conditions between adjacent blade rows via a mixing plane. Because the flow field at each mixing plane is essentially time-averaged, nonperiodic circumferential conditions that result from dissimilar blade counts are not an issue. Therefore, only one passage needs to be analyzed for each blade row. As a result, the problem size and calculation time are considerably reduced, compared to an unsteady blade-row interaction analysis. The mixing plane approach has been taken by Dawes [62], with his multistage program, and has also been applied to the method of Hah and Wennerstrom [63].

Adamczyk [64] has developed an alternative approach for multiple blade-row analyses, which utilizes an "average-passage" model. The governing equations in this model provide a time-averaged 3D representation of the flow through a typical passage of each blade row. Individual solutions are performed for each blade row, with the effects of adjacent rows being modeled by averaged blockage and body forces. A correlation model is used to represent the interaction between blade rows. The computational cost of the average-passage model is intermediate between the mixing plane model and the unsteady blade-row interaction analysis. However, the average-passage simulation becomes more complex and costly as the number of blade rows increases.

The decision to utilize a full unsteady analysis technique depends largely on what type of information is desired. If only time-averaged flow properties are of interest, then a steady, isolated blade-row analysis or a simplified blade-row interaction model should suffice, with a considerable savings in computational effort. However, in other cases, the ability to resolve the time-unsteady nature of the flow is essential, to model such effects as vortex shedding, wake passage, or blade-row interaction. Then a full unsteady analysis is required.

Numerical Solution Techniques

The subject of numerical solution techniques is too extensive to be covered in any detail in this chapter. Only a cursory discussion of methods appropriate to the solution of the time-dependent Reynolds-averaged

Navier–Stokes equations will be presented. Details of the various solution techniques may be found in texts by Hirsch [65] and Anderson et al. [66]. In addition, an excellent survey is provided by Lakshminarayana [41] in his review of CFD techniques for turbomachinery applications.

In order to numerically solve the set of governing equations for a particular turbomachinery flow field, the partial differential or integral equations of the continuous solution domain must first be discretized into a set of algebraic equations, which are applied at discrete points or cells in the computational grid. These algebraic equations are then solved, using a numerical solution technique that can be implemented as a computational algorithm.

Depending on the formulation of the governing equations, they may be discretized into a finite-difference, finite-volume, or finite-element representation. The finite-difference method approximates the derivatives in the differential form of the governing equations by difference expressions formulated at discrete points in space. Because the finite-difference method relies on the construction of differences between adjacent points, it requires the use of a structured computational grid. In contrast, finite-volume methods discretize the integral form of the governing equations. The integral equations are applied to a small control volume around every point in the computational grid. This approach ensures that mass, momentum, and energy remain conserved in the discretized formulation. Because the finite-volume method utilizes a control volume concept, arbitrary computational grids may be accommodated. The finite-element method also employs an integral formulation of the governing equations, as obtained from the differential form, through the use of the method of weighted residuals. As with the finite-volume method, finite-element approximations may utilize computational grid cells of arbitrary shape and size. Hirsch [65] presents a detailed discussion of each of the discretization techniques.

Finite-volume schemes are experiencing widespread usage today for turbomachinery CFD applications, replacing the previously dominant finite-difference discretization. Finite-element schemes, although popular for mechanical applications, have received less attention in computational fluid dynamics. The increasing usage of finite-volume techniques recognizes their improved ability to conserve mass, momentum, and energy, relative to the finite-difference methods. The flexibility afforded by the use of arbitrary computational grids is also a distinct advantage for the finite-volume methods.

Once the governing equations have been discretized, the resulting set of algebraic equations must be solved numerically. The most appropriate solution techniques for the discretized time-dependent Reynolds-averaged

Navier–Stokes equations are time-marching schemes. Both explicit and implicit time-marching solutions are used; however, each has advantages and disadvantages. Explicit time-marching methods are simpler, in that they allow the solution to be directly calculated at each cell, using known conditions at the old time level. However, they impose a stability criterion on the size of the time step used in the marching process. That stability criterion is a function of the grid cell size and may require the solution to proceed very slowly in time, if small cells are present in the computational space. In contrast, implicit solution schemes are not limited by such a stability criterion and may use larger time steps; however, they are formulated as a set of simultaneous equations, which must be solved as a system. To avoid the substantial computation time required for matrix inversion, other techniques, such as approximate factorization, are often employed to simplify the computation for implicit methods.

To achieve better performance, other hybrid algorithms have also been developed, which employ characteristics of both implicit and explicit schemes. Jameson and Baker [66] introduced implicit residual smoothing in an explicit Runge–Kutta technique to relax the stability criterion imposed by the explicit technique. Also, Dawes [67] devised a two-step explicit and one-step implicit variation on the implicit Beam and Warming algorithm.

Another approach to improve performance involves the use of local time stepping. If only a steady-state solution is desired, as opposed to a true unsteady analysis, then explicit time marching may be performed with unequal time intervals at various cells within the computational grid. This allows stability constraints to be locally satisfied, while still permitting the solution to converge as rapidly as possible, on highly stretched grids.

To analyze flow phenomena that are unsteady, such as vortex shedding, wake passing, and blade-row interaction, requires that the time-marching solution be performed with uniform time steps, such that the entire flow is advanced in time by the same amount with every time step. It is also necessary that the solution be allowed to proceed long enough in time, from an initialized state, to establish periodic flow behavior. This can impose very long calculation times on the solution, particularly when stability criteria governed by dense packed grids require that small time steps be taken.

As Lakshminarayana [41] points out in his review of CFD techniques, both explicit and implicit schemes offer similar levels of maturity and have been used successfully for turbomachinery flow analyses. Neither approach provides overriding advantages in terms of accuracy; however, explicit methods tend to require less computation time and are better suited for application on vector- and parallel-processor computers.

Geometric Modeling

The physical complexity of advanced technology turbomachinery necessitates a sophisticated approach to the description of component and flow-path geometry and the generation of computational grids within the resulting solution domain.

Geometry Description. Before a computational grid can be imposed on a particular flow-path solution domain, the geometry of the flow-path boundaries must be modeled. This numerical definition of the flow-path shape provides the framework upon which to build the computational grid.

The approach taken to describe the flow-path geometry will be determined, in part, by the complexity of the flow-path boundary shapes. Simple axisymmetric ducts, or single blade rows, could be treated with reasonably unsophisticated techniques, such as tabular representations of flow-path coordinates at selected streamwise locations. However, as the flow-path geometry becomes more complex, and as multiple objects are introduced into the analysis, the process of defining the configuration becomes more involved. Nonaxisymmetric ducts with substantial turning, flow paths with multiple blade rows and flow splitters, blades with complex shapes, tip clearance, internal cooling flow passages, etc. cannot be described with the simple approach that would suffice for less complicated geometries. Thus, the technique selected for the geometric description of components and flow paths should offer sufficient generality to accommodate complex configurations.

Another issue that must be considered in the description of flow-path geometry is that of the transfer of consistent information to other functional groups during the design process. Particularly in a concurrent engineering environment, it is essential that all functional organizations have access to and work with the same ''master'' geometric model of an object or flow path. To maintain consistency of the geometric definition of turbomachinery components throughout all functional organizations during the design and manufacturing processes, a standard method of description is required. Of equal importance is the ability to communicate this geometric description efficiently between groups. This can be accomplished using a ''neutral'' file, written in a format that makes the data accessible to all parties involved. By taking this approach, a consistent definition of component geometry is guaranteed across all interfaces during the design and manufacturing processes.

Because component and flow-path shapes constantly evolve during the design process, modification of the geometric model of the flow-path boundaries must also be easily accomplished, and the updated model must be made rapidly available to all functional groups.

To satisfy these requirements, it is desirable to utilize the geometric modeling capabilities of a computer-aided design (CAD) system, if possible. These systems offer the ability to efficiently model complex shapes, using representations such as Beziers and NURBS (Non-Uniform Rational B-Splines) to precisely define surfaces. Use of such surface-description devices allows for a relatively automated scheme for the description and modification of component geometry. CAD tools also permit easy access by different user groups via the concept of neutral files, typically written in a standard IGES format. This facilitates the concept of a master model, used by both design and manufacturing functional organizations within a concurrent engineering environment.

Grid Generation. Once the geometric model of the turbomachinery component has been established, the next step in the process of communicating this configuration to the CFD analysis program is to define the computational grid within the physical domain.

The boundaries of this region are typically defined by the flow-path surfaces (end walls, blades, etc.) and by the periodic boundaries between blade passages, where appropriate. Inlet and exit boundaries are established at points upstream and downstream, where the necessary flow conditions are assumed to be known. Within this region, a three-dimensional computational grid is applied, such that the governing equations will be solved at every point on the grid, or within every cell formed by the grid. The grid imposed on the physical domain must conform to the boundaries of that domain and must provide adequate resolution in all areas of the flow field to permit accurate prediction of the flow behavior.

Computational grids may be classified by their type of construction. A structured grid has a fixed number of points in each of three directions, and the grid lines are arranged according to some scheme that is related to the geometric configuration of the physical domain. Common types of structured grids include H-grids, C-grids, and O-grids. In contrast, unstructured grids are not oriented in predetermined directions, nor do they have a fixed number of points in any particular direction. Unstructured grids typically utilize tetrahedral elements, or volumes, as opposed to the hexahedral elements of structured grids. Because the unstructured grid is not restricted in its formation, it is well suited to complex geometric regions, where structured grids would be difficult to construct.

Grid generation for structured grids may be performed using either algebraic methods or differential equation methods. In the algebraic approach, grid coordinates are interpolated between boundary surfaces using algebraic functions. In contrast, the differential equation method uses partial differential equations, such as Poisson's equation, to determine the

position of grid node coordinates. Anderson et al. [68] discusses these techniques in more detail. In addition, Eiseman [69] presents a thorough study of both algebraic and differential equation methods for grid generation. Thompson [70] also surveys structured grid generation techniques in his review paper.

Unstructured computational grids are generated by first establishing a suitable distribution of grid points on each boundary surface of the physical domain, without imposing any predetermined connectivity on the points. Then the domain is filled with a triangular mesh, based on these boundary points, using a Delaunay triangulation technique. This method is discussed by Mavriplis [71] for two-dimensional applications, and the equivalent procedure for three dimensions is presented by Baker [72].

Due to the nature of unstructured grids, the grid points or cells may be easily clustered in any location, to improve resolution of local flow conditions. For example, a grid may be clustered in a high-gradient region to resolve a boundary layer or a shock. Structured grids may also employ grid clustering, to improve the resolution of the analysis in particular areas of the flow field; however, this clustering must be performed within the limitations of the grid structure.

Because of the relatively flexible nature of unstructured grids, they lend themselves well to the application of adaptive gridding techniques. With a solution-adaptive grid, the clustering of grid points or cells is modified as the solution develops to better resolve selected gradients of flow properties or other characteristics of interest. Adaptive gridding techniques are of utility because high-gradient regions of the computational domain may not always be identifiable a priori; e.g., the precise position of a shock may not be known at the outset of the analysis. With an adaptive grid, resolution may be enhanced at appropriate locations, as the solution evolves. Adaptive gridding techniques are discussed by Anderson [68] and Thompson [70] for structured grids, and by Kennon and Anderson [73] and Palmerio and Dervieux [74] for unstructured grids.

As the complexity of the physical domain increases, the application of a structured grid becomes more difficult, and special gridding techniques must be employed. For example, to effectively deal with physical domains containing multiple objects, such as multiple blade rows, flow splitters, midspan dampers, etc., the domain could be decomposed into smaller subregions, each of which could be gridded independently. This multiblock grid generation technique allows structured grids to be generated more easily for complex configurations, by simplifying the definition of surface boundaries. However, the bookkeeping effort related to the connectivity of the subdomains and the communication between them can require considerable computational effort. Multiblock grid generation techniques

are discussed by a number of authors in the proceedings of the Second Conference on Grid Generation in Computational Fluid Dynamics [75].

In some cases, however, the complexity of the physical domain can render even multiblock techniques ineffective. For example, an analysis of flow through complex internal cooling passages in a turbine combined with the flow in the primary gas path poses such a challenge. To satisfactorily discretize such a complex domain, the most effective approach would be to apply an unstructured grid. With the unstructured grid methodology, the entire domain could be gridded as a single block. Because unstructured grids are not sensitive to the complexity of the physical domain, they can be generated with much less effort, and in much less time, than is required for structured grids.

The development of any grid, either structured or unstructured, relies on the specification of physical domain boundaries as a basis for grid construction. As the geometry of the physical domain becomes perturbed during design iterations, those grid boundaries will change, necessitating reconstruction of the computational grid. It therefore would be desirable to tie the grid boundary specification directly to the description of the flow-path geometry during the design process. This can be achieved by integrating the grid generator and the CAD solid modeling software, such that the boundary surface grid generation is performed on the actual CAD geometry definition, e.g., a set of NURBS surfaces. Such an approach maintains the link between the CFD computational grid and the master CAD model as it evolves. One example of such an integrated CAD solid modeler/grid generator package is discussed by Rout [76], with capabilities for treating both structured and unstructured grids, in single or multiple blocks.

Analysis Tool Performance

Turbomachinery component design efforts are almost always limited by schedule and resources. As a result, the application of computationally intensive CFD analysis tools may be restricted during a design. For this reason, improvements in analysis tool performance can offer substantial benefits. Faster solutions permit the analysis of more candidate designs within a given time, thereby ensuring a greater chance of success in meeting the aerodynamic performance goals of the component. Alternatively, by performing fewer analyses but completing them more quickly, the design cycle time for a particular component may be compressed, which can free resources for other activities. With sufficient reduction in computation time, it becomes possible to use advanced CFD analysis tools that would otherwise be impractical to apply during design. As a result, complex flow

physics can be modeled more accurately, providing a much more realistic picture of the flow behavior before critical design decisions are made.

CFD analysis tool performance improvements can be achieved through both software and hardware. Solution acceleration algorithms can provide a significant reduction in computation time. However, a major source of analysis tool performance improvement today comes from the rapidly improving speed of the platforms themselves. It has been estimated that the processor speed of computers doubles every 12 to 18 months (Moore's law). Thus, to minimize the computation time for a CFD analysis tool, both software and hardware aspects of performance need to be considered.

Software-based performance improvements are dependent upon the numerical solution technique employed in the analysis. For time-marching methods applied to the solution of the time-dependent Navier–Stokes equations, a multigrid technique offers significant reduction in the time required to achieve convergence. In a multigrid algorithm, the solution is performed at each time step on a series of grids of increasing coarseness, to reduce the low-frequency errors in the solution. This convergence acceleration technique is described by Jameson and Baker [66] and has been applied to many analysis methods, including that of Dawes [77]. Multigrid schemes are ideally suited to structured grids, because the coarser grids can be easily generated by combining cells from the denser grid. However, a multigrid technique has recently been applied to an unstructured grid analysis, as described by Smith [78].

Additional performance benefits are being achieved through consistent and dramatic reductions in computational speed. These reductions are occurring as a result of improvements in computer hardware due to such technologies as RISC architecture, vector processing, and parallel processing.

Much of this technology has been implemented in workstations, to the extent that their performance is rapidly approaching that of supercomputers, but at much more affordable prices. As a result, these computational speed improvements are readily accessible in the design environment, permitting more widespread use of CFD analysis tools.

In particular, parallel processing offers an opportunity for significant performance improvements. Parallel processing allows a problem to be split among two or more processors that operate together, such that each of them executes different instructions within the same program. At the lowest level, parallel processing may be applied on workstations that have multiple processors. The compilers with such platforms automatically perform a basic level of parallelization of the software, using an autotasker. The autotasker enables the compiler to identify independent segments of the

source code, and to assign each segment to a different processor, in order to minimize idle processor time. In this way, existing software that has not been optimized for parallel processing can be compiled to achieve substantial improvements in solution speed. If the source code is modified to allow for more optimum application of parallel processing, then even better results can be achieved.

To take maximum advantage of this particular computer architecture, it is convenient to utilize multiblock grids when discretizing the computational space. By defining a number of subdomains or grid blocks equal to the number of processors, the solution of each subdomain may be assigned to a particular processor, and the solution time may be reduced by a factor almost equal to the number of processors.

Thus, through the use of affordable, state-of-the-art hardware, coupled with appropriate software techniques for solution acceleration, it becomes possible to achieve the performance necessary to utilize CFD analyses as practical design tools.

Pre- and Postprocessing Considerations

A significant percentage of the total time spent on a CFD analysis is involved in pre- and postprocessing activities. Both the setup for an analysis and the evaluation of results require considerable effort on the part of the component designer. Therefore, the use of software tools to automate or facilitate these activities has the potential to substantially reduce the time required for the analysis and improve the overall efficiency of the process.

Both the pre- and postprocessing functions must rely heavily on interactive computer graphics, due to the need for visualization of 3D objects. Display capabilities such as zooming, rotation, and translation are required in order to view the flow-path geometry, the computational grid, or the analysis results within the computational domain. The display of multiple images on the screen is also desirable, to allow inspection or evaluation of more than one view at a time. Displays must also be generated rapidly, to provide utility to the component designer.

A graphical user interface can provide ease of use for the pre- and postprocessors by allowing control, from the screen, for the displays and functions provided by the tools. Dials, buttons, and menus on the screen can be mouse-driven by the user. To support pre- and postprocessors with such capabilities typically requires the use of a graphics workstation.

Both pre- and postprocessing can be made more efficient through the application of automation. During the design process, analyses are usually performed on a number of components that are very similar in configuration. For each of these component variations, the initial computational grid

setup would typically be the same. Thus, the ability to automatically specify a preliminary grid would offer considerable efficiency in the preprocessing phase of the analysis. Also, the same types of results would be evaluated and compared during the design, requiring the same series of plots to be produced for each variation in the configuration. Therefore, automation would also be desirable, to reduce the workload on the designer during postprocessing. Automation of this form can typically be achieved through the use of scripts, to drive the pre- and postprocessors in those instances when interaction is not necessary.

Many preprocessing functions can be supported by CAD packages. These tools offer a convenient method for defining and viewing flow-path and component surfaces. Geometric modeling using Beziers or NURBS surface representations can accommodate the complex configurations encountered in advanced technology turbomachinery. Some CAD packages may also provide an interactive grid generation function, using the actual CAD geometry definition of NURBS surfaces, etc. In some cases, however, the grid generation capability is available within the CFD package itself. Whatever the source of the grid generator, the ability to view the computational grid and interactively modify the distribution of nodal points or cells is essential to the efficient preparation for a CFD analysis. Parametric modeling techniques also offer the possibility of tying the location of computational grid nodes to the configuration of the geometric model, such that the grid is automatically modified or adjusted as the geometry is varied during design iterations.

The postprocessing function for a CFD analysis provides a numerical flow visualization capability. This facility is essential for understanding and interpreting analysis results that consist of five or more dependent variables at thousands of discrete locations within the flow field. For these CFD visualization tools to be useful to the component designer, they must be highly interactive, and also "user-friendly," requiring only minimal training, in order to achieve effective utilization.

Because the postprocessor is dealing with highly three-dimensional flowfields, many traditional two-dimensional display techniques are no longer adequate. To obtain useful information in a 3D environment, the visualization tool must have the capability to display color contours of scalar properties on flow-path and component surfaces, and also on user-specified, arbitrarily oriented slices through the flow path. Vector properties at discrete grid nodes or cells are best represented by arrows, oriented in the direction of the vector, and scaled to its magnitude. Additional scalar property information may be communicated in a vector display, by superimposing a color scale on the vectors themselves. Particle traces may be generated to visualize flow behavior, by positioning "rakes" at user-

selected locations in the flow path. Particles are then released from these rakes, and their paths are determined by integrating through time, given the local velocity vector distribution.

Among other features of value in a postprocessor is the ability to compute additional functions or flow properties for display, using the standard set of dependent variables typically calculated in a CFD analysis. In some types of displays, the ability to overlay results from multiple datasets can facilitate the comparison and evaluation of component designs. Animation can also be extremely valuable as a visualization tool. The ability to display color contour plots or vector plots on a series of cutting planes sweeping through the flow path can provide significant insight into the behavior of a highly three-dimensional flow.

Software packages offering many of these pre- and postprocessing capabilities are available commercially or have been developed by NASA. Much of the necessary surface modeling capability may be found in commercial CAD packages. Grid generation is also available in some CAD packages and is often included within CFD packages themselves, along with postprocessing functions. Additional standalone postprocessors for CFD applications are available from several commercial companies, as well as NASA.

The FAST (Flow Analysis Software Toolkit) package, developed by NASA Ames Research Center, provides many of the desired features of a CFD postprocessor. FAST utilizes a mouse-driven graphical user interface to produce displays of shaded surfaces, function-mapped surfaces, flow-field vectors, particle traces, isosurfaces, and displays on arbitrary surfaces. In addition, more traditional two-dimensional plots can also be produced.

NASA-Ames has also produced similar software packages specifically for unsteady flow simulations. PLOT4D has many of the features of the FAST package, with the added capability of depicting unsteady flow via animation techniques. STREAKER generates streaklines in a manner similar to the steady-flow particle traces found in FAST.

Analysis Tool Selection

When establishing the specifications for a CFD analysis tool, prior to its acquisition or development, it is important not to restrict the program's capabilities unnecessarily. In most cases, the component designers will soon find applications for the tool that go beyond those limits. Demands will be placed on the program to analyze more complex geometries and a wider range of flow conditions than were originally intended by the program's specifications. Thus, to avoid the problem of rapidly "outgrowing" the analysis tool, due to its limitations, it is advisable to define the tool's

specifications to exceed the narrowest requirements initially envisioned as being necessary.

Specifying a higher level of capability for a CFD analysis tool can be of benefit to the entire aerodynamic design system. A program that is more general in its function can serve a wider variety of applications and may therefore reduce the need for multiple programs that are more specialized or narrowly defined.

This potential reduction in complexity of the design system has many economic benefits. A considerable investment is made, in terms of both time and money, to bring a CFD analysis program into service as a design tool, and to maintain it over its life cycle. With fewer, more general, programs in the design system, the development and maintenance efforts can be made more efficient, and possibly reduced in scope, thereby freeing resources for other activities.

A limited number of analysis tools also can have an impact on user proficiency. The aerodynamic component designer will be able to function far more efficiently as a user if the analysis tools in the design system are valid for all geometries and flow conditions that might reasonably be encountered. This reduces the number of analysis programs with which the designer must be proficient, and therefore simplifies the process of ''user calibration,'' through which the designer gains experience in how well a particular tool may be expected to predict certain flows. Application of a more general tool also reduces the possibility that an analysis program will unknowingly be extended beyond its capabilities, thereby producing inaccurate results.

Once the specifications for the CFD analysis tool have been established, it then becomes necessary to determine whether to develop the software, or to acquire existing software from an outside source.

Commercially developed CFD analysis tools and support software are becoming quite prevalent. In many cases, an entire package, including pre- and postprocessors, is provided by one vendor. An increasing number of these commercial CFD packages are specifically targeted to turbomachinery, and some are general enough in capability to treat not only blade rows, but other related configurations, including inlets and nozzles. In addition to the commercial packages, various programs, including support software, are available through NASA.

However, the ''make-or-buy'' decision must be based on the examination of many factors beyond merely the capability of the software to analyze complex turbomachinery flows. The cost of leasing or purchasing commercial software must be compared with the manpower requirements and cost of developing software in-house. In addition, from a competitive standpoint, the lead time required to place the completed tool in the hands

of the component designers must be accounted for. Once the software is in production as a design tool, the ongoing costs and manpower resources necessary to maintain and upgrade an in-house program throughout its life cycle must also be addressed. In contrast, when commercial software is leased or purchased, program upgrades and maintenance services from the vendor are often included.

Therefore, except in those circumstances when no commercial software packages meet the specifications for the CFD analysis tool, or when it is recognized that other special requirements would dictate in-house development, it would often be more cost-effective to acquire a commercial software product.

FUTURE EXPECTATIONS

The preceding sections of this chapter have presented a view of the characteristics of turbomachinery flow fields and the current status of analysis techniques used to model these flows. In the following paragraphs, an attempt will be made to focus on the trends that appear to be developing, as a result of the increasingly strong interrelationship between the aerodynamic design of turbomachinery components and the ability to realistically model and analyze the flow fields associated with those components.

Trends in Component Design

A primary driver determining the trends in turbomachinery component design in the near future will be the IHPTET program. With its goal of doubling propulsion engine performance capability by the year 2003, relative to 1980s base technology levels, revolutionary advances will be achieved in terms of reductions in specific fuel consumption (SFC) and increases in power-to-weight or thrust-to-weight ratios. As an example [79], for turbine engines in the small/medium size class, the IHPTET goals are to reduce SFC by 30% and increase power-to-weight ratio by 100%. In addition to these performance improvements, the engines are expected to be approximately 70% smaller in diameter and weight than 1980s technology engines.

While IHPTET represents revolutionary technology, the advances achieved along the way to the final goals will be progressively implemented in existing or new engine applications to improve performance. Thus, the benefits of this advanced technology program will be appearing in the design of commercial and military engines long before the program's conclusion in

2003. For this reason, it is instructive to review some of the ongoing accomplishments of the IHPTET program that would be expected to see implementation in engine applications in the near future [79].

Not only are IHPTET power plants achieving substantial improvements in SFC and specific weight, relative to 1980s technology engines, but also parts counts have been reduced by half, largely by reducing the number of compressor and turbine stages. This action also has yielded a substantial decrease in weight. Reductions in the number of compressor stages have been achieved by operating each stage at significantly higher rotor speeds and pressure ratios. Overall engine cycle pressure ratios are also being increased. In addition, higher turbine temperature levels are contributing to improved performance.

These advances in engine design would not be possible without corresponding advances in the design of individual turbomachinery components, in order to maximize aerodynamic performance.

As an example, axial and centrifugal compressor rotors are being swept to reduce shock losses and improve efficiency. In addition, axial compressor rotors are employing splitters, to achieve higher pressure ratios without incurring flow separation. The distance between axial and centrifugal compressor stages has been reduced by almost half, compared to 1980s technology engines, requiring vanes that utilize lean to improve efficiency in a more closely coupled compressor system.

Advanced turbine cooling technology is being employed to allow turbine operation at higher temperatures. Complex internal cooling passages with three-dimensional, aerodynamically shaped holes are being utilized, which require detailed aerodynamic and heat-transfer analysis for successful design.

In general, component design is experiencing an increased use of highly three-dimensional component shapes, including such devices as bow, lean, and scallop of blade rows, in order to locally control the flow, minimizing loss-producing mechanisms and maximizing performance-enhancing features of the flow.

Also, hybrid components, such as mixed-flow fans and turbines, are being employed. These devices feature characteristics of both axial and radial components, with the primary benefit of achieving a higher pressure ratio in a single stage than a pure axial device, with less radius ratio than a centrifugal impeller or radial turbine.

The increasingly complex shapes of these advanced technology components will be enabled by the application of CFD analysis tools, to model three-dimensional viscous flows and to provide the insight into the flow behavior required to achieve maximum aerodynamic performance under extremely demanding flow conditions.

Trends in Flow Modeling Capabilities

The primary trend, which will affect all others in turbomachinery flow modeling, is the steady increase in available computing power. With greater computer performance will come the ability to more rapidly perform any given level of flow analysis. As a result, design/development cycle times can be reduced, more design options can be explored, and more advanced flow analyses can be performed, leading to a better, more competitive turbomachinery component design process.

In the near term, the primary impact on flow modeling will result from faster processor speed and the increased accessibility of computing power via faster and cheaper workstations. Computer speed has been steadily increasing by an order of magnitude every 5 years. Microprocessor performance has been increasing at such a rapid rate that it is now approaching that of conventional supercomputers. As a result, the price–performance advantage of engineering workstations relative to mainframe computers is increasing substantially, accelerating the trend toward distributed computing on workstations.

Over the longer term, the introduction of parallel-processor computers will have an increasing impact on how CFD analyses are performed. Parallel–processing architectures can range from relatively simple multiprocessor workstations, to massively parallel machines containing several hundred to thousands of processors.

While massively parallel processing offers the promise of extraordinary reductions in computation time, this goal will not be easily achieved. The greatest performance efficiency is attained by tailoring the CFD software to the parallel-processor architecture. Thus, existing software is often not readily transportable to parallel machines. In some cases, the algorithms being used are simply not well suited to parallelization, and therefore will require a complete redesign. As a result, programming for massively parallel processors requires specialized skill, and the development of efficient software for these platforms can represent a major challenge.

While it should be recognized that massively parallel processing is not a panacea, and design application of this computing technology is not yet practical, it has the potential to substantially change the character of CFD analyses and aerodynamic design tools when massively parallel systems reach a higher level of maturity.

As computer performance increases, a number of benefits will be realized that will significantly impact the aerodynamic component design process. Modeling of the flow physics will become more realistic, including aspects of the flow that previously could not feasibly be treated, analysis tools will become more advanced, and eventually the flow simulations will

be coupled with mechanical and heat-transfer modeling to provide a multidisciplinary analysis system.

In the area of flow physics modeling, near-term activity will see the integration of 3D viscous flow and heat-transfer analyses, improved turbulence modeling using higher-order closure, and improved transition modeling. Unsteady analyses will be more frequently used. Multicomponent analyses will also become more common for blade-row interaction predictions, initially using simpler models, such as average-passage analyses of multistage systems, and later employing unsteady multistage analyses.

In addition to increased sophistication of the physics modeling, analysis tools will also be able to accommodate more complex flow-path configurations. These improved capabilities will permit detailed analyses of critical features, such as tip clearance flows in the presence of tip treatment, and cooling flows coupled with main gas-path flows.

As massively parallel-processing technology gains more maturity for CFD applications, the field of multidisciplinary analyses will be expected to grow. Not yet feasible with the level of computing power typically available for turbomachinery component design, a multidisciplinary analysis would couple the fluid dynamics analysis with other aspects of the design, such as heat-transfer, mechanical, and structural dynamics modeling. By integrating all aspects of the component design, it would eventually be possible to apply optimization techniques to the entire system of disciplines.

Taking this concept a step further, Simoneau and Hudson [1] suggest that, by utilizing various levels of modeling detail for each component, an entire gas turbine engine could be modeled as an integrated, coupled system, where changes in one component affect all other components. In this way, a full propulsion system analysis could be performed, applying a highly sophisticated model to one particular component of interest, and treating the remainder of the system with a simpler level of modeling accuracy.

SUMMARY

The driving forces in the design of gas turbine engines for aerospace applications are requiring, in general, greater performance in smaller packages. As a result, the performance demands on each turbomachinery component are becoming much more severe. To meet these requirements, component designs must minimize loss-generating mechanisms and maximize efficiency.

The successful accomplishment of these goals requires a thorough understanding of the highly complex fluid dynamics of turbomachinery components, and the ability to design the components to control and

optimize the flow behavior. The effects of three-dimensionality, compressibility, turbulence, heat transfer, and unsteady flow are all contributors to the aerodynamic performance of turbomachinery components. To achieve the desired levels of performance, component designs must become more complex, utilizing highly three-dimensional blade and flow-path shapes to optimize the flow behavior.

To design such components, advanced CFD analysis tools are required that are capable of accurately modeling the complex flows encountered in turbomachinery applications. These models must reflect the three-dimensional, turbulent, transonic, and often unsteady nature of the actual flows. In addition, they must be usable within the context of the design process; i.e., they must allow analyses to be performed in reasonable amounts of time that can be accommodated within a typical design cycle.

The general trends seen in turbomachinery design, as applied to aero engines, indicate a continuing push for improved component performance, and also a continuing improvement in CFD modeling capabilities. The primary factor governing the level of CFD modeling that can be applied to the aerodynamic component design process is the performance of the computer platform on which the CFD package is installed. As workstation processor speeds and parallel-processing technology improve, more advanced CFD analysis tools will be able to move into the mainstream of the component design process.

REFERENCES

1. R. J. Simoneau and D. A. Hudson, "CFD in the Context of IHPTET—The Integrated High Performance Turbine Technology Program," AIAA/ASME/SAE/ASEE 25th Joint Propulsion Conference, AIAA-89-2904 (1989).
2. S. Deutsch and W. C. Zierke, "The Measurement of Boundary Layers on a Compressor Blade in Cascade. Part 2: Suction Surface Boundary Layers," Gas Turbine Conference and Exhibition, ASME-87-GT-249 (1987).
3. S. Deutsch and W. C. Zierke, "The Measurement of Boundary Layers on a Compressor Blade in Cascade. Part 3: Pressure Surface Boundary Layers and the Near Wake," Gas Turbine Conference and Exhibition, ASME-87-GT-250 (1987).
4. M. Pouagare, J. M. Galmes, and B. Lakshminarayana, "An Experimental Study of the Compressor Rotor Blade Boundary Layer," Turbomachinery Laboratory, Department of Aerospace Engineering, The Pensylvania State University, PSU/TURBO R84-1 (1984).
5. J. H. Wagner, R. P. Dring, and H. D. Joslyn, "Inlet Boundary Layer Effects in an Axial Compressor Rotor: Part I—Blade-to-Blade Effects," *ASME J. Eng. Gas Turbines Power, 107*: 374 (1985).

6. J. H. Wagner, R. P. Dring, and H. D. Joslyn, "Inlet Boundary Layer Effects in an Axial Compressor Rotor: Part II—Throughflow Effects," *ASME J. Eng. Gas Turbines Power, 107*: 381 (1985).
7. B. Lakshminarayana, N. Sitaram, and J. Zhang, "End-Wall and Profile Losses in a Low-Speed Axial Flow Compressor Rotor," International Gas Turbine Conference and Exhibit, ASME-85-GT-174 (1985).
8. K. N. S. Murthy and B. Lakshminarayana, "Laser Doppler Velocimeter Measurement in the Tip Region of a Compressor Rotor," *AIAA J., 24*: 807 (1986).
9. B. Lakshminarayana and K. N. S. Murthy, "Laser Doppler Velocimeter Measurement of Annulus Wall Boundary Layer Development in a Compressor Rotor," Gas Turbine Conference and Exhibition, ASME-87-GT-251 (1987).
10. M. Inoue, M. Kuroumaru, and M. Fukuhara, "Behavior of Tip Leakage Flow Behind an Axial Compressor Rotor," International Gas Turbine Conference and Exhibit, ASME-85-GT-62 (1985).
11. A. J. Strazisar and J. A. Powell, "Laser Anemometry Measurements in a Transonic Axial Flow Compressor Rotor," *ASME J. Eng. Power, 103*: 430 (1981).
12. R. J. Dunker, P. E. Strinning, and H. B. Weyer, "Experimental Study of the Flow Field Within a Transonic Axial Compressor Rotor by Laser Velocimetry and Comparison With Through-Flow Calculations," Gas Turbine Conference, ASME-77-GT-28 (1977).
13. R. J. Dunker and H. G. Hungenberg, "Transonic Axial Compressor Using Laser Anemometry and Unsteady Pressure Measurements," *AIAA J., 18*: 973 (1980).
14. R. W. Paterson and H. D. Weingold, "Experimental Investigation of a Simulated Compressor Airfoil Trailing-Edge Flowfield," *AIAA J., 23*: 768 (1985).
15. J. Prato and B. Lakshminarayana, "Investigation of Compressor Rotor Wake Structure at Peak Pressure Rise Coefficient and Effects of Loading," International Gas Turbine and Aeroengine Congress and Exposition, ASME-92-GT-32 (1992).
16. T. H. Okiishi, M. D. Hathaway, and J. L. Hansen, "A Note on Blade Wake Interaction Influence on Compressor Stator Row Aerodynamic Performance," *ASME J. Eng. Gas Turbines Power, 107*: 549 (1985).
17. M. D. Hathaway, K. L. Suder, T. H. Okiishi, A. J. Strazisar, and J. J. Adamczyk, "Measurements of the Unsteady Flow Field Within the Stator Row of a Transonic Axial-Flow Fan. II—Results and Discussion," Gas Turbine Conference and Exhibition, ASME-87-GT-227 (1987).
18. M. A. Cherrett and J. D. Bryce, "Unsteady Viscous Flow in a High Speed Core Compressor," International Gas Turbine and Aeroengine Congress and Exposition, ASME-91-GT-91 (1991).
19. D. Eckardt, "Detailed Flow Investigations Within a High-Speed Centrifugal Compressor Impeller," *ASME J. Fluids Eng. 98*: 390 (1976).

20. D. Eckardt, "Flow Field Analysis of Radial and Backswept Centrifugal Compressor Impellers. Part I: Flow Measurements Using a Laser Velocimeter," *Performance Prediction of Centrifugal Pumps and Compressors*, ASME Publication, p. 77 (1980).
21. H. Krain, "A Study on Centrifugal Impeller and Diffuser Flow," International Gas Turbine Conference, ASME-81-GT-9 (1981).
22. L. S. Langston, M. L. Nice, and R. M. Hooper, "Three-Dimensional Flow Within a Turbine Cascade Passage," Gas Turbine Conference and Products Show, ASME-76-GT-50 (1976).
23. C. H. Sieverding, "Recent Progress in the Understanding of Basic Aspects of Secondary Flows in Turbine Blade Passages," *ASME J. Eng. Gas Turbines Power, 107*: 248 (1985).
24. O. P. Sharma and T. L. Butler, "Predictions of Endwall Losses and Secondary Flows in Axial Flow Turbine Cascades," International Gas Turbine Conference and Exhibit, ASME-86-GT-228 (1986).
25. E. Detemple-Laake, "Detailed Measurements of the Flow Field in a Transonic Turbine Cascade," International Gas Turbine and Aeroengine Congress and Exposition, ASME-91-GT-29 (1991).
26. M. Stastny and P. Safarik, "Boundary Layer Effects on the Transonic Flow in a Straight Turbine Cascade," International Gas Turbine and Aeroengine Congress and Exposition, ASME-92-GT-155 (1992).
27. A. Binder and R. Romey, "Secondary Flow Effects and Mixing of the Wake Behind a Turbine Stator," International Gas Turbine Conference, ASME-82-GT-46 (1982).
28. C. G. Graham and F. H. Kost, "Shock Boundary Layer Interaction on High Turning Transonic Turbine Cascades," Gas Turbine Conference and Exhibit, ASME-79-GT-37 (1979).
29. J. Zeschky and H. E. Gallus, "Effects of Stator Wakes and Spanwise Nonuniform Inlet Conditions on the Rotor Flow of an Axial Turbine Stage," International Gas Turbine and Aeroengine Congress and Exposition, ASME-91-GT-93 (1991).
30. N. Arndt, "Blade Row Interaction in a Multistage Low-Pressure Turbine," International Gas Turbine and Aeroengine Congress and Exposition, ASME-91-GT-283 (1991).
31. J. C. Collie, H. L. Moses, J. A. Schetz, and B. A. Gregory, "Recent Advances in Simulating Unsteady Flow Phenomena Brought About by Passage of Shock Waves in a Linear Turbine Cascade," International Gas Turbine and Aeroengine Congress and Exposition, ASME-92-GT-4 (1992).
32. M. F. Blair, "An Experimental Study of Heat Transfer in a Large-Scale Turbine Rotor Passage," International Gas Turbine and Aeroengine Congress and Exposition, ASME-92-GT-195 (1992).
33. R. J. Roback and R. P. Dring, "Hot Streaks and Phantom Cooling in a Turbine Rotor Passage. Part 1—Separate Effects," International Gas Turbine and Aeroengine Congress and Exposition, ASME-92-GT-75 (1992).

34. R. J. Roback and R. P. Dring, "Hot Streaks and Phantom Cooling in a Turbine Rotor Passage. Part 2—Combined Effects and Analytical Modeling," International Gas Turbine and Aeroengine Congress and Exposition, ASME-92-GT-76 (1992).
35. D. Joslyn and R. Dring, "Three-Dimensional Flow in an Axial Turbine. Part 2—Profile Attenuation," Gas Turbine and Aeroengine Congress and Exposition, ASME-90-GT-57 (1990).
36. B. R. Haller and J.-J. Camus, "Aerodynamic Loss Penalty Produced by Film Cooling Transonic Turbine Blades," International Gas Turbine Conference and Exhibit, ASME-83-GT-77 (1983).
37. M. F. Malak, A. Hamed, and W. Tabakoff, "Three-Dimensional Flow Field Measurements in a Radial Inflow Turbine Scroll Using LDV," International Gas Turbine Conference and Exhibit, ASME-86-GT-122 (1986).
38. H. Eroglu and W. Tabakoff, "LDV Measurements and Investigation of Flow Field Through Radial Turbine Guide Vanes," Gas Turbine and Aeroengine Congress and Exposition, ASME-89-GT-162 (1989).
39. A. N. Lakshminarasimha, W. Tabakoff, and A. M. Metwally, "LDV Measurements and the Flow Analysis in the Vaneless Region of a Radial Inflow Turbine," Gas Turbine and Aeroengine Congress and Exposition, ASME-89-GT-157 (1989).
40. M. Zangeneh-Kazemi, W. N. Dawes, and W. R. Hawthorne, "Three Dimensional Flow in Radial-Inflow Turbines," Gas Turbine and Aeroengine Congress, ASME-88-GT-103 (1988).
41. B. Lakshminarayana, "An Assessment of Computational Fluid Dynamic Techniques in the Analysis and Design of Turbomachinery—The 1990 Freeman Scholar Lecture," *ASME J. Fluids Eng., 113*: 315 (1991).
42. W. N. Dawes, "The Simulation of Three-Dimensional Viscous Flow in Turbomachinery Geometries Using a Solution-Adaptive Unstructured Mesh Methodology," International Gas Turbine and Aeroengine Congress and Exposition, ASME-91-GT-124 (1991).
43. B. Baldwin and H. Lomax, "Thin Layer Approximations and Algebraic Model for Separated Flow," AIAA 16th Aerospace Sciences Meeting, AIAA-78-257 (1978).
44. C. K. G. Lam and K. Bremhorst, "A Modified Form of the k-ε Model for Predicting Wall Turbulence," *ASME J. Fluids Eng., 103*: 456 (1981).
45. K. Hanjalic and B. E. Launder, "Sensitizing the Dissipation Equation to Irrotational Strains," *ASME J. Fluids Eng., 102*: 34 (1980).
46. Y. Nagano and M. Tagawa, "An Improved k-ε Model for Boundary Layer Flows," *ASME J. Fluids Eng., 112*: 33 (1990).
47. R. Abid, "A Two-Equation Turbulence Model for Compressible Flows," AIAA 22nd Fluid Dynamics, Plasma Dynamics, and Lasers Conference, AIAA-91-1781 (1991).
48. V. Yakhot and S. A. Orszag, "Renormalization Group Analysis of Turbulence: I. Basic Theory," *J. Sci. Computation, 1*: 3 (1986).

49. K. R. Kirtley, "An Algebraic RNG-Based Turbulence Model for Three-Dimensional Turbomachinery Flows," AIAA 29th Aerospace Sciences Meeting, AIAA-91-0172 (1991).
50. W. Rodi and G. Scheuerer, "Calculation of Curved Shear Layers with Two-Equation Turbulence Models," *Phys. Fluids, 26*: 1422 (1983).
51. J. Zhang and B. Lakshminarayana, "Computation and Turbulence Modeling for Three-Dimensional Boundary Layers Including Turbomachinery Rotor Flows," *AIAA J., 28*: 1861 (1990).
52. V. C. Patel, W. Rodi, and G. Scheuerer, "Turbulence Models for Near-Wall and Low Reynolds Number Flows: A Review," *AIAA J., 23*: 1308 (1985).
53. B. Lakshminarayana, "Turbulence Modeling for Complex Shear Flows," *AIAA J., 24*: 1900 (1986).
54. C. G. Speziale, "Analytical Methods for the Development of Reynolds-Stress Closures in Turbulence," *Annu. Rev. Fluid Mechanics, 23*: 107 (1991).
55. R. E. Mayle, "The Role of Laminar-Turbulent Transition in Gas Turbine Engines," *ASME J. Turbomachinery, 113*: 509 (1991).
56. G. J. Walker, "The Role of Laminar-Turbulent Transition in Gas Turbine Engines: A Discussion," International Gas Turbine and Aeroengine Congress and Exposition, ASME-92-GT-301 (1992).
57. J. N. Scott and W. L. Hankey, "Boundary Conditions for Navier-Stokes Solutions of Unsteady Flow in a Compressor Rotor," *Three-Dimensional Flow Phenomena in Fluid Machinery* (A. Hamed, J. Herring, L. Povinelli, eds.), ASME Winter Annual Meeting, p. 141 (1985).
58. J. N. Scott and W. L. Hankey, "Navier-Strokes Solutions of Unsteady Flow in a Compressor Rotor," International Gas Turbine Conference and Exhibit, ASME-86-GT-226 (1986).
59. M. Furukawa, T. Nakano, and M. Inoue, "Unsteady Navier-Stokes Simulation of Transonic Cascade Flow Using an Unfactored Implicit Upwind Relaxation Scheme with Inner Iterations," International Gas Turbine and Aeroengine Congress and Exposition, ASME-91-GT-223 (1991).
60. M. M. Rai, "Navier-Stokes Simulations of Rotor-Stator Interaction Using Patched and Overlaid Grids," *J. Propulsion Power, 3*: 387 (1987).
61. K. L. Gundy-Burlet, M. M. Rai, and R. P. Dring, "Two-Dimensional Computations of Multi-Stage Compressor Flows Using a Zonal Approach," AIAA/ASME/SAE/ASEE 25th Joint Propulsion Conference, AIAA-89-2452 (1989).
62. W. N. Dawes, "Towards Improved Throughflow Capability: The Use of 3D Viscous Flow Solvers in a Multistage Environment," International Gas Turbine and Aeroengine Congress and Exposition, ASME-90-GT-18 (1990).
63. W. W. Copenhaver, C. Hah, and S. L. Puterbaugh, "Three-Dimensional Flow Phenomena in a Transonic, High-Through-Flow, Axial-Flow Compressor Stage," International Gas Turbine and Aeroengine Congress and Exposition, ASME-92-GT-169 (1992).

64. J. J. Adamczyk, "Model Equation for Simulating Flows in Multistage Turbomachinery," International Gas Turbine Conference and Exhibit, ASME-85-GT-226 (1985).
65. C. Hirsch, *Numerical Computation of Internal and External Flows*, Volumes 1 and 2, John Wiley and Sons, New York (1988, 1990).
66. A. Jameson, and T. J. Baker, "Multigrid Solutions of Euler Equations for Aircraft Configurations," AIAA 22nd Aerospace Sciences Meeting, AIAA-84-0093 (1984).
67. W. N. Dawes, "A Numerical Analysis of the Three-Dimensional Viscous Flow in a Transonic Compressor Rotor and Comparison with Experiment," *ASME J. Turbomachinery, 109*: 83 (1987).
68. D. A. Anderson, J. C. Tannehill, and R. H. Pletcher, *Computational Fluid Mechanics and Heat Transfer*, Hemisphere Publishing, New York (1984).
69. P. R. Eiseman, "Grid Generation for Fluid Mechanics Computations," *Annu. Rev. Fluid Mechanics, 17*: 487 (1985).
70. J. F. Thompson, "Grid Generation Techniques in Computational Fluid Dynamics," *AIAA J., 22*: 1505 (1984).
71. D. J. Mavriplis, "Adaptive Mesh Generation for Viscous Flows Using Delaunay Triangulation," NASA CR-181699 (1988).
72. T. J. Baker, "Generation of Tetrahedral Meshes Around Complete Aircraft," *Numerical Grid Generation in Computational Fluid Mechanics '88* (S. Sengupta, J. Hauser, P. R. Eiseman, J. F. Thompson, eds.), Pineridge Press, Swansea, U.K., p. 675 (1988).
73. S. R. Kennon and D. A. Anderson, "Unstructured Grid Adaption for Non-Convex Domains," *Numerical Grid Generation in Computational Fluid Mechanics '88* (S. Sengupta, J. Hauser, P. R. Eiseman, J. F. Thompson, eds.), Pineridge Press, Swansea, U.K., p. 599 (1988).
74. P. Palmerio and A. Dervieux, "2-D and 3-D Unstructured Mesh Adaption Relying on Physical Analogy," *Numerical Grid Generation in Computational Fluid Mechanics '88* (S. Sengupta, J. Hauser, P. R. Eiseman, J. F. Thompson, eds.), Pineridge Press, Swansea, U.K., p. 653 (1988).
75. S. Sengupta, J. Hauser, P. R. Eiseman, and J. F. Thompson, eds., *Numerical Grid Generation in Computational Fluid Mechanics '88*, Pineridge Press, Swansea, U.K. (1988).
76. R. K. Rout, "Application of I-DEAS Grid Generator for Three-Dimensional Transonic Flow Analysis," *Numerical Grid Generation in Computational Fluid Mechanics '88* (S. Sengupta, J. Hauser, P. R. Eiseman, J. F. Thompson, eds.), Pineridge Press, Swansea, U.K., p. 761 (1988).
77. W. N. Dawes, "The Application of Multigrid to Navier-Stokes Simulation of 3D Flow in Axial and Radial Flow Turbomachinery," *International J. Numerical Methods in Fluids, 8*: 1217 (1988).
78. W. A. Smith, "Multigrid Solution of Transonic Flow on Unstructured Grids," ASME Winter Annual Meeting, ASME Special Publications (1990).
79. S. W. Kandebo, "Textron Lycoming to Renew JTAGG Tests This Spring," *Aviation Week Space Technol.*, p. 48, January 11, 1993.

3

Turbine Gas-Path Heat Transfer

Charles MacArthur
Wright-Patterson Air Force Base, Ohio, U.S.A.

INTRODUCTION

The introduction of turbomachinery in the late 1940s and early 1950s as a means of propelling military and, later, civilian aircraft led to a large increase of research in fluid mechanics and heat transfer centered on the gas turbine engine. Durable, efficient, high-performance engines were needed for a large number of new aircraft performing a wide variety of missions. Also gas turbines became increasingly popular for ground power and marine applications. The designers of these new machines faced more and more challenges in terms of size, time between overhaul, and power output. Each new generation of engines needed to operate at the highest practical turbine inlet temperature for maximum thrust or power output and highest thermodynamic (fuel) efficiency.

As the turbine inlet temperature was raised, accurate means of predicting the new flow and heat transfer in the hot section were generally not available, resulting in the need for expensive series of tests. This problem, in particular, motivated analytical research into fundamental fluid mechanics and convective heat transfer to minimize testing. At the same time, new ways to learn more from the testing that was done were needed.

The story of turbomachinery research over the last approximately 50 years is one of advances in both theory and experiment that have continually reduced development costs. New theory and, in particular, computational methods, have now developed to the point where fully three-dimensional, time-accurate (unsteady) numerical simulations are, if not routine, certainly possible in the design of a turbine.

In this chapter we will make an attempt to summarize the progress in just one part of a very large body of research and discovery. We have limited our discussion to external turbine heat transfer, and then to only that part that does not include film cooling. But even then it has been difficult to write a comprehensive summary that can fit into the practical limits of this handbook. Our objective, then, is to highlight major accomplishments in understanding turbine flow-path heat transfer, both through theory and experiment, starting at the beginning of the 1950s and continuing through today. As mentioned above, much of this story deals with the improved fluid dynamic computational tools, allowing the gas turbine industry to refine and verify its design systems. The computational tools must, of course, be verified themselves, and the consequent need for more accurate, more engine relevant data has led to significant improvements in experimental methods and instrumentation.

Because of the direct link between fluid boundary-layer skin friction and heat transfer, our review has been made much easier by the very comprehensive presentation of turbomachinery fluid dynamics given in Chapter 2.

What has been the result of all this research and development effort? An easy way to appreciate the effect that improved understanding of turbine heat transfer has had is to compare take-off high-pressure turbine inlet temperature for engines developed in the 1950s through those of today. Figure 1 shows this comparison for a large number of engines, both commercial and military. We see that inlet temperature has been nearly doubled in approximately the last 50 years. Engines of the future may reach nearly stoichiometric temperatures that would provide the maximum power output for a given engine overall pressure ratio.

The maximum turbine inlet temperature is a function of many factors, but primarily it is the more effective cooling schemes plus the higher usage temperature materials that have allowed the significant increases shown in the figure. Development of better cooling schemes is due in part to better understanding of the turbine heat-transfer mechanisms and the heat load that must be tolerated. This understanding includes knowing the behavior of the main stream flow and all of the wall boundary layers, wakes, separation bubbles, vortices, etc. As we shall see, these have been the subjects of many individual studies of the separate phenomena as well as measurements of all

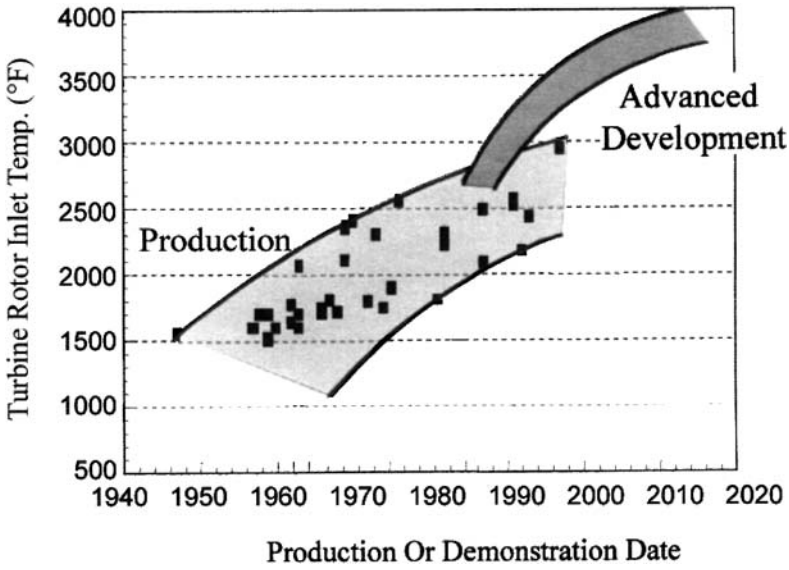

Figure 1 Maximum turbine rotor inlet temperature vs. year of service introduction.

or nearly all of the phenomena combining in fully scaled experiments and detailed computations.

SYMBOLS

A_x, A_θ, A_r	Control volume face area elements perpendicular to the x, θ, r directions respectively (m^2)
C_p	Fluid specific heat at constant pressure (kcal/kgm-K)
E	Flow total energy per unit mass (J/kg)
h_0	Fluid stagnation enthalpy per unit mass (J/kg)
h	Convective heat-transfer coefficient (W/m^2-K)
k	Turbulence kinetic energy ($kg/m\text{-}s^2$)
P	Fluid pressure (N/m^2)
r	Radial coordinate in an orthogonal cylindrical coordinate system (m)
Re_0	Reynolds number based on momentum thickness
Re_x	Reynolds number based on distance (x)

St	Stanton number $h/(\rho C_p u_\infty)$
u_∞	Free-stream fluid velocity (m/s)
V	Control volume (m^3)
V_x, V_θ, V_f	Velocity components in the x, θ, r directions, respectively (m/s)
x	Axial direction in an orthogonal cylindrical coordinate system (m)
ε	Fluid turbulence kinetic energy dissipation rate (kg/m-s)
γ	Intermittancy
ν	Kinematic viscosity (m^2/s)
θ	Azimuthal coordinate in an orthogonal cylindrical system (rad)
ρ	Fluid density (kg/m^3)

EARLY COMPUTATIONAL METHODS

The first turbines representing what we now think of as "modern" turbomachinery appeared with the invention of the axial flow steam turbine by Parsons in the 1880s. (See, for example, Horlock [1].) Turbine aerodynamic design methods at that time consisted of little more than guess work as to the nozzle guide vane and rotor blade shapes, the optimum number of blades, reaction, and other features. However, World War II led to quasi-empirical databases and design methods from marine, ground power turbines, and aircraft turbo-supercharger designs. Heat transfer to the airfoils was generally not a major consideration, as the maximum material use temperatures were higher than inlet gas total temperatures.

After the war, the development of computers allowed the use of computational fluid dynamics (CFD) in many engineering fields including turbomachinery, albeit primitive by today's standards. As simplified as these early CFD tools were—dealing with only inviscid flow, for example—their results were often quite successful, and many are still in use today. In Fig. 2, we illustrate one of the first major advances in turbomachinery CFD after World War II: Wu's Quasi-3-D stream surface model of the mainstream flow [2]. Wu's calculation method introduced the concept of the blade-to-blade stream surfaces (S1) and the meridional (hub-to-tip) stream surfaces (S2) on which sets of 3D models (the governing equations) of the flow could be written. In writing a 3D model on a 2D surface, we mean that one must assume the surface normal velocity component to S1 or S2 is known. The surface normal component at a point on, say, the S1 surface will be one of

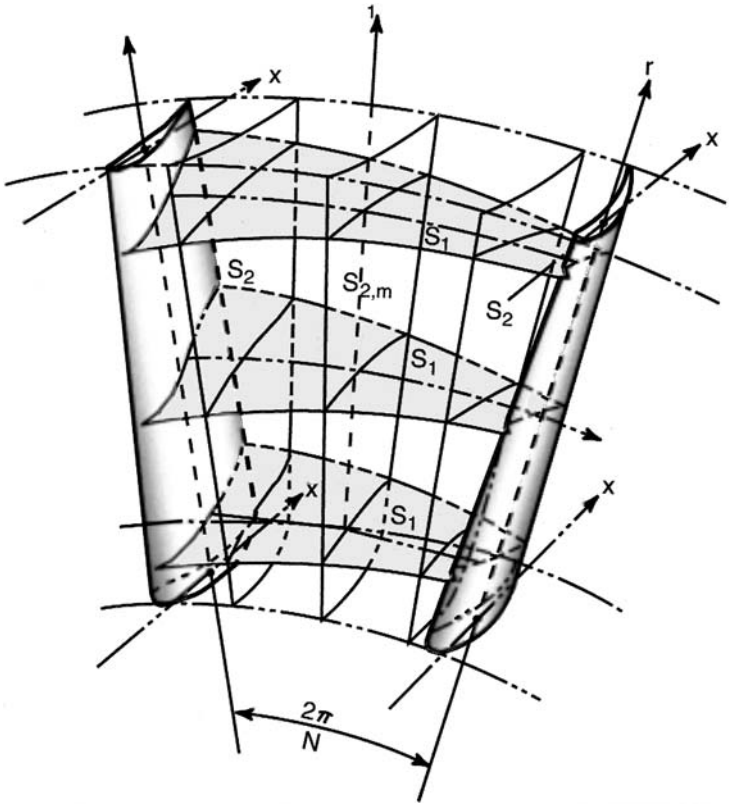

Figure 2 Intersecting S_1 and S_2 surfaces in a blade row. (Wu [2]).

the unknown components at the same point on the intersecting S2 surface. Therefore, the "Quasi-3-D" solutions for each plane are coupled through the out-of-plane velocity components. Using an iterative (guess-and-correct) technique and the continuity equation, the final Quasi-3-D solution can be achieved, but not without considerable work.

Computer performance restrictions as well as a lack of good turbulence modeling capability usually required that the assumption of inviscid flow (potential or Euler form) be made for the bulk flow through the turbine. Use of these inviscid assumptions, of course, limits accuracy primarily because we cannot deal with flow separation.

Wu's method or derivatives thereof became quite popular through the 1950s until the mid-1980s, when sufficient computing power became

available to explore fully viscous solutions of the 3D Navier–Stokes equations in reasonable times. Because external surface heat transfer is essentially driven by the main stream flow conditions (through the structure of the intervening boundary layer), standard heat-transfer correlations could be used along the predicted streamlines to compute the heat transfer to the surface.

Wu's method was "packaged" and improved by researchers at what is now the USA's NASA/Glenn Research Center as the well-known computer codes MERIDL and TSONIC [3, 4]. These codes are still used in many CFD calculations, for example, to quickly generate an approximate starting solution for more complex and time-consuming Navier–Stokes numerical solutions. A major drawback of Wu's Quasi-3D method is that it is only approximate (by design, of course). The procedure also requires much human intervention and application of design experience during the iterative solution process to obtain the most useful results. Researchers therefore continued to look for both faster and more accurate methods, particularly those that incorporate viscosity and other effects naturally.

The first major step for including viscosity became available in the late 1960s and early 1970s through numerical analysis of flow-path boundary layers. The publication that started much of the work was by Patankar and Spalding [5] in which the authors numerically solved the 2D, steady boundary-layer equations (simplified forms of the Navier–Stokes equations) using a scaled coordinate system that adapts to the boundary-layer thickness as it grows downstream. The boundary-layer differential equations are of the parabolic type; thus only the values of the upstream independent variables are needed to solve for the downstream values. Variation in the solution is wholly determined by the variations in the free stream and the solid surface over which the fluid flows. This technique formed the vehicle for many, many studies of skin friction drag and heat transfer, for *attached* boundary layers. Patankar–Spalding also became the workhorse numerical technique for many studies of boundary-layer turbulence that popularized the k-ε turbulence model [6] and others.

Parabolic boundary-layer solvers using the Patankar–Spalding procedure were written by NASA and others under the names of STAN5 [7] and TEXSTAN [8]. Many others were developed in academia and industry. These codes were used with the TSONIC/MERDIL passage-flow solvers to give a technique fast and robust enough for design work but with greater accuracy than the part-calculation, part-correlation techniques used previously. Separation still had to be dealt with empirically because of the inability of the parabolic equations to be solved under conditions favoring separation, i.e., strong adverse pressure gradients. The transition starting point and transition lengths also need empirical expressions for their

determination. Nothing in the simplified governing equations will generate this information from first principles.

TRANSITION AND TURBULENCE MODELING

Emmons [9] is generally credited with the recognition that laminar boundary layers in turbomachines may not undergo the "natural" transition to turbulence process seen in the relatively undisturbed boundary layers in the laboratory. He observed boundary layers that undergo the high strain rates (rates of acceleration or deceleration) typical of turbomachinery and noticed the phenomena known as "turbulent spots", islands of turbulent flow in the surrounding laminar boundary layer. As shown schematically in Fig. 3, these spots grow while moving down stream to eventually coalesce to form the fully turbulent boundary layer. Flow over the suction surface of a turbine blade is often in the Reynolds number range where turbulent spots are observed and the boundary layer is unstable.

The significance of Emmons' observation was that empirical results taken from studies of relatively lightly strained boundary layers—those that transition by the classic Tollmien-Schlichting process (see White [10])—do not translate to turbines because of the turbulent spot transition phenomena described above. New correlations and analysis were needed.

To quantify this phenomenon and point in the direction of these new correlations, Emmons used a measure of turbulence distribution called intermittancy. Intermittancy, often denoted by γ, can be considered for any

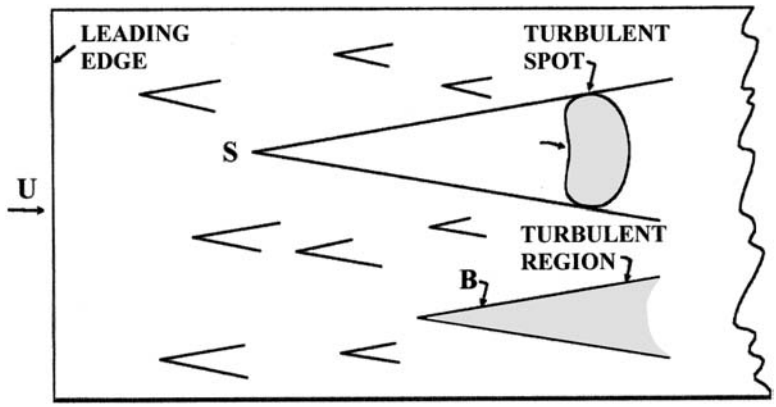

Figure 3 Transition on a flat plate (Emmons [9]).

point in the flow as the fraction of time in which the flow is turbulent at that point. Where the flow is all laminar γ is 0 and where it is fully turbulent γ is 1.

As turbulent spots in the boundary layer move down stream and coalesce into full turbulence, intermittancy can be used to scale (or weight) the values of quantities of interest through transition. The non-dimensional heat transfer coefficient, St, may be given in this manner. If the momentum thickness Reynolds number (Re_θ) of 162 is used as the start of transition (Kays and Crawford [11]), and intermittancy is expressed by Emmon's relationship

$$\gamma(x) = 1 - \exp[-n\sigma(\mathrm{Re}_x - \mathrm{Re}_{xt})^2] \tag{1}$$

Where

Re_{xt} is the x (surface distance) Reynolds number at the start of transition.
n and σ are experimentally determined parameters.

Then we can write the heat-transfer coefficient as

$$\mathrm{St}(x) = (1 - \gamma)\mathrm{St}_{\mathrm{lam}} + \gamma\mathrm{St}_{\mathrm{turb}} \tag{2}$$

In other words, the Stanton number in the transition zone is a linear combination of the fully laminar and fully turbulent heat-transfer coefficients at the same surface distance.

While this approach serves well to estimate how the heat transfer and other quantities change through the transition zone, designers must still find a method to predict the intermittancy values from transition onset to finish. Clark et al. [12] is an example of this approach.

LOW-SPEED, LARGE-SCALE EXPERIMENTS

Virtually all of the turbine experimental heat-transfer studies through the mid-1970s were done either in flat-plate wind tunnels or in cascades of vanes or blades. The study of three-dimensional flow in a turbine cascade by Langston et al. [13] is typical of many similar investigations.

The flow in these facilities could be compressible but more often was not because of the expense involved. Further, earlier experiments were most often steady and run at relatively low temperature differences between the wall and mainstream gas. The large scale of these facilities allowed matching of the Reynolds numbers in the experiments to the design Reynolds numbers of actual machines. But, as mentioned, Mach numbers could rarely

be well matched with the engine. The effect of upstream wakes was sometime included as in the work of Doorley et al. [14], where a moving wake simulator was used. Matching the gas properties and temperature effects with those of the engine were often ignored or assumed to be of secondary importance.

Nevertheless, because of the usually medium to large size of the facilities (≈ 1–$10\times$ engine scale), high-quality steady flow data could be obtained that demonstrated the complexity of the turning flow in cascades. Such features as the passage vortex and separation near the end walls were observed and their influence on heat transfer measured. For example, the work by Langston et al. showed the importance of three-dimensional separation in cascades and demonstrated that end walls could not be well modeled by the existing design methods.

Around the middle of the 1980s, there began to appear large-scale (equal to or greater than engine-scale) facilities that added rotation to the experiments. A noted large-scale rotating turbine facility is shown in Fig. 4. The motivation for building large-scale facilities shows the importance to the gas turbine industry of better defined heat-transfer information.

To give a sense of the scale of the facility, the turbine tip diameter is about 60 in. (2 m) and a typical blade might be 12 in. (30 cm) long. The capability of the GE facility to measure boundary-layer properties may be seen in the very detailed data given by Dorney et al. [15]. A facility of similar scale exists at United Technologies Research Center [16], and a number of others may be found in Europe.

The large size and slower speed of these test "rigs" allow more detailed surface measurement and the easier use of some advanced measurement techniques such as Laser Doppler Velocimetry (LDV) and Particle Image Velocimetry (PIV) for in-passage flow velocity measurements.

Exploring variable fluid properties, high Mach numbers, and strong rotational effects still would have to wait, however, for further developments.

CALCULATIONS USING QUASI-3D AND BOUNDARY-LAYER METHODS

Figure 5 shows the results of a study of the performance of several 2D boundary-layer codes used with a 2D inviscid main flow solution by Harasgama et al. [17]. The experimental plots are heat-transfer coefficient, h, versus distance along a surface streamline from the leading edge for a vane. These boundary-layer codes were executed using the same initial, free-stream, and surface conditions, but with different turbulence models, in this

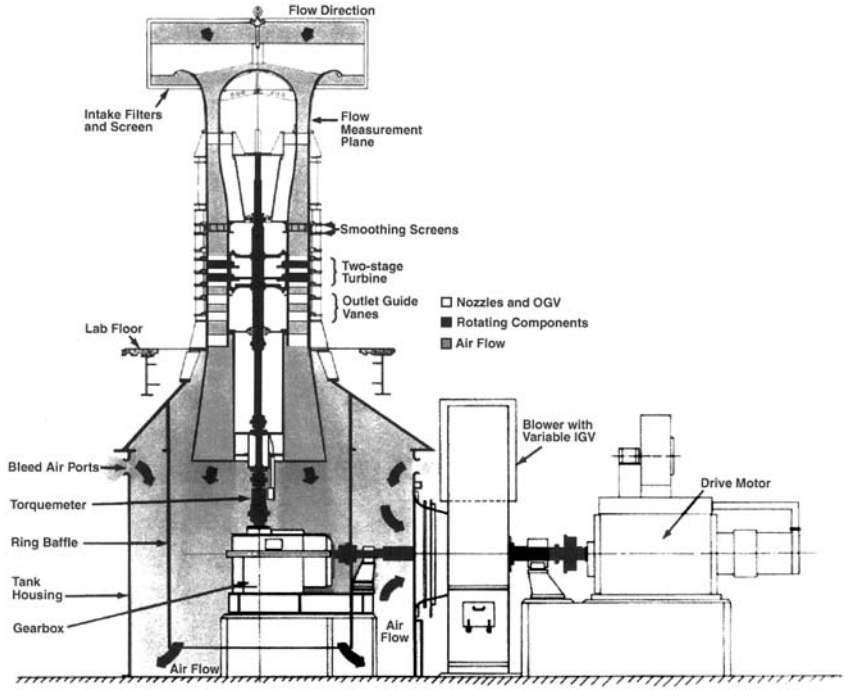

Figure 4 GE low speed research turbine.

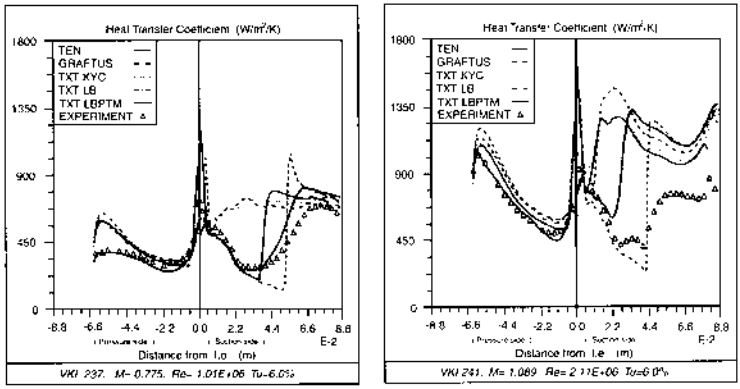

Figure 5 Heat transfer coefficient predictions vs. air foil surface length. 5(a) subsonic exit Mach number 5(b) supersonic exit Mach number

case different forms of the popular k-ε "two-equation" model. The models/codes were TEXSTAN (Crawford [8]), GRAFTUS (Haas & Shoenung [18]), and TEN (Tarada [19]). The turbulence models used in the codes were those by Lam and Bremhorst [20] and K. Y. Chen [21]. The results show how well (and also how poorly) one can do when the boundary-layer external flow conditions are carefully documented. In all cases the pressure side heat transfer is well predicted where laminar flow appears to occur from the leading edge to the trailing edge. On the suction side, however, all the models fail in predicting the start of transition and are, therefore, greatly overpredicting the heat transfer for about half the suction side.

The heat transfer is the greatest at the leading edge of the airfoils, as one would expect, because of the thin, highly accelerated boundary layers at the stagnation point. However, measuring an accurate stagnation point heat transfer is difficult because of instrumentation limits. Similarly, predicting the heat transfer at stagnation is also a problem because the exact location for starting the boundary-layer calculation can be hard to determine. Given these problems, the codes nevertheless do reasonably well at stagnation. We can conclude from this that if we know the starting point of the boundary layer and the free-stream conditions (and these conditions are such as to avoid transition and separation) we can make a reasonably accurate heat-transfer prediction.

FLOW CALCULATIONS USING THE EULER EQUATIONS

From the mid-1970s to the early 1980s, major steps was taken to improve the accuracy of CFD for turbines. The quasi-3D methods were replaced by fully 3D methods for at first inviscid and then viscid flows. Researchers were able to do this because of the increasing storage and speed available in the new computer systems available and because of newly created schemes for solving the Euler equations. This overcame the inherent uncertainty in solutions by the quasi-3D techniques caused by the human judgment necessary in selecting relaxation factors and knowing when the solution had converged to the desired accuracy.

Denton [22] was probably the first author to present a fully 3D method for solving the Euler and Navier–Stokes equations. He used a finite-volume equation form on a quasi-orthogonal grid, consisting of interlocking control volumes. The grid, shown in two views in Fig. 6 for a typical airfoil, can be extended to a multigrid form in order to speed convergence. (Note that the grid used in an actual problem will be much finer.)

The general form of each difference equation is that the sum of the flux of a property over the control volume faces plus any source in the control

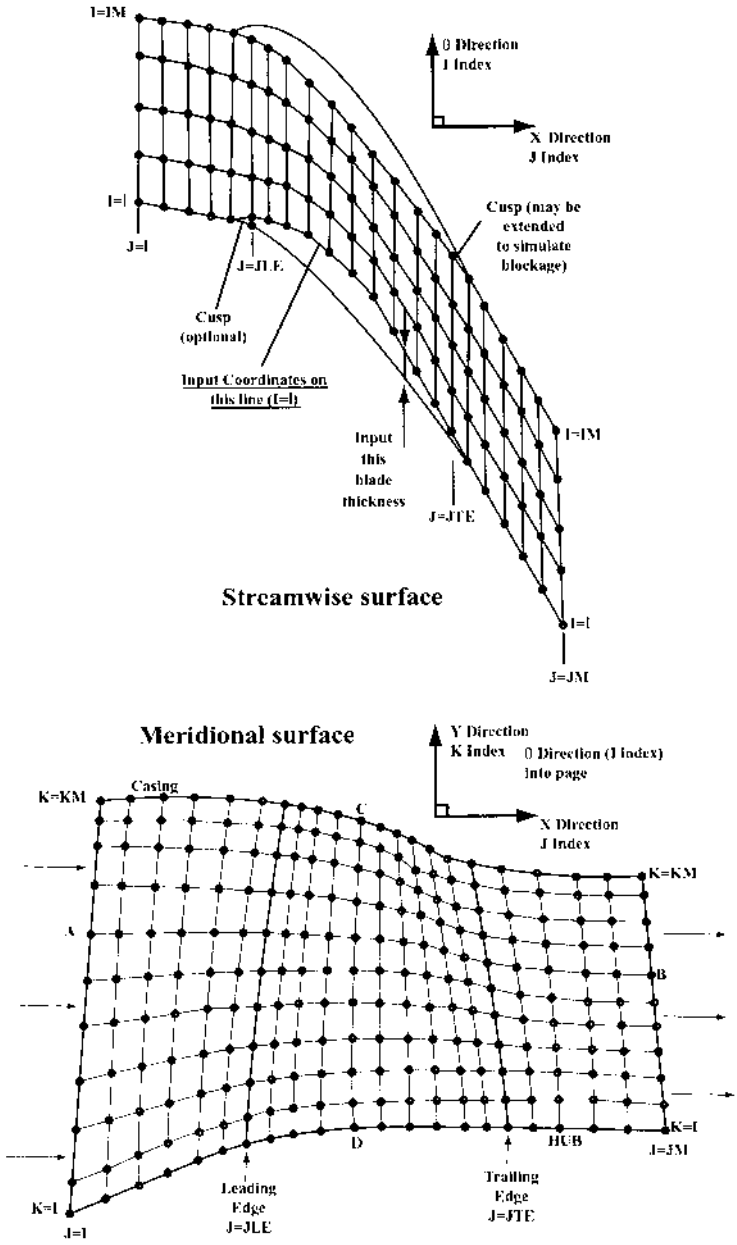

Figure 6 Interlocking grid of control volumes in Denton's method.

volume will be equal to the accumulation rate in the control volume with time. In this general scheme the continuity, energy, and x-momentum equations to be solved on the grid are

$$\begin{aligned}
&\text{mass :} && \Sigma(\rho V_x\, dA_x + \rho V_\theta + \rho V_r dA_r) = && (\Delta V/\Delta t)\Delta\rho \\
&\text{energy :} && \Sigma(\rho V_x h_o dA_x + \rho V_\theta h_o dA_\theta + \rho V_r h_o dA_r) = && (\Delta V/\Delta t)\Delta(\rho E) \\
&x-\text{momentum :} && \Sigma((P+\rho V_x^2)dA_x + \rho V_\theta V_x dA_\theta + \rho V_r V_x dA_r) = && \Delta V/\Delta t(\Delta(\rho V_x))
\end{aligned} \tag{3}$$

Similar relationships govern the r-momentum and the moment of momentum.

There are many important details left unmentioned here on Denton's method concerning the numerical solution technique, stability and damping, convergence, etc. These are available in the extensive literature on his method that Denton and his colleagues have published. Some other early developers of similar fully 3D methods deserving mention include Rai [23], Ni [24], and Ha [25]. Most of these follow the basic finite-volume, multigrid idea. For details on these methods, the reader is referred to the respective citations.

CALCULATIONS AND MEASUREMENTS—FULLY 3D METHODS

Figure 7 shows a single-stage, high rim speed, high-pressure turbine with a significant 3D design studied by Kingcombe et al. [26] at the Defense Equipment Research Agency (DERA) in the United Kingdom. The rig-measured turbine aerodynamics were compared to the 3D Denton code. The vane drawing, Fig. 8, shows measured and computed isentropic Mach number profiles over the vane pressure surface. Agreement with the experiment is reasonably good, demonstrating the power of applying a true 3D code to the analysis of this very 3D geometry.

For the heat transfer, Fig. 9 gives the measured vane midspan heat-transfer coefficient, expressed as Nu, taken from the vane cascade in DERA's test facility. Also shown on the plot is a prediction using the Denton 3D Euler method and the STAN5 boundary-layer code incorporating the Van Driest damping function (see [11]), transition start length correlation by Seyb [27], and transition length correlation by Chen and Thyson [28]. (Note that contrary to usual custom, the suction side is on the left.) Kingcombe et al. state that the transition location and length were "quite well" predicted although at some points the predictions and measurements were in better agreement than others. What is important is

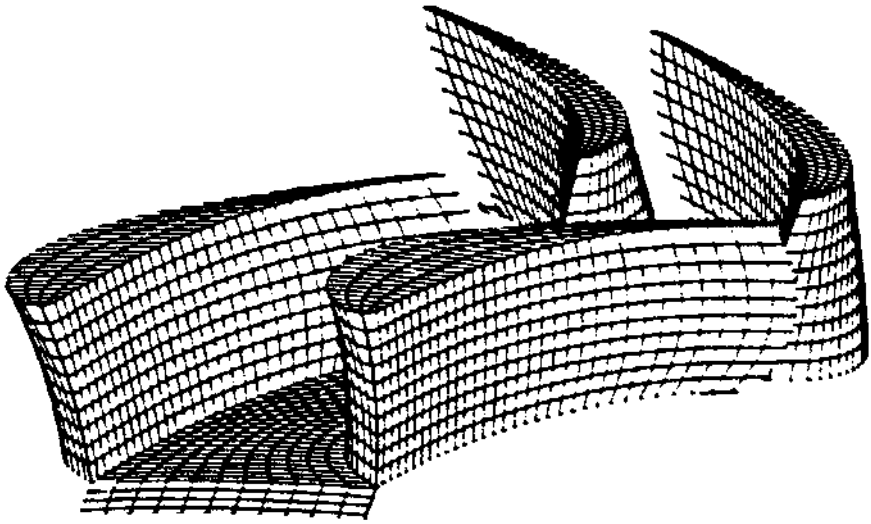

Figure 7 3-D high pressure turbine design of Kingcombe et al. [26].

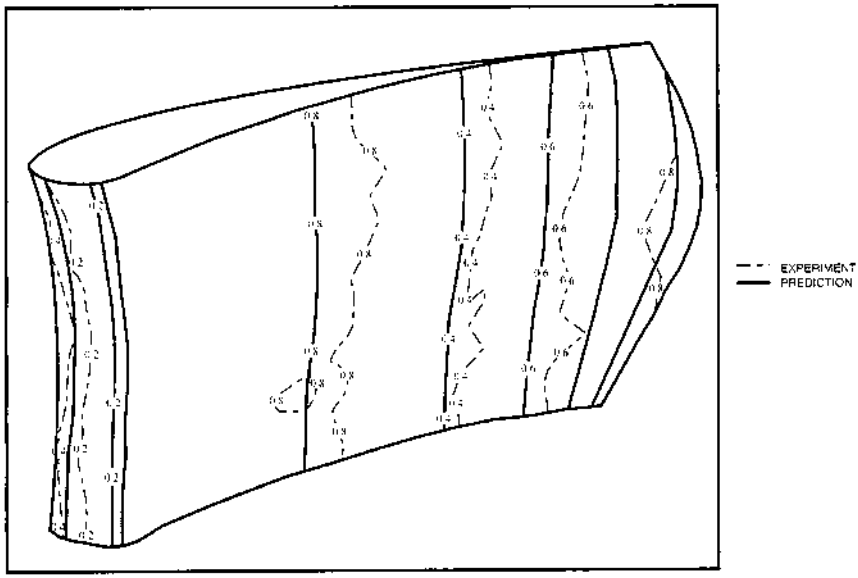

Figure 8a Predicted and measured contours of isentropic Mach number for the vane in the turbine of Kingcombe.

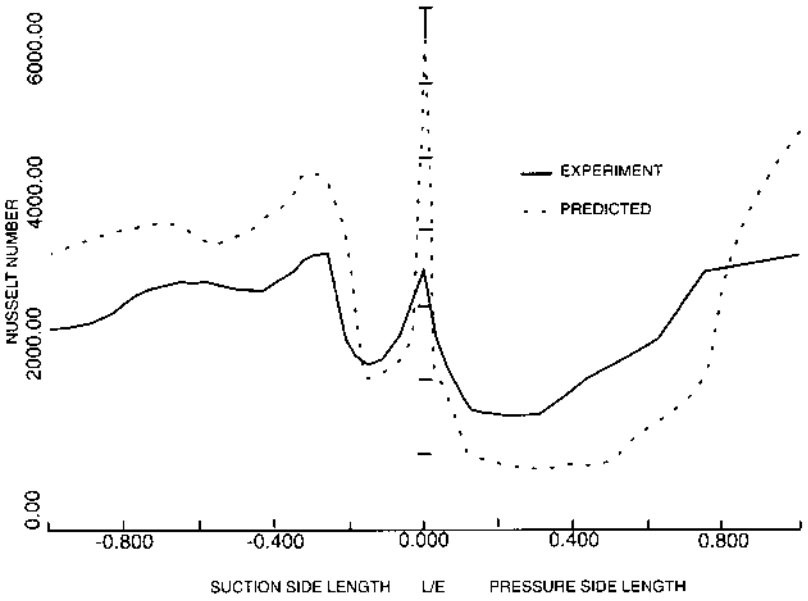

Figure 9 Nusselt number vs. vane surface length. Comparison of predicted and measured vane surface mid-span Nusselt number at design.

that this is one of the first reasonably successful fully 3D heat-transfer predictions.

THIN-LAYER NAVIER–STOKES ANALYSIS

At this point we have examined two approaches for the fluid dynamic solution in the main flow region and the boundary layers. The first was a quasi-3D approach based on potential flow solutions coupled with a 2D boundary-layer code operating along the streamlines at the surface. Second, we looked at a fully 3D main flow solution of the nonviscous Euler equations again with a 2D boundary-layer code following the surface streamlines. An intermediate method that takes into account viscous effects in more detail is known as thin-layer Navier–Stokes analysis, in which the Navier–Stokes (N–S) equations are used in a quasi-3D approach. Here the full Navier–Stokes equations are solved on the blade-to-blade surface, and the solution extends across the passage from wall to wall, eliminating the

need for a separate boundary code. Perhaps the most attractive feature of this technique is that the governing equations are now elliptic and thus can incorporate regions of flow separation. A drawback is that the governing equations require iterative solution and so add considerable computer time.

Figure 10 shows calculations by Boyle [29] using the thin-layer N–S method. The curve marked "predicted" assumes 1.5% free-stream turbulence. A prediction for zero free-stream turbulence is also given in the figure. Note the high sensitivity of the heat-transfer results to the assumptions made about free-stream turbulence levels, a topic discussed further below.

Boyle's paper also gives comparisons for a number of other phenomena influencing heat transfer at the airfoil surface, such as eddy viscosity, near-wall turbulence damping, among others. This author agrees with Boyle, who states that the predictions are generally better than if an inviscid blade-to-blade solution was used. There is still, however, the issue of the approximate nature of Quasi-3D analysis.

ADVANCES IN TRANSITION AND TURBULENCE

The advent of fully viscous, Quasi-3D, and fully 3D calculation methods spurred the research on transition and turbulence because these codes more accurately computed situations that were not just simple, 2D shear flows.

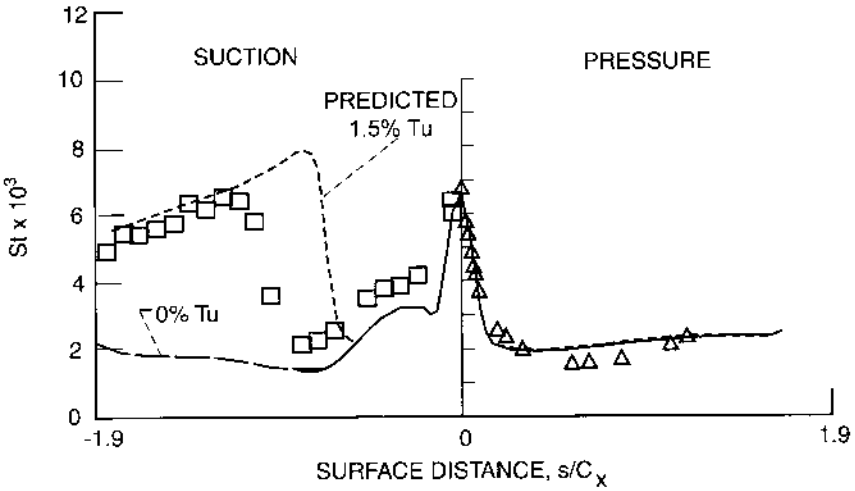

Figure 10 Predicted and measured heat transfer on a vane by Boyle [29] using thin layer Navier-Stokes analysis.

Furthermore, to keep computer time to a minimum, given the computer speeds available, it was necessary to use as simple a turbulence model as possible. Simple algebraic models, if sufficiently accurate, are preferred over more complex methods that may require, say, the solution of additional differential equations.

Predicting the onset and length of transition is presently the most challenging task in turbine heat-transfer design. The practical forms of turbulence models are still empirical or semi-empirical, although some of the most sophisticated physical theory has been applied to the problem.

Figure 11 from Mayle [30] shows the trends in boundary layer development for a high-pressure stage operating at or near design. The strong accelerations and decelerations add to or subtract from the influences of free-stream turbulence, film cooling, etc. to control whether the transitional boundary layer is evolving toward or away from a fully turbulent condition. The figure also shows a rough relationship between momentum thickness Reynolds number, Re_θ, and flow acceleration parameter $[v/(u^2 du/dx)]$. Boundaries for different behaviors as functions of imposed influences are shown. For a more comprehensive review of progress in transition modeling, see Mayle.

FULL NAVIER–STOKES PREDICTIONS

To show the effect of turbulence modeling used in 3D computations, Fig. 12 compares three computations differing by only the turbulence model used (Boyle and Jackson [31]). The figure shows three views of an "unwrapped" vane surface with contours of scaled heat-transfer coefficient $(\mathrm{St} \times 10^{-3})$ on the vane surfaces. The calculations used "engineering" (simple algebraic) turbulence models to save computer time instead of those requiring solution of added differential equations.. These models are one by Baldwin and Lomax [32], one by Chima [33], and one by Cebeci and Smith [34]. Each of these models was used in the three-dimensional fluid dynamics computer code of Chima [35] to predict the vane surface heat-transfer coefficient map over the vane and end-wall surface. Other than the method of predicting the turbulent viscosity (the model), nothing else was changed in the three cases.

Examining the figures, we see there are large differences in the predicted values, particularly near the leading edge. However, the overall shape of the profiles is similar, showing that the predicted main stream flow is not especially different among the three cases. The problem, not unexpectedly, lies in the details of the boundary-layer profiles where good prediction of shear stress (and so heat transfer) is required.

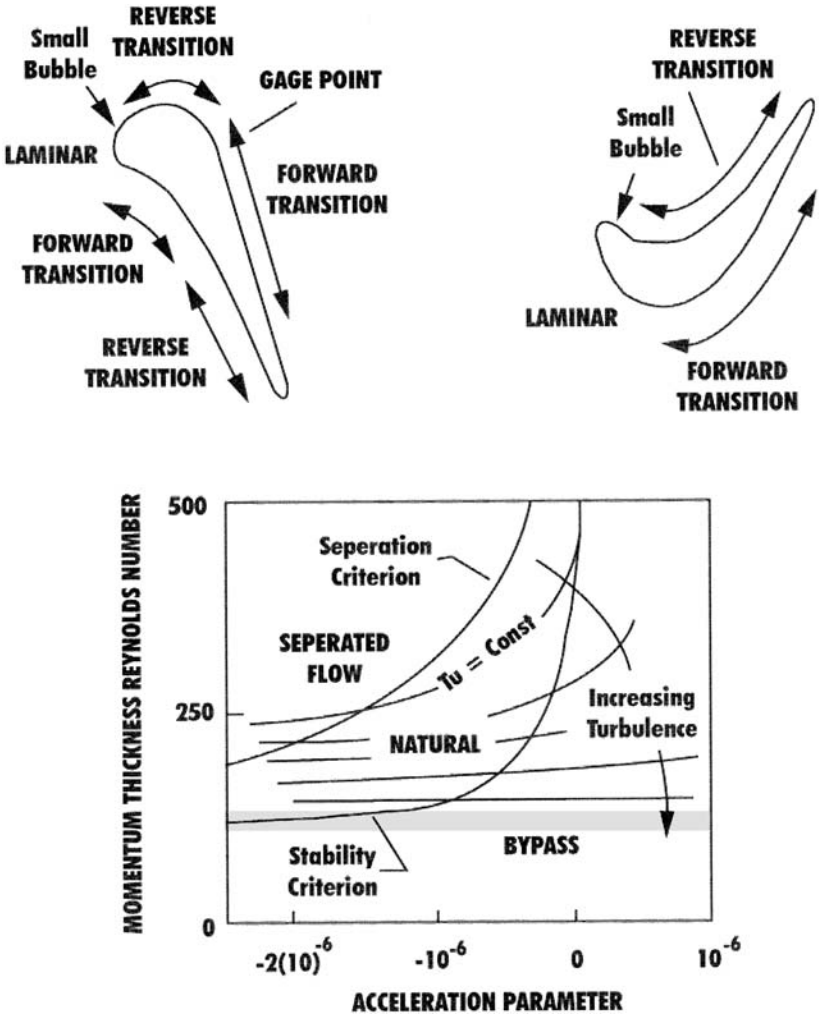

Figure 11 General boundary layer trends over the airfoil surface and regions of boundary layer behavior vs. momentum thickness Reynolds number and acceleration parameter.

St contours on the end walls (not shown) were in general in even more poor agreement because of the complex main stream flow driving the sheared boundary layers. Separating vortices at the junctions between the end wall and airfoils severely complicate the flow.

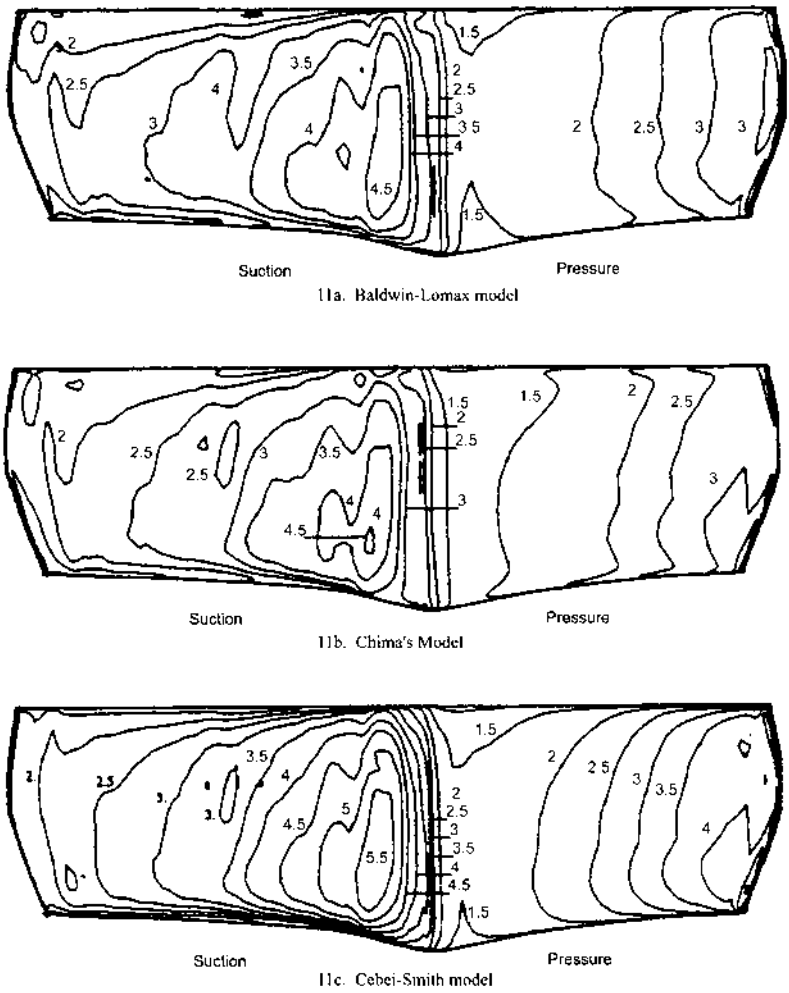

Figure 12 Comparison of three turbulence models used in the code of Chima [33] (see Boyle and Jackson [31]).

We can conclude that a simplified turbulence model for the main stream flow may produce acceptable aerodynamic results—as in the example given by Fig. 8—but acceptable prediction of heat-transfer coefficient distribution generally needs more sophisticated turbulence modeling.

HIGH-SPEED ROTATING, TRANSIENT EXPERIMENTS

Verification of turbine heat-transfer theories and design techniques by experiment has always been difficult because of the complex geometry and extreme fluid dynamic conditions involved. Fortunately, many designs and theories can be partially tested using static cascades of both vanes and blades. Combining all the important influences (transonic flow, rotation, vane-blade interaction, etc.), however, requires measurements in a facility that can provide full rotation, correctly modeled pressure ratio, correct gas-to-wall temperature ratio, and correct gas properties, i.e., ratio of specific heats and Prandtl number. If, in any test, these values match those for operation of the actual engine, we can be assured that the data we take (aerodynamic loss and heat transfer) will properly represent true engine values when the appropriate scaling is applied. This is the idea behind the new generation of experimental devices described in this section.

The early advances in high-speed turbine testing were made by Ainsworth et al. [36] at Oxford University and by Dunn [37] and his co-workers now at the Ohio State University. Both groups used the idea of full-stage, transient, rotational testing under properly scaled conditions. The Oxford group built several piston compression tubes to rapidly compress air to the desired conditions (temperature and pressure.) A fast-acting valve is then opened and this flow driven through a turbine for a few seconds while data are taken. The turbine in these experiments is spun up to operating speed by an air motor just before the flow begins. A novel aerodynamic brake holds the turbine at an almost-constant speed for the test time.

Heat transfer on the turbine surfaces is measured using transient heat-transfer gauges that are based on measuring the rate of rise of turbine surface temperature. Fast-response pressure sensors also are used to measure the aerodynamic loading.

The Oxford Group collaborated with the U.K. Defence Research Agency to build a larger diameter piston tube at the Defence Research Establishment (DERA) facility at Piestock in the United Kingdom. This facility is capable of accepting full-sized engine hardware and has been used to conduct a number of groundbreaking experiments. This facility was used to make the DERA measurements discussed above.

Dunn and his colleagues use the basically the same transient heat-transfer measurement approach, but instead substitute a shock tube for the piston tube as the flow source. Dunn's measurement times are much shorter than that of the Oxford and DERA devices, on the order of few milliseconds. The shock tube, however, eliminates the piston oscillations giving oscillating turbine inlet pressures sometimes seen in piston tubes. Dunn has an extensive literature on use of the shock tube method to large

and small and cooled and uncooled turbines. For further information, see his writings.

A third technique developed by Guenette et al. [38] at the Massachusetts Institute of Technology uses the adiabatic exhaust from a vessel of fixed volume as the flow source. While this does not provide a truly steady pressure into the turbine during the test period, the pressure decay rate is slow compared to typical characteristic times of the phenomena being measured. So for short periods (milliseconds) the inlet conditions may be assumed constant.

In a development similar to what occurred in the United Kingdom, U.S. researchers have built a larger-scale version (shown in Fig. 13) of the MIT "blow-down" rig at the U.S. Air Force Research Laboratory. As in the case of the relation between the Oxford and DRA facilities, the U.S. Air Force facility, the Turbine Research Facility (TRF), can perform heat-transfer measurements on full-scale engine turbines up to about 1 m in diameter.

The attractive feature of all three of these experimental facilities is that they are capable of reproducing the values of all five nondimensional

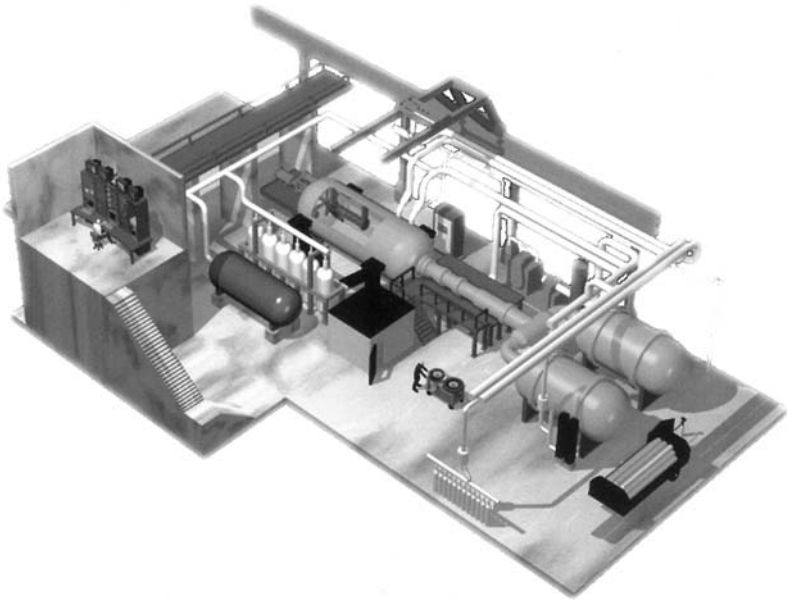

Figure 13 The Turbine Research Laboratory at the U.S. Air Force Research Laboratory.

quantities that are key to simulating an operating engine. These five nondimensional quantities are flow-path gas specific heat ratio, main stream gas-to-surface temperature ratio, fluid Prandtl number, blade-relative Mach number, and Reynolds number. When the experimental conditions are set to match these values in the laboratory and engine, the dependent variables of the problem—turbine work (and thus efficiency) and heat transfer—also become identical to the engine value when represented nondimensionally.

High-speed facilities, of course, need high-frequency response instrumentation. This instrumentation must also be of very small size in order that sufficient gauges be placed to resolve changes over the important turbine airfoil surfaces.

Figures 14 and 15 show, respectively, "miniature" pressure and temperature gauges that respond at rates approaching 100,000 Hz. The pressure gauges that use very small piezoelectric silicon wafers are set flush with the airfoil surface. These gauges have been well enough developed to be available commercially. An excellent introduction to the use of these pressure gauges, particularly calibration issues, is given by Dunn and Haldeman [39].

The miniature heat-flux gauges, of the type developed by Shultz and Jones [40] and others, operate by measuring the surface temperature of one

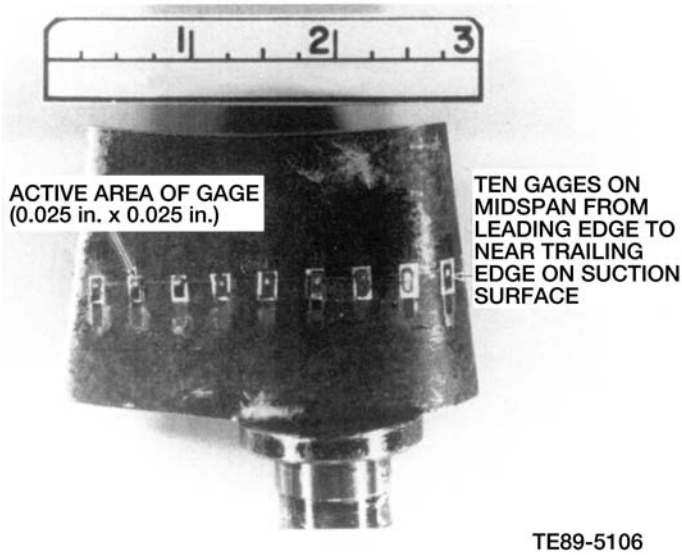

Figure 14 Miniature pressure gauges.

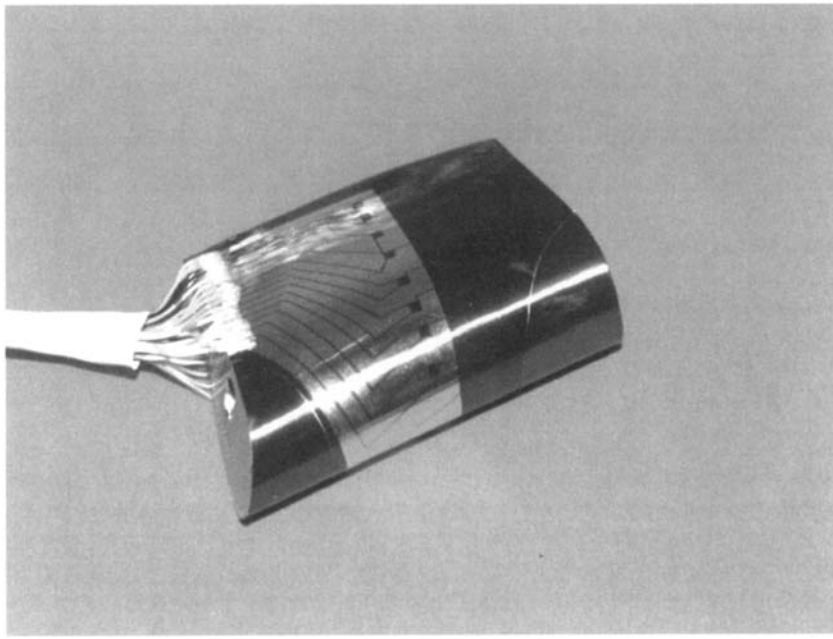

Figure 15 Miniature heat flux gauges.

or both sides of a thin plastic film. Because the testing is of short duration, the surface on which they are mounted may be assumed to be that of a semi-infinite body. Then the gauge-measured heating rate at the surface can be transformed into a heat-flux history using the Laplace transform technique (see [40]).

The literature also describes examples of several other types of high-frequency pressure and temperature gauges and the challenges involved in their use. For a representative example, see Dunn and Haldeman [39], where surface pressure and temperature fluctuations on a rotor blade surface from upstream wake passing were measured on a rotor blade surface revolving at 20,000 rpm.

Figures 16 and 17 present time-resolved, midspan heat-flux data from a moving blade in the MIT turbine blow-down turbine rig by Abhari et al. [41]. The plots are scaled heat-flux versus blade passing period (about two and a half passings in each case) at various positions on the blade for two different incidence angles, 0° (14a) and -10° (14b). As the figure shows, the heat flux is highly variable and depends primarily on the location on the

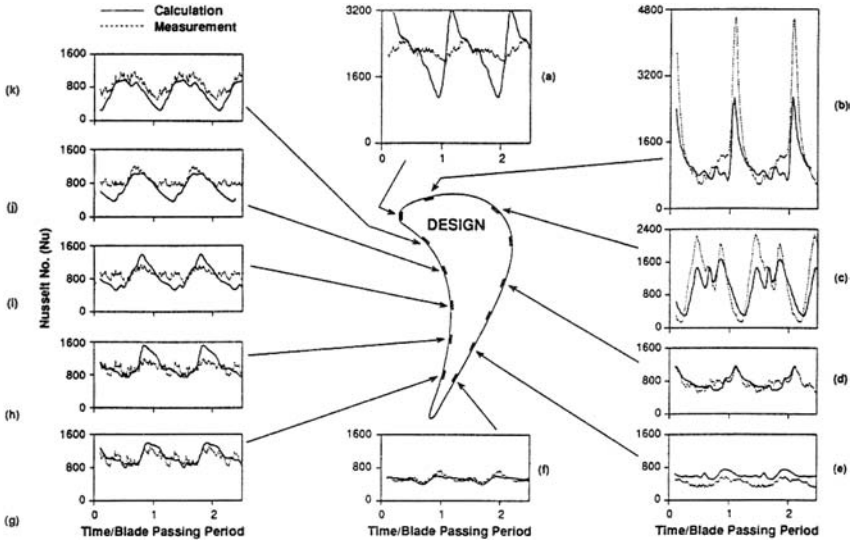

Figure 16 Time resolved heat transfer measurements and predictions at 0° incidence, Abhari et al. [41].

blade. Variations in magnitude of about a factor of up to 8 occur at each measurement point, but location on the blade surface is by far the most important determiner of heat-flux magnitude.

The results of the prediction are also given. The code is the 2D thin-layer Navier–Stokes code, called UNSFLO, developed by Giles and described in [42]. The code generally does very well, at least in a qualitative sense, at predicting the variation of heat flux with rotor position. Heat-flux magnitude is sometimes greater than observed and sometimes lower. In comparing the differences between incidence angles, it is the stagnation point and the suction side near the leading edge that seem to differ most. This is probably due the fluctuating state of the boundary layer as the wakes and shocks move over the leading edge and into the rotor passage. Much more concerning the detailed flow structure is given in [42].

Aerodynamic performance measurements made in short-duration facilities have been relatively few to date due mostly to concerns about accuracy. One can argue, however, that with proper care acceptable aerodynamic results are possible. Figure 17 shows results from a turbine vane cascade test in the AFRL TRF (Joe et al. [45]), which measured loading and loss, velocity traverses, and uncooled vane surface heat flux.

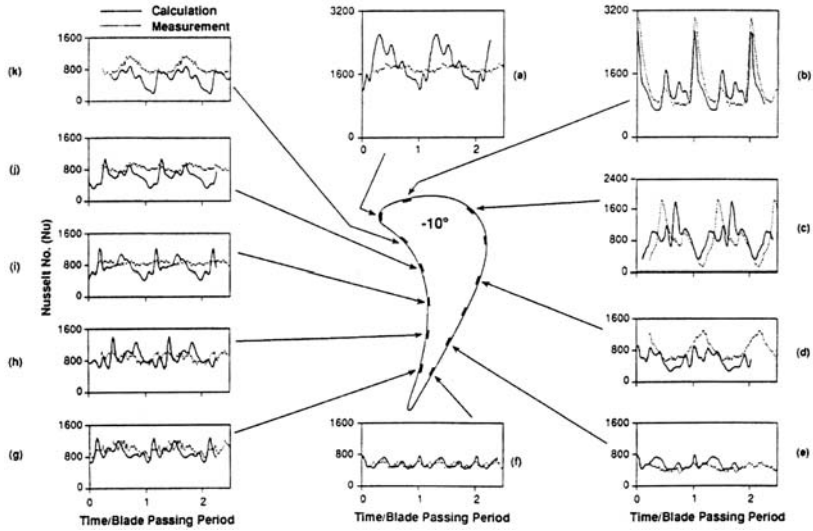

Figure 17 Time resolved heat transfer measurements and predictions at -10° incidence.

The figure shows good agreement between the measured vane surface pressure and an industrial design system predictive code. The total loss as a function of exit Mach number correlates reasonably well, and the measured and predicted total pressure loss in the vane wakes is a very good fit. For the heat transfer, once again, the predictive system misses the suction-side transition, while the pressure-side prediction is reasonable. The primary reason, of course, that good aerodynamic prediction is important is that the best knowledge of the free-stream state needs to be available to correctly determine boundary behavior.

ROTOR–STATOR INTERACTION MODELING

In addition to the heat-transfer analysis capability demonstrated in [Fig. 16] is the development many other of 3D unsteady CFD codes for turbines reached the literature in the early 1990s. As computing power continued to rise, researchers began to attempt computation of the full 3D rotating flow, sometimes with heat transfer and other times not.

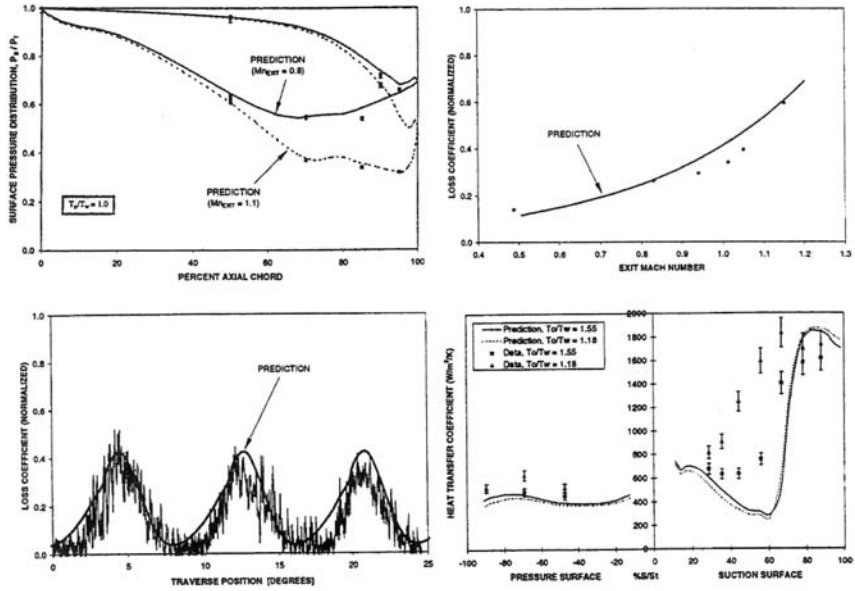

Figure 18 Aerodynamic and heat transfer results from the vane measurements of Joe et al. [43].

Often the key to making these calculations work is the gridding scheme chosen. Figure 19 shows a comparison between computation and experiment of surface static pressure normalized to total pressure for the code of Rao and Delaney [44] as compared to data taken by Dunn [37]. The computation is made on overlapping "O" and "H" grids between which information is shared iteratively as the solution is integrated forward in time. "O" grids consist of lines radiating outward from the airfoil surface, which intersect with concentric closed loops starting at the airfoil surface and moving outward. "H" grids are lines in the flow direction intersecting with lines from one blade surface to the next. This combination of grid schemes gives maximum solution accuracy both near the surface and throughout the main stream.

In these types of codes the boundary conditions must be nonreflecting in that as the solution proceeds (converges on a periodic unsteady solution), "waves" generated in the solution do not "bounce off" the edges of the solution grid and become artificially "trapped" in the grid.

Figure 19 gives the results of the 2D, unsteady, full Navier–Stokes calculations of the surface pressure over a full cord at midspan by Rao and

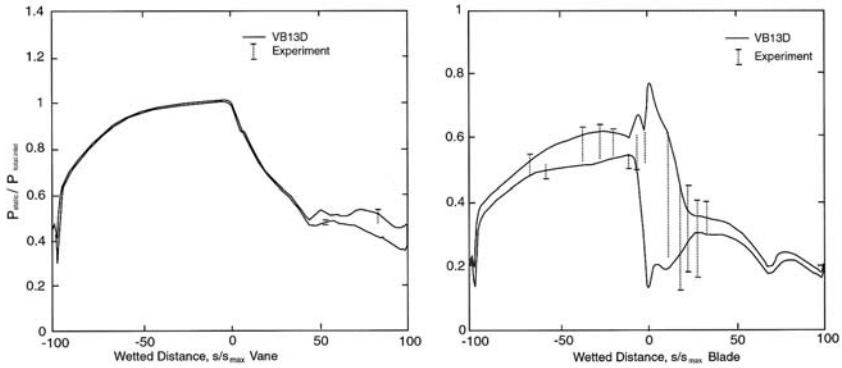

Figure 19 Surface pressure changes measured and computed for the turbine of Rao and Delaney. [44] Data and calculations shown for one complete rotor revolution.

Delaney. The solid lines show the variation of surface pressure versus chord. The data-range variations are given by the discrete symbols. Measurements were taken on a turbine of the same design in a shock tube facility. Given the difficulty of these measurements and the 2D form of the code, the comparison of experiment to computation is encouraging.

The computer time necessary to converge to a periodic unsteady 3D solution for even the most advanced current codes or computer systems is still prohibitive for day-to-day design. Fortunately a promising alternative technique, the Average Passage Method (APM), developed by Adamczyk [46] is now becoming more widely known and used. The APM is an approximate technique that takes into account unsteady vane-blade interaction effects in steady calculations of turbine and compressor through flow.

The idea of the Average Passage Method is to apply assumptions similar to those of Reynolds averaging and define new averaging operators, reducing the problem of computing the complex 3D unsteady flow through the stage (or stages) to an equivalent 3D steady flow system. The central assumption is that the flow can be decomposed into three parts, each part representing a portion of the total unsteady motion.

In the first part, the flow is decomposed into an unsteady, deterministic part plus a nondeterministic (random) part, essentially turbulence. Once the turbulence is ensemble-averaged out, then the remaining unsteady deterministic flow is divided into two more parts: one is the steady part of the flow, and the other the deterministic, but unsteady part. The

deterministic unsteady part arises from rotor–stator interactions and the rotor motion through the stator field (or vice versa, depending on the location of the reference axis). If this is a multistage turbine, there will also be unsteady effects from wakes of upstream stages, but these will not be repeating in the same time cycle as the influences from the immediate upstream airfoil row. To remove the unsteadiness due to upstream stages, the last of the three averaging processes is applied.

Because each new averaging creates new correlation terms, by the time we have completed the last averaging there are 25 correlation terms in just the *r*-momentum equation alone. As in the Reynolds averaging of the Navier–Stokes equations, a model must be provided for each of these correlation terms.

Despite the effort needed to apply models for all the correlation terms, the finished (fully derived) model can be implemented as a reasonably efficient computer code. Whereas the analysis of a given design may require several hundred hours with a massively parallel computer for a fully unsteady calculation, in the same time several hundred runs of a code using the APM could be made. This should certainly be enough to firm up the design of a given machine.

Figure 20 shows some comparisons of using average passage calculations to predict the total pressure and total temperature profiles after a LPT stage. (No heat-transfer results seem to be available as yet from Average Passage Methods.) Looking at the figure, especially when noting the increment of the scale shown, the prediction of the shape and magnitude of the profiles is close to—if not actually superior to—most steady 3D methods.

How the APM approach will perform in heat-flux calculations is yet to be tested.

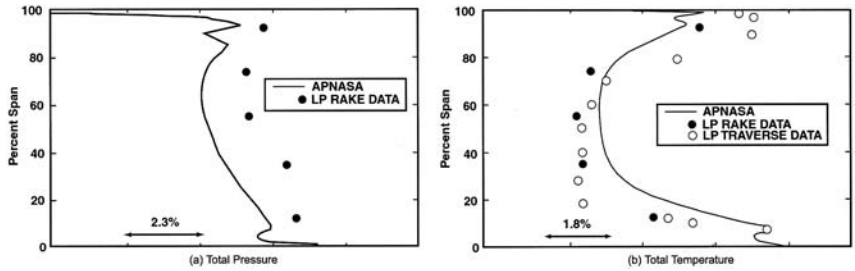

Figure 20 Results of APNASA calculations of flow through a low pressure turbine. A high pressure stage is located upstream.

NONUNIFORM INLET FLOW

All gas turbines operate with a combustor that supplies the energy to the flow through the addition of the enthalpy (heat) of combustion. Because combustor space and weight generally must be kept to a minimum, designs tend to have features that present a more or less nonuniform flow to the turbine, i.e., hot and cold streaks relative to the average flow temperature. In addition, cooling gas may be introduced through the combustor and vane walls to protect them from the hottest gases. Inertia forces separate this mixture of hotter and cooler flow as it is accelerated and turned through the vanes and blades. This process sets up secondary flows in the blade passages; that is, gas movement not directly aligned with the center of the passage because of the density differences between the hot and cold flows. This is often called the Kerrebrock–Mikolaczak effect after a study by these authors of similar phenomena in compressor inlets [47].

One of the first experimental studies of nonuniform inlet flow effects was by Roback and Dring [48]. These authors used a large-scale rotating rig (Fig. 21), with a mixture of air and carbon dioxide to simulate the density difference between typical hot and cold flows. They found that the "rectification" process, as they define it, caused hot gas to accumulate on the pressure sides of rotating blades (an often-observed phenomenon revealed by higher rates of heat transfer on the pressure sides) and cold gas to accumulate on the suction sides. In cooled turbines, stator coolant injected upstream can add to the accumulating flow on the rotor suction side. Other parts of the rectification process observed defined the effect of the ratios of temperature (density) between the hot and cold streaks in radial movement toward the tips and end walls.

FREE-STREAM TURBULENCE

Free-stream turbulence (FST) is known to have very significant effects on transition and separation, and therefore on heat transfer. This may be above and beyond the FST effect on the magnitude of the heat transfer in a boundary that has not yet separated. Some of the first work on FST effects is that of Kestin et al. [49], which was followed by several others and continues today. Figure 22, from [50], demonstrates the sensitivity of airfoil heat transfer to lower levels of FST. Many more recent studies have been done with higher levels of FST that are expected to exist at the combustor outlet. A good summary of the earlier work is found in Thole and Bogard [51], where a correlation is presented, given in Fig. 23, based on data provided from Hancock and Bradshaw [52] and others. The correlation

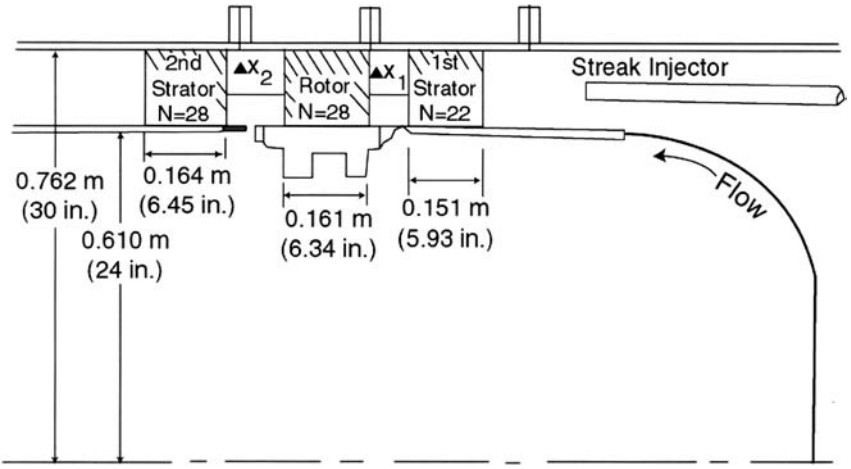

Figure 21 The UTRC large scale $1\frac{1}{2}$ stage turbine facility for the study of inlet flow effects.

recognizes the two characterizations (or descriptors) of isotropic turbulence, intensity and length scale in the ranges expected to be found in the turbine inlet flow. (Most researchers have assumed that combustor exit turbulence can be well modeled as isotropic, despite characteristics of combustor design that might suggest otherwise.) While generally following the trend of experimental results, Thole and Bogrard's correlation needs further validation through comparison with additional data before it is suitable for design.

CONCLUDING REMARKS

Clearly, there has been great progress in understanding and predicting turbine heat transfer in the last 50 years. The physical and mathematical modeling of the fluid flow and heat transfer through these seemingly simple yet actually complex devices has improved our design capability greatly. Better design methods have been the key to continually higher operating temperatures and longer component lives.

If we are to continue these trends there are still many phenomena to investigate. The following are the highest-priority issues to be addressed in the next decades:

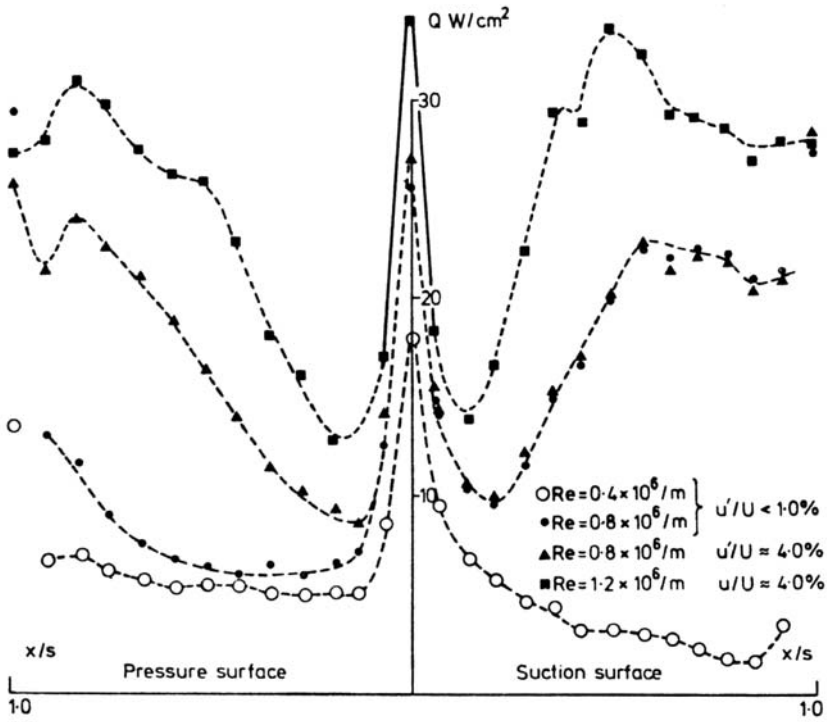

Figure 22 Typical distributions of heat transfer around a nozzle guide vane at different levels of grid-produced turbulence, U′/U. From Jones [50].

1. Rotor–stator interaction effects on transition and separation. The effect of wake passing from an upstream blade row through a downstream blade row (stage) can now be computed, but modeling the wake's effects on transition, separation, and, possibly, reattachment and relaminarization are only approximately understood.

2. Off-design performance, particularly low Reynolds number performance. A number of current conceptual aircraft designs, both civilian and military, operate at very high altitudes or are powered by smaller engines. Most of these engine concepts have low-pressure turbines that will operate at Reynolds numbers where separation on the airfoil suction side is a major problem. The heat-transfer consequences of this low Reynolds number operation are only now being addressed.

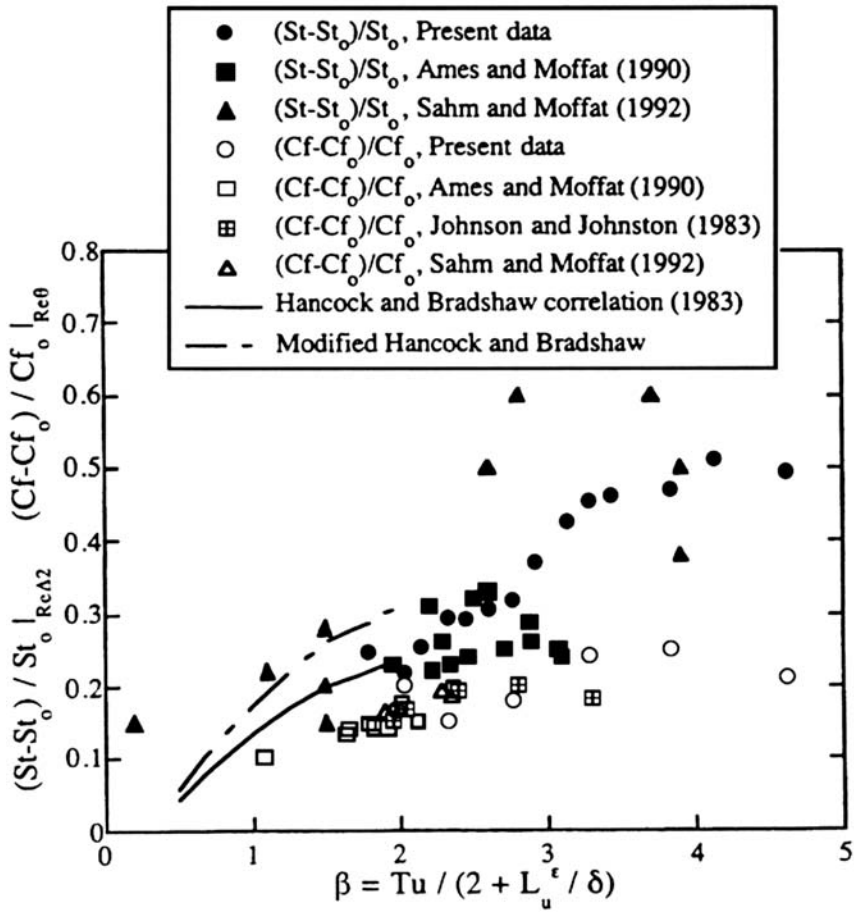

Figure 23 Comparison between heat transfer and skin friction enhancements collected by Thole and Bogard [51].

3. Active or passive boundary-layer control. This is perhaps the most fruitful area of research in turbine heat transfer. Modern high-performance aero engines may use upwards of 25% of the flow entering the inlet to cool parts in the hot section, with the majority of cooling flow going to the turbines. If workable control of boundary-layer behavior can be realized, the amount of cooling air needed could be reduced significantly (see Rivir et al. [53]). Film cooling and its characteristics, of course, form another very rich category of heat-transfer research, which is covered in the next chapter.

4. Better instrumentation for heat-transfer and aerodynamic studies. There is a great need for nonintrusive wide-area sensing devices, particularly for temperature and pressure that can be read at high rates. The sensors or sensing media will most likely need to be read optically to give a 2D surface field of information at one time. This would solve a number of difficult problems encountered using today's technology. In particular, limitations on sensor placement and wire routing and breaking would be eliminated.

Acknowldgements

The author wishes to thank Dr. Richard Rivir, Mr. Jeffrey Stricker, and Ms. Renee Kaffenbarger of the Air Force Research Laboratory, Prof. Michael Dunn of Ohio State University, and Prof Michael Crawford of University of Texas. Thanks, too, to Dr. Louis Povinelli, Dr. Raymond Gaugler, and Mr. Robert Boyle of NASA/Glenn Research Center, and to Dr. David Wistler of the General Electric Company for their kind assistance. Ms. Dayna Groeber of RCF Information Systems Inc. did outstanding work in preparing the illustrations. Finally, I'd like to thank my loving wife, Joanne, for her contribution.

REFERENCES

1. J. H. Horlock, *Axial Flow Turbines Fluid Mechanics and Thermodynamics*, Butterworth and Co. Ltd., London, 1966.
2. C. H. Wu, "A Generalized Theory of Three-Dimensional Flow in Subsonic and Supersonic Turbomachines of Axial, Radial, and Mixed Flow Types," NACA Tech. Note 2604 (1952).
3. T. Katsanis and McNally, "FORTRAN Program for Calculating Velocities and Streamlines on the Hub-Shroud Mid-Channel Stream Surface of an Axial-, Radial-, or Mixed Flow Turbomachine or Annular, Duct, Vol. 1 User's Manual, Vol. 11 Programmer's Manual," NASA TND-8430, 8431 (1977). See also: R. A. Novak and Hearsay, "A Nearly Three Dimensional Intrablade Computing System for Turbomachinery," ASME-76-FE-19 and -20, 1976.
4. T. Katsanis "FORTRAN Program for Calculating Transonic Velocities on a Blade-to-Blade Stream Surface of a Turbomachine," NASA TN D5427 (1969).
5. S. V. Patankar and D. B. Spalding, *Heat and Mass Transfer in Boundary Layers*, Morgan-Grampian Press, London, 1967.
6. D. A. Anderson, J. C. Tannehill, and R. H. Pletcher, *Computational Fluid Mechanics and Heat Transfer*, Hemisphere Publishing Co., New York, 1984.
7. M. E. Crawford, "Simulation Codes for Calculation of Heat Transfer to Convectively Cooled Turbine Blades," in *Convective Heat Transfer and Film*

Cooling in Turbomachinery (T. Arts, ed.), Lecture Series 1986–06, von Karman Institute for Fluid Dynamics, Rhode-Saint-Genese, Belgium, 1986.
8. M. E. Crawford, "Simulation Codes for the Calculation of Heat Transfer to Convectively Cooled Turbine Blades," 130 pp, a set of four lectures in Convective Heat Transfer and Film Cooling in Turbomachinery, T. Artz Ed. Lecture Series 1986–06, Von Karman Institute for Fluid Dynamics, Rhode-Saint-Genese, Belgium, 1986.
9. H. W. Emmons, and A. E. Bryson, "The Laminar–Turbulent Transition in a Boundary Layer Part," *J. Aeo. Sci., 18*: 490–498 (1951).
10. F. M. White, *Viscous Fluid Flow*, McGraw Hill, New York (1974).
11. W. M. Kays and M. E. Crawford, *Convective Heat Transfer*, McGraw Hill, New York (1980).
12. J. P. Clark, J. E. LaGraff, P. J. Magari, and T. V. Jones, "Measurement of Turbulent Spots and Intermittency Modeling at Gas Turbine Conditions," Presented at the 80th Symposium of the Propulsion and Energetics Panel Heat Transfer and Cooling in Gas Turbines, Antalya, Turkey, October 12–16, 1992.
13. L. S. Langston, M. L. Nice, and R. M. Hooper, *J. of Eng. for Power* (1977).
14. D. J. Doorly and M. J. Oldfield, "Simulation of the Effects of Shock Wave Passing on a Turbine Rotor Blade," *International J. of Eng. for Gas Turbines and Power, 107*: 998–1006 (1985).
15. D. J. Dorney, D. E. Ashpis, D. E. Halstead, and D. C. Wisler, "Study of Boundary Layer Development in a Two Stage Low Pressure Turbine," NASA/TM-1999-208913 (1999).
16. M. F. Blair, "An Experimental Study of Heat Transfer in a Large Scale Turbine Rotor Passage," ASME Paper 92-GT-195 (1992).
17. S. P. Harasgama, F. H. Tarada, R. Baumann, M. Crawford, and S. Neelakantan, "Calculation of Heat Transfer to Turbine Blading Using Two-Dimensional Boundary Methods," ASME Paper 93-GT-79 (1993).
18. W. Haas and B. Shoenung, "Erweiterte Version des Filmkuehlmodells im Grenzschichtverfahren GRAFTUS/R zur erfassung von Dichteunterschieden bei Filmkuelstroemungen," *Institut fuer Hydromechanik TH Karlssruhe Nr. 662* (1988).
19. F. Tarada, "Prediction of Rough Wall Boundary Layers Using a Low Reynolds Number k-epsilon Model," *Intl. J. of Heat and Fluid Flow. 4*: 331–345 (1990).
20. C. K. G. Lam and K. Bremhorst, "A Modified Form of the k-epsilon Model for Predicting Wall Turbulence," *Trans. ASME J. of Fluid Eng., 103*: 456–460 (1981).
21. K. Y. Chen, "Predictions of Channel and Boundary Layer Flows with a Low Reynolds Number Turbulence Model," *AIAA J., 20*: 33–38 (1982).
22. J. D. Denton, "Extension of the Finite Volume Time Marching Method to Three Dimensions," *Von Karman Institute Lecture Series Transonic Flows in Turbomachinery* (1976).
23. M. M. Rai, "Navier–Stokes Simulations of Rotor-Stator Interactions Using Patched and Overlaid Grids," AIAA Paper 85–1519 (1985).

24. R. H. Ni, "A Multiple Grid Scheme for Solving the Euler Equations," *AIAA J. 20*(11): 1565–1571, Nov. (1982).
25. C. Ha, "A Navier–Stokes Analysis of Three Dimensional Turbulent Flows Inside Turbine Blade Rows," ASME Paper 83-GT-40 (1983).
26. R. C. Kingcombe, S. P. Harasgama, Leversuch, and E. T. Wedlake, Aerodynamic and Heat Transfer Measurements on Blading for a High Rim Speed Transonic Turbine," ASME Paper 89-GT-228 (1989).
27. N. J. Seyb, "The Role of Boundary Layers in Axial Flow Turbomachinery and the Prediction of Their Effects," AGARD-AG-164, pp. 241–259 (1972).
28. K. K. Chen and N. A. Thyson, "Extension of Emmon's Spot Theory to Flows on Blunt Bodies," *AIAA J. 9*(5): 821–825 (1971).
29. R. J. Boyle, "Navier–Stokes Analysis of Turbine Blade Heat Transfer," ASME 90-GT-42 (1990).
30. R. E. Mayle, "The Role of Laminar-Turbulent Transition in Gas Turbine Engines," *J. Turbomachinery, 113* 509–537 (1991).
31. R. J. Boyle and Jackson, "Heat Transfer Predictions for Two Turbine Nozzle Geometries at High Reynolds and Mach Numbers," NASA TM 106956 (1995).
32. B. S. Baldwin and H. Lomax, "Thin Layer Approximation and Algebraic Model for Separated Turbine Flows," AIAA Paper AIAA-78-257 (1978).
33. R. V. Chima, W. J. Giel and R. J. Boyle, "An Algebraic Turbulence Model for Three Dimensional Viscous Flows," AIAA Paper 93-0083 (NASA TM-105931) (1993).
34. T. Cebeci and A. M. O. Smith, *Analysis of Turbulent Boundary Layers*, Academic Press, New York (1974).
35. R. V. Chima, "Explicit Multi-Grid Algorithm for Quasi Three Dimensional Flows in Turbomachinery," *AIAA J. Propulsion and Power, 3*(5): 397–405 (1987).
36. R. W. Ainsworth, D. L. Shultz, M. R. D. Davies, C. J. P. Forth, M. A. Hilditch, M. L. G. Oldfield, and A. G. Sheard, "A Transient Flow Facility for the Study of Thermofluid-Dynamics under Engine Representative Conditions," ASME 88-GT-144 (1988).
37. M. G. Dunn, International Gas Turbine Institute Scholar Lecture, "Convective Heat Transfer and Aerodynamics in Axial Flow Turbines," ASME 2001-GT-0506 (2001).
38. G. R. Guenette, A. H. Epstein, M. B. Giles, R. Hames, R. J. G. Norton, "Fully Scaled Turbine Rotor Heat Transfer Measurements," *ASME J. Turbomachinery, 111*: 1, Jan. (1989).
39. M. G. Dunn and C. W. Haldeman, Jr., "High Accuracy Turbine Performance Measurements in Short Duration Facilities," *ASME J. Turbomachinery, 120*: 1–9, Jan. (1998).
40. D. L. Shultz and T. V. Jones, "Heat Transfer Measurements in Short Duration Hypersonic Facilities," AGARDograph, No. 165 (1973).
41. R. S. Abhari, Guenette, A. H. Epstein, and M. B. Giles, "Comparison of Time-Resolved Turbine Rotor Blade Heat Transfer Measurements and Numerical Calculations," ASME 91-GT-268 (1991).

42. M. B. Giles, "Calculation of Unsteady Wake Rotor Interaction," *AIAA J. Propulsion and Power, 4*(4): 356–362 (1988).
43. K. V. Rao and R. A. Delaney, "Vane-Blade Interaction in a Transonic Turbine, Part I Aerodynamics," *AIAA J. Propulsion and Power, 10*(3): 305–311 (1994).
44. K. V. Rao, R. A. Delaney, and M. G. Dunn, "Vane-Blade Interaction in a Transonic Turbine, Part II—Heat Transfer," *AIAA J. Propulsion and Power, 10*(3): 312–317 (1994).
45. C. R. Joe, X. A. Montesdeoca, F. O. Soechting, C. D. MacArthur, and M. Meininger, "High Pressure Turbine Vane Cascade Heat Flux and Aerodynamic Measurements with Comparisons to Predictions," ASME 98-GT-430 (1998).
46. J. J. Adamczyk, "Aerodynamic Analysis of Multistage Turbomachinery Flows in Support of Aerodynamic Design, 1999 International Gas Turbine Institute Scholar Lecture," *ASME J. Turbomachinery, 122*: 189–217, April (2000).
47. J. L. Kerrebrock and A. A. Mikolajczak, "Intra Stator Transport of Rotor Wakes and Its Effect on Compressor Performance," *ASME J. Eng. for Power*, pp
48. R. J. Roback and R. P. Dring, "Hot Streaks and Phantom Cooling in a Turbine Rotor Passage, Part 1—Separate Effects, Part 2—Combined Effects and Analytical Modeling," *ASME J. Turbomachinery, 115*: 657–674.
49. J. Kestin, P. F. Maeder, and Wang, "Influence of Turbulence on the Heat Transfer from Plates with and Without a Pressure Gradient," *Int. J. Heat and Mass Transfer, 3*: 133 (1961).
50. T. V. Jones, "Gas Turbine Studies at Oxford 1969–1987," ASME Paper 88-GT-112 (1988).
51. K. A. Thole and D. Bogard, "Enhanced Heat Transfer and Shear Stress Due to High Free Stream Turbulence," ASME Paper 94-GT-296 (1994).
52. P. E. Hancock and P. Bradshaw, "The Effect of Free-Stream Turbulent Boundary Layers," *ASME J. Fluids Engineering, 105*: 284–289 (1983).
53. R. B. Rivir, R. Sondergaard, J. P. Bons, and J. P. Lake, "Passive and Active Control of Separation Control in Gas Turbines," AIAA Paper 2000–2235 (2000).

4

Selection of a Gas Turbine Cooling System

Boris Glezer

Optimized Turbine Solutions, San Diego, California, U.S.A.

This chapter focuses primarily on the heat- and mass transfer issues as they are applied to cooling of turbomachinery components, and the reader is expected to be familiar with fundamentals in these fields. A number of excellent books [1–7] can be recommended in reviewing these fundamentals, including Streeter, *Fluid Dynamics*, Eckert and Drake, *Analysis of Heat and Mass Transfer*, Incropera and DeWitt, *Fundamentals of Heat and Mass Transfer*, Rohsenow and Hartnett, *Handbook of Heat Transfer*, Kays, *Convective Heat and Mass Transfer*, Schlichting, *Boundary Layer Theory*, and Shapiro, *The Dynamics and Thermodynamics of Compressible Fluid Flow*.

When a comprehensive source of information is available, the author of this chapter refers the reader to such a source; however, when data are spread over various papers, the author attempts to summarize this data in the chapter.

NOMENCLATURE

a—speed of sound
b—linear dimension in rotational number
A—reference area, annular area of gas path
A_g—airfoil outer surface
$\mathrm{Bo} = \mathrm{Gr}/\mathrm{Re}^2$—buoyancy number
BR, M—blowing rate
C_p—specific heat at constant pressure
d—hydraulic diameter
e—turbulator height
$\mathrm{Ec} = (\gamma - 1)M^2T/2\Delta T$—Eckert number
FP—flow parameter for cooling air
g—gravitational acceleration
G—heat-transfer roughness parameter
$\mathrm{Gr} = \mathrm{R}\omega^2\beta\Delta T d_h^3/v^2$—Grashof number
h—heat-transfer coefficient
h_t—heat-transfer coefficient augmented by turbulators
$\rho_f V_f^2/\rho_\infty V_\infty^2$—momentum flux ratio
k—thermal conductivity
kf—thermal conductivity of fluid
L—a reference length
m—mass flow rate
m_c—cooling flow rate
$M = \rho_f V_f/\rho_\infty V_\infty$—blowing rate
$\mathrm{Ma} = \mathrm{V}/\mathrm{a}$—Mach number
N, rpm—rotor speed
$\mathrm{Nu_L} = hL/k_f$—Nusselt number
$\mathrm{Pr} = \mu c_p/k$—Prandtl number
PR—compressor pressure ratio
Ps—static pressure
P_t—total pressure
P_{tin}—inlet total pressure
Q—heat-transfer rate, energy transfer rate
q''—heat flux
p—pitch of turbulators
r—radial position
R—mean radius, radius of combustor, resistance, gas constant
R_i—blade local radius
R_T—blade-tip radius
R_h—blade hub radius
$\mathrm{Re}d = \rho V d/\mu$—Reynolds number based on hydraulic diameter

$\mathrm{Re}\,L = \rho VL/\mu$—Reynolds number based on L
$\mathrm{Ro} = \omega b/U$—rotational number
$\mathrm{Ros} = 1/\mathrm{Ro}$—Rossby number
s—normalized surface distance
St—Stanton number
t—time
T_c—cooling air temperature, also compressor discharge temperature
Tf—surface film temperature
T_g—gas temperature
T_{gin}—inlet gas temperature
T_m—metal temperature, also mixing-layer temperature
T_{ref}—reference temperature
T_{st}—local static temperature
Tu—turbulence intensity
u'—local axial velocity fluctuation
u_{in}—inlet gas velocity
U, V, W—main-stream or cooling flow stream velocity components in x, y, z directions
w—width
α—film jet inclination angle
β—angle between film jet and main-stream vectors
γ—specific heat ratio
ε—volumetric coefficient of thermal expansion, surface roughness
ε_h—eddy thermal diffusivity
ε_m—eddy momentum diffusivity
ξ—heat-transfer effectiveness
η_c—cooling effectiveness
$\dot{\eta}$—thermal efficiency
μ—absolute gas viscosity
ρ—density
σ—rupture stress limit
ω—rotational frequency

Subscripts

aw—adiabatic wall
b—bulk
c—coolant
d—based on leading-edge (cylinder) diameter
f—film
hc—hot cascade
o—total

tur—turbine
w—wall
∞—mainstream (free-stream) condition

TURBINE COOLING AS A KEY TECHNOLOGY FOR ADVANCEMENT OF GAS TURBINE ENGINES

The performance of a gas turbine engine is strongly influenced by turbine inlet temperature, and substantial performance increases can be achieved with the maximum allowable turbine inlet temperature. From a performance standpoint, stoichiometric combustion with turbine inlet temperature around 2,000 °C (3,650 °F) would be a thermodynamic ideal because no work would be "wasted" to compress air needed to dilute combustion products. Therefore, the current industry trend pushes the turbine inlet temperature closer to the fuel stoichiometric temperature, especially for military engines. However, allowable component metal temperatures, even for the most advanced alloys and manufacturing processes, cannot exceed 930–980 °C (1,700–1,800 °F). To operate at gas temperatures well above this limit, a highly efficient component cooling system is required. Advancement in cooling is a major means to achieve higher turbine inlet temperatures, leading to improved performance and life of the turbine. Heat transfer is thus a very important design element for all parts of a modern gas turbine, but especially the combustor and turbine sections. In discussing the state-of-the-art cooling design of the hot section it is important to keep in mind that the turbine designer is constantly under extreme pressures of development schedule, affordability, durability, and various other interdisciplinary constraints, all these strongly affecting the selection of a cooling design.

Cooling Challenges for Constantly Increasing Gas Temperatures and Compressor Pressure Ratio

Progress in modern high-efficiency and high specific power gas turbine engines is typically measured by the increases in operating temperature and overall compressor pressure ratio. The most common simple cycle engines with higher pressure ratios and correspondingly increased gas temperatures can achieve greater power for the same size and weight and better overall engine fuel efficiency. Engines with recuperators do not benefit thermodynamically from high compressor pressure ratio. Advanced alloys for turbine airfoils can safely operate at metal temperatures below 980 °C (1,800 °F) and alloys for discs and stationary structures are limited to 700 °C

(1,300 °F). But modern gas turbines operate at turbine inlet temperatures that are well above these limits. There is also a significant difference in the operating temperature between advanced aircraft turbines and industrial turbines. This is the result of fundamental differences in the required life, weight, fuel/air quality, and restrictions on emissions.

For advanced aero engines turbine rotor inlet temperatures (TRIT) close to 1,650 °C (3,000 °F) and compressor pressure ratios around 40:1 are becoming a reality. A high specific power, which is a primary objective for this type of engine, is usually obtained along with high efficiency. Such extreme operating conditions inherently require frequent engine inspections and continuous health monitoring. For industrial engines the leading requirement is long-term durability without frequent inspections and overhauls. Typically, major industrial turbine components are expected to endure at least 30,000 hours between overhauls, with potential to be repairable such that the engine life can be extended to 100,000 hours. This compares to aircraft turbine component lives of only a few thousand hours. This factor, as well as the usual requirement of a compressor discharge pressure to be below the available gas pipeline fuel supply pressure, leads to a moderately high turbine rotor inlet temperature. The TRIT limit for a modern industrial gas turbine is established presently in the range of 1,260–1,370 °C (2,300–2,500 °F). Figure 1 illustrates the recent history of continuously rising TRIT and compressor pressure ratios. This rising temperature trend results in the operating gas temperatures significantly exceeding acceptable material capability limits and requires the application of cooling in various engine hot section components, particularly in the components exposed to the high-temperature environment. Relatively cold air from the compressor discharge and, in some cases, from intermediate compressor stages is the traditional source to cool turbine components. After performing the cooling task, this air is discharged into the main stream. The cooling air discharged within each particular cooled stage practically does not perform any work on this stage before it is accelerated to the mainstream velocity. This leads to significant losses in engine performance. In summary, disadvantages of the open air cooling system include a relatively low cooling effectiveness, significant losses of work required to compress cooling air, and mixing losses that reduce aerodynamic efficiency of the turbine. The main advantage of the open air cooling system making it the most common for gas turbines is its simplicity, compared to a close loop cooling system.

With compressed air pressure ratios for modern aero engines exceeding 30:1 and reaching 40:1, the temperature of the compressor discharge air approaches 650 °C (1,200 °F). This creates a significant difficulty in using this air to cool the turbine discs, stators, and vicinity of

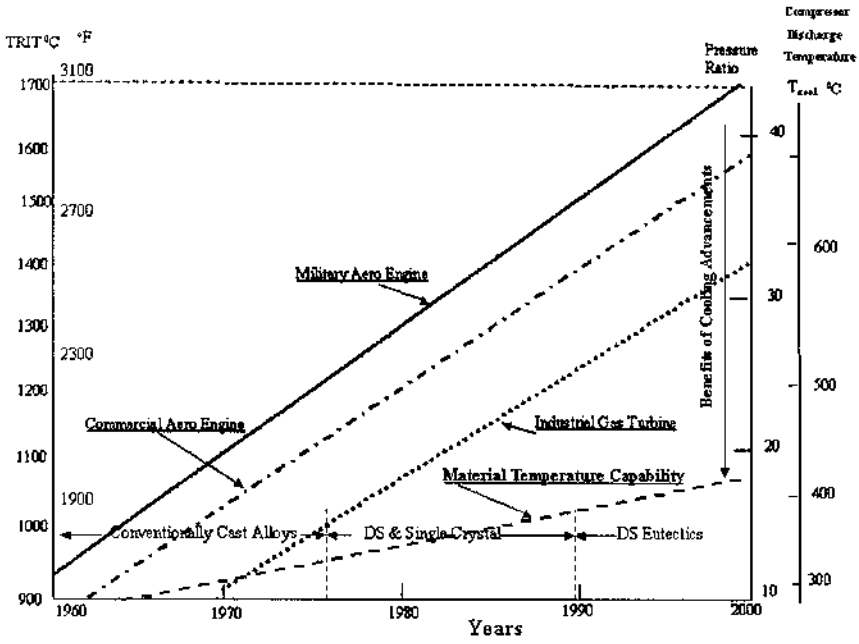

Figure 1 Trend or growth for key engine operating parameters.

the last stages of a compressor rotor, considering that temperature capability of the material for these components is limited to about 700 °C (1,300 °F). Application of a lower-temperature air from an intermediate compressor stages can be beneficial if this air has a sufficient pressure margin over the exterior pressure of the cooled component. In some cases, the temperature of the discharge air can be reduced in an external heat exchanger, for example, using in the cooling circuit a low-temperature bypass air in aero engines or water in combined cycle industrial turbines.

A closed cooling system, where the coolant continuously circulates in a closed loop, presents a more efficient but more complex alternative to the open system. Closed-loop systems using liquid metal coolants are known for space application. A closed-loop steam cooling system that had been tried decades ago is regaining its popularity for heavy-duty industrial gas turbines, particularly in combined cycle power generation plants.

Advancements in cooling technology are a critical means, together with improvements in high-temperature materials, to achieve higher turbine inlet temperatures. Cooling systems must be designed to assure that the maximum component temperatures and temperature gradients experienced

during engine operation are compatible with the maximum stress limits imposed by the specified operating life of the component. The cooling system design and development process requires innovative design experience, proven analytical methods, and sophisticated experimental facilities, as well as advanced materials and manufacturing techniques. This establishes the required confidence in the prediction of turbine component temperatures affecting life and performance of the engine.

A major design challenge in achieving high turbine efficiency is to minimize the flow rate of turbine cooling air with the best utilization of its cooling potential for providing the required component temperatures. An additional factor that should be considered, particularly in the industrial environment, is the fuel/air quality, which is often responsible for erosion of the coatings that protect the hot section components. Operation in such environment also requires larger cooling passages to avoid their blockage.

Major gas turbine components typically requiring cooling include:

Stage 1 and Stage 2 nozzle vanes
Stage 1 blades
Support structure for the nozzles and tip shrouds (nozzle case, diaphragms)
Turbine disc/rotor assemblies
Combustor liners

In addition to component temperature reduction, another important role for the cooling system is to control "passively" or "actively" the relative position between rotor and stator, maintaining turbine blade-tip clearances.

Commonly Used Cooling Techniques

The most common cooling techniques, for the reasons stated above, are based on the application of the air bled from the compressor discharge or intermediate stages. Figure 2 illustrates a generic turbine hot section with main elements of turbine and combustor cooling system. Introduction of the turbine cooling air downstream of the combustor results in degradation of turbine performance because less work is extracted from the compressed cooling air. At the same time the reduced amount of air available for the combustor makes liner cooling and emission control more difficult. This poses a major challenge for the designer of the cooling system: select a system that requires a minimal amount of cooling air to achieve targeted metal temperature of the turbine components and produces the smallest negative impact on engine durability, performance, weight, emission, cost, and fabrication complexity. Out of these most important engine characteristics, weight reduction is a major design criterion for aero engines, and

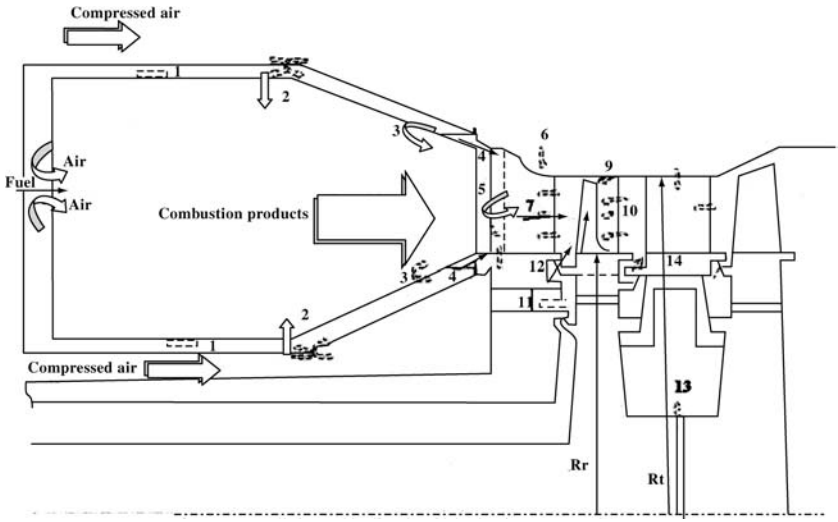

Figure 2 Generic turbine hot section cooling system: 1. back side cooling in-series with combustion air, 2. dilution air, 3. liner exit film, 4. nozzle endwall film, 5. nozzle shower head film, 6. tip clearance control modulated air, 7. nozzle trailing edge discharge, 8. blade leading edge air, 9. blade tip discharge, 10. blade trailing edge discharge, 11. preswirled air, 12. disc forward cavity buffer air/blade platform film, 13. interstage buffer air, 14. disc aft cooling air/stage 2 nozzle endwall film.

long-term durability and emission reduction are often critical targets for industrial engines.

Stage 1 nozzle vanes operate at the highest cycle gas temperatures and blades experience a combination of high temperatures and centrifugal loads. Accordingly, cooling them presents the most challenging task in turbine cooling system design.

Typical thermal loads for the blades (thermal boundary conditions on the external surfaces) can be presented in a simplified form as a combination of the local heat-transfer coefficients and relative turbine rotor inlet gas temperatures (TRIT). Internal airfoil cooling is arranged to counterbalance thermal loads in order to keep the metal temperatures at an acceptable level.

A number of sophisticated cooling techniques (Fig. 3) have been developed to allow gas temperatures of nearly 540 °C (1,000 °F) above material temperature limit. These cooling techniques could be grouped in three categories:

1. Internal convective cooling, where the cooling is performed by convection only (without providing further cooling effect by the spent air). This category can be subdivided into six subgroups:

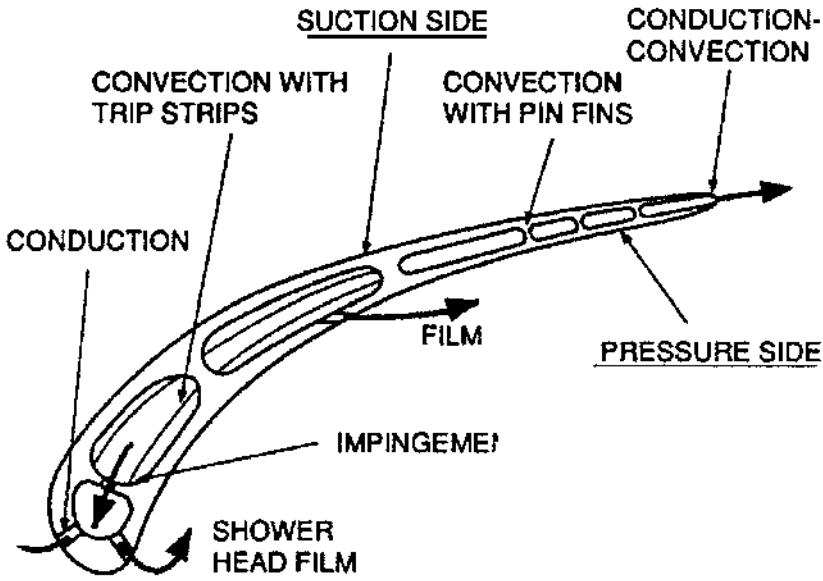

Figure 3 Airfoil cooling techniques.

(a) smooth channels
(b) internal passage augmented with longitudinal ribs
(c) channels with normal or angled ribs (trip-strips)
(d) channels augmented with pedestals or pin-fins
(e) jet impingement cooling with and without cross flow
(f) swirling flow of the coolant

2. External film cooling, where the coolant forms a protective film barrier on the component surface. In most of the cases this type of cooling is coupled with internal convection using spent cooling air for the film protection. A Particular attention should be paid to film cooling of the leading-edge vicinity, which is known as "shower head" cooling.
3. Transpiration cooling, where the coolant penetrates the airfoil surface through a porous wall, is the most efficient air cooling scheme available, but it has significant limitations due to required small size of the pores and the potential problem of their blockage. Also, aerodynamic losses can be significant because of normal injection of a low velocity cooling air into the boundary layer of a main stream. However, when this technique is applied for a combustor liner in the form of effusion cooling, using a significant amount of cooling air, the aforementioned limitation is not

relevant because the air can be discharged through relatively large holes mixing subsequently with a relatively small velocity mainstream flow.

Cooling Effectiveness

The main challenge in the development of a cooling system is to support the highest turbine inlet gas temperature at the existing stress and life requirements using a minimum amount of cooling air. Cooling effectiveness, defined as $\eta_c = (T_g - T_m)/(T_g - T_c)$, becomes a major criterion when different cooling techniques are considered. At a given difference between local gas temperature T_g and temperature of the cooling air T_c, the required cooling effectiveness is directly proportional to a specified ΔT between T_g and component bulk metal temperature T_m. Cooling effectiveness curves are usually presented as experimental correlations with cooling flows. The most common practice is to use a flow parameter $FP = m_c h_c / AC_p$.

Figure 4 compares the effectiveness of various combinations of blade cooling techniques. Effectiveness of the traditional convective cooling usually limits TRIT to 1,120 °C (2,050 °F). Impingement cooling of the leading edge of a turbine blade improves effectiveness and allows TRIT up to 1,150 °C (2,100 °F). More recent advancements in leading-edge cooling, which are based on swirling cooling air flow in the blade passage, are

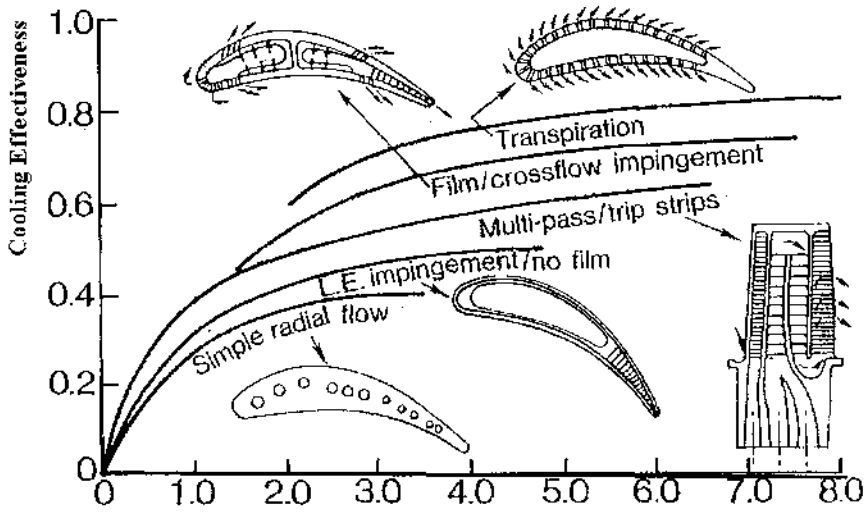

Figure 4 Cooling air flow (% of compressor flow).

expected to increase this limit to 1,260 °C (2,300 °F). Further increases in TRIT require a combination of convection, impingement, and film cooling, thus bringing the present technology limit of the turbine inlet temperature for industrial turbines to 1,370 °C (2,500 °F) and to 1,540 °C (2,800 °F) for advanced aero engines.

Internal convective and film cooling or their combinations are the techniques most commonly applied to turbine airfoil cooling. The airfoil internal convective cooling that shares a common knowledge base with heat exchangers has been thoroughly studied for many decades enabling relatively accurate analytical predictions. Much of the design information for this cooling group appears in the open literature. A reader will find some details and design guidance for particular applications of internal cooling in the sections of this chapter that follow.

In spite of its advancements and favorable manufacturing and cost considerations, internal cooling is not usually sufficient for the first-stage turbine airfoils operating in modern high-temperature engines. When local gas temperatures exceed 1,200–1,260 °C (2,200–2,300 °F), internal cooling cannot provide the metal temperature reduction that can be achieved with advanced film cooling. It takes a combination of internal and film cooling to achieve the required cooling effectiveness. Considering the effect of specified life on allowable metal temperatures of the component, a higher cooling effectiveness for similar components (nozzle, blade, etc.) is required for longer-life industrial turbines compared to aero engines. It can be easily concluded that a cooling technique becomes inefficient when a significant increase in the cooling flow results in a small gain in cooling effectiveness. A specified ΔT between the local hot gas and cooled component metal temperatures corresponds to a certain required cooling effectiveness that can be achieved for each specified cooling technique at the allowed cooling flow.

With the levels of cooling air supply pressures generally available in turbines and constantly rising air temperature at the compressor discharge, it becomes very difficult to convectively cool airfoils beyond an average cooling effectiveness level of 0.5. This level indicates that the component metal temperature is halfway between the cooling air and gas temperatures. This also means that an increase of gas temperature by 40 °F (22 °C) will result in a rise of the metal temperature of the cooled component by 20 °F (11 °C), cutting the life of this component approximately in half. Also, with high convective cooling effectiveness levels, the component metal temperature gradients tend to become very large and thus cause concerns for local thermal stress problems. When the combination of turbine gas temperature, coolant temperature and allowable metal temperature requires a higher effectiveness level, film cooling is generally applied. Although the film cooling air is used mainly to shield the airfoil surface from the hot gas, it

also performs a very important convective cooling function within the film discharge holes. The most effective system combines internal convective and external film cooling. In an ideal situation where film cooling approaches transpiration cooling, the film cooling source air temperature might be close to the targeted metal temperature. The cooling effectiveness in this case can be close to 1. This, however, requires large cooling flows and multiple rows of film holes to achieve full film coverage of the component without degradation of the film cooling effectiveness between the holes.

Cooling Penalties

For a modern industrial turbine, the cooling airflow requirements are in the order of 20–25% of the total compressor flow. This large quantity of air is a source of a significant loss to the engine cycle performance as a whole and has three effects that tend to partially offset the performance improvement of high turbine inlet temperature operation. The first is that the air used for cooling enters the turbine at a lower temperature, reducing temperature of the gas downstream of combustor. Thus, to deliver a specified power, the engine has to run at a higher turbine inlet temperature than would an uncooled engine. The second is that the cooling air bypasses the combustor, subsequently leading to greater challenges to control emissions and provide desirable temperature distribution at the combustor exit. The third is related to aerodynamic losses when the cooling air is reintroduced and mixes with the higher-velocity main gas stream. The aerodynamic loss, often called the mixing loss, is caused by the injection of coolant into a turbine airfoil passage, and its subsequent mixing with the main-stream flow. This is generally reported in terms of a decrease, or loss, in the total pressure of the mainstream. Vigorous steps must therefore be taken to minimize both the quantity of cooling air used and the losses associated with its use, in order to achieve maximum benefits of the high cycle temperature. This can be a severe restraint on the degree of freedom with which the cooling design is performed.

Regardless of what type of open cooling technique is used—internal or film cooling—the spent air has to be discharged through the wall along the surface of the airfoil or through its trailing edge. For this reason, when the applied cooling technique is based on internal cooling, an effort should be made to utilize the spent air for some film protection. And, for the same reason, when film cooling is applied an effort has to be made to utilize the cooler air for some convective cooling along the channels of the film discharge holes.

Two main objectives related to the penalty reduction have to be considered during airfoil internal cooling design:

1. Reduce the effect of main-stream temperature dilution by utilizing the maximum potential of internal cooling and discharging the spent air at temperature that is close to the allowable metal temperature.
2. Minimize pressure drop in the internal cooling passages of the airfoil to enable discharge of the spent cooling air on the pressure side of the airfoil upstream of the throat or through the trailing edge at a velocity that matches the main-stream velocity. This results in reduced aerodynamic losses and improved turbine performance.

These design rules are often compromised when the internal cooling is applied for the leading edge, which is usually the highest thermally loaded part of an airfoil. Internal cooling of the blade leading edges is often preferred for modestly high inlet temperatures due to their lower manufacturing cost and elimination of stress concentration versus film cooling. More effective internal cooling techniques based on impingement or swirl cooling are required for this region of the airfoil. These techniques typically require a larger pressure drop of the cooling air and air has to be discharged in less favorable locations for aerodynamic penalties—on the suction side or at the trailing edge of the airfoil at a velocity lower than the main stream.

Somewhat limited information can be found in the open literature concerning the effect of film cooling on aerodynamic losses, particularly for the typical turbine airfoil flow that is characterized by large pressure gradients and multiple rows of film injection. Figures 5 and 6 present a summary data [8, 9] obtained for typical cooling flows and penalties associated with different locations of cooling discharge along a nozzle vane and a turbine blade. These data clearly illustrate a relatively small impact of the air discharged at low main-stream Mach number locations like stagnation point or a significant portion of the pressure side. However, a very strong adverse effect can be observed at high main-stream Mach number locations such as the suction side, particularly closer to the throat of the passage.

An analytical treatment for the mixing loss due to film blowing, based on the hypothesis that the injected coolant mixes with the main-stream flow rather than remaining entrained in the boundary layer, is recommended by Hartsel [10], providing the following simplified one-dimensional total pressure loss equation:

$$\Delta P/P_\infty = \gamma m_c/m_\infty Ma^2/2(1 + T_c/T_\infty - 2V_c/V_\infty \cos\alpha)$$

Where

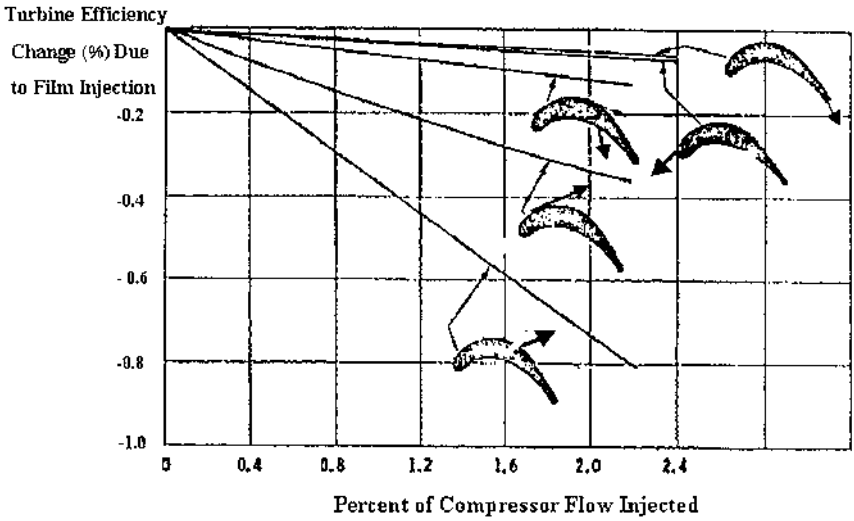

Figure 5 Effect of cooling film injection on turbine efficiency.

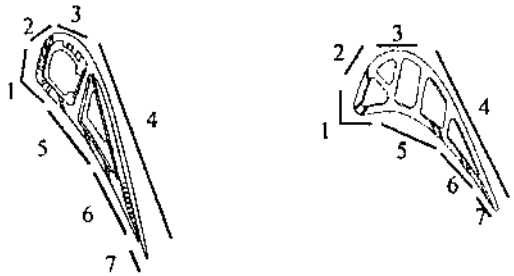

	NGV			Blade		
	Flow %	Normalised Loss/unit flow %	Freestream Mach No	Flow %	Normalised Loss/unit flow %	Freestream Mach No
1	2 - 3	10	0 - .15	0.5 - 1.5	120	0 - .15
2	0.5 - 1	39	.15 - .4	0.4 - 0.8	120	.15 - .4
3	1.5 - 2	Datum	.4 - .6			
4	0 - 1.5	250	.8 - 1.1	0	800	.8 - 1.1
5	1 - 2	10	0 - .2	0.3 - 0.6	190	.2 - .4
6	0.75 - 2	33	.2 - .4	0.3 - 0.6	190	.2 - .4
7	2 - 3.5	45	.75 - 1	0.8 - 1.3	225	.75 - 1
Total	9 - 12			3 - 4		

Figure 6 Typical cooling air losses and flows.

P_∞ is total inlet pressure.
T_c/T_∞ is local mixing cooling layer and main-stream temperatures ratio.
m_c/m_∞ is the coolant to total main-stream mass flows ratio.
α is the angle of injection.

The loss in total pressure of the main-stream flow due to injection decreases with decreasing angle of injection is directly proportional to the local main-stream Mach number squared and is strongly influenced by the blowing rate. When the injection angle decreases, the effect of coolant-to-main-stream temperature ratio T_c/T_∞ becomes less pronounced for higher-temperature ratios and more evident for lower ratios. Limited test data have shown this loss prediction to be reasonable and consistent with test results. The important end result of this method is that it gives a certain guidance in the optimum location of film cooling holes. It is apparent that film cooling near the stagnation point and on the pressure surface of airfoils (where the Mach numbers are low) will give small total pressure losses, whereas film cooling on the suction side near the throat (where Mach numbers are high) will give high total pressure losses.

It is quite often argued that the trailing-edge ejection of the coolant flow might reduce the aerodynamic losses by filling in the wake. Several investigations showed a positive effect of cooling discharge into the trailing-edge wake, especially when significant amount of high momentum flux cooling flow had been discharged. However, due to manufacturing and cost considerations, most of the advanced airfoils are designed with air discharged on the pressure side immediately upstream of the trailing edge.

Significant attention over the last few years was paid to the penalties associated with end-wall film cooling. Some of the studies have indicated that when film is properly introduced upstream of the stagnation plane of the airfoils, it might control the secondary flow formation such as a horseshoe vortex initiated at the fillet junction between an airfoil and the end wall (more details about end-wall cooling and secondary flow control can be found later in this chapter).

An important role in cooling penalties is also played by the cooling air that cools turbine discs and buffers disc cavities from hot gas ingress. The amount and manner of discharging this air into the main stream can significantly affect the performance losses. A recently performed study [11] indicates that the most beneficial location and direction for discharging the air from disc cavity is an immediate vicinity of the vane trailing edges near the inner end wall at a velocity vector that closely matches the nozzle exit velocity.

General rules for minimizing cooling air discharge penalties affecting turbine performance can be summarized as follows:

Discharge any cooling flow as far upstream along the gas path as possible.

Use benefits of a shower head cooling for the leading edge of the first stages of airfoils as a preferred cooling technique, even using larger cooling flows, if sufficient cooling budget is allowed and when fabrication cost is not prohibitive.

Attempt to design the cooling system that discharges cooling air at a temperature that is close to (or slightly below) allowable local metal surface temperature.

Minimize mixing losses by closely matching velocity vectors between main-stream and discharged cooling flows.

Avoid film discharge on the suction side of an airfoil at close vicinity of the boundary-layer transition.

Exercise maximum effort in avoiding cooling flow discharge from the suction side of an airfoil in the vicinity upstream of the throat and especially downstream of the throat.

Minimize pressure losses in the internal cooling passages to retain the total pressure in the cooling flow.

Use preswirling mechanism for blade cooling supply system, lowering the relative temperature of the coolant and reducing disc friction losses.

Combination of Cooling with Thermal Barrier Coatings

The use of thermal barrier coatings (TBC) presents a great benefit in reducing the heat load on the airfoil alloy particularly for internally cooled airfoils. Airfoils dressed in thermal barrier coatings are fabricated in a conventional manner with the exception of a thin layer of a high-temperature insulating material. TBC material usually can withstand very high temperatures and has a thermal conductivity in order of one tenth that of conventional superalloys. Due to the additional thermal resistance, airfoils coated in this manner can operate with much less cooling air at a given gas temperature or, conversely, can withstand much higher gas temperatures at a given level of cooling flow than uncoated airfoils. It is quite clear that TBC applied on the external surface cannot do the job of protecting the airfoil material from high temperature without applying cooling on the inner surface.

Designing cooled airfoils with thermal barrier coatings presents certain problems. Even when polished, the material has an inherent roughness,

thereby increasing both the skin-friction and heat-transfer coefficients. The application of a layer of thermal barrier coating also results in thicker trailing edges, with associated aerodynamic penalties. At given internal heat-transfer coefficient and temperature of the coolant, the temperature gradient across the thickness of the coating is driven primarily by the gas temperature and external heat-transfer coefficient. The greatest benefit from application of TBC or the highest temperature gradient through the coating can be gained in the environment where the large temperature difference between hot gas and cooling air is combined with high heat-transfer coefficients on both sides. This environment exists often in certain areas of airfoils, end walls, and combustor liners that are cooled by backside convection. The greatest concern affecting the use of thermal barrier coatings is their life, caused by their brittleness and flaking due to differential thermal expansion relative to the airfoil base material. Recent advancements in materials for TBC and improved coating application techniques have provided significant extension of their life. This allows a lesser conservatism in life prediction for coated nozzles and blades, including thermal resistance of the coating in the component temperature analysis. Selection of the coating thickness for blades should also consider the fact that coating strength is very low relative to the base alloy causing increased inertial (centrifugal) stresses in the blade material. Design of airfoils with thermal barrier coatings must obviously weigh all of these factors.

Airfoil Cooling Development Process

Figure 7 presents a typical development process for airfoil cooling. The starting point for the airfoil cooling system design specifies the component life requirements, which dictate an acceptable metal temperature limit. Local metal temperature of the airfoil is driven mainly by a combination of three factors:

1. External heat load to the surface from the main-stream gas by convection through a boundary layer or through a film cooling layer (when cooling air is discharged through the film holes)
2. Internal convective cooling of the part by cooling air
3. Thermal conduction and heat sink within the component

A preliminary turbine aerodynamic design provides the airfoil geometry, estimates cooling air flows, and specifies pressures, temperatures, and velocities of the main-stream flow. Previous experience is essential for correct assumptions in the analysis and cooling concept selection.

Recent advancements in computer-based analytical methods, and particularly in computer graphics, provide sophisticated tools for con-

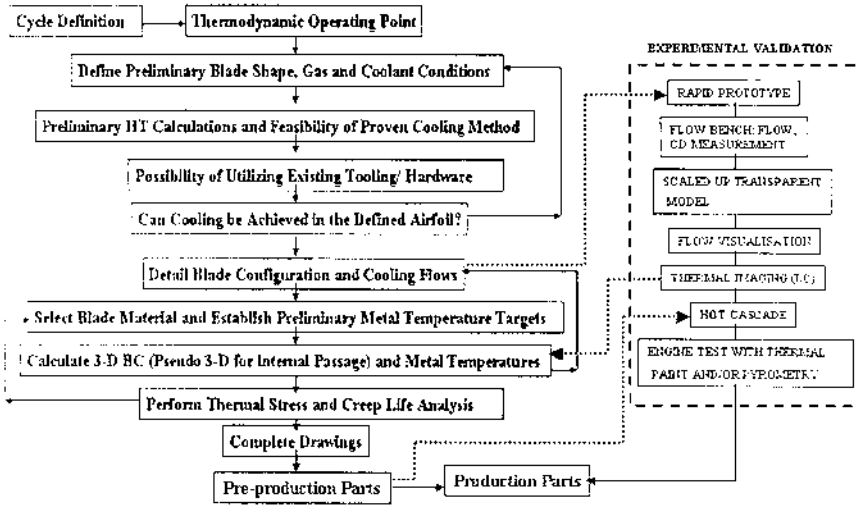

Figure 7 Development process for cooled turbine airfoil.

current engineering using a three-dimensional (3D) database for solid modeling, flow, heat transfer, and mechanical analyses. Solid modeling gives a comprehensive graphical representation of the most intricate component geometry.

The calculation of the local component heat-transfer coefficients is based on defined boundary conditions around external and internal surfaces of the airfoil. Existing computational fluid dynamic codes for the main-stream flow (often 3D), correlations and flow codes (often 1D or pseudo-3D) for the internal flows through the cooling passages establish these boundary conditions. Iterative thermal analyses of the airfoil are usually performed, combining the heat-transfer data, physical properties of the alloy, and thermodynamic parameters of the main-stream and cooling flows, until the required metal temperatures are satisfied. Effects of free-stream turbulence, secondary flows, and rotation (for the blades) are essential for meaningful results of the thermal analyses.

The expected radial temperature profile of the main-stream flow is applied as input for the turbine blade analysis. The circumferential peak temperature (hot-spot) in a nonuniform combustor temperature pattern factor is used as the boundary condition for the nozzle vane temperature prediction. Analytically predicted airfoil temperatures are interpolated within the computer solid model and applied as input for mechanical analysis.

After four decades of advancement in numerical analysis and turbomachinery studies, the state-of-the-art analytical techniques are still limited in providing an accurate life prediction for the components. Therefore, experimental calibration and verification of the analysis are playing a major role in the development cycle. Experimental validation of the analysis is performed after a design team is satisfied with the concept and analytical prediction. The section on combustor cooling describes major elements of experimental validation.

DEFINITION OF MAJOR HEAT- AND MASS TRANSFER SIMILARITY PARAMETERS

Three distinct heat-transfer phenomena should be considered when turbine components are analyzed:

1. Heat transfer by conduction
2. Heat transfer by convection
3. Heat transfer by radiation

Radiative heat transfer is often important in the analytical prediction of combustor liner and stage 1 nozzle vanes facing a combustor liner. Typical so-called conjugate heat transfer in a turbine component, for example, a cooled turbine vane, involves a combination of convective external heat transfer from the hot gas to the vanes, conduction through the wall of the hollow vane, convective internal heat transfer from the vane to the cooling air, and possible flame radiation as well as radiative heat transfer from higher-temperature walls of the liner.

Heat–Mass Transfer Interaction in the Airfoil Boundary Layer

The transfer of heat in a fluid can occur through conduction as well as advection through the movement of the fluid (it is customary to use term ''convection'' when referring to cumulative transport by random motion of molecules and the term ''advection'' when referring to transport due to bulk fluid motion). The overall heat transfer combining advection and conduction in a moving media is usually referred to as convective heat transfer. The heat and mass transfer defining the temperature and velocity field are closely coupled and interact, strongly affecting each other. Forced convection plays the dominant role for most of the turbine components compared to natural convection. The critical elements in the external heat transfer from the hot gas to the wall of a blade are the boundary layer developing on the surface and the free-stream total temperature. The boundary layers, which act as a

buffer between the main stream and solid, represent resistance to the heat transfer. The heat transfer occurs in this layer between the solid and fluid through both conduction and convection mechanisms. If the component surface is at a higher temperature, the heat transfer will occur from the surface to the fluid, and vice versa if the fluid temperature is higher than the surface. Once the heat has penetrated into the flow, the energy transport occurs mainly through the convection by the moving media. Therefore, the buffer region, or boundary layer, plays a very critical role in the heat transfer. The condition and properties of this layer determine the rate at which the heat is transferred.

A good physical understanding of convective heat transfer can be obtained by examining the energy equation, where one side of the equation denotes the advection of energy and another side denotes, respectively, the heat transfer by molecular conduction in the fluid, the work done by pressure forces, the work done by laminar stresses, the work done by turbulent stresses, and heat transfer by turbulent velocity and temperature fluctuations.

The relative heat-transfer distribution on a typical turbine blade is illustrated in Fig. 8. The highest heat fluxes generally occur at the leading-edge stagnation region and toward the trailing edge of the blade. The large gas-side heat-transfer variations must be appropriately matched by

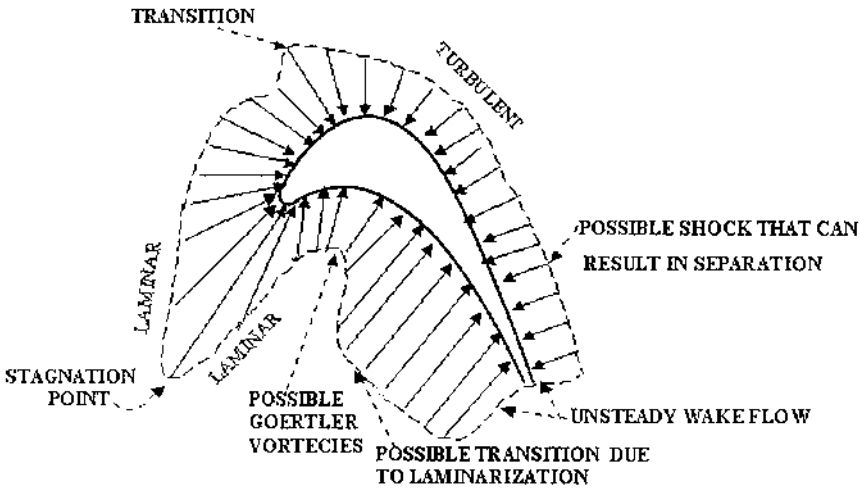

Figure 8 Typical heat-transfer distribution around turbine airfoil.

correspondingly high coolant-side thermal effectiveness so as to achieve acceptable temperature distributions. At least seven distinctly different regions of blade heat transfer can be identified:

1. Stagnation point
2. Laminar boundary layer
3. Transitional boundary layer
4. Turbulent boundary layer
5. Shock/boundary-layer interaction
6. Separation with reattachment
7. Separation without reattachment

Since the heat transfer is closely coupled to fluid mechanics phenomena, each of these regions involves a separate analysis valid for that particular region. The heat transfer depends on Mach number, Reynolds number, free-stream turbulence, free stream-to-wall temperature ratio, blade curvature and roughness, material, and the gas properties.

In heat-transfer applications, the use of dimensional analysis is important as the heat transfer depends on a large number of parameters. Dimensional analysis enables reduction of the large numbers of variables to a manageable number of nondimensional groups. This, in turn, enables experimentalists to design experiments to carry out a parametric study.

There is considerable empiricism in the analysis of convective heat transfer because of complicated geometry involved and complex interaction between the flow and heat-transfer fields. The following groups can be identified by a dimensional analysis:

Reynolds number $\mathrm{Re_L} = \rho VL/\mu$, based on a reference length or $\mathrm{Re_d} = \rho \mathrm{V}d/\mu$, based on hydraulic diameter
Mach number $\mathrm{Ma} = V/a$
Prandtl number $\mathrm{Pr} = \mu c_\mathrm{p}/k$
Eckert's number $\mathrm{Ec} = (\gamma - 1)\mathrm{Ma}^2 T/2\Delta T$

In heat transfer (internal as well as external) applications, several additional nondimensional groups are important. The overall heat transfer is related to the temperature difference between the fluid (T_∞) and the solid wall (T_w) through Newton's cooling law: $Q(x) = h(x)A(T_\mathrm{w} - T_\infty) = -kA(\partial T/\partial y)_\mathrm{w}$.

The heat transfer coefficient h can be nondimensionalized as Nusselt number $\mathrm{Nu} = h(x)\, L/k = -L(\partial T/\partial y)_\mathrm{w}/(T_\mathrm{w} - T_\infty)$

As indicated earlier, the boundary layer acts as a resistance to the heat transfer and this property is characterized by the shear stress. The nondimensional group called the Stanton number St represents the

nondimensional heat transfer coefficient:

$$St = q''_w/\left[\rho o_p U(T_w - T_\infty)\right] = k(\partial T/\partial y)_w/\left[\rho o_p U(T_\infty - T_w)\right]$$

$$\text{also St} = \text{Nu}/\text{RePr}$$

The heat transfer is a function of Reynolds number and Prandtl number and is directly proportional in the case of turbulent boundary layer to the skin friction $C_f = 0.058(\text{Re})^{-1/5}$; $\text{Nu} = C_f/2(\text{RePr}^{1/3})$, or $\text{Nu} = 0.029\,\text{Re}^{4/3}\text{Pr}^{1/3}$.

A thin boundary layer (smaller resistance) permits a greater heat transfer. The case of zero boundary-layer thickness (as in stagnation point) has the maximum heat transfer. The thickness of thermal and velocity boundary layers is about the same for air, and the velocity and temperature $(T_w - T_\infty)$ profiles are similar for a flat plate (zero pressure gradient).

In a turbulent boundary layer, the turbulent heat flux can be treated much the same way as the Reynolds stress. The velocity temperature correlation is assumed to be proportional to the temperature gradient in the y direction (normal to wall). Hence, the heat flux due to turbulent fluctuations can be written as

$$q''_t = -\rho c_p \varepsilon_h \partial T/\partial y$$

where ε_h is the eddy thermal diffusivity.

The similarities between the exchanges of heat and momentum by turbulence fluctuations should be emphasized in the presence of velocity gradient. There is a close coupling between heat transfer and momentum transfer, which translates into a close coupling between heat flux and shearstress. Since the major concern here is the heat transfer between fluid and solid, the shear stress at the wall plays a key role. The dimensionless turbulent Prandtl number $\text{Pr}_h = \varepsilon_m/\varepsilon_h$ provides a relation between closely coupled momentum and heat transfer.

Role of Similarity in Experimental Emulation of a Turbine Airfoil Heat and Mass Transfer

One of the most critical measures affecting turbine blade and nozzle vane life is their metal temperature. A 20–30 °F (12–18 °C) underprediction in metal temperature may easily result in a 50% reduction in blade creep-rupture life. Accurate prediction of this temperature is often based on high-quality experimental simulation of the component heat transfer representing actual engine conditions. This is particularly important for a cooled turbine airfoil where both external and internal convective heat transfer have to be considered as boundary conditions for the conduction heat transfer in the

component. Use of a hot cascade for steady-state experiments or short-duration facilities for transient experiments becomes a necessity for obtaining reliable data and validation of the airfoil cooling systems. Realistically simulated steady-state hot cascade experiments using actual engine hardware with proper external/internal cooling arrangements can be extremely beneficial for turbine airfoil local temperature prediction in the early stage of turbine development. A few of the experiments using actual engine configuration were reported [12–16]. However, heat-transfer experiments including evaluation and comparison of the cooling effectiveness in both engine and hot cascade environments are rarely discussed in the open literature.

The solutions of the Navier–Stokes and energy equations for compressible flow depend on a number of dimensionless groups. These equations suggest that the similarity of fluid streamlines and the isotherms in forced convection heat transfer can be enforced by using the same magnitudes of these nondimensional groups for both the actual phenomenon and the simulation experiment. When the momentum and energy equations are nondimensionalized, the solution strongly depends on four nondimensional parameters: Re, $\mathrm{Gr}/\mathrm{Re}^2$, $1/(\mathrm{Pr}\,\mathrm{Re})$, and Ec.

For most of the forced convection problems of interest to us such as external heat transfer on a gas turbine blade, buoyancy forces are considered negligible compared to inertial forces. The Eckert number Ec can be expressed in terms of free-stream Mach number, Ma, wall-to-free-stream total temperature ratio, and the specific heat ratio: $\mathrm{Ec} = (\gamma - 1)\mathrm{Ma}^2 (\mathrm{T}\infty/\mathrm{T}\infty_0)/(1 - \mathrm{Tw}/\mathrm{T}\infty_0)$

The static to total temperature ratio can be replaced by using the isentropic relation, to obtain

$$\mathrm{Ec} = (\gamma - 1)\mathrm{Ma}^2\left\{1/\left[1 + (\gamma - 1)\mathrm{Ma}^2/2\right]\right\}/(1 - T_{\mathrm{w}}/T_{\infty_0})$$

STEADY-STATE AND TRANSIENT HEAT-TRANSFER ISSUES IN THE ENGINE HOT SECTION

Over the past three decades, turbine heat-transfer calculations and experimental data have been reported in the open literature by numerous industry, government, and university authors. The detail reported for a particular calculation generally depends on the competition sensitive nature of the data. Understandably, the company design codes distinguish the manufacturers, and detail about these codes will be kept proprietary.

Government- and university-authored papers usually provide a greater detail about the calculation but generally for a geometry that is often not representative of actual components in the industry. Efforts focused on understanding turbine airfoil heat transfer have traditionally been overshadowed by the work done on the associated aerodynamics. This was not due to a lack of appreciation for heat-transfer problems, but rather the difficulty of the problem that became more prominent as the turbine inlet temperature increased.

Most conceptual models for heat transfer in a modern 3D airfoil require significantly more information than is required for aerodynamic calculations. The computational grid required for the heat-transfer calculation is much finer than required for the corresponding aerodynamic calculation. This is because the temperature gradient at the airfoil wall drives the heat-flux calculation and the grid resolution in the boundary layer must be significantly finer. The boundary-layer approximation assumes a constant pressure through the boundary-layer thickness, but the temperature through the boundary-layer thickness is not constant. The codes have progressed from boundary-layer codes that have their origin in correlations of early flat-plate data, through the 2D or quasi-3D steady codes to the full 3D unsteady Navier–Stokes codes.

In addition to analyses of the individual cooled turbine components, it is very common that turbine cooling designers with expertise in heat transfer and fluid mechanics are also responsible for secondary flow analysis and overall engine thermal management. This includes analyses of the cooling flows and seal leakages, and temperature distribution for most of the hot section components at steady-state and transient operating conditions. The cooling designers are also expected to provide design input for transient behavior of the entire turbine structure, including interaction between the turbine rotor and stator.

Metal Temperatures and Their Effect on Life of the Turbine Components

In most of the cases, steady-state temperatures define the life of turbine components for the selected turbine materials. An exception is the low cycle fatigue life, which is defined by transient temperature gradients.

A cooling designer starts by either being given or assuming certain component life requirements based on oxidation/corrosion/erosion, creep-rupture, and thermal (low cycle) fatigue, which dictate acceptable metal temperature limits. For each component these life and temperature requirements must be met under given duty cycle conditions. Life of combustor liners, for example, and, in most of the cases, that of stage one

nozzle vanes is limited by their oxidation. In some cases a low cycle fatigue can be detrimental for trailing edges of the nozzle vanes, particularly when they are very thin compared to the rest of the nozzle. Life of the turbine blades is usually limited by creep-rupture characteristics of a selected blade material, except for tips of unshrouded blades, which are typically exposed to low stresses from inertial forces and limited by the oxidation. Fifty percent reduction in the creep-rupture life of an advanced airfoil might result from the metal temperatures in stressed sections being only 20–30 °F (12–18 °C) above nominal design. For nozzles or oxidation-limited tip sections of the blade, the same life reduction results from metal temperatures at about 40–50 °F (25–32 °C) above nominal.

The basic airfoil shape arises from the aerodynamic design, but modified by the knowledge that some, as yet unspecified, cooling system will have to be accommodated. Certain preliminary cooling assessments must be performed prior to a full specification of the airfoils. In order to keep metal temperatures within limits, the airfoil internal cooling must be arranged in a way so as to most effectively counterbalance external thermal loads. The designer can usually decide from past experience and design practices what type of cooling will be necessary (convective or film cooling) on each surface to be cooled.

Depending on a specified life, the recommended metal temperature limits for advanced alloys are 1,800–1,900 °F (980–1,040 °C) for combustor liners and transitional parts, 1,900–2,000 °F (1,040–1,095 °C) for the nozzle vanes and end walls, 1,500–1,650 °F (815–900 °C) at blade highly stressed sections with allowance to rise to 1,800–1,900 °F (980–1,040 °C) in the oxidation limited tip section. Large turbine components like turbine discs and nozzle support structures, produced from forgings, are usually limited to temperatures below 1,400 °F (760 °C), and even at these relatively low temperatures might require oxidation protective coatings.

Turbine discs and relatively high-temperature stationary structures that support turbine nozzles are susceptible to significant, mainly radial, transient temperature gradients inducing a low cycle fatigue. Effective protection (isolation) of these components from ingress of the high-temperature main-stream flow is essential for life of the components. Application of low-conductivity thermal barrier coatings can also provide significant assistance in confronting excessive transient temperature gradients in these components.

Transient Rotor-to-Stator Thermal Displacements Issues and Tip Clearance Control

A general case of transient three-dimensional conduction is governed by the Fourier equation:

$$k\nabla^2 T/(\rho c_p) + Q/\rho c_p = \partial T/\partial t$$

Where

∇ is a Laplace operator.
The parameter $k/(\rho c_p)$ is thermal diffusivity α of the conducting material.
Q is amount of heat added (or lost) within the body per unit of time and volume.

Providing proper relative positioning of the rotor and stator components of the engine is a major objective at an early conceptual design of a turbine hot section. Many issues, which are often called "thermal management" of a turbine design, have to be addressed at this stage. This include

Location of a thrust bearing strongly affecting relative axial displacement of a rotor
Transient thermal matching between interacting rotor and stator components defining operating clearances
Transient behavior of turbine components during various modes of operation that might be quite different from a steady-state positioning
Behavior of a bearing housing structure affecting concentricity between rotor and stator, particularly after engine shutdown when bearing housing might experience bowing from circumferentially nonuniform temperatures
Ability of the seals between different components to accommodate transient radial and axial displacements without losing their effectiveness

Figure 9 presents an example of the entire turbine stator finite-element computer model, which is required to perform the analyses of both radial and axial displacements induced by the transient thermal and pressure loads. Rotor displacement analysis should include the effect of both thermal and centrifugal forces. During the early layout effort both models can be significantly simplified using an axisymmetric 2D structures with the exception of the nozzle vanes and blades. The airfoils can be modeled at this stage as constant-thickness beams with moments of inertia and circumferentially averaged densities that represent actual geometry of

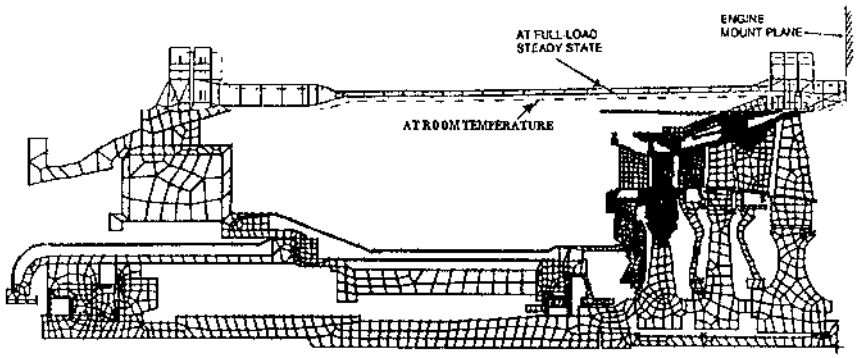

Figure 9 Typical turbine hot section finite-element model.

hollow components. One of the most challenging engineering objectives in turbomachinery design and a crucial factor for engine performance is to minimize and maintain tight turbine blade-tip clearances over the life of the engine. This requires a full range of comprehensive design and analysis, including concept development combined with intricate transient fluid mechanics, heat transfer, and stress-deflection analysis of the entire multicomponent structure, followed by engine test verification. Turbine blade-tip leakages represent one of the largest sources of turbine efficiency loss. Maintaining tight operating tip clearances without tip rubs is a major task for a cross-disciplinary design. Proper thermal management of the entire engine rotor-to-stator transient behavior, particularly for the nonshrouded blades in the diverging gas path, creates an extraordinary challenge. Both thermal and inertial transient displacements as well as some aerodynamic loading effects should be considered. Passive tip clearance control, which is based on close matching between transient growth of rotor and stator, typically requires a bulky stationary structure, unacceptable for aero engines. Active and semiactive [17–20] tip clearance controlling techniques, based on modulation of the cooling air supply to the stationary structure during transient operation, present an alternative solution when lighter structures are required.

Several factors must be considered to insure minimal tip clearance at steady state without rubs, particularly in the case of unshrouded blades:

Differences in thermal radial growth between the turbine rotor assembly and nozzle tip shroud support structure during transients. This is usually the most severe during hot restarts, when tip

clearances are drastically reduced due to more rapid cooling of the stator than of the rotor.

Relative axial rotor-to-stator thermal displacements in the cases when the blade tips are flared.

Circumferential thermal distortion of the tip shroud support structure resulting from nonuniform combustor exit temperatures during transient or steady-state operation.

Bowing of tip shroud segments during transients due to radial temperature gradients across the shroud wall.

Changes in rotor-to-shroud position caused by variations of rotor speed, turbine inlet temperature, cooling air temperature, and bearing clearance.

The efficiency of the stage 1 and 2 high-pressure turbine, often called gas producer turbine, has a major impact on overall engine performance and thus justifies all efforts to minimize the blade-tip clearance to the blade height ratio. Tip clearance reduction based on the active control of transient thermal growth of the stationary components by modulation of the cooling air flow became a popular concept over the last two decades among leading aircraft engine manufacturers. However, major concerns associated with the high cost, complexity, and reliability of this system for industrial engines led to development of more suitable concepts for the application. These concepts can be based on passive (versus active) or semiactive (simplified open or closed air supply) tip clearance management system.

The turbine static structure plays a dominant role in turbine clearance control and the positioning of the stationary tip shrouds over the blade tips. To perform this function, the stator structure must first of all be mechanically restrained and thermally isolated from the gas stream. It is essential that the structural elements of the stator be protected from conduction, radiation, and hot gas ingestion to minimize the influence of the gas-stream temperature changes and circumferential temperature patterns.

In actual industrial turbine design practice, the nozzle support structure must be cooled to about the same average temperature as the rotor in order to achieve the proper thermal match. This requires cooling the structure to within 100–200 °F (55–111 °C) of the cooling air temperature. Even local hot spots on the inner surfaces of a support structure can cause out-of-roundness under running conditions, sometimes resulting in permanent distortion. Sufficient thickness of the nozzle support case helps to reduce circumferential temperature gradients, but weight concerns usually exclude this option from aero engine design, often requiring an active tip clearance control. The air plenums must be sealed and have a metered flow for cooling and purging adequate to prevent hot gas ingestion. Another

important factor to consider for transient tip clearance control is the number of tip shroud segments needed to minimize radial bowing. It is a tradeoff between a larger number of segments, needed for roundness control, and fewer segments, required to reduce the leakage between them.

In addition to the above factors, other design objectives such as cost, maintainability, ease of inspection, and repair of the components have to be addressed.

Turbine shrouds and blade tips must tolerate tip rubs without seriously affecting tip clearances. Reliable abrasive turbine blade-tip materials or abradable shroud material have not yet been demonstrated to withstand long-term operation. (Typically, solid metal shrouds will pick up particles worn from the blade tips when rub occurs leading to local weldlike buildup, increased tip clearance, and loss in performance.) This led to the application of a rub-tolerant material that is approximately five times less dense than the blade material and is resistant to surface erosion. Introduction of the cylindrical first-stage nozzle shroud eliminates the effect of axial rotor-to-stator displacements on tip clearance.

In order to establish the most critical period, during which turbine blade tip rubs are most likely to occur, five operating conditions must be considered:

1. Start transients, from a "cold" (effectively room temperature) condition
2. Full load steady-state operation, for which clearances are usually designed to be a minimum
3. Load transients, where sudden gas-stream temperature changes result in different thermal responses of the component parts, due to differing thermal capacitances and heat-transfer boundary conditions
4. Shutdown transients, which include a rotor rundown period and a cooling period after the rotor stops
5. "Hot" restart, after a shutdown from a steady-state full load operating condition

Effective diaphragm and clamp ring cooling, in spite of nonuniform combustor exhaust temperature distribution, provides a negligible circumferential temperature differential in the diaphragm assembly. This allows the diaphragm assembly structure to be analytically treated as axisymmetrical. The most delicate part of validation for a selected design is the direct transient blade-tip clearance measurements. A number of microprocessor-controlled electromechanical actuators with customized traversable tip probes are available that can be spring-loaded onto the tip shroud outer surfaces.

TURBINE NOZZLE COOLING

In the design of air-cooled turbine nozzles, a number of factors have to be considered in order to achieve an optimized design (more details for cooling design optimization can be found in the section on advanced experimental heat transfer and cooling validation). In addition to the specified engine thermodynamic performance, these should include

Life requirements
Field operating conditions
Aerodynamic design
Combustor characteristics
Emission constraints
Coolant supply system
Material properties
Geometric constraints
Manufacturability and cost

Selection of the nozzle cooling design concept is strongly affected by the component life target and environment where the engine is operated. The presence of foreign particles in the compressed air and corrosive chemicals in the fuel as well as the number of thermal cycles over the life of the component, and off-design operation result in certain decisions regarding the selected design concept. Examples of design constraints associated with these factors are the smallest allowable size of the cooling holes, application of thermal barrier coatings, expected erosion-induced surface roughness and corresponding changes in the external heat-transfer coefficients, cooling air supply pressure margins over downstream pressures at the air discharge locations, etc.

The shape of a turbine airfoil that is selected for the best aerodynamic performance might be compromised to be acceptable from a cooling design standpoint. Constraints associated with the cooling might require redistribution of the external heat-transfer coefficients, resulting in a larger diameter of the leading edge, changes in velocity distribution and airfoil shape, and even the number and size of the airfoils. Figure 10 illustrates the evolution of these changes using Rolls Royce nozzles as an example.

Interaction with Combustor

Combustors are responsible for generating the upstream turbulence of various intensity and scale, temperature profile (pattern factor), and velocity boundary conditions for turbine nozzles. Emissivity characteristics of the combustor also often play an important part in the thermal loading of the

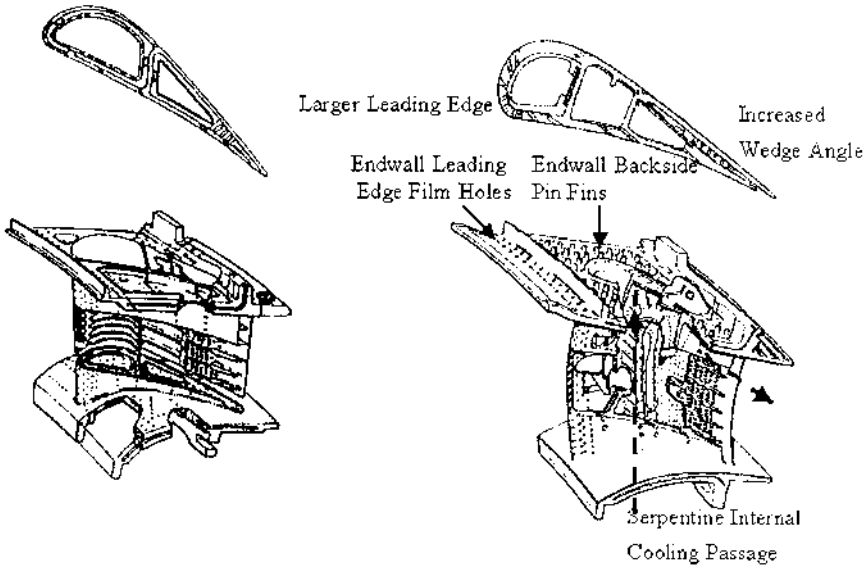

Figure 10 Evolution of nozzle geometry and cooling design.

nozzle downstream. The flow field of the gas exiting the combustor and entering the stage 1 turbine nozzle is complicated including nonuniform radial and circumferential temperature profiles (hot streaks) and free-stream turbulence of some unknown intensity and scale. The parameter describing the degree of nonuniformity of combustor exit temperature is called pattern factor:

$$PF = (Tg_{max} - TIT)/(TIT - Tc)$$

Where

Tg_{max} is the highest gas temperature found at combustor exit plane.
TIT (called sometimes CET) is the average turbine inlet (or combustor exit temperature).
Tc is the compressor discharge temperature (recuperator exit temperature for an engine with recuperator).

It is understandable that a lower PF at a given TIT requires a lower cooling effectiveness (lesser amount of cooling air for the same cooling technique). Typical PF values vary between 0.15 and 0.3.

Because of difficulties with measurements in operating combustors, designers have often guessed what the appropriate turbulence intensity and scale might be. Techniques to incorporate combustor-generated turbulence into heat-transfer design systems have been under development for many years, but with limited results. A significant portion of the experimental information used for this purpose has come from programs utilizing flat plates as the test article. It has been often assumed that the turbulence intensity values generated for these measurements are representative of typical engine combustors. Seldom for these studies has there been an attempt to simultaneously duplicate the "thought to be" turbulence intensity and scale of the turbine free-stream inlet turbulence. In addition, a significant obstacle for the turbine heat-transfer design community has been that flat-plate flows have not been demonstrated to be representative of the unsteady flow-field environment associated with a turbine stage. There are many coupled phenomena associated with the unsteady turbine stage flow field, and recent experimental results suggest that the influences of free-stream turbulence, wakes, fluid injection or ejection, and shock interaction may not be individually separable.

Very limited data of the flow and thermal fields usually exist for an actual gas turbine engine due to the extremely harsh operating conditions in the engine. Consequently, development of computational models for predicting heat transfer in the turbine section has relied on experimental simulations of the turbine environment. Simulations of film-cooled airfoils have become much more sophisticated over the last decade, including high-density coolants, curved and rough walls, and geometrically more complicated airfoils. Over the past 10 years, much effort has been put into correctly simulating the main-stream turbulence conditions characteristic of the flow entering the turbine section. Studies have shown that very high turbulence levels can cause dramatic increases in heat transfer and rapid diffusion of film-cooling jets. Many heat-transfer-related papers begin by making the assertion that the flow leaving the combustor and entering the turbine has very high turbulence intensity with numbers cited ranging from 6 to 20%. Seldom do these publications cite an available reference with a measurement of turbulence intensity or turbulence length scale for an operating combustor. For this reason, a comprehensive understanding of the effects of highly turbulent main stream is still lacking, particularly in regard to the influence of the length scale of the turbulent eddies. All these factors explain a limited ability for reliable computational modeling of these flows and the associated heat transfer.

It is well known that the flow exiting the combustor and entering the turbine has significant radial and circumferential temperature distortion or "hot streaks/hot spots." It is not surprising that the number of hot streaks at

the exit of the combustor section frequently corresponds with the number and circumferential positions of combustor fuel nozzles. It becomes important to model as accurately as possible hot streak migration through the turbine. Among the papers describing this effort are references [21–24].

It is possible in certain cases to position stage 1 turbine nozzles in a such way that the hot streaks stay in the middle of a gas path without a direct effect on metal temperatures of the vane or at least its leading edge.

The combustor–turbine junction (transition section) is a critical region that has a significant influence on stage 1 turbine aerodynamics and cooling. It is important to make sure that the cycle efficiency gain expected with the increased gas temperature is not significantly compromised by a loss in turbine performance due to turbine cooling. Combustor liner geometry has a significant effect on first-stage turbine performance and end-wall cooling. A larger combustor exit cone area corresponds to reduced main-stream velocities and can have the positive effect of reduced heat load along the exit cone. It has also been observed in a number of studies that a thicker boundary layer formed on the liner walls, upstream of the stage 1 nozzle, encourages formation of the near-end-wall secondary flows and particularly the generation of a horseshoe vortex. To avoid thickening of the boundary layer, it is important to provide continuously converging/flow accelerating geometry through the transitional portion of the liner and the following stage 1 nozzle. If this task is accomplished, the challenge of effective cooling of the nozzle end walls can be handled without significant performance penalties.

Highly converging end walls in the front part of the nozzle minimize the cross flow on the end walls within the nozzle. This suppresses the horseshoe vortex formation. As a result, the nozzle secondary losses are significantly reduced. Modern gas turbines require significant cooling of the combustor exit transition and nozzle end walls (Fig. 11). This task is often achieved with application of film cooling although in some cases attempts are made to use backside convective cooling. The location and the manner in which the film cooling is introduced into the main stream are very important for both cooling effectiveness and performance penalties. Requirements for nozzle end-wall cooling can be reduced by a proper arrangement of the combustor liner exit cooling flow, which can be injected upstream of the nozzle leading edges in a such way that a more favorable, cooler toward the end walls radial temperature profile is obtained. Some of the recently introduced designs and future generation of industrial gas turbines will use advanced low-emission combustion systems. Peak combustion temperatures have to be limited to minimize the formation of nitric oxides (NOx). Consequently, the use of combustor and nozzle cooling air will be strictly limited. Some designs will need to rely more on thermal

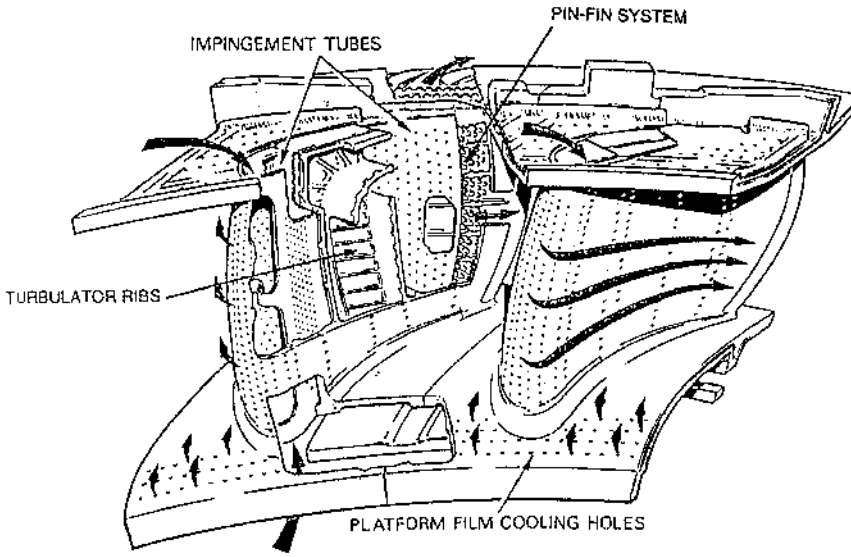

Figure 11 Nozzle vane and end-wall cooling with end-wall film discharged upstream of the leading edge.

barrier coatings and internal cooling methods and less on film-cooling air to achieve the required component life. Other designs will involve unique film-cooling configurations designed as an integrated system, including the transition, airfoils, and end walls. These new combustors will also produce different turbulence conditions and flatter temperature profiles than present aero-derivative combustors. Effects of temperature migration are expected to be less important, and cooling the end walls will be more critical to component life. Heat transfer and internal cooling will have to be further integrated with aerodynamic performance and combustion.

Vane Heat Transfer

One of the most critical inputs to cooling design calculations for turbine airfoils is the prediction of the gas-side heat-transfer coefficients distribution and corresponding heat fluxes. The relative heat-flux distribution on a typical high-pressure turbine airfoil is illustrated in Fig. 12. The highest heat fluxes generally occur at the leading-edge stagnation region and toward the trailing edge of the airfoil. The large gas-side heat-flux variations must be

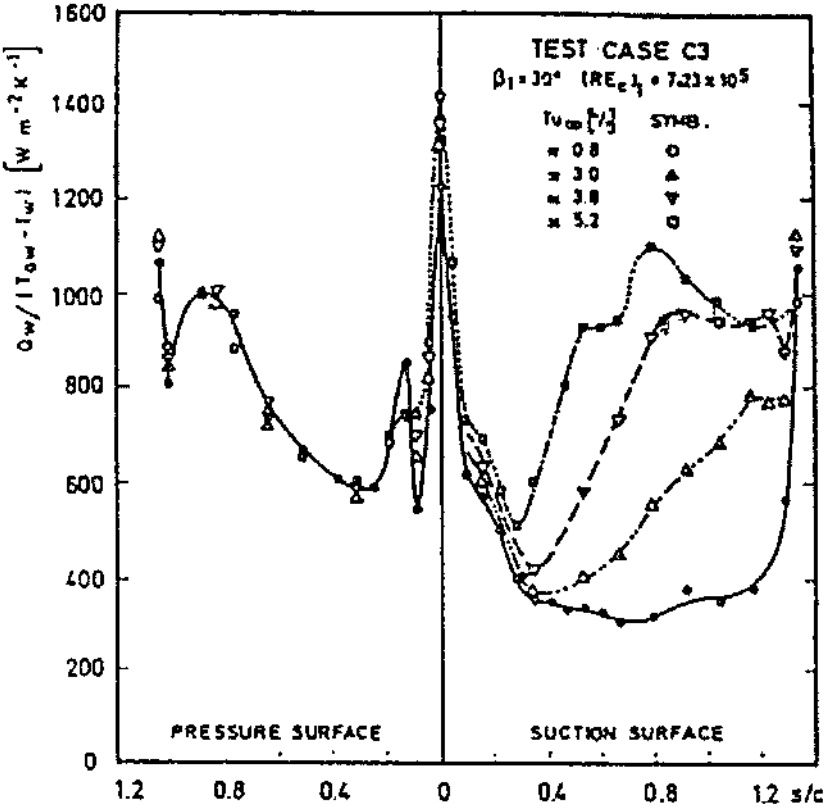

Figure 12 Inlet turbulence effect on vane heat transfer.

appropriately matched by correspondingly high coolant-side effectiveness so as to achieve acceptable temperature distributions.

The general approach often used in the calculation of turbine airfoil heat-transfer coefficients is based on two-dimensional boundary-layer calculation using either finite-difference or integral formulations. Proper aerodynamic description of the flow field, which provides the basis (boundary conditions) for the heat-transfer calculation, is essential for a meaningful prediction of the heat-transfer distribution on the surface of an airfoil. Many of the existing codes have been developed for two-dimensional flow, even though it was well known that for modern highly curved airfoils a three-dimensional calculation is necessary to account for secondary flows

usually originated near the end walls. During last two decades the airfoil external heat-transfer prediction techniques moved from coupling the two-dimensional inviscid flow codes [25] (used for generation of the local pressure or velocity field information for the airfoil) with a two-dimensional parabolic boundary-layer code STAN 5 [26] or later version of the code TEXTAN [27], to more sophisticated (two- and three-dimensional Euler and Navier–Stokes) codes used in conjunction with an appropriate two-dimensional or three-dimensional boundary-layer code to calculate heat-transfer coefficients. A good example of the later technique can be found in [28]. Depending on a number of factors, laminar flow that is usually present on the suction surface of the airfoil goes through sudden transition to turbulent flow at some point downstream of the leading edge. The boundary layer on the pressure surface is generally assumed to be turbulent. The heat-transfer coefficient calculation at the leading edge is typically based on either laminar boundary-layer calculations or standard correlations of stagnation region heat transfer for a cylinder in cross flow.

Heat-transfer coefficients depend mainly on gas pressure level, airfoil size, airfoil shape, and hence surface velocity distribution, and particularly on the location of the boundary-layer transition. The most important factors can be outlined as follows:

Surface curvature
Surface roughness
Local pressure gradient
Mainstream turbulence
Flow injection (film cooling)
Wakes (for second-stage vanes)
End-wall effects (secondary flow)
Radiation

Data on each of the above individual factors are available in the literature, but generally do not represent their combined effects. A limited number of experimental investigations of the effects of main-stream turbulence and film injection on turbine airfoils have also been published. However, systematic investigations of the above parameters in realistic airfoil applications are grossly lacking. As a result, the limited amount of turbine airfoil heat-transfer data available cannot always be interpreted or correlated on the basis of current understanding of the effects of individual parameters present in turbine airfoil applications. At best, only qualitative predictions of the effects of various factors are possible.

The external airfoil heat transfer is mainly governed by streamline aerodynamics over most of the airfoil span. In general, there is little influence of unsteadiness on vane heat transfer. Typically there is an increase

in heat transfer as the Reynolds number is increased. The converse is true as the Mach number is increased. This follows the classical trends for flat-plate boundary layers, and the only difference in the present case is the effect of curvature and pressure gradient which modify the onset and length of transition. The effects of turbulence are well catalogued by a number of authors, for example by Arts et al. [29] and Consigny et al. [30]. Their studies show (Fig. 12) that as inlet turbulence is increased, the location of transition moves upstream and generally leads to an increase in the heat transfer to the suction side of the airfoil.

Curvature

It has been established that the aerodynamics on the pressure side is mainly two-dimensional. Therefore, the heat transfer on the pressure side is also mainly two-dimensional and can be predicted, in most cases, using two-dimensional boundary-layer computer programs. It has been observed that the presence of Goertler vortex on concave surfaces [[31] and [32]] (Volino et al., Dring et al.) can increase the heat transfer to turbine pressure sides particularly at low inlet turbulence intensity. However, experiments on actual turbine vanes and blades that exhibit high inlet free-stream turbulence ($Tu > 5\%$) do not appear to confirm such phenomena. It may also be that the convex to concave curvature transition near the leading edge in real engine airfoils (test cascades and engine vanes) eliminates or destroys the growth of the Goertler vortex, which is quite sensitive to curvature effects and inlet turbulence.

The effect of streamwise surface curvature is to stabilize the boundary layer on a convex surface and to destabilize the boundary layer on a concave surface. The destabilizing effect of centrifugal forces on the concave wall induces an instability, which results in Goertler vortices with axes in the same direction as the main-stream flow. It has been shown that the heat transfer on a concave wall is increased with surface curvature and that for a convex wall the heat transfer is decreased. Turbulence intensities in the boundary layer are significantly reduced on a convex wall and enhanced on a concave wall. The results of some studies also suggest that the effect of surface curvature is nonlinear, being very strong at small curvature values but increasing less than proportionately as curvature increases.

Vane suction surfaces are more influenced by secondary flows. It has been shown that the end-wall boundary layers migrate across the suction surface of the vane. In case of a blade, the tip section has a more intensive secondary flow resulting from the radial pressure gradient (tip to hub) that tends to push more fluid along the airfoil suction side. The secondary flows affect the heat transfer close to the tip and hub sections of the nozzle.

However, this situation is not harmful because the heat transfer in these regions is usually lower than at the midspan. This is due to the thicker momentum and thermal boundary layers in such secondary flow regions caused by the roll-up of the end-wall boundary layers with the airfoil boundary layer. Usually the suction-side heat transfer is lowest close to hub and tip at all Reynolds numbers and Mach numbers. In most cases the onset and length of transition on the suction side is the most difficult to predict. Stagnation-region (leading-edge) heat transfer is affected by inlet turbulence, inlet Reynolds number, and Mach number [33–35] (Lowery and Vachon; Wadia and Nealy; and Garg and Gaugler). The prediction of heat transfer at the leading edge is often performed using correlations established for the circular cylinders. The use of 2D boundary-layer techniques usually yields erroneous results in the leading-edge region because the boundary layer is only just beginning to form and most 2D methods cannot accurately predict the phenomena in this region. The measured leading-edge heat-transfer coefficient is about 1.25 times that calculated for an equivalent cylinder in cross flow. This is to be expected in view of the known marked effect of main-stream turbulence on the local heat-transfer coefficient for a cylinder in cross flow and on laminar boundary layers in the presence of favorable pressure gradients.

The pressure surface heat-transfer coefficients appear to agree well with turbulent flat-plate calculated values. This seems to imply that the combination of the effects of main-stream turbulence, surface curvature, and pressure gradient tend to balance each other and thus results in heat-transfer coefficient levels corresponding to zero pressure gradient and zero curvature turbulent flow.

For the most of the suction surface, heat-transfer coefficients range from 1.0 to 1.25 times turbulent flat-plate values. The transitional flow region on the suction side of the airfoil corresponds to the highest static pressure gradient and requires very close attention [36], particularly if film cooling is discharged in this region. Some consideration should be given to the effects of thermal radiation, particularly for liquid fuel combustors and also when a significant amount of soot and water vapor are present in the products of combustion. It can often account for 10% of the vane heat load. An analytical method for calculation of the radiation heat transfer can be found in a work [109] referenced later.

As shown in Fig. 12, the heat-transfer coefficient reaches the highest level at the leading edge often defining life of the cooled vane due to typically high metal temperature. Presence of erosive particles in the product of combustion makes this area of the nozzle vane even more critical. Therefore, an accurate prediction of the local heat transfer is very important. During an initial design phase its value can be assessed

reasonably well using correlations established for a cylinder in cross flow:

$$\mathrm{Nu}\alpha = \mathrm{Nu}_\mathrm{d}\left[1 - (\alpha/90)^3 K_\mathrm{tu}\right]$$

Where

$\mathrm{Nu}_\mathrm{d} = 1.14\,\mathrm{Re}_\mathrm{d}^{0.5}\mathrm{Pr}^{0.4}$.

α-angular location on cylinder from the leading-edge stagnation point (valid to 60° at either side of the stagnation point).
$K_\mathrm{tu} = 0.267\,\mathrm{Re}^{0.15}$—correction for main-stream turbulence effect [37] (Dyban, Kurosh).
Re_d = Reynolds number, based on airfoil leading-edge diameter.

Roughness Effects

Elevated levels of surface roughness, which are particularly typical for industrial turbines, operating long hours without maintenance often at harsh environments, have a significant effect on the skin friction and heat transfer of turbine engine blades. For aero engines, which operate usually in a better environment, thermal barrier coating roughness and spallation are main modes of the heat-transfer increase due to airfoil surface roughness

The increased roughness causes an increase in the external heat-transfer coefficient on all surfaces exposed to the hot gas stream. The increased heat transfer arises from the addional turbulence (from vortex shedding) generated close to the surface by the roughness elements and also the extra surface area due to the roughness elements. Experimental work by [38] Turner et al. shows that roughness can increase the heat load quite significantly to the aerofoil. A number of other studies [39–41] by Abuaf et al., Tolpadi and Crawford, and Guo et. al. have also reported a higher heat transfer that is associated with increased roughness on turbine blades. The experiments indicate that, when the inlet turbulence is low, the increase in heat transfer is approximately 50% on the suction side and around 100% on the pressure side. Clearly, some of this increase is attributable to the fact that roughness initiates transition. However, for higher turbulence intensity (Tu = 7% with an installed turbulence grid) the authors note that there is an increase of heat transfer on the pressure side of around 25%, while the suction-side heat transfer is hardly changed.

In general, the influence of roughness only becomes important for gas turbines using fuels of poor quality when operated for extended periods of time. These applications typically include industrial gas turbines for power generation and mechanical drive. In the case of the aircraft gas turbine, roughness is less of a problem because the airfoils generally remain smooth

throughout the operational life. The only situation where roughness can be a generic problem is with thermal barrier coated (TBC) components where the TBC can have an initial roughness of up to 12 microns. However, even here modern coating methods can deliver smooth TBC components, albeit with a significantly higher cost.

Turbulence

The effects of main-stream turbulence on turbine airfoil heat transfer can be summarized by the following:

- Main-stream turbulence significantly influences the start of transition from a laminar to a turbulent boundary layer with increased turbulence promoting early transition.
- Turbulence has a very marked effect on laminar boundary layers; increased turbulence results in increased heat-transfer coefficients in the laminar boundary-layer region of turbine airfoils, such as the leading edge, and in the transitional flow regions.
- Main-stream turbulence level has little effect on the heat transfer in the turbulent boundary-layer region.

It is well known that favorable pressure gradients suppress and adverse pressure gradients amplify turbulence in a boundary layer.

Vane Film Cooling

This section considers the main practical aspects of film-cooling application to turbines. Both internal convective and external film-cooling techniques, or more often their combination, are applied in nozzle cooling design. Localized injection of a cooler fluid into the boundary layer of a high-temperature fluid along a wall to control the wall surface temperature is called film cooling. The cooling air, usually bled from the compressor, shields the turbine airfoil surface by creating an insulating layer between the main stream and the surface, thereby achieving a reduction in heat flux to the surface. Because the coolant mixes with the main-stream flow, the film is generally not a very effective method of cooling by itself. However, film cooling used in combination with convective cooling can result in significant reductions in metal temperature and thereby contribute to high overall cooling effectiveness. Figure 11 provided an example of advanced nozzle cooling. The fundamental reason for using film cooling arises from those situations in which purely internal convective cooling has been found to be inadequate. Details of internal convective cooling techniques are presented

in the section on blade cooling that follows, where application of film cooling is often somewhat limited compared to nozzles.

Film-cooling application for turbine airfoils is very common in advanced gas turbines. For this reason the following section considers most of the factors that influence film cooling. A comprehensive early guide to the methodology of film cooling was given by Goldstein (1971) [42]. However, these generic early data have very limited application for the modern airfoil shapes and realistic main-stream velocity distribution. The most recent bibliography of the film cooling can be found in [43, 44].

With film cooling the heat flux q''_f is given by the following relation: $q''_f = h_f(T_{aw} - T_w)$; the heat-transfer coefficient, h_f, is often assumed to be that which would exist without film injection, although it may deviate significantly from this value in the near-hole region. The adiabatic wall temperature T_{aw} is the temperature assumed at the wall in the absence of heat flow (without film cooling, the adiabatic wall temperature for low Mach number is equal to the main-stream gas temperature), and T_w is the actual wall temperature. In the presence of film cooling, the adiabatic wall temperature is defined by a dimensionless wall temperature called film-cooling effectiveness generally designated by η and defined as

$$\eta = (T_g - T_f)/(T_g - T_c)$$

where

T_g and T_c are the gas stream and coolant exit temperatures, respectively.
T_f is the film temperature (adiabatic wall temperature resulting from film injection).

The film temperature is a function of distance downstream from the injection point and must be experimentally determined for a given film-cooling geometry. Film temperature is generally correlated in terms of local film effectiveness as

$$T_f = T_g - \eta(T_g - T_c)$$

There are two main types of geometry used in film cooling: slots and rows of discrete holes. However, slots are not often used in airfoils because of thermal stress and mechanical design considerations. High thermal stresses are caused by the fact that the airfoil region just upstream of a slot is hot, while just downstream of a slot it is cold. Provision of slots causes difficulty in holding the airfoil together at the slot, especially in the presence of the high thermal stresses. Replacing the slot with a row of holes tends to reduce these problems considerably because the metal between the holes

relieves the thermal gradients and stresses and holds the airfoil together. An exception to the use of film hole rows rather than slots is in the pressure-side trailing-edge region of vanes and blades, where a row of short slots are often used. With this specific geometry the thermal stress and mechanical problems associated with the use of slots are minimized. Rows of holes may solve some problems, but they do so at the expense of others. In general, film-cooling effectiveness from discrete holes is less effective than from slot injection and the flow fields are more difficult to predict or correlate. The lower film-cooling effectiveness is due to the jets from the individual holes penetrating into the main stream and thereby permitting the hot main-stream gas to flow under the film along the cooled surface. As the jet emerges into the free stream, it is deflected toward the surface, and consequently a pressure gradient is set up within the jet with a low-pressure zone beneath the jet and a high-pressure zone above the jet. This causes the jet to roll up into a kidney-shaped vortex, which then entrains main-stream fluid toward the surface, which is being cooled. This penetration and mixing are not present with injection slots. However, for the reason mentioned above, slots are not often used in airfoils. Therefore, the following discussion will be limited to the film-cooling air discharged through discrete holes. For average film effectiveness values of about 0.20–0.30, airfoil surface heat-flux reductions of 30–45% can be achieved.

One of the efforts in film-cooling design has to be focused on avoiding separation of a film jet from the surface (blow-off phenomenon). Two primary parameters affecting film jet behavior are: blowing rate M (or mass flux ratio) and momentum flux ratio I:

$$M = \rho_f V_f^1 / \rho_\infty V_\infty; \qquad I = \rho_f V_f^2 / \rho_\infty V_\infty^2$$

The blow-off phenomenon represents an obvious limitation to the use of single-row film-cooling configurations. The problem, however, can be alleviated by improved film-cooling design configurations, which minimize or reduce jet penetration. Two alternate design approaches that have been successful in achieving this are the use of staggered rows of inclined holes and the use of shaped holes.

The film-cooling performance of two staggered rows of holes inclined 35° to the mainstream was studied by Jabbari and Goldstein [45]. It was shown that unlike the single-row case, no blow-off is apparent. The film-cooling effectiveness following injection through two staggered rows of holes increased with increasing blowing rate without exhibiting a decrease in the range of values of M covered by the test. The indicated improvement was attributed to the lower jet penetration resulting from the jet interaction obtained in the configuration. It was observed that for the same injected

mass flow rate (e.g., $M = 1$ for a single row of holes and $M = 0.5$ for a double row of holes) the staggered row configuration provides higher film-cooling effectiveness than the single-row configuration at blowing rates that result in "blow-off" in single-row configurations. At lower blowing rates, $M < 0.5$, the film-cooling effectiveness obtained for both configurations is about the same. A further advantage in the use of staggered rows is derived from the spanwise, more uniform film cooling. It has been shown that the use of double rows of staggered holes or shaped holes in order to eliminate blow-off is advantageous for suction surface applications. To improve pressure surface effectiveness, use of multiple rows with film accumulation from preceding rows is required.

Application of shaped holes that are diverged in the lateral direction normal to the direction of the main-stream flow can significantly improve attachment of the film jet to the surface. The most common shaped hole geometry consists of a circular metering hole, which controls the film flow rate, with a flared diffuser section at the discharge of the hole. For values of $M = 0.5$, the shaped hole film effectiveness continues to increase with increasing blowing rate, whereas the cylindrical hole effectiveness exhibits a sharp decline, particularly in the region near the holes. This sharp decline in effectiveness is attributed to jet blow-off. Additionally, the shaped hole contributes to improved lateral distribution of the secondary flow so that the film-cooling effectiveness between holes is significantly greater than that obtained with straight cylindrical holes. The improved effectiveness is attributed to the reduced injection velocity of the secondary flow due to the larger discharge area. This lower velocity causes the jet to stay closer to the wall rather than penetrate into the main stream and accounts for the higher film effectiveness than obtained at high blowing rates for the same hole geometry.

It is apparent from the preceding discussion that the use of shaped holes or double hole rows in order to eliminate blow-off only appears to be advantageous for suction surface applications.

Where a turbine airfoil is cooled with the aid of films, there is an added benefit in that the film-cooling holes can constitute quite a powerful convection heat-transfer system locally. While this is not usually a sufficient reason in itself to warrant the provision of a film-cooling hole row (or rows) in a design, it nevertheless provides a useful bonus when film cooling is added. This effect is particularly beneficial in the leading-edge region of an airfoil when a shower head configuration is used. Radially inclining the film holes increases the local convection cooling effect by increasing the length of the holes.

In summary, the main factors affecting the performance of film cooling include hole size, shape, spacing and angle, number of rows, row

spacing, location coordinated with a hot spot and internal cooling geometry, blowing ratio, surface curvature, pressure gradient, density ratio, and mainstream turbulence level. Some of these will be discussed in more detail below. A single row of holes, even for optimized geometry of the holes, cannot usually provide sufficient cooling effectiveness along a turbine airfoil due to certain decay in film effectiveness. Figure 13 provides an example of the film effectiveness decay along the pressure and suction surfaces of a realistic airfoil. In general, as far as defining and using experimental data, film-cooling effectiveness is a function of the injection geometry on the airfoil including hole diameter (d_h), hole spacing (X_n) to diameter ratio (X_n/d_h), and axial inclination of hole axis to the surface α (for radially inclined holes, the angle α is defined relative to the vertical), together with the blowing rate M and the distance correlation parameter (X/Ms). In this correlation parameter, X is the downstream distance from the point of injection, and s is the equivalent slot width of a film hole row. For multiple-row film correlations, unless otherwise stated, the distance X is measured from the center of the last row of holes and the coolant mass velocity V_f used in calculating M is based on the average for all blowing holes.

A large variety of geometries that have been studied can be found in the open literature for film hole rows, showing their effects on film effectiveness. The majority of the design data is for circular holes, although with interest shifting to shaped holes, more data are becoming available for this geometry. As mentioned earlier, a typical shaped film hole configuration contributes to improved laterally (spanwise) averaged film-cooling effectiveness especially in the region immediately downstream of the film

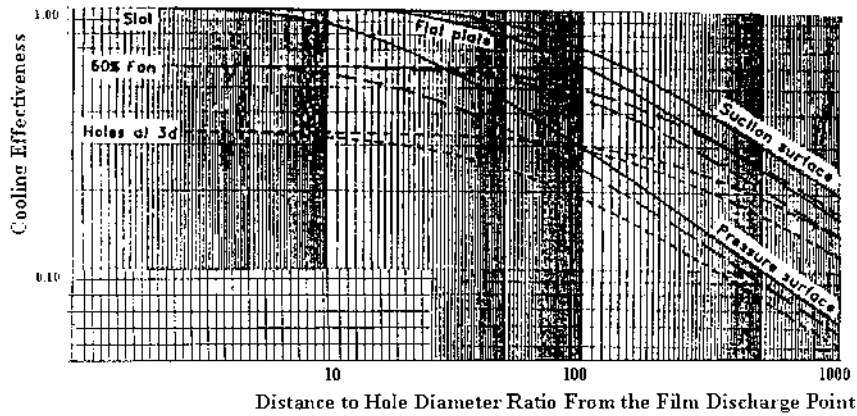

Figure 13 Film-cooling effectiveness decay downstream of a discharge hole/slot.

holes. Cooling hole pattern is an important parameter in film cooling. In general, decreasing the film injection angle increases the film effectiveness, particularly when operating close to a blow-off situation. Compound angles are used in some applications, especially where better spanwise film coverage is required with large film hole spacing. Decreasing the hole spacing increases the film effectiveness and also makes it more laterally uniform. For practical situations it is recommended that film injection angles be designed between 15° and 40° to the local airfoil tangent surface. However, this rule does not apply to the leading-edge shower head holes where the angle, by geometric necessity, will tend to be greater. In general and where possible, hole spacing should be maintained at a ratio of between 3 and 4 times the hole diameter in order to provide an effective film. Obviously, there may be other factors that will control the film hole spacing such as the necessity to minimize flows where there is a high film hole pressure ratio. A larger number of film hole rows requires smaller hole sizes for a given cooling budget and might not be practical due to increased hole blockage problem.

Blowing Ratio

In film cooling, the effectiveness can generally be correlated as a function of the blowing ratio, as defined above, or the mass flux ratio. Increasing the blowing ratio M up to a certain limit increases cooling effectiveness. Further increase in the blowing ratio beyond this limit decreases film-cooling effectiveness due to jet blow-off into the main stream. The effect of blow-off is generally the strongest near the holes and weaker farther downstream. The limiting value of the blowing ratio at a coolant density ratio $\rho_f/\rho_\infty = 1$ is between 0.4 and 0.6 for 35° injection angle. Recent studies on the effects of density ratio, free-stream turbulence, unsteadiness, and surface roughness show that these factors have a tendency to make the blowing ratio limit higher. There is also a difference between concave and convex surfaces, the limiting value being greater for the concave surface.

Early experimental work on film cooling was mostly conducted with heated injection air, resulting in a density ratio equal to or less than unity. In real engines, the density ratio is greater than 1.8 due to the large temperature ratio between the gas stream and cooling air.

The coolant-to-mainstream density ratio is an important factor. As the density ratio is increased, the film-cooling effectiveness is also increased. The physics of the process is such that the heat transfer under the film is reduced as the density ratio is increased for the same gas-to-coolant temperature ratio.

Surface Curvature

Curvature plays a very important role in achieving required film-cooling effectiveness. For the same blowing rate ($M = 0.5$), the suction-side effectiveness is higher than that for an equivalent flat plate by up to 100%; on the pressure side the cooling effectiveness is reduced by around 50%. The effect is evident for all coolant-to-gas density ratios. The observed curvature effects on film-cooling effectiveness have been attributed to the balance of the forces exerted on the injected fluid jet by the static pressure and the centrifugal force along the path of the injected jet. These forces have been shown, for low-momentum jets, to act on the injected jet in the direction that moves the jet toward the surface on the suction side and away from the surface on the pressure side. For high-momentum jets, the opposite occurs. Hence, for low-momentum jets, the general trend for film-cooling effectiveness is low on the pressure side and high on the suction side, relative to a flat plate. These trends are reversed for high-momentum jets. Suction surface data exhibited the characteristic limiting value caused by blow-off and observed with flat-plate data. Clearly then, it is necessary for the turbine cooling designer to have a sufficiently large database or appropriately calibrated numerical methods to be able to assess the impact of film cooling during the design process.

Pressure Gradient

Very little data are available to define the effect of pressure gradient on film-cooling performance. Its effect is generally combined with surface curvature when airfoils are tested under simulated main-stream conditions. In this situation it is not possible to separate the two interrelated effects. However, it is generally understood that both favorable (accelerating) and adverse (decelerating) main-stream pressure gradients can cause a slight degradation of film-cooling effectiveness as compared to that for zero main-stream pressure gradient flow (constant velocity).

Main-Stream Turbulence

Early studies on film cooling were all performed under low free-stream turbulence conditions. In an actual gas turbine, airfoils experience combustor-generated turbulence as well as the unsteady wake effect generated by upstream airfoil trailing edges. These effects have received more attention in recent years because the results obtained under low-turbulence conditions may lead to significant overprediction of the film-cooling effectiveness. Free-stream turbulence and unsteady wake may damage the film protection on a surface due to greater mixing of the injected

coolant flow with the main stream, resulting in reduced film-cooling effectiveness. In addition, free-stream turbulence and unsteady wake may increase heat-transfer coefficients, causing further increases in heat transfer to the surface. Experimental data indicate that increased main-stream turbulence reduces the effectiveness of films that often depends on the blowing ratio. Optimum blowing ratio for high turbulence levels were found to be much higher and wider in range than is reported for the low-turbulence level. The data show that film effectiveness for low blowing ratio decreases dramatically in the region close to injection with increasing main-stream turbulence. The effect is reduced at higher blowing ratios. Downstream from injection, film effectiveness is reduced with increasing turbulence for all blowing ratios studied.

A very important consideration when looking at film cooling of an airfoil is to ensure that an adequate margin exists between the internal pressure supplying the film cooling air and the local external static pressure at the film injection point. This is to avoid the possibility of hot gas ingestion into the airfoil. The amount by which the film air supply pressure exceeds the exit pressure is usually referred to as the "backflow margin."

Among other important effects of film cooling that the designer must consider are momentum losses associated with mixing of the coolant with the main-stream flow and its effects on turbine aerodynamic performance. Considering the complexity of film-cooling interaction with the main stream and the large number of factors affecting film-cooling effectiveness, it is recommended to validate turbine airfoil film-cooling design data in cascades where geometry, Reynolds number, Mach number, coolant-to-main-stream density and temperature ratios, and main-stream turbulence are all closely simulated to represent engine design conditions. The available literature can be used for guidance in these tests.

Film-Cooling Slots

Trailing-edge pressure-side slots, often replacing traditional (in the past) trailing-edge ejection, is the most common application of slots (often shaped as gill slots). They provide an improvement in the turbine aerodynamic efficiency by allowing the trailing-edge thickness to be reduced. Even though an increase in cooling flow is required for the pressure-side slots to achieve the same metal temperature, the reduction in trailing-edge thickness still produces a net performance improvement. With this configuration, the temperature of the trailing-edge region depends strongly on the heat-transfer coefficient and the film effectiveness in the area downstream of the slot exit.

A considerable amount of early film-cooling experimental work was performed using two-dimensional slot configurations. A number of these studies were reviewed in detail, together with a comprehensive development of theoretical analyses relating to the subject of film coolant. Most of the empirical expressions for slot film-cooling effectiveness have been developed using heat sink models for two-dimensional incompressible flow film-cooling injection. Several are discussed in detail in [46]. The equation developed by this work is

$$\eta_c = 1.53/\left\{1 + 0.329\,\mathrm{Re}_s^{-0.2}[X/(Ms)]^{0.8}\,K\right\}$$

where $K = 1 + 1.5 \times 10^{-4}\,\mathrm{Re}_s \sin\beta$ with the slot Reynolds number $\mathrm{Re}_s = \mathrm{m\,s}/\mu$.

The above correlation is recommended as a generalized slot film-cooling correlation.

Film Accumulation

For most high-temperature turbine airfoil cooling designs, film-cooling schemes are employed on the leading edge as well as along both the suction and pressure surfaces. This is because the coolant film must be periodically renewed as decay of the film and mixing with the hot gas stream bring the adiabatic wall temperature back to the gas-stream temperature. In this situation, where there are two or more film rows provided on an airfoil surface, it is necessary to be able to estimate the combined effects of these films. The following equation for the overall film-cooling effectiveness is recommended for use where there is a film-cooling additive effect:

$$\eta_f = \eta_1 + \eta_2(1-\eta_1) + \eta_3(1-\eta_1)(1-\eta_2) + \cdots + \eta_n(1-\eta_1)(1-\eta_2)(\cdots\cdots\cdots)(1-\eta_{n-1})$$

where n is the number of film rows.

This simple superposition model is based on the assumption that the accumulated film effectiveness due to multiple rows of holes can be represented from data or correlations for a single row of holes. It was derived from the concept that the gas temperature used to determine the film effectiveness downstream of an injection location should be the adiabatic film temperature due to all injections upstream of that location. Industry comparison of this method with multiple row data has, in general, shown good agreement. The film superposition equation was further studied for multiple row of injection holes over an airfoil suction surface. An excellent agreement between measured and predicted overall film-cooling effectiveness was demonstrated in a number of studies. It should be noted that the

above equation assumes a constant film injection temperature for each row of holes. In some cases this assumption may be acceptable; however, if there is a significant variation in the film injection temperature from row to row, then the equation for overall film effectiveness needs to be modified.

Effect of Film-Cooling Air Ejection on Surface Heat Transfer

The application of film cooling to the design of an airfoil requires the accurate prediction of both the film-cooling effectiveness and the heat-transfer coefficient under the film. The majority of film-cooling designs have been based on the assumption that the heat transfer to a film-cooled surface can be approximated sufficiently well by using the heat-transfer coefficient of the surface without injection, in conjunction with the difference between the adiabatic wall temperature with injection and the actual wall temperature. This approximation is good for slot injection at low blowing rates. For higher blowing rates ($M > 1.0$) and for hole row injection, studies show that the heat-transfer coefficient is higher than without injection, particularly in the region close to the point of injection. However, this effect of heat-transfer augmentation by the film injection is not observed far downstream from the point of injection. The heat-transfer coefficient under the injected film, similar to film effectiveness, is a function of more factors than just the blowing rate. These include geometry, pressure gradient, density ratio, turbulence, etc.

End-Wall Cooling Issues

End-wall high-temperature oxidation or "hot corrosion" is known as one of the factors that limit the life of a turbine hot section. Surface irregularities resulting from this oxidation lead to increased local heat transfer and accelerated material loss due to oxidation. Complicated secondary flow phenomena [47] and high local heat-transfer coefficients near the end walls are considered to be major factors in the oxidation damage. Effective cooling of these areas is certainly required for advanced gas turbines.

Numerous studies dealing with heat transfer to the end-wall region of the vane have been reported in the literature. Sharma et al. [28] compare the results of a 3D boundary-layer calculation with experimental results near the hub and tip end walls for a low aspect ratio turbine vane. Good agreement is demonstrated with the measurements on both end walls near the suction surface and at midpitch, but they underpredict the heat-transfer values near the pressure surface for both cases. The end-wall aerodynamics and heat transfer are dominated by secondary flows. The fluid dynamic phenomenon is illustrated in Fig. 14. Flow visualization shows that the inlet

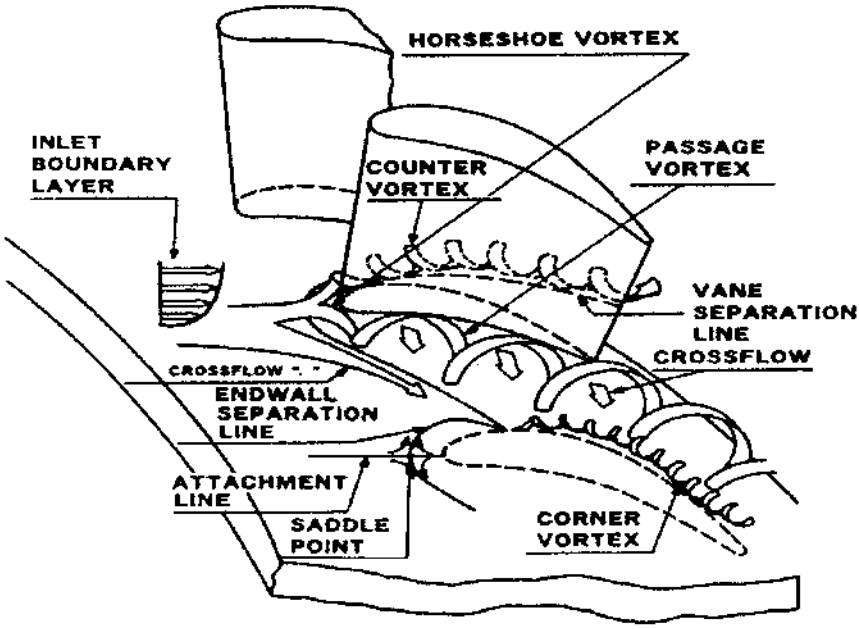

Figure 14 Nozzle end-wall secondary flows.

boundary layer is skewed toward the suction side of the passage due to the vane-to-vane pressure gradient. As the end-wall boundary layer is swept toward the suction side, a new boundary layer is formed downstream of the separation line and this results in a high heat-transfer region. Several investigators have demonstrated the phenomena in linear cascades.

Figure 15 shows the film-cooling configuration that was utilized by Harasgama and Burton [48,49]. The film-cooling holes were placed along a computed iso-Mach line (constant pressure) in order to achieve a uniform momentum flux ratio (and blowing rate) across the whole platform. There is a steep reduction in effectiveness from suction side to pressure side as well as the expected streamwise decay of effectiveness. The pressure-side effectiveness is typically lower than the suction-side value by 20% (for low x/d) to 75% (for large x/d). This results from the film being swept toward the suction side.

In the case of turbine blades, the end-wall heat transfer is also strongly dependent on the spanwise pressure gradient. The heat-transfer data for inner and outer end walls obtained in annular cascades at engine representative conditions were shown to differ (Harasgama and Wedlake,

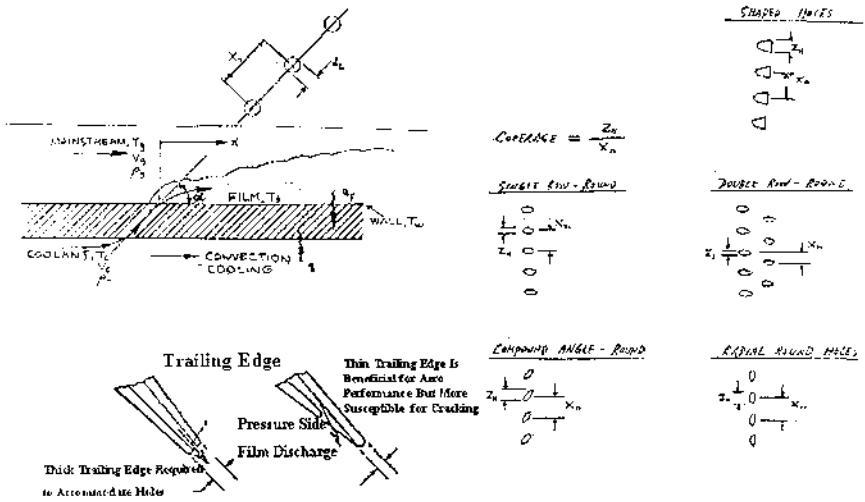

Figure 15 Definition of film-cooling hole geometry.

Arts and Heider) [50, 51]. It was concluded also that the heat transfer depends on the operational Mach number and Reynolds number. The observed differences were related to the changes in the spanwise pressure distribution, conditions of the inlet boundary layer, and the blade-to-blade loading of the turbine. It was concluded that results of the annular cascade heat-transfer data are well representative of an actual engine and can be applied as a basis for cooling design. At larger Reynolds numbers a high heat-transfer region migrates upstream of the trailing edge along the inner end wall and is centered midway between pressure and suction sides. For the outer end wall the high heat transfer is usually found near the pressure side closer to the trailing edge. At low Re, the high heat-transfer region moves toward the trailing edge, also near the pressure side. The effect of Mach number is found to be much less significant than that of Reynolds number.

Two cooling techniques have been used for nozzle end walls: backside convective (often impingement) cooling and film cooling. Significant pressure losses associated with the backside impingement cooling usually exclude its combination with film cooling at upstream locations near the leading edge of the end wall. This requires discharging the spent cooling air further downstream, resulting in significant performance penalties. A similar negative effect is observed when film cooling is introduced in the vicinity of end wall next to the nozzle throat.

Positioning the film-cooling jets upstream of the leading edge is the most beneficial for overall stage performance. However, this approach has to overcome certain challenges imposed by the secondary flows. Over the last few years, a number of numerical and experimental studies (Friedrichs, 1996, 1997) [52, 53] have addressed this approach with a goal to effectively cool nozzle end walls relying primarily on the upstream film jets. Some of the recently published data by Friedrichs and also by Simon [54, 55] clearly show that properly positioned film jets discharged at optimized blowing ratio can provide effective end-wall cooling all the way to the nozzle throat without premature sweeping of the film toward the suction side. Although it might require a significant amount of the film flow, the overall stage performance improvement can be achieved by suppression of the secondary flow and associated performance losses. Coolant distribution is strongly influenced by the momentum flux ratio. At a lower momentum flux, there is strong migration toward the suction side due to the cross flow. As the momentum flux ratio increases, there is better pressure-side cooling, as some coolant accumulates in the vicinity of the pressure surface. Comparing a single-slot injection case with a double-slot injection case, it was observed that uniformity of coolant distribution across the leading edge is better for the single-slot injection case, due to the higher momentum flux ratio. Direct comparison of single- and double-slot injection for the same momentum flux ratio shows that the distributions of cooling effectiveness for both cases are similar in shape but different in magnitude, providing higher values for the double-slot injection due to the higher coolant mass flow rate. Other very important factors affecting secondary flow and film effectiveness are the shape and degree of converging contouring of the end wall. Improved numerical prediction techniques [56, 57, 58] might be very useful in optimizing design of the film-cooled end wall.

TURBINE BLADE COOLING

In addition to high thermal and aerodynamic loads turbine blades operate at extremely high inertial stresses. Creep and rupture life of the blade material at certain temperatures often defines the life of the entire engine. The criticality of a blade failure explains the level of attention paid to the blade-cooling design that is required to support the constantly increasing turbine rotor inlet temperatures (TRIT). Similarly to nozzle vanes, the shape of a turbine blade that is selected for the best aerodynamic performance often has to be compromised to be acceptable from a cooling design standpoint. Constraints associated with the cooling of modern blades, which are highly loaded and have a large main-stream turning angle, might require

redistribution of the external heat-transfer coefficients, resulting in a larger diameter of the leading edge, changes in velocity distribution and airfoil shape, and modifications even to the number and size of the airfoils. Figure 16 illustrates the evolution of these changes from an early blade with a simple cooling scheme (a) to more advanced internal cooling with a minor film cooling (b) and finally to a modern full-film coverage cooling that approaches effectiveness of transpiration cooling (c).

The aerodynamics of rotor blade internal cooling and external gas flows differ from that of the nozzle vane due to presence of the rotational forces, unsteady wakes from the upstream nozzle vanes, and more pronounced 3D effects along the blade surface particularly on the pressure side and near the tip of a blade. Blade-cooling techniques are often different from the nozzle vane-cooling methods. Much higher performance penalties that are associated with blade cooling, compared to upstream nozzle cooling, impose significant limitation on the blade-cooling flow budget. Due to blade rotation, the main-stream gas temperature is averaged in the tangential direction, thereby subjecting the blade to only the radial combustor temperature variation (radial temperature profile). For this reason blades operate under the same radial profile whose peak is lower than that at the vanes. Due to rotation, only the relative main-stream velocity affects the total relative gas temperature T_{rel} that is "seen" by the blade. The difference between TRIT and T_{rel} is proportional to $(V_{abs}^2 - V_{rel}^2)$.

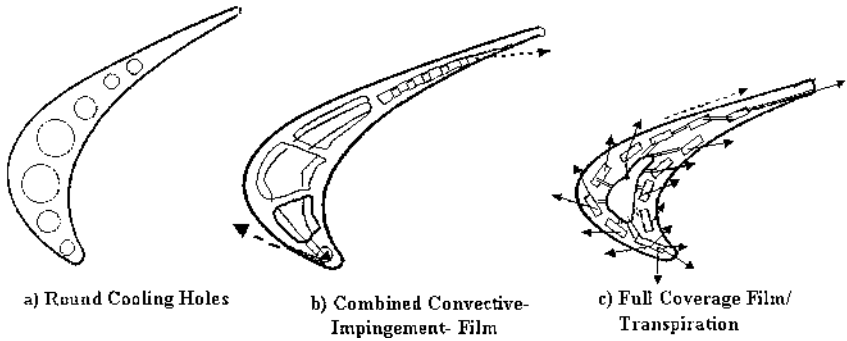

Figure 16 Evolution of cooled blade profile and geometry of interior.

Rotational and Three-Dimensional Effects on Blade Heat Transfer

Rotational Forces

Rotation-induced body forces give rise to two effects that must be considered for their influence on the heat transfer in coolant passages of turbine blades. These are free convection or buoyancy effect, and Coriolis effect. An indication of whether these effects may be significant is obtained from the magnitude of the appropriate dimensionless parameters derived by comparing the magnitudes of the rotation-induced body force and the inertia force of the passage coolant flows. It is common in experimental studies to characterize the fluid flow in a rotating blade by a buoyancy number (ratio of centrifugal to inertial forces), a rotational parameter (ratio of Coriolis to inertial forces), and the Reynolds number. The inverse of the rotational parameter Ro is the Rossby number Ros (ratio of inertial to Coriolis forces). These parameters can be described in several ways, but are often expressed as follows: $\mathrm{Bo} = \mathrm{Gr}/\mathrm{Re}^2$; $\mathrm{Ro} = \omega b/U$; and $\mathrm{Ros} = 1/\mathrm{Ro}$, where $\omega =$ angular velocity, $b =$ passage height, and $U =$ fluid mean velocity in the passage.

Buoyancy effects become important when the magnitude of the buoyancy number is of the order of unity or greater. In general, buoyancy effects are found to be small or negligible in a high-pressure turbine blade coolant passage application. The results of investigations of Coriolis force effects on the flow in rotating radial passages indicate that even at relatively low values of rotation number $\mathrm{Ro} \approx .01$, significant effects on the wall shear and the turbulent structure of the flow may occur. Coriolis forces in radial flow passages result in transverse pressure gradients across the channel, giving rise to secondary flows. Most of the rotating heat-transfer measurements reported in the literature were obtained in cylindrical tubes and were limited to average heat-transfer coefficient measurements. In turbine blade applications, due to large heat-flux variations, calculations based on average heat-transfer coefficients may not be adequate, particularly when these variations are large.

A rotation number of $\mathrm{Ro} = .05$ is typical in turbine blade-cooling passage applications. On this basis, one might expect that significant Coriolis effects may be encountered in turbine blade coolant passages and that calculations based on average heat-transfer coefficients may lead to significant errors. Over the last decade a number of heat-transfer studies have been performed for realistic Ro numbers in rotating channels simulating turbine blade-cooling passages [59–64]. As expected, a noticeable increase of the heat transfer near the pressure-side wall and reduction of the heat transfer adjacent to the suction side have been observed as result of the Coriolis forces.

Three-Dimensional Effects

The three-dimensional flow characteristic in a turbine passage in a cascade environment is well understood, and there is good agreement among investigators regarding the major flow structures (Sieverding and Langston) [65–66]. Recent experimental measurements suggest that the local efficiency gains from a pressure-side tip platform extension can be significant. A number of studies revealed that there is considerable secondary flow that is directed toward the tip region especially between the leading edge and around 30% axial chord. This is explained by Dring & Joslyn [67] as a relative eddy, which carries the fluid toward the blade tip. It is a simple physical phenomenon where the secondary flow vorticity locally dominates the main-stream flow because in this region of the blade the axial Mach numbers are quite low ($\leqslant 0.3$). The secondary flow can result in a slightly higher heat transfer due to skewing of the near-wall flow.

One of the significant effects of rotor flow is the redistribution of inlet temperature radial profile along the blade passage. There is also an unsteady circumferential effect generated by combustor burners. It is observed that the secondary flow within the passage can be augmented due to temperature distortion. As the rotor blade passes through a combustor hot streak, the flow within the blade passage becomes density-stratified and suffers incidence changes and additional secondary vorticity. The accompanying Mach number distributions result in quite high velocities in the tip gap region, which generate correspondingly high shear stress and heat transfer in the blade-tip gap. As the hot gas reaches the trailing edge of the blade, it migrates to the suction surface and also penetrates through the tip gap.

Radial Gas Temperature Profile

Due to the typical distribution of centrifugal forces along the blade height with its maximum at the root section and minimum at the tip, a decline in gas temperature toward the blade platform is necessary to achieve uniform creep-rupture life through the blade height. In addition, blade material properties usually allow significantly higher metal temperature than the surrounding end-wall structures: turbine disc under the platform and stator components that form the radial clearance between rotor and stator. For these reasons, a blade inlet radial temperature profile has to be skewed toward the end walls with the peak temperatures located usually between 50% and 70% of the blade height [68]. This radial temperature profile has to be formed in the combustor and include effects of the cooling air that enters the main gas flow upstream of the blade, after cooling the nozzle end walls, vanes, and disc forward faces. Cooling air discharged from the upstream

vane trailing edges usually does not undergo uniform circumferential mixing and is often skewed toward the tip of a blade at the suction side. Actual measurements in engines and analytical predictions show that inlet radial temperature profile along the gas path is usually further skewed toward the outer radius, creating additional challenges for cooling the tip sections of blades toward trailing edges.

Effects of Unsteadiness

Unsteady interaction between stator and downstream rotor has a significant effect on heat transfer. Heat-transfer measurements for a full turbine rotor stage have first been reported by Dunn et al [69]. Their study showed that the wakes from upstream vanes cause an intermittent increase in the heat transfer on the rotor blade surfaces. The highest enhancement of heat transfer could be seen mainly near the leading edge and just around the first part of the suction surface. Further downstream on the suction surface the enhancement of heat transfer decays quickly. On the pressure surface the increase in heat transfer persists all the way back to the trailing edge, although the enhancement near the leading-edge region up to 20% axial chord is not as high as that on the suction surface.

Later aerodynamic and heat-transfer measurements on a rotating turbine made by Hodson [70] showed that the rotor blade boundary layer undergoes transition from laminar to turbulent flow as the wake from upstream vanes pass through the rotor blade passage. This results in increased shear stress and aerodynamic loss. The increased shear stress is also expected to increase the heat transfer. A number of studies have shown that there is an intermittent increase in heat transfer over the suction and pressure sides of a blade. Measurements that were made even at a low turbulence level (4%) showed that the moving turbulence simulating grid induces wakes and results in increased heat transfer. Usually the increase on the pressure side is greater than that on the suction side. In a similar experiment Dullenkoph et al. [71] have also demonstrated similar effects on the time-averaged heat transfer for upstream wakes on a rotor blade cascade. Strong increases in heat transfer are shown by Johnson et al. [72] for the case of shock waves from upstream vanes impinging on the rotor blade surface. This phenomenon has been analyzed more recently by Abhari et al. [73] and Rao et al. [74] using comprehensive numerical models.

Internal Blade-Cooling Techniques

Because of its high thermal load combined with large inertial and dynamic forces, the turbine blade is the most critical component for engine durability.

In order to achieve the bulk metal temperatures capability of about 1,500 °F, required by creep-rupture life characteristics for advanced blade alloys, highly effective blade-cooling techniques are inevitable for long-term durability. For sustaining the bulk metal temperatures at a TRIT of 2,200 °F and compressor discharge temperatures of 840 °F, the required cooling effectiveness parameter, as defined below, is approximately 0.5:

$$\eta_c = (T_\infty - T_\mathrm{m})/(T_\infty - T_\mathrm{c})$$

Even for advanced cooling designs utilizing film cooling, the efficient use of the air by internal convection cooling, prior to being ejected as a film still forms an important part of the overall design. There are many variations on the internal construction of blade-cooling passages. These variations often include ribs, inclined ribs, roughened ribs, etc. which are designed to trip the internal boundary layer to turbulent in order to increase the internal cooling capacity above what it would be for a smooth wall laminar boundary layer. Based on engine experience, designers can often estimate the internal heat transfer using standard pipe flow correlations and adding an experience factor to the correlations. However, in the case of the rotating hot turbine blade, Coriolis and buoyancy forces, as defined earlier, induce secondary flow vortices that result in different heat loads to the different internal walls depending on their specific orientation.

The combination of Coriolis forces, buoyancy forces, and forced convection determines the internal heat transfer. For this case, the common practice among designers is still to use the available database obtained for nonrotating airfoil and then to introduce enhancement factors to correct for the effect of rotation missing from the dataset being used. For the past 8 to 10 years, experiments have been designed to supplement the existing nonrotating data and to provide insight into internal heat transfer for the turbine blade. It is generally agreed among the research community that the experiments designed to produce data applicable to the blade must be rotating to produce the proper Coriolis forces, and they must be heated to produce the proper buoyancy forces.

For some applications (closed-loop cooling systems), the coolant gas (or liquid) remains confined to the internal passages of the blade and is not discharged into the main stream, thus avoiding the associated performance penalties. In the case of large industrial power-generating turbines, the cooling medium of choice is sometimes steam or water. Some experimental advanced propulsion gas turbine engines have used liquid metals (sodium or sodium-potassium) heat pipes that transform the coolant phase from solid to liquid in a closed-loop cycle. One of the advantages of the heat pipe technique is that it does not rely upon compressor bleed air, but rather uses

a phase changing liquid as a heat sink coupled with a condenser to remove the absorbed heat.

Although the following section is devoted primarily to the blades, many features that are common to both vanes and blades can be found.

Smooth Internal Passages

In general, a blade convection cooling techniques can be subdivided into:

- Schemes employing straight-through radial holes or channels that may be connected to form multipass, or serpentine, systems in which the air passes through the blade/vane several times before exiting
- Schemes involving enhanced heat transfer by means of ribs, dimples, matrixes, pin-fins, or similar devices to extend the cooled surface and promote turbulence
- Schemes using impingement cooling to more closely match the cooling to external thermal loads
- Swirl cooling schemes utilizing heat-transfer augmentation due to centrifugal force field in a strong vortex that is induced inside the blade, primarily for leading edges

Since the level of internal convection cooling depends on the internal cooling passage surface area and the convection heat-transfer coefficient acting over this area, both of these parameters must be maximized for an efficient cooling design. For all cooling systems covered by first two groups, custom tailoring of the cooling passage cross-sectional flow area provides an effective means of controlling the local Reynolds number, and thereby the local heat-transfer coefficient. A convectively cooled airfoil usually uses air that is brought in at the root or tip (for vanes only) of the airfoil and then discharged at the other end of the airfoil or through its trailing edge. Properly designed internal cooling is quite efficient and is usually preferred where it can satisfy the required cooling effectiveness.

The simplest form of internal cooling system used in airfoil designs generally consists of smooth radial passages of circular, elliptical, or triangular cross section. Matching locally of the cooling capacity to the external airfoil heat load is achieved through appropriate combinations of cooling flow rate and passage cross-sectional area, which affect the cooling air velocity and hence the internal heat-transfer coefficient, and cooling surface area.

The flow in typical airfoil cooling passages is usually assumed to be turbulent. For this condition the fully developed smooth wall heat-transfer

coefficient is given by

$$\mathrm{Nu}d = hd/kc = 0.023(\mathrm{m}cd/\mu)^{0.8}(Taw/T\mathrm{c})^{0.8}(\mu cp/k)^{0.333}$$

Ribs/Fins (Longitudinal or Angled Trip-Strips)

Ribs or fins offer a simple means of enhancing heat-transfer performance. The function of fins is basically twofold; first to increase the internal heat-transfer surface area, and second to reduce the coolant flow area, thereby increasing the internal heat-transfer coefficient. Although there are numerous practical fin (rib) shapes, the majority of longitudinal ribs to be found in gas turbine cooling systems are of a square or rectangular section. For vane and in some cases blade-cooling design using tube insert, the fin length is oriented along the vane, parallel to the main-stream flow. In this application the tube insert is positioned against the fins. In addition to the effect of extended heat-transfer area that is provided by the fins, some heat dissipation is achieved due to thermal conduction between the fins and the tube. However, due to uncertainty of the metal contact area, such effects are generally neglected in analysis. The heat-transfer coefficient for cooling passages with fins is calculated in the same manner as for smooth wall passages. However, the heat-transfer characteristics of the extended fin surface must be accounted for. The heat-transfer coefficients are based on the total exposed area of both fin and its base, and on an average surface temperature (again, fin and its base). In thermal modeling of fins, either the fins must be physically modeled or the fin effectiveness must be accounted for.

The heat-transfer effectiveness of a fin is measured by a parameter called the fin efficiency ξ, which is defined as $\xi =$ (actual heat transfer from fin) / (heat transfer from fin if entire fin were at its base temperature).

To obtain the total efficiency of a surface with fins ξ_Σ, the unfinned portion of the surface at 100% efficiency is combined with the surface area of the fins at ξ_Σ, or: $\xi_\Sigma = 1 - (A_\mathrm{f}/A_\Sigma)(1 - \xi)$, where A_f and A_Σ are the heat-transfer area of the fins and total area, respectively.

When the ribs are positioned at an angle to the direction of the cooling flow, they act as turbulators and are often called trip-strips due to effect of tripping boundary layer of the coolant. The vast majority of cooling designs utilizing turbulators are typically rectangular in shape, with only the passage walls adjacent to the pressure and suction surfaces carrying the turbulators. This is done in order to minimize premature heat pick-up by the coolant, and also to minimize the thermal gradients between the cross-airfoil webs and the pressure- and suction-side walls. This type of geometry also results in reduced frictional pressure drop as compared to the fully turbulated

channel. Any cooling channel entrance effects should be accounted for by using the same methodology as for the smooth channel geometry.

The most common for blade internal cooling is the application of cross flow or inclined ribs. Only a few studies have addressed inclined turbulators in rotating cooling passages. The following correlation, based on the data of Han and Park [75], can be recommended for both plain and inclined turbulators.

For the fully turbulated walls (see Fig. 17 for nomenclature):

$$h_t d_h/k = f \ \mathrm{Re}_{d_h} \ \mathrm{Pr}/\left\{2\left[(G-R)(f/2)^{1/2}+1\right]\right\}$$

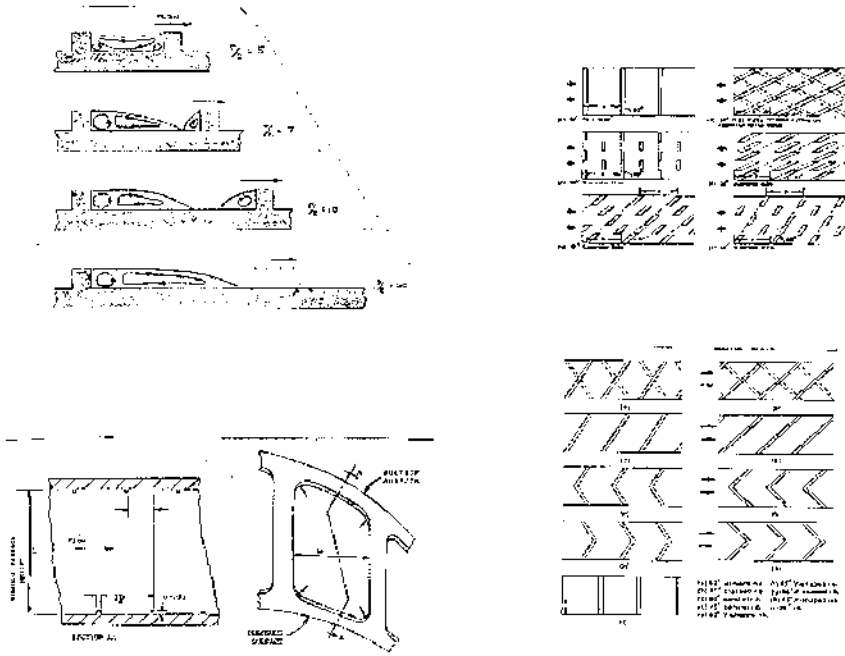

Figure 17 Various rib (trip-strip) geometries.

Where

$G = 2.24(w/t)^{0.1}(\mathrm{Re_e})^{0.35}(\alpha/90)^m(p/e/10)^n$, heat-transfer roughness function.

$w/t =$ ratio of channel width to the channel depth.

roughness Reynolds number $\mathrm{Re_e} = (e/d_\mathrm{h})\mathrm{Re}_{d_\mathrm{h}}(f/2)^{1/2}$.

$\alpha =$ rib angle of attack, defined relative to the flow direction.

$p/e =$ ratio of turbulator pitch over its height.

$m = 0.35, n = 0.1$ for square channels; $m = 0, n = 0$ for rectangular channels.

$R = \left[12.3 - 27.07(\alpha/90) + 17.86(\alpha/90)^2\right] / \left[(p/e/10)^{0.35}\ (w/t)^Z\right]$,

friction roughness function.

$z = 0$ for $\alpha = 90^\circ; z = 0.35$ for $\alpha < 90^\circ$; also, if $w/t > 2$, use $w/t = 2$.

$f = 2/\{R - 2.5 \ln [(2e/d_\mathrm{h})(2w/(t + w))] - 2.5\}^2$.

For the combined smooth/turbulated (st) walls,

$$h_\mathrm{st} = h + (w/t)(h - h_\mathrm{t})$$

Where

$$h_\mathrm{t} = fk\mathrm{Re}_{d_\mathrm{h}}\,\mathrm{Pr} \,/ \left\{2d_\mathrm{h}\left[(1.2G - R)(f/2)^{1/2} + 1\right]\right\}$$

is an average heat-transfer coefficient for turbulated and smooth walls.

The applicability limits for these correlations are

$$\begin{aligned}
\mathrm{Re_e} &\geqslant 50 \\
30^\circ &\leqslant \alpha \leqslant 90^\circ \\
0.021 &\leqslant e/d_\mathrm{h} \leqslant 0.078 \\
10 &\leqslant p/e \leqslant 20 \\
1 &\leqslant w/t \leqslant 4 \\
8,000 &\leqslant \mathrm{Re}_{d_\mathrm{h}} \leqslant 80,000
\end{aligned}$$

In continuing studies to optimize turbulator design, a range of geometries have been tested. Continuous and discrete (interrupted) ribs were evaluated for both heat-transfer augmentation and pressure losses. A study on the heat-transfer and friction characteristics of a square channel with angled discrete ribs was conducted for two opposite walls roughened with 90° continuous ribs, parallel and crossed continuous ribs with angles of attack of 60° and 45°, 90° discrete ribs, and parallel and crossed discrete ribs with 60°, 45°, and 30° angles. The results showed that parallel-angled discrete ribs

were superior to both 90° discrete ribs and parallel-angled continuous ribs and were recommended for internal cooling passage designs. For 60° and 45°, parallel discrete ribs had higher ribbed wall heat transfer, lower smooth wall heat transfer, and lower channel pressure drop than parallel full ribs. Parallel 60° discrete ribs had the highest ribbed wall heat transfer, and parallel 30° discrete ribs caused the lowest pressure drop. The heat transfer and pressure drops in crossed-angled continuous and discrete rib cases were all lower than those in the corresponding 90° and parallel-angled rib cases. Crossed arrays of angled ribs had poor thermal performance and were not recommended. Correlations of Stanton number and friction factor are provided for turbine-cooling design.

More recent work by Han et al. [76] has studied the effects of ribs with different configurations and channel orientation on heat transfer for a rectangular channel with width-to-depth aspect ratio about 2:1. The local heat-transfer coefficient distribution in a rotating frame is different from that of a stationary frame. Heat-transfer coefficient patterns in radial outward flow and radial inward flow conditions show different dependence on rotation. This is primarily due to the reversal of the Coriolis force acting on the moving fluid in a rotating flow. The results of this study confirm a similar heat-transfer effect in a two-pass rotating rectangular channel as is observed in a two-pass rotating square channel from the previous work. In general, the rib-roughened surfaces in a rectangular channel perform similarly to smooth surfaces with increasing rotational speed. However, the average heat-transfer coefficient magnitude in a rectangular channel with ribbed wall is much higher than that of the smooth walls. Ribs placed at an angle to the bulk flow direction induce greater heat-transfer enhancement. Comparative studies suggest that a 45° parallel rib configuration in a rectangular channel is more suitable to enhance heat transfer than a 45° cross configuration for both nonrotating and rotating cases. The effect of channel orientation on heat transfer shows that a 90° channel orientation has more effect on leading and trailing surfaces than a 135° orientation due to rotation. The difference in Nusselt number ratios between trailing and leading surfaces in a smooth channel is smaller in a 135° channel orientation than a 90° channel orientation. Han et al. [77] studied the heat-transfer and friction performance of a square channel with parallel, crossed, and V-shaped angled ribs. Nine rib configurations were tested: 90° rib; 60° and 45° parallel ribs; 60° and 45° crossed ribs; 60° and 45° V-shaped ribs; and 60° and 45° A-shaped ribs. The results showed that the 60°/45° V-shaped rib performed better than the 60°/45° parallel rib, and better than the 60°/45° crossed rib and the 90° rib. The V-shaped rib produced the highest heat-transfer augmentation, while the A-shaped rib generated the greatest

pressure drop. The 60°/45° V-shaped rib configuration was the recommended geometry.

It should be noted that some of the recommended above rib geometries may not be suitable for certain cooling passage geometries due to difficulty of their fabrication.

Pin Fins

A commonly used method for enhancing the heat-transfer rate in airfoil cooling passages is to introduce pin fins, or pedestals, across the flow passage. These act in three ways:

1. Provide obstacles in the path of the coolant flow, raising its level of turbulence to enhance heat transfer.
2. Act as extended surface area increasing the heat-transfer rate between the wall of a cooling passage and the coolant.
3. Provide a conducting pass between two opposite walls to reduce temperature differences between these walls and improve the structural integrity of the airfoil.

Typical pin fin applications in airfoil cooling designs are found in the narrowing toward the trailing-edge cooling passages, where full-height pins (or pedestals) improve also structural integrity of the airfoil and provide conduction path between pressure and suction sides (Figs. 11 and 18). In general, pin fins are more effective from a cooling performance standpoint than turbulators, but they induce a substantially higher pressure drop. In cases where the available cooling air pressure drop is minimal, pin fin designs can become much more challenging, or even may not be feasible. Pin fins commonly used in turbine-cooling applications generally take the form

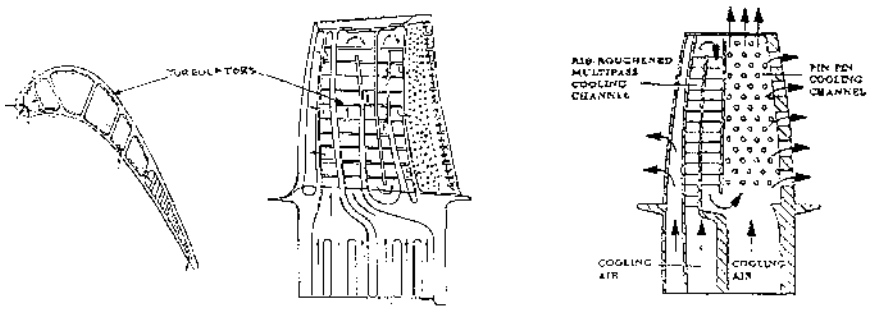

Figure 18 Examples of combined rib-roughened and pin finned cooling enhancement.

of arrays of circular cylinders embedded inside a turbine airfoil cooling passage such that they are oriented normal to the flow direction. The two most common arrangements are the in-line and staggered arrays. They are typically, although not exclusively, employed in narrow channels where the castability of trip-strips (ribs) is in question. The majority of data available on pin fins is for the staggered array geometry, and unless otherwise stated all correlations are given for this geometry. This is generally the geometry of choice for a designer.

The heat transfer in turbine airfoil pin fin banks combines the pin heat transfer with the pin end-wall heat transfer. Pin fin heat transfer averaged over the array appears to vary with Reynolds number to a power of between 0.6 and 0.7, depending on the pin height. The local heat transfer in rows of pin fins increases for the first three to five rows for arrays with nonrestricted entrances; in-line array heat-transfer exhibits a fully developed behavior after the third row, while staggered arrays exhibit a peak in the third to fifth rows, followed by a slight decay in the succeeding downstream rows.

The majority of turbine pin fin applications are to be found in the trailing-edge region of airfoils. Here, aerodynamic considerations demand a small wedge angle for the trailing edge, and as a result the internal passages become so narrow that the choice of cooling scheme is limited. Pin fins in the trailing-edge region also serve a structural purpose by holding the suction and pressure surfaces together. It is not always possible to manufacture pins of optimum length for heat-transfer purposes in the trailing-edge region due to limits in casting technology, which is not capable of reliably producing pins much smaller than about 0.02 in. in diameter. Typically in this region, pin fins have height-to-diameter ratios between 4 and 1, or even lower. In these "short" pin fin arrays, the heat transfer has been shown to be lower than from longer pin fins. A few studies showed that for height-to-diameter ratios less than 3, there is no effect of the ratio on array averaged heat transfer. However, for the ratio greater than 3, the heat transfer was found to increase significantly with length. For short pin fins the cylinder/end-wall interaction becomes important, and the array total heat transfer must include heat transfer from both the cylinder surface and the uncovered region on the end wall. This presents a fundamental difference from arrays having long cylinders in which the end-wall effects become insignificant. Also, the addition of short pin fin arrays to a cooling passage may actually cover up more wall surface area than they add in pin surface area. Thus, the term "extended surface" does not really apply to this configuration. Therefore, in this situation, the predominant mechanism of heat-transfer augmentation lies in promoting flow turbulence rather than the addition of heat-transfer area.

Some of the studies have found that converging cooling passages, such as found in trailing-edge applications, can reduce heat transfer by as much as 20% compared to the constant-pin height case. A clearance above partial pins (typical of vane geometries where truncated, or partial length, pin fins are used adjacent to an impingement tube insert) or gaps between opposing truncated pins result in reduced heat transfer and friction compared to full length pins. For these partial length pin fin geometries, the heat-transfer rate has been found to decrease linearly with increasing clearance from the full pin value to that for the smooth channel. However, friction loss reduction was found to be more pronounced than the reduction in heat-transfer coefficient. Partial length pin fins could be effectively employed in situations where there is a significant difference between the heat loads of opposite walls in a cooling passage. The partial-length pin fins would often be used on the surface where a higher rate of heat transfer is desired. Also these geometries, with their lower friction loss characteristics, could be employed in designs where the available pressure drop is limited to preclude full-length pin fins. For further information and test data on these geometry cases, see [63].

Pin fins have been effectively combined with turbulators for moderate increases in heat transfer and friction (Fig. 19). By staggering the turbulators, a 35% increase in heat transfer can be obtained. A comprehensive review of pin fin literature related to turbine-cooling applications is given in [78].

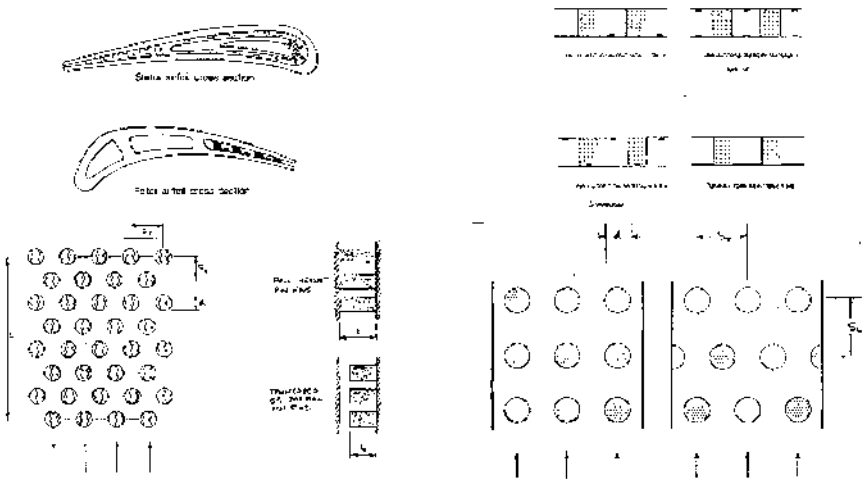

Figure 19 Pin fin geometry definition.

For turbine airfoil-cooling applications, it is recommended that two basic correlations be used to characterize cylindrical pin fin heat transfer. Separate correlations should be used for short and long pin fins. Short pin fin ($H/d \leqslant 3$) heat-transfer performance can be predicted using an equation defined by Metzger et al. [79]. This correlation should cover the majority of trailing-edge applications and is given by

$$\mathrm{Nu_d} = 0.135\mathrm{Re_d^{0.69}}(S_\mathrm{L}/d)^{-0.34}$$

(Refer to the figure for nomenclature)

where

$$\mathrm{Re_d} = Wd/(A_{\min}\mu).$$

$A_{\min}$ =minimum flow area of pin fin array for the ranges

$\mathrm{Re_d}$	from	10^3	to	10^5,
H/d	from	0.5	to	3.0,
S_L/d	from	1.5	to	5,
S_T/d	from	2.0	to	4.0.

For long pin fin ($H/d > 3$) applications, the heat-transfer performance should be predicted using a correlation established by Faulkner [80].

The use of pin fins to cool turbine airfoils is generally not limited to the simple uniform arrays in a constant flow area duct discussed earlier, but may require more complex geometries. Complex pin fin arrays might include various strategies for manipulation of the local row by row heat transfer to obtain a desired distribution, such as interarray changes in pin diameter or spacing and interruptions in the pin pattern. Such arrays may also be located in ducts that converge in the mean flow direction.

For the situation where the pin fin array is located in a converging channel, the measured Nusselt numbers were found to be consistently lower than predicted by applying the constant flow area results using the local row value of Reynolds number. This degradation was thought to be due to accelerating flow effects. To account for this, a multiplying factor of 2.28 $\mathrm{Re_d^{-0.096}}$ to the average heat-transfer coefficient was proposed for converging channels.

In certain airfoil-cooling applications, such as in the trailing-edge region of blades, air enters at the root of the blade and flows radially through a pin fin channel, with some of the flow exhausting through holes in the tip of the blade while the rest of the air is ejected through slots in the trailing edge. The gradually decreasing mass flow due to the lateral ejection

of the cooling air and the turning of the ejection air toward the trailing edge affect the heat transfer to the cooling air. Data and correlations for this type of configuration could be found in [81]. In numerical heat-transfer prediction, either the pin fins must be physically modeled, or the pin fin surface effectiveness must be specified.

Jet Impingement

A combination of the highest airfoil external heat-transfer rate coupled with wake-induced turbulence and an unfavorable area ratio between inner and outer surfaces makes the blade leading edge the most difficult region to cool. Deviation of the stagnation point during off-design operation complicates the problem even further.

Cooling techniques based on film protection of the leading edge (shower head) provide adequate cooling effectiveness, but produce a number of negative effects:

Increased local stress concentration
Additional aerodynamic penalties
Concerns about engine durability associated with the potential of plugging of the small film holes, especially for long-term operation in an industrial environment

For aero engines, all these concerns are easily outweighed by the requirement of very high cooling effectiveness, which justifies a large amount of cooling air and the application of blade film cooling. For a moderate TRIT of 2,050–2,200 °F, a maximum effort should be made to avoid blade film cooling until all means of augmentation of internal heat transfer are exhausted. A variety of straight, angled, chevron, and "broken" trip-strips (ribs), pin fins, and other more exotic geometries intended to trip the boundary layer in the internal passage have been applied or considered over the last decade. Unfortunately, some of the promising intricate vortex generating geometries that were studied in up-scaled models cannot always be reproduced in actual-size blade castings or are very sensitive to the manufacturing tolerances, particularly when small internal holes and sharp-edged features are required.

The heat-flux distribution on the turbine airfoil must be appropriately matched with an effective cooling system that will achieve the desired design temperature distribution while minimizing the amount of cooling air used. In the leading-edge region of the airfoil, this often results in the use of impingement cooling. Impingement cooling refers to the use of orifices through which the coolant flow is accelerated and the resulting jets impinge normal to the target surface. Heat-transfer coefficients generated by normal

impingement of air jets are generally considerably higher than those obtainable by other conventional methods.

Jet impingement cooling, which has been proven to be highly effective for turbine nozzles, and where spent air is removed toward the trailing edge through the passage between airfoil inner wall and insert, is usually not practical for the blades without immediate film discharge of the spent air. Without this, the presence of cross flow results in a significant reduction of the impingement cooling effectiveness (Kercher and Tabakoff) [82].

An important advantage of impingement cooling, particularly if the design uses sheet metal inserts, is that it is usually relatively easy to modify the geometry for engine temperature uprates or if shortfalls are encountered in a design. However, it must be noted that an impingement design can add complexity to a part, especially if the impingement holes are a cast-in feature. Difficulties in the internal casting core design, core yield rate, and control of impingement hole size can become limiting factors. This method of cooling has been recognized for some time as being highly effective and, therefore, has received much attention from researchers. As a result, a considerable amount of experimental data and correlations exist for impingement cooling heat transfer. With such an extensive collection of data, it simplifies matters to classify the data by geometry. The first classification relates to the impinged surface, which can be flat or curved (concave). In the context of turbine airfoil cooling, the leading-edge internal area forms a concave surface, but further back in the midchord region the impinged surface is nearly flat. The second classification relates to the impinging jet and this can be either two-dimensional (slot) or axisymmetric (hole). Then there is the possibility of a single jet, a row of jets, or an array of jets. With an array of jets there is the added complication of spent air cross flow, which interferes with the jets and reduces their effectiveness.

The first and most important task for the designer is to identify the impingement geometry most suited to the particular design under consideration and select the data or correlations that most closely relate to that geometry. It is quite possible that a cooling design may embody several types of flow geometry at various locations. A considerable amount of data on impingement heat transfer is available in the literature for various impingement configurations. The local impingement heat-transfer coefficient data of Chupp et al. [83] and the average heat-transfer coefficient data of Metzger et al. [84] were obtained with test models simulating turbine airfoil leading-edge configurations and are therefore particularly useful in turbine airfoil leading-edge cooling design applications.

For most practical turbine airfoil-cooling applications, there are two main geometries of interest (Fig. 20). The first is impingement from an array

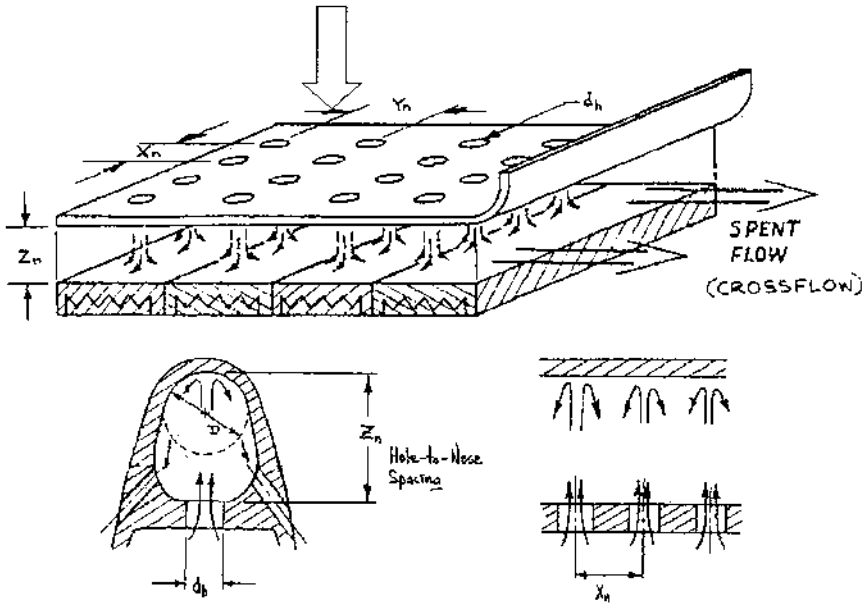

Figure 20 Impingement geometry definition.

of holes onto a flat surface, and the second impingement from a row of holes onto a concave surface.

A method for producing relatively large forced convection heat-transfer coefficients on a surface is by the use of a multiplicity, or array, of jets impinging normal to the surface from a perforated parallel plate placed close to the surface. As the air jets approach the impinged surface, they make a 90° turn and thereby become what are called wall jets. As the wall jets from two adjacent impinging jets approach each other, their interference forces the flow to separate from the surface and form a stream, often of relatively low velocity, flowing past the impinging jets to reach the exit where the air is removed. This spent flow is called "cross flow" and tends to deflect the impinging jets from their initial direction and can thereby reduce the average convective heat-transfer coefficient.

Design features approximating a square array of jets impinging on a flat plate with cross-flow air exhausting to one side can be based on the correlation of Kercher and Tabakoff [82]. This correlation is

$$\mathrm{Nu_d} = h_{\mathrm{av}} d_{\mathrm{h}}/k = \phi_1 \phi_2 (\rho V_3 d_{\mathrm{h}}/\mu)^m (\mathrm{Z}_n/d_{\mathrm{h}})^{0.09} (\mu Cp/k)^{1/3}$$

for the ranges:

Re from 300 to 3×10^4,
Z_n/d_h from 1.0 to 4.8,
X_n/d_h from 3.1 to 12.5.

h_{av} is based on an area one half-pitch on either side of any row in the cross-flow direction. Values of m and ϕ_1 are each a function of both (X_n/d_h) and Re. The function ϕ_2 is used to express the degradation effect of cross flow caused by the accumulation of fluid from multiple rows of impingement jets, it being unity when this effect is negligible.

In the absence of cross-flow effects, the simpler square array correlation of Gardon and Cobonpue [85] is recommended:

$$Nu_d = 0.286(\rho V_a \ X_n/\mu)^{0.625}$$

It should be noted that in-line hole rows appear to be superior in heat-transfer performance to staggered rows.

In the leading-edge region of an airfoil, where the external heat load generally tends to be at its highest, the application of impingement cooling becomes particularly valuable. Here, a row or array of impinging jets are directed at the inside concave wall of a vane or blade leading edge from either a tube insert (typical of a vane application) or from a cast-in or machined feature (typical of a blade application). In these types of applications, the impinged air is generally designed to flow in a chordwise direction, either then exiting as a film or being utilized for further internal cooling. Radial flow of the impinged air is largely avoided as this produces a degradation of the system resulting from cross-flow effects.

The detailed impingement data of Chupp et al. [83] were obtained with test models simulating turbine airfoil leading-edge configurations and is therefore particularly useful in turbine airfoil leading-edge cooling design applications. The experimental model used is typical of a vane airfoil application with a single row of holes impinging into the leading edge from a tube insert, with spent air flowing, unrestricted, in a chordwise direction around the impingement tube. An equal flow split around each side of the tube is assumed. The Chupp et al. correlations are recommended for this geometry type. Heat-transfer coefficients were correlated over the leading-edge radius region. Information on the distribution of the heat-transfer coefficient was also obtained. The average (over an arc of 180° of the impinged target) and stagnation point (an arc of approximately 25° of the impinged target) heat-transfer coefficients are

correlated by

$$\mathrm{Nu}_{\mathrm{d}}^{\mathrm{a}} = 0.63(Gd/\mu)^{0.7}(d_{\mathrm{h}}/X_n)^{0.5}(d_{\mathrm{h}}/D)^{0.6}\exp\left[-1.27(Z_n/d_{\mathrm{h}})(d_{\mathrm{h}}/X_n)^{0.5}(d_{\mathrm{h}}/D)^{1.2}\right]$$

$$\mathrm{Nu}_{\mathrm{d}}^{\mathrm{star}} = 0.44(Gd/\mu)^{0.7}(d_{\mathrm{h}}/X_n)^{0.8}\exp\left[-1.27(Z_n/d_{\mathrm{h}})(d_{\mathrm{h}}/X_n)^{0.5}(d_{\mathrm{h}}/D)^{1.2}\right]$$

for the ranges:

Re from 3×10^3 to 1.5×10^4,
Z_n/d_{h} from 1.0 to 10.0,
X_n/d_{h} from 4.0 to 16.0,
D/d_{h} from 1.5 to 16.0.

A typical heat-transfer coefficient distribution away from the stagnation point was found to be only a weak function of the dimensionless hole spacing parameter, X_n/d_{h}, and practically independent of Re. Although this correlation is good for the vane type of geometry, industry experience has shown that this correlation should be modified for the typical blade impingement geometry because a more restricted exit of the impingement flow with the greater possibility of interaction between the impingement and cross flow in a blade. Industry test experience of actual blade geometries has shown that the numerical multiplier of 0.5 should be used in place of 0.63 (reduction of 20%) for the ranges

Z_n/d_{h} from 1.5 to 4.0; X_n/d_{h} from 2.1 to 9.7; D/d_{h} from 2.0 to 5.8.

The work of Metzger et al. [84] covered a wide range of geometric variables, and in particular the effects of concave surface radius on heat-transfer performance. Only average heat-transfer coefficients were measured.

For details of application of the correlation, the reader is referred to the referenced work.

As stated earlier, a leading-edge impingement system should be designed to avoid cross-flow effects, which result in jet bending and the consequent degradation of impingent heat-transfer performance. This is generally achieved by exhausting the spent impingement flow in a chordwise direction. In the application of impingement cooling, special consideration must be given to the manner in which the spent impingement air is discharged from the impingement cavity. In many designs, the spent impingement flow is discharged through radially angled film cooling holes in the leading edge and through tangential film cooling holes on airfoil sidewalls. The design is particularly effective since the high impingement heat transfer at the leading edge is further complemented with convective cooling in the radial holes. Additionally, the spent impingement air is

further used to provide a film on the pressure and suction surfaces, thereby providing a design having high thermal efficiency.

This above summary indicates that development of more effective internal cooling techniques that can counterbalance high external heat loads for the blade leading edge and tip section is required, particularly for moderate turbine inlet temperatures, when the application of film cooling can be avoided.

Swirling Flow

Extensive studies of heat exchangers show that one of the effective heat-transfer augmentation techniques is based on swirling flow. Swirling flow is commonly referred to as a vortical flow that can be generated by a number of methods, including twisted tape inserts, coil wires, inlet guide vanes, and tangential injection of the fluid. Some of these methods generate swirl continuously along the entire length of the test section, often a cylindrical tube, whereas others are placed at the inlet with the decay of swirl along the tube. A technique based on tangential jet-induced swirl flow that has been recently developed [86, 87] is of particular interest for the leading edge of a blade. It utilizes a three-dimensional screw-shaped swirl flow induced by tangential slot jets swiping the interior of the leading edge as shown in Fig. 21. Multiple jets along the channel provide energized in radial direction swirl flow motion, which is sustained over the entire height of the blade. Heat transfer along the concave surface is augmented by the unsteady Görtler vortices formed in the near-wall region. The high-momentum jet, introduced

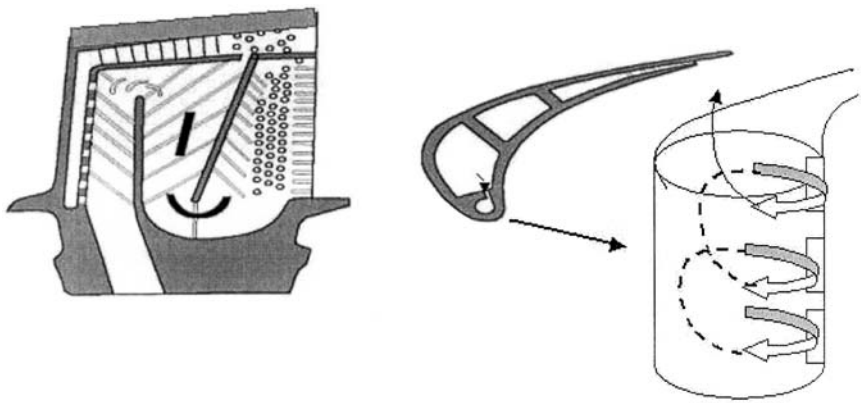

Figure 21 Illustration of blade leading-edge swirl cooling.

tangentially to the inner wall, behaves initially as quasi-impingement and becomes unstable due to interaction with the concave surface of a circular channel. The swirl motion results in a longer path for coolant air to travel for a given axial length. Highly turbulent flow near the surface leads to a thin boundary layer. Additional cooling benefits can be obtained due to centrifugal forces, which push the cool high-density air toward the hot surface. The Görtler vortices are known to significantly enhance heat transfer by its downwash and upwash vortical motion near the wall and by continuous interaction and intermingling with each other.

A comparison of the three different swirl cooling configurations versus impingement cooling with and without cross flow and versus smooth and trip-strip augmented channel surface is presented in Fig. 22. For the purpose of this comparison, the Nusselt number based on hydraulic diameter was calculated and averaged over $\pm 60^\circ$ angle from the leading edge. Reynolds numbers were calculated based on the assumptions that all of the flow went through the cross-sectional area of the leading-edge chamber. For impingement cooling, Chupp and Helm's correlation (1968) was used for a given geometry: $D/d_n = 4$, and $x_n/d_n = 3$. Kercher and Tabakoff's data (1970) were used for cross-flow effects on the impingement cooling. The heat transfer in a channel with normal trip-strips was obtained from the correlation of Webb et al. (1971) [88]. It can be seen from Fig. 21 that the

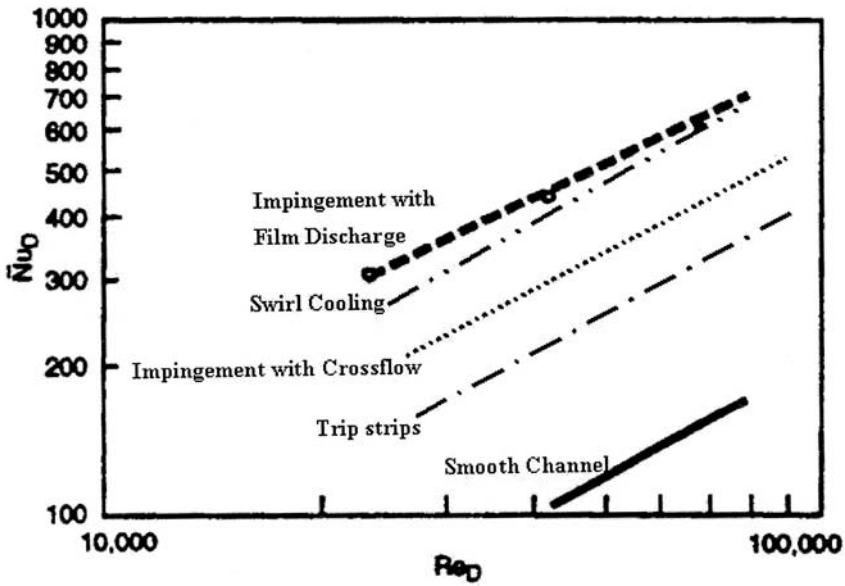

Figure 22 Comparison of internal blade-cooling techniques.

swirl cooling technique provides internal heat-transfer augmentation comparable with the impingement coupled with film discharge of the spent air and is more effective than impingement with cross flow or trip-strips. Application of this technique might allow extension of the range of internal blade cooling for moderately high turbine inlet gas temperatures, further avoiding the use of film cooling for the leading edge.

Film Cooling

There is relatively little published data on the effects of film cooling on rotating turbine blades. Most of the studies were performed for the stationary environment. A number of ongoing studies address the effects of rotation on film flow and heat transfer.

Very early work by Dring et al. [89] in a low-speed rotating test facility examined a single film-cooling hole placed on the suction and pressure sides of a rotor blade. Contrary to the nature of a film on a nonrotating aerofoil, it could be seen that the pressure-side coolant becomes entrained into the spanwise secondary flow and migrates toward the tip. On the suction side of the aerofoil, the coolant behaves as though rotation has only a small effect. The tests were for cases where the density ratios of 1.0 and 4.0 were examined. It was observed that the higher-density ratio gives rise to more effective cooling as is the case for nonrotating airfoils. The experiments by Dring have demonstrated that film cooling on rotating blades behaves differently from nonrotating vanes. Unfortunately, however, the data are too limited to derive any design correlation for film cooling on rotating airfoils.

More recently, the work by Takeishi et al. [90] on a full-scale rotating turbine has also shown that pressure-side film-cooling behavior on rotating blades is quite different from that found on nonrotating airfoils. It was observed that on the suction side the film effectiveness values are similar. However, in the case of the rotating blades the pressure-side film effectiveness decays very rapidly for a film near the leading edge. In a similar work, Abhari & Epstein (1992) [91] have confirmed these findings. They showed that at both low and high blowing rates the film has almost no effect on reducing the heat transfer on the pressure surface. At low blowing rates the suction side is relatively well cooled, but at high blowing there appears to be film lift-off and poor film cooling. From these limited data, the effect of rotation can be summarized as follows:

The effectiveness of a leading-edge film flowing along the suction surface compares well with stationary blade data.

The effectiveness of a leading-edge film flowing along the pressure surface decreases more rapidly compared to stationary blade data.

The effectiveness of a suction surface film compares well with stationary data close to injection but decays faster, dropping by 30% close to the trailing edge.

The effectiveness of a pressure surface film decays much faster than at stationary condition. Critical to all airfoil-cooling designs is the method of discharging the cooling air into the gas path. The flow characteristics of blade-tip discharge holes and trailing-edge or film-cooling ejection holes must be precisely known, as these features play a major role in controlling the cooling air mass flow rate and distribution along the blade height. Published literature on the discharge coefficients of these geometries can provide a good estimate (see, for example, Camci [92]), but the data are usually applicable to only a limited range of parameters. If the design geometry is outside this range, extrapolation of the data is not recommended. Instead, flow testing of the design geometry using an upscaled model is suggested.

Tip and Platform Cooling Issues

It has long been recognized that the effectiveness of blade-tip design, which strongly influences hot gas leakage over the tip, is a major contributor to the aerodynamic efficiency of turbines. Blade tips are typically comprised of extended surfaces at the furthest radial position of the rotating blade, which are exposed to hot gases on all sides, difficult to cool, and subjected to the potential for wear due to rubbing against the outer stationary casing (shroud).

There is very little experimental data for heat-transfer distributions in the vicinity of recessed tips that have been obtained for full-scale rotating turbines operating at the conditions that simulate actual engine environment. It is well known that the pressure difference between the pressure and suction sides of the blade drives flow through the tip clearance gap. A flat tip is unacceptable in most of the cases due to severe damages that can be associated with tip rubs in the case of solid tip design. Most of the blade-tip designs use a squealer cavity with thin walls along the pressure and suction sides that are less damaging in the tip rub situation. However, presence of this cavity at the tip results in a significantly more complicated flow field than one would encounter on a flat tip blade. Near the leading edge of the blade, a strong vortex flow exiting the vane near the stationary shroud enters the tip region head on or from the suction surface side of the blade.

Ameri et al. [93] demonstrate in their numerical study of the tip region flow that the flow field is three-dimensional with many vortices interacting. Their results suggest that there are at least two distinct sources of vortices in

the cavity region and that vortices persist throughout the length of the cavity. Their modeling of this flow suggests that one of the vortices is the result of separation off the pressure side of the tip edge and that this vortex rolls over the cavity pressure side wall. The second vortex is the result of a flow separation again at the tip edge on the blade suction side. There appears to be a dividing line where the main stream starts rolling into the gap from the pressure side of the blade. Flow separation occurs because of the edge of the tip. Strong secondary flows can be expected to be present in the gas path. This can have the effect of bringing very hot portions of the mainstream gas to the vicinity of the clearance gap, downstream of the blade leading-edge lip. This lip acts like a rearward-facing step with resulting flow separation and attachment in the recessed cavity. As the flow emerges from the suction side of the gap, it usually observed to roll into a vortex as it meets the oncoming shroud wall flow.

A significant portion of the literature relevant to experimental studies of tip gap flows has dealt with flat tip blades. Distributions of blade-tip static pressure were measured in a 2D cascade by Bindon [94]. He included the effects of clearance gap and pressure-side edge radius on a flat tip. Special attention was given to the separation bubble formed at the tip entry along the pressure side. The same study addressed the effects of profiling of tip geometry in both stationary and rotating cascades using a pressure-side edge radius, suction-side squealer, or full squealer. The study also focused on effect of leakages on losses and stage performance. It concluded that for all tested configurations the flat tip performed best, and relative motion was of importance.

A recent study (Bunker 2001 [95]) of the effects of squealer cavity depth on tip cavity heat-transfer distribution has used a stationary blade-tip cascade, representing a high-pressure turbine blade with actual aerodynamic pressure distribution. The effect of cavity depth was found to be not uniform over the tip cavity surface. The general observation is that a deeper cavity produces lower heat-transfer coefficients. A shallow squealer cavity is shown to be very close to the flat tip behavior. A depth often found in practical design tip cavity is shown to reduce overall heat load by 50%.

Several researchers have investigated ways of reducing performance losses by controlling tip leakage. Mixing of the leakage flow with the rotor passage flow causes total pressure loss and reduces turbine stage efficiency. The losses originate during the formation of a leakage vortex and its interaction with the passage vortex. Recently published [96, 97] (Camci, and Harvey) studies use the concept of a tip platform extension that is a very short ''winglet'' obtained by slightly extending the tip platform in the tangential direction. The use of a pressure-side tip extension can significantly affect the local aerodynamic field by weakening the leakage

vortex structure. Their studies shows that significant total-to-total efficiency gain is possible by the use of tip platform extensions.

For more detailed information dealing with turbine blade-tip heat transfer, the reader is referred to a recently published review by Bunker [98].

COOLING OF ROTOR AND STATOR STRUCTURES

Cooling Supply and Secondary Air Systems

The role of a secondary air system, which is often also called internal cooling system, is to deliver cooling air to the cooled gas-path components, cool rotor, and stator structures and prevent hot gas ingress into internal cavities and seal leakages between turbine stages. Traditionally, the combustor secondary air flows were treated independently from the turbine section using pressure losses through a combustor that were specified by engine designers. However, the secondary air circuits in the combustor and turbine sections are closely coupled being supplied from the same pressure source—the compressor discharge. For this reason, more recently the entire (often very complicated) flow network of the secondary air system is being analyzed to provide accurate prediction of local pressure and flow distributions. Also advanced analytical tools, which must include heat-transfer effects in the flow calculations, started to use pseudo-3D or true 3D flow modeling for the secondary cooling systems.

Delivering cooling air to the cooled component has to be performed at lowest pressure losses and with minimal heat pick-up on the way to the component. Lowest pressure losses in the delivery system are particularly critical for a shower-cooled leading edge of the stage 1 nozzle, especially for modern industrial gas turbines designed with a low combustor pressure drop. A combustor pressure drop in order of 3% of the total compressor discharge pressure that is often found in these engines leads to a very small pressure margin at the shower head film discharge holes in the leading edges.

Secondary flow and heat-transfer issues in the disc cavities and blade-cooling delivery systems play a crucial role in the life and structural integrity of these components. Blade- and rotor-cooling delivery system deserves special attention—its significant impact on engine performance losses associated with the cooling air discharge into the main stream must also be considered. Some issues related to flows and heat transfer in the disc cavities are discussed in the following section. Minimal heat pick-up is very important for the cooled stage 1 disc rim and blade structure. There are four main ways to deliver air from a turbine stator to the blades:

1. Impinging air from the stator in the direction normal to rim section of the turbine rotor disc
2. Providing radial outflow of the cooling air in the disc cavity toward blade root air inlet passages
3. Preswirling cooling air prior to its discharge into a disc cavity
4. Supplying air close to the center of the disc into a channel formed between turbine disc and corotating cover plate attached to the disc

The first two methods are rarely found in the first stage of modern gas turbines due to significant heat pick-up by the air from the disc and due to work required for tangentially accelerating the air until the disc tangential velocity is matched.

Application of preswirl nozzles accelerates the air in tangential direction, reducing the relative temperature of the air and minimizing frictional losses in the system (Fig. 23). Usually the relative temperature of the swirled air should be set at about 100 °F below the allowable disc rim temperature. The preswirl nozzles are often positioned at approximately the same radius as the entries into the blade-cooling passages on the rotor (Fig. 24, left configuration). A sealed subplenum supplying the preswirled air is recommended to prevent hot gas ingress and reduce mixing between the blade-cooling and disc-cooling flows.

The fourth method (Fig. 24, right configuration), using various types of corotating cover plates, is usually applied when additional air pumping is required for the blades, particularly when a high-pressure margin has to be provided, for example, for the blade shower head cooling. This method makes cooling air delivery system more expensive but less sensitive to rim seal leakages than open disc systems.

The cooling air from intermediate compressor stages is often provided to the turbine components downstream of stage 1. This helps to improve the overall engine performance by saving compression work and also provides lower-temperature cooling air bled from an intermediate stage. The first two methods, as described above, are typical options for delivering air to cool stage 2 (and sometimes stage 3) blades and discs.

A small portion of the internal air flow has to be assigned for buffering of the sealed bearing housing cavities. The air pressure in the cavities should be carefully balanced as a part of the whole internal flow network to avoid ingress of the hot gas, oil leakages into the turbine, and proper ventilation of the oil vapor. Performance and long-term durability of the rotor-to-stator seals are often crucial for reliable supply of the cooling air and for overall engine performance. Figure 25 provides a good summary of the flow characteristics for traditional labyrinth seals [99]. More recently, a new

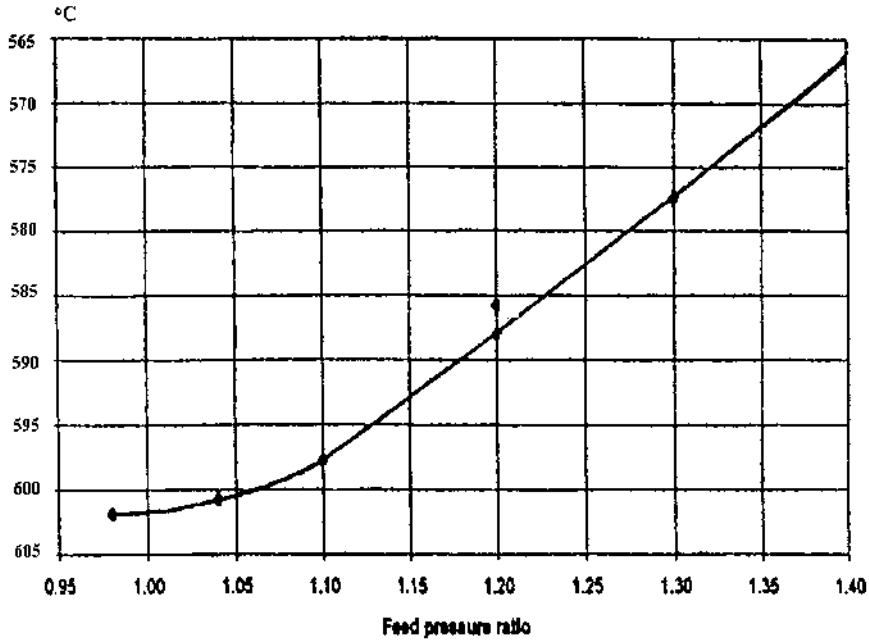

Figure 23 Effect of preswirler pressure ratio on blade air feed temperature.

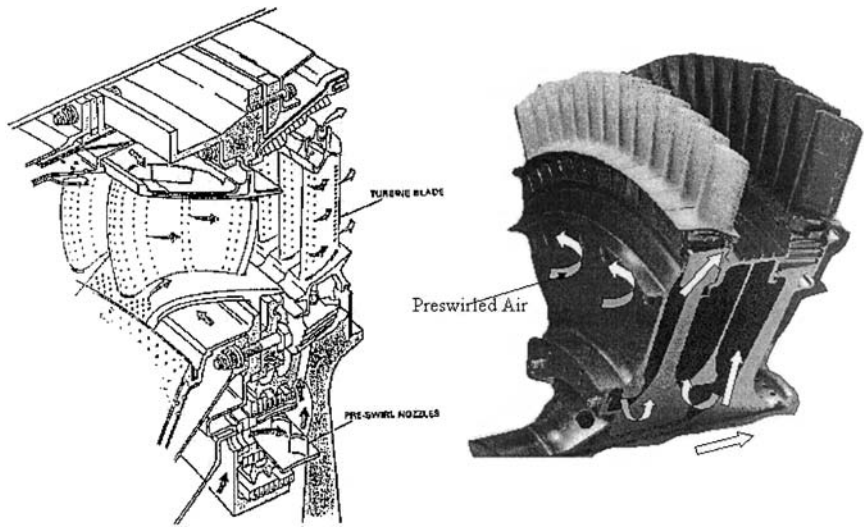

Figure 24 Examples of internal cooling air delivery systems.

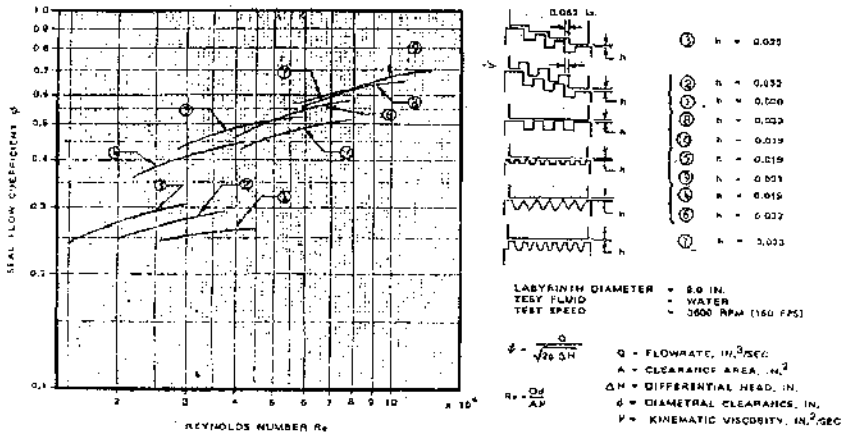

Figure 25 Variation of flow coefficient for various geometries of labyrinth seals.

generation of seals, called brush seals, has been introduced and successfully applied to critical high-pressure gradient regions in many advanced gas turbines [100].

Disc Plenum Buffering and Disc-Cooling Methods

Although turbine airfoils are exposed to higher thermal loads, the turbine disc should be treated as the most critical component when failure is considered. Because disc alloys have temperature capabilities significantly lower than airfoil materials, cooling of the discs and prevention of the hot gas ingress into a disc cavity present a challenge for a design team. The flow in the disc cavity must also be understood so that proper cooling of the disc can be ensured in order to prevent thermal distress. Typical disc-cooling techniques can be based on

- Radial outflow of the cooling air (directly injected or preswirled) in the disc cavity between stator and rotor or between disc and corotating cover plate
- Jet impingement of the disc surface particularly at the critical disc rim location
- Cooling air leakages from the forward to aft cavity of the disc through small gaps in the blade-disc attachments

Typically the cooling air source has a static pressure that is significantly higher than the static pressure in a disc cavity. This pressure differential can be utilized in a preswirling system to provide a tangential velocity

component to the cooling air that closely matches the tangential velocity of the disc. This design feature has two positive results: first it reduces disc frictional losses, and even more importantly, when this air is used for blade cooling, it reduces the relative temperature of the cooling air (Meierhofer and Franklin) [101].

The rim seal between the rotor and the stationary vane will usually experience some leakage under the best of conditions, allowing hot gas from the flow path to move into the disk cavity, thus presenting a potential problem for the disc.

A significant portion of the database applicable to these problem areas can be found in papers and books authored by Owen and co-workers at the University of Bath and by Bohn and co-workers at Aachen University of Technology. Wilson et al. [102] used a preswirl rotor–stator rig similar to that used by El-Oun and Owen [103] to perform detailed heat-transfer, velocity, and temperature measurements for the surface of the disc. In the United States, generic flow and heat-transfer investigations of various rotor–stator systems were originated by Metzger [104] and continued at Arizona State University by his co-workers. The most recent studies including both experimental and numerical methods are led by Roy [105] and focus on practical disc gas turbine geometries integrating the disc cavity with main-stream flow.

Flow and heat transfer of the three main generic disc cavity configurations commonly used in the engine design practice have been studied, including (Fig. 26)

Rotor–stator system with an axial cavity gap that is open toward the main stream (1–3)
Rotor–stator system positively sealed from the main stream (4–6)
Rotating cavity found in corotating discs (7,8) or counterrotating discs (9)

Each of these configurations with or without superposed radial or axial air flow has practical application in the disc internal air systems. Comprehensive experimental and numerical data obtained for many of these configurations have been summarized by Owen and Rogers [106, 107].

A number of CFD codes that can predict quite complicated turbulent flows in the disc cavity have been developed over last few years. However, these codes still require experimental calibration, particularly when the cavity flow due to its interaction with the main-stream flow is not axis-symmetric and 3D analysis has to be performed.

During the early turbine-cooling design phase, when disc cavity geometry and values of main parameters influencing the flow and ingress into the cavity are not well defined, it is important to estimate the disc

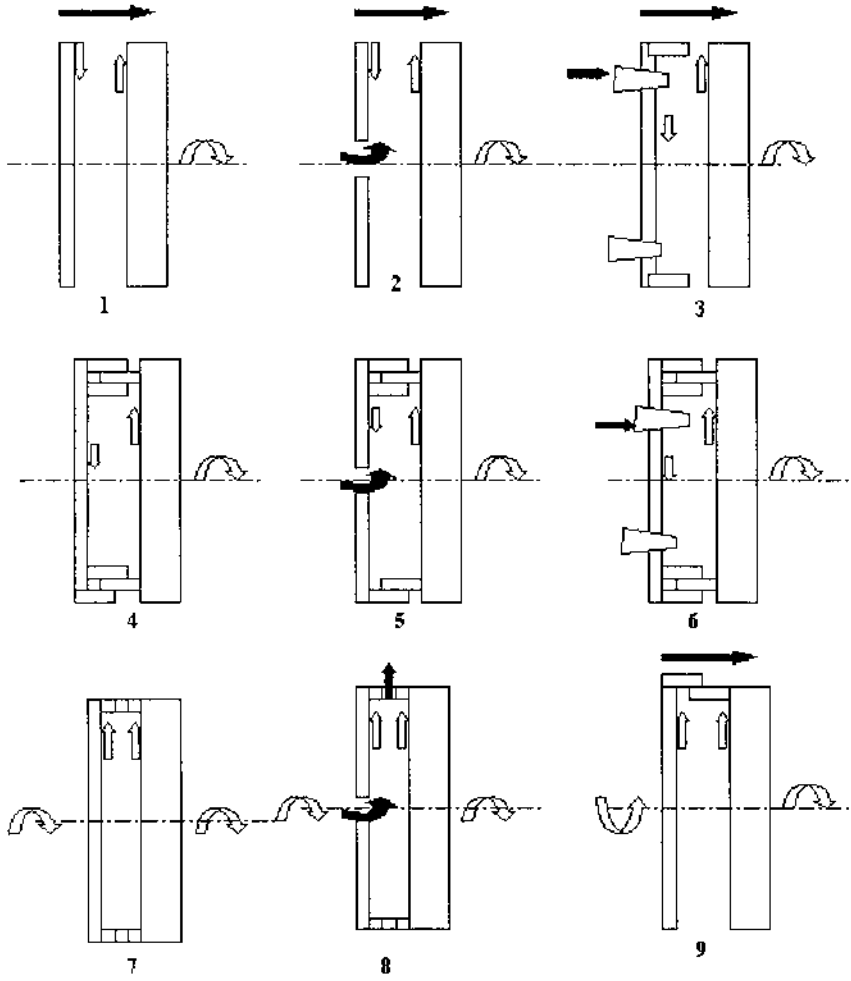

Figure 26 Schematics of disc–stator and disc–disc systems.

pumping flow and a required buffer flow to overcome or drastically reduce potential ingress from the main stream. Simplified calculations that are based primarily on experimental data have to be applied during this phase.

It has been recognized that the hot gas ingress mechanism resulting from disc pumping outflow in rotor–stator systems, particularly with the cavity open toward the main stream, is strongly affected by circumferential steady and unsteady pressure variations observed above the disc plenum

axial gap. A static pressure variation propagating from the nozzle trailing edges downstream to the gap causes the steady pressure nonuniformity. At the same time, the static pressure variation propagating from the blade leading edges upstream to the gap causes the unsteady pressure fluctuation. Both sources encourage hot gas ingress into the disc plenum. Some techniques intended to reduce these pressure variations have been developed recently to minimize these effects (Glezer, Fox) [108]. However, implementation of these techniques requires close interaction between different disciplines participating in the engine design. Compromises between cost and efficiency when using established life target are also required when disc material and disc cavity seal design configurations are considered. Axially overlapping seal is required to avoid hot gas ingress into the disc rim plenum, but this results in increased rotor span affecting entire engine rotor dynamics. These factors must be addressed in a true multidisciplinary design optimization process.

The ingress phenomena in stator–rotor systems is also strongly influenced by the cavity fluid core tangential velocity that is about 50% of the disc angular velocity for the cases where there is no superposed radial inflow. Studies show that introduction of the radial air flow leads to reduced core velocity and reduced ingress. Additional details related to disc flow and heat-transfer studies are presented later.

Cooling of Nozzle Support Structure and Turbine Housing

Maintaining a small variation of transient thermal growth is the essential task of cooling that is applied to a nozzle support structure, which is connected to the turbine housing. The nozzle support structure (sometimes also called a nozzle case) is typically positioned between the gas path and outer housing, thus often experiencing significant radial and circumferential temperature gradients. Low thermal expansion materials would be the most desirable choice for the nozzle support structure. However, very few alloys with low expansion properties can tolerate operating temperatures above 1,200–1,300 °F. For this reason it is essential to cool the nozzle support structure. The cooling flow budget is usually very restricted to avoid significant turbine performance penalties. Use of air from intermediate compressor stages for the cooling is often encouraged to minimize performance penalties. All means must be exercised to limit the area of conduction heat transfer with the nozzles without sacrificing integrity of their support. The cavities between the nozzle support structure and nozzles have to be well sealed and are often buffered with the cooling air to prevent hot gas leakages through these cavities. This important task requires a thorough flow analysis as a part of the internal cooling flow system.

Impingement cooling is the most common technique for cooling of the nozzle support structure. Impingement jets are often directed toward the outer radius of the nozzle hooks that position nozzles in the support structure. This allows reduction of hoop stresses in the nozzle support structure, particularly when there is a concern for excessive radial temperature gradients through this structure. Another benefit of nozzle support structure cooling in addition to lowering metal temperature is a reduction of circumferential temperature gradients within the structure. This is a very important factor in achieving circumferentially uniform blade-tip clearances. Modulation of the cooling flow directed to the nozzle support structure can be used for active control of the tip clearances.

The temperature of the turbine housing outer surface is often limited for reasons of safety and constraints from external engine hardware, including lube system and instrumentation. The U.S. standard for industrial gas turbines limits this outer shell temperature to about 450 °F. This is usually a tradeoff between housing cooling and external insulation. Use of a highly effective external insulation is costly and also results in increased turbine housing temperatures that require application of more expensive, higher-grade alloys for the housing. Cooling of the housing results in additional heat losses with corresponding penalties for engine thermal efficiency and complications in design and engine maintenance. It is quite common to use ambient air for housing cooling utilizing energy of the spent cooling air from the turbine (or from the engine exhaust gas) to create suction (ejection) and flow of the ambient air along the housing.

COMBUSTOR COOLING

Effect of Combustor Design Evolution on Cooling Techniques

This section will focus primarily on the liner, which usually consumes most of the combustor cooling flow budget. Other parts of the combustor including dome and transition to the nozzles are prone to design specifics and their cooling is not described in this section. However, some of the transition cooling issues were addressed earlier.

Cooling requirements for the liner vary with a number of parameters, which have continually changed in the past 20 years of engine development. The major parameters are

Hot gas temperature and type of fuel
Cooling air temperature and allowable combustor pressure drop
Allowable material temperatures, expected life, and durability

Weight, cost, and complexity constraints

Considering that liner heat load is driven primarily by the flame radiation, the calculation of the flame temperature and the heat flux through the liner wall requires good understanding of the combustion process. A comprehensive monograph by Lefebre [109] provides an excellent review of various gas turbine combustor systems. It also details the calculation procedures for the main factors that affect liner cooling.

Many early gas turbine combustors were a single- or multiple-can design and required a transition between combustor exit and turbine inlet. Liners for many of these combustors were assembled from a group of cylindrical shells that formed a series of annular passages at the shell intersection points. These passages created the louvers permitting a film of cooling air to be injected along the hot side of the liner wall to provide a protective thermal barrier. The annular gap heights were maintained by simple "wiggle-strip" louvers (Fig. 27). Air metering was a major problem with this technique. Application of splash-cooling devices provided control of the cooling air entering the liner through a row of small-diameter holes with air jets impinging on a cooling skirt, which deflected the air along the inside of the liner wall. Annular combustors, which were introduced later, originally also used wiggle-strip and splash-cooling configurations. Since then, the "machined-ring" or "rolled-ring" approach, which features accurately machined holes instead of louvers and combines accurate air-

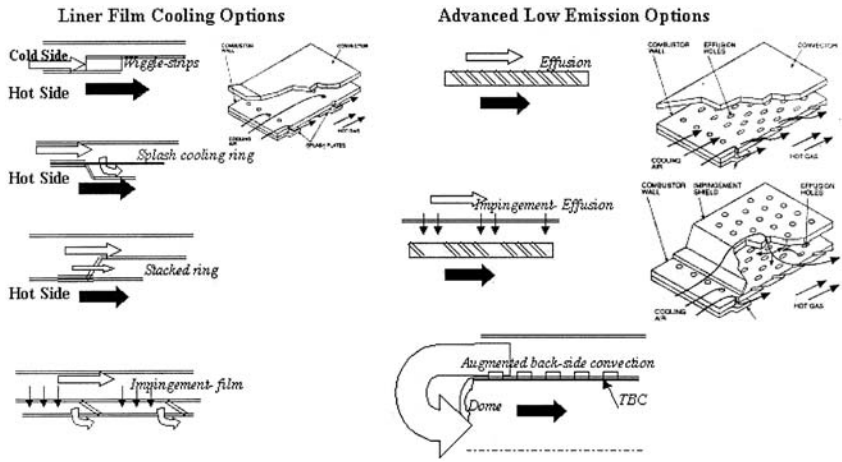

Figure 27 Combustor liner cooling techniques.

flow metering with good mechanical strength, has been widely adopted in one form or another.

Modern cooling techniques include angled effusion cooling (EC) using multiple rows of small holes drilled through the liner wall at a shallow angle to its surface. With this scheme, the cooling air flows through the liner wall, first removing heat from the wall by convection–conduction, and then providing a thermal film barrier between the wall and the hot combustion gases. EC is presently considered to be the most promising option among advanced combustor-cooling techniques that are being actively developed for the new generation of industrial and aero engines. For some advanced aero engines, it has reduced the conventional cooling air requirement by 30%. The main drawback of EC is an increase in liner weight of around 20%, which stems from the need for a thicker wall to achieve the required hole length and provide buckling strength.

A common alternative to increasing the efficiency of cooling techniques is to spray protective and thermal barrier coatings on the inner liner wall. As it has for the past 60 years, the search continues for new liner materials that will allow operation at higher temperatures. Current production liners are typically fabricated from nickel-based alloys such as Haynes 230.

Application of combined impingement-film or impingement-effusion techniques are often considered when a higher cooling effectiveness is required. These techniques require a double-walled liner design where the outer (in relation to the gas path) wall in the double-walled region is perforated. The advantage of the method derives from its use of cooling air to serve a dual purpose. First, the air is shaped into multiple small jets, which provide impingement cooling to the front (primary zone) section of the liner wall, and then the jets merge to form an annular sheet, which operates in a conventional film-cooling mode to cool a downstream section of the inner liner wall. Another advantage of impingement cooling is that the impingement jets can be positioned to provide extra cooling on liner hot spots. The higher cooling effectiveness of these techniques comes with certain penalties in terms of cost, weight, and higher pressure losses that affect overall engine efficiency. Another concern stems from the significant difference in temperature between the two walls, leading to a differential expansion that might result in buckling of the inner wall if the local hot spots become too severe. Also, the high heat-transfer coefficients that are normally associated with impingement cooling cannot be realized fully in the downstream section, because the film of air discharged from the upstream protects the downstream section, reducing the inner wall metal temperature and thus lowering the effectiveness of impingement cooling.

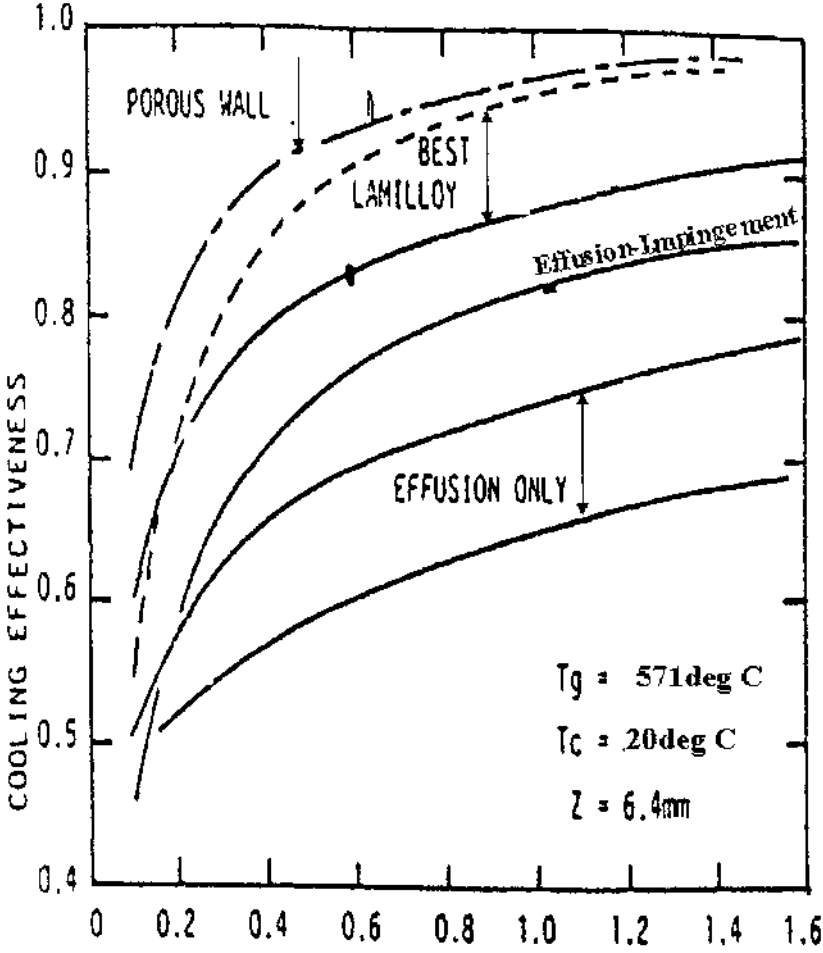

Figure 28 Effectiveness of liner cooling methods.

Similar to other cooled turbine components, the combustor air inlet and hot gas outlet temperatures can be combined together with the maximum allowable liner wall temperature into a single parameter called "cooling effectiveness" reflecting the thermal load on the wall at given heat-transfer conditions. The larger this parameter, the more cooling air is needed, or the more effective the cooling method must be (Fig. 28).

Advanced large engines are clearly approaching the limit above which pure film cooling is no longer sufficient. In the past, therefore, an iterative solution was found in reducing the surface in need of cooling by shortening the flame tube. This was made possible by the adoption of improved fuel preparation systems. Over the years the ratio of the liner length to its height dropped from about 4 for old engines to about 2 for new engines.

Cooling configurations are usually tested in model rigs, where the cooling action is determined at defined constraints. When applying the cooling configuration to real combustors, the exact constraints are unfortunately not known. This applies in particular to constraints on the hot gas side. The flow pattern and the local temperature in the flame tube, familiarity with which is a prerequisite for determining the constraints, cannot normally be measured. For this reason, these quantities must be computed using 3D CFD computations for the combustor flow, where the local release of heat is to be determined accurately enough to derive local temperatures, velocities, and radiation load. Codes for this purpose already exist, although the confidence in the results they provide is still limited. However, the recent improvements in accuracy of the analytical predictions suggest that future designs of combustor-cooling configurations should be made in combination with CFD computations.

Transpiration Cooling

For the cooling air to be utilized much more effectively than in traditional film-cooling-based designs, the single-layer perforated sheet must be replaced with a multiple-layer sheet structure where the cooling air is routed through a winding path between and through the layers. This arrangement is referred to as "transpiration cooling." This method approaches an ideal wall-cooling system that can maintain the entire liner at the maximum temperature of the material, avoiding cooler regions that would represent a wasteful use of cooling air. The transpiration cooled liner wall is constructed from a porous material that provides a large contact area for heat transfer to the air passing through it. Because the pores are uniformly dispersed over the surface of the wall, the tiny air jets emerging from each pore rapidly form a protective layer of a relatively cold air over the entire inner surface of the liner. While passing through the pores, the cooling air removes a significant amount of heat from the wall. When this combined convection–conduction wall heat transfer is coupled with the protective layer of discharged film, the overall cooling effectiveness is sufficient to counterbalance very high heat loads that include radiation from the flame. This means that, in addition to acting as a porous medium, the wall must also have good heat-transfer properties and be of adequate

thickness. A problem this poses is that, in order to form a stable boundary layer on the inner surface of the wall, the coolant flow should emerge with as low a velocity as possible, whereas for maximum heat transfer within the wall a high velocity is required. Although transpiration cooling is potentially the most efficient method of liner cooling, its practical implementation has been very limited due to the availability of required porous materials. The porous materials developed to date have failed to demonstrate the required tolerance to oxidation, which has led to the small passages becoming blocked. These passages are also sensitive to blockage by foreign particles in the air.

Effusion Cooling

The simplest approach to a practical form of transpiration cooling is a wall perforated by a large number of small holes. Ideally, the holes should be large enough to remain free from blockage by impurities, but small enough to prevent excessive penetration of the air jets into the main stream. Provided that the jet penetration is small, it is possible to produce along the inner surface of the liner a fairly uniform film of cooling air. If, however, the penetration is too high, the air jets rapidly mix with the hot gases and provide little cooling of the wall downstream. Effusion cooling can be applied to all or any portion of the liner wall, but due to the high rate of cooling flow required it is best used for treating local hot spots in the liner wall. Another useful role of effusion cooling is in improving the effectiveness of a conventional film-cooling slot. As the film of air from this slot moves downstream, its temperature gradually rises due to entrainment of the surrounding combustion gases. Eventually, it becomes so hot that it starts to heat the liner wall instead of cooling it. If effusion cooling is applied before this point is reached, the injection of cold air into the film enables it to maintain its cooling effectiveness for a longer distance downstream.

In conventional effusion cooling, the holes are drilled normal to the liner wall. The advantages to be gained from angled effusion cooling with the holes drilled at a shallower angle are twofold:

1. An increase in the internal surface area available for heat removal. This area is inversely proportional to the square of the hole diameter and the sine of the hole angle. Thus, for example, a hole drilled at 20° to the liner wall has almost three times the surface area of a hole drilled normal to the wall.
2. Jets emerging from the wall at a shallow angle have low penetration and are better able to form a film along the surface of the wall. The cooling effectiveness of this film also improves as the hole size and angle are decreased.

Some studies showed that the cooling effectiveness can be increased by 60% at a realistic pressure ratio of 1.03, if the hole is made at an angle of 20° versus being normal to the wall surface. It is clear that practical implementation of angled effusion cooling is highly dependent on an ability to accurately, consistently, and economically manufacture large numbers of oblique holes of very small diameter. Advances in laser drilling have made this possible, and this cooling method is now regarded as a viable and economically acceptable technique. At the present time, the lower limit on a hole diameter is about 0.4 mm, whereas the lowest attainable hole angle is just below 20°. Andrews [110–113] presents a number of papers that are widely used for advanced liner cooling design. Full coverage discrete hole impingement cooling and effusion film cooling are extensively used in gas turbine blade and combustor wall cooling. However, most applications and most experimental investigations for these cooling techniques are used separately. The combination of impingement and effusion cooling offers a good means of improving the overall cooling effectiveness of both turbine blades and combustor walls and of minimizing the coolant flow required to achieve the desired cooling effectiveness. Combined impingement/effusion cooling with equal numbers of holes, but the main pressure loss at the impingement holes, has very good internal wall heat-transfer characteristics with increases of 45% and 30% found for two designs, relative to the impingement-only situation. Studies of combined impingement–effusion cooling yielded the following conclusions:

The combined impingement–effusion cooling heat transfer was not greatly influenced by the effusion wall design for the effusion–impingement hole diameter ratios.

The measured combined impingement–effusion heat-transfer coefficients were lower than the sum of the separate impingement and effusion wall heat transfer by approximately 15–20% for the two designs tested. This indicates that there was an interaction between the two heat-transfer modes, which reduced the net heat transfer.

The overall cooling effectiveness results demonstrated the large benefits to be obtained from the addition of impingement cooling to effusion cooling. However, the film-cooling part of the process, which was strongly dependent on the effusion hole size, had a strong influence on the wall impingement–effusion heat-transfer coefficient.

Cost, increased weight, durability, and ability to repair the angled effusion-cooled liners are the main concerns that limit their application. These issues can only be fully resolved by extensive service experience.

Future developments in angled effusion cooling will tend to focus on the optimization of hole geometry. A diffuser-shaped expansion at the exit

portion of the hole has been shown to improve cooling effectiveness due to lower exit velocity and reduced penetration of the air jet into the hot gas stream. However, a cost-effective method of producing the shaped holes has yet to be developed.

Augmented Back-side Convection

The introduction of low-emission combustors has resulted in partly changed challenges compared to those associated with conventional combustion chambers. Low-emission combustors for advanced industrial engines target very low NOx emission using the lean-combustion principle. In the lean-combustion concept the objective is to use a large fraction of the air for combustion in the primary combustor zone to achieve reduction in combustion temperature and NOx emissions. The resultant effects on the available cooling air flow are shown in Fig. 29. As expected, the amount of air required increases for lean combustion. As illustrated in the figure, the amount of cooling air available decreases proportionately. Consequently, with a primary zone temperature of 3,150 °F and a combustion chamber exit temperature of 2,780 °F, the portion of air available for cooling is only about 20%. Therefore, it is necessary to find methods of cooling that require less air or methods that can use the air in sequence for liner cooling and then for the primary zone "quenching."

This application of in-series cooling can make most of the combustor air available for cooling the liner back side. The convective heat-transfer rate on the back side of the liner can be increased by the application of fins, pedestals, ribs, or any other form of secondary surface that augments convective heat transfer and increases the effective area for heat exchange. Details and some heat-transfer correlations for such augmentation techniques were described earlier. Usually this cooling technique will require an additional "cold" wall to control the air passage. Such dual-wall cooling structures are not necessarily easy to translate into practical designs. The inner wall being hot and the outer wall cold result in excessively high differential temperatures and hence differential expansions between inner and outer walls such that a fixed joint is made impossible. Therefore, the outer wall is normally designed as a supporting structure, while the inner wall is designed as shingle-type individual plates with sufficient clearance between them to accommodate the difference in thermal growth. Some of the design concepts, however, can be based on a reversed scheme, where the hot wall is a continuous structure and outer wall is sectioned and spring loaded against the liner (Glezer et al.) [114].

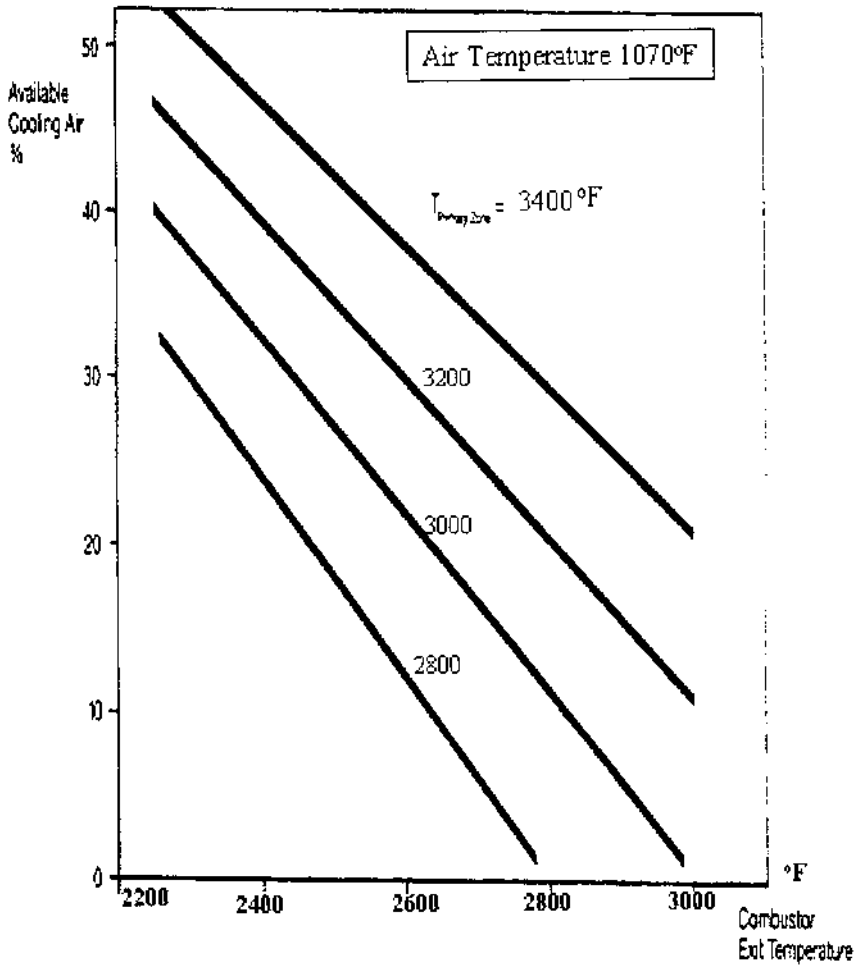

Figure 29 Influence of combustor exit and primary zone temperature on the available amount of cooling air.

Specific information on the use and performance of various extended-surface configurations for the liners, including ribs, fins, and pedestals, may be found in Gardner [115] and Evans and Noble [116].

One of the critical parameters that can limit application of these techniques is the pressure loss of the cooling system, which should not exceed 1.5–2% of the total compressor discharge pressure, otherwise causing

unacceptable engine performance penalties. Among the various heat-transfer augmentation techniques that might be attractive for this application is a surface with periodic concavities often called dimples, which has been recently introduced to the industry. Application of the dimpled back-side-cooled surface, when optimized for certain geometry, showed significant improvement in heat transfer at remarkably small pressure loss (Moon et al.) [117]. Fabrication of a liner wall that is smooth on the gas side and dimpled on the cold side can result in certain manufacturing challenges, however. Combination of this cooling method with a thermal barrier coating (see following section) might provide promising design alternatives to more complicated low-emission combustor systems.

Thermal Barrier Coatings

One attractive approach to the problem of achieving satisfactory liner life is to coat the inside of the liner with a thin layer of a very low thermal conductivity material, which is often called thermal barrier coating (TBC). A suitable material of low emissivity and low thermal conductivity could reduce the wall temperature in two ways: by reflecting a significant portion of the radiation heat flux from the flame and by providing a layer of thermal insulation between the hot gas and the wall of a base metal. The steep temperature drop through the TBC varies with the thermal conductivity and thickness of the layer, and the heat flux through the layer that is greatly affected by the heat transfer from the hot gas and to the cooling air. If the TBC coated wall is not provided with sufficient back-side cooling, the barrier helps little in lowering the temperature. A further benefit may be gained if an oxidation-resistant base coat is applied, because it reduces the oxidation constraint on the choice of liner-wall material.

An ideal TBC would be chemically inert and have good mechanical strength, resilience to thermal shock, and resistance to wear and erosion. Above all, it would have a low thermal conductivity and a thermal expansion coefficient that is similar to that of the base metal. A typical thermal spray-deposited TBC comprises a metallic base coat (such as 0.1 mm of Ni Cr AL Y), plus one or two layers of ceramic (such as yttrium-stabilized zirconium oxide ZrO_2).

Recent developments in the strain tolerance of the TBC have reduced the necessity for an intermediate coat, and two-layer coatings are now sometimes specified for improved mechanical integrity.

Plasma flame spraying is often used to apply the ceramic and base-coat layers because it is found to provide durable and reproducible coatings. A typical overall coating thickness is around 0.4 to 0.5 mm, which gives metal

temperature reductions of the order of 100 to 160 °F, depending on the heat flux through the liner wall. In this context it was noted earlier that for a TBC to be fully effective there must be adequate heat removal from the "cold" side of the liner wall. The most favorable temperature reduction in the base material that results from implementation of TBC is obtained at highest convection heat-transfer coefficients on both hot gas side and air-cooled back side of the liner wall. Inevitably, this means that liner geometries will become more complex as various features (such as fins, ribs, etc.) are added to augment the convective heat transfer from the cooled side of the wall in order to derive full benefit from the TBC coating on the inner wall.

The reduction in wall temperature obtained from using a TBC can be calculated by adding a term of TBC resistance $R_{TBC} = (k/t)(T_h - T_i)$ and solving one-dimensional heat transfer equations for the composite liner wall,

Where

k = TBC conductivity.
t = TBC thickness.
T_h = hot-side surface temperature of TBC.
T_i = temperature at interface between TBC and liner wall.

Many details of practical combustor designs and liner-cooling features can be found in [118–120].

ADVANCED EXPERIMENTAL HEAT TRANSFER AND COOLING VALIDATION

The state-of-the art analytical methods of predicting external and internal airfoil walls boundary conditions have improved significantly within recent years as a result of continuous advancements in numerical simulation models. However, even these improvements cannot predict local airfoil metal temperatures to an accuracy of better than 25–30 °F under real engine conditions. This limited accuracy can result in error in the prediction of component life of over 100%. For this reason, experimental verification of the analytically predicted metal temperatures and required cooling flows remains a critically important task for accurate estimates of engine life and performance. Experimental verification of various aspects of the analysis are performed after the design team is satisfied with the cooling concept and the analytical predictions.

Modern computational fluid dynamics and heat-transfer methods allow for the complete analysis of cooled turbine components. However, the complexity of internal and external boundary conditions for cooled airfoils requires detailed experimental calibration and test verification of the

analysis, in order to provide accurate life prediction for the components. When a component design is completed, its specific geometries are determined by the particular constraints of the overall engine design. The new design may differ sufficiently from reference existing design with proven operating experience to warrant model testing of specific new design features and, if necessary, hot cascade and/or engine testing.

External Heat-Transfer Measurements and Cooling Validation Techniques

Direct measurements of the turbine airfoil external heat transfer (or local heat-flux values) in a stator–rotor interacting system, even when only time-averaged data are recorded, are known to be quite complex and require very sophisticated experimental rigs. Such rigs are usually configured as low-speed, long-duration or near-full-speed, short-duration (blowdown, shock-tunnel, or light piston) facilities. Heat-transfer measurements are often performed in these rigs using a thin-film heat-flux measuring gauge. The thin-film gauge is a device consisting of a thin metal element having a very small heat capacity bonded to the surface of an insulator that is mounted in the studied component. Some examples of these facilities and measurements can be found in a recent Scholar Lecture presented by Dunn [121].

Takeishi et al. [122] report the results of a study for which the film-cooling effectiveness was measured for the same scaled model blades mounted either in a two-dimensional, low-speed stationary cascade or in a high-speed air turbine rotating rig. The specific application was for a stationary power plant turbine. The turbine stage consisted of 32 vanes and 72 blades. Two of the blades were configured so that heated or cooled air or CO_2 could be injected through them. Film-cooling effectiveness was determined based on surface temperature measurements and by using gas chromatography to analyze the relative amounts of CO_2 collected at selected locations along the blade surface. The authors used engine hardware, but were not able to reproduce the proper density ratio (density ratio is known to have an influence on film effectiveness) for the operating conditions.

More often, especially for turbine nozzle vanes, the heat-transfer measurements are performed in stationary cascades using traditional mass-heat-transfer analogy techniques such as naphthalene, liquid crystal, or other physical methods. When film-cooling effectiveness has to be measured, a higher spatial resolution technique needs to be applied. A recently developed application of pressure–sensitive paint for these measurements has demonstrated significant benefits for obtaining qualitative as well as quantitative results.

Pressure-Sensitive Paint

Using the pressure-sensitive paint (PSP) technique, film-cooling effectiveness can be measured on turbine vane surfaces [123, 124]. Nitrogen gas is used to simulate film-cooling flow providing an oxygen concentration map corresponding to an effectiveness map by the mass transfer analogy.

PSP technique is based on oxygen-quenched photoluminescence. Photoluminescence is a property of some compounds (active component of PSP) to emit light after being illuminated by a suitable light source. The emitted light intensity is related to the pressure of test fluid containing oxygen—for example, the blue wavelength (450 nm) can be used to excite the active molecules with the return signal in the yellow wavelength (600 nm). To detect and record the emitted light, which contains both pressure and concentration information, a filter and a CCD camera can be used. In addition to measuring the static pressure distribution at the test plate, the oxygen sensitivity is used to indicate oxygen concentration in the gas mixture. Nitrogen gas is heated to the temperature of the free stream to eliminate possible errors related to a difference in temperature. It is then injected through the film-cooling holes into the main flow. The mass concentration of oxygen in the nitrogen–air mixture downstream from the point of injection is measured to obtain film effectiveness by using the mass transfer analogy. The mass fraction of the tracer gas (oxygen) in the mixture near the wall surface is related to the adiabatic wall temperature for the analogous heat-transfer situation. In the referenced study [124] the main stream contains approximately 79% nitrogen and the cooling flow contains approximately 100% nitrogen. The film effectiveness can be expressed by oxygen concentrations, which can be measured by the PSP. The highest (100%) concentration of nitrogen (0% of oxygen) should be expected inside the film-cooling hole.

The test setup of the PSP application to obtain film effectiveness includes a test vane, a CCD camera, and light sources. The test vane, made of stainless steel and coated with PSP, is mounted at the middle (for viewing the leading edge and the suction surface) or at the mid-left position (for viewing the pressure surface) in the cascade. Transparent windows are located immediately upstream and downstream of the cascade. The CCD camera is mounted in front of these windows to view the vane surfaces from four positions as shown in Fig. 30—two for viewing the pressure surface (camera positions 1 and 2); one for viewing the leading edge (camera position 3); and one for viewing the suction surface (camera position 4). In this particular study, the data obtained by viewing from camera position 1 were used to validate data taken viewed from camera position 2, which contained information for the entire pressure surface. Three halogen lamps,

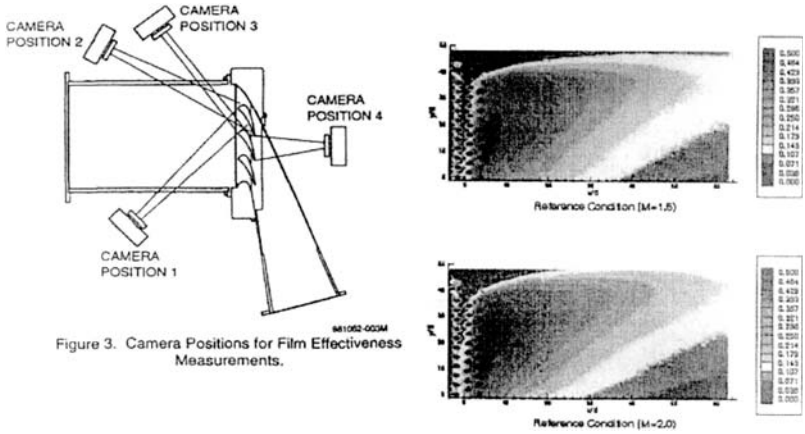

Figure 30 Application of PSP for film effectiveness mapping.

located around the camera, provided the light source for each of the camera positions. The images of luminescence intensity distribution from the nozzle surfaces, recorded by the CCD camera, are originally gray scaled. A data reduction program compared the recorded intensity values with the calibration data to obtain surface pressure and film effectiveness distributions. For the PSP film-cooling test, four images are required: a dark image (light off, wind off); a reference image (wind off, light on); an air injection image (wind on, light on, hot air injection); and a nitrogen injection image (wind on, light on, hot nitrogen injection). Hot refers to the temperature of the main stream, about 170 °F (77 °C) and cold means the reference temperature, controlled at 70 °F (21 °C). The air injection image contains information of surface static pressure only, while the nitrogen injection image contains both the surface static pressure and the oxygen concentration information. The PSP is also sensitive to the surface temperature. Therefore, the nozzles are allowed to stabilize at the free-stream temperature. By obtaining ratios of intensities of the described four images, the oxygen concentration on the airfoil surface downstream from the injection can be separated from the pressure distribution. Adjusted images provide the whole picture of the airfoil surface viewed with detailed qualitative and quantitative data of local cooling effectiveness.

Indirect Turbulence Measurement

The most difficult requirement in a turbine heat-transfer experiment is to reproduce the character of the actual engine free-stream turbulence. The

main challenge for a properly designed experiment is not only to provide basic aerodynamic and heat-transfer similarity with an actual engine, but also to emulate the free-stream turbulence level produced by the actual engine combustor and stator–rotor wake interaction when rotor blades are tested. For this reason, it is very important to measure the effect of free-stream turbulence on local main-stream convective heat transfer in an actual engine. When such data are recorded for at least a stagnation point of the airfoil, a corresponding level of free-stream turbulence can be closely estimated. The correlation between convective heat transfer and free-stream turbulence intensity obtained at the stagnation point under realistic conditions is particularly useful for achieving this important similarity requirement in a hot cascade emulation. Conventional methods of direct measurement of turbulence intensity and its effect on airfoil heat transfer require relatively sophisticated experimental techniques including Laser Doppler Anemometry or hot-wire anemometry combined with available methods of heat-transfer measurements. As a result of these direct measurements performed during the last decade, useful correlations of Frosling number $\mathrm{Nu}/(\mathrm{Re})^{0.5} = f(\mathrm{Tu})$ have been established not only for the stagnation point of the airfoil but also for the pressure and suction side. Practical application of such correlations in the turbine airfoil development process presents a significant difficulty due to the unknown free-stream turbulence produced by each combustor. Direct measurement of the turbulence intensity in a combustor above 2,000 °F (1,100 °C) is particularly difficult with conventional methods. In the turbine airfoil cooling design process, the knowledge of the turbulence intensity presents only a reference value, resulting in a search for simplified experimental methods of the heat-transfer evaluation in the actual engine.

The methodology described in [125] is based on indirect measurement of turbulence intensity using a heat-flux probe. Positioned downstream of the combustor, this instrument provides stagnation point heat-transfer data that correspond to a particular free-stream turbulence intensity defined in the prior studies. The heat-flux probe fits a 6.3-mm-diameter cylinder with a heat-flux sensor located at the side of the probe. The heat-flux sensor is a 1.5-mm-diameter Gardon-type thin foil heat-flux gauge. The stagnation point heat-transfer coefficient can be obtained from the measured stagnation heat flux, stagnation point wall temperature, and gas temperature using the equation

$$h = q''/(T\mathrm{aw} - T\mathrm{w})$$

Adiabatic wall temperature is calculated based on gas static temperature, pressure, and flow rate. Stagnation point temperature is measured by a

thermocouple positioned close to the heat-flux sensor. The calculated heat-transfer coefficient is then used to predict turbulence intensity. The described method remains an effective, practical tool for estimating heat-transfer augmentation produced by actual combustor discharge free-stream turbulence. Reproduction of this augmentation in the hot cascade environment provides more realistic measurements of heat load for the development of cooled airfoils.

Internal Flow and Heat-Transfer Measurements

Internal flow studies include two major tasks:

1. Measurements of the pressure distribution for the cooling passage
2. Flow visualization to reveal potential problems such as local flow stagnation or separation

Measurement of the pressure distribution and flow behavior in blade- and vane-cooling passages is critical to the calibration of the flow network models used in cooling design. Static pressure measurements are used to verify the pressure losses (inlet, frictional, turning, impingement/film hole losses, etc.) through the cooling passages.

In the early stages of a cooled component development cycle, when actual engine hardware is not available, scaled-up models are often used. Developed nearly a decade ago, the rapid prototyping stereolithography process based on application of a laser light-sensitive acrylic photopolymer is widely used at present for fabrication of the full size or up-scaled blade models providing accurate geometric similarity of all details of internal cooling passages and heat-transfer augmentation features. The stereolithography process uses a computer-generated 3D geometry file to control the motion of the focused laser beam, which solidifies a liquid photopolymer, layer by layer. The process produces accurate translucent models even for the most complicated geometries. Polishing of the model is required to achieve a full transparency for internal flow studies. Due to the complete geometric similarity between the scaled-up model and the full-scale design, the required ratio of their flow rates is equal to the square of the model scale factor. A scaled-up model provides the very important benefit of obtaining detailed measurement of the pressure distribution in the cooling passages. Final verification of the pressure loss distribution can be performed in a full-scale engine hardware instrumented with local pressure taps.

Complicated flow phenomena within cooling passages can be understood with the application of a flow visualization technique. Flow visualization is a powerful experimental tool that can save valuable development time and assist in the interpretation of other test data. In

addition, quantitative flow velocity measurements can be made simultaneously if the visualization technique allows for the motion of discrete particles to be viewed by high-speed optical devices. This study is performed usually inside an up-scaled transparent model. One of the rather simple visualization techniques can be based on application of neutrally buoyant helium-filled soap bubbles of controlled size that are produced by a separate bubble generator. The bubbles trace air-flow patterns at speeds as high as 200 fps. Since they follow the flow streamlines, the bubbles rarely collide with objects in the airstream and are extremely durable. The motion of the bubbles at lower speeds, up to 30 fps, can be photographed using conventional film and lighting. For higher speeds, special film and lighting are required. With an interrupted light source, the motion appears as broken streaks on the photograph, which can be used to obtain a quantitative measurement of local velocities. The primary objective of these experiments is to quickly identify any stagnant zones, recirculation, and separation, or any anomalies in the flow behavior that could compromise the projected cooling performance. If any of these flow phenomena exist, it may be necessary to incorporate design changes to overcome them.

A highly recommenced experimental technique, which is known as thermal imaging, was introduced by Hippensteele et al. [126] and since then has been used extensively for direct local convective heat-transfer measurements within cooling passages. Improvements in video systems brought tremendous enhancement of the imaging method. The Thermochromic Liquid Crystal (TLC) coating may be described as an organic compound existing in the state between its solid and liquid phases. When its molecules are in a disturbed state (caused, for example, by increased temperature or mechanical shear), their axes are rotated, leading to bright reflected colors of light. The visible effect is shown through a change from colorless to red. As the temperature is raised further, the colors pass through a range of the visible spectrum to blue/violet and finally to colorless again at higher temperatures. A primary advantage of the liquid-crystal coating is its reversible state, which allows a number of experiments to be performed without reapplying the coating and also provides redundant data during the same test if transitions of more than one color are recorded. Data reduced from thermal imaging can be presented in a pseudo-color plot of very fine-size pixels, representing the heat-transfer matrix of the entire airfoil internal passage or one particular area. Each color corresponds to a particular range of heat-transfer coefficients. These values define internal heat-transfer boundary conditions required for thermal analysis.

The liquid crystal (for example, Hallcrest, R35C1W) is sprayed evenly on the inner surface of the transparent model before testing. For an optimum visual background for the liquid crystal display, the test surface is

spray-painted black (Hallcrest, BB-GI). Optical viewing and nonglaring illuminating devices are installed outside. The example of image processing system including a Y-C camera (Cohu 82100) and Silicon Graphics Indy workstation (R4000SC) can be found in [127]. The local heat-transfer coefficients are measured with the technique described by Metzger and Larson [128] and Wang et al. [129] using a transient heat-transfer solution for the semi-infinite plate. The imaging technique is illustrated in Fig. 31. Pre-established air flows that provide aerodynamic similarity to actual airfoil pass through an in-line electrical heater before the air enters the test section. Initially the heated air is diverted away from the model to keep the model at a uniform (room) temperature. The experiment begins with opening the diverter valve suddenly to direct the heated air flow through the model. With the heated air temperature reaching the transition temperature, the TLC color change takes place at various points on the model, transitioning first in the region of highest convective heat transfer. The color change information is directed to a data acquisition system (real-time

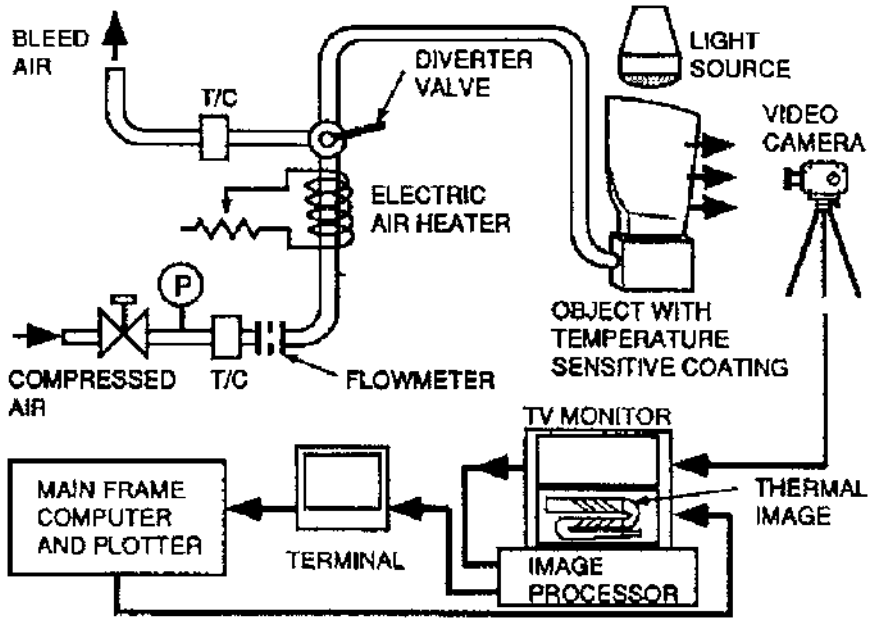

Figure 31 Schematics of internal blade heat-transfer measurement using liquid crystals.

image grabber). The software examines the transient transformation (pixel by pixel) and produces matrices of times.

Local convective heat-transfer coefficients are calculated at any point on the surface from the liquid-crystal response to convective heating. The data reduction technique converts the transient response data to local convective heat-transfer coefficients or Nusselt numbers. The test is usually performed in scaled-up transparent acrylic models simulating the actual geometry and Reynolds number range. Each pixel generates a local heat-transfer coefficient or Nusselt number. Heat-transfer coefficients generated by this means are compared to initial design values, and any necessary adjustments are made to the thermal analysis.

Conjugate Heat-Transfer Simulation and Cooling Validation in a Hot Cascade

Blade-Cooling Effectiveness Validation in Hot Cascade

The aerodynamic and heat-transfer similarity parameters discussed earlier have to be applied to simulate the actual engine flow and thermal fields in the hot cascade experiments. There are two main types of hot cascades: transient blow-down facility and steady-state rigs with the capability to perform transient experiments as well. The steady-state hot cascade [127] is more preferable due to lesser uncertainties of the experiment; however, in certain cases when large main-stream flow rate is required, the blow-down facility can provide some advantages. Figure 32 shows typical features of a steady-state cascade which includes an annular sector of the gas path with 5 to 7 airfoils providing realistic boundary conditions for the airfoils in the middle of the cascade. In an ideal case, the temperature and velocity distribution in the hot cascade and engine should be identical. However, difficulties in simulating the actual radial (along the blade) profiles in the stationary cascade rig, as well as complicated blade platform and tip region flows, usually limit simulation to the midspan values only. The similarity parameters identified for the boundary layers developing on gas turbine blade surfaces include Re, Pr, Ma, T_w/T_g, and C_p/C_v Pr, T_w/T_g, and C_p/C_v can be matched exactly when the hot cascade total temperature is set equal to the actual turbine rotor relative total temperature. Even though the facility might not have the capability of running close to the engine operating conditions, lower operating temperatures and pressures can be chosen for longevity of the instrumentation and safety. However, the similarity parameters Pr, T_w/T_g, and C_p/C_v are expected to be close to the engine condition. The hot

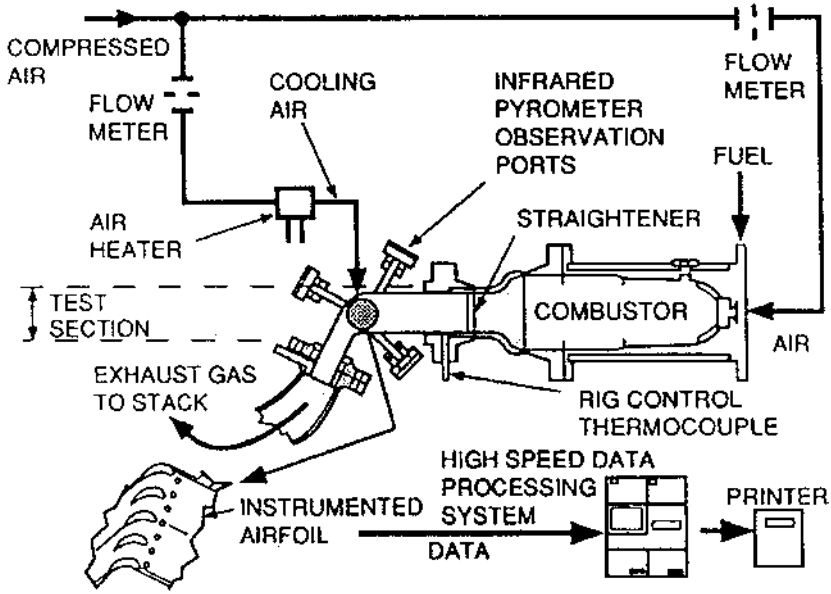

Figure 32 Schematics of a hot cascade for airfoil-cooling validation.

cascade local total temperatures and pressures, simulating engine conditions, are recommended to be measured with an automatic traversing Kiel probe and thermocouples.

The similarity principles applied to the main-stream gas side of the hot cascade also have to be applied to the coolant side of the airfoil under investigation. Additionally, the gas-to-coolant mass flow rate and the gas-to-coolant total temperature (T_g/T_c) ratios must be matched. Emulation of the forced convection heat-transfer process on gas turbine blade surfaces requires the similarity of Re, Pr, Ma, T_x/T_{go}, and C_p/C_v. The Nusselt number in the turbine (inlet) and in the hot cascade (inlet) will be the same if the similarity of all of these parameters is enforced, because the Nusselt number has a direct functional dependency on the local Reynolds number, the Prandtl number, and the free stream-to-wall temperature ratio. It should be noted that the list of similarity parameters used results from the unsteady form of the momentum and energy equations. In addition, the free-stream turbulence also affects airfoil heat transfer and should be reproduced during heat-transfer simulation experiments. Ideally, the intensity of free-stream turbulence and a typical length scale of the characteristic turbulent eddies as well as the inherent periodic unsteadiness of the turbine environment should

be provided in the simulation environment. It is a known that turbulent flow imposes a different momentum balance because of the existence of turbulent shear forces in addition to the shear forces due to molecular viscosity. Fluid elements also experience additional forces due to inherent periodic unsteadiness in the turbine. Thus the convective heat transfer to the surface is increased by the additional heat flux due to turbulence as well as inherent unsteadiness.

To simulate the external convective heat transfer, the local Reynolds number at the inlet of the blade (or nozzle) is calculated under engine conditions. The same Reynolds number needs to be reproduced at the inlet of the hot cascade. The total pressure at the inlet section of the cascade can then be calculated in such a way that both the inlet Reynolds number and the Mach number values are matched for the prescribed cascade operating temperature. The geometric similarity condition or the characteristic length in the expression for the Nusselt and Reynolds numbers can be satisfied easily by using a full-scale model in the cascade test section. For the same Reynolds number in the turbine and hot cascade, by using the equation of state and the definition of the Mach number, the free-stream mass flux rate can be defined as

$$\rho_{\mathrm{hc}} U_{\mathrm{hc}} = \frac{\mu_{\mathrm{hc}}}{\mu_{\mathrm{tur}}} \rho_{\mathrm{tur}} W_{\mathrm{tur}} = \frac{P_{\mathrm{hc}}}{R_{\mathrm{hc}} T_{\mathrm{hc}}} \mathrm{Ma} \sqrt{\gamma_{\mathrm{hc}} R_{\mathrm{hc}} T_{\mathrm{hc}}}$$

If the component simulated is a rotor blade, then W_{tur} corresponds to the relative velocity with respect to the rotor. The static pressure, P_{hc}, and temperature T_{hc}, values for the hot cascade can be replaced with the total quantities by using the isentropic relations. The expression for the total pressure of the hot cascade corresponding to an operator-selected cascade total temperature can then be obtained from

$$P_{\mathrm{o_{hc}}} = \frac{\mu_{\mathrm{hc}} \rho_{\mathrm{tur}} W_{\mathrm{tur}}}{\mu_{\mathrm{tur}} \mathrm{Ma} \sqrt{\frac{\gamma_{\mathrm{hc}}}{R_{\mathrm{hc}}}}} \left(1 + \frac{(\gamma_{\mathrm{hc}} - 1)}{2} \mathrm{Ma}^2\right)^{\frac{\gamma_{\mathrm{hc}}}{\gamma_{\mathrm{hc}} - 1}} \sqrt{\frac{T_{\mathrm{o_{hc}}}}{(1 + \frac{(\gamma_{\mathrm{hc}} - 1)}{2} \mathrm{Ma}^2)}}$$

At this stage, turbine conditions including the local Mach and Reynolds numbers are known. The total temperature can easily be controlled by changing the combustor operating conditions. Calculation of the hot cascade total pressure requires an iterative procedure because the specific heat ratio and the gas constant in the hot cascade are not known initially. Although the static temperature in the cascade is not known yet also, the total temperature is defined. The specific heat ratio has some nonnegligible static temperature dependence. Since the hot cascade static temperature is not known initially, the fluid properties can be approximately evaluated at

the turbine static temperature (rotor exit). This approach allows the first approximate calculation of total pressure, static temperature, and static pressure in the hot cascade. At this step, there is some error in the three quantities calculated initially because of the first approximation made of the specific heat ratio and gas constant. The resulting hot cascade static temperature, T_{hc}, is much more accurate than the first approximation, which is $T_{hc} = T_{tur}$. If one obtains the necessary properties with the new static temperature and recalculates the total pressure, static temperature, and static pressure in the hot cascade, the new result will be more accurate than the results obtained in the previous steps. If this process is repeated a few times until the properties converge to a stable value, an exact solution to the hot cascade total pressure can be obtained.

Once the free-stream total temperature is chosen in the simulating experiment, the total coolant temperature is calculated by matching the ratio of total coolant to free-stream temperature of the engine. Although engine coolant flow rate is usually expressed as a fraction of the main-stream gas flow rate, different total temperature conditions existing in the turbine and the simulating experiment may result in significantly different values of the coolant mass flow rates when the coolant Reynolds number is kept the same for both the turbine and the simulator (hot cascade rig) due to coolant viscosity variation. Therefore, the ratio of the hot cascade coolant to free-stream mass flow rate should be adjusted in such a way that it matches the coolant Reynolds number of the turbine. If the internal cooling passage is designed with a high coolant velocity, a match of the coolant local Mach number should be imposed.

Application of actual airfoils (or their prototypes) in the hot cascade ensures similarity in the conduction heat transfer. Practically useful (for the final design) conjugate heat-transfer experimental data can be obtained when external and internal convective heat-transfer similarity is achieved in addition to similarity in the conduction heat transfer.

Turbine Disc Experimental Boundary Conditions

For the last 30 years there has been a growing interest in fluid mechanics and heat transfer for the rotating disc systems. Dorfman (1960) [130] published analytical solutions based on the Reynolds analogy, for the rotating disc–stator system. Most of the early experimental studies performed for simplified generic case (unbladed disc rotating in the unshrouded plenum) were redirected toward practical turbine disc–cooling application. Later studies have addressed effects of the preswirler, which feeds cooling air into the blade and disc rim seal to prevent disc plenum from hot gas ingress.

Two major practical requirements exist when the turbine rotor–stator system is developed:

1. Define turbine disc local heat-transfer coefficients for specified rotational speed, geometry, and disc-cooling configuration.
2. Provide a system that prevents hot gas ingress into the disc plenum.

Disc heat-transfer prediction based on flow visualization (Pincombe, 1989) and measured angular velocity of the flow core in the plenum between disc and stator was a traditional method along with complicated direct measurements of the local disc temperatures or heat fluxes.

Some of the early flow visualization methods for the air in the plenum were based on application of $TiCl_4$ reacting chemically with the humid air to produce high-density white smoke. This method of flow visualization is practically obsolete at the present time because of product toxicity. It was noticed (Glezer, 1969) [131] and Phadke and Owen, 1988 [132] that nonaxisimmetric pressure distribution in the main-stream flow over disc–stator gap can produce a standing wave pattern of "hot gas" ingress into the plenum even when outward supply of "cooling" air flow exceeded disc pumping flow. (Turbine nozzle vane wakes present a typical example of nonaxisimmetric pressure distribution.) This phenomenon has to be addressed when an actual rotor–stator system is developed.

A very promising experimental technique to study both "hot gas" ingress and local convective heat transfer distribution along turbine disc and stator, based on application of liquid-crystal coating in a thermal transient test, was described by Metzger et al. [133]. More recent results performed at ASU for some practical rotor–stator geometries were referred earlier [105]. An additional study of effect of rotation on the accuracy of the liquid-crystal experiment was performed by Camci et al. [134] who replaced an acrylic disc with high-strength aluminum disc dressed with a balsa layer that was required to meet one-dimensional transient response of "semi-infinite solid." Balsa face surface was painted black and coated with thin liquid crystal. Coating of the disc face and acrylic stator with liquid crystals, which have significant difference in transitional temperature, allows performing heat-transfer thermal imagining for both disc and stator during one test. This approach was used and tested in a full-scale industrial turbine rotor–stator system rig (Fig. 33). Significant design features required for this rig included

Full-scale turbine disc with rim seal and preswirler air delivery system (feeding air into angular disc holes that represent blade-cooling passages)

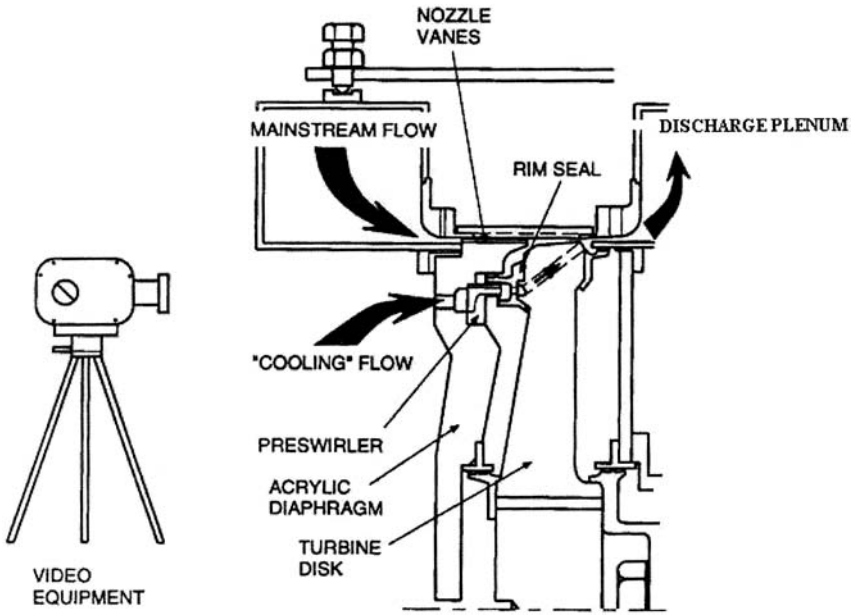

Figure 33 Experimental rig for investigation of turbine disc–stator interaction.

Adjustable-rim seal clearances and axial disc-to-stator diaphragm distances
Transparent stationary diaphragm that allows flow visualization and heat-transfer study in the disc plenum
Annular main-stream passage with nozzle vanes (simulating actual gas turbine aerodynamics in the vicinity of the disc rim axial gap)
Variable-speed driver
Adjustable radial inward and outward flow in the plenum

The rig can be designed to operate at close to ambient temperature providing aerodynamic similarity of the flow between the rig and the actual turbine environment. Both main-stream (simulating hot gas) and preswirler (simulating cooling air) flows are measured and adjusted to the required rates. Flow visualization in the disc–stator plenum and thermal imaging (liquid crystal) experiments to obtain the disc local convective heat-transfer coefficients were similar to the previously described for blade internal passage studies. Diverter valves can instantly introduce preheated air into

the main stream or into the preswirler (when ''reversed'' heat transfer is simulated).

An important contribution to this subject, including the effect of downstream blades on hot gas ingress, was made over the last few years by the research team at Aachen University of Technology [135], providing valuable experimental validation of numerical models that were generated by the university.

Cooling Verification in an Engine Test

Traditional Instrumentation

Final validation of the selected cooling system is typically performed in a prototype engine using detailed instrumentation with pressure and temperature sensors in the cooled components of the hot section as well as in the rotor–stator cavities supplying the cooling air. In the past, instrumenting the airfoils with thermocouples in the full-scale turbine test was the main technique for validating a design. The most expensive and time-consuming factor was the instrumentation of the rotating components. Furthermore, test data collection through a slip ring or telemetry system provided only local temperature information. More recently, some new techniques have been developed and implemented, which require much less test preparation time and provide more detailed information about component surface temperature distribution.

Borescope Port Inserted Pyrometer

This system is often based on a 90° side-viewing air-cooled pyrometer probe that can be inserted radially through an existing borescope port. Air cooling makes this system more convenient than nitrogen- or water-cooled pyrometers. The optical head of the pyrometer is connected by a fiber optic cable to a photodiode converter with outputs to an electronic amplifier, a control and recording system, and a display system. The high-speed recording system stores, displays, and plots the data identifying each individual blade on the recording chart. The system is calibrated against thermocouples installed in the blades and is qualified as a valuable diagnostic tool to identify potential blade-cooling problems (cooling passage blockage or restricted air entry orifice).

High-Temperature Thermal Paints

Another component temperature evaluation technique is based on the application of high-temperature thermal paints, which permanently change

their color when exposed to higher temperatures. The color transition is sensitive to both temperature and time at the temperature. This technique provides a very representative map of surface temperatures with resolution of $\pm$ 50 °F, although highly trained operators can interpret results with an accuracy of $\pm$ 20 °F. The thermal paint technique has become an important tool for the final qualification of cooled turbine components before production parts are fabricated. Slight variations in the geometry of the cooling passages can be produced with the application of rapid prototyping. This allows for the testing of "rainbow" configurations of the component in a single thermal paint test, thus qualifying the best configuration for future production. Further improvements in the technique include an automatic computer color-recognition method. This method provides fast, accurate nonsubjective color recognition when an object is properly illuminated. Proper assessment of experimental uncertainties should be performed during all stages described in the above section. Moffat [136] provides good guidance to evaluation of experimental uncertainties.

Thermal paint testing usually completes the development cycle for advanced airfoil cooling. After that, the selected design is ready for extended gas turbine endurance testing and production.

MULTIDISCIPLINARY CONSIDERATIONS IN SELECTION OF TURBINE COOLING SYSTEM

Advancements in modern high-efficiency and high specific power gas turbine engines are typically measured by the increases in overall pressure ratio and operating temperature. This trend results in the operating gas temperature significantly exceeding acceptable material capability limits, relying on application of cooling for various engine hot section components. Introduction of turbine cooling air further downstream of the combustor in an air-based open-cycle cooling system increases its negative impact on cycle performance. At the same time, reduction of the amount of the air available for the combustor makes the liner cooling task and emission control more difficult. This results in a major challenge for the designer of cooling system: select a system that requires minimal amount of cooling air and produces the smallest negative impact on engine durability, performance, weight (particularly for aero engines), emission (particularly for industrial engines), cost, and fabrication complexity. Such a task can benefit significantly from a multidisciplinary optimization effort, with each discipline effectively contributing to a successful design.

The traditional step-by-step engine hot section design process that has been following the sequential loop of thermodynamic cycle analysis–

aerodynamic design–mechanical design–cooling design (and back to the cycle analysis) is being recognized as outdated due to boundaries historically established within each discipline. A significant improvement in the development process for advanced gas turbine engines can be achieved through close interaction between various disciplines participating in the development. This approach often requires compromises within each of the disciplines to accommodate major interdisciplinary constraints (Fig. 34). The engine development program starts with a specification of the application, performance, cost, emission limits, and size/weight targets, and subsequently progresses through thermodynamic cycle analysis and gas-path geometry definition. Even at this early stage of development, the cooling issues play an equally important role with aerodynamic and structural considerations affecting blade-tip-to-hub-diameter ratio, work splits between stages, combustor liner surface-to-volume ratio, etc. For a development program to be successful, a true concurrent engineering process is essential during these conceptual and preliminary design phases. Risk-sharing between disciplines, which leads to justifiable safety margins and is based on probabilistic risk analysis, must replace the traditional more conservative approach, which is based on overconservative summation of

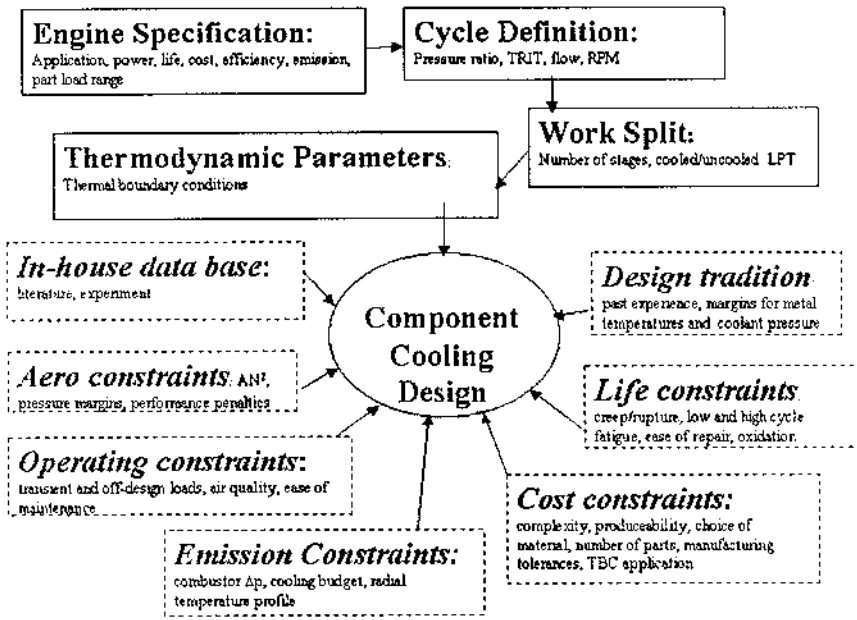

Figure 34 Factors affecting turbine cooling design.

margins defined within each discipline. This change in design culture is critical for development of a high-performance, cost-effective engine.

High turbine inlet temperature is required to increase the specific power of an engine resulting in continuously reducing weight-to-power ratio that is critically important for aero engines. Optimized compressor pressure ratio has to increase with higher gas temperature. The increased pressure ratio is a major factor in improving engine efficiency. Unfortunately, higher gas temperature and increased temperature of the cooling air, resulting from the higher compressor pressure ratio, require significantly higher turbine cooling flows, producing a diminishing effect on engine performance improvement.

For industrial engines, which are not as sensitive to size and weight as are aero engines, this factor often leads to the use of moderately high turbine inlet temperatures. Cost of the engine is expected to rise from the use of advanced materials, more complicated cooling systems and associated manufacturing processes, thermal barrier and oxidation resistant coatings, and more sophisticated and usually more complicated design of the hot section components. Figure 35 shows the typical trend in increasing engine efficiency, specific cost, and turbine-cooling flow requirements corresponding to rising turbine inlet temperature. An accelerated increase of the cooling air budget at gas temperatures above 2,200–2,350 °F (1,200–1,300 °C) is driven by the necessity to use a large amount of the air for film cooling, particularly when the compressor pressure ratio exceeds 30–35 and cooling air temperature increases above 1,100 °F (600 °C). Preliminary cooling design of turbine components can begin after the engine thermodynamic parameters and gas-path geometry are conceptually defined. At this juncture, a designer of cooling system should consider a number of major multidisciplinary factors: company past design history, life limiting factors, manufacturing and material cost affecting factors, emission limit imposed constraints, field operating conditions, aerodynamic design imposed constraints, and availability of in-house database and facility to validate advanced cooling methods. A company that achieves close cross-disciplinary interaction is more likely to establish an integrated design methodology and experience-based optimization algorithms linking together the different factors.

One of the most critical design decisions affecting not only selection of the cooling system, but also the entire turbine hot section design, is related to the turbine stage 1 work load and the corresponding stage pressure ratio. Higher stage 1 loading leads to a proportionally greater difference between stage 1 blade total and relative temperatures, resulting in lower cooling flow requirements for the blade and the possibility of using only internal blade cooling for moderately high turbine inlet gas temperatures, without assistance of film cooling.

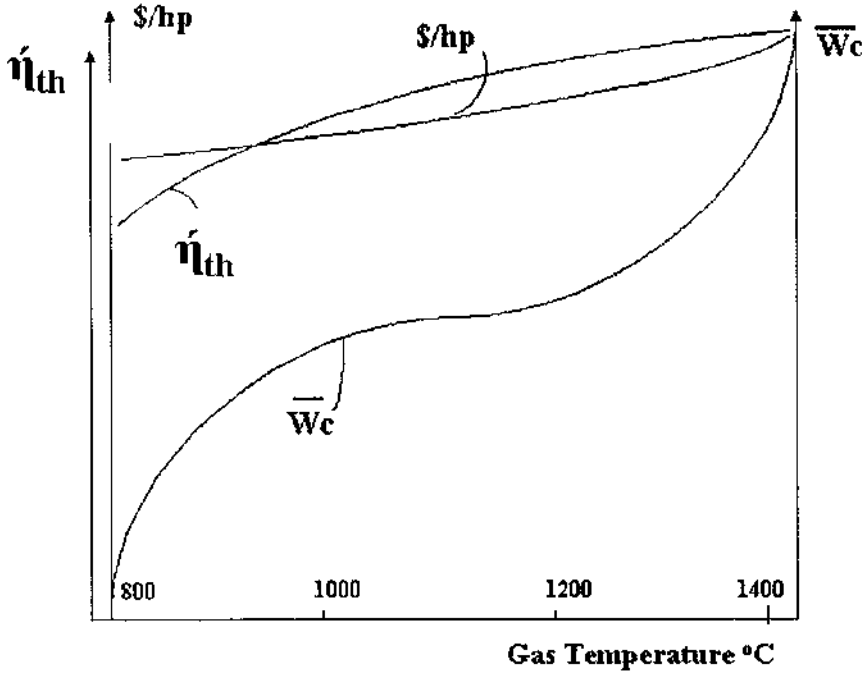

Figure 35 Cost, efficiency, and cooling flows versus TRIT.

But even more importantly, this cross-disciplinary team decision can provide an opportunity to significantly reduce cooling of downstream turbine components, avoiding in some cases any stage 2 blade cooling. The higher stage 1 pressure ratio might also lead to fewer turbine stages, resulting in a larger gas-path divergence angle. This leads to a larger gas-path area for the blades, which should be optimized between longer blades and larger tip diameter, which holds an acceptable $\mathbf{AN}^2$ stress parameter limit (where **A** is an annular gas-path area and **N** is the rotational speed of the rotor). Longer blades are less sensitive to performance losses associated with tip leakages for the same tip clearance. This makes the option of a highly loaded stage 1 with longer and smaller tip diameter blades more attractive for a single-stage high-pressure turbine provided the rotor speed can be maintained at a stress-limiting maximum. However, longer blades with smaller tip and hub diameters have their own, primarily mechanical, stress limitations associated with smaller circumferential disc spaces available for the blade fir tree attachments and the disc posts separating

them. The larger gas-path divergence angle is associated with a reduced number of stages. This should be taken into consideration regarding control of the blade-tip clearances that becomes more difficult due to a greater effect of relative transient axial displacements in a rotor–stator system.

In cases where the turbine rotor speed is limited by the tip speed of the larger diameter of the downstream stages, an option of a shorter stage 1 blades at larger tip diameter (retaining the equivalent gas-path area) can be more beneficial for the turbine thermodynamic efficiency. This option typically requires a higher blade count and larger cooling flow for the stage blade–disc system with increased disc pumping, which might negatively affect gains in the turbine thermal efficiency. The larger blade-tip diameter also results in a larger and usually heavier and more costly engine package. Optimization between these options has to involve a cross-disciplinary team that primarily addresses aerodynamic, stress, heat-transfer, and cost factors. The optimized blade height and tip diameter determine the height of stage 1 nozzle exit, consequently strongly affecting the height of the nozzle leading edge and the shape of combustor liner exit transition. Establishment of correlations between these various influencing factors and development of physically and/or statistically proven algorithms are necessary steps toward an optimized turbine multidisciplinary design system. A number of multivariable design optimization tools using deterministic or stochastic approaches (Goel et al.; Egorov et al.; Tappeta et al.) [137–139] have been developed and applied in certain areas of gas turbine engine design. However, development of algorithms that may be unique for each turbine manufacturer due to the differences in design criteria for each company continues to be a major obstacle in applying these optimizers.

A proper combustor design cannot be performed in isolation either. Higher compressed air-to-fuel flow ratios required to control nitrogen oxide emission by lowering the flame temperature demand a larger amount of compressor discharge air to be introduced in the combustor primary zone. This limits the cooling air budget available for the combustor liner and for the turbine components, particularly when the line-cooling air circuit is in parallel (not in series) with the primary air for fuel injectors. Back-side liner convective cooling methods are becoming more preferred to avoid relatively cold carbon oxide formation zones resulting from a more traditional film-cooling method. Particularly interesting for this application are the techniques based on a low-pressure-drop convective back-side cooling, allowing the use of the spent liner cooling air in series with the primary combustion air. With growing demands for air in the primary combustion zone, to control nitrogen oxide emission, the amount of air available for dilution decreases. This leads to a flatter combustor exit radial temperature profile and results in higher gas temperature near the end walls.

Existing challenges associated with cooling of the nozzle end walls and combustor liner exit transition walls require close interaction between combustor and turbine section designers. Maintaining a thin boundary layer at the combustor exit by constantly converging the liner walls toward the nozzles, and then converging the nozzle end walls via contouring, help reduce secondary flow losses originated at the nozzle end wall. An earlier study [55] has shown that introduction of end-wall film cooling upstream of the leading edge in combination with end-wall contouring suppresses the formation of horseshoe vortex at the nozzle leading edge, providing marked reduction in aerodynamic losses and preventing the cooler film layer from being diverted from the end wall. The studies also show that higher film blowing ratios utilizing maximum available pressure head, equivalent to the pressure drop through combustor, lead to significant improvement in the end-wall film coverage.

As a result of the flatter radial temperature profile mentioned earlier, turbine component cooling design strategy has to change beginning with the stage 1 nozzle, which typically consumes nearly 50% of the total turbine cooling budget in high-temperature engines. Tightening emission control requirements justify efforts toward reduction of nozzle-cooling flows by using spent air from combustor liner cooling and also by applying advanced thermal barrier coatings in combination with nozzle internal convective cooling, instead of full-coverage film cooling. These options represent a tradeoff between product cost and engine efficiency to satisfy emission and life requirements. Reduced amount of the turbine nozzle-cooling flow also assists in reducing combustor exit temperature for a fixed rotor inlet temperature.

Similar considerations regarding emission, flatter radial temperature profiles, and product cost must be applied during the selection of a blade-cooling design. Recent advances in internal blade cooling, particularly for highly thermally loaded leading edges of blades, including a technique based on swirling flow [86, 140, 141], as well as increased confidence in durability of blade thermal barrier coatings, improve the potential for a nonfilm-cooled blade leading-edge option for turbine inlet temperatures up to 2,370 °F (1,300 °C).

A four-quadrants chart shown in Fig. 36 illustrates a logical sequence for preliminary cross-disciplinary selection of the blade leading-edge cooling [142]. Two applications are considered in parallel: one for 15,000 h of operation, representing typical aero-engine blade life, and another for 60,000 h of operation, representing industrial engine blade life expectancy. Both engines are assumed to have similar thermodynamic cycle, design and materials. For both specified applications, quadrant I shows a correlation between initially assumed blade stresses σ and maximum allowable metal

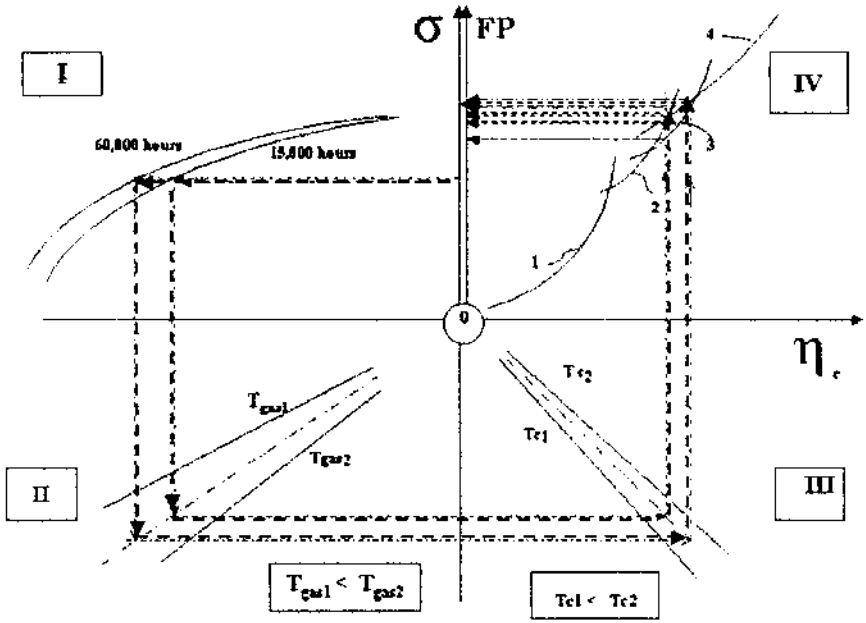

Figure 36 Blade-cooling selection diagram.

temperatures T_m that is based on the creep-rupture data for a selected blade material. The assumed difference in lives of the blade corresponds to about 80 °F (27 °C) in blade metal temperatures (as calculated from Larson–Miller parameter for advanced blade alloys). Moving vertically down to quadrant II to the intersection with specified blade inlet relative gas temperature line T_{gas} and then horizontally to quadrant III to the intersection with specified blade-cooling air temperature line T_c and finally to quadrant IV, a designer arrives to a point where a choice has to be made between available cooling options to satisfy the required cooling effectiveness $\eta_c = (T_{gas} - T_m)/(T_{gas} - T_c)$. Quadrant IV represents a typical correlation between cooling effectiveness and blade leading-edge cooling flow parameter $FP = (W_e o_p)/(A_{gas} h_{gas})$ for four different blade leading-edge cooling techniques, including (1) trip-strip augmented passage, (2) impingement of the leading edge without cross flow, (3) swirl cooling technique, and (4) shower head film cooling. Curves for the internally cooled techniques include the effect of a TBC coating. As can be seen from the chart, the 15,000-h application may use any of the techniques 2, 3, or 4. The 60,000-h application is limited only to techniques 3 and 4. The swirl cooling option

(3) coupled with TBC is able to match the cooling effectiveness of the shower head cooled blades (4) for moderately high turbine inlet temperatures. In addition to reduced cooling flow, this option may also provide improved cost and durability associated with elimination of the rows of shower head film-cooling holes. Comparing with jet impingement (2) this technique provides almost uniformly high heat-transfer coefficient along the entire circumference of the leading-edge cooling passage interior. This addresses a concern for off-design operation with the impingement cooling (2) when the nominal design stagnation point on the leading edge shifts away due to a change in the incidence angle.

Flatter radial gas temperature profiles, more typical for the industrial engines, produce higher thermal loads in the blade root, platform, and tip, creating significant challenges for a cooling designer. Interdisciplinary considerations might allow higher metal temperatures in the blade root section without changes in the creep-rupture life, for example, by tapering blade wall thickness. An increased tapering of the airfoil toward the tip combined with more a favorable ratio between root and tip cross-sectional areas might be required in certain cases to meet life targets. The increased gas temperatures near the blade tips, which are usually oxidation life-limiting (for nonshrouded blades) due to high local heat-transfer coefficients and unfavorable heating-to-cooling surface area ratio, can be counter-balanced by a redistribution of aerodynamic loading away from the tips. Finding improved concepts for blade-tip design, combining effective cooling with minimized tip leakages and reduced aerodynamic losses, continues to present a major challenge for cross-disciplinary turbine design teams and the gas turbine research community.

REFERENCES

1. Streeter, *Fluid Dynamics*, McGraw-Hill, New York (1971).
2. E. R. C. Eckert and R. M. Drake, *Analysis of Heat and Mass Transfer*, McGraw-Hill, New York (1972).
3. F. P. Incropera and D. P. DeWitt, *Fundamentals of Heat and Mass Transfer*, 2nd ed., J. Wiley & Sons, New York (1985).
4. W. M. Rohsenow and J. P. Hartnett, *Handbook of Heat Transfer*, McGraw-Hill, New York (1973).
5. W. M. Kays, *Convective Heat and Mass Transfer*, 5th ed., McGraw-Hill, New York (1966).
6. H. Schlichting, *Boundary Layer Theory*, 7th ed., McGraw-Hill, New York (1979).
7. A. H. Shapiro, *The Dynamics and Thermodynamics of Compressible Fluid Flow*, Ronald Press, New York (1954).

8. B. Barry, *Turbine Blade Cooling: Aerodynamic Penalties Associated with Turbine Blade Cooling*, von Karman Institute for Fluid Dynamics (VKI), Lecture Series 83 (1976).
9. G. M. Dailey, *Aero-Thermal Performance of Internal Cooling Systems in Turbomachines: Design and Calculation Issues*, VKI Lecture Series 2000–03, pp. 1–70 (2000).
10. J. E. Hartsel, "Prediction of Effects of Cooling Mass Transfer on the Blade-Row Efficiency of Turbine Airfoils," AIAA Paper 72-11, Jan. (1972).
11. C. McLean, C. Camci and B. Glezer, "Mainstream Aerodynamic Effects Due to Wheelspace Coolant Injection in a High-Pressure Turbine Stage: Part II—Aerodynamic Measurements in the Rotational Frame," ASME Paper 2001-GT-120.
12. R. W. Ainsworth, D. L. Schultz, M. R. D. Davies, C. J. P. Forth, M. A. Hilditch, M. L. G. Oldfield and A. G. Sheard, "A Transient Flow Facility for the Study of the Thermofluid-Dynamics of a Full Stage Turbine Under Engine Representative Conditions," ASME 88-GT-144 (1988).
13. A. H. Epstein, G. R. Guenette and R. Norton, "The MIT Blowdown Turbine Facility," ASME 84-GT-116 (1984).
14. R. S. Abhari, G. R. Guenette, A. H. Epstein and M. B. Giles, "Comparison of Time Resolved Turbine Rotor Blade Heat Transfer Measurements and Numerical Calculations." ASME Paper No. 91-GT-268 (1991).
15. C. W. Haldeman, M. G. Dunn, C. D. MacArthur and C. G. Murawski, "The USAF Advanced Turbine Aerothermal Research Rig (ATARR)," AGARD Conference Proceedings 527, 80, Symposium of the Propulsion and Energetics Panel, Antalya, Turkey (1992).
16. M. G. Dunn, "Phase and Time Resolved Measurements of Unsteady Heat Transfer and Pressure in a Full Stage Rotating Turbine," *J. Turbomachinery, 112*: 531–538 (1990).
17. S. E. Rich and W. A. Fasching, "CF6 Jet Engine Performance Improvement—High Pressure Turbine Active Clearance Control," NASA Report CR-165556 (1982).
18. R. S. Beitler and G. W. Bennett, "Energy Efficient Engine–Control System Component Performance Report," NASA Report CR-174651, pp. 31–43 (1984).
19. B. Glezer, "Turbine Blade Tip Clearance Improvement," ASME Paper 91-GT-164 (1991).
20. B. Glezer and H. Bagheri, Turbine Blade Clearance Control System, *U.S. Patent No. 5779436* (1998).
21. A. P. Saxer and H. M. Felici, "Numerical Analysis of Three-Dimensional Unsteady Hot Streak Migration and Shock Interaction in a Turbine Stage," *ASME J. Turbomachinery, 118*: 268–277 (1996).
22. D. J. Dorney and D. L. Sondak, "Study of Hot Streak Phenomena in Subsonic and Transonic Flows," ASME Paper No. 96-GT-98 (1996).

23. D. Bohn, H. Funke, T. Heuer, J. Bütikofer, "Numerical and Experimental Investigations of the Influence of Different Swirl Ratios on the Temperature Streak Development in a 4-stage Turbine, ASME Paper 2000-GT-250 (2000).
24. K. Gundy-Burlet and D. J. Dorney, "Influence of 3D Hot Streaks on Turbine Heat Transfer," ASME Paper No. 97-GT-422 (1997).
25. T. Katsanis and W. D. McNally, *Revised FORTRAN Program for Calculating Velocities and Streamlines on the Hub-Shroud Mid-Channel Stream Surface of an Axial-Radial- or Mixed-Flow Turbomachine or Annular Duct Vol. 1, User's Manual, Vol. II, Programmer's Manual*, NASA TN 8430,8431 (1977).
26. M. E. Crawford and W. M. Kays, "STAN5—A Program for Numerical Computation of Two-Dimensional Internal and External Boundary Layer Flows," NASA CR-2742 (1976).
27. S. P. Harasgama, F. H. Tarada, R. Baumann, M. E. Crawford and S. Neelakantan, "Calculation of Heat Transfer to Turbine Blading Using Two-Dimensional Boundary Layer Methods," ASME Paper 93-GT-79 (1993).
28. O. P. Sharma, P. Nguyen, R. H. Ni, C. M. Rhie, J. A. White and A. K. Finke, "Aerodynamics and Heat Transfer Analysis of a Low Aspect Ratio Turbine," AIAA Paper No. AIAA-87-1916 (1987).
29. T. Arts and R. Heider, "Aerodynamic and Thermal Performance of a Three Dimensional Annular Transonic Nozzle Guide Vane. Part I: Experimental Investigation," AIAA Paper AIAA-94-2929 (1994).
30. H. Consigny and B. E. Richards, "Short Duration Measurements of Heat Transfer Rate to a Gas Turbine Rotor Blade," ASME 81-GT-146 (1981).
31. R. J. Volino, "A New Model for Free-Stream Turbulence Effects on Boundary Layers," *ASME J. Turbomachinery, 120*: 613–620 (1998).
32. R. P. Dring, M. F. Blair and H. D. Joslyn, "An Experimental Investigation of Film Cooling on a Turbine Rotor Blade," *ASME J. Engineering for Power, 102*: 81–87 (1980).
33. G. W. Lowery and R. I. Vachon, "The Effect of Turbulence on Heat Transfer From Heated Cylinders," *Int. J. Heat and Mass Transfer, 18*: 1229–1242 (1975).
34. A. R. Wadia and D. A. Nealy, "Development of a Design Model for Airfoil Leading Edge Film Cooling," ASME Paper 85-GT-120 (1985).
35. V. J. Garg and R. E. Gaugler, "Prediction of Film Cooling on Gas Turbine Airfoils," ASME Paper 94-GT-16 (1994).
36. R. E. Mayle, "The Role of Laminar-Turbulent Transition in Gas Turbine Engines," *ASME J. Turbomachinery, 113*: 509–537 (1991).
37. Y. P. Dyban and V. D. Kurosh, "Heat Transfer at the Leading Edge of a Turbine Blade," *Heat Transfer—Soviet Research, 2*(1) Jan. (1970).
38. A. Turner, F. Tarada and F. Bayley, "Effects of Surface Roughness on Heat Transfer to Gas Turbine Blades," AGARD-CP-390, pp. 9–1 to 9–9 (1985).
39. N. Abuaf, R. S. Bunker and C. P. Lee, "Effects of Surface Roughness on Heat Transfer and Aerodynamic Performance of Turbine Airfoils," *ASME J. Turbomachinery, 120*: 522–529 (1998).

40. A. K. Tolpadi and M. E. Crawford, "Predictions of the Effect of Roughness on Heat Transfer from Turbine Airfoils," ASME Paper 98-GT-087 (1998).
41. S. M. Guo, T. V. Jones, G. D. Lock and S. N. Dancer, "Computational Prediction of Heat Transfer to Gas Turbine Nozzle Guide Vanes with Roughness Surfaces," *ASME J. Turbomachinery, 120*: 343–350 (1998).
42. R. J. Goldstein, *Film Cooling Advances in Heat Transfer, Vol. 7*, Academic Press, New York, pp. 321–379 (1970).
43. D. M. Kercher, "A Film-Cooling CFD Bibliography: 1971–1996," *Intl. J. Rotating Machinery, 4*(1): 61–72 (1998).
44. D. M. Kercher, "Turbine Airfoil Leading Edge Film Cooling Bibliography: 1972–1998," *Intl. J. Rotating Machinery, 6*(5): 313–319 (2000).
45. M. Y. Jabbari and R. J. Goldstein, "Adiabatic Wall Temperature and Heat Transfer Downstream of Injection Through Two Rows of Holes," ASME Paper 77-GT-50 (1977).
46. R. J. Goldstein and A. Haji-Sheikh, "Prediction of Film Cooling Effectiveness," Japan SME, International Symposium, pp. 213–218 (1967).
47. L. S. Langston, "Crossflows in a Turbine Cascade Passage," *ASME J. Engineering for Power, 102*(4): 866–874 (1980).
48. S. P. Harasgama and C. D. Burton, "Film Cooling Research on the Endwall of a Turbine Nozzle Guide Vane in a Short Duration Annular Cascade," ASME 91-GT-253 (1991).
49. S. P. Harasgama, "Heat Transfer and Cooling in Gas Turbines: Aero-Thermal Aspects of Gas Turbine Flows," VKI Lecture Series 1995–05 (1995).
50. S. P. Harasgama and E. T. Wedlake, "Heat Transfer and Aerodynamics of a High Rim Speed Turbine Nozzle Guide Vane Tested in the RAE Isentropic Light Piston Cascade (ILPC)," *J. Turbomachinery, 113*: 384–391 (1991).
51. T. Arts and R. Heider, "Aerodynamic and Thermal Performance of a Three-Dimensional Annual Transonic Nozzle Guide Vane, Part 1 Experimental Investigation," Paper No. 1994–31, 30th AIAA/ASME/SAE/ASEE Joint Propulsion Conference (1994).
52. S. Friedrichs, H. P. Hodson and W. N. Dawes, "Distribution of Film-Cooling Effectiveness on a Turbine Endwall Measured Using the Ammonia and Diazo Technique," *ASME J. Turbomachinery, 118*: 613–621.
53. S. Friedrichs, H. P. Hodson and W. N. Dawes, "Aerodynamic Aspects of Endwall Film-Cooling," *ASME J. Turbomachinery, 119*: 786–793 (1997).
54. S. Friedrichs, H. P. Hodson and W. N. Dawes, "The Design of an Improved Endwall Film-Cooling Configuration," *ASME J. Turbomachinery, 121*: 772–780 (1999).
55. R. Oke, S. Burd, T. Simon and R. Vahlberg, "Measurements in a Turbine Cascade Over a Contoured Endwall: Discrete Hole Injection of Bleed Flow." ASME Paper 2000-GT-214 (2000).
56. O. P. Sharma and T. L. Buffer, "Prediction of Endwall Losses and Secondary Flows in Axial Flow" (1987).

57. R. P. Roy, K. D. Squires, M. Gerendas and S. Song, "Flow and Heat Transfer at the Hub Endwall of Inlet Vane Passages, Experiments and Simulations, 1," ASME Paper 00-GT-198 (2000).
58. T. Shih, Y. L. Lin and T. Simon, "Control of Secondary Flows in a Turbine Nozzle Guide Vane by Endwall Contouring," ASME Paper 2000-GT-556 (2000).
59. J. H. Wagner, B. V. Johnson and T. Hajek, "Heat Transfer in Rotating Passages With Smooth Walls and Radial Outward Flow," *ASME J. Turbomachinery, 113*: 42–51 (1991).
60. J. H. Wagner, B. V. Johnson and F. C. Kopper, "Heat Transfer in Rotating Serpentine Passage With Smooth Walls," *ASME J. Turbomachinery, 113*: 321–330 (1991).
61. J. H. Wagner, B. V. Johnson, R. A. Graziani and F. C. Yeh, "Heat Transfer in Rotating Serpentine Passages with Trips Normal to the Flow," *ASME J. Turbomachinery, 114*: 847–857 (1992).
62. B. V. Johnson, J. H. Wagner, G. D. Steuber and F. C. Yeh, "Heat Transfer in Rotating Serpentine Passage with Trips Skewed to the Flow," *ASME J. Turbomachinery, 116*: 113–123 (1994).
63. J.-C. Han, S. Dutta and S. Ekkad, *Gas Turbine Heat Transfer and Cooling Technology*, Taylor & Francis, London (2000).
64. M. Taslim, *Convection Cooling in Non-rotating and Rotating Channels—Experimental Aspects*, T. Arts, ed. VKI Lecture Series 2000-03 (2000).
65. C. H. Sieverding, "Recent Progress in the Understanding of Basic Aspects of Secondary Flows in Turbine Blade Passages," *ASME J. Turbomachinery, 114*: 248–257 (1985).
66. L. S. Langston, "Secondary Flow in Axial Turbines—A Review," Presented at ICHMT Turbine Symposium 2000, Cesme, Turkey, Aug. 13–18 (2000).
67. R. P. Dring and H. D. Joslyn, "Measurement of Turbine Rotor Blade Flows," *J. Eng. for Power, Trans. ASME, Ser. A, 103*: 400–405, April (1981).
68. E. Elovic and W. K. Koffel, "Some Considerations in the Thermal Design of Turbine Airfoil Cooling Systems," *Intl. J. for Turbo and Jet Engines, 1*: 45–65 (1983).
69. M. G. Dunn, W. J. Rae and J. L. Holt, "Measurement and Analysis of Heat Flux in a Turbine Stage: Part II—Discussion of Results and Comparison With Prediction," *ASME J. Engineering for Gas Turbines and Power, 106*: 234–240 (1984).
70. H. P. Hodson, "Boundary-Layer Transition and Separation Near the Leading Edge of a High-Speed Turbine Blade," ASME Paper 84-GT-179 (1984).
71. K. Dullenkopf and R. E. Mayle, "The Effects of Incident Turbulence and Moving Wakes on Laminar Heat Transfer in Gas Turbines," ASME Paper 92-GT-377 (1992).
72. A. B. Johnson, M. L. G. Oldfield, M. J. Rigby and M. B. Giles, "Nozzle Guide Vane Shock Wave Propagation and Bifurcation in a Transonic Turbine Rotor," ASME Paper 90-GT-310 (1990).

73. R. S. Abhari, "Comparison of Time Resolved Turbine Rotor Blade Heat Transfer Measurements and Numerical Solution," ASME Paper 91-GT-268 (1991).
74. K. V. Rao, R. A. Delaney and M. G. Dunn, "Vane-Blade Interaction in a Transonic Turbine, Part I-Aerodynamics," *AIAA J. Propulsion and Power, 10*(3): 305–311 (1994).
75. J. C. Han and J. S. Park, "Developing Heat Transfer in Rectangular Channel with Rib Turbulators," *Intl. Heat and Mass Transfer, 31*(1): 183–195 (1988).
76. G. S. Azad, M. J. Uddin, J.-C. Han, H.-K. Moon and B. Glezer, "Heat Transfer in a Two-Pass Rectangular Rotating Channel with 45° Angled Rib Turbulators," 2001-GT-186 (2001).
77. J. C. Han and S. Dutta, *Internal Convection Heat Transfer and Cooling—An Experimental Approach*, VKI Lecture Series 1995-05, Parts I, II, III, IV (1995).
78. D. E. Metzger, W. B. Shepard and S. W. Haley, "Row Resolved Heat Transfer Variations in Pin Fin Arrays Including Effects of Non-Uniform Arrays and Flow Convergence," ASME Paper 86-GT-132, June (1986).
79. D. E. Metzger, C. S. Fan and S. W. Haley, "Effects of Pin Shape and Array Orientation on Heat Transfer and Pressure Loss in Pin Fin Arrays," *J. Eng. for Gas Turbines and Power, 106*: 252–257 (1984).
80. F. E. Faulkner, "Analytical Investigation of Chord Size and Cooling Methods on Turbine Blade Requirements," NASA CR-120882, pp. 189–194 (1971).
81. S. C. Lau, J. C. Han and Y. S. Kim, "Turbulent Heat Transfer and Friction in Pin Fin Channels with Lateral Flow Ejection," *J. Heat Transfer, 111*: 51–58, Feb. (1989).
82. D. M. Kercher and W. Tabakoff, "Heat Transfer by a Square Array of Round Air Jets Impinging Perpendicular to a Flat Surface Including the Effect of Spent Air," *ASME J. Engineering for Power, 92*(1): 73–82 (1970).
83. R. E. Chupp, H. E. Helms, P. W. McFadden and T. R. Brown, "Evaluation of Internal Heat Transfer Coefficients for Impingement Cooled Turbine Airfoils," AIAA Paper No. 68-564 (1968).
84. D. E. Metzger, R. T. Baltzer and C. W. Jenkins, "Impingement Cooling Performance in Gas Turbine Airfoil Including Effect of Leading Edge Sharpness," ASME Paper 72-GT-07 (1972).
85. R. Gardon and J. Cobonpue, "Heat Transfer Between a Flat Plate and Jets of Air Impinging on It," *International Developments in Heat Transfer Part II* (1961).
86. B. Glezer and H.-K. Moon, "A Novel Technique for the Internal Blade Cooling," ASME Paper 96-GT-181 (1996).
87. C. R. Hedlund, P. M. Ligrani, H.-K. Moon and B. Glezer, "Heat Transfer and Flow Phenomena in a Swirl Chamber Simulating Turbine Blade Internal Cooling," *ASME J. Turbomachinery, 121*: 804–813 (1998).
88. R. L. Webb, E. R. G. Eckert and R. J. Goldstein, "Heat Transfer and Friction in Tubes with Repeated-Rib Roughness," *J. Heat and Mass Transfer, 14*: 601–617, Pergamon Press (1971).

89. R. P. Dring, M. F. Blair and H. D. Joslyn, "An Experimental Investigation of Film Cooling on a Turbine Rotor Blade," *ASME J. Engineering for Power, 102*: 81–87 (1980).
90. K. Takeishi, S. Aoki, T. Sato and K. Tsukagoshi, "Film Cooling on a Gas Turbine Rotor Blade," ASME Paper 91-GT-279 (1991).
91. R. S. Abhari and A. H. Epstein, "An Experimental Study of Film Cooling in a Rotating Transonic Turbine," ASME Paper 92-GT-187 (1992).
92. O. Uzo and C. Camci, "Aerodynamic Loss Characteristics of a Turbine Blade with Trailing Edge Coolant Ejection Part 2, External Aerodynamics, Total Pressure Losses and Predictions," ASME Paper 2000-GT-258 (2000).
93. A. A. Ameri and R. S. Bunker, "Heat Transfer and Flow on the First Stage Blade Tip of a Power Generation Gas Turbine Part 2; Simulation Results," ASME Paper 99-GT-283 (1999).
94. J. P. Bindon, "Pressure and Flowfield Measurements of Axial Turbine Tip Clearance Flow in a Linear Cascade," Cambridge University Engineering Department, TR 123 (1986).
95. R. S. Bunker and J. C. Bailey, "Effect of Squealer Cavity Depth and Oxidation on Turbine Blade Tip Heat Transfer," ASME Paper 2000-GT-0155D (2000).
96. D. Dey and C. Camci, "Aerodynamic Tip Desensitization of an Axial Turbine Rotor Using Tip Platform Extension," ASME Paper 2001-GT-484 (2001).
97. N. W. Harvey and K. Ramsden, "A Computational Study of a Novel Turbine Partial Shroud," ASME Paper 2000-GT-668 (2000).
98. R. S. Bunker, "Review of Turbine Blade Tip Heat Transfer," Turbine 2000 Symposium on Heat Transfer in Gas Turbine Systems, Cesme, Turkey (2000).
99. NASA Report, "Liquid Rocket Engine Turbopump Rotating Shaft Seals," SP-8121 (1978).
100. J. G. Ferguson, "Brushes as High Performance Gas Turbine Seals," ASME Paper 88-GT-182 (1988).
101. B. Meierhofer and C. J. Franklin, "An Investigation of a Preswirled Cooling Airflow to a Gas Turbine Disc by Measuring the Air Temperature in the Rotating Channels," ASME Paper 81-GT-132 (1981).
102. M. Wilson, R. Pilbrow and J. M. Owen, "Flow and Heat Transfer in a Preswirl Rotor–Stator System," *ASME J. Turbomachinery, 119*: 364–373 (1997).
103. Z. El-Oun and J. M. Owen, "Pre-Swirl Blade Cooling Effectiveness in an Adiabatic Rotor–Stator System," *ASME J. Turbomachinery, 111*: 522–529 (1989).
104. D. E. Metzger, W. J. Mathis and L. D. Grochowsky, "Jet Cooling at the Rim of a Rotating Disc," ASME Paper 78-GT-25 (1978).
105. R. P. Roy, G. Xu, J. Feng and S. Kang, "Pressure Field and Mainstream Gas Ingestion in a Rotor–Stator Disk Cavity," ASME Paper 2001-GT-0564 (2001).

106. J. M. Owen and R. H. Rogers, *Flow and Heat Transfer in Rotating-Disc Systems, Vol.1*, Research Studies Press, Taunton; UK Wiley, New York (1989).
107. J. M. Owen and R. H. Rogers, *Flow and Heat Transfer in Rotating-Disc Systems, Vol.2 Rotor–Stator Systems*, Research Studies Press, Taunton, UK; Wiley, New York (1995).
108. B. Glezer and M. Fox, Turbine Ingress Prevention Method and Apparatus, U.S. Patent 5759012 (1998).
109. A. H. Lefebvre, *Gas Turbine Combustion*, 2nd ed., Tailor & Francis, Philadelphia-London (1998).
110. G. E. Andrews, A. A. Asere, C. I. Hussain and M. C. Mkpadi, "Transpiration and Impingement/Effusion Cooling of Gas Turbine Combustion Chambers," Seventh International Symposium on Air Breathing Engines, Beijing, China, pp. 794–803, AIAA/ISABE 85-7095, Sept. (1985).
111. G. E. Andrews and C. I. Hussain, "Impingement Cooling of Gas Turbine Components," Tokyo International Gas Turbine Conference, pp. 67–74 (1983).
112. G. E. Andrews, A. A. Asere, M. C. Mkpadi and A. Tirmahi, "Transpiration Cooling: Contribution of Film Cooling to the Overall Cooling Effectiveness." ASME Paper 86-GT-136. *Int. J. Turbo and Jet Engines, 3*: 245–256 (1986).
113. G. E. Andrews and C. I. Hussain, "Full Coverage Impingement Heat Transfer: The Influence of Cross Flow," Presented at the AIAA/ASME/sAE/ASEE 23rd Joint Propulsion Conference, San Diego, AIAA Paper 87-2010 (1987).
114. B. Glezer, S. Greenwood, P. Dutta and H.-K. Moon, Combustor for a Low-Emissions Gas Turbine Engine, U.S. Patent 6,098,397 (2000).
115. K. A. Gardner, "The Efficiency of Extended Surfaces," *Trans. of ASME, 67*: 621–631 (1945).
116. D. M. Evans and M. Noble, "Gas Turbine Combustor Cooling by Augmenting Backside Cooling," ASME Paper 78-GT-33 (1978).
117. H.-K. Moon, T. O'Connell and B. Glezer, "Channel Height Effect on Heat Transfer and Friction in a Dimpled Passage," ASME Paper 99-GT-163 (1999).
118. S. Burkhardt, "Advanced Gas Turbine Combustor Cooling Configurations," *Proc. Intl. Symposium on Heat Transfer in Turbomachinery*, pp. 261–285, Begell House Bahr, D.W., Technology for Design of High Temperature Rise Combustors, AIAA Paper No. 85-1292 (1985).
119. D. A. Nealy, S. B. Reider and H. C. Mongia, "Alternate Cooling Configuration for Gas Turbine Combustion Systems," AGARD PEP 65th Meeting, Bergen (1985).
120. D. W. Bahr, "Gas Turbine Combustion and Emission Abatement Technology Current and Projected Status," *Proc. Intl. Gas Turbine Congress*, Kobe, Japan, pp. 15–25 (1999).
121. M. G. Dunn, "Convective Heat Transfer and Aerodynamics in Axial Flow Turbines," ASME Scholar Award Lecture 2001-GT-506 (2001).

122. K. Takeishi, S. Aoki, T. Sato and K. Tsukagoshi, "Film Cooling on a Gas Turbine Rotor Blade," ASME Paper 91-GT-279 (1991).
123. L. Zhang and M. Fox, "Flat Plate Film Cooling Measurement Using PSP and Gas Chromatography Techniques," 5th ASME/JSME Joint Thermal Engineering Conference, San Diego, CA (1999).
124. L. Zhang and R. Pudupatty, "Turbine Nozzle Leading Edge Film Cooling Study in a High Speed Wind Tunnel," 33rd National Heat Transfer Conference, Albuquerque, NM (1999).
125. L. Zhang and B. Glezer, "Indirect Turbulence Measurement in Gas Turbine Stages Using Heat Flux Probe," ASME Paper 95-GT-153 (1995).
126. S. A. Hippensteele, L. M. Russell and F. J. Torres, "Use of a Liquid-Crystal, Heater-Element Composite for Quantitative, High-Resolution Heat Transfer Coefficients on a Turbine Airfoil, Including Turbulence and Surface Roughness Effects," NASA TM-87355 (1984).
127. H. K. Moon and B. Glezer, "Application of Advanced Experimental Techniques in the Development of a Cooled Turbine Nozzle," ASME Paper 96-GT-233 (1996).
128. D. D. Metzger and D. E. Larson, "Use of Melting Point Surface Coating for Local Convection Heat Transfer Measurements in Rectangular Channels with 90-Degree Turns," *J. of Heat Transfer, Trans. ASME, 1098*: 48–54 (1986).
129. Z. Wang, P. T. Ireland and T. V. Jones, "A Color Image Processing System for Transient Liquid Crystal Heat Transfer Experiments," ASME Paper 94-GT-290 (1994).
130. L. A. Dorfman, *Hydrodynamic Resistance and Heat Transfer of Rotating Solids*, English trans., Oliver & Boyd, Edinburgh, London (1963).
131. B. Glezer, "Investigation of the Flow Between Rotating Disc and Stator," *Energetica*, *3*, University Press, Moscow (1969).
132. U. P. Phadke and J. M. Owen, "An Investigation of an Air-Cooled Shrouded Rotating Disc System with Radial-Clearance Seals," ASME Paper 82-GT-145 (1982).
133. D. E. Metzger, R. S. Bunker and G. Bosch, "Transient Liquid Crystal Measurement of Local Heat Transfer on a Rotating Disc with Impingement," ASME Paper 89-GT-287 (1989).
134. C. Camci, B. Glezer, J. M. Owen, R. G. Pilbrow and B. J. Syson, "Application of Theremochromic Liquid Crystal to Rotating Surfaces," ASME Paper 96-GT-138 (1996).
135. D. Bohn, B. Rudzinski and N. Surken, "Experimental and Numerical Investigation of the Influence of Rotor Blades on Hot Gas Ingestion into the Upstream Cavity of an Axial Turbine Stage," ASME Paper 2000-GT-284 (2000).
136. R. J. Moffat, "Describing the Uncertainties in Experimental Results," *Experimental Thermal and Fluid Science*, *1*(1): 3–17.
137. S. Goel, J. Cofer and H. Singn, "Turbine Airfoil Design Optimization," ASME Paper 96-GT-158 (1996).

138. I. Egorov, G. Kretinin, I. Leshcenko and S. Kostiuk, "Technology of Multipurpose Optimization of Gas Turbine Engines and Their Components," ASME Paper 98-GT-512 (1998).
139. R. Tappeta, S. Nagendra and J. Renaud, "A Multidisciplinary Design Optimization Approach for High Temperature Aircraft Engine Components," 35th Joint Jet Propulsion Conference, AIAA Paper 98-1819 (1998).
140. A. A. Khalatov, N. Syred, P. J. Bowen and R. Al-Ajmi, "Quasi-Two-Dimensional Cyclone Jet Cooling Configuration: Evaluation of Heat Transfer and Pressure Losses," ASME Paper 2001-GT-182 (2001).
141. G. Pamula, S. Ekkad and S. Acharya, "Influence of Cross-Flow Induced Swirl and Impingement on Heat Transfer in a Two-Pass Channel Connected by Two Rows of Holes," ASME Paper 2000-GT-235 (2000).
142. B. Glezer, "Integration of Multi-Disciplinary Factors into Turbine Cooling Design," ASME Paper 2001-GT-179 (2001).

5

Unsteady Flow and Aeroelasticity

L He

School of Engineering, University of Durham, Durham, England

INTRODUCTION

An unsteady flow may vary in time either randomly (turbulence) or periodically. It is the latter type that we are dealing with here. Regarding turbomachinery performances, there are two main aspects associated with unsteady flow effects: (1) aerothermal performance due to blade-row interaction and flow instability (stall/surge); (2) blade mechanical integrity due to flow-induced vibrations (forced response and flutter).

For conventional blading at design conditions, blade-row interaction effects (and unsteady losses) are normally small, and blades do not normally experience serious vibration problems. This should be self-evident considering current blading designs with high aerothermal efficiency have been achieved so far largely by using steady-flow methodologies. Consequently, the main design issues have been to find sufficient aerodynamic and aeroelastic stability margins. However, the drive in the future developments toward higher loads and more compact configurations will result in intensified unsteadiness even at design conditions, and its effects on time-averaged performances need to be assessed during a design process from a purely aerothermal point of view. In addition, the blade mechanical

integrity (stress levels) will have to be more adequately examined if aero loading is to be increased, which challenges widely used empirical design rules on blade flutter and forced responses. All these requirements would point to closer coupling and more simultaneous (concurrent) interaction between aerodynamic design and structural mechanical design, since a lengthy aeromechanical iterative path can be very costly.

The competitive situation demanding better understanding and prediction of unsteady effects is further compounded by "nonstandard" problems arising from increasingly important environmental concerns and legislation. For example, a situation may arise where a required low NOx combustion has to generate a large-scale circumferential temperature distortion which can pass through a 5-stage low-pressure turbine with little decay (Manwaring et al. 1997) [1]. The analysis of the blade aeromechanical responses in this kind of nonstandard environments is becoming a necessary part of standard procedures. An aero design that has a high efficiency in a normal undistorted flow condition but produces an excessive stress level under the distortion condition is obviously not to be accepted. A similar example is the increasing priority to reduce aerodynamics-related noise generation and propagation in future aero-engine developments due to increasingly important environmental concerns and legislation. Again, an aerodynamically efficient blading design will not be acceptable if its associated noise level (especially that of fans or LP turbines at off-design conditions) is high.

Today computation of unsteady turbomachinery flows has become a very active research and development area. Carefully executed and analyzed unsteady CFD computations have provided useful information and insights to help our understanding of complex unsteady flow problems. However, it needs to be recognized that with computer resources currently available, full-scale time-dependent CFD calculations for unsteady turbomachinery flows are still very expensive and are not suitable for daily design purposes. In order to make effective use of CFD methods, we need to have a clear appreciation of relevant flow physics and length scales and be aware of the capabilities as well as the limitations of different flow models and numerical methods.

In this chapter, various basic sources of periodic unsteady disturbances and their aerodynamic and aeroelastic impacts are described first. Relevant parameters controlling the basic unsteady flow characteristics are then described. Particular attention is paid to the role of circumferential wavelength. Finally several modeling issues on computational efficiency and accuracy are discussed.

SOURCES AND EFFECTS OF UNSTEADINESS

Propagation of Wake and Pressure Disturbances

Unsteady disturbances travel in the form of flow characteristics. Each characteristic has a distinct traveling velocity (magnitude and direction). Although the basic characteristics are obtained from the linear Euler equations (hence inviscid without any dissipation mechanisms), they are extremely useful as the basis for developing computational models, understanding flow physics, and interpreting computational (as well as experimental) results. For a 2D inviscid compressible flow with "V" being the local flow velocity and "A" the local speed of sound, there are four flow characteristics: (1) entropy disturbance, convected at a local flow velocity V, running downstream; (2) vorticity disturbance, convected at local velocity V, also running downstream; (3) an acoustic (pressure wave) disturbance, propagated at a speed of $V + A$, always running downstream; and (4) another acoustic (pressure wave) disturbance, propagated at a speed of $V - A$, which runs either upstream for a subsonic flow, or downstream for a supersonic flow.

In a turbomachinery context, the spatial nonuniform velocity and pressure distributions in a blade row are sensed as unsteady disturbances in adjacent blade rows. More specifically, wakes shed from upstream blades contain both entropy and vorticity components and normally have little static pressure nonuniformity (until they impinge on downstream blades). Therefore, a wake disturbance is convected downstream at a local flow velocity. An example is shown in Fig. 1, where incoming unsteady wakes are convected through a turbine passage and distorted in the nonuniform velocity field. For both compressor and turbine situation, a wake disturbance mainly affects downstream rows, though unsteady pressures generated when it hits the downstream blade also propagate upstream.

On the other hand, nonuniform "steady" static pressure necessarily associated with blade loading in one blade row can be seen as unsteadiness by both upstream and downstream relatively moving blade rows, assuming that the axial-flow velocity is subsonic. The propagation of acoustic (pressure) waves is largely an inviscid phenomenon, which is probably why an interference with unsteady pressure disturbances is often called "potential interaction." Wakes have measurable velocity gradients and therefore viscous dissipation always coexists with wake convection, although the kinemics of wake convective transportation itself can be described in an inviscid manner. An example of the potential interaction can be seen in Fig. 2 for a transonic turbine stage, where pitchwise nonuniform pressures of the upstream stator interact with the rotor in a complex manner, largely due to reflection of pressure disturbances. It is noted from

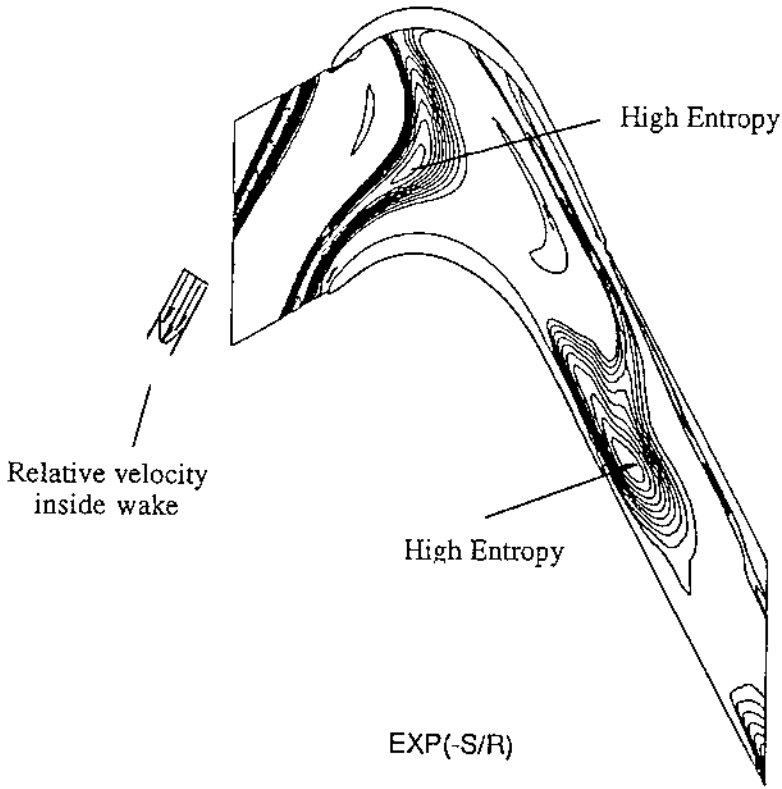

Figure 1 Instant entropy contours of turbine blade passage subject to incoming wakes.

these snapshot contours that the downstream stator passage is more affected by the potential interaction. This is typical because of higher loading and flow speed in the rear part of turbine blading. Conversely for a compressor case, an upstream blade row will typically be more affected by a potential interaction, because of a typical frontal loading of the downstream row.

Blade-Row Interference Effects

Having had some basic ideas about how unsteady disturbances propagate, now we look at the aerodynamic and aeroelastic impacts due to the inherent blade-row relative motion.

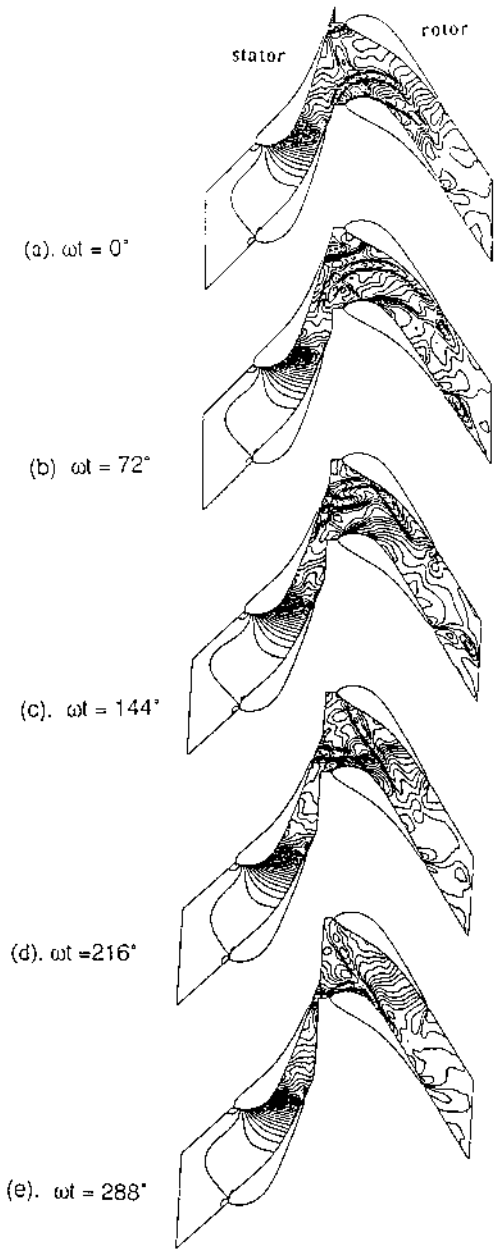

Figure 2 Instant static pressure contours for a transonic turbine stage.

Aerodynamic Interaction (Unsteady Losses)

Regarding aerothermal influences of a wake shed from an upstream blade on a downstream relatively moving blade row, there are several different but related issues:

1. *How do we quantify flow loss in an unsteady environment*?
2. *How is the mixing loss of wake velocity deficit influenced by the presence of a downstream blade row*?
3. *How does a wake disturbance affect the loss generation of downstream blade rows*?

Entropy/stagnation Pressure Decoupling. This is a basic issue concerning transportation of flow losses in an unsteady environment, relevant to presentation and interpretation of unsteady losses computationally and experimentally. For a thermodynamic process, we have

$$T_0 dS = dh_0 \frac{1}{\rho_0} dP_0 \tag{1}$$

Hence, in a *steady* adiabatic flow situation, a higher entropy is always associated with a lower stagnation pressure, because the stagnation enthalpy h_0 remains constant along a streamline. Essentially, stagnation pressure deficit is a proper measure of entropy rise (loss) in steady flows. For an unsteady flow, however, this is not the case. Neglecting the viscous and heat conduction terms, the unsteady energy equation can be written as

$$\frac{dh_0}{dt} = \frac{1}{\rho} \frac{\partial P}{\partial t} \tag{2}$$

Therefore, $h_0(T_0)$ will not be constant along a stream line if static pressure is varying in time, as it would be once an unsteady wake impinges on blade surface.

An inviscid unsteady flow calculation by the author [2] for a low-pressure turbine cascade subject to periodic unsteady incoming wakes is used to illustrate this point. Wakes shed from the upstream blade row are modeled by specifying inlet wake profiles, traveling relatively in the circumferential direction at the rotor rotating speed. As can be seen from the instantaneous entropy contours (Fig. 1), for the region upstream of the blade passage, wakes are convected at an essentially uniform velocity, and the time-averaged stagnation pressure and entropy would be more or less uniformly distributed along the pitch upstream of the blade row. By looking at the velocity triangles, we can see that within the wake there would be a relative velocity component. The entropy within a moving wake is thus convected relatively along the wake. Each wake first hits the pressure surface

and acts like a "negative jet" [3]. Kinematically, these "negative jets" effectively convect the high entropy within the wake toward the suction surface (recall that entropy disturbances are convected at a local flow velocity). If we look at the pitchwise distribution of time-averaged flow parameters downstream of the blade row, we should have a higher loss (entropy) region near the suction surface. This can be shown in Fig. 3(a), which is the pitchwise distribution of time-averaged entropy rise at the exit plane (about 50% chord downstream of the trailing edge). However, due to unsteadiness, stagnation pressure deficit is decoupled from entropy rise in this unsteady flow case, as shown in Fig. 3(b). Note that at the position around 60% pitch, we have a peak of stagnation pressure deficit, while the entropy rise is almost zero at the same position! Therefore, in an unsteady situation, the time-averaged stagnation pressure variation might not correspond to the true flow loss (time-averaged entropy rise) at all.

Wake/blade-row Interaction. First of all, we note that the velocity deficit of a wake shed from an upstream blade row will be eventually mixed out, resulting in mixing loss. What is the effect of a downstream relatively moving blade row on this mixing loss generation process? There are some theories in a 2D context that the wake mixing loss can be reduced ("recovered") when passing through a compressor blade row, but it would be increased when passing through a turbine row [4, 5]. The argument is based on a simple kinematic consideration as shown in Fig. 4. One can see that a wake passing through a compressor passage [Fig. 4(a)] is "stretched" (elongated) by the velocity difference between the suction surface and pressure surface, noting again a wake is convected at a local flow velocity. We can simplify the argument by first considering how the velocity deficit would be changed in a purely inviscid flow situation, and then thinking about the consequent mixing loss due to the viscous dissipation of the resultant velocity deficit. An inviscid argument based on the conservation of total vorticity (Kelvin theorem) would give a reduced velocity deficit in this stretched wake. It follows then that the corresponding mixing loss of the wake passing through a downstream compressor blade row will be smaller in comparison to that when the wake were mixed out in absence of the downstream blade row. Following the same reasoning, one can reach the opposite conclusion for an unsteady wake passing through a turbine blade row [Fig. 4(b)] where the velocity deficit is enlarged (hence larger viscous dissipation and mixing loss) since the wake is "compressed" due to the corresponding velocity difference between the suction and pressure surfaces. A corollary is that a smaller intrarow gap should reduce wake-mixing losses for compressors, but not for turbines.

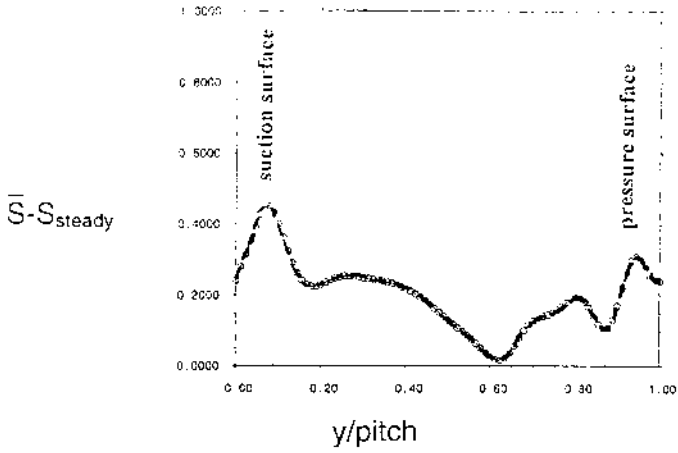

(a). Entropy Rise

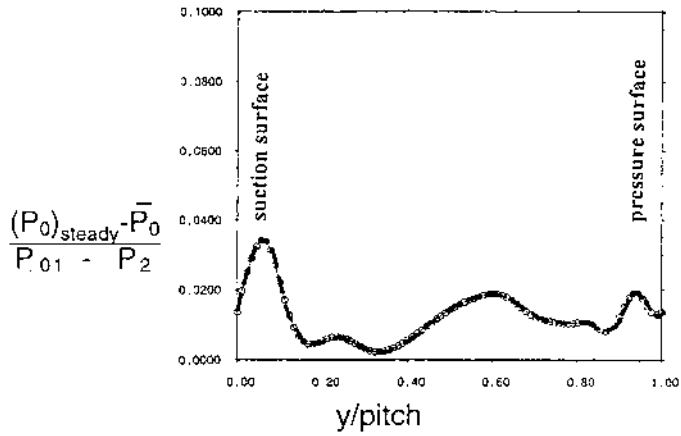

(b). Stagnation Pressure 'Loss'

Figure 3 Pitchwise time-averaged entropy rise and stagnation pressure distributions (downstream of a turbine cascade subject to incoming wakes).

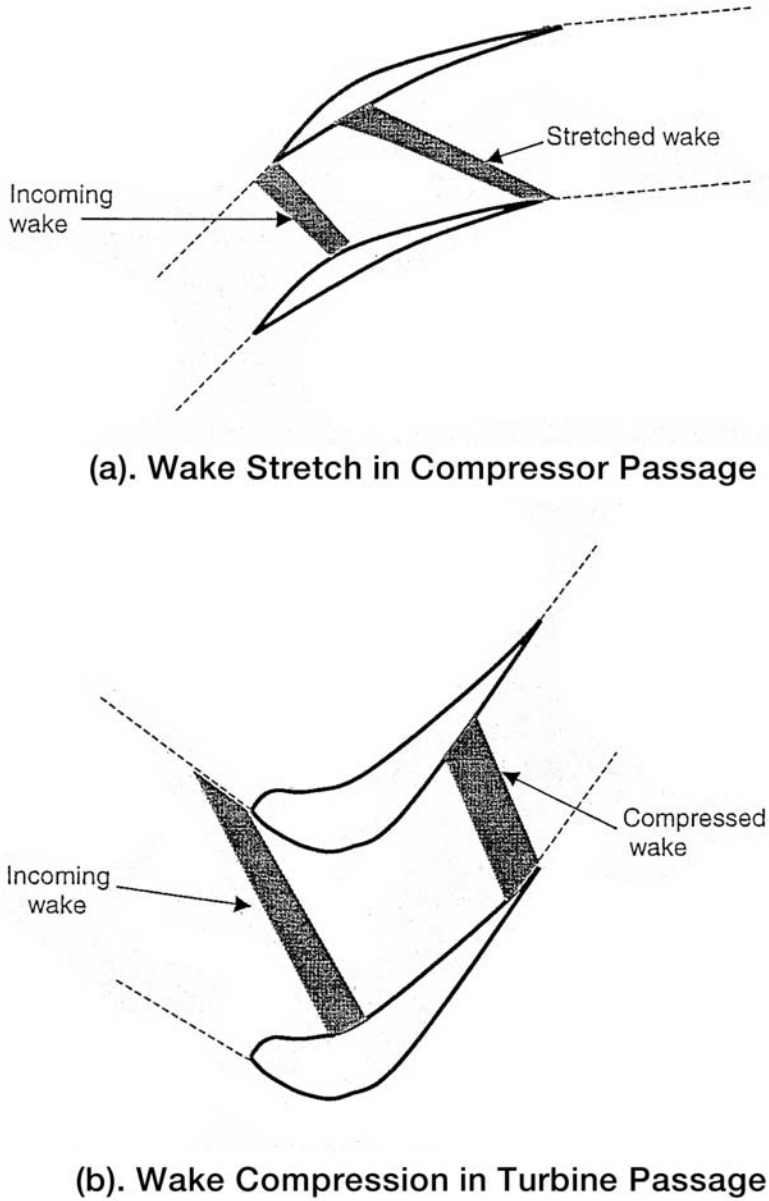

Figure 4 Schematic of wake distortion through a downstream blade row (*kinematics due to suction/pressure surface velocity difference*).

The above considerations are all for pure 2D and highly simplified situations. It should be noted that even in a 2D case with realistic blading geometry, wakes may not be stretched all the time in a compressor passage or compressed all the time in a turbine passage as depicted in Fig. 4. The 2D computational result in Fig. 1 shows just how the wakes can be both compressed in the frontal passage part and stretched in the rear in addition to being distorted, giving a much more complex picture.

Furthermore, attention is drawn to the very 3D nature of wake–blade row interaction in the near end-wall regions. An unsteady wake shed from an upstream row is characterized by the cross-passage transportation by the ''negative jet'' within the wake, which convects low-momentum fluid from the pressure surface to the suction surface for turbines and conversely for compressors. On the other hand, end-wall flows in the blade row under consideration are characterized by 3D secondary flow structures with dominant streamiwse vorticity, e.g., passage vortex, tip-leakage vortex. A basic feature of all these 3D flow structures is that the associated cross-passage fluid movement near an end wall has an opposite sense to that close to midspan. Here one can use a simple ''phasing'' argument to examine the interaction between an incoming largely 2D unsteady wake with a 3D ''steady'' passage vortex. Just imagine two separate activities that could behave linearly and thus be superimposed. One is the 2D incoming wake, and the other is a steady passage vortex. Note that the sense of the cross-passage fluid movement due to the incoming wake is the same regardless of spanwise positions, while the cross-passage movement due to the passage vortex changes the directions depending on the spanwise position. In the very near-wall regions, the low-energy fluid is transported by the passage vortex from the pressure to the suction surface and thus is in the same direction as the wake transportation (for a turbine). On the other hand, in a region away from the end wall, the cross-passage movement due to the passage vortex will have an opposite sense to that due to the wake. Consequently, the resultant flow structure when a 2D wake is interacting with a passage vortex will have to be strongly 3D. The suppression or enhancement of cross-passage movements at different spanwise sections has been shown to generate a radial redistribution time-averaged entropy loss in comparison with a steady flow without incoming wakes [6]. Given that a major portion of aerodynamic losses is generated in highly 3D end-wall regions for typical blading designs, one does need to be cautious in applying the 2D flow arguments. More work is needed to identify 3D blade-row interaction effects and understand the corresponding mechanisms.

Rotor–rotor Interaction (Clocking and Aperiodic Effects). If a wake is not completely mixed out after passing through the immediate downstream blade row, the remaining disturbance will interfere with a further downstream but relatively stationary blade row, causing a rotor–rotor (or stator–stator) interaction. Although by intuition we might expect much smaller rotor–rotor (or stator–stator) interactions than rotor–stator interactions, the picture is not entirely clear and may vary depending on different designs and flow conditions. It can be argued that rotor–rotor (stator–stator) interactions should be much smaller in compressors than in turbines because of the wake recovery mechanism described earlier. Some recent analysis using a multistage computational method [7], however, indicates a marked difference between a rotor–rotor interaction and a stator–stator interaction in a transonic compressor.

We first note that the effects of rotor–rotor (or stator–stator) interactions strongly depend on blade counts. This can be highlighted in two extreme cases: (1) both rotors have the same number of blades; and (2) two rotors have such different blade counts that a relative circumferential positioning between two blades in the two rows can only repeat after the whole annulus. Consider a two-stage compressor consisting of rotor-1, stator-1, rotor-2, and stator-2. If both rotors have the same blade count, every blade passage in one rotor row will see the same pattern of spatial (time-averaged) disturbance from the other blade row. Hence the time-averaged rotor–rotor interaction pattern will be spatially periodic with a wavelength of one blade pitch. In this case, we can change the relative circumferential position (clocking or indexing) between the two rotors by up to one blade pitch. Thus, for the case with an equal rotor blade counts, we have the full range (one pitch) to identify the maximum clocking effect.

However, the clocking effect can be significantly reduced when the two rotors have different blade counts. For example, if rotor-1 has 21 blades and rotor-2 has 20 blades, then adjacent blades in rotor-2 will have slightly different circumferential positions relative to their counterparts in rotor-1, and the maximum clocking range would only be 1/20 blade pitch. In this case, although the clocking effect is expected to be negligible, the time-averaged flow patterns in the passages in each rotor row will not be spatially periodic. This aperiodic effect needs to be assessed if a single-passage domain/traverse area is adopted for either computation or experimental measurement. It is worth pointing out that for rotor-2, although the magnitude of velocity deficit of wakes from rotor-1 might be smaller than those from the immediate upstream stator row, the circumferential wavelength of the disturbance due to the rotor–rotor interference mode might be much longer. In this case with 21 rotor-1 blades and 20 rotor-2

blades, the wavelength of the disturbance is the whole circumference. As will be discussed later, disturbances with long circumferential length scales can have marked effects on downstream blade rows.

So far, most of clocking studies have been carried out for stators, e.g., the experimental work for a low-speed compressor by Barankiewicz and Hathaway [8]. Rotor–rotor interactions (clocking and aperiodicity) might, however, behave differently in particular when a downstream rotor row is transonic. A relevant mechanism to be taken into consideration is that associated with the passage shock wave of rotor-2 interacting with the wake shed from rotor-1. The mixing loss of a wake would be higher when the wake is subject to an adverse pressure gradient [9]. Thus, in this transonic "mean" flow condition, the mixing loss of rotor-1 wake is certainly expected to rise when passing through the rotor-2 passage shock wave, as shown by the schematic in Fig. 5. Given that the strength of the rotor passage shock varies pitchwise (typically stronger near the suction side), it would not be surprising that the rotor–rotor interaction loss is dependent on the clocking position.

In contrast to typical flow conditions for transonic rotors, the "mean" flow in which two stator rows interact is subsonic. Therefore, it seems reasonable to expect more pronounced rotor–rotor interference (aperidoic

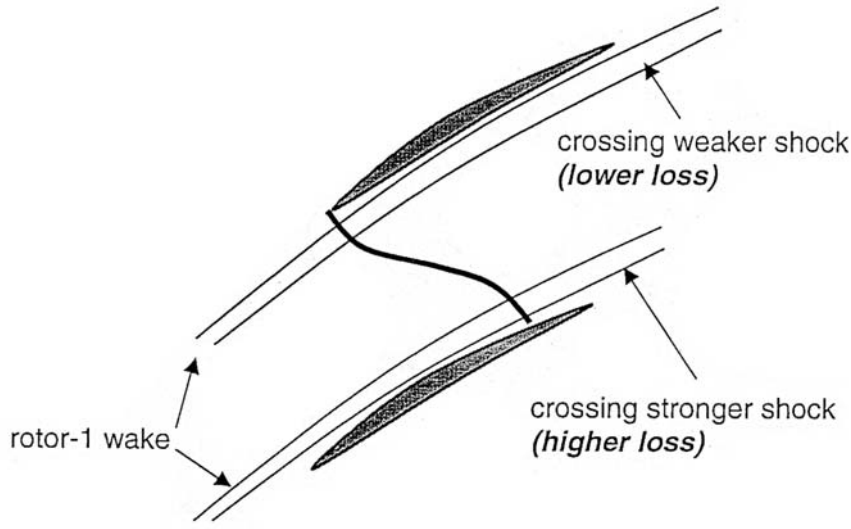

Figure 5 Rotor-1 wakes crossing rotor-2 passage shock at two different clocking positions.

and/or clocking) effects than their stator–stator counterparts for transonic compressors.

Aeroelastic Interaction (Blade Forced Response)

All the aforementioned interaction effects are of a pure aerodynamic nature where the main concern is the corresponding *time-averaged* unsteady losses resulting from the interactions, which are usually small. The blade mechanical responses under those unsteady disturbances can have very important consequences. Excessive stress levels at a blade resonant condition, in which the frequency of an unsteady disturbance coincides with that of a particular blade vibration mode, may occur due to lack of damping (aerodynamic and/or mechanical). The frequencies of the blade vibration modes at risk can be identified from the Campbell diagram (Fig. 6), when the frequency curves (e.g., those for the first flap "1F" and the first torsion "1T") cross the engine order excitation lines (1EO, 2EO . . .). Even if the designer can choose an appropriate condition to avoid resonance at design, it is difficult or impossible to do so at off-design conditions. When the machine is started off or shut down, blades will have to go through some resonance conditions, and it is important to be able to assess the unsteady

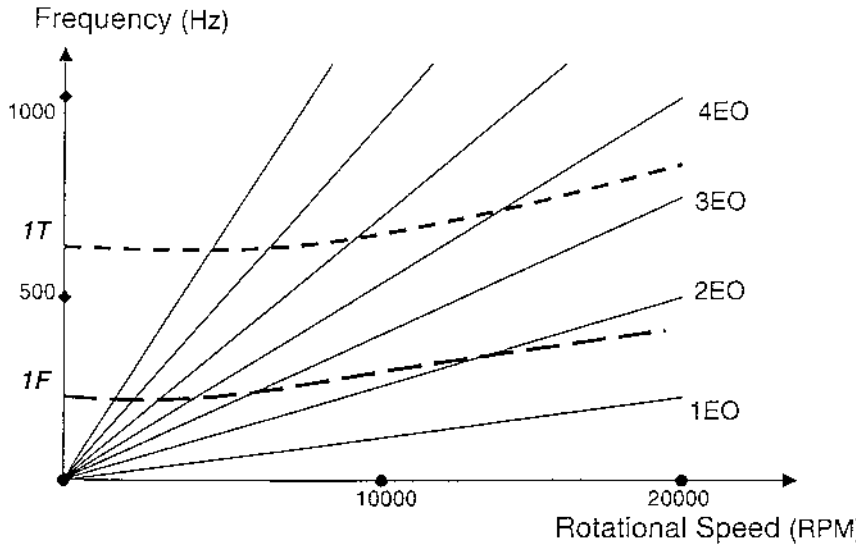

Figure 6 Campbell diagram.

forcing and damping, and hence the blade stress levels at these crossing-over points. Given that a component fatigue cycle life span is inversely related to alternating stress levels, high cycle fatigue has to be an important blading design aspect, if blades are to be designed to last for a required life span to give an optimum economic benefit (e.g., in terms of manufacture as well as maintenance costs) and reliability.

The aerodynamic sources of excitation (forcing) are those nonuniformities due to blade wakes, pressure waves, and inlet/exit distortions. On the aerodynamic side, there are two essential parts required for predicting a blade stress level in a forced response problem:

1. Unsteady aerodynamic forces on blades generated by relative motions of adjacent blade rows and/or circumferential distortions
2. Aerodynamic damping, effectively the unsteady aerodynamic forces induced by vibration of a blade once excited

Predictions of unsteady forcing/excitation as well as blade aerodynamic damping with adequate accuracies are challenging tasks. In the past they were largely avoided by adopting empirical design rules based on experiences. But this situation with regard to blade forced response is about to change. Currently, there are active developments in using advanced unsteady flow methods to improve the capability for forcing and damping prediction, as required for current and future high-load blading designs.

There are some basic aeromechanical considerations in designs. The main objective here is, of course, to reduce or sustain unsteady forcing, when steady aero loading is increased. It has been shown that the main contributor to unsteady forces in compressors is the incidence variation, while the velocity variation in wakes is mainly responsible for forcing in turbines [10]. The 3D blading with radially leaned blades is widely used in designs. Although the leaned blading may well be chosen to reduce aerodynamic losses from a steady flow point of view, it does have a lower unsteady loading compared to a radially straight one, since a wake shed from an upstream blade with radial staking will not hit different radial sections of a downstream blade at the same time (a simple example of 3D relief of unsteady loading). Given that 3D blading designs are currently exploited for benefits in aerodynamic performances, it is equally (if not more) important that such 3D aerodynamic designs are aero-mechanically sound.

Self-Excited Unsteadiness

All the unsteady disturbances generated by blade-row interactions share one common feature. Their frequencies are simply related to rotor speed and blades counts in a form

$$f = N_n f_r \tag{3}$$

Where

f_r is the machine rotation speed (in Hz).
N_n is the number of blades in the exciting row (in general, N_n is the number of nodes of a circumferential distortion pattern rotating relatively at a frequency f_r).

On the other hand, when an unsteady flow pattern is triggered by a self-excited aerodynamic or aeroelastic instability, there would be no such simple frequency correlation.

Aerodynamic Instability

Vortex Shedding and Self-excited Shock Oscillation. Vortex shedding is a significant source of profile loss for turbine blading with a thick trailing edge [9]. Prediction of the base pressure at the trailing edge is dictated by proper modeling of unsteady periodic vortex shedding. But for most steady CFD methods used in current blading designs, the trailing-edge vortex shedding phenomenon and its associated effects on profile loss are completely missed out. Even when a time-accurate method is adopted, vortex shedding may still not be captured due to excessive numerical dissipation and/or inadequate mesh resolution. An alternative approach is to introduce the deterministic stress terms to the *steady* flow equations, and it has been shown that a time-independent solution of the time-averaged flow field due to a vortex shedding can be obtained by using a steady flow solution method [11]. For an unsteady flow field influenced by unsteadiness with a short wavelength, the spatial gradient can be much steeper than its time-averaged counterpart. Hence, a time-independent solution to the time-averaged flow equations would not demand as high resolution as a time-domain unsteady calculation. A practical question that remains to be answered is how to model the deterministic stresses without resorting to full time-domain unsteady calculations.

In an undisturbed flow, frequency characteristics of a vortex shedding are largely dependent on the boundary-layer state and the geometry of the trailing edge. However, its frequency can be easily locked into frequencies of external disturbances. For example, in a turbine stage configuration, a shedding from the upstream blade row can be locked into the blade passing

frequency and its higher harmonics [12]. Furthermore, because of its sensitivity to flow conditions, vortex shedding may well couple with other oscillatory acoustic or blade structural dynamic modes, and act as an excitation source.

For passage shock oscillations, the flow physical mechanism is typically associated with shock/boundary-layer interaction, resulting in a thickened or separating boundary layer at the foot of passage shock wave. The oscillating shock patterns (frequencies) are very often suspected to be associated with acoustical modes within blade passages, similar to those found in transonic ducts (e.g., [13]). An oscillating shock wave produces a higher time-averaged loss than its steady counterpart. The existence of shock oscillation can be easily identified from "steady" (time-averaged) experimental data showing a "smeared" shock wave. The range of smearing is normally a pretty good indication of the magnitude of the shock oscillation.

Rotating Stall. Rotating stall is a circumferential flow instability, which is normally regarded as a precursor of compressor and engine surge. Apart from seriously detrimental effects on aerodynamic performances, it should also be noted that stall onset generates severe blade vibration problems. The vortical and reversal flow pattern produces transient aerodynamic loading of a considerable magnitude, causing blades to be overstressed. There is a need to estimate the maximum stress level in this fairly hostile environment, especially if the stability boundary can only be identified by crossing the boundary during experimental rig tests.

There has been a considerable amount of work recently resulting in enhanced understanding of stall inception mechanisms based on experimental observations, e.g., [14]. It should also be mentioned that full-scale CFD simulations of stall inception have started to emerge which can help to understand complex physical mechanisms involved and identify relevant influencing parameters. For instance, computational studies using an unsteady Navier–Stokes time-domain flow solver for a compressor stage indicate that the initial stall inception pattern (number of cells, circumferential wavelength, and rotating speed) corresponds to that set by rotor–stator blade counts [15]. Figure 7 shows the results at an initial stage of stall inception for the rotor and stator rows with blade numbers of 10 and 12, respectively. With these blade counts, the rotor and stator disturbances beat circumferentially twice per rotor revolution, resulting in an interference disturbance with a wavelength of half an annulus. This should explain why a two-cell structure is triggered as shown by a snapshot of entropy contours at the inception [Fig. 7(b)]. Figure 7(a) shows the time traces of axial velocities from four circumferential stationary positions upstream of the rotor row.

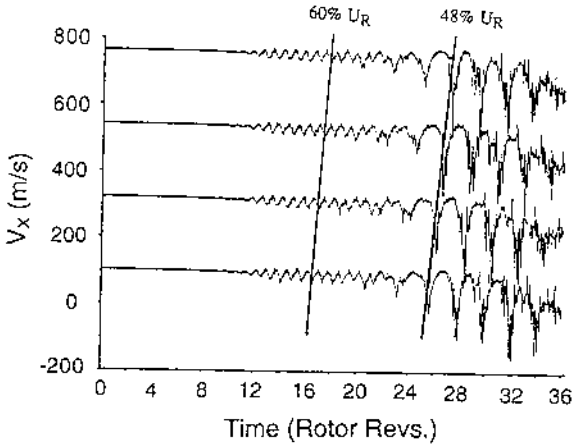

(a). Time traces of axial velocity from 4 circumferential positions upstream of rotor

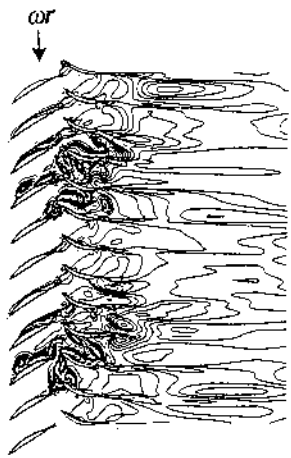

(b). Instantaneous Entropy Contours
(Two-cell Pattern at Initial Stage of Stall Inception)

Figure 7 Navier–Stokes solution of stall inception for a compressor stage configuration (10 rotor blades, 12 stator blades).

The two-cell pattern with a relatively short circumferential wavelength rotates in the absolute frame of reference at a faster speed (60% of rotation speed) before merging to a more common single-cell pattern rotating at a slower speed (48% of rotation speed). However, if the rotor–stator blade counts are such that the interference wavelength is the whole annulus, a single-cell pattern will be triggered directly, as shown in Fig. 8, where the rotor and stator blade numbers are 10 and 9, respectively. The overall observation is that although a single-cell pattern rotating at about 50% rotor speed is the most common one, a multiple-cell structure might occur at an initial stage of stall inception if the stalling blade row is subject a distortion disturbance of the same circumferential wave pattern. A numerical analysis of 3D unsteady CFD results for a fan rotor at subsonic and relatively supersonic flow conditions [16] suggests that the basic stall inception mechanisms in high-speed transonic flows might be qualitatively different from that at low speeds due to the difference between propagating information upstream in subsonic flow and in supersonic flow.

So far, most of the research activities are largely aimed at providing detailed (even qualitative) information to help understanding, motivated by the prospect of active control/depression of rotating stall. We must appreciate that true prediction of exact stall onset conditions for determining suitable stall margins during designs is still extremely difficult, depending strongly on numerical resolution, turbulence modeling, and boundary condition treatment of truncated computational domains.

Aeroelastic Instability (Flutter)

Blade flutter is a self-excited aeroelastic instability phenomenon. When working blades are disturbed aerodynamically or mechanically, they tend to vibrate in their natural modes with small amplitudes, which will in turn induce unsteady aerodynamic forces. At certain conditions, the unsteady forces resulting from the initial blade vibration will do a net work (energy input) to the blade in each period of vibration. As a result, the initially small vibration will be amplified and the instability (flutter) will occur, often leading to blade failure if there is not enough mechanical damping to dissipate the energy.

Flutter can be a serious problem for frontal stages of compressors, in particular fans of aero-engines, and needs to be addressed during a design process. Figure 9 shows typical blade flutter boundaries in an axial-flow compressor/fan performance map. Corresponding aerodynamic conditions of the instabilities are indicated by the names given, which clearly suggest that steady and unsteady aerodynamics play an essential part in the aeroelastic instability. At low off-design speeds, danger exists under high

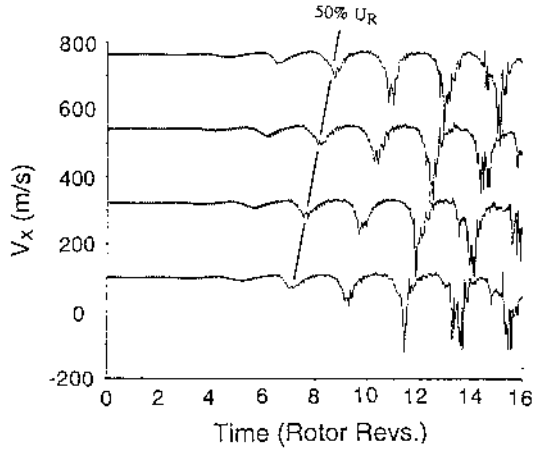

(a). Time traces of axial velocity from 4 circumferential positions upstream of rotor

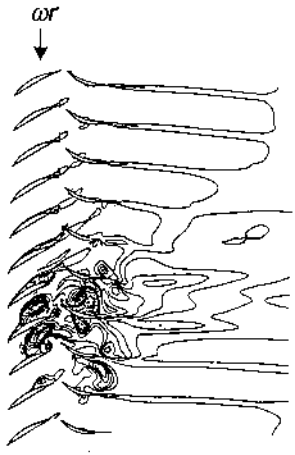

(b). Instantaneous Entropy Contours
(**Single-cell Pattern** at Initial Stage of Stall Inception)

Figure 8 Navier–Stokes solution of stall inception for a compressor stage configuration (10 rotor blades, 9 stator blades).

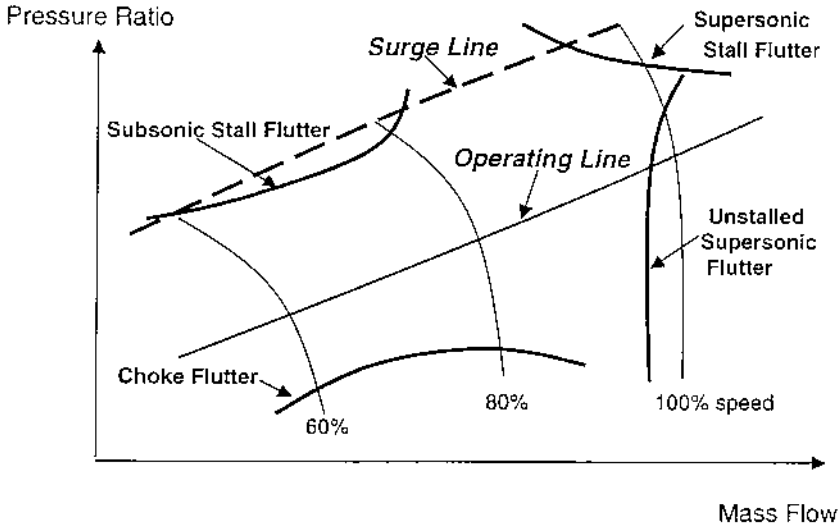

Figure 9 Typical blade flutter boundaries on compressor map.

incidence (high-pressure ratio) conditions, where flow separation on the blade suction surface is likely to occur. The highly loaded blades (especially with separating boundary layers) are very sensitive to small disturbances and a separating flow pattern can easily couple with blade vibration, giving a negative aerodynamic damping (i.e., a net energy input to blade vibration). At higher operating speeds, a strong shock system is expected to play a role in flutter onset, either by intensive unsteady loading around an oscillating shock ("supersonic unstalled flutter") or by inducing periodic boundary-layer separation ("supersonic stalled flutter"). At medium speeds, throttle opening (reducing incidence) might lead to choked blade passages, where a supersonic region is ended by a weak shock wave. This kind of transonic flow pattern is very "stiff" and can produce a large flow response to a small disturbance and is likely to be responsible for "choke flutter."

It must be pointed out, however, that these names of the flutter boundaries need to be taken with caution—the real mechanisms may be far more complicated than they suggest. For instance, although it is expected that "subsonic stall flutter" should be associated with separated flows, there have been some experimental results showing that this may not necessarily be the case [17], and it is argued the instability may be better called "high incidence flutter."

Flutter has been mainly a problem on the compressor/fan side, but turbine flutter (especially of low-pressure stages) has also been of concern.

Overall it is fair to say that because of the complex aerodynamic and aeroelastic mechanisms involved in these instabilities, both current understanding and predictive capability are far from being satisfactory. The situation will be more pressing as the trend of future designs heads toward higher aero loading.

RELEVANT PARAMETERS

Reduced Frequency

One of the most important parameters for unsteady flow problems is the *reduced frequency* defined as

$$K = \frac{\omega L}{V} \tag{4}$$

Where

$\omega = 2\pi f$ is the angular frequency.
f(Hz) is the physical frequency of the unsteadiness.
L is a reference length scale, usually taken to be the chord length C.
V is a reference velocity, usually taken to be the inlet flow velocity.

The reduced frequency can be interpreted as

$$K = \frac{\text{time scale for flow particles to be convected over } 2\pi L}{\text{time scale of unsteadiness}} \tag{5a}$$

or

$$K = \frac{2\pi L}{\text{spatial length scale of a convected wave}} \tag{5b}$$

When modeling an unsteady flow problem, one must ensure that the reduced frequency is the same as that in the real situation. The reduced frequency is a measure of both temporal and spatial length scales. Thus at a high reduced frequency, we need to use a scheme with high enough temporal accuracy as well as fine enough spatial resolution since the high-frequency unsteadiness would vary on a short spatial length scale.

As a simple measure of a true unsteady behavior against a steady one, if the reduced frequency is much smaller than 1 (say $K < 0.1$), the behavior can be regarded as *quasi-steady*, then the time-derivative terms in the unsteady flow equations (and hence the temporal accuracy) can simply be neglected. In other words, at each time instant, an effectively steady flow

field is generated to satisfy the time-varying boundary conditions at that instant.

For unsteady flows in turbomachinery, values of the reduced frequency vary considerably. Resolving all different frequencies (length scales) will be extremely difficult. Before doing unsteady flow calculations, we should have some ideas about the relevant length scales of interest, so that adequate and efficient discretization schemes and mesh arrangements can be adopted.

For rotor–stator interactions, unsteadiness experienced by a blade row is caused by pitchwise blade-to-blade nonuniformities of adjacent blade rows. Obviously, the dominant spatial length scale would be the blade pitch (or chord) length, and the time scale would be blade passing period. A typical value of the reduced frequency is about 5–10.

A high-frequency (short spatial wavelength) example is the blade trailing-edge vortex shedding. By analogy to the Karman vortex street behind a cylinder, the corresponding spatial length scale is of the blade trailing-edge thickness δ, and the corresponding time scale is mainly subject to the convection time δ/u, where u is the free-stream velocity. Both the temporal and the spatial length scales may be by one order of magnitude smaller than those due to rotor–stator interactions. A low-frequency (long wavelength) example is a rotating stall. A typical stall cell can cover several blade passages and circumferentially travels at a speed about 50% of the blade rotation speed. So both the temporal and spatial length scales can be much longer than those for rotor–stator interaction problems.

For blade flutter problems, the time scale is given by the blade vibration frequency. Usually the chord length is taken as the reference length scale. A typical value of the reduced frequency for the first bending/flap mode is around 0.3, while that for the first torsion is around 1. Simple aeroelastic design guidance can be based on the observations that blades tend to flutter in low-order vibration modes and are less stable at lower frequencies. Thus, blade-reduced frequencies need to be above certain (empirical!) limiting values, e.g., $K > 0.2$ for the first bending/flap and $K > 0.6$ for the first torsion mode. These can be achieved by either increasing blade natural frequencies (stiffness) or reducing flow velocity (loading).

Blade Count and Interblade Phase Angle (Influence of Circumferential Wavelength)

All practical turbomachinery stages have different numbers of blades in neighboring rotor and stator rows to avoid resonance. And this difference in blade counts defines the circumferential interference wavelength. Consider a hypothetical compressor stage, for instance. If we have 10 rotor blades and 9

stator blades, the unsteady disturbances from the two rows can only "beat" each other after the whole annulus, so the circumferential wavelength is the whole annulus, as indicated by the instantaneous static pressure pattern shown in Fig. 10. On the other hand, if the stator blade number is changed to 12, the two rows beat twice for the whole annulus, so the wavelength is half the annulus (Fig. 11). The fundamental interference wavelength is thus determined by the difference of the blade numbers of the two blade rows.

On the aeroelastic side, for both flutter and forced response problems we have similar patterns. Vibratory patterns of blade and disk assemblies are typically featured by a cyclic symmetry mode, rotating circumferentially at a constant speed. For this kind of traveling wave modes, the radial lines with zero displacements are called "nodal diameters". So the circumferential wavelength is defined by the number of nodal diameters.

In both blade-row aerodynamic interaction and aeroelastic problems, each blade will be subject to unsteadiness of a circumferential traveling wave pattern. Since the circumferential wavelength is not the same as the blade pitch (usually much longer for those problems of interest), we no longer have the direct periodicity between adjacent blade passages. Instead, there is

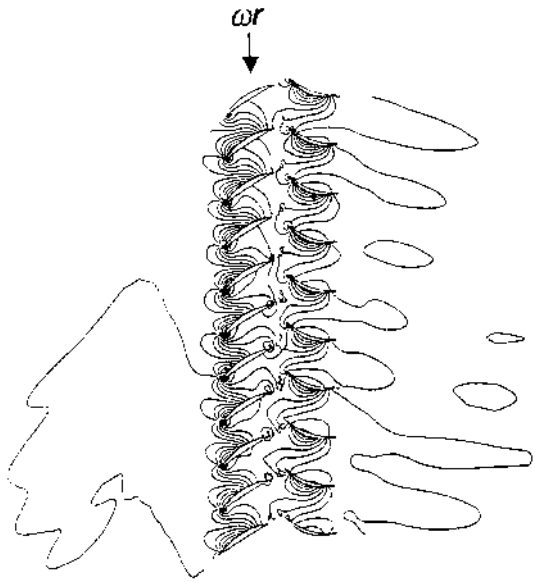

Figure 10 Instant static pressure contours (NBr = 10, NBs = 9, circumferential interference wavelength = whole annulus).

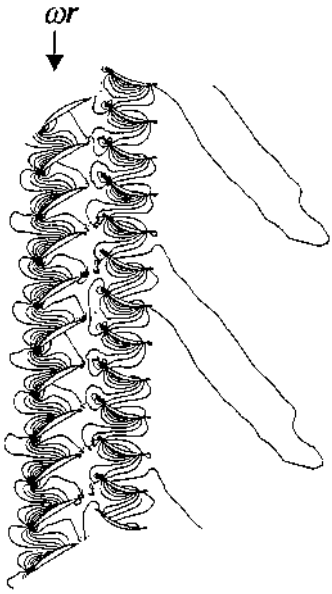

Figure 11 Instant static pressure contours (NBr = 10, NBs = 12, circumferential interference wavelength = half-annulus).

a constant phase lead or lag, called "inter blade phase angle" σ (in radians):

$$\sigma = \frac{2\pi n}{N} \tag{6}$$

Where

N is the number of blades of the blade row under consideration.
n the number of nodal diameters of the disturbance.

Hence, for a given number of blades, σ also defines the circumferential wavelength. Typically the flutter instability occurs corresponding to an interblade phase angle with a small number of nodal diameters.

For blade-row interaction, if a row of N blades is subject to unsteady disturbances generated by an adjacent blade row with M blades, the most

apparent value of interblade phase angle would be

$$\sigma = 2\pi \frac{M}{N} \tag{7a}$$

In general, there are multiple values of interblade phase angles corresponding to multiple possible interaction modes, as permitted by the circular functions. For instance, the interference wavelengths shown in Figs. 10 and 11 will correspond to a form

$$\sigma = 2\pi \frac{N - M}{N} \tag{7b}$$

The circumferential wavelength has a direct implication on computational modeling, as will be seen later. It also has important physical influences on unsteady aerodynamic and aeroelastic characteristics. For blade flutter analysis, it has been well established that the aerodynamic damping at a given blade vibration frequency and mode shape can change from a positive value to a negative one depending on the interblade phase angle. For aerodynamic interactions under a circumferential distortion, the spatial wavelength is normally tied together with the temporal frequency, so it is not easy to isolate the spatial wavelength effects. Nevertheless, the following two examples should be able to illustrate the impacts of the circumferential wavelength of disturbances on unsteady responses within blade passages as well as on axial decay of the disturbances.

The first example concerns the steam turbine operation at a practical partial admission condition, in which one or several circumferential segments of annular flow path are blocked to adjust the total mass flow rate (and hence power output). Figure 12 shows computed instantaneous entropy contours for two different blocking arrangements at the first stator leading-edge plane to achieve a 50% flow rate, "$1 \times 50\%$" and "$2 \times 25\%$" admissions for a two-stage high-pressure turbine [18]. For both cases, the entropy contours clearly show considerable boundary-layer separation on blade pressure surfaces of the second stator row. Figure 13 shows the pitchwise time-mean static pressure distribution downstream of the first stator row and that downstream of the second stator row. Clearly there is very strong circumferential static pressure nonuniformity due to the partial admission. Comparing Fig. 13(a) with Fig. 13(b), we note that the pitchwise pressure nonuniformity at the $2 \times 25\%$ admission has a significantly faster decay rate than that at the $1 \times 50\%$ admission. The magnitudes of the pitchwise pressure nonuniformity for both cases are roughly the same at the position downstream of the first stator row. However, downstream of the second stator row, the magnitude of the nonuniformity for the $2 \times 25\%$

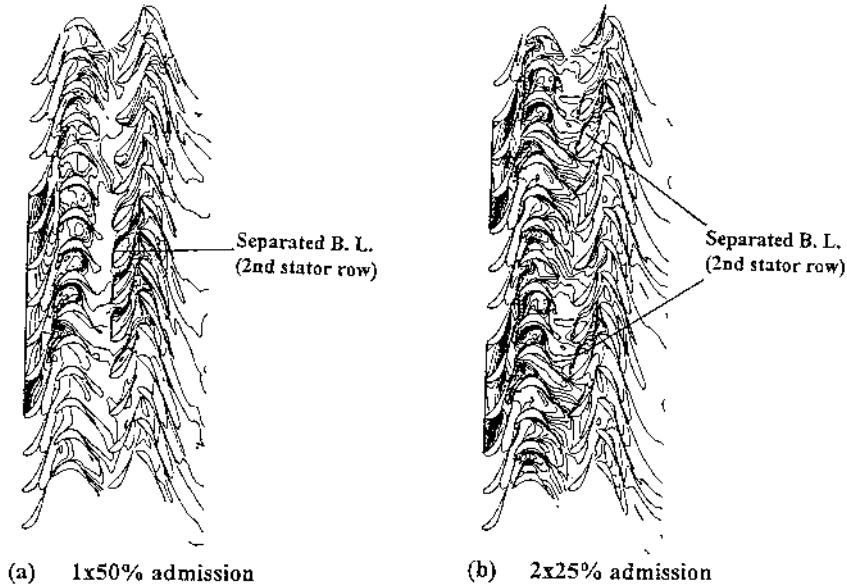

Figure 12 Calculated instantaneous entropy contours for two-stage turbine at partial admission.

admission is less than half of that for the $1 \times 50\%$ admission. Therefore, we see that the nonuniformity with a longer circumferential wavelength decays at a much slower rate in the axial direction.

The second example concerns responses of a blade row to inlet distortions. In this case, stationary stagnation pressure distortions are specified at the inlet to a transonic fan rotor row. And the results obtained at the same distortion amplitude of 15% are compared for two different circumferential wavelengths [19]. The distortion pattern in the first case has 11 nodal diameters (wavelength = 2 passages). In the second case, the distortion has 1 nodal diameter (wavelength = whole annulus, 22 passages). The influence of the circumferential distortion wavelength can probably be best illustrated by *time-space* static pressure contours on the suction surface at 90% span, as shown in Fig. 14. Note that at this spanwise section, the passage shock wave in a steady solution is situated on the suction surface around 85–90% chord. The results demonstrate that the passage shock oscillation is strongly dependent on the distortion wavelength. For the short wavelength case [Fig. 14(a)] the shock oscillation is confined to 3–5% chord,

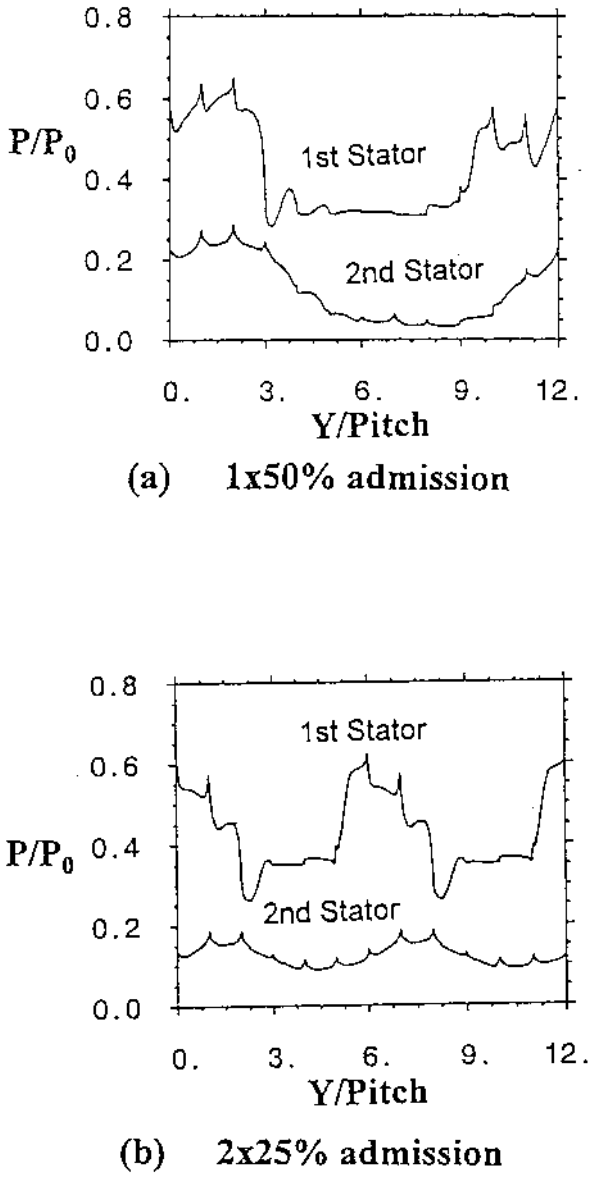

Figure 13 Time-averaged pitchwise static pressure distributions downstream of the first and second stator rows of a turbine at partial admission (Y = *pitchwise distance; pitch = stator blade pitch length*).

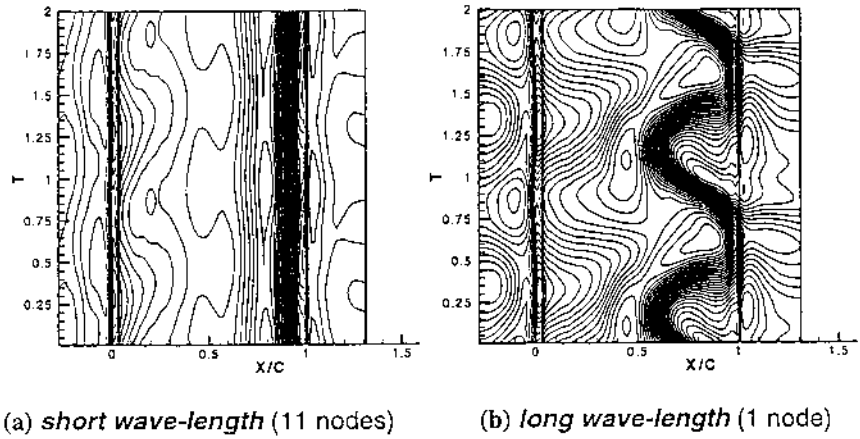

Figure 14 Time-space static pressure contours on suction surface at 90% span under different inlet distortion wavelengths.

while for the case with a long length scale [Fig. 14(b)] the moving shock covers nearly 50% chord. Clearly, this long wavelength case with a large shock oscillation is strongly nonlinear.

Given the importance of circumferential length scales, one should be cautious about the practice of "slightly" changing blade counts to obtain a much reduced multipassage computational domain—a drastic change in the corresponding circumferential wavelength by doing so may result in a very different unsteady response!

Phasing of Unsteady Disturbances

It must be kept in mind that influences of an unsteady disturbance depend on its phase angle, not just the amplitude. The most obvious example is the use of "antisound" where an acoustical noise disturbance can be completely cancelled by artificially introducing an acoustical disturbance with the same amplitude but a 180° phase shift.

Phasing Between Wake and Potential Disturbances

In the context of blade forced responses, there is a scope of utilizing the phase difference between wake and potential disturbances to produce positive results. For example, a higher unsteady loading might not

necessarily be generated at a higher steady loading condition if the wake and potential disturbances are closer to being antiphase [10]. The phasing effect is caused simply by the fact that a wake shed from an upstream row is always convected downstream at the local flow velocity in the relative streamwise direction, but the pressure disturbances from the upstream row do not follow the same pattern at all! The resultant response is dictated by the difference in propagation directions and speeds between the wake (entropy and vorticity) and the pressure disturbances. A downstream relatively rotating blade would see the pressure peaks originated from the two disturbances at different times in one passing period, depending on its axial location (the axial gap). Given that potential and wake disturbances propagate in different paths, there might therefore be an optimum gap to minimize the net unsteady forcing, where the two peaks due to the two disturbances are 180° apart circumferentially.

Phasing Between Aerodynamic Force and Blade Vibration (Energy Transfer in Blade Flutter)

As mentioned earlier, energy transfer is the fundamental consideration in blade flutter, and the role played by phasing in the instability is illustrated here. Assume a blade is initiated (e.g., disturbed by mechanical or aerodynamic noise) to vibrate in a sinusoidal form with a small amplitude. Its vibration displacement X_B is

$$X_B = A_X \sin(\omega t) \tag{8}$$

Consider that this blade vibration movement induces an unsteady aerodynamic force F_A, in a sinusoidal form with a phase angle ϕ_{FX} relative to the blade vibration displacement [although higher-order harmonics of flow response may arise due to nonlinearity, as was seen earlier, it can be shown that only the fundamental harmonic component of the flow response will contribute to the net energy transfer between the blade oscillating in the form Eq. (8) and the flow].

$$F_A = A_F \sin(\omega t + \phi_{FX}) \tag{9}$$

The rate at which the aerodynamic force does work to the blade is

$$w = F_A V_B \tag{10}$$

where V_B is the blade vibratory velocity. The net work input to the blade in

one period T_p (neglecting change of the vibration amplitude) will be

$$W_{\mathrm{A}} = \int^{\mathrm{T_p}} F_{\mathrm{A}} V_{\mathrm{B}} dt = \pi A_F A_X \sin(\phi_{FX}) \tag{11}$$

A flutter instability would occur when the net work input to blade vibration is positive (i.e., a negative aerodynamic damping when the induced unsteady force leads the blade vibration displacement, $0 < \phi_{FX} < \pi$).

MODELING ISSUES

As for any other engineering problems, there are two basic considerations in prediction of unsteady flow effects: accuracy versus efficiency. Very often, a blading designer or method developer may face a choice between a seemingly more complete model and a truncated/reduced one. Usefulness of a complete model is likely to be dictated by numerical resolution limited by computing power, while the truncated model apparently would neglect some phenomena deemed to be unimportant for the problems of interest. In the unsteady aerodynamics and aeroelasticity area, a judgment can be helped by appreciation of a common modeling issue, flow nonlinearity.

Unsteadiness/Time-Averaged Flow Interaction (*Nonlinearity and Deterministic Stresses*)

In relation to blading designs, aerodynamic designers normally are only interested in time-mean performances, rather than details of unsteady disturbances. The basic question is, can we obtain the time-mean parameters by solving the *steady* flow equations under the time-mean flow conditions? Effectively, what we ask is the difference between the steady flow equations and the time-averaged unsteady flow equations. The fundamental principles can be illustrated in a very simple situation. Let us consider a *1D inviscid* flow governed by the following equations:

$$\textit{Continuity}: \quad \frac{\partial \rho}{\partial t} + \frac{\partial \rho u}{\partial x} = 0 \tag{12a}$$

$$\textit{Momentum}: \quad \frac{\partial \rho u}{\partial t} + \frac{\partial \rho u u}{\partial x} = -\frac{\partial P}{\partial x} \tag{12b}$$

$$\textit{Energy}: \quad \frac{\partial \rho e}{\partial t} + \frac{\partial \rho u h_0}{\partial x} = 0 \tag{12c}$$

This set of equations is applicable to one-dimensional steady and unsteady

(*random and periodic*) flows. A purely steady flow will satisfy the equations with the time derivatives being zero. To answer the question raised earlier, we apply the standard time-averaging technique. An instantaneous flow variable can be expressed in terms of a time-averaged part and a fluctuation:

$$f(x,t) = \overline{f(x)} + f'(x,t) \tag{13}$$

where

$$\overline{f(x)} = \frac{1}{T}\int f(x,t)dt \qquad \text{and} \qquad \overline{f'(x,t)} = 0$$

If the flow is randomly unsteady (turbulent), the time scale T over which the averaging is carried out should be much larger than the scales of turbulence fluctuations. For a periodic flow, T is the time length of the period. We substitute the time-averaged and fluctuation parts into the unsteady flow equations [Eq. (12)]. Then the time-averaged equations would be as follows:

$$\frac{\partial \overline{\rho u}}{\partial x} = 0 \tag{14a}$$

$$\frac{\partial \overline{\rho u u}}{\partial x} + \frac{\partial \overline{(\rho u)' u'}}{\partial x} = -\frac{\partial \bar{P}}{\partial x} \tag{14b}$$

$$\frac{\partial \overline{\rho u h_0}}{\partial x} + \frac{\partial \overline{(\rho u)' h_0'}}{\partial x} = 0 \tag{14c}$$

The above *time-averaged* equations can be compared to their counterparts for purely *steady* flows:

$$\frac{\partial \rho u}{\partial x} = 0 \tag{15a}$$

$$\frac{\partial \rho u u}{\partial x} = -\frac{\partial P}{\partial x} \tag{15b}$$

$$\frac{\partial \rho u h_0}{\partial x} = 0 \tag{15c}$$

Comparing the time-averaged equations [Eq. (14)] with the steady equations [Eq. (15)], we have the following observations:

1. The mass continuity equation remains unchanged, i.e., the time-averaged mass flow at the inlet and outlet of a flow domain must be conserved.
2. For the momentum and energy equations, the time-averaging generates extra terms, due to *nonlinearity* of the equations. These terms need extra relationships or equations to close.

It should be noted that the effects of the extra terms depend on the spatial gradients of the unsteady disturbances (not just their absolute magnitudes). Also note that the pressure term remains unchanged since it is linear. Thus, an unsteady flow with large velocity fluctuations (e.g., unsteady vortices) is likely to be have more significant effect on the time-averaged flow than one with mainly pressure fluctuation (e.g., pressure waves). Clearly, the time-averaged results of an unsteady flow cannot be obtained by simply solving the steady flow equations.

The most common and probably most complicated type of unsteady flows is "steady" turbulent flows. It is somehow ironic that we hear much more about how turbulence affects our "steady" flow results than we do about a periodic unsteadiness. In a case of a turbulent flow, the extra terms (e.g., $\overline{\rho u' v'}$ in a 2D case) are the turbulence (Reynolds) stress terms, which need to be closed by turbulence modeling in one form or another. The basic mechanism to generate turbulence stress terms is exactly the same as what is illustrated above using the 1D flow equations, i.e., by the nonlinearity of the *inviscid* part of the equations. The only difference is that the Reynolds stresses are generated by essentially random unsteadiness, while for the cases we consider here, the stresses terms are generated by unsteadiness with distinctive frequencies, and for this reason they are called deterministic stresses as cast in the framework for blade-row interactions by Adamczyk [20].

Likewise, an appreciation of the effects of turbulence is helpful in identifying those of a periodic unsteadiness on time-averaged flows. For instance, we know that magnitudes of turbulence fluctuations are generally much smaller than an averaged flow velocity. It is therefore not surprising that a periodic unsteadiness with a small magnitude could have a significant effect on a time-averaged flow. In general, as far as a time-averaged flow is concerned, periodic unsteadiness might be regarded as "*regular turbulence*." The main difference is that the extra terms due to periodic disturbances can be directly evaluated by unsteady flow calculations or modeling with less uncertainties than conventional turbulence modeling for the Reynolds stress terms.

Here are some simple examples concerning the loss associated with a periodic unsteady flow. Firstly, consider a shock wave in a quasi 1D duct flow (Fig. 15). In a steady flow situation with fixed upstream conditions, the solution of the shock wave (position, strength, and entropy rise, etc.) is determined by the downstream static pressure P_2. Now the shock wave is made to oscillate by the downstream static pressure changing in the following form:

$$P = P_2 + A_m \sin(\omega t + \phi) \tag{16}$$

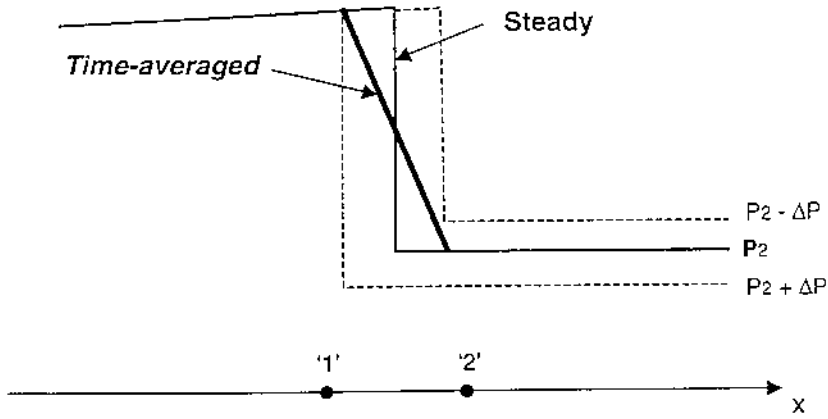

Figure 15 Steady and time-averaged unsteady pressures around shock wave.

Assume the shock wave oscillates over the distance between location 1 and location 2. We can then compare the time-averaged flow to a steady one at the same steady (time-averaged) back pressure P_2. First it should be noticed that the time-averaged pressure distribution is smeared between these two extreme locations by the unsteadiness (not the artificial viscosity!). For a steady flow, conservation of mass, momentum, and energy will sufficiently determine the jump conditions across a shock (i.e., the Rankine–Hugoniout relations), so that the entropy loss across the shock will simply follow a control volume analysis. Now we can take a control volume between locations 1 and 2 that covers the region of shock motion. Then the downstream momentum at the boundary surface of the control volume is

For the steady flow:

$$(\rho uu)_2 = (\rho uu)_1 - (P_2 - P_1) \tag{17a}$$

For the time-averaged unsteady flow:

$$(\overline{\rho uu})_2 = (\rho uu)_1 - (P_2 - P_1) - (\overline{(\rho u)' u'})_2 \tag{17b}$$

The unsteady stress term $(\overline{(\rho u)' u'})_2$ can be roughly approximated by $(\rho \overline{u'^2})_2$, which is a positive term. Therefore, for the unsteady flow case, there would be less time-averaged downstream momentum, compared to the steady flow case. Hence we would expect an extra aerodynamic loss in the case of an oscillating shock.

There are some further points to note about the dependence of shock oscillation characteristics on the mean shock wave strength. A quasisteady analysis [2] shows that at the same relative amplitude of upstream Mach number variation, a weak shock wave gives a higher relative increase of time-averaged entropy rise than a strong shock wave. It is also observed based on a time-domain CFD simulation (He, 1990) [21] that under the same blade oscillation amplitude and frequency, a weak shock wave moves over a larger blade surface distance with a more pronounced nonlinear behavior than a strong one.

In addition to the difference between a time-averaged flow and a steady flow, nonlinearity also manifests itself in the temporal form of unsteady flow responses to incoming disturbances. For instance, for a given blade *sinusoidal* oscillation:

$$X_b = A_x \sin(\omega t) \tag{18}$$

where A_x is the amplitude of the blade vibration. Corresponding flow velocity fluctuating components will in general be in a Fourier series form:

$$u' = A_1 \sin(\omega t + \phi_{u1}) + A_2 \sin(2\omega t + \phi_{u2}) + \cdots \tag{19a}$$

$$v' = B_1 \sin(\omega t + \phi_{v1}) + B_2 \sin(2\omega t + \phi_{v2}) + \cdots \tag{19b}$$

If the flow responds to the blade oscillation (input) in a linear manner, then any unsteady flow parameter should also vary in a pure sinusoidal form with negligible higher harmonics, i.e.:

$$u' = A_1 \sin(\omega t + \phi_{u1}), \qquad v' = B_1 \sin(\omega t + \phi_{v1}) \tag{20}$$

Thus in the way, a linear response will be in the same harmonic form as that of a boundary disturbance.

If, however, nonlinear effects are measurable, the flow response will be influenced by the nonlinear product terms of the flow equations. Then the fundamental harmonic components can be seen to "generate" higher harmonics:

$$\begin{aligned} u'v' &= [A_1 \sin(\omega t + \phi_{u1})][B_1 \sin(\omega t + \phi_{v1})] + \cdots \\ &= \frac{A_1 B_1}{2}\left[\cos(\phi_{u1} - \phi_{v1}) - \cos(2\omega t + \phi_{u1} + \phi_{v1})\right] + \cdots \end{aligned} \tag{21}$$

Hence, we can see that in addition to an extra "steady" (time-average) part, there would also be a second harmonic component in the solution, which is "produced" by the first harmonics due to nonlinearity. In this way, a nonlinear interaction can create other harmonics that are not present in the "forcing" disturbances at domain boundaries. Thus, for a system subject to

only the first harmonic disturbances at boundaries, an appearance of the second- or higher-order harmonics is an indication of nonlinearity.

An example to illustrate a linear or nonlinear behavior is given for an NACA-65 airfoil oscillating sinusoidally in a torsion mode. In this case, surface unsteady pressure and shear stress were measured at different mean incidence conditions [22]. Figure 16 shows ensemble-averaged unsteady pressures for two periods measured at different chordwise surface locations at 0° mean incidence. We can see that the pressure variations are almost sinusoidal, indicating a linear response to the sinusoidal oscillatory movement of the airfoil. However, at a high mean incidence of 10°, there is a separation bubble around the leading edge on the suction surface as shown in the smoke flow visualisation [Fig. 17(a)]. The corresponding ensemble-averaged unsteady pressure variations are nonsinusoidal [Fig. 17(b)], indicating a nonlinear pressure response due to the bubble-type separation. In this case, subject to a sinusoidal unsteady disturbance of a single frequency (blade vibration), the nonlinear effects manifest in the higher harmonics.

In a more complex situation subject to two fundamental external disturbances with frequencies ω_1 and ω_2, it can be shown following the

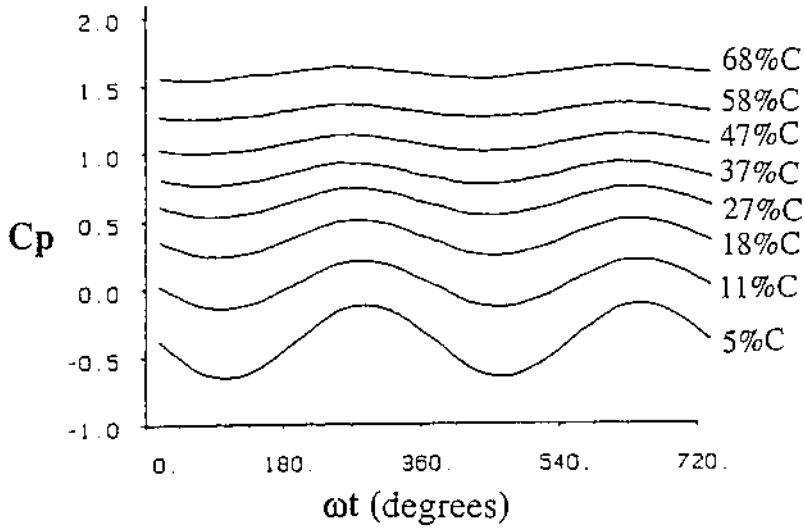

Figure 16 Ensemble-averaged unsteady pressure data at various suction surface locations of oscillating airfoil at a mean incidence of 0° *(torsional oscillation at 2° amplitude)*.

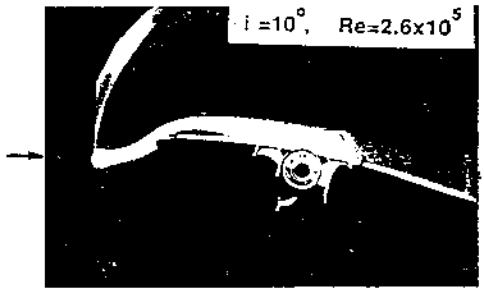

(a). Smoke Visualisation (*steady flow*)

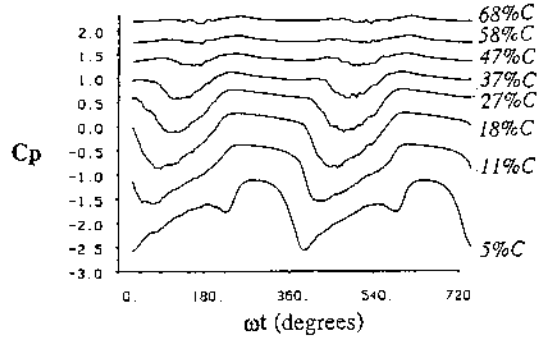

(b). Ensemble-averaged unsteady pressures (*blade oscillation in torsion*)

Figure 17 Flow around an NACA-65 airfoil at a mean incidence of 10°.

above reasoning that nonlinearity will result in secondary or induced disturbances with frequencies: $\omega_1 + \omega_2, \omega_1 - \omega_2$, and their higher harmonics. It is normally the long wavelength component at the low frequency $\omega_1 - \omega_2$ that has a more pronounced influence. Generally speaking, in all situations with measurable nonlinear effects, Fourier-transformed unsteady pressure or velocities will reveal other harmonic components, which are not present in the unsteady "forcing" disturbances at domain boundaries (inlet/exit/blade surface).

Aerodynamic/Structural Dynamic Interaction

For flutter and forced response problems, we must address how unsteady aerodynamics interacts with blade structural dynamics. The situation

regarding the aeroelastic coupling effects for turbomachinery blades is largely influenced by the structural/flow mass ratio, measured by the mass coefficient defined as:

$$C_{\text{mass}} = \frac{m}{\rho\pi(C/2)^2} \tag{22}$$

Where

m is the mass per unit span of blade or airfoil.
C is the chord length.
ρ is the air/gas density.

Typical values of the mass coefficient for conventional turbomachinery blades are by an order of magnitude higher than those of aircraft wings (or wind turbine blades). Thus, the changes of blade vibration mode shapes and the frequencies due to aerodynamic damping and forcing are usually small and may be neglected. This fundamental blade structural dynamic characteristic has a significant bearing in the ways blade flutter and forced response problems are dealt with.

Flutter Prediction

At a flutter inception, blade vibratory movements (mode shape and frequency) can be assumed to be the same as in the natural (i.e., without unsteady aerodynamic forces) modes and frequencies. Then the stability of the blade-flow aeroelastic system can be simply determined by the energy transfer between the blade and its surrounding flow. The above energy consideration forms the basis for the conventional blade aeroelastic calculation procedure, the "energy method" [23].

In a flutter prediction using the energy method, there are three main steps. First, the blade natural vibration modes shapes and frequencies are obtained by a finite-element (FE) analysis. Second, the unsteady aerodynamic forces induced by a specified blade vibration in a natural mode (typically a lower-order one, e.g., first flap or first torsion) will be calculated. Third, the blade aeroelastic stability will be determined purely based on the total energy transfer (work sum) in one period between the blade vibration and the flow. The mode shape only gives the relative displacement of different points on a blade surface. An aerodynamic damping calculation can in practice be carried out by taking a small maximum displacement (say 0.5% chord for the first bending mode or 0.5 degree for first torsion). If a blade surface is covered by N_c mesh cells, then the total aerodynamic work done to the blade in one period of vibration at a frequency ω is [see Eq. (8)–

(11) for a simple case]:

$$W_A = \pi \sum_{i=1}^{Nc} [A_f A_x \sin(\phi_{fx})]_i \tag{23}$$

Where

A_f is the amplitude of the induced aerodynamic force component on mesh cell i in the direction of the vibratory motion.
A_x is the amplitude of the vibrating displacement of the cell.
ϕ_{fx} is the phase lead of the induced aerodynamic force relative to the displacement for the cell.

Aerodynamic damping can be defined as

$$D_A = -W_A \tag{24}$$

The total damping of the blade aeroelastic system is

$$D = D_M + D_A \tag{25}$$

A conservative prediction can be made by neglecting the mechanical damping, D_M, which is always positive. Aeroelastic stability of a blade is directly indicated by a damping coefficient taking a form of

$$C_A = \frac{W_A}{A_m^2} \tag{26}$$

where A_m is the maximum vibration amplitude taken in the unsteady aerodynamic calculation. So, the somehow arbitrary vibrating amplitude taken in the damping calculation does not matter provided the aerodynamic response is of a linear nature.

Apparently, given natural vibration mode shapes and frequencies, a blade flutter analysis using the energy method will be solely determined by unsteady aerodynamic calculations. This is why unsteady aerodynamics around oscillating blades in a specified mode has attracted so much attention and effort in flutter analysis and predictions for turbomachinery blades.

Forced Response Prediction

Forced response is more complex, because it involves two separate aerodynamic elements, aerodynamic damping and aerodynamic forcing. The analysis may be most effectively carried out in a *Modal* space, where the original structural dynamic equations with N degrees-of-freedom are decoupled into N single-degree-of-freedom equations. Each of these

decoupled equations corresponds to one vibration mode. For instance, if mode k is identified in the Campbell diagram as the one with resonance crossing, the natural mode at frequency ω_k is governed by

$$\ddot{q}_k + \omega_k^2 q_k = 0 \tag{27}$$

where q_k is the modal displacement for this mode, relating to the physical displacements through the mode shape matrix. Assuming that the mode shape is not affected by the aerodynamics, the vibration displacement under an external aerodynamic force should be a simple solution to an equivalent equation:

$$\ddot{q}_k + c_k \dot{q}_k + \omega_k^2 q_k = f_k \tag{28}$$

where f_k and c_k are the modal aerodynamic force and damping coefficient, respectively. The key link among different parts in the process is the mode shape.

An alternative and somewhat simpler approach can be entirely based on the energy consideration, similar to the energy method applied to flutter analysis. At an equilibrium (steady-state) vibration, the energy input from the aerodynamic forcing to the blade must be balanced by the dissipation work done by the aerodamping. So the question becomes one to find a finite blade vibration displacement to satisfy

$$W_F = D_A \tag{29}$$

where W_F is the work input to the blade by the aerodynamic forcing. This work sum can be calculated similarly to the aerodynamic damping work in Eq. (23), as long as the phase between the aerodynamic forcing and the blade response vibratory movement is given. It is known that for a forced oscillator in a single degree of freedom, the response displacement will lag the forcing by exactly 90° if the frequency shift can be neglected.

The overall observation is that aerodynamic and structural interactions for conventional turbomachinery blades can be dealt with in a loosely coupled manner. Caution should be taken about the linear assumptions implied here about both aerodynamics and structural dynamics. On the blade structural dynamic side, nonlinear effects are evident when underplatform dampers are used, resulting in measurable frequency shifts [24]. On the unsteady aerodynamic side, the aerodamping characteristic for blade flutter is normally considered to be linear, but the situation for forced responses is less clear. Nonlinear aerodynamic behavior has been revealed for transonic fans under influences of inlet distortions. But its impacts on aeroelastic coupling are still to be identified.

Regardless whether loosely coupled approaches or fully time-domain coupled approaches (e.g., Bakhle et al. [25], Vahdati and Imregun [26]) are adopted, it is well recognized that the computing efforts for solving an aeroelastic problem in turbomachinery is dominated by that required for solving the unsteady aerodynamics.

Efficient Unsteady Flow Modeling Approaches

The most straightforward way to solve an unsteady nonlinear multipassage multirow flow field is to integrate the spatially discretized flow equations in time (time-domain solutions). This kind of full-scale time-domain unsteady CFD runs are very time-consuming. The following brief estimate can give some indication of typical CPU requirements for a time-domain unsteady solution compared to a steady flow solution:

1. *Time accuracy*: for the same number of mesh points, a time-accurate solution would typically require about 15–20 times more CPU than a steady solution for blade-row interaction problems (e.g., Graf et al. [27]). The difference can be much more for low-frequency long wavelength (e.g., inlet distortion driven low engine order forced response) problems.

2. *Multiple-passage domain*: to model proper circumferential length scales would normally lead to use of a whole annulus computational domain, resulting in another factor between 20 and 100, depending on numbers of blade passages.

Hence, a full-scale unsteady time-domain calculation would be by two to three orders of magnitude more time-consuming than a steady calculation. There certainly is a need for developing efficient numerical modeling techniques.

Single-Passage Domain Methods

The large requirement for computing time can be reduced if we can truncate the computational domain in the axial direction to a single blade row, or in the circumferential direction to a single blade passage.

First some comments should be made on the axial truncation. Single-row domains have been widely used in conjunction with nonreflective inlet and exit boundary conditions. The problem is that the presence of adjacent blade rows will always reflect! It has been shown recently [28] that the potential interaction effects between adjacent blade rows can significantly change unsteady flow responses within the blade row concerned. Realistic ''semireflecting'' boundary conditions have not been available. It seems that coupled (nontruncated) multiple-row solutions may become the only way to include the complex interaction effects. Nevertheless, single-row solutions

with nonreflecting boundary conditions are still useful when compared with well-established analytic solutions (only available for single-row configurations) or specially designed single-row experimental tests for method validation purposes.

Regarding the circumferential domain truncation, for both blade flutter and rotor–stator interaction problems, adjacent blades in one blade row would usually experience unsteadiness with a constant phase difference (interblade phase angle). Therefore, if a single-blade passage computation domain is taken (Fig. 18), a flow variable at the upper periodic boundary U_U and that at the lower periodic boundary U_L will have to satisfy the phase-shifted (or time-lagged) periodic condition:

$$U_L(x, t) = U_U(x, t - \Delta t) \tag{30}$$

Where

$\Delta t (= \sigma/\omega)$ is the time lag of the flow variable at the lower boundary compared to that at the upper boundary.
ω is blade vibration (or blade passing) angular frequency.
σ is the interblade phase angle [Eqs. (6) and (7)].

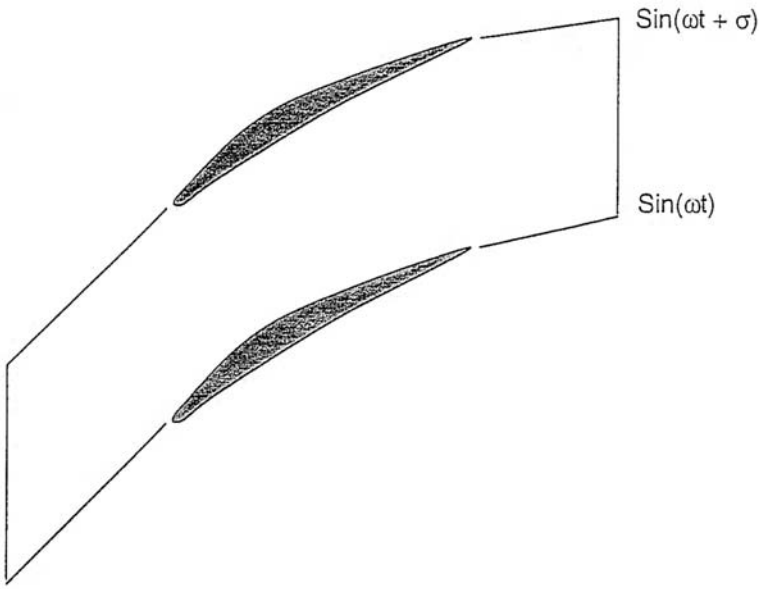

Figure 18 Single-passage computational domain with the phase-shifted periodicity ($\sigma =$ *interblade phase angle*).

Several methods have been developed to deal with the phase-shifted periodicity. The first method has been proposed by Erdos et al. [29], known as the "direct store." In this method, flow variables at the periodic boundaries are stored for one period of time. Then the stored parameters and the current solution correct each other according to the phase-shifted periodicity. An apparent disadvantage of the direct store method is that a large amount of computer storage is required. The lower the frequency, the more the storage. For a low-frequency case the storage required for the periodic boundary condition can be 10 times more than that for the rest of the computation. In a 3D flow situation, this restriction on computer memory can be significant.

Giles [30] has proposed a space-time transformation (time-inclination) method to implement the phase-shifted periodic condition. In his method the time plane in computational domain is inclined along the blade pitchwise direction according to a given interblade phase angle. The phase-shifted periodic condition can then be directly applied by equating flow variables at the periodic boundaries on the transformed computational plane. Therefore, no extra storage is required, and the convergence rate is much faster because the solution procedure is less influenced by the initial guess, compared to the direct store method. However, the time-inclination angles (and therefore allowed interblade phase angles) are very severely restricted by the characteristics of the governing equations.

As described earlier, nonlinearity of a periodic flow manifests in terms of the difference between the time-averaged flow and a pure steady one. It also leads to higher harmonics generated by products of lower ones [Eq. (21)]. In general, a nonlinear periodic flow variable for a known fundamental frequency can be expressed by the Fourier series with its zeroth order corresponding to a time-averaged value. Thus the Fourier series can be used to implement the phase-shift periodicity at single-passage domain boundaries, even when the flow unsteadiness is nonlinear. This is the basis for a Fourier series-based method, called "shape correction" [21, 31] for single-passage domain calculations. At the lower and upper periodic boundaries (Fig. 18), we write an Nth-order timewise Fourier series for the flow variables as

$$U_{\mathrm{L}}(x,t) = \overline{U}(x) + \sum_{n=1}^{N} \left[A_n(x)\sin(n\omega t) + B_n(x)\cos(n\omega t) \right] \tag{31a}$$

$$U_{\mathrm{U}}(x,t) = \overline{U}(x) + \sum_{n=1}^{N} \left[A_n(x)\sin[n(\omega t+\sigma)] + B_n(x)\cos[n(\omega t+\sigma)) \right] \tag{31b}$$

where $\overline{U}(x)$ is the time-averaged flow part. Then the stored Fourier components and the current solution can correct each other accordingly.

For most practical situations of interest, first few harmonics (typically less than 5) have been shown to be sufficient.

A major advantage of expressing unsteadiness in a Fourier series is its ability to include multiple disturbances with unrelated frequencies. If the total number of unsteady disturbances of interest is N_d, a flow variable at periodic boundaries is expressed in the following general form:

$$U(x,t) = \overline{U}(x) + \sum_{i=1}^{N_d} U_i(x,t) \tag{32}$$

Each disturbance U_i is identified by its fundamental and higher harmonics in a Fourier series as in Eq. (31). The capability of including multiple disturbances has been demonstrated for a transonic fan rotor subject to inlet distortion and blade oscillation [19].

Frequency-Domain Modeling

Frequency domain methods have been well established for unsteady flow calculations, mainly for blade aeroelasticity applications, e.g., Verdon and Caspar [32], Hall et al. [33]. The methodology of this kind starts with decomposing a flow variable U into a *steady* part and an unsteady part:

$$U(x,t) = U_0(x) + U'(x,t) \tag{33}$$

And the unsteady part is assumed to be very small so that nonlinear effects (product terms of the unsteady perturbations) can be neglected. It follows then that the time-averaged flow is the same as the steady one. On the basis of a steady flow, a linear equation can be formed with respect to the unsteady perturbation. The linear unsteady perturbation is normally cast in a complex harmonic form, to remove the time dependence, resulting in the perturbation equation with respect to the complex amplitude. The real and imaginary parts of the complex amplitude determine the phase and amplitude of unsteadiness. A solution to the complex harmonic amplitude is obtained at a given frequency, thus is in "frequency domain." Compared to unsteady time-domain (time-marching) methods, frequency-domain methods are much more efficient. A frequency-domain unsteady calculation can be regarded as being equivalent to solving two "steady" flow problems since the amplitude is not time-dependent, and can be conveniently solved in a single-passage domain. The key limitation of the conventional frequency-domain methods is the linear assumption about unsteadiness.

To include nonlinear effects, a new methodology, called nonlinear harmonic method, has been proposed [2] and developed for analysis of blade aeroelasticity [34], [35] and blade-row interactions [6]. Here, a simple but

significant difference is introduced to the flow decomposition:

$$U(x,t) = \overline{U}(x) + U'(x,t) \tag{34}$$

where $\overline{U}(x)$ is a *time-averaged* variable, instead of a *steady* one as defined in Eq. (33). For a general case with N_p disturbances, each disturbance at a frequency ω_k can be expressed by a pair of complex conjugates, $\widetilde{U}_{\mathrm{k}}$ and $\widetilde{U}_{-\mathrm{k}}$, so:

$$U'(x,t) = \sum_{k=1}^{N_p} \left[\widetilde{U}_k(x) e^{i\omega_k t} + \widetilde{U}_{-\mathrm{k}}(x) e^{-i\omega_k t} \right] \tag{35}$$

The flow decomposition as defined in Eq. (34) leads to two sets of equations, one for the time-averaged flow, the other for the unsteady perturbations. The set of N_p unsteady perturbation equations are obtained by balancing harmonic terms for each frequency.

Following the earlier discussion, we know that the time-averaged equations will contain extra deterministic stress terms, which depend on the unsteady solution. On the other hand, the unsteady perturbation equations cannot be solved without a "known" time-averaged flow. This interdependence between the two sets of equations reflects the physical interaction between the two parts of flow and is modeled by a simultaneous coupling in the solution process of the nonlinear harmonic method, as shown in Fig. 19.

The nonlinear harmonic method offers a significant gain in computational efficiency, since neither a time-accurate integration, nor a multi-

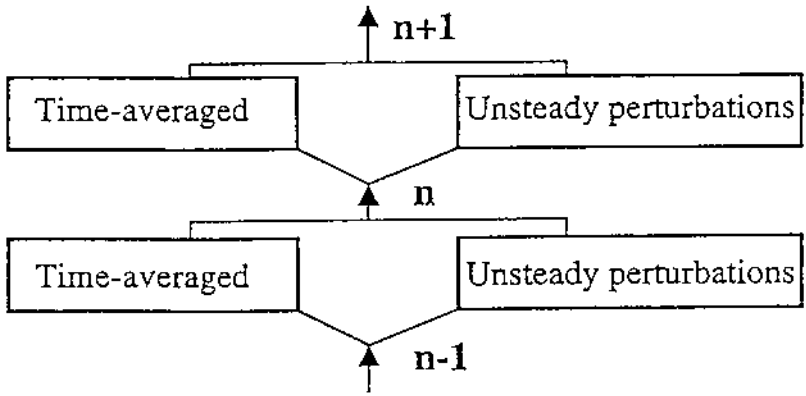

Figure 19 Strongly coupled solution between two sets of decomposed flow equations (n = number of pseudotime iterations).

passage domain is required. The method is currently extended to a multistage environment to analyze rotor–stator and rotor–rotor (stator–stator) interaction (aperiodic and clocking) effects on both aerothermal and aeromechanical performances. The whole annulus unsteady flow field is reconstructed from the single-passage result according to the phase-shifted periodicity. By introducing the nonrotating spatial harmonics, representing upstream wakes, the aperiodic disturbances due to different rotor–rotor blade counts as well as the clocking effects are efficiently included in a single-passage solution.

Some further comments need to be made on this kind of unsteady flow modeling based on flow decomposition, which is seemingly more complex (undesirable!) than the straightforward time-domain unsteady CFD methods. First, the unsteady disturbances we are dealing with are generally small in magnitudes, though their effects may not be. To ensure small unsteadiness to be adequately resolved, numerical errors (artificial dissipation and dispersion) need to be much smaller compared to the physical signals to give a reasonable "signal-to-noise" ratio. For instance, in the field of computational aeroacoustics, it has been evident that conventional unsteady CFD algorithms with second-order temporal and spatial discretizations are unable to adequately extract small but meaningful physical acoustical disturbances from a background flow. In the context of unsteady turbomachinery flows, it won't be difficult to find situations where physical unsteady disturbances are easily "washed off" by numerical dissipations. Since magnitudes of numerical errors are normally in proportion to those of flow variables, it would be more accurate to directly solve the unsteady perturbations. Second, by decomposing the time-averaged flow and the unsteady part, we can use the same numerical algorithms and boundary condition treatments for both a time-averaged flow and a pure steady flow. The past experiences suggest that usefulness of comparing different unsteady CFD computations depends measurably on the consistency of the ways these computations are carried out. Hence use of the same numerics in both steady and time-averaged calculations should help to identify and understand true unsteady effects.

Some Comments on Turbulence/Transition Modeling

It has been a standard practice that turbulence models tuned for steady flows are used quasisteadily for unsteady flows. The uncertainties associated with this must be recognized. At the same time, it is felt that this should not always be used as an explanation (or excuse!) for poor agreements between computational and experimental results. For instance, one may find the turbulence/transition modeling will strongly affect blade aerodynamic

losses, but it may affect to a minimal extent pressure distributions for attached boundary layers. Figure 20 shows measured surface shear-stress and corresponding unsteady pressures for an oscillating NACA-65 airfoil in a low-speed wind tunnel [22]. The shear stress data clearly indicate that the transition point periodically moves over a very large range on the airfoil surface during one oscillating period [Fig. 20(a)], but the unsteady pressure over the major portion of the surface appears to be almost unaffected [Fig. 20(b)]. So for this case, an accurate modeling of the large-scale movement of the transition point (most likely to be nonlinear) should make a negligible difference in an aerodynamic loading (aerodamping prediction).

A more complex situation where turbulence/transition modeling can be important is with a bubble-type boundary-layer separation. Bubble-type separations are common on both compressor and turbine blades at typical Reynolds numbers. Depending on the bubble size, this type of flow separation can affect local as well as global unsteady pressures. A typical scenario is that a boundary layer separates at a laminar state, and a transition happens in the separated shear layer. The reattachment point of separation zone and its movement will strongly depend on the transition and its modeling. For aerodynamic damping calculations involving blade vibration at a small amplitude, a simple bubble separation/transition model developed for steady low-speed flows [36] can be implemented, assuming that an unsteady laminar separation bubble behaves quasisteadily [37]. In transonic flows, the passage shock position at a highly loaded condition is very sensitive to small blockage variations. In these cases, unsteady transition would certainly influence the unsteady shock boundary-layer interaction and the shock oscillation. The associated aerodamping can be thus dependent on the transition modeling [38].

For typical off-design conditions with much thickened and/or separated boundary layers, it is probably fair to say that none of the existing turbulence/transition models is shown to be reliable. Given that viscous effects at off-design conditions are likely to be influenced by large turbulence eddy structures, which in turn interact with short-scale periodic unsteadiness, large eddy simulation (LES) looks to be the way forward. The need to pursue LES can also be viewed from a slightly different angle, relating to mesh dependence of unsteady solutions. Generally it is more difficult to get a mesh-independent solution for unsteady flows than for steady flows. This is because that when we refine meshes (which would normally be associated with using smaller time steps), we will pick up disturbances at smaller scales. And this would be a neverending process (imagine that at some stage down the line, we might start to pick up large-scale ''random'' turbulence!). This fundamental uncertainty of modeling turbulence while resolving it at the same time needs to be clearly appreciated

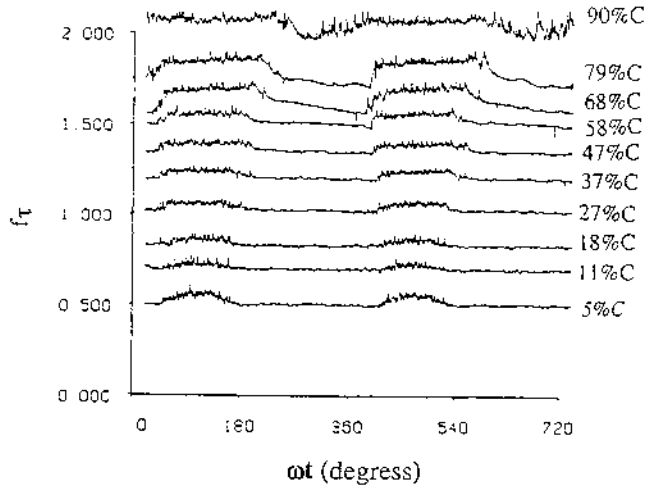

(a). Shear stress (*hot-film data showing large scale unsteady transition*)

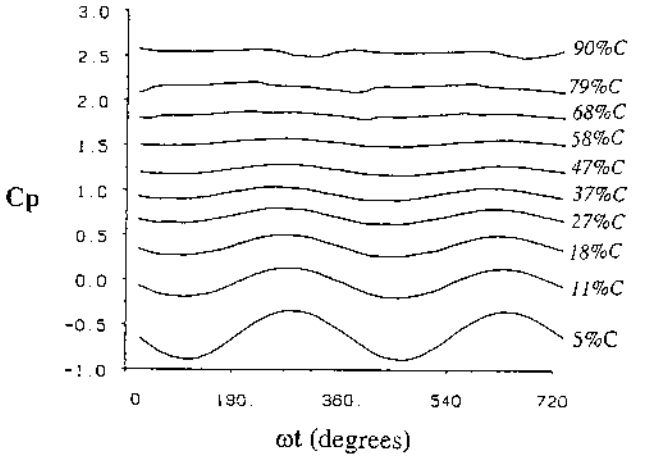

(b). Unsteady pressure

Figure 20 Unsteady shear stress and pressure on suction surface of NACA-65 airfoil (torsion oscillation at a mean incidence of 2.5°).

when we refine a mesh in an unsteady calculation. Again, the issue can be consistently addressed in the framework of LES. It is anticipated that use of finer and finer temporal and special resolutions for small deterministic unsteadiness would lead to earlier rather than later realization of LES in practical turbomachinery applications.

CONCLUDING REMARKS

On aerothermal performances, efforts have been (and continue to be) made to enhance understanding and predictability of blade-row (wake and potential) interactions. Generally speaking, unsteady effects tend to be more significant at off-design (or "bad design"!) conditions than at conventional design conditions where unsteady losses tend to be relatively small. However, future "design conditions" may be much more prone to unsteadiness due to higher loading and/or other nonstandard requirements.

Aerodynamics-related vibration (flutter and forced response) problems directly affect reliability, cost, and life span of turbomachinery blades. This is likely to be a major area where blading design procedures will further evolve in the future with ever-closer coupling and more concurrent integration between aerodynamics and structural dynamics.

Basic understanding of unsteady effects and appreciation of unsteady flow modeling issues can be gained by examining how an unsteady disturbance affects a time-averaged flow field through *nonlinearity* in the momentum and energy equations. The same principle applies to both random turbulence fluctuations and periodic unsteadiness.

With development of computer hardware, it is now possible to carry out multipassage nonlinear time-domain calculations. While this kind of full-scale unsteady CFD simulations will be increasingly applied, we should ensure that relevant unsteady flow information is adequately and consistently extracted from the results to enhance understanding and to help design processes. It is expected that various truncated or reduced computational models aimed at efficiently including relevant unsteady flow physics will continue to be developed, validated, and implemented in design environments.

ACKNOWLEDGEMENTS

The author wishes to thank Stuart Moffatt (School of Engineering, University of Durham) for his help to improve the presentation.

Figures 1, 2, and 3 are originally published in L. He, "II. Time-Marching Calculations for Blade Row Interaction and Flutter," VKI Lecture Series, *Unsteady Flows in Turbomachines*, by von Karman Institute for Fluid Dynamics, March 1996, reprinted with permission.

Figures 7, 8, 10, and 11 were originally published in L. He, "Computational Study of Rotating Stall Inception in Axial Compressors" *J. Power and Propulsion, 13*(1), copyright© 1997 by American Institute of Aeronautics and Astronautics, reprinted with permission.

Figures 12 and 13 are reproduced from L. He, *Proc IMechE*, Part A Issue A3 *211*(1997) titled "Computational Study of Unsteady Flows in Steam Turbine Blade Rows at Partial Admission" by permission of the Council of the Institution of Mechanical Engineers.

Figures 16, 17, and 20 are reproduced from the ASME Paper 91-GT-181 "An Experiment on Unsteady Flow over Oscillating Airfoil" by L. He and J. D. Denton with permission from the American Society of Mechanical Engineers.

REFERENCES

1. S. R. Manwaring and K. L. Kirkeng, "Forced Response Vibrations of a Low Pressure Turbine Due to Circumferential Temperature Distortions," *Proc of 8th International Symposium on Unsteady Aerodynamics and Aeroelasticity of Turbomachines*, Stockholm, Sweden, Sept. (1997).
2. L. He, "I. Modelling Issues for Computations of Unsteady Turbo-machinery Flows; II Time-marching Calculations for Blade Row Interaction and Flutter," VKI Lecture Series, *Unsteady Flows in Turbomachines*, von Karman Institute for Fluid Dynamics, Belgium, (1996).
3. J. L. Kerrebrock and A. A. Mikolajczak, "Intra-Stator Transport of Rotor Wakes and Its Effect on Compressor Performance," *ASME J. of Engineering for Gas Turbine and Power*, pp. 359–370, Oct. (1970).
4. L. H. Smith, "Wake Dispersion in Turbomachines," *ASME J. of Basic Engineering 88:* 688–690 (1966).
5. J. J. Adamczyk, "Wake Mixing in Axial-Flow Compressors," ASME Paper 96-GT-29 (1996).
6. L. He, "Three-Dimensional Unsteady Navier–Stokes Analysis of Stator-Rotor Interaction in Axial-Flow Turbines," *IMechE J. of Power and Energy, 214:* 13–22 (2000).
7. T. Chen, P. Vasanthakumar, and L. He, "Analysis of Unsteady Blade Row Interaction Using Nonlinear Harmonic Approach," *AIAA J. Power and Propulsion, 17*(3), May (2001).

8. W. S. Barankiewicz and M. D. Hathaway. "Effects of Stator Indexing on Performance in a Low Speed Multi-Stage Axial Compressor," ASME Paper 97-GT-496 (1997).
9. J. D. Denton. "Loss Mechanisms in Turbomachines," IGTI Scholar Lecture, ASME Paper 93-GT-435 (1993).
10. R. Kielb, "Forced Response," VKI Lecture Series, *Aeroelasticity in Axial Flow Turbomachines*, von Karman Institute for Fluid Dynamics, May (1999).
11. W. Ning and L. He. "Some Modelling Issues on Trailing-Edge Vortex Shedding," *AIAA J. 39*(5) (2001).
12. D. L. Sondak and D. J. Dorney. "Simulation of Vortex Shedding in a Turbine Stage," *ASME J. Turbomachinery, 121*:(3) 428–435 (1999).
13. T. J. Bogar, M. Sajben, and J. C. Kroutil, "Characteristic Frequencies of Transonic Diffuser Flow Oscillations," *AIAA J. 21*(8) (1983).
14. I. J. Day, "Stall Inception in Axial Flow Compressors." *ASME J. Turbomachinery, 115:* 1–9, Jan. (1993).
15. L. He, "Computational Study of Rotating Stall Inception in Axial Compressors," *AIAA J. Power and Propulsion, 13* (1) (1997).
16. L. He and J. O. Ismael, "Computation of Blade Row Stall Inception in Transonic Flows," *Aeronautical J. 103* (1025): 317–324 (1999).
17. F. O. Carta, "Unsteady Aerodynamics and Gapwise Periodicty of Oscillating Airfoils," *ASME J. Engineering for Power, 105*(3) (1983).
18. L. He, "Computation of Unsteady Flows in Steam Turbine Blade Rows at Partial Admission," *IMech.E J. Power and Energy, 211:* 197–205 (1997).
19. H. D. Li and L. He, "Prediction of Flutter and Inlet Distortion Driven Response of a Transonic Fan Rotor Using Phase-Lagged Boundary Conditions," ASME Paper 2001-GT-0272 (2001).
20. J. J. Adamczyk, "Model Equations for Simulating Flows in Multistage Turbomachinery," ASME Paper 85-GT-226 (1985).
21. L. He, "An Euler Solution for Unsteady Flows Around Oscillating Blades," *ASME J. Turbomachinery, 112*(4): 714–722 (1990).
22. L. He and J. D. Denton, "An Experiment on Unsteady Flow over Oscillating Airfoil," ASME Paper 91-GT-181 (1991).
23. F. O. Carta, "Coupled Blade-Disk-Sroud Flutter Instabilities in Turbojet Engine Rotors," *ASME J. Engineering for Power, 89:* 419–427, July (1967).
24. J. S. Green and J. G. Marshall, "Forced Response Prediction within the Design Process," *Proc. of 3rd European Conference on Turbomachinery*, Paper C557/076/99, London, March (1999).
25. M. A. Bakhle, R. Srivastava, G. L. Stefko, and J. M. Janus, "Development of an Aeroelastic Code Based on an Euler/Navier-Stokes Aerodynamic Solver," ASME Paper 96-GT-311 (1996).
26. M. Vahdati and M. Imregun. "Non-linear Aeroelastic Analysis using Unstructured Dynamic Meshes," *Proc. of the 7th International Symposium on Unsteady Aerodynamics and Aeroelasticity in Turbomachines*, Fukuoka, Japan, Sept. (1994).

27. M. B. Graf, E. M. Greitzer, F. E. Marble, and O. P. Sharma, "Effects of Stator Pressure Field on Upstream Rotor Performance," ASME Paper 99-GT-99 (1999).
28. P. D. Silowski and K. C. Hall, "A Coupled Mode Analysis of Unsteady Multi-Stage Flows in Turbomachinery," *ASME J. Turbomachinery, 120*(3) (1998).
29. J. I. Erdos, E. Alzner, and W. McNally, "Numerical Solution of Periodic Transonic Flow Through a Fan Stage," *AIAA J. 15*(11) (1977).
30. M. B. Giles, "Calculation of Unsteady Wake Rotor Interaction," *AIAA J. Propulsion and Power, 4*(4): 356–362 (1988).
31. L. He, "A Method of Simulating Unsteady Turbomachinery Flows with Multiple Perturbations," *AIAA J. 30*(12) (1992).
32. J. M. Verdon and J. R. Caspar. "A Linearized Unsteady Aerodynamic Analysis for Transonic Cascades," *J. Fluid Mechanics, 149*: 403–429 (1983).
33. K. C. Hall, W. S. Clark, and C. B. Lorence, "A Linearized Euler Analysis of Unsteady Transonic Flows in Turbomachinery," *ASME J. Turbomachinery, 116*(3) (1994).
34. W. Ning and L. He, "Computation of Unsteady Flows around Oscillating Blades using Linear and Nonlinear Harmonic Euler Methods," *ASME J. Turbomachinery, 120*(3): 508–514 (1998).
35. L. He and W. Ning, "Efficient Approach for Analysis of Unsteady Viscous Flows in Turbomachines," *AIAA J. 36*(11): 2005–2012 (1998).
36. H. P. Horton, "A Semi-Empirical Theory for Growth and Bursting of Laminar Separation Bubble," A.R.C. Report, CP-1073 (1969).
37. L. He, "Unsteady Flows in Oscillating Turbine Cascade, Part 1. Linear Cascade Experiment; Part 2. Computational Study," *ASME J. Turbomachinery, 120*(2): 262–275 (1998).
38. K. Isomura and M. B. Giles, "A Numiercal Study of Flutter in a Transonic Fan," *ASME J. Turbomachinery, 120*(3) (1998).

6

Fundamentals of Compressor Design

Robert O. Bullock*

Allied Signal Company, Phoenix, Arizona, U.S.A.

INTRODUCTION

Compressors raise the pressure of a gas by transferring mechanical energy from a rotating shaft to the gas. Many ingenious methods have been devised for this purpose, but the compressors discussed herein are limited to those that are similar to the axial-flow and centrifugal units illustrated in Figures 1–4. Figure 1 is a cutaway photograph of a TFE 731 turbofan engine manufactured by the Allied Signal Corporation. Figure 2 is a drawing of the projection of the engine on a plane through the axis of rotation. The fan is a single-stage axial compressor. A four-stage axial compressor follows, and to the right is a centrifugal compressor. Figures 3 and 4 illustrate a two-stage centrifugal compressor that is part of the Allied Signal TPE 331 turboprop engine.

All of these compressors have rows of blades that are mounted on rotating disks. The blades provide conservative forces that increase the angular momentum of the gases flowing between them; Euler's turbine

* Deceased

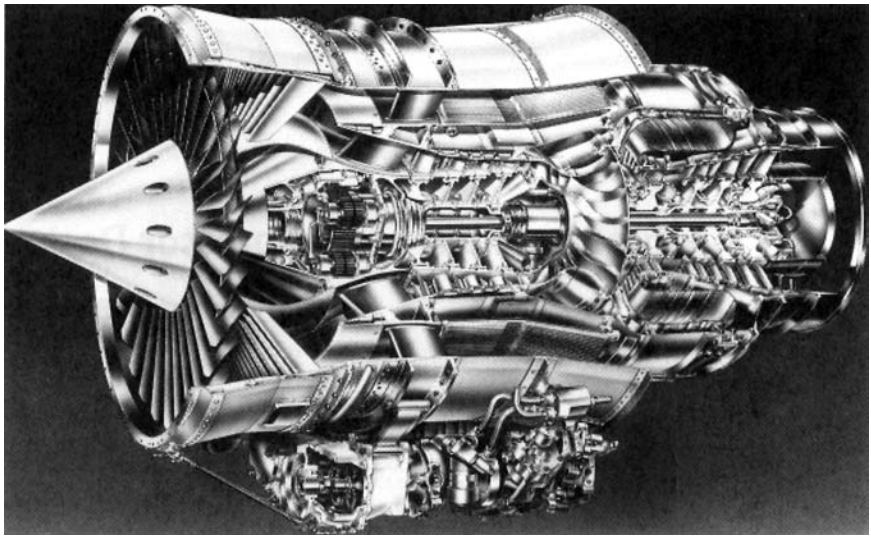

Figure 1 AlliedSignal 731 turbofan engine.

equation determines the amount of energy thus transferred. A row of stationary blades is placed behind each rotor in order to remove part or all of the angular velocity produced by the previous rotating blade row. Note that another type of compressor, a mixed-flow compressor, is similar to centrifugal units.

The concepts for these compressors were originally used for the design of pumps for liquids, and pump efficiencies of 0.90 or more have been attainable for about a century. This design technology relied on empirical correlations derived from experiments; it was also adequate for the design of

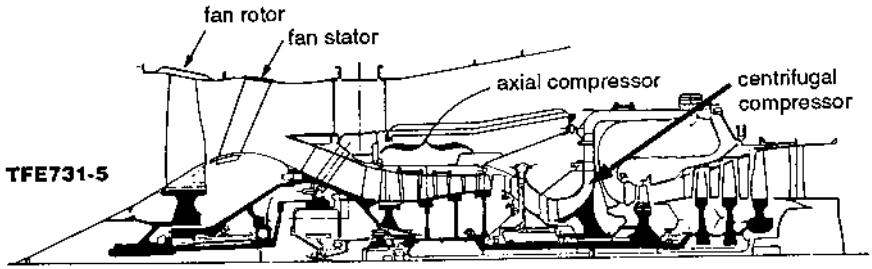

Figure 2 Flowpath of AlliedSignal 731 turbofan. (Designate compressors and fan.)

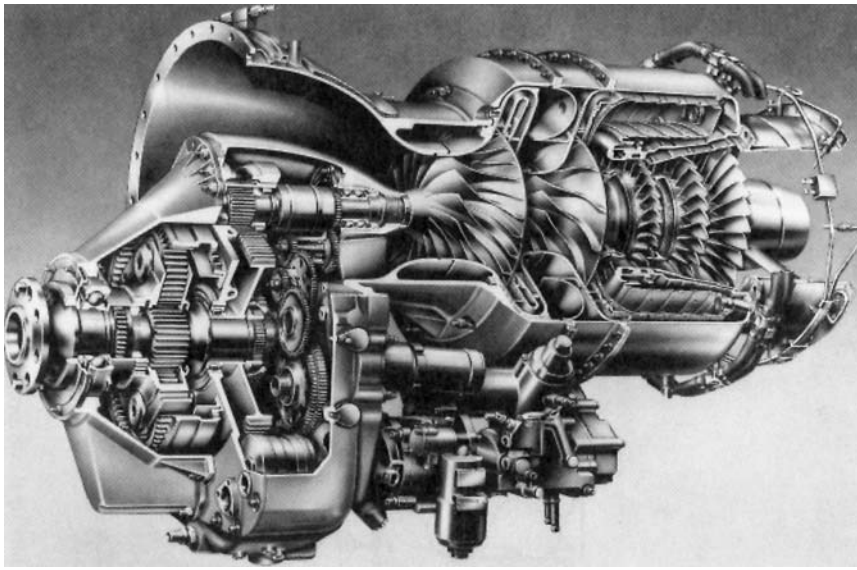

Figure 3 AlliedSignal 331 turboprop engine.

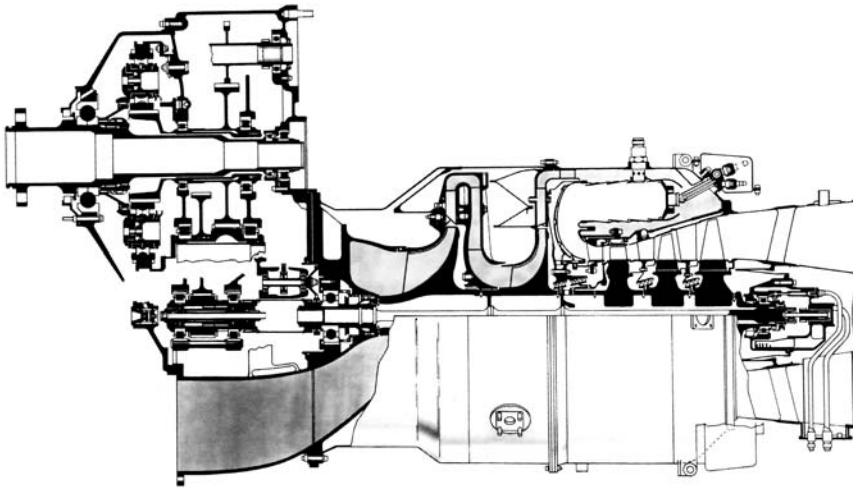

Figure 4 Flowpath of AlliedSignal turboprop 331 engine. (Designate centrifugal compressors.)

compressors as long as the desired pressure rise was low enough to be conveniently measured in inches of water. Compressor efficiency deteriorated when greater pressure increases were sought, falling below the order of 0.7 when pressure ratios of about 2, or higher, were needed.

During the mid-1930s the interest in compact, lightweight compressors for supercharging the reciprocating engines of military aircraft spurred research and development efforts having the goal of realizing efficiencies of 0.8 or higher when the developed pressure ratio was at least 3. By this time, other research had augmented the understanding of fluid mechanics and aerodynamics to the point where the important interactions between blades and fluid could be identified and the chief causes of losses in efficiency understood.

Of particular value was the concept of boundary layers, which contained most of the fluid affected by friction and which partially blocked the area provided for the flow. It had also been discovered that boundary layers, when once formed, often moved in different directions than that of the adjacent main stream.

Systematic work could then be planned to attack the problems. A summary of this effort on axial-flow compressors, up to about 1955, is presented in Reference [1]. A subsequent review is provided by Lakshminarayana [2]. Research has continued, and compressors developing pressure ratios of the order of 20 with adiabatic efficiencies 0.80 or more are feasible. Pertinent references to similar research on centrifugal compressors and to the more recent work on all compressors are noted as the need arises.

The design of compressors usually requires a number of steps. After studying the various requirements for an intended compressor, a designer selects for the design point the values for the total pressure and temperature of the inlet gas flow, the rate of mass flow, the pressure ratio, and the target efficiency. The designer also selects tentative values for both the outer and inner diameters of the annulus for the first row of blades. A rotating speed for the rotor is also assumed. These choices are usually made at the condition where either the highest efficiency or the greatest pressure ratio is demanded. In addition, the designer decides how to compromise the often conflicting requirements of low operating costs, low manufacturing costs, small size, light weight, and high reliability.

A designer then chooses the mean gas velocity, or Mach number, at the compressor inlet, and also decides what changes in velocity components each of the blade rows should produce. These estimates are made at a number of radii in the inlet annulus of the flow passage.

The designer can then estimate the radial movement of the streamlines as the flow passes through the first set of blades. Changes in the pressure and temperature produced by the row can now be calculated. This is done at

each of the selected radii. The properties of the gas flow, as a function of radius, are thus established behind the blade row or ahead of the following blade row, if there is one.

A preliminary shape for the blades is then defined. This may be done from personal experience or by correlated experimental data.

The next task is to estimate the actual changes in gas velocities and entropy created by the blades. Correlated experimental data may again be used for this purpose. Greater accuracy would be available if these changes could be mathematically computed.

Thermodynamic equations provide estimates of the resulting changes in gas temperature, pressure, and density. If these quantities are acceptable, attention is directed to the following blade row. If not, the blade shapes are modified to eliminate unwanted behavior.

Once a blade has been defined, modern computers and computing techniques can effectively solve the applicable inviscid and time-steady form of the Navier–Stokes equations. Proper accounting for the attendant viscous effects and then the time-unsteady effects could then produce the knowledge for designing compressors. Some empirical correlations are presently necessary to achieve this result, and it will be some time before the complete Navier–Stokes equations can be used by themselves for compressor design. Further remarks about this situation are made in a later section.

Note that if a blade is for a rotor, the chosen shape must allow the centrifugal forces to be safely resisted. Both rotors and stators must be able to withstand aerodynamic forces that could cause them to vibrate and break.

The work just described is repeated, blade row by blade row, until the desired overall pressure ratio is attained. The overall efficiency of the compressor is then checked to be sure that it is not below the target value. If it is, the design calculations are reviewed to identify the assumptions that are responsible for excessive losses in available energy. The suspected assumptions are modified and the procedure is repeated until an acceptable efficiency is predicted.

If performance levels at other flow rates and speeds of rotation are specified, the pressure ratios and efficiencies for these conditions are estimated also. Indicated changes again must be made in the appropriate assumptions to cope with any adverse situation. Stresses are also checked. However, even if performance is specified only at the design point, this work is done at several of the rotating speeds and air flows anticipated during an acceleration of the unit from standstill to the maximum expected rotating speed. The objective is to be sure that acceptable efficiencies together with stable and reliable operation are provided at every critical off-design condition. Be aware that very unsteady flows may be found in several

operating regimes; if a problem seems to arise at these off-design conditions, another design of the blades and flow passages is prescribed and the routine just described is repeated until a satisfactory compromise is found. Another design point may have to be selected to resolve a problem.

The design process is thus seen to require accurate thermodynamic and aerodynamic calculations in order to determine the changes in the flow properties produced by each blade row. These calculations should be based on the fundamental laws of motion, the Navier–Stokes equations, whenever possible. In one form or another, these equations, which are reviewed in Chapter 2, provide a skeleton for the necessary design calculations.

Many of the computing techniques that are necessary to cope with even the time-steady and inviscous forms of these equations are often not readily available and recourse to other procedures is required. Any treatment of compressor design methods must therefore make assumptions about what computing resources are available to the designer. The kind and the quality of any correlated experimental compressor data accessible must also be presumed. (Many of the data used by current manufacturers of compressors were obtained at their own expense and are often not generally available.)

For the present purpose, it seemed reasonable to believe that the greatest value of this chapter would obtain if it had two goals: first, to describe and appraise the important design problems, and second, to identify some of the better techniques that have been developed for executing the calculations needed for compressor design.

The object of this chapter, therefore, is to select calculation procedures for executing the aerodynamic design and development of those compressors indicated in the opening paragraph. NASA SP [1] Lakshminarayana [2] and Serovy [3] should be consulted for a more extensive review of the fundamental aerodynamics of compressor design. Serovy [3] is especially useful, because it contains a valuable bibliography concerning many aspects of this subject.

Frequent distinctions are made between axial and centrifugal compressors. We note at this time that the former are essentially curved diffusers. The latter depend on centrifugal force for producing a significant part of the increase in pressure.

The text first calls attention to important operating regimes that are revealed by typical performance curves, or maps, of compressors. The applicable equations of thermodynamics and aerodynamics are introduced and discussed. Causes of energy degradation and inefficiences are examined. The phenomena of choked flow and shock waves associated with compressible flow are studied. Methods of selecting the magnitude of the

components of gas velocity upstream and downstream of a blade row are discussed.

The principles involved in the selection of tentative shapes for blades can now be considered; axial and centrifugal compressors are often treated separately in this discussion. Factors governing the compromises necessary for practical multistage units are noted.

Estimating the behavior of a compressor at various inlet flow conditions and rotating speeds is the next subject to be discussed. Here again, some separate procedures are given for axial and centrifugal compressors.

The subjects of unsteady flows and excessive losses in useful energy are reviewed and methods of coping with these problems are suggested. Mechanical stresses and vibrations that may be troublesome are identified and relevant references are cited. The subject of compressor noise is briefly noted.

Bear in mind that compressor design is not an exact science. Experimental development is nearly always required to make the best use of a particular configuration when the desired pressure ratio is about 3 or higher. Development testing is therefore the final subject included in this chapter. Emphasis is placed on the objectives of the tests and the precautions that should be taken. Details about instrumentation and other testing techniques are left to publications dealing with these particulars.

COMPRESSOR MAPS

Compressors can and do operate over a range of speeds and gas flows. This ability is shown by the curves of Fig. 5, which presents a typical compressor map. Each of the coordinates and parameters of this figure can be shown to be equal to a dimensionless variable multiplied by some constant.

Corrected Weight Flow and Pressure Ratio

Corrected weight flow, $W\sqrt{\theta_1}/\delta_1$, is the abscissa of Fig. 5. This variable is almost a standard in the United States and is proportional to the rate of mass flow of the gas entering the compressor (see Symbols). Note that this term is also proportional to $W\sqrt{T_T}/P_1$, which is frequently used in other countries. Both of these terms are functions of the Mach number of the flow at the compressor inlet. The ordinate is the ratio of the total pressure at the compressor outlet to that at the inlet. One of the parameters is the corrected speed, $N/\sqrt{\theta_1}$; it too is often replaced by another term, $N/\sqrt{T_1}$, which is proportional to it.

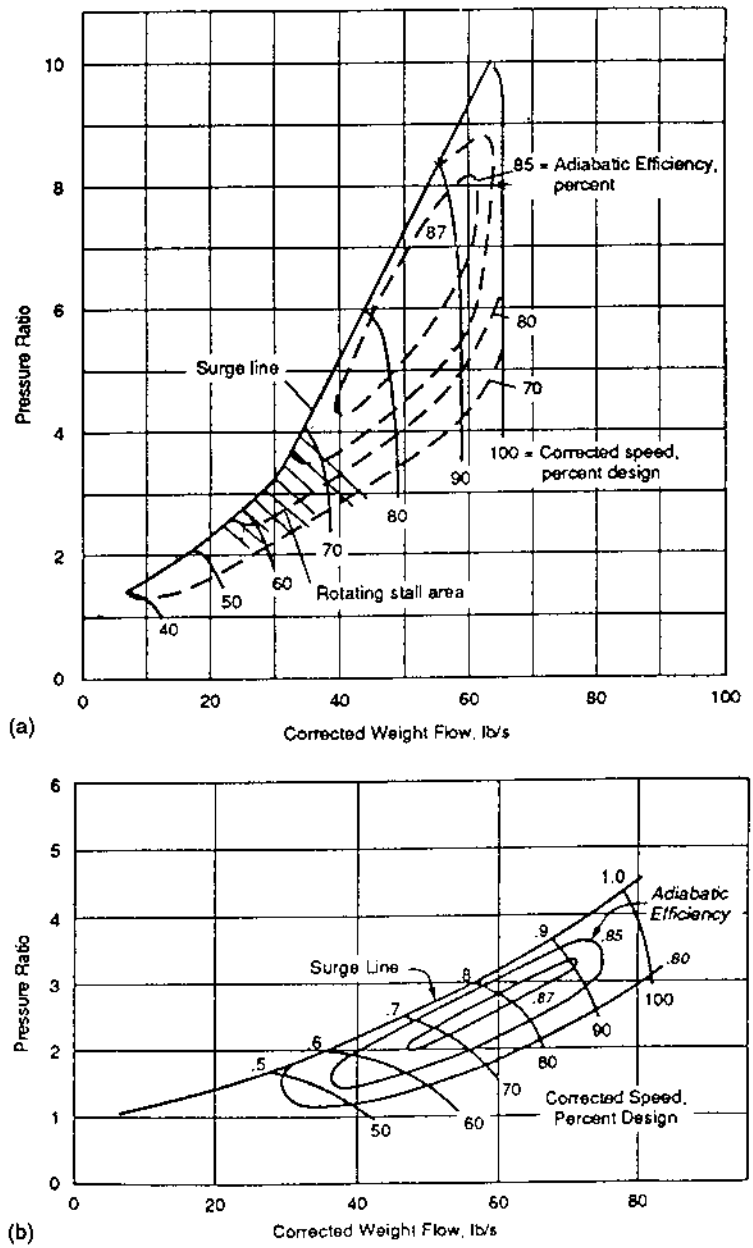

Figure 5 Design and development: (a) high-pressure ratio (b) low-pressure ratio.

Observe that each of the curves for constant $N/\sqrt{\theta_1}$ is terminated on the left by another curve known as the surge line. Attempts to operate to the left of this line produce effects ranging from pulsating flow to a complete deterioration of pressure ratio and efficiency. Prolonged operation here can be disastrous. At lower corrected speeds, an unsteady flow known as rotating stall is encountered in the region indicated by the dashed lines. Operating here has caused blades and vanes to vibrate and fail.

Note that the corrected weight flow generally increases with corrected speed, but the rate of change diminishes at the higher speeds. This could invite trouble if proper attention is not paid to this trend at the beginning of the design.

Compressor Adiabatic Efficiency, η_{ad}

This is another parameter of Fig. 5, and it is defined in the section on symbols. Note that this quantity is equal to the ratio of the ideal energy (that of an isentropic process) required to produce the given pressure ratio to the energy actually needed. Other definitions of efficiency are sometimes used. Two of these are

1. Polytropic efficiency, η_p, which is the average efficiency that each small increment of pressure rise must experience in order to achieve the observed overall adiabatic efficiency. It is often used in Great Britain.
2. Compression efficiency, η^*. Reference to Symbols shows that the denominator for this efficiency is the same as that for η_{ad}, but the ideal energy is that which could be recovered if the gas at the compressor outlet were expanded isentropically to the total pressure at the compressor inlet. This definition has some theoretical and some empirical merits that are noted later.

For general information, an idea of the relative values of these efficiencies is provided by Table 1, using the ideal thermodynamic properties of air. It is clear that any cited efficiency should be defined. One should be mindful that Reynolds number, based on some characteristic dimension, is also an important operating variable—the useful operating range, pressure ratio, and efficiency deteriorate when Reynolds number becomes too small. Wassel [4] and Bullock [5] discuss this subject, which is important when compressors are small or when they operate with low-density gases such as air at high altitudes.

It is also important to realize that an effort was made to supply uniform flow to the compressor while the data for the map were being generated. The useful range of mass flow rate, the pressure ratio, and the efficiency deteriorate when the entering flow is nonuniform or distorted.

Table 1 Relative Values of η_{ad}, η_p, and η^*

	Pressure Ratio			
Efficiency	2	4	8	16
η_{ad}	0.9	0.89	0.88	0.869
η_p	0.909	0.909	0.909	0.909
η^*	0.918	0.926	0.934	0.941

Pertinent information about this subject is presented in Steenken [6], and additional information about Reynolds number is presented in the discussion of testing.

APPLICABLE EQUATIONS OF THERMODYNAMICS

Flow in Stators

The applicable equations of thermodynamics are readily written. Since there is no change in enthalpy between the inlet and the outlet of any stator, the energy equation can be expressed by

$$H_1 = gJc_p t_1 + \frac{1}{2}(V_{z,1}^2 + V_{r,1}^2 + V_{\theta,1}^2)$$
$$= gJc_p t_2 + \frac{1}{2}(V_{z,2}^2 + V_{r,2}^2 + V_{\theta,2}^2) = H_2 \quad (1)$$

(When c_p is a function of temperature, then either tables, such as those given in Ref. [7], or actual integration must be used to find H.)

This equation may be used to denote the change in static temperature that stems from changes in the individual components of velocity. (Note from Figs. 1–4 that the gas velocity, in general, can be expected to have components in the axial, circumferential, and radial directions.)

The mass rate of flow at any station is expressed by

$$\dot{m} = 2\pi \int_{r_1}^{r_2} \rho V_z r \, dr \quad (2)$$

The quantity $\dot{m}$ is constant throughout a blade row unless gas is removed, either deliberately or by leakage.

The conservation of angular momentum requires that

$$\int_{r_1}^{r_2} \rho V_z (rV_\theta) r\, dr = \text{constant between blade rows} \tag{3}$$

When there is also a change in entropy through any stream tube (e.g., from friction or from a transfer of heat into or out of a stream tube), the total pressure changes according to the equation:

$$(P_2/P_1)^{(\gamma-1)/\gamma} = \exp[-(J/R)\Delta S] \tag{4}$$

The corresponding static pressure and density are related by Eqs. (5) and (6):

$$p_2/p_1 = (t_2/t_1)^{\gamma/(\gamma-1)} p_2/p_1 \tag{5}$$

$$p_2/p_1 = (p_2/p_1)/(t_2/t_1) \tag{6}$$

Flow in Rotors

Rotors supply energy to the gas, and change the enthalpy in accordance with Euler's turbine equation:

$$J(H_2 - H_1) = (r_2 V_{\theta,2} - r_1 V_{\theta,1}) \tag{7}$$

Be aware, however, that any recirculation of gas between the inlet and outlet of a rotor augments the enthalpy of the gas stream and causes H_2 to be greater than that given by Eq. (7). This phenomenon also increases the entropy.

The relation corresponding to Eq. (1) is

$$\begin{aligned} I_2 &= gJc_p t_2 + \frac{1}{2}(V_{z,2}^2 + V_{r,2}^2 + V_{\theta,2}^2) \\ &= gJc_p t_1 + \frac{1}{2}(V_{z,1}^2 + V_{r,1}^2 + V_{\theta,1}^2) = I_2 \end{aligned} \tag{8}$$

and Eq. (4) is changed to

$$(P_2/P_1)^{(\gamma-1)/\gamma} = (T_2/T_1)\exp[-(J/R)\Delta S] \tag{9}$$

Equation (5) becomes

$$(p_2/p_1) = (t_2/t_1)^{\gamma/(\theta-1)}(P_2/P_1)/(T_2/T_1)^{\gamma/(\theta-1)} \tag{10}$$

Equations (2) and (6) are applicable to rotors as well as stators.

ENERGY DEGRADATION AND INEFFICIENCIES

Providing good efficiency is always a goal of compressor design. Recall that compressors transfer energy from a shaft to the gas, and that the pressure ratio realized depends on the efficiency of the adiabatic process. This fact is implied by the definitions of efficiencies in Symbols. Equation (9) shows the relation between an increase in entropy and the total pressure ratio realized from a given total temperature ratio.

A loss in efficiency can thus be expressed either as a loss in total pressure or as an increase in entropy. It is useful to consider four types of losses: ideal shock losses, friction losses, mixing losses, and secondary flow losses.

Ideal Shock Losses

These losses are generated by the sudden irreversible change in gas speed from a uniform supersonic to a uniform subsonic value. The mass flow rate, the energy, and the momentum of the subsonic and supersonic flows are unchanged. There is a loss in total pressure, however, which may be calculated using published gas flow tables (e.g., Keenan et al. [7]). It may also be calculated with the aid of Eq. (11), presented in the section on mixing losses. Interactions between a shock and a boundary layer aggravate these losses, but experiments with flat plates have shown that the magnitudes of the ideal losses are approximately valid as long as the static pressure ratio across the shock is equal to or lower than that shown by Fig. 6. A maximum

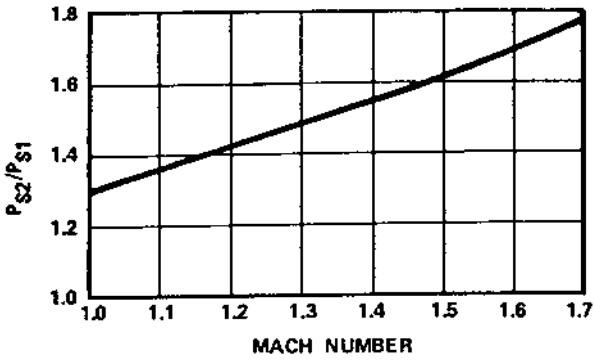

Figure 6 Separation static pressure ration versus Mach number on a straight surface, single-shock.

allowable static pressure ratio of 1.4 seems to be a better guide for this event when the surface is curved.

Friction Losses

Losses of this type are listed in published data concerning the flow in pipes and other ducts. These losses are relatively low. Friction is also involved in the actual mechanism of ideal shock losses. The principal action of friction in compressors, however, is to create boundary layers, which are a zone between the part of the fluid not retarded by friction and the solid boundaries confining the flow. The relative speed of a fluid within the boundary layers ranges from 0 at a bounding surface to that attained by the flow particles undisturbed by friction. McDonald [8] summarizes some of the basic concepts about boundary layers, which are the source of mixing losses and secondary flows.

Mixing Losses

The low speeds of the fluid in boundary layers effectively block part of the available passage area; continuity then requires the speed of the undisturbed flow to increase and the local static pressures to be less than their ideal value. However, if the static pressure is required to increase in the direction of flow, as it does in diffusers, the flow in the boundary layer becomes even more retarded and the thickness of the layer increases even further. This adverse pressure gradient can completely stop part of the flow in a boundary layer and even reverse it—a phenomenon known as flow separation.

At this point we must recognize the importance of other pressure gradients that are at once perpendicular to both the bounding surfaces and the direction of the flow itself. We also need to distinguish situations in which the principal through-flow component is axial from those in which it is radial. Pressure gradients perpendicular, or normal, to the fluid velocity are created by curvature of the flow passages and by Coriolis accelerations. These gradients have important effects in both radial and axial flows. The Coriolis accelerations, however, which predominate in radial flows when the blades are rotating, are more potent by an order of magnitude. Observe that the normal pressure gradients associated with curved flow are proportional to V_s^2/R; the gradients caused by Coriolis accelerations are proportional to $2\omega V_r$. It can be shown that boundary layers are unstable when the scalar product of the normal pressure gradient with the normal entropy gradient is positive. They become unstable and thin on the high-pressure side of a blade, especially in centrifugal compressors. Conversely, they are stable and relatively thick on the low-pressure side; local turbulence can be so

suppressed that flow separation is almost inevitable in the presence of even small adverse pressure gradients. (See Ref. Haleen and Johnson [9] and Johnston [10]; Session II of Ref. [2] is devoted to this subject.) On the other hand, even small surface asperities in centrifugal compressors can exacerbate friction losses on the high-pressure side.

It should be realized that the behavior of the wakes created by rotating blades is also different for the two types of flows. The equations describing the losses due to the wakes are also different. This difference is rarely acknowledged, however, for reasons that are given in the next section.

Mixing Losses in One-Directional Flow

The flow in axial compressor blades is essentially the flow in curved diffusers. The growth of boundary layers along a blade surface, without secondary flow effects, is shown in Fig. 7. The shaded areas indicate the regions of the retarded flow, which become the wake when it moves downstream of the trailing edges of the blades. (Note that the absolute tangential velocity of the wakes from rotors approaches that of the blades and is usually greater than that of the main stream.) The wake must eventually mix with the main flow. The mass flow rate, flow power, and momentum are conserved during this mixing. Because mixing is an irreversible process, the entropy must increase and a loss in total pressure is suffered. When a frame of reference is available in which the fluid velocity has only one direction, the conserved quantities are expressed by Eq. (11). Note that $W\sqrt{T}/AP$ is proportional to A^*/A.

$$\dot{W} = \Sigma(P/\sqrt{T})\psi\Delta A \tag{11a}$$

$$\dot{H} = \Sigma c_p T \Delta \dot{W} \tag{11b}$$

$$f = \Sigma p \mu \Delta A \tag{11c}$$

Equation (11c) is a function of the Mach number for uniform flow, and it must be the same as that calculated for nonuniform flow. One can therefore determine the Mach number of the uniform mixed flow with the aid of Eq. (11c). The other properties of the mixed flow can then be determined.

If the growth of a boundary layer is calculated, the mixing losses must be included in the loss estimates. If one uses experimental data, note that these data are often the average of the losses in a wake, weighted either by the the incremental mass flow rate of the sample data or by the incremental area. The former underestimates the loss, while the latter overestimates it. How the losses were calculated is thus a necessary guide for the application of the data.

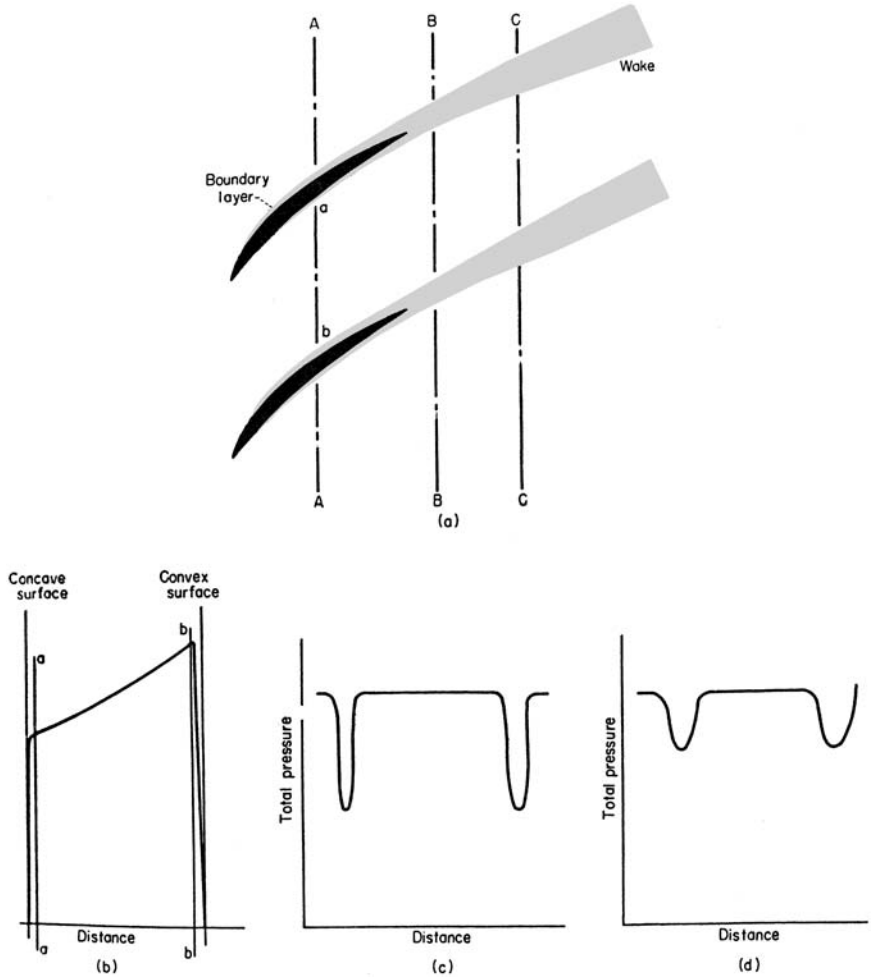

Figure 7 Boundary layers and wakes formed by cascade elements. (a) Sketch of boundary layers and wakes, (b) velocity distribution along A-A, (c) total-pressure distribution along B-B, (d) total-pressure distribution along C-C.

Observe from Fig. 8 that boundary layers also form along the outer casing and the hub. Although these boundary layers also represent losses, their principal effect is to block part of the flow area.

As previously noted, Eq. (11) is not strictly applicable when there are significant radial components of velocity (Dean and Senoco [11]). It can be

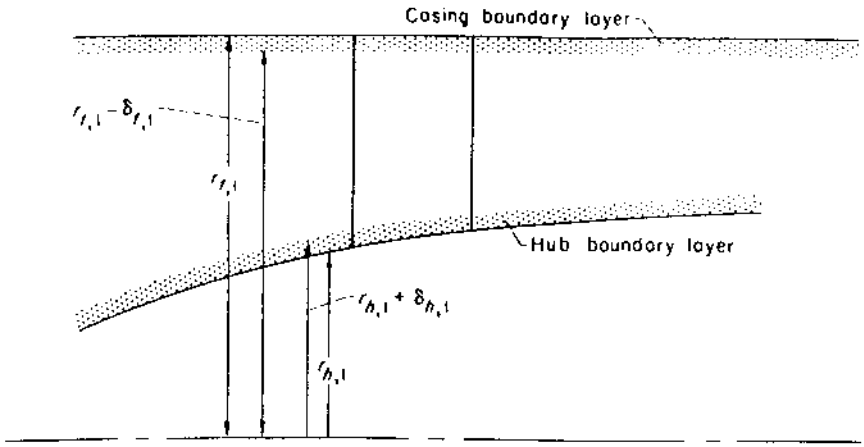

Figure 8 Boundary layers at hub and casing.

shown that an integration of the pressure along a radial line is involved. Since the attendant mixing process is accelerated by the conservation of angular momentum and by the difference between the radial pressure gradients in the wake and in the main flow, Eq. (11) does provide a useful estimate even if the flow has radial and tangential components.

Secondary Flows

A descriptive review of this subject is presented in Chapter 15 of NASA SP [1]. A fund of information is reviewed in Ref. [12]. Pertinent data are also presented in Ref. [13]. Besides the normal static pressure gradients previously discussed, gradients perpendicular to the flow but parallel to a bounding surface can develop. One of these gradients is a result of curved streamlines, and it is directed outward along the radius of curvature of a streamline. The other is in a radial direction and is the result of the difference between the rotating speed of the blades and that of the adjacent main flow.

Recall that the static pressure within a boundary layer is the same as the local pressure of the main flow and that the radial static pressure must be in equilibrium with the term V_s^2/R_C. Because of its lower velocities, the adjacent boundary layer cannot be in equilibrium with the external gradient unless the bounding surface itself is rotating at the same speed. Consequently, the flow within a boundary layer must have a velocity

component that is perpendicular to the main flow. This movement is called secondary flow. Some secondary flows move through the gas stream in the same way that steam bubbles rise from the bottom of a steam kettle toward the surface. This motion is related to boundary-layer stability.

Of interest at this time are two secondary flows. One crawls along the casing or hub from the high- to the low-pressure side of the passage between two blades. The other moves up and down the blades. The former originates near the leading edge of a blade. The boundary layer at the hub or casing comes under the influence of the stagnation pressure created by the main stream near the leading edge. The boundary layer cannot overcome the retarding pressure gradient and rolls up into an eddy. Most of this eddy moves across the channel to the low-pressure side of the passage; from there the slowly moving fluid within the eddy proceeds downstream to the trailing edge (see Fig. 9).

A secondary flow eddy is very stable, and the momentum normally supplied to a boundary layer by the turbulence of the main stream does not penetrate it. The retarded flow is thus easily disturbed by the adverse pressure gradients usually found on the low-pressure side and near the trailing edge of compressor blades.

The other type of secondary flow is generated along blade surfaces and in the blade wakes when the circumferential speed of a blade differs from that of the neighboring gas. The flow is radially inward when the rotating speed of the gas exceeds that of the blades; otherwise it is radially outward. Many of the losses generated on the blades thus ultimately appear near the hub or casing.

Still another source of secondary flow is the leakage of gas through the clearance between the ends of the rotor or stator blades and the cylindrical surfaces forming the outer casing or hub. This flow (Fig. 10) is from the high- to the low-pressure surfaces of a blade, and it forms another slowly moving stable vortex on the low-pressure side. Flow of gas over the end of a blade also lowers the pressure difference across it. The useful work delivered to the gas near a rotor tip is diminished, even though the local gas temperature is raised by nonconservative forces that increase the entropy. Smith [13] offers information about this subject.

Although secondary flows contain a large portion of the friction losses in compressors and turbines, they are still poorly understood. It is important to appreciate that they concentrate thick and stable boundary layers, in the form of eddies, on the low-pressure side of blades near the hub and casing. When an adverse pressure gradient is then imposed by the main stream, the area occupied by the eddy is considerably enlarged; flow separation may even be observed. The resulting diffusion losses are aggravated. This behavior is particularly obvious at rotor tips, and the blade loading that can

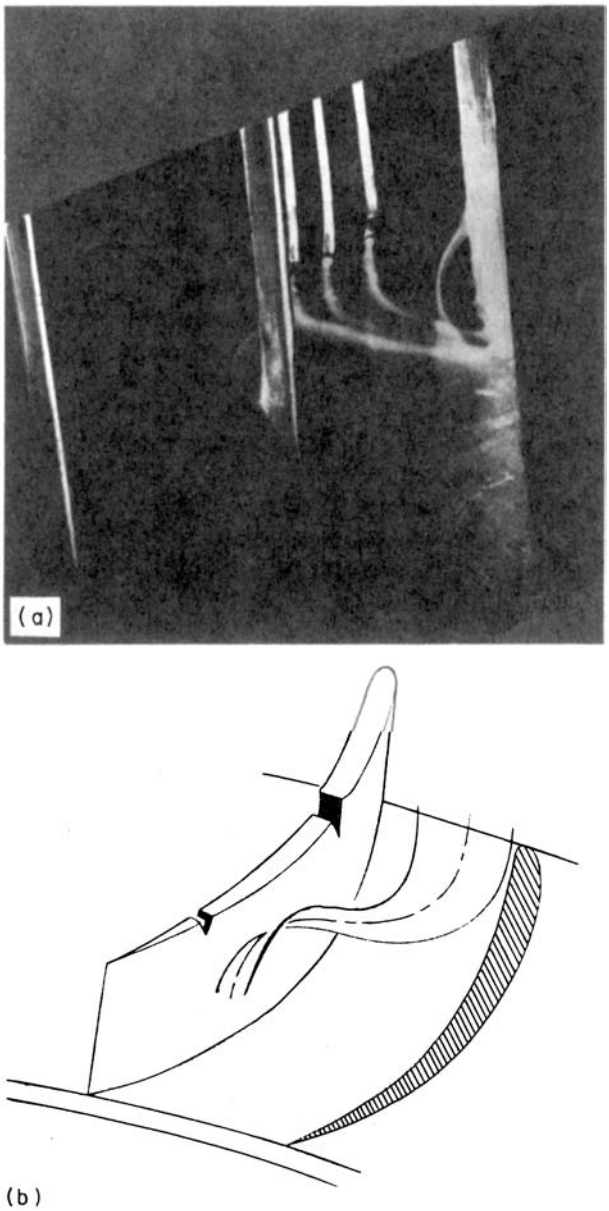

Figure 9 (a) Convergence of streamlines, (b) spanwise deflection and vortex roll-up.

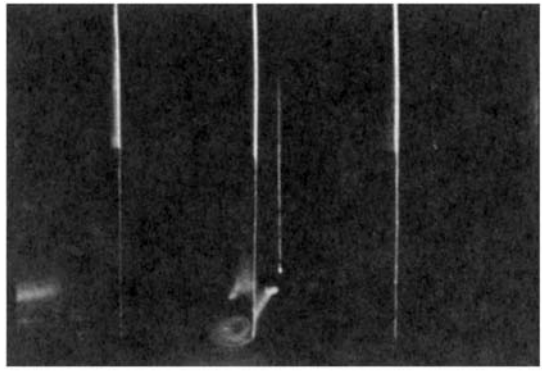

(a)

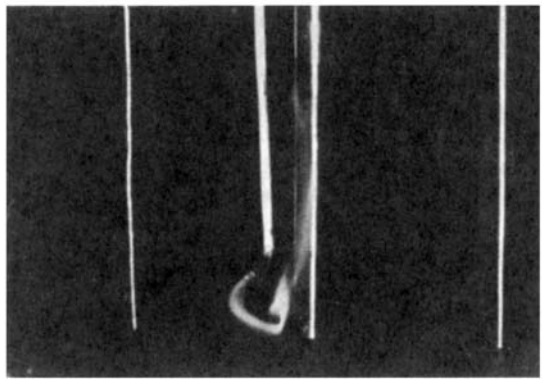

(b)

Figure 10 (a) Deflection of flow off pressure surface at blade end and through tip-clearance region to roll-up as vortex near suction surface, (b) displacement of passage vortex by tip-clearance vortex.

be tolerated there is limited. Moreover, the retarded flow occupies space and reduces the effective flow area.

One must acknowledge that classic methods of calculating boundary layers (e.g., McDonald [8]) do not include the realities of secondary flows. This fact has stimulated much of the efforts for devising numerical techniques capable of estimating three-dimensional viscous flow phenomena.

CHOKED FLOW AND SHOCK WAVES

Special considerations are necessary when the relative flow ahead of a blade row approaches or exceeds the speed of sound. Here again we must

distinguish flows that have large tangential and radial velocities from those that do not.

The latter case is treated in most texts on gas dynamics. It is shown that the flow area must converge in the direction of flow in order to lower the speed of supersonic flow. After the speed of sound has been attained, the area must diverge in order to lower the gas speed further. The flow area of such a diffuser must thus be a minimum, the throat, when the local speed of the gas is sonic.

As an example, assume ideal flow and suppose that the Mach number is to be lowered from 1.3 to 0.8. If we assign a value of 1.0 to the area at the inlet, the ideal area of the throat should have a value of 0.9355, and the exit area would be 0.9624. The corresponding ideal ratio of inlet total pressure to outlet static pressure is 1.5. These numbers can be deduced using tables for the compressible flow of air (e.g., Keenan et al. [7]).

When the flow in the diffuser has to be started from rest, however, the diffuser would choke when the inlet Mach number becomes 0.803—the point where the Mach number at the throat is 1.0. No higher inlet Mach could be generated if all the flow had to be contained within fixed boundaries.

Consider now the situation when the diffuser has a relative motion with respect to the flow. Such would be the case if the diffuser were mounted on an airplane. The diffuser would still choke at the inlet Mach number of 0.803, but the relative Mach number ahead of the inlet could be now increased because the part of the mass flow approaching the diffuser would bypass it.

When the inlet Mach number exceeds 1.0, a normal shock wave forms ahead of the inlet. The normal shock persists as the inlet Mach number increases. It is still there when the desired inlet Mach number of 1.3 is reached. The Mach number behind the shock is then 0.786, and the throat area would have to be equal to or greater than 0.9567 to pass the required flow, instead of the ideal value of 0.9355. The total pressure loss in the shock wave accounts for the difference.

The total incoming flow cannot pass through the throat until the Mach number immediately behind the shock is 0.741. The corresponding inlet Mach number is 1.40, and the ratio of inlet total to outlet static pressure becomes 1.60 instead of 1.50. The flow at the throat is supersonic, and normal shock waves are generated downstream of the throat in order to get a subsonic Mach number at the diffuser exit. In a very real sense, the diffuser has swallowed the inlet shock wave. If the downstream flow is now throttled to raise the static pressure to its design value, the inlet Mach number would be reduced to 1.3 and the design intent of the diffuser would be theoretically realized. This is an unstable condition because a slight

increase in the downstream pressure would force the shock wave upstream to a position ahead of the inlet.

A great deal of research has been devoted to the problem of starting inlet diffusers in supersonic aircraft without excessive shock losses. Younghans and Paul [14] review this subject. The same basic problem is confronted by the rotors of all compressors whenever the Mach number relative to any portion of a blade exceeds about 0.7. Recall that axial-flow compressor blades resemble curved diffusers—the flow area at the trailing edges of two adjacent blades edges is greater than that at the inlet. Moreover, blades have finite thickness, so the passage area available for the flow first converges, then diverges. This is also a characteristic feature of supersonic diffusers.

There is an important difference, however: the inlet Mach numbers relative to the blades, as well as the areas of the inlet, throat, and trailing edge, all vary with the radius. As the rotating speed of the unit is increased, the values of both the tangential and axial components of the relative Mach number increase.

Choking within a row of rotor blades initially occurs near their tips. As the rotor speed increases, the choked portions of the blade move inward. If the rotor speed is high enough and the blades are long enough, the inlet shock wave is eventually swallowed at the tips while the choked area continues to move closer to the hub. When choking occurs at any radius, however, the streamlines of the incoming flow are forced into regions of higher or lower radii where the throats are not choked. The need for a normal shock wave ahead of the leading edge tends to be mitigated. It is this fact that enables transonic and supersonic relative flows to be effectively used in compressors.

A special problem occurs when rotor blades are separated by a solid ring near their tips. This is often done in the fans of turbofan engines to prevent damage to the blades due to vibration or due to impact with large birds. Such rings are visible in Fig. 1. If the available flow area within or outside of the ring is too low, this area may contain choked flow. Such situations must be avoided to forestall crippling shock loses. The designer should verify that the minimum flow area between the casing and the ring and that between the ring and the hub are large enough to pass all the flow immediately behind any normal shock. (After the inlet shock losses are taken into account, the value of A at the critical area should be no less than that for the speed of sound.)

A different problem is faced when there are both radially outward and tangential components of gas velocity. Consider such a flow between two parallel walls. As the gas moves radially outward, the tangential component of velocity decreases because angular momentum is conserved. Shock-free

transition from supersonic to subsonic gas speeds is therefore possible as long as the combined vector of radial and axial velocity components is subsonic. This behavior is often used to advantage in the design of diffusers for centrifugal and mixed-flow compressors. The transition from supersonic to subsonic flow is allowed to take place in a vaneless space between the rotating and stationary vanes.

VELOCITY COMPONENTS UPSTREAM AND DOWNSTREAM OF BLADES

Inlet Conditions

The flow just upstream of the first blade row is assumed to be uniform and in the axial direction. Care should be taken to assure uniform flow, otherwise operation will be impaired by aerodynamic problems. High rotor speeds are frequently demanded to minimize compressor length. Small diameters are usually desired, so one often aims for a large subsonic axial inlet Mach number. Supersonic inlet Mach numbers relative to rotors, particularly near the outer casing, are thus attractive. Be aware, however, that selecting too high a value for the axial component of the inlet Mach number causes the performance curves at constant $N/\sqrt{\theta_1}$ to crowd together. Table 2 indicates the reason.

The axial velocity of the gas, denoted by V_z/a, is ideally proportional to $N/\sqrt{T_1}$, but we note that equal increments in $N/\sqrt{T}$ produce successively smaller increases in $W\sqrt{T}/P$. In fact, the magnitude of this quantity cannot exceed 0.528, which obtains when M_z is 1.0. The selected inlet Mach number at the design point must accommodate any foreseen need for gas flow rates above that selected for the design value of $N/\sqrt{T_1}$. Choosing the rotor speed and the inlet axial Mach number deserves considerable thought, and several iterations may be required to find a suitable compromise. Note that the

Table 2 Cause of Nonlinear Variation of $W\sqrt{T}/P$ with $N/\sqrt{T}$

$N/\sqrt{T_1}$	V_z/a_1	M_z	$W\sqrt{T_1}/P_1$
800	0.40	0.459	0.359
900	0.45	0.458	0.364
1000	0.50	0.511	0.395
1100	0.55	0.565	0.423
1200	0.60	0.619	0.447

Mach number at a compressor outlet is inherently prescribed by the intended use of the unit.

Relative Mach Number

Figure 11(a) is a typical diagram of the velocity vectors at the tip of a rotor blade. Note that inlet velocity is assumed to be axial. Figure 11(b) presents the case when the inlet flow has a tangential component. Both the gas velocity and Mach number relative to the moving blades are determined by the selections of the inlet Mach number and the blade speed. As a rule, relative Mach numbers up to about 1.3 may be routinely accepted if the blades are thin. Higher relative Mach numbers can be used effectively, but extra considerations are necessary, as noted later.

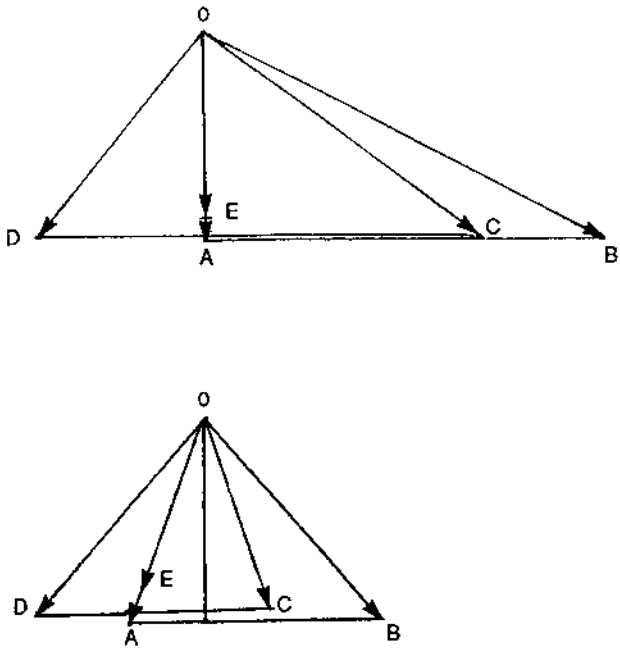

Figure 11 Velocity diagram of typical stages: (a) axial velocity ahead of rotor, (b) rotating flow ahead of rotor. OA: absolute inlet velocity, OB: relative inlet velocity for rotor, OC: relative exit velocity for rotor, OD: relative inlet velocity for stator, OE: relative exit velocity for stator.

FACTORS GOVERNING THE SELECTION OF BLADE SHAPES

The general design process is to assume a shape for each row of blades, together with the configuration of the hub and casing. Some method is then employed to anticipate the changes that the blade row should produce in the tangential, axial, and radial components of velocity of the gas. The accompanying losses in available energy are estimated at the same time—in fact, the loss estimates play a vital role in selecting the proposed changes in velocity components.

The loss estimates should be based on the fundamental equations of flow whenever possible. When all the details involved in loss calculations cannot be treated analytically, recourse must be made to empirical procedures that rely on correlated experimental data.

A brief description of the empirical material is now in order. A similar discussion of centrifugal and mixed-flow compressor design is presented later.

Axial-Flow Compressors

A practical review of the subject of blade selection is offered by L. C. Wright under Session V of Lakshminarayana [2]. This work is an extension of many of the ideas more thoroughly covered in Ref. [1]. These methods are useful for developing a preliminary design, which can be analyzed and refined by more advanced techniques.

The flow is initially assumed to lie on surfaces of revolution. It is also assumed that important radial gradients in the flow can subsequently be identified with sufficient accuracy to generate a useful design.

Flow Lies on the Surface of a Right Circular Cylinder

Figure 12 depicts this concept. It is initially assumed that there are no radial components of gas velocity. We shall see that this assumption cannot be actually realized, but it does provide a basis for further development. Note that the intersection of such a surface with a blade or vane describes an airfoil, which is called a blade element. Moreover, the velocity distribution between any two adjacent blades or vanes must be the same as that between any other two in a particular row. It is useful to express the equations of motion with cylindrical coordinates. The equation for continuity is

$$\frac{\partial(\rho V_z)}{\partial z} + \frac{\partial(\rho V_\theta)}{r\partial\theta} = 0 \tag{12}$$

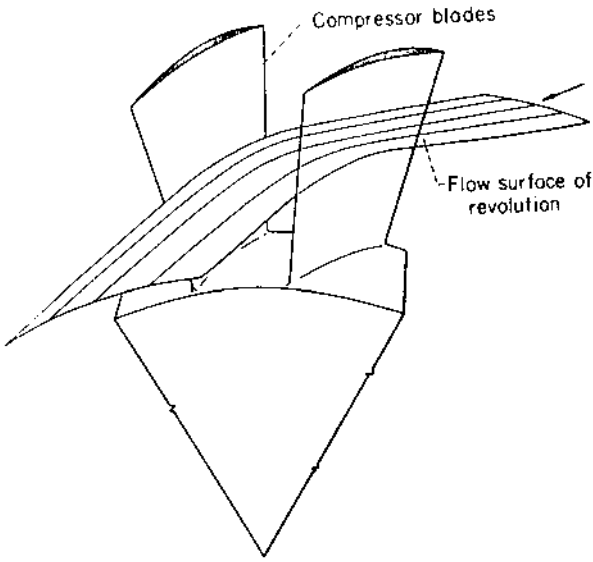

Figure 12 Sketch of flow surface and streamlines when assumed flow lies on the surface of a right circular cylinder.

Equations (13a), (13b), and (13c) express the components of vorticity in the radial, axial, and circumferential directions, respectively:

$$\frac{\partial V_z}{r\partial\theta} - \frac{\partial V_\theta}{\partial z} = \zeta_r \tag{13a}$$

$$\frac{V}{r}\frac{\partial(rV_\theta)}{\partial r} - \frac{\partial V_r}{V\partial\theta} = \zeta z \tag{13b}$$

$$\frac{\partial V_r}{\partial z} - \frac{\partial V_z}{\partial r} = \zeta_\theta \tag{13c}$$

The values of V_r and its derivatives vanish under our assumptions. If the assumed inviscid flow upstream of a blade row has no radial component of vorticity, then this condition must prevail throughout the blade row. The right-hand side of Eq. (13a) is thus 0. [The significance of the right-hand side of Eqs. (13b) and (13c) is discussed later.]

Two-Dimensional Cascades

Inasmuch as r is assumed to be constant on any stream surface, the equations may be altered so that $dz = dx$ and $r\,d\theta = dy$. Hence, Eqs. (12)

and (13a) also represent two-dimensional flow through a cascade of airfoils that lie in a plane containing the cartesian coordinates x and y.

This result shows why tests of the flow through two-dimensional cascades of blades have been used to determine important features about the flow through blades, except for secondary flows. The use of ideal two-dimensional flow calculations, together with conventional boundary-layer analyses, is also suggested by these equations. The variables for two-dimensional cascade tests are blade shape, inlet gas angle, blade angle, and solidity. The last three quantities are denoted in Fig. 13 by β_i, β_b, and σ, respectively. The Mach number of the flow is also a test variable. (Without special equipment, however, attempts to obtain valid data between inlet Mach numbers of about 0.7 and 1.3 would be unsuccessful.)

The derived test data are the deviation angle, δ, and some weighted average of the total pressure loss, ΔP, through the blades. Numerous data have been published (see Refs. Lakschminarayana [2] and Serovy [3]), and

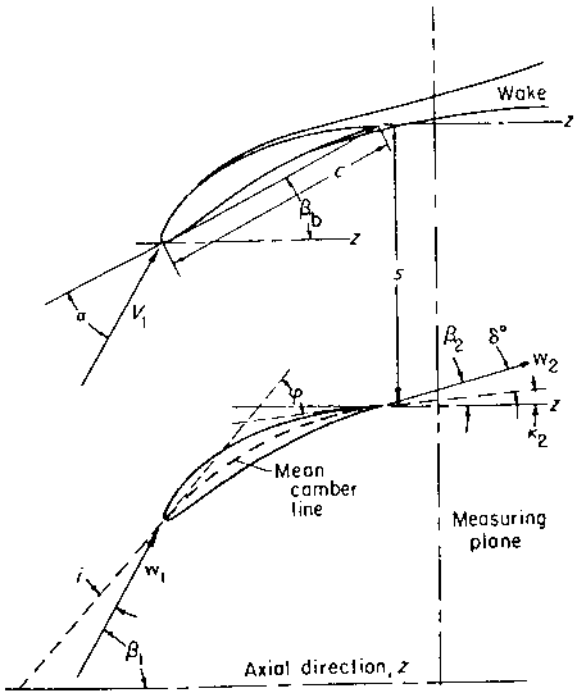

Figure 13 Nomenclature for cascade blade, $\delta = C/s$.

useful shapes and orientations of blades can be selected for a wide range of design points.

All of the early experimental results were obtained with low gas speeds; the axial velocity was virtually constant through the cascade. In real compressors, however, this component usually decreases through a blade row. We must anticipate that some correction for this event is necessary.

The published data also permit estimates of off-design performance. A summary and correlation of some of the results of this work are summarized by S. Lieblein in Chapter 6 of NASA SP [1], and in Refs. Lieblein [15] and [16]. (Observe that calculations of the ideal flow through two-dimensional cascades, together with boundary-layer calculations, should yield design information also.) Probably more reliable data, with fewer corrections for radial gradients, are potentially obtainable from measurements made upstream and downstream of the rotors and stators of actual stages. Chapter 7 of NASA SP [1] considers this topic.

A correlation of the inherent limits that can be imposed on the change in tangential velocity produced by a row of blades is furnished by Chapter VI of NASA SP [1]. It is shown that a function called the diffusion (or D) factor and defined by

$$D = V_2/V_1 + \Delta(V_\theta r)/(2r_1 V_1) \tag{14}$$

should not exceed about 0.6 for efficient cascade performance (see Fig. 14). In Chapter 8 of NASA SP [1], Robbins, Jackson, and Lieblein show that the retarded secondary flow vorticities at a rotor tip reduce the limiting value of D to 0.4 or lower. The effect of incidence angles is correlated in Lieblein [16]. This is useful information for the analysis of off-design conditions.

In practice, the changes in the axial component of velocity from blade row to blade row are chosen to be consistent with the selected compressor inlet and outlet Mach numbers, which have an effect on the D factor. Note that once this choice has been made, a change in the relative gas velocity through a blade row depends only on the change in the tangential velocity through it. Changes in axial velocity also accompany radial shifts of the stream surfaces. (The causes of these shifts are reviewed in the next subsection.) The effect on axial velocity is estimated after the magnitude of these shifts have been calculated. Some iteration may be required to accomplish this.

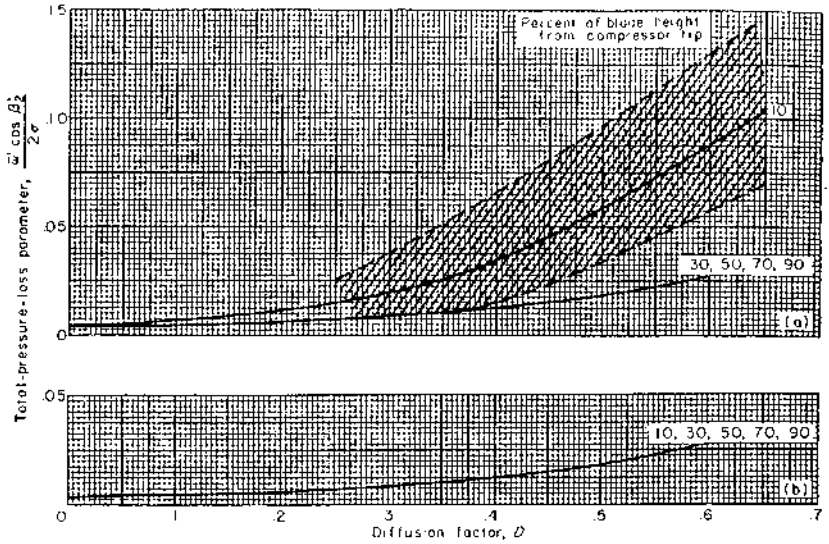

Figure 14 Deduced variation of total pressure-loss parameter with diffusion factor at incidence angle for minimum loss, NACA 65-(A_{10})-series and double-circular-arc blades. (a) stator, (b) rotor.

Radial Velocities

Observe first from Fig. 2 that the shapes of the hub and shroud surfaces are also a source of radial components of velocity. Equations (13b) and (13c) reveal other sources.

Radial Velocity Gradients Caused by Vorticity

A better insight, however, is suggested by Eq. (15), which combines the energy equation with the conditions necessary for radial equilibrium of an ideal flow when radial components of velocity are ignored:

$$-(1/p)(\partial p/\partial r) = -(V_\theta^2/r)$$
$$= V_z(\partial V_z/\partial r) + V_\theta(\partial V_\theta/\partial r) - \frac{\partial}{\partial r}(\omega_0 r V_\theta) \tag{15}$$

Let us further assume that

$$V_\theta = \Gamma/r + \omega_a r \tag{16}$$

where Γ and ω_a are constant along a radial line. We can then write:

$$V_z(\partial V_z/\partial r) = 2\omega_a(\omega_0 - \omega_a)\mathrm{r} - 2\omega_a(\Gamma/r) \tag{17}$$

Observe that V_z does not change with r when $\omega_a = 0$. In this case, $V_\theta = \Gamma/r$. This situation is called a free vortex rotation and is selected for many designs. Equation (17) then becomes

$$\frac{1}{2}(V_{z,2}^2 - V_{z,1}^2) = \omega_a(\omega_0 - \omega_a)(r_2^2 - r_1^2) + 2\omega_a\Gamma\ln(r_1/r_2) \tag{18}$$

Subscripts 1 and 2 refer to the hub and outer casing, respectively.

Consider the situation when $\Gamma = 0$. It is evident that $V_{z,2} = V_{z,1}$ when $\omega_a = 0$ or ω_0. *The difference between the two velocities is a maximum when* $\omega_a = 0.5\omega_0$. Figure 15 illustrates a typical shape of the stream surfaces suggested by Eq. (18). Observe that radial flow is necessary, however, to actually achieve the differences in axial velocity and that this flow reduces the magnitude of these differences. Significant gradients in axial velocity, which are primarily functions of ω_0, ω_a, and (r_2/r_1), must still be present when the rotation of the fluid is not that of a free vortex.

The relative simplicity of a free vortex design encourages its use in many applications. Note, however, that the stagger angle of the blades of such designs must change with radius—the blade is twisted. Consequently, bending moments near hubs are produced in rotor blades by centrifugal force. (This is especially true for centrifugal and mixed-flow compressors where the change in tangential velocity is large. The variation of tangential

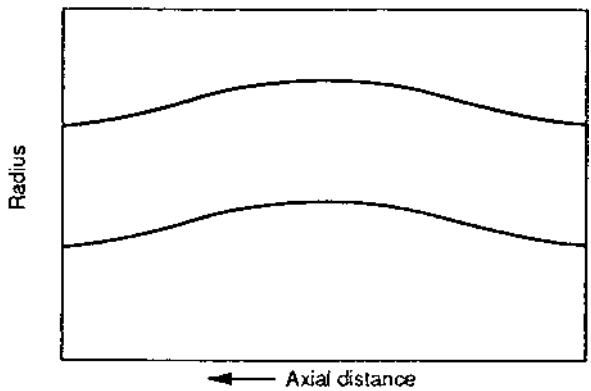

Figure 15 Ideal shape of streamline in a rotating blade row imparting solid body rotation to a gas.

velocity with radius and axial distance in these units is indeed often limited by mechanical stresses.)

Radial Velocities Implied by Flow Continuity

The mass rate of flow between the hub and an arbitrary radius may be expressed by

$$2\pi\int_{r_1}^{r_2}\rho V_z r dr = \dot{m} \tag{19}$$

The term V_z is calculated from

$$V_z = V\cos\beta \tag{20}$$

Equation (15) shows that the static pressure normally increases with the radius whenever the tangential component of velocity is finite. Changes in the radial gradient of gas density are therefore expected whenever the tangential velocity of a gas changes in the direction of flow. The same effect is also produced when the axial velocity is a function of the radius. In either case, β_2 must change with radius because of the radial movements of the gas.

In order to recognize this case, we now assume that the flow lies on conical surfaces and that we can estimate any resulting change in deviation angles by the equations presented by L. C. Wright in Session V of Lakshminarayana [2]. These equations include an estimate for the changes in axial velocity that were previously noted:

$$\tan\beta'_{2,\mathrm{e}} = (r_2 V_{z,2})/(\mathrm{r}_1 V_{z,1})\tan\beta_z + (U_1/U_{z,1})[1-(r_2/r_1)^2]$$

and

$$\tan\beta_{2,\mathrm{e}} = (r_2 V_{z,2})/(r_1 V_{z,1})\tan\beta_2$$

Since the details of the flow in the compressor hub and casing boundary layers are rarely known, Eq. (19) is often integrated between the limits of $r_1+\Delta r_1$ and $r_2-\Delta r_2$. The terms Δr_1 and Δr_2 are estimates of the thickness of the hub and casing boundary layers. As previously noted, part of these boundary layers contains gas particles that were originally retarded by the blades and have been displaced by secondary flows. The information necessary for predicting these boundary-layer properties cannot be obtained at this writing. Instead, the left side of Eq. (19) is usually multiplied by a blockage factor, B. Be aware that the output of a design is very sensitive to the selected values of Δr and B. Unfortunately, the data in the open literature on this subject are sparse, and even the use of the best data available often leads to designs that require experimental development.

There is a good reason for this situation. It is difficult to determine by tests when the physical area for the flow is just right. Gas will always fill the space available for it, and the performance of diffusers is best when the flow through them is on the verge of separating. A value of 0.98 has been used for the value of B in the first stage and 0.96 for subsequent stages. This is admittedly crude, and it suggests a fertile area for future research.

A practical review of the various blockages and losses in axial flow compressors is presented in Koch and Smith [17]. This reference also offers a good insight into some of the important items a compressor designer should consider.

CENTRIFUGAL AND MIXED-FLOW COMPRESSORS

Attention must be given to all three directions of flow in the usual configuration of these compressors (e.g., those shown in Figs. 3 and 4). No experiments have been devised that provide credible correlations about how blade shapes affect the deviation angles, the optimum incidence angles, or the losses. Consequently, the initial concepts for the shapes of both rotors and stators are individually derived for each application.

Specific Speed

A quantity known as specific speed provides a correlation between compressor efficiency and the energy that can efficiently add to the gas flow by the compressor. Specific speed is defined by

$$N_s = (N\sqrt{Q})/(\Delta H)^{0.75} \tag{21}$$

A relation between specific speed and the best attainable compression efficiency, derived from tests of a number of centrifugal impellers, is shown by the data points of Fig. 16. (Be aware of the definitions for both η^* and Q.)

$$\eta_c^* = \frac{1 - \left(\frac{P_1}{P_2}\right)^{\frac{\gamma-1}{\gamma}}}{\frac{\Delta T}{T}}$$

$$N_s = \frac{N\sqrt{Q_{AV}}}{\Delta H^{.75}}$$

$$Q_{Av} = \sqrt{Q_{IN} Q_{OUT}}$$

The solid line of this figure represents a similar and widely used correlation

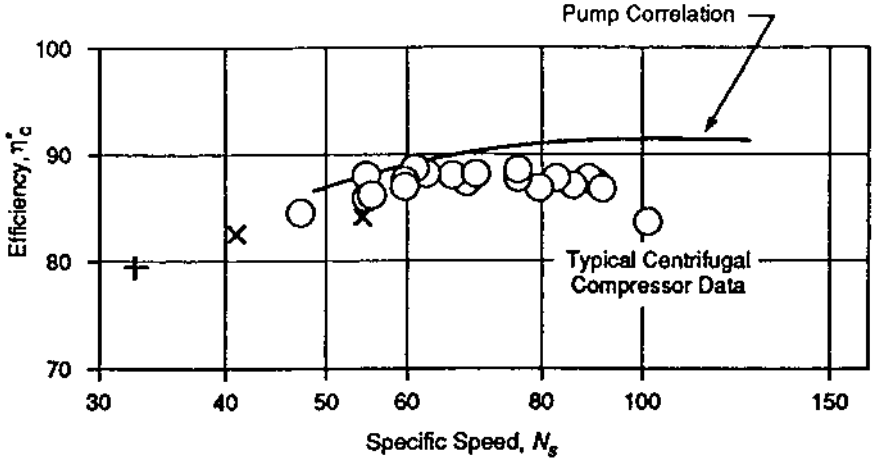

Figure 16 Use of specific speed to correlate compressor efficiency.

for centrifugal and mixed-flow pumps. The agreement among the data suggests that the curve can be used with confidence for both centrifugal and mixed-flow compressors. A preliminary estimate of the specific speed necessary to get a given compressor efficiency is thus obtained.

The conditions at the compressor inlet, including the mass flow rate, are assumed to be known. If N is also known, then one is required to estimate a value for ΔH to assure the attainment of at least a given level of efficiency. A trial value of ΔH is assumed and the corresponding value of the compressor temperature ratio is found. The selected efficiency then determines the pressure ratio, and the magnitude of Q can be calculated. The corresponding value of N_s is found and the associated efficiency is compared with that desired. Successive iterations eventually establish the magnitude of ΔH. (Observe that the value of N necessary for a required efficiency is easily obtained if ΔH is included with the specified data.) The preliminary design of rotors and stators will be separately treated in the following sections.

ROTORS

The first paper of Session V of Lakshminarayana [2] reviews this subject in depth. Supplementary information is presented next.

Projected Shape in Meridional Plane

Let us first consider the shape projected by a rotor on the meridional plane, which is a plane through the axis of rotation. This shape is illustrated by the contours shown for the centrifugal impellers in Figs. 2 and 4. The boundaries of the indicated flow passage turn the flow radially outward and thereby produce additional velocity gradients normal to the stream surfaces. The velocity of a gas is higher at the casing than at the hub.

Blade Shapes

Refer now to Eq. (16) and note that ω_a must have finite values in centrifugal and mixed-flow impellers. The velocity gradients described by Eq. (17) augment those noted in the previous subsection when the magnitude of ω_a is less than one half of the angular velocity of the impeller. Both the vorticities and the curvatures of the hub and shroud induce high gas velocities at the outer casing and low velocities at the hub. The effect of vorticity is reversed at greater values of ω_a. Vorticity and the outward curvature of the flow have been responsible for stagnated flow at the hub and separated flow at the casing. Outward curvature of the hub and casing should thus be deferred until the value of ω_a is about 50% of the angular velocity of the rotor. For this preliminary design, one may estimate the gradients by assuming that the path of the flow follows the shape of the blades.

One should strive to design the blades so that as much free vortex rotation as possible is imparted to the gas in the regions where the flow has a strong axial component. Recall, however, that mechanical stresses can limit this objective.

As a tentative diffusion limit, the relative velocity at the impeller outlet should be no less than 60% of the maximum relative velocity at the inlet. If the resulting relative velocity component at the impeller outlet is uncomfortably high, the use of relative tangential velocities opposite to those of the impeller blades should be considered. The blades of such impellers are said to have backward curvature. The absolute value of the outlet tangential component of gas velocity is reduced, which lessens the task of the following stator or diffuser. Impeller cost, size, stresses, and possibly efficiency are the principal limitations to the amount of backward curvature that may be selected.

Slip Factor

Unfortunately, there is no good general rule for estimating the deviation angle or an equivalent angle. A quantity known as slip factor is an

alternative frequently employed. If the relative angle of the flow leaving an impeller were parallel to the impeller blades at the trailing edge, the absolute value of the tangential component of the exit velocity would be $V_{\theta,\mathrm{i}}$. The ratio of $V_{\theta,2}$, the tangential velocity actually realized, to $V_{\theta,\mathrm{i}}$ is called the slip factor. Various formulas for estimating slip factor have been published, but most are unreliable. Most of the values were deduced by measuring the temperature rise in the impeller and calculating the value of ΔH and the value of $V_{\theta,2}$ by using Eq. (7). In nearly all impellers, however, some flow is recirculated between stations somewhere between the inlet and discharge. The actual value of $V_{\theta,2}$ is lower than that calculated. In fact, slip factors greater than unity have been reported, and this is absurd. A practical solution is to estimate the slip factor by Eq. (22), and then increase the impeller diameter by about 5%. The impeller tip is gradually cut back to the proper value during development testing. Chapter 4 of Balje [19] has a good discussion about slip factor. One of the equations noted there is

$$\text{Slip factor} = 1 - (3 \sin \beta_{\mathrm{b},2})/Z \tag{22}$$

STATORS OR DIFFUSERS

Four types of stators or diffusers have been used. They have been designated as vaneless, vane island, cascade, and pipe diffusers. Most often, nearly all the diffusion takes place while the gas velocity has a significant radial component. The flow then is usually either turned to the axial direction, as shown in Figs. 1–4, or collected by a scroll, which changes the flow direction to a tangential one. Chapter 6 of Balje [19] reviews the design of scrolls.

Vaneless Diffusers

These diffusers are rarely used in industry except when some efficiency can be sacrificed to reduce manufacturing costs, when size is not a criterion, or if a wide range of flow rates between the maximum flow and surge is mandatory. Scrolls are generally used with these diffusers. Chapter 6 of Balje [19] reviews the design of these diffusers. As previously noted, deceleration of the tangential component of velocity leaving the impeller is automatically accomplished as the radius of the flow increases. Deceleration of the radial and axial components, which is controlled by the space between the two walls, must be kept small.

Short, vaneless diffusers also offer a cost-effective way to execute part of the development testing of centrifugal and mixed-flow compressors. The

inherent flow range of the impeller is disclosed by this test. The inlet angles of the impeller can be deliberately set for flow rates that are lower than desired. After the initial test, the leading edges of the blades are machined back in appropriate steps to realize maximum impeller efficiency at the design flow rate. Similarly, the diameter of the impeller tips can be made extra large and then machined back so that the desired useful energy is imparted to the gas.

Vane Island Diffusers

These are the diffusers used for the centrifugal compressors of Figs. 1–4. In other applications, scroll collectors may be used with these diffusers also. Vane island diffusers usually have thin leading edges and can be used in both subsonic and supersonic flow. Note that the vane heights are usually too limited to alleviate the choking effects noted in the discussion of supersonic diffusers. Many designers leave sufficient radial distance between the impeller and the vanes to allow the flow to become subsonic, that is, to reduce the Mach number to a value of 0.8 or lower.

The diffusion process is mainly controlled by the flow area between the vanes, although the curvature of the vanes has a noticeable effect. Reneau et al. [20] and Sagi et al. [21] offer relevent data on these subjects. These references also show that the efficiency of diffusers is strongly dependent on the thickness of the boundary layer at the diffuser inlet. The maximum thickness used in the references should be assumed for the design of these diffusers.

The leading edges of the diffuser vanes must be properly aligned to the incoming flow, because this usually controls both the maximum flow rate and the surge point at rated speed. Measurements of flow angles during tests with vaneless diffusers are a useful guide. The vanes usually have no twist; however, determining the flow angle as a function of passage width provides data for specifying the angle of the leading edge along the span of the blade. The ability to adjust the vanes during development testing to precisely define the usable range of flow rates is often cost-effective.

Cascade Diffusers

These diffusers resemble vane island diffusers. Blades similar to those of axial-flow compressors are placed in one or more rings around an impeller. The height-to-spacing ratio of the blades for these diffusers is of the order of unity. Experience with them is limited to subsonic flows. The diffusion factor developed for axial-flow blades is used to determine how much each ring may reduce the angular momentum of the gas flow. Unlike axial

compressor blades, however, the blades of cascade diffusers do not influence the direction of the incoming air far upstream (see the appendix of Bullock [22]). On the other hand, they have a larger effect on the tangential velocities at greater radii. The correlations of both [15] and [16] are therefore not completely applicable, and the best results are obtained when adjustable blades are used during development in order to find the optimum blade orientation.

Testing impellers with vaneless diffusers before installing a cascade diffuser is recommended. Beneficial results have been derived from twisted diffuser blades and using test data to specify the variation of the angle of the leading edge along the span of the blade. These diffusers have demonstrated high efficiency in the laboratory, but they have not been extensively used by industry because the blades are relatively thin and are subjected to high gas velocities. It has been feared that their life would be limited by erosion or by foreign object damage in applications where the incoming gas may carry dust particles.

Pipe Diffusers

These are tapered holes drilled through a solid annulus. The annulus, in turn, is defined by the selected inner and outer radii of the diffuser as well as the gap between the inner and outer walls. Kenney [23] and Kenney and Morris [24] may be used as a guide for determining how much the flow area in the diffuser can be increased. These diffusers are inexpensive, are easy to fabricate, and may also be castings. Their efficiency is more or less comparable to that of vaned diffusers. Some experiments should be made to find the best orientation for the center line of the tapered passages.

MULTISTAGE COMPRESSORS

A four-stage axial compressor is shown in Figs. 1 and 2, while a two-stage centrifugal compressor is presented in Figs. 3 and 4. A single stage usually consists of a rotor followed by a stator. Occasionally, a stator is used in order to establish a prescribed distribution of tangential velocity ahead of the first blade row. The first stage would then include this stator. Two more stators have been used behind a rotor, particularly the final rotor, in order to remove all circumferential components of velocity. Two or more multistage axial compressors may also be placed in series to provide a given pressure ratio (see Figs. 3 and 4).

The methods previously mentioned may be used for the initial definition of shapes for the blades and passages of multistage axial

compressors. Multistage centrifugal compressors are also designed one stage at a time. As depicted in Figs. 3 and 4, however, the flow leaving the diffuser of an upstream stage must be turned three times—axially rearward, radially inward, and axially rearward again. Any residual swirl existing behind the radial inflow section must be removed to obviate a large swirl ahead of the next impeller, due to the conservation of angular momentum. Additional vanes near the outer radii are often used for this purpose.

Problems with Multistage Compressors at Part Speed

Certain precautions should be observed in defining the specifications of each stage in order to preclude problems when the rotating speed is increased from rest to its design value. There is an instinctive desire to operate each stage at its maximum efficiency at the selected design point. When the design point pressure ratio is too high, however, difficulties may be encountered while the unit is being accelerated from rest. An example illustrates the problem.

Assume that the data for Fig. 5 were generated by a compressor that has the following specifications at its design point:

Blade-tip speed	1000 ft/s
Inlet axial Mach number	0.6
Outlet axial Mach number	0.3
Relative air angle at inlet	57°
Relative air angle at outlet	65°

Consider now the corresponding data at 60% of design speed:

Blade-tip speed	600 ft/s
Inlet axial Mach number	0.2
Outlet axial Mach number	0.35
Relative air angle at inlet	70°
Relative air angle at outlet	52°

Observe the large increase in the relative air angle at the inlet and the accompanying large decrease in air angle at the outlet. These changes not only cause the inlet rotor blades to stall—that is, separated flow occurs—but they usually cause choked flow to degrade the performance of the outlet blades.

Note that the losses in stalling blades tend to increase as the flow is reduced. A stalling blade row thus offers a negative dynamic resistance to the flow: the loss in pressure increases as the flow reduces.

Since any compressor blade row is really a group of diffusers in parallel, a stalled blade row often develops several circumferential zones of separated flow, more or less equally spaced around the row. The stall zones rotate at a speed that is about half that of the rotors. A typical operating regime where this occurs in noted in the map of Fig. 5.

Had the compressor been designed for optimum efficiency at rated speed, the incidence angle at the inlet for part speed would be much higher than optimum, while the incidence angles for the outlet stages would be much too low. The inlet blade rows would be severely stalled, and choked flow would further impair the usefulness of the outlet rows.

The inlet rows of such an "ideal" design have been known to remain stalled, while the inlet blades were choked, until the operating speed approached 120% of rated speed. After the outlet stages became unchoked, the rotating speed could be continuously reduced to its rated value, where the higher efficiency of the "ideal" design could be realized. Observe that the map of such a compressor is not unique; there could be two curves for some constant speed. The applicable one would depend on how the speed was approached.

There are not many applications that could tolerate this situation. For the design point, compresser designers often use lower than optimum incidence angles for the initial stages and higher than optimum values near the outlet. Leaning too far in this direction, however, has produced premature surging at the higher speeds, which reduced the potential efficiency and range of performance. Notice that the areas defined by the hub and casing diameters throughout the compressor are critical. Experimentally adjusting these areas is sometimes needed to balance performance at design speed, part speed, and overspeed.

The problems at part speed can be further relieved in three ways.

First, adjustable stators blades have been used to partially control the incidence angles of the blades that are in danger of stalling or choking at part speed. Trial-and-error experiments are usually necessary, however, to properly schedule the setting of the stators as a function of rotating speed.

A second way is to provide a scheme for removing part of the gas flow from the compressor at one or more stations downstream of the initial stages. Removing gas at part speed increases the flow through the inlet stages, thus diminishing their tendency to stall. It also increases the pressure ratio they produce. This result, together with the reduced mass flow through the latter stages, removes the tendency of the outlet stages to choke.

The third, and most usual, way is to develop the required pressure ratio by putting two or more compressors in series. Each compressor has an independent shaft and rotating speed. The compressors illustrated in Fig. 1 are examples of such an arrangement, which is frequently used in gas

turbines. In these designs the high-pressure unit is started first. This approach not only eases the part speed problems, but the resulting unit is able to attain higher efficiencies: the equivalent speed of each compressor can be more exactly tailored to the equivalent flow through it. Such a system is still apt to exerience part speed problems when the overall pressure ratio is high enough.

A practical example of the part speed problem is given in O'Brien and Boyer [25]. This experience lends additional support to the recommendation that analysis of the potential problems is always a good idea before any hardware is built. Observe that similar reasoning with the same conclusions is valid for centrifugal compressors.

ESTIMATING DESIGN AND PART SPEED PERFORMANCE

The data generated during the preliminary design also provided the first estimate of design-point performance. Now that the shapes for the blades in each row, as well as the hub and shroud contours, have been defined, a review of design-point pressure ratio and efficiency is in order. An estimate of these quantities at other speeds and weight flows should be made also.

For each case we must again determine deviation angles or slip factors as well as the total pressure losses experienced by each stream surface as it passes through a blade row. The increases in enthalpy through a rotor and the pressure ratio and efficiency of every stage are then calculated. The resulting data are combined to predict overall design and off-design performance.

A number of procedures, based on different simplifying assumptions, have been devised for estimating deviation angles and losses. Some of these are now presented.

AXIAL-FLOW COMPRESSORS

Six different concepts have been used for axial-flow compressors.

Information from Two-Dimensional Experimental Data

Blade elements were originally defined by the intersection of a blade with cylindrical surfaces. Radial movements of the flow through a blade row were subsequently recognized by assuming the streamlines to lie on conical surfaces. The surfaces, in turn, were determined from the requirements of flow continuity and vorticity. The deviation angles and the two-dimensional

losses in available energy are determined directly from experimental cascade data or from correlations of such data. Losses due to the boundary layers at a hub or casing and those caused by flow through clearances at the blade ends are estimated with the aid of other empirical correlations. Smith [13], Lieblein [16], and Koch and Smith [17] are again cited as examples of this procedure. Chapter 7 of NASA SP [1] provides additional information and references. The examples described in NASA SP [1] are based on the assumption that streamlines lie on conical surfaces. If experimental cascade data have been measured over a range of inlet air angles, they may be used for off-design performance estimates also. These experimental data have been presented in many forms. One may deduce from any of them how the tested blade shapes, solidities, stagger angles, and incidence angles affect both the turning angles and the observed losses in total pressure. (The turning angle measures the angle through which the flow is deflected by a blade.)

It should be observed that data from two-dimensional cascades are unavailable for cases where the inlet Mach number ranges from about 0.7 to 1.3. The previously discussed flow phenomena in compressor blade elements at transonic gas speeds preclude the establishment of the required flows without special equipment. Reliable transonic blade element data for rotors have been obtained, however, from tests of actual units. Data for higher supersonic Mach numbers have been obtained in two-dimensional cascades. Starken and Lichtfuss [26] is an example.

Use of Two-Dimensional Flow Theory

This procedure differs from the preceding one in that mathematical theory is used to estimate the changes in tangential velocity imparted to a gas by a blade element. Boundary-layer analysis then provides an estimate of the two-dimensional losses. Separate correlations are again needed for the losses and blockage at the hub and casing. Dodge [27] is an example of a procedure for calculating the inviscid two-dimensional flow field. The method of characteristics is sometimes used to estimate the velocity distributions in the regions of supersonic flow. As an alternative, the work described in Dodge [28] can be used. McDonald [8] discusses procedures for calculating the boundary layers and losses associated with the blade elements.

It was initially assumed that the streamlines within a blade row are confined to cylindrical surfaces. In order to account for inevitable radial shifts of the flow, it was then assumed that streamlines lay on conical surfaces. A more satisfactory technique takes into account, one way or another, the curvatures of the streamlines, as projected on a plane through the axis of rotation. This is discussed in the next four concepts.

Corrections for Streamline Curvature

Hamrick et al. [29] reports an early attack on this problem, which is very important in centrifugal compressors. The position of the projected streamlines is assumed; the radial pressure gradients induced by the curvature of the streamlines and the rotation of the gas are then calculated. The resulting changes in the velocities and gas densities are evaluated. One then revises the positions of the streamlines as required by flow continuity. This of course changes the curvature of the streamlines, so the previous calculations are repeated and the radial pressure gradients are corrected. This iterative process is continued until satisfactory agreements are reached. Novak and Hearsey [30] improves this concept and shows how it can be extended to axial-flow compressor design.

Combination of Separate Two-Dimensional Flow Calculations

Simultaneous equations of flow on two surfaces, designated as S_1 and S_2, are formed from the three-dimensional equations for inviscid flow. These surfaces are more or less orthogonal to each other. The resulting equations are used to determine ideal gas velocities throughout a blade row.

This procedure allows the effects of entropy gradients to be considered, but not the local effects of viscous action. Entropy gradients are initially assumed, and the velocities are calculated. These velocities, together with boundary-layer theory, shock loss calculations, and blockage estimates, are used to reevaluate the entropy gradients. The calculations are reiterated as often as required in order to establish a consistent distribution of velocities and losses.

This concept was originated in 1952 by Chung Hua Wu and has been continuously developed by him over the intervening period. Wu et al. [31] and Wu et al. [32] demonstrate the usefulness of this approach and provide an extensive list of supporting references. This method is often preferred to other inviscid calculations.

Use of Three-Dimensional Inviscid Flow Theory

Finite-difference or finite-element forms of the inviscid equations of flow in three dimensions are written. Corrections for boundary layers on the blades and on the inner and outer walls are made as indicated in the preceding two methods. Katsanis and McNally [33] presents a typical procedure that can use this concept.

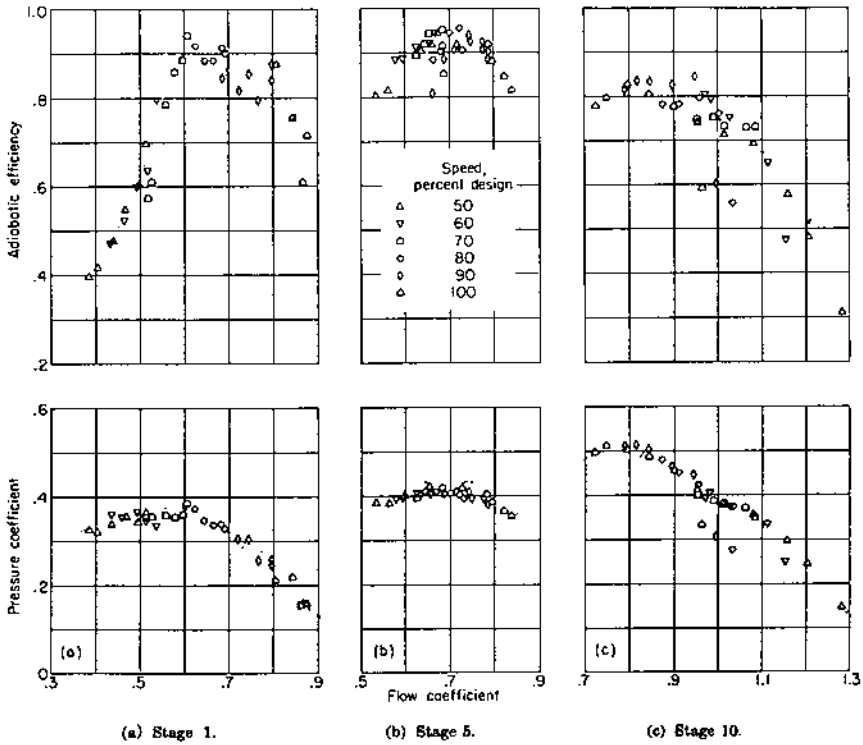

Figure 17 Generalized stage performance for stages (a) 1, (b) 5, and (c) 10 of a 10-stage compressor.

Three-Dimensional Equations of Viscous Flow

These equations can be solved by using an assumed model for the viscous turbulence together with a numerical process known as equation splitting. The velocity vector is decomposed into one that has no divergence and another that has no curl. The equations are coupled by the provision that fluid pressures must be the same for both velocity fields. This idea, which is an extension of the conventional boundary-layer technique, has the potential of accounting for all the the effects of viscosity, even secondary flows. This procedure was conceived by P. Dodge and was first presented in Waterman and Tall [34]. Future work may enable one to include the losses caused by flow through the clearances at the blade ends.

Preparation of Maps

Once the losses and energy changes have been established, compressor maps are conveniently estimated by preparing individual stage curves similar to those of Fig. 16. Note that the variables selected tend to collapse the curves for a wide range of rotor speeds into one curve. A set of curves is prepared for each stage. The abscissa is the flow coefficient: the ratio of the mean axial component of velocity at the inlet of a stage to a characteristic speed of the rotor. A diabatic efficiency is the ordinate for one set of curves, and pressure coefficient is the ordinate for the other. (This coefficient is the ratio of the useful energy transferred to the gas to the square of a characteristic rotor speed.)

These curves are created by first selecting the flow coefficients of each stage being considered. Blade elements for each blade row are then identified. Allowances for the blockage at the hub and casing are made; then the gas velocities and incidence angles at the inlet of each element are determined. Changes in the tangential component of velocity can be calculated, and the change in enthalpy through a rotor is determined. The total pressure loss within each blade element is converted into an increase in entropy. Pressure coefficient and efficiency for each complete stage are then readily found.

Chapter 10 of NASA SP [1] demonstrates the validity of this approach. The same reference indicates how these data are used to synthesize a map for a range of rotating speed and gas flows. A rotor speed and a gas flow rate at the inlet of the first stage are assumed; the pressure and temperature changes through the stage are then calculated with the aid of the estimated stage curves. The flow coefficient of the following stage is then determined, together with the changes in pressure and temperature through it. This procedure is repeated for all the stages of the compressor. The entire routine is also repeated for other gas flow rates and rotor speeds. This work provides the data necessary to plot the desired map. Chapter 13 of NASA SP [1] provides a number of examples of this procedure. Novak [35] contains supplementary information.

Defining the surge point at each speed requires special attention. Chapter 12 of NASA SP [1] and Bullock et al. [36], Greitzer [37], and Greitzer [38] present important details about the subject of surging. Note that surging may occur whenever the pressure ratio being developed at a fixed rotor speed drops while the flow rate decreases: the slope of the performance curve for a constant speed is then either positive or discontinuous. Although the former condition is necessary for surging to occur, it is not sufficient. The degree to which positive slopes may be tolerated depends on both the volume and the momentum of the gas within

the compressor system, as well as the pressure ratio being developed. The slope at the surge point is practically zero for large volumes or high pressure ratios.

Observe that a positive slope of a constant-speed curve requires a cell of separated flow to be either developing or growing within a blade row. Chapter 13 of NASA SP [1] contains a discussion of some of the factors influencing the slope. However, experience has not yet produced a method of precisely anticipating the surge point of a given design. At this time, it is prudent to assume that surge will occur whenever the incidence angle of any part of any blade row starts to exceed the angle for stall. If part of a blade row is already stalled, however, the compressor will probably be free from surging as long as none of the blade rows is either beginning to stall or experiencing the growth of an established stall zone. This discussion admittedly lacks the positive directions that one desires, but this is the current state of the art.

Centrifugal and Mixed-Flow Compressors

Energy Addition and Losses

The very nature of the shape of these compressors precludes the existence of anything similar to the two-dimensional cascade data that are available for axial-flow compressor design. The latter four techniques discussed for axial-flow compressors are equally applicable to these units.

The third method of the previous section, corrections for streamline curvature, is used when calculating facilities are limited. The slip factor is estimated as previously noted to determine the energy added to the flow. The effect of off-design incidence angles is approximated by resolving the relative inlet velocity into two components—one parallel to the convex surface of a blade at the inlet and the other perpendicular to it. The kinetic energy of the second component is presumed to be lost. The losses thus calculated are added to that estimated from the curve of efficiency versus specific speed. Although this concept is not precise, it does account for the trends generally observed in both rotors and stators. The compressor map is prepared by using the calculated increase in enthalpy and the losses to compute the pressure ratio and efficiency of each stage. The overall performance is then readily found.

UNSTEADY FLOW

The importance of and interest in this subject are evidenced by Reference [39]. There are several sources of unsteady flow in compressors. Notice first

that circumferential gradients measured by a stationary observer produce time-unsteady flows relative to a rotor. This condition at the inlet is thus a source of unsteady flow in the rotors. Wakes or pressure fields generated by stator blades and other structures within the flow passages also cause rotors to be exposed to time-unsteady flow.

Time-unsteady flows in stators are similarly produced by circumferential gradients in rotors. The magnitude of the unsteadiness produced by stators on rotors or rotors on stators decreases as the distance between them increases.

Axial-flow compressors, which depend on adverse pressure gradients for all the increases in pressure, are quite sensitive to nonuniform, or distorted, inlet flow. Centrifugal and mixed-flow compressors are more tolerant, probably because centrifugal force plays a large part in the development of pressure ratio.

Rotating stall obviously causes unsteady flow in both rotors and stators. Surging, which is primarily a pulsation of the axial component of velocity, is another source of unsteady flow in both rotors and stators.

Time-unsteady flow has adverse aerodynamic and mechanical consequences. There is some evidence, however, that performance improves slightly when the unsteady flow caused by blade wakes is augmented by placing rotors and stators close together. This benefit is usually small in comparison to the danger of destructive vibrations that may be induced by the increased unsteady forces on the blades. Noise generated within a compressor is also increased when rotor and stator blades are close together.

Surging is manifested by either pulsating flow or an abrupt deterioration of pressure ratio and efficiency. The pulsations may be either gentle or violent. Sustained operation during surge is to be avoided.

MECHANICAL DESIGN CONSIDERATIONS

This chapter is primarily devoted to the aerodynamic design of compressors. However, mechanical problems can curtail operating life or even cause structural failure. Either event limits the freedom of aerodynamic design. Centrifugal force causes tensile stresses in rotor blades and disks that could rupture them if proper provisions were not made in the design. Calculating the expected steady-state and vibratory stresses, together with the thermal growth of the various parts, offers the biggest challenge to the mechanical designer. The placement of structural elements such as struts within the flow passages also causes aerodynamic problems that must be recognized.

Steady-State Stresses and Thermal Growth

Rotor blades, which are subject to centrifugal force, are one of the principal elements subject to steady-state stresses. The forces exerted by high-pressure gases are another stress. Centrifugal stresses can usually be readily estimated when the surfaces of each blade element lie on radial lines. If a blade is only slightly twisted, this analysis can be extended to shapes in which the center of gravity of each element lies on a radial line. (Recall that a blade element now is defined as the shape generated by the intersection of a blade with a conical surface.) This configuration has allowed conventional one-dimensional analysis to be used for estimating the stresses. Conventional techniques have also been used to assess stresses in the supporting disks and to evaluate stress concentrations at the junctures of blades with the disks. Chapter 3 of Balje [19] presents representative simplified procedures for estimating some of the principal steady-state stress in turbomachines. Such methods have been used in practice, but their success depends on the designer's experience with compressors having similar shapes and applications. Factors of safety must be employed; too small a factor invites trouble, while too large a one increases the size, weight, and cost of the unit. The pressure ratio and efficiency of the compressor could be compromised as well. In general, more sophisticated methods than those just outlined are advised.

Observe also that the temperatures within compressors increase as the units are accelerated from rest and that this causes the dimensions of each element to change. The casing and the tips of the rotor blades move radially outward. Depending on the relative rates of expansion, these two parts could rub against each other. The heat from friction then causes additional growth and possible failure. Since the running clearance at the blade tips must be small in order to avoid unwanted gas flow between blades and casing, good estimates of the relative expansions are required.

An alternate design uses solid rings, or shrouds, that are placed around the blade tips to prevent flow over the tips. A labyrinth seal or some form of face seal then limits the leakage from the high- to the low-pressure side of the blade row. The danger of catastrophic failure due to rubbing is thus reduced, but the centrifugal stresses in the blades are increased. Notice that shrouds can also limit blade vibrations.

The hub also expands radially outward, but the tips of stator blades move radially inward. Unless sufficient clearance is provided, the stators and the rotating hub will contact each other and rub. The heat from the rubbing exacerbates the interference. Shrouds, with seals, are often placed under stator tips to mitigate this possibility.

In order to cope with the problems associated with twisted blades and thermal expansions, designers often rely on computer programs such as

Nastran, which was developed by NASA. They can then more accurately forecast steady-state stresses and thermal growth.

The combination of centrifugal forces and thermal expansions distorts the shape of centrifugal and mixed-flow units. This event alone can be a possible cause of structural failure. Moreover, the clearance between the rotor blades and the casing can be decreased in one area and increased in another, resulting in a failure by rubbing in one region of the component even though there is excess clearance in another region. Growth analysis using computer programs is almost mandatory in this case.

Blade Flutter and Impact Stresses

Rotating stall and blade flutter instigate blade vibrations and cause fatigue failure in both rotors and stators. Failures have also resulted from impacts between rotor blades and foreign objects, such as tools, rags, or birds. Computer programs such as Nastran can analyze and identify the natural frequencies of the bending and torsional modes of blade vibration. Other programs have been developed within the industry for calculating thermal growth and the effects of internal pressures. Note that these phenomena are functions of the rotating blade speed. Similar programs have been developed that can estimate the damage to be expected from impacts with foreign objects. These analyses are preferably done by someone experienced in stress and vibration calculations for compressors.

Carta [40] offers a good overview of the mechanism of flutter. Contending with vibration problems triggered by rotating stall unfortunately requires some experience, because neither the frequency nor the magnitude of the forcing functions can be accurately defined in advance. We know only that the stall zones probably excite blades at frequencies corresponding to multiples of 40 to 60% of rotor speed. The lack of accurate calculation procedures is the main reason why the design and development of new compressors can sometimes be a time-consuming and expensive venture.

Other Design Considerations

It might seem convenient to design compressors with hollow struts immediately behind the last row of blades, or close to the inlet blading. These struts would enclose accessory items such as tubes for delivering oil to and from the bearings. They could also be part of the structural support of the bearings. This arrangement should be avoided, particularly in axial compressors where the close axial spacing of the blades inhibits circumferential movement of gas between successive rows of blades. An

anomaly in the flow is then effectively trapped and confined within a limited sector of the circumference. This subject is discussed in Bullock [22].

The field of relatively high pressure at the leading edge of the strut behind the blade rows thus influences the flow several stages upstream. Not only are the temperature rise and pressure ratio within the affected sector higher than the neighboring values, but premature stalling can be instigated. The same thing is true of similar obstructions, such as clusters of instruments, inserted in the gas stream during testing.

NOISE GENERATION

The noise radiated from a compressor is often limited by national and local laws. Note that even a single rotor blade will generate noise because there are pressure gradients around the blade and the gas pressures vary with time at a given point. This source of noise is accentuated when the flow relative to the blade is supersonic and shock waves are generated. The unsteady flows instigated by the relative motion of rotors and stators are another source of noise. Cumpsty [41] is recommended for a good overview of this topic.

DEVELOPMENT TESTING

At the very least, a designer should confirm to his or her own satisfaction that a compressor can develop the expected pressure ratios, efficiencies, and ranges of surge-free operation when the inlet flow conditions are within specified limits. If the desired compressor output fails to be realized, diagnostic tests are necessary to identify the corrections that must be made in the design in order to meet the specifications.

Performance Tests

The initial tests should be made with uniform inlet gas flow and with no external struts or other partial obstructions to the flow within several chord lengths upstream or downstream of the blades. Otherwise pressure ratio, efficiency, and the range of surge-free operation would be adversely affected. The conditions noted previously that trap circumferential variations in the flow also cause inlet flow anomalies to persist within a narrow annular sector throughout the length of a compressor.

Radial disturbances in the inlet flow have also impaired performance. These disturbances should thus be avoided during the initial performance

tests. One should take pains to provide compressors with uniform flow rates and properties at the inlet during these tests.

If compressor specifications require it to operate with gradients in the flow at the inlet, this ability can be verified by separate tests. Usually, specified deviations from uniform flow can be established with the use of overlapping screens upstream of the inlet. Under some conditions, however, ingenuity is required to effect suitable tests.

Instrumentation

The object of overall tests is to determine how the rotating speed and flow rate affect the pressure ratio, the temperature rise, and the position of the surge line. A number of instruments are available for sensing and measuring rotating speed, flow rate, pressures, temperatures, and velocities, as well as variations of the last four items with time. Torque measurements are useful for confirming the amount of energy added by the rotors: the effect of any backflow over rotor blade tips is then properly identified as an increase in entropy instead of a transfer of mechanical energy.

The location of the sensing elements deserves careful study. Figure 18 illustrates a typical problem. This figure shows how the total pressure, as measured behind the last blade row of a compressor, can vary throughout the annulus. This result was observed even though uniform flow was presented to the compressor inlet. Measurements of total temperature often exhibit similar trends. Experience shows that this type of distribution can change with flow rate and speed. The section on energy degradation noted how this flow is subsequently mixed as it moves downstream. The mass flow rate, the power, and the momentum of the gas are preserved during mixing, while the available total pressure is reduced. Many data points can be required to obtain the information necessary to accurately evaluate the available total pressure or the true total temperature.

Whenever possible, the data should be taken far enough downstream so that the flow is sufficiently uniform that the effects of subsequent mixing can be ignored. In this case the data at the measuring points can be weighted either by the local mass flow rate or by volume flow rate. The result is practically the same.

When gradients in flow are inevitable at the measuring station, some method must be used to get meaningful averages. Some measure of the statistical variance is also required. Previous discussions have demonstrated that both radial and circumferential gradients in pressure may have been the result of the design and inlet conditions. They are not random in a statistical sense. The method of averaging must recognize this situation, and those

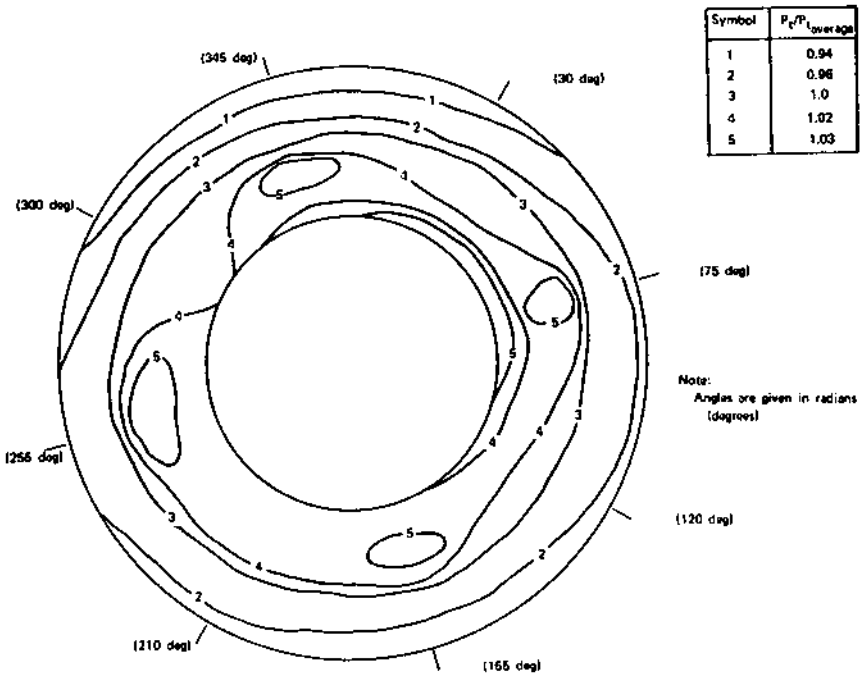

Figure 18 Total pressure map of compressor discharge, no engine inlet distortion.

deviations from the average are not an indication of statistical variance. A measureable payoff is usually provided by a careful evaluation of the data.

Diagnostic Tests

If tests reveal that a compressor fails to meet its objective performance, diagnostic tests may be required. The specifications for such a test depend on the problem being addressed. In general, however, one must acquire data to evaluate the individual performance of one or more stages. Measurements of pressures and temperatures in a field containing gradients and unsteady flows are necessary. The precautions noted previously need to be observed.

Notice also that the wakes behind a rotating blade row rotate at greater speeds than that of the main stream; the total pressure or temperature sensed by an ordinary probe behind a rotor will thus be higher than that of the gas in the main stream. The magnitude of the error cannot

be predicted in advance. Total pressure probes and hot-wire anemometers having very fast time responses overcome this difficulty and thus are invaluable diagnostic tools. Laser anemometry is frequently used for this purpose also.

O'Brien and Boyer [42] discusses some of the equipment and procedures that have been used to examine the internal behavior of the gas flow. Procedures used in other diagnostic tests and the results obtained are described in O'Brien and Boyer [42], Ostdiek et al. [43], Budinger and Thomson [44], and Budinger [45]. Chapters XI and XII of Ref. [1] provide additional information. More information and additional references are given in Lakshminarayana [2] and Serovy [3]. The examples cited describe good diagnostic test procedures.

When there is a problem of locating the stages responsible for stall and surge, one may be guided by an analysis of the overall performance data. The variation of the ratio $(W\sqrt{T}/P)/[U/(N\sqrt{T})]$ with rotating speed provides a measure of how the relative inlet air angles of the initial blade rows change with speed. This ratio is proportional to the flow coefficient, $V_{z,1}/U$. When it is divided by the quantity $(P_2/P_1)/(T_2/T_1)$, one obtains a corresponding measure of $V_{z,2}/U$ and the relative air angles in the final blade rows. Selecting approximate values of P and T for the divisor enables one to appraise the situation at intermediate stages. An example for air is given by Table 3. (The numbers in the first two columns indicate the percent of design value, while those in the last two columns are proportional to the actual values.)

The low and nearly identical values under $V_{z,1}/U$ at the two lowest rotor speeds are an indication that the initial stages were stalling and were responsible for the incidence of surge at these speeds. The same type of

Table 3 Effect of Speed on Value of Flow Coefficients, at Stall, of First and Last Stages

N	$W\sqrt{T}/P$	P_2/P_1	T_2/T_1	$V_{z,1}/U$	$V_{z,2}/U$
0.5	8.7	1.8	1.26	17.4	12.2
0.6	10.8	2.5	1.40	17.2	10.1
0.7	13.5	3.5	1.57	19.3	8.7
0.75	15.0	4.05	1.66	20.0	8.2
0.8	18.0	5.0	1.74	22.5	7.9
0.9	25.4	7.6	1.98	28.2	7.4
1.0	33.6	9.8	2.10	33.6	7.1

evidence strongly suggests that the stalling of the later stages induces the surging at the higher speeds.

This use of overall data can be employed for other diagnostic information. For instance, the existence of relatively large axial velocities and negative incidence angles in the latter stages at the lower speeds is confirmed. The initial stages are shown to be exposed to this condition at the higher speeds.

Important diagnostic information is obtained from the measurement of the clearance between the ends of rotor blades and the casing. Measuring the instantaneous electrical capacitance between the casing and the passing rotor blades is a good way to do this. Unexpected distortions of the structure caused by thermal expansion and pressure are often revealed by such measurements.

Useful knowledge is also derived by spraying talcum powder, diatomaceous earth, or a mixture of lampblack and light oil into the gas stream ahead of a compressor. Regions of reverse flow and flow leakage are disclosed by such tests.

CONCLUDING COMMENTS

The discussion in this chapter was directed to compressors in which the pressure ratio exceeds about 1.1. What are generally called fans are excluded.

Axial compressors for pressure ratios of the order of 4 to 1 can usually be designed without much risk if the inlet Mach number is 0.5 or lower, if the pressure ratio per stage is limited to about 1.2 or lower, and if the rotor blades have little twist.

Aiming for higher values of these quantities entails exposure to aerodynamic and mechanical problems unless sophisticated computing techniques and experienced personnel are employed. Facilities for making state-of-the-art aerodynamic and mechanical tests are also necessary in this case if one intends to be competitive. The potential designer should be aware that U.S. government organizations such as NASA are usually willing to provide information about various problems in this field.

SYMBOLS

A Area
B Blockage, ratio of effective flow area to physical area
C_p Coefficient of heat at constant pressure

C_v	Coefficient of heat at constant volume
D	Diffusion factor [Eq. (14)]
f	$PA(1+\gamma M^2)/(1+\frac{\gamma-1}{2}M)$
g	Acceleration of gravity
H	Enthalpy ($= C_p T$ for ideal gas)
I	Rothalpy ($= H-(1/2)\omega^2 r$)
i	Incidence angle; see Fig. 13
J	Ratio, unit of work per unit of thermal energy
N	Rotating speed
$\dot{m}$	Rate of mass flow
m_1	$=\frac{1}{2}\frac{\gamma+1}{\gamma-1}$
m	$=\frac{\gamma}{\gamma-1}$
P	Total pressure
p	Static pressure
r	Radius
S	Entropy
T	Absolute total temperature
t	Absolute static temperature
z	Axial distance
V	Velocity, referred to stationary coordinates
W	Relative velocity
Z	Number of blades
β	Angle; see Fig. 13
γ	Ratio of specific heats $= C_p/C_v$
Γ	Circulation, $2rV_\theta$
ζ	Vorticity
δ	Deviation angle; see Fig. 13
δ	P/P_{SL}
θ	Circumferential angle
θ	T/T_{SL}
μ	$\frac{f}{PA}=(1+\gamma M^2)/(1+\frac{\gamma-1}{2}M^2)^{m_e}$
ρ	Density
ϕ	$f/(W\sqrt{T})=(f/PA)/((W\sqrt{T})/PA)^{m_2}$
ψ	$(W\sqrt{T})/(PA)=g/RM/((1+(\gamma-1)/2)M^2)^{M_1}\sqrt{\gamma g/R}M/(1+\frac{\gamma-1}{2}M^2)^{m_1}$
ω	Angular velocity

Subscripts

1	Inlet of flow section, or hub
2	Outlet of flow section, or casing

SL Standard sea-level condition
e Designates the equivalent value in a two-dimensional cascade
i ideal

Superscript

1 Denotes value for a rotor

REFERENCES

1. NASA SP 36 (1965).
2. B. Lakshminarayana, W. R. Britsch, and W. S. Gearhaart, eds., *Fluid Mechanics, Acoustics, and Design of Turbomachinery*, Parts I and II, Scientific and Technical Information Office, NASA, Washington, D.C. (1974).
3. G. K. Serovy, *Aerothermodynamics of Aircraft Engine Components* (G. C. Oates, ed.), AIAA Education Series, American Institute of Aeronautics and Astronautics, Inc., New York (1985).
4. A. B. Wassel, *J. Eng. Power, Trans. ASME, Ser. A, 90*: 149–156 (1968).
5. R. O. Bullock, *J. Eng. Power, Trans. ASME, Ser. A, 86*: 247–256 (1964).
6. W. G. Steenken, *Aerothermodynamics of Aircraft Engine Components* (G. C. Oates, ed.), AIAA Education Series, American Institute of Aeronautics and Astronautics, Inc., New York (1985).
7. J. H. Keenan, J. Chao, and J. Kaye, *Gas Tables*, John Wiley and Sons, New York (1983).
8. H. McDonald, *Aerothermodynamics of Aircraft Engine Components* (G. C. Oates, ed.), AIAA Education Series, American Institute of Aeronautics and Astronautics, Inc., New York (1985).
9. R. M. Haleen and J. J. Johnston, "The Influence of Rotation on Flow in a Long Rectangular Channel—An Experimental Study," Report M.D. 18, Mechanical Engineering Dept., Stanford University, Stanford, Calif.
10. J. J. Johnston, "The Effect of Rotation on Boundary Layers in Turbomachine Rotors," Report M.D. 24, Mechanical Engineering Dept., Stanford University, Stanford, Calif.
11. R. C. Dean and Y. S. Senoo, *Trans. J. Basic Eng., ASME, Ser. D*, Sept. (1960).
12. "Secondary Flows in Turbomachines," *AGARD Conference Proceedings*, no. 469 (1990).
13. L. H. Smith, Jr., *Casing Boundary Layers in Multistage Axial Flow Compressors, Flow Research on Blading*, Elsevier, Amsterdam (1969).
14. J. I. Younghans and G. L. Paul, *Aircraft Propulsion Technology and Design* (G. C. Oates, ed.), AIAA Education Series, American Institute of Aeronautics and Astronautics, Inc., New York (1989).

15. S. Lieblein, *J. Basic Eng., Trans. ASME, Ser. D, 82*: 575–587 (1960).
16. S. Lieblein, *Basic Eng., Trans. ASME, Ser. D. 81*: 387–400 (1959).
17. C. C. Koch and L. H. Smith, Jr., *J. Eng. Power, Trans. ASME, Ser. A, 8*: 411–424 (1976).
18. W. C. Swan, *J. Eng. Power, Trans. ASME, Ser. A, 83*: 322–330 (1961).
19. O. E. Balje, *Turbomachines, A Guide to Design, Selection and Theory*, Chapter 4, John Wiley and Sons, New York (1981).
20. L. R. Reneau, J. P. Johnston, and S. Kline, "Performance and Design of Straight Two-Dimensional Diffusers," Thermosciences Division, Dept. of Mechanical Engineering, Stanford University, Stanford, Calif., Report PD-8 (1964).
21. C. J. Sagi, J. P. Johnston, and S. J. Kline, *Diffuser Design Manual, Part II. The Design and Performance of Two-Dimensional Curved Diffusers*, Thermosciences Division, Dept. of Mechanical Engineering, Stanford University, Stanford, Calif., Report PD-9 (1964).
22. R. O. Bullock, *Aircraft Propulsion Systems Technology* (G. C. Oates, ed.), AIAA Education Series, American Institute of Aeronautics and Astronautics, Inc., New York (1989).
23. D. P. Kenney, "A Novel Low Cost Diffuser for High Performance Centrifugal Compressors," ASME Paper 72-GT-54 (1972).
24. D. P. Kenney and R. E. Morris, "High Pressure Ratio Centrifugal Compressors for Small Gas Turbine Engines." Prepared for 31st Meeting of the Propulsion and Energetics Panel of AGARD, Helicopter Propulsion Systems, Ottawa, Canada, June 10–14 (1968).
25. W. F. O'Brien and K. M. Boyer, "Stall and Recovery in Multistage Axial Compressors," *AGARD Conference Proceedings* no. 468 (1990).
26. H. Starken and H. J. Lichtfuss, *J. Eng. Power, Trans. ASME, Ser. A, 92*: 267–274 (1970).
27. P. R. Dodge, *J. Eng. Power, Trans. ASME, Ser. A, 95*: 185–190 (1973).
28. P. R. Dodge, "A Non-Orthogonal Numerical Method for Solving Transonic Cascade Flows," ASME Paper 76-GT-63 (1976).
29. J. T. Hamrick, A. Ginsberg, and W. M. Osborn, "Method of Analysis for Compressible Flow Through Mixed-Flow Compressors of Arbitrary Design," NACA Report 1082 (1952).
30. R. K. Novak and R. M. Hearsey, *J. Fluids Eng. Trans. ASME, Ser. 1, 99*: 154–166 (1977).
31. C.-H. Wu, Z. Wang, and H. Chen, "Three-Dimensional Rotational Flow in Transonic Turbomachines, Part 1, Solution Obtained Using a Number of S Stream Filaments of Revolution and a Central S Stream Filament," ASME Paper 90-GT-18 (1990).
32. C.-H. Wu, X. Zhao, and D. L. Oin, "Three-Dimensional Rotational Flow in Transonic Turbomachines, Part II, Full 3D Flow in CA#S Rotor Obtained Using a Number of S and S Stream Filaments," ASME Paper 90-GT-13 (1990).
33. T. Katsanis and W. D. McNally, "Revised Fortran Program for Calculating Velocities and Streamlines on the Hub-Shroud Midchannel Stream Surface of

an Axial-, Radial- or Mixed-Flow Turbomachine, or Annular Duct," NASA Technical Note No. C-8430 (1977).
34. W. F. Waterman and W. A. Tall, "Measurement and Prediction of 3-D Viscous Flows in Low-Aspect-Ratio Turbine Blades," ASME Paper 75-GT-73 (1973).
35. R. A. Novak, "Flow Field and Performances Map Computation for Axial-Flow Compressors and Turbines," Modern Prediction Methods for Turbomachine Performance, AGARD-LS-83 (1976).
36. R. O. Bullock, W. W. Wilcox, and J. J. Moses, "Experimental and Theoretical Studies of Surging in Continuous-Flow Compressors," NACA Report 861 (1946).
37. E. M. Greitzer, *J. Eng. Power, Trans. ASME, Ser. A, 98*: 190–198 (1976).
38. E. M. Greitzer, *J. Eng. Power, Trans. ASME, Ser. A, 98*: 199–217 (1976).
39. "Unsteady Aerodynamic Phenomena in Turbomachines," *AGARD Conference Proceedings* no. 468 (1990).
40. F. O. Carta, *Aircraft Propulsion Technology and Design* (G. C. Oates, ed.), AIAA Education Series, American Institute of Aeronautics and Astronautics, Inc., New York (1989).
41. N. Cumpsty, *Aerothermodynamics of Aircraft Engine Components* (G. C. Oates, ed.), AIAA Education Series, American Institute of Aeronautics and Astronautics, Inc., New York (1985).
42. W. F. O'Brien and K. M. Boyer, "Stall and Recovery in Multistage Axial Compressors," *AGARD Conference Proceedings* no. 468 (1990).
43. F. R. Ostdiek, W. W. Copenhaver, and D. C. Rabe, "Compressor Performance Tests in the Compressor Research Facility," *AGARD Conference Proceedings* no. 468 (1990).
44. R. E. Budinger and A. R. Thomson, "Investigation of a 10-Stage Subsonic Axial-Flow Compressor, II—Preliminary Analysis of Overall Performance," NACA RM E52C04 (1952).
45. R. E. Budinger, "Investigation of a 10-Stage Subsonic Axial-Flow Compressor, VI—Performance Evaluation and Flow Distributions in the First, Fifth and Tenth Stages," NACA RM E62F28 (1954).

7

Fundamentals of Turbine Design

David M. Mathis
Honeywell Aerospace, Tempe, Arizona, U.S.A.

INTRODUCTION

Turbines are used to convert the energy contained in a continuous flow of fluid into rotational mechanical energy of a shaft. Turbines are used in a wide range of applications, in a wide variety of sizes. Large single-stage turbines are used for power generation in hydroelectric dams, while large multistage turbines are used in steam power plants. Aircraft propulsion engines (turbofans, turbojets, and turboprops) use multistage turbines in their power and gas generator sections. Other, less obvious uses of turbines for aircraft are in auxiliary power units, ground power units, starters for main engines, turboexpanders in environmental controls, and constant-speed drives for electrical and hydraulic power generation. Rocket engines use turbines to power pumps to pressurize the propellants before they reach the combustion chamber. Two familiar consumer applications of turbines are turbochargers for passenger vehicles and wind turbines (windmills).

Many excellent texts have been written regarding the design and analyses of turbines [1–3]. There is also a large institutional body of knowledge and practices for the design and performance prediction of

power plant and aircraft propulsion engine turbines. Here we make no attempt to cover these areas. The purpose of this text is to familiarize a mechanical or aerospace engineer who does not specialize in turbines with basic turbine design and analysis. The emphasis will be on smaller turbines for applications other than propulsion or electrical power generation. Further restricting our emphasis, detailed design activities such as geometric specification of blades, vanes, etc. will not be covered. Our intent is to give the system engineer the necessary information to choose the correct type of turbine, estimate its performance, and determine its overall geometry (diameter, blade height, and chord).

This chapter will first cover those equations and concepts that apply to all types of turbines. Subsequently, the two main turbine types will be discussed, specifically, axial-flow turbines and radial-inflow turbines.

BASIC TURBINE CONCEPTS

Flow Through a Turbine

Figure 1 shows cross sections of generic single-stage axial-flow and radial-inflow turbines. The figure shows the station notation used for subsequent analyses. The high-pressure flow enters the turbine at station "in," passes through the inlet, and is guided to the stator inlet (station 0), where vanes turn the flow in the tangential direction. The flow leaves the stator vanes and enters the rotor blades (at station 1), which turn the flow back in the opposite direction, extracting energy from the flow. The flow leaving the rotor blades (station 2), now at a pressure lower than inlet, passes through a diffuser where a controlled increase in flow area converts dynamic head to static pressure. Following the diffuser, the flow exits to the discharge conditions (station dis).

The purpose of the inlet is to guide the flow from the supply source to the stator vanes with a minimum loss in total pressure. Several types of inlets are shown in Fig. 2. Most auxiliary types of turbines such as starters and drive units are supplied from ducts and typically have axial inlets such as that shown in Fig. 2(a) or a tangential entry like that of Fig. 2(b). The axial inlet acts as a transition between the small diameter of the supply duct and the larger diameter of the turbine. No flow turning or significant acceleration is done in this type of inlet. In the tangential-entry scroll of Fig. 2(b), the flow is accelerated and turned tangentially before entering the stator, reducing the flow turning done by the stator. Another type of inlet for an auxiliary turbine is the plenum shown in Fig. 2(c). For turbines that are part of an engine, the inlet is typically integrated with the combustor [Fig. 2(d)] or the discharge of a previous turbine stage [Fig. 2(e)].

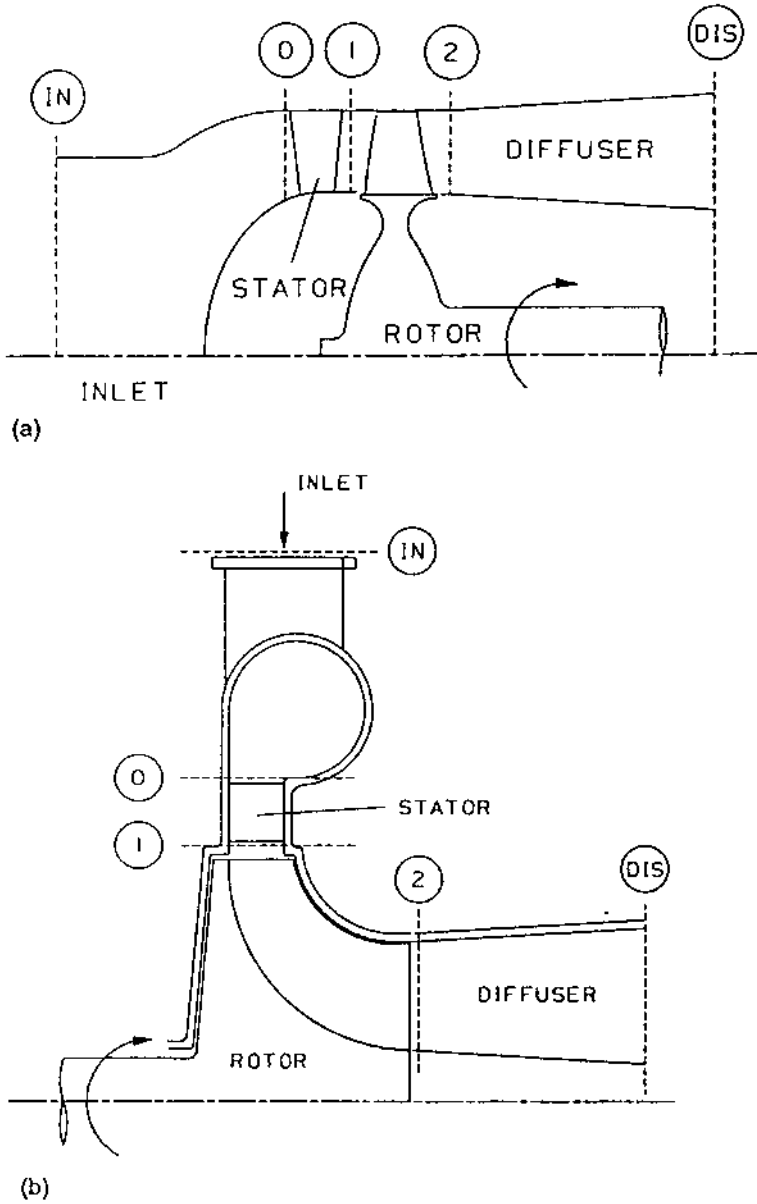

Figure 1 Cross sections of generic single-stage turbines: (a) axial-flow turbine, (b) radial-inflow turbine.

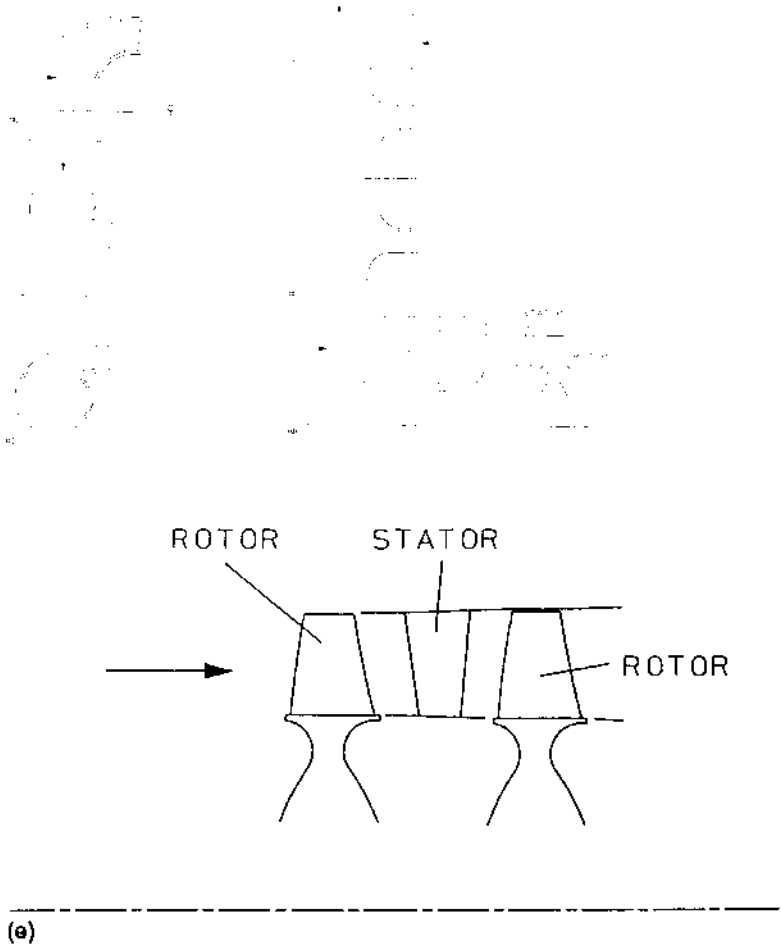

Figure 2 Common types of turbine inlets: (a) in-line axial inlet, (b) tangential-entry scroll inlet for axial-flow turbine, (c) plenum inlet with radial or axial entry, (d) turbine stage downstream of combustor, (e) turbine stage in multistage turbine.

The sole purpose of the stator is to induce a swirl component to the flow so that a torque can be imparted to the rotor blades. Stators are typically equipped with numerous curved airfoils called vanes that turn the flow in the tangential direction. Cross sections of an axial-flow turbine stator and a radial-inflow turbine stator are shown in Fig. 3(a) and 3(b),

respectively. Radial-inflow turbines supplied from a scroll, such as turbocharger turbines, often have no vanes in the stator. For turbines that must operate efficiently over a wide range of inlet flow conditions, variable-geometry stators are used, typically with pivoting stator vanes. For high-temperature applications, the stator vanes are cooled using lower-temperature fluid, usually compressor bleed air.

The purpose of the rotor is to extract energy from the flow, converting it to shaft power. The rotor blades are attached to a rotating disk that transfers the torque of the rotor blades to the turbine output shaft. Like the stator, the rotor has a number of individual curved airfoils called rotor or turbine blades. The blades are angled to accept the flow from the stator with minimum disturbance when the turbine is operating at design conditions. The flow from the stator is then turned back in the opposite direction in a controlled manner, causing a change in tangential momentum and a force to be exerted on the blades. Figure 4 shows cross sections of generic axial-flow and radial-inflow turbine blades. Axial-flow rotors have been constructed with blades integral with the disk and with blades individually inserted into the disk using a dovetail arrangement. Cooling is often used for rotors in high-temperature applications. Exotic materials are sometimes used for both rotors and stators to withstand the high temperatures encountered in high-performance applications.

The flow leaving the turbine rotor can have a significant amount of kinetic energy. If this kinetic energy is converted to static pressure in an efficient manner, the turbine can be operated with a rotor discharge static pressure lower than the static pressure at diffuser discharge. This increases the turbine power output for given inlet and discharge conditions. Diffusers used with turbines are generally of the form shown in Fig. 5(a) and 5(b) and increase the flow area gradually by changes in passage height, mean radius of the passage, or a combination of the two. Diffusers with a change in radius have the advantage of diffusing the swirl component of the rotor discharge velocity as well as the throughflow component.

Turbine Energy Transfer

The combined parts of the turbine allow energy to be extracted from the flow and converted to useful mechanical energy at the shaft. The amount of energy extraction is some fraction of the energy available to the turbine. The following describes the calculation of the available energy for a turbine and assumes familiarity with thermodynamics and compressible flow.

Flow through a turbine is usually modeled as an adiabatic expansion. The process is considered adiabatic since the amount of energy transferred as heat is generally insignificant compared to the energy transferred as work.

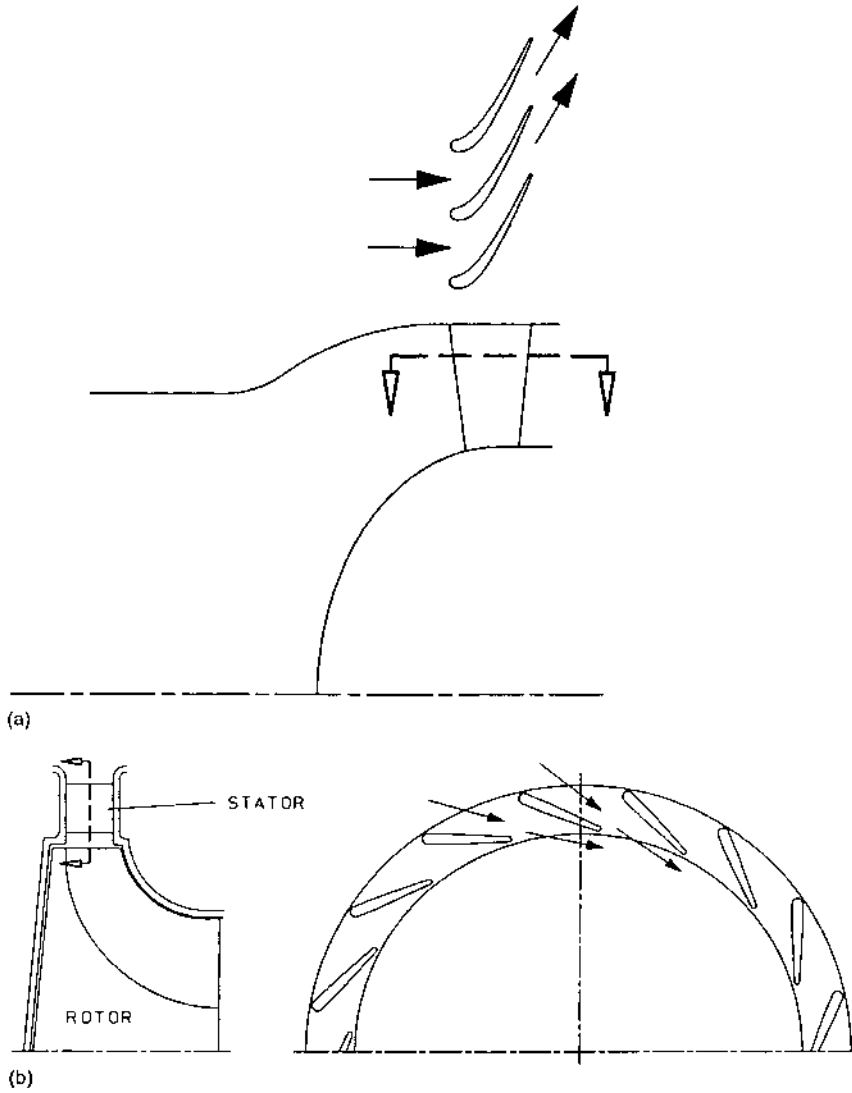

Figure 3 Typical stator vane shapes: (a) axial-flow stator, (b) radial-inflow stator.

In the ideal case, the expansion is isentropic, as shown in Fig. 6(a) in an enthalpy–entropy (h–s) diagram. The inlet to the turbine is at pressure p'_{in} and the exit is at p'_{dis}. The isentropic enthalpy change is the most specific

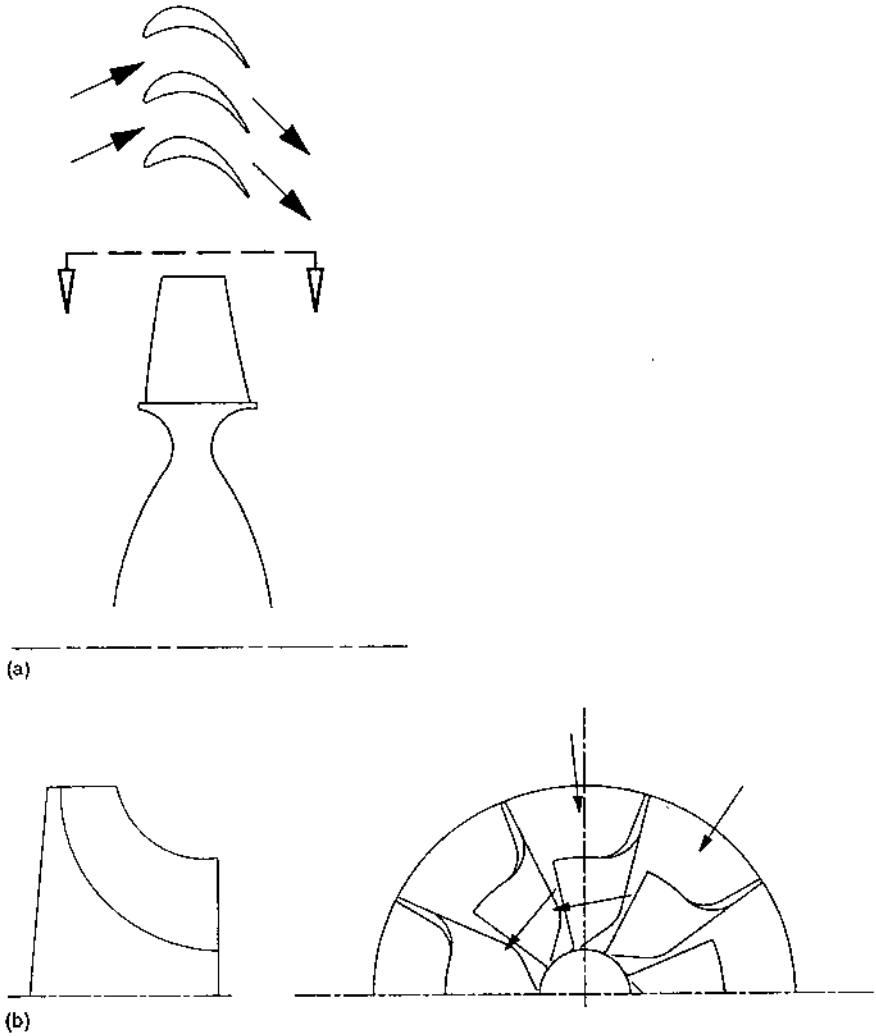

Figure 4 Typical rotor blade shapes: (a) axial-flow rotor, (b) radial-inflow rotor.

energy that can be extracted from the fluid. Thus, if the inlet pressure and temperature and the exit pressure from a turbine are known, the maximum specific energy extraction can be easily determined from a state diagram for the turbine working fluid. For an ideal gas with constant specific heats, the

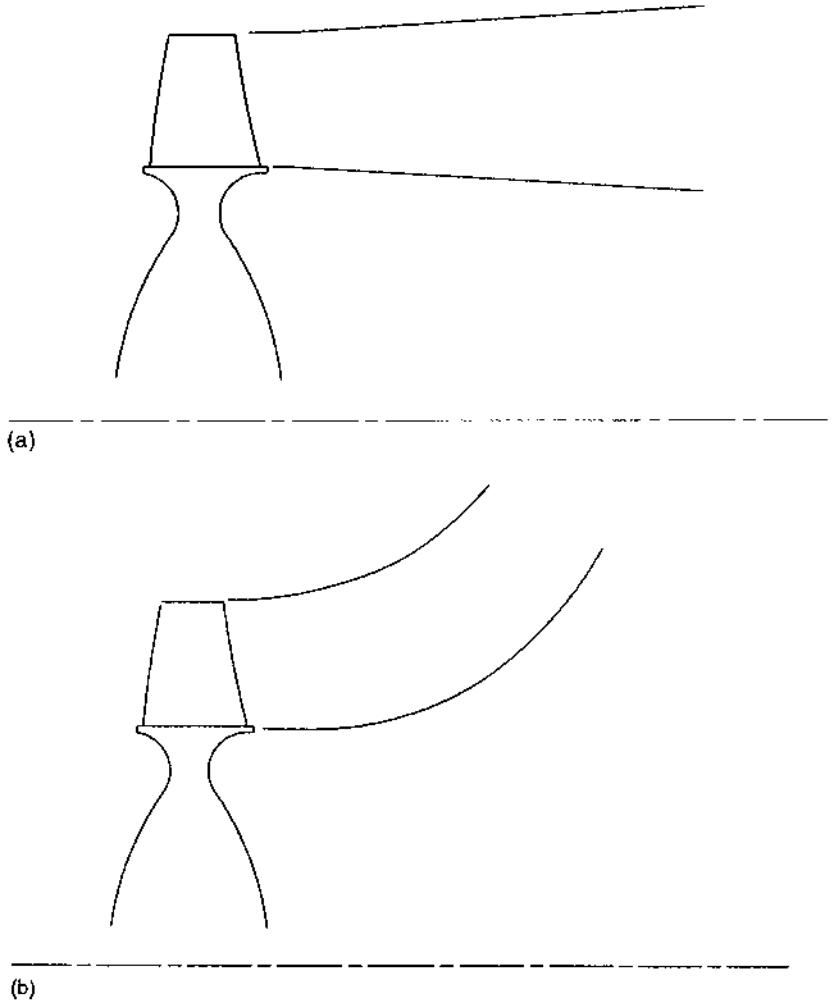

Figure 5 Turbine diffuser configurations: (a) constant mean-diameter diffuser, (b) increasing mean-diameter curved diffuser.

isentropic enthalpy drop is calculated from

$$\Delta h_{\text{isentropic}} = c_{\text{p}} T'_{\text{in}} \left[1 - \left(\frac{p_{\text{dis}}}{p'_{\text{in}}} \right)^{(\gamma-1)/\gamma} \right] \tag{1}$$

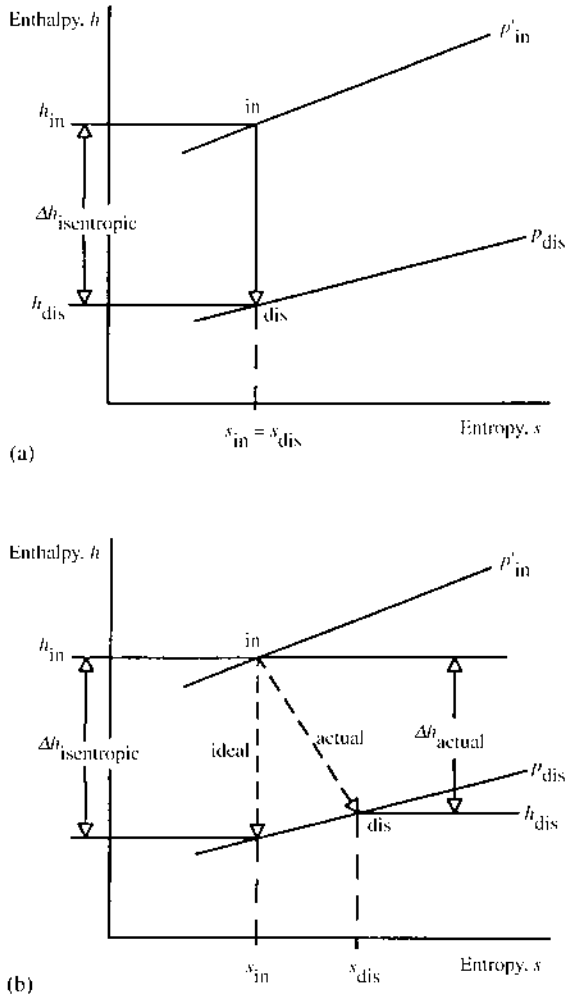

Figure 6 The expansion process across a turbine: (a) idealized isentropic expansion, (b) actual expansion.

Where

T'_{in} = inlet absolute total temperature.
O_p = specific heat at constant pressure.
γ = ratio of specific heats.

The approximation of Eq. (1) is adequate for turbines operating on air and other common gases at moderate pressures and temperatures. Total conditions are normally used for both temperature and pressure at the inlet to the turbine, so that the inlet pressure is correctly referred to as p'_{in} in Eq. (1).

As discussed earlier, the actual energy transfer in a turbine is smaller than the isentropic value due to irreversibilities in the flow. The actual process is marked by an increase in entropy and is represented in the h–s diagram of Fig. 6(b) by a dotted line. The actual path is uncertain, as the details of the entropy changes within the turbine are usually not known. Due to the curvature of the isobars, the enthalpy change associated with an entropy increase is less than that for an isentropic process. The degree of entropy rise is usually described indirectly by the ratio of the actual enthalpy drop to the isentropic enthalpy drop. This quantity is referred to as the isentropic (sometimes adiabatic) efficiency, η, and is calculated from

$$\eta_{OA} = \frac{h_{in} - h_{dis}}{\Delta h_{isentropic}} \tag{2}$$

The subscript OA indicates the overall efficiency, since the enthalpy drop is taken across the entire turbine. The efficiency is one of the critical parameters that describe turbine performance.

So far we have not specified whether the total or static pressure should be used at the turbine exit for calculating the isentropic enthalpy drop. (Note that this does not affect the actual enthalpy drop, just the ideal enthalpy drop.) Usage depends on application. For applications where the kinetic energy leaving the turbine rotor is useful, total pressure is used. Such cases include all but the last stage in a multistage turbine (the kinetic energy of the exhaust can be converted into useful work by the following stage) and cases where the turbine exhaust is used to generate thrust, such as in a turbojet. For most power-generating applications, the turbine is rated using static exit pressure, since the exit kinetic energy is usually dissipated in the atmosphere. Note that the total-to-static efficiency will be lower than the total-to-total efficiency since the static exit pressure is lower than the total.

With the energy available to the turbine established by the inlet and exit conditions, let's take a closer look at the actual mechanism of energy transfer within the turbine. Figure 7 shows a generalized turbine rotor. Flow enters the upstream side of the rotor at point 1 with velocity $\vec{V}_1$ and exits from the downstream side at point 2 with velocity $\vec{V}_2$. The rotor spins about its centerline coincident with the x-axis with rotational velocity ω. The location of points 1 and 2 is arbitrary (as long as they are on the rotor), as are the two velocity vectors. The velocity vectors are assumed to represent

the average for the gas flowing through the turbine. The net torque Γ acting on the rotor can be represented as the difference of two torques on either side of the rotor:

$$\Gamma = r_1 F_{\theta 1} - r_2 F_{\theta 2} \tag{3}$$

where F_θ is the force in the tangential direction and r is the radius to the point. From Newton's second law, the tangential force is equal to the rate of

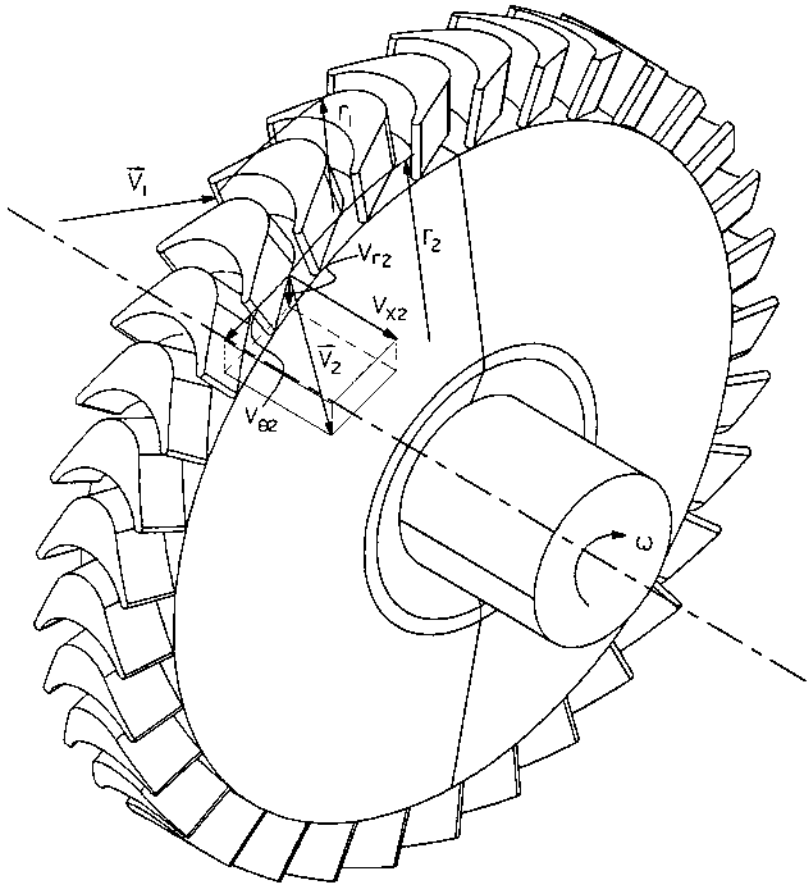

Figure 7 Velocities at the inlet and exit of a turbine rotor.

change of angular momentum:

$$F_\theta = \frac{d(mV_\theta)}{dt} \tag{4}$$

Performing the derivative, assuming constant V_θ and mass flow rate $\dot{m}$, results in

$$\Gamma = \dot{m}(V_{\theta 1} r_1 - V_{\theta 2} r_2) \tag{5}$$

The energy transfer per time (power) is obtained by multiplying both sides of Eq. (5) by the rotational velocity ω:

$$P = \Gamma\omega = \omega\dot{m}(V_{\theta 1} r_1 - V_{\theta 2} r_2) \tag{6}$$

The power P can also be calculated from the h–s diagram for the actual process as

$$P = \dot{m}(h_{\text{in}} - h_{\text{dis}}) = \dot{m}\Delta h_{\text{actual}} \tag{7}$$

Combining Eqs. (6) and (7) and defining the wheel speed U as

$$U = \omega r \tag{8}$$

results in the Euler equation for energy transfer in a turbomachine:

$$\Delta h_{\text{actual}} = U_1 V_{\theta 1} - U_2 V_{\theta 2} \tag{9}$$

The Euler equation, as derived here, assumes adiabatic flow through the turbine, since enthalpy change is allowed only across the rotor. The Euler equation relates the thermodynamic energy transfer to the change in velocities at the inlet and exit of the rotor. This leads us to examine these velocities more closely, since they determine the work extracted from the turbine.

Velocity Diagrams

Euler's equation shows that energy transfer in a turbine is directly related to the velocities in the turbine. It is convenient to graphically display these velocities at the rotor inlet and exit in diagrams called velocity or vector diagrams. These diagrams are drawn in a single plane. For an axial-flow turbine, they are drawn in the x–θ plane at a specific value of r. At the inlet of a radial-inflow turbine, where the flow is generally in the r–θ plane, the diagram is drawn in that plane at a specific value of x. The exit diagram for a radial-inflow turbine is drawn in the x–θ plane at a specific value of r.

Figure 8(a) shows the velocity diagram at the inlet to an axial-flow rotor. The stator and rotor blade shapes are included to show the relation

between the velocity diagram and the physical geometry of the turbine. The flow leaves the stator at an angle of α_1 from the axial direction. The velocity vector $\overrightarrow{V}_1$ can be broken into two components, V_{x1} in the axial direction and $V_{\theta 1}$ in the tangential direction. Note that the turbine work is controlled by the tangential component, while the turbine flow rate is controlled by the axial component (for an axial-flow turbine). The vector $\overrightarrow{V}_1$ is measured in an absolute, nonrotating reference frame and is referred to as the absolute rotor inlet velocity. Likewise, the angle α_1 is called the absolute flow angle at rotor inlet. A rotating reference frame can also be fixed to the rotor. Velocities in this reference are determined by subtracting the rotor velocity from the absolute velocity. Defining the relative velocity vector at the inlet to be $\overrightarrow{W}_1$, we can write

$$\overrightarrow{W}_1 = \overrightarrow{V}_1 - U_1 \tag{10}$$

The vector notation is not used for the rotor velocity U_1 as it is always in the tangential direction. The relative velocity vector is also shown in Fig. 8(a). The relative flow angle β_1 is defined as the angle between the relative velocity vector and the axial direction. Inspection of the diagram of Fig. 8(a) reveals

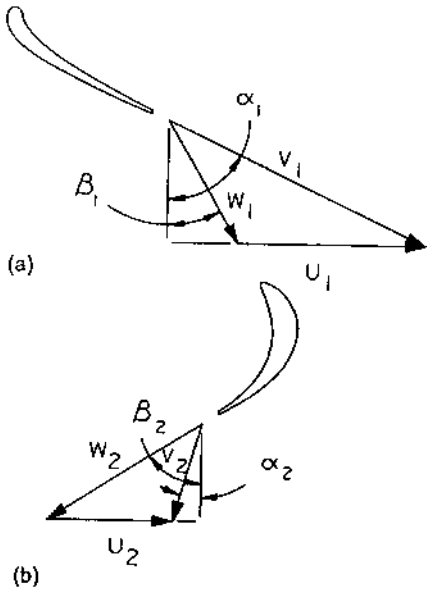

Figure 8 Velocity diagrams for an axial-flow turbine: (a) rotor inlet velocity diagram, (b) rotor exit velocity diagram.

several relationships between the relative velocity and absolute velocity and their components:

$$V_1^2 = V_{x1}^2 + V_{\theta 1}^2 \tag{11}$$

$$W_1^2 = W_{x1}^2 + W_{\theta 1}^2 \tag{12}$$

$$W_{\theta 1} = V_{\theta 1} - U_1 \tag{13}$$

$$W_{x1} = V_{x1} \tag{14}$$

The sign convention used here is that tangential components in the direction of the wheel speed are positive. This implies that both α_1 and β_1 are positive angles. Figure 8(b) shows the vector diagram at the outlet of the rotor. Note that in this diagram, both the absolute and relative tangential components are opposite the direction of the blade speed and are referred to as negative values. The two angles are also negative.

In addition to the relative velocities and flow angles, we can also define other relative quantities such as relative total temperature and relative total pressure. In the absolute frame of reference, the total temperature is defined as

$$T' = T + \frac{V^2}{2c_p} \tag{15}$$

In the relative frame of reference, the relative total temperature T'' is defined as

$$T'' = T + \frac{W^2}{2c_p} \tag{16}$$

The static temperature is invariant with regard to reference frame. Combining Eqs. (15) and (16), we have

$$T'' = T' + \frac{W^2 - V^2}{2c_p} \tag{17}$$

The relative total temperature is the stagnation temperature in the rotating reference; hence it is the temperature that the rotor material is subjected to. Equation (17) shows that if the relative velocity is lower than the absolute velocity, the relative total temperature will be lower than the absolute. This is an important consideration to the mechanical integrity of the turbine.

As with the static temperature, the static pressure is also invariant with reference frame. The relative total pressure can then be calculated from the

gas dynamics relation

$$\frac{p''}{p} = \left(\frac{T''}{T}\right)^{\gamma/(\gamma-1)} \tag{18}$$

Types of Velocity Diagrams

There are an infinite number of variations of the velocity diagrams shown in Fig. 8. To help distinguish and classify them, the vector diagrams are identified according to reaction, exit swirl, stage loading, and flow coefficient. The reaction is the ratio of the change in static enthalpy across the rotor to the change in total enthalpy across the stage. In terms of velocities, the change in total enthalpy is given by Eq. (9). The change in static enthalpy (denoted as h_s) can be found from

$$\begin{aligned} h_{s1} - h_{s2} &= \left(h_1 - \frac{V_1^2}{2}\right) - \left(h_2 - \frac{V_2^2}{2}\right) \\ &= U_1 V_{\theta 1} - U_2 V_{\theta 2} - \frac{1}{2}(V_1^2 - V_2^2) \end{aligned} \tag{19}$$

Geometric manipulation of the vector diagram of Fig. 8 results in

$$UV_\theta = \frac{1}{2}(V^2 + U^2 - W^2) \tag{20}$$

Applying to Eqs. (9) and (19), the stage reaction can be expressed as

$$R_{stg} = \frac{(U_1^2 - U_2^2) - (W_1^2 - W_2^2)}{(V_1^2 - V_2^2) + (U_1^2 - U_2^2) - (W_1^2 - W_2^2)} \tag{21}$$

Stage reaction is normally held to values greater than or equal to 0. For an axial-flow turbine with no change in mean radius between rotor inlet and rotor outlet, $U_1 = U_2$ and the reaction is controlled by the change in relative velocity across the rotor. Negative reaction implies that $W_1 > W_2$, indicating diffusion occurs in the rotor. Due to the increased boundary-layer losses and possible flow separation associated with diffusion, negative reaction is generally avoided. Diagrams with zero reaction (no change in magnitude of relative velocity across the rotor) are referred to as impulse diagrams and are used in turbines with large work extraction. Diagrams with reactions greater than 0 are referred to as reaction diagrams. Stage reaction is usually limited to about 0.5 due to exit kinetic energy considerations.

Exit swirl refers to the value of $V_{\theta 2}$. For turbines discharging to ambient, the most efficient diagram has zero exit swirl. While a negative value of exit swirl increases the work extraction, the magnitude of the turbine discharge velocity increases, leading to a larger difference between the exit static and total pressures. For turbines rated on exit static pressure, the tradeoff between increased work and lower exit static pressure results in lower efficiency levels. Most turbines operating in air with pressure ratios of 3:1 or less use zero exit swirl vector diagrams.

The stage loading is measured by the loading coefficient λ. The loading coefficient is defined here as

$$\lambda = \frac{\Delta h_{\text{actual}}}{U^2} \tag{22}$$

which can also be written as

$$\lambda = \frac{\Delta V_\theta}{U} \tag{23}$$

for turbines with no change in U between inlet and outlet. The loading coefficient is usually calculated for an axial-flow turbine stage at either the hub or mean radius. For a radial-inflow turbine, the rotor tip speed is used in Eq. (23).

The stage flow is controlled by the flow coefficient, defined as

$$\phi = \frac{V_x}{U} \tag{24}$$

These four parameters are related to each other through the vector diagram. Specification of three of them completely defines the vector diagram.

Figure 9 presents examples of a variety of vector diagrams, with exit swirl, reaction, and loading coefficient tabulated. Figure 9(a) shows a vector diagram appropriate for an auxiliary turbine application, with relatively high loading (near impulse) and zero exit swirl. A diagram more typical of a stage in a multistage turbine is shown in Fig. 9(b), since the exit kinetic energy can be utilized in the following stage, the diagram does show significant exit swirl. Both Fig. 9(a) and 9(b) are for axial turbines; 9(c) is the vector diagram for a radial-inflow turbine. The major difference is the change in U between the inlet and exit of the turbine.

Turbine Losses

The difference between the ideal turbine work and the actual turbine work is made up of the losses in the turbine. The losses can be apportioned to each

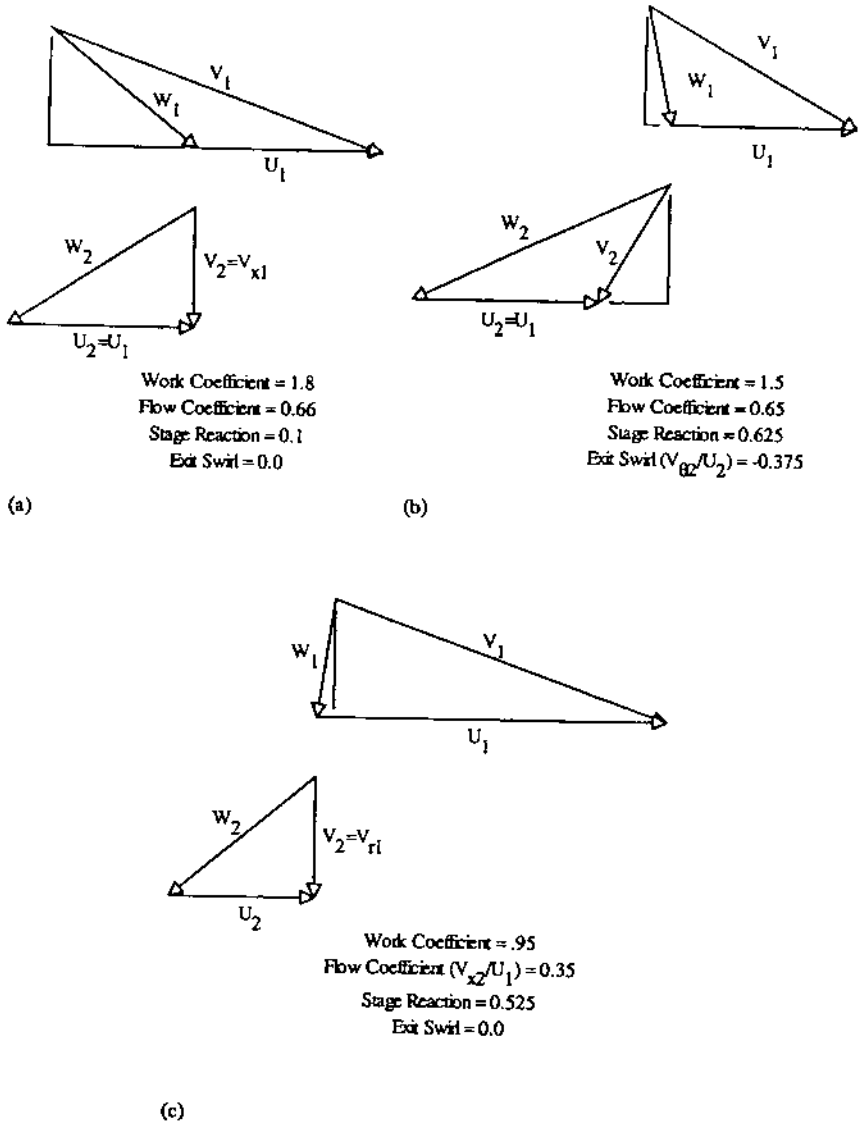

Figure 9 Variations in turbine velocity diagrams: (a) axial-flow diagram for single-stage auxiliary turbine, (b) axial-flow diagram for one stage in multistage turbine, (c) radial-inflow turbine velocity diagram.

component so that we may write

$$\Delta h_{\text{ideal}} = \Delta h_{\text{actual}} + L_{\text{inlet}} + L_{\text{stator}} + L_{\text{rotor}} + L_{\text{diffuser}} + L_{\text{exit}} \tag{25}$$

where the L terms represent losses in enthalpy in each component. Losses can also be looked at from a pressure viewpoint. An ideal exit pressure can be determined from

$$\Delta h_{\text{actual}} = c_{\text{p}} T'_{\text{in}} \left[1 - \left(\frac{(p_{\text{dis}})_{\text{ideal}}}{p'_{\text{in}}} \right)^{(\gamma-1)/\gamma} \right] \tag{26}$$

The component losses are then represented as losses in total pressure, the sum of which is equal to the difference between the actual and ideal exit pressure:

$$P_{\text{dis}} = (p_{\text{dis}})_{\text{ideal}} - \Delta p'_{\text{inlet}} - \Delta p'_{\text{stator}} - \Delta p''_{\text{rotor}} - \Delta p'_{\text{diffuser}} - \Delta p'_{\text{exit}} \tag{27}$$

Most loss models incorporate the pressure loss concept.

Inlet Losses

Losses in inlets are usually modeled with a total pressure loss coefficient K_{t} defined as

$$\Delta p'_{\text{inlet}} = (K_{\text{t}})_{\text{inlet}} \left(\frac{1}{2} \rho V^2_{\text{inlet}} \right) \tag{28}$$

Where

V_{inlet} = velocity at the upstream end of the inlet.
ρ = density of the working fluid.

The losses in an inlet primarily arise from frictional and turning effects. Within packaging constraints, the inlet should be made as large as possible to reduce velocities and minimize losses. Axial inlets such as that of Fig. 2(a) have low frictional losses (due to their short length and relatively low velocities), but often suffer from turning losses due to flow separation along their outer diameter. Longer axial inlets with more gradual changes in outer diameter tend to reduce the turning losses and prevent separation, but adversely impact turbine envelope. Tangential entry inlets tend to have higher losses due to the tangential turning and acceleration of the flow. The spiral flow path also tends to be longer, increasing frictional losses. Typically, loss coefficients for practical axial inlets are in the range of 0.5 to 2.0, while tangential inlets are in the range of 1.0 to 3.0. In terms of inlet

pressure, inlet losses are usually on the order of 1–3% of the inlet total pressure. For turbines in engines, there is usually no real inlet, as they are closely coupled to the combustor or the preceding turbine stage. In this case, the duct losses are usually assessed to the upstream component.

Stator Losses

The stator losses arise primarily from friction within the vane row, the secondary flows caused by the flow turning, and exit losses due to blockage at the vane row trailing edge. The stator loss coefficient can be defined in several ways. Two popular definitions are

$$\Delta p'_{\text{stator}} = Y_{\text{stator}}\left(\frac{1}{2}\rho V_1^2\right) \tag{29}$$

or

$$\Delta p'_{\text{stator}} = Y_{\text{stator}}\left[\frac{1}{2}\rho\left(\frac{V_0^2 + V_1^2}{2}\right)\right] \tag{30}$$

In either case, the loss coefficient is made up of the sum of coefficients for each loss contributor:

$$Y_{\text{stator}} = Y_{\text{profile}} + Y_{\text{secondary}} + Y_{\text{trailing edge}} \tag{31}$$

Profile refers to frictional losses. There can be additional loss contributions due to incidence (the flow coming into the stator is not aligned with the leading edge), shock losses (when the stator exit velocity is supersonic), and others. Much work has been dedicated to determining the proper values for the coefficients, and several very satisfactory loss model systems have been developed. As loss models differ for axial-flow and radial-inflow turbines, these models will be discussed in the individual sections that follow.

Rotor Losses

Rotor losses are modeled in a manner similar to that for stators. However, the pressure loss is measured as a difference in relative total pressures and the kinetic energy is based on relative velocities. As with stators, the rotor loss is based on either the exit relative kinetic energy or the average of the inlet and exit relative kinetic energies:

$$\Delta p''_{\text{rotor}} = X_{\text{rotor}}\left(\frac{1}{2}\rho W_2^2\right) \tag{32}$$

or

$$\Delta p''_{\text{rotor}} = X_{\text{rotor}} \left[\frac{1}{2} \rho \left(\frac{W_1^2 + W_2^2}{2} \right) \right] \tag{33}$$

With rotors, incidence loss can be significant, so we include that contributor in the expression for the rotor loss coefficient:

$$X_{\text{rotor}} = X_{\text{profile}} + X_{\text{secondary}} + X_{\text{trailing edge}} + X_{\text{incidence}} \tag{34}$$

Other losses associated with the rotor are tip clearance and windage losses. Turbine rotors operate with a small clearance between the tips of the blades and the turbine housing. Flow leaks across this gap from the high-pressure side of the blade to the low-pressure side, causing a reduction in the pressure difference at the tip of the blade. This reduces the tangential force on the blade, decreasing the torque delivered to the shaft. Tip clearance effects can be reduced by "shrouding" the turbine blades with a ring, but this introduces manufacturing and mechanical integrity challenges. The loss associated with tip clearance can be modeled either using a pressure loss coefficient or directly as a reduction in the turbine efficiency. The specific models differ with turbine type and will be discussed in following sections.

Windage losses arise from the drag of the turbine disk. As the disk spins in the housing, the no-slip condition on the rotating surface induces rotation of the neighboring fluid, establishing a radial pressure gradient in the cavity. This is commonly referred to as disk pumping. For low-head turbines operating in dense fluids, the windage losses can be considerable. Windage effects are handled by calculating the windage torque from a disk moment coefficient defined as

$$\Gamma_{\text{windage}} = \frac{2C_{\text{m}}}{\frac{1}{2}\rho\omega^2 r_{\text{disk}}^5} \tag{35}$$

The output torque of the turbine is reduced by the windage torque. Values of the moment coefficient C_{m} depend on the geometry of the disk cavity and the speed of the disk. Nece and Daily [4–6] are reliable sources of moment coefficient data.

Diffuser Losses

Losses in the diffuser arise from sources similar to those in other flow passages, namely, friction and flow turning. The diffuser loss can be expressed in terms of a loss coefficient for accounting in turbine performance, but diffuser performance is usually expressed in terms of

diffuser recovery, defined as

$$R_p = \frac{p_{dis} - p_2}{p_2' - p_2} \tag{36}$$

The diffuser recovery measures how much of the kinetic energy at diffuser inlet is converted to a rise in static pressure. Recovery is a function of area ratio (A_{dis}/A_2), length, and curvature. For an ideal diffuser of infinite area ratio, the recovery is 1.0. Peak recovery of a real diffuser of given length takes place when the area ratio is set large enough so that the flow is on the verge of separating from the walls of the diffuser. When the flow separates within the diffuser, the diffuser is said to be stalled. Once stalled, diffuser recovery drops dramatically. Curvature of the mean radius of the diffuser tends to decrease the attainable recovery, since the boundary layer on one of the diffuser walls is subjected to a curvature-induced adverse pressure gradient in addition to the adverse pressure gradient caused by the increase in flow area.

Even with the recent advances in general-use computational fluid dynamics (CFD) tools, analytical prediction of diffuser recovery is not normally performed as part of the preliminary turbine design. Diffuser performance is normally obtained from empirically derived plots such as that shown in Fig. 10. Diffuser recovery is plotted as a function of area ratio and diffuser length. The curvature of the contours of recovery shows the large fall-off in diffuser recovery after the diffuser stall. The locus of maximum recovery is referred to as the line of impending stall. Diffusers should not be designed to operate above this line. Runstadler et al. [7, 8] and Sovran and Klomp [9] present charts of diffuser recovery as a function of inlet Mach number and blockage, as well as the three geometric factors noted earlier.

The total pressure loss across a diffuser operating in incompressible flow can be calculated using continuity and the definition of diffuser recovery. The recovery for an ideal diffuser (no total pressure loss) is given by

$$(R_p)_{ideal} = 1 - \left(\frac{A_2}{A_{dis}}\right)^2 \tag{37}$$

The total pressure loss for a nonideal diffuser in incompressible flow is given by

$$\frac{p_2' - p_{dis}'}{\frac{1}{2}\rho V_2^2} = (K_t)_{diff} = (R_p)_{ideal} - R_p \tag{38}$$

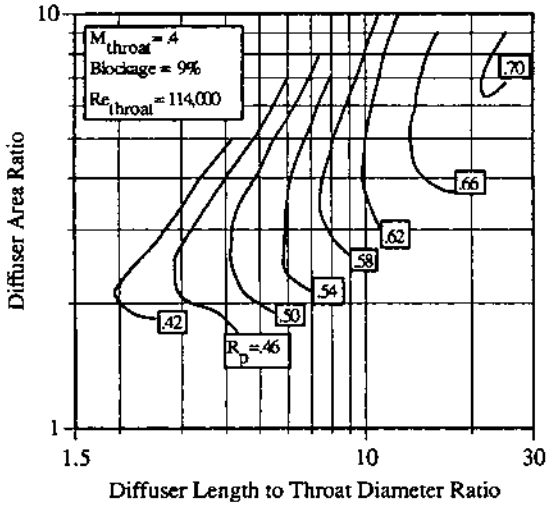

Figure 10 Conical diffuser performance chart. (Replotted from Ref. 8).

This can be used to calculate the diffuser loss when compressibility is not important. If the Mach number at the inlet to the diffuser is above 0.2–0.3, this can be used as a starting guess, and the actual value can be determined by iteration. The diffuser recovery is a function of the inlet Mach number, blockage, and geometry (straight, curved, conical, or annular); it is critical to use the correct diffuser performance chart when estimating diffuser recovery.

Exit Losses

Exit losses are quite simple. If the kinetic energy of the flow exiting the diffuser is used in following stages, or contributes to thrust, the exit losses are zero. If, however, the diffuser discharge energy is not utilized, the exit loss is the exit kinetic energy of the flow. For this case,

$$\Delta p'_{\text{exit}} = p'_{\text{dis}} - p_{\text{dis}} \tag{39}$$

Nondimensional Parameters

Turbine performance is dependent on rotational speed, size, working fluid, enthalpy drop or head, and flow rate. To make comparisons between

different turbines easier, dimensional analysis leads to the formation of several dimensionless parameters that can be used to describe turbines.

Specific Speed and Specific Diameter

The specific speed of a turbine is defined as

$$N_s = \frac{\omega\sqrt{Q_2}}{(\Delta h_{ideal})^{3/4}} \tag{40}$$

where Q_2 is the volumetric flow rate through the turbine at rotor exit. The specific speed is used to relate the performance of geometrically similar turbines of different size. In general, turbine efficiency for two turbines of the same specific speed will be the same, except for differences in tip clearance and Reynolds number. Maintaining specific speed of a turbine is a common approach to scaling of a turbine to different flow rates.

The specific diameter is defined as

$$D_s = \frac{d_{tip}(\Delta h_{ideal})^{1/4}}{\sqrt{Q_2}} \tag{41}$$

where d_{tip} is the tip diameter of the turbine rotor, either radial in-flow or axial flow. Specific diameter and specific speed are used to correlate turbine performance. Balje [3] presents extensive analytical studies that result in maps of peak turbine efficiency versus specific speed and diameter for various types of turbines. These charts can be quite valuable during initial turbine sizing and performance estimation.

Blade-Jet Speed Ratio

Turbine performance can also be correlated against the blade-jet speed ratio, which is a measure of the blade speed relative to the ideal stator exit velocity. Primarily used in impulse turbines, where the entire static enthalpy drop is taken across the stator, the ideal stator exit velocity, C_0, is calculated assuming the entire ideal enthalpy drop is converted into kinetic energy:

$$C_0 = \sqrt{2\Delta h_{ideal}} \tag{42}$$

The blade-jet speed ratio is then calculated from

$$\frac{U}{C_0} = \frac{U}{\sqrt{2\Delta h_{ideal}}} \tag{43}$$

The value of blade speed at the mean turbine blade radius is typically used in

Eq. (43) for axial turbines; for radial-inflow turbines, the rotor tip speed is used.

Reynolds Number

The Reynolds number for a turbine is usually defined as

$$\mathrm{Re} = \frac{\rho U_{\mathrm{tip}} d_{\mathrm{tip}}}{\mu} \tag{44}$$

where μ is the viscosity of the working fluid. Sometimes ωd_{tip} is substituted for U_{tip}, resulting in a value twice that of Eq. (44). The Reynolds number relates the viscous and inertial effects in the fluid flow. For most turbomachinery operating on air, the Reynolds number is of secondary importance. However, when turbomachinery is scaled (either larger or smaller), the Reynolds number changes, resulting in a change in turbine efficiency. Glassman [1] suggests the following for adjusting turbine losses to account for Reynolds number changes:

$$\frac{1-\eta'_a}{1-\eta'_b} = A + B\left(\frac{\mathrm{Re}_b}{\mathrm{Re}_a}\right)^{0.2} \tag{45}$$

where η' indicates total-to-total efficiency and A and B sum to 1.0. That all the loss is not scaled by the Reynolds number ratio reflects that not all losses are viscous in origin. Also, total-to-total efficiency is used since the kinetic energy of the exit loss is not affected by Reynolds number. Glassman [1] suggests values of 0.3–0.4 for A (the nonviscous loss) and from 0.7 to 0.6 for B (the viscous loss).

Equivalent or Corrected Quantities

In order to eliminate the dependence of turbine performance maps on the values of inlet temperature and pressure, corrected quantities such as corrected flow, corrected speed, corrected torque, and corrected power were developed. Using corrected quantities, turbine performance can be represented by just a few curves for a wide variety of operating conditions. Corrected quantities are not nondimensional. Glassman [1] provides a detailed derivation of the corrected quantities. The corrected flow is defined as

$$w_{\mathrm{corr}} = \frac{w\sqrt{\theta}}{\delta} \tag{46}$$

where

$$\theta = \frac{T'_{\text{in}}}{T_{\text{STD}}} \tag{47}$$

and

$$\delta = \frac{p'_{\text{in}}}{p_{\text{STD}}} \tag{48}$$

The standard conditions are usually taken to be 518.7 R and 14.7 psia. Corrected speed is defined as

$$N_{\text{corr}} = \frac{N}{\sqrt{\theta}} \tag{49}$$

Equation (5) shows torque to be the product of flow rate and the change in tangential velocity across the rotor. Corrected flow is defined above; corrected velocities appear with $\theta^{1/2}$ in the denominator from the corrected shaft speed. Therefore, corrected torque is defined as

$$\Gamma_{\text{corr}} = \frac{\Gamma}{\delta} \tag{50}$$

The form of the corrected power is determined from the product of corrected torque and corrected speed:

$$P_{\text{corr}} = \frac{P}{\delta\sqrt{\theta}} \tag{51}$$

These corrected quantities are used to reduce turbine performance data to curves of constant-pressure ratio on two charts. Figure 11 presents typical turbine performance maps using the corrected quantities. Figure 11(a) presents corrected flow as a function of corrected speed and pressure ratio, while Fig. 11(b) shows corrected torque versus corrected speed and pressure ratio. Characteristics typical of both radial-inflow and axial-flow turbines are presented in Fig. 11.

AXIAL-FLOW TURBINE SIZING

Axial-Flow Turbine Performance Prediction

Prediction methods for axial-flow turbine performance methods can be roughly broken into two groups according to Sieverding [10]. The first group bases turbine stage performance on overall parameters such as work coefficient and flow coefficient. These are most often used in preliminary

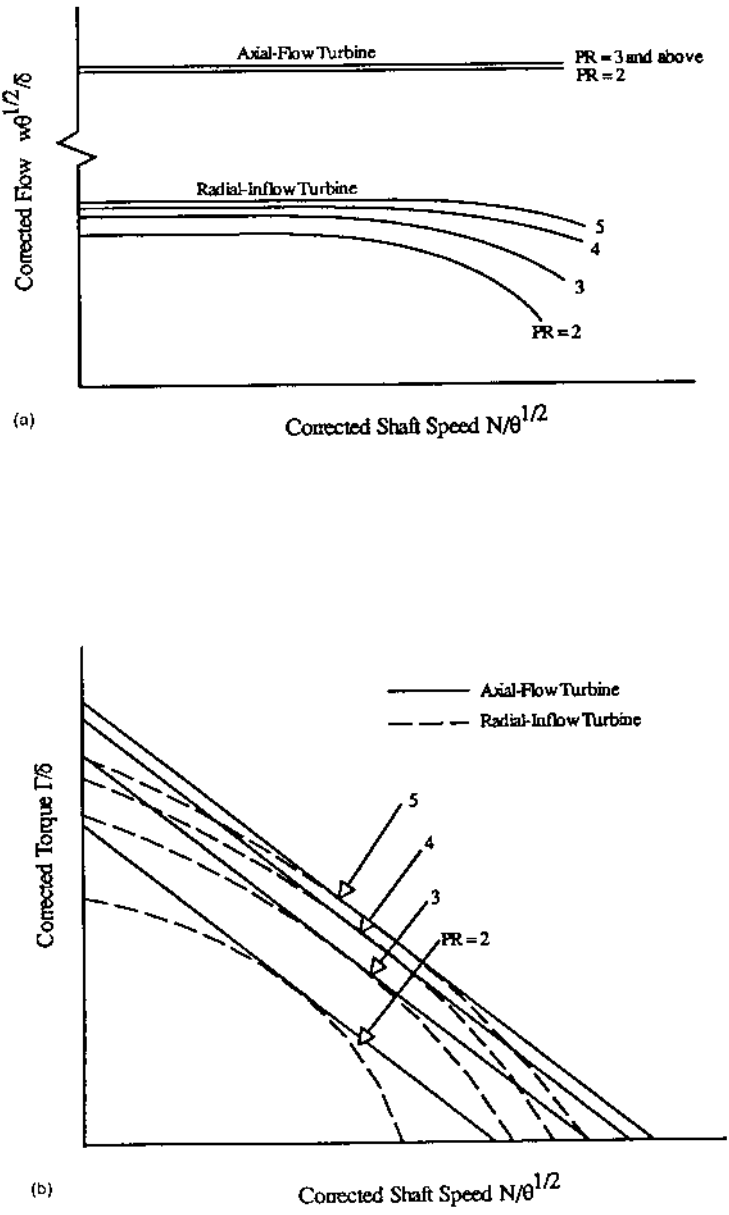

Figure 11 Typical performance maps using corrected quantities for axial-flow and radial-inflow turbines: (a) corrected flow vs. pressure ratio and corrected speed; (b) corrected torque vs. pressure ratio and corrected speed.

sizing exercises where the details of the turbine design are unknown. Smith [11] and Soderberg [12] are both examples of this "black box" approach, as are Balje's [3] maps of turbine efficiency as a function of specific speed and specific diameter.

The second grouping is based on the approach outlined earlier where turbine losses are broken down to a much finer level. In these methods, a large number of individual losses are summed to arrive at the total loss. Each of these loss components is dependent on geometric and aerodynamic parameters. This requires more knowledge of the turbine configuration, such as flow path and blading geometry, before a performance estimate can be made. As such, these methods are better suited for more detailed turbine design studies.

Among the loss component methods, Sieverding [10] gives an excellent review of the more popular component loss models. The progenitor of a family of loss models is that developed by Ainley and Mathieson [13]. It has been modified and "improved" by Dunham and Came [14] and, more recently, by Kacker and Okapuu [15]. A somewhat different approach is taken by Craig and Cox [16]. All these methods are based on correlations of experimental data.

An alternate approach is to analytically predict the major loss components such as profile or friction losses and trailing-edge thickness losses by computing the boundary layers along the blade surfaces. Profile losses are then computed from the momentum thickness of the boundary layers on the pressure and suction surfaces of the blades or vanes. Glassman [1] gives a detailed explanation of this method. Note that this technique requires even more information on the turbine design; to calculate the boundary layer it is necessary to know both the surface contour and the velocities along the blade surface. Thus, this method cannot be used until blade geometries have been completely specified and detailed flow channel calculations have been made.

In addition to the published prediction methods just noted, each of the major turbine design houses (such as AlliedSignal, Allison, General Electric, Lycoming, Pratt & Whitney, Sundstrand, and Williams) has its own proprietary models based on a large turbine performance database. Of course, it is not possible to report those here.

For our purposes (determining the size and approximate performance of a turbine) we will concentrate on the overall performance prediction methods, specifically Smith's chart and Soderberg's correlation. Figure 12 shows Smith's [11] chart, where contours of total-to-total efficiency are plotted versus flow coefficient and work factor [see Eqs. (23) and (24)]. Both the flow coefficient and stage work coefficient are defined using velocities at the mean radius of the turbine. The efficiency contours are based on the

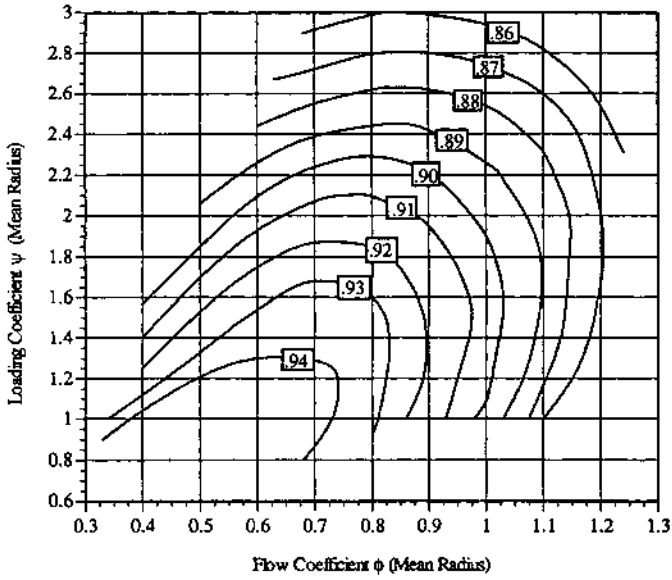

Figure 12 Smith's chart for stage zero-clearance total-to-total efficiency as function of mean-radius flow and loading coefficient. (Replotted from Ref. 11 with permission of the Royal Aeronautical Society).

measured efficiency for 70 turbines. All the turbines have a constant axial velocity across the stage, zero incidence at design point, and reactions ranging from 20% to 60%. Reynolds number for the turbines range from 100,000 to 300,000. Aspect ratio (blade height to axial chord) for the tested turbines is in the range of 3–4. Smith's chart does not account for the effects of blade aspect ratio, Mach number effects, or trailing-edge thickness variations. The data have been corrected to reflect zero tip clearance, so the efficiencies must be adjusted for the tip clearance loss of the application.

Sieverding [10] considers Soderberg's correlation to be outdated but still useful in preliminary design stages due to its simplicity. In Soderberg's [12] correlation, blade-row kinetic energy losses are calculated from

$$\frac{(V_o)^2_{\text{ideal}} - V_o^2}{V_o^2} = \xi = \left(\frac{10^5}{R_{\text{th}}}\right)^{1/4} \left\{(1 + \xi_{\text{ref}})\left[0.975 + 0.075\left(\frac{c_x}{h} - 1\right)\right]\right\} \quad (52)$$

where R_{th} is the Reynolds number based on the hydraulic diameter at the blade passage minimum area (referred to as the throat) defined as

$$R_{th} = \frac{\rho_o V_o}{\mu_o} \frac{2hs\cos(\alpha_o)}{h + s\cos(\alpha_o)} \tag{53}$$

where h is the blade height and s is the spacing between the blades at the mean radius. The blade axial chord is identified by c_x. In both Eqs. (52) and (53), the subscript "o" refers to blade-row outlet conditions, either stator or rotor (for the rotor, the absolute velocity V is replaced by the relative velocity W, standard practice for all "blade-row" relations). The reference loss coefficient ξ_{ref} is a function of blade turning and thickness and can be found in Fig. 13. Compared to Smith's chart, this correlation requires more knowledge of the turbine geometry, but no more than would be required in a conceptual turbine design. The losses predicted by this method are only valid for the optimum blade chord-to-spacing ratio and for zero incidence. Tip clearance losses must also be added in the final determination of turbine efficiency. Like Smith's chart, this correlation results in a total-to-total efficiency for the turbine.

The optimum value of blade chord-to-spacing ratio can be found using the definition of the Zweifel coefficient [17]:

$$\zeta = \left| \frac{2}{c_x/s} \frac{\cos\alpha_o}{\cos\alpha_i} \sin(\alpha_i - \alpha_o) \right| \tag{54}$$

where the subscript "i" refers to blade-row inlet. Zweifel [17] states that optimum solidity (c_x/s) occurs when $\zeta = 0.8$.

Tip clearance losses are caused by flow leakage through the gap between the turbine blade and the stationary shroud. This flow does not get turned by the turbine blade; so it does not result in work extraction. In addition, the flow through the clearance region causes a reduction of the pressure loading across the blade tip, further reducing the turbine efficiency. The leakage flow is primarily controlled by the radial clearance, but is also affected by the geometry of the shroud and the blade reaction. Leakage effects can be reduced by attaching a shroud to the turbine blade tips, which eliminates the tip unloading phenomenon. For preliminary design purposes, the tip clearance loss for unshrouded turbine wheels can be approximated by

$$\frac{\eta}{\eta_{zc}} = 1 - K_c \frac{r_{tip}}{r_{mean}} \frac{c_r}{h} \tag{55}$$

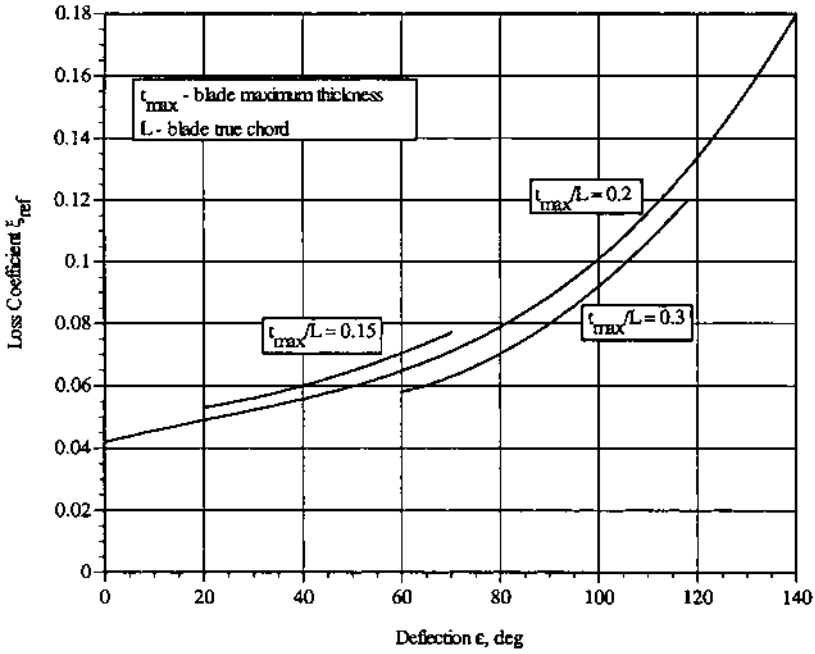

Figure 13 Soderberg's loss coefficient as function of deflection angle and blade thickness. (Replotted from Ref. 12 with permission from Pergamon Press Ltd.)

Where

η_{zc} = zero clearance efficiency.
o_r = radial tip clearance.
r_{tip} = passage tip radius.
r_{mean} = mean passage radius.
K_c = empirically derived constant.

Based on measurements reported by Haas and Kofskey [18], the value of K_c is between 1.5 and 2.0, depending on geometric configuration. For preliminary design purposes, the conservative value should be used. When using Soderberg's correlation, the value of K_c should be taken as 1, since Soderberg corrected his data using that value for K_c.

With the information above, the turbine efficiency (total-to-total) can be determined from the stator inlet (station 0) to rotor exit (station 2). In

order to determine the overall turbine efficiency, it is necessary to include the inlet, diffuser, and exit losses. These losses do not affect the turbine work extraction, but result in the overall pressure ratio across the turbine being larger than the stage pressure ratio. The overall efficiency can be calculated from

$$\eta_{OA} = (\eta_{0'-2'}) \frac{1 - (p'_2/p'_0)^{(\gamma-1)/\gamma}}{1 - (p_{dis}/p'_{in})^{(\gamma-1)/\gamma}} \tag{56}$$

The pressure losses in the inlet, diffuser, and exit are calculated from the information presented earlier.

Mechanical, Geometric, and Manufacturing Constraints

Turbine design is as much or more affected by mechanical considerations as it is by aerodynamic considerations. Aerodynamic performance is normally constrained by the stress limitations of the turbine material. At this point in the history of turbine design, turbine performance at elevated temperatures is limited by materials, not aerodynamics. Material and manufacturing limitations affect both the geometry of the turbine wheel and its operating conditions.

Turbine blade speed is limited by the centrifugal stresses in the disk and by the tensile stress at the blade root (where the blade attaches to the disk). The allowable stress limit is affected by the turbine material, turbine temperature, and turbine life requirements. Typical turbine materials for aircraft auxiliary turbines are titanium in moderate-temperature applications (turbine relative temperatures below 1,000 °F) and superalloys for higher temperatures.

Allowable blade-tip speed for axial-flow turbines is a complex function of inlet temperature, availability of cooling air, thermal cycling (low cycle fatigue damage), and desired operating life. In general, design point blade speeds are held below 2,200 ft/sec, but higher blade speeds can be withstood for shorter lifetimes, if temperatures permit. For auxiliary turbine applications with inlet temperatures below 300 °F and pressure ratios of 3 or below, blade speed limits are generally not a design driver.

Both stress and manufacturing considerations limit the turbine blade hub-to-tip radius ratio to values greater than about 0.6. If the hub diameter is much smaller, it is difficult to physically accommodate the required number of blades on the hub. Also, the twist of the turbine blade increases, leading to sections at the tip not being directly supported by the hub section. This leads to high bending loads in the blade and higher stress levels. For

performance reasons (secondary flow losses and tip clearance losses), it is desirable to keep the hub-to-tip radius ratio below 0.8.

Manufacturing considerations limit blade angles on rotors to less than 60° and stator vane exit angles to less than 75°. Casting capabilities limit stator trailing-edge thickness (t_{te}) to no less than 0.015 in., restricting stator vane count. For performance reasons, the trailing-edge blockage should be kept less than 10% at all radii. The trailing-edge blockage is defined here as the ratio of the trailing-edge tangential thickness (b) to the blade or vane spacing (s):

$$\frac{b}{s} = \frac{t_{te}/\cos\alpha_{te}}{2\pi r/Z} \tag{57}$$

where Z is the blade or vane count. Rotor blades are usually machined, but for stress and tolerance reasons the trailing-edge thickness is normally no less than 0.015 in. The 10% limitation on blockage is also valid for rotors.

Auxiliary turbines often are required to survive free-run conditions. Free run occurs when the turbine load is removed but the air supply is not. This can happen if an output shaft fails or if an inlet control valve fails to close. Without any load, the turbine accelerates until the power output of the turbine is matched by the geartrain and aerodynamic losses. Free-run speed is roughly twice design-point speed for most aircraft auxiliary turbines. This restricts the allowable design-point speeds and stress levels further, since the disk and blade may be required to survive free-run operation.

Hub-to-Tip Variation in Vector Diagram

Up to this point we have only considered the vector diagram at the mean radius of the turbine. For turbines with high hub-to-tip radius ratios (above 0.85), the variation in vector diagram is not important. For a turbine with relatively tall blades, however, the variation is significant.

The change in vector diagram with radius is due to the change in blade speed and the balance between pressure and body forces acting on the working fluid as it goes through the turbine. Examples of body forces include the centrifugal force acting on a fluid element that has a tangential velocity (such as between the stator and rotor), and the accelerations caused by a change in flow direction if the flow path is curved in the meridional plane. The balance of these forces (body and pressure) is referred to as radial equilibrium. Glassman [1] presents a detailed mathematical development of the equations that govern radial equilibrium. For our purposes, we will concentrate on the conditions that satisfy radial equilibrium.

The classical approach to satisfying radial equilibrium is to use a free vortex variation in the vector diagram from the hub to the tip of the rotor blade. A free vortex variation is obtained by holding the product of the radius and tangential velocity constant ($rV_\theta = \text{constant}$). When this is done, the axial velocity V_x is invariant with radius. Until the widespread use of computers in turbine design, almost all turbines employed free vortex diagrams due to their simplicity. For preliminary design purposes, the free vortex diagram is more than satisfactory.

Aside from its simplicity, the free vortex diagram has other advantages. Holding rV_θ constant implies that the work extraction is constant with radius. With V_x constant, the mass flow varies little with radius. This implies that the mean section vector diagram is an excellent representation of the entire turbine from both a work and mass flow standpoint.

When using a free vortex distribution, there are two key items to examine in addition to the mean vector diagram. The hub diagram suffers from low reaction due to the increase in V_θ and should be checked to ensure at least a zero value of reaction. From hub to tip, the reduction in V_θ and increase in U cause a large change in the rotor inlet relative flow angle, with the rotor tip section tending to overhang the hub section. By choosing a moderate hub-to-tip radius ratio (if possible), both low hub reaction and excessive rotor blade twist can be avoided.

For a zero exit swirl vector diagram, some simple relations can be developed for the allowable mean radius work coefficient and the hub-to-tip twist of the rotor blade. For a zero exit swirl diagram, zero reaction occurs for a work coefficient of 2.0. Using this as an upper limit at the hub, the work coefficient at mean radius is found from

$$\lambda_m = 2\left(\frac{r_h}{r_m}\right)^2 \tag{58}$$

For a turbine with a hub-to-tip radius ratio of 0.7, the maximum work coefficient at mean radius for impulse conditions at the hub is 1.356. The deviation in inlet flow angle to the rotor from hub to tip for a free vortex distribution is given by

$$\begin{aligned}\Delta\beta_1 &= \beta_{1h} - \beta_{1t} \\ &= \tan^{-1}\left[\frac{\lambda_m(r_m/r_h)^2 - 1}{\phi_m(r_m/r_h)}\right] - \tan^{-1}\left[\frac{\lambda_m(r_m/r_t)^2 - 1}{\phi_m(r_m/r_t)}\right]\end{aligned} \tag{59}$$

For a vector diagram with $\lambda_m = 1.356, r_h/r_t = 0.7$, and

$\phi_m = 0.6, \Delta\beta_1 = 56.1°$, which is acceptable from a manufacturing viewpoint. Large negative inlet angles at the blade tip are to be avoided.

An Example of Turbine Sizing

In order to demonstrate the concepts described in this and preceding sections, an example is presented of the sizing of a "typical" auxiliary turbine for use in an aircraft application. The turbine is to be sized to meet the following requirements:

1. Generates 100 hp at design point.
2. Operates at an overall pressure ratio of 3:1 in air.
3. Inlet pressure is 44.1 psia, and inlet temperature is 300 °F.

The object of this exercise is to determine the turbine size, flow rate, and operating speed with a turbine design meeting the mechanical, geometric, and manufacturing constraints outlined earlier. The following procedure will be followed to perform this exercise:

1. Determine available energy (isentropic enthalpy drop).
2. Guesstimate overall efficiency to calculate flow rate.
3. Select the vector diagram parameters.
4. Calculate the vector diagram.
5. Determine the rotor overall geometry.
6. Calculate the overall efficiency based on Smith's chart both with and without a diffuser.

The process is iterative in that the efficiency determined in step 6 is then used as the guess in step 2, with the process repeated until no change is found in the predicted efficiency. We will also predict the turbine efficiency using Soderberg's correlation.

The first step is to calculate the energy available to the turbine using Eq. (1). For air, typical values for the specific heat and the ratio of specific heats are $0.24\,\mathrm{Btu}/(\mathrm{lb_m} - \mathrm{R})$ and 1.4, respectively. It is also necessary to convert the inlet temperature to the absolute scale. We then have

$$\Delta h_{\text{isentropic}} = \left(0.24\frac{\text{Btu}}{\text{lb}_\text{m}\cdot\text{R}}\right)(760\,\text{R})\left[1 - \left(\frac{1}{3}\right)^{0.4/1.4}\right] = 49.14\frac{\text{Btu}}{\text{lb}_\text{m}}$$

Note that more digits are carried through the calculations than indicated, so exact agreement may not occur in all instances. The vector diagram is calculated using the work actually done by the blade row; therefore, we need to start with a guess to the overall efficiency of the turbine. A good starting point is usually an overall efficiency of 0.8, including the effects of tip

clearance. Since tip clearance represents a loss at the tip of the blade, the rest of the blade does more than the average work. Therefore, the vector diagram is calculated using the zero-clearance efficiency. Since we do not know the turbine geometry at this point, we must make another assumption: we assume that the tip clearance loss is 5%, so that the overall zero-clearance efficiency is 0.84. Note that the required flow rate is calculated using the overall efficiency with clearance, since that represents the energy available at the turbine shaft. Equation (2) is used to calculate the actual enthalpy drops:

$$\Delta h_{\mathrm{OA}} = (0.8)\left(49.14\ \frac{\mathrm{Btu}}{\mathrm{lb_m}}\right) = 39.31\ \frac{\mathrm{Btu}}{\mathrm{lb_m}}$$

and

$$\Delta h_{\mathrm{OA\ ZC}} = (0.84)\left(49.14\ \frac{\mathrm{Btu}}{\mathrm{lb_m}}\right) = 41.28\ \frac{\mathrm{Btu}}{\mathrm{lb_m}}$$

The required turbine flow is found using Eq. (7):

$$\dot{m} = \frac{P}{\Delta h_{\mathrm{OA}}} = \frac{(100\,\mathrm{hp})(.7069\,\mathrm{Btu/sec/hp})}{39.31\,\mathrm{Btu/lb_m}} = 1.798\,\mathrm{lb_m/\,sec}$$

The mass flow rate is needed to calculate turbine flow area and is also a system requirement.

We specify the vector diagram by selecting values of the turbine work and flow coefficients. We also select a turbine hub-to-tip radius ratio of 0.7, restricting the choice of mean work coefficient to values less than 1.356 in order to avoid negative reaction at the hub. From Smith's chart (Fig. 12), we initially choose a work coefficient of 1.3 and a flow coefficient of 0.6 to result in a zero-clearance, stator inlet to rotor exit total-to-total efficiency of 0.94. We apply these coefficients at the mean radius of the turbine. From Eq. (22) we calculate the mean blade speed, U_{m}:

$$U_{\mathrm{m}} = \sqrt{\frac{\Delta h_{\mathrm{OA\ ZC}}}{\lambda}} = \sqrt{\frac{(32.174\,\mathrm{ft\cdot lb_f/(lb_m\cdot sec^2)})(778.16\,\mathrm{ft\cdot lb_f/Btu})(41.28\,\mathrm{Btu/lb_m})}{1.3}}$$
$$= 891.6\,\mathrm{ft/\,sec}$$

The axial velocity is calculated from Eq. (51):

$$V_{x2} = (0.6)(891.6\,\mathrm{ft/\,sec}) = 535.0\,\mathrm{ft/\,sec}$$

In order to construct the vector diagram, we make two more assumptions: (1) there is zero swirl leaving the turbine stage in order to minimize the exit kinetic energy loss, and (2) the axial velocity is constant through the stage.

By assuming that $V_{\theta 2}$ is zero, Eq. (23) reduces to

$$V_{\theta 1} = \lambda U_{\mathrm{m}} = (1.3)(891.6\,\mathrm{ft/sec}) = 1159.1\,\mathrm{ft/sec}$$

Using Eqs. (10) through (14) results in the vector diagram shown in Fig. 14. Note that the critical stator and rotor exit angles are within the guidelines presented earlier.

The rotor blade height and mean radius are determined by the required rotor exit flow area and the hub-to-tip radius ratio. The rotor exit flow area is determined from continuity:

$$A_2 = \frac{\rho_2 V_{x2}}{\dot{m}}$$

The mass flow rate and axial velocity have previously been calculated; the density is dependent on the rotor exit temperature and pressure. For a turbine without a diffuser, the rotor exit static pressure is the same as the discharge pressure, assuming the rotor exit annulus is not choked. For a

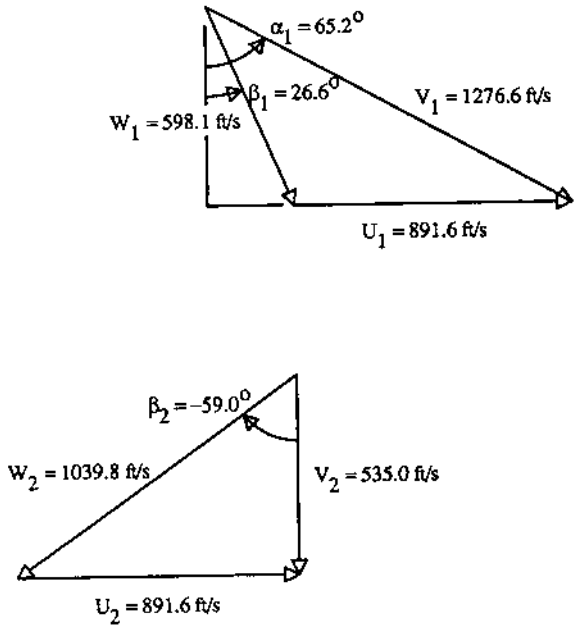

Figure 14 Mean-radius velocity diagrams for first iteration of axial-flow turbine sizing example.

turbine with an effective diffuser, the rotor exit static pressure will be less than the discharge value. We will examine both cases.

Turbine Without Diffuser

First we consider the turbine without a diffuser. Assuming perfect gas behavior, the density is calculated from

$$\rho_2 = \frac{p_2}{R_{\text{gas}} T_2}$$

where the temperature and pressure are static values and R_{gas} is the gas constant. The rotor exit total temperature is determined from

$$T_2' = T_0' - \frac{\Delta h_{\text{OA ZC}}}{C_{\text{p}}} = 760\,\text{R} - \frac{41.28\,\text{Btu/lb}_\text{m}}{0.24\,\text{Btu/(lb}_\text{m} \cdot \text{R)}} 588.0\,\text{R}$$

The zero-clearance enthalpy drop is used because the local temperature over the majority of the blade will reflect the higher work (a higher discharge temperature will be measured downstream of the turbine after mixing of the tip clearance flow has occurred). Next we calculate the rotor exit critical Mach number to determine the static temperature. The critical sonic velocity is calculated from

$$a_{\text{cr}} = \sqrt{\frac{2\gamma}{\gamma + 1} g R_{\text{gas}} T'}$$

where g is a conversion factor. For air at low temperatures, $R_{\text{gas}} = 53.34\,\text{ft-lb}_\text{f}/\text{lb}_\text{m} - \text{R}$, resulting in

$$a_{\text{cr2}} = \sqrt{\frac{2(1.4)}{1 + 1.4} \left(32.174 \frac{\text{ft} \cdot \text{lb}_\text{f}}{\text{lb}_\text{m} \cdot \text{sec}^2}\right) \left(53.34 \frac{\text{ft} \cdot \text{lb}_\text{f}}{\text{lb}_\text{m} \cdot \text{R}}\right) 588\,\text{R}}$$

$$= 1085\,\text{ft/sec}$$

The static temperature is found from

$$T_2 = T_2' \left[1 - \frac{\gamma - 1}{\gamma + 1} \left(\frac{V_2}{a_{\text{cr2}}}\right)^2\right]$$

with zero exit swirl, $V_2 = V_{x2}$ resulting in

$$T_2 = (588\,\text{R}) \left[1 - \frac{1.4 - 1}{1 + 1.4} \left(\frac{535\,\text{ft/sec}}{1085\,\text{ft/sec}}\right)^2\right] = 564.2\,\text{R}$$

The density can now be determined:

$$\rho_2 = \frac{\left(\frac{44.1\,\mathrm{lb_f/in^2}}{3}\right)\left(144\,\frac{\mathrm{in^2}}{\mathrm{ft^2}}\right)}{\left(53.34\,\frac{\mathrm{ft\cdot lb_f}}{\mathrm{lb_m\cdot R}}\right)(564.2\,\mathrm{R})} = 0.0703\,\frac{\mathrm{lb_m}}{\mathrm{ft^3}}$$

and the required flow area:

$$A_2 = \frac{1.798\,\mathrm{lb_m/sec}}{(0.0703\,\mathrm{lb_m/ft^3})(535.0\,\mathrm{ft/sec})}\left(144\,\frac{\mathrm{in.^2}}{\mathrm{ft^2}}\right) = 6.882\,\mathrm{in.^2}$$

The rotor exit hub and tip radii cannot be uniquely determined until either shaft speed, blade height, or hub-to-tip radius ratio is specified. Once one parameter is specified, the others are determined. For this example, we choose a hub-to-tip ratio of 0.7 as a compromise between performance and manufacturability. If the turbine shaft speed were restricted to a certain value or range of values, it would make more sense to specify the shaft speed. The turbine tip radius is determined from

$$r_{t2} = \sqrt{\frac{A_2}{\pi[1-(r_h/r_t)^2]}} = \sqrt{\frac{6.882\,\mathrm{in.^2}}{\pi[1-(0.7)^2]}} = 2.073\,\mathrm{in.}$$

This results in a hub radius of 1.451 in., a mean radius of 1.762 in. and a blade height of 0.622 in. The shaft speed is found from Eq. (8):

$$\omega = U_m/r_m = \frac{891.6\,\mathrm{ft/sec}}{(1.762\,\mathrm{in})(1\,\mathrm{ft}/12\,\mathrm{in})} = 6073\,\mathrm{rad/sec}$$

or 57,600 rpm. The tip speed of the turbine is 1,049 ft/sec, well within our guidelines.

The next step is to calculate the overall efficiency. From Smith's chart, a stator inlet to rotor exit total-to-total efficiency at zero clearance is available. We must correct this for tip clearance effects, the inlet loss, and the exit kinetic energy loss. At $\lambda = 1.3$ and $\phi = 0.6$, Smith's chart predicts

$$\eta_{0'-2'ZC} = 0.94$$

Assuming a tip clearance of 0.015 in., the total-to-total efficiency including the tip clearance loss is calculated from Eq. (55) using a value of 2 for K_c:

$$\eta_{0'-2'} = (\eta_{0'-2'ZC})\left(1 - 2\frac{r_t}{r_m}\frac{\delta}{h}\right) = 0.94\left(1 - 2\frac{2.073}{1.762}\frac{0.015}{0.622}\right) = 0.8867$$

Equation (56) is used to determine the overall efficiency including inlet and exit losses. From the problem statement, we know that the overall pressure

ratio (p'_{in}/p_{dis}) is 3. The stator inlet to rotor exit total-to-total pressure ratio is calculated from

$$\frac{p'_2}{p'_0} = \left(\frac{p_{dis}}{p'_{in}}\right)\left(\frac{p'_2}{p_{dis}}\right)\left(\frac{p'_{in}}{p'_0}\right)$$

Based on earlier discussions, we assume an inlet total pressure loss ratio of 0.99. With no diffuser, the discharge and rotor exit stations are the same, so the ratio of static to total pressure is found from the rotor exit Mach number:

$$\frac{p_{dis}}{p'_2} = \frac{p_2}{p'_2} = \left[1 - \frac{\gamma - 1}{\gamma + 1}\left(\frac{V_2}{a_{cr2}}\right)^2\right]^{\frac{\gamma}{\gamma-1}} = \left[1 - \frac{1}{6}\left(\frac{535}{1085}\right)^2\right]^{3.5} = 0.8652$$

We can now calculate the total-to-total pressure ratio from stator inlet to rotor exit and the overall efficiency:

$$\frac{p'_2}{p'_0} = \left(\frac{1}{3}\right)\left(\frac{1}{0.8652}\right)\left(\frac{1}{0.99}\right) = 0.3891$$

and

$$\eta_{OA} = (0.8867)\frac{1 - (0.3891)^{0.4/1.4}}{1 - \left(\frac{1}{3}\right)^{0.4/1.4}} = 0.7779$$

This completes the first iteration on the turbine size and performance for the case without a diffuser. To improve the accuracy of the result, the preceding calculations would be repeated using the new values of overall efficiency and tip clearance loss.

Turbine with Diffuser

For an auxiliary type of turbine such as this, a diffuser recovery of 0.4 is reasonable to expect with a well-designed diffuser. The rotor exit total pressure is calculated from the definition of diffuser recovery given in Eq. (35):

$$p'_2 = \frac{p_{dis}}{R_p(1 - p_2/p'_2) + p_2/p'_2} = \frac{44.1\,\text{psia}/3}{0.4(1 - 0.8652) + 0.8652} = 15.99\,\text{psia}$$

and the rotor exit static pressure is

$$p_2 = (15.99\,\text{psia})(0.8652) = 13.84\,\text{psia}$$

This is a considerable reduction compared to the discharge pressure of 14.7 psia. From this point, the rotor exit geometry is calculated in the same way as that presented for the case without the diffuser. The following results are obtained:

$$\rho_2 = 0.0662\,\mathrm{lb_m/ft^3}$$
$$A_2 = 7.311\,\mathrm{in.^2}$$
$$r_{t2} = 2.136\,\mathrm{in.}$$
$$r_{h2} = 1.495\,\mathrm{in.}$$
$$r_{m2} = 1.816\,\mathrm{in.}$$
$$h_2 = 0.641\,\mathrm{in.}$$
$$N = 56{,}270\,\mathrm{rpm}$$

The tip speed is the same as the turbine without the diffuser, since the mean blade speed is unchanged, as is the hub-to-tip radius ratio of the rotor. The efficiency calculations also proceed in the same manner as the earlier case with the following results (using the same inlet pressure loss assumption):

$$\eta_{0'-2'} = 0.8882$$
$$\frac{p'_2}{p'_0} = 0.3663$$
$$\eta_{OA} = 0.8224$$

Since this result differs from our original assumption for overall efficiency, further iterations would be performed to obtain a more accurate answer. Note the almost 6% increase in overall efficiency due to the inclusion of a diffuser. This indicates a large amount of energy is contained in the turbine exhaust. The efficiency gain associated with a diffuser is dependent on diffuser recovery, rotor exit Mach number, and overall pressure ratio and is easily calculated. Figure 15 shows the efficiency benefit associated with a diffuser for an overall turbine pressure ratio (total-to-static) of 3. Efficiency gains are plotted as a function of rotor exit critical Mach number and diffuser recovery. As rotor exit Mach number increases, the advantages of including a diffuser become larger. This tradeoff is important to consider when sizing the turbine. For a given flow or power level, turbine rotor diameter can be reduced by accepting high rotor exit velocities (high values of flow coefficient); however, turbine efficiency will suffer unless a diffuser is included, adversely impacting the axial envelope.

Automation of Calculations and Trade Studies

The calculations outlined in this example can be easily automated in either a computer program or a spreadsheet with iteration capability. An example of the latter is presented in Fig. 16, which contains the iterated final results for the example turbine when equipped with a diffuser. The advantage of automation is the capability to quickly perform trade studies to optimize the turbine preliminary design. Prospective variables for study include work and flow coefficients, diffuser recovery, shaft speed or hub-to-tip radius ratio, inlet loss, tip clearance, exit swirl, and others.

Soderberg's Method

We conclude this example by calculating the turbine performance using Soderberg's correlation. We will use the iterated turbine design results shown in the spreadsheet of Fig. 16. Soderberg's correlation [Eq. (52)] requires the vane and blade chords in order to calculate the aspect ratio (c_x/h). We first determine the blade number by setting the blockage level at mean radius to 10% and the trailing-edge thickness for both the rotor and

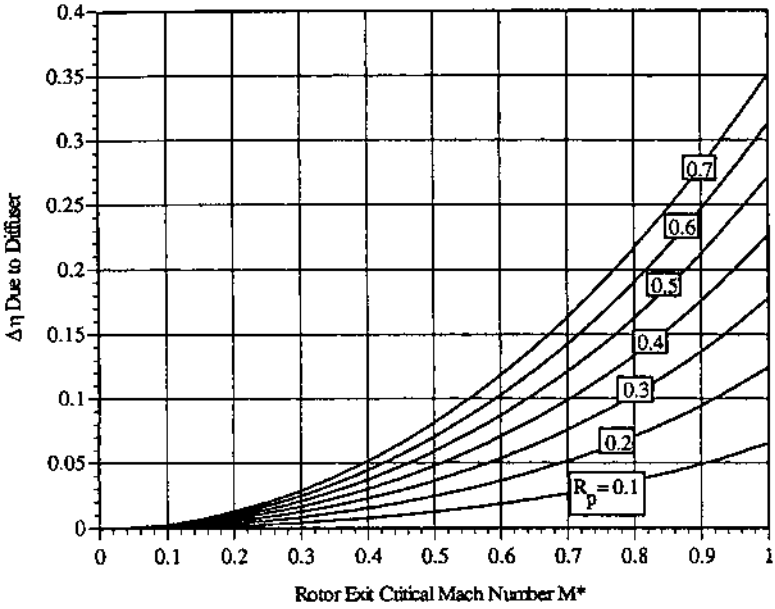

Figure 15 Effect of diffuser on turbine efficiency at an overall pressure ratio of 3.0.

Operating Conditions				Design parameters			
T)inlet	P)inlet	Pressure Ratio	Shaft Power	Hub-tip Ratio	Diffuser Recovery	Inlet Loss Ratio	Tip Clearance
(R)	(psia)		(hp)				(in)
760	44.1	3	100	0.7	0.4	0.99	0.015

Ideal Work	acr)1
(Btu/lbm)	(ft/s)
49.1386	1233.61

Case	Overall Efficiency	Work Coefficient	Flow Coefficient	Eta)0'-2' ZC from Smith's Chart	Actual Delta h	Flow Rate	U)mean	Vx
					(Btu/lbm)	(lbm/s)	(ft/s)	(ft/s)
1	0.8187	1.3	0.6	0.94	42.636	1.7572	906.15	543.69
T')2	M*)2	p/p')2	p)dis/p')2	PR)0'-2'	p)2	rho)2	rt)2	rh)2
R					(psia)	(lbm/ft3)	(in)	(in)
582.35	0.5035	0.8598	0.9159	2.7201	13.800	0.0668	2.086	1.460
eta/eta)zc	eta)0'-2'	eta)oa	Shaft Speed	M*)1	Alpha)1	Beta)1	W)1/Acr)1	Beta)2
			(rpm)		(deg)	(deg)		(deg)
0.9436	0.8870	0.8187	58577	1.0517	65.22	26.57	0.4928	-59.04
W)2/Acr)2	acr)2	V)2/acr)2	Reaction	Hub Work Coefficient	Beta)1 t (deg)	Beta)1 h (deg)		
0.9786	1079.86	0.5035	0.3500	1.9168	-6.79	51.53		

Figure 16 Spreadsheet for preliminary axial-flow turbine sizing showing iterated results for example turbine.

stator at 0.020 in. These values are selected based on the guidelines given earlier in the chapter. Solving Eq. (57) for the blade number results in

$$Z = \frac{(b/s)2\pi r_{\mathrm{m}}}{t_{\mathrm{te}}/\cos(\alpha_{\mathrm{te}})}$$

For the stator, the flow angle α_1 is used for α_{te}; for the rotor, the relative flow angle β_2 is substituted for α_{te}. The blade angle is slightly different from the flow angle due to blockage effects, but for preliminary sizing, the approximation is acceptable. For the stator, we have

$$Z_{\mathrm{stator}} = \frac{(0.1)(2\pi)(1.773\,\mathrm{in})}{(0.020\,\mathrm{in})/\cos(65.22^\circ)} = 23.35$$

and for the rotor

$$Z_{\text{rotor}} = \frac{(0.1)(2\pi)(1.773\,\text{in})}{(0.020\,\text{in})/\cos(-59.04^\circ)} = 28.65$$

Of course, only integral number of blades are allowed, so we choose 23 vanes for the stator and 29 rotor blades, resulting in a blade spacing of 0.484 in. for the stator and 0.384 in. for the rotor. Normal practice is to avoid even blade counts for both the rotor and stator to reduce rotor blade vibration response. The blade chord is now calculated from Zweifel's relation given in Eq. (54) using the optimum value of 0.8 for the Zweifel coefficient:

$$c_x = \left| \frac{2}{\zeta/s} \frac{\cos(\alpha_o)}{\cos(\alpha_i)} \sin(\alpha_i - \alpha_o) \right|$$

For the stator,

$$(c_x)_{\text{stator}} = \left| \frac{2}{0.8/(0.484\,\text{in.})} \frac{\cos(65.22^\circ)}{\cos(0^\circ)} \sin(-65.22^\circ) \right| = 0.460\,\text{in.}$$

and for the rotor,

$$(c_x)_{\text{rotor}} = \left| \frac{2}{0.8/(0.384\,\text{in.})} \frac{\cos(-59.04^\circ)}{\cos(26.57^\circ)} \sin[26.57^\circ - (-59.04^\circ)] \right|$$
$$= 0.551\,\text{in.}$$

The Reynolds number for each blade row is calculated from Eq. (53). At the exit of each blade row, the static temperature and pressure are required to calculate the density. The viscosity is calculated using the total temperature to approximate the temperature in the boundary layers where viscous effects dominate. For the stator, the exit total temperature is the same as the inlet temperature. We assume a 1% total pressure loss across the stator. Using the stator exit Mach number, the static pressure is calculated:

$$p_1 = 44.1\,\text{psia}(0.99)(0.99)\left[1 - \frac{1}{6}(1.0517)^2\right]^{3.5} = 21.18\,\text{psia}$$

as is the static temperature:

$$T_1 = (760\,\text{R})\left[1 - \frac{1}{6}(1.0517)^2\right] = 619.9\,\text{R}$$

Using the perfect gas relation, the stator exit density ρ_1 is calculated to be $0.09225\,\text{lb}_\text{m}/\text{ft}^3$. The viscosity is determined using an expression derived

from that presented by ASHRAE [19]:

$$\mu = \frac{\sqrt{T}}{1.34103 + 306.288/T - 13658.3/T^2 + 1,239,069/T^3} \times 10^{-6} \frac{\text{lb}_\text{m}}{\text{ft-sec}}$$

The original expression was in SI units. For the stator, the viscosity $\mu_1 = 1.5998 \times 10^{-5}$ lb$_\text{m}$/ft-sec. The Reynolds number is then calculated using Eq. (53):

$$(R_{\text{th}})_{\text{stator}} = \frac{(0.09225 \frac{\text{lb}_\text{m}}{\text{ft}^3})(1297.4 \frac{\text{ft}}{\text{sec}})}{1.5998 \times 10^{-5} \frac{\text{lb}_\text{m}}{\text{ft-sec}}} \frac{2(0.626\,\text{in.})(0.484\,\text{in.})\cos(65.22^\circ)}{12 \frac{\text{ft}}{\text{in}}(0.626\,\text{in.}) + (0.484\,\text{in.})\cos(65.22^\circ)}$$

resulting in a Reynolds number of 1.9103×10^5. A similar procedure is used for the rotor, except the relative velocity and angle at the rotor exit (station 2) are used. The viscosity is calculated using the relative total temperature determined using Eq. (17). For the rotor, the Reynolds number is 1.2356×10^5.

The reference value of the loss coefficient ξ is found from Fig. 13 as a function of the deflection across the blade row. The deflection is the difference between the inlet and outlet flow angles. For the stator, the deflection is 65.22°, and for the rotor it is 85.61°, resulting in $\xi_{\text{ref s}} = 0.068$ and $\xi_{\text{ref r}} = 0.083$, assuming a blade thickness ratio of 0.2. The adjusted loss coefficients are calculated from Eq. (52):

$$\xi_{\text{stator}} = \left(\frac{10^5}{1.9103 \times 10^5}\right)^{1/4} \left[(1 + 0.068)\left(0.975 + 0.075\frac{0.460}{0.626}\right) - 1\right] = 0.0852$$

and for the rotor

$$\xi_{\text{rotor}} = \left(\frac{10^5}{1.2356 \times 10^5}\right)^{1/4} \left[(1 + 0.083)\left(0.975 + 0.075\frac{0.551}{0.626}\right) - 1\right] = 0.1209$$

The stator inlet to rotor exit total-to-total efficiency is calculated from the ratio of the energy extracted from the flow ($U\Delta V_\theta$) divided by the sum of

the energy extracted and the rotor and stator losses:

$$\eta_{0'-2'ZC} = \frac{U\Delta V_\theta}{U\Delta V_\theta + \frac{1}{2}V_2^2\xi_{\text{stator}} + \frac{1}{2}W_2^2\xi_{\text{rotor}}}$$

Numerically, we have

$$\eta_{0'-2'ZC} = \frac{1.3(906.15\ \frac{\text{ft}}{\text{sec}})^2}{1.3(906.15\ \frac{\text{ft}}{\text{sec}})^2 + \frac{0.0852}{2}(1297.39\ \frac{\text{ft}}{\text{sec}})^2 + \frac{0.1209}{2}(1056.75\ \frac{\text{ft}}{\text{sec}})^2}$$
$$= 0.8846$$

which is considerably lower than the 0.94 value from Smith's chart. Correcting for tip clearance using a value of 1 for K_c in Eq. (55) yields

$$\eta_{0'-2'} = 0.8846\left(1 - \frac{1}{0.85}\frac{0.015}{0.626}\right) = 0.8597$$

and correcting for overall pressure ratio using the total-to-total pressure ratio from Fig. 16 results in the overall efficiency:

$$\eta_{OA} = 0.8597\frac{1 - (1/2.7201)^{(\gamma-1)/\gamma}}{1 - (1/3.0)^{(\gamma-1)/\gamma}} = 0.7935$$

This value is 0.025 lower than the value of 0.8187 from Fig. 16 predicted using Smith's chart. Sieverding [10] notes that Smith's chart was developed for blades with high aspect ratios (h/c_x in the range of 3–4), which will result in higher efficiency than lower aspect ratios, such as in this example. For preliminary sizing purposes, the conservative result should be used.

Partial Admission Turbines

For applications where the shaft speed is restricted to low values or the volumetric flow rate is very low, higher efficiency can sometimes be obtained with a turbine stator that only admits flow to the rotor over a portion of its circumference. Such a turbine is called a partial-admission turbine. Partial-admission turbines are indicated when the specific speed of the turbine is low. Balje [3] indicates partial admission to be desirable for specific speeds less than 0.1. Several conditions can contribute to low specific speed. Typically, drive turbines operate most efficiently at shaft speeds higher than the loads they are coupled to, such as generators, hydraulic pumps, and, in the case of an air turbine starter, the main engine of an aircraft. For low-cost applications, it may be desirable to eliminate the speed-reducing gearbox and couple the load directly to the turbine shaft. In order to attain adequate

blade speed at the reduced shaft speed, it is necessary to increase the turbine diameter, which causes the blade height to decrease. The short blades cause an increase in secondary flow losses reducing turbine efficiency. With partial admission, the blade height can be increased, reducing secondary flow losses. In a low-flow-rate situation, maintaining a given hub-to-tip radius ratio results in an increase in the design shaft speed and a decrease in the overall size of the turbine. However, manufacturing limits restrict the radial tip clearance and blade thickness. With a small blade height, tip clearance losses are increased. With a limitation on how thin blades can be made, it is necessary to reduce blade count in order to keep trailing-edge blockage to a reasonable level. Fewer blades result in longer blade chord and reduced aspect ratio, leading to higher secondary flow losses. The taller blades associated with partial admission can increase turbine performance. For high-head applications a high blade speed is necessary for peak efficiency. With shaft speed restricted by bearing and manufacturing limitations, an increase in turbine diameter is required, resulting in a situation similar to the no-gearbox case discussed earlier. Here, too, partial admission can result in improved turbine efficiency.

The penalty for partial admission is two additional losses not found in full-admission turbines. These are the pumping loss and sector loss. The pumping loss accounts for the drag of the rotor blades as they pass through the inactive arc, the portion of the circumference not supplied with flow from the stator. The sector loss arises from the decrease in momentum caused by the mixing of the stator exit flow with the relatively stagnant fluid occupying the blade passage just as it enters the active arc. Instead of being converted into useful shaft work, the stator exit flow is used to accelerate this stagnant fluid up to the rotor exit velocity. An additional loss occurs at the other end of the active arc as the blade passages leave the active zone. Just as a blade passage is at the edge of the last active stator vane passage, the flow into the rotor blade passage is reduced. This reduced flow has the entire blade passage to expand into. The sudden expansion causes a loss in momentum resulting in decreased power output from the turbine. Loss models for partial-admission effects are not as well developed as those for conventional, full-admission turbines. As a historical basis, Glassman [1] presents Stodola's [20] pumping loss model and Stenning's [21] sector loss model in an understandable form and discusses their use. More recently, Macchi and Lozza [22] have compiled a number of more modern loss models and exercised them during the design of partial-admission turbines. The reader is referred to those sources for detailed information regarding the estimation of partial-admission losses.

RADIAL-INFLOW TURBINE SIZING

Differences Between Radial-Inflow and Axial-Flow Turbines

Radial-inflow turbines enjoy widespread use in automotive turbochargers and in small gas turbine engines (auxiliary power units, turboprops, and expendable turbine engines). One advantage is their low cost relative to machined axial turbines, as most of these applications use integrally bladed cast radial-inflow turbine wheels.

The obvious difference between radial-inflow and axial-flow turbines is easily seen in Fig. 1; a radial-inflow turbine has a significant change in the mean radius between rotor inlet and rotor outlet, whereas an axial-flow turbine has only a minimal change in mean radius, if any. Because of this geometric difference, there are considerable differences in the performance characteristics of these two types of turbines. Referring to the "typical" radial-inflow vector diagram of Fig. 9(c), the radius change causes a considerable decrease in wheel speed U between rotor inlet and outlet. For zero exit swirl, this results in a reduced relative exit velocity compared to an axial turbine with the same inlet vector diagram (since $U_2 \approx U_1$ for an axial rotor). Since frictional losses are proportional to the square of velocity, this results in higher rotor efficiency for the radial-inflow turbine. However, the effect of reduced velocity level is somewhat offset by the long, low-aspect-ratio blade passages of a radial-inflow rotor.

Compared to the axial-flow diagram of Fig. 9(a), there is a much larger difference between the rotor inlet relative and absolute velocities for the radial-inflow diagram. Referring to Eq. (17), this results in a lower relative inlet total temperature at design point for the radial-inflow turbine. In addition, due to the decrease in rotor speed with radius, the relative total temperature decreases toward the root of radial-inflow turbine blades (see Mathis [23]). This is a major advantage for high inlet temperature applications, since material properties are strongly temperature-dependent. The combination of radial blades at rotor inlet (eliminating bending stresses due to wheel rotation) and the decreased temperature in the high-stress blade root areas allows the radial-inflow turbine to operate at significantly higher wheel speeds than an axial-flow turbine, providing an appreciable increase in turbine efficiency for high-pressure-ratio, high-work applications.

For applications with moderate inlet temperatures (less than 500 °F) and pressure ratios (less than 4:1), the blade speed of an axial wheel is not constrained by stress considerations and the radial-inflow turbine is at a size disadvantage. Due to bending stress considerations in the rotor blades, radial blades are used at the inlet to eliminate bending loads. This limits the $V_{\theta 1}/U_1$ ratio to 1 or less, meaning that the tip speed for an equal work

radial-inflow turbine will be higher than that for an axial-flow turbine, which can have $V_{\theta 1}/U_1 > 1$ with only a small impact on efficiency. This assumes zero exit swirl. For a fixed shaft speed, this means that the radial-inflow turbine will be larger (and heavier) than an axial-flow turbine. Stage work can be increased by adding exit swirl; however, the radial-inflow turbine is again at a disadvantage. The lower wheel speed at exit for the radial-inflow turbine means that more $V_{\theta 2}$ must be added for the same amount of work increase, resulting in higher exit absolute velocities compared to an axial-flow turbine. In addition, high values of exit swirl negatively impact obtainable diffuser recoveries.

Packaging considerations may lead to the selection of a radial-inflow turbine. The outside diameter of a radial-inflow turbine is considerably larger than the rotor tip diameter, due to the stator and inlet scroll or torus. Compared to an axial-flow turbine, the radial-inflow package diameter may be twice as large or more. However, the axial length of the package is typically considerably less than for an axial turbine when the inlet and diffuser are included. Thus, if the envelope is axially limited but large in diameter, a radial-inflow turbine may be best suited for the application, considering performance requirements can be met.

For auxiliary turbine applications where free run may be encountered, radial-inflow turbines have the advantage of lower free-run speed than an axial turbine of comparable design-point performance. Figure 11 shows the off-design performance characteristics of both radial-inflow and axial-flow turbines. At higher shaft speeds, the reduction in mass flow for the radial-inflow turbine leads to lower torque output and a lower free-run speed. Because of the change in radius in the rotor, the flow through the rotor must overcome a centrifugal pressure gradient caused by wheel rotation. As shaft speed increases, this pressure gradient becomes stronger. For a given overall pressure ratio, this increases the pressure ratio across the rotor and decreases the pressure ratio across the stator, leading to a reduced mass flow rate. A complete description of this phenomenon and its effect on relative temperature at free-run conditions is presented by Mathis [23]. However, the rotor disk weight savings from the lower free-run speed of a radial-inflow turbine is offset by the heavier containment armor required due to the increased length of a radial-inflow turbine rotor compared to an axial turbine.

Radial-Inflow Turbine Performance

The literature on performance prediction and loss modeling for radial-inflow turbines is substantially less than that for axial-flow turbines. Wilson [2] states that most radial-inflow turbine designs are small extrapolations or

interpolations from existing designs and that new designs are executed using a "cut-and-try" approach. Rodgers [24] says that minimal applicable cascade test information exists (such as that used to develop many of the axial-flow turbine loss models) and that exact analytical treatment of the flow within the rotor is difficult due to the strong three-dimensional character of the flow. Glassman [1] presents a description of radial-inflow turbine performance trends based on both analytical modeling and experimental results and also describes design methods for the rotor and stator blades. More recently, Rodgers [24] has published an empirically derived performance prediction method based on meanline quantities for radial-inflow turbines used in small gas turbines. Balje [3] presents analytical performance predictions in the form of efficiency versus specific speed and specific diameter maps.

For our purposes, we will use the results of Kofskey and Nusbaum [25], who performed a systematic experimental study investigating the effect of specific speed on radial-inflow turbine performance. Kofskey and Nusbaum used five different stators of varying flow area to cover a wide range of specific speeds (0.2 to 0.8). Three rotors were used in conjunction with these stators in an attempt to attain optimum performance at both extremes of the specific speed range. Results of their testing are presented in Fig. 17, which shows the maximum efficiency envelopes for both total-to-total and total-to-static efficiencies. These efficiencies were measured from scroll inlet flange to rotor exit and include the effects of tip clearance. Axial tip clearance was approximately 2.2% of the inlet blade height, while the radial tip clearance was about 1.2% of the exit blade height. Efficiencies above 0.90 were measured for both total-to-total and total-to-static efficiencies. The turbine tested was designed for maximum efficiency and likely represents a "maximum attainable" performance level. For predicting the performance of new turbine designs, the efficiency obtained from this data should likely be derated to account for nonoptimum factors in the new design such as constraints on scroll size, different blade counts, etc.

Tip clearance losses in a radial-inflow turbine arise from two sources: axial clearance at the rotor blade inlet, and radial clearance at the rotor blade exit. Of the two, the radial clearance is by far the more important. Futral and Holeski [26] found that for axial clearances in the range of 1–7% of inlet blade height, an increase in clearance of 1% (say from 2% to 3% of inlet blade height) caused a decrease in total-to-total efficiency of only 0.15%. For radial clearances in the range of 1–3% of exit blade height, Futral and Holeski measured a 1.6% decrease in total-to-total efficiency for a 1% increase in radial clearance, roughly 10 times greater than the change for axial clearance. In a radial-inflow turbine, the majority of flow turning in the rotor is done in the exit portion of the blading, called the exducer.

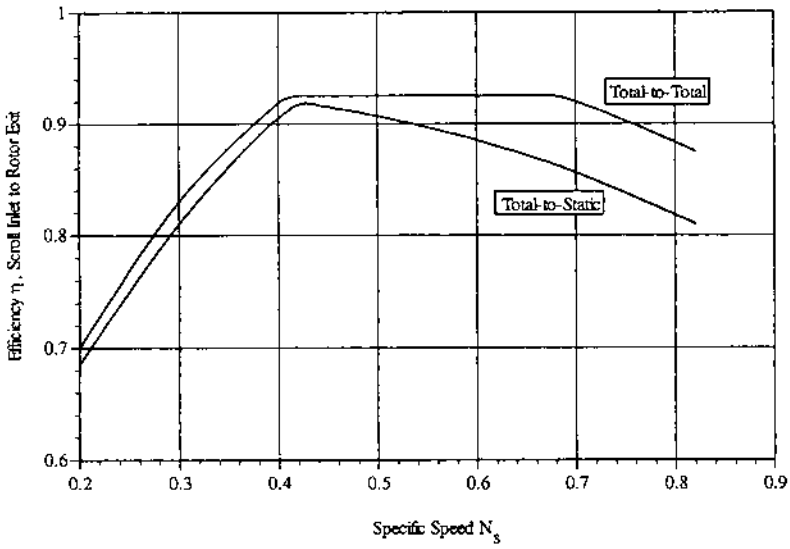

Figure 17 Effect of specific speed on radial-inflow turbine efficiency. (Replotted from Ref. 25.)

Because of radial clearance in the exducer, some fraction of the flow is underturned and does less work (similar to the situation at the tip of an axial-flow turbine blade). Since little flow turning is done in the inlet portion of the blade, the axial clearance has a smaller effect.

As with axial-flow turbines, peak total-to-static efficiency in radial turbines usually occurs when there is no exit swirl ($V_{\theta 2} = 0$). Rodgers [27] reports that the exit vector diagram is optimized for maximum total-to-static efficiency when the exit flow coefficient ϕ_2, defined as

$$\phi_2 = \frac{V_{x2}}{U_1} \tag{60}$$

has a value between 0.2 and 0.3. Rodgers [27] also reports that the geometry of the exit is optimized when the ratio of the rotor inlet radius to the rotor exit root mean squared radius is 1.8. Regarding the rotor inlet vector diagram, maximum efficiency occurs when the mean rotor inlet flow enters the normally radially bladed rotor at some incidence angle. According to

Glassman [1], the optimum ratio of $V_{\theta 1}$ to U_1 is given by

$$\frac{V_{\theta 1}}{U_1} = 1 - \frac{2}{Z_r} \tag{61}$$

where Z_r is the rotor blade count at the inlet (includes both full and partial blades). The optimum blade speed occurs for $U/C_0 = 0.7$ [see Eq. (43)] according to empirical data from Rodgers [27] and analytical results from Rohlik [28]. Specification of the optimum rotor inlet vector diagram is completed by choosing a stator exit angle of approximately 75° (measured from radial) based on data from Rohlik [28].

Due to the change in radius through the rotor, local blade solidity (the ratio of blade spacing to chord) changes appreciably. At the rotor inlet, more blades are needed than at the rotor exit if uniform blade loading is to be maintained. This situation can be treated by adding partial blades at the rotor inlet. These partial blades, called splitters, end before the exducer. The intent of adding the splitter blades is to reduce the blade loading in the inlet portion of the rotor and so reduce the boundary-layer losses. However, the splitters increase the rotor surface area, counteracting some of the benefit of reduced loading. Futral and Wasserbauer [29] tested a radial-inflow turbine both with and without splitters (the splitters were machined off for the second test) and found only slight differences in turbine performance. In this particular case, the benefits of reduced blade loading were almost completely offset by the increased surface area frictional losses. It is not clear that this result can be universally extended, but it does indicate that splitters should not always be included in a radial-inflow turbine design.

For low-cost turbines such as those in automotive turbochargers, no nozzle vanes are used, with all flow turning being done in the scroll. This increases the scroll frictional losses due to the increased velocity and also decreases the obtainable rotor inlet absolute flow angle. Balje [3] has calculated the efficiency ratio for radial-inflow turbines with and without nozzles and found it to be approximately 0.92, regardless of specific speed.

Adjustments for the effects of diffusers and Reynolds number changes are similar to those previously presented for axial turbines.

Mechanical, Geometric, and Manufacturing Constraints

Radial-inflow turbine design is as much affected by mechanical considerations as axial-inflow turbines. As with axial-flow turbines, turbine efficiency for high-temperature applications is limited by materials, not aerodynamics. Material and manufacturing limitations affect both the geometry of the turbine wheel and its operating conditions.

When Rohlik performed his analytical study in 1968, he limited the rotor exit hub-to-tip radius ratio to values greater than 0.4. The turbine investigated by Kofskey and Nusbaum [25] had a hub-to-tip radius ratio at the exit of 0.53. However, with the desire for smaller and less expensive turbine wheels, hub-to-tip radius ratios now are seen as low as 0.25 and less. Along with inertia and stress considerations, this limits rotor blade count from 10 to 14 (Rodgers [27]).

Typical materials for radial-inflow turbine wheels are cast superalloys for high-temperature applications and cast or forged steel for lower temperatures. Ceramics have been used in production turbochargers and are in a research stage for small gas turbines. Radial-inflow turbine wheels have three critical stress locations: inlet blade root, exducer blade root, and hub centerline. Rodgers [27] notes that the tip speed of current superalloy radial-inflow turbine wheels is limited to approximately 2,200 ft/sec. The exact value is dependent on both operating temperature and desired life. For moderate inlet temperatures and pressure ratios ($T'_{in} < 500\,^{\circ}\mathrm{F}$ and $p'_{in}/p_{dis} < 4$), stress considerations, while they must be addressed in the mechanical design, usually do not constrain the aerodynamic design of the turbine. This includes free-run operation.

As previously mentioned, radial-inflow turbine blades are usually radial at the inlet to eliminate bending loads. At the exit, the rotor blade angle is limited to about 60° from axial for manufacturing reasons. With casting being the preferred method of construction, rotor trailing-edge thickness should be greater than 0.020 in. Limitations on the radial-inflow stator are similar to those for an axial-flow stator: exit blade angle should be less than 75° (for a radial-inflow stator, this is measured from the radial direction) and trailing-edge thickness should be 0.015 in. or greater. Significantly thicker trailing edges are needed if the stator vanes are cooled. Trailing-edge blockage for both stators and rotors should be kept below 10% for best performance. With low hub-to-tip radius ratios at rotor exit, this guideline is frequently violated at the hub, where the blade spacing is smallest and the trailing-edge thickness is large for mechanical reasons.

Overall package diameter is determined by rotor tip diameter, radius ratio across the stator, and the size of the scroll. In addition, there is normally a vaneless space between the stator and rotor, similar to the axial gap between the stator and rotor in an axial-flow turbine. The vaneless space radius ratio is usually held to 1.05 or less. Stator vane radius ratio is controlled by stator vane count and stator turning. In most radial-inflow turbines, a scroll provides a significant amount of tangential component at stator inlet, resulting in relatively low amounts of flow deflection in the stator vane row. This results in reduced solidity requirements, so that fewer and shorter stator vanes can be used. Rodgers [24] states that a common

design fault in the radial-inflow turbine stator is too high a value of solidity, resulting in excessive frictional losses. Based on turbine designs presented by Rodgers [27] and the turbine used by Kofskey and Nusbaum [25], stator vane radius ratios range from 1.2 to 1.3. For preliminary sizing exercises, a value of about 1.25 may be taken as typical. The radius to the centerline of the scroll inlet of the turbine from Kofskey and Nusbaum [25] is twice the radius at stator inlet. Cross-section radius at scroll inlet is approximately two thirds the stator inlet radius, so the maximum package radius is roughly 2.67 times the stator inlet radius. This represents a fairly large scroll, commensurate with the high efficiency levels obtained during testing. For a reduction in efficiency, the scroll size can be reduced.

An Example of Radial-Inflow Turbine Sizing

To demonstrate the concepts and guidelines described in this and preceding sections, we will size a radial-inflow turbine for the same application as the axial-flow turbine example presented earlier. The design requirements for that turbine were:

1. Generates 100 hp at design point.
2. Operates at an overall pressure ratio of 3:1 in air.
3. Inlet pressure is 44.1 psia, and inlet temperature is 300 °F.

A procedure similar to that used in the axial-flow turbine sizing example will be used here with a few modifications:

1. Determine available energy (isentropic enthalpy drop).
2. Guesstimate overall efficiency to calculate flow rate.
3. Calculate vector diagram based on optimum parameters.
4. Select specific speed based on Fig. 17.
5. Determine overall geometry.
6. Determine overall efficiency when equipped with a diffuser.

The process is iterative, since the efficiency determined in step 6 is used to improve the efficiency guess made in step 2. The process is repeated until the efficiencies from steps 2 and 6 agree. Perfect gas behavior is assumed, with $c_p = 0.24\,\text{Btu/lb}_m$, $\gamma = 1.4$, and $R_{gas} = 53.34\,\text{ft-lb}_f/\text{lb}_m\text{-sec}$.

The isentropic overall enthalpy drop across the turbine is the same as in the axial-flow turbine example:

$$\Delta h_{\text{isentropic}} = \left(0.24\frac{\text{Btu}}{\text{lb}_m \cdot \text{R}}\right)(760\ \text{R})\left[1 - \left(\frac{1}{3}\right)^{0.4/1.4}\right] = 49.14\frac{\text{Btu}}{\text{lb}_m}$$

Note that more digits are carried through the calculations than indicated, so

exact agreement may not occur in all instances. Since we expect a higher efficiency with the radial-inflow turbine, we will assume an overall efficiency, including tip clearance effects, of 0.85. As with the axial-flow turbine, the vector diagram needs to be calculated using the zero-clearance work. We assume that the tip clearance loss is 5%. The actual enthalpy drop is

$$\Delta h_{\mathrm{OA}} = (0.85)\left(49.14\frac{\mathrm{Btu}}{\mathrm{lb_m}}\right) = 41.77\frac{\mathrm{Btu}}{\mathrm{lb_m}}$$

and the zero-clearance work is

$$\Delta h_{\mathrm{OAZC}} = \frac{0.85}{0.95}\left(49.14\frac{\mathrm{Btu}}{\mathrm{lb_m}}\right) = 43.97\frac{\mathrm{Btu}}{\mathrm{lb_m}}$$

The required turbine flow is found using Eq. (7):

$$\dot{m} = \frac{P}{\Delta h_{\mathrm{OA}}} = \frac{(100\,\mathrm{hp})(0.7069\,\mathrm{Btu/sec/hp})}{41.77\,\mathrm{Btu/lb_m}} = 1.693\,\mathrm{lb_m/\,sec}$$

The mass flow rate is needed to calculate turbine flow area and is also a system requirement.

We calculate the tip speed of the turbine based on the optimum value (0.7) of blade-jet speed ratio U_1/C_0. From Eq. (42) we have

$$C_0 = \sqrt{2\Delta h_{\mathrm{isentropic}}} = \left[(2)\left(32.174\,\frac{\mathrm{ft\cdot lb_m}}{\mathrm{lb_f\cdot sec^2}}\right)\left(778.16\,\frac{\mathrm{ft\cdot lb_f}}{\mathrm{Btu}}\right)\left(49.14\frac{\mathrm{Btu}}{\mathrm{lb_m}}\right)\right]^{1/2}$$
$$= 1569\,\mathrm{ft/\,sec}$$

For $U_1/C_0 = 0.7$, the wheel speed is calculated to be

$$U_1 = (0.7)(1569\,\mathrm{ft/\,sec}) = 1098\,\mathrm{ft/\,sec}$$

Assuming zero exit swirl, we calculate the rotor inlet absolute tangential velocity component using Eq. (9):

$$V_{\theta 1} = \frac{\Delta h_{\mathrm{OA\ ZC}}}{U_1} = \frac{\left(32.174\,\frac{\mathrm{ft\cdot lb_m}}{\mathrm{lb_f\cdot sec^2}}\right)\left(778.16\,\frac{\mathrm{ft\cdot lb_f}}{\mathrm{Btu}}\right)\left(43.97\,\frac{\mathrm{Btu}}{\mathrm{lb_m}}\right)}{1098\,\mathrm{ft/\,sec}}$$
$$= 1002\,\mathrm{ft/\,sec}$$

The required rotor blade count is obtained from Eq. (61):

$$Z_{\mathrm{r}} = \frac{2}{1-(V_{\theta 1}/U_1)} = \frac{2}{1-(1002/1098)} = 23$$

This blade count is much higher than the 10–14 guideline given by Rodgers

[27]. In order to avoid manufacturing problems at the rotor exit, we choose 11 full blades and 11 splitter blades, for a total of 22 blades at the rotor inlet. We now recalculate the ratio of absolute rotor inlet tangential velocity to the wheel speed from Eq. (61):

$$\frac{V_{\theta 1}}{U_1} = 1 - \frac{2}{22} = 0.9091$$

From Eq. (9) we calculate the required wheel speed:

$$U_1 = \sqrt{\frac{\Delta h_{\text{OA ZC}}}{V_{\theta 1}/U_1}} = \sqrt{\frac{\left(32.174 \frac{\text{lb}_\text{m}\cdot\text{ft}}{\text{lb}_\text{f}\cdot\text{sec}^2}\right)\left(778.16 \frac{\text{ft}\cdot\text{lb}_\text{f}}{\text{Btu}}\right)\left(43.97 \frac{\text{Btu}}{\text{lb}_\text{m}}\right)}{0.9091}}$$
$$= 1100\,\text{ft/sec}$$

As a check, we recalculate the blade-jet speed ratio:

$$\frac{U_1}{C_0} = \frac{1100\,\text{ft/sec}}{1569\,\text{ft/sec}} = 0.7015$$

which is very close to our original intent. The absolute tangential velocity at rotor inlet is

$$V_{\theta 1} = \frac{V_{\theta 1}}{U_1} U_1 = (0.9091)(1100\,\text{ft/sec}) = 1000\,\text{ft/sec}$$

Next, we specify an inlet absolute flow angle of 75° from the radial direction. We can now calculate the remainder of the inlet velocity triangle, the results of which appear in Fig. 18. To determine the rotor inlet blade height, we will need the rotor inlet density. From the vector diagram of Fig. 18, the value of the rotor inlet absolute velocity, V_1, is 1036 ft/sec. The inlet critical velocity is

$$a_{\text{cr1}} = \sqrt{\frac{2(1.4)}{1+1.4}\left(32.174 \frac{\text{ft}\cdot\text{lb}_\text{f}}{\text{lb}_\text{m}\cdot\text{sec}^2}\right)\left(53.34 \frac{\text{ft}\cdot\text{lb}_\text{f}}{\text{lb}_\text{m}\cdot\text{R}}\right)760\ \text{R}}$$
$$= 1234\,\text{ft/sec}$$

The rotor inlet density is determined (assuming a 2% inlet and stator total pressure loss) from

$$\rho_1 = \frac{p_1'}{R_{\text{gas}} T_1'}\left[1 - \frac{\gamma - 1}{\gamma + 1}\left(\frac{V_1}{a_{\text{cr1}}}\right)^2\right]^{1/(\gamma-1)} = \frac{(0.98)(44.1\,\text{psia})(144\,\text{in}^2/\text{ft}^2)}{(53.34\,\text{ft}\cdot\text{lb}_\text{f}/\text{lb}_\text{m}\cdot\text{R})(760\,\text{R})}\left[1 - \frac{1}{6}\left(\frac{1036}{1234}\right)^2\right]^{2.5}$$
$$= 0.1123\,\text{lb}_\text{m}/\text{ft}^3$$

For the rotor exit vector diagram, we assume an exit flow coefficient ϕ_2 value of 0.3. The exit axial velocity is then calculated from Eq. (60):

$$V_{x2} = \phi_2 U_1 = 0.3(1100\,\text{ft/sec}) = 330.1\,\text{ft/sec}$$

To calculate the rotor exit pressure, we need to know the critical Mach number at the exit. The rotor exit total temperature is given by

$$T_2' = T_0' - \frac{\Delta h_{\text{OAZC}}}{C_p} = 760\,\text{R} - \frac{43.97\,\text{Btu/lb}_m}{0.24\,\text{Btu/lb}_m \cdot \text{R}} = 576.8\,\text{R}$$

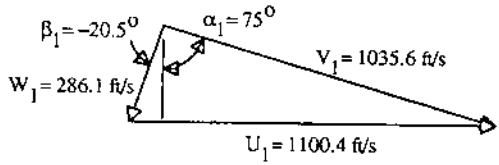

Inlet Vector Diagram

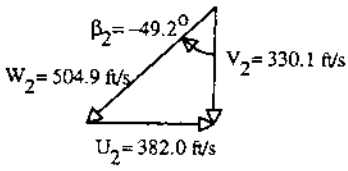

Exit Vector Diagram - Hub

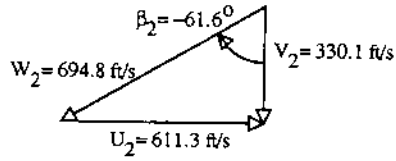

Exit Vector Diagram - RMS

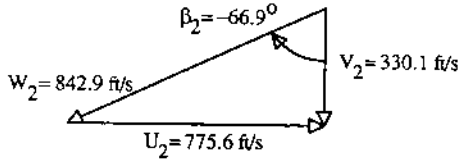

Exit Vector Diagram - Tip

Figure 18 Inlet and exit vector diagrams for first iteration of radial-inflow turbine sizing example.

The rotor exit critical velocity is

$$a_{cr2} = \sqrt{\frac{2(1.4)}{1+1.4}\left(32.174\ \frac{\text{ft}\cdot\text{lb}_f}{\text{lb}_m\cdot\text{sec}^2}\right)\left(53.34\ \frac{\text{ft}\cdot\text{lb}_f}{\text{lb}_m\cdot\text{R}}\right)576.8\ \text{R}}$$
$$= 1075\ \text{ft/sec}$$

The static-to-total pressure ratio at rotor exit is calculated from the gas dynamics relation,

$$\frac{p_2}{p_2'} = \left[1 - \frac{\gamma-1}{\gamma+1}\left(\frac{V_2}{a_{cr2}}\right)^2\right]^{\gamma/(\gamma-1)} = \left[1 - \frac{1}{6}\left(\frac{330.1}{1075}\right)^2\right]^{3.5} = 0.9460$$

With a diffuser recovery assumed to be 0.4, the rotor exit total pressure is determined from Eq. (35):

$$p_2' = \frac{p_{dis}}{R_p(1 - p_2/p_2') + p_2/p_2'} = \frac{(44.1\ \text{psia})/3}{0.4(1-0.9460)+0.9460} = 15.19\ \text{psia}$$

The rotor exit density is calculated from

$$\rho_2 = \frac{p_2'}{R_{gas}T_2'}\left[1 - \frac{\gamma-1}{\gamma+1}\left(\frac{V_2}{a_{cr2}}\right)^2\right]^{1/(\gamma-1)} = \frac{(15.19\ \text{psia})(144\ \text{in.}^2/\text{ft}^2)}{(53.34\ \text{ft}\cdot\text{lb}_f/\text{lb}_m\cdot\text{R})(576.8\ \text{R})}\left[1 - \frac{1}{6}\left(\frac{330.1}{1075}\right)^2\right]^{2.5}$$
$$= 0.06834\ \text{lb}_m/\text{ft}^3$$

The rotor exit volumetric flow is

$$Q_2 = \frac{\dot{m}}{\rho_2} = \frac{1.693\ \text{lb}_m/\text{sec}}{0.06834\ \text{lb}_m/\text{ft}^3} = 24.77\ \text{ft}^3/\text{sec}$$

The required rotor exit flow area is calculated from continuity:

$$A_2 = \frac{\rho_2 V_{x2}}{\dot{m}} = \frac{(0.06834\ \text{lb}_m/\text{ft}^3)(330.1\ \text{ft/sec})}{1.693\ \text{lb}_m/\text{sec}}(144\ \text{in.}^2/\text{ft}^2)$$
$$= 10.80\ \text{in.}^2$$

Before we can proceed further, we must determine the turbine shaft speed. We do this by selecting a specific speed from Fig. 17. In order to minimize turbine size, a high specific speed is desired. However, the data of Fig. 17 show a reduction in total-to-static efficiency at high specific speeds. As a compromise we select $N_s = 0.6$. The rotational speed ω is calculated from Eq. (40). The ideal head used by Kofskey and Nusbaum [25] is based on the inlet to rotor exit total-to-total pressure ratio, so we must first

calculate the correct head ($\Delta h^*_{\text{isentropic}}$) to use in Eq. (40):

$$\Delta h^*_{\text{isentropic}} = \left(0.24\,\frac{\text{Btu}}{\text{lb}_\text{m}\cdot\text{R}}\right)(760\,\text{R})\left[1-\left(\frac{15.19}{44.1}\right)^{0.4/1.4}\right]$$
$$= 47.88\,\text{Btu/lb}_\text{m}$$

The rotational speed is then

$$\omega = \frac{N_\text{s}(\Delta h^*_{\text{isentropic}})^{3/4}}{(Q_2)^{1/2}} = \frac{0.6\left[\left(32.174\,\frac{\text{ft}\cdot\text{lb}_\text{m}}{\text{lb}_\text{f}\cdot\text{s}^2}\right)\left(778.16\,\frac{\text{ft}\cdot\text{lb}_\text{f}}{\text{Btu}}\right)\left(47.88\,\frac{\text{Btu}}{\text{lb}_\text{m}}\right)\right]^{3/4}}{(24.77\,\text{ft}^3/\text{sec})^{1/2}}$$
$$= 4368\,\text{rad/sec}$$

The rotor inlet tip radius is found from Eq. (8):

$$r_1 = \frac{U_1}{\omega} = \frac{1100\,\text{ft/sec}}{4368\,\text{rad/sec}}\,12\,\frac{\text{in.}}{\text{ft}} = 3.023\,\text{in.}$$

The rotor inlet blade height h_1, commonly referred to as the "*b*-width," is calculated from continuity at rotor inlet:

$$h_1 = \frac{\dot{m}}{\rho_1 V_{r1} 2\pi r_1} = \frac{1.693\,\text{lb}_\text{m}/\text{sec}}{(0.1123\,\text{lb}_\text{m}/\text{ft}^3)(268.0\,\text{ft/sec})(2\pi)(3.023\,\text{in.})(1\,\text{ft}/12\,\text{in.})}\,12\,\frac{\text{in.}}{\text{ft}}$$
$$= 0.426\,\text{in.}$$

The rotor exit geometry can be determined in several ways. A hub-to-tip radius ratio can be assumed, the ratio of the exit tip radius to the inlet radius can be specified, or the ratio of the rotor exit root-mean-squared radius to the inlet radius can be chosen. Following Rodgers [27], we choose $r_1/r_{\text{rms2}} = 1.8$. The root-mean-squared radius is that radius that divides the flow area into two equal parts. The rotor exit hub and tip radius are calculated from

$$\frac{A_2}{2} = \pi(r^2_{\text{rms2}} - r^2_{\text{h2}}) = \pi(r^2_{\text{t2}} - r^2_{\text{rms2}})$$

The following results are obtained:

$$r_{\text{rms2}} = \frac{3.023\,\text{in.}}{1.8} = 1.680\,\text{in.}$$
$$r_{\text{h2}} = \sqrt{(1.680\,\text{in.})^2 - \frac{10.80\,\text{in.}^2}{2\pi}} = 1.049\,\text{in.}$$
$$r_{\text{t2}} = \sqrt{(1.680\,\text{in.})^2 + \frac{10.80\,\text{in.}^2}{2\pi}} = 2.131\,\text{in.}$$

The hub-to-tip radius ratio at the exit is 0.493, above the lower limit suggested by Rohlik [28]. The ratio of the exit tip radius to the inlet tip radius is also of concern, since a large value implies sharp curvature along the tip shroud and possible flow separation. Rohlik [28] used an upper limit of 0.7 on this ratio. For the geometry determined here, the value of the ratio r_{t2}/r_1 is 0.705, which should be acceptable. We also need to check on the blade angles at the rotor exit. The vector diagrams for the three radii at rotor exit are shown in Fig. 18. The axial velocity is constant with radius to satisfy radial equilibrium, since we have specified zero swirl at the exit. The relative flow angles decrease from -49.17° at the hub to -66.94° at the tip of the blade. Because this angle exceeds our guideline of 60°, alternate values of the design parameters should be investigated further to try to reduce the tip relative flow angle. One method is to increase the value of the exit flow coefficient ϕ_2. The drawback to this is that the increased velocity at rotor exit leads to larger exit kinetic energy losses and decreased efficiency.

Rotor blade trailing-edge blockage is calculated using Eq. (57). Assuming a blade thickness tapering from 0.040 in. at the hub to 0.020 in. at the tip and a blade count of 11 at the exit results in a hub blockage of 10.2% and a tip blockage of 4.2%. These values should result in no performance impact.

The next step is to update our overall efficiency estimate. From Fig. 17, for a specific speed of 0.6 a scroll inlet to rotor exit total-to-total efficiency of 0.92 is found. Recall that these data were taken with an axial clearance of 2.2% of the inlet blade height and a radial clearance of 1.2% of the exit blade height. For our turbine, we assume that both the radial and axial clearances are 0.015 in. In terms of their respective blade heights,

$$\frac{c_x}{h_1} = \frac{0.015\,\text{in.}}{0.426\,\text{in.}} = 0.0352 \text{ and } \frac{c_\text{r}}{h_2} = \frac{0.015\,\text{in.}}{2.131\,\text{in.} - 1.049\,\text{in.}} = 0.0139$$

where c_x in this case is the axial clearance, not axial chord as used earlier; and c_r is the radial clearance. The efficiency is corrected for these different clearance levels based on the conclusions of Futral and Holeski [26], summarized earlier. The change in efficiency is given by

$$\frac{\Delta\eta}{\eta} = \frac{-0.0015}{0.01}\left[\frac{c_x}{h_1} - \left(\frac{c_x}{h_1}\right)_\text{KN}\right] + \frac{-0.016}{0.01}\left[\frac{c_r}{h_2} - \left(\frac{c_r}{h_2}\right)_\text{KN}\right]$$

where the subscript KN refers to the values for the turbine tested by Kofskey and Nusbaum [25]. Inserting the appropriate values, the change

in total-to-total efficiency is

$$\frac{\Delta\eta}{\eta} = \frac{-0.0015}{0.01}(0.0352 - 0.022) + \frac{-0.016}{0.01}(0.0139 - 0.012) = -0.0050$$

Corrected for clearance differences, the predicted scroll inlet to rotor exit total-to-total efficiency is

$$\eta_{0'-2'} = 0.92(1 - 0.0050) = 0.9154$$

Correcting to diffuser exit static pressure to obtain the overall total-to-static efficiency, we have

$$\eta_{OA} = .9154\frac{1 - (15.19/44.1)^{0.4/1.4}}{1 - (1/3.0)^{0.4/1.4}} = 0.8919$$

Since this is considerably higher than our initial guess of 0.85, iteration will be needed to arrive at a converged result. However, at this point some conclusions may be drawn by comparing these results to those for the axial-flow turbine. For the axial-flow turbine an overall efficiency of 0.793 was predicted, almost 10 points lower than the result for the radial-inflow turbine designed for the same conditions. The increased efficiency does come with a packaging penalty, however. Comparing turbine rotor tip radii, we see that the radial-inflow rotor is almost 2 in. larger in diameter than the axial-flow rotor. Using the radius ratios suggested earlier and neglecting the vaneless space between the stator exit and rotor inlet, the stator inlet radius is estimated to be

$$r_0 = 1.25r_1 = 1.25(3.023\,\text{in.}) = 3.78\,\text{in.}$$

The maximum package radius is given by

$$r_{max} = 2.67r_0 = 2.67(3.78\,\text{in.}) = 10.09\,\text{in.}$$

Even with an axial-to-radial curved diffuser, the maximum package radius for the axial-flow turbine is likely to be less than 5 in., a considerable savings in both envelope and weight. The diameter of the radial-inflow turbine could be reduced if a higher specific speed were specified and a smaller scroll were used, but these changes would cause a reduction in overall efficiency. In general, for moderate-temperature auxiliary turbine applications, a radial-inflow design will result in a larger and heavier turbine than an axial-flow configuration.

REFERENCES

1. A. J. Glassman (ed.), *Turbine Design and Application*, NASA SP-290, Washington, DC (1972).
2. D. G. Wilson, *The Design of High Efficiency Gas Turbines*, MIT Press, Cambridge, MA (1984).
3. O. E. Balje, *Turbomachines*, Wiley, New York (1981).
4. R. E. Nece and J. W. Daily, "Roughness Effects on Frictional Resistance of Enclosed Rotating Disks," *Trans. ASME J. Basic Eng., 82*: 553 (1960).
5. J. W. Daily and R. E. Nece, "Chamber Dimension Effects on Induced Flow and Frictional Resistance of Enclosed Rotating Disks," *Trans. ASME J. Basic Eng., 82*: 218 (1960).
6. J. W. Daily, W. D. Ernst, and V. V. Absedian, "Enclosed Rotating Disks with Superposed Throughflow: Mean Steady and Periodic Unsteady Characteristics of Induced Flow," Report No. 64, Hydrodynamics Lab, MIT, Cambridge, MA (1964).
7. P. W. Runstadler, Jr., F. X. Dolan, and R. C. Dean, Jr., *Diffuser Data Book*, Creare Technical Note 186, Creare, Inc., Hanover, NH (1975).
8. F. X. Dolan and P. W. Runstadler, Jr., "Pressure Recovery Performance of Conical Diffusers at High Subsonic Mach Numbers," NASA CR-2299, Washington, DC (1973).
9. G. Sovran and E. D. Klomp, "Experimentally Determined Optimum Geometries for Rectilinear Diffusers with Rectangular, Conical, or Annular Cross-Section," *Fluid Mechanics of Internal Flow* (G. Sovran, ed.), Elsevier Publishing Co., New York, pp. 270–319 (1967).
10. C. H. Sieverding, "Axial Turbine Performance Prediction Methods," *Thermodynamics and Fluid Mechanics of Turbomachinery*, Vol. 2, Martinus Nijhoff, Dordrecht, pp. 737–784 (1985).
11. S. F. Smith, "A Simple Correlation of Turbine Efficiency," *J. R. Aeronaut. Soc., 69*: 467 (1965).
12. J. H. Horlock, "Losses and Efficiencies in Axial-Flow Turbines," *Int. J. Mech. Sci, 2*: 48 (1960).
13. D. G. Ainley and G. C. R. Mathieson, "A Method of Performance Estimation for Axial-Flow Turbines," British ARC, R & M 2974 (1951).
14. J. Dunham and P. M. Came, "Improvements to the Ainley-Mathieson Method of Turbine Performance Prediction," *Trans. ASME J Eng. Power*, July: 252 (1970).
15. S. C. Kacker and U. Okapuu, "A Mean Line Prediction Method for Axial Flow Turbine Efficiency," ASME Paper 81-GT-58 (1981).
16. H. R. M. Craig and H. J. A. Cox, "Performance Estimation of Axial Flow Turbines," *Proc. Inst. Mech. Engineers, 185*: 407 (1971).
17. O. Zweifel, "The Spacing of Turbomachine Blading, Especially with Large Angular Deflection," *Brown Boveri Rev., 32*: 436 (1945).

18. J. E. Haas and M. G. Kofskey, "Effect of Rotor Tip Clearance and Configuration on Overall Performance of a 12.77-Centimeter Tip Diameter Axial-Flow Turbine," ASME Paper 79-GT-42 (1979).
19. *Thermophysical Properties of Refrigerants*, American Society of Heating, Refrigeration, and Air-Conditioning Engineers (ASHRAE), Atlanta, GA, p. 171 (1976).
20. A. Stodola, *Steam and Gas Turbines*, Vol 1 (L. C. Loewenstein, trans.), McGraw-Hill, New York, pp. 200–201 (1927).
21. A. H. Stenning, "Design of Turbines for High-Energy-Fuel Low-Power-Output Applications," Report 79, Dynamics Analysis and Controls Lab, MIT, Cambridge, MA (1953).
22. E. Macchi and G. Lozza, "Comparison of Partial vs Full Admission for Small Turbines at Low Specific Speeds," ASME Paper 85-GT-220 (1985).
23. D. M. Mathis, "Turbine Wheel Relative Temperature at Freerun Conditions," SAE Paper 921949 (1992).
24. C. Rodgers, "Meanline Performance Prediction for Radial Turbines," Lecture Series 1987–07, von Karman Institute for Fluid Dynamics, Rhode Saint Genese, Belgium (1987).
25. M. G. Kofskey and W. J. Nusbaum, "Effects of Specific Speed on Experimental Performance of a Radial-Inflow Turbine," NASA Technical Note TN D-6605, Washington, DC (1972).
26. S. M. Futral, Jr., and D. E. Holeski, "Experimental Results of Varying the Blade-Shroud Clearance in a 6.02-Inch Radial-Inflow Turbine," NASA Technical Note TN D-5513, Washington, DC (1970).
27. C. Rodgers, "High Pressure Ratio Radial Turbine Design Constraints," Lecture Series 1987–07, von Karman Institute for Fluid Dynamics, Rhode Saint Genese, Belgium (1987).
28. H. E. Rohlik, "Analytical Determination of Radial-Inflow Turbine Design Geometry for Maximum Efficiency," NASA Technical Note TN D-4384, Washington, DC (1968).
29. S. M. Futral, Jr., and C. A. Wasserbauer, "Experimental Performance Evaluation of a 4.59-Inch Radial-Inflow Turbine With and Without Splitter Blades," NASA Technical Note TN D-7015, Washington, DC (1970).

8

Steam Turbines

Thomas H. McCloskey
Aptech Engineering Services, Sunnyvale, California, U.S.A.

INTRODUCTION AND HISTORICAL BACKGROUND TO STEAM TURBINES

The potential for steam turbine power was recognized by the ancients, with descriptions of potential steam weapons or novelties contained in works by Archimedes and Hero of Alexandria (a reaction design) (see Fig. 1) [1].

Similarly and independently, in 1629 Giovanni de Branca suggested a steam jet to blow against a modified waterwheel and turn a roasting spit (an impulse design) (see Fig. 2) [2].

Steam power, used in reciprocating steam engines, drove the industrial revolution and many contributors slowly added improvements to the basic device invented by Thomas Savery in 1698 (see Fig. 3) [3, 4].

In contrast, the development of a steam turbine started much later but had a shorter development period. Throughout the late 18th and 19th centuries, a series of investigators worked toward designing a practical steam turbine. More than 100 patents granted up to 1880 allowed the basic developments to occur that led finally in the 1880s to the point when the technology to build practical working steam turbines caught up to the vision. At this time Carl Gustaf de Laval and Charles Parsons built practical

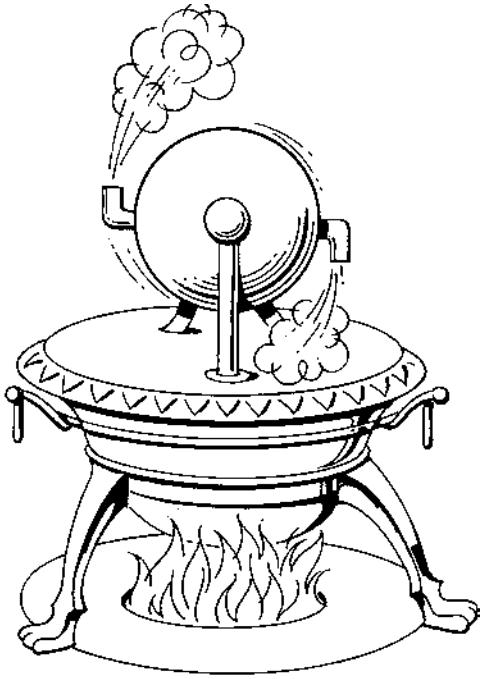

Figure 1 Reaction steam turbine designed by Hero of Alexandria (B.C.).

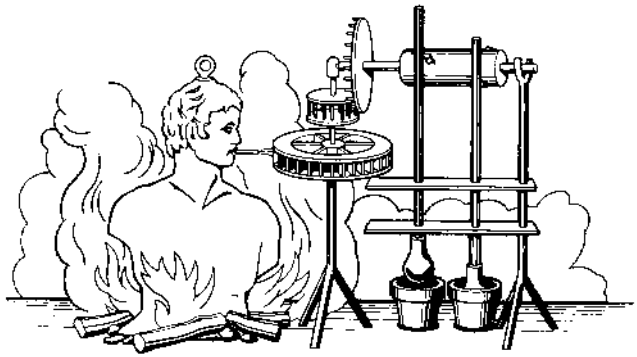

Figure 2 Impulse steam turbine designed by Giovanni de Branca (1629).

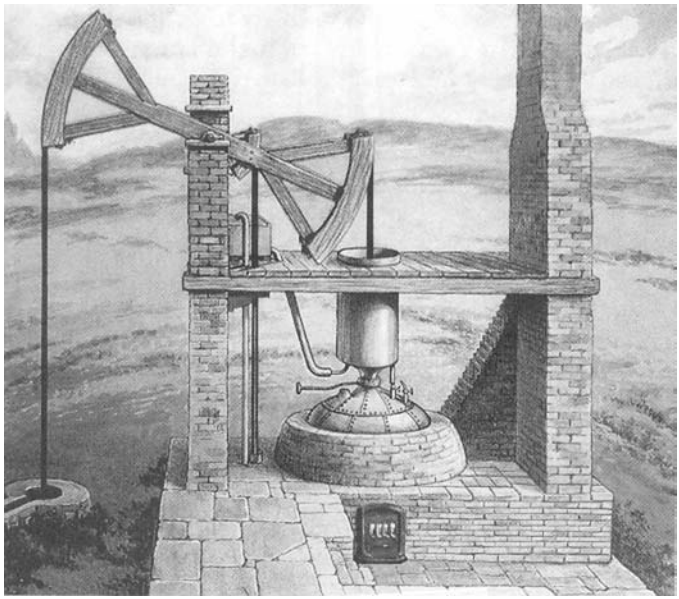

Figure 3 Reciprocating steam engine (1750).

steam turbines of two different designs: an impulse type and a reaction type, respectively.

In 1883 de Laval built his first practical steam turbine, using high-velocity steam jets to push blades of a turbine wheel. That single-stage, single-wheel turbine operated at speeds up to 26,000 rpm with tip speeds of the larger rotors over 365 m/sec (1,200 fps). de Laval had to solve several problems that are still central to turbine design including (1) how to lower the high centrifugal forces, (2) how to eliminate vibration, and (3) how to ensure steady operation. He recognized the phenomenon of critical speed. In the mid-1880s Charles Curtis patented a turbine design based on this concept of expanding steam through a nozzle, then impacting the high-velocity, low-pressure steam jet on the blades of a rotating wheel. It included velocity compounding for the first time. This design was acquired by General Electric in 1897 and has been the subject of constant improvement since, including, for example, the issue of patents for reheating steam in 1905 and 1906, although the use of regenerative feedwater heating and reheat were not actually incorporated until the 1920s.

In 1884 Parsons took a different approach and built a turbine that in concept is very similar to today's machines [3]. The steam entered a single

casing and flowed axially in opposite directions through two groups of turbine wheels, each containing 14 consecutive wheels. The design was intended to subdivide the pressure drop among the stages and reduce the required rpm. An early experimental turbine, producing 0.746 kW (1.0 hp), with 7.6-cm (3-in.) wheels operated at 17,000 rpm. In 1887 Parsons designed a compound turbine with a high-pressure and a low-pressure turbine mounted on the same shaft. Parsons went on to develop a radial-flow reaction turbine and a condensing turbine. The condensing turbine, developed only seven years after Parson's initial turbine, was more efficient than steam engines of the time, which had seen over 200 years of development. The rights to manufacture the Parsons reaction turbines were acquired by Westinghouse in 1895 (Fig. 4). Allis-Chalmers also acquired rights to manufacture the Parsons design. The first power station to produce electricity from a steam turbine was in 1888 in a Newcastle-upon-Tyne, England, power station using a Parsons generating set.

The improvement of design, operation, and efficiency continues today and makes interesting historical reading. For example, standardization to 1,800- and 3,600-rpm machines (from a variety of speeds—720, 750, 1,200, 1,500, and 1,800 rpm) occurred in North America when 25 Hz power stopped being used by utilities and the frequency was standardized to 60 Hz.

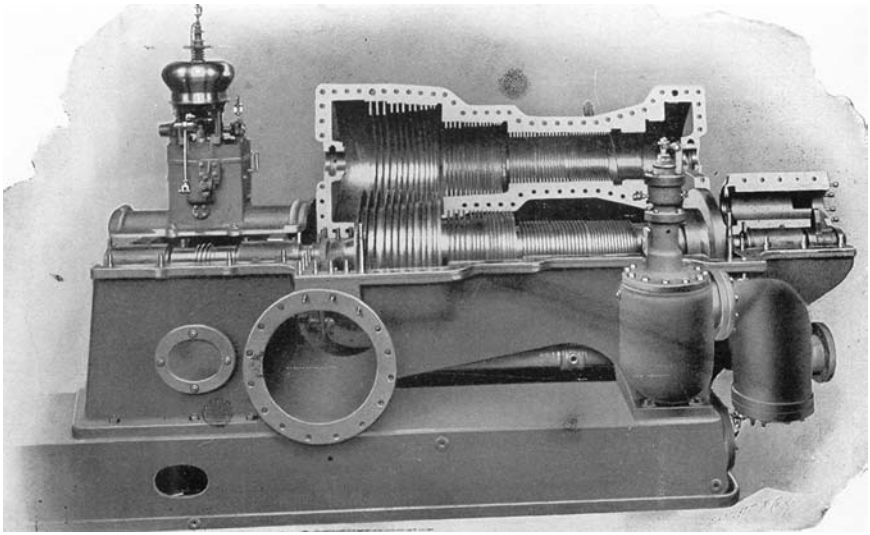

Figure 4 500-KW reaction steam turbine (1900).

This process began in the 1920s, although at least one major U.S. utility continued to use 50 Hz until the 1940s [5].

By the year 2001, the design and manufacturing capabilities of manufacturers have resulted in nuclear steam turbines of 1500 Mw in capacity at 1,500 rpm (see Fig. 5).

STEAM TURBINE THERMODYNAMIC CYCLES

A basic understanding of the thermodynamics of the steam turbine is essential to understanding the how a steam turbine is designed, operated, and maintained. There is a controlled and continual drop of both pressure and temperature as the working steam expands through the turbine flow path. As the pressure is reduced, the steam specific volume and volumetric flow increase. The pressure, temperature, and moisture content of steam control the efficiency of the process and impose severe performance requirements on turbine components [6].

Review of Thermodynamic Principles

Historical Developments

The importance of thermodynamics in the history of technology cannot be overstated. Bernal has said: "The central and most far-reaching discovery in the physical science of the nineteenth century was that of the conservation of energy—the first law of thermodynamics" [7]. The second law of thermodynamics was discovered by Sadi Carnot. In 1824, in *Réflexions sur la puissance motrice du feu et sur les machines propre à developper cette puissance*, Carnot outlined the second law as a theoretical limit on the efficiency of reversible cycles. Carnot also discovered the first law and a value for the mechanical equivalence of heat in 1830, but those were unpublished and lost in his notes until their rediscovery in 1878.

Rudolf Clausius generalized Carnot's work and by so doing began formal thermodynamics. Clausius pointed out in 1850 that "It is impossible to construct a device which, when operating in a cycle, will produce no effect other than the transference of heat from a colder to a hotter body."

> The final acceptance of the new views was due to the work of two academic scientists, William Thompson (Lord Kelvin), in his paper 'On the Dynamical Equivalent of Heat' and Herman Ludwig Ferdinand Helmholtz in his paper 'On the Conservation of Force', who fitted them into the accepted scheme of classical physics and almost succeeded in obscuring the fact that a great revolution in human thought had been achieved [11].

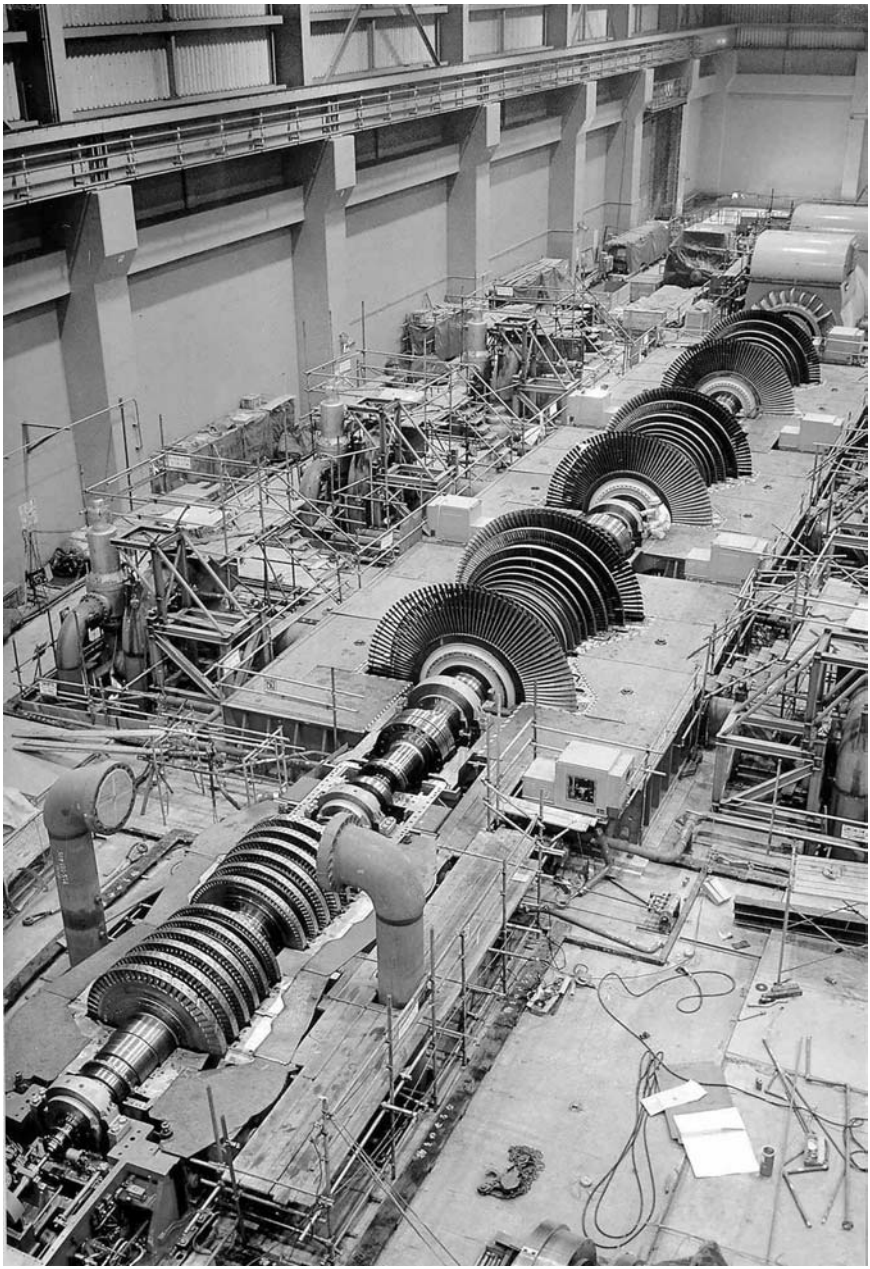

Figure 5 1,500-MW nuclear steam turbine (1995).

First Law of Thermodynamics

The first law of thermodynamics or the law of conservation of energy states that energy can neither be created nor destroyed. It describes the change of energy between forms (heat to work and work to heat) and allows for accounting for the transfer of energy to and from a system and changes of energy within a system. One typical form of the first law is

$$\Delta Q = W^* + \Delta U \tag{1}$$

Where

$\Delta Q =$ heat added to the system.
$W =$ work done by the system to the surroundings.
$\Delta U =$ increase in energy storage within the system.

A useful property for flow processes, such as in steam turbines, is the concept of enthalpy. Enthalpy per unit mass is defined as

$$H^* \cong u + Pv \tag{2}$$

Where

$H^* =$ enthalpy.
$u =$ internal energy per unit of mass.
$P =$ pressure.
$v =$ volume per unit mass.

In the case of an ideal flow system with no heat exchange with the surroundings or change in potential or kinetic energy, the work done by the system is the change in enthalpy between two states:

$$W = \Delta h \tag{3}$$

Second Law of Thermodynamics

Simply stated, the second law of thermodynamics is that not all of a given quantity of heat can be converted to useful work. The second law of thermodynamics places strict limits on the available performance of any heat engine, including a steam turbine. For example, one of the implications of the second law is that all real cycles must reject heat. The second law is typically discussed by considering the entropy of a thermodynamic system. Entropy is defined as the quantity of heat added during a reversible process

divided by the absolute temperature at which the addition takes place:

$$\Delta S = \int_1^2 \frac{dQ}{T} \quad \text{(reversible)} \tag{4}$$

The second law of thermodynamics is the postulate that the entropy of an isolated system cannot decrease:

$$\Delta S \geqslant 0 \tag{5}$$

Processes that would decrease entropy are therefore not possible; processes that increase entropy are possible.

Steam Properties

The state of steam (single phase) can be completely defined by specifying any two of six properties: temperature, pressure, specific volume, internal energy, enthalpy, and entropy. The first three of these are both observable and measurable; the second three must be calculated.

Steam Tables and Equations

The properties of steam have been historically, and continue to be, of tremendous importance. Steam tables provide compilations of key steam properties such as pressure, the corresponding saturation temperature, specific volume, sensible heat of the liquid, latent heat, and internal energy.

The documentation of those properties continues under the auspices of the International Association for the Properties of Water and Steam (IAPWS). The most recent official compilation is the Release on the IAPWS Industrial Formulation 1997 for the Thermodynamic Properties of Water and Steam (IAPWS-IF-97). These tables have replaced the 1967 Formulation for Industrial Use (IFC-67), which was the basis for the ASME Steam Tables. The changes have resulted in improved accuracy, speed of calculation, and internal consistency. However, there are differences between the two formulations, which users need to consider. There are differences of up to 3.48 kJ/kg (1.5 Btu/lbm) in some values for the latent heat of vaporization, and there are enthalpy differences at various points in the superheat region of up to 2.32 kJ/kg (1 Btu/lbm).

Calculated heat rates can have a substantial financial impact on industry costs. If calculations are made for the same power plant using the IFC-67 and IAPWS-IF97 formulations, different values will be obtained for the heat input from the boiler and for turbine section efficiencies, although

the amount of fuel burned and the power output do not change. The changes would make the boiler appear to be more efficient (more enthalpy added to the turbine cycle for the same amount of fuel burned), and decrease the apparent efficiency of the turbine. The total change for a typical 16.55-MPa (2400 psig), 538 °C/538 °C (1000 °F/1000 °F) unit could be on the order of 21–26 kJ/kW-hr (~20–25 Btu/kW-hr). This amount could have significant consequences to contract performances for either new plant or for changes to existing plant. It is therefore recommended that designers, vendors, and purchasers avoid mixing results calculated from the two formulations, and explicitly state which formulation is being used. Specifically, "a unit tested with IAPWS-IF97 properties cannot be expected to meet guarantees of specifications calculated using IFC-67" [14].

Process Representations

Process representations provide information about key thermodynamic variables during a cycle. Two valuable process representations for the analysis of thermodynamic cycles in steam turbines are the temperature–entropy diagram and the enthalpy–entropy (Mollier) diagram.

The temperature–entropy (T–s) diagram for steam is shown in Fig. 6. In the central part of the figure is the "steam dome," which is formed by the saturated liquid (0% quality) line and the saturated vapor (100% quality) line. For steam conditions falling under the dome, there will be a two-phase (vapor and liquid) system; in this region pressure is fixed for a given temperature, independent of quality. The point at the top of the steam dome is the critical point defined by the critical pressure 22.12 MPa (3208.2 psia) and temperature 374.15 °C (705.47 °F). Two other regions can be defined. Subcooled liquid is represented by the region of the diagram to the left of the saturated liquid line and below the critical pressure. At temperatures above the critical point, only a single phase substance exists independent of pressure. In the superheated region, the vapor is superheated and the temperature elevation above the saturation temperature corresponding to the prevalent pressure is termed the superheat.

Figure 7 shows schematically temperature–entropy diagrams for three power plant cycles: (1) operating predominantly in the superheated steam region; (2) operating predominately in the wet-steam region without reheat; and (3) with reheat.

The enthalpy–entropy (h–s) diagram or Mollier diagram for steam is shown in Fig. 8. The Mollier diagram, developed by Prof. Mollier at Dresden University circa 1898, is used extensively as an aid to understanding thermodynamic cycles. Lines of constant pressure run diagonally

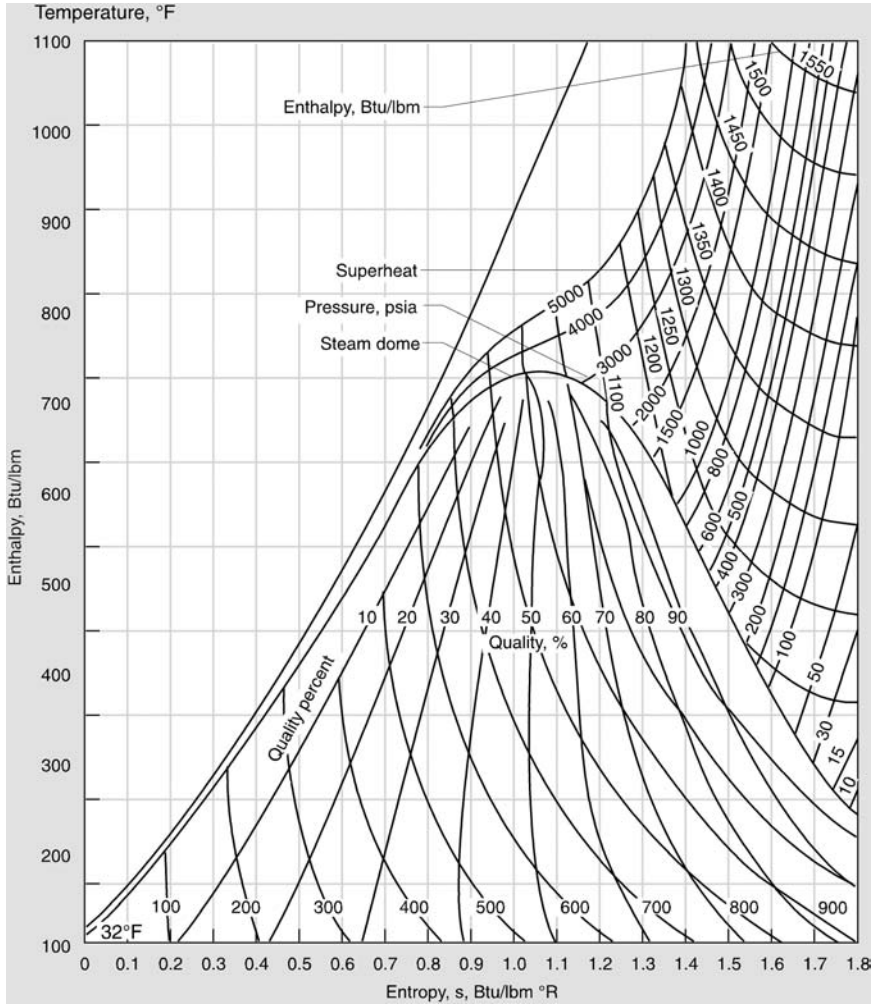

Figure 6 Steam cycle temperature entropy diagram.

across the diagram from the lower left to upper right. Along those lines of constant pressure, at any point, the values of the corresponding enthalpy and entropy can be read. Vertical distances on the diagram (changes in enthalpy) are proportional to the energy transfer as work for a turbine. They would be identically equal to the work of the turbine if the turbine was 100% efficient (isentropic efficiency). However, as there are losses in real turbines, the actual work done will be somewhat less than the difference in enthalpies

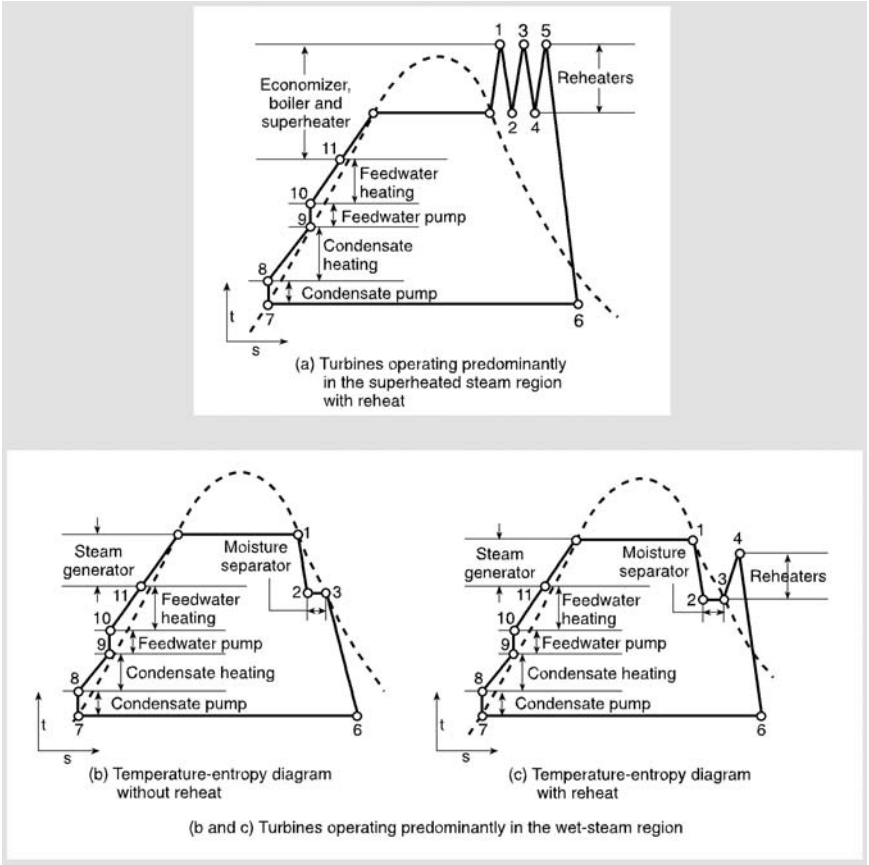

Figure 7 Rankine cycle temperature–entropy diagrams.

between two points. Turbine losses are associated with an increase in entropy. Turbine efficiency is discussed in more detail in the sections on steam cycles ahead.

The saturation line drawn on the Mollier diagram separates steam conditions that are superheated (above and to the right of the saturation line) and "wet" steam (below and to the left of the saturation line). The cross-hatched area on Fig. 8 is the phase-transition zone (PTZ), which is the below the saturation lines and at a point where significant condensation will occur, typically at a moisture level around 1–3%. The Mollier diagram is an equilibrium or static diagram and does not take into account the actual dynamic process.

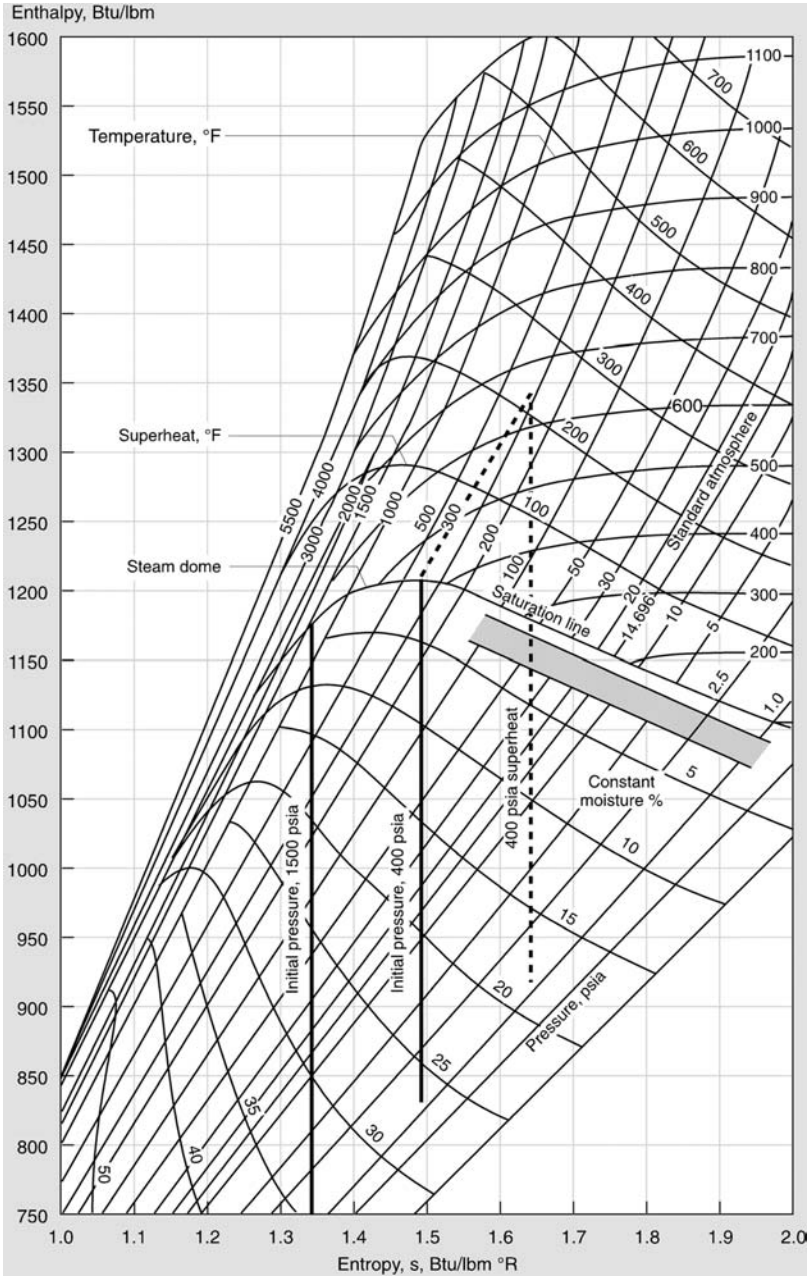

Figure 8 Steam turbine Mollier diagram (H–S).

The Mollier diagram is quite useful for diagnosing the influence of moisture and impurities on various damage mechanisms. A first step in the evaluation of blade damage may often be plotting the damage location on the Mollier diagram to determine its relationship to the start of the phase-transition zone.

Steam Cycles—Theory

A power plant cycle is the paths and processes through which a working fluid passes, in a cyclic fashion, in the production of power by a prime mover [7]. The efficiency of a power plant depends on the type of cycle, temperatures and pressures in the cycle, the distribution of the working fluid, and system losses. It is useful in the analysis of real systems to analyze the so-called ideal cycles. Such analyses provide insights about the upper bounds on efficiency, help characterize losses, and provide suggestions for improvements in real-world equipment.

Here we examine three such cycles: the Carnot cycle; the simple or base Rankine cycle; and the regenerative cycle.

Carnot Cycle

The Carnot cycle is illustrative because it represents the upper limit for performance in a real system. The Carnot cycle is illustrated on a temperature–entropy diagram in Fig. 9. It consists of two isothermal processes and two isentropic processes. The Carnot cycle is completely reversible, has no losses nor increases in entropy, and therefore represents the ideal condition.

The Carnot efficiency is equal to

$$\eta_{\text{Carnot}} = 1 - \left(\frac{T_A}{T_B}\right) \tag{6}$$

Where

T_A = temperature of heat transfer into steam engine.
T_B = temperature of environment.

Efficiency will be the highest where the temperature of heat transfer into the engine is at the highest possible temperature and the heat rejection is at the lowest possible temperature. For example, for $T_A = 1500\,^{\circ}\text{F}(1960^{\circ}\text{R})$ and $T_B = 60\,^{\circ}\text{F}(560^{\circ}\text{R})$, the maximum thermal efficiency is approximately 73.5%. No real-world devices, which are all inherently irreversible, operate at efficiencies as high as the ideal Carnot efficiency.

The expected efficiency of real-world energy conversion is also less by

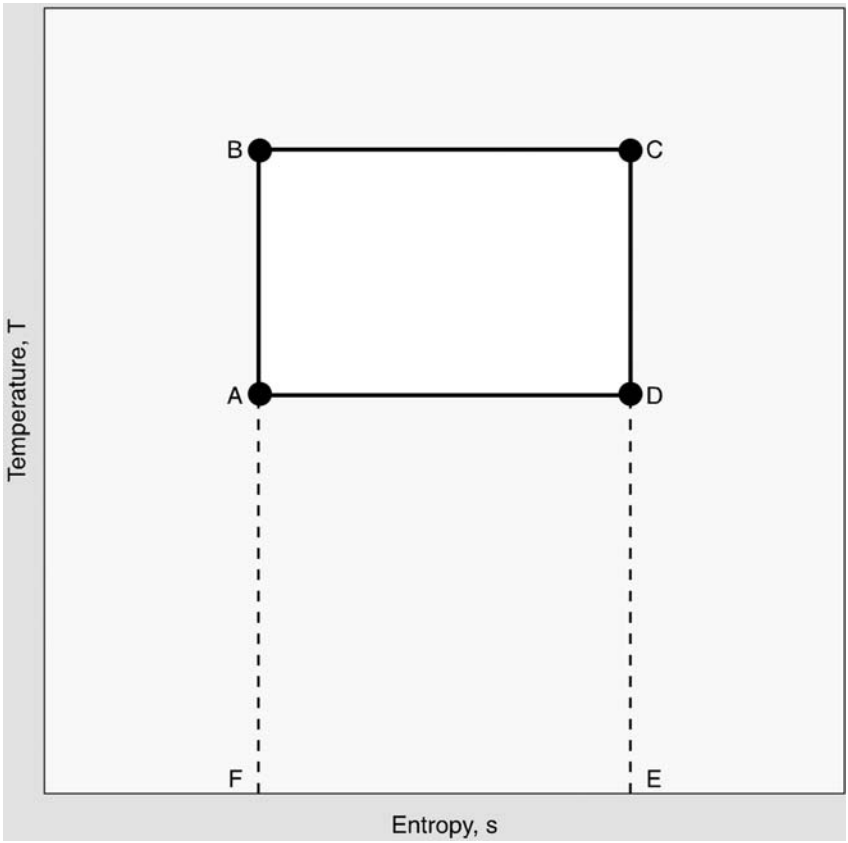

Figure 9 Theoretical Carnot thermal efficiency diagram.

an amount known as the isentropic efficiency, that amount by which an actual device output differs because of adiabatic instead of isentropic processes. This efficiency differs by machinery type from 60–80% for small, single-stage steam turbines up to about 90–95% for modern, large steam turbines [8].

Rankine Cycle

The basic Rankine cycle was used in power plants early in the 20th century. It consists of a single heat addition (from the boiler), expansion of the steam through an engine, and condensation (heat rejection) of the exhaust. The *T–s* diagram for the basic Rankine cycle is shown in Fig. 10. Heating of the

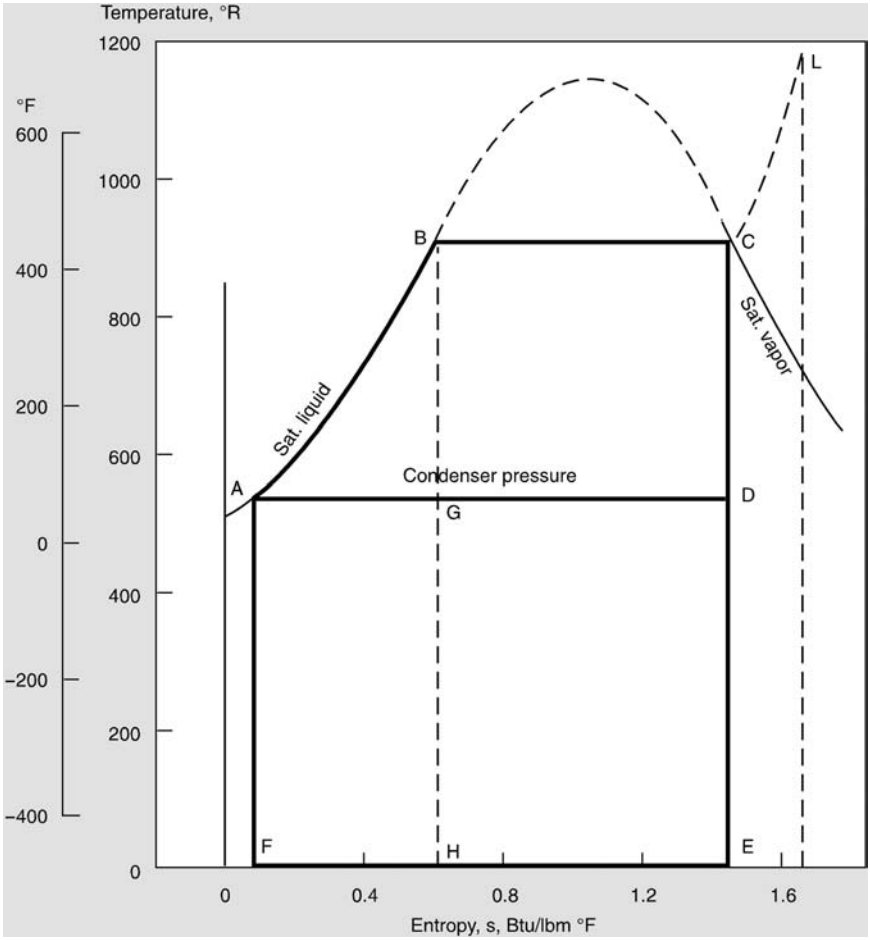

Figure 10 Theoretical Rankine cycle diagram.

liquid occurs along the segment AB; BC is the evaporation to steam; CD is the expansion in the turbine; and DA is condensation. The efficiency of the Rankine cycle can be found by dividing the work performed by the heat added:

$$\eta = \frac{(h_C - h_D)}{(h_C - h_A)} \tag{7}$$

The Rankine cycle efficiency is a function of the steam conditions in the unit

only, including pressure, temperature, and exhaust pressure. The actual or thermal efficiency of a power plant is the Rankine efficiency multiplied by the efficiency of the turbine. Because the overall unit efficiency is a function of both the thermodynamic and turbine efficiencies, an alternative performance criterion has been established in terms of heat rates. The heat rate is the ratio of the heat supplied to the turbine (or plant) divided by the output of the generator (or plant).

The earliest plants used an open thermodynamic steam cycle, thus a primary problem was with contaminants in the feedwater supply. Control methods included water treatment and boiler blowdown. Evolution to a closed cycle led to easier and better control of water/steam purity.

There were two other significant problems with the basic Rankine cycle. The moisture in the exhaust was high, which decreased the overall efficiency and led to significant blade erosion. The second drawback was the low efficiencies that were caused by the nonequilibrium heating of the compressed liquid along AB. The solution to these problems was to evolve to a regenerative (with reheat) Rankine cycle.

Reheat

The efficiency of the Rankine cycle is highest for the highest turbine inlet temperatures. However, there are limitations to how high a temperature can be used, such as material capability. Further, when pressures are raised to increase the work that can be produced, there is an increase in exhaust moisture that lowers the efficiency and increases the amount of liquid droplet erosion damage. To overcome these difficulties and also generate higher cycle efficiencies, the reheat cycle is used. The steam starts at a maximum temperature, then is partially expanded through a turbine section, and is subsequently returned to the reheater section of the boiler. There may be one or more reheats, the number being a matter of economics and efficiency. The use of reheat led to an increase in operating pressure.

In a typical steam turbine unit, going to a single reheat Rankine cycle increases the efficiency (decreases the heat rate) by about 4–6%. Heat rate is a measure of fuel economy in a unit and can be defined as

$$\text{Plant heat rate} = \frac{\text{Heat equivalent of fuelburned}}{\text{Net useful kWhr generated}} \tag{8}$$

The plant efficiency is

$$\eta = \frac{3412.14 \frac{\text{BTU}}{\text{kWhr}}}{\text{Heat rate}} \times 100\% \tag{9}$$

An additional advantage of reheat is that the steam going through later

stages of the turbine is at a higher temperature and thus lower moisture content (with the double benefit of higher efficiencies and less moisture-induced damage). Double reheating provides an additional improvement in efficiency, typically about one half of the improvement obtained in going from no reheat to a single reheat [9]. In order to avoid superheated exhaust, it is necessary to go to higher throttle pressures, and as a result double reheat has been used in practice only in plants with supercritical throttle pressure [7].

The Regenerative Cycle

Further improvement to the basic Rankine cycle is the regenerative cycle, a form of reheat in which steam extracted from various stages of the turbine is directed to feedwater heaters. Modern conventional fossil fuel power plants use regeneration to increase the efficiency of the cycle. The larger the number of feedwater heaters, the greater the efficiency of the cycle, although the overall economics of the additional equipment and piping limit the practical number of feedwater heaters used. In heat recovery steam generators (HRSGs) there are usually no feedwater heaters [10].

The manner in which the improvement of efficiency is obtained can be seen by reference to Fig. 11. The Rankine cycle is ABCDA made up of three reversible processes: isothermal processes BC and DA, the isentropic process CD, and the irreversible heating process AC. If the irreversible process AC could be made reversible, then the cycle would have Carnot efficiency [1]. Regeneration allows part of the turbine steam thermal energy to be used to heat the feedwater. As shown in Fig. 6, the steam at C is first partially expanded through the turbine. An extraction reduces the steam thermal energy from 1 to 2 and that thermal energy is used to heat the feedwater from 11 to 12. Similarly, after the next incremental expansion through turbine from 2 to 3, extraction can be used to heat feedwater from 10 to 11. In the limit of smallest steps, the heating process approaches a reversible process as the temperature difference between the extracted steam and fluid being heated is infinitesimal. In the limit, as lines AB and EC become parallel, the efficiency of this cycle becomes that of the ideal Carnot cycle.

Use of Superheat

If superheated steam is used, the thermal and aerodynamic efficiencies of the cycle are improved and the moisture content of the steam is reduced. The improvement in the thermal efficiency of the cycle by the use of superheating can be seen in Fig. 10; the segment CL is the superheated portion of the cycle.

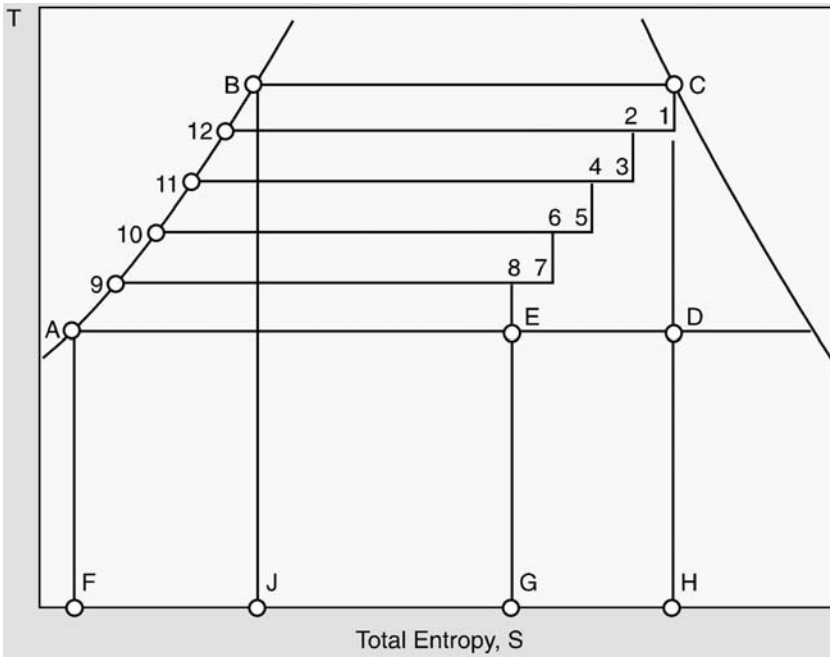

Figure 11 Saturated steam regenerative cycle.

Limits to the level of superheating that can be used are primarily determined by the properties of boiler materials, specifically the creep and thermal fatigue resistance of the superheater tube materials used. Higher pressures that result with higher superheat temperatures also result in thicker tube walls, which slow unit startup and load changing and greatly affect the thermal fatigue life of the component.

Typical supercritical unit conditions are 23.13 MPa (3500 psia) and 538 °C/538 °C (1000 °F/1000 °F) for single reheat and 23.13 MPa (3500 psia), 538 °C/551 °C/565 °C (1000 °F/1025 °F/1050 °F) for double reheat units.

Turbine Efficiency and Overview of Losses

Fundamental to understanding the effect of many of the damage mechanisms in steam turbines is understanding how the damage creates efficiency losses in the turbine. At some stage in the analysis of repair and prevention strategies, an economic analysis will be required. Being able to

calculate the relevant thermodynamic losses and to predict the likely magnitude of the changes in those losses will be central to such an economic analysis and will help determine which options are viable.

As befits the central importance of thermodynamic losses in turbine design, maintenance, and operation, numerous references describe these contributions in great detail [11, 12].

Three groups of losses can be considered: pressure drops that occur with the passage of steam through valves, piping, and exhaust between sections; turbine section losses; and individual turbine stage losses. Figure 12 shows that the relative mix and magnitude of efficiency losses varies by type of stage. The figure shows the major losses for a typical 700 MW single reheat turbine.

Pressure Drop Losses

A rule of thumb is that every 1% pressure reduction results in a reduced heat rate of about 0.1% in a fossil unit and 0.15% in a nuclear unit [9].

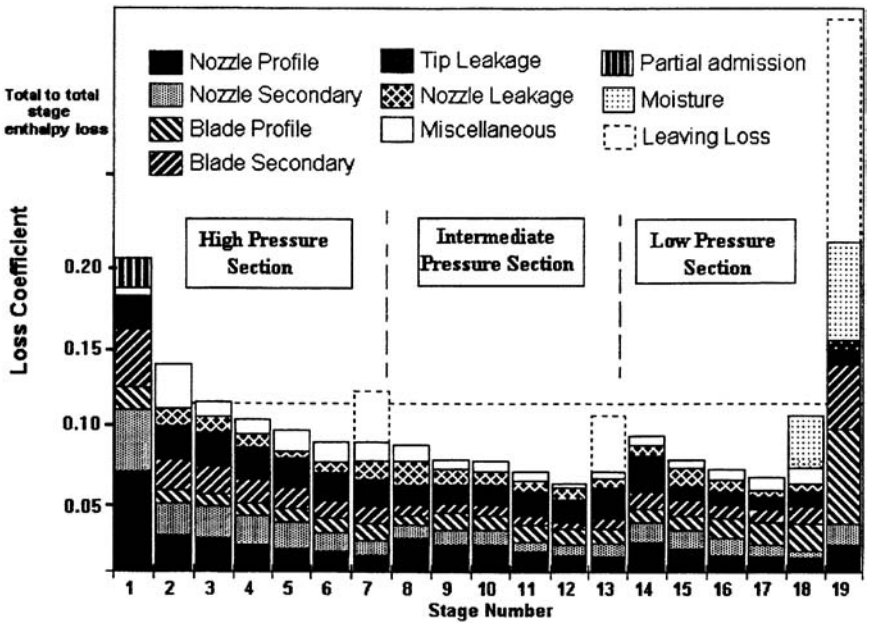

Figure 12 Stage and section efficiency losses for a 700-Mw single reheat turbine.

Turbine Section Losses

A survey of 31 steam path audits indicated that the average section efficiency deterioration was 12.5% for the HP, 9.1% for the IP, and 3% for the LP. Most of the total loss in these turbines was caused by either leakage (about 50% of the total) or surface roughness (about 36% of the total). The worst leakage losses were from (1) radial spill strips, tip seals, or shroud seals, (2) diaphragm packing or interstage shaft packing, (3) end packing or shaft packing, and (4) miscellaneous leakages such as midspan balance hole plugs, inner shell, and seal rings.

Figures 13 and 14 show typical leakage paths in impulse and reaction designs, respectively. Losses from leakage steam reentry between the

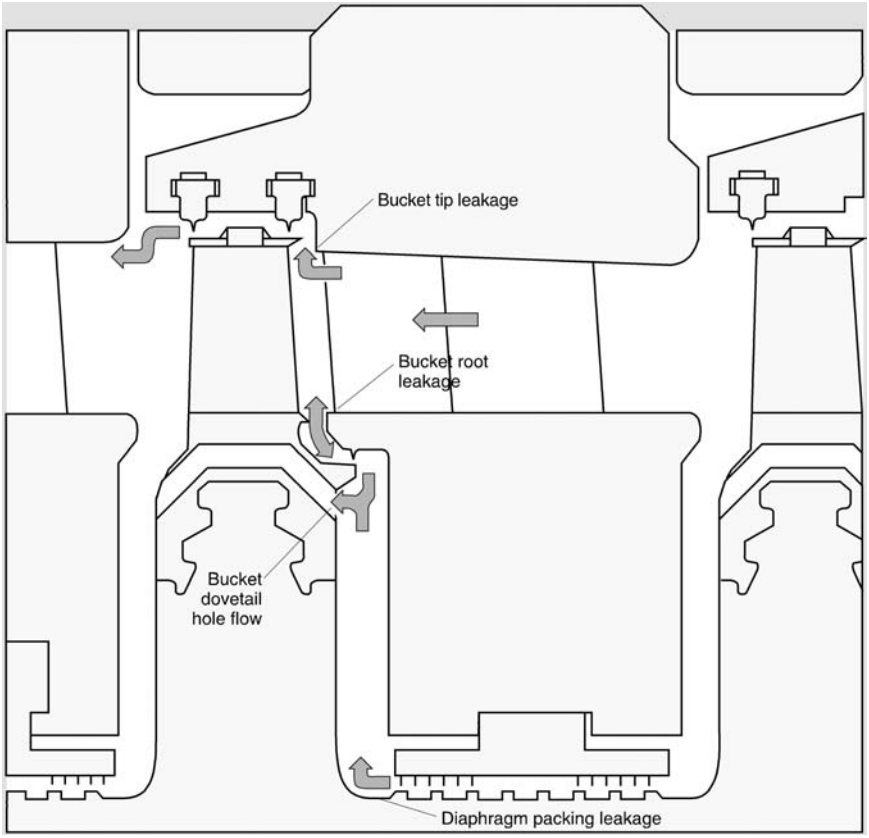

Figure 13 Steam leakage losses for an impulse stage design.

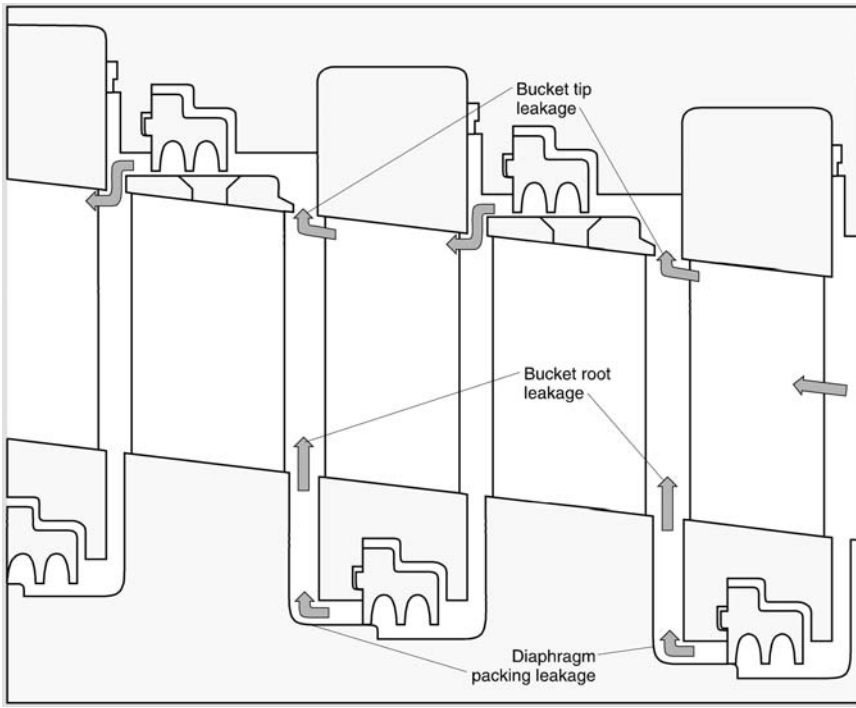

Figure 14 Steam leakage losses for a reaction stage design.

stationary and rotating rows of a low-reaction stage will be higher than on a conventional reaction stage. Impulse-style blading has increased base section reactions to prevent the reentry of leakage steam between the stationary and rotating blades of a stage. Typical stage reactions at the mean diameter of low-reaction blading in intermediate-pressure turbines are about 30 to 35%.

Surface roughening occurs as a result of (1) deposits, (2) solid particle erosion, and (3) steam path damage such as weld beads, tools, thick deposits, and surface finish losses. The calculated percent change in turbine efficiency by stage as a function of surface finish is shown in Fig. 15.

Turbine Stage Losses

The primary contribution to the overall turbine generator efficiency is the efficiencies of the individual turbine stages. The ideal stage efficiency is the

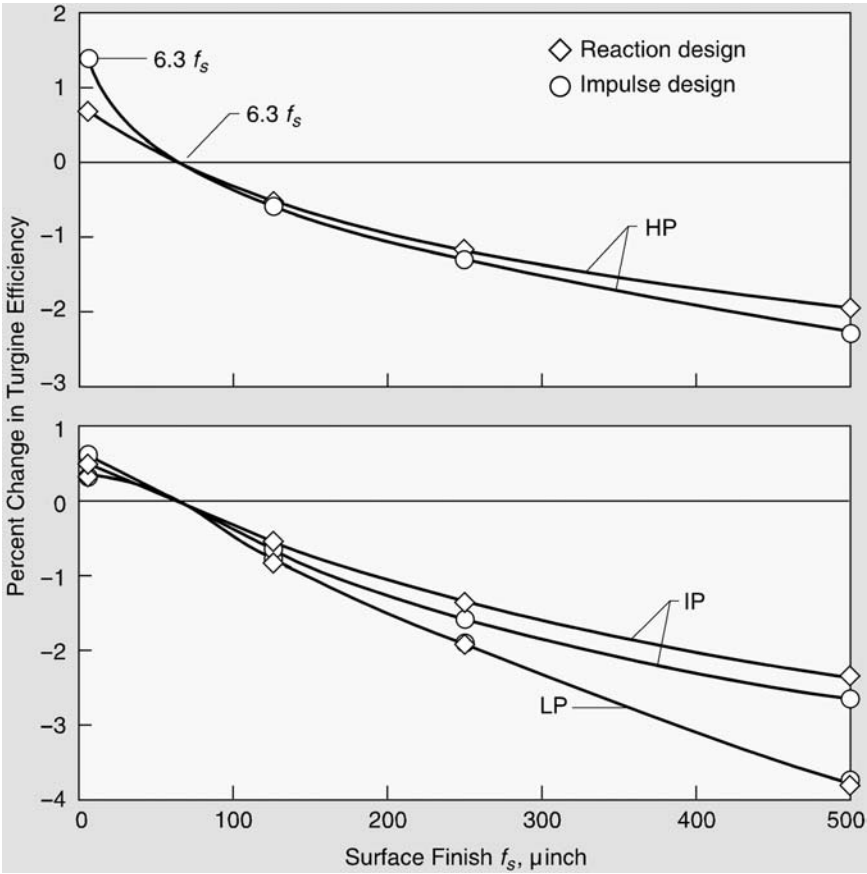

Figure 15 Percent change in turbine efficiency for HP and LP turbines as a function of material surface finish.

ratio of the energy of steam converted into mechanical work to the available energy in a given stage.

Maximum Load Testing

A maximum load test can be used as a simple indicator of efficiency.

Measuring Changes in Stage Efficiency

An enthalpy drop test can provide a simple check on the condition of turbine nozzles and blades. Plots of stage efficiency and stage pressure ratio

can reveal nozzle and/or blade erosion or fouling. Measurement of the turbine section efficiency by an enthalpy drop test is the most simple and useful test of turbine stages operating in the superheated steam region; for accurate results, one needs to have accurate measurements of the pressures and temperatures at the inlet and outlet of the stage [13–16].

Enthalpy drops for the HP and IP sections of the turbine are fixed by known temperatures and pressures, whereas that for the LP is not. Until recently there has been no means to measure the wetness of the interstage and exhaust steam, and thus LP turbine power and efficiency could only be inferred indirectly from a heat balance calculation. However, wetness probes have now been developed that can measure the distribution of wetness at the interstage and turbine exhaust planes. These data, when combined with aerodynamic data from pitot tube measurements, can quantify the LP discharge mass flow, flow-weighted total/static pressure, and turbine exhaust state point [17]. From the state point, the thermodynamic efficiency of the last stage can be determined. This allows for baseline data to be established in efficiency or flow path improvement projects [17–19].

Steam Cycles—Practice

Components of a power plant can be divided into heat sources (the boiler or steam generator) and the turbine cycle. The turbine cycle includes the turbine, generator, condenser, pumps, and feedwater heaters.

Fossil Power Plant Cycles—Illustrative Example

Figure 16 shows a typical turbine–heater cycle in a fossil fuel power plant. In this example the turbine has high-pressure (HP), intermediate-pressure (IP), and low-pressure (LP) sections. Also shown are a typical feedwater heater arrangement, the condenser, and the auxiliary turbine. Figure 17 shows the superposition of the steam cycle for this unit on an outline of the Mollier diagram. A few pressure curves are shown as dotted lines. The saturation line is shown as a solid line and located approximately in the middle of the figure. The expansions through various cycles are shown with solid lines. The lines for expansion through fossil fuel HP, IP, and LP turbines are in the upper part of the figure. Typical efficiencies for each of these turbine sections and typical nuclear reheat and nonreheat cycles are also shown in Fig. 17.

Note that unlike the idealized regenerative Rankine cycle, typical fossil and nuclear unit cycles are not isentropic. This is evidenced by the slight slope toward increasing entropy during the expansions through the turbine

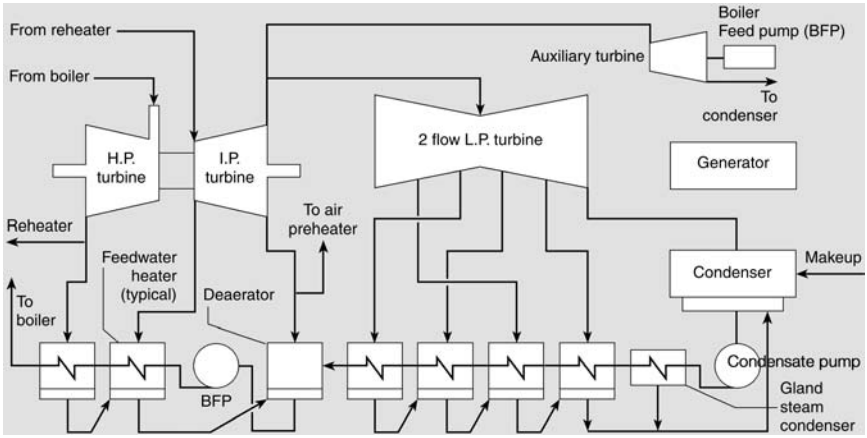

Figure 16 Typical fossil fuel turbine heater cycle.

stages (offset from vertical lines on the Mollier diagram). At the same time, no heat is added to or rejected, indicating an adiabatic process.

Typical fossil units operate with main steam conditions of at 538–566 °C (1000–1050 °F) and pressures typically in the range 16–20 MPa (2300 to 2900 psia) for subcritical units and up to 24 MPa (3500 psia) for supercritical units. Advanced steam conditions in fossil fired units, of increasing interest because of the potential for greatly improved efficiencies, are typically at 24 MPa (~3500 psia or 240 bar) and above with main and reheat temperatures of 565 °C (1050 °F) and above. Internationally, units are in operation with steam conditions as high as 31 MPa (4500 psia or 310 bar)/565 °C (1050 °F)/656 °C (1212 °F)/565 °C (1050 °F). An example of the efficiency improvement has been cited by one manufacturer at about 8% for a unit at 300 bar/600 °C/600 °C/600 °C compared to conventional technology at 180 bar/540 °C/540 °C [20].

Mass and flow diagrams are used to summarize key information about the fluid at each process end point in the cycle. Typical mass flow diagrams can be found in a number of references (see, for example, [13]). They indicate flow rates, pressures, enthalpy, and temperature throughout the cycle.

Nuclear Power Plant Cycles—Illustrative-Example

Typical nuclear power plant cycles for both pressurized water reactors (PWR) and boiling water reactors (BWR) differ considerably from typical

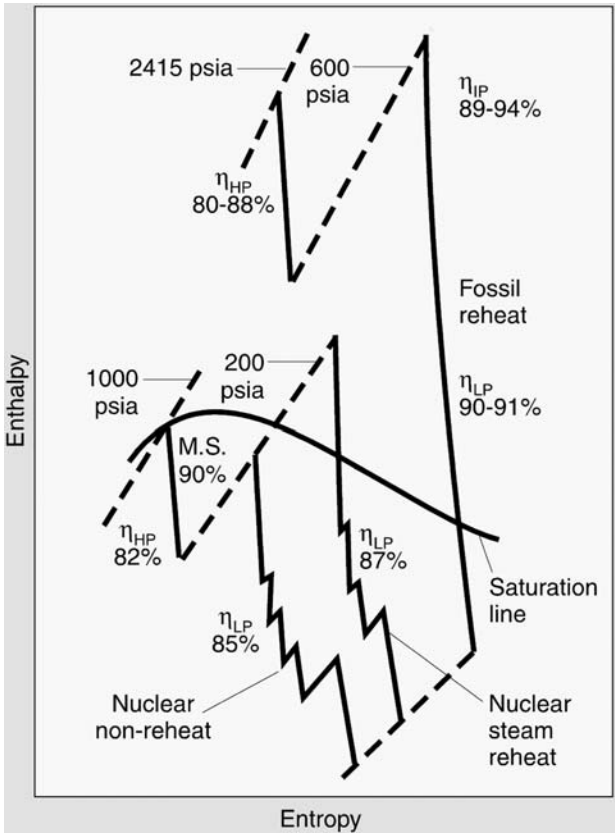

Figure 17 Enlarged portion of the Mollier diagram illustrating typical fossil and nuclear turbine expansion lines.

fossil unit cycles. This can be seen by reference to Fig. 17, which shows the lower pressures and enthalpies of the steam in both nonreheat and reheat nuclear cycles when compared to fossil units. Nuclear cycles have lower steam parameters, typically 6–7 MPa (870–1015 psia or 60–70 bar) and (260–290 °C 500–554 °F), with around 0.25% moisture and very large flow rates (approximately 4,000 lbm of steam per second in a 1200 MW plant). In some PWR designs, steam is produced at a slight superheat. As a result of these steam conditions, there is considerable difference between the HP turbine of nuclear and fossil units. Predicted exit wetness ranges typically are 13–17%, with actual values being somewhat less because of moisture removal by drainage devices and steam extraction.

Peripheral (blade-tip) speeds in the HP turbines of nuclear units range from about 100 to 200 m/s ($\sim$ 325 to 650 ft/s) depending on unit size, rotor speed, and type of blading used. These tip speeds are significantly slower than in fossil units, and as a result there are fewer problems with liquid droplet erosion than in fossil unit LP turbines which have approximately the same moisture levels, but considerably higher blade-tip speeds. Expansion in the HP turbine is typically followed by a moisture separator; at the exit to the moisture separator, steam quality is typically close to unity.

LP turbines in most nuclear cycles operate under similar moisture conditions to those in fossil units because of reheating in the moisture separator reheaters (MSR). Last-stage blades typically range in overall length from about 900 mm to 1320 mm (35 to 52 in.). Continuing improvements in materials and design will almost certainly allow for progressively longer blades in future machines.

A circuit diagram for a state-of-the-art nuclear plant is shown in Fig. 18.

Co-Generation Cycles

In co-generation cycles, steam is typically generated at a higher temperature and pressure than required for a particular industrial process. The steam is expanded through a turbine to produce electricity, and the resulting steam flow extractions at the discharge are at the temperature and pressure required by the process. Turbines can be of condensing or noncondensing design typically with large mass flows and comparably low output [7].

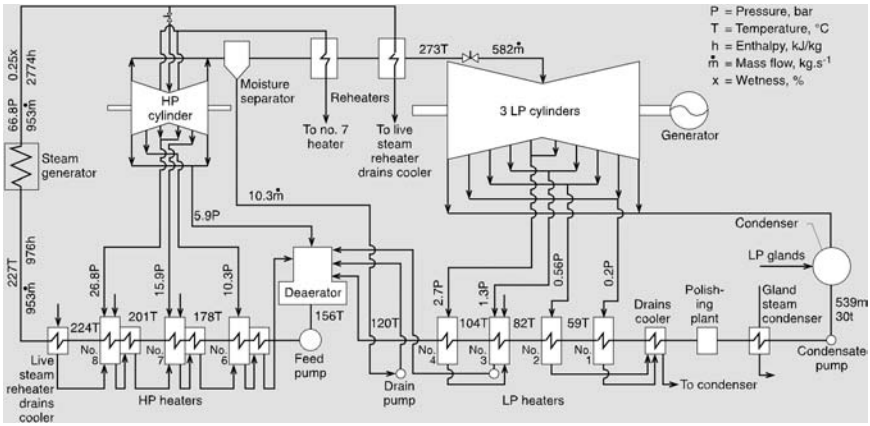

Figure 18 Schematic diagram of a typical PWR nuclear turbine cycle.

Traditionally, pressures have been 6.21 MPa (900 psig) and below with temperatures 441 °C (825 °F) or lower, although the trend toward higher levels for each continues. There are now a considerable number of co-generation steam turbines with initial steam pressures in the 8.63–10 MPa (1250–1450 psig) range and steam temperatures of 482–510 °C (900–950 °F).

Combined Cycle Plants

Combined cycle plants use the exhaust from advanced gas turbines [which is typically in the range from 560 °C to 600 °C (1040 °F to 1110 °F)] to feed a fired or unfired heat recovery steam generator (HRSG) and subsequently drive conventional steam turbines with main and reheat temperatures at 540 °C (1000 °F) and 590 °C (1100 °F), respectively. Flow diagrams for two arrangements are shown in Figs. 19 and 20.

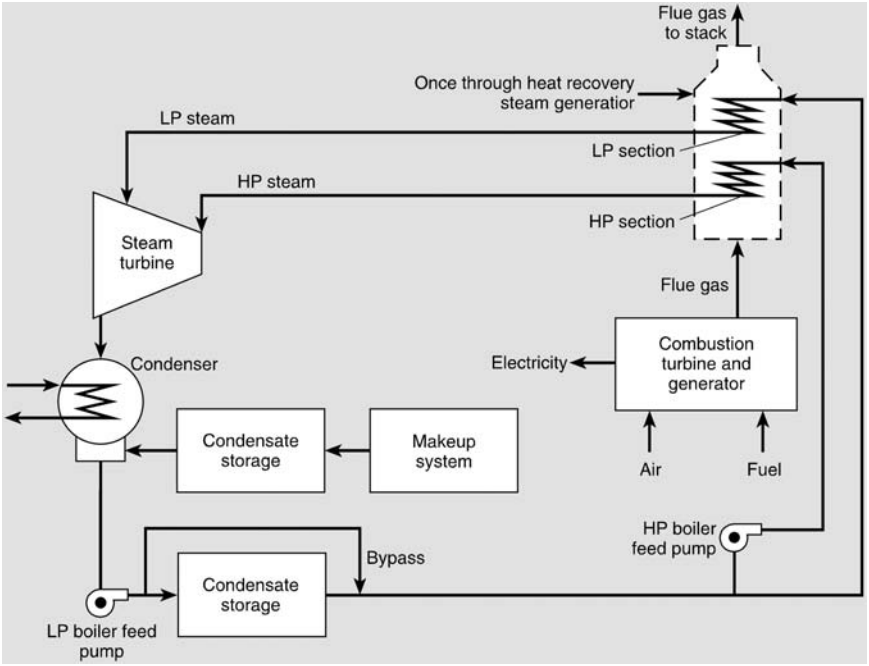

Figure 19 Thermodynamic diagram for a once-through combustion turbine and steam turbine combined cycle.

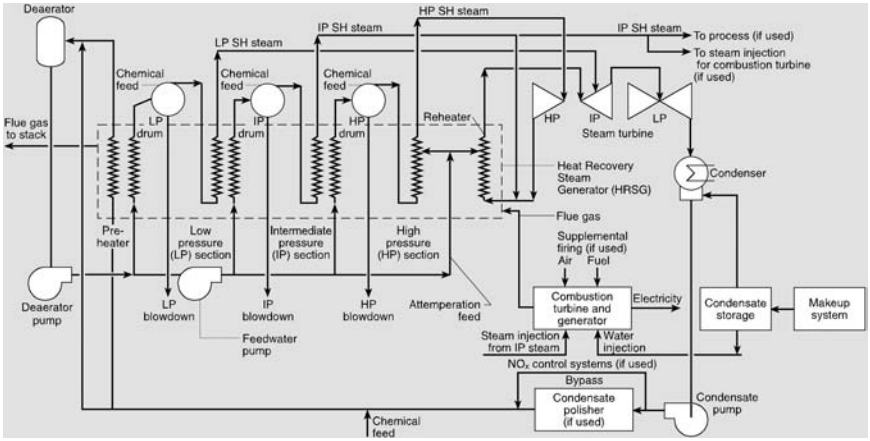

Figure 20 Thermodynamic diagram for combined cycle with three reheat cycles.

Geothermal Plants

Steam conditions (and as a result, efficiencies) in geothermal plants are usually low, typically below 7 MPa (1015 psi) and 170 °C (340 °F). The low available enthalpy means that very large flows are necessary. For example, in a typical 150 MW unit, the flow is 600 lbm/sec.

Moisture Limitations

A practical limit on the usable temperatures and pressures of steam is also imposed by the entrained moisture. Severe erosion, caused by excessive moisture levels at the inlet to the last few blade rows, was found in LP blades in early turbine designs and led to a limitation of about 12% on turbine exit wetness [21].

Furthermore, the efficiency, η, of the LP turbine decreases by approximately 1% for every 1% increase in wetness in the wet stages. The overall loss caused by moisture consists of a supersaturation loss and a moisture loss as illustrated in Fig. 21 for results obtained from a development laboratory LP turbine. The supersaturation loss occurs because the expansion in the turbine is more rapid than indicated by equilibrium expansion. Under these conditions, the temperature drops much more rapidly, and there is less available energy than equilibrium. Beyond the "Wilson line," condensation occurs and the stage efficiency drops by about 0.76% per 1% increase in moisture. The overall loss introduced from zero

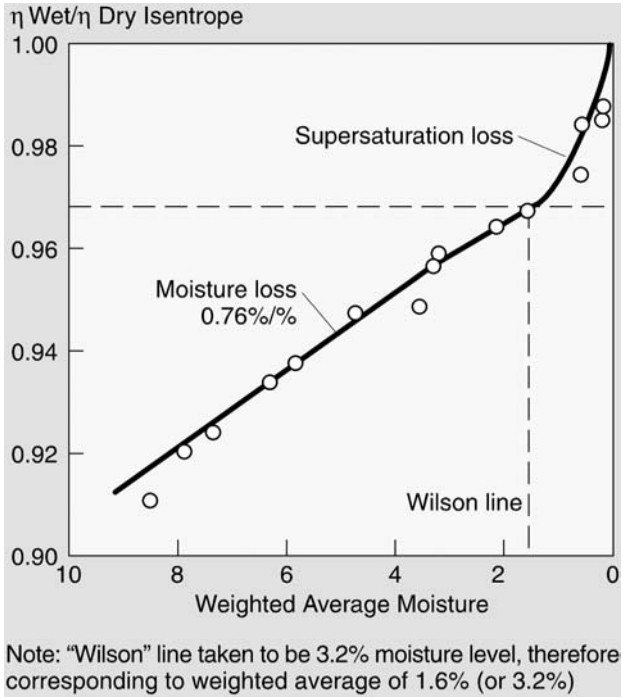

Figure 21 Wetness thermodynamic losses versus percent average moisture.

moisture to about 8% weighted average moisture including supersaturation loss is about 1% per percent of average moisture. Thus, there is a decrease in the overall efficiency of the LP turbine of about 8%.

Double reheat systems, introduced in the 1950s, operate optimally with a cycle that results in about 6–10% wetness, well within the limits applicable to prevent LP blade erosion. The concern over moisture level, however, continues as

Larger unit designs introduced in the 1960s led to longer blades and higher blade-tip speeds and therefore more potential for erosion damage

Single reheat systems, which have optimal cycles with higher moisture levels, may be favored over double reheat systems because of economic advantages related to the cost of additional equipment, controls, and floor space.

Light water reactor (LWR) nuclear units generate saturated, high-pressure steam for use in the HP turbine. Expansion of even slightly

wet steam results in moisture content of 15% at a pressure level of about 5 bar (72.5 psi); straightforward expansion at the vacuum end could raise the level to 20–25%. As a result, moisture separators are placed between the HP and LP, along with reheaters to limit the moisture content at the LP exit.

STEAM TURBINE DESIGN AND CONSTRUCTION FUNDAMENTALS

Steam Flow Orientation

Steam flow can be radial or axial. Axial is by far the most common for large power plant steam turbines. Figure 22 shows a typical axial flow LP turbine. Figure 23 shows a typical radial-flow Ljöngstrom IP turbine. In the radial-flow turbines, steam enters at the centerline and exits radially outward.

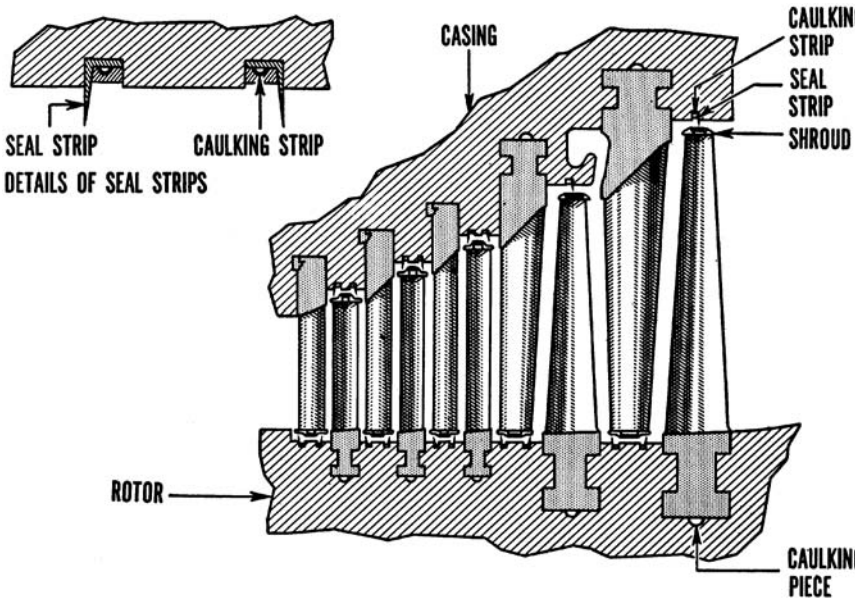

Figure 22 Low-pressure double-flow axial design steam turbine.

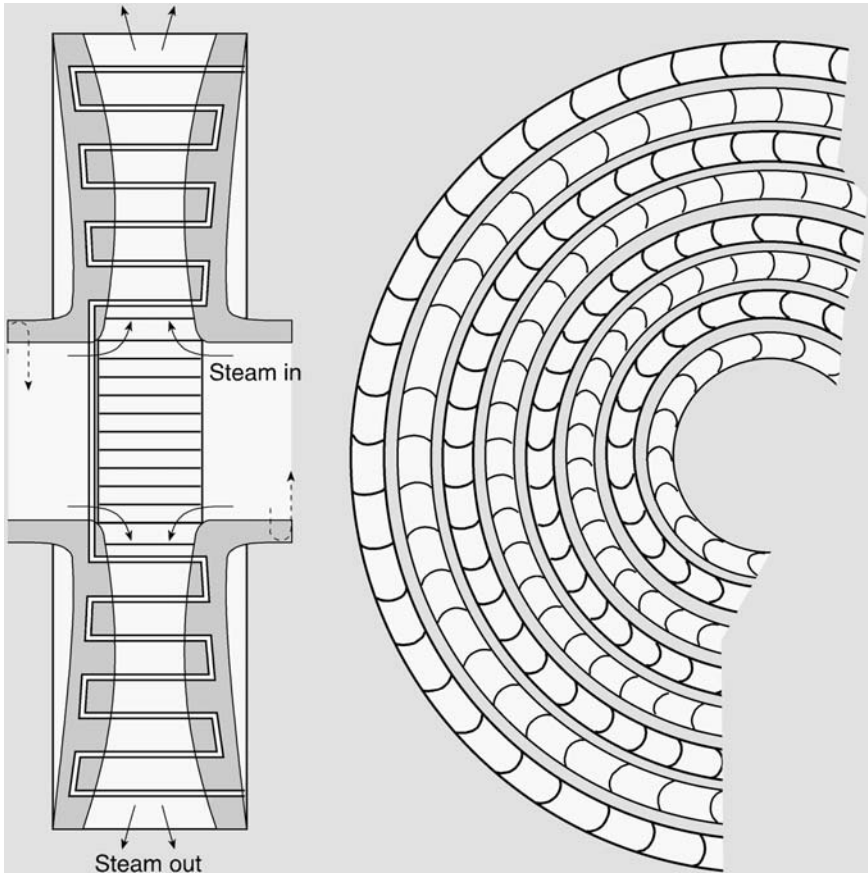

Figure 23 Radial steam turbine flow schematic.

Impulse Versus Reaction Design

A distinction is made between ''impulse'' and ''reaction'' turbine designs based on the relative pressure drop across the stage. There are two measures for pressure drop, the pressure ratio and the percent reaction. Pressure ratio is the pressure at the stage exit divided by the pressure at the stage entrance. Reaction is the percentage isentropic enthalpy drop across the rotating blade or bucket compared to the total stage enthalpy drop; some manufacturers utilize percent pressure drop across stage to define reaction [22].

In an impulse design, most of the pressure drop is across the stationary blade or nozzle. In a "pure" impulse design, all the pressure drop would occur across the nozzle; this would be termed 0% "reaction." In practice, there must be some pressure drop across the rotating blades in order to generate flow. For example, the control stage of the HP turbine is typically an "impulse" stage by design but still has on average about 5% reaction at full load. Note that a stage will pass flow even if there is negative reaction; what is required is that the ratio of the total to static pressure drop across the rotating row be a positive value (see Fig. 24).

In a reaction design, work is performed by a jet exiting from stationary blades similar to the impulse design; however, an additional reaction from the jet created by the moving blades also occurs. For a symmetric reaction design, equal pressure drop occurs across the stationary and rotating blades and thus reaction is equal to 50%. Figures 24 and 25 show the percent reaction versus stage number for fossil and nuclear units, respectively, with both impulse and reaction turbine types plotted on each figure. Note that the tip and root reaction percentages are different to counteract the effect of

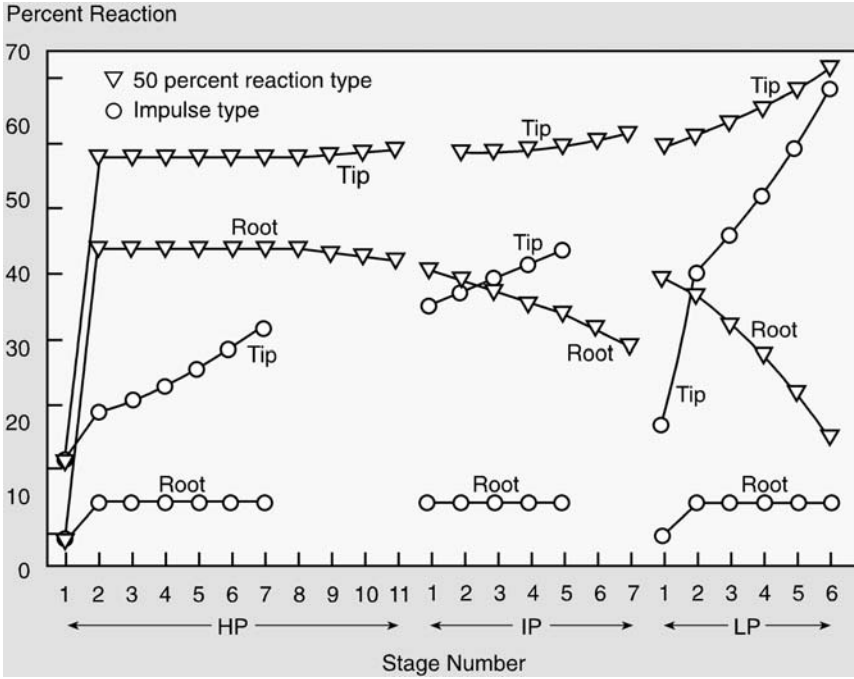

Figure 24 Percentage stage reactions for fossil steam turbines.

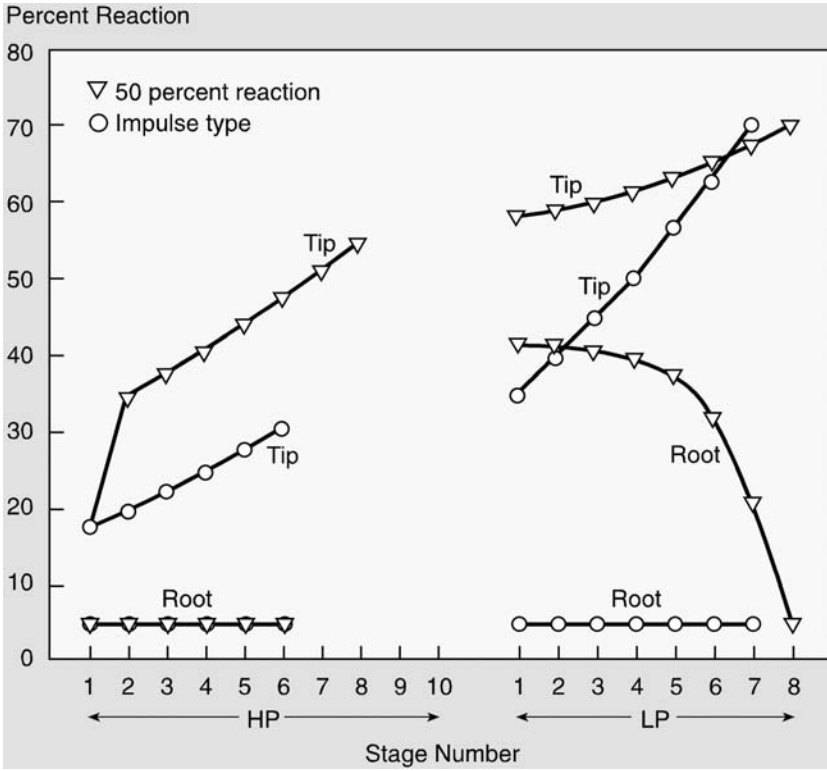

Figure 25 Percentage stage reactions of nuclear steam turbines.

centrifugal forces on the steam flow. If this was not done, too much flow would migrate to the blade tips and reduce stage efficiency. Bowed blades, for a given mean diameter reaction, increase the base section reaction and reduce the tip reaction [104].

Flow Through a Stage (Velocity Triangles)

"Velocity triangles" for an impulse stage are shown in Fig. 26. This vector representation is an important tool used to understand the flow of steam through real turbine stages. The stationary blades (or nozzles) accelerate the flow by altering the flow area and turn the flow toward the rotating blades. The velocity of steam leaving the stationary blade, V_1, is approximately equal to the theoretical steam velocity V_0, which would be the velocity of the

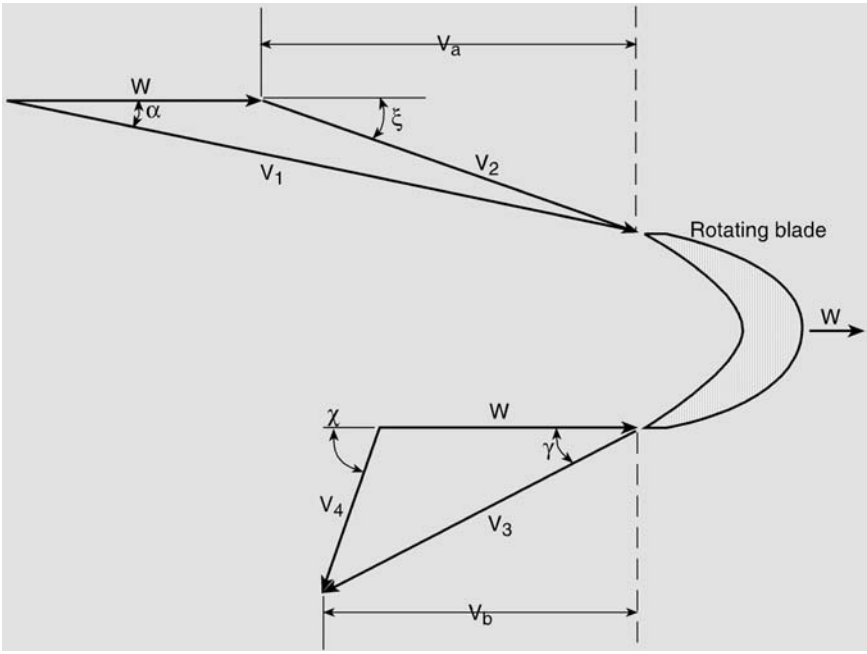

Figure 26 Velocity triangle of steam through a steam turbine stage.

steam expanded from the pressure upstream of a stage to the downstream pressure without losses.

The velocity of the rotating blades or wheel velocity, is designated W, and the vector result of V_1 and W is the velocity of the entering steam relative to the rotating blade, V_2. α is the angle at which the steam leaves the stationary blade relative to the plane of rotation of the rotating blade. α is sometimes referred to as the "nozzle angle" although it is actually the steam angle and typically about 2° larger than the nozzle passage angle.

In an impulse design, there is little pressure drop across the rotating blades so that the relative velocity leaving the rotating blade, V_3 (Fig. 26), would be equal to the entering velocity V_2 if there were no frictional losses. The absolute velocity of the exiting steam is V_4, the vector sum of V_3 and the wheel speed, W. A goal of the stage design process is to have the direction of the flow at exit be as close as possible to axial for entry into the next stage [9].

The force on the blade is proportional to the change in tangential components of the velocity, i.e., the entering tangential velocity, V_a, less the exit tangential velocity, V_b.

The power output of the stage can be determined from impulse–momentum considerations. Efficiency is shown to be [6]

$$\eta = 2\frac{w}{V_0}\left(\frac{V_a}{V_0} + \frac{V_b}{V_0}\right) \tag{10}$$

Where

w = the mass of steam flowing per second.

Alternatively,

$$\eta = \frac{V_1^2 - V_2^2 + V_3^2 - V_4^2}{V_0^2} \tag{11}$$

The theoretical efficiency of stages with reactions is shown in Fig. 27. The parameter X indicates the fraction of stage energy released in the blades. As shown in the figure, in a pure impulse stage, where $X = 0$, the optimum ratio of W/V_0 is 0.5. Optimum ratios for other percent reactions are shown in Fig. 27. Note that in reality, as the velocity ratio, W/V_0, changes, the fractional reaction will also change. Thus the change in efficiency of an actual turbine stage efficiency would cut across the velocity ratio curves with changes in imposed reaction. Rotating steam turbine blades utilized in impulse type of construction are often referred to as "buckets."

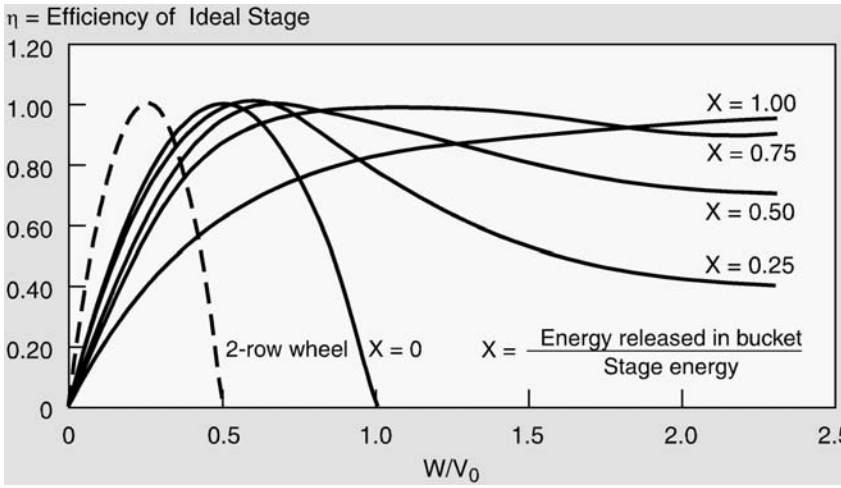

Figure 27 Thermodynamic efficiency of a turbine stage versus velocity ratio for various bucket/blade reactions.

Pressure or Velocity Compounding

Multistage turbines can use either pressure or velocity compounding. In pressure compounding, each blade row is preceded by a row of nozzles. In velocity compounding, one row of nozzles guides steam onto two or more rows.

Condensing and Noncondensing Units

Condensing units allow for the steam to expand to the lowest possible pressure before being condensed. The exhaust steam pressure is termed the "back pressure" and is equal to the pressure in the condenser plus a small incremental pressure that results from pressure losses in the exhaust hood. The condenser pressure, and hence turbine back pressure, depend on the flow rate and temperature of the cooling water, contamination or fouling of the condenser tubes, and other condenser factors. High back pressures can result in large vibratory blade stresses from flow recirculation and in the overheating of last-stage blades by windage friction. In noncondensing turbines, the steam is exhausted before being fully expanded. The exhaust may be used to supply steam to a condensing turbine or for process heating. A noncondensing turbine is sometimes referred to as a "back-pressure" turbine.

Number of Sections (Cylinders) and Stages

Although early machines were one section or cylinder (because of design and manufacturing limitations), most commonly, power plant turbines consist of two or more sections designated high-pressure (HP), intermediate-pressure (IP) and low-pressure (LP) in order to improve overall efficiency. The optimum number of stages depends on a number of factors, including (1) the amount of available energy from steam boiler conditions, allowable exhaust pressure, etc. and (2) stage percent reaction, rotor mean diameter, and rotor speed.

There are three basic types of shaft and casing arrangements: single casing, tandem-compound, and cross-compound. In turbines with a single casing, all sections are contained within one casing and the steam path flows from throttle valve to exhaust through that casing.

In the tandem-compound design, two or more casings are connected in series on a single shaft. In a common arrangement, the HP and IP turbines are in one casing, with the HP exhaust returned for reheating and entering or sent to the IP turbine The IP exhausts into crossover piping and on to one or more low-pressure turbines. LP turbines are typically characterized by the number of parallel paths available to the steam. The steam path through

the LP turbines is split into parallel flows because of steam conditions and practical limitations on blade length. Typically several LP flows in parallel are required to handle the large volumetric flow rates. Figure 28 shows a typical tandem-compound turbine with two casings—one HP and IP, and the second, a two-flow LP.

A cross-compound design typically has two or more casings, coupled in series on two shafts, with each shaft connected to a generator. In cross-compound arrangements, the rotors can rotate at different speeds but cannot operate independently, as they are electrically coupled. The cross-compound design is inherently more expensive than the tandem-compound design, but has a better heat rate, so that the choice between the two is one of economics.

Schematics of Common Arrangements

A variety of common steam path arrangements is shown schematically in Fig. 29. Figure 29(a) shows a simple path where steam enters a turbine and is exhausted to the atmosphere or a condenser. In Fig. 29(b) two sections are used, an HP and an LP section. Figure 29(c) indicates a condition where split steam is used in a double-flow, low-pressure (DFLP) section.

Figure 29(d) indicates a three-section turbine including the IP section, along with reheating of steam exiting the HP section (indicated by the "R" in the figure). Figure 29(e) is a similar configuration except that the flow is to two DFLP sections. Figure 29(f) shows a double-flow IP (DFIP), followed by three DFLP sections.

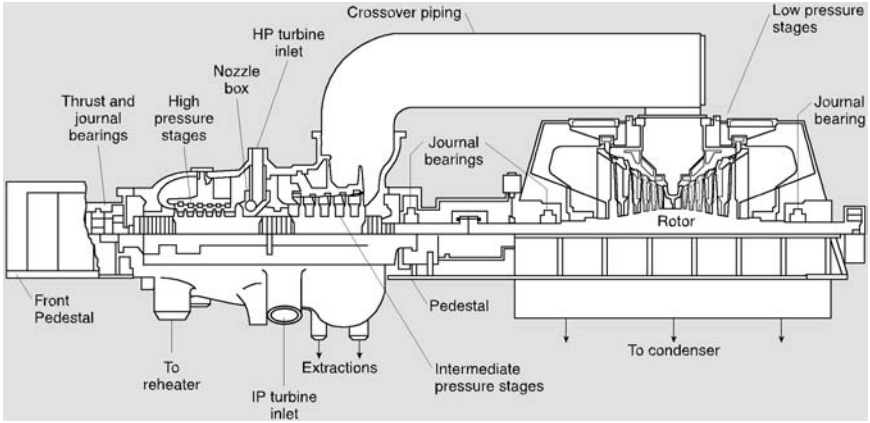

Figure 28 Typical tandem compound single-reheat condensing steam turbine.

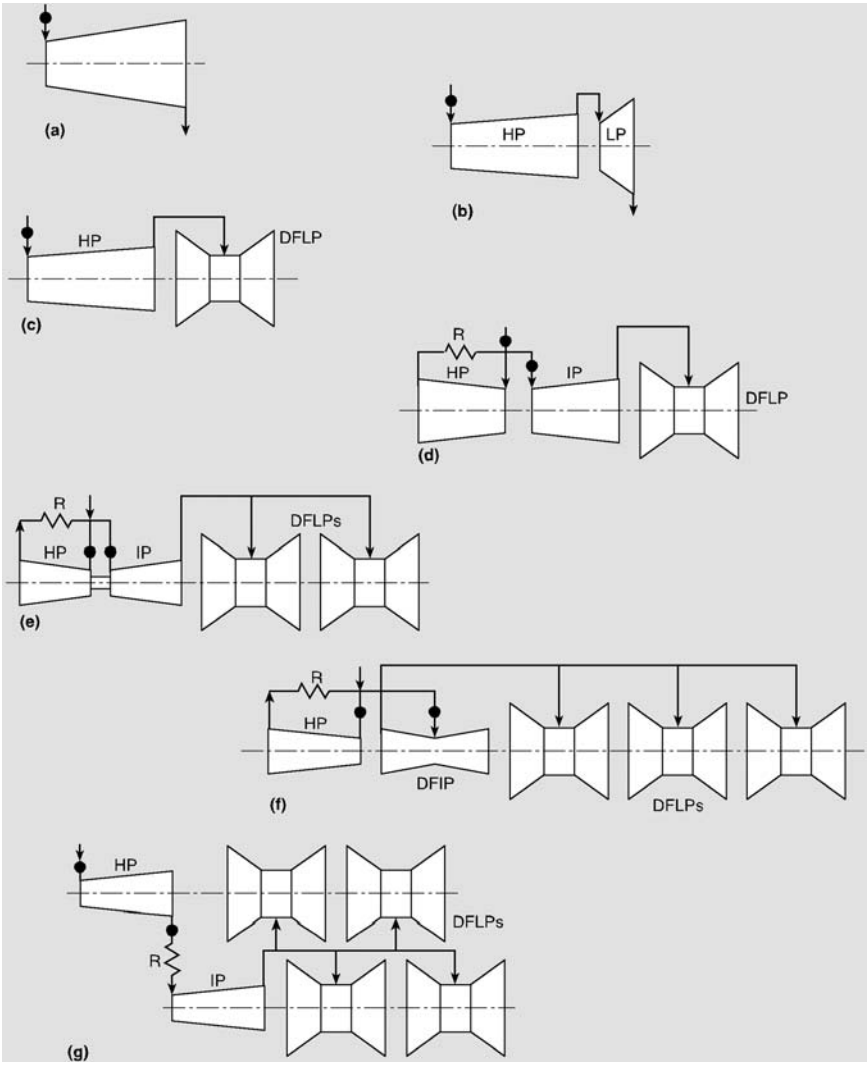

Figure 29 Alternative arrangements of steam turbine construction.

In arrangements shown in Fig. 29(a–f), all rotors are coupled or contained on a common shaft, a tandem-compound arrangement. Figure 29(g) shows the cross-compound arrangement where the units have more than one rotor shaft [22].

Turbine Inlet

Two stages in particular have very specific design considerations—the first (“inlet” or “control”) stage, and the exhaust stage. The inlet stage serves a control function, and flow through it may vary widely (for example, during partial-arc admission). If the first stage is a full-arc admission stage, either impulse or reaction, the flow control is accomplished by control valve action. A true control stage is a partial-arc admission stage where flow control is achieved both by varying the active steam admission arc as well as by throttling on the control valves. Consequently, a control stage is a low-reaction design with partial-arc admission. Because of the variable admission, the stage pressure ratio increases as load is reduced with an accompanying increase in the steam velocity leaving the nozzles.

The space between the inlet stage and the following stage allows for equalization of the flow. In most turbines, even those with subsequent stages of the reaction design, the first stage is typically an impulse stage in order to achieve a large temperature drop and thus control the temperature of the steam to the rotor.

The first stage of the HP is typically divided into several arcs of admission fed by separate control valves, allowing it to be operated with either full-arc or partial-arc admission. In partial-arc admission, startup is often accomplished by opening stop valves wide open and controlling the steam flow with the first control valve.

Turbine Exhaust—Last Stage and Exhaust Hood

As it produces about 10% of the total power output of the turbine, the exhaust stage of the LP is one of the most critical to the economics of the entire turbine. There is considerable economic pressure to increase unit sizes by increased steam mass flow rates. A key limitation is the last LP stage, specifically the allowable blade length, annulus area, and tip speed. Raising the annulus area increases the turbine capacity and efficiency but also increases the turbine and blade size. Increasing the last-stage blade length allows more power to be extracted from the working fluid (or alternatively a more compact machine with fewer stages can be built to extract the same amount of energy). The disadvantage is the increased centrifugal stress, which quickly limits the length of the blades constructed of a particular material.

From a damage viewpoint, the last stage also sees a high proportion of blade failures. This is due to the combined effects of high stresses, caused by the length of the blades, entrained moisture droplets, and any chemical contaminants.

Even though designers make the exhaust hood as large as possible, because of the large volume of steam flow, sonic velocities can be reached at the steam exit. As a result, losses accumulate similar to flow through a pipe, and the exhaust hood is potentially subject to flow-accelerated corrosion. Exhaust hood redesign to optimize flow paths is an area that is showing considerable economic payback [23]. These redesigns are being performed using tools such as computational fluid dynamics (CFD), a technique that was not available to the early designers.

Fossil and Nuclear Turbine Designs Compared

Fossil Turbine Designs

An overall schematic of a typical fossil turbine is shown in Fig. 28. Steam enters from the main steam lines through stop and control valves into the HP section or cylinder. As noted earlier, the first or control stage is spaced somewhat apart from subsequent stages to allow for stabilization of the flow.

After passing through the HP turbine, cold reheat piping carries the steam to the reheater and returns in the hot reheat piping to the integrated HP and IP cylinder to pass through the IP turbine. The return to the IP turbine typically passes through a stop and intercept valve. The flow exits the IP through the IP exhaust hood and typically passes back along the spacing between the inner and outer casing of the combined HP and IP turbine. The flow then passes through crossover piping to the LP.

During its expansion through the LP turbine(s), the steam crosses the steam saturation line, also termed the phase-transition zone (PTZ). Exit is through the LP exhaust hood. The typical modern steam turbine has a number of extraction points throughout all its sections, the extracted steam being supplied to the feedwater heaters.

Nuclear Turbine Designs

Nuclear steam supply is generally at lower pressures and temperatures than in fossil fuel units; as a result, considerably higher flow rates are required to generate the same power output. There is generally an HP section coupled with several LP sections.

Nuclear HP turbines are usually of a double-flow design. Because the supplied steam has little or no superheat, expansion through the nuclear HP turbine leads to high moisture levels (typically 10–15%). If it were exhausted directly to the LP turbine, exit moisture from the LP would be on the order

of 20%, which would cause excessive erosion of the last stages of the LP and large losses in efficiency. As a result, a moisture separator (in which the steam is dried or separated mechanically) and a one- or two-stage reheater are provided for the steam exhausted from the HP before returning it to the LP.

Piping from the HP turbine exhaust to the moisture separator/reheater is termed cold reheat or crossunder piping; that from the reheater to the LP turbine called hot reheat or crossover piping. In nuclear nonreheat units, there is typically only a moisture separator between the HP and LP turbines.

The LP turbines for nuclear reactors are subject to nearly identical conditions as those in fossil units and have led to the use of the designs that are often identical. However, as the steam volumetric flows are 60–70% larger, the exhaust annulus area must be increased or the number of LP turbines increased to reduce exhaust losses [23].

In the United States, the use of larger-sized components needed to handle the high steam flow rates in nuclear units has led to the use of lower speeds such as 1800 rpm for 60-Hz units, compared to 3,600 rpm for fossil units. The stresses that result in the turbine blades of fossil and nuclear units are roughly the same order of magnitude, as the allowable blade lengths are longer in the slower-turning nuclear-powered turbines. For 50-Hz systems, 1,500 rpm and 3,000 rpm machines have been used in nuclear units.

Steam Turbines for Co-Generation, Combined Cycle, and Geothermal Plants

Co-Generation Turbines

Steam turbines for co-generation may be of standard designs or incorporate specific features to improve the delivery of district heating, such as extra cylinders to allow more freedom in automatic extraction [9].

Combined Cycle Turbines

Combined cycle units may consist of a single gas turbine and single steam turbine on a common shaft with the generator, or multiple gas turbines and a single steam turbine. Depending on the steam conditions and flow, the steam turbine for combined cycle units may be a single cylinder or multiple cylinders, such as with an HP and a double-flow LP turbine. Combined cycle turbines typically do not employ regeneration cycles employing feedwater heaters.

Geothermal Unit Turbines

Because of the low-enthalpy steam conditions in most geothermal units, very large flow rates are required; as a result, such units may typically contain setups such as two double-flow, low-pressure cylinders.

Rotors

Rotors are coupled together, except for cross-compound designs where there may be two shafts driving two generators that are coupled electrically. The rotors rest in one or, more typically, two journal bearings. The journal bearings help hold the rotor in the proper radial position and provide support that will withstand the reaction from shaft rotation. Thrust bearings are typically located between the HP and IP and first LP sections in fossil units. They take axial thrust and hold the position of the turbine rotor axially relative to the stationary stages. Rotors are equipped with a turning gear to allow them to be turned during shutdown and startup to prevent thermal bending or warping caused by uneven cooling or warming.

This section briefly reviews the design features, materials of construction, and damage mechanisms pertinent to steam turbine rotors.

Overview of Rotor Design and Features

Three general types of rotor construction are shown schematically in Fig. 30.

In HP and IP turbines of fossil plants, rotors are ordinarily of the monoblock or welded construction. In nuclear units, the earliest HP rotors tended to be of monoblock construction, followed for a period of time by the use of shrunk-on construction. Most recently the trend has been back to monoblock construction in these machines [24].

Most commonly, because of their large size, LP turbines have tended to be the built-up (shrunk-on) design with an integrally forged shaft onto which disks are shrunk and keyed. However, all three types of rotor construction are in use in the LP rotors; Figure 31 shows, for example, a welded LP rotor.

Rotor Materials of Construction

Fossil HP and IP rotors. Rotors in the 1950s were made of 1 CrMoV (typical composition is 0.9 to 1.5% Cr, 0.7 to 1.5% Mo, and 0.2 to 0.35% V), prepared in open hearth furnaces (“C” grade). In the late 1950s, electric furnace steel making and vacuum deoxidation and degasing techniques led to improved quality and cleanliness (“D” grade). Some manufacturers use a

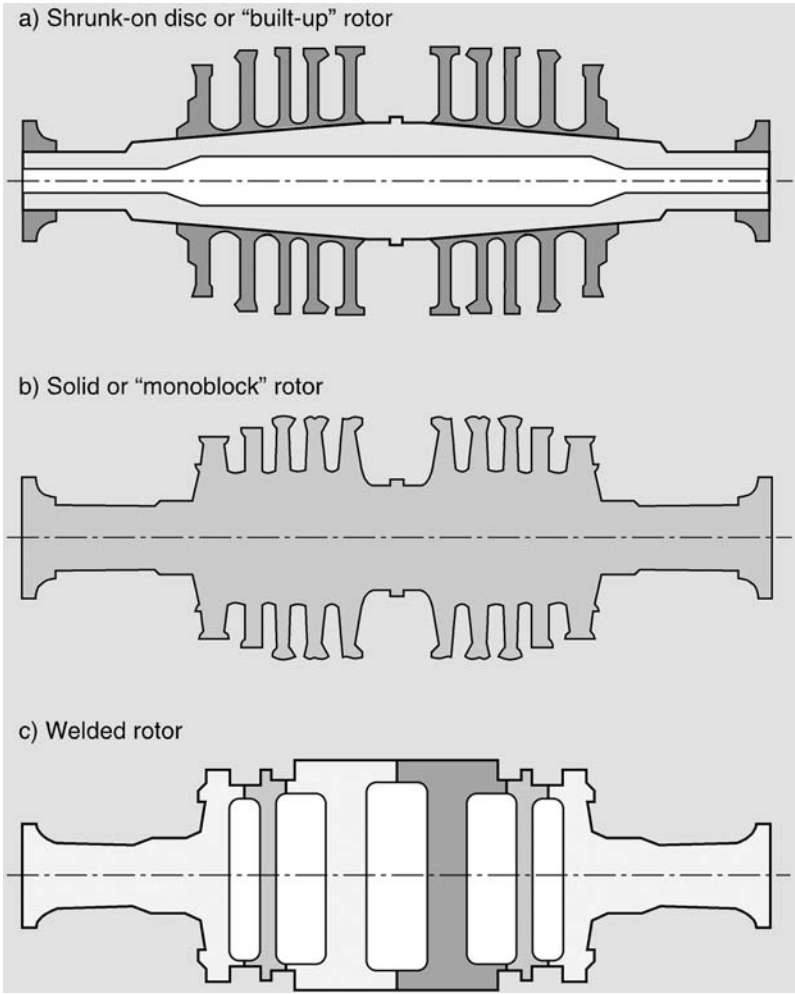

Figure 30 Typical low-pressure steam turbine rotor construction.

12% Cr steel (typical compositional ranges 10 to 12.5% Cr, 0.8 to 1.2% Mo, and 0.15 to 0.35% V) for more highly stressed rotors.

Fossil LP rotors. Fossil LP rotors are typically constructed of forgings conforming to ASTM A293, Class 2 to 5 or ASTM A470, Class 2 to 7 materials. Corresponding European alloys include 26 NiCrMo 11 5 (DIN 1.2726), 30 NiCrMoV 5 11 (DIN, 1.6946), or ~21 CrMoV 5 11 (DIN,

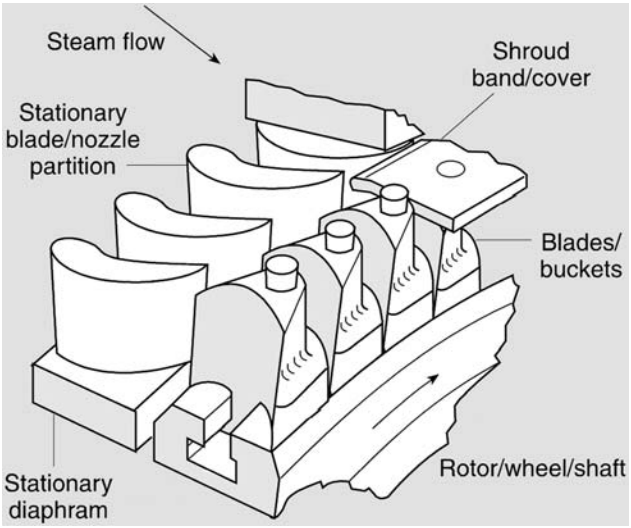

Figure 31 Schematic arrangement of stationary and rotating blades.

1.8070) [8]. LP rotors are mostly typically constructed of NiMoV or NiCrMoV materials, particularly 3.5 NiCrMoV. Shrunk-on disks, when used, are made from forgings of similar NiCrMoV materials, conforming to ASTM A294 Grade B or C, or ASTM 471, Classes 1 to 3.

Nuclear rotors. Nuclear HP rotors are also typically manufactured out of NiCrMoV materials.

Rotor Damage Mechanisms

Fossil HP and IP rotors. Damage mechanisms include creep, low cycle fatigue (thermal mechanical), creep-fatigue interactions, fatigue from rotating weight (''self-bending''), and embrittlement. Key areas of concern in the HP rotors of fossil fired units are the accumulation of damage at the bore and in other areas of stress concentration resulting from cyclic loading and elevated temperature operation. Stress concentrations of concern are bores, keyways, heat and seal grooves, locking slots, ventilation holes, fillets, and the blade attachments—tangential entry, triple pin, and axial fir-tree designs.

Early development of rotor forgings concentrated on heat treating the rotor to give maximum creep resistance. The material was austenitized at 1010 °C (1850 °F). This high creep strength was accompanied by poor creep

ductility and poor toughness, since as the creep-rupture strength increases, so does the fracture appearance transition temperature (FATT). More recently, toughness has been improved through changes in steel-making practices, alloy content, heat treatment, and increased steel purity. Maximizing creep-rupture strength has been relaxed in favor of improving creep ductility. However, creep cracking at the blade attachment areas continues to be a problem for many operators.

The range of service conditions of rotors has changed over the years. Under continuous service at temperatures up to 565 °C (1050 °F), creep damage was the primary threat to integrity, and considerable long-term (100,000 hr) creep data have been generated. However, as rotors have become increasingly subject to cyclic service conditions (load cycling and full startup/shutdown cycles), other potential damage mechanisms such as low cycle fatigue and creep-fatigue have been introduced. Startup and shutdown induce thermal stresses that become a maximum at temperatures substantially lower than those that occur at steady state. Fracture toughness becomes the dominant property in the resistance of the steel to brittle fracture.

Fossil and nuclear Lp rotors. Typical damage mechanisms for LP rotors are (1) low cycle fatigue cracking in the rotor bore, (2) high cycle fatigue cracking of the shaft, (3) stress corrosion cracking of discs in areas of condensation, especially in shrunk-on disks, and (4) stress corrosion cracking of the blade attachment areas.

Most of the potential problem areas on the LP rotor are in regions where stress concentrations are present. These stress concentrations may be further aggravated by erosion and/or pitting. Corrosion caused by chemical pitting at the surface of the rotor can lead to crack initiation and subsequent propagation by rotating bending fatigue (transverse cracking). High levels of concentrated bending stress can exist in the shaft beneath certain disks, during conditions of journal bearing misalignment.

The disk and shaft assembly of large LP rotors includes either keys or locking pins at each shrink-fit interface to prevent rotation of the disk relative to the shaft. Keyways are stress concentrators and provide interstices for deposition of chemical contaminants from the steam. Both of these factors are important in assessing the problems associated with disk cracking.

As with HP and IP rotors, the LP bores are highly stressed largely by thermal transients that can lead to low cycle fatigue damage. Unlike the high-temperature rotors, creep is not a factor because the maximum temperature of operation is below the creep regime, which simplifies evaluation. However, the older NiMoV and newer NiCrMoV steels are

more susceptible to temper embrittlement during service, even at the lower temperatures of operation.

Casings

Casing Design and Features

Turbine casings (or shells) must contain the steam pressure and maintain support and alignment for the internal stationary components. Casings are designed to withstand temperature and pressure up to the maximum steam condition.

Early designs of casings (prior to about 1963) were classic pressure vessel shapes with single-walled cylinders and hemispherical ends, together with a horizontal, bolted, flanged joint for access. The casings were designed to withstand steady-state pressure loads at high temperatures. Conservative design led to thick sections. As technology advanced, steam temperatures and pressures increased and more severe thermal transients were imposed on casings during startup, load changes, and shutdown. This led to the occurrence of fatigue, creep, and distortion.

Turbine casing design has evolved over the years and casings are now multiple pressure vessels (for example, an inner and outer casing in the HP and IP cylinder, or a triple casing), allowing smaller pressure differentials and realizing thinner wall thickness and sections. These thinner sections allow for lower temperature drop across the casing section and thus lower thermal stresses. The exhaust steam flows back along the turbine axis through the space between casings to allow for quicker warming of the turbine during starts. LP casings may also be of multiple part design with the inner casing containing the diaphragms supports and the outer casing directing the exhaust to the condensers.

Steam chests and valves were often integral to older turbine casings. Standard design practice now is to separate these components. However, the materials of construction and degradation of these components is similar to casings and, as a result, the methods for condition assessment of casings are also appropriate to steam chests and valves.

Casing Materials of Construction

In the 1940s casings were manufactured from C-Mo steels; by about 1947, CrMo and CrMoV steels were introduced to prevent graphitization. In the 1950s, the primary emphasis was on creep strength, and these early materials had poor creep-rupture ductility (and high notch sensitivity). High carbon levels were typical, as were relatively high contents of detrimental elements such as P, S, Sn, As, and Sb. Modern materials have strict controls on these

"tramp" elements to minimize temper embrittlement. Lower carbon and sulfur levels reduce the likelihood of hot tearing during solidification of the castings.

Common materials for HP and IP casings are $2\frac{1}{4}$Cr-1Mo, for temperatures up to 538 °C (1000°F), and $\frac{1}{2}$Cr-$\frac{1}{2}$Mo-$\frac{1}{4}$V, for temperatures up to 565 °C (1050 °F). For advanced steam conditions, modern HP and IP casings are often made of 9–12% Cr materials. In addition to ferritic steels, the Type 300 series stainless steels have been used for high-temperature applications. Castings are used in the higher-temperature HP and IP casings. In lower-temperature applications such as the nuclear HP shell, carbon steel castings may be used.

LP turbines casings, which are significantly larger in size and operate at lower temperatures, are typically either fabricated or constructed of fabricated and cast components. Materials that are structurally sufficient for lower temperatures such as carbon steel plate may also be used.

Casing Damage Mechanisms

Major casing damage mechanisms include (1) creep, (2) thermal fatigue (low cycle), (3) creep-fatigue interactions, (4) embrittlement, and (5) flow-accelerated corrosion. In the majority of failures, there is evidence of more than one damage mechanism.

Valves

Valve Design and Features

Valves control the flow rate of steam through the turbine. Key valves include

- Main stop valves. These valves primarily protect the turbine against overspeed, but may also regulate steam flow rate during startup. Stop and control valves regulate the flow of steam from the steam leads into the HP turbine [25].
- Control or throttling valves. These valves control steam flow rate during operation. During startup, control valves are used to govern turbine speed and acceleration.
- Intercept valves. Intercept and reheat stop valves are used between the boiler reheater and the IP turbine inlet. Intercept valves are used to prevent overspeed from the steam stored in the reheater and connecting lines in the event of a large load reduction [26].

Valving Options for Partial Load and Startup

Partial load operation is determined by the method of steam control and the turbine exhaust loss. There are three basic options for steam control: throttle control (single admission), nozzle control (partial admission), and variable pressure. In throttle control, the valves open together and progressively as the load increases [9]. In contrast, under nozzle control, valves are opened sequentially to full pressure. In variable-pressure operation, control is on steam pressure coming from the boiler.

Partial admission has the benefit of improved heat rate compared to throttle control. Two HP turbine blade damage mechanisms that may be exacerbated by partial-arc admission are solid particle erosion and fatigue.

An additional consideration is the thermal stress induced in the rotor as a result of the unit ramp rate. This rate is typically controlled by the change in first-stage shell temperature, which will vary with the type of admission used.

Valve Materials of Construction

Valve materials are similar to those used for turbine casings. To slow valve seat erosion, a wear-resistant material such as Stellite may be inlaid into the base material.

Valve Damage Mechanisms

Damage to turbine valves includes (1) breaking or jamming of the valve stem, (2) moisture erosion or wear, such as between the valve body and seat which can cause steam leakage, and (3) cracking of valve casings or housings as a result of thermal stresses. Turbine valves may be particularly sensitive problem items in cyclic plants.

Seals

Various seals are used to minimize leakage losses. Seal leakage is important as it is the largest single cause of performance reduction in HP turbines; IP and LP stages also suffer significant losses because of poor sealing.

Interstage Seals

These include seals to prevent leakage around the rotating and stationary stage. They are typically called diaphragm seals in impulse stages and undershroud/overshroud seals in reaction stages. They are generally of a labyrinth design.

End Seals

End seals or packing glands are used to minimize leakage at the ends of cylinders. They are intended to prevent air inleakage into the LP and condenser, and in the case of nuclear units employing boiling water reactors to prevent leaking of radioactive steam from the cylinders to the atmosphere. End seals are of the labyrinth design. There are typically several sections of end seals at the end of each cylinder.

Bypass Systems

Turbine bypass systems offer a variety of benefits, including the following:

1. Ability to match steam and metal temperatures during startups. A primary function of bypass systems is to permit sufficient firing rates in the boiler to achieve acceptable throttle temperatures and pressure while minimizing damage to ancillary systems (such as overheating of tubes). Bypasses are often considered in conjunction with moving from base load to two-shift or cycling operation as a means of reducing the thermal damage induced and to improve startups [26].
2. Use as relief valves during severe load fluctuations.
3. Operation as overload or bypass during turbine trips or when the turbine is run back to house load.
4. Operation as a boiler safety valve. Note that the ASME Boiler and Pressure Vessel Code, Section I, limits such use to once-through boilers with a minimum of two spring loaded valves.
5. Allows faster unit startups, thereby decreasing startup energy.
6. Provides cooling of all boiler components by providing fluid flow during all firing conditions.
7. Reduces solid particle erosion on turbine valves and blading by minimizing the carryover of oxide particles during startups.

Extensive surveys of bypass usage, operation, and design were conducted in the mid-1980s [11, 12]. Some of the results of those studies indicated:

1. The bypass system size is governed by turbine rotor diameter and thermal energy distribution in the boiler, as well as startup, loading, unloading, and shutdown practices.
2. A large bypass system, one capable of diverting at least 40% of the boiler's steam, is necessary to avoid boiler shutdown after a turbine trip at full load.
3. Systems diverting at least 15% of the steam enhance startup flexibility and load changing capabilities. These systems, sufficient

to match turbine component and steam temperatures, can reduce average startup time by 30 minutes.

Small Bypass Systems

The simplest bypass systems consist of a pipe and shutoff valve that can exhaust steam from the boiler to the condenser, bypassing the turbine. Such bypasses originate from one or more of the following locations [25]: primary superheater inlet, primary superheater outlet, secondary superheater outlet, or turbine inlet.

Small Bypass Systems with Division Values

A more complex superheater bypass systems adds a pressure-reducing valve (division valve) between the primary and secondary superheater, and secondary superheater and reheater steam attemperator valves. This permits bottling up, or shutting off, the boiler drum at high pressure during overnight outages while providing throttle steam to the turbine at reduced pressure. This conserves energy and supplies high-temperature steam at the turbine rotor by avoiding large temperature drops through the turbine inlet valves and control stage.

Large Turbine Bypass Systems

European power plants use large HP and IP/LP bypasses. The HP bypass line takes steam from the superheater outlet to the reheater, bypassing the HP turbine. The IP/LP bypass line takes steam from the reheater to the condenser, bypassing the IP and LP turbines. These types of systems accomplish the following objectives:

Steam flows through the reheater as well as the superheater, cooling the tubes.

Large bypass systems permit firing up the boiler to a minimum stable load before opening the turbine valves. Thus, the boiler can be operated at stable conditions and steam outlet temperatures can be controlled with the need to synchronize the turbine startup with the boiler startup.

Load rejections can be sustained without tripping the boiler.

This may allow for bypassing of exfoliated oxide during startup periods and thus reduce or eliminate solid particle erosion damage to the turbine.

This allows complete feedwater cleanup before admitting steam to the turbine.

Drains

Condensate can form during startup as steam contacts cooler metal surfaces, or during operation when steam and metal temperature differences occur such as with changes in load or steam conditions. The drain system removes the condensate from critical areas of the turbine, main and reheat piping, and gland steam piping to prevent water buildup and subsequent damage such as by water induction. Drains may be either continuous operation (such as those that ensure that condensate in the LP turbine is continuously removed during operation) or intermittent (such as those opened and closed automatically during startup). Drains are located at the low point of each piping system or turbine location. The removed condensate is returned into the steam cycle [28].

STEAM TURBINE BLADE PATH MECHANICAL DESIGN AND MATERIALS

Steam enthalpy is converted into rotational energy as it passes through a turbine stage. A turbine stage consists of a stationary blade (or nozzle) and a rotating blade (or bucket). Stationary blades convert the potential energy of the steam (temperature and pressure) into kinetic energy (velocity) and direct the flow onto the rotating blades. The rotating blades convert the kinetic energy into impulse and reaction forces, caused by pressure drop, which together result in the rotation of the turbine shaft or rotor.

Features and Structure of HP and IP Blades

HP and IP Rotating Blades

The blades in the high-pressure (HP) turbine are small because of the low volumetric steam flow. Basic features of the short blades typical of HP turbines are identified in Fig. 31. Rotating HP blades are usually straight; however, the use of leaned and bowed blades has recently introduced a three-dimensional aspect to designs. Shrouds (also called covers or connecting bands) provide a sealing surface for radial steam seals and are used to minimize losses due to leakage. Shrouds also tie the blades together structurally and allow for some control over the damping and natural frequencies of the blades. The shrouds are typically attached either by peened tenons or are integral with the blade airfoil.

Various methods of attaching both HP and LP blades to the rotor are used, depending on the manufacturer. Figure 32 shows the most common types of root attachments. The choice of type of attachment will

depend on a number of factors. For example, for one manufacturer, a side-entry fir-tree root design is used in the HP control stage for ease of replacement if required because of solid particle erosion For longer blades in the control stage, however, a triple-pin construction is sometimes used as the side-entry design has too many modes close to the nozzle wake frequency [8].

A particular challenge in HP blading design is the first (control) stage where operation with partial-arc admission leads to high dynamic stresses. Design factors such as choice of leading-edge configuration and blade groupings are chosen to reduce the vibratory stresses produced. Blades in IP turbines are very similar in design to those in the HP, with somewhat more twist (and most recently bowing and leaning) to account for greater radial variation in the flow.

Design of HP turbine blades in nuclear units manifest similar features as those in fossil units; for example, use of the same root attachment designs. HP blades in nuclear units are longer in order to handle the higher volumetric flows.

HP and IP Stationary Blades or Nozzles

In HP and IP turbines, stationary blades (or nozzles) can be classified into two general design categories: a wheel and diaphragm construction is used for impulse stages; the drum-rotor construction for reaction stages.

A nozzle or diaphragm, used in impulse stages, consists of (1) nozzles or stationary blades, (2) a ring that locates them in the casing, and (3) a web that extends down between the rotor wheels and supports the shaft packing. Figure 33 indicates the typical construction. Diaphragms in the HP and IP are typically of welded construction. In the control (first) stage, nozzles are divided into segments, arranged in separate nozzle ''chests'' or ''boxes'' and each segment has an associated control valve or control valve group [29].

In reaction stages, stationary blades or nozzles are manufactured in a manner similar to that for rotating blades with a root attachment and in some cases a sealing shroud. The blades are fitted by the root attachment on a blade carrier, which is located in the outer casing.

Nozzles and diaphragms are typically exposed to pressure differentials that bend them in the plane perpendicular to the turbine axis. These pressure differentials are highest in the HP, although the shorter blade length limits the bending stresses that develop.

The relationship between the stationary (nozzles) and rotating blades (buckets) in typical stages is shown in Fig. 31 and 34.

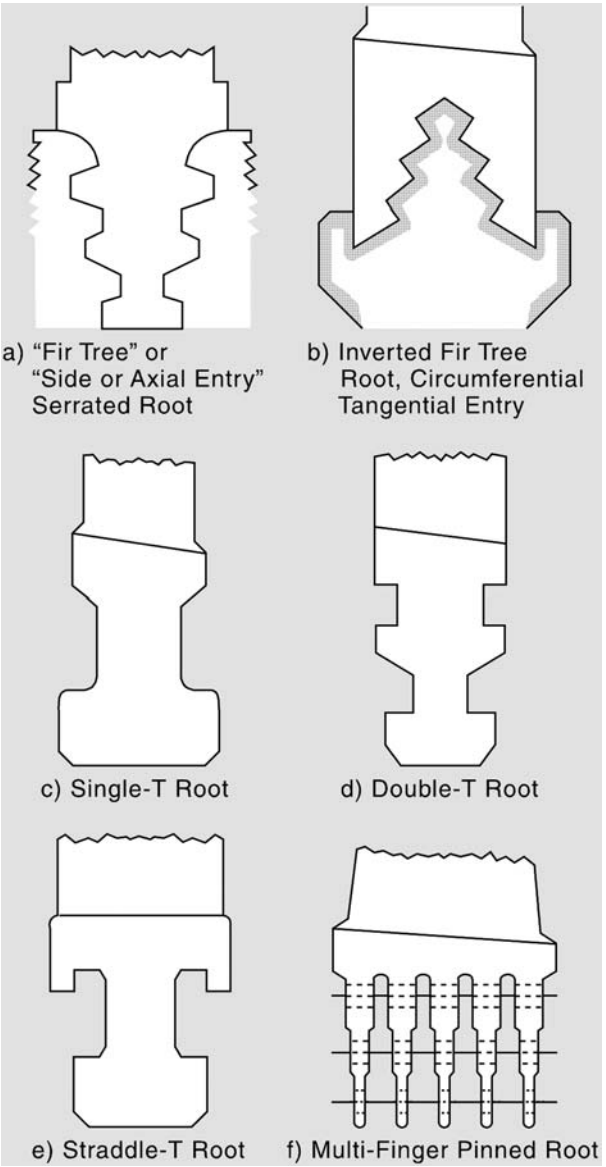

Figure 32 Steam turbine blade roots.

Features and Structure of LP Blades

Figure 35 shows the nomenclature for a rotating LP blade. Rotating LP turbine blades may be "free-standing," that is, not connected to each other in any way; they may be connected in "groups" or "packets", each comprising several blades (generally between 2 and 8); or all blades in the whole row may be "continuously" connected. Free-standing blades have the following characteristics compared to grouped blades: (1) they have less inherent damping at the blade tips; (2) their resonances are more easily defined (i.e., no mechanical interactions with neighboring blades); (3) they have more aerodynamic interactions; and (4) they are easier to install and disassemble, as there are no welds or rivets [30, 31].

In connected blades, there are a number of design choices. The connections may consist of shrouds (or bands) over the tips of the blades, or of tiewires (or lashing or lacing wires) located along the blade height as illustrated in Fig. 36. As with HP blades, connections made at the blade tip are termed shrouding. Shrouds may be inserted over tenons protruding above the blade tips, and these tenons then riveted down to secure the shrouds, or they may consist of integrally forged stubs in a welded or brazed-together assembly. Other types of riveted connections are also used. Tiewires may consist of either integrally forged stubs welded or brazed

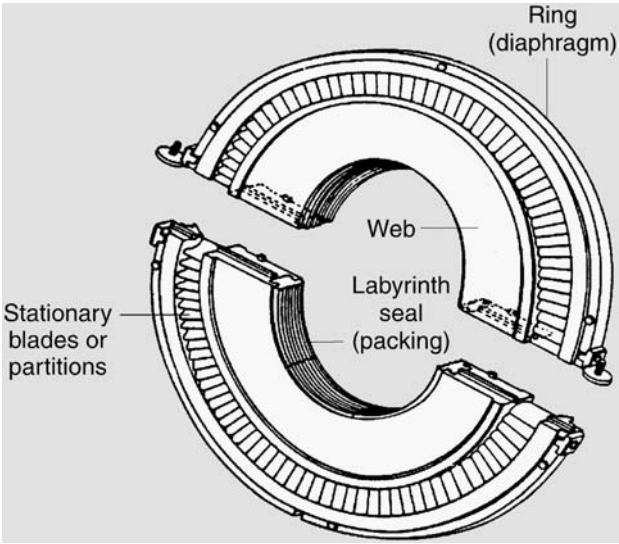

Figure 33 Steam turbine diaphragm construction.

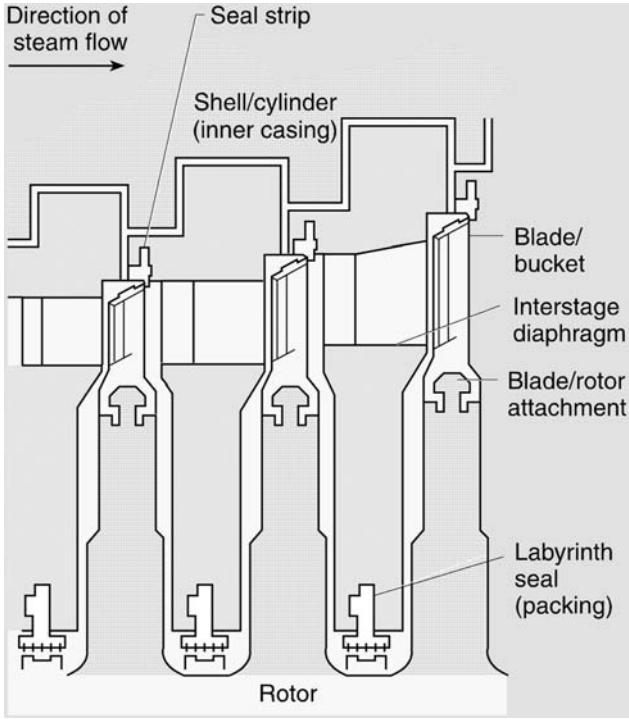

Figure 34 Cross-section view of three turbine stages.

together, or cylindrical "wires" or rods inserted through a hole (usually in a forged boss) in each blade foil [32, 33].

In order to add mechanical damping, some wire or rod-type lashing wires are left loose in their holes, and there are also some shroud-type connections that merely abut each other and are not permanently attached. Continuous connections must make some provision to accommodate thermal expansion of the connection. Shrouds and lacing wires sometimes are introduced to decrease vibratory stresses, but can act as "crud traps."

Blades are connected at the root to the rotor or disk by several configurations as shown in Fig. 32. The blade roots may be of the "serrated" or "fir-tree" configuration, inserted into individual axial slots in the disk or a similar serrated or T-shape, inserted into a continuous circumferential slot in the disk (this requires a special insertion gap), or may comprise one or several flat "fingers" fitting into circumferential slots in the disk and secured

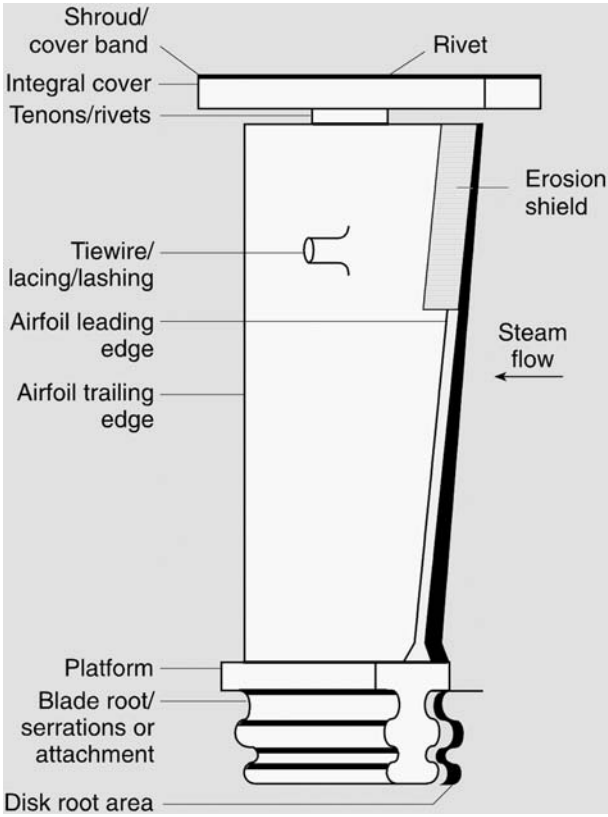

Figure 35 Low-pressure turbine blade (bucket) construction.

by axially inserted pins. Serrated or T-roots, furthermore, may be of male or female type.

The airfoil of blades may be of constant section and constant width for short blades, but twisted for longer ones. The longest blades for the last few rows of the LP are twisted, to match the aerodynamics at different radii and improve aerodynamic efficiency. Most recent designs have also begun to be leaned or bowed in both the radial as well as axial directions.

Nozzles or stationary blades in LP stages are typically arranged in diaphragms like those for HP and IP impulse stages. However, the construction may be simpler than those in the HP and IP, consisting, for example, of only fixed blades, constrained by inner and outer (hub and rim)

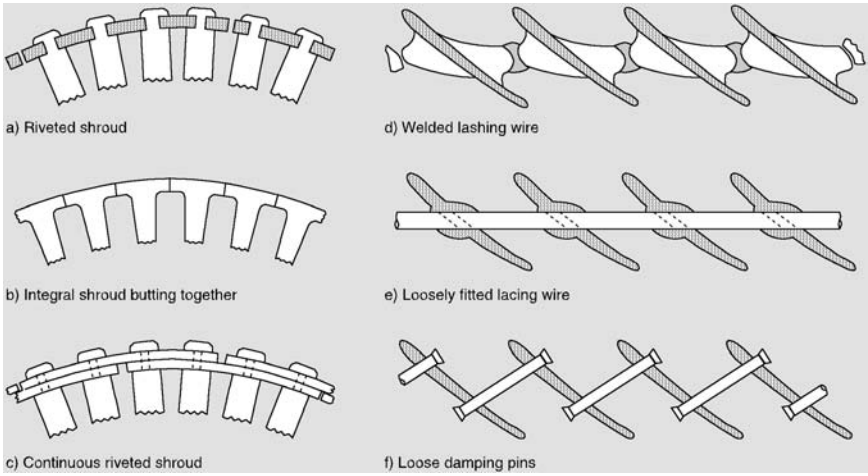

Figure 36 Interblade shroud and Tiewire blade construction.

annular bands. Diaphragms in the LP are of cast or welded construction. In wet stages, stationary diaphragms may incorporate hollow, perforated blade vanes or other design features as a means of drawing off moisture that would otherwise lead to liquid droplet erosion.

LP turbine blades in nuclear units show similar design features and materials of construction to those in fossil units. Nuclear blades are longer, reflecting the higher volumetric flows and slower speeds. Typically in fossil units, the maximum last-stage blades are on the order of 83 cm (33 in.) for stainless steel and 101 cm (40 in.) for titanium. In nuclear units, the corresponding lengths are 111 cm (44 in.) for steel blades and 135 cm (53 in.) for titanium. Because nuclear units typically operate at half the speed of fossil units (1,800 or 1,500 rpm versus 3,600 or 3,000 rpm in fossil units), the developed blade centrifugal stresses for both types of units are roughly equivalent by design.

Required Material Properties

Choosing the optimum blade material is an ongoing tradeoff between desirable material properties. Demands placed on HP and LP blades emphasize different material properties. In addition, it is important that

blading material be weldable, particularly last-stage LP blading, as many designs require that cover bands, tiewires, and erosion shields be attached by thermal joining. Weldability is also important for blade repairs. It is important to note that up to about 1990 welding of blades and rotors was considered ''impossible'' by many major manufacturers [33].

Creep Strength and Creep-fatigue Resistance. Creep resistance is important in the first two or three rows of the HP and IP turbines to resist elongation and accumulation of strain at the higher operating temperatures, particularly at stress concentrations such as at the blade-to-rotor attachments.

Tensile strength is required to withstand steady centrifugal and steam-bending loads. Corrosion resistance is important to maintain blade life in the turbine environment. Ductility is required for three reasons:

1. To allow localized plastic flow to relieve stress peaks and concentrations, which can occur in the local regions of complex geometries, e.g., at the blade root, and interblade connections such as lashing wires and shrouds.
2. To allow for rivet formation from blade tenons, which is required in many designs to attach shrouds to blades.
3. To provide for plastic deformation that can accommodate stress from a rub or impact of a foreign body and thus limit damage to a localized region instead of a brittle fracture followed by multiple consequential failures.

High impact strength will also help resist failure from sudden contact by foreign bodies such as a fragment from a failed blade.

Fatigue strength is important to prevent failures from the vibratory stresses imposed by steam flow and system resonances. In LP blades, even more important than simple fatigue strength is the resistance of the material to cyclic loads in aggressive or corrosive environments in order to avoid corrosion fatigue.

Notch Sensitivity. Notch sensitivity describes the effect of stress concentration on fatigue strength. Since blades have a variety of stress concentrations, low notch sensitivity is a desirable characteristic. There are, however, tradeoffs. Higher tensile strengths tend toward improved fatigue strength, but unfortunately, increasing tensile strength also leads to increased notch sensitivity. The practical implication is that the designer must balance the benefits of selecting a stronger material against the reduction of fatigue strength [34].

The influence of notch sensitivity can be determined from

$$F_s = \frac{S_e}{[q(K_t - 1) + 1]\sigma_a} \tag{12}$$

Where

F_s = factor of safety against fatigue.
S_e = endurance limit of material without stress concentration (adjusted for steady stress).
q = notch sensitivity factor ($0 \leqslant q \leqslant 1$) (compiled in standard references such as Peterson [34]).
K_t = stress concentration factor (>1).
σ_d = nominal alternating stress, disregarding stress concentration.

Damping. Damping is a primary consideration in blading design and operation. Analysis of damping is complicated by the number of factors to be considered including (1) the inherent damping of the blade material, (2) the effect of damping geometries such as tiewires or shrouding, and (3) the problems associated with defining the damping at the root attachment. At the root attachment, small differences in tolerances and clearances can make large differences in the actual damping capability [35–37].

There are three general means of damping vibrations in LP blading: material, mechanical, and aerodynamic.

1. **Material damping.** Material damping occurs as a result of crystal slip and distortion. It is an inherent property of the blade material depending on the dynamic stress amplitude, on preload (steady stress), and to a lesser extent on the temperature of operation and blade frequency of vibration.
   Material damping is described by Lazan's law as

$$D^* = \int D_o dV^* \tag{13}$$

   Where

   D^* = the damping energy dissipated within volume V^*.
   D_o = the energy loss per unit volume = $J\sigma_D^n$.
   J and n = materials constants.
   σ_D = the vibratory stress.

   Data on J and n have been obtained by many researchers and were summarized by Lazan. The validity of Lazan's law for turbine

blade materials has been demonstrated experimentally by Wagner, Gotoda, and Rieger [35–37].

2. **Mechanical or interface damping.** Mechanical or interface damping occurs by Coulomb friction. Mechanical damping arises from the relative motion (slip) between contacting parts such as damping pins, shrouds, and root cover sealing plates [39]. Friction values must be established from tests in actual turbines or accurate experimental simulations and not from simple laboratory tests [18]. Mechanical damping is the most widely applied form of damping and, as a result, in the careful selection of blade root connection, tiewires and shroud-tenon connections.
3. **Aerodynamic or gas dynamic damping.** Aerodynamic damping in the turbine rotating stage can be either positive or negative depending on the direction of the energy transmitted between the flow and the airfoil. Aerodynamic damping occurs as a result of work done on the gas stream (positive blade damping), or by the gas stream (negative blade damping) as it passes over the vibrating airfoil. In most cases, in turbine bladed disks, the aerodynamic damping is positive and constitutes a significant portion of the total damping available in the rotating stage, ranging from -1% to $+1\%$ of the total system damping. In contrast, tests have shown that material damping is insignificant. Mechanical damping can be as high as 2% if damping elements such as a "Z" shroud or snubber are used. If the aerodynamic damping becomes negative and, if the mechanical damping is low, the bladed disk becomes unstable.

This aero-elastic phenomena is dependent on the flow velocity and the vibration mode of the blade known as the "reduced velocity". Whitehead and Hall have developed computer programs to evaluate aerodynamic damping in the bladed disk. Using these computational fluid dynamics programs, aerodynamic damping can be evaluated quite accurately.

Erosion Resistance. HP and IP turbine blades can be subjected to erosion by solid particles. The particles are oxides exfoliated from superheater/reheater tubing and steam leads. The oxide scale grows as a natural result of the material's continued exposure to high temperature operation. For this reason, although this problem can be controlled, it typically cannot be eliminated completely from most units. This places a premium on the use of materials (either for complete blades or applied as surface treatments) that have good erosion resistance as a means of limiting the time-to-repair.

Similarly, LP turbine blades are subjected to liquid droplet erosion, especially in the last stages of the turbine. For both solid particle and liquid droplet erosion, there is a general trend that increased hardness of the target material (blade) within a given class of materials leads to improved resistance to erosion. Outside these general guidelines, however, the development of quantitative predictions of erosion resistance from basic material properties is still evolving.

Materials of Construction for HP and IP Blades

The most common material for HP and IP rotating and stationary blades and nozzles is 12 Cr martensitic stainless steel. Three generic martensitic stainless steels are widely used for turbine blading, most commonly Type AISI 422 for HP blading and Types AISI 403 and AISI 410 in LP blading. There are numerous specific application materials where turbine manufacturers have customized the generic grade by the addition or deletion of specific alloying elements, or by modification of the production or heat-treating process. The final properties of these steels are strongly influenced by tempering temperature.

Austenitic stainless steels (AISI series 300) are used in some high-temperature applications [42]. An example is Bohler's Turbotherm 17 13 W (a 16 Cr–13.5 Ni variety). Austenitic stainless steels have excellent mechanical properties at elevated temperatures and are typically readily weldable. There is a thermal expansion coefficient difference between martensitic and austenitic stainless steels so that care is required when designing attachment clearances for fitting austenitic blades into martensitic disks. Also there is a potential for stress corrosion cracking when 300 series stainless steels are used in wet-steam conditions.

The rings and webs of HP and IP nozzle diaphragms are commonly manufactured from stainless steels, although if the working steam temperature does not exceed 350 °C (660 °F), then welded diaphragms can be made from carbon steels.

A number of superalloys have been investigated for use in blading, particularly for combustion turbines, primarily because of their high-temperature tensile and creep strength. However, these materials have typically not been used in steam turbines due to their higher manufacturing costs.

Materials of Construction for LP Blades

Early LP blade materials included cartridge brass (72 Cu, 28 Zn), nickel brass (50 Cu, 10 Ni, 40 Zn), and Monel (typically 66 Ni, 31 Cu, 1.3 Fe).

With the advent of larger turbines in the 1920s, a 5% Ni steel became commonly used. Since the 1930s, most LP turbine blades have been manufactured from a 12% Cr stainless steel; typically Type AISI 403, 410, or 410-Cb has been chosen depending on the strength required. Types 403 and 410 have better corrosion resistance than Type 422, an important characteristic for use in the wet stages of the LP turbine.

There are numerous specifically customized versions of these generic materials, for example, Carpenter H-46 and Jethete M152. Jethete M152 has higher hardness and is thus more resistant to liquid droplet erosion in the LP than Types 403 and 410. So far it has only been used in LP turbines, but could be used in the HP and IP if needed. European designations for 12% Cr blading alloys include X20CrMoV121 and X20Cr13.

More recently the precipitation-hardened stainless steel designated 17-4 PH (AISI 630) was developed by one manufacturer for the last blades of the LP turbine in the largest 3,600 rpm machines. It has a nominal composition that is 17% Cr, 4% Mn, and 4% P. The hardening temperature can control a wide range of mechanical properties. Alloy 17-4 PH is somewhat difficult to weld and requires postweld heat treatment. Other precipitation hardened steels that have been investigated for blade construction in Europe include 15-5 PH (European designation: X5CrNi-MoCu145) and 13-8 PH (designation: X3CrNiMoAl1382).

Titanium alloys, chiefly Ti-6Al-4V (6% aluminum and 4% vanadium), have been used for turbine blades since at least the early 1960s. The use of titanium in the last few rows of the LP offers a number of advantages over other materials:

1. Titanium has about half the density of 12 Cr steels, which allows for longer last-stage blades without an increase in centrifugal stresses in the blade and thus an increase in annular area and improved turbine efficiency. The capability of LP turbines to produce power is limited by the long last row of blading and the strength of the rotor to support the blades. The practical limitation for blades constructed of 12% Cr martensitic steel was reached with 840-mm (33.5-in.) blades operating in 3,600 rpm machines and 1,200-mm (48-in.) blades operating in 3,000 rpm machines. In contrast, titanium offers an opportunity to go to 1,000-mm (40-in.) and 1,350-mm (54-in.) blades for 3,600 rpm and 3,000 rpm machines, respectively. This represents a marked increase in power and makes possible a new generation of LP steam turbines [47].

2. Titanium has particularly favorable mechanical properties in applications involving high stresses at low temperatures. Because titanium has half the density and about half the elastic modulus of steel, the natural vibration frequencies and mode shapes of titanium blades are very similar to

those made of steel. Note, however, that the elastic modulus is dependent on the particular titanium composition.

3. Titanium has greater corrosion resistance and as a result may have better performance in dry/wet transition-phase regions of the LP.
4. Titanium also has excellent resistance to impact and water droplet erosion damage and, in many applications, can be used without erosion shields.

The drawbacks to titanium include:

1. Higher cost than steel, even though titanium's lower density means that more blades can be manufactured for a given mass of material, which somewhat offsets the higher cost per pound of the material.
2. More difficult to machine.
3. More difficult to weld. Titanium requires a high state of cleanliness and an inert welding atmosphere.
4. Poor resistance to sliding wear, which can allow fretting corrosion in some conditions, although fretting has not been found to be as much of a problem as was once anticipated.
5. Lower internal material damping than stainless steel.
6. Finally, a disadvantage of titanium for blades is that recent high cycle fatigue studies have shown an endurance limit in air and in steam smaller than for 12% Cr stainless steels. However, shot peening has been successfully used to restore the fatigue life lost after machining, production, or repair processes.

Duplex stainless steels are those stainless steels that contain very high levels of chromium and about equal amounts of ferrite and austenite. They have been evaluated for use for LP blading, primarily in Europe. There are a variety of duplex stainless steels with ferrite contents ranging from about 45–75%. The composition of an alloy produced in the United States (Ferralium 255) is the same as the composition of a European alloy (X3CrMnNiMoN2264). The duplex stainless steels have excellent corrosion fatigue properties. Their primary drawback for blading may be somewhat lower yield strength than Type 403/410 (in general, although the specific properties for the Ferralium alloy indicate that good yield and tensile strength can be achieved) and they do show some long time service embrittlement at temperatures above 300 °C (570 °F).

STEAM TURBINE BLADE PATH DYNAMICS AND AERODYNAMICS

Figure 37 illustrates the primary factors that affect blade life in both fossil and nuclear units: stresses, the environment, and the material properties. Loading on rotating blades includes both steady-state loads (centrifugal and steam pressure loads) and dynamic loads (nonsteady steam forces, nozzle wakes, recirculation, etc.). The steady and dynamic stresses produced are determined by the nature of the loads. The level of dynamic stresses is also determined by the structural stiffness, frictional dampening, mass properties of individual blades, and groups of connected blades.

Turbine Blade Design Dynamics

The steam environment imposed on blades and connections can have a major detrimental effect on the blade life. This occurs through the transport and concentration of steam impurities. Similarly, the choice of material and key properties such as fatigue strength, yield and ultimate strength, corrosion fatigue strength, and material damping characteristics will affect the expected lifetime of the blade in service [32].

Many of the most serious damage mechanisms in blades occur in the phase-transition zone (PTZ) where the expansion and cooling of steam leads to condensation. This region typically starts in LP turbines around the L-O or L-1 rows in fossil units and around the L-3 to L-6 rows of nuclear units. In addition to operating in the most severe environment in the turbine, blades in these rows are also typically subjected to the highest stresses. As a

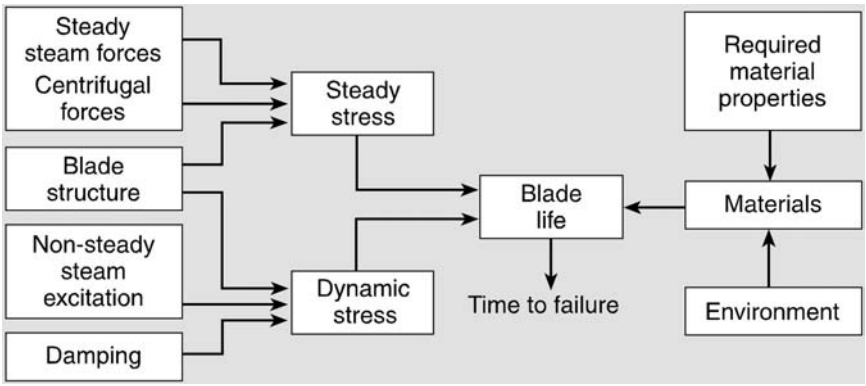

Figure 37 Stress, operational, and maintenance effects on steam turbine blade life.

result, significant attention must be paid to understanding how these effects develop and how their interactions lead to steam path damage.

Analysis of the actual stress state in a blade is complicated by a number of factors. In fact, until about 20 years ago, turbine blades were designed primarily by extrapolation from prior field experience and laboratory tests, and, as vibratory stresses could not be accurately determined, blade strength was based primarily on calculated steady stresses [31]. Dynamic stresses are complex and usually require verification by aerodynamic testing. The analysis of blade stresses is complicated by the geometric complexity (tapered/twisted configurations and asymmetric sections) and the interactions of the various modes of damping (material, frictional and aerodynamic) in the blade.

Blade designs represent an ongoing compromise between aerodynamic design, thermodynamic efficiency, and structural reliability. A primary concern is vibration, which can induce significant damage over a short period. Vibration can be either synchronous or nonsynchronous. In simplest terms, loads are synchronous when the blades are exposed to the same dynamic forces during each rotation and the excitation frequencies are integral multiples of running speed. Unsteady (nonsynchronous) steam flows that cause excitation forces that result in frequencies that are not multiples of the running speed are termed nonsynchronous.

It is important to understand the accuracy to which the various stress contributions can be determined. Centrifugal stresses are usually the major load and are typically accurately known as a function of speed (within 1%). Aerodynamic (steam) loads are often much smaller and depend on stage power output; they are typically known to within 2–5% [34]. As a general rule, steady loads can be defined to within 2–5% of actual values.

Dynamic loads are much more difficult to predict. Measurements of blade excitation can be made in the low-pressure turbine directly using strain gages, or indirectly by measuring pressures with a pitot tube. However, it is difficult to make measurements on high-temperature/pressure rotating blades at operating conditions. As a result, experimental determination in the laboratory has been most commonly performed using air turbine tests and water table studies [31, 53, 54]. In water table studies, the water flows radially outward, passing first through a stationary row, then through a rotating row of blades. The height of the water table flow is proportional to the steam pressure in an operating turbine and thus can be related to the forces of excitation on the rotating blades.

The probable accuracy with which nonsteady forces can be predicted from laboratory tests is between 20–40%. Excitations arising from nozzle wakes, diaphragm vane spacing errors, and partial-arc admission have all

been addressed using the water table approach and, in some cases, have been verified in the field.

These various estimates of accuracy pertain to both fossil and nuclear turbine blading.

Turbine Blade Stresses

There is a myriad of static and dynamic stresses and loads on turbine blades, particularly the longer blades of the LP turbine.

Blades in nuclear and fossil turbines are mostly affected by the same types of stresses; further, the magnitude of the stresses tend to be about the same. Blades in nuclear units are longer, but the machines typically rotate at 1,500 or 1,800 rpm instead of 3,000 or 3,600 rpm, and thus the magnitude of the centrifugal stress (the highest magnitude blade stress), by design, is about the same.

Centrifugal Stresses

Centrifugal loads, caused by rotation, are the primary source of stress on blades. The centrifugal loads on HP and IP blades are relatively small as the blades are short and the diameter small because of the relatively low volumetric flows. In contrast, as a rule of thumb, in typical last-row LP turbine blades (unshrouded), the steady stresses will be roughly 0.5 S_y over about half the blade airfoil length, and in excess of 0.25 S_y over about 80% of that length, where S_y is the yield strength of the material. Figure 38 shows a typical distribution of centrifugal stresses and the benefits associated with the use of titanium (because of its lower material density).

Centrifugal stresses are generally proportional to the square of the speed, i.e., a 120% overspeed will produce a 1.44 times increase in the centrifugal load. As a result, during overspeed tests, the centrifugal stresses on a blade can increase to as high as 75% of the material's yield strength [38, 39]. See Figure 38.

Centrifugal stresses can also have a dramatic effect in those locations where there are stress concentrations such as in the root attachment and at tiewire holes. For example, in the blade root, where stress concentrations are high, design steady stresses are lower than the aforementioned maximum, perhaps in the range of 0.2 to 0.4 S_y. However, during startup, dynamic centrifugal stresses near to these stress concentrations can exceed the yield strength. Also, actual stresses are strongly influenced by the local geometry. For example, in those designs where multiple hooks share the load, variations in the gap between blade and disk in the root attachment can lead

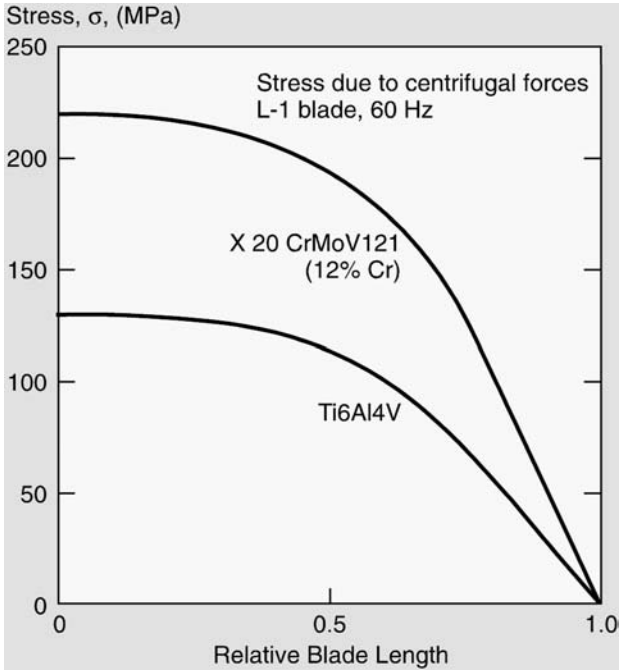

Figure 38 Centrifugal stresses on a steam turbine blade airfoil.

to a wide variation in actual stresses. This is discussed in more detail below, in the section on manufacturing and assembly stresses.

High mean stresses, such as those induced by centrifugal loads, have a pronounced detrimental effect on the fatigue strength of high-strength materials such as blading alloys.

Geometric Untwisting

Centrifugal forces can induce untwisting of the blade. Such a shape change causes direct blade stresses, changes the blade's natural frequency, and causes flow geometry distortion. This loading, and the next, centrifugal bending, affect longer blades of the LP turbine much more than blades in the HP or IP turbine.

Centrifugal Bending Stresses

This stress component arises when the cross-section centroids at different blade heights do not fall on the same radial line. Especially in long blades, designers typically use this effect to help offset the steam-bending stresses, as illustrated in Fig. 39.

Steam-Bending Loads

Both steady-state and dynamic bending loads are induced on the blade as a result of the flow of steam within the blade path. Steady steam-bending loads are discussed here, the effect of nonuniform flows in the next section. Steam-bending loads are important in both HP/IP and LP blade design.

Steady steam-bending stresses in the blade airfoil are typically low, less than 10% of the centrifugal stresses in rotating blades. In the lashing wires, steady steam stresses may be several times higher than in the airfoil because of stress concentration effects, but the centrifugal stresses are lower.

A method for calculating steady steam-bending forces in rotating blades has been reported by Hong *et al*. [60, 62, 63] based on a streamline curvature method. Values of the thermodynamic and aerodynamic properties of the steam as it moves through a stage are calculated and then used to evaluate static pressure and velocity distributions, which are in turn used to determine the steam-bending forces in both axial and tangential directions.

Steady steam-bending stresses can significantly affect stationary blades or diaphragms as the differential pressure across the section tends to try to bend them in the axial direction; this effect is greatest in the HP turbine, where interstage pressure differentials are the highest, particularly in impulse designs. However, because the blades are shorter, the maximum stresses may not occur in stages with the highest pressure differentials.

Synchronous Resonance of a Blade with a Harmonic of the Unit Running Speed

A primary goal of blade design is to tune the longer turbine blades away from multiples of unit running speed (harmonics). Blades typically have a sharp frequency response, typically the bandwidth being on the order of $\pm$ a few Hz, and thus virtually no vibrational amplitude unless the exciting force is relatively close to, or at, a resonance frequency. Thus, even a nominal degree of tuning off resonance by 3 to 5 Hz for lower modes (less than 300 Hz) can dramatically reduce the dynamic stresses that develop. If such tuning is not performed, high cycle fatigue failures caused by resonance can occur within a relatively short period (several weeks to less than a year). A

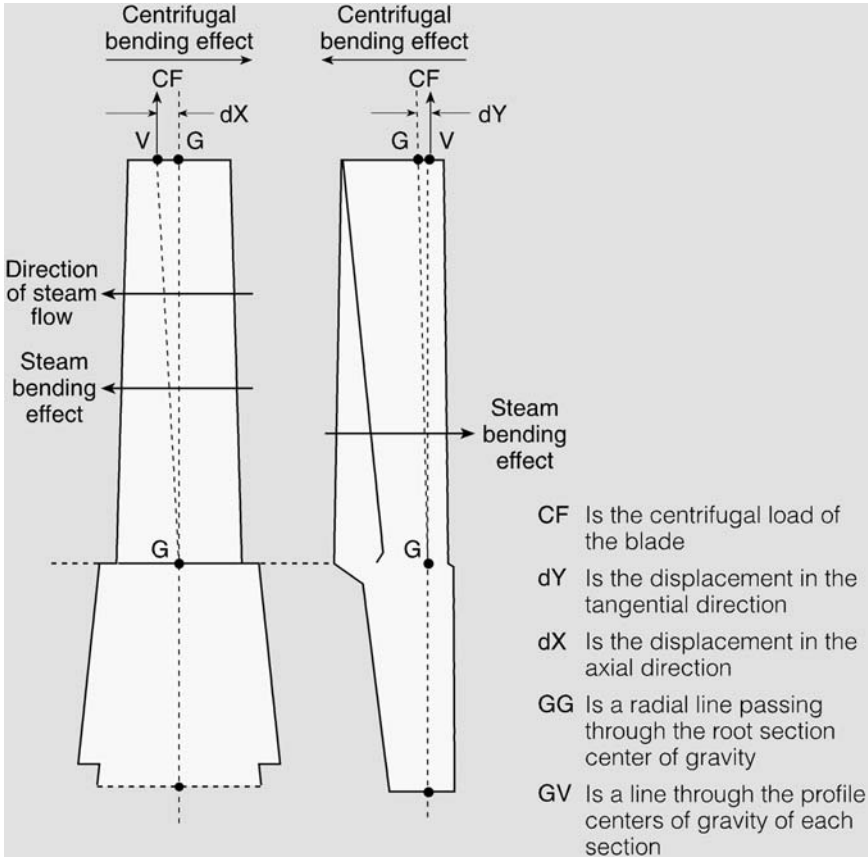

Figure 39 Centrifugal bending stresses on a rotating turbine blade.

3% margin is typically used in tuned rows to allow for scatter from installation, manufacturing, and materials [63].

Unsteady Nonuniform Flows

A variety of sources of nonuniform flows leads to dynamic (and either synchronous or nonsynchronous) stresses on all turbine blading. The following are a list of some of the most common sources of nonuniform flows:

1. Nozzle-wake interactions and other nonuniformities produced by stationary blades. Nozzle-wake interactions are the aerodynamic force

fluctuations seen by a rotating blade as it passes each stationary blade or traverses each stationary blade pitch They are among the most pervasive sources of synchronous excitation in steam turbines. They occur at the nozzle passing frequency and its harmonics. Key contributors to nozzle-wake excitations occur from [46]

Viscous wake caused by the presence of a boundary layer.

Trailing-edge thickness. A turbulent wake is formed by the passage of flow past a stationary blade. There is a design tradeoff pertaining to the thickness of the blade's trailing edge. Too thick leads to increased wake, while too thin is difficult to manufacture and has unacceptable strength levels.

Separation wake caused by premature separation of the flow before reaching the trailing edge. These wakes can be caused by inadequate design or by operating at off-design conditions and can lead to a larger wake with potentially large flow fluctuations.

Nonuniform deposits on blade airfoil surfaces can trip boundary layers.

Shock waves and expansion waves. Shock waves can be formed when supersonic velocities are reached in the stationary blade passages. Another flow condition that can result in an unsteady flow is the formation of a choked, underexpanded jet. This latter condition can cause excitation in the passing rotating blade as well as disturb the flow through the rotating blade rows.

Wave reinforcement. It has been proposed that reinforcement of waves bouncing between rotating and stationary blades in the same stage may occur leading to increased wave amplitudes and corresponding blade vibrations [66].

Moisture impingement. The impingement of moisture coming off stationary blades and hitting the rotating blades can result in forces on LP blades (as well as erosion) and thus induce vibration.

Of these sources the first three (viscous wakes, trailing-edge thickness, and separation wakes) affect HP, IP, and LP turbine blades. The last three (shock waves, wave reinforcement, and moisture impingement) occur in LP turbines.

Figure 40 shows one example of these types of nonuniform flows. The figure illustrates the variation of the steam force across the discharge from a fixed blade row that will result in nonuniform loading on the passing rotating blades.

2. Spatially nonuniform flows caused by geometric asymmetries. This category includes nonuniform pressures, velocities, or angles of flow

onto the rotating blade. These can be caused by asymmetry of major geometrical features, such as

Partial-admission or sequential arc operation. Partial-arc admission is utilized to minimize throttling losses in the HP control valves and thus improve heat rate at low-load operation. The blades experience asymmetric (stepwise) load transients as they move in and out of steam admission arcs. Details of such loadings were first obtained by Kroon [68]. This problem is typically a major source of excitation in some small turbines and in the high-pressure control stage of large turbines.

Figure 41 illustrates the effect as determined from water table testing. The stationary row was set up to allow flow through a limited number of open arcs (shown by the shaded arcs in the left side of the figure). The water table blade response curve (right side of Fig. 41) is indicative of the response of the rotating blade of an operating turbine under partial-admission conditions. The key observation is the periodic stimulus applied to the blade as it passes the open arc.

Pigott and Warner found that the effect of partial admission could be divided into shock and a nozzle-wake component and the separate effects superimposed to determine the combined vibration response.

The pressure differences across the first (control) stage between areas of open and closed arc can be as high as 100–200% of the nominal stage pressure (Fig. 41). The results of a finite-element-based numerical analysis found that operating in the 1–2 mode (valves 1 and 2 were open) led to steady steam-bending stresses that were approximately 2–4 times higher than in the 1–2–3 or full-admission mode. As a result, in this instance, a

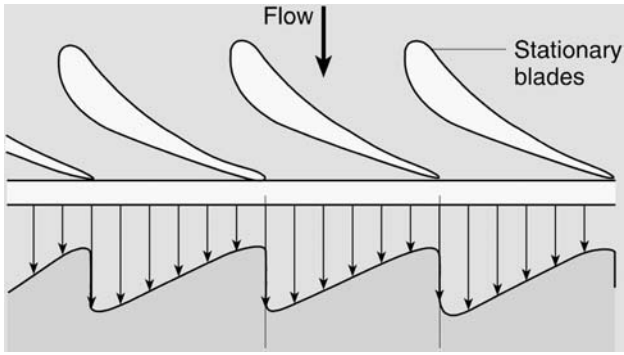

Figure 40 Steam turbine pressure and force variations exiting from a stationary blade row.

recommendation was made to minimize the amount of operating time in the 1–2 mode. It should be noted that this was a precautionary measure, as it was also indicated that the stress increase was probably not sufficient by itself to cause crack initiation by high cycle fatigue [51].

Sanders [67] has suggested that the stress effects of partial-arc admission are applicable for any active arc less than 96% of full arc.

Flow bending at radial inlet and exhaust of steam. Radial inlet and exhaust of steam at a turbine element require turning of the flow and thus can cause circumferential pressure or velocity nonuniformities.
Steam extraction paths.

3. Unsteadiness in the flow passages. Flow perturbations can be introduced by unsteadiness in the stationary flow passages, including

Acoustical resonances in inlet passages, extraction lines, or other cavities excited by flow past them
Vortex shedding from stay-bars, etc. [52]
Unsteady flow separation from stationary blades
Unsteady shocks in choked stationary blade passages
Surface pressure fluctuations caused by impingement of turbulent flow onto rotating blade shrouds, disks, etc.
"Edge tones" or other acoustical noise generation phenomena

4. Flow over rotating blades can also induce unsteadiness such as by

Boundary-layer pressure fluctuations

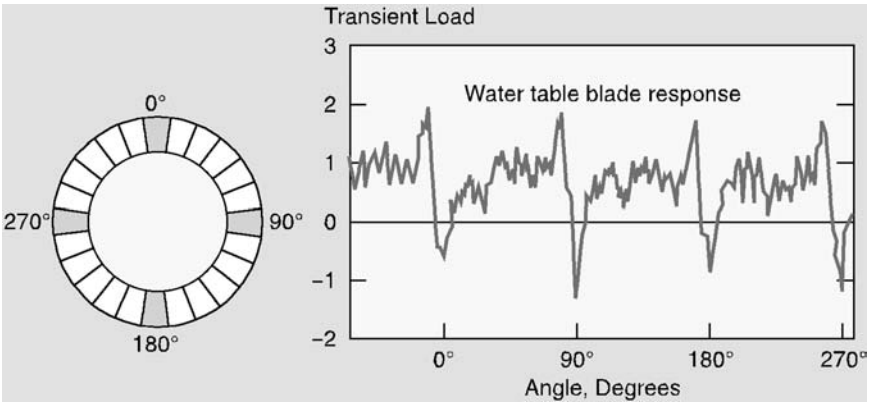

Figure 41 Transient forced load response on rotating blades as a function of turbine arc of admission.

Vortex shedding from blade trailing edges, causing unsteady aerodynamic force

5. Per-revolution diaphragm harmonics can result from dimensional imperfections in the flow passage geometry, particularly from variations in nozzle throat dimensions.[3]

6. Other structural features. Flow disturbances can also be caused from structural features (other than from stationary blades) such as (1) staybars (struts) in the inlet chamber and in exhaust hood, (2) moisture removal slots, and (3) axial or radial spacing between seal ends or stationary blade shroud ends.

The term "stimulus" is used to describe unsteady blade loading. Stimulus is the ratio of the blade unsteady loading amplitude at a given harmonic to the steady component magnitude.

Blade Vibration Induced from Rotor or Disk Torsional Vibrations

Several potential sources of blade vibration can be induced through the attachment to the rotor or disk. The vibrational modes created by the interaction of the disk mass/stiffness and blades must be taken into account to clearly identify all potential resonance modes, particularly for shrunk-on or flexible disk constructions. The lower-frequency torsional resonances in the shaft do not generally interact with blades; however, the higher frequencies, particularly the frequency at twice the power system frequency, can be a significant problem. These loads are typically in the range that interact with the natural frequencies of the longer (tuned) blades of the LP turbine.

Blade–disk Interactions. Blade and disk vibrations can be strongly interconnected. If this coupling action occurs, resonance conditions are not well predicted by the traditional methods of plotting blade frequencies versus machine frequencies, e.g., Campbell diagram [53–71]. Lam *et al.* provide a procedure for analyzing blade–disk response and a case study comparing the results of an analysis of a blade group versus a blade–disk analysis. The most important result of that analysis was that significant differences did exist between the blade–group and blade–disk models, particularly when predicting axial and torsional modes of vibration.

System Disruptions Leading to Rotor Torsional Modes. Rotor torsional vibrations can be excited by electrical faults in the distribution system. These torsional vibrations can lead to considerable damage to the rotor and blading and have led to a number of blade failures in the power industry [55]. The turbine generator system may respond to subsynchronous, synchronous, or supersynchronous (typically two times the running speed, e.g., 120 Hz for 60-Hz turbines) frequencies.

Design of pre-1975 machines typically evaluated the potential for synchronous vibrations, but were not designed for frequency resonances equal to two times the running speed. These resonances occur as a result of load imbalance on the three phases which can induce secondary currents in the generator stator. These stator currents, termed "negative sequence currents," cause an alternating torque to act on the rotor system at twice the transmission grid frequency of 60 Hz. Sources of such load imbalance can include: cutoff of load, line accidents, subsynchronous resonance, or a short in the generator terminals [73, 74].

Torsional modes near this frequency tend to be highly coupled to disk–blade modes and, as a result, considerable high cycle fatigue damage can be imparted to LP blades, particularly in the last stages, from the phenomenon illustrated schematically in Fig. 42. Failures caused by this mechanism have been reported in fossil units and in nuclear units.

A number of researchers have reported on the analysis of disk–blade interactions, specifically related to avoiding unwanted resonances (see, for example, Refs. [55–63]). The aims of such analyses are to evaluate blade and disk dynamics and to avoid resonances with the electrical grid frequency. Two examples illustrate the typical methodology.

Higuchi and Tsuda performed a torsional vibration analysis of the LP turbine in a 1,160-MW nuclear unit; of particular concern were frequencies near 120 Hz. They found as many as 45 torsional natural modes in the frequency range below 180 Hz. The natural modes included fundamental modes, higher modes of the shaft, and blade–shaft interactions. Torsional modes above 70 Hz were mostly caused by coupled effects between the blade, shaft, and disk. Field tests measured the blade induced vibrations caused by short circuits induced at the generator terminals and concluded that, in this case, the blades of the L-0 row were tuned well away from 120 Hz.

Reid provided a detailed case study that evaluated coupled blade–rotor torsional vibration in anticipation of a major low-pressure blade retrofit. That analysis analyzed the natural frequencies and response stresses for a system that included a combined HP, IP and two LP turbines along with a generator and exciter. Bladed disks were modeled as branch elements. The model developed was confirmed using impact or "bump" testing on the

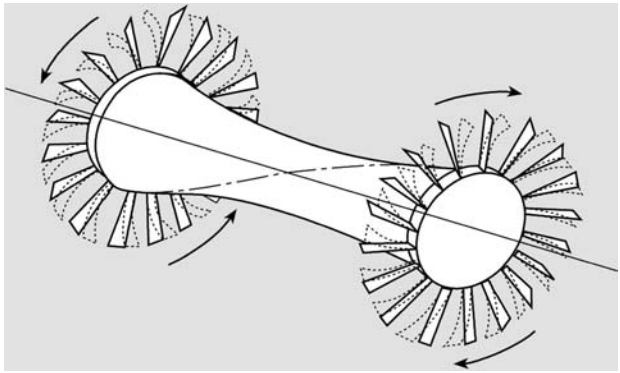

Figure 42 Torsional coupled vibration of a turbine rotor/blade.

rotor with and without blades. It was important that impact test data be obtained for all blades with interactions in the frequency range of interest. For fossil units, this is typically the L-0 stage only; in nuclear units, the last three rows are typically required. Following a redesign and retrofit of the L-0 row, field torsional testing was done using a system transient bump test. The test was used to detect torsional modes around 60 and 120 Hz. The test was performed by manually synchronizing and tripping the machine and measuring the resulting noise spikes A single-phase ramp test was also used to excite the system at double-line frequency [73].

There are considerable differences in torsional stiffness of the various rotor disk designs, such as monoblock, shrunk-on disk, and welded construction, and as a result of these differences, in the torsional response characteristics of each, particularly in the higher torsional modes.

Over- and Underfrequency Operation. Prolonged operation at small variations from 60 Hz (islanding) can cause increased dynamic loading on tuned blades. Figure 43 shows a composite of the limits on frequency operation from five manufacturers. The figure shows that operation in the range 59.5–60.5 Hz would not affect blade life, while outside this range blade life will be affected. Note that this figure indicates worst-case allowable times at particular operating levels; specific turbines may not have such restrictive values [81, 82].

Self-Excitation

Three primary types of self-excited turbine blade vibration phenomena have been defined: stall flutter, unstalled flutter, and unsteady condensation shocks.

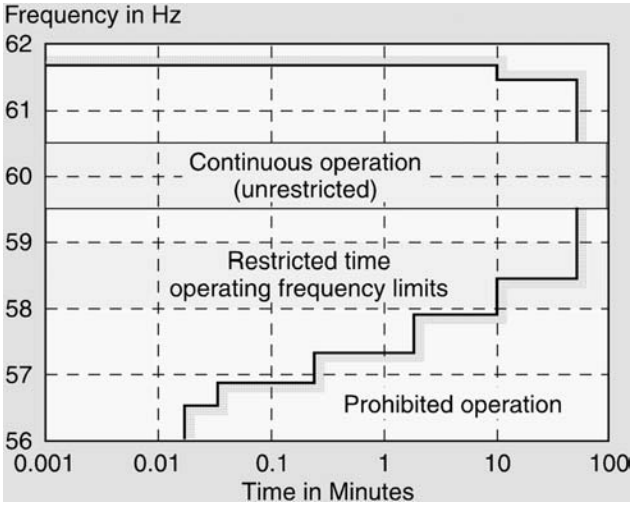

Figure 43 System frequency limitations versus maximum turbine operation time.

Stall Flutter. Stall flutter is similar to the well-known "stall" of an airplane wing. In steam turbines, it occurs in the last row of LP turbines at low load and high back pressures when the blades experience a negative angle of attack at least over the upper portion of their length. This condition is illustrated in Fig. 44, where the angle of attack approaching the rotating blade is shown for normal operation (velocity vector labeled V_2) and, in contrast, for off-design or low-load conditions (velocity vector labeled V_2 off). A region of stall can form on the trailing side of the blade as shown in the figure and will result in a form of unstable vibration termed stall flutter. Stall flutter is a serious potential cause of blade damage as a considerable number of cycles can accumulate in a very short period of time, leading to blade failure by high cycle fatigue.

Investigation of stall flutter has a long history including fundamental work by Sisto in the early 1950s [83]. Flutter is an aeroelastic instability that occurs when energy is exchanged between the fluid and the structure in a manner that creates self-excitation. Flutter is limited only by the damping capability of the blade material and the structural damping. Stable flutter can occur only when the aerodynamic power flow to the blade is equal to or greater than the dissipative power of the blade and structure. As it is difficult to measure or calculate structural damping, a conservative analysis ignores that component. An extensive study of the potential for flutter was

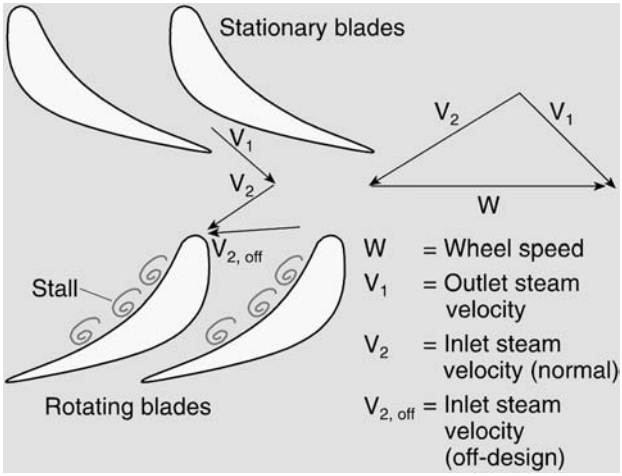

Figure 44 Stall flutter of low-pressure rotating blades during low-load and high-exhaust pressure operation.

conducted by Omprakash *et al.* [84] for last-stage blading in a 3,600 rpm machine. The model developed is described along with the results of a particular analysis. They concluded that the bladed disk under analysis was not susceptible to flutter at loads of 50, 75, or 100% off the design condenser back pressure of 5.08 kPa (1.5-in. Hg). However, at a higher back pressure of 10.16 kPa (3.0-in. Hg), the first tangential mode became aerodynamically unstable. A further increase in back pressure would make all the modes aerodynamically unstable.

Flutter stability can be determined by the net power flow to the bladed disk at various amplitudes of vibration. Normal modes of vibration are calculated by a bladed disk modal analysis at the operating speed. Aerodynamic forces can be calculated from the pressure distribution derived from a separate two-dimensional cascade analysis using compressible inviscid flow for a range of flow angles corresponding to different operating conditions.

Considerable effort has been spent analyzing and developing design methods to avoid stall flutter. Common testing methods include cascade, model, and/or full-scale testing. An alternative approach is to make the blade strong enough to resist the dynamic stresses resulting from stall flutter.

Unstalled Flutter. Unstalled flutter occurs without stall conditions, particularly in low-pressure turbines that operate at relatively high flow rates. In unstalled flutter there is generally no actual flow separation (the flow remains attached to the airfoil at all times), and the flow is not obstructed due to a high back pressure. Unstalled flutter is more likely to affect free-standing blades that lack frictional damping. Unstalled flutter was first detected in the field after the development and application of a blade vibration monitor (BVM) [89].

Some of the methods available for the analysis of unstalled flutter are reviewed by Evans [68] and include (1) the FINSUP computer code [41], which calculates work for a vibrating blade as determined by modal analysis, and (2) the influence coefficient method, which determines unstalled flutter boundaries from experimental data. Whitehead's method determines the unsteady forces acting on the blade. It also determines work coefficients that, when coupled with steam density and blade stiffness, can then be converted to aerodynamic damping. If the aerodynamic damping is negative, the aerodynamic forces reinforce blade motion and the blade becomes unstable [41].

An Aeroelastic Stability Index (ASI) has been defined that combines calculation of aerodynamic damping, mechanical damping based on blade vibration test data, and a moisture effect deduced from BVM tests. Blade response rises rapidly as a function of increase in steam density, indicating that unsteady aerodynamic forces required for unstalled flutter are more likely at maximum load conditions.

In one particular case, cracking occurred in groups of free-standing titanium blades of an L-1 row [90]. An analysis showed that for certain interblade acoustic phase angles, the aerodynamic damping was significantly negative: the condition was worse at high-load than low-load operation. One potential solution to unstalled flutter is the mixed tuning of blades.

Unsteady Condensation Shocks. When steam expands through a diverging passage, condensation will be delayed as the saturation line is crossed. This time delay is caused by thermodynamic nonequilibrium in the high-velocity steam. A certain amount of supersaturation of the fluid will occur and then a relatively large amount of moisture will condense in a small region. Such a phenomenon has been suggested as an additional loading on blades that should be incorporated into the design of LP turbine blades. Condensation shock may also lead to a pressure recovery that can give rise to a variable loading problem. It has also been suggested that the shock may move back and forth in the flow passage, interacting with the boundary layer in low-pressure steam turbines, producing a self sustained, nonsynchronous vibration.

Start–Stop Transients/Overspeeds

Large cyclic stresses on blades can occur during turbine run-ups and during overspeeds. The effect is shown schematically in Fig. 45. Blades will experience a half-stress cycle from zero centrifugal load to full centrifugal load as the unit starts up. During operation, vibratory stresses are imposed on the high mean centrifugal stresses as indicated schematically by the numerous vibratory stress cycles shown in Fig. 45. With unit shutdown the centrifugal stress cycle is completed.

These large cyclic stresses are most prominent on those blades subject to the highest centrifugal stresses, e.g., the longest blades in the last few stages of the LP turbine. Distribution of blade loads can occur that lead to stresses that exceed local yield level and subsequently to low cycle fatigue failures. This problem is particularly acute in locations of high stress concentration such as blade root hooks and tiewire holes. It is less common in the disk rim attachment hooks, where design stress levels are typically lower.

Rotating blade failure can occur in a relatively few number of cycles. For example, crack initiation has been experienced in L-0 blades in 200–1,000 start–stop cycles depending on steam environmental conditions. Clearly, for units cycled on a regular basis, a design low cycle fatigue life of less than 500 start–stop cycles is marginal, particularly given the potential for adverse environmental effects or the added stresses that result from stress concentration in the gaps between the blade root and disk hooks.

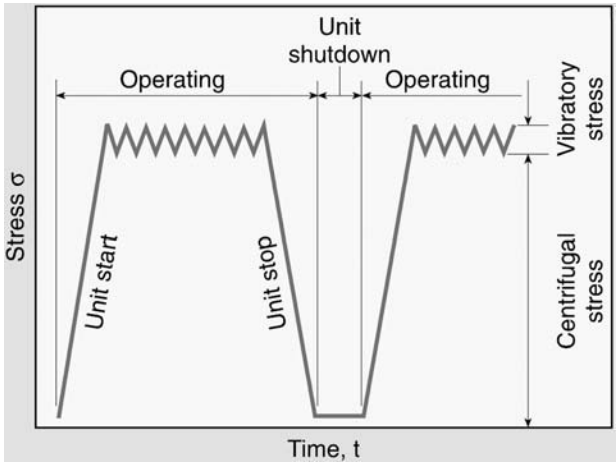

Figure 45 Dynamic and static stresses during turbine start–stop operation.

Manufacture and Assembly Stresses

There are a number of sources of added static and dynamic stresses such as abnormal manufacturing and assembly tolerances

Assembly and Attachment Tolerances. The attachment between blade and disk presents a complicated stress analysis problem. Not only are there stress concentration effects in the typical interlocking geometries, but there are often gaps in the contact locations [93]. The distribution of load among the disk and blade hooks can significantly influence the low cycle fatigue life of the localized area. Computation of peak stresses in the blade roots is vital for evaluation of the structural integrity and life assessment of turbine blades. Two examples of this type of analysis are presented below.

Srivastav et al. performed a displacement-based finite-element analysis to address the contact/friction problem between blades and disks including an axial entry blade with three hooks in which four cases of varying gaps sizes were examined. The analysis showed that as the gap size on the lower two hooks grew larger (up to a maximum of 1.0 mil), the stress overload on the top hook grew significantly. A 23% increase in the value of the peak effective stress and a 25% increase of the peak principal tensile stress were calculated. The conclusion was that careful consideration of relative clearances and contact areas is needed to avoid significant underestimation of the blade attachment stresses.

Sarlashkar et al. performed a study of gap sizes (defined as the clearance between the root and disk groove bearing lands when at least one bearing land was in contact between the root and disk steeple). The results showed a potential for low cycle fatigue failures where stress concentrations in this region were excessive.

Attachment Constraints. This component of blade stress can arise from shroud and lashing wire loads on the blade and the resultant bending stresses and deformations.

Residual Stresses Induced by Assembly Such as by Tenon Cold Working. Cracks can also be induced when riveting is overdone. A case study indicating that microcracks in tenons grew during operation by a combination of steady-state and dynamic stresses in the first tangential mode of vibration, leading to eventual blade failures in the L-1 stage of a 300-MW unit, is discussed in Ref. [94].

Dynamic stresses can also result from manufacturing imperfections such as (1) inexact matching of stationary blade geometry at horizontal joints, (2) leakage through gaps in stationary blade shrouds and diaphragm disks at horizontal joints, (3) eccentricity (“run-out”) of rotating blade assembly with respect to stationary seals, end walls, or nozzle diaphragms,

(4) ellipiticity, such as caused by thermal distortion of stationary parts such as end walls, seals, and nozzle diaphragms, (5) nonuniform spacing, gauging, or thickness of stationary blades.

Frequency Response and the Campbell Diagram

Natural modes of vibration for turbine blades can be divided into three basic categories: (1) tangential modes where blades vibrate perpendicular to the axis of the turbine in the plane of maximum blade flexibility; (2) axial modes; and (3) torsional (twisting) vibration. Figure 46 shows a schematic of the typical first three modes of vibration of a single blade. These are tangential (first mode), axial (second mode), and torsional (third mode). In practice, actual blade vibration modes will usually be a combination of these simple modes, and thus actual measured vibration will be considerably more complex even for single blades and for grouped blades. Because of the complexity in the shape of blade vibrations, a number of physical terms for the higher modes have been developed and can lead to significant confusion unless specifically defined for the particular problem being analyzed. The use of computer-generated mode shape diagrams, visually identifying the displacements and shapes, can be of significant benefit in understanding how the actual deformations are occurring.

High cycle fatigue of LP turbine blades usually occurs because of structural resonances at frequencies synchronous with harmonics of the running speed. The tuning of longer blades so that no structural resonances occur with the first several harmonics of rotational frequency has been standard design practice ever since the principle was introduced by W. Campbell in 1924. Parallel work was done by D. Smith. Subsequent refinement was introduced by M. Prohl [96]. Blades are also tuned to avoid frequencies close to harmonics to allow a margin to account for slight differences in manufacturing and assembly tolerances. If these goals are achieved, only aerodynamic flow excitations should remain as forcing functions for dynamic stresses.

The Campbell diagram provides a representation of blade natural frequencies against rotational speed and machine harmonics as shown in Fig. 47. Note that at the rated speed, N_R, the blades are tuned such that none of the blade natural frequencies (horizontal bands in the figure) intersects a machine harmonic (or multiple of operating speed), H. The width of the horizontal bands indicate expected scatter from manufacturing and assembly tolerances. The rise in blade frequencies from zero to rated speed of the turbine is caused by "speed" or "spin" stiffening.

If the machine speed is above or below the rated level, there can be an intersection of the two lines leading to a condition of resonance. Turbines

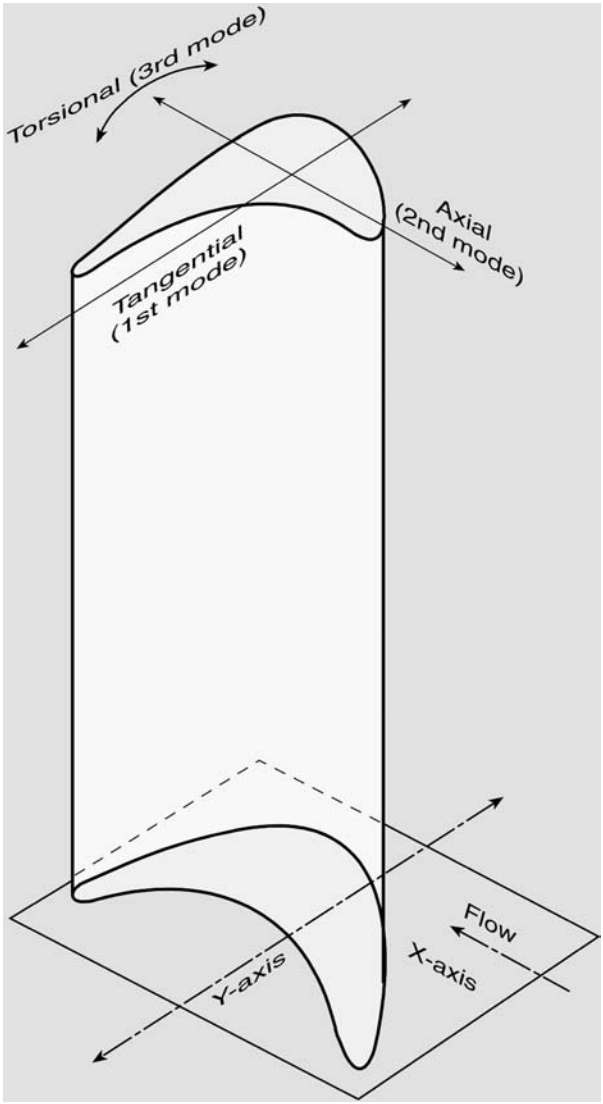

Figure 46 Typical tangential, axial, and torsional modes of blade vibration.

being brought up to speed will undergo multiple resonances, but the flows are typically low and thus the magnitude of the stress, even when amplified by the resonance behavior, tends to be low.

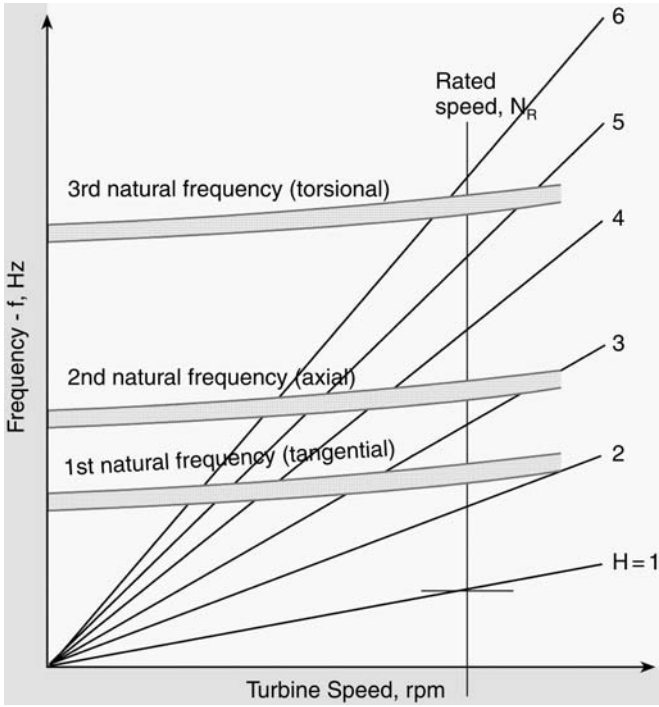

Figure 47 Campbell diagram (frequency versus turbine speed) for a 60 Hz last-row turbine blade.

Manufacturers generally tune through the first three families of modes (tangential, axial, torsional) to avoid resonance up through the seventh or eighth harmonic (420–480 Hz) of running speed. This is generally sufficient as the lower modes have higher associated energies. However, tenon fatigue failures have occurred in the 4th mode (second bending mode) excited by 12th- or 13th-order harmonics.

There is a limitation on the number of modes that can be tuned, because this is a function of off-frequency requirements and manufacturing capability, illustrated schematically by example in Fig. 48. If, for example, the requirement is that the blade should be off a resonant frequency by ± 1.5 Hz and the manufacturer can produce blades of a population that fits within a 40-Hz band, then it is only possible to tune modes with frequencies

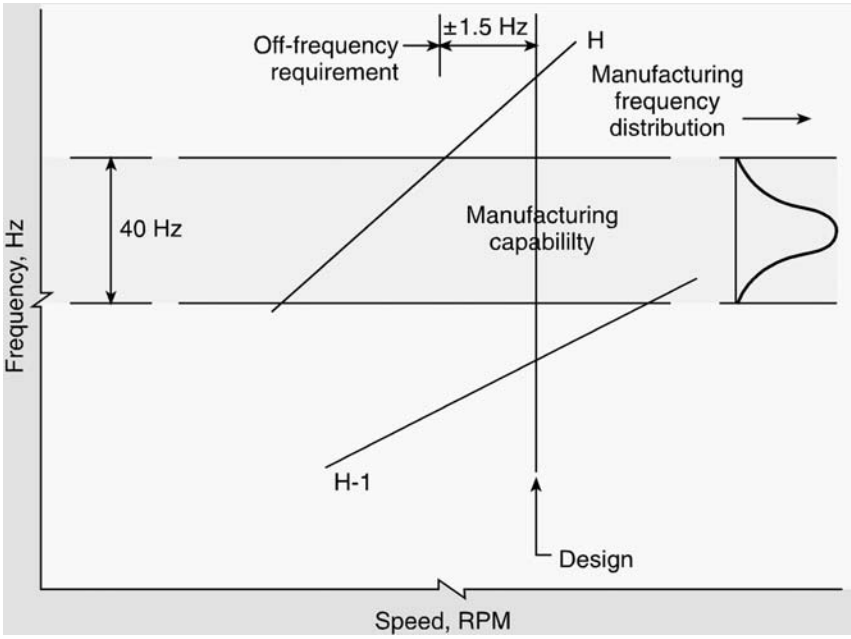

Figure 48 Campbell diagram with limitations based on manufacturing and tuning requirements.

below the seventh harmonic:

$$H \approx \left(\frac{60-40}{2}\right)\frac{1}{1.5} \approx 7 \tag{14}$$

The frequency response of blades is typically verified as part of the manufacturing and quality-control process and compared to the permissible frequencies evaluated using a Campbell diagram. Then all other effects such as blade fixation and rotor-blade coupling are added to the frequency calculation and compared to the permissible frequency window.

At higher modes, the frequencies are more difficult to calculate and test. Also, factors such as manufacturing tolerances, material properties, root attachment or disk effects, and the effects of deposits and/or erosion on the blade vane leading edge tend to cause the individual blade frequencies to scatter about the calculated frequency. Fortunately, at the higher harmonics the dynamic forces generated are usually lower.

Furthermore, in practice each manufactured and assembled blade has a slightly different natural frequency, which complicates the analysis for a row of blades but does reduce the aerodynamic coupling between blades and therefore makes the row less unstable than if all blades were perfectly matched. In fact, it is possible to stabilize an aerodynamically unstable row by deliberate mistuning if the average self-damping of a single fixed blade is positive, but not if it is negative. The variation in individual blade natural frequencies also explains why, in a potentially unstable row, some blades fail while others do not: adjacent blades that are not aerodynamically coupled will vibrate independently of one another.

The implication to blade design is that blade rows should be aerodynamically stable with the use of deliberate mistuning (or mixing) of actual blade natural frequencies to achieve stability if necessary. Mechanical damping, primarily a result of mechanical friction, decreases with increasing amplitude and should not be relied upon unless specifically confirmed in rotating tests under worst-case operating conditions. Monitoring of all blades in a suspect row is necessary, and tests should be run under worst-case flow conditions. *In situ* blade vibration can also be measured by noncontacting methods using strain gage, telemetry, electromagnetic, eddy current, or optical devices. Use of such methods are the preferred means of measurement of nonsynchronous vibration.

Vibratory stresses can also arise from variation in the geometry of the steam inlet passages in the stationary blades. There is no practical way to tune the blade against these high-frequency per-rev harmonics. The deflections and stresses that result are fortunately generally low; however, poor environmental conditions can lower the life of the blade under such loadings.

Asymmetric variations in the flow path that are both temporally and spatially periodic result in flow-induced vibrations in the blade by buffeting from random fluctuations in the flow, by aerodynamic instability (which can lead to blade flutter), or by a combination of the two. Such excitations are the result of random fluctuations in the flow and, as a result, the frequency spectrum is continuous or broad band and the Campbell-type plot and methods cannot be used to guard against failure.

The Campbell diagram can, however, be used to predict the frequencies of individual blades, or some groups of blades. Where the blade groups are attached to rigid drum-type rotors, finite-element models and a plot of the Campbell diagram are sufficient to detect potential conditions of resonance. However, in turbines with more flexible disks, there may be structural interaction between the blades and the disks that is not easily detected using only the Campbell diagram. The dominant shapes of the deformation of the disk tend to be sinusoidal waves around the

circumference of the disk, although a variety of other shapes are possible. Figure 49 illustrates these dominant sinusoidal shapes. The one nodal diameter figure shows the simplest of these modes. In this mode there are two zero points or nodes (indicated by the solid points on the circle) and a displacement around the disk equal to one sine wave. The displacement reaches a maximum positive displacement on the right side of the drawing and a maximum negative displacement 180° around the disk from that point.

The interference diagram has been developed to calculate the effect of nodal disc vibrations on blade vibrations. The interference diagram plots the disk–blade modal shapes (using nodal diameters) against frequency. An example of the interference diagram is shown in Fig. 50 for an analysis of a six-blade group. The basic premise of the interference diagram is that resonance cannot occur unless the nodal diameter of the mode in question coincides with the per-rev excitation, i.e., four per-rev interfering with the fourth nodal diameter. The nodal diameter concept is used to describe the mode shapes in terms of the number of nodes (locations of zero motion) observed in a given mode. Thus, Fig. 50 shows the relationship between the blade group natural frequency, the blade–disk mode shape (expressed in terms of nodal diameters), and per-rev excitation. The closed symbols represent single modes. The data used on the interference diagram are from a finite-element analysis [80].

A constant-speed line (1,800 rpm in Fig. 50) is drawn on the interference diagram. Wherever the speed line crosses a set of nodal diameter modes, a resonant condition is possible. In this example, the speed line passes near the fourth nodal diameter of the first tangential mode set, indicating a possible resonance. The advantage of the interference diagram over the Campbell diagram is that the latter would not have identified this potential resonance since it does not include the disk modal effects.

Aerodynamic Analysis and Flow Analysis of Blades

Aerodynamic and flow analysis has always been important in the design and analysis of turbines. However, recent developments in computational fluid dynamic (CFD) codes have allowed significantly better analysis than was available even in the recent past. Such tools were not available to the turbine manufacturers when most units were originally designed.

Turbine heat rate and output improvements of 2–6% have been reportedly achieved in turbines from several manufacturers as a result of optimizing the aerodynamics of the original turbine flow paths [103, 104]. Complex three-dimensional CFD codes have been increasingly used to evaluate the redesign of turbine components such as exhaust hoods and/or

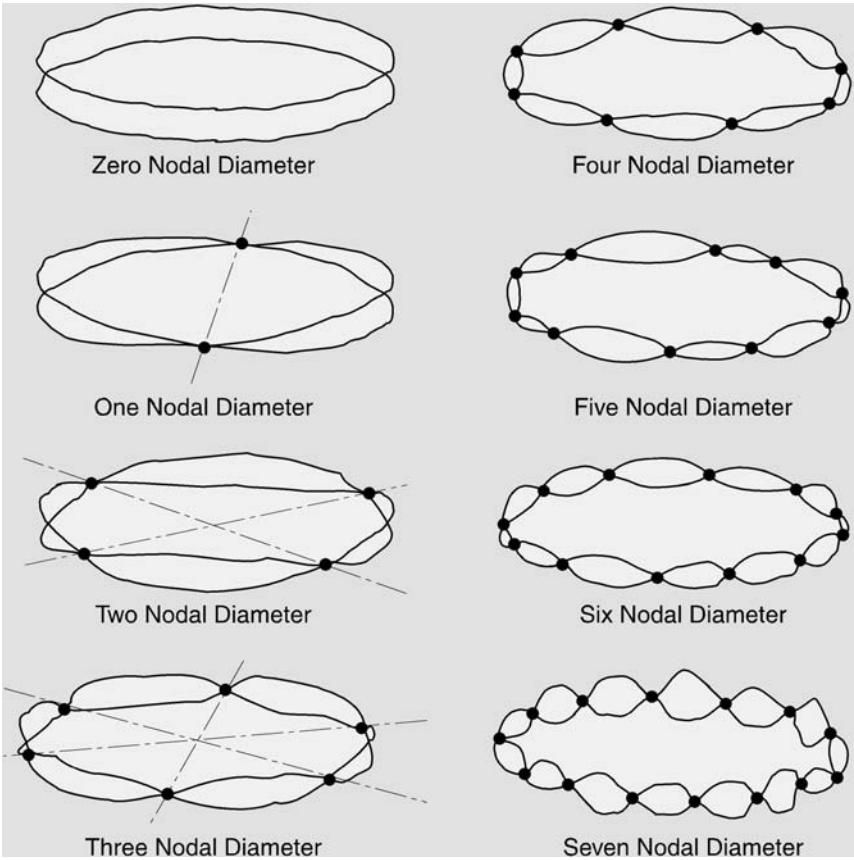

Figure 49 Modal diameters of a low-pressure turbine disk.

blading modifications and have been used to assess the potential payback for such changes. In a number of cases, the need to replace worn or eroded airfoils and the nature of the replacement have been established by the use of three-dimensional CFD studies.

Prior to the early 1990s, flow analysis was performed primarily with axisymmetric flow field computer programs (one-dimensional and later two-dimensional models). However, in the final stages of the LP turbine, the flow undergoes a phase change because of steam expansion and is significantly three-dimensional (Fig. 51). Furthermore, this nonequilibrium phase change produces vapor subcooling (supersaturation), which can locally alter the velocity triangles in the critical area near the leading edges of fixed as well as rotating blades.

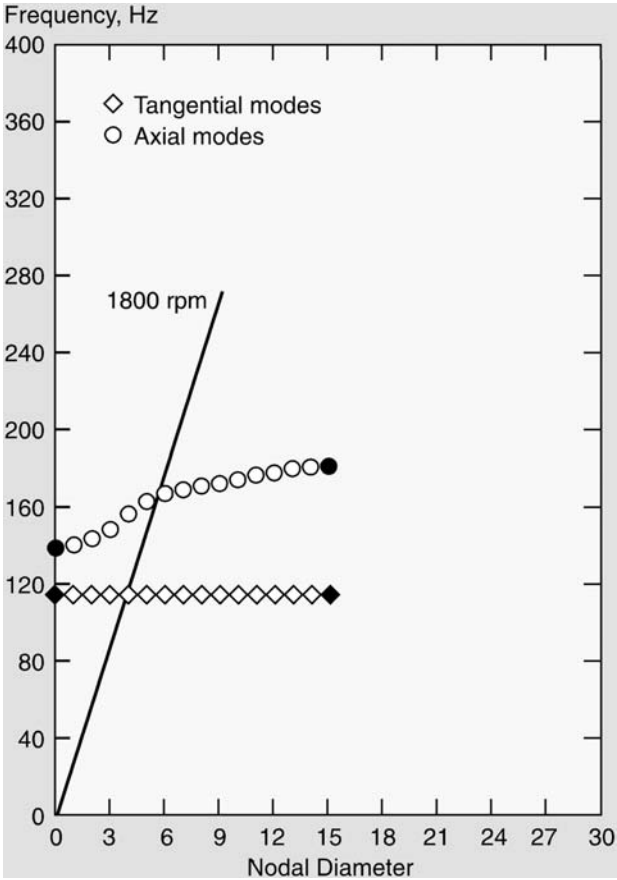

Figure 50 Interference diagram (frequency versus nodal diameter) for a six-blade group (packet).

Earlier programs could not take into account these complex radial flows because of the lack of computational tools. The state of the art for analysis of flows is that three-dimensional flows within blade rows can be calculated and two-dimensional calculations of condensing flows can be calculated. The next step is the calculation of three-dimensional condensing flows and to combine the effects of vapor subcooling (supersaturation), shock wave development, spontaneous condensation, and three-dimensional flow on overall stage losses.

The results of three-dimensional CFD are used to improve blade designs that optimize the shape of the concave (pressure) and convex

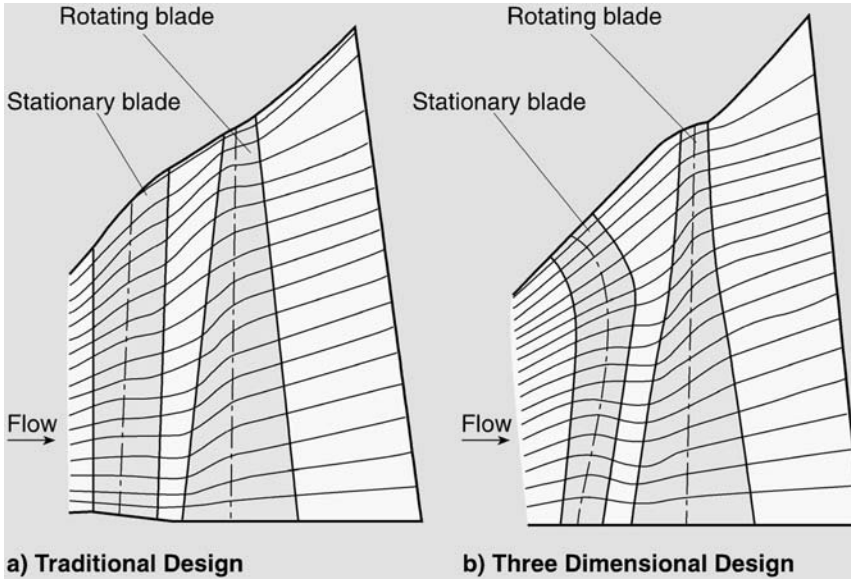

Figure 51 Three-dimensional computational fluid dynamics analysis (3D CFD) of a steam turbine low-pressure last stage.

(suction) sides of the blade and produce optimized steam flow passage profiles that can reduce shock-induced losses.

It is ironic that, despite the recent advances in three-dimensional aerodynamic analysis design, the last LP stage remains the least thermodynamically efficient row in the steam path, even though it has the largest available energy. This should be a challenge to future design engineers.

STEAM TURBINE BEARING SYSTEMS

The main bearings, both thrust and journal, of a steam turbine are of the fluid-film type. The reasons for the use of this type of bearing are that they exhibit little or no wear and the bearings can operate for long periods of time with no inspection or change. Fluid-film bearings can pass some dirt as foreign material with little or no serious damage and also exhibit strong damping, thus permitting some unbalance of the rotor and allow for passing through the critical speeds with acceptable amplitudes of vibration. Dirt is intolerable in antifriction bearings because of failure, as they exhibit no damping whatsoever [110].

In a steam turbine, a thrust bearing is used to locate the rotor axially with respect to the stationary parts and at the same time carry any axial steam loads that may be imposed on the rotor. Journal bearings are used to carry the weight of the rotors and any transverse steam loads imposed on the rotor, and also to locate the rotor radially with respect to the stationary parts.

A thin film of lubricant, which provides the necessary load support function, separates the journal and bearing surfaces. The function of the lubrication supply system is to provide a continuous supply of oil into the clearance space between the bearing and the rotating journal. Once the oil is within the clearance space, actual separation of the journal surface from the bearing surface is achieved by formation of the load-supporting oil film via hydrodynamic action (Fig. 52).

The oil film develops because oil adheres to the journal and when the journal is rotated, it pulls some oil with it. Since the radius of the journal is smaller than the radius of the bearing, the surfaces form a converging wedge and the clearance between them will be a minimum at one circumferential position. When oil is pulled from a position with greater clearance into the position of minimum clearance, oil pressure within the film becomes established. The film pressure increases to equal the journal loads and push the journal away from the bearing.

The two main criteria of bearing performance are the coefficient of friction and the minimum thickness of the oil film. When full film lubrication is achieved, the rotor glides along without any metal-to-metal contact because the oil film supports the journal. Without full film lubrication, metal-to-metal contact of the rotating journal with the bearing occurs and results in a marked increase in frictional resistance. While the resulting increase of drive torque required to overcome the increased frictional resistance is of very little concern, the side effects of increased bearing temperature and wear of the bearing and/or journal surfaces are of major concern.

A closer look at the operating geometry and fluid-film pressure distribution of the journal bearing in Fig. 52 shows that the journal center, $0'$, is displaced radically from the bearing center, 0. The resulting line of centers is not in line with the direction of the applied radial load but is at an angle to it. Choosing the angular location of maximum film thickness as a reference ($o = 0$), the minimum film thickness will be at $o = 180$. The solid-line pressure distribution is typical for incompressible fluid-film journal bearings. In this case, positive pressures are generated within the converging film thickness zone with peak pressure obtained just before the location of minimum film thickness. The pressure is reduced to ambient pressure just after the location of minimum film thickness. Beyond this point of return to

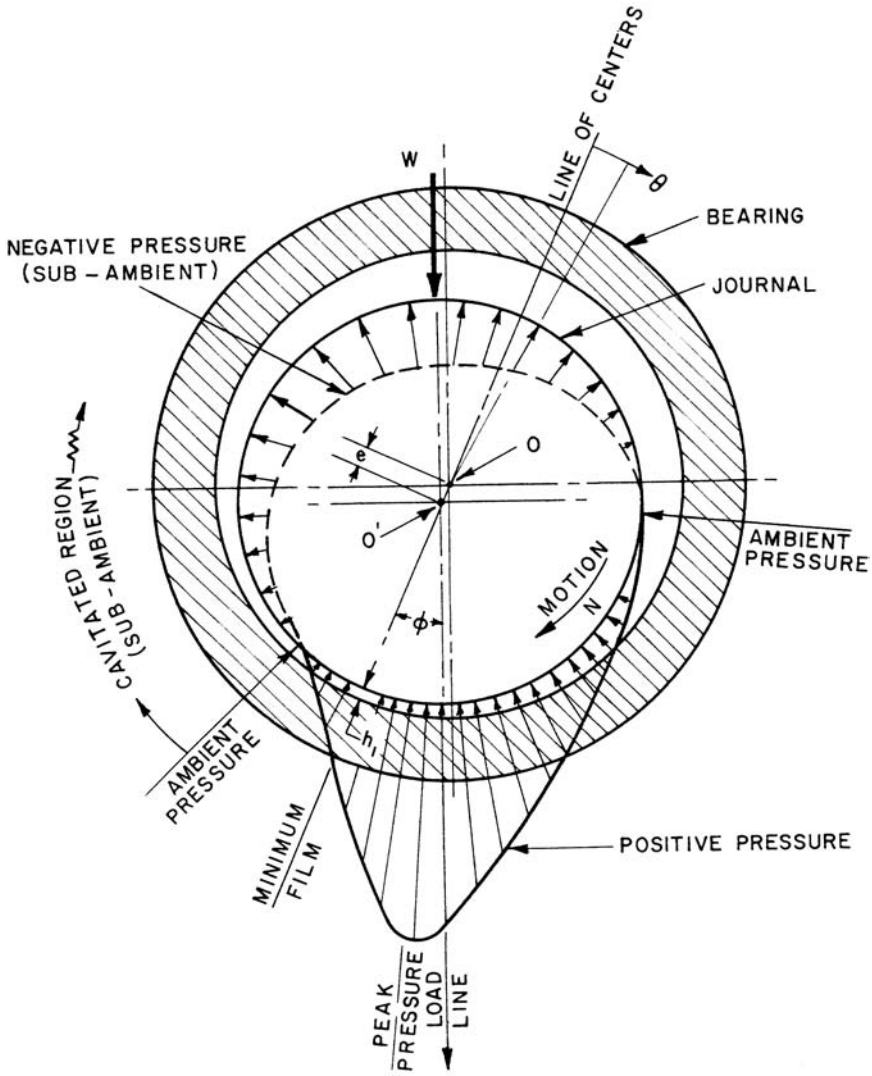

Figure 52 Converging wedge and resulting pressure distribution in a hydrodynamic journal bearing.

ambient pressure, an incompressible fluid cavitates (unless the ambient is a pressure environment) because of the rapidly diverging (expanding) film

thickness. In the case of a compressible fluid, subambient pressure can exist and is of the form indicated by the dashed pressure distribution in Fig. 52.

The solid curve in Fig. 53 represents the actual coefficient of friction and the dashed curve represents the theoretical coefficient of friction when there is no metal-to-metal contact. At very high values of uv/p, the actual and theoretical coefficient of friction (f) is relatively low and decreases in

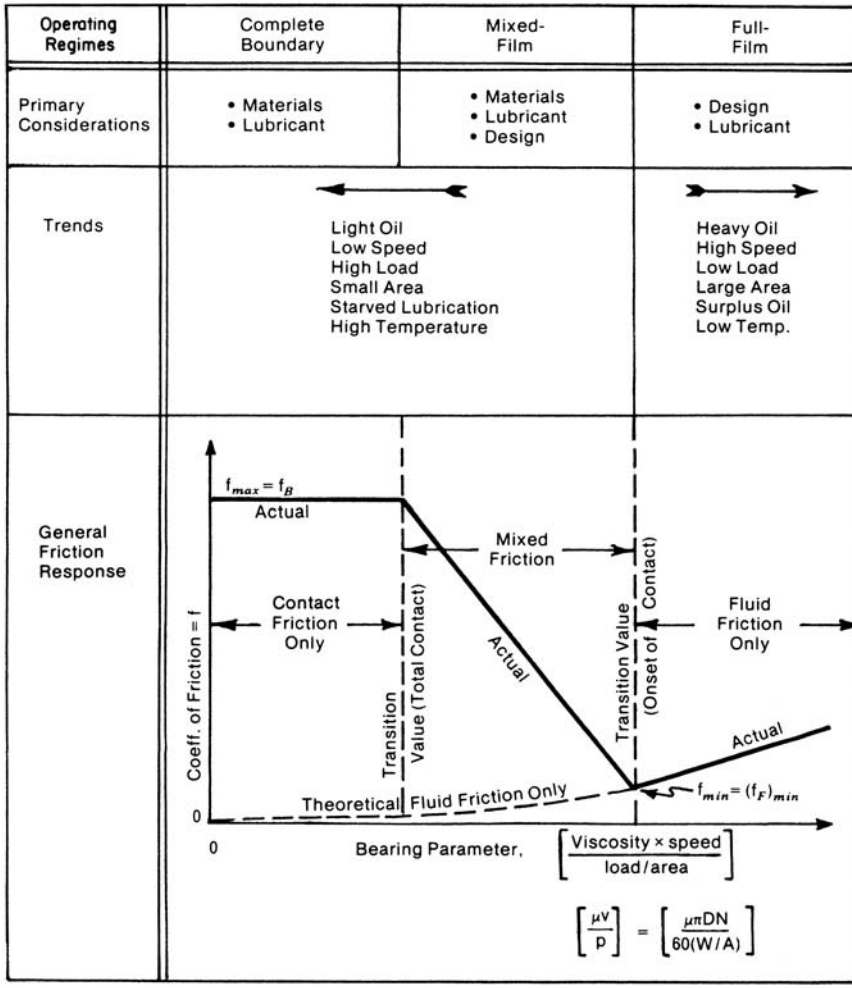

Figure 53 Steam turbine operating regime versus nondimensional bearing parameter.

value as the operating value of uv/p decreases. Theoretically, this decreasing trend of f with decreasing uv/p continues downward to a value of $f=0$ at $uv/p=0$. However, a transition value of uv/p exists below which the actual value of f increases with decreasing uv/p. This transition signifies the onset of metal-to-metal contact. As the value of uv/p continues to decrease, the value of f increases very rapidly due to more and more of the load being supported by metal-to-metal contact. This trend of increasing actual value of f with decreasing value of uv/p continues until yet another transition value of uv/p occurs, below which the actual coefficient of friction remains at a high value. This second transition point signifies total loss of oil-film load-carrying capacity, and the entire load is supported by metal-to-metal contact.

Dirt, deformations, misalignments, surface roughness, and reduced oil flow rate all have deleterious effects on the resulting coefficient of friction. When such considerations exist, the onset of metal-to-metal contact occurs at higher values of uv/p. Wearing-in as opposed to wearing-out of the bearing has a beneficial effect since hydrodynamic full film operation is maintained to lower values of uv/p. In the full film hydrodynamic regime, increasing clearance has a beneficial effect since bearing oil flow rates increase, which lowers oil-film temperature and increase lubricant viscosity.

At full-speed operation, the bearing operates in a "full film friction and lubrication" regime with relatively low coefficient of friction. When running at the much lower turning gear speed, the bearing operates in a "complete boundary friction and lubrication" regime with very high coefficient of friction. Using these coefficient of friction characteristics, a schematic is depicted in Fig. 54. The solid-line curve is quite similar to field observations in a bearing that has been scored or wiped. Solid particle contaminants in the lubricant and/or deformations and misalignments of the bearing members would also result in similar contact-induced transient temperature rise of the bearing during coastdown.

Steam Turbine Lubrication Supply Systems

The lubrication system of a steam turbine generator unit performs the vital function of supplying lubricating oil to the thrust and journal-type bearings at all times under all operating conditions. Without proper design, installation, operation, and maintenance of the lubrication system, reliable performance of the turbine generator unit cannot be achieved. Failure of the lubrication system to perform its function can cause significant damage to the turbine generator. While lubrication system failures are not common occurrences, they can result in extended unit outrages to repair or replace damage turbine generator components such as blades, casings, rotor windings, and entire shafts [111–113].

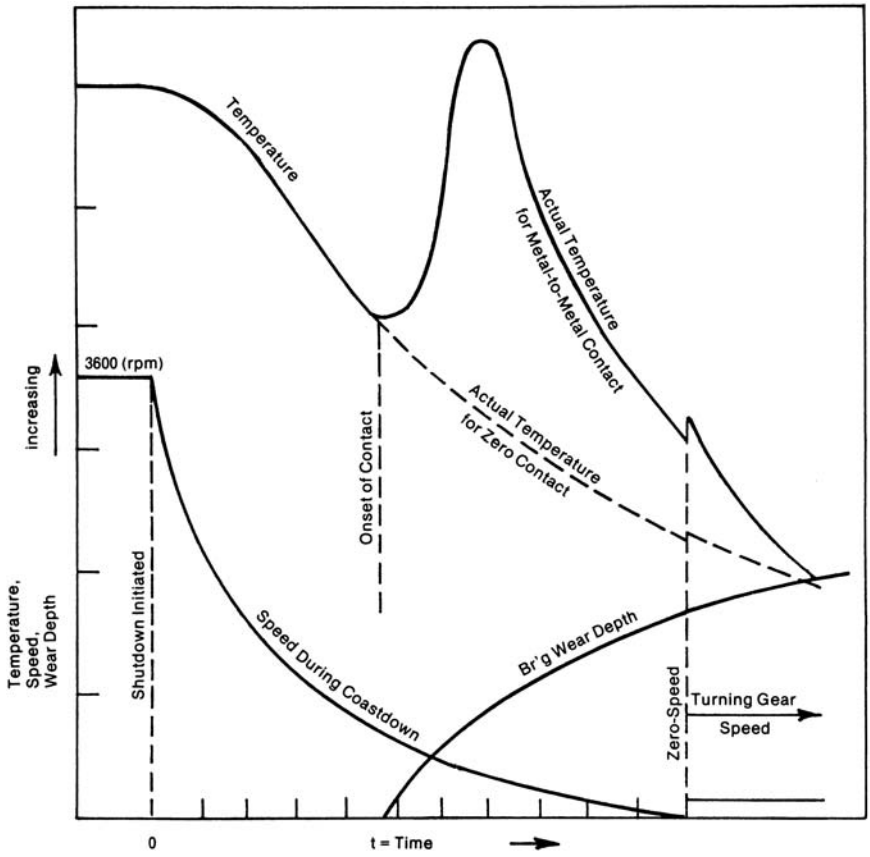

Figure 54 Bearing temperature during coast down of a turbine as a function of speed.

The lubrication system provides a clean, cool, and copious supply of refined petroleum oil for lubrication of the multiple journal bearings and the thrust bearing of a steam turbine generator unit. The lubrication system also provides for retention of the generator hydrogen cooling gas and may provide for emergency closure of the turbine steam regulation valves. The lubricant must also provide for corrosion protection of the lubrication system internal seal and contact surfaces.

Lubrication Supply System Design

Design of the lubrication system is usually provided by the original equipment manufacturer (OEM) as part of the scope of supply for the main steam turbine generator unit. The utility as owner and operator must provide specifications for the system and the numerous interfaces for power supplies, oil supply, and instrumentation and control. To aid in obtaining satisfactory performance of the lubrication system, the American Society for Testing and Materials (ASTM) has issued a standard practice titled "Design of Steam Turbine Generator Oil Systems (D 4248-83)" [112]. This standard provides recommended practices for design of the turbine generator lubrication system including the high-pressure supply, bearing oil, control oil, generator seal oil, and drain oil return subsystems [114–116].

Operation of the lubrication system is relatively simple when the turbine generator unit is at full operating speed. A main shaft oil pump (MSOP) connected to the turbine shaft provides high-pressure oil to the system. The complexity of the lubrication system is increased when the turbine generator unit is below full operating speed because the MSOP is not capable of providing high-pressure oil when the shaft speed is below approximately 90% of full operating speed. Auxiliary motor-driven oil pumps (AOP) and subsystems are necessary to replace the MSOP during turbine generator startups and shutdowns. Emergency oil pumps (EOP) and subsystems are provided as backup to the MSOP and AOP subsystems to allow safe shutdown of the turbine generator unit. Either a dc electric motor or a steam turbine may drive the EOP. Elaborate instrumentation and power supply schemes are involved to start up the AOP and/or EOP when the bearing oil pressure decays below a specific set point (Fig. 55).

Steam Turbine Lubrication System Pumping Systems

The primary pumping system supplies oil during the full-speed operation through the main shaft oil pump. The MSOP is driven by the main turbine generator rotor shaft. The MSOP is usually a centrifugal pump that is not self-priming, and since it is located above the oil reservoir it must be supplied with oil from the reservoir by another means. Oil to the MSOP suction is supplied by a motor-driven suction pump (MSP), an oil turbine driven booster pump, or oil ejectors. The MSP supplies suction oil when the turbine generator shaft is rotating below approximately 90% of its normal speed. When the turbine generator shaft is rotating above 90% of its normal speed, oil from the MSOP discharge can be used to supply either an oil turbine-driven booster pump or oil ejectors located in the main oil reservoir along with associated flow regulation valves.

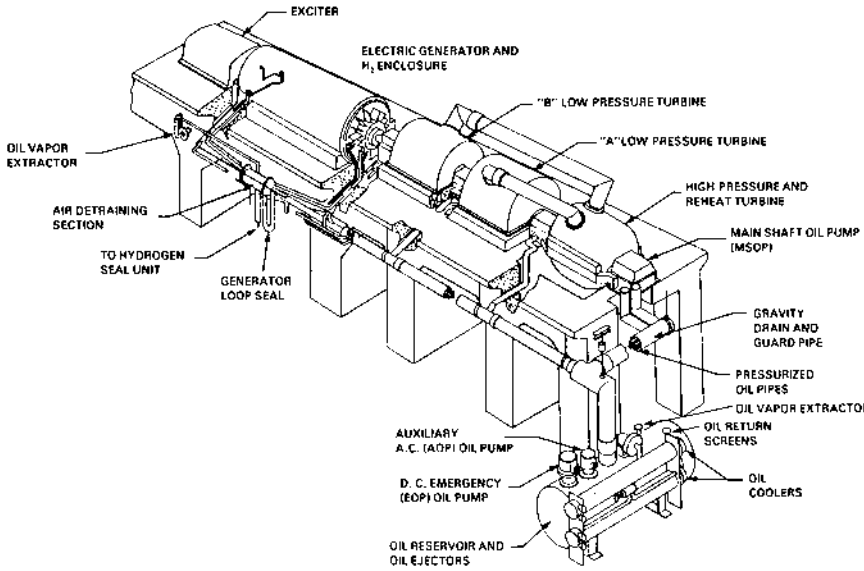

Figure 55 Steam turbine lubrication supply system.

When an oil turbine-driven booster pump is used as shown in Figs. 56 and 57, two baffler valves and a relief valve are provided for adjustment of the oil pressure and flow. The booster nozzle baffler valve controls the oil supply from the discharge of the MSOP to the oil turbine. The bypass baffler valve allows oil from the discharge of the MSOP to flow around the oil turbine. These two valves are adjusted to provide the following conditions:

1. The booster nozzle baffler valve must pass sufficient oil to supply power to the oil turbine for pumping oil to the suction of the MSOP. MSOP suction pressure should be approximately 15 psig. The valve plug is drilled to allow a minimum of 60% of the bearing oil flow requirement to pass should the valve be unintentionally closed.
2. The flow through the oil turbine plus the bypass baffler valve must be sufficient to supply all the turbine bearings plus maintain some flow through the relief valve. The relief valve is commonly adjusted to hold bearing pressure at 25 psig at the turbine centerline.

The backup pumping system consists of one or more ac motor-driven auxiliary pumps and a dc motor-driven or steam turbine-driven emergency pump. The auxiliary and emergency pump drivers are sized to provide adequate capacity even when operating with a high oil viscosity such as can

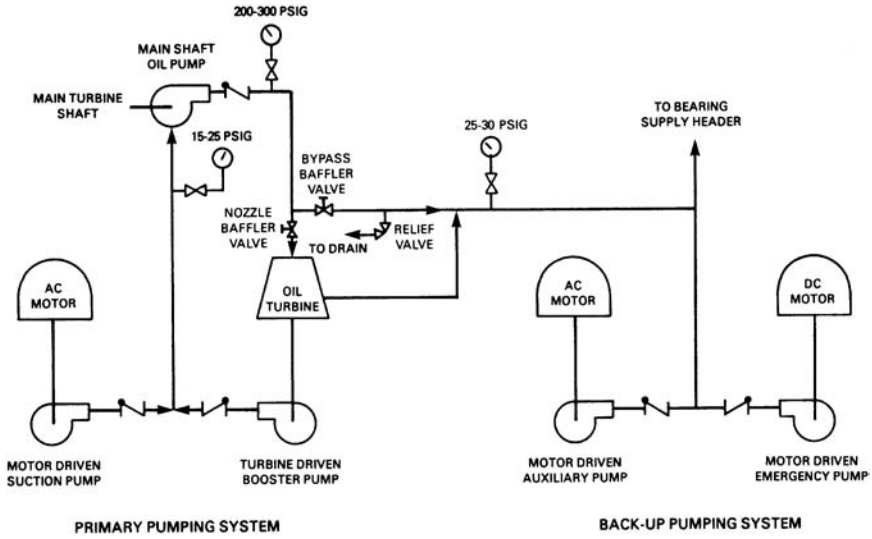

Figure 56 Steam turbine oil system utilizing an oil turbine-driven booster pump.

be obtained during cold startups of the unit. The auxiliary oil pump has enough capacity to permit continued turbine generator operation if the MSOP fails; however, unit shutdown should commence upon MSOP failure. The emergency pump should be sized to supply oil during unit coast down upon failure of the main and auxiliary oil pumps.

All pumps except the MSOP are located within the main oil reservoir to provide for positive suction. The pumps are submerged with their suction inlet located at least 6 in. below the minimum operating level and 6 in. above the bottom of the reservoir. They are arranged to avoid air pockets in the suction piping and entrainment of air. Emergency oil pump suction is lower than that of other pumps in the reservoir. The suction systems of all pumps are provided with coarse mesh strainers for protection from large pieces of debris.

Lubrication System Oil Reservoirs

Oil reservoirs or oil tanks are required to provide an oil reserve during turbine generator operation and for oil storage when the unit is shut down. One main oil reservoir is usually provided for each turbine generator unit with sufficient capacity to store a full charge of oil. A full charge is the amount of oil being circulated in the lubrication system piping and bearing

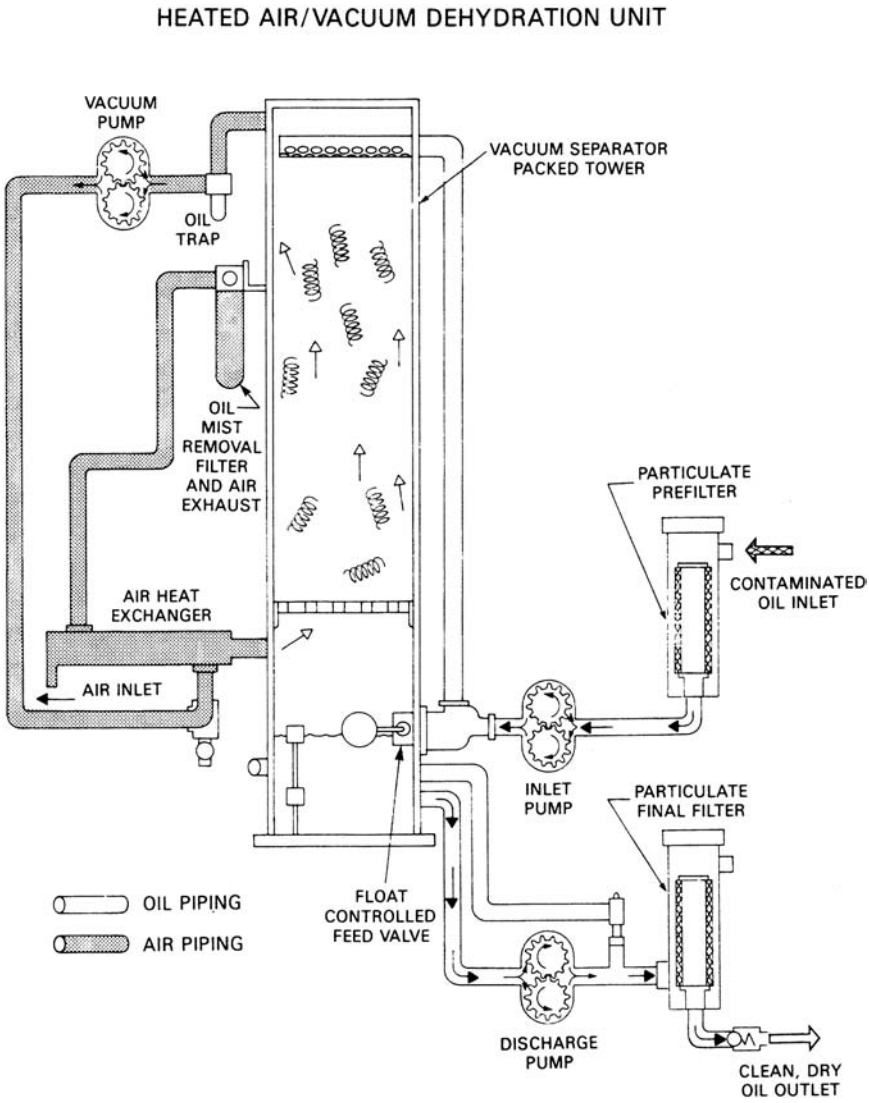

Figure 57 Turbine oil filtration system utilizing heated air/vacuum dehydration.

plus the volume of oil in the reservoir required for oil pump submergence. The bearing pedestals or housings also serve as small reservoirs to collect oil used for lubrication and cooling and to direct the oil into the return piping.

The main oil reservoir is located below the turbine generator operating floor so that oil returns to the reservoir from the bearings by the force of gravity. To allow separation of entrained air and settling by gravity of water and solid contaminants, retention time of oil in the reservoir should be approximately 8 min. Division panels or baffles may be employed to provide a longer flow path through the reservoir.

Air in the oil can result in excessive oil foaming, air entrainment, and oxidation. Design of the reservoir should minimize turbulence at the oil return line discharge and maximize oil deaeration. The reservoir should provide surface area and retention time to enhance air separation from the oil. API Standard 614 specifies a minimum of 0.25 ft^2 of free oil surface for each gal/min of normal oil flow.

Lubrication System Oil Conditioners

Oil conditioners are provided to remove water and solid particle contaminants that enter or are produced in the lubrication system. Usually these components are used in a bypass or supplementary mode in which oil flows from the reservoir, through the conditioner, and directly back to the reservoir. Various types of conditioners are employed including particulate filters, oil centrifuges, precipitation chambers, vacuum dehydration tanks, and coalescence cartridge (Fig. 58). Adsorption purification that utilizes an active medium such as fuller's earth is not recommended since some of the additives in inhibited oil may be removed by this material [110]. Water washing of oils containing rust and oxidation inhibitors is also not recommended since experience indicates that this method may cause some reduction in inhibitor content [121, 122].

In the bypass method, a percentage of the oil volume in the system is pumped through the oil conditioner each hour. Several utilities recommended 20% as the minimum based on their experience. They have updated older units to this standard in order to maintain desired contamination limits. The higher percentage of bypass flow allows more rapid removal of contamination and lower equilibrium level of contaminants. Bypass circulation should be continuous to reduce the possibility that contaminants will accumulate and exceed an acceptable purity level.

The turbine generator manufacturer establishes oil requirements since bearing and lubrication system designs are dependent on oil properties. As a guide to defining the properties of mineral oil-based turbine lubricating oil, ASTM has approved the standard specification titled "Mineral Lubricating Oil Used in Steam or Gas Turbines" (D 4304-84) [116]. Exceptions to specific items in this standard may be required and agreed upon between the user and supplier. This standard is intended to define only new lubricating

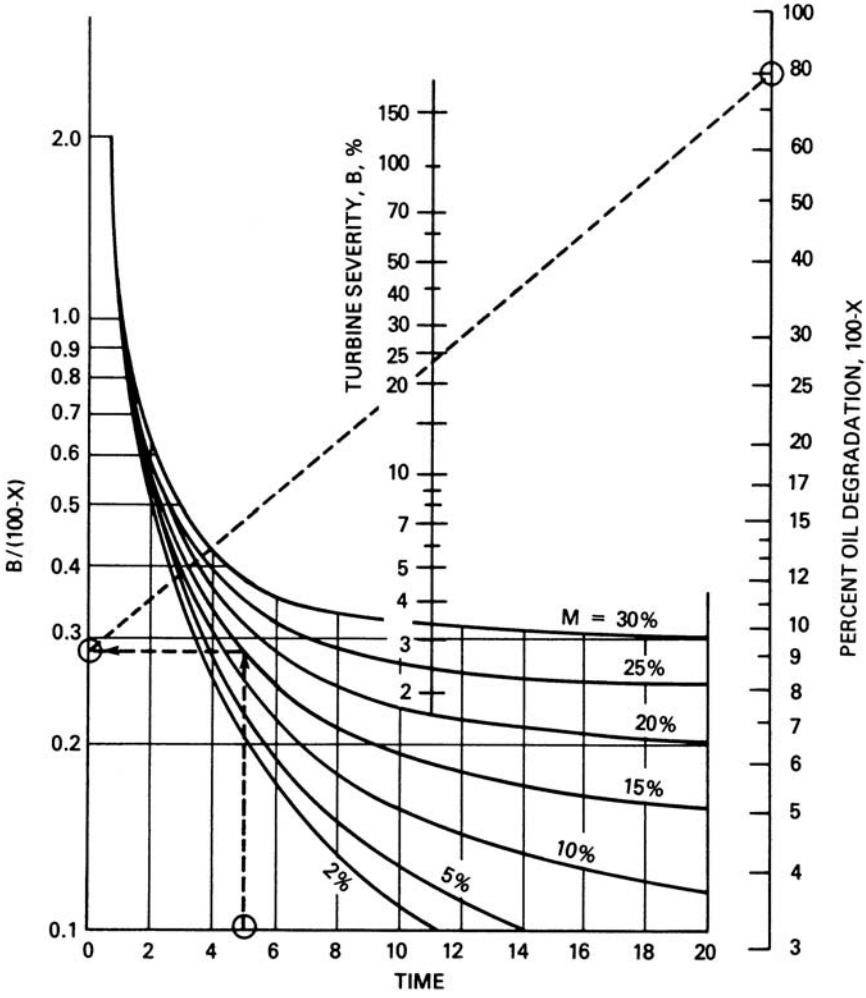

Figure 58 Effect of turbine oil severity (B) and makeup rate (M) on oil degradation rate.

oil before it is installed in the machinery. ASTM D 4293-83 defines the requirements for the phosphate ester-based fire-resistant fluid when used as turbine generator lubricant [117].

Oil used for turbine generator units is considered "light" oil because it has a relatively low viscosity rating. This reduces frictional drag in the bearing and lowers power loss from the turbine generator bearings.

Although a light oil does provide a relatively full film between the rotating shaft journal and the bearing at operating speed, some metal-to-metal contact occurs between these members during starting, stopping, and slow-speed turning gear operation. The oil must therefore have adequate film strength to minimize friction and to protect against wear when journal speed is low. A properly refined petroleum-based lubricating oil will have a high film strength value.

Lubrication System Oil Service Life

Turbine generator oil is expected to have a long service life, on the order of 15–20 years. Certain environmental conditions, however, can result in or accelerate oil degradation and reduce service life. Primary environmental conditions that influence oil life are exposure to high temperature in the presence of oxygen, and contamination by particulate materials and water.

The degree of exposure to these environmental conditions and capability of the oil (oil quality) to resist them are factors that determine the exact period of service life obtained from the oil. Other important factors affecting the oil service life are type and design of the lubricating system, condition of the system after construction, and oil makeup rate (Fig. 59).

Combinations of these factors vary from unit to unit so that service life of the oil is difficult to predict solely from original oil properties.

Each turbine generator lubrication system is unique due to exclusive conditions that occur during construction and operation of the system. These conditions set the rate at which a new charge of fresh oil will lose its oxidation resistance. A property called turbine severity (B) level has been established that can be used to take these conditions into consideration when monitoring the remaining oxidation resistance of the oil during its service life [111]. "B" is defined as the percentage of fresh oil oxidation resistance lost per year due to the oil reactions in the turbine generator lubrication system.

The severity level for a particular lubrication system should be determined over a period of time beginning with initial operation or installation of fresh oil charge. Accurate record keeping of the amount of oil makeup is essential, and a rotating bomb oxidation test (RBOT) should be conducted at three- to six-month intervals for one to two years. By knowing the oil makeup and degradation of the oil with time, the turbine system with a high severity level requires frequent makeup or completely new charges, whereas one with a low severity level may have no problems with routine makeup. Turbine generator units of recent design have higher "B" levels than units installed before 1965. Increases in lubrication system

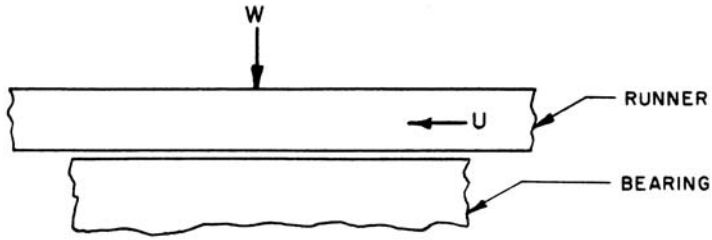

(a) Plain Thrust Surface (no pressure generated)

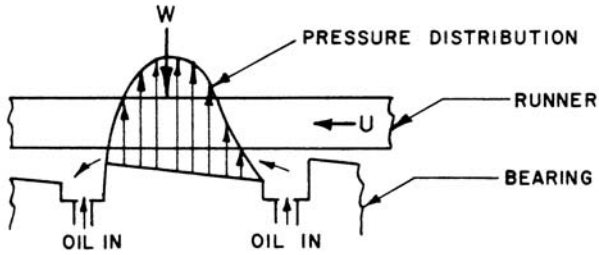

(b) Altered Thrust Surface To Provide Converging Wedge

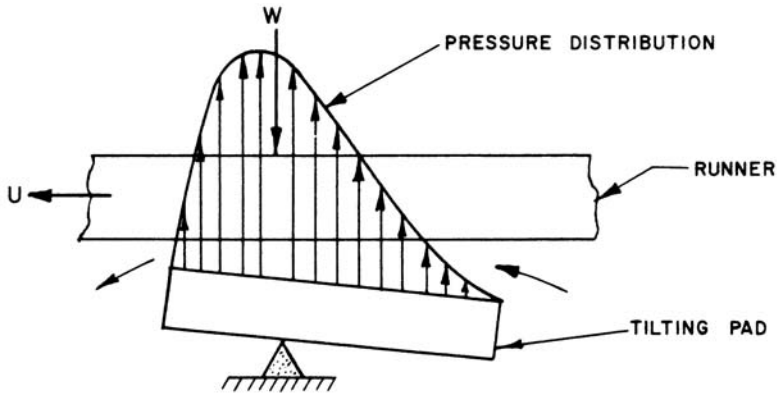

Figure 59 Bearing pressure wedge profiles for various thrust-bearing designs.

temperatures are suspected as reasons for the higher "B" levels obtained in new turbines. Larger shafts, turning gears, and couplings, and smaller oil mist transfer per hour to the pressurized furnaces has also been a factor.

Steam Turbine-Bearing Design

Three journal-bearing designs are widely used in steam turbine generator sets. These are the circular-overshot bearing, the elliptical-overshot bearing, and the tilting pad bearing. Other design variations may be found in support equipment, such as fans, blowers, and pumps. Several pertinent bearing design factors and geometry of both the circular-overshot and the tilting pad bearings are in use by turbine manufacturers and users.

The generation and maintenance of full-film lubrication by hydrodynamic action requires a working fluid (typically mineral oil), motion of the bearing members to drag fluid between their surfaces, and a converging, wedge-shaped fluid film in the direction of the motion. The combination of these three factors results in pressurization of the interposed fluid, thereby providing the necessary load support without metal-to-metal contact. In a steam turbine journal bearing, a converging wedge is automatically formed by virtue of the eccentricity of the cylindrical bearing, as shown previously in Fig. 52. This is not the case for thrust bearings, as shown in Fig. 60. Plain, flat bearing surfaces, in a thrust bearing or wear plate, do not provide a converging wedge. To promote fluid-film lubrication, one of the surfaces must be altered to provide a hydrodynamic shape.

Another means of providing a converging wedge in flat-surface hydrodynamic lubrication is by use of a pivoted pad. This allows the bearing pad to automatically incline itself in the direction of motion to the degree required to support the load. Tilting pad thrust bearings are frequently used in steam turbines to provide hydrodynamic lubrication.

Bearing/Journal Minimum Oil-Film Thickness

Every discussion of bearing performance involves the term "load capacity," which normally refers to the load a bearing can support at a given minimum film thickness. In journal bearings, this minimum film thickness occurs at the angular position of the line of centers; and for an aligned case, it stretches along the entire length of the bearing. The minimum film thickness (H-min) is important because it gives indication of:

- The likelihood of physical contact between the mating surfaces, which would lead to failure
- The intensities of the peak pressures and temperatures, which tend to rise steeply with a decrease in H-min

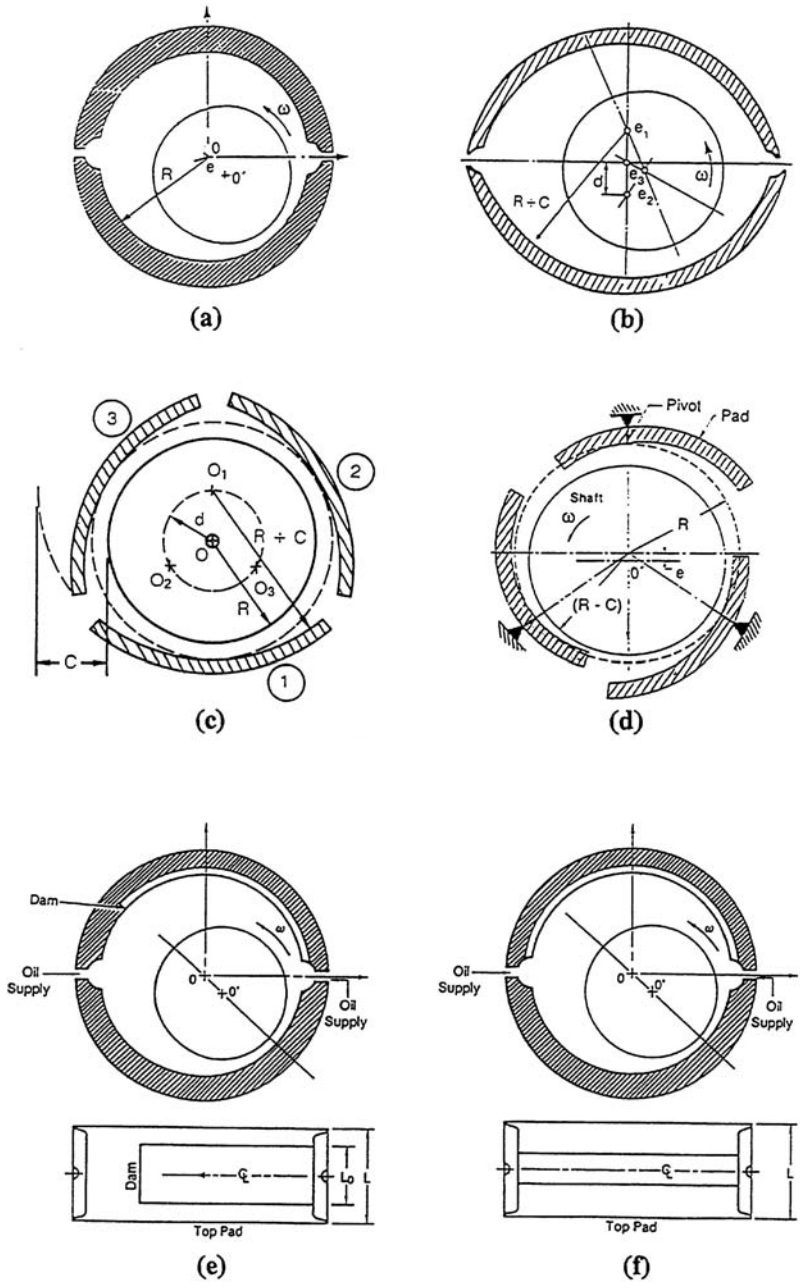

Figure 60 Steam turbine journal and tilting pad design configurations.

There is no fixed or absolute value for a satisfactory H-min. The value depends on the size of the bearing, the nature of the application, the operating conditions, the degree of reliability required, and other factors including industrial practice. In no case, however, should the calculated H-min be smaller than the sum of the surface roughness of the two mating surfaces.

Maximum Bearing Oil-Film Temperature

Knowing the value of the film maximum temperature T-max is as important as knowing that of H-min. While too small an H-min can cause damage by physical contact, excessive temperatures may cause failure by either softening or melting of the bearing surface, and this can occur even when there is an ample film thickness. T-max usually occurs ahead of the trailing edge of the bearing pad due primarily to the presence of cool lubricant and heat-transfer effects at the downstream boundary of the pad. In aligned journal bearings, T-max occurs along the centerline.

It is common practice in industry to use the oil temperature rise, ΔT, as a criterion of bearing performance, where AT is the difference between the bulk temperatures of the oil discharging from the bearing and the oil supply temperature. While monitoring ΔT may be helpful in spotting sudden changes in bearing behavior, it is a poor indicator of the magnitude of T-max.

Since the value of ΔT is determined by power loss and oil flow, raising the oil inlet pressure or increasing the size of groove chamfers will reduce ΔT.

Thus, while ΔT remains a useful overall indicator of the amount of total heat generation and of any untoward changes in bearing behavior, it cannot represent or replace the crucial quantity T-max. This can be obtained only from an appropriate variable temperature analysis, and it has to be viewed as an independent indicator of bearing safety and performance.

Bearing/Journal Dynamic Stability

The third important criterion of journal-bearing operation is stability. Hydrodynamic forces may induce instabilities, even though there may be no external stimuli. The nature of the bearing dynamics dictates that a journal displacement in one direction produces resisting force F_x along x, as well as a force F_y in the y direction (Fig. 61). These two resisting forces are accompanied by two stiffness coefficients K_{xx} and K_{xy}, where the first subscript refers to the direction of the displacement and the second subscript to the direction of the resisting force. A similar situation arises with a

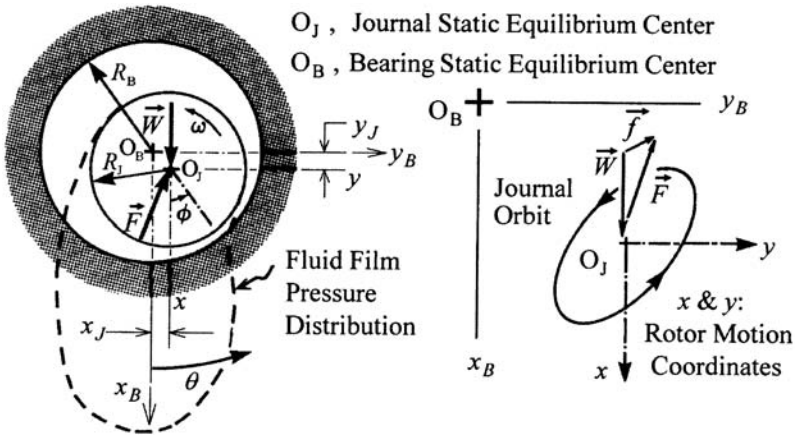

Figure 61 Journal bearing fluid-film pressure distribution and journal orbit displacements and force vectors.

displacement in the y direction. Consequently, there are four stiffness coefficients: K_{xx}, K_{xy}, K_{yy}, and K_{yx}.

Motion of the shaft center generates a resisting force that is expressed as the shaft center velocity by a damping coefficient, B. Cross-coupling effects occur here also, and consequently there are four damping coefficients: B_{xx}, B_{xy}, B_{yy}, and B_{yx}.

Fixed Versus Tilting Pad Bearings

There are basically two types of bearings used in steam turbines. They are the fixed type and the tilting pad type. Typically, the fixed types consist of the axial groove and elliptical configurations for the journal bearings and the tapered land configuration for the thrust bearing. The tilting pad configurations are utilized for both journal and thrust bearings (Fig. 62).

The reason for going from a fixed geometry to a tilting pad type depends on the application. For the journal-bearing application, the major reason is dynamics. The tilting pad journal bearing is inherently stable (free of bearing half-frequency whirl). Another advantage of a tilt pad journal bearing is that it is superior for a start–stop and turning gear operation. The reason for this is that pads can pitch and form a good hydrodynamic film shape at all speeds. Therefore, the shaft lifts off at a lower speed and thus reduces startup and shutdown wear. A third advantage is that spherical

pivots incorporated in this bearing configuration make it truly self-aligning (Fig. 62).

However, there are some disadvantages related to tilt pad bearings. Normally, they have higher power losses and operate at higher temperatures for a given set of supply oil flow conditions. Tilt pad bearings operate at a smaller minimum film thickness during maintenance inspections. If properly designed, however, these disadvantages can be minimized.

For the thrust-bearing application, tilt pad bearings are often utilized because of their superior characteristics relating to alignment and thermal distortion. This is accomplished because each pad can toll and pitch to adjust to misalignment and thermal distortion. Also, for fully equalized thrust bearings, the linkage behind the pads ensures good load sharing among all the pads. One manufacturer has had success using a copper material, which helps compensate for deleterious thermal effects in their fixed thrust-bearing configurations.

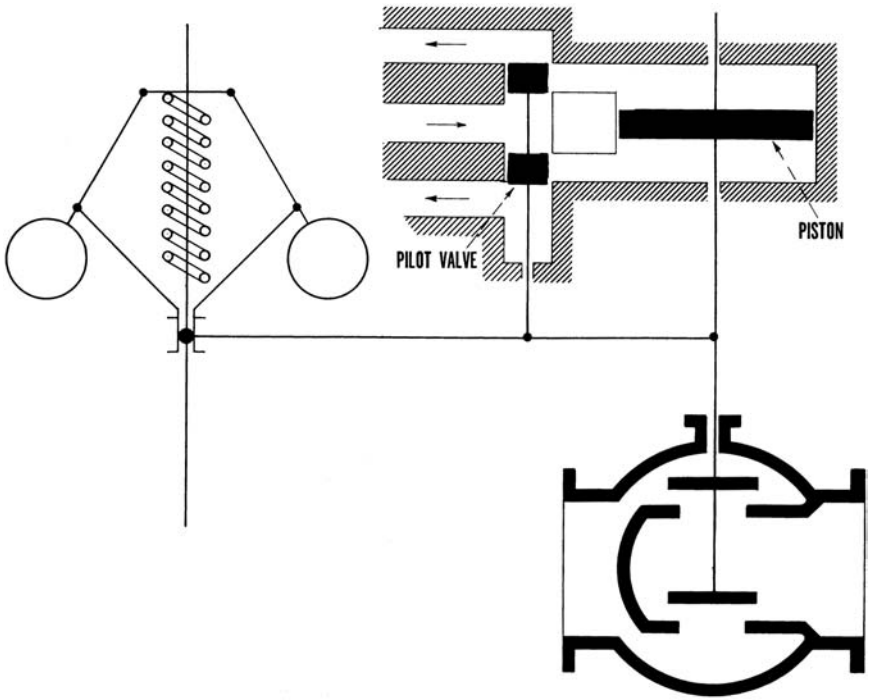

Figure 62 Steam turbine speed and load control system utilizing a flyball governor connected to a hydraulic relay piston combination.

The disadvantages associated with the tilt pad thrust bearing are the complexity and wear of the additional moving parts (linkages and pivots). Also, the initial cost of tilting pad bearings is greater than that of the fixed-type bearings. Furthermore, because of their relative complexity, a higher level of skill is required for their maintenance and repair. Therefore, when designing bearings for large steam turbines, the choice as to which type of bearing is most suitable is not clear-cut but depends on the specific requirements of a particular application. Usually, combinations of fixed- and tilting pad-types of bearings are incorporated in a given turbine generator unit design [119].

Steam Turbine-Bearing System Problems

Foaming

Foaming of the oil may result when air is entrained by the oil and is thoroughly mixed by agitation and churning. Normally only a thin layer of foam will be present on the oil surface due to turbulence in oil return lines, especially as they discharge into the reservoir. High-quality oil should have good resistance to excessive foaming, and the air bubbles formed on the surface should break up quickly. Foaming increases the rate of oil oxidation, since more oil is exposed to the entrapped air than would be in nonfoaming situations. Oxidation products, in turn, promote the formation and stabilization of the foam. Contaminants in the oil also reduce the capability of the oil to resist excessive foaming. Excessive foam accumulation can result in loss of oil by overflow or seepage. In some instances, foam weeping from generator bearings has been drawn into the electrical windings or onto the collector rings to cause insulation damage, short circuits, and sparking. ASTM Test Method D 892-74, ''Foaming Characteristics of Lubricating Oils,'' can determine the foaming properties of oil [120].

Bearing System Contamination

The remaining factor that influences the rate of oil oxidation is the amount of contamination present in the oil. Metal particles and water contaminants promote oil oxidation and contribute to formation of foam, deposits, and sludge.

Particle Contamination

Pulverized coal, fly ash, airborne dirt, and sand can enter the lubrication system through openings at the bearing housings and at the oil reservoir

covers and doors. Pipe scale, rust, and other metal particles may enter the system during construction and remain there even after the postconstruction lubrication system flush. Fine metal particles act as a catalyst to the oil oxidation process. All solid contaminants have the potential to cause excessive wear or scoring of the bearings and journals, and damage to other lubrication system components.

Rusting of oil system piping and other carbon steel components can occur in service on both submerged and exposed locations. Rust can be produced in both the hematite (red color) form and the magnetite (black color, magnetic) form. Rust particles can be swept up by the flow of oil and transported throughout the lubrication system. Rust inhibitors are added to the oil to protect against rusting of oil-wetted metal surfaces. Volatile vapor-phase inhibitors (VPI) may also be added to protect the nonoil-wetted locations. ASTM Test Methods D 665-82 and D 3603-82, ''Rust Preventing Characteristics of Steam Turbine Oil in the Presence of Water,'' are used to evaluate the corrosion protection of the oil [121–123]. However, the most effective method of preventing rust is to keep the lubrication system and the oil free from water.

Water Contamination

The most common contaminant in a lubrication system is water. Water may enter the system from leaks in water-cooled heat exchangers, from condensation of humid air, and from leakage of the steam turbine shaft seals. Water in the oil results in promotion of rust, formation of emulsions, and accumulation of sludge. Consequently, the water-separating ability of the oil is an important characteristic and water must separate quickly from the oil so that it can be collected in and removed from the bottom of the oil reservoir. Large amounts of water form persistent emulsions that join with insoluble oxidation products to form sludge. Accumulation of sludge in oil piping, passages, and coolers impairs circulation of the oil and causes higher bearing and oil temperatures. Higher oil system temperatures, in turn, increase the oil oxidation rate. Sludge also can cause sluggishness or sticking of oil pressure relays and governor pilot valves if the oil is used as the hydraulic control fluid.

Water exists in the dissolved state in oil and will precipitate as free water when it exceeds the saturation (concentration) point. The saturation point of oil varies with its additive package and its temperature. Generally, more additives in oil increase its solubility limit. Hot oil dissolves more water than cold oil so that a drop in oil temperature can result in conversion of part of the dissolved water to free water that collects in low spots or low-flow branches of the lubrication system. Even periodic excursions in the

water content can cause corrosive attack of lubrication system components, resulting in rust spots, corrosion pits, or rapid corrosive removal of bearing surfaces.

STEAM TURBINE CONTROL SYSTEMS

In the past, turbine control technology had to satisfy the demands of a few isolated turbine generators. This was accomplished by the application of a relatively simple mechanical control system. Even when generators were interconnected to larger power pools, this system was the only means of controlling speed and load of steam turbines. The earliest steam turbine control systems were purely mechanical with a "fly ball" governor controlling speed through a series of levers, cams, and springs [124–125].

Since large steam turbines are essentially designed for constant-speed service, the operating governors are designed primarily for speed response. The governor weights in operation rotate with the main shaft, and centrifugal force causes the weights to move away from the shaft upon increase of shaft speed (Fig. 63). These weights are restrained by a helical spring and revolve around the spindle, causing the link attached to the horizontal arm overhead to be moved either up or down. An increase in speed will cause the weight to move outward and change the position of the overhead arm so as to push the relay valve downward. Oil is used as a fluid medium under pressure to move the pilot or relay cylinder pistons. When the piston has assumed a new position under the action of oil admitted through the relay valve, a horizontal link moved by the pilot or relay-cylinder piston rods through linkages connected back to the relay pilot or valve repositions the latter in a neutral or mid-position.

Mechanical Hydraulic Control Systems

As the sizes of steam turbines have grown in capacity, so have the throttle, stop, and control valves, which require larger motive forces to operate the control system quickly and reliably. Fundamentally, all mechanical hydraulic controls are operated utilizing the lubricating oil supplied by the shaft-mounted main oil pump. This hydraulic motive oil pressure is used to obtain the necessary force to actuate the servomotor pistons. The same high-pressure oil is orificed and regulated by various controllers to obtain the lower pressures necessary to monitor the position of the servomotors, by means of automatic stop and oil control pressures (Fig. 63).

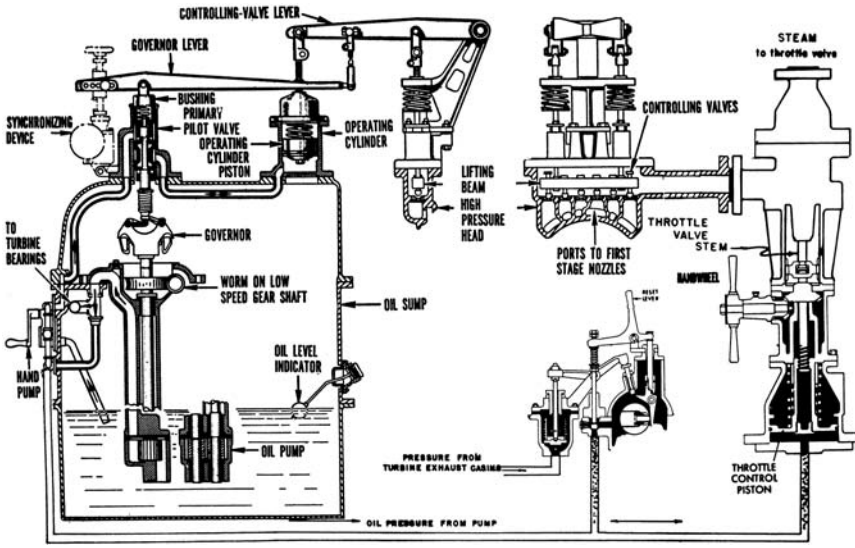

Figure 63 Mechanical hydraulic control/governor/actuator system.

Main and Auxiliary Governors

The main governor with a conventional motor operated speed changer controls the speed or load of the turbine. This governor controls the positioning of the steam inlet (or governing) valves through servomotors, one of which is connected to each steam chest.

The main governor produces a governing control oil pressure that varies in accordance with the turbine speed with a fixed setting of the speed changer. When operating in parallel with a utility system or with large units in the same plant, the electrical tie of the generators controls the turbine speed. Under such operating conditions, the speed changer actually becomes a load changer. This is true because changing the steam flow can only change the torque, while the speed of the turbine is scarcely affected. Accordingly then, there is a different load for every position of the speed changer. The auxiliary governor, mounted on the control block with the main governor, is hydraulically connected to the governing control oil system and has no speed changer or speed setting.

In the event of the complete or partial loss of electrical load, the speed will rise sharply since the main governor speed changer is in such a position that the speed with no power load is higher than normal operating speed. This sudden speed rise will cause the acceleration response feature of the

auxiliary governor to momentarily assume control of the turbine by decreasing the control oil pressure, causing the governing and interceptor valves to close rapidly.

With the governing and interceptor valves closed, the speed of the unit will decrease at a rate depending on the residual load left on the generators. As the unit reaches a speed, which will be determined by the setting of the valve speed changer, the interceptor valves will regulate the flow of steam, holding the speed of the unit constant.

As the pressure in the reheater circuit decreases, the interceptor valves will continue to open. The speed will then tend to drop and the governing valves open to control at the no-load speed corresponding to the setting of the speed changer.

Electro-Hydraulic Control Systems

In the early 1960s, the large turbine generator manufacturers recognized the need for a faster and more accurate steam turbine control system. Solid-state electronic techniques had successfully proven their reliability in other fields such as aerospace and computers. This technology and the use of an even-higher-pressure hydraulic system were combined in the development of the Electro Hydraulic Control System [126–128].

EH Control Systems provide the following main advantages:

Improved reliability
Improved load and frequency control
Simplified interfacing with external systems
More compact valve actuators

Today, complete remote-control operation, supplemented by diagnostic monitoring, automatic startup, and interlocking functions, greatly overshadow the basic control system. Since these more modern functions require a high degree of flexibility, steam turbine engineers recognized the need for a digital computer to be used as the heart of a new control system. Large steam turbine manufacturers now provide fully digital Electro Hydraulic Control Systems.

The spring-loaded steam control and throttle valves are positioned by hydraulic actuators, which receive their motive fluid from a fire-retardant pressurized fluid supply system. In the event of a trip contingency, a high-pressure emergency trip system is interfaced to the lube oil systems by means of a diaphragm or mechanical trip valve (Fig. 64).

The digital controller positions the throttle and governing valves by means of electro-hydraulic servo loops. In the event of a partial load drop, energizing a solenoid valve on the appropriate valve actuators closes the

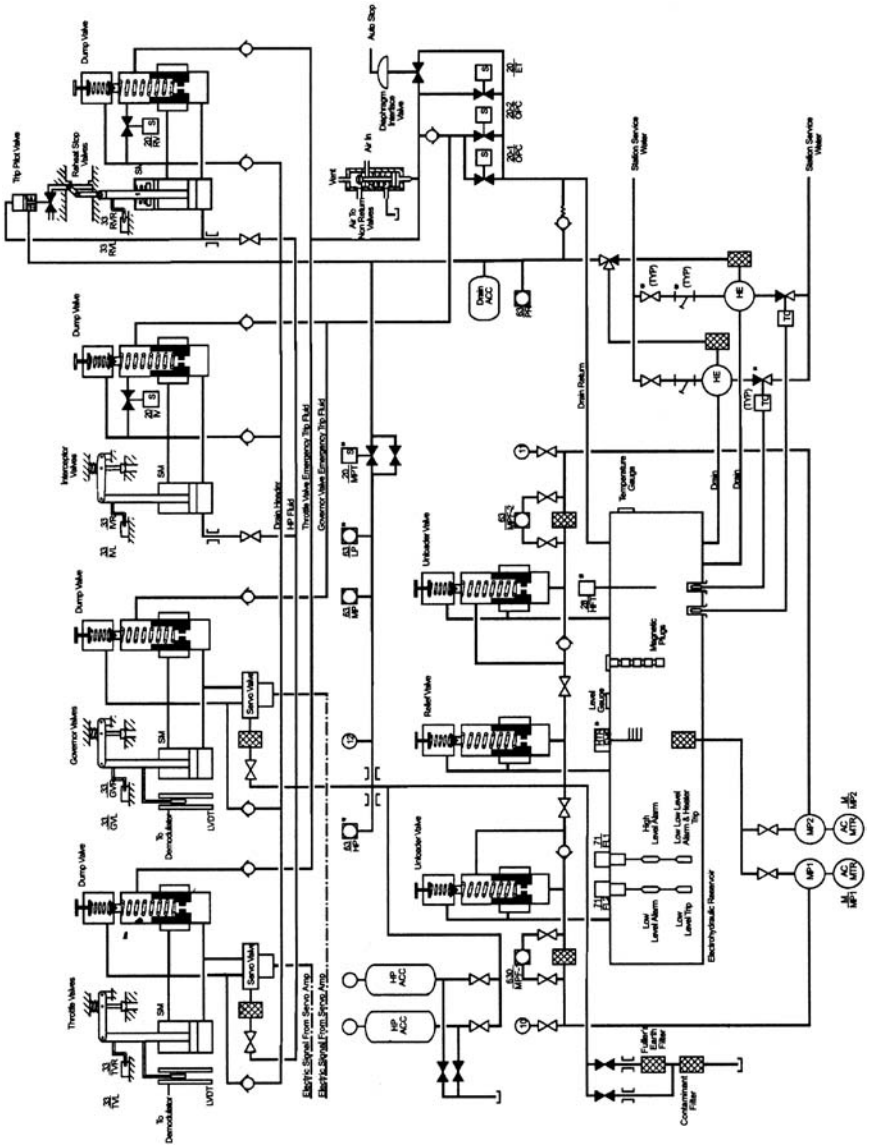

Figure 64 Steam turbine electro-hydraulic control system.

interceptor valves. The digital controller receives three feedbacks from the turbine: speed, generator megawatt output, and first-stage pressure, which are proportional to turbine load. The operator controls the turbine and

receives his or her information from the operator's panel located on the main control board.

Electro-Hydraulic Fluid Supply Control Systems

A typical isolated unloading-type high-pressure fluid supply system is represented in Fig. 64. A 200-gal stainless steel reservoir serves as the housing and focal point of the supply. Stored within the reservoir is the hydraulic motive fluid, a synthetic base phosphate ester type that possesses lubricity, fluid stability, and fire retardance. Self-sustaining oxidation does not result even when subjected to open flame test exceeding 1,000 °F. A dual positive displacement pump fluid supply system accomplishes delivery of the motive fluid. One motor and pump is used as a standby in the event of contingency involving the primary system. A pressure switch on the high-pressure header initiates operation of the second pump, ensuring constant supply to valve positioning demands. Each pump is nominally rated at 20 gpm at 2,500 psig discharge pressure. Drive motors are 30 hp, totally enclosed, fan-cooled. High-pressure fluid is filtered through 10-micron metal mesh filters enroute to unloader valves and isolation check valves. A bank of 1,250-psig nitrogen-charged, piston-type accumulators maintains header pressure. The unloader valve regulates the system pressure at 200 psig. At this point, the pump discharge is diverted to a drain, relieving motor and pump load while the accumulators meet valve actuator demands. As system pressure decays to 1,700 psig, the unloading valve reseats to initiate another loading cycle. A nominal one to four load–unload cycling of the pumps reduces power consumption and greatly extends pump life. Other OEM systems utilize variable displacement pumps to supply EH motive oil supply and pressure [128, 129].

Fluid returning to the reservoir receives polishing filtration cleansing before passing through coolers. Ten-micron system filtration maintains cleanliness equivalent to a class 2 hydraulic fluid as per SAE, ASTM, and AIA Hydraulic Contamination Standards. "Fuller's earth" filters are provided adjacent to the reservoir for control of acidity. On-line maintenance is readily performed as a result of numerous isolation and check valves located between the pumps and the valve actuators.

Emergency Trip Headers

Interfacing of the turbine protective system with the emergency and overspeed protection controller trip systems is illustrated in Fig. 64. Appropriate orificing of the high-pressure lubricating oil-operated trip system establishes the "auto stop header," which physically interfaces the

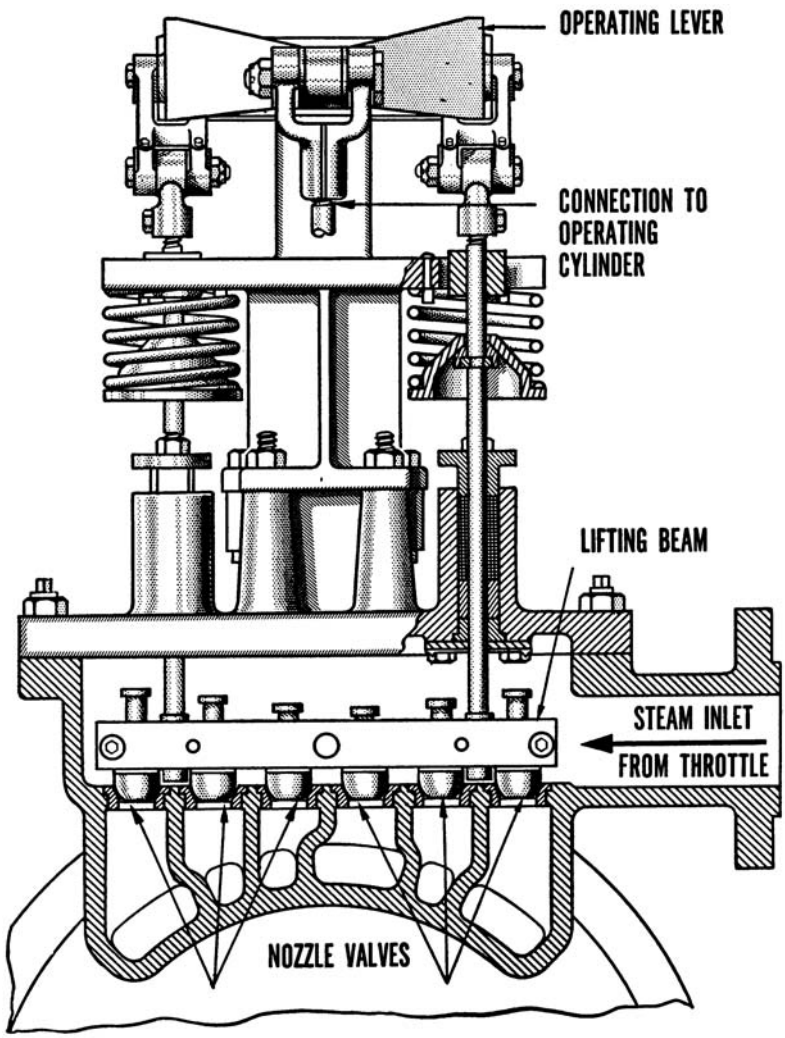

Figure 65 Steam turbine electro-hydraulic fluid supply control system.

emergency system trip header. Any trip function (low bearing oil, low vacuum, thrust bearing, or solenoid) associated with the auto stop unbalances the counteracting forces on the emergency trip diaphragm valve that diverts all actuator motive fluid into the drain system. A pressure switch-operated solenoid valve paralleled with the emergency trip valve as the auto stop pressure collapses achieves redundancy.

A unidirectional check valve isolates the emergency trip header from the overspeed protection controller trip header. Under the condition of an emergency trip, actuating fluid is dumped from beneath all turbine valve actuators. The overspeed protection controller trip closes only the control and interceptor valves. Thus, as the overspeed protection controller solenoids are energized, the governor valves and the interceptor valves immediately close while the check valve maintains emergency trip header pressure to keep the throttle and reheat stop valves in a wide open state. All protective system solenoids are located on the turbine governor pedestal.

Emergency Trip Systems

A hydraulic emergency trip, or mechanical trip valve, and solenoid valves as shown in Fig. 64 typically control the high-pressure fluid trip headers connected to each valve actuator assembly. The mechanical overspeed trip arrangement, which controls the diaphragm-operated emergency trip valve, is retained. When the trip valve is opened by either overspeed or other emergency conditions, the pressure in the two headers is released, initiating quick closing of all steam valve actuators.

A solenoid valve arrangement controls the trip header for the governor and interceptor valves. These solenoid valves are energized by the overspeed protection controller to limit overspeed. Each interceptor valve is equipped with a separate solenoid valve mounted on the actuator block as mentioned before. These solenoid valves are energized to close the interceptor valves during a partial load loss to limit the accelerating steam torque acting on the unit.

Steam Turbine Control and Stop Valving

The steam valves on a large turbine can be classified into four categories. The steam flows through the main stop valve and then a control valve before entering the high-pressure turbine. After the steam leaves a reheater or a moisture separator, the steam will flow through a reheat stop valve and then an interceptor valve before entering an intermediate or low-pressure turbine. The number of each valve, its size, and its type are dependent on the original equipment manufacturer's design criteria and operating utilities' requirement specifications [129, 130].

The primary functions of the steam valves are to provide turbine load control and to protect the turbine from potential overspeed. Two valves are always provided in series to ensure safe closure of either valve during a turbine trip. With increases in turbine steam pressure and temperature to improve cycle efficiency, the relationship between power output and turbine

generator rotor moment of inertia has increased substantially. This design condition, coupled with increased entrapped steam volumes in the main and reheat steam lines, requires a decrease in valve closure times from approximately 0.5 sec to as little as 0.1 sec. These new requirements have prompted a change from the conventional mechanical hydraulic control system (MHC) to the more modern electro-hydraulic control systems (EHC) with improved time response, accurate positioning, and increased operational control.

Earlier steam valves on turbine ratings of approximately 150 MW and less were mounted directing on the turbine casings. This becomes impractical for larger ratings, and so the steam valves were repositioned to either separate steam chests or casings. Some OEM valves are mounted rigidly to the turbine generator foundation. This feature permits the plant designer to accept larger forces and moments on the inlet connections of the valves from either the superheater or hot reheat steam lines. This will generally result in shorter steam lines from the boiler exit to the turbine inlet connections. Other OEM design configuration mount the valve casings or steam chests on conventional or constant-load spring support hangers, resulting in a considerable reduction in allowable forces and moments on the valve inlet connections.

The steam turbine valves are opened by hydraulic forces and closed by springs to ensure maximum safety from potential overspeed. Stop valves are designed to be "bottle-tight"-type valves and generally must not leak more than the rate of two pints per minute during hydrostatic testing. Control and interceptor valves are usually "pressure-balanced" valves, which are permitted increased leakage characteristics depending on OEM and functional requirements (Fig. 65).

Main Stop Valves

The main stop valve is, as the name implies, the principal shut-off valve for steam entering the turbine. The main stop valve is a "bottle-tight" type of valve. The stop valve assembly usually has some form of bypass, or pilot, system, which may be either internal or external to the valve body. This will allow for slow and even heating of the turbine elements prior to unit synchronization. It also provides for a balancing of steam pressure across the main valve. By keeping the steam pressure against which the main stop valve has to work low, the size of the closing springs and that of actuator are significantly reduced. The pilot valve also is frequently used for speed control of the turbine prior to synchronization (Fig. 66).

Usually the main stop valve is designed to operate as a two-position valve after a unit is on-line. It is designed to close quickly in order to protect

Figure 66 Steam turbine stop/throttle and multiple control valves.

the turbine against overspeed. This valve is usually the last valve to receive the signal to close on overspeed, since when this valve closes, a complete restart will be required.

Control Valves

The control valve, which may also be called a governor valve or steam chest valve, provides for load control and is a variable lift type of valve. The operating sequence of the valve is designed to include balanced steam force loading on the turbine, the avoidance of double stock loading in the nozzle area, and an efficient heat rate at various loads.

Steam is typically fed through several control valves and an equal number of inlet pipes to the double control stage as shown in Fig. 67. Four

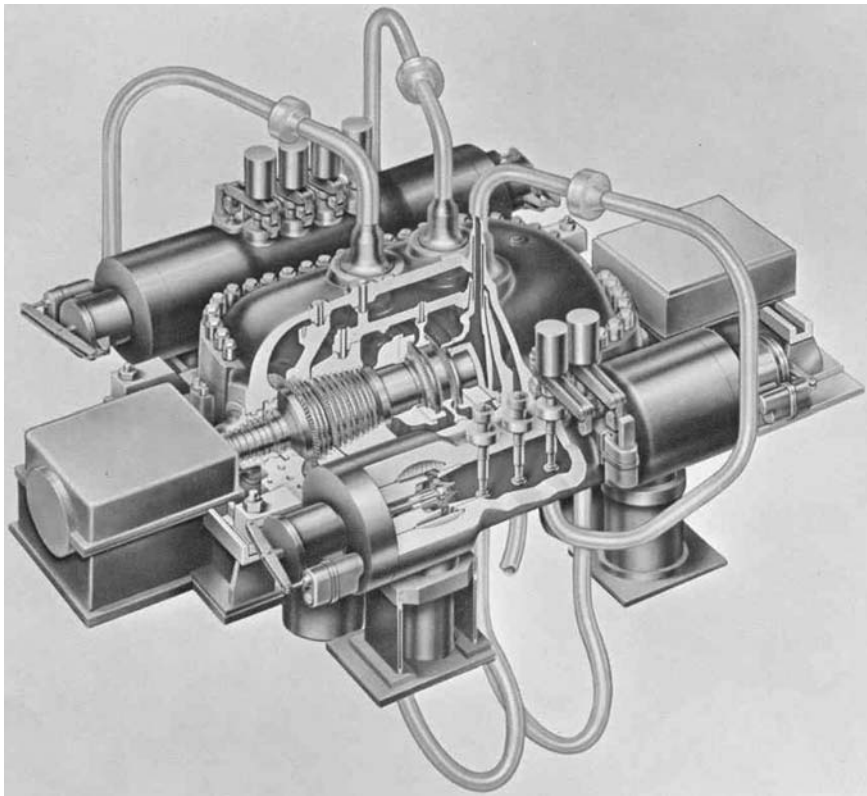

Figure 67 Steam turbine main steam nozzle and control stage inlet configuration.

90° arc nozzle chambers feed each half of the control stage. The control valves are so arranged that the valves open in pairs and feed chambers that are opposite in direction (one chamber of each stage) and diametrically opposite. An equal force on the opposite wheel balances the torque force on one control stage wheel. The only dynamic reaction that remains on the spindle is the torque produced by the diametrically opposite forces on the individual control stages.

Protective Trip and Supervisory Systems

The main steam valves are under the control of autostop oil, which is produced by latching the overspeed trip valve. The trip devices operate directly to rapidly close the throttle valves and reheat stop valves. The governing valves and interceptor valves are hydraulically interlocked with the protective trip devices and remain closed whenever the turbine is tripped. The protective trip devices normally include an overspeed trip, a low-bearing-oil pressure trip, a solenoid trip, a thrust-bearing trip, and a low vacuum trip. The protective devices are included in a separate assembly but connected hydraulically to the overspeed trip valve through the trip relay.

Overspeed Trip Mechanism

This mechanism consists of an eccentric weight or ring mounted at the end of the turbine shaft, which is balanced in position by a spring until the speed reaches approximately 111% of normal operating speed. Its centrifugal force then overcomes the holding spring and the weight or ring flies out striking a trigger, which trips the overspeed trip valve releasing the autostop pressure to drain.

The autostop control pressure is connected to a governing emergency trip valve, which releases the control oil pressure. Therefore, all valves capable of admitting steam into the turbine will close. An air pilot valve used to monitor the extraction nonreturn valves is also triggered from the autostop pressure. The autostop is also tripped when any one of the protective devices, such as the low-bearing oil, low vacuum, solenoid, thrust-bearing trip, etc. are actuated.

Provision is made for testing the overspeed trip mechanism without actually overspeeding the turbine. If the overspeed trip mechanism reset lever is held to prevent the trip valve from opening, it can be tested without taking the unit off the line or removing load. This is accomplished by admitting oil under pressure to the chamber beneath the trip weight and noting the pressure required to move the weight outward. On EHC systems,

an additional electronic overspeed trip is provided through a "toothed wheel" and proximity probe mounted in the front standard or pedestal.

Low-Bearing-Oil Pressure Trip

This device typically consists of a spring-loaded diaphragm exposed to bearing oil pressure. Excessively low-bearing-oil pressure can cause overheating or scoring of journal bearings. A diaphragm is connected to a dump relay through a linkage mechanism. If the bearing pressure falls below a preset valve of 5 to 6 psig, it will release the oil from the overspeed trip valve through an intermediate relay. Other OEM design configurations utilize a dual system of hydraulic pressure switches for the low-bearing-oil pressure switch.

Low Vacuum Trip

The low vacuum trip protects the turbine from operation without adequate condenser vacuum. Low condenser vacuum can cause "stall-flutter" of the last row of rotating turbine blades, particularly at low operating loads. This device typically utilizes a pressure-responsive bellow, which is exposed to the turbine exhaust pressure. When the exhaust pressure drops below a preset value, adjustable between 18 and 25 in. of mercury, it causes the trip relay to release the overspeed trip valve. A means of latching the vacuum trip is provided, which when engaged prevents the device from operating during startup when the exhaust vacuum is less than the normal trip setting. However, it will function with the latch engaged should the exhaust pressure increase to $2\frac{1}{2}$ to $3\frac{1}{2}$ psig during the starting cycle. The latch will fall out of engagement when the exhaust vacuum has reached a value of 20 to 28 in. of mercury and will thereafter trip at the normal value of 18 to 25 in. of mercury, unless relatched. This function can also be accomplished through the use of a dual system of hydraulic pressure switches.

Emergency Solenoid Trip

A protective trip is provided that, when energized, operates through the same mechanism as the vacuum trip device. The solenoid trip feature permits remote tripping from the control room or by means of protective relays.

Thrust-Bearing Trip

The thrust-bearing trip device is used to warn the operator of abnormal wear of the thrust-bearing shoes and to shut down the unit in case shoe wear increases to the point where it may cause serious damage to close-fitting other turbine parts such as seals or stationary and rotating blading. It typically consists of two small nozzles whose openings are close to the thrust collar faces. High-pressure oil is supplied to each nozzle through an orifice and pressure is built up in the line through ball check valves to a spring-loaded diaphragm. Should excessive thrust-bearing wear occur, the thrust-bearing collar will move toward one of the nozzles and the oil pressure in the line will increase. When this pressure rises to 30 psig, a pressure switch will close and sound an alarm. Should wear continue, the pressure will continue to rise; when it reaches 80 psig the diaphragm will overcome the spring load and open the dump relay through the same mechanism as the other protective devices and thus release the overspeed trip valve. On EHC systems the thrust remains the trip device, which detects thrust-bearing wear using an eddy current probe to determine the axial distance between rotating and stationary components.

Supervisory Systems

Turbine generator control systems are also provided with a supervisory system, which senses, records, and alarms a number of measured variables (Fig. 68).

The measured variables, which vary with turbine design and individual purchaser's requirements, include the following:

Lateral vibration
Vibration phase angle
Differential expansion between casing and rotor
Valve positions
Turbine speed
Rotor eccentricity
Casing temperatures
Casing expansion
Bearing, and casing temperatures
Exhaust pressure

Earlier MHC supervisory systems were limited to recording on circular or strip chart recorders. Modern EHC systems are capable of both magnetic tape recording of data for long-term storage capability as well as

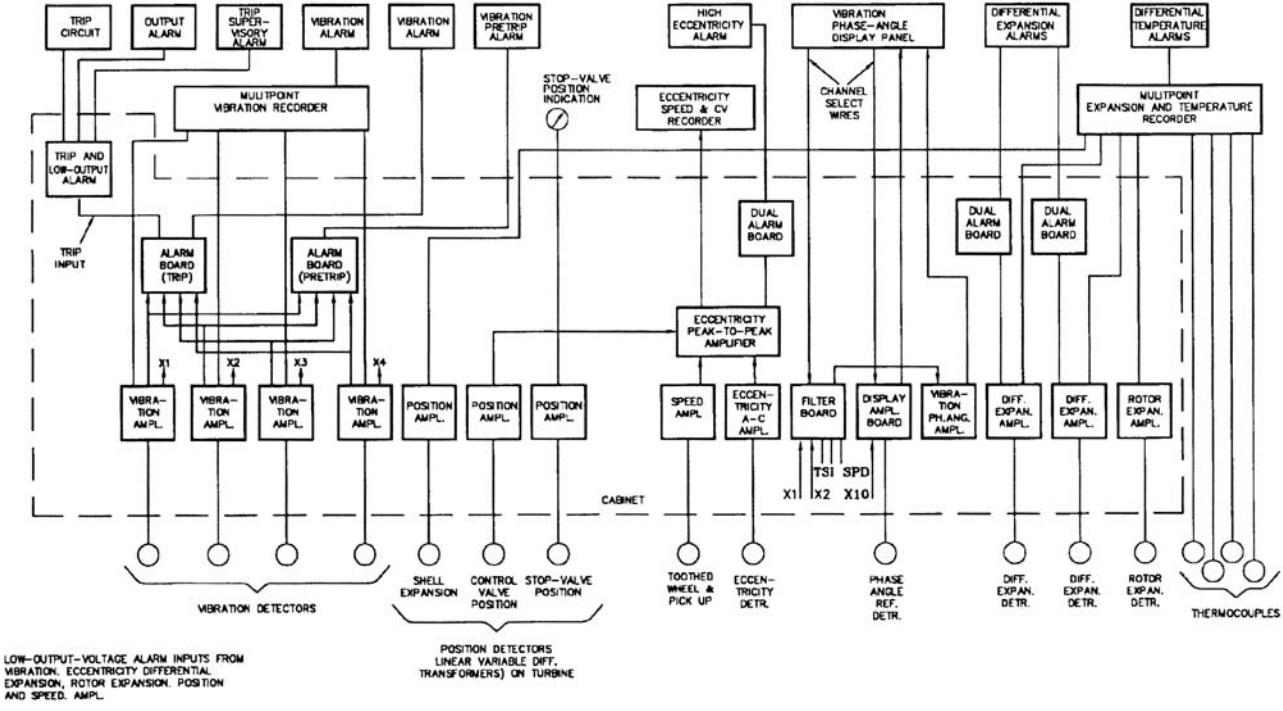

Figure 68 Steam turbine protective trip and supervisory alarm control systems.

instantaneous video graphic computerized display and processing of supervisory data.

FUTURE STEAM TURBINE DEVELOPMENTS

1. Moving to longer intervals between maintenance outages. A significant need in today's competitive climate is to maximize the interval between major turbine generator inspections and overhauls, while still operating safely and protecting these major plant assets. The key questions inherent in such a change are whether existing damage can be detected, and future accumulation of damage predicted and controlled (Fig. 69).

2. Methods to shorten maintenance outage periods. Continued development of innovative maintenance and inspection approaches will enable utilities to reduce turbine generator outage time and cost. Innovations required include (1) specific techniques to reduce the duration of the sequence of outage actions, such as quick opening/closure techniques, assembly/disassembly techniques, or advanced bolting and coupling systems, (2) identification and assessment of innovative in-situ turbine inspection technologies and practices, and (3) continued development and verification of "on-deck" and factory rotor/blading weld repairs [115, 117, 120].

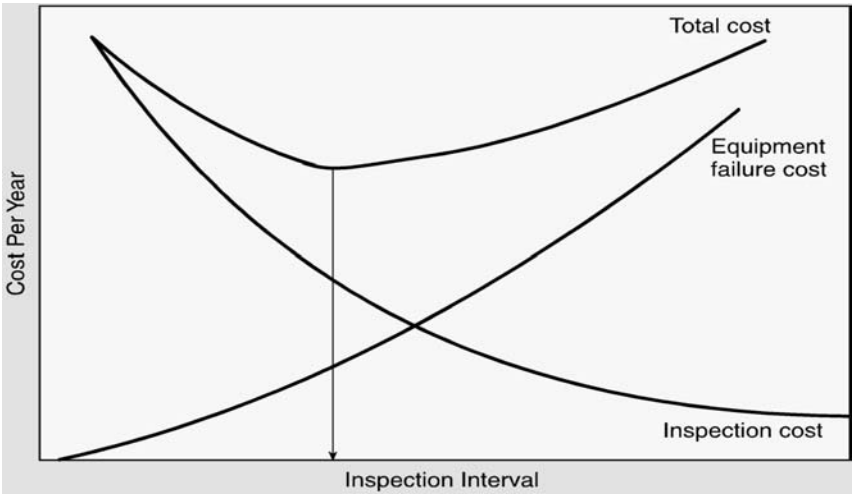

Figure 69 Optimized steam turbine inspection intervals based on economic net present value (NPV).

3. Need for better understanding of the economics needed to justify changes in turbine design, materials, and operating practice. Throughout this chapter it is noted that economic analysis is needed in order to properly weigh run/repair/replace options when steam path damage is found. Ultimately, the constraints of a particular economic analysis are owner-specific. However, there is need for more comprehensive models that can perform sensitivity studies quickly to key variables [134–141].

4. Need for better understanding of the fundamentals of the deposition process. Control of deposition would lead to significant benefit, most notably improvements to the efficiency in all turbine stages. Control of deposition may be achieved by several methods including improved surface finish and improvements in steam chemistry (Fig. 70) [136].

5. Modification of the processes of nucleation, condensation, and formation of liquid films and deposition. Significant benefits will be achieved if these basic processes can be controlled. Efficiency improvements will be realized by better control over moisture levels (such as through moisture removal techniques) and slowing down the dynamics of droplet formation.

6. Improving flow-path design, particularly in the last stage of the LP and in exhausts hoods. It is ironic that despite the recent advances in three-dimensional aerodynamic analysis design, the last LP stage in fossil fired units remains the least thermodynamically efficient row in the steam path, even though it has the largest available energy. Programs to use advanced tools such as three-dimensional CFD codes to optimize the design of the

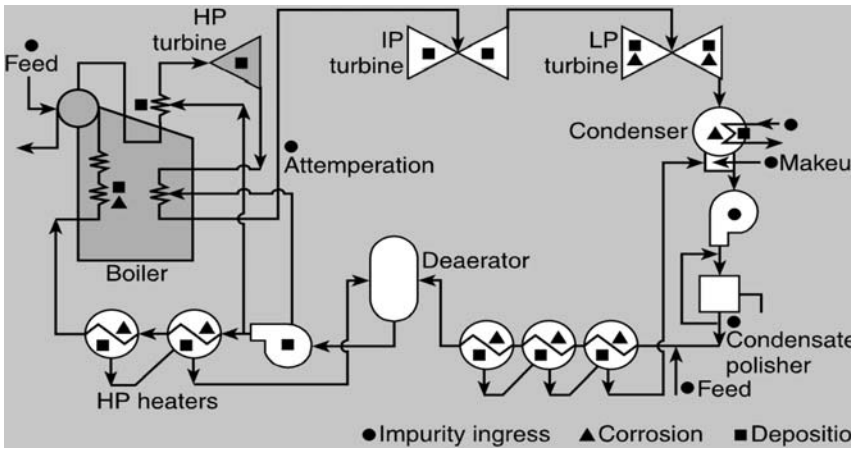

Figure 70 Rankine cycle deposition and corrosion sites.

flow path will continue to be developed and see an increasingly larger role in the design and retrofitting of large steam turbines.

Improvements in turbine exhaust hoods and/or last-row blade performance can have some substantial consequences. Reducing hood loss will increase leaving loss and may increase the loss in last-row exit turning because of jet deflection. Only a fraction of the reduced hood loss in the last rotating row can be recovered. Similarly, increased blading efficiency also results in increased exit jet velocity and consequently higher hood loss. Neither of these tradeoffs implies that there is no improvement in turbine performance.

7. Moving to advanced steam conditions. Challenges to the integrity of the steam path will result from the constant push toward more aggressive operating conditions such as higher temperatures associated with advanced steam plants. Such advanced steam conditions may lead to higher thermodynamic efficiencies utilizing combined cycles employing cooling of the gas turbine blades with steam from the steam turbine (approaching 60% Rankine cycle efficiencies) (Fig. 71). However, moving toward advanced steam conditions will tend to exacerbate many of the damage types currently affecting the steam path, thus imposing greater requirement for the evaluation and control of damage.

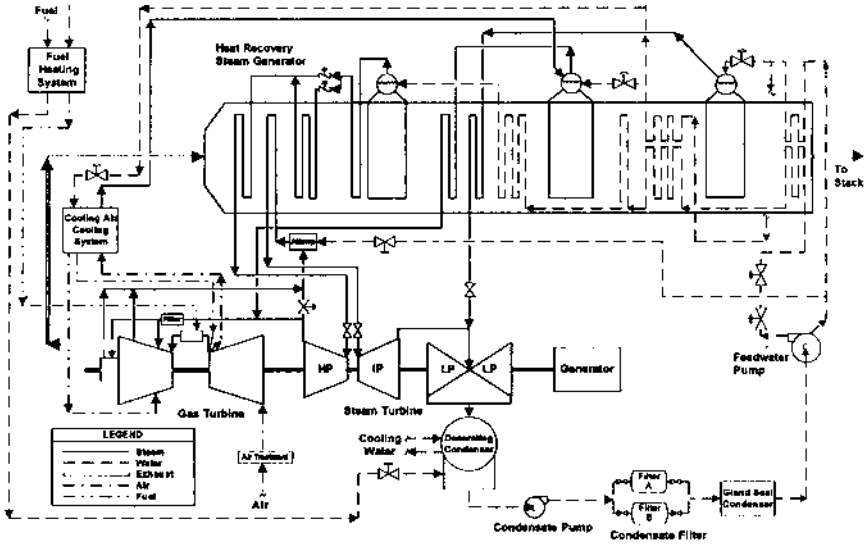

Figure 71 Combined Rankine and Brayton cycles for improved overall cycle efficiency.

REFERENCES

1. J. C. Zink, "Steam Turbines Power—An Industry," *Power Engineering*, pp. 24–30, Aug. (1996).
2. A. Stodola, *Steam Turbines with an Appendix on Gas Turbines and the Future of Heat Engines*, 1905 and 1927 editions (L. C. Loewenstein, trans.), D. Van Nostrand Company, New York (1945).
3. C. A. Parsons, "The Steam Turbine," The Rede Lecture, Cambridge University Press (1911).
4. J. D. Storer, *A Simple History of the Steam Engine*, John Baker, London (1969).
5. E. L. Robinson, "The Steam Turbine in the United States. III—Developments by the General Electric Co.," *Mechanical Engineering*, April (1937).
6. J. K. Salisbury, *Steam Turbines and Their Cycles*, 1950, reprinted by Krieger Publishing Company, Malabar, FL (1974).
7. W. Traupel, *Thermische Turbomachinen*, Springer-Verlag, New York (1958).
8. H. Craig and H. Cox, "Performance Estimation of Axial Flow Turbines," *IMECHE Proc. 185*: 32–71 (1970–1971).
9. K. C. Cotton, *Evaluating and Improving Steam Turbine Performance*, Cotton Fact, Inc., Rexford, NY (1993).
10. P. Cohen, ed., *The ASME Handbook on Water Technology for Thermal Systems*, The American Society of Mechanical Engineers, New York (1989).
11. J. D. Bernal, *Science and Industry in the Nineteenth Century*, Indiana University Press, Bloomington, IN (1970).
12. G. J. Silvestri, "Steam Turbines," Chapter 1 in P. Cohen, ed., *The ASME Handbook on Water Technology for Thermal Systems*, The American Society of Mechanical Engineers, New York, pp. 1–40 (1989).
13. International Association for the Properties of Water and Steam, *IAPWS IF97 Industrial Formulation 1997 for the Thermodynamic Properties of Water and Steam*, published by the International Association for the Properties of Water and Steam, copies available from Dr. R. B. Dooley, EPRI, Palo Alto, CA (1997). See also W. Wagner and A. Kruse, *Properties of Water and Steam: The Industrial Standard IAPWS-IF97 for the Thermodynamic Properties and Supplementary Equations for Other Properties*, Springer-Verlag, New York, (1998).
14. W. T. Parry, "New Steam Properties Now and for the 21st Century," ASME Research Subcommittee for the Properties of Water and Steam, presented at the International Joint Power Conference, Baltimore, MD (1998). Paper to be separately published in 1999.
15. American Society of Mechanical Engineers, *Performance Test Code 6 on Steam Turbines*, ASME PTC 6-1996, American Society of Mechanical Engineers, New York (1996).
16. A. Stodola, *Steam Turbines with an Appendix on Gas Turbines and the Future of Heat Engines*, 1905 and 1927 editions (L. C. Loewenstein, trans.), D. Van Nostrand Company, New York (1945).

17. P. Schofield, "Steam Turbines," Chapter 3 in P. Cohen, ed., *The ASME Handbook on Water Technology for Thermal Systems*, The American Society of Mechanical Engineers, New York, pp. 113–177 (1989).
18. C. Rice, J. C. Harris, S. F. Gibson, J. L. Ellis, N. E. Cowden, and D. H. Cioffi, "Steam Turbine Performance Survey Compiled from Steam Path Audits," *Proc. 1992 EPRI Heat Rate Improvement Conference*, TR-102098, EPRI, Palo Alto, CA, March (1993).
19. T. McCloskey, R. Dewey, S. Hesler, and M. Pollard, "Low Pressure Steam Turbine Thermal Performance Improvements," *Thirteenth Annual Plant Performance Enhancement Program*, held August 12–14, 1997, in San Antonio, TX, Plant Support Engineering, EPRI, Charlotte, NC (1997).
20. A. N. Paterson, G. Simonin, and J. G. Neft, "Steam Turbines for Advanced Steam Conditions," in *Symposium on Steam Turbines and Generators*, held in Monaco, October 12–14, 1994, GEC Alsthom (1994).
21. G. Gyarmathy, "Basic Notations," Chapter 1 in M. J. Moore and C. H. Sieverding, eds., *Two-Phase Steam Flow in Turbines and Separators: Theory, Instrumentation, Engineering*, Hemisphere Publishing Company, Washington, pp. 1–57 (1976).
22. W. P. Sanders, *Turbine Steam Path Engineering for Operations and Maintenance Staff*, Turbo-Technic Services Incorporated, Toronto, Ontario, Canada, Dec. (1988).
23. T. McCloskey, R.Dewey, S. Hesler, and M. Pollard, "Low Pressure Steam Turbine Thermal Performance Improvements," *Thirteenth Annual Plant Performance Enhancement Program*, held August 12–14, 1997, in San Antonio, TX, Plant Support Engineering, EPRI, Charlotte, NC (1997).
24. D. W. Gandy, S. J. Findlan, R. Munson, W. F. Newell, and J. T. Stover, *State-of-the-Art Weld Repair Technology for Rotating Components, Volume 1: Weld Repair of Steam Turbine Discs and Rotors*, Final Report TR-107021, Electric Power Research Institute, Palo Alto, CA, Oct. (1996).
25. A. Juntke, W. R. Sylvester, and M. J. Hargrove, "Experience with Turbine Bypass Systems and Solid Particle Erosion," in S. R. Murphy, ed., *Solid Particle Erosion of Steam Turbine Components: 1989 Workshop*, held March 7–9, 1989, in New Orleans, LA, Proceedings GS-6535, EPRI, Palo Alto, CA, pp. 5-17–5-30 (1989).
26. W. G. Steltz, D. D. Rosard, O. W. Durrant, L. G. Crispin, K. H. Haller, J. Price, R. Friedman, H. Termuehlen, G. Gartner, P. Anderson, and A. Bose, *Assessment of Fossil Steam Bypass Systems*, Final Report CS-3717, EPRI, Palo Alto, CA (1984).
27. American Society of Mechanical Engineers, "Recommended Practices for the Prevention of Water Damage to Steam Turbines Used for Electric Power Generation," ASME Standard TDP-1-1980, Part 1—Fossil Fueled Plants, American Society of Mechanical Engineers, New York (1980).
28. ASME Turbine Water Damage Prevention Committee, "Recommended Practices for the Prevention of Water Damage to Steam Turbines Used for Electric Power Generation—Part 1: Fossil Fueled Plants," ASME Standard

No. TWDPS-1, The American Society of Mechanical Engineers, New York (1972).
29. F. L. Weaver, "Turbine Bucket Design," ASME Paper No. 74-Pet-30 (1974).
30. R. C. Bates, J. W. Cunningham, N. E. Dowling, F. J. Heymann, O. Jonas, L. D. Kunsman, A. R. Pebler, V. P. Swaminathan, L. E. Willertz, and T. M. Rust, *Corrosion Fatigue of Steam Turbine-Blading Alloys in Operational Environments*, Final Report CS-2932, EPRI, Palo Alto, CA (1984).
31. R. Pigott, and R. E. Warner, "Steam Turbine Blade Developments," presented at the Joint ASME/IEEE Power Generation Conference held in Portland, OR, October 19–23 (1986).
32. R. C. Bates, F. J. Heymann, V. P. Swaminathan, and J. W. Cunningham, *Steam Turbine Blades: Considerations in Design and a Survey of Blade Failures*, Final Report CS-1967, EPRI, Palo Alto, CA (1981).
33. D. W. Gandy, S. J. Findlan, J. T. Stover, M. Breslin, S. Allgood, and E. V. Clark, *State-of-the-Art Weld Repair Technology for Rotating Components. Volume 2: Repair of Steam Turbine Blading*, Final Report TR-107021, EPRI, Palo Alto, CA (1996).
34. R. E. Peterson, *Stress Concentration Factors*, John Wiley & Sons, New York (1974).
35. B. J. Lazan, *Damping of Materials and Members in Structural Mechanics*, Pergamon Press, New York (1968).
36. J. T. Wagner, "Blade Damping Tests," Westinghouse Engineering Report, ED-401, NOGS N00024-67-C-5494, May (1969).
37. H. Gotoda, "An Analysis on Resonant Stress and Damping in Turbine Blades," Turbine Designing Department, Kawasaki Heavy Industries, Ltd., Kobe, Japan (1974).
38. N. F. Rieger, "Damping Properties of Steam Turbine Blades," *Proc. WPAFB Materials Laboratory: Vibration Damping Workshop*, Queen Mary Hilton, Long Beach, CA, Feb. (1984).
39. J. M. Allen, "Characteristics of Nonsynchronous Vibration of Turbine Blades," in Stress Technology, Inc., *Proc. Steam and Combustion Turbine-Blading Conference and Workshop—1992*, Orlando, FL, Jan. 29–31, 1992, Proceedings TR-102061, EPRI, Palo Alto, CA, pp. 4-45–4-81 (1993).
40. K. Namura, K. Ikeuchi, T. Tan, T. Lam, and E. Wan, "Development of New 20.9-Inch Next-to-Last Stage Blade for Improved Turbine Reliability and Efficiency," *American Power Conference* (1998).
41. D. S. Whitehead, "A Finite Element Solution of Unsteady Flow in Cascades," *International J. Numerical Methods for Fluids, 10*: 13–34 (1990).
42. W. P. Sanders, *The Procurement of Replacement Steam Turbine Blading*, Forham Printing Company, Ltd., Toronto, Canada (1993). Distributed by Turbomachinery International, Norwich, CT.
43. J. L. Ray, "Investigation of Materials to Reduce Steam Turbine Blade Wear," *Power*, May 26, pp. 804–808 (1931).
44. W. H. Lloyd, "Avoid Blade Corrosion and Erosion," *Power*, April, pp. 94–97, 204 (1952).

45. J. Drahy, "Water Droplet Erosion of Titanium Alloy Steam Turbine Blading," in R. I. Jaffee, ed., *Titanium Steam Turbine Blading*, held Nov. 9–10, 1988, Palo Alto, CA, Workshop Proceedings ER-6538, EPRI, Palo Alto, CA, and Pergamon Press, pp. 405–426 (1990).
46. T. H. McCloskey and N. F. Rieger, "Assessment Technology for Turbine Blades," in R. Viswanathan and R. W. Porter, eds., *Life Assessment Technology for Fossil Power Plants, Proceedings of the American Power Conference, 57* (III), American Power Conference, Illinois Institute of Technology, Chicago, IL, pp. 1965–1979.
47. R. I. Jaffee, "Foreword" in R. I. Jaffee, ed., *Titanium Steam Turbine Blading*, held Nov. 9–10, 1988, Palo Alto, CA, Workshop Proceedings ER-6538, EPRI, Palo Alto, CA, and Pergamon Press (1996).
48. M. O. Speidel, "Corrosion-Fatigue of Steam Turbine Blade Materials," in R. I. Jaffee, ed., *Corrosion Fatigue of Steam Turbine Blade Materials*, Workshop Proceedings held in Palo Alto, CA, Sept. 21–24, 1981, Pergamon Press, New York, pp. 1-1–1-23 (1983).
49. D. B. Roach, *The Potential for Duplex Stainless Steels for Utility Applications*, Final Report RD-3401, EPRI, Palo Alto, CA (1984).
50. T. H. McCloskey and N. F. Rieger, "Assessment Technology for Turbine Blades," in R. Viswanathan and R. W. Porter, eds., *Life Assessment Technology for Fossil Power Plants, Proceedings of the American Power Conference, 57* (III), American Power Conference, Illinois Institute of Technology, Chicago, IL, pp. 1965–1979.
51. R. Pigott, and R. E. Warner, "Steam Turbine Blade Developments," presented at the Joint ASME/IEEE Power Generation Conference held in Portland, OR, Oct. 19–23 (1986).
52. N. F. Rieger, and T. H. McCloskey, "Turbine Blade Life Assessment," in *International Conference on Life Assessment and Extension*, The Hague, The Netherlands, June 13–15, pp. 219–233 (1988).
53. H. K. Heen and R. W. Mann, "The Hydraulic Analogy Applied to Non-Steady Two-Dimensional Flows in the Partial Admission Turbine," *Trans. ASME J. Basic Engineering*, Series D, Sept., pp. 408–421 (1961).
54. N. F. Rieger, "Diagnosis and Correction of Vibration Problems in Turbine Generator Units," *Proc. EPRI Workshop on Power Plant Availability*, Dearborn, MI (1982).
55. A. J. Partington, "Vibration Analysis of Steam Turbine Pinned Root Control Blades," *Rotordynamic Problems in Power Plants: Proceedings of the FToMM International Conference*, Rome, Italy, Sept. 28–Oct. 1 (1982).
56. A. Atrens, H. Meyer, G. Faber, and K. Schneider, "Steam Turbine Blades," in M. O. Speidel and A. Atrens, eds., *Corrosion in Power Generating Equipment*, Plenum Press, New York, pp. 299–328 (1984).
57. R. C. Bates, F. J. Heymann, V. P. Swaminathan, and J. W. Cunningham, *Steam Turbine Blades: Considerations in Design and a Survey of Blade Failures*, Final Report CS-1967, EPRI, Palo Alto, CA (1981).

58. A. V. Sarlashkar and T. C. T. Lam, "Blade Root Attachment Evaluation Low-Cycle Fatigue Estimates Based on Probabilistic Approach," in *Proc. 1996 International Joint Power Generation Conference, Volume 2: Power*, American Society of Mechanical Engineers, New York, pp. 511–516 (1996).
59. S. Sakurai, and H. Miyata, "Failure Analysis and Life Assessment of Low Pressure Turbine Blades," in D. M. Rasmussen, ed., *Latest Advances in Steam Turbine Design, Blading, Repairs, Condition Assessment and Condenser Interaction*, 1989 Joint Power Generation Conference held in Dallas, TX, Oct. 22–26, 1989, PWR-Vol. 7, American Society of Mechanical Engineers, New York, pp. 9–15 (1989).
60. C. Hong, T. C. Lam, and S. H. Hesler, "Steady and Nonsteady Steam Bending Force Analysis and Its Application to Blade Life Assessment," in L. D. Nottingham and P. F. Sabourin, eds., *Proceedings: EPRI Steam Turbine and Generator NDE, Life Assessment, and Maintenance Workshop*, held July 16–19, 1991, Charlotte, NC, Proceedings TR-101333, EPRI, Palo Alto, CA, pp. 43-1–43-18 (1992).
61. M. J. Moore, and C. H. Sieverding, eds., *Aerothermodynamics of Low Pressure Steam Turbines and Condensers*, Hemisphere Publishing Corporation, Washington (1987).
62. W. G. Steltz, "A Simplified and Generalized Approach to Design and Analysis of Axial Flow Steam and Gas Turbine Blade Paths," in C. P. Bellanca, ed., *Advances in Steam Turbine Technology for Power Generation* ASME Book No. G00518, American Society of Mechanical Engineers, New York (1991).
63. R. P. Dewey, and A. V. Sarlashkar, *Low-Pressure Turbine Blade Design Evaluation*, Final Report TR-105839, EPRI, Palo Alto, CA (1995).
64. M. D. Lefcourt, "An Investigation into Unsteady Blade Forces in Turbomachines," *J. Engrg. for Power Trans. ASME, 87*, Ser. A: 345–354 (1965).
65. W. P. Sanders, *The Procurement of Replacement Steam Turbine Blading*, Forham Printing Company, Ltd., Toronto, Canada (1993). Distributed by Turbomachinery International, Norwich, CT.
66. J. A. Owczarek, "On a Wave Phenomenon in Turbines," *J. Engrg. for Power Trans. ASME, 91*, Ser. A: 223–238 (1969).
67. W. P. Sanders, *Turbine Steam Path Engineering for Operations and Maintenance Staff*, Turbo-Technic Services Incorporated, Toronto, Canada (1988).
68. R. Kroon, "Turbine-Blade Vibration Due to Partial Admission," *Applied Mechanics*, Dec. (1940).
69. M. A. Pollard, R. P. Dewey, and H. Yu, "Analysis of Solid Particle Erosion Damage to an HP Turbine First Stage Bucket," in I. Fruchtman, S. Hartman, B. Moore, R. Henry, D. Karg, M. Curley, S. Reid, and B. Sykes, eds., *Proc. International Joint Power Generation Conference: Volume 3: Power*, Papers from the 1995 International Joint Power Generation Conference held in

Minneapolis, MN, Oct. 8–12, 1995, PWR-Vol. 28, American Society of Mechanical Engineers, New York, pp. 415–422 (1995).
70. J. S. Alford, "Protecting Turbomachinery from Unstable and Oscillatory Flows," *J. Engrg. for Power Trans. ASME, 89*: 513–528 (1967).
71. W. Campbell, "Protection of Steam Turbine Disk Wheels from Axial Vibration," *Trans. ASME, 46*(1920) (1924).
72. T. Lam, R. Dewey, and A. Sarlashkar, "The Importance of Blade-Disk Modeling for Defining Resonant Operation Conditions," in Stress Technology, Inc., *Proc. Steam and Combustion Turbine-Blading Conference and Workshop—1992*, held in Orlando, FL, Jan. 29–31, 1992, Proceedings TR-102061, EPRI, Palo Alto, CA, pp. 4-21–4-41 (1993).
73. S. R. Reid, "Coupled Blade-Rotor Torsional Vibration Component and Low Pressure Blade Retrofit Issues," in I. Fruchtman, S. Hartman, B. Moore, R. Henry, D. Karg, M. Curley, S. Reid, and B. Sykes, eds., *Proc. International Joint Power Generation Conference: Volume 3: Power*, Papers from the 1995 International Joint Power Generation Conference held in Minneapolis, MN, Oct. 8–12, 1995, PWR-Vol. 28, American Society of Mechanical Engineers, New York, pp. 251–259 (1995).
74. E. Tsunoda, H. Mimuro, S. Hisa, H. Sakakida, and S. Mori, "Torsional Vibration Evaluation Technique for Large-Capacity Steam Turbine," *Proc. American Power Conference, 51*, Illinois Institute of Technology, Chicago, IL, pp. 109–114 (1989).
75. K. Kuwamoto, and T. Sugitani, "Reliability Enhancement of Turbine-Generator System Against Blade-Shaft Coupled Vibration," *50th Annual Meeting of the American Power Conference*, Chicago, IL, April 18–20 (1988).
76. J. A. LaRosa, *et al.*, "Analysis of Turbine Blade Vibrations Induced by Electrical-Mechanical Interactions," *Proc. 1980 Joint Power Generation Conference*, Phoenix, AZ, Sept. 28–Oct. 2 (1980).
77. O. Matsushita, K. Naura, T. Yoshi, R. Kaneko, and A. Okabe, "Torsional Vibration Analysis of Turbine-Generator-Blade Coupled System," *Proc. American Power Conference, 51*, Illinois Institute of Technology, Chicago, IL, pp. 81–86 (1989).
78. M. Higuchi, and T. Tsuda, "Telemetry Test of Blade Shaft Coupled Torsional Vibration at the Tsuruga No. 2 Power Plant," *Proc. American Power Conference, 51*, Illinois Institute of Technology, Chicago, IL, pp. 103–108 (1989).
79. J. D. Hurley, and S. A. Welhoelter, "Turbine-Generator Design, Analysis, and Testing for Prevention of Double-Frequency Torsional Resonance," *Proc. American Power Conference, 51*, Illinois Institute of Technology, Chicago, IL, pp. 87–93 (1989).
80. K. Steigleder and E. Kramer, "Coupled Vibrations of Steam Turbine Blades and Rotors Due to Torsional Excitation by Negative Sequence Currents," *Proc. American Power Conference, 51*, Illinois Institute of Technology, Chicago, IL, pp. 94–102 (1989).

81. *IEEE Guide for Abnormal Frequency Protection for Power Generating Plant*, ANSI/IEEE Standard C37.106-1987, American National Standards Institute, New York (1987).
82. P. Kundur, *Power System Stability and Control*, McGraw-Hill, Inc., New York (1993).
83. F. Sisto, "Stall Flutter in Cascades," *J. Aeronautical Sci., 20*(9): 598–604 (1953).
84. V. Omprakash, A. V. Sarlashkar, T. C. T. Lam, L. H. Shuster, and T. H. McCloskey, "Flutter Stability Investigation of Low-Pressure Steam Turbine Bladed Disks," in W. G. Moore, ed., *Advances in Steam Turbine Technology for the Power Generation Industry*, Papers from the 1994 International Joint Power Generation Conference held in Phoenix, AZ, Oct. 2–6, 1994, PWR-Vol. 26, American Society of Mechanical Engineers, New York, pp. 57–65 (1994).
85. A. D. Maddaus, A. Morson, and M. F. O'Conner, "Continuously Coupled Last-Stage Bucket Design and Experience," *Proc. American Power Conference*, April 26–28, Chicago, IL (1982).
86. D. H. Evans, "Comparison of Unstalled Flutter Predictions and Field Measurements for Steam Turbine Blades," in Stress Technology, Inc., *Proc. Steam and Combustion Turbine-Blading Conference and Workshop—1992*, held in Orlando, FL, Jan. 29–31, 1992, Proceedings TR-102061, EPRI, Palo Alto, CA, pp. 4-85–4-99 (1993).
87. D. S. Whitehead, and S. G. Newton, "A Finite Element Method for the Solution of Two-Dimensional Transonic Flows in Cascades," *International J. Numerical Methods for Fluids, 5*: 115–132 (1985).
88. D. S. Whitehead, "A Finite Element Solution of Unsteady Flow in Cascades," *International J. Numerical Methods for Fluids, 10*: 13–34 (1990).
89. P. F. Rozelle, D. H. Evans, and B. B. Seth, "Development and Application of a Blade Vibration Monitor," in D. M. Rasmussen, ed., *Latest Advances in Steam Turbine Design, Blading, Repairs, Condition Assessment and Condenser Interaction*, 1989 Joint Power Generation Conference held in Dallas, TX, Oct. 22–26, 1989, PWR-Vol. 7, American Society of Mechanical Engineers, New York, pp. 37–45 (1989).
90. S. I. Nedeljkovic, P. F. Rozelle, and B. B. Seth, "Design and Verification of Mixed-Tuned Titanium Freestanding Low Pressure Steam Turbine Blades," in A. S. Warnock, ed., *Design, Repair, and Refurbishment of Steam Turbines*, Papers from the 1991 International Joint Power Generation Conference held in San Diego, CA, Oct. 6–10, 1991, PWR-Vol. 13, American Society of Mechanical Engineers, New York, pp. 203–208 (1991).
91. J. M. Allen, "Characteristics of Nonsynchronous Vibration of Turbine Blades," in Stress Technology, Inc., *Proc. Steam and Combustion Turbine-Blading Conference and Workshop—1992*, held in Orlando, FL, Jan. 29–31, 1992, Proceedings TR-102061, EPRI, Palo Alto, CA, pp. 4-45–4-81 (1993).
92. J. Davids, C. L. S. Farn, J. R. Kadambi, and D. K. Whirlow, *Steam Turbine Condensation–Shock Wave Interaction*, Final Report CS-3251, EPRI, Palo Alto, CA (1983).

93. S. Srivastav, M. Redding, and T. H. McCloskey, "3-D Modeling of Imperfect Contact Conditions Between Turbine Blades and Disk," in W. G. Moore, ed., *Advances in Steam Turbine Technology for the Power Generation Industry*, Papers from the 1994 International Joint Power Generation Conference held in Phoenix, AZ, Oct. 2–6, 1994, PWR-Vol. 26, American Society of Mechanical Engineers, New York, pp. 197–204 (1994).
94. J. A. Kubiak, A. Carnero, and Z. Mazur, "Modification of L-1 Moving Blades," in I. Fruchtman, S. Hartman, B. Moore, R. Henry, D. Karg, M. Curley, S. Reid, and B. Sykes, eds., *Proc. International Joint Power Generation Conference: Volume 3: Power*, Papers from the 1995 International Joint Power Generation Conference held in Minneapolis, MN, Oct. 8–12, 1995, PWR-Vol. 28, American Society of Mechanical Engineers, New York, pp. 289–294 (1995).
95. D. Smith, "The Transverse Vibration of Uniform Beams," *Engineering, 120*:808 (1951).
96. M. Prohl, "A Method for Calculating Vibration Frequency and Stress of a Banded Group of Turbine Buckets," *Trans. ASME*, American Society of Mechanical Engineers, New York (1956).
97. R. Pigott, L. D. Kramer, R. J. Ortolano, and R. I. Jaffee, "Increasing Availability in Low Pressure Steam Turbines by Design and Materials Selection," *44th Annual Meeting of the American Power Conference*, held in Chicago, IL, April 26–28 (1982).
98. R. Dewey, M. Redding, T. Lam, S. Hesler, and T. McCloskey, "A Finite Element Diagnostic Tool for Turbine Blade Failures," in C. P. Bellanca, ed., *Advances in Steam Turbine Technology for Power Generation*, 1990 International Joint Power Generation Conference, Boston, MA, Oct. 21–25, 1990, PWR-Vol. 10, American Society of Mechanical Engineers, New York, pp. 71–79 (1990).
99. R. E. Warner, T. L. Dillman, and M. S. Baldwin, "Off-Frequency Turbine-Generator Unit Operation," *Proc. American Power Conference*, Chicago, IL, pp. 570–580 (1976).
100. W. Burton, and R. Ortolano, *Field Telemetry Testing of Long-Arc, Low-Pressure Turbine Blading*, Final Report TR-100216, Research Project 1856-3, Electric Power Research Institute, Palo Alto, CA (1992).
101. M. P. Singh, J. J. Vargo, D. M. Schiffer, and J. D. Dello, "SAFE Diagram—A Design and Reliability Tool for Turbine Blading," *Proc. 17th Turbomachinery Symposium*, held in Dallas, TX, Nov. 8–10, pp. 93–101 (1988).
102. J. Grant, N. Wood, P. Walters, "Development and Site Test Evaluation of Some Blading Retrofit Packages for Improving the Efficiency of Low-Pressure Turbines in UK Power Stations," *IMechE*, C423/63 (1991).
103. T. Miyawaki, H. Tashiro, M. Honjo, and E. Watanabe, "Improvement of LP Turbine Efficiency by Fully 3D Designed Blade," in W. G. Steltz, ed., *Steam Turbine-Generator Developments for the Power Generation Industry*, Papers from the 1992 International Joint Power Generation Conference held in

Atlanta, GA, Oct. 18–22, 1992, PWR-Vol. 18, American Society of Mechanical Engineers, New York, pp. 75–80 (1992).
104. M. Gloger, K. Neumann, D. Bergmann, and H. Termuehlen, "Advanced LP Turbine Blading: A Reliable and Highly Efficient Design," in W. G. Steltz, ed., *Steam Turbine-Generator Developments for the Power Generation Industry*, Papers from the 1992 International Joint Power Generation Conference held in Atlanta, GA, Oct. 18–22, 1992, PWR-Vol. 18, American Society of Mechanical Engineers, New York, pp. 41–51 (1992).
105. Y. Kadoya, Y. Kuramoto, T. Sato, and E. Watanabe, "New Reaction Blade for Steam Performance Improvement," ASME/IEEE (1987).
106. K. C. Cotton, *Evaluating and Improving Steam Turbine Performance*, Cotton Fact, Inc., Rexford, NY (1993).
107. T. McCloskey, R. Dewey, S. Hesler, and M. Pollard, "Low Pressure Steam Turbine Thermal Performance Improvements," *Thirteenth Annual Plant Performance Enhancement Program*, held Aug. 12–14, 1997, in San Antonio, TX, Plant Support Engineering, EPRI, Charlotte, NC (1997).
108. O. Jonas and N. F. Rieger, *Turbine Steam, Chemistry, and Corrosion*, Final Report TR-103738, EPRI, Palo Alto, CA (1994)
109. A. P. Weiss, "Aerodynamic Design of Advanced LP Steam Path," *ABB Review*, May (1998).
110. T. McCloskey, "Troubleshooting Bearing and Lube Oil System Problems," 24th Turbomachinery Conference, Houston TX, Sept. (1995).
111. G. A. Lamping, J. P. Cuellar, H. S. Silvus, "Summary of Maintenance Practices for Large Steam Turbine-Generator Lubrication Systems," ASME 86-JPGC-PWR-14 Oct. (1986).
112. American Society for Testing and Materials (ASTM), "Standard Practice for Design of Steam-Turbine Generator Oil Systems, D 4248-83," *1984 Annual Book of ASTM Standards: Petroleum Products and Lubricants* (III)/Vol. 05.03, ASTM Philadelphia (1984).
113. "Recommended Practices for the Cleaning, Flushing, and Purification of Steam and Gas Turbine Lubrication Systems, LOS—1M 1980," ASME, New York, p. 15 (1980).
114. "Turbine Lube Oil (Recommended Properties and Maintenance Practices), General Electric Report GEK-46506B," Schenectady, New York, Nov. (1979).
115. J. R. Conklin, "Design Philosophy—Turbine Generator Lubricating Oil Systems," American Society of Lubrication Engineers, Park Ridge, IL, ASLE Preprint Number 69AM6B-3, p. 17 (1969).
116. ASTM, "Standard Specification for Mineral Lubricating Oil Used in Steam or Gas Turbines, D4304-83," *1984 Annual Book of ASTM Standards: Petroleum Products and Lubricants (III). Vol. 05.03*, ASTM, Philadelphia (1984).
117. ASTM, "Standard Specification for Phosphate Ester Based Fluids for Turbine Lubrication, D4293-83," *1984 Annual Book of ASTM Standards: Petroleum Products and Lubricants (III). Vol. 05.03*, ASTM, Philadelphia (1984).

118. M. J. DenHerder and P. C. Vienna, "Control of Turbine Oil Degradation During Use," *Lubrication Eng., 37*: 67–71 (1981).
119. "COJOUR Users Guide: Dynamic Coefficients for Fluid Film Journal Bearings," EPRICS-4093-CCM, Aug. (1985).
120. ASTM, "Standard Test Method for Foaming Characteristics of Lubricating Oils, D 892-74," *1984 Annual Book of ASTM Standards: Petroleum Products and Lubricants (I). Vol. 05.01*, ASTM, Philadelphia (1984).
121. ASTM, "Standard Test Method for Rust Preventing Characteristics of Steam Turbine Oil in Presence of Water, D 665-82," *1984 Annual Book of ASTM Standards: Petroleum Products and Lubricants (I). Vol. 05.01*, ASTM, Philadelphia (1984).
122. ASTM, "Standard Test Method for Rust-Preventing Characteristics of Steam-Turbine Oil in the Presence of Water, D 3603-82," *1984 Annual Book of ASTM Standards: Petroleum Products and Lubricants (III). Vol. 05.03*, ASTM, Philadelphia (1984).
123. H. P. Block, "Criteria for Water Removal from Mechanical Drive Steam Turbine Lube Oils," *Lubrication Eng., 36*:703 (1980).
124. E. Lewis and H. Stern, *Design of Hydraulic Control Systems*, McGraw Hill, New York (1962). See also G. Gaffert, *Steam Power Stations*, McGraw-Hill, New York (1946).
125. J. Kure-Jensen, "Control of Large Modern Steam Turbine-Generators," General-Electric Large Steam Turbine Seminar, 81T7 (1975).
126. L. B. Podolsky, *The Electro Hydraulic Governor* (1972).
127. L. H. Johnson, P. C. Callan, and J. Kure-Jensen, *Designing for Reliability—The Large Steam Turbine Mark II Control System*, ASME JPGC (1977).
128. R. L. Olson, "Mark II EHC System for General Electric Large Steam Turbine-Generators," Large Steam Turbine Seminar, 81T8 (1981).
129. R. L. Carson, "Design and Experience with Steam Valves for Large Steam-Turbines," GE Large Steam Turbine Seminar, 81T10 (1981).
130. F. A. Artusa, "Turbines and Cycle for Nuclear Power Plant Application," 1967 American Power Conference (1967).
131. M. A. Eggenberger, *Introduction to the Basic Elements of Control Systems for Large Steam Turbine-Generators*, GET-3096F (1965).
132. H. H. Nelken, W. P. Gorzegno and C. J. Brigida, "Coordinating Power Plant Components for Cycling Service," American Power Conference, April (1979).
133. S. Hesler, A. Liberson, R. Maurer, and T. McCloskey, "Optical Probe for Measurement of Steam Wetness Fraction in LP Turbines," in EPRI Workshop on Nuclear Performance (unpublished), held in San Antonio, TX, Aug. 1997.
134. R. P. Dewey, M. J. Roemer, M. A. Pollard, and T. H. McCloskey, "Optimization of Outage Interval for a Large Steam Turbine Unit," *Proc. International Joint Power Generation Conference*, Baltimore, MD (1998).
135. T. McCloskey, R. Dewey, S. Hesler, and M. Pollard, "Low Pressure Steam Turbine Thermal Performance Improvements," *Thirteenth Annual Plant*

Performance Enhancement Program, held Aug. 12–14, 1997, in San Antonio, TX, Plant Support Engineering, EPRI, Charlotte, NC (1999).
136. T. McCloskey, B. Dooley, and W. McNaughton, "Turbine Steam Path Damage: Theory and Practice (Vol. 1 Fundamentals, Vol. 2 Damage Mechanisms)," EPRI TR-108943 (1999).
137. T. McCloskey, A. Lieberson, and S. Hesler, "Inviscid and Viscous Numerical Simulation for Non-Equilibrium Spontaneously Condensing Flows in Steam Turbine Blade Passages.," ASME IJPGC, Baltimore, MD (1998).
138. T. McCloskey, S. Hesler, R. Maurer, and L. Shuster, "Optical Probe for Measurement of Steam Wetness Fraction in LP Turbines," ASME IJPGC, Baltimore, MD (1998).
139. T. McCloskey, R. Viswanathan, J. Foulds, and R. Swaminathan, "Condition Assessment of High Temperature Steam Turbine Rotors," R POWER-GEN '97 International Dallas, TX, Dec. (1997).
140. T. McCloskey, T. Lam, and R. Dewey, "Reliability Assessment of Turbine Disc Rim Under Stress Corrosion Cracking," International Joint Power Generation Conference, Denver, CO, Nov. (1997).
141. T. McCloskey, M. Pollard, and J. Schimmels, "Development and Implementation of a Turbine-Generator Outage Interval Extension Strategy," ASME International Joint Generation Conference, Minneapolis, MN, Oct. (1995).

9

Multidisciplinary Design Optimization for Turbomachinery

John N. Rajadas

Arizona State University East, Mesa, Arizona, U.S.A.

INTRODUCTION

Modern engineering design processes exhibit a multidisciplinary outlook involving high-fidelity analyses and fast and efficient computational tools. The design processes are capable of addressing multiple disciplines in a coupled and structured format unlike the ad-hoc and empirical methods used in the recent past. More accurate models are replacing empirical and/or simplified ones and, with the advent of powerful computers, more detailed and accurate evaluation of performance characteristics of complex engineering systems is feasible now. Of particular significance in this regard is the recent advances made in the area of aerospace systems design. The development of highly accurate flow solvers and efficient computational algorithms has led to a wide range of design applications such as aircraft wing design, helicopter rotor blade design, and turbomachinery design. The primary goal of any design process is to end up with an optimum design that meets all the design objectives subject to all the constraints imposed on the design. Formal optimization techniques are increasingly being used as part

of the design process toward achieving optimum design of overall systems as well as components. While formal optimization procedures have not yet been fully integrated into all present-day engineering designs, their potential utility and adaptability have led to increased efforts in developing robust and efficient optimization techniques. A brief glimpse into the evolving area of design optimization with specific application in the area of gas turbine design is provided here.

Turbomachinery design is a complex task involving strong coupling between a number of disciplines such as fluid dynamics, heat transfer, aeroelasticity, structures, vibration, and materials. The design parameters associated with such designs are large in number, and hence maximizing the performance characteristics of a design using traditional methods is very difficult. Traditionally, the designer relies on experience and intuition for the initial design and then uses appropriate analyses to evaluate the design. If redesign is indicated, the entire process is repeated until a satisfactory design is achieved. Such a process is time-consuming and could involve significant cost to complete. Formal optimization techniques will be appropriate for such problems. In gas turbine engine designs, there are usually multiple design objectives (minimum blade temperature, minimum aerodynamic losses, minimum coolant flow rate, etc.) that must be simultaneously met due to the strong coupling between different disciplines. However, some of these objectives may impose conflicting requirements on the design parameters, thus requiring a robust process for accommodating all the resultant constraints. Multidisciplinary design optimization (MDO) techniques, which allow the designer to include a large number of design parameters while addressing multiple design objectives and constraints simultaneously, are better suited for such design applications. Robust MDO techniques are adaptable to a number of design processes such as component design applications, overall systems design, configuration optimization, and design cycle cost/time minimization.

The gas turbine design community has yet to take full advantage of formal optimization techniques in the design process. There have been a number of turbomachinery design applications involving optimization procedures during the past few years. The technological challenges associated with the optimum design of gas turbine systems are immense. A number of complex issues such as the constraints imposed by material properties (due to the high-temperature environment), design objectives that impose opposing requirements on the design parameters, simultaneous coupling of different disciplines, manufacturability constraints on the optimum design, validity of the analysis tools, resources to couple comprehensive analysis tools [such as 3D computational fluid dynamics (CFD) solvers], efficient and accurate sensitivity analyses involving a large

number of design variables, robust optimization algorithms that are capable of addressing multiple disciplines and design objectives simultaneously, and low computational turnaround time so that the design changes can be addressed in a reasonable time need to be addressed. A robust and efficient optimization procedure that is capable of addressing all these concerns will be a very valuable tool for the designer. Improvements in existing designs for better-performance, new designs that, in addition to optimum performance, also involve low design cycle cost, the ability to investigate the impact of new concepts on the overall design, and material cost savings associated with cooler blade temperatures are some of the capabilities of such a procedure.

The main areas that need to be addressed in establishing a multidisciplinary optimization procedure for gas turbine application are (1) disciplines to be addressed, (2) appropriate design objectives, (3) relevant design variables, (4) constraints, (5) optimization algorithm(s), (6) analysis tools (available or to be developed), (7) geometry specifications (e.g., Bezier–Bernstein polynomials for blade geometry), (8) computational resources and strategy, (9) sensitivity analysis, and (10) validation of the procedure. Usually, the disciplines that need to be addressed will be dictated by the design objectives.

One of the best means of achieving higher efficiency in gas turbine engines is to raise the temperature of the gas flow entering the turbine. Since the high-temperature environment in the turbine affects the life of the blade and its structural integrity, the efficient removal of heat from the blade interior is very important. Also, the geometry of the blade and the choice of appropriate materials that are capable of withstanding the high temperatures will be affected by manufacturability and structural integrity concerns. A method to alleviate this problem is to use effective turbine blade-cooling mechanisms and blade geometry such that the temperatures stay within acceptable levels in the blade. Since the cooling air is supplied by the compressor, it is essential to maintain the coolant air-flow rate low so that overall engine performance is not degraded. Another area of interest is the need to minimize aerodynamic losses in order to improve overall performance. Thus, the design of gas turbine blades is a multidisciplinary problem that requires the integration of several disciplines such as aerodynamics, heat transfer, structures, vibration, etc. For an efficient and comprehensive design, these disciplines need to be addressed simultaneously. In general, such an optimization problem is nonlinear and has several objective functions, constraints, and design variables. Many of the existing optimization procedures can address only a single objective function and multiple constraints at a time. A multidisciplinary design optimization

procedure capable of addressing multiple design objectives simultaneously can thus be a valuable tool.

Design of an efficient cooling mechanism for the gas turbine blades is an important part of the overall design process. Cooling of turbine blades can be done internally and/or externally. Internal cooling is achieved by circulating coolant air through the passages that extend from the hub to the tip of the blade interior. For improved heat-transfer characteristics, baffles are sometimes placed in the internal passages to increase the surface area of contact, which can increase the pressure loss. Another method of internal cooling is impingement cooling, where the coolant fluid is impinged on the inside surface of the blade leading edge, thus lowering its temperature. Efficient shaping of the blade geometry will help to augment surface-cooling mechanisms while keeping the aerodynamic losses low. External cooling of the surface of the turbine blade is achieved by injecting cooling air along the blade surface through discrete holes on the blade surface (film cooling). Film cooling, combined with the flow field around the blade, has the advantage of thermal protection not only in the immediate vicinity of injection but also in the surrounding regions of the blade surface. Extensive experimental and computational investigations directed at understanding the complex thermal and fluid interaction associated with film cooling have been done in recent years [1–5]. The effects of coolant hole geometry, secondary fluid density, blowing rates and modes, and main-stream boundary layer on film cooling are some of the characteristics that have been studied. The impact of complex flow interactions near the hub and the tip regions of the turbine blade, the sensitivity of the surface heat-transfer coefficient to the boundary layer, turbulence modeling, and the associated near-wall treatment are some of the associated issues that have also been studied extensively.

In the design optimization problem for cooled turbine blades, some of the relevant design objectives are minimum blade interior temperature, improved aerodynamic performance (smooth flow field around the blade, reduced pressure loss), minimum coolant flow rate and pressure drop, improved structural integrity and vibration performance, and reduced tip losses. The major disciplines that need to be included are aerodynamics (3D), heat transfer, modal analysis, and structural analysis. The design variables set will include geometric as well as other parameters such as coolant flow injection rates, temperature of the coolant air, etc. The constraints may be based on thermal and material properties, stress field, coolant flow rate-related factors, manufacturability, as well as the allowable limits on the design variables. The optimization algorithm should be capable of addressing the design objectives simultaneously.

The main aim of this chapter is to emphasize the applicability and utility of MDO techniques for turbomachinery design. A brief description of

relevant optimization techniques for turbomachinery design applications is given. The main focus of discussion is the use of MDO procedures for component design applications associated with gas turbine engines. The design of turbine blade geometry for improved heat-transfer performance is used to demonstrate one particular multidisciplinary, multiobjective optimization technique. Particular emphasis has been placed on the blade-cooling (internal and external) aspect of the design.

Development of formal optimization techniques for engineering design applications has reached a high level today [6, 7]. Most of the optimization techniques developed for engineering applications are typically capable of addressing only a single design objective at a time subject to several constraints, which restricts the applicability of the procedure [8] since such problems usually involve multiple design objectives. A common practice in addressing multiobjective optimization problems has been to combine individual objective functions in a linear fashion using weight factors [9] that are user-specified, thus requiring input based on user intuition and/or prior experience. Another common method, called the modified global criterion approach [8], combines the individual objective functions into a single composite function using separately determined target values for the objective functions. Optimization of the composite function corresponds to optimizing the individual objective functions. This requires that separate optimization be performed for each objective function in order to obtain the target values, which could be computationally prohibitive for complex designs. Several efforts for developing multidisciplinary, multiobjective design optimization procedures have been initiated during the past few years. One such procedure is the Kreisselmeier–Steinhauser (K–S) function technique [10, 11], which is capable of addressing design problems with multiple objectives and inequality constraints. The multiobjective optimization formulation used in the design optimization problem described in the present chapter is based on the K–S function technique [12–17], and a brief description of this approach is given later.

A popular design optimization technique used in aerospace applications, especially in gas turbine design, is the inverse design method in which the required performance characteristics, such as a pressure distribution or velocity distribution about the turbine blade, are prescribed and the geometric parameters are modified iteratively to arrive at a configuration that satisfies the prescribed criteria. An extensive review of inverse design methodologies for aerodynamic shape design has been presented by Dulikravich [18]. Such a procedure for the design of blade coolant passages with specified temperatures and heat fluxes has been developed by Dulikravich et al. [19, 20]. An iterative procedure for three-dimensional blade design using a transpiration model along with a modified Euler solver

to achieve a specific target pressure distribution about the blade has been developed by Demeulenaere and Braembussche [21]. A three-dimensional inverse method for aerodynamic design of turbomachinery blades with prescribed circumferential mass-averaged tangential velocity (blade loading) has been developed by Dang and Isgro [22]. A numerical automation procedure in conjunction with an inverse hodograph method for the design of controlled-diffusion blades has been developed by Sanz [23] with the associated controlling parameters of blade solidity, inlet Mach number, inlet air-flow angle, and trailing-edge thickness, along with a prescribed surface pressure distribution. Borges [24] has developed a three-dimensional method for turbomachinery blades that uses a prescribed distribution of mean swirl as the target performance criterion. Foster and Dulikravich [25] have developed two hybrid optimization methods based on gradient methods and genetic algorithm (GA), for preliminary aerodynamic designs. In the work reported above, the important coupling between blade heat transfer and the external shape of the blade has not been considered. Huang et al. [26] have developed an inverse methodology for the design of internal cooling passages in turbine blades for a prescribed temperature distribution on the external surface using the conjugate gradient method. One of the major drawbacks of the inverse methods is the practice of prescribing a performance criterion (e.g., pressure distribution, velocity distribution, etc.) by the designer, thus directly linking the quality and feasibility of the resultant design with the accuracy of the prescribed criteria. Also, integration of multiple design criteria in the design process is difficult to achieve, and the method does not lend itself adequately to imposing geometric constraints that are usually needed to address considerations such as manufacturability. Formal optimization techniques have a distinct advantage over inverse methods in complex design problems in this regard. In typical applications using formal optimization techniques, the overall design objectives (such as minimum blade average temperature, minimum coolant flow rate, etc.) and constraints are specified along with the relevant design variables. The resultant optimum design provides the detailed information such as pressure and temperature distributions, thus eliminating the need for accurate input from the user as required by the inverse methods. Also, geometric constraints can be easily incorporated in the design process.

The application of formal design optimization procedures for turbine blade designs has been mostly limited to single objective function formulations, and coupling between different disciplines is usually achieved through the incorporation of design sensitivities of discipline-based subsystems. In problems where multiple objective functions need to be considered, either the additional objectives are treated as constraints or a

single composite function is developed by combining the objective functions using weight factors. This approach tends to be highly empirical in nature and relies heavily on the experience of the designer to devise the proper arrangement of the design objectives in the optimization process.

There have been a number of gas turbine design applications coupling formal optimization techniques in the recent past. Haendler et al. [27] developed an aerothermal design procedure for highly thermally loaded film-cooled first-stage gas turbine blade. Goel and Lamson [28] have used a combination of heuristic-search and numerical optimization techniques with a quasi-3D aerodynamic analysis for the design of turbine blades. Chattopadhyay et al. [12] have developed an optimization procedure for efficient aerodynamic design of turbine blades that eliminated the sharp variations in the velocity field near the blade leading edge without compromising overall blade performance. A sensitivity analysis procedure for turbine blade components was developed by Kolonay and Nagendra [29] using a Jacobian derivative-based methodology to determine semianalytic sensitivities of isotropic eight-noded (hexahedron) isoparametric finite elements with respect to geometric shape design variables. Kodiyalam et al. [30] have coupled heat-transfer and structural analysis to optimize a composite engine structure using a modified method of feasible directions algorithm. The optimization procedure used was a variation of the weighted summation method and did not include the effect of heat transfer on the blade shape. A coupled aerodynamic-structural shape optimization procedure was developed and demonstrated on a low-pressure turbine blade by Kao et al. [31]. Fatigue strength at high operating temperatures was used as the design criterion. The coupling between the two disciplines (aerodynamics and structures) was achieved though sensitivities of the optimum solutions from the subsystem designs. Tappeta et al. [32] have developed a multidisciplinary optimization approach using a concurrent subspace optimization procedure for designing an engine blade with internal cavities. The blade was modeled as a stepped beam with rectangular cavities, and the weight of the structure was used as the objective function. Optimal design of turbine blade for minimum weight has been carried out by Queau and Trompette [33].

The application of artificial neural networks and genetic algorithm (GA) for turbine blade optimization is gaining popularity. A neural network-based parametric coupling in turbine design was developed by Goel and Hajela [34]. The effect of heat transfer on the blade external shape was not considered in the development. The technique was applied to a three-stage power turbine and an aircraft engine turbine design. Shelton et al. [35] optimized a 2D transonic turbine airfoil using an artificial intelligence engineering design shell coupled with an inviscid, adaptive CFD solver. The

objective was to minimize the downstream static pressure variation resulting from the trailing-edge shock structure. An artificial neural network-based method was used by Pierret and Braembussche [36] for the automatic design of turbomachinery blades. Simulated annealing (SA) coupled with a Navier–Stokes solver was used for optimization. Trigg et al. [37] developed an optimizer based on GA for the design of two-dimensional blade profiles for steam turbines. The blade profile loss was minimized with limits on 17 parameters that defined the blade geometry, and the effect of blade heat transfer on the blade geometry was not considered.

During the past few years, Chattopadhyay et al. [12–17] have been using the K–S function technique (multiobjective formulation capable of addressing multiple disciplines simultaneously) for a variety of aerospace engineering design problems, including gas turbine blade design applications involving the coupling of aerodynamics and heat transfer, and have extended the procedure to include structural analysis and vibration [17]. Narayan et al. [13] have developed a multidisciplinary optimization procedure, integrating aerodynamic and heat-transfer effects to design an internally cooled turbine blade. Multidisciplinary design optimization of film-cooled gas turbine blades, including the coupling of aerodynamics and heat transfer, was done by Talya et al. [14–16]. Film cooling was modeled by appropriately changing the boundary conditions on the turbine blade surface. Considerable improvement in blade temperature was achieved by changing the film-cooling parameters like the hole position, blowing rate, and temperature of film-cooling air. Talya [17] extended this work to include structural and modal analyses and applied it for the optimum design of a cooled 3D turbine blade. The design optimization application example given in this chapter is based on this work.

APPLICATION OF MULTIOBJECTIVE OPTIMIZATION PROCEDURE FOR GAS TURBINE BLADE DESIGN OPTIMIZATION METHODOLOGY

Most of the efforts to include multiple objective functions in an optimization method can be divided into two techniques. The first is to form a single composite objective function using weighting factors (e.g., the utility function method). The second approach is to solve the optimization problem once for each single objective function and then to use the resulting optimum objective function or design variable vector as a target, solving an additional optimization problem to attain a suitable compromise. Examples of this approach are the global criterion formulation, game theory approach, goal programming method, and goal attainment method [8]. A

promising technique capable of addressing multiple objectives and constraints without relying on user input is the Kreisselmeier–Steinhauser (K–S) function approach [10, 11]. In this approach, the multiple objective functions and constraints are combined using the K–S function to form a single envelope function, which is then optimized. The optimization procedure presented in this chapter uses the K–S function technique. The following section briefly describes the K–S function technique.

Kreisselmeier-Steinhauser (K–S) Function Technique

In this technique, the original objective functions and constraints are modified into reduced objective functions. Depending on whether the individual objective functions are to be minimized or maximized, these reduced objective functions assume one of the two following forms:

$$F^*_k(\Phi) = \frac{F_k(\Phi)}{F_{k_0}} - 1.0 - g_{\max} \leqslant 0, \qquad k = 1, \ldots, \text{NOBJ}_{\min}$$
$$F^*_k(\Phi) = 1.0 - \frac{F_k(\Phi)}{F_{k_0}} - g_{\max} \leqslant 0, \qquad k = 1, \ldots, \text{NOBJ}_{\max} \tag{1}$$

where F_{k_0} represents the original value of the kth objective function (F_k) calculated at the beginning of each optimization cycle and Φ is the design variable vector. $g_{\max}$ represents the largest constraint in the original constraint vector, $g_j(\Phi)$, and is held constant during each cycle. $\text{NOBJ}_{\min}$ and $\text{NOBJ}_{\max}$ represent the number of objective functions that are to be minimized or maximized, respectively. The reduced objective functions are analogous to constraints. Therefore, a new constraint vector, $\mathbf{f}_m(\Phi)$ ($m = 1, 2, \ldots, M$, where $M = NC + \text{NOBJ}$), that includes the original constraints and the reduced objective functions is introduced. Here NC is the total number of original constraints. The new objective function to be minimized is defined as

$$F_{\text{KS}}(\Phi) = f_{\max} + \frac{1}{\rho} \log_e \sum_{m=1}^{M} e^{\rho(\mathbf{f}_m(\Phi) - f_{\max})} \tag{2}$$

where $f_{\max}$ is the largest constraint in the new constraint vector $\mathbf{f}_m(\Phi)$. The composite function $F_{\text{KS}}(\Phi)$, which represents an envelope function of the original objective functions and constraints, can now be minimized using a suitable unconstrained optimization technique. The parameter ρ is a drawdown factor that may vary between optimization cycles. Large values of ρ "draw down" the K–S function closer to the value of the largest constraint. Typically, ρ is progressively increased such that the K–S function

more closely represents the largest constraint (or the most violated reduced objective function) as optimization proceeds. The optimization technique used here is gradient-based and hence requires the evaluation of the objective functions and constraints many times during every cycle of optimization. Since it is computationally expensive to evaluate these functions through exact analysis at all times, an approximation technique is used within each cycle of the optimization. The two-point exponential approximation technique developed by Fadel et al. [38] has been found to be well suited for nonlinear optimization problems and has been used in the work reported here for approximating the objective functions and the constraints within the optimizer.

In the example below, a procedure developed for the multidisciplinary design optimization of gas turbine blades is demonstrated. The blade is cooled both internally (internal coolant passage) and externally (film cooling). The optimization procedure couples aerodynamic and heat-transfer disciplines. The 3D blade is divided into 12 sections along the blade span, and each section is represented by a Bezier–Bernstein polynomial [39]. A 3D Navier–Stokes solver [40, 41] is used to evaluate the external flow field, and a finite-element method is used to evaluate the blade interior temperatures at each section. A constrained multiobjective optimization formulation based on the Kreisselmeier–Steinhauser (K–S) function approach [10, 11] has been used for optimizing the blade geometry.

BLADE MODELING AND ANALYSIS

3D Blade Model

The full blade geometry is defined by a set of discrete points on the blade surface. The blade is divided into different slices along the span, with each slice represented by a Bezier–Bernstein polynomial [39]. A two-dimensional boundary is defined by a Bezier–Bernstein curve of degree n as

$$b^n(t) = \sum_{j=0}^{n} \mathbf{b}_j B_j^n(t) \tag{3}$$

where

$b^n(t)$ is a point on the boundary.
$\mathbf{b}_j$ is the vector of Bezier control points.
$B_j^n(t)$ is the Bernstein polynomial.
t varies from 0.0 to 1.0.

Depending on the number of points required on the boundary, the incremental step for t can be specified. The vector of Bezier control points $\mathbf{b}_j$ consists of $(n+1)$ values of x- and y-coordinates of the control points. The nth-degree Bernstein polynomials are given by

$$B_j^n(t) = \frac{n!}{j!(n-j)!} t^j (1-t)^{n-j} \tag{4}$$

These equations are used to calculate the coordinates of the points on the surface of the blade section from a given set of Bezier control points which are used as design variables in the optimization problem (Fig. 1). In the present optimization problem, a Bezier polynomial of order 15 is used to represent the blade section.

As mentioned earlier, blade cooling is done using both internal (coolant flow through internal passages) and external (film cooling) methods. The coolant fluid is compressed air from the engine compressor. The coolant air circulating through the internal coolant passages is routed through the film-cooling ports for external cooling, where the flow of cooler air along the blade surface helps keep the blade surface at a lower

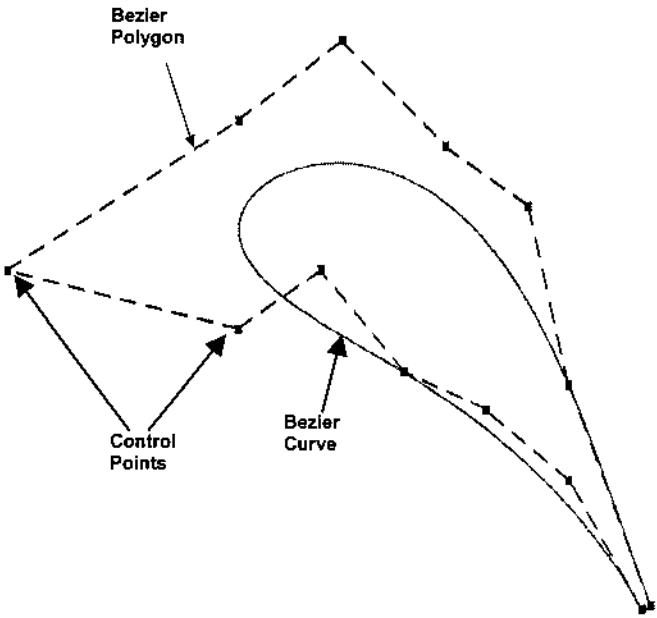

Figure 1 Bezier–Bernstein representation of blade geometry.

temperature by forming a thin film over it. Geometric and flow parameters associated with the cooling mechanisms (internal and external) form part of the design variables set for the optimization problem. The internal coolant passage has five sections, each spanning the blade span (root to tip). Each blade section has six film cooling holes connected to the appropriate sections of the internal coolant passage (Fig. 2). The set of design variables includes the locations of the Bezier control points, the positions of the center of each film-cooling hole, and the positions of the side boundaries of each internal coolant passage section. The surface boundary conditions are appropriately modified to account for film-cooling flow when evaluating the external flow field.

Aerodynamic Analysis

A three-dimensional, thin-layer Navier–Stokes solver (RVC3D) is used to evaluate the flow field around the blade [40, 41]. The computational grid for the flow solver is generated using the grid generator TCGRID [42]. The Navier–Stokes equations in the Cartesian coordinate system rotating with the angular velocity Ω about the x-axis are mapped to a general body-fitted (ξ, η, ζ)-coordinate system with the ξ-coordinate following the flow

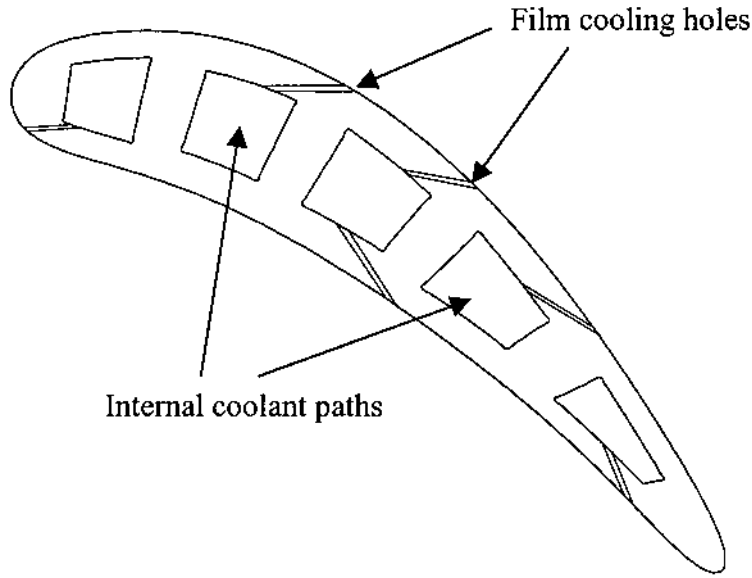

Figure 2 Blade model: 2D view of blade section with coolant paths.

(streamwise), the η-coordinate along the blade-to-blade direction, and the ζ-coordinate positioned along the spanwise direction. Viscous terms in the streamwise direction are neglected and turbulence effects are modeled using the Baldwin–Lomax turbulence model. The resulting time-dependent governing equations are as follows:

$$\frac{\partial \mathbf{q}}{\partial t} + J\left[\frac{\partial \hat{E}}{\partial \xi} + \frac{\partial \hat{F}}{\partial \eta} + \frac{\partial \hat{G}}{\partial \zeta} - \mathrm{Re}^{-1}\left(\frac{\partial \hat{F}_v}{\partial \eta} + \frac{\partial \hat{G}_v}{\partial \zeta}\right)\right] = \hat{H} \tag{5}$$

Where

t is time.
$\mathbf{q}$ is the vector of conserved flow variables.
$\hat{E}, \hat{F}, \hat{G}$ are the inviscid flux terms.
$\hat{F}_v, \hat{G}_v$ are the viscous flux terms.
$\hat{H}$ is a source term due to blade rotation.
J is the Jacobian of coordinate transformation.

The equations are nondimensionalized using appropriate reference quantities, and the Reynolds number (Re) and Prandtl number (Pr) are defined in terms of these quantities. The specific heats, C_p and C_v, and Prandtl number are assumed to be constant. A multistage Runge–Kutta scheme is used to solve the discretized form of the equations.

Boundary Conditions

The total temperature and total pressure are specified upstream of the turbine blade (inlet). For supersonic inflow, all flow variables are specified at the inlet. For subsonic outflow, the exit static pressure is specified and the conserved flow variables are derived using extrapolation. On the blade surface the normal velocity component is set to be zero. For viscous flows, the velocity (all components) is set to be zero at the blade surface. At the film-cooling holes, the boundary conditions of the flow solver are modified to account for the mass flow rate, temperature, and pressure of the film-cooling air entering the external flow field.

Internal Cooling

The internal coolant flow in a gas turbine blade is complex and three-dimensional. The complexity of the computations is increased further due to factors such as thermal buoyancy, Coriolis effects on the internal flow, etc. As a result, the computational effort and resources needed for a detailed evaluation of the coolant flow are prohibitive in an optimization procedure

such as the one described here. For the problem at hand, this is circumvented by the specification of convective heat-transfer coefficients and bulk fluid temperatures of the coolant fluid in each section of the internal passage at each of the spanwise sections. Semiempirical correlations have been used to determine the coolant heat-transfer coefficients, $h_{\text{cool},n}$, and the bulk coolant temperatures, $T_{\text{cool},n}$, for each section (n) of the coolant passage with appropriate modifications included to reflect the temperature distributions around the cooling passage boundary in the interior of the blade. Thermal buoyancy, centripetal, and Coriolis forces are neglected. The heat-transfer correlations were based on the hydraulic diameter of the coolant passages, $D_h = 4A/P$, where P is the wetted perimeter of the nth coolant passage. The Reynolds analogy gives

$$St = \frac{f/8}{1 + 12.7(\text{Pr}^{2/3} - 1)\sqrt{f/8}} \tag{6}$$

Where

St is the Stanton number.
f is the friction factor, defined as $f = 8\tau_w/(\rho w^2)$.

The effect of placing trip-strips to increase the heat-transfer coefficients in the coolant passages was simulated with large wall roughness values. The friction factor was evaluated from the correlation

$$\frac{1}{\sqrt{f}} = -1.8 \log\left[\frac{6.9}{\text{Re}_D} + \left(\frac{\varepsilon/D_h}{3.7}\right)^{1.11}\right] \tag{7}$$

During the numerical optimization procedure, the relative wall roughness heights of each coolant passage was set by specifying $\varepsilon/D_h = 0.2$.

The temperature of the coolant air is specified at both the inlet and the exit of the internal coolant passage (using representative values from a companion design problem) during the optimization process. Since the coolant air gets heated as it moves through the blade interior, the temperature of the coolant air at each spanwise section and in each section of the passage is calculated by extrapolating between the temperature at the inlet and the exit of the passage. The coolant mass flow rate at the entrance to the internal cooling passage is specified as a boundary condition and is held fixed during the optimization process. This mass flow rate is an important design parameter since it impacts the effectiveness of the compressor on the overall engine performance. The coolant mass flow rate at each section of the passage at every spanwise section is evaluated taking into account the amount of coolant air that is used for film cooling,

leading to an overall reduction in mass flow rate at the exit of the section. The convective heat-transfer coefficient, $h_{\text{cool},n}$, is evaluated from the Stanton number, and the bulk fluid temperature is obtained from the above calculations by extrapolation. The convective heat-transfer coefficient and the bulk fluid temperature are specified as boundary conditions on the walls of the internal coolant passages for the heat-transfer analysis of the blade interior.

Film Cooling

Film cooling is simulated by specifying appropriate temperature, pressure, and velocity values on the blade surface at discrete locations. The location of the center and the radius of each film-cooling hole is specified. The eight finite-difference grid points surrounding the grid point corresponding to the center of each film-cooling hole are moved to lie on the circumference of the hole, thus modeling the circular cross section of the film-cooling ports. Film-cooling boundary conditions such as the velocity, temperature, and angle of injection are specified at the nine grid points. Each film-cooling hole is associated with one of the five internal coolant passages depending on the location of the hole. Thus the mass flow rate, temperature, and pressure of the cooling air from each hole are determined from the corresponding section of the internal passage. The angle of blowing is specified with respect to the flow direction along the blade surface.

The temperature distribution on the blade surface is obtained as part of the flow field evaluation using the 3D Navier–Stokes solver. This temperature distribution is used as boundary condition along with the temperatures that are specified on the internal coolant passage walls, for the finite-element heat-transfer analysis of the blade interior. For the sake of simplicity, the iterative process that will help to couple the external and internal temperature distributions is left out in the present calculations.

Heat-Transfer Analysis

The temperature distribution within the blade is determined at each spanwise section as the solution of a two-dimensional heat conduction problem using finite elements. The corresponding governing equation is

$$\frac{\partial}{\partial x}\left(\kappa\frac{\partial T}{\partial x}\right)+\frac{\partial}{\partial y}\left(\kappa\frac{\partial T}{\partial y}\right)=0 \tag{8}$$

Where

T is the local blade temperature.

κ is the thermal conductivity of the blade material.

The computational domain (blade section with internal coolant passages) is discretized using linear triangular elements. A typical finite-element computational mesh is shown in Fig. 3.

Dirichlet boundary condition is specified on the blade surface and convective boundary condition is used for the internal coolant passage walls. Using the Galerkin approach, the above boundary-value problem is reduced to the following system of linear simultaneous equations for the unknown nodal temperatures:

$$[\mathbf{K}]\overline{T} \equiv \mathbf{F} \tag{9}$$

where

[**K**] is the global stiffness matrix and **F** is the forcing vector.

The solution to this equation yields the nodal temperatures, $\bar{T}$, from which the blade average and maximum temperatures are evaluated. Since the geometry of the blade and internal coolant passages change during optimization, the finite-element grid as well as the computational grid for the external flow are regenerated after each optimization cycle.

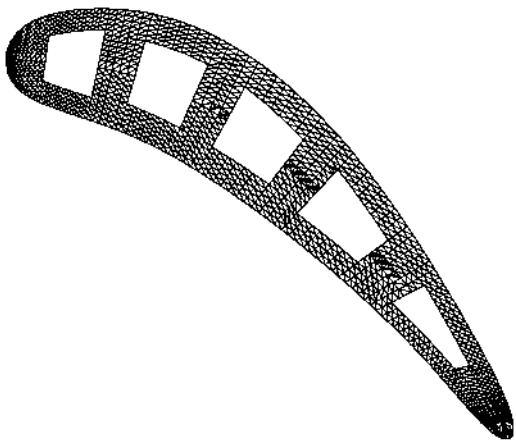

Figure 3 Finite-element grid arrangement for heat–transfer analysis.

Optimization Problem

For the design optimization problem considered, a wide range of design objectives can be addressed even with the coupling between two disciplines. In the results described below, the average and maximum temperatures at each spanwise section are used as objective functions. The trailing-edge thickness is held constant during the optimization, and the ratio of maximum thickness to chord for each section is constrained to within 10% of the reference value, which results in better aerodynamic characteristics for the blade.

The results discussed below are for a simplified optimization problem involving two design objectives per section since the main purpose here is the demonstration of the optimization procedure. The two objectives are minimum average temperature and minimum peak temperatures in each blade section. A more detailed optimization problem with more design objectives is given in Ref. [17]. The constraints are

$$
\begin{aligned}
t_{\mathrm{tr}} &\leqslant t_{\mathrm{tr\_ref}} \\
t_{\mathrm{tr}} &\geqslant t_{\mathrm{tr\_ref}} \\
\frac{t_{\max}}{C} &\leqslant 1.1\,\frac{t_{\max\_\mathrm{ref}}}{C_{\mathrm{ref}}} \\
\frac{t_{\max}}{C} &\geqslant 0.9\,\frac{t_{\max\_\mathrm{ref}}}{C_{\mathrm{ref}}} \\
\mathbf{X}_{\mathrm{lower},i} \leqslant \mathbf{X}(\mathbf{i}) &\leqslant \mathbf{X}_{\mathrm{upper},i}, \qquad i = 1, \ldots, \mathrm{NDV}
\end{aligned}
\tag{10}
$$

Where

t_{tr} is the trailing-edge thickness.
$t_{\max}$ is maximum blade thickness.
C is the blade chord. The subscript "ref separate" stands for reference value.
$\mathbf{X}(\mathbf{i})$ is the vector of design variables, which includes the y-coordinate of the Bezier control points of each section, end locations of each internal coolant passage in each section, and the location of the film-cooling ports (centers) along the blade.

For all the sections combined, there are 24 objective functions, 48 constraints, and 384 design variables [17] in the optimization problem.

Sensitivity Analysis

The sensitivities of the objective function and constraints with respect to the design variables (required for the optimization procedure) are evaluated

through finite differences. Mathematically, the finite-difference sensitivities can be expressed as follows:

$$\frac{dF(\mathbf{x})}{dx} = \frac{F(\mathbf{x} + \Delta\mathbf{x}) - F(\mathbf{x})}{\Delta x} \tag{11}$$

Where

F(x) is any objective function or constraint.
x is the vector of design variables.
Δx is the increment in each design variable.

The solver used for flow field evaluation (3D Navier–Stokes solver RVC3D) is CPU-intensive (6.0 h of CPU time for each run). Due to the large number of design variables used in the present problem, an alternative method is used for evaluating the sensitivities in order to avoid the large computational times involved. The converged solution from the 3D Navier–Stokes solver (RVC3D) is used as a starting solution for the quasi-3D solver (RVCQ3D), which is used in every spanwise section for evaluating the sensitivities. Exploratory calculations [17] indicate that the sensitivities obtained in this fashion are very close to those obtained by using the full 3D solver RVC3D.

RESULTS AND DISCUSSION

The angle of blowing of film-cooling air is held constant at 30° to the blade surface in the spanwise direction and 30° to the blade surface in the streamwise direction. The size of the film-cooling holes is kept constant during the optimization cycle. The finite-difference grid for the flow solver is generated using 158 points in the streamwise direction, 51 points in the circumferential direction, and 63 points in the spanwise direction around each blade. The blade section is represented using 106 surface points. For the blade heat-transfer problem, the finite-element mesh is generated using approximately 1,200 nodes and 2,100 elements at each blade section. The blade material properties are density = 8,200 kg/m^3 and thermal conductivity = 78 W/m.K. The free-stream temperature is 2000 °C; the temperatures at the inlet and exit of the internal coolant passage are 300 °C and 700 °C, respectively (based on a companion design problem). The other relevant parameters are Pr = 0.65 and $\mathrm{Re}_c = 6.651 \times 10^6$ (based on the chord length and incoming flow conditions).

The design variable vector for this problem includes the x-coordinates of the Bezier control points at each section, the x-coordinates of the centers of the film-cooling holes, and the end locations (x-direction) of each internal

passage at each section. Here x is measured in the streamwise direction along the blade surface. The widths of the internal passages are held fixed during the optimization cycle. The design variables associated with the blade surface (x-coordinates of Bezier control points) are allowed to vary up to $\pm 10\%$ of the reference value, and the design variables associated with internal cooling and film cooling are allowed to vary up to $\pm 5\%$ of their respective reference values. The lower limiting value of $\pm 5\%$ is used for the internal cooling design variables in order to prevent the walls between adjacent internal passages from becoming very thin. The trailing-edge thickness is specified to be constant. In order to maintain good aerodynamic characteristics, constraints are specified on the maximum thickness-to-chord ratio for each section ($\pm 10\%$ of the reference value).

A detailed listing of all the design variables before and after optimization is available in Ref. [17]. There are considerable changes in the design variables as a result of optimization. The optimized design variable values for internal cooling differ from the corresponding reference values by less than $\pm 5\%$, which is surprising. From the heat-transfer perspective, the internal coolant passages should have reached their maximum size, leading to larger areas of coolant flow available for cooling the hot interior. Since the inlet mass flow rate of the coolant air in the internal passages is constant, an increase in the size of the coolant passage means a reduction in the coolant air velocity, which leads to a reduction in heat-transfer rate. Thus, an optimum value is reached by balancing these two contradicting factors, which is what a good optimization procedure should do. Since the film-cooling hole size is held fixed during optimization, better cooling performance is achieved by repositioning the film-cooling holes in the neighborhood of hot spots in the blade.

The reference blade and optimum blade shapes are compared for the root section in Fig. 4. The center of each film-cooling hole is indicated by a dot. The shape and position of the internal passages and the shift in position of film-cooling holes can be seen in these figures. The film-cooling holes have shifted considerably, resulting in a more efficient cooling configuration. The internal passages have also increased in size.

The maximum thickness-to-chord ratio is reduced by almost 10% (the allowable limit for that constraint), making this an "active" constraint for all the sections considered, which means that this constraint is critical, playing a major role in defining the external shape of the optimum blade. As mentioned before, the maximum thickness-to-chord ratio constraint is enforced to maintain good aerodynamic characteristics of the blade and to avoid drastic changes in the blade external shape. A comparison of the objective function values for the reference and optimum blade configurations shows significant reductions in the maximum and average tempera-

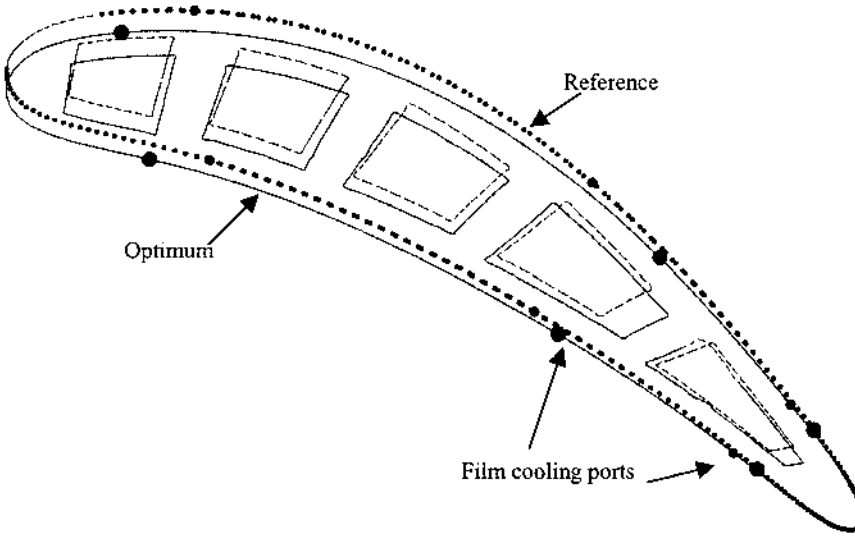

Figure 4 Comparison of blade cross-section (at the root) geometry.

tures for each of the 12 sections. At the blade root, the maximum and average temperatures are reduced by 14% and 12.5%, respectively, and the corresponding reductions at the blade tip are 10% in the maximum temperature and 8.2% in the average temperature. A combination of blade external surface parameters, film-cooling parameters, and internal cooling parameters has resulted in a blade that is much cooler than the reference blade. The interior temperature distributions for the reference and optimum blades are shown for the root section in Fig. 5. The effect of the shift in the film-cooling ports in reducing blade temperatures can be seen in these figures.

CONCLUSIONS

The suitability and the need for a robust multidisciplinary design optimization procedure are an integral part of the design process associated with gas turbine blade designs, as has been demonstrated above. The example problem is a simplified version of a typical design optimization problem in that it includes only two of the multiple disciplines associated with such a design. A multiobjective optimization procedure with the

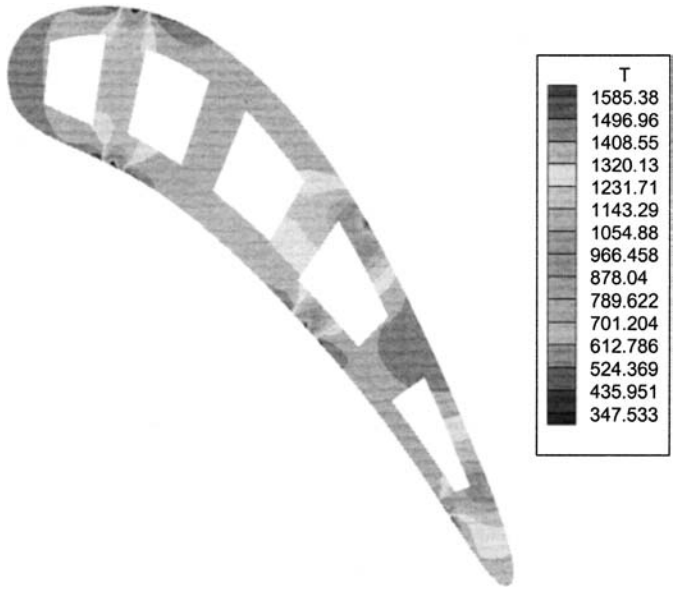

Figure 5 (a) **Temperature distribution: reference blade (root section).**

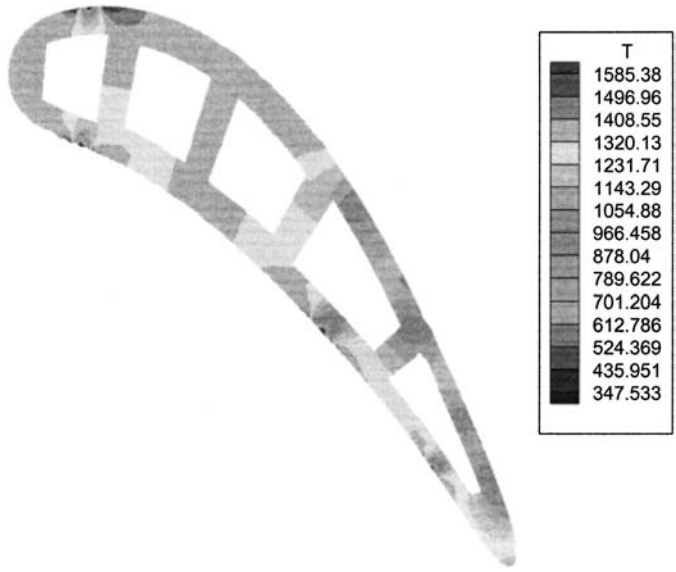

Figure 5 (b) **Temperature distribution: optimized blade (root section).**

integration of multiple disciplines (aerodynamics and heat transfer) developed for the design of cooled gas turbine blades has been used. The blade model is simplified for the heat-transfer analysis by using 12 sections of the blade rather than the full 3D blade. All the above simplifications were incorporated in order to keep the computational effort at a reasonable level. However, it must be pointed out that the optimization framework can be easily adapted to include more detailed analyses, additional disciplines, and additional design objectives and constraints.

Bezier–Bernstein polynomials for surface definition have been used to represent each of the 12 spanwise sections of the blade, leading to a relatively small set of design variables. Viscous blade-to-blade flow is calculated using the thin-layer 3D Navier–Stokes equations. The maximum and average temperatures at selected sections of the blade (obtained through a finite-element analysis) are minimized. The K–S function approach is used to solve the multiobjective constrained nonlinear optimization problem, and the results for the generic blade design show significant improvements in all the objective functions. The maximum and average temperatures at each section decreased considerably, resulting in a cooler blade. Design constraints such as fixed trailing-edge thickness and maximum thickness-to-chord ratio were satisfied. The maximum thickness-to-chord ratio constraint was found to be an active constraint, thus playing a major role in defining the external shape of the optimum blade.

The topic addressed here is a relevant one in modern engineering design applications. The area of gas turbine blade design was used as a means of demonstrating the utility and the need for formal optimization procedures as integral elements of the overall design processes for various engineering applications. The benefits to be derived are enormous. The computational cost associated with the optimization process (not discussed here) is considerable for such a complex design application. However, computational tools are continuously improving in both efficiency and speed. Cleverly arranged configurations of computing resources (distributed computing, parallel algorithms, etc.) and a gradual scaling-up approach [starting with simpler models and gradually fine-tuning the models while eliminating design variables that do not impact the design very much (via sensitivity analysis)] will make such a process viable for practical applications.

REFERENCES

1. R. J. Goldstein, "Film Cooling," *Advances in Heat Transfer*, *Vol. 7*, Academic Press, New York and London, pp. 321–379 (1971).

2. D. T. Vogel, "Navier–Stokes Simulation of the Flow Around a Leading Edge Film-Cooled Turbine Blade Including the Interior Cooling System and Comparison with Experimental Data," ASME Paper No. 96-GT-71 (1996).
3. E. R. G. Eckert, "Analysis of Film Cooling and Full-Coverage Film Cooling of Gas Turbine Blades," Paper No. ASME 95-GT-2 (1995).
4. B. Weigand and S. P. Harasgama, "Computations of a Film Cooled Turbine Rotor Blade With Non-Uniform Inlet Temperature Distribution Using a Three-Dimensional Viscous Procedure," ASME 94-GT-15 (1994).
5. D. K. Walters and J. H. Leylek, "A Systematic Computational Methodology Applied to a Three-Dimensional Film-Cooling Flowfield," *Journal of Turbomachinery*, *119*: 777–785 (1997).
6. J. Sobieszczanski-Sobieski and R. T. Haftka, "Multidisciplinary Aerospace Design Optimization: Survey of Recent Developments," AIAA 96-0711, *Proc. 34th Aerospace Sciences Meeting and Exhibit*, Reno, NV (1996).
7. H. Ashley, "On Making Things the Best—Aeronautical Use of Optimization," *AIAA J. Aircraft*, *19*(1) (1982).
8. A. Chattopadhyay and T. R. McCarthy, "Multiobjective Design Optimization of Helicopter Rotor Blades with Multidisciplinary Couplings," *Optimization of Structural Systems and Industrial Applications*, S. Hernandez and C. A. Brebbia, eds. Computational Mechanics Publications, pp. 451–462 (1991).
9. R. T. Haftka, Z. Gurdal, and M. P. Kamat, *Elements of Structural Optimization*, third revised and expanded edition, Kulwer Academic Publishers, Boston (1992).
10. A. Kreisselmeier and R. Steinhauser, "Systemic Control Design by Optimizing a Vector Performance Index," *IFAC Symposium on Computer Aided Design of Control Systems*, Zurich, Switzerland, pp. 113–117 (1979).
11. A. G. Wrenn, "An Indirect Method for Numerical Optimization Using the Kriesselmeir–Steinhauser Function," NASA Contract Report No. 4220 (1989).
12. A. Chattopadhyay, N. Pagaldipti, and K. T. Chang, "A Design Optimization Procedure for Efficient Turbine Airfoil Design," *J. Computers and Mathematics with Applications*, *26*(4): 21–31 (1993).
13. J. R. Narayan, A. Chattopadhyay, N. Pagaldipti, and S. Zhang, "Integrated Aerodynamics and Heat Transfer Optimization Procedure for Turbine Blade Design," AIAA-95-1479-CP (1995).
14. S. S. Talya, J. N. Rajadas, and A. Chattopadhyay, "Multidisciplinary Design Optimization of Film-Cooled Gas Turbine Blades," *Mathematical Problems in Engineering*, *5*(2): 97–119 (1999).
15. S. S. Talya, J. N. Rajadas, and A. Chattopadhyay, "Multidisciplinary Optimization of Gas Turbine Blade Design," *7th AIAA/USAF/NASA/ISSMO Symp. Multidisciplinary Analysis and Optimization*, Paper No. AIAA-98-4864, St. Louis, MO (1998).
16. S. S. Talya, R. Jha, A. Chattopadhyay, and J. N. Rajadas, "Development of Multidisciplinary Optimization Procedure for Gas Turbine Blade Design," *37th AIAA Aerospace Sciences Meeting and Exhibit*, Paper No. AIAA-99-0364, Reno, NV (1999).

17. S. S. Talya, "Multidisciplinary Design Optimization Procedure for Turbomachinery Blades and Sensitivity Analysis Technique for Aerospace Applications," Ph.D. Thesis, Arizona State University, Tempe, AZ (2000).
18. G. S. Dulikravich, "Aerodynamic Shape Design and Optimization: Status and Trends," *J. Aircraft, 29*(6): 1020–1026 (1992).
19. G. S. Dulikravich and T. J. Martin, "Three-Dimensional Coolant Passage Design for Specified Temperature and Heat Fluxes," AIAA Paper No. 94-0348, *32nd Aerospace Sciences Meeting and Exhibit*, Reno, NV (1994).
20. G. S. Dulikravich and T. J. Martin, "Inverse Design of Super Elliptic Coolant Passages in Coated Turbine Blades with Specified Temperatures and Heat Fluxes," AIAA Paper No. 92-4714, *4th AIAA/USAF/NASA/OAI Symp. Multidisciplinary Analysis and Optimization*, Cleveland, OH (1992).
21. A. Demeulenaere and V. R. Braembussche, "Three-Dimensional Inverse Method for Turbomachinery Blade Design," *J. Turbomachinery*, *120*: 247–255 (1998).
22. T. Dang and V. Isgro, "Euler-Based Inverse Method for Turbomachine Blades Part 1: Two-Dimensional Cascade," *AIAA J. 33*(12): 2309–2315 (1995).
23. J. M. Sanz, "Automated Design of Controlled-Diffusion Blades," *J. Turbomachinery*, *110*: 540–544 (1988).
24. J. E. Borges, "A Three-Dimensional Inverse Method for Turbomachinery: Part 1—Theory," *J. Turbomachinery*, *112*: 346–354 (1990).
25. F. N. Foster and G. S. Dulikravich, "Three-Dimensional Aerodynamic Shape Optimization Using Genetic and Gradient Search Algorithms," *J. Spacecraft and Rockets*, *34*(1): 36–42 (1997).
26. C. Huang and T. Hsiung, "An Inverse Design Problem of Estimating Optimal Shape of Cooling Passages in Turbine Blades," *Intl. J. Heat and Mass Transfer*, *42*: 4307–4319 (1999).
27. M. Haendler, D. Raake, and M. Scheurlen, "Aero-thermal Design and Testing of Advanced Turbine Blades," Presented at the International Gas Turbine and Aeroengine Congress and Exposition, Orlando, FL, Paper No. 97-GT-66 (1997).
28. S. Goel and S. Lamson, "Automating the Design Process for 3D Turbine Blades," *CFD for Design and Optimization*, *ASME*, *FED 232*: 85–86 (1995).
29. R. M. Kolonay and S. Nagendra, "Sensitivity Analysis for Turbine Blade Components," AIAA Paper no. AIAA-99-1315 (1999).
30. S. Kodiyalam, V. N. Parthasarathy, M. S. Hartle, and R. L. Mcknight, "Optimization of Composite Engine Structures for Mechanical and Thermal Loads," AIAA Paper No. AIAA-93-1583-CP (1993).
31. P. Kao, V. N. Parthasarathy, S. Kodiyalam, and S. H. Lamson, "Coupled Aerodynamic-Structural Shape Optimal Design of Engine Blades," AIAA Paper No. AIAA-94-1479-CP (1994).
32. R. Tappeta, S. Nagendra, and J. E. Renaud, "A Multidisciplinary Design Optimization Approach for High Temperature Aircraft Engine Components," AIAA Paper No. AIAA-98-1819 (1998).

33. J. P. Queau and P. Trompette, "Optimal Shape Design of Turbine Blades," *J. Vibration, Acoustics, Stress and Reliability in Design*, *105*: 444–448 (1983).
34. S. Goel and P. Hajela, "Identification of Parameter Coupling in Turbine Design Using Neural Networks," *J. Propulsion and Power*, *12*(3): 503–508 (1996).
35. M. L. Shelton, B. A. Gregory, S. H. Lamson, H. L. Moses, R. L. Doughty, and T. Kiss, "Optimization of a Transonic Turbine Airfoil Using Artificial Intelligence, CFD and Cascade Testing," Presented at the International Gas Turbine and Aeroengine Congress and Exposition, Cincinnati, OH, Paper No. 93-GT-161 (1993).
36. S. Pierret and V. R. A. Braembussche, "Turbomachinery Blade Design Using a Navier–Stokes Solver and Artificial Neural Network," *J. Turbomachinery*, *121*: 326–332 (1999).
37. M. A. Trigg, G. R. Tubby, and A. G. Sheard, "Automatic Genetic Optimization Approach to Two-Dimensional Blade Profile Design for Steam Turbines," *J. Turbomachinery*, *121*: 11–17 (1999).
38. G. M. Fadel, M. F. Riley and J. F. M. Barthelemy, "Two-Point Exponential Approximation Method for Structural Optimization," *Structural Optimization*, *2*: 117–124 (1991).
39. G. Farin, *Curves and Surfaces for Computer Aided Geometric Design, A Practical Guide*, 3rd ed., Academic Press, New York (1993).
40. R. V. Chima and J. W. Yokota, "Numerical Analysis of Three-Dimensional Viscous Internal Flows," *AIAA J. 28*(5) (1990).
41. R. V. Chima, *RVC3D—Rotor Viscous Code 3-D*, user manual and documentation (1996).
42. R. V. Chima, *TCGRID—3-D Grid Generator for Turbomachinery*, user manual and documentation (1998).

10

Rotordynamic Considerations

Harold D. Nelson
Arizona State University, Tempe, Arizona, U.S.A.
Paul B. Talbert
Honeywell Engines, Systems and Services, Phoenix, Arizona, U.S.A.

INTRODUCTION

The discipline of rotordynamics is concerned with the free and forced response of structural systems that contain high-speed rotating assemblies. The concern here is with the dynamic characteristics of systems with rotor assemblies that spin nominally about their longitudinal axes. Examples of such systems, Fig. 1, include gas turbines, steam turbines, pumps, compressors, turbochargers, electric motors and generators, etc. A completely separate area of rotordynamics, not addressed here, is concerned with structural systems with rotor assemblies that spin nominally about an axis perpendicular to the axis of the rotor such as encountered with helicopter blades or propellers. The interest here focuses primarily on the displacement components (both translation and bending rotation) and associated forces and moments that are linked with motion of a shaft perpendicular to the shaft centerline.

Vibration problems that exist in rotordynamic systems are caused by a variety of different excitation sources. Residual rotating unbalance and self-excitation mechanisms are two of the more prevalent. The rotating unbalance

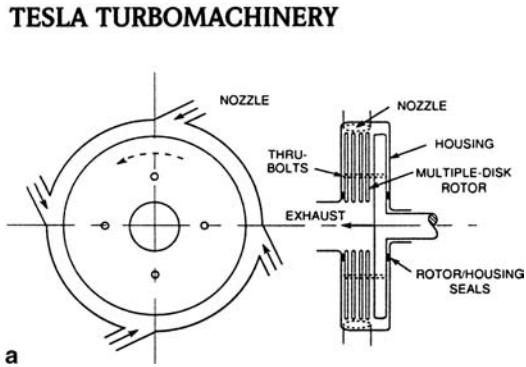

Figure 1 Examples of rotordynamic systems. (a) Schematic diagram of a Tesla-type turbine.

forces are synchronous with the spin-speed of each associated rotating assembly, while the self-excited free-vibration responses generally have a more complex frequency content. These self-excitation mechanisms are typically associated with system components such as fluid-film bearings and dampers,

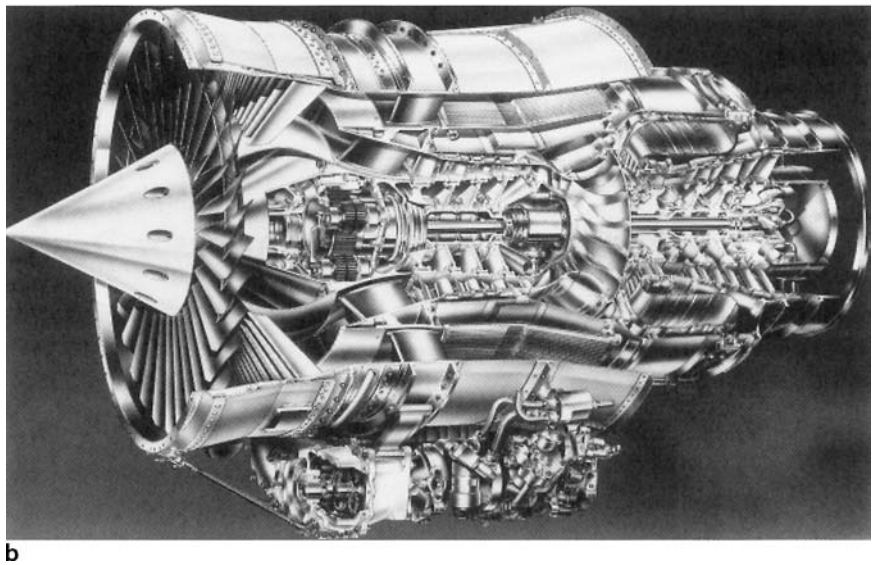

Figure 1 (b) AlliedSignal 731 turbofan engine.

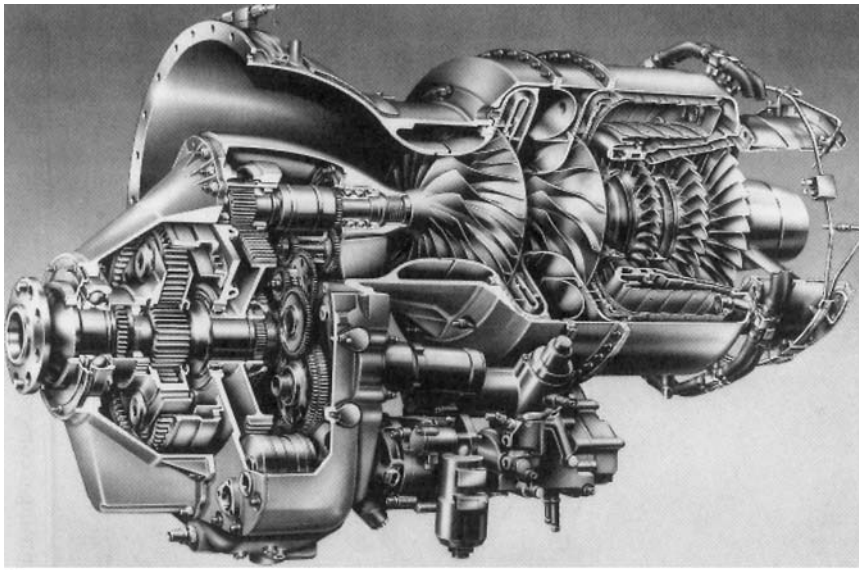

c

Figure 1 (c) AlliedSignal 331 turboprop engine.

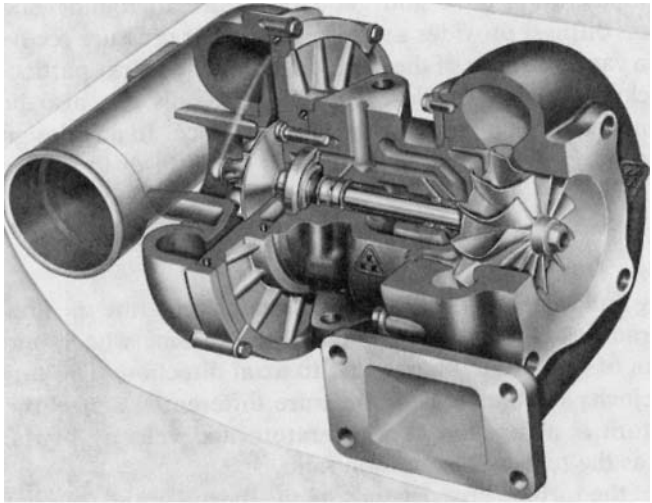

d

Figure 1 (d) Turbocharger for a spark ignition engine. (Courtesy Kuhnle, Kopp, and Kausch AG.)

working fluid interactions, couplings, seals, splines, internal damping, etc. Some technical issues of concern to development engineers include the frequency order of the response relative to the rotation speed, noise generation (decibel level and steady versus beating), possible rotor–structure rubs and/or rotor–rotor rubs, deflection of the rotating assembly at seal locations, and bearing loads and their influence on bearing life and failure.

The dynamic characteristics of rotor systems that are of primary interest to the machine analyst and designer include

- Natural frequencies of whirl (whirl speeds) and associated mode shapes
- Critical speeds and associated mode shapes
- Range of dynamically stable operation
- Steady spin-speed unbalance response (deflections and bearing loads)
- Steady response due to maneuvers (turns, rolls, etc.)
- Transient response
  - Startup and shutdown operation (variable spin-speed)
  - Foreign substance ingestion (e.g., birds)
  - Blade-loss excitation (step change in unbalance)
  - Hard landings and maneuvers
  - Response from self-excitation mechanisms

Knowledge of these characteristics is helpful in assisting a design engineer in selecting design parameters to avoid unstable regions of operation and/or large-amplitude response within the operating range of the system. Rotordynamic simulation may be used to assist the designer in the preliminary design of a new system, in the redesign of an existing system, or in determining the cause of undesirable response characteristics of an existing system.

The motion of a rotor system is usually described in terms of physical coordinates as observed from a fixed reference (Fig. 2). Most analyses are posed in terms of these physical coordinates as long as the number of coordinates does not present significant computational problems. Many coordinate reduction procedures and/or modal analysis procedures have been successfully employed in the rotordynamic simulation of "very large"-order systems. The interested reader is referred to more extensive treatment of these topics in references such as Ehrich [6].

Rotordynamic systems are normally modeled as a finite set of interconnecting flexible-shaft elements, bearings and dampers, working fluid mechanisms, rigid and/or flexible disks, rotational springs to connect rotor sections, and the support structure. The system components are typically defined by using a lumped-mass or consistent-mass (finite-element) idealization, or a combination of these two approaches. The system

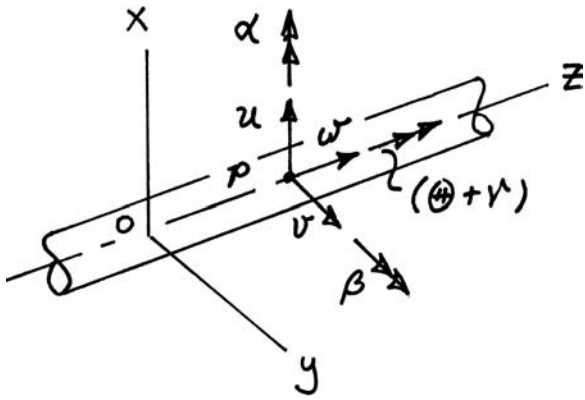

Figure 2 Rotor system displacements.

equations of motion are then developed and analyzed by either the direct stiffness or transfer matrix method, Ehrich [6]. Classical linear analysis techniques apply for those systems where the nonlinear mechanisms are weak and linear modeling assumptions are acceptable. Fortunately, this condition exists in many practical applications. Linear system response analyses may be conducted using established classical techniques, and several commercial numerical and/or symbolic computer software packages are available for conducting these analyses. The analysis of strongly nonlinear systems, however, is more limited in terms of currently available mathematical software. Direct numerical integration of the nonlinear equations of motion is presently the most widely used technique for simulating the behavior of nonlinear rotor systems.

The present literature on the subject of rotordynamics consists of several books and a wealth of technical manuscripts in mechanics, mechanical engineering, and aerospace engineering technical transactions. Several of these works are included in the References. A list of rotordynamics books is contained in the bibliography of the vibrations text by Dimaragonas [4].

Steady-State Rotor Motion

The motion of a rotor system is most conveniently described in a fixed (inertial) Cartesian (x, y, z)-coordinate system as illustrated in Fig. 2. One of the coordinate axes, say the z-axis, is selected along the axis of the shaft and the x- and y-axes form a plane perpendicular to the shaft. The origin of the

system, o, coincides with an arbitrarily defined reference position of the shaft centerline (e.g., the static equilibrium position). The lateral motion of the shaft is then defined by translations and rotations (using the right-hand rule) in the (x, y)-plane. Small motion assumptions are generally made so both the translation and rotation components of motion may be treated as vector quantities.

The displacement of a typical structural point on a rotating assembly includes axial, lateral, and torsional components. The lateral motion (perpendicular to the axis of rotation) typically includes small-amplitude translation (u, v) and rotation (α, β) components in two perpendicular directions. The torsional motion is usually represented as a superposition of a rigid-body rotation Θ plus a torsional deformation γ. The six components of displacement at a typical structural point p are illustrated in the rotor system schematic shown in Fig. 2.

In most rotor systems, the axial component of motion, w, is usually negligible. In addition, the static and dynamic coupling between the torsional motion, γ, and lateral components of motion, $(u, v; \alpha, \beta)$, are generally weak. Thus, most rotor system models treat the lateral vibration and torsional vibration problems as separate and decoupled problems. For the case of geared systems, however, there may be strong static and dynamic coupling between the torsional and lateral motions of the rotating assemblies.

Elliptic Lateral Whirl

The most elementary steady-state motion of a typical station p of a rotor system is simple harmonic motion occurring simultaneously in the x- and y-directions with common frequency ω, as illustrated in Fig. 3. This frequency of motion is referred to as the *whirl frequency* of the shaft centerline. This whirling motion may be either a free-vibration motion at a natural whirl frequency or forced response at a specific excitation frequency. The translation displacement components (the rotation displacements have the same form) in the x- and y-directions and may be expressed in the form

$$\begin{aligned} u(t) &= u_c \cos \omega t + u_s \sin \omega t \\ v(t) &= v_c \cos \omega t + v_s \sin \omega t \end{aligned} \tag{1}$$

As the point p moves along the orbit path, the radius vector **op** rotates at an angular rate referred to as the *precessional rate*. This rate, $\dot{\varphi}$, varies around the orbit and is a minimum at an apogee (maximum radius) of the orbit and is a maximum at a perigee (minimum radius) of the orbit. The minimum and maximum precession rates each occur twice for a complete orbit, and the

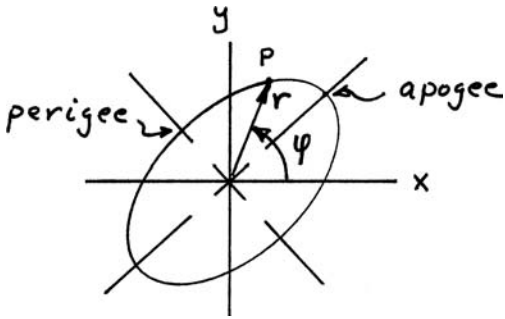

Figure 3 Elliptic lateral whirl.

average processional rate over a complete orbit is equal to the whirl frequency of the orbit.

Differentiation of Eq. (1) twice with respect to time provides the x- and y-components of the acceleration for point p. These components are equal to negative the square of the whirl frequency times the displacement components. Thus, the acceleration of point p is always directed toward the center of the elliptical orbit (the negative radial direction), and the transverse acceleration component is always zero. The type of elliptical lateral motion described by Eq. (1) is referred to as *elliptic vibration*. The elliptical nature of steady rotor motion is caused by stiffness and/or damping forces that are not isotropic, i.e., the stiffness in the horizontal direction may be different than in the vertical direction. If all support properties are isotropic, the steady elliptic motion degenerates to circular motion.

Two special cases of elliptic vibration occur quite often in the observation of rotor motion. These two cases are referred to as *forward circular whirl* and *backward circular whirl*. Forward circular whirl is the normal motion of a rotor. Backward circular whirl, however, occurs infrequently except for systems that have coupled counter-rotating assemblies.

Forward Circular Whirl. This special whirl condition exists when $u_s = -v_c$ and $v_s = u_c$. For illustration purposes, let $u_c = f$ and $v_c = g$. The orbit Eq. (1) then simplifies to

$$\begin{aligned} u(t) &= f\cos\omega t - g\sin\omega t \\ v(t) &= g\cos\omega t + f\sin\omega t \end{aligned} \tag{2}$$

and describes a forward-whirl circular orbit as illustrated in Fig. 4(a). For this case, the precessional rate of the radius vector **op** is constant over the orbit and is equal to the whirl frequency, ω, of the orbit.

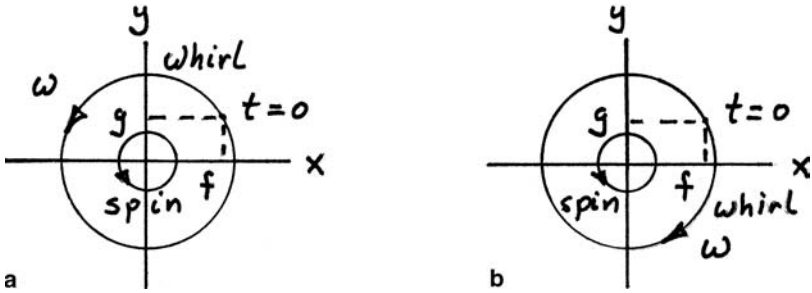

Figure 4 Forward (a) and backward, (b) whirl circular orbits.

Backward Circular Whirl. This special whirl condition exists when $u_s = v_c$ and $v_s = -u_c$. Again, for illustration purposes, let $u_c = f$ and $v_c = g$. The orbit Eq. (2) then simplifies to

$$\begin{aligned} u(t) &= f\cos\omega t + g\sin\omega t \\ v(t) &= g\cos\omega t - f\sin\omega t \end{aligned} \tag{3}$$

and describes a backward-whirl circular orbit as illustrated in Fig. 4(b). For this case, the precessional rate of the radius vector **op** is also constant over the orbit and is equal to negative the whirl frequency ω of the orbit.

Superposition of Elliptic Vibrations

The steady-state motion of a rotor system frequently involves the superposition of several frequency components, e.g., natural frequencies of whirl, rotor spin-speeds, and external excitation sources. This situation can often be represented at a typical structural point as the superposition of several elliptic vibration components of the motion.

If all the frequencies are commensurate (i.e., the ratios of all possible frequencies are rational numbers), then the resulting superposed motion is periodic. If any one ratio is not commensurate, the resulting motion still possesses a discrete frequency content; however, the motion is not periodic.

Several special cases exist in the superposition of elliptic vibrations that are often of interest to rotordynamists.

1. *Identical frequency superposition.* If all the frequencies in a superposition of elliptic vibrations are identical with whirl frequency ω, then the resulting motion is also an elliptic vibration with the same whirl frequency.

2. *Subharmonic superposition.* This situation occurs when an elliptic vibration with whirl frequency ω is superposed with a second elliptic

vibration (either forward or backward) with a frequency equal to a submultiple of ω (i.e., ω/n). This situation may exist when the rotor tends to respond at one of the natural frequencies of whirl and is simultaneously excited by a mechanism at the rotor spin-speed or by a self-excitation mechanism. When n is an integer, the period of the superposed motion is $n(2\pi/\omega)$.

Two examples of superposed elliptic vibrations are illustrated in Fig. 5. The first case [Fig. 5(a)] is a superposition of two forward circular orbits. Both orbits have an amplitude of 1.0, one with a whirl frequency ω, and the other with a frequency of $\omega/2$. The second case [Fig. 5(b)] is a superposition of a forward circular orbit with amplitude 1.0 and frequency ω, and a backward circular orbit with an amplitude 1.0 and frequency $\omega/2$. More discussion on the superposition of elliptic vibrations is included in Tondl [19].

SINGLE-DISK ROTOR SYSTEMS

The Laval–Jeffcott Rotor: Translational Motion

An elementary rotor system model, frequently used by designers and analysts to study and simulate basic rotordynamic system characteristics, is a single rigid disk centrally located on a uniform flexible shaft as illustrated in Fig. 6. The shaft is considered to have negligible mass and is supported on bearings that are considered to be infinitely stiff. A form of this single-disk rotor model was first presented by A. Föppl [8] in Germany in 1895. Föppl named this elementary model the Laval rotor in recognition of the contributions made in the area of turbomachinery by the Swedish engineer Gustav Patric De Laval. In 1919, the English engineer, H. H. Jeffcott [11] subsequently presented a study using the same elementary model. As the result of references made to these two pioneering works over the past several decades, this single-disk rotor model is referred to as the Laval rotor in some sections of the world and as the Jeffcott rotor in others. In order to recognize the early work of both Föppl and Jeffcott, the name Laval–Jeffcott rotor is adopted here.

The rigid disk is of negligible axial extent and has a mass, m, with mass center located a distance, e, in the ξ-direction from the geometric disk center, o. The diametral and polar mass moments of inertia for the disk are I_d and I_p, respectively. The shaft has a translational stiffness, k_t (associated with shaft bending), which depends in magnitude on the shaft geometrical and material properties. For a simply supported shaft with modulus of elasticity, E, and diametral area moment of inertia, I, the translational stiffness at the center of the beam is $k_t = 48EI/L^3$. Only the undamped translational motion of the disk in the (x, y)-plane is included for this classic

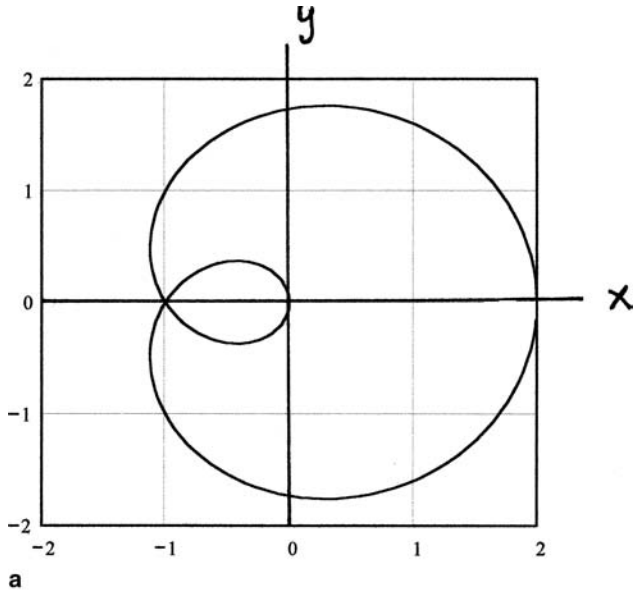

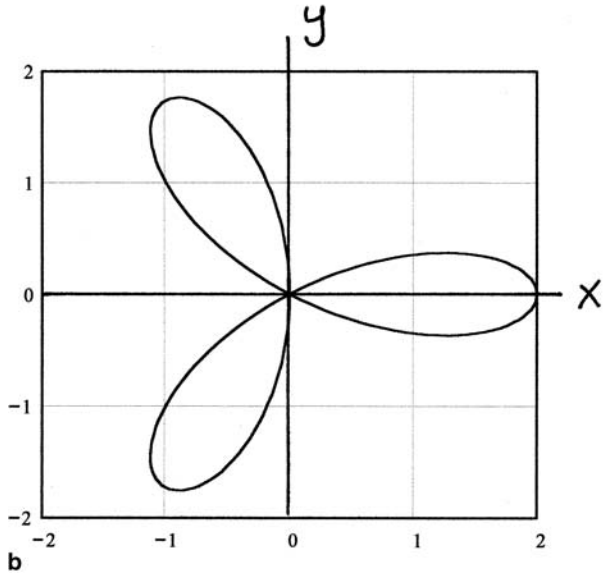

Figure 5 Superposition of elliptic vibrations. (a) Forward subharmonic, (b) backward subharmonic.

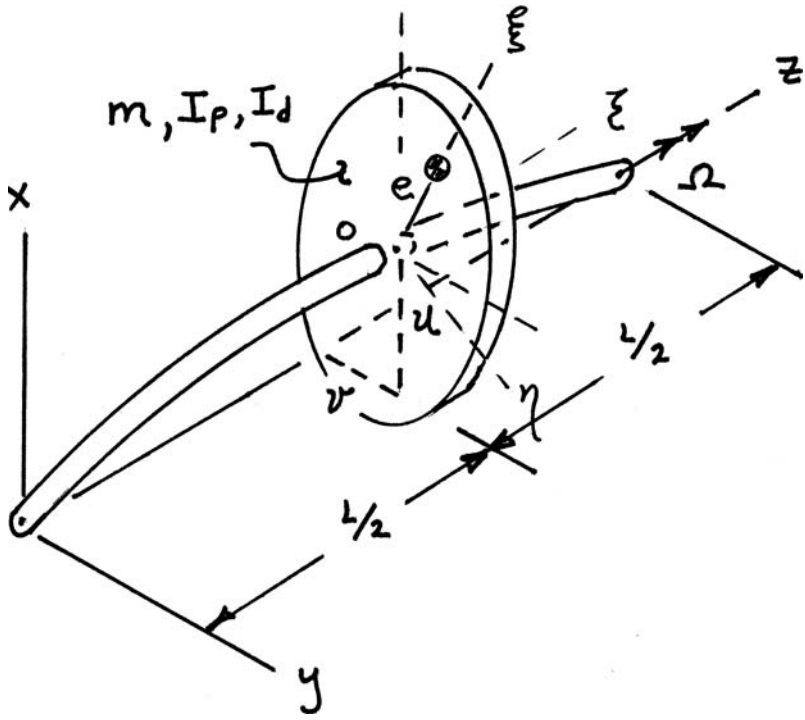

Figure 6 The Laval–Jeffcott rotor.

Laval–Jeffcott rotor model. The influence of both external and internal viscous damping on the translational motion is discussed later in this chapter. A discussion on the effects of rotatory (rotation perpendicular to the shaft centerline) inertia and gyroscopic moments of the disk are also included. The translational displacement components of the disk geometrical center, o, are denoted by (u, v) relative to the (x, y)-directions respectively.

Undamped Response

Relative to the (x, y, z) reference, the equation of motion of the undamped two degree-of-freedom disk is

$$\begin{bmatrix} m & 0 \\ 0 & m \end{bmatrix} \begin{Bmatrix} \ddot{u} \\ \ddot{v} \end{Bmatrix} + \begin{bmatrix} k_t & 0 \\ 0 & k_t \end{bmatrix} \begin{Bmatrix} u \\ v \end{Bmatrix} = me\Omega^2 \begin{Bmatrix} \cos(\Omega t) \\ \sin(\Omega t) \end{Bmatrix} \tag{4}$$

An inspection of Eq. (4) reveals that the u and v motions are both dynamically and statically decoupled for this undamped model. The equations of motion for the u and v displacements are identical in form with the exception that the mass unbalance forces differ in phase by 90°.

Undamped Forced Response. The forced response, or particular solution, includes only the influence of steady unbalance associated with the mass eccentricity. This unbalance excitation is harmonic relative to a nonrotating observer in (x,y,z). From Eq. (4), the forced response solutions are

$$u(t) = r_t(\Omega)\cos(\Omega t) = \frac{e(\Omega/\omega_t)^2}{1-(\Omega/\omega_t)^2}\cos(\Omega t) \tag{5a}$$

$$v(t) = r_t(\Omega)\sin(\Omega t) = \frac{e(\Omega/\omega_t)^2}{1-(\Omega/\omega_t)^2}\sin(\Omega t) \tag{5b}$$

where the undamped translational natural frequency of the system is $\omega_t = \sqrt{k_t/m}$. The (u, v) motion, associated with Eqs. (5), describes a circular orbit in (x, y, z) with a radius $|r_t(\Omega)|$, which is dependent on the spin-speed, Ω. This amplitude function, $|r_t(\Omega)|$, (normalized with respect to e), is plotted in Fig. 7 versus the spin-speed ratio, Ω/ω_t. This function changes from positive to negative polarity when the spin-speed passes through the rotor critical speed, ω_t. This change is due to a 180° phase shift in the position of the rotor center relative to the mass center. When the rotor speed is less than the rotor critical speed, the rotor center and mass centers are in-phase (i.e., the bearing center, rotor center, and mass center form a straight line). After passing through the rotor critical speed, the rotor center and mass centers

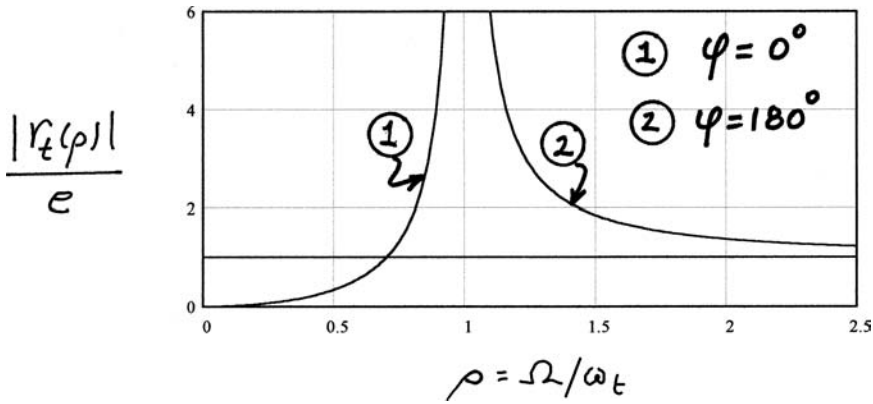

Figure 7 Laval–Jeffcott rotor: undamped steady unbalance response re: (x, y, z).

are 180° out of phase (i.e., the bearing center, mass center, and rotor center form a straight line). As the rotor speed approaches infinity, the amplitude of the response approaches the cg eccentricity, e, of the rotor. Thus, at very high speeds, the rotor tends to spin about its mass center, providing an orbit radius equal to the cg eccentricity.

Undamped Free Response. The free response, or homogeneous solution, is obtained from Eq. (4) with the excitation forces excluded, i.e.,

$$\begin{bmatrix} m & 0 \\ 0 & m \end{bmatrix} \begin{Bmatrix} \ddot{u} \\ \ddot{v} \end{Bmatrix} + \begin{bmatrix} k_t & 0 \\ 0 & k_t \end{bmatrix} \begin{Bmatrix} u \\ v \end{Bmatrix} = \begin{Bmatrix} 0 \\ 0 \end{Bmatrix} \tag{6}$$

For an arbitrary set of initial conditions,

$$\begin{matrix} u(0) = u_o \\ v(0) = v_o \end{matrix} \quad \text{and} \quad \begin{matrix} \dot{u}(0) = \dot{u}_o \\ \dot{v}(0) = \dot{v}_o \end{matrix} \tag{7}$$

the solution of Eq. (6) yields

$$u(t) = u_o \cos \omega_t t + \frac{\dot{u}_o}{\omega_t} \sin \omega_t t \tag{8a}$$

$$v(t) = v_o \cos \omega_t t + \frac{\dot{v}_o}{\omega_t} \sin \omega_t t \tag{8b}$$

This free-vibration response is clearly harmonic with the same natural undamped frequency $\omega_t = \sqrt{k_t/m}$ in both the x- and y-directions of motion. A typical free-vibration orbit, relative to an observer in (x, y, z), is illustrated in Fig. 8. The orbit may precess either in a forward or backward direction depending on the initial conditions. The precession direction is defined as forward if it is in the same direction as the rotor spin-speed and backward if in the opposite direction.

The orbit is generally a standard ellipse, however, a few special degenerate cases may exist. First, if the initial conditions for the x- and y-components of displacement and velocity are proportionally related, i.e., $v(0) = u(0) \tan \theta$ and $\dot{v}(0) = \dot{u}(0) \tan \theta$, the orbit reduces to an oscillatory straight-line motion at the angle θ relative to the x-axis, i.e., an ellipse with zero semi-minor axis. A second special case exists if the initial conditions satisfy the relations $\dot{u}(0) = -v(0)\omega_t$ and $\dot{v}(0) = u(0)\omega_t$. For this case, the resulting orbit is circular, i.e., an ellipse with zero eccentricity. These two special cases are illustrated in Fig. 9.

It is common practice in rotordynamics to graph the natural frequencies of the rotor system as a function of the rotor spin-speed. These graphs are typically referred to as "whirl speed maps" or "Campbell diagrams for whirl speeds." For the case of the classic Laval–Jeffcott rotor,

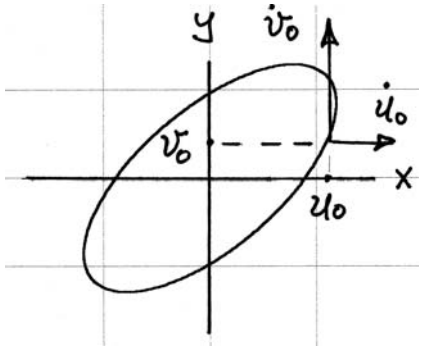

Figure 8 Typical undamped free-vibration orbit: Laval–Jeffcott rotor.

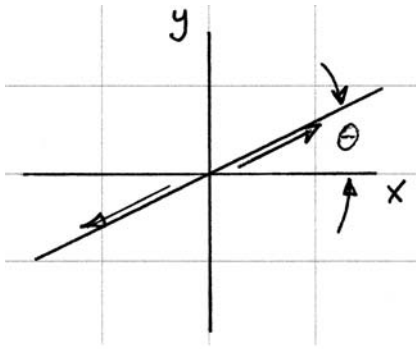

a

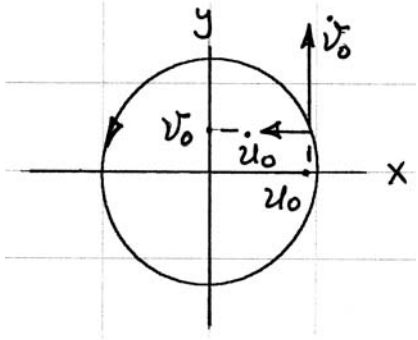

b

Figure 9 Special free-vibration orbits: Laval–Jeffcott rotor. (a) Straight-line orbit, (b) circular orbit.

this graph is quite simple; however, it is presented here to introduce the concept as a forerunner of whirl speed maps for more complicated systems.

For the case of a Laval–Jeffcott rotor in translation only, two natural frequencies of whirl exist. The first is a forward whirl (denoted as 1f) with natural whirl frequency, ω_t, and the second is a backward whirl (denoted as 1b) at the frequency, $-\omega_t$. These natural frequencies are not a function of the rotor spin-speed since the natural motion of the rigid disk is pure translation. Thus, gyroscopic moments are not present for this simple translational model.

One option is to graph the positive and negative natural whirl frequencies as a function of the spin-speed including the entire range of positive and negative spin-speeds (i.e., a four-quadrant map). This graph is illustrated in Fig. 10(a) for the Laval–Jeffcott rotor. When the rotor is defined as having a positive spin-speed, a positive whirl frequency corresponds to a forward mode and a negative whirl frequency corresponds to a backward mode. When the rotor is defined as having a negative spin-speed, a positive whirl frequency corresponds to a backward mode and a negative whirl frequency corresponds to a forward mode. Recall: a forward mode is simply defined as a whirling motion in the same sense as the spin while a backward mode is in the opposite sense.

Because of the polar symmetry of the four-quadrant graph, it is common practice to present a whirl speed map as a single-quadrant graph associated with a positive spin-speed and include both the positive and negative whirl frequencies in the first quadrant. Quite often, different line types are used to distinguish the positive (e.g., solid) and negative (e.g., dashed) whirl frequencies. A single-quadrant whirl speed map for the Laval–Jeffcott rotor is illustrated in Fig. 10(b). For this simple system, the positive and negative whirl frequencies have the same absolute value and are therefore coincident on the graph.

It is common practice to include an excitation frequency line, e.g., $\omega_{\text{exc}} = \rho\Omega$, on whirl speed maps. This line indicates an excitation frequency that is a multiple, ρ, of the rotor spin-speed, Ω. The line shown in Fig. 10(a) and (b) corresponds to $\rho = 1$ and indicates an excitation frequency that is synchronous with the rotor spin-speed. This excitation is generally of interest because rotating unbalance is always present in a rotor system, and the associated excitation is synchronous with the rotor spin-speed, i.e., $\rho = 1$. An intersection of the excitation frequency line with a whirl speed line identifies a "critical speed" or rotor spin-speed, n, associated with a resonance condition. For the Laval–Jeffcott rotor, only one forward critical speed exists for synchronous spin-speed excitation, with a value of $n_f = \omega_t$.

A second type of graph that is often used by designers to assist in making design parameter decisions is called a "critical speed map." This

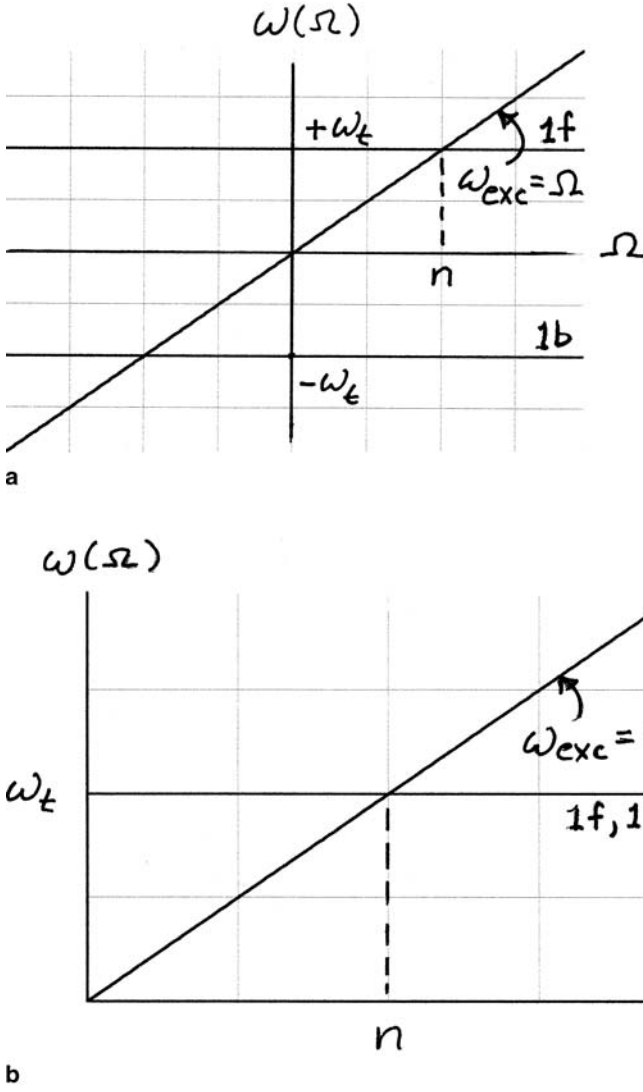

Figure 10 Whirl speed map for a Laval–Jeffcott rotor. (a) Four-quadrant graph, (b) single-quadrant graph.

graph plots the critical speed(s) of the system versus a design parameter of the system. In addition, the operating spin-speed range of the system is usually included on the graph. A second design parameter may also be

included on these types of graphs by adding a family of plots. As an illustration for the Laval–Jeffcott rotor, consider the shaft stiffness, k_t, as a design parameter and allow the rotor mass to take on values of 15, 20, and 25 kg (33.07, 44.09, and 55.12 lb_m). Define the operating spin-speed range (including design margins) for the rotor to be between 2,000 and 4,000 rpm. Typically the upper and lower speeds in the operating range include a margin of approximately 30% to provide for inaccuracies in simulated results associated with deficiencies in modeling and the inability to accurately evaluate many system parameters. A critical speed map for this rotor system is illustrated in Fig. 11.

This critical speed map indicates that, for a rotor mass of 20 kg (44.09 lb_m), a shaft stiffness less than 0.88 MN/m (5,025 lb_f/in.) places the synchronous forward critical speed below the lowest operating speed and that a value above 3.51 MN/m (20,043 lb_f/in.) positions the critical speed above the highest operating speed. This critical speed map then provides a designer with information that may be used to assist in selecting the shaft stiffness. The family of curves associated with the rotor mass generalizes the critical speed map and provides additional information to assist a designer in sizing the system.

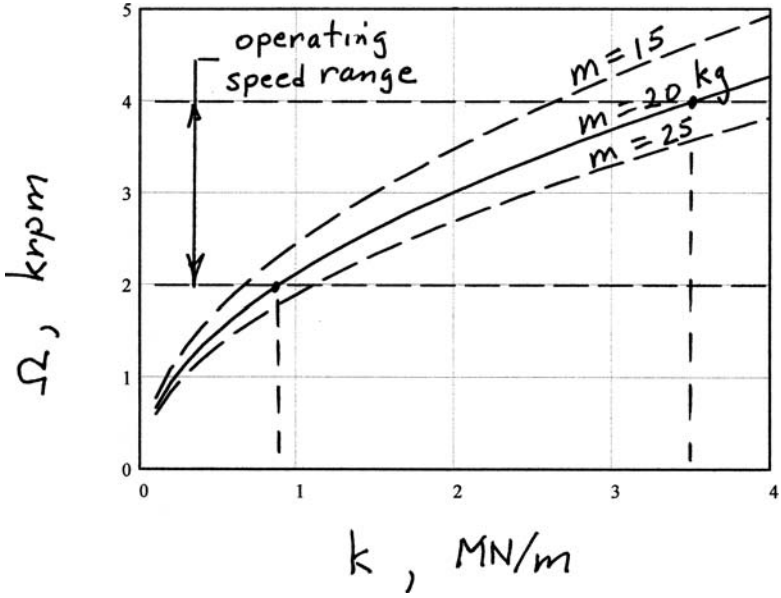

Figure 11 Critical speed map for a Laval–Jeffcott rotor.

Internal and External Viscous Damping Effects

The Laval–Jeffcott rotor, discussed above, is generalized in this section to include the effects of both external and internal viscous damping. An external viscous damping force is proportional to the velocity of the disk relative to the (x, y, z) reference, and an internal viscous damping force is proportional to the velocity of the disk relative to the rotating shaft. These external and internal viscous damping coefficients are denoted by c_e and c_i, respectively.

Relative to the fixed reference frame, (x, y, z), the equation of motion of the two degree-of-freedom disk is

$$\begin{bmatrix} m & 0 \\ 0 & m \end{bmatrix} \begin{Bmatrix} \ddot{u} \\ \ddot{v} \end{Bmatrix} + \begin{bmatrix} c_e + c_i & 0 \\ 0 & c_e + c_i \end{bmatrix} \begin{Bmatrix} \dot{u} \\ \dot{v} \end{Bmatrix} + \begin{bmatrix} k & +c_i\Omega \\ -c_i\Omega & k \end{bmatrix} \begin{Bmatrix} u \\ v \end{Bmatrix} = me\Omega^2 \begin{Bmatrix} \cos(\Omega t) \\ \sin(\Omega t) \end{Bmatrix} \tag{9}$$

The internal damping mechanism introduces a spin-speed dependent skew-symmetric contribution to the system "stiffness" matrix. This internal force is a destabilizing influence on the system and can cause dynamic instability for certain combinations of parameters. For additional discussion on this model, see Loewy and Piarulli [12].

Damped Steady Forced Response. The forced response, or particular solution, consists only of the contribution from steady unbalance associated with the mass unbalance force. The harmonic nature relative to (x, y, z) of the mass unbalance force is evident by inspection of Eq. (9), and the associated steady-state unbalance response is

$$u(t) = \frac{e(\Omega/\omega_t)^2}{\sqrt{(1 - (\Omega/\omega_t)^2)^2 + (2\zeta_e(\Omega/\omega_t))^2}} \cos(\Omega t - \psi_o(\Omega)) \tag{10a}$$

$$v(t) = \frac{e(\Omega/\omega_t)^2}{\sqrt{(1 - (\Omega/\omega_t)^2)^2 + (2\zeta_e(\Omega/\omega_t))^2}} \sin(\Omega t - \psi_o(\Omega)) \tag{10b}$$

where $\psi_o(\Omega)$ represents the phase lag of the response relative to the unbalance force excitation and is given by the expression

$$\psi_o(\rho) = \tan^{-1}\left(\frac{2\zeta_e(\Omega/\omega_t)}{1 - (\Omega/\omega_t)^2}\right) \tag{11}$$

$\zeta_e = c_e/2\sqrt{k_t m}$ is a damping ratio associated with the external damping mechanism of the model. Since the response of the rotor is synchronous with the rotor spin and is circular relative to (x, y, z), the strain rate of any point

on the shaft is zero. Thus, the steady-state unbalance response is not influenced by the internal damping mechanism. The normalized amplitude and the phase of the unbalance response are graphed in Bode and polar plot format in Fig. 12 versus the normalized spin-speed.

When the rotor spin-speed equals the undamped natural frequency, ω_t, the phase lag is 90°. This condition is referred to as the *phase resonance* condition of the rotor. The peak unbalance response for the rotor, however, occurs at a slightly higher spin-speed of $\omega_t/\left(1-2\zeta_e^2\right)^{1/2}$. This condition is referred to as the *amplitude resonance* condition of the rotor. For small values of damping, the difference between the two conditions is negligible in a practical sense.

Several configurations of the steady response are also shown in Fig. 13. These configurations display the location of the disk geometric center o and mass center c for the cases associated when with the shaft spin-speed is less than, equal to, and greater than the undamped natural frequency ω_t. The geometric center lags the excitation associated with the mass center c as the result of a transverse viscous damping force that is opposite in direction to the motion of the rotor geometric center. This phase lag ranges from near zero at low spin-speeds to 90° (the phase resonance) when the spin-speed equals the undamped natural frequency, to nearly 180° at very high spin-speeds.

Inspection of Eqs. (10) and (11) and the associated response plots in Fig. 12 reveal that the radial position of the mass center c approaches zero as the spin-speed approaches infinity. Thus, the rotor tends to spin about its mass center at high spin-speeds, and the geometric center o then approaches a circular orbit with amplitude equal to the mass eccentricity, e, of the disk.

Damped Free Response—External Damping Only. It is instructive to initially consider the situation when only external damping is present. For this case, the homogeneous form of the rotor equations of motion relative to (x, y, z), Eq. (9), reduces to

$$\begin{bmatrix} m & 0 \\ 0 & m \end{bmatrix} \begin{Bmatrix} \ddot{u} \\ \ddot{v} \end{Bmatrix} + \begin{bmatrix} c_e & 0 \\ 0 & c_e \end{bmatrix} \begin{Bmatrix} \dot{u} \\ \dot{v} \end{Bmatrix} + \begin{bmatrix} k & 0 \\ 0 & k \end{bmatrix} \begin{Bmatrix} u \\ v \end{Bmatrix} = \begin{Bmatrix} 0 \\ 0 \end{Bmatrix} \tag{12}$$

For lightly (under) damped systems, i.e., $0 < \zeta_e < 1$, the solutions from Eq. (12), for an arbitrary set of initial conditions,

$$\begin{aligned} u(0) &= u_o \\ v(0) &= v_o \end{aligned} \quad \text{and} \quad \begin{aligned} \dot{u}(0) &= \dot{u}_o \\ \dot{v}(0) &= \dot{v}_o \end{aligned} \tag{13}$$

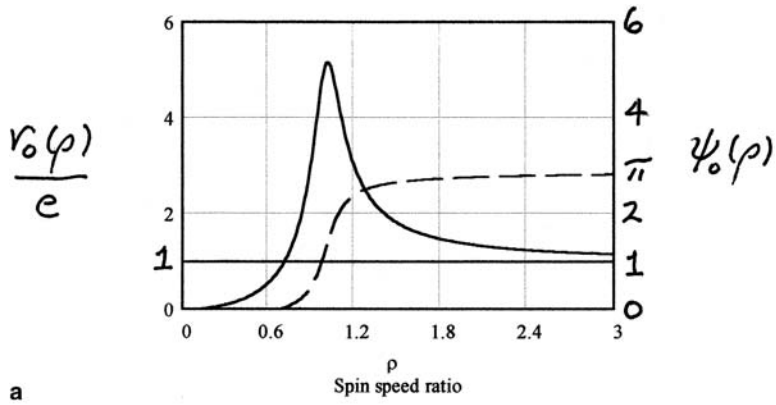

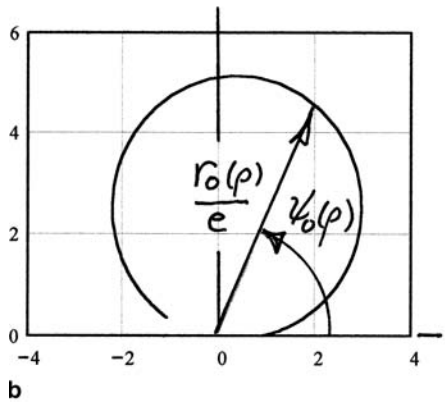

Figure 12 Laval–Jeffcott rotor damped unbalance response. (a) Bode plot, (b) polar plot.

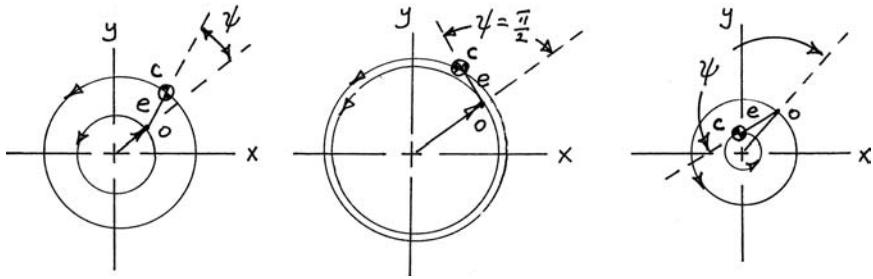

Figure 13 Response configurations. (a) $\Omega < \omega_t$, (b) $\Omega = \omega_t$, (c) $\Omega > \omega_t$.

are

$$u(t) = e^{-\zeta_e \omega_t t}\left(u_o \cos \overline{\omega}_t t + \frac{\dot{u}_o + \zeta_e \omega_t u_o}{\overline{\omega}_t} \sin \overline{\omega}_t t\right) \tag{14a}$$

$$v(t) = e^{-\zeta_e \omega_t t}\left(v_o \cos \overline{\omega}_t t + \frac{\dot{v}_o + \zeta_e \omega_t v_o}{\overline{\omega}_t} \sin \overline{\omega}_t t\right) \tag{14b}$$

The frequency $\overline{\omega}_t = \omega_t(1 - \zeta_e^2)$ is the damped natural frequency of vibration of the disk relative to the fixed (x, y, z) reference. As the magnitude of external damping increases, the damped natural frequency decreases in magnitude from ω_t to zero when the external damping equals the critical damping value of $(c_e)_{cr} = 2\sqrt{km}$, i.e., $\zeta_e = 1$. When the external damping is zero, Eqs. (14) reduce to the undamped solution provided by Eqs. (8).

The free-vibration response is an exponentially damped harmonic motion with the same damped natural frequency $\overline{\omega}_t$ in both the x- and y-directions of motion. A typical free-vibration time response, relative to an observer in (x, y, z), is illustrated in Fig. 14(a). This response may precess either in a forward or backward direction depending on the initial conditions.

For heavily (over) damped systems, i.e., $\zeta_e > 1$, the solution to Eqs. (12) is aperiodic. A typical free-vibration response for this situation is illustrated in Fig. 14(b). Additional information on free vibration of viscously damped systems may be obtained in standard vibration texts such as Dimaragonas [4].

Damped Free Response—External and Internal Damping. The equation of motion, relative to the (x, y, z) reference, for the Laval–Jeffcott rotor including both external and internal viscous damping is given by Eq. (9). A normalized homogeneous form of Eq. (9) is repeated below for quick reference.

$$\begin{bmatrix} 1 & 0 \\ 0 & 1 \end{bmatrix} \begin{Bmatrix} \ddot{u} \\ \ddot{v} \end{Bmatrix} + 2\omega_t \begin{bmatrix} \zeta_e + \zeta_i & 0 \\ 0 & \zeta_e + \zeta_i \end{bmatrix} \begin{Bmatrix} \dot{u} \\ \dot{v} \end{Bmatrix} + \omega_t^2 \begin{bmatrix} 1 & +2\zeta_i\rho \\ -2\zeta_i\rho & 1 \end{bmatrix} \begin{Bmatrix} u \\ v \end{Bmatrix} = \begin{Bmatrix} 0 \\ 0 \end{Bmatrix} \tag{15}$$

Where

$$2\zeta_e\omega_t = c_e/m \qquad 2\zeta_i\omega_t = c_i/m \qquad \text{and} \qquad \omega_t = \sqrt{k_t/m} \tag{16}$$

The dynamic characteristics of a Laval–Jeffcott rotor with external and internal viscous damping are established from the characteristic roots of

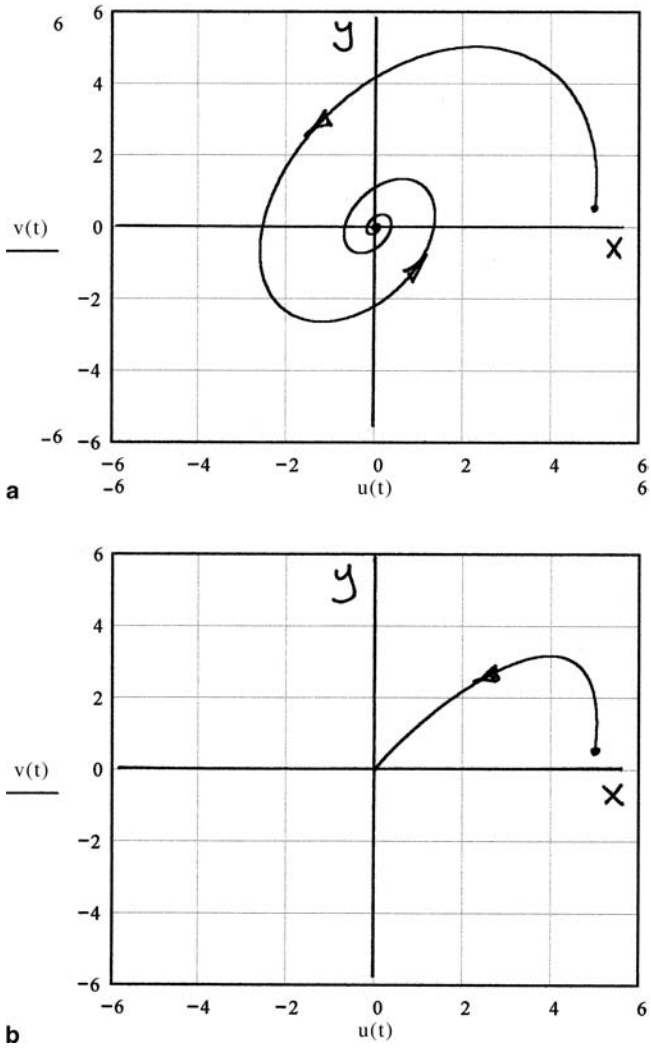

Figure 14 Typical free response: externally damped Laval–Jeffcott rotor. (a) Underdamped response, (b) overdamped response.

Eq. (15). For simplicity of presentation, the details of this analysis are not included here. Tondl [20], Dimaragonas and Paipetis [5], and Loewy and Piarulli [12] include additional information on this topic.

An analysis of the characteristic roots of this linear model reveals that the Laval–Jeffcott rotor is stable (in the linear sense) if the spin-speed, Ω,

satisfies the inequality

$$\Omega < \omega_t \left(1 + \frac{c_e}{c_i}\right) \tag{17}$$

An onset of instability speed, Ω_{oi}, is defined as the value of rotor spin-speed that satisfies the equality associated with Eq. (17), i.e.,

$$\Omega_{oi} = \omega_t \left(1 + \frac{c_e}{c_i}\right) \tag{18}$$

For spin-speeds below the onset of instability, the free-vibration (transient) motion of the rotor is stable. Above the onset of instability, the rotor motion diverges. Of course, as the amplitude increases, nonlinear mechanisms become more significant and the validity of the linear model decreases. If the internal viscous damping coefficient is zero, the spin-speed range of dynamic stability is theoretically infinite. As the level of internal viscous damping increases, the onset of instability speed, Ω_{oi}, decreases toward the undamped natural frequency, ω_t, of the rotor. A whirl speed map for a viscously damped Laval–Jeffcott rotor is shown in Fig. 15.

Simulations of a typical transient rotor response are presented in Fig. 16 for the case when Ω is below the onset of instability speed Ω_{oi} and a second case when Ω is above the onset of instability speed.

Residual Shaft Bow Effects

If a rotor assembly is not straight, it is said to have a *residual shaft bow*. A shaft bow may occur as the result of several situations including assembly imperfections and thermal effects. When a shaft is bowed, a rotating force that is synchronous with the spin-speed is introduced to the system. This force is similar to the rotating force associated with mass unbalance. The difference is that the amplitude of a shaft bow force is constant while the amplitude of an unbalance force changes with the square of the spin-speed. Both, however, have a tendency to produce large-amplitude rotor response in the vicinity of a rotor critical speed. These two effects superpose and may add or subtract depending on the unbalance and bow distributions and the spin-speed. For additional information on this topic, refer to the contributions by Nicholas et al. [15, 16].

The Laval–Jeffcott Rotor: Rotational Motion

This special configuration is identical with the Laval–Jeffcott rotor presented earlier. For the rigid disk located in the center of the shaft, as

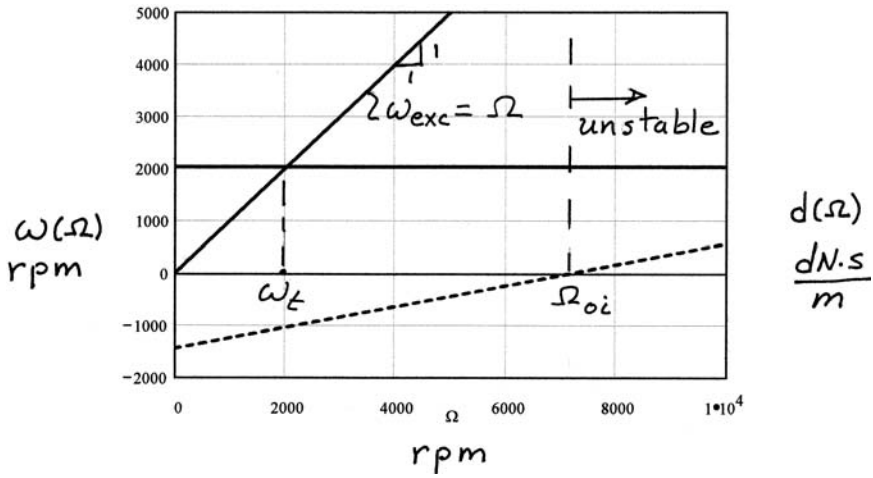

Figure 15 Whirl speed map: viscously damped Laval–Jeffcott rotor.

illustrated in the schematic in Fig. 17, the translational and rotational (also referred to as rotatory) motions are statically and dynamically decoupled. The translational dynamic characteristics of the Laval–Jeffcott rotor were discussed previously in this chapter. The emphasis here is on the rotatory motion defined by the rotation coordinates (α, β) about the (x, y)-axes, respectively. The translational displacements, (u, v), are constrained to zero for this discussion.

Free Vibration

The free undamped rotatory motion, (α, β), for a Laval–Jeffcott rotor configuration is governed by the equation

$$\begin{bmatrix} I_d & 0 \\ 0 & I_d \end{bmatrix} \begin{Bmatrix} \ddot{\alpha} \\ \ddot{\beta} \end{Bmatrix} - \Omega \begin{bmatrix} 0 & -I_p \\ +I_p & 0 \end{bmatrix} \begin{Bmatrix} \dot{\alpha} \\ \dot{\beta} \end{Bmatrix} + \begin{bmatrix} k_r & 0 \\ 0 & k_r \end{bmatrix} \begin{Bmatrix} \alpha \\ \beta \end{Bmatrix} = \begin{Bmatrix} 0 \\ 0 \end{Bmatrix} \tag{19}$$

The rotational shaft-bending stiffness for this disk-centered configuration with simple supports is $k_r = 12EI/L$. The natural frequencies of whirl for this system are dependent on the rotor spin-speed, Ω (i.e., on the gyroscopic

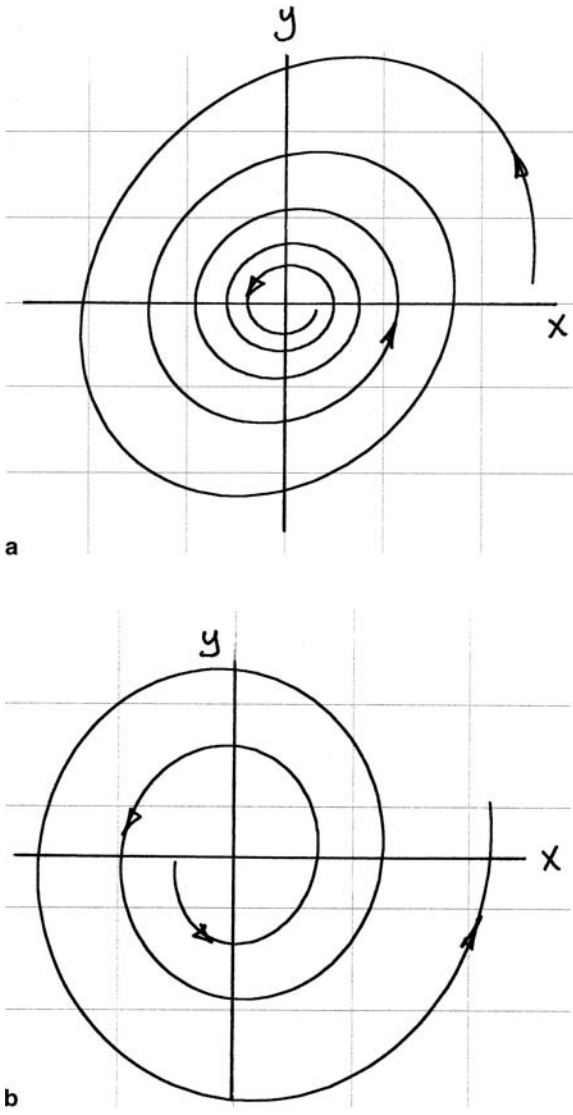

Figure 16 Laval–Jeffcott rotor transient vibration response: with external and internal damping. (a) $\Omega < \Omega_{oi}$, (b) $\Omega > \Omega_{oi}$.

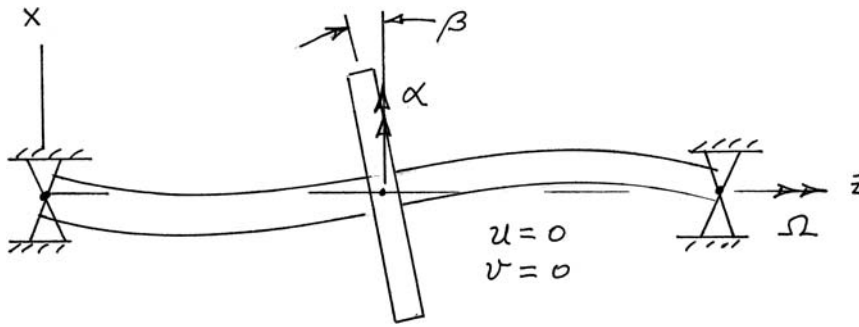

Figure 17 Laval–Jeffcott rotor: rotatory motion.

effects of the disk) and are given by the relations

$$\omega_b(\Omega) = \frac{\Omega I_p}{2I_d} - \sqrt{\left(\frac{\Omega I_p}{2I_d}\right)^2 + \frac{k_r}{I_d}} \tag{20a}$$

$$\omega_f(\Omega) = \frac{\Omega I_p}{2I_d} + \sqrt{\left(\frac{\Omega I_p}{2I_d}\right)^2 + \frac{k_r}{I_d}} \tag{20b}$$

The natural whirl frequency, $\omega_b(\Omega)$, is associated with a backward circular whirl of the rotor system and the frequency, $\omega_f(\Omega)$, is a forward-whirl speed. These undamped natural whirl frequencies are plotted in a whirl speed map, Fig. 18, for the following arbitrary choice of system parameters: $I_d = 0.094\,\text{kg-m}^2$ ($321.2\,\text{lb}_\text{m}\text{-in.}^2$), $k_r = 95.43\,\text{kNm}$ ($844.6\,10^3\,\text{lb}_\text{f}\text{-in.}$) and two different values of the polar mass moment of inertia ($I_p = 0.80I_d$ and $I_p = 1.10I_d$).

The forward synchronous critical speed is associated with an intersection of the forward natural frequency line in Fig. 18 with an excitation frequency equal to the rotor spin-speed, i.e., $\omega_{\text{exc}} = \Omega$. The forward synchronous critical speed is

$$n_f = \sqrt{\frac{k_r}{I_d - I_p}} \tag{21a}$$

Similarly, the backward synchronous critical speed is associated with the intersection of the excitation line with the backward natural frequency line.

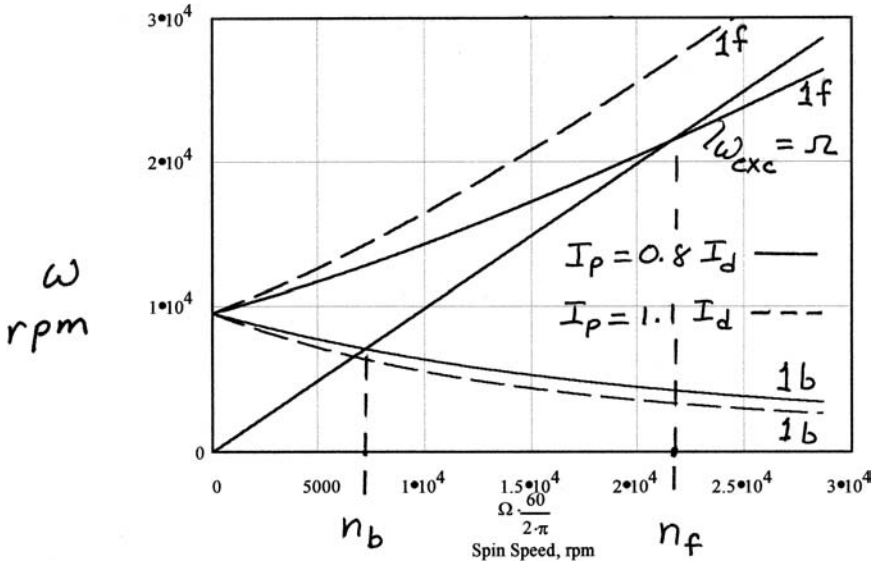

Figure 18 Whirl speed map: Laval–Jeffcott rotor rotatory motion.

The backward synchronous critical speed is

$$n_b = \sqrt{\frac{k_r}{I_d + I_p}} \tag{21b}$$

For the choice when $I_p = 0.80 I_d$, these two critical speeds are $n_f = 21,540$ rpm and $n_b = 7,181$ rpm.

Note that Eq. (21a) is singular when $I_p = I_d$ and that this equation yields an extraneous solution when $I_p > I_d$. When $I_p = I_d$, the disk is said to be "inertially spherical." As illustrated in Fig. 18, when I_p is larger than I_d, an intersection of the synchronous excitation line and the forward natural frequency line does not exist. In general, forward natural whirl speeds increase in value due to a "gyroscopic stiffening" of the shaft as the rotor spin-speed increases, and backward natural whirl speeds decrease due to a "gyroscopic softening." For the special case when $I_p > I_d$, the Laval–Jeffcott rotor system "stiffens" such that the forward natural frequency is always larger than the rotor spin-speed. Thus, a forward critical speed does not exist for this situation. For additional information on the effects of rotatory inertia and gyroscopic moments, refer to the vibrations book by Den Hartog [3].

Disk-Skew Excitation

As was established earlier, a rotating unbalance force provides a spin-speed squared translational force at the connection of the disk to the shaft. A similar excitation exists if the disk happens to be assembled on the shaft such that the disk is skewed, at an angle ε, relative to the shaft as illustrated in Fig. 19.

The "disk-skew" moment vector, associated with the (x, y) rotatory displacement coordinates (β, γ), for this imperfect configuration is given by

$$\Omega^2\left(\begin{Bmatrix} -(I_d - I_p)\sin\varepsilon\cos\varepsilon \\ 0 \end{Bmatrix}\cos\Omega t + \begin{Bmatrix} 0 \\ -(I_d - I_p)\sin\varepsilon\cos\varepsilon \end{Bmatrix}\sin\Omega t\right) \quad (22)$$

Thus, the disk-skew excitation forces are similar to unbalance forces associated with a mass center that does not coincide with the spin axis. The difference is that a disk-skew produces a moment of force at the connection of the disk to the shaft while a mass eccentricity produces a translational force. The steady disk-skew amplitude response, normalized with respect to the skew-angle ε, is shown in Fig. 20 for a Laval–Jeffcott rotor with a positive disk-skew angle. A resonance condition is encountered when the spin-speed equals the first critical speed, $\Omega_f = \omega_r/\sqrt{1 - I_p/I_d}$, where $\omega_r = \sqrt{k_r/I_d}$ represents the disk rotatory natural frequency for a nonspinning shaft. As the spin-speed increases to very high speeds, the gyroscopic stiffening effect of the disk dominates, and the amplitude of the disk angular rotation approaches the disk-skew angle. In effect, the disk spins, without nutating, about its axial principle axis that becomes co-aligned with the bearing centerline.

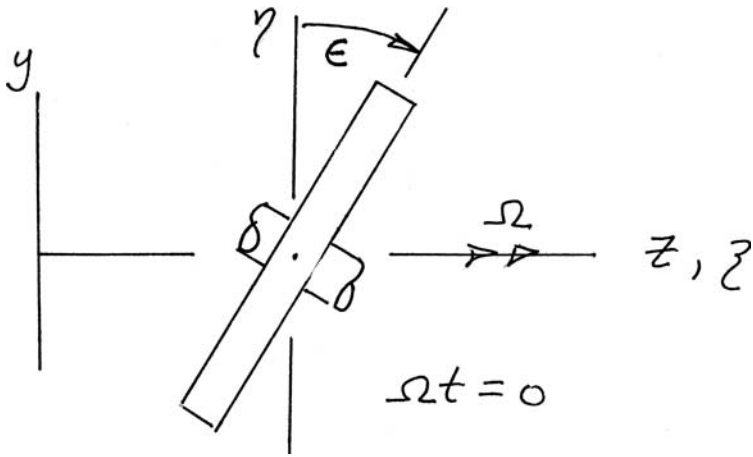

Figure 19 Typical disk-skew configuration.

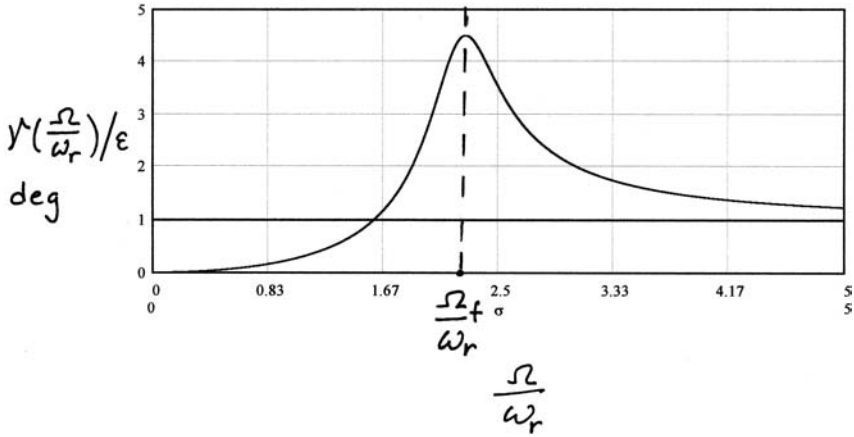

Figure 20 Laval–Jeffcott rotor: steady disk-skew response.

The Laval–Jeffcott Rotor: Coupled Translational and Rotational Motion

In previous sections the decoupled translational and rotational motions of a Laval–Jeffcott rotor configuration were considered. To illustrate a more general situation in rotordynamics, consider a generalized version of the Laval–Jeffcott rotor with the disk located off-center as illustrated by the schematic in Fig. 21. No damping is included in the shaft-disk model for this study. The linear matrix equation of motion for the system is

$$\begin{bmatrix} m & 0 & 0 & 0 \\ 0 & m & 0 & 0 \\ 0 & 0 & I_d & 0 \\ 0 & 0 & 0 & I_d \end{bmatrix} \begin{Bmatrix} \ddot{u} \\ \ddot{v} \\ \ddot{\alpha} \\ \ddot{\beta} \end{Bmatrix} - \Omega \begin{bmatrix} 0 & 0 & 0 & 0 \\ 0 & 0 & 0 & 0 \\ 0 & 0 & 0 & -I_p \\ 0 & 0 & I_p & 0 \end{bmatrix} \begin{Bmatrix} \dot{u} \\ \dot{v} \\ \dot{\alpha} \\ \dot{\beta} \end{Bmatrix}$$
$$+ \frac{EI}{8L^3} \begin{bmatrix} 729 & 0 & 0 & -162L \\ 0 & 729 & 162L & 0 \\ 0 & 162L & 108L^2 & 0 \\ -162L & 0 & 0 & 108L^2 \end{bmatrix} \begin{Bmatrix} u \\ v \\ \alpha \\ \beta \end{Bmatrix}$$
$$= \Omega^2 \begin{Bmatrix} me \\ 0 \\ -(I_d - I_p) \sin \varepsilon \cos \varepsilon \\ 0 \end{Bmatrix} \cos \Omega t + \Omega^2 \begin{Bmatrix} 0 \\ me \\ 0 \\ -(I_d - I_p) \sin \varepsilon \cos \varepsilon \end{Bmatrix} \sin \Omega t \tag{23}$$

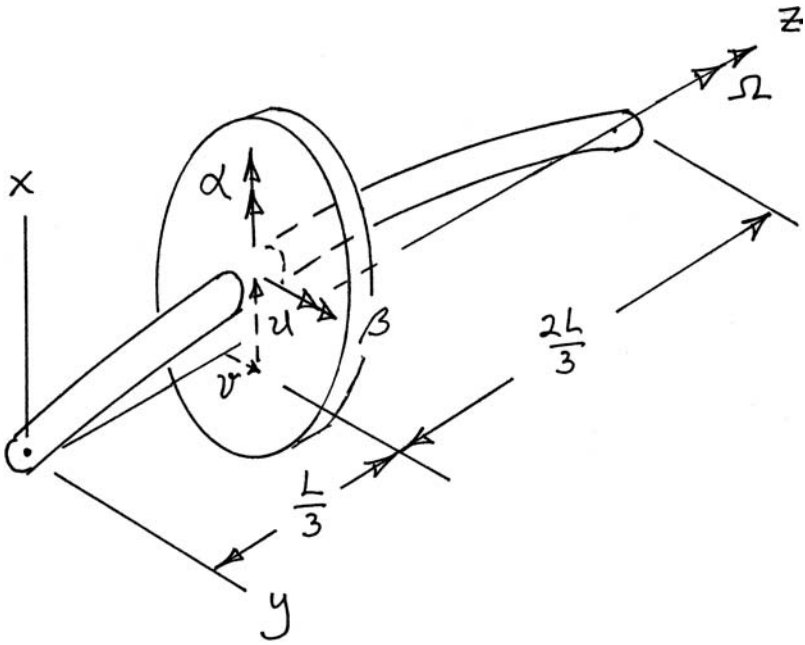

Figure 21 Generalized Laval–Jeffcott rotor.

This system is a 4-degree-of-freedom model with two translations (u, v) and two rotations (β, γ) at the disk center. The translations at both boundary points are constrained to zero. The excitation force for this model includes both rotating unbalance and rotating disk-skew terms.

The four precessional modes are circular with two of the natural modes whirling in the same direction as the rotor spin (forward modes) and two whirling in the opposite direction (backward modes). Typical first forward and second forward mode shapes are illustrated in Fig. 22 for a rotational speed of 3,000 rpm. The backward modes are similar in shape to the forward modes.

The natural frequencies of whirl, and associated modes are a function of the rotor spin-speed, and the system parameters. A typical whirl speed map for this system is illustrated in Fig. 23 for the following selection of parameters: $m = 10\,\text{lb}_\text{m}$ (4.5359 kg), $I_d = 90\,\text{lb}_\text{m}\text{-in.}^2$ (0.0263 kg-m^2), $I_p = 0.5\,I_d$, $E = 30 \cdot 10^6\,\text{lb}_\text{f}/\text{in.}^2$ (206.84 GPa), $r = 0.5$ in. (1.27 cm), and $L = 12$ in. (30.48 cm). The shaft mass is neglected in this example system. The translational and rotational coordinates are statically coupled for this system. As a result, all natural modes of motion are affected by the gyroscopic moments associated with the spinning of the disk.

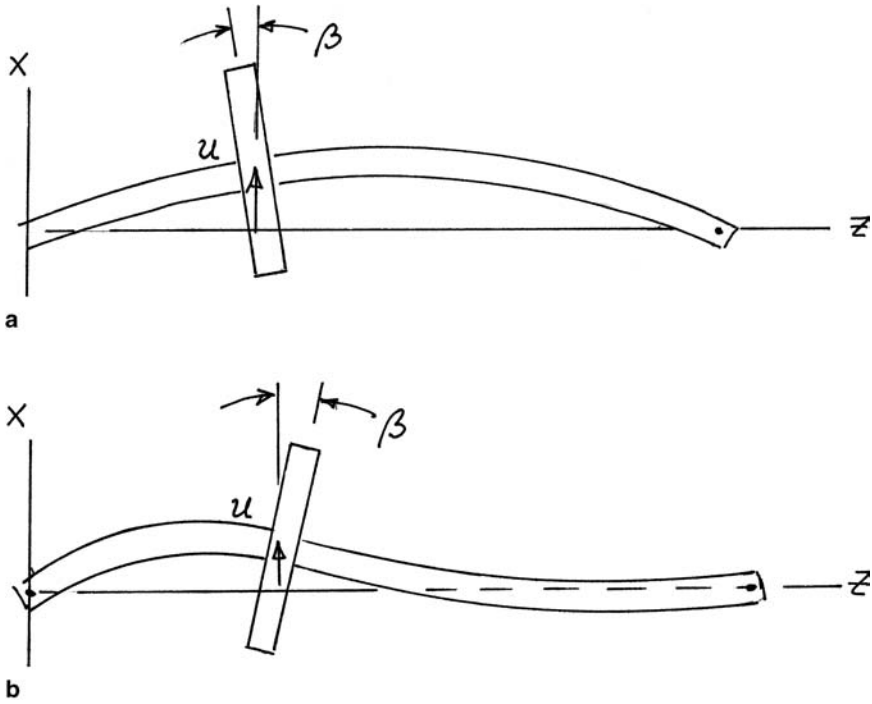

Figure 22 Typical precessional modes: generalized Laval–Jeffcott rotor. (a) First forward mode, (b) second forward mode.

Disk Flexibility Effects

Rotordynamics analyst should carefully evaluate whether disk flexibility may significantly influence the lateral dynamics of a rotating assembly. A flexible disk or bladed disk assembly is usually cyclosymmetric. These flexible disks have a large number of natural frequencies consisting of "umbrella-type" modes that have only circular nodal lines, and "diametral-type" modes where diametral and circular nodal lines may exist. Examples of these types of modes are illustrated in Fig. 24.

The umbrella-type modes are coupled only with the axial motion of the rotating assembly. Since axial motion is usually of minor importance for rotordynamics systems, these modes are generally not of concern. All of the remaining modes, those with diametral nodal lines, are self-equilibrating with the exception of modes with a single nodal diameter such as illustrated in Fig. 24(b). The term "self-equilibrating" implies that the summations of

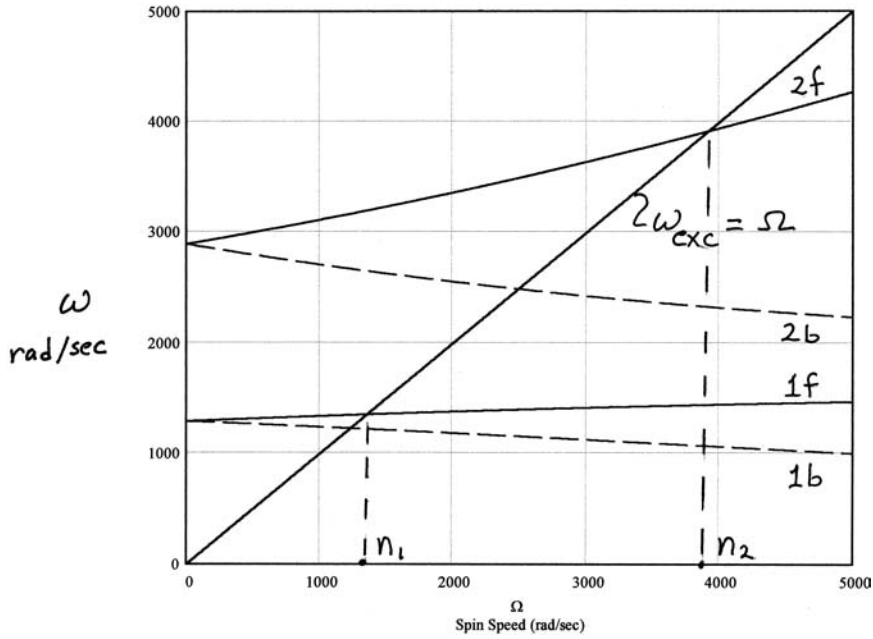

Figure 23 Whirl speed map: generalized Laval–Jeffcott rotor.

all distributed interaction forces and moments, at the shaft-disk interface, are zero.

A relatively simple procedure for including the first diametral mode in a disk model is to consider the disk to consist of an inner hub and an outer annulus. The hub and annulus are assumed to be rigidly connected in translation, but are rotationally flexible. By carefully selecting the inertia properties of the hub and annulus and the rotational stiffness between the hub and annulus, it is possible to develop a model that closely approximates the frequency response characteristics of a flexible disk in the neighborhood of a first diametral mode natural frequency. A more effective way to study flexible disk effects is to create a detailed finite-element model of the flexible disk appropriately connected to the shaft. Additional information on this topic may be found in references such as Ehrich [6] and Vance [21].

MULTIDISK STRADDLE-MOUNT ROTOR

This example multidisk rotor system is supported at its two endpoints by identical isotropic bearings as illustrated in Fig. 25. The entire rotating

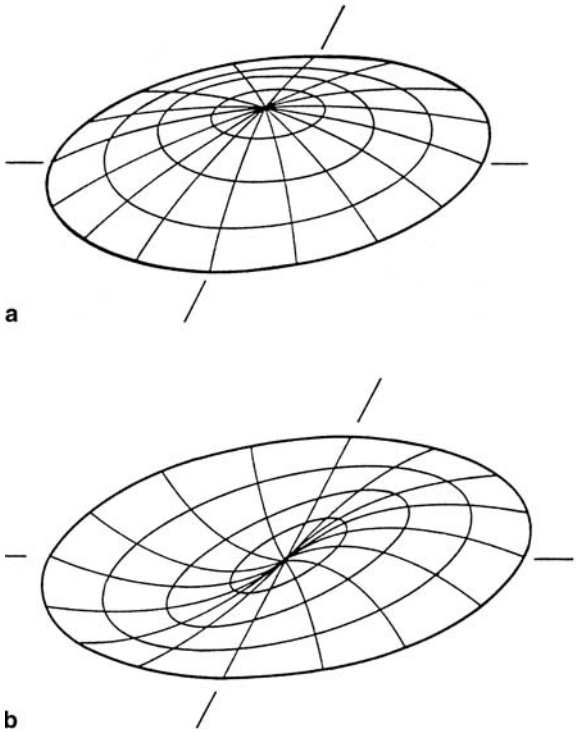

Figure 24 Examples of flexible disk modes. (a) "Umbrella" mode, (b) "diametral" mode.

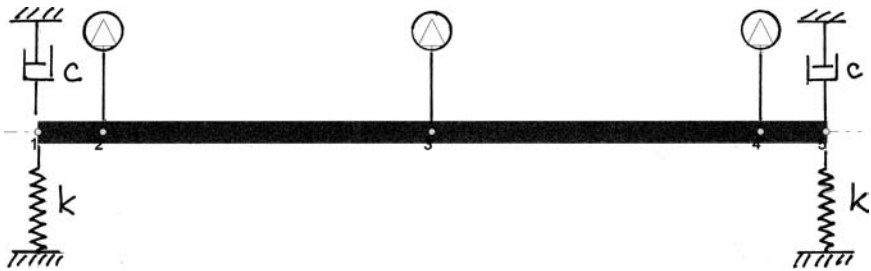

Figure 25 Straddle-mount rotor system.

assembly "straddles" the two bearing supports and is often referred to as a straddle-mount rotor. The rotor consists of a single solid steel shaft [$\rho = 7{,}832\,\text{kg/m}^3$ ($0.283\,\text{lb}_\text{m}/\text{in.}^3$), $E = 200\,\text{GPa}$ ($29 \cdot 10^6\,\text{lb}_\text{f}/\text{in.}^2$), $G = 77\,\text{GPa}$ ($11.17 \cdot 10^6\,\text{lb}_\text{f}/\text{in.}^2$)] of length equal to 30 cm (11.81 in.) and diameter equal to 5 cm (1.97 in.). Three rigid disks of equal size [$m = 3.3\,\text{kg}$ ($7.28\,\text{lb}_\text{m}$), $I_d = 0.006\,\text{kg-m}^2$ ($20.50\,\text{lb}_\text{m}\text{-in.}^2$), $I_p = 0.011\,\text{kg-m}^2$ ($37.59\,\text{lb}_\text{m}\text{-in.}^2$)] are attached to the shaft—one nominally at each end and one at the center of the shaft. The isotropic bearings each have a stiffness $k = 10\,\text{MN/m}$ ($57{,}100\,\text{lb}_\text{f}/\text{in.}$) and viscous damping coefficient $c = 1.0\,\text{kN-s/m}$ ($5.71\,\text{lb}_\text{f}\text{-s}/\text{in.}$).

A graph of the natural frequencies of whirl versus the rotor spin-speed (whirl speed map) is presented in Fig. 26. The first forward and first backward whirl speeds are nearly identical; thus, their values appear essentially as a single line on the graph. These modes are nearly cylindrical (i.e., small rotatory motion of the disks) and, as a result, the gyroscopic effects are negligible, providing essentially constant values for the whirl speeds as the rotor spin-speed changes. The second and third forward and

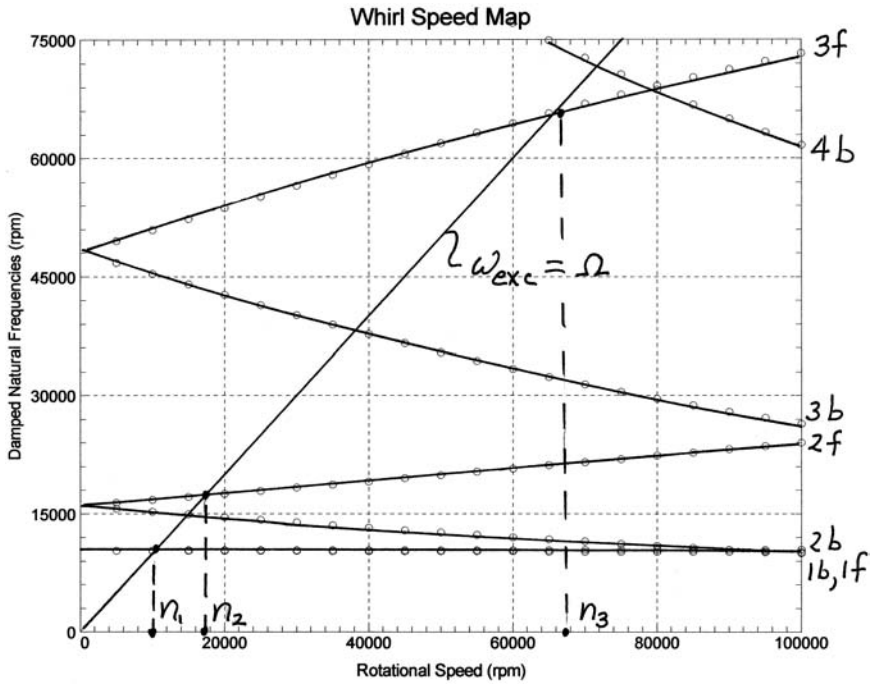

Figure 26 Whirl speed map: straddle-mount rotor.

backward modes, however, involve considerable rotatory motion of the disks such that the gyroscopic moments have a significant influence on the whirl frequencies. The mode shapes for the first three forward modes are shown in Fig. 27 for the case when the spin-speed is equal to 40,000 rpm.

A critical speed map is shown in Fig. 28 for this straddle-mount rotor system for the case when the bearing stiffness (considered to be the same at each support) is treated as a design parameter. The range of bearing stiffness on this graph is $k = 1\,\text{MN/m}$ ($5.71 \cdot 10^3\,\text{lb}_\text{f}/\text{in.}$) to $1\,\text{GN/m}$ ($5.71 \cdot 10^6\,\text{lb}_\text{f}/\text{in.}$). For a bearing stiffness of 1 MN/m, the rotor responds essentially as a rigid rotating assembly supported by flexible bearings, and the first two modes are in effect rigid-body modes. At the opposite extreme of the graph for a bearing stiffness of 1 GN/m, the rotor responds essentially as a flexible rotating assembly supported by bearings of infinite stiffness. The mode shapes for low, intermediate, and stiff bearings are displayed on the critical speed map. If the operating speed range, including design margins, of this rotor system is between 20,000 and 50,000 rpm, the critical speed map indicates that none of the first three forward critical speeds will lie within this range so long as the bearing stiffness is less than approximately 14 MN/m ($7.994 \cdot 10^4\,\text{lb}_\text{f}/\text{in.}$). A critical speed map, as displayed in Fig. 28, is a valuable tool for assisting engineers in evaluating the effect of changing a design parameter, e.g., the bearing stiffness used in this example.

For rotor dynamic systems and particularly for flexible systems, the distribution of any mass unbalance, due to manufacturing imperfections, has a significant effect on the response of the system. As an illustration of this fact, consider the steady-state response of the flexible straddle-mount rotor of Fig. 25 for two different unbalance cases. Case (1): each disk has a mass eccentricity of 100 μm (3.94 mils) at the same angle relative to an

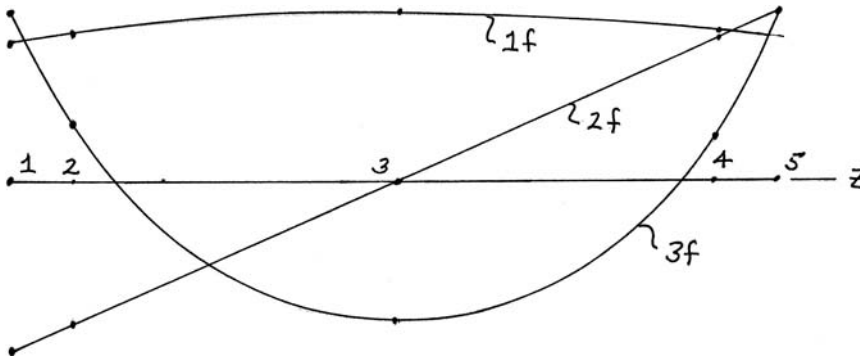

Figure 27 Forward whirl modes: straddle-mount rotor @ 40,000 rpm.

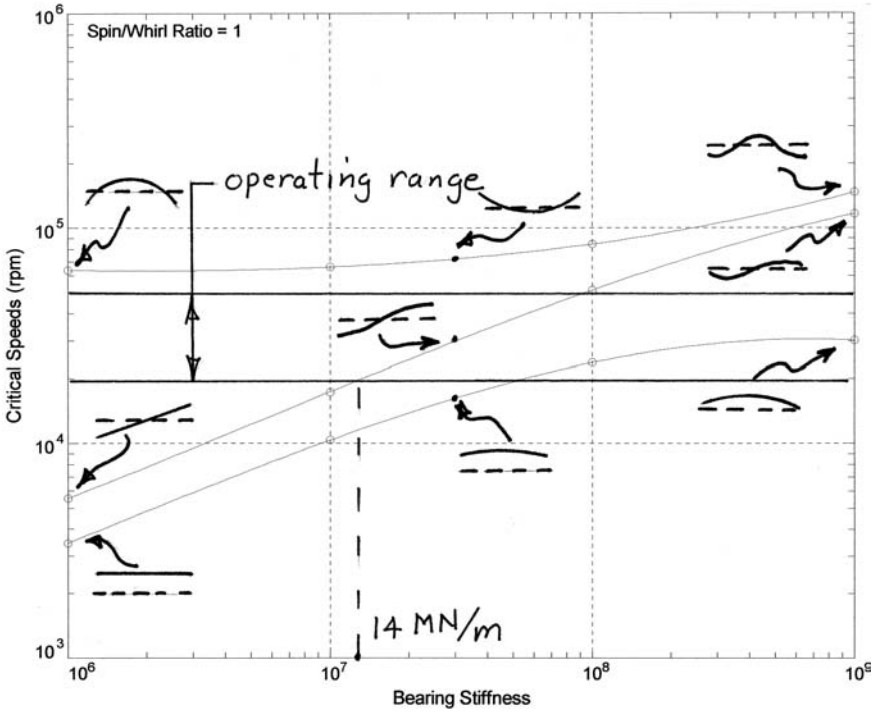

Figure 28 Critical speed map: straddle-mount rotor.

angular reference on the rotor. Case (2): each disk has a mass eccentricity of 100 μm, and the angular location of the unbalance for the station 3 disk is 180° out of phase with the unbalance of the other two disks.

The amplitude of the steady unbalance response for this rotor system is shown in the Bode plot of Fig. 29 for the two unbalance cases defined above. Only the response of the station 2 disk is included in the plot. Since the unbalance distribution is similar in shape to the first rigid-body mode (cylindrical mode) of the rotor, a relatively large "modal" unbalance force exists for this mode and a large unbalance response is noted at the critical speed associated with this mode. A modal unbalance force for the second rigid-body mode (conical mode), however, is zero in this example since the two end disks are out of phase and the amplitude of the center disk is zero. The third forward critical speed has a mode shape that is symmetric such that the symmetric unbalance distribution of Case (1) also provides a plausibly large modal unbalance force. The unbalance plot of Fig. 29 shows that the first and third modes experience relatively large steady-state

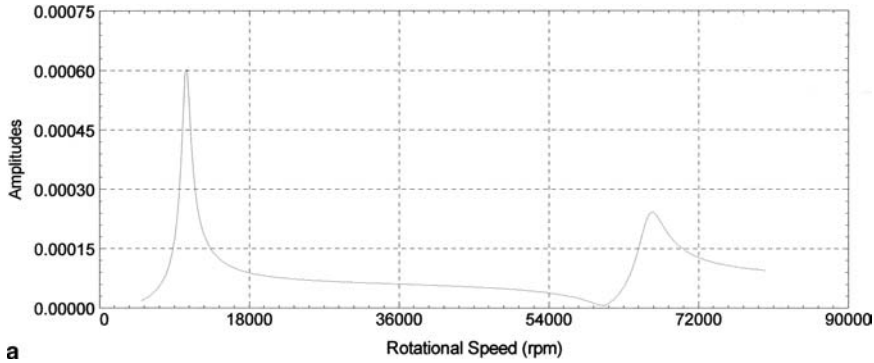

Figure 29 Steady unbalance response: straddle-mount rotor. (a) Case (1) unbalance.

amplitude responses for Case (1) unbalance distribution. The unbalance distribution of Case (2), however, does not provide a significant excitation of either the first mode (cylindrical rigid-body mode) or the second mode (conical rigid-body mode). It does, however, strongly excite the third mode (flexible). This situation is also illustrated by the response shown in Fig. 29. In general, if the unbalance distribution is similar in shape to a forward critical speed mode, the associated modal unbalance force will tend to be high.

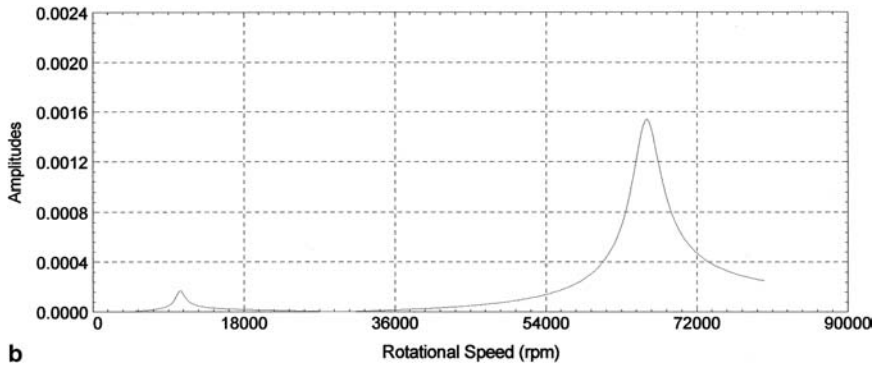

Figure 29 (b) Case (2) unbalance.

LARGE-ORDER FLEXIBLE SYSTEMS

A typical rotor dynamic system consists of a large number of interconnected and interacting components with various structural, thermal, and/or electrical functions. From a structural viewpoint a system includes three primary component groups: a rotating assembly, (or assemblies); a support structure (also referred to as a casing, frame, housing or stator); and a set of interconnection components that provide physical links between a rotating assembly and the support structure or another rotating assembly.

Interconnecting Mechanisms

Typical interconnection components include rolling element bearings, fluid-film (journal) bearings, magnetic bearings (passive and active), fluid-film (squeeze film) dampers, solid dampers, seals, couplings, gearing systems, and a variety of working fluid interactions. A brief description of the forces associated with some of these interconnection mechanisms is provided below. More detailed information may be found in references such as Childs [1], Ehrich [6], and Vance [21].

Rolling Element Bearings

Rolling element bearings are widely used in situations where large loads exist and where impacts due to various shock conditions are prevalent. These bearings exist in a variety of forms, including spherical ball, cylindrical roller, and tapered roller. They may be designed to carry transverse and/or axial thrust loads. The force–deformation relation of these types of bearings is approximately linear under normal operating conditions. General information on determining the stiffness of a rolling element bearing and other design information may be found in references such as Shaw and Macks [18] and Ehrich [6]. More detailed information about specific designs is usually available from the bearing manufacturer. The damping forces in rolling element bearings are quite low, and other damping mechanisms must generally be included in a system design to assist in attenuating high-amplitude response and/or controlling system instabilities.

Fluid-Film Bearings

Fluid-film bearings (journal bearings) have been successfully utilized in rotating machinery for a long period of time. These bearings are capable of generating high fluid pressure and thereby can carry relatively large transverse loads. In addition, they inherently possess the ability to provide large damping forces that can, if suitably located on the rotating assembly,

assist in attenuating high vibration levels in rotating machinery. Since the fluid used in these bearings is often flammable, the bearings are not generally used in extreme-temperature areas of a turbomachine.

Fluid-film bearings have been developed in a number of various configurations with descriptive names such as cylindrical, partial arc, elliptical, axial groove, multilobe, offset cylindrical, and tilting pad, e.g., Ehrich [6]. The interaction forces that these bearings develop between the rotating assembly and nonrotating support structure are nonlinear and are a function of the relative motion (displacement and velocity) between these two structural groups. Tribologists have been quite successful in modeling fluid-film bearing characteristics; detailed information on the modeling, analysis, and computational assumptions and procedures may be found in references such as Childs [1] and Ehrich [6]. For small motion in the neighborhood of a steady operating position of the rotating assembly within the bearing, it is often practical to linearize the bearing force–motion relationship and use these linear forces for rotordynamic performance and design evaluation. In this situation, the typical bearing force, acting on the rotating assembly, may be approximated in a form illustrated by Eq. (24):

$$\begin{Bmatrix} F_x \\ F_y \end{Bmatrix} = -\begin{bmatrix} k_{xx} & k_{xy} \\ k_{yx} & k_{yy} \end{bmatrix} \begin{Bmatrix} v \\ w \end{Bmatrix}_{\text{rel}} - \begin{bmatrix} c_{xx} & c_{xy} \\ c_{yx} & c_{yy} \end{bmatrix} \begin{Bmatrix} \dot{u} \\ \dot{v} \end{Bmatrix}_{\text{rel}} \tag{24}$$

The eight linear bearing coefficients (4—stiffness and 4—damping) are dependent of the bearing properties (fluid viscosity, clearance, radius, length, etc.) and differ depending on the bearing type. They are also strongly dependent on the rotor spin-speed. These forces may tend to stabilize the rotor system response for some spin-speed ranges and may destabilize for other speed ranges. Thus, a designer/analyst must collect as much information as possible about the characteristics of these bearings to successfully design and develop a properly performing machine.

Magnetic Bearings

Magnetic bearings are constructed to levitate the rotating assembly within a bearing enclosure. This condition is accomplished by opposing magnetic forces and may be completely passive or coupled with an active control system. The forces generated by these bearings are typically much lower than for other types of bearings, and this fact limits the areas of application. The main advantage, however, is that there is no mechanical or liquid contact between the rotating assembly and support structure so bearing life is increased substantially and rotating drag is very low. For actively controlled bearings, it is necessary to provide for sensors and other appropriate electronics. This requirement may significantly increase the

system weight and/or space requirements. There are generally quite severe temperature constraints on the placement of these bearings due to possible destruction of the properties of the magnetic material and electronic components. The improvement of these bearings is continuing at a rapid pace, and they are a highly desirable option for certain applications.

Fluid-Film Dampers

Fluid-film dampers (also called squeeze film dampers) have been successfully utilized for a relatively long time as a means of providing vibrational energy dissipation in rotating machinery. They are often used in conjunction with rolling element bearings that typically possess low damping characteristics. A fluid-film damper is similar to a fluid-film bearing except it is constructed so the relative angular velocity between the inner and outer surfaces of the damper are constrained to zero or at least to a low rate. A schematic of a series-connected rolling element bearing and a squeeze film damper is shown in Fig. 30. As the center of the rotating assembly moves laterally, the fluid in the damper is "squeezed," providing a large velocity-dependent force. By

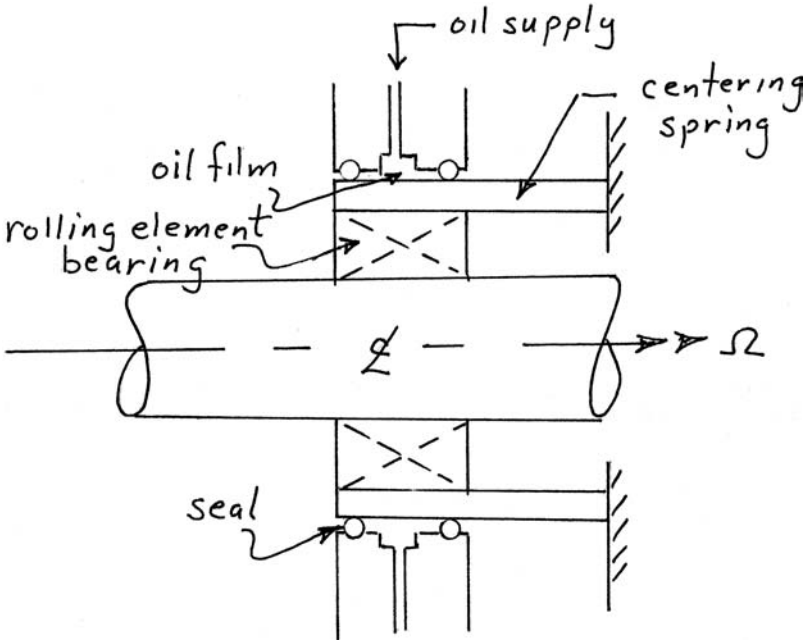

Figure 30 Fluid-film damper schematic.

properly sizing the damper, a highly effective and relatively inexpensive design can be achieved for attenuating vibration levels. The correct sizing of a fluid-film bearing is essential to proper system operation, and improper sizing may lead to serious problems. Additional information on the design of squeeze film dampers may be found in Vance [21].

Solid Dampers

There are a few alternatives to fluid-film dampers—often referred to solid dampers. One of these options is a device that operates in a manner similar to a fluid-film damper except the fluid is replaced by a solid elastomeric material. The viscoelastic properties of this material provide an energy dissipative effect that assists in attenuating the vibration levels in rotating machinery. These dampers possess the advantage of being simple in design, are relatively low in cost, and do not require a fluid with all the associated components required for fluid collection and recirculation. The main disadvantage, however, is that the damping forces generated by the solid damper are relatively low in comparison with those generated by fluid-film dampers. In addition, there are also temperature limitations to protect the elastomeric material from deterioration.

Seals

A seal is a mechanical component designed to minimize the flow of fluid (liquid or gas) from one region of a turbomachine to another. The goal of a design for such a device is to reduce the flow to zero and minimize the absorption of power and any tendency of the forces generated by the device to destabilize the transverse vibrational response of the rotating assembly. Numerous seal configurations have been developed over the years including designs referred to as floating contact, face, and labyrinth seals. The forces that exist between the rotating assembly and support structure for most seals are generally small and do not significantly affect the rotordynamic characteristics of the system. For certain configurations and operating conditions, however, the seal forces may be large enough to be considered in a rotordynamics performance evaluation. The seal in these situations serves not only as a seal to restrict axial-fluid flow, but also as a pseudo-bearing or damper. More detail concerning the properties of seals and their associated forces may be found in Childs [1].

Working Fluid Mechanisms

Fluid of some type (liquid, gas, steam) always flows through a turbomachine usually at high velocities and with complicated flow paths. Interaction forces

between the rotating assembly and the support structure (stator) accompany the flow of the fluid through the turbomachine. Usually, these forces are large enough to significantly impact the rotordynamic characteristics of the system. Examples of these fluid forces are associated with aerodynamic cross coupling, impeller–diffuser interaction, propeller whirl, turbomachinery whirl, and fluid entrapment. Fluid dynamicists have been quite successful in modeling the fluid flow through turbomachinery using computational fluid dynamics and/or empirical techniques and are able to provide a reasonable prediction of the fluid forces. This information can then be used in a structural dynamics design/analysis to predict the rotordynamic characteristics of the machine.

The Rotating Assembly

A rotating assembly for a high-speed rotor dynamic system is a straight axisymmetric structural group. Rotating asymmetries tend to introduce destabilizing conditions that should be avoided in rotor designs, e.g., Tondi [20]. A rotor consists of many possible components, depending on the application, and includes compressor wheels, impellers, turbine disks, and shaft segments (constant or variable cross section). For analysis and design purposes, rotating assemblies are usually approximated by a set of interconnected idealized components that include rigid or flexible disks and rigid or flexible shaft segments. For example, the generalized Laval–Jeffcott rotor system of Fig. 21 and the straddle-mounted rotor system of Fig. 25 include rigid disks and uniform flexible shaft segments. To demonstrate this concept more clearly, a suggested physical model is shown for the rotating assembly of the gas turbine illustrated in Fig. 31.

Rigid Disk

A rigid disk, as used in the generalized Laval–Jeffcott rotor system of Fig. 21, is a four-degree-of-freedom component whose position is defined by two transverse translational displacements (u,v) and two small-order transverse rotational displacements (β,γ) as illustrated in Fig. 21 and also in Fig. 32(a). The properties of the disk are defined by its mass, mass center location (cgx), diametral moment of inertia, and polar moment of inertia. The disk is referred to as "thin" if the axial extent of the disk, at the connection point, is negligible compared to the overall length of the rotating assembly. If the disk occupies a significant axial space, as part of the rotating assembly, the disk is usually modeled as a thick rigid disk, as illustrated in Fig. 32(b). In this situation, a rigid-body constraint exists

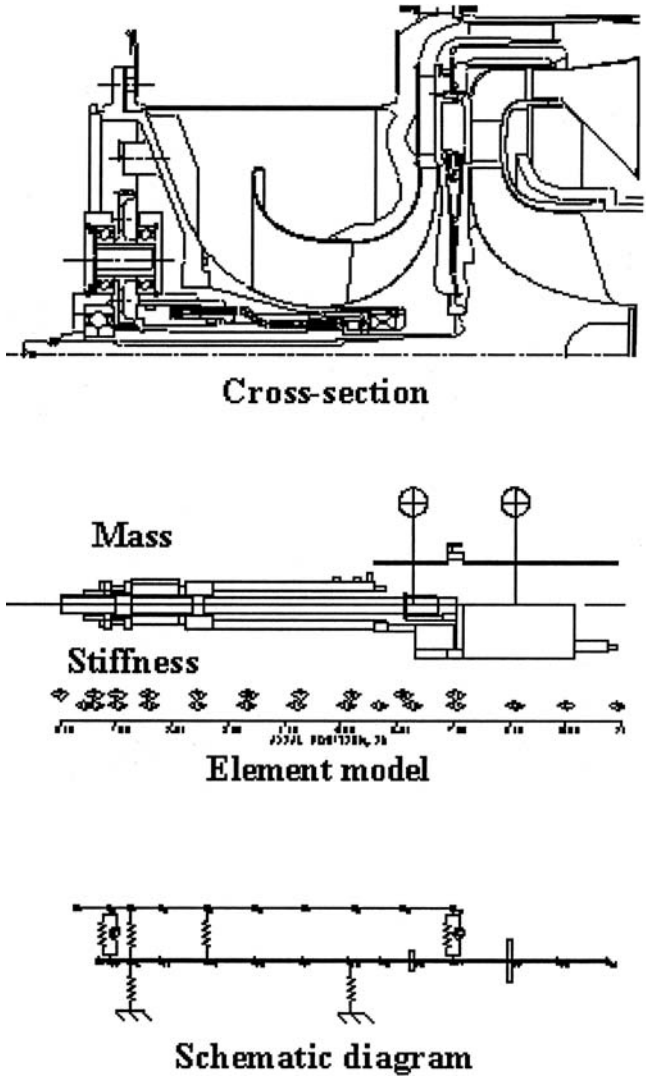

Figure 31 Gas turbine schematic and idealized physical model.

between the motion of the disk center and the ends of the disk. As a result, the disk may still be modeled as a four-degree-of-freedom component.

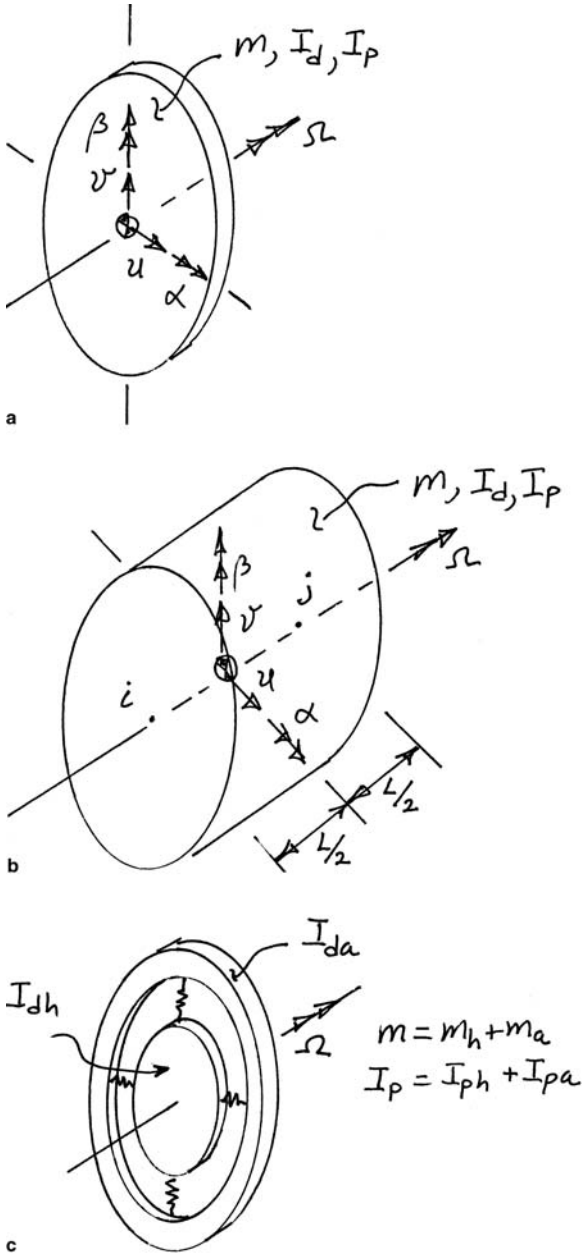

Figure 32 Rigid and flexible disk models. (a) "Thin" disk, (b) "thick" disk, (c) "flexible" disk.

Flexible Disk

If the frequency of a first diametral mode of a "disk component" is within the general operating range of the rotor system, it is probably advisable to investigate the effects of this flexibility on the dynamic characteristics of the overall rotordynamic system. A simple flexible disk model, as illustrated in Fig. 32(c), is often used. This model is a six-degree-of-freedom system whose configuration is defined by two transverse translational displacements (u, v), two transverse rotations (α_h, β_h) of the hub center, and two transverse rotations (α_a, β_a) of the annular ring. The hub and annulus are constrained to equal lateral translations and spin rotation. The dynamic characteristics of this flexible disk model are determined by its mass, diametral and polar moments of inertia of the hub, diametral and polar moments of inertia of the annular ring, and the rotational stiffness between the hub and annular ring. These parameters must be carefully selected to provide realistic frequency response characteristics for the component. As the rotational stiffness is increased, this flexible disk model tends toward a rigid disk component.

If more accuracy is required for a rotordynamic performance evaluation, a reasonable strategy is to develop a detailed finite-element model of the disk component and then couple this model to a model of the rotating assembly at the appropriate connection point. This approach, of course, significantly increases the degrees of freedom of the model but also provides more accuracy to the prediction of system dynamic characteristics.

Rotating Shaft Segments

A uniform rotating shaft segment (finite shaft element) is illustrated in Fig. 33(a). This element is an eight-degree-of-freedom component consisting of two transverse translations and rotations, as shown in Fig. 33(a), at either end of the segment. The equations of motion of this flexible component have been established using standard beam theory and may include the effects of shear deformation, rotatory inertia, gyroscopic moments, and mass unbalance, e.g., Nelson and McVaugh [13] and Nelson [14]. Excitation due to distributed mass unbalance and residual shaft bow may also be included. Finite-element equations have also been developed for conical rotating shaft elements as presented by Rouch and Kao [17] and others.

The cross sections of most shaft segments for complex rotating machinery, however, do not vary continuously as for a uniform or conical segment. Rather, they are typically a complex assemblage of subsegments of different diameters and lengths (i.e., a compound cross-section element) as illustrated in Fig. 33(b). The equations of motion for a rotating shaft segment of this type can be established by assembling the equations of

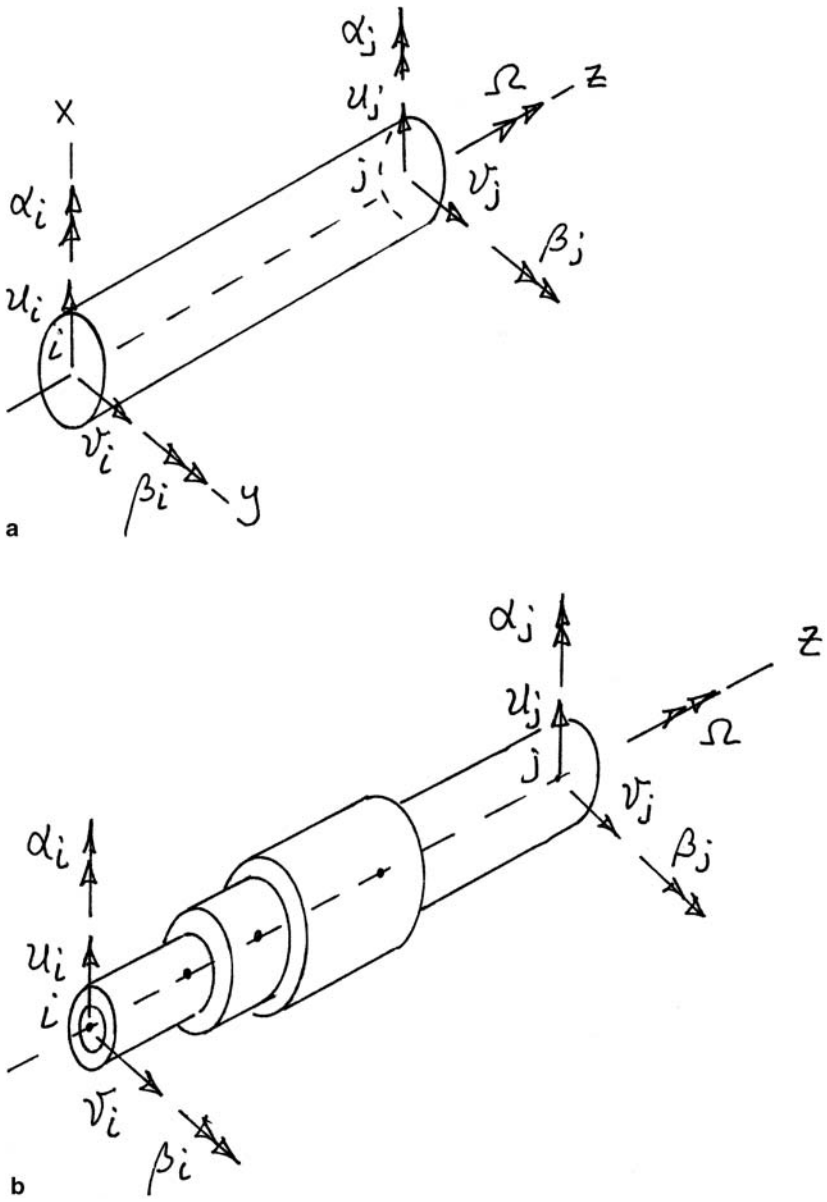

Figure 33 Rotating shaft elements. (a) Uniform shaft element, (b) compound cross-section element.

motion for each subsegment to form a "super-shaft element." These equations can then be condensed to establish an equivalent eight-degree-of-freedom model, as illustrated in Ehrich [6].

The Support Structure

The support structure (casing, housing, frame, stator, foundation) for a rotor dynamic system is typically a complex structural assemblage of many components each with a specific function (thermodynamic, electrical, structural, etc.) in the overall design. The schematic of a gas turbine engine shown in Fig. 31 illustrates the complexity of these types of machines. The rotating assembly, rolling element bearings, and squeeze film dampers are present, as well as the complex structure that holds the system together and attaches it to the outside environment (e.g., aircraft, ship, oil-drilling rig, etc.).

The overall system performance is quite clearly dependent on the characteristics of the entire system, i.e., rotating assemblies, interconnection components, and the support structure. Quite often, the design of the rotating groups and the placement of bearings, dampers, and other interconnection mechanisms are quite firmly established. The basic design of the support structure is also usually visualized in a preliminary design. All components of a system are clearly candidates for design variation; however, it is frequently easier to modify the static support structure configuration and/or design parameters than to alter the high-speed rotating groups or interconnection components. As a result, it is important for engineers to understand how the dynamics of the support structure affects the overall system dynamics. A thorough knowledge of the support structure dynamic characteristics, as a stand-alone structure, provides useful information to a design engineer in sizing or modifying the support structure to ensure satisfactory overall system performance from a rotordynamics perspective.

Lumped Mass Pedestals

To illustrate the influence of the support structure dynamics on overall rotordynamics performance, consider the system shown in Fig. 34. The rotating assembly and linear bearings are identical with the system presented earlier, Fig. 25, which was used to study the influence of gyroscopic moments on natural frequencies of whirl. This rotating assembly with bearings is supported by a nonrotating annular-shaped pedestal of mass m_p at each bearing location. These pedestals are in turn connected to a rigid base by isotropic springs with stiffness k_p and viscous damping coefficient

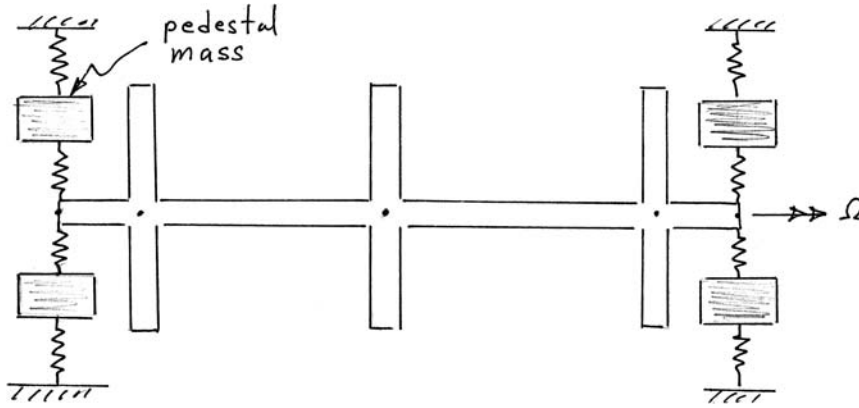

Figure 34 Rotor-bearing-support structure model.

c_p, respectively. This simple modeling scheme (i.e., lumped mass pedestals) is often used by designers/analysts to obtain a "rough sense" of the influence of the support structure frequency response on the rotordynamic performance of the system.

The critical speed map for this system without inclusion of the pedestal mass and stiffness is presented in Fig. 28. For example, with a bearing stiffness of 10 MN/m (5.71 10^4 lb_f/in.), the first three forward critical speeds, as shown on the critical speed map, are 10,358, 17,369, and 65,924 rpm. If the pedestal mass and stiffness are included for each bearing support as illustrated in Fig. 35, these critical speeds may change considerably depending on the natural frequency of the support structure.

For instance, if m_p is chosen as 91.75 kg (202.3 lb_m) and k_p as 367 MN/m ($2.10 \cdot 10^6$ lb_f/in.) the natural frequency of each pedestal, as a stand-alone structure, is approximately 19,098 rpm. This natural frequency is roughly 10% higher than the second forward critical speed of the system with rigid supports. A whirl speed map for this system is shown in Fig. 35. Whenever it is observed that a natural frequency of a rotor-bearing-casing system does not change significantly with rotor spin-speed, it is highly probable that the associated mode is associated with the nonrotating portion of the system.

The inclusion of additional flexibility to the system, by adding the pedestal masses, changes the forward critical speeds of the system to 10,184, 16,515, 19,424, 20,086, and 65,930 rpm. The first two forward critical speeds are lowered in comparison with those associated with a rigid support, and two additional critical speeds enter the operating range of the system. These two new modes are essentially foundation modes with relatively large

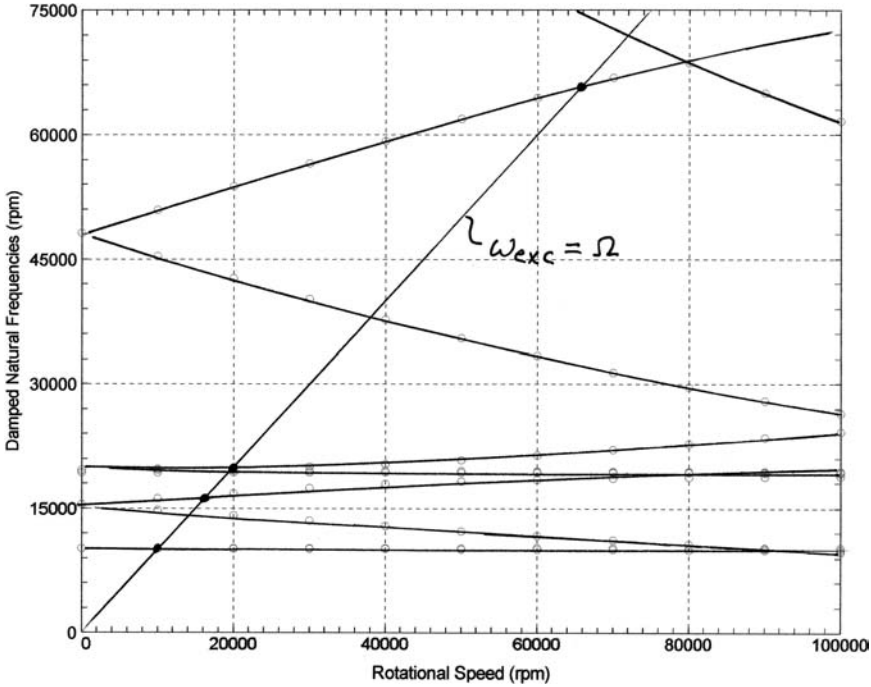

Figure 35 Whirl speed map—straddle-mount rotor with pedestal supports.

motion of the pedestal masses and small motion of the rotating assembly. The fifth critical speed mode primarily involves bending of the rotating assembly and is essentially identical with the third critical speed mode with rigid supports.

If the pedestal stiffness k_p is increased by a factor of 10, so the pedestal natural frequency is increased by $\sqrt{10}$ to 60,393 rpm, the first three forward critical speeds then become 10,345, 17,343, and 60,440 rpm. Thus, this higher-frequency (very stiff) pedestal design approaches the equivalent of a rigid support and the critical speeds are only slightly changed from those with a rigid support.

A foundation model, which includes only lumped pedestal masses at each bearing location, is useful in many situations; however, it possesses serious deficiencies. The pedestal mass only allows for the inclusion of one foundation frequency at each bearing location and does not provide for either static or dynamic coupling between bearing locations. If the true support structure is quite flexible and includes several natural frequencies

within or close to the operating range of the system, a lumped mass pedestal model is probably not advisable.

A slightly better modeling assumption may be to treat the support structure as a nonrotating shell, as illustrated in Fig. 36. This model provides for both static and dynamic coupling between the bearing connection points and also allows for the inclusion of several support structure natural frequencies. A major difficulty, however, exists in that it is difficult to establish appropriate parameters that will provide the desired dynamic characteristics of the foundation. Thus, from a practical perspective, this concept is difficult to implement unless the casing closely approximates a shell-type structure.

Finite-Element Model

Several finite-element-based structural analysis programs are available and provide a rotor dynamicist with the capability of developing detailed models of the static support structure for a rotordynamic system. A schematic of such a system is illustrated in Fig. 37. For example, a system may include n_{ra} degrees-of-freedom for the rotating assembly and n_{ss} degrees of freedom for the support structure. The motion of the rotating assembly and support structure are then coupled by means of various interconnection components (bearings, dampers, seals, fluid–structure interaction mechanisms, etc.) at a

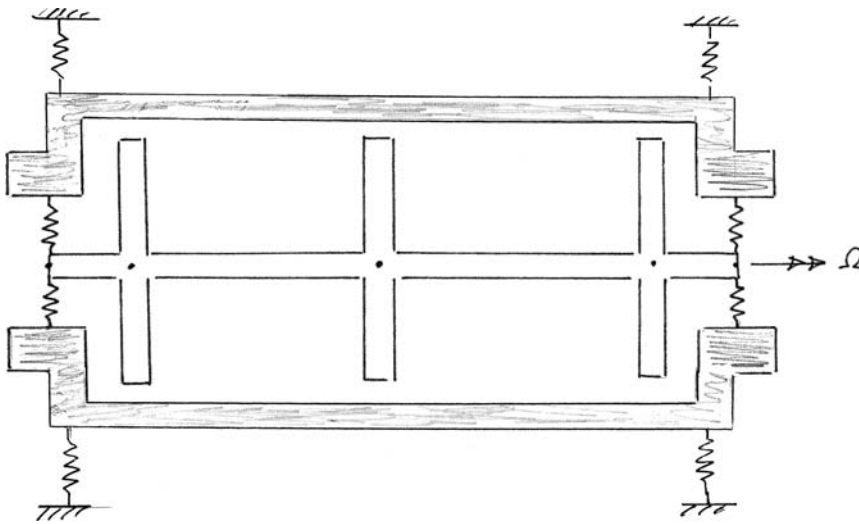

Figure 36 Shell-type support structure model.

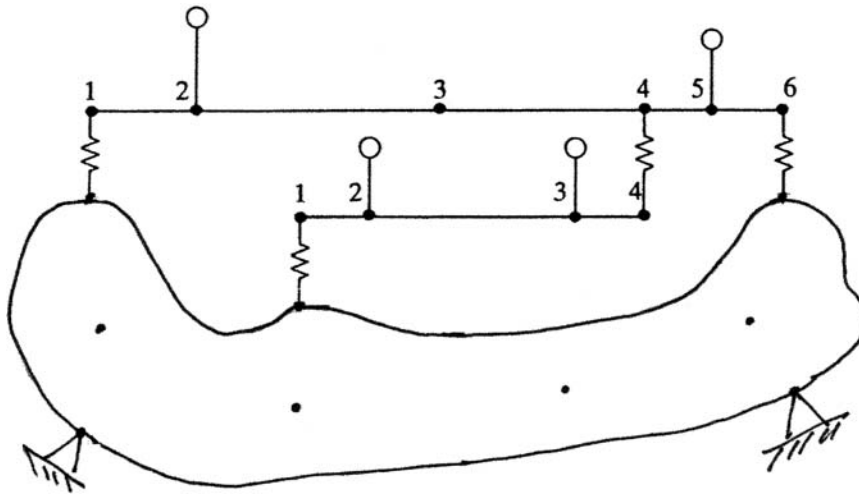

Figure 37 Rotor-bearing-support structure schematic.

finite subset of the rotating assembly and support structure coordinates. Additional details on a procedure for assembling the equations of motion for this type of system are provided in Ehrich [6].

A typical rotating assembly can generally be modeled with sufficient accuracy by using a 5–10 finite-element station (20–40 degrees of freedom) model. A complex support structure finite-element model, however, often requires several hundred degrees of freedom. There are a number of different strategies, however, that can be applied to reduce the order of the support structure model to a much smaller number of so-called retained coordinates. These "retained coordinates" include the coordinates associated with the interconnection components and as many other coordinates as deemed necessary to accurately model the dynamic characteristics of the support structure. These same coordinate reduction procedures may also be used, if desired, to reduce the order of the model for a rotating assembly. By using "engineering judgment," a typical single-rotor dynamic system can generally be modeled with less than 100 degrees of freedom. For instance, the multidisk model displayed in Fig. 35 includes 24 degrees of freedom (20 for the rotating assembly and 2 for each pedestal).

Dynamic Stiffness Representation

The *receptance* (*dynamic flexibility*) frequency response function (FRF), $F_{ij}(\omega)$, of a structure is defined as the harmonic response (amplitude and

phase lag relative to the input) of the ith displacement coordinate of the structure due to a unit amplitude harmonic force associated with the jth coordinate. The complete set of dynamic flexibility FRFs forms the *dynamic flexibility matrix*, $[F_{ss}(\omega)]$, for the structure, and the inverse of this matrix is the *dynamic stiffness matrix*, $[S_{ss}(\omega)]$, for the structure. A typical *dynamic stiffness* FRF, $S_{ij}(\omega)$, may be interpreted as the ith harmonic force associated with a unit amplitude harmonic displacement of the jth coordinate with all other coordinates constrained to zero.

The dynamic flexibility matrix for a support structure may be established experimentally using modal testing techniques, e.g., Ewins [7], or analytically from a finite-element model of the support structure. Typically, only the support structure coordinates that dynamic flexibility modeling of the support structure. The dynamic stiffness matrices for the rotating assembly(s), $[S_{ra}(\omega)]$, and interconnecting components, $[S_{ic}(\omega)]$, may be determined analytically from their respective governing equations. The dynamic stiffness matrix for the system is then assembled and appears typically in the form shown in Eq. (25). It is mathematically convenient to express this type of equation in complex form. The coordinates linked with the interconnecting components constitute a subset of both the rotating assembly and support structure components, i.e., $\{q_{ra}(\omega)\}$ and $\{q_{ss}(\omega)\}$, respectively. Thus, the interconnection components are not separately identified in Eq. (25). For additional information on rotor-foundation effects and analysis, see Gasch [9, 10].

$$\begin{bmatrix} S_{ra}(\omega) & & \\ & S_{ic}(\omega) & \\ & & S_{ss}(\omega) \end{bmatrix} \begin{Bmatrix} \{q_{ra}(\omega)\} \\ \{q_{ra}(\omega)\} \end{Bmatrix} = \begin{Bmatrix} \{F_{ra}(\omega)\} \\ \{0\} \end{Bmatrix} \tag{25}$$

The harmonic force vector, $\{\mathbf{F}_{ra}(\omega)\}$, is typically the steady rotating assembly unbalance force vector, which is synchronous with the rotor spin-speed. The solution of Eq. (25) for a range of spin-speeds provides coordinate response information as well as the location of the critical speeds for the rotor-bearing-support structure system. When the rotor spins near a support structure natural frequency, the dynamic stiffness of the support structure tends to diminish significantly and the rotating assembly behaves as if it were decoupled from the support structure. A model such as suggested in Eq. (25) provides an analyst with a valuable tool to investigate the effect of the support structure design on the overall system dynamic characteristics. Based on this information, it may be possible to make support structure design changes to improve the overall system performance.

DESIGN STRATEGIES AND PROCEDURES

Rotordynamic system response presents the following concerns: generated noise, rotor deflection at close clearance components (e.g., seals, rotor-to-structure rubs and rotor-to-rotor rubs), lateral bearing loads, and support structure loads. All of these are concerns associated with the overall goal of minimizing the response of a rotor-bearing system for both synchronous and nonsynchronous whirl. The largest responses usually occur when a forcing function acting on the system, e.g., mass unbalance, excites a natural frequency with its inherent dynamic magnification. Strategies for designing rotor-bearing systems with acceptable rotordynamic response characteristics thus focus on the critical speeds and associated mode shapes.

For most rotor systems the preferred design sequence to minimize dynamic response is

1. Size the system, whenever possible, so the natural frequencies are outside the machine's operating range.
2. Introduce damping if design constraints place natural frequencies within the operating range.
3. Reduce the excitation levels acting on the system.

Designing the system so the natural frequencies are outside the operating range is an obvious benefit to improving rotor dynamic response characteristics. This strategy, however, can place severe constraints on the key design parameters perhaps requiring unrealistically stiff bearings and/or support structure, large shaft diameters, short bearing spans, etc. Larger shaft diameters naturally lead to larger diameter bearings, seals, compressors, and turbines. These larger components then limit the maximum allowable speed for overall system durability. The introduction of damping to minimize response near a system natural frequency is typically accomplished using an oil film between a bearing outer ring and the support structure. These "squeeze film dampers" can be quite effective in adding the beneficial external damping to the rotor provided that the excitation does not drive the oil film beyond its useful linear range. The excitations acting on the system should obviously be minimized (e.g., balancing the individual components) whenever possible even if the natural frequencies are outside the operating range. This method of controlling response, however, typically adds significantly to the manufacturing cost.

Straddle-Mounted Rotor: Disks Inside the Bearings

Consider, as an illustrative example, a straddle-mounted rotor-bearing system: 20.0-in. (50.8-cm) steel shaft with a 0.70-in. (1.78-cm) inner radius

and a 1.00-in. (2.54-cm) outer radius, bearings at 2.0 and 18.0 in. (5.08 and 45.72 cm), a 15.44-lb_m (7.00-kg) disk at 5.0 in. (12.70 cm), and a 23.16-lb_m (10.51-kg) disk at 15.0 in. (38.10 cm). The critical speed map of Fig. 38(a) shows how the first four synchronous whirl speeds change with bearing support stiffness. The corresponding mode shapes are shown in Fig. 38(b) for a bearing support stiffness of 100,000 lb_f/in. (17.51 MN/m). The first two critical speeds are support dominated "rigid-body" modes with most of the strain energy in the bearing supports. These critical speeds are associated with the "cylindrical" and "conical" modes in which the two ends of the rotor whirl in-phase and out-of-phase, respectively. The third and fourth critical speeds are associated with "bending modes" with most of the strain energy in the rotating assembly. The bending modes are not significantly affected by bearing supports stiffness until the stiffness becomes very large. Note that the node points for the "bending modes" coincide with the disks and their associated relatively large inertias. If the design goal for this configuration is to operate below the first critical speed, the bearings must to be very stiff and the maximum spin-speed must be limited to about 20,000 rpm.

Most designs probably do not have a sufficiently large design envelope, i.e., weight and performance freedom, to allow for the placement of the first critical speed above the operating range. A combination of the three design approaches, listed above, is often required to develop a practical design with acceptable rotordynamic response characteristics. A machine will typically need to operate above at least one of the "rigid-body" critical speeds. Ideally the "rigid-body" critical speed(s) will occur below idle, and the critical speed response will be a brief transient condition as the machine is accelerated to either its idle or operating speed.

If the bearings are "hard-mounted" and the rotor operates above the "rigid-body" critical speed(s), large response should be expected as the rotor accelerates through the critical speeds. Assuming that structural damping produces 5% critical damping, the dynamic magnification would be approximately 10 (i.e., $1/2\zeta_e$). This situation may be acceptable if the rotor has sufficient clearance relative to the structure and the bearings have adequate load capacity for the large response as the rotor accelerates through the critical speed(s). However, a preferred design option is to add damping via a squeeze film damper at one or both of the bearings to reduce the response at the critical speed(s).

The unbalance response for the "hard-mounted" and "squeeze film-mounted" configurations may be estimated by assuming a mass eccentricity for the two disks [i.e., 1.0 mils (25.4 μm)] and performing an unbalance response analysis. For the "hard-mounted" configuration, an equivalent viscous damping coefficient ($c = 2\zeta_e k/\omega$) may be calculated based on the

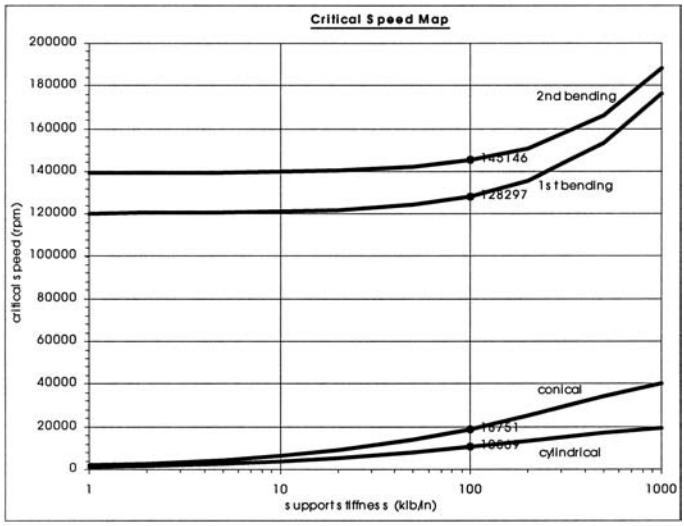

a

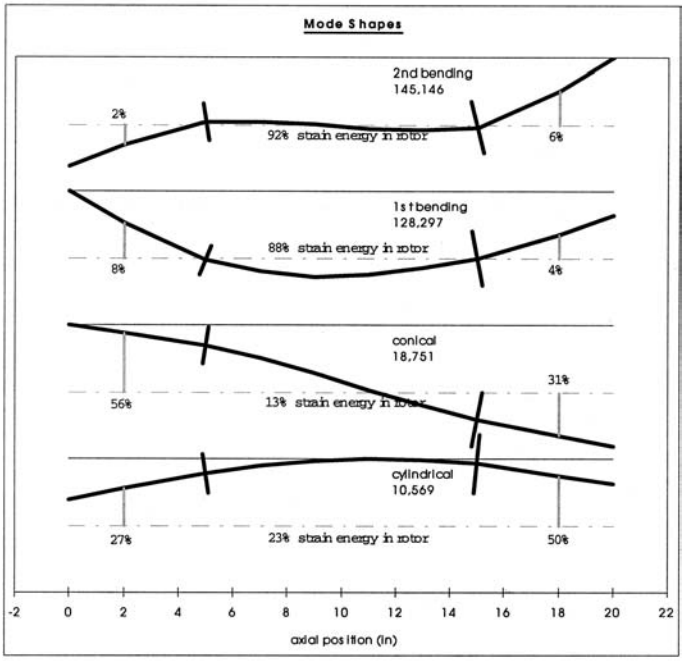

b

Figure 38 Straddle mounted rotor. (a) Critical speed map, (b) mode shapes.

support stiffness and the spin speed. For the "squeeze film-mounted" configuration, the radial stiffness k and transverse viscous damping coefficient c of the squeeze film may be calculated from closed-form equations, e.g., Vance [21], based on short bearing theory and a centered, circular orbit assumption:

$$k = \frac{2RL^3\mu\omega\varepsilon}{C^3(1-\varepsilon^2)^2} \qquad c = \frac{\pi RL^3\mu}{2C^3(1-\varepsilon^2)^{3/2}}$$

Where

R = radius.
L = length.
C = radial clearance.
μ = oil viscosity.
ω = whirl speed.
ε = eccentricity ratio (orbit magnitude/clearance).

Note that both the stiffness and damping coefficients become very large as the eccentricity ratio approaches 1.0.

Figure 39 illustrates typical response characteristics for in-phase and out-of-phase unbalance of the two disks. For the in-phase unbalance and "hard-mounted" bearings, the "cylindrical" mode responds strongly with a dynamic magnification slightly greater than 10 (0.014-in. (356 μm) whirl radius/0.001-in. (25.4 μm) mass eccentricity) while the "conical" mode does not respond significantly. With the out-of-phase unbalance condition, the response is larger at the "conical" mode. The maximum response for a given mode occurs when the unbalance distribution is aligned with the mode shape, thus producing the maximum modal force. Although not shown in this example, the response at the either the third or fourth critical speed could be very large if the unbalance distribution resulted in a significant modal excitation force. The beneficial external damping from the bearing support structure and/or squeeze film dampers would be largely ineffective due to the low percent strain energy at the bearings (see Fig. 38). Figure 39 also illustrates the dramatic reduction in response at both of the "rigid-body" critical speeds with squeeze film dampers at both bearings. Response at the first and second critical speeds is reduced by factors of five and two, respectively. The axial length or radial clearance of the squeeze film dampers could be changed to better balance the response at the critical speeds, recognizing that their stiffness increases linearly with the whirl frequency.

Some high-speed machines have been designed that operate between the first and second bending modes. These types of machines are usually referred to as "supercritical rotors." Since most of the strain energy is in the

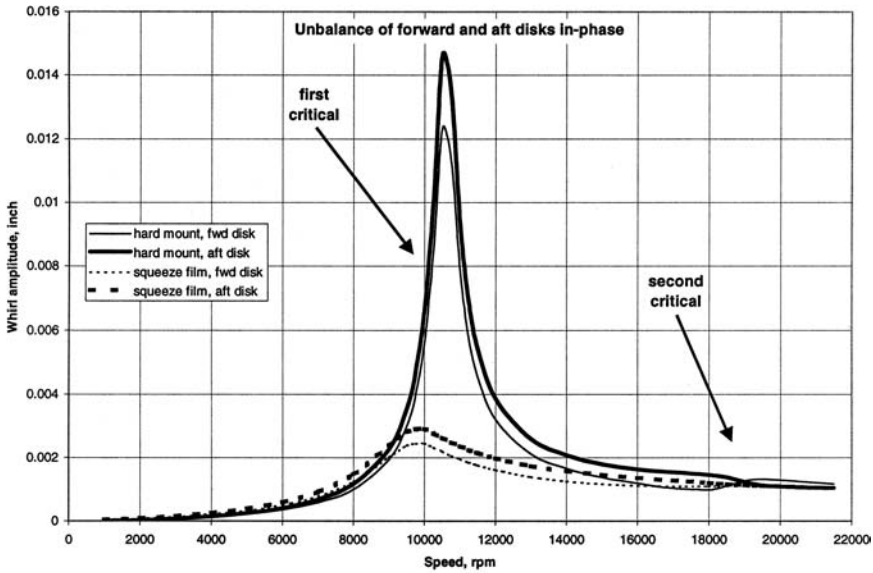

a

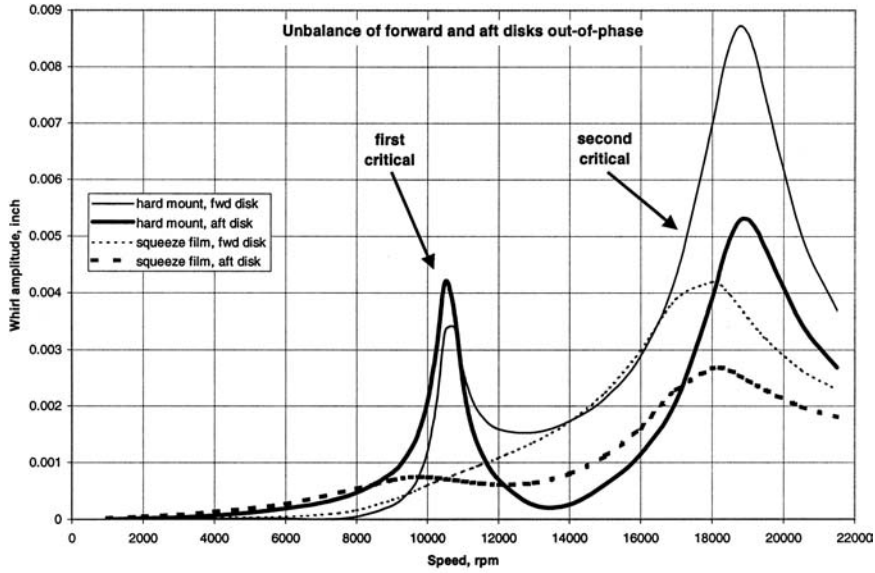

b

Figure 39 Unbalance response: straddle-mounted configuration.

rotating assembly for these modes, the external damping at the bearing supports will be less effective and the response will be significantly larger than at the rigid-body critical speeds. Mass eccentricity limits may need to be reduced and rotor–structure clearances increased in order for a supercritical rotor to be reliable.

Double Overhung Rotor: Disks Outside the Bearings

Next, consider the same rotor-bearing system except with the disks at the ends of the rotor instead of between the bearings. The critical speed map of Fig. 40(a) shows how the first four synchronous whirl speeds change with bearing support stiffness, and the corresponding mode shapes are shown in Fig. 40(b) for a bearing support stiffness of 100,000 lb_f/in. (17.51 MN/m). The critical speed associated with the "cylindrical" mode does not change significantly, but the critical speed associated with the "conical" mode is three times lower than in the "straddle-mounted" configuration. The "cylindrical" mode does not change because it is controlled by the weight of the rotor and the bearing stiffness. The "conical" mode changed because it is controlled by the diametral mass moment of inertia of the rotor assembly (which increased significantly) and the coupled stiffness of the bearing supports.

Note that the node points for the "bending modes" again coincide with the disks and their relatively large inertias. Due to the change in its mode shape, the first bending mode of this configuration is reduced about 67% from that of the "straddle-mounted" configuration. The nodes in the first "bending mode" are located closer to the bearings, thus increasing the percent strain energy in the rotating assembly. "Supercritical" operation through this critical speed would result in increased response compared to that of the original straddle-mounted configuration.

Single Overhung Rotor

Next consider a rotor configuration with both disks overhung at the aft end of the rotor and the aft bearing moved forward 4.0 in. (10.16 cm). The critical speed map of Fig. 41(a) shows how the first four synchronous whirl speeds change with bearing support stiffness. The corresponding mode shapes are shown in Fig. 41(b) for a bearing support stiffness of 100,000 lb_f/in. (17.51 MN/m). The critical speed associated with the "cylindrical" mode is significantly reduced since the aft bearing now effectively supports the inertia of both disks. The critical speed associated with the "conical" mode is roughly the same as in the straddle-mounted configuration because both the diametral mass moment of inertia of the rotor and the coupled stiffness of the

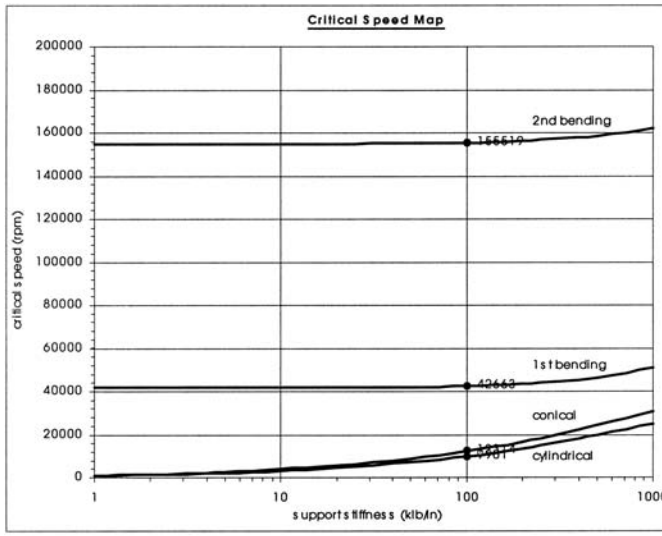

a

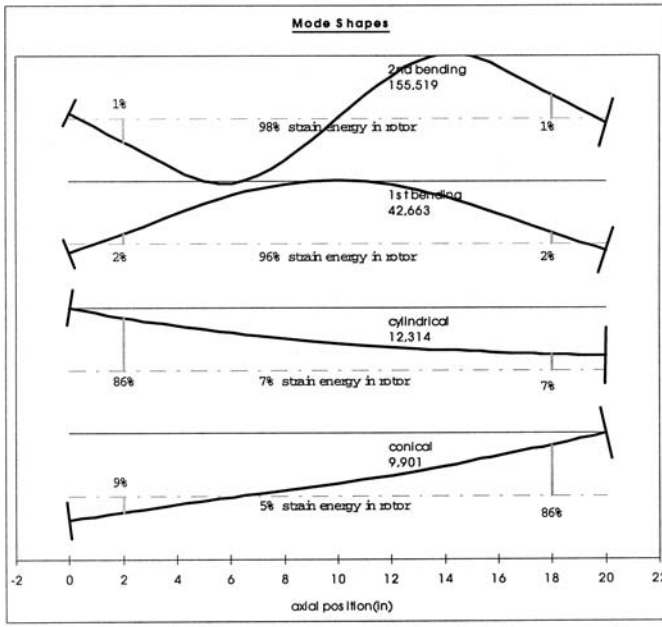

b

Figure 40 Double overhung rotor—disks outside the bearings. (a) Critical speed map, (b) mode shapes.

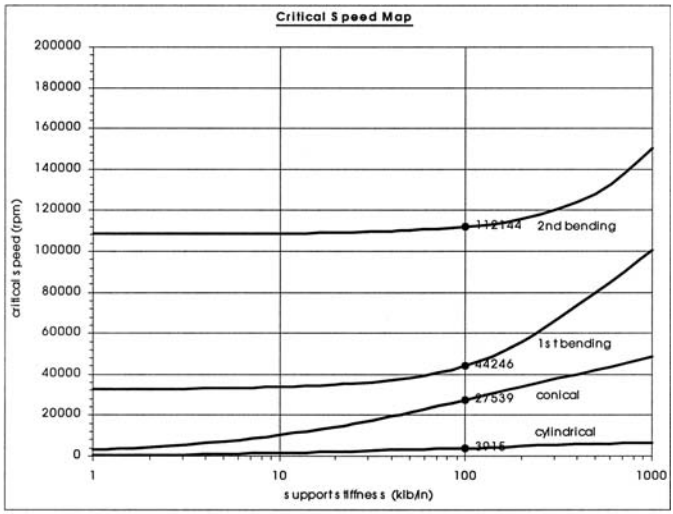

a

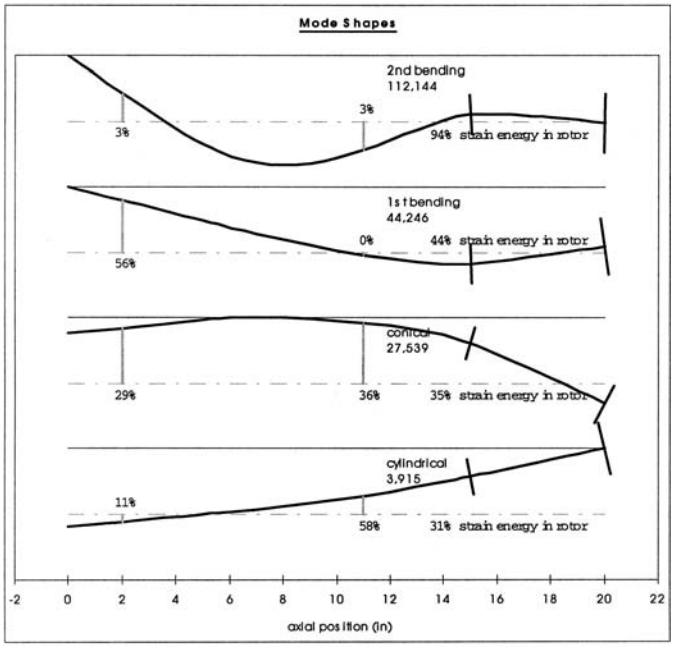

b

Figure 41 Single overhung rotor. (a) Critical speed map, (b) mode shapes.

bearing supports are reduced. The third critical speed is no longer a pure bending mode since the forward bearing possesses a significant percentage of the total strain energy.

A single overhung configuration, as discussed here, has a packaging advantage in that it allows both bearings to reside in a single sump; however, this design configuration presents several rotordynamic challenges. For comparable support stiffness, external damping, and mass eccentricity, overhung disks will have larger response at the "cylindrical" mode than a straddle-mounted configuration. Larger response at the disks increases the probability of encountering nonlinear behavior, possibly resulting in rotor instability. The unbalance response at the "conical" mode will be very sensitive to an out-of-phase unbalance distribution of the disks.

Bearing Mount Considerations

Several factors should be considered if a bearing outer ring is "hard-mounted" to the bearing support structure:

1. The bearing internal clearance must be properly accounted for in any unbalance response calculations by using the secant stiffness of the bearing's nonlinear load-deflection relationship [6].
2. Between rest speed and approximately 50% of the critical speed, the dynamic magnification is small and the bearing load is almost equal to the mass unbalance force ($me\omega^2$).
3. The motion of the bearing support structure will essentially be the same as the rotor whirl at that location.

A soft connection between the rotor and the bearing support structure allows the rotor to whirl about its mass center without imparting that motion to the support structure and case. Reducing the transmissibility via a soft rotor–structure interface, e.g., a squeeze film damper, can thus effectively isolate the structure from the rotor motion.

Blade-Out

Most turbomachinery must be designed to shut down safely in the event of failure/loss of an entire blade. For a propulsion engine, a safe shutdown implies that an engine blade-out unbalance response does not adversely affect the aircraft other than the loss of the engine's thrust. The engine mounts must not fail and damage to the rotating and static components must not result in a fire. To maintain rotordynamic integrity, sufficient axial clamp-load must be maintained on the rotating components to overcome

the large bending moments that tend to separate these components. A good estimate of the blade-out response is required.

The loss of a full blade causes an instantaneous change of the mass eccentricity of that bladed component from its ''balanced condition'' [e.g., 0.5 mils (12.7 μm) *cgx*] to a grossly unbalanced condition [e.g., 250 mils (6.35 mm) *cgx*]. Within a few revolutions the response grows so large that severe rubs occur between the blade tips and their shrouds. Close-clearance seals will also experience severe rubs, and rubs between rotating assemblies in multispool engines may also occur. These rubs act as additional ''bearings,'' and their associated stiffness and damping may significantly change the system critical speeds and associated mode shapes. Figure 42 illustrates the rapid growth in lateral response of a rotor to a blade-out event. Note the rapid (noncommanded) decrease in speed caused by the large amplitude whirl of the rotor.

The large amplitude response during a blade-out event typically bottoms out any squeeze film dampers in the system. The associated high stiffness of a damper under this condition renders its damping ineffective

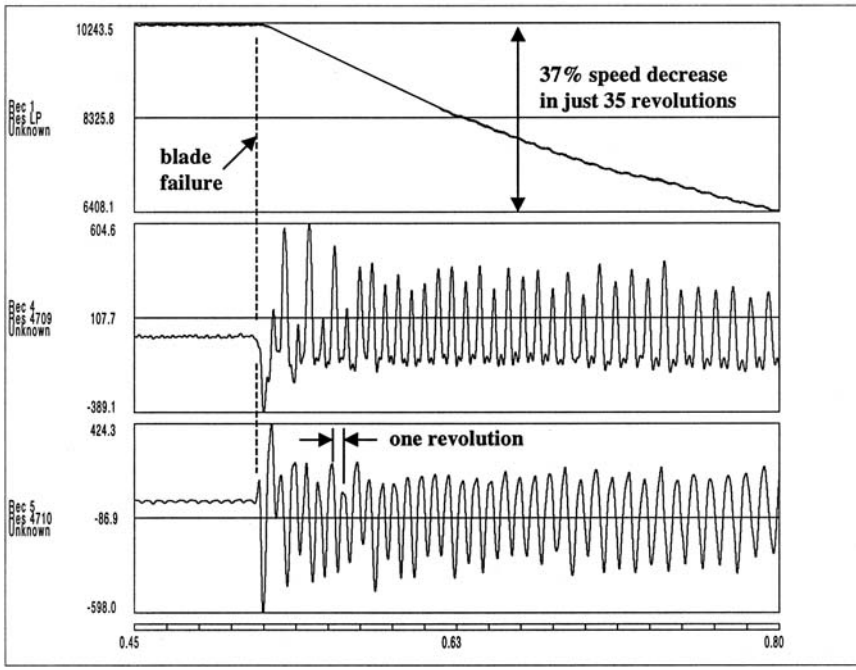

Figure 42 Blade-out response transient.

and also increases the critical speeds to those determined by the bearing support structure. The structural damping (i.e., 5% of critical damping) then determines the magnitude of the unbalance response as the rotor decelerates through its critical speeds.

The large amplitude response and resulting rubs render the system nonlinear. Most blade-out unbalance response analyses are conducted using piecewise linear equivalent springs and dampers at the rub locations. The rub can be modeled as a bilinear spring with zero stiffness until the deflection equals the clearance between the rotating assembly (i.e., the blade tips) and "hard" metal. The stiffness after hard contact is based on the lateral bending and ovalization of the casing. The steady-state response at each spin-speed is determined using an iterative process, continuing until the assumed response at each rub location matches the predicted response within a convergence criterion.

Figure 43 illustrates a typical steady-state blade-out response using the straddle-mounted example with squeeze film dampers presented earlier. Assuming a 0.10-in. (2.54 mm) *cgx* of the aft disk after a blade failure and no rubs, the response at the first critical speed resembles that of the hard-mounted, in-phase unbalance case shown in Fig. 39a except it is over 60 times greater. Due to the large rotor whirl both of the squeeze film dampers

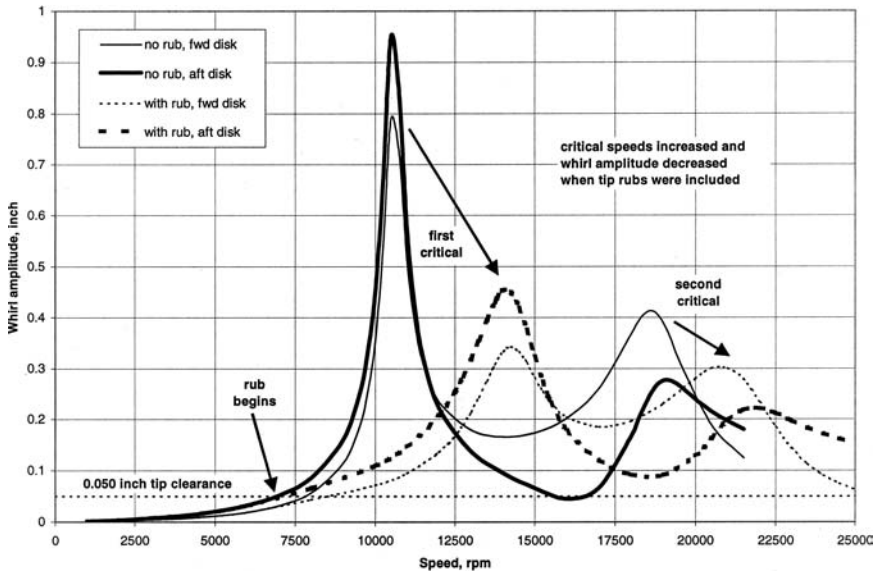

Figure 43 Steady-state blade-out response: straddle-mounted rotor.

have bottomed-out and become very stiff. Rotor–structure rubs can be modeled using a secant value for the stiffness and viscous damping based on this stiffness value and an assumed friction coefficient:

$$K_{\text{rub}} = K_{\text{structure}} \times \left(1 - \frac{\text{clearance}}{\text{deflection}}\right) \qquad \text{and} \qquad C = \frac{\mu K_{\text{rub}}}{\omega}$$

Assuming a $K_{\text{structure}}$ of 100,000 lb_f/in. (17.51 MN/m), a clearance of 0.050 in. (1.27 mm), and a μ of 0.3, the critical speeds increase and their amplitudes decrease due to the additional stiffness and damping at the rub locations. Note that the deviation from the no-rub response curves begins after the response exceeds the assumed tip clearance of 0.050 in. (1.27 mm).

The characteristics described above for blade-out response are for typical configurations with a stiff-bearing support structure and close clearance between the bladed components and shrouds. An alternative approach is to design a "fuse" into the support structure that yields or fractures at a level above normal lateral loads. This type of design prevents large lateral loads on the support structure during blade-out events, thus allowing for a lighter weight structure. If the bearing support structure is designed with sufficient radial clearance and the "fuse" has failed, the rotor will then spin about its post blade-out eccentric mass center without generating large bearing loads. This approach requires equally large clearance between the blade tips and "hard" metal. Thus a thick region of "soft" material must be incorporated into the design of the shroud to prevent large lateral loads between the rotor and case.

Extent of the Rotor-Bearing System Model

The simple models for a rigid rotor on flexible supports or a flexible rotor with pinned–pinned supports will suffice if the rotor-bearing system under study fits their assumptions. The rotor dynamic response of most systems will contain a combination of displacement of the bearing supports and bending of the rotor; thus a detailed finite-element or transfer matrix model is usually required. The rotor dynamic analyst must decide how much of the rotating assembly and static support structure to include in the model.

During the design phase, a flexible rotor model with springs to ground at the bearing locations is usually sufficient to predict the critical speeds. The goal at this stage is to define the basic configuration (disk and bearing axial locations, the required shaft diameters), which will have sufficient critical speed margin. The static structure does not need to be included in the rotordynamics model unless its basic dynamic characteristics will impact the bearing support structure stiffness or result in a coupled mode involving motion of both the rotor and the structure.

Examples of structure modes coupling with a rotor mode include (1) "back-bone bending mode" of the entire engine case, and (2) lateral natural frequency of a bearing support housing. Their natural frequencies should be estimated before making the decision to exclude or include these factors in the rotor dynamics analysis.

BALANCING PROCEDURES

The process of "balancing" a high-speed rotating machine is an inverse engineering problem. The response (amplitude and phase of various system outputs) of the machine may be measured at specific rotor speeds. Based on this measured information, a balance procedure identifies, in some equivalent sense, the unbalance distribution that is present in the rotor assembly(s). A balance correction is then imposed with the intent of effectively canceling the effects of the residual unbalance.

Many different strategies have been developed for balancing, and the specific strategy to be used generally differs depending on the application. Numerous publications discuss this important area of rotordynamics. An excellent source is the book by Darlow [2] that discusses the balancing of high-speed machinery in considerable detail and also provides an important list of references.

NOMENCLATURE

c = viscous damping coefficient.
cgx = center of gravity eccentricity.
C = radial clearance.
d = deci.
$d(\Omega)$ = damping exponent.
$e = cg$ eccentricity in ξ-direction.
EI = bending stiffness.
f, g = elliptic whirl components.
F = force, dynamic flexibility coefficient.
I = mass moment of inertia.
k = stiffness coefficient.
L = length.
m = mass.
n = critical spin-speed, subharmonic order.
q = typical displacement component.
r = radial displacement.

R = radius.
S = dynamic stiffness coefficient.
t = time.
u, v, $w = x$, y, z translational displacements.
x, y, z = fixed reference.

$\alpha, \beta, \gamma = x, y, z$ rotational displacements.
ε = disk-skew angle about η-axis, eccentricity ratio.
μ = viscosity, Coulomb friction coefficient.
ψ = phase lag.
$\dot{\varphi}$ = precession rate.
ρ = multiplier, spin-speed ratio, density.
θ = straight-line orbit angle.
Θ = rigid-body rotation.
ω = whirl frequency.
$\bar{\omega}$ = damped whirl frequency.
Ω = spin-speed.
ξ, η, ζ = body reference.
ζ = damping ratio.

Subscripts

a = annular ring.
b, f = backward, forward.
c, s = cosine, sine.
cr = critical.
d, p = diametral, polar.
da, dh = disk annular ring, disk hub.
e, i = external, internal.
exc = excitation.
h = hub.
ic = interconnecting components.
o = initial value.
p = pedestal.
oi = onset of instability.
ra = rotating assembly.
ss = support structure.
t, r = translational, rotational.
x, y = x-, y-components.

REFERENCES

1. D. Childs, *Turbomachinery Rotordynamics: Phenomena, Modeling, & Analysis*, John Wiley & Sons, New York (1993).
2. M. S. Darlow, *Balancing of High-Speed Machinery*, Springer-Verlag, New York (1989).
3. J. P. Den Hartog, *Mechanical Vibrations*, McGraw-Hill Book Co., New York (1956).
4. A. Dimaragonas, *Vibration for Engineers*, Prentice-Hall, Englewood Cliffs, NJ (1996).
5. A. D. Dimaragonas and S. A. Paipetis, *Analytical Methods in Rotordynamics*, Applied Science Publishers (1983).
6. F. F. Ehrich, *Handbook of Rotordynamics*, McGraw-Hill, New York (1992).
7. D. J. Ewins, *Modal Testing: Theory and Practice*, John Wiley & Sons, Chichester, England (1984).
8. A. Föppl, "Das Problem der Laval'schen Turbinewelle," *Civilingenieur*, *41*: 332–342 (1985).
9. R. Gasch and H. Pfützner, *Rotordynamik-Eine Einführung*, Springer-Verlag, Berlin (1975).
10. R. Gasch, "Vibration of Large Turbo-Rotors in Fluid-Film Bearings on an Elastic Foundation," *J. Sound and Vibration*, *47*(1): 53–73 (1976).
11. H. H. Jeffcott, "Lateral Vibration of Loaded Shafts in the Neighbourhood of a Whirling Speed—The Effect of Want of Balance," *Philosophical Magazine*, *37*:304–314 (1919).
12. R. G. Loewy and V. J. Piarulli, *Dynamics of Rotating Shafts*, SVM-4, Shock and Vibration Information Center, U.S. Department of Defense (1969).
13. H. D. Nelson and J. M. McVaugh, "The Dynamics of Rotor-Bearing Systems Using Finite Elements," *ASME Trans. J. Engineering for Industry*, *98*(2): 593–600 (1976).
14. H. D. Nelson, "A Finite Rotating Shaft Element Using Timoshenko Beam Theory," *ASME Trans. J. Mechanical Design*, *102*: 793–803 (1980).
15. J. C. Nicholas, E. J. Gunter, and P. E. Allaire, "Effect of Residual Shaft Bow on Unbalance Response and Balancing of a Single Mass Flexible Rotor: Part I Unbalance Response," *J. Engineering for Power*, April: 171–181 (1976).
16. J. C. Nicholas, E. J. Gunter, and P. E. Allaire, "Effect of Residual Shaft Bow on Unbalance Response and Balancing of a Single Mass Flexible Rotor: Part II Balancing," *J. Engineering for Power*, April: 182–187 (1976).
17. K. E. Rouch and J. S. Kao, "Tapered Beam Element for Rotor Dynamics," *J. Sound and Vibration*, *66*(1): 1–22 (1979).
18. M. C. Shaw and E. F. Macks, *Analysis and Lubrication of Bearings*, McGraw-Hill, New York (1949).
19. A. Tondl, "Notes on the Identification of Subharmonic Responses of Rotors," *J. Sound and Vibration*, *31*(1): 119–127 (1973).
20. A. Tondl, *Some Problems of Rotor Dynamics*, Chapman and Hall, London (1965).
21. J. M. Vance, *Rotordynamics of Turbomachinery*, John Wiley & Sons, New York (1988).

11

Turbomachines in Rocket Propulsion Systems

David Mohr
D&E Propulsion, Inc., Mims, Florida, U.S.A.

INTRODUCTION

In this chapter, we focus our attention on the application of turbomachinery to use in rocket propulsion systems. Probably no other single area of application has placed such high demands on turbomachinery performance, especially in the last 15–20 years. It is my intention to explore the evolution of turbomachinery systems as well as some of their components beginning approximately in the early 1950s.

This is not a "how to design turbomachinery" chapter. The relevant principles of fluid mechanics, as well as the design considerations involved, are treated very thoroughly in the published literature as well as in other chapters of this book. This treatment is by experts in the field. My intent is for this chapter to bridge a gap that I feel exists between the purely analytical treatments and the "practical experience" side of a relatively exotic field.

This chapter begins with a rather broad historical account of some of the key milestones in the development of rocket turbomachinery. This

section is intended to place today's capabilities (and shortcomings) in a somewhat better perspective. Following this, sections are devoted to each of several key components of rocket turbomachinery systems. Where it is necessary or particularly insightful, various design issues are discussed as they relate to the various rocket engine thermodynamic cycles in existence today or in the recent past. Some cycles may be discussed together in relation to a particular component when the cycles place similar demands or restrictions on component design or performance.

Although this chapter is not intended to function as a design guide, I have found it necessary to make certain assumptions as to the reader's familiarity with the subject. A knowledge of the fundamental concepts of turbomachinery energy exchange will be needed, as well as a grasp of velocity diagrams and their relationship to machinery performance. Topics such as these are not specifically covered, but a certain familiarity with them will make discussions regarding things like design tradeoffs much more intuitive.

It is hoped that this chapter will serve as a starting point for readers (both advanced students and practicing engineers at the BSE level) who wish to efficiently learn some aspect of turbomachinery as it relates to rocket propulsion systems. I attempt to present a collection of my own experiences and the experiences of others as related to me, as well as a collection of the references I have found most helpful.

The development of turbomachinery for use in rocket engines has involved both the government of the United States and large portions of the American industrial base. Examples of firms that are deeply involved include the Aerojet General Corp., Pratt and Whitney Division of United Technologies Corp., Rocketdyne Division of Rockwell International, and the Turbomachinery Division of Sunstrand Corp., to name just a few. With the help of firms such as these, the design, development, and production of turbomachinery have reached quite a high state of refinement. For example, the combined turbomachinery of a cluster of three Space Shuttle main engines (SSMEs) moves nearly 1,600,000 lb of cryogenic propellant through the engines in approximately 510–520 sec. In the process, head rises approaching 200,000 ft are achieved in the engine's fuel systems.

In more than 100 Space Shuttle flights to date, not a single turbomachinery failure has occurred. Similar systems have been in operation on several expendable launch vehicles for nearly 30 years with comparable records of success. As a result of the talent brought to bear on the turbomachinery problem, the record of reliability achieved thus far is truly outstanding. Enormous quantities of propellant have been moved against high pressures by marvelously compact machinery with rarely a failure.

As might be expected, the state of the art has moved rapidly forward, thanks to the intense effort expended by both the government and industry. Particular factors that imposed limitations on the performance of one machine have been systematically addressed during development of the next generation of machinery. As a result, the contemporary design community now finds itself dealing with limitations more fundamental than ever before. These include constraints imposed by material properties, as well as the long-term durability of these materials in turbomachinery service. In the last half-dozen years, the interests of potential customers of rocket engine systems have shifted significantly. Whereas interest was previously on engine ballistic performance and performance-to-weight ratio to the practical exclusion of all else, this is beginning to be tempered by serious interest in satisfactory long-term service as well as minimizing requirements for maintenance between uses of the system. It is probably safe to say that a significant portion of future development effort will be expended in this area.

Finally, a rather disturbing report must be made. At one time, the United States was the undisputed world leader in development of the high-performance turbomachinery common in rocket engine systems. Unfortunately, the lead we once possessed has been badly eroded, and in some cases all but nullified, by other countries. Japan, for instance, is displaying development capabilities disquietingly close to our own. Also, in the areas where they are known to be still behind, they have undertaken fundamental research and development efforts that should bear substantial fruit if carried through to completion. If we are to continue to lead the world in the years ahead, we must be committed to maintaining a high level of effort in this regard on a long-term basis.

This author is grateful for the opportunity to participate with Professor Logan in this book and humbly solicits any comments and/or suggestions on the content of this chapter.

ROCKET PROPULSION SYSTEMS—A SHORT HISTORY

The application of turbomachinery to rocket systems has a long history, which can be both instructive and somewhat entertaining. We explore some of this history (as well as some of its products) in order to put today's capabilities in better perspective.

Most rocket enthusiasts are aware of the experiments Dr. Robert H. Goddard in the 1920s and beyond, and we do not dwell on the details here. However, in the mid-1930s, Dr. Goddard had apparently reached the conclusion that his experiments were pointing out the limitations of

pressure-fed propellant systems. His notes from this time period indicate his belief that a propellant pumping system was going to be necessary if very high altitudes were to be achieved. Accordingly, beginning in October 1938, he began a series of component-level tests of five models of small, high-speed centrifugal pumps. These pumps incorporated features that, at the time, were considered radical. The last problem to be addressed was a source of drive gas for the turbopump turbine. This was handled by a device that Dr. Goddard referred to as a "boiler." Rocket enthusiasts will recognize it as the precursor to regenerative cooling. It used some of the waste heat of the rocket combustion chamber to vaporize a portion of the liquid oxygen flow to function as turbine drive fluid. Component-level tests along with turbopump system-level tests progressed until mid-1940. The development of the turbopump was acknowledged by Dr. Goddard as the most challenging technical problem of his career to that point. It seems fitting that this new propellant delivery device enabled Dr. Goddard's engines to record both the longest thrust durations and highest thrust generated up to that time.

Even as Dr. Goddard's turbomachinery tests were progressing, work was proceeding in Germany that would leave Goddard's achievements far behind, at least as far as scale is concerned. In the spring of 1936, the now-famous German rocket scientists captured such interest from the military that they were eventually assigned to develop a rocket-powered weapon that would totally eclipse the largest artillery for range and payload. To do so would require a rocket engine with in excess of 50,000 lb of thrust. This was far beyond any power plant yet conceived, and considerations similiar to those of Dr. Goddard led Dr. Walter Thiel, placed in charge of engine development, to begin the development of a turbopump to supply propellants to the engine. The missile they developed is, of course, the infamous V-2, whose success is a matter of history. However, for our purposes, a somewhat closer look at this pioneering turbomachinery development is warranted.

In order to support operation of the the V-2's main combustion chamber, the turbopump was required to supply fuel (ethyl alcohol) at a flow rate of approximately 128 lb/sec and the oxidizer (liquid oxygen) at 158 lb/sec. These flow rates had to be supplied against the combustion chamber's pressure of 220 psia, requiring a discharge pressure from both pumps in the neighborhood of 360–370 psia. Lacking a ready reference from which to proceed, versions of high-performance fire-fighting water pumps were suitably modified and formed the basis for the V-2's fuel and oxidizer pumps. For the turbine, products of catalytic decomposition of hydrogen peroxide (H_2O_2) were employed as the drive fluid, probably due to past experience with it. The turbine itself was a two-stage pressure-compounded

unit with a shaft speed of approximately 3,800 revolutions per minute (rpm). The turbine working fluid flow rate required was about 3.7 lb/sec, with the turbine expanding the flow through a pressure ratio of 19:1. The turbine rotors and blades were a single integral unit, cast of aluminum. The mechanical arrangement of the turbopump as a whole placed the turbine on a common shaft with both fuel and oxidizer pumps. This arrangement would later become something of a standard in the United States. In the V-2 turbopump, however, the common shaft arrangement appears to this author to have been done in the interest of simplicity, as opposed to being the product of some type of analysis. The turbopump shaft bearings were implemented as plain journal bearings, which were impregnated with a semisolid lubricant. The designers themselves acknowledge the implementation as being "very rudimentary, but sufficient, because this unit has only to operate once, for a period of about 70 seconds." Rudimentary or not, the turbomachinery system of the V-2 guided missile represented a pinnacle in development up to that time. It is also interesting to note that this system formed the basic pattern for at least two production models of turbopump systems in the United States following World War II.

The small piece of history covered in the preceding paragraph is intended to give the reader/engineer some appreciation for the events that led to the start of implementation of turbomachinery in the rocket engine systems of the United States. Having done so, let's take an "overall" look into some of the special considerations of this branch of machines.

The chief distinction between turbomachines as implemented in rocket engines versus most other applications concerns packaging. To this author's knowledge, nowhere else is the machine designer more keenly aware that the hardware is part of a "system." The consequence of this, of course, is that the design engineers are usually required to develop a turbine/pump package along with the necessary peripheral hardware that fits neatly into the allowable envelope for a given engine. This "envelope" is frequently specified explicitly by the vehicle designer, who is, understandably, actively trying to minimize linear dimensions and volumes that are not either propellant or payload-containing. This carries the implication (either understood or specified) that all supporting systems, including the engines and turbomachinery, be packaged in the minimum practical volume. This fundamental size/weight constraint is at once the glory and the bane of the existence of rocket turbomachinery. A "common" industrial machine may have several different criteria that played key roles in its design iterations. These may include thermodynamic efficiency, satisfactory service life, acceptable life cycle costs, and others. In a rocket engine application, however, criteria such as those just listed generally become secondary to the fundamental problem of packaging an adequately performing machine within what would

normally be considered a very small space. This situation has intensified over the years, since the general desire has been to place an engine of a given thrust in a progressively smaller volume. One may also view this as continuing to increase the thrust of a constant volume engine. In any event, turbomachine designers are confronted with the problem of displacing ever-increasing quantities of propellant against increasing pressures within a volume that is decreasing. The specific problems inherent with these trends are covered in more detail in subsequent sections of this chapter.

To illustrate on a semiquantitative basis the trends in machine design over the last 40 years, we consider some particular examples.

In the early 1950s, the Army Ballistic Missile Agency (ABMA) called for the development of a 200-mile-range battlefield missile. This missile came to the be the Redstone. The vehicle was, in almost every respect, an Americanized V-2, including the use of liquid oxygen (LOX) and ethyl alcohol as propellants. The engine was required to generate 78,000 lb of thrust at a chamber pressure of approximately 300 psia, or almost 50% greater than the V-2. To support the thrust chamber operation, the turbopump was required to move 150 lb/sec of ethyl alcohol fuel (1,190 gal/min) along with 205 lb/sec of LOX (1,290 gal/min). The head rises required of the fuel and oxidizer pumps were approximately 1,140 ft and 600 ft, respectively. Both pumps were arranged on a common shaft, which was driven at a rotational speed of 4,700–4,800 rpm. With efficiencies of both pumps on the order of 70%, approximately 740 hp of shaft power was required. The turbine configuration was a two-row velocity-compounded unit, also known as a Curtis staged turbine. Arranged in the middle of the turbopump shaft, the turbine's pitch diameter was approximately 20 in. The drive fluid employed was decomposition products of concentrated hydrogen peroxide, again similar to its German counterpart. These products of decomposition were ducted to the turbine inlet manifold at a total inlet pressure of slightly less than 400 psia at a temperature of nearly 700 °F. The turbine expanded the working fluid through a pressure ratio of 22, with the exhaust products leaving the turbine at just slightly higher than sea-level pressure. This pressure ratio is of the order of magnitude of the majority of rocket engines that operate on the so-called gas generator cycle. These conditions provide high work per pound of turbine drive fluid, although extracting this energy efficiently is problematic, as evidenced by the unit's efficiency of just under 40%.

A rather useful (though not all-important) parameter by which rocket turbomachinery performance is gauged is by the use of a "power density" term. This is simply the shaft power supplied by the turbopump per unit of machine weight. In the case of the Redstone engine turbopump, this term computes to slightly over 2 hp/lb.

The next generation of machinery entered design at about the same time as the Redstone engine was beginning flight operations. The U.S. Air Force called for the design of an intermediate-range ballistic missile (IRBM) to be stationed in England. The missile carried the name Thor and was designed for a range of 1,500 miles. The engine required for the Thor represented a large jump in capability from the Redstone engine. Thrust of the engine was to double, as was the chamber pressure, reaching just under 600 psi. Liquid oxygen was retained as the oxidizer, with kerosene being substituted for ethyl alcohol as the fuel for higher performance. Fuel and oxidizer flow rates required increased to 200 lb/sec and 450 lb/sec, respectively. The corresponding pump head rises were 1,650 ft and 2,340 ft. Simple calculations will show that the required turbine power for this application was in excess of four times that of its Redstone predecessor. This large increase in required performance resulted in a number of significant evolutionary changes.

First, the large turbine power requirement rendered the previous hydrogen peroxide monopropellant drive system less practical. In order to more compactly package both the turbine and its drive system, a small combustor was incorporated to produce the turbine drive gas. Called (predictably) a *gas generator*, this small chamber burned the engine's main propellants to produce hot, fuel-rich gas at a temperature of approximately 1,200 °F. The output of the gas generator was, of course, ducted directly to the turbine inlet where the gas was expanded through a two-stage impulse turbine. To produce the required power (approximately 3,100 hp), the turbine's two stages expanded 15 lb/sec of drive gas through a pressure ratio of 17.6. Upon exit from the turbine, the gases were exhausted to the atmosphere.

Another fundamental change also concerned turbine packaging. In order to produce the required shaft power with reasonable efficiency, a much higher turbine blade speed was required. To accomplish this along with reducing the turbine weight and volume, turbine rotational speed was increased by a factor of in excess of 7, to 30,500 revolutions per minute. Together with a decrease in turbine pitchline diameter from 20 in. to 9 in., a blade speed increase from 400 to 1,200 ft/sec was obtained.

The centrifugal pumps for the Thor engine also underwent noticeable improvements. Since the fuel and oxidizer were of comparable density, the required head rises from both pumps were also similar. This enabled both pumps to again be placed back to back on a common driveshaft, which required both pumps to run at the same angular velocity. To generate the increased head required over that of the Redstone engine, the diameter of both pump impellers was increased, and their operating speed was increased to 6,300 rpm. The increased performance demand resulted in a great

increase of required suction performance from both pumps. This resulted in the introduction of a device known as an inducer at the inlet of both fuel and oxidizer pumps. An inducer is simply a single-stage axial pumping element whose diameter matches that of the main impeller inlet. For those who have never seen one, the geometry of an inducer is somewhat reminiscent of a screw or propeller. The inducer is usually fairly lightly loaded and imparts just enough head to the pumped fluid that the main impeller inlet does not experience adverse effects due to cavitation. Although the inducers fitted to the Thor engine pumps were somewhat primitive by today's standards, they caused the suction performance capability of these pumps to be nearly tripled.

Lastly, we must address the problem of coupling turbine and pump shafts. In the design of the Redstone engine turbopump, turbine and pumps were on a common driveshaft. This was impossible in the Thor engine turbopump. In order to increase turbine efficiency and to minimize turbine weight, the turbine shaft speed was optimized separately from the pumps. At more than 30,000 rpm, the turbine was running at a speed that was far beyond the capability of centrifugal pump stages to support.

The only practical answer was to link the turbine and pump shafts together via a gear reduction system. As it turned out, this gearbox formed the structural backbone of the Thor turbopump. Fabricated from an aluminum sandcasting, the gearbox contained a 4.8:1 reduction gear train to link turbine and pump shafts. In addition, it contained provisions for an accessory drive pad (which could be used by a missile hydraulic pump, for example), as well as connect points for both centrifugal pumps as well as the turbine assembly. The fuel pump was bolted to the gearbox, while the LOX pump was attached by radial pins around the circumference of the pump rear. This technique provided radial load relief for the LOX pump housing to permit thermal contraction of the housing without causing any undue radial direction loads. It is also worth mentioning that this gear reduction train proved to be one of the largest technical challenges of the turbopump development. The desire to keep inert weight to a minimum caused the gearbox to be sized as small as was practical. This reduced the gear diameters, and therefore their pitchline velocity. The transmission of in excess of 3,000 hp to a main driveshaft moving relatively slowly through gears that have low pitchline velocity caused very high forces between gear teeth. This condition resulted in a number of cases of premature fatigue failure of turbopump gears. Modifications to the gear tooth involute profile yielded a wider tooth root with greater load capacity, as well as a reduction in shear loading at the tooth root. This, along with careful processing of the gear material and somewhat unique fabrication techniques, resulted in

a gear train that has performed satisfactorily in over 2,500 production units. The experience gained to date in turbomachinery design was also evident. At approximately $5\frac{1}{2}$ hp per pound of weight, the Thor engine turbopump more than doubled the specific power of its Redstone predecessor.

During the mid- and late 1950s, this geared turbopump arrangement was a common design selection used by several aerospace companies. Several distinct variations emerged. Among these were

A common pump drive where a single gear train linked the turbine to both pumps. This arrangement was used where both pumps could operate at the same angular velocity.

Independent gear drives where each pump was geared separately to the turbine. This arrangement allowed each pump to run at a different angular velocity. This could be necessary for a number of reasons, such as a large density difference between propellants.

Turbine direct drive to one propellant pump, with a gear train to the other propellant pump. This arrangement was particularly applicable to an engine that had a large difference in the power requirements for the two pumps. It has the potential to avoid large reductions in turbopump system efficiency caused by a low-power design for a separate turbine for the low-power pump.

It should be pointed out that the original necessity for gear drive of a turbopump was the inability of the centrifugal pumps to operate at the same angular velocity as the turbine. This was due to a number of factors, all based on fundamental technology that did not exist in the 1950s. The U.S. government and industry have invested considerable effort in research since that time. As a result, the obstacles that made gear drives necessary are now largely absent. For this reason, a "common shaft" arrangement with both pump(s) and turbine on the same shaft is now essentially a standard. This configuration obviously benefits in both weight and bulk from the absence of the gearbox and the internal gear train.

In the late 1950s, the U.S. government perceived the need to develop a very high thrust single-chamber rocket engine. This perception was based on understanding (and speculation) of the propulsion capability of the Soviet Union at the time. The engine was to produce 1.5 million lb of thrust burning liquid oxygen and kerosene propellants. This engine was the F-1. A cluster of five such engines provided the first-stage muscle for the Saturn V launch vehicle and until the late 1980s was the most powerful operational rocket engine in the world. To support the engine thrust level of over 750 tons, enormous quantities of propellants had to be moved from the vehicle tanks to the thrust chamber. With the combustion chamber pressure set at approximately 1,000 psi, 2 tons of liquid oxygen per second had to be

displaced by the F-1 oxidizer pump and brought to a discharge pressure of 1,500 psi. Fuel flow amounted to another ton per second, with a required discharge pressure of 2,000 psi. With efficiency of both pumps in the 75% range, the F-1 turbine was required to produce approximately 55,000 hp at a shaft speed of 5,500 revolutions per minute. This demand for turbine power would remain unsurpassed for 20 years.

The development and success of the F-1 engine turbopump represent (in this author's opinion) another quantum jump in turbomachinery technology for a number of reasons. We touch on only a few. To harness 55,000 hp of shaft power productively is in itself a task that would daunt most engineers. Additionally, providing flow paths of reasonable size for 3 tons of pumped fluids (as well as 170 lb of turbine drive fluid) per second required component sizes that were quite without precedent. For example, to obtain the tangential blade velocity required for good efficiency, the pitch diameter of the turbine rotors was sized at 35 in. The second row of rotor blades (a two-row velocity-compounded configuration was chosen) had blade heights of nearly 4 in. The centrifugal fuel and oxidizer pumps in this machine had similarly impressive proportions. Both impellers were quite large, with tip diameters of nearly 20 in. for the LOX pump, and nearly 2 ft for the fuel pump. To obtain maximum suction performance from both pumps, both were equipped with a new type of inducer, which contained blades that were canted forward. Called (predictably) a *canted inducer*, it represented another step forward in dealing with the problem of pump suction performance. With blades canted forward, centrifugal loading on the blades partially balanced the force due to fluid traversing the blade passage. The result was a higher allowable loading of the inducer and an accompanying increase in performance. Obtaining maximum suction performance from the F-1 pumps was particularly important. With several tens of thousands of horsepower being transmitted, a reduction gear between turbine and pumps was probably less than practical. This mandated a common driveshaft arrangement, with both turbine and pumps operating at the same angular velocity. This has two effects: to restrict turbine blade speed to stay within pump operating capability, and to demand increased pump cavitation resistance in order to maintain acceptable turbine efficiency. This mutually conflicting state of affairs represented a substantial design problem, and required compromises by both turbine and pump designers to arrive at a workable solution.

Once design was complete, fabrication began, fraught with its own set of problems.

For the turbine inlet manifold and associated structure, designers had chosen a nickel-based material called Rene 41, which at that time was new. Due to size of the structure involved (the F-1 turbine housing was about 4 ft

across), hand forming and welding of large pieces of relatively thin Rene 41 sheet were required. As readers with manufacturing experience are aware, the heat-resistant nickel-based materials pose their own brand of fabrication and welding difficulties. These difficulties (particularly regarding welding) are accentuated when workpieces become large, with resulting loss of stiffness. Although automated welding procedures were eventually implemented, the success of this machine is owed in large part to the craftsmanship of the individuals involved.

The fuel and oxidizer pumps of the F-1 engine were, in a hydraulic sense, relatively straightforward. The difficulties encountered were, for the most part, due to their size. The oxidizer pump, in particular, was a source of some difficulty. Due to the highly reactive nature of liquid oxygen, as well as the ability of most metals to serve as a fuel, any substantial internal malfunction in a LOX pump normally results in total devastation. Any useful physical evidence is usually consumed. This makes failure investigations difficult. Diagnoses normally require substantial experience and judgment. In the case of the F-1 LOX pump, development engineers were also assisted by an unlikely event. In examining the hardware from a test that did not run satisfactorily, a suspected structural inadequacy of the LOX impeller was confirmed when an impeller blade was found separated from the impeller and lodged in a pump flow passage. This evidence led to modifications that permitted subsequent successful operation of the pump assembly. The F-1 turbopump went on to operate with 100% success in the Saturn V flight program. With every Saturn V launch, in excess of 2,200 tons of propellant was pumped through the 5 F-1 engines in just 160 sec. Another interesting note concerns the F-1 turbopump specific power. At more than 16 hp/lb, it represented an increase of nearly an order of magnitude in less than 10 years of rocket turbomachinery development.

While one group in industry wrestled with the large-sized machinery for the F-1 engine, another was coming to terms with the requirement to pump a new fuel: liquid hydrogen (LH_2). The impetus behind this new fuel was primarily its high performance. A simple analysis reveals available specific impulse of in excess of 400 sec at only moderate chamber pressure. However, as always seems to be the case, new problems loomed that required new solutions.

The first of these centered around LH_2's temperature. At atmospheric pressure, hydrogen has a saturation temperature of approximately 37 °R (−423 °F). The only fluid known to maintain a vapor phase under these conditions is helium. As a result, all systems containing hydrogen in the liquid phase must be completely inerted with gaseous helium prior to the introduction of LH_2. Also, uninsulated vessels containing LH_2 quickly condense air on their exteriors. Hardware not intended for cryogenic

exposure may be subjected to impingement by cryogenic air with unpredictable results. Finally, the unusually low fuel temperature creates an external heat leakage problem that is usually impossible to ignore. The result is that most liquid hydrogen propellant systems contain large amounts of thermal insulation, and sometimes protective shells to prevent damage to the insulation.

Another problem unique to LH_2 concerns its low density. Since changes in head and pressure are proportional to each other by the reciprocal of the fluid density, lower-density fluids require higher developed heads to impart a given pressure rise. In the case of hydrogen near saturation conditions, head rises required to develop a given pressure rise from a pump are an order of magnitude higher than that required for denser propellants such as kerosene, liquid oxygen, and others. Pump designs for LH_2 service, therefore, typically require comparatively large amounts of input power, have near-maximum impeller tip speeds, and are often multistage machines.

The Rocketdyne Division of North American Aviation was the builder of the J-2 engine under contract to NASA. As it happened, the company had already been engaged in the development of a liquid hydrogen pump for a nuclear rocket engine project not related to the J-2 program. The LH_2 pump, called the Mark 9, worked to performance requirements similar to those of the J-2. The Mark 9 was an axial-flow pump with six main stages, plus an inducer. Although not a common design for a rocket pump, the axial-flow configuration had advantages in weight, packaging, efficiency and was relatively easy to multistage. For these reasons, as well as the lack of a throttling requirement (the J-2 was a fixed-thrust engine), the J-2 fuel pump was designed to a configuration very much akin to the Mark 9, although a seventh main stage was added to provide satisfactory stall margin. This pump (known as the Mark 15-F) went on to see a great deal of operational service in the upper stages of the Saturn 1B and Saturn V vehicles.

In the late 1960s, the U.S. government decided that the next large launch vehicle development effort would center around a reuseable vehicle to ferry astronauts and cargo to and from low earth orbit. This vehicle was to become the Space Transportation System (STS) or Space Shuttle, which is currently operating. The system went through many incarnations during definition, the details of which are beyond the scope of this text. When, in 1972, the vehicle configuration was chosen, the resulting propulsion system requirements were unlike any previously stipulated. First, the STS's main propulsion system (later named the Space Shuttle main engine, or SSME) was to use LOX/LH_2 propellants and operate at a chamber pressure of 3,000 psi. This was three times higher than the highest pressure production engine prior to it. Second, the engine was to operate on a thermodynamic

cycle known as staged combustion (some refer to it as a topping cycle). Third, the engine was to be capable of throttling, or varying its thrust to support the ascent trajectory requirements of the Space Shuttle vehicle. From a design thrust level of (appropriately) 100% rated power (referred to as RPL), the engine was to be capable of reduction in thrust to a minimum of 65% of design. This is referred to as minimum power level, or MPL. Also, thrust was to be capable of increasing to 109% of the design thrust. This high thrust was to be used for emergency conditions. As such, it was referred to as emergency power level, or EPL. Thrust variations were to be controllable to increments of 1%. Another notable feature of the original engine design was the requirement for a variable mixture ratio, or ratio of oxidizer to fuel being consumed by the engine. This ratio was to be variable from 5:1 to 7:1 as commanded from the Shuttle orbiter. This feature was to be an attempt to ensure simultaneous depletion of both fuel and oxidizer tanks. This combination of operating conditions placed demands on the turbomachinery systems that remain unmatched 20 years later.

Before proceeding further, a short comparison of the SSME operating cycle with those of its ancestors would be helpful. The Thor engine and its descendants, along with the F-1 and J-2 engines, shared a common thermodynamic cycle, the *gas generator* cycle. In this cycle, propellants from the vehicle tanks reach the turbopump inlets under tank pressure. Turbopump discharge ducting routes most of the fuel and oxidizer to the thrust chamber inlet manifolds. A small amount of both propellants, typically 2–3% of the total flow, is carried from the pump outlets to another combustor, referred to as a gas generator. Usually quite small in comparison to the main thrust chamber, the gas generator burns its propellants at a mixture ratio to produce gas (usually fuel rich) to serve as turbine drive fluid. Typically, these gases are in the 1000 to 1700 °F range. Although it would certainly be possible to create turbine drive gas that is oxidizer-rich rather than fuel-rich, the generally adverse chemistry associated with this situation normally renders fuel-rich gas a better choice. To this author's knowledge, oxidizer-rich gas generators have not been employed in any production engines produced in the United States, although they have been (and still are) in use by other countries. Upon exit from the gas generator, the drive gas is transported to the inlet manifold of the turbine(s). Following expansion through whatever turbine arrangement has been provided, the gas is typically either dumped to atmosphere through an exhaust duct or is transported to the divergent section of the engine exhaust nozzle, where it is injected into the supersonic flow stream. Being relatively cool, this gas can provide what is referred to as *dump cooling* of some portion of the nozzle divergent section. Incidentally, if drive gas is simply ducted overboard, a restricting orifice is normally placed in

the exhaust duct. Sized to create sonic flow of the exhaust, this choked orifice ensures that turbine exhaust pressure remains constant such that turbine power will not increase with altitude. From the preceding description, it can be seen that in gas generator cycle engines, turbine inlet pressure is close to turbopump discharge pressure (less the losses in the gas generator system itself) and that turbine exhaust pressure is kept slightly above local ambient pressure. This results in an available turbine pressure ratio that is (by most standards) fairly high, with values in the range of 20 being rather common. As a result, theoretical gas specific work values are rather high, allowing a low turbine flow rate. As stated above, turbine fluid flow rates of 2–3% of total engine propellant flow rate are representative. Given the large available pressure ratio along with the usual guidelines for turbine packaging (which dictate a minimum number of stages), these turbines, almost without exception, contain stages that operate with supersonic gas spouting velocities. Considering the range of blade speeds normally permitted, impulse blade rows have been the usual choice. This choice is based on a turbine design parameter known as the turbine stage velocity ratio. In this operating regime, turbine efficiencies are normally on the order of 30–60%, with the latter somewhat irregularly achieved. This is not particularly detrimental, since turbine flow constitutes but a small portion of the total engine flow.

The staged combustion cycle, however, necessitates a realignment of some of these thought processes. The mechanics of this engine cycle make the establishment of design requirements for turbomachinery and the engine system anything but straightforward. We attempt to impart to the reader a small sample of this quandary.

The main motivation behind staged combustion is to avoid the parasitic losses associated with overboard dump of turbine exhaust gases. These gases are rich with unburned fuel, and such losses are a characteristic of the gas generator power cycle. To avoid these losses, it is necessary to redirect the turbine exhaust gases to the inlet of the thrust chamber injector. This raises the turbine exhaust pressure to somewhat in excess (typically to 110–120%) of the main combustion chamber pressure. Now a balance must be achieved between pump flow rates, pump discharge pressures, and turbine flows, as well as pump and turbine efficiencies. The interested reader can certainly see that a ''low'' turbine flow rate would increase the pump discharge pressure required to perform a given rate of turbine work. Turbine pressure ratios similar to those used in gas generator cycle engines would require pump discharge pressures that are unreasonably high. To keep this situation under control, the philosophy followed was to increase the turbine flow rate to nearly its limiting condition, that is, to where all the engine fuel flow becomes turbine drive fluid. This acts to decrease the turbine

pressure ratio that is required and also lowers the pump discharge pressure required.

Turbine efficiency also becomes a significant problem with which the designer must be concerned. In gas generator cycle engines, turbine efficiency had relatively little effect on engine performance, since turbine flow was small, and pump discharge pressure was set (practically speaking) only by thrust chamber injector inlet pressure requirements. In a staged combustion cycle engine, however, the turbine pressure drop is in series between the thrust chamber injector and the turbopump discharge. Reduced turbine efficiency requires a higher turbine pressure ratio, which in turn increases the needed pump discharge pressure. It is therefore desirable to maximize the turbine efficiency in order to meet the main combustion chamber pressure requirement with the lowest possible pump discharge pressure.

During the engine definition effort, a fundamental design decision was made to drive fuel and oxidizer pumps by separate turbines rather than by a common turbine. Since the engine required not only throttling capability but active mixture ratio control, it would be necessary to vary the speed of fuel and oxidizer pumps independently. This would necessitate a separate gas generator (referred to as a *preburner*) for both turbopumps, with an oxidizer flow control valve in series with each preburner for turbine gas temperature control. The early design studies for fuel and oxidizer pump turbines focused on basic configuration issues. Studies were performed for turbines with from one to three stages, with diameters from 10 to 12 in., with blading varying from impulse to substantial degrees of reaction. The final choices made were for both fuel and oxidizer turbines to have two stages of reaction blading, with diameters of 10 in. Although this was not absolutely optimum from a turbine performance standpoint, it optimized the turbomachinery system for size, weight, and efficiency when integrated with the overall engine system. This is a good example of where thermodynamic performance of a component is intentionally compromised to bring about net gains in overall engine system performance or suitability. In the case of these turbines, a 12-in. diameter would have been desirable for higher machine efficiency. However, the turbines are enclosed in a hot gas manifold structure, which is comprised of relatively thick sections of high-temperature material. Reduction of the turbine diameter to 10 in. resulted in adequate turbine performance, while reducing engine weight significantly.

The early design selection effort for the SSME fuel and oxidizer pumps brought about some interesting choices and a novel configuration. Let us focus on the fuel pump system first. The fuel turbopump system of the SSME has the task of displacing about 150 lb/sec of LH_2 and raising its pressure from about 35 psi (set by allowable propellant tank pressure) to in

excess of 6,000 psi for consumption by the engine. This equates to a head rise of approximately 200,000 ft. Although past design practices would have suggested the use of an axial-flow pump (and one was considered), the need to throttle over nearly a 2:1 range of thrust requires the fuel pump to operate over a range of inlet flows that axial machinery would have difficulty supporting. The throttling requirement was a major factor that dictated a centrifugal pump configuration. Also, since the head rise requirement was clearly beyond the capability of a single stage; a multistage machine would be required. Centrifugal pump configurations with from two to four stages were considered, with a three-stage configuration being selected. Designed for a shaft angular velocity of 37,000 rpm, it was the best compromise for weight, complexity, efficiency, impeller speed, and hydrodynamic stability over the required operating range.

Another outcome of the early fuel pump design process is worth special mention. Initial pump sizing efforts showed that the propellant tank pressure (approximately 35 psi) was much too low to support operation of a fuel turbopump that was optimized for size and weight. While a single pump to perform this job could certainly be designed, its bulk and performance would be clearly undesirable. However, if a large inducer stage was placed upstream of the main fuel pump inlet, and provided approximately 4% of the required total head rise, a much more compact and higher-performing main fuel pump could be devised. As it happened, such a large inducer stage (referred to as a *pre-inducer*) had been the object of some previous development work for an experimental version of the J-2 engine. This pre-inducer took the form of an entirely separate *low-pressure fuel turbopump*. Driven by warm gaseous hydrogen extracted from elsewhere in the engine, the low-pressure fuel turbopump generates a discharge pressure of approximately 250 psi. With this available inlet pressure, the main pump (referred to as the *high-pressure fuel torbopump*) can operate under much more favorable conditions. This machine has gone on to become what is perhaps the most visible single piece of turbomachinery engineering in the world today.

Like the fuel turbopump system, the oxidizer turbopump system of the SSME is a somewhat novel configuration that is a direct result of the unique demands placed on it. This system must move approximately 1,000 lb/sec of LOX, which is ingested at a propellant tank pressure of approximately 100 psi. For reasons analogous to the fuel pump system, a separate low-pressure oxidizer turbopump was contrived to enable the high-pressure oxidizer turbopump to be considerably smaller and lighter than would be possible otherwise. Approximately 90% of the engine LOX flow is destined for the main combustion chamber, which requires a pump discharge pressure of 4,000 psi. The other 10% is required to operate the two

preburners, one each for the high-pressure fuel and oxidizer turbopump turbines. The preburner oxidizer system requires a pump discharge pressure of nearly 7,500 psi. A basic pump configuration question now arose as to whether the oxidizer pump should include one pump stage or two. Using a single pump stage would certainly minimize complexity. This single stage would discharge the entire LOX flow at a pressure of 7,500 psi, with the main combustion chamber flow being throttled to 4,000 psi through a pressure-reducing valve on its way to the thrust chamber. The use of two pump stages added somewhat to the turbopump complexity. The first pump stage would raise the LOX pressure to 4,000 psi. Most of this would flow to the main combustion chamber. The LOX required for preburner operation would be tapped off and ingested by a separate preburner boost pump that would generate the required preburner oxidizer system pressure. The single-stage configuration, although simpler, would require on the order of 12,000 hp of additional turbine power to raise the entire LOX flow to preburner system pressure. Since this is not required, it is best avoided. Also, the single-stage configuration could very well have been heavier, with a single large pump volute sized for a working pressure of almost twice what is needed.

The turbomachinery system of the SSME represents the present state of the art as far as performance is concerned. The high-pressure fuel turbopump in particular operates at a specific power of approximately 100 hp/lb at conditions of maximum engine thrust. This figure is (in this author's opinion) not likely to be exceeded in the near future. The capabilities of available materials are being pushed near their limits under these conditions, and issues regarding durability and ultimate cost-effectiveness are urging new priorities in future designs.

ROCKET PROPULSION SYSTEMS—TURBINES

Turbines are, of course, the power production device in rocket turbomachinery systems. Pump-fed rocket engines could not exist in their present form without them. Although alternate means of energy generation could probably be found, the performance per unit weight and envelope of modern gas turbines are not so easily exceeded. Rocket engine turbines operate on exactly the same principles as any other type of turbine, and the physics of their operation is well documented in the literature. There are, however, a number of areas in which these machines are somewhat unique, and these deserve mention.

A turbine design engineer delving into rocket turbines for the first time faces his or her biggest "cultural shock" concerning the issue of design

lifetime. With very few exceptions, rocket engine turbines have lives that are exceedingly short when compared with more conventional turbine applications. A German engineer who participated in the development of the F-1 engine turbine once told me, "The design lifetime of our machines was intended to be 25 years [he was referring to hydrodynamic power plant turbines in Europe]. Then I start to work on this machine, and I asked about the intended design life. They told me it was 160 seconds!" While the current trend is toward lives considerably in excess of this, the basic idea is still valid.

Rapidity of startup is another somewhat unique problem area. Rocket turbines are often required to transition from a "cold start" to rated power output in 2–3 sec. The transient loading resulting from this very rapid power buildup has been the cause of turbine blade failures. It should also be pointed out that the startup loads issue has a strong thermal component as well as a mechanical one. Since rocket turbines are normally powered by gases that are products of combustion, the gas temperature increases from nearly ambient to its full value within the same 2- to 3-sec time period. This may be accompanied by transient overshoots in both gas temperature and chemical composition due to the action of the engine's control system. The turbine must tolerate these, and they must not compromise design life.

Rocket turbines operate with working fluids of a very high energy content, and this energy must be extracted in as efficient a manner as possible. This is somewhat problematic (as mentioned earlier) due to relatively strict size and weight limitations placed on the turbine package. With the advent of hydrogen-based working fluids, old problems are compounded and new ones created. For a number of reasons, blade speed in rocket turbines is normally lower than desired. Also, due to hydrogen's high specific heat value, gas spouting velocities tend to be higher in hydrogen-operated turbines than in turbines operated with other propellant combinations over the same pressure ratio. This combination of factors tends to move the operating point for a turbine stage toward a lower range of velocity ratio, where maintaining a given efficiency is difficult. In addition, a heated hydrogen environment under elevated pressure creates the potential for a turbine blade environment that is chemically adverse. A great many metallic materials are subject to premature embrittlement and failure in a hydrogen environment. Although this failure mechanism may not represent a serious problem for an expendable rocket turbine, it may have to be considered in the design of longer-lived and reusable machinery. What represents "consideration" varies from case to case. In one instance, a problem may be avoided by wise choice of blade or disk material and/or processing methods. In a more acute case, blade speed may be limited or derated by the necessity of keeping blade loading below a threshold value.

The design of a turbine package for a rocket engine system may be reasonably thought of as following a somewhat generic sequence of steps. We try to touch on the high points of these in the following paragraphs. This discussion, unless otherwise specified, refers to axial-flow turbines whose working fluid is in the gaseous phase. Radial-flow turbines, as well as liquid-operated (hydraulic) machines, are discussed separately.

In the design of rocket turbines, the selection of turbine working fluid is, almost without exception, somewhat reflexive. In a monopropellant turbine drive system, such as the Redstone engine system or numerous small auxiliary power units, the selection is obviously limited to those fluids that will satisfactorily decompose on demand. Engines operating on the gas generator cycle typically burn a small percentage of the engine's main propellants to produce the turbine working fluid. The variable that is left up to the turbine designer is, in this case, the turbine inlet gas temperature. The usual desire would be to maximize this temperature to provide high working fluid specific energy. In practice, however, certain limitations emerge. To achieve the most compact package, stage mechanical loads are deliberately sized high, and at times may approach material limits. Gas temperature distributions within the turbine stage(s), blade speed, and blade loadings may require an iterative analysis and mutual compromise to achieve a satisfactory state of affairs. Another point to be borne in mind concerns turbine gas properties as they are affected by temperature. Since the turbine working fluid is being produced by combustion of, in general, two reactants, all thermodynamic properties of the resulting combustion products are continuously varying functions of the input ratio of the reactants. If we specify a target working fluid temperature, then the rest of the properties with which we are concerned are automatically selected (constant-pressure specific heat c_p, gas constant R, specific heat ratio γ, gas chemical species, etc.). It should also be remembered that gas specific energy is proportional to the product of temperature and constant-pressure specific heat. Under certain conditions, this product may not be a linear function of temperature, and experience is required to assess the maximum desired temperature. There may be other considerations unrelated to the turbine package proper that influence the selection of a working fluid temperature. For example, when the reactants are of the variety that exotherm prior to combustion (such as the hydrazine family and nitrogen tetroxide), certain chemical stability issues may become important. For example, with several hydrazines and nitrogen tetroxide, the temperature range of 1,000–1,400 °F is often avoided. This is due to an oscillatory catalytic reaction of the hydrazine, which can occur in the mixture ratios of reactants that produce these temperatures. For this reason, turbine inlet temperatures of either below 1,000 or above 1,400 °F are normally specified. In another example, turbines

using hydrocarbon fuel combustion products have suffered progressive coking of the turbine nozzles. This gradual reduction in nozzle flow area resulted in decreasing turbine performance. To avoid this, the turbine inlet temperature was adjusted to move out of the range that accentuated the coking problem. Ironically, one production turbine had its inlet temperature lowered, while another responded favorably only with increased inlet temperature. Finally, a brief mention of the working fluid chemical properties is worthwhile. In the range of turbine inlet temperatures typically specified (800–1,700 °F is representative), the mixture ratio of oxidizer to fuel required is quite heavily biased by combustion system standards. This could, of course, be accomplished by biasing toward either excess fuel or excess oxidizer. Almost without exception, fuel-rich combustion products are specified for the working fluid of rocket turbines. There are two main reasons for this: first, the chemistry of fuel-rich gases, is typically favorable while that of oxidizer-rich gases can be quite adverse; and second, turbine mass flow requirements are normally lower with fuel-rich gases since they tend to have lower molecular weight than equivalent oxidizer-rich gas. It should be noted, however, that these conditions scarcely prohibit the use of oxidizer-rich gases for turbine drive with proper attention to detail. Several engines operating with this type of turbine working fluid have been in use in other countries for many years. These engines have been developed to a high degree of refinement.

Engines that operate on the expander cycle typically use the engine's fuel (and/or oxidizer) heated in the combustion chamber cooling circuit for turbine drive. The success of this arrangement depends on the combustion chamber coolant fluid undergoing an adequate enthalpy increase in the chamber cooling process to satisfy turbine energy requirements. For this reason, the successful operation of this cycle can be thought of as a significant technical accomplishment. Fluids used in this application to date include supercritical hydrogen and oxygen.

Given the turbine working fluid and its properties, we next discuss specification of the turbine inlet and exit pressures. Monopropellant turbine drive cycles probably have the greatest flexibility in this area, since the turbine working fluid is contained in an independent system. In these applications, turbine inlet pressure is determined by the allowable monopropellant tank pressure, while accounting for the losses between the monopropellant tank and the turbine inlet. Also, since the turbine fluid is exhausted to atmosphere in this cycle, high turbine pressure ratios are possible. The most recent example of such a system in a production rocket engine in the United States is the Redstone engine, built by the Rocketdyne Division of Rockwell International (then North American Aviation Inc.). This system employed a two-row velocity-compounded impulse turbine

using products of decomposition of hydrogen peroxide (H_2O_2) as working fluid. Expanding its gas through a pressure ratio of approximately 22, this turbine delivered just under 800 hp at a shaft speed of 4,800 rpm. The most serious limitation suffered by systems of this sort is relatively low-power output due to low specific energy of the turbine working fluid. Despite this comparative limitation, monopropellant drive turbomachinery remains in quite high-volume use in countries other than the United States.

Rocket engines employing the gas generator cycle comprise the bulk of the engines being produced in the United States today, or that have been produced in the past. In this cycle, a small combustor is supplied with fuel and oxidizer in parallel with the engine's main combustion chamber. The resulting products of combustion are fed directly to the turbine inlet manifold. Thus, the turbine inlet pressure is, for practical purposes, set at the turbopump discharge pressure less the pressure losses in the gas generator combustion system. Typical values of inlet pressure for gas generator cycle turbines have ranged from 400 to 1,000 psi. The turbine designer could, of course, reduce the turbine inlet pressure by means of pressure reducing or regulating devices in the gas generator propellant systems, although this is not common practice.

The turbine exhaust pressure in gas generator cycle turbines may or may not be dependent on other engine cycle considerations. In the simplest instances, turbine exhaust gases are simply transported to the base plane of the engine by a suitable exhaust duct, where they vent to atmosphere. In these cases, turbine exhaust pressures are only slightly above atmospheric pressure. Such systems also typically include a restricting orifice in the turbine exhaust duct. This orifice, along with the turbine exhaust pressure level, is sized to induce sonic flow through the orifice. This technique ensures that the turbine pressure ratio (and thus turbine power) will not vary with altitude. The other popular method of disposal of gas generator cycle turbine exhaust gas involves transporting the gas to an annular manifold around the divergent section of the engine exhaust nozzle. Here, the gas is injected into the nozzle's supersonic flow stream. The turbine exhaust is cool relative to the total temperature of the main chamber gas and is used in this instance to provide a boundary layer adjacent to the nozzle wall that is cool enough to negate the requirement for regenerative cooling in the lower portion of the nozzle section. This practice is referred to as dump cooling and has certain advantages. The smaller the fraction of the nozzle length that must be regeneratively cooled, the lower is the discharge pressure requirement of the propellant pump that is delivering the coolant fluid. Since the regenerative cooling process depends on high coolant velocities, the pressure losses across a large nozzle's coolant circuit can be substantial. Even a relatively small reduction in the regeneratively cooled nozzle length

can yield noticeable savings in required turbopump power. Locating the turbine exhaust within the engine nozzle sets the turbine exhaust pressure at the level that exists within the nozzle at the plane where the dump coolant injection will occur. The larger the fraction of the nozzle length that is dump-cooled, the further upstream in the nozzle flow the dump coolant will be introduced. Moving the turbine exhaust manifold further upstream exposes the turbine exhaust to progressively higher static pressures. This results in lower available turbine pressure ratios. Whether or not this method of turbine exhaust disposal is to be used depends, of course, on a number of factors. During the engine preliminary design, parametric studies involving turbine pressure ratio, pump discharge pressure, nozzle coolant jacket pressure drop, and others must be performed to assess the desirability of dump cooling. As a general rule, nozzles intended for operation at or near sea level may not benefit substantially from dump cooling, while nozzles optimized for high-altitude operation can benefit greatly.

The staged combustion cycle and expander cycle (of which several derivatives have emerged) mandate a somewhat different approach than the gas generator cycle to the issue of setting turbine inlet and outlet pressures. As stated earlier, the turbine inlet pressure in the gas generator cycle is determined by the turbopump discharge pressure that is required to meet the target main combustion chamber pressure. Gas generator propellant flow is then determined by turbine efficiency at the specified pressure ratio. Staged combustion and expander cycles, in contrast, generally use most or all of the flow of one of the propellants for turbine drive. (A prototype engine recently built worked on a variant of the expander cycle known as the *dual expander*. In this case, both fuel and oxidizer were used for cooling of different portions of the combustion chamber and nozzle. Separate turbines were employed for each pump, and each used its own pumped fluid for turbine drive.) The pump discharge pressure is then determined from the turbine pressure ratio needed to meet the turbine work requirement. If the reader detects an element of circular logic here, that detection is to be applauded! As can be seen from the schematic representations in Figs. 1–5, both staged combustion and expander cycles set the turbine exhaust pressure from the required pressure in the main combustion chamber injector's fuel manifold. The turbine inlet pressure is then set by the turbine work required by the propellant pump(s) being driven. At this point, the efficiencies of both turbine(s) and pump(s) come into play. Since pump discharge pressure and turbine inlet pressure must be identical (neglecting losses in between these two points), this pressure must be determined iteratively. A representative method could involve a set of parametric computations as shown in Figs. 6, 7, and 8. Shown is a family of curves of turbine work generated and pump work input required versus pump discharge pressure. As can be seen, lower

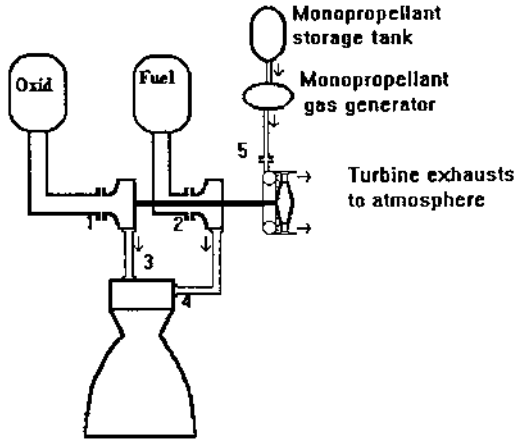

Figure 1 Rocket engine system schematic, monopropellant gas generator cycle: 1, oxidizer pump inlet; 2, fuel pump inlet; 3, thrust chamber injector oxidizer inlet; 4, thrust chamber injector fuel inlet; 5, turbine hot-gas inlet.

values of component efficiencies cause these curves to approach parallelism, intersecting at progressively higher values of pump discharge pressure. If these curves cannot be made to intersect at an achievable pressure, a working system is obviously impossible. Further, it can be shown that with

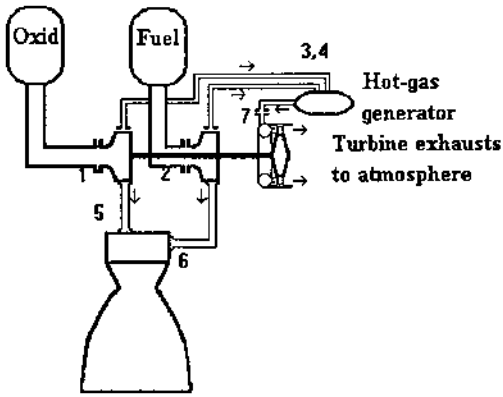

Figure 2 Rocket engine system schematic, bipropellant gas generator cycle: 1, oxidizer pump inlet; 2, fuel pump inlet; 3, gas generator fuel inlet; 4, gas generator oxidizer inlet; 5, thrust chamber injector oxidizer inlet; 6, thrust chamber fuel manifold inlet; 7, turbine hot-gas inlet.

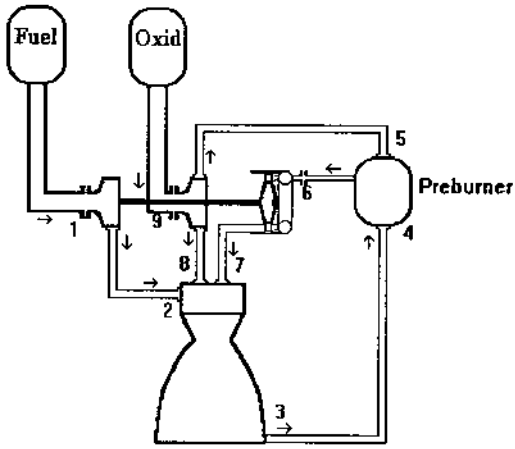

Figure 3 Rocket engine system schematic, staged combustion cycle: 1, fuel pump inlet; 2, fuel jacket inlet; 3, fuel jacket outlet; 4, preburner fuel inlet; 5, preburner oxidizer inlet; 6, turbine hot-gas inlet; 7, main injector fuel inlet; 8, main injector oxidizer inlet; 9, oxidizer pump inlet.

specified pump and/or turbine efficiencies, the maximum achievable main combustion chamber pressure is a function only of pump discharge pressure. For this reason, turbine and pump component efficiencies take

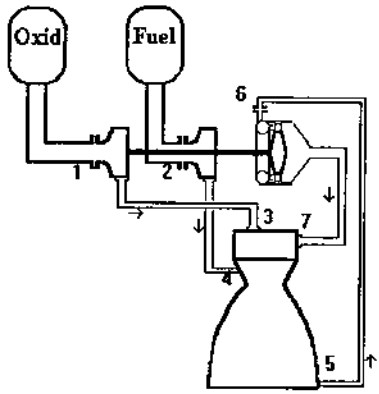

Figure 4 Rocket engine system schematic, expander cycle: 1, oxidizer pump inlet; 2, fuel pump inlet; 3, thrust chamber injector oxidizer inlet; 4, thrust chamber fuel jacket inlet; 5, thrust chamber fuel jacket outlet; 6, turbine inlet manifold; 7, thrust chamber injector fuel inlet.

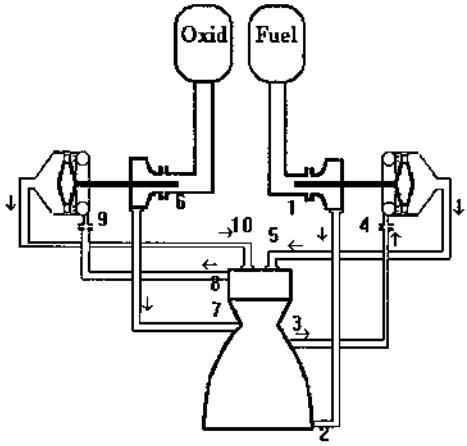

Figure 5 Rocket engine system schematic, dual expander cycle: 1, fuel pump inlet; 2, nozzle fuel manifold inlet; 3, nozzle fuel manifold exit; 4, fuel turbopump turbine inlet; 5, thrust chamber injector fuel inlet; 6, oxidizer pump inlet; 7, main combustion chamber coolant inlet; 8, main combustion chamber coolant outlet; 9, oxidizer turbopump turbine inlet; 10, thrust chamber oxidizer inlet.

on a somewhat central role in these cycles. A survey of turbine efficiencies from several staged combustion cycle engines shows significantly higher values than for even the most efficient gas generator cycle turbines. The same can be said for turbines in expander cycle engines. Also, as explained earlier, turbine pressure ratios are kept as low as possible to limit the needed pump discharge pressures. Turbine pressure ratios in engines using these cycles are typically less than 2 to 1.

Turbine blade speed (by *blade speed* we mean blade tangential velocity) is a quantity that, in general, is sized to the maximum permitted by other turbopump design considerations. In the majority of cases, blade speed winds up being constrained to a value that is less than the designer would prefer from a pure turbine performance standpoint. In a direct-drive turbopump application, for example, centrifugal pump suction performance limitations will be very likely to constrain the shaft angular velocity. In a particularly high-power application with bearings placed between the turbine and the load, the *DN number* (which is the product of the bearing bore diameter in millimeters and the shaft speed in revolutions per minute) for the large bearings may be the limiting factor. In instances such as these, the turbine designer may have no option but to increase turbine pitch diameter to effect an increase in blade speed. However, due to the usually

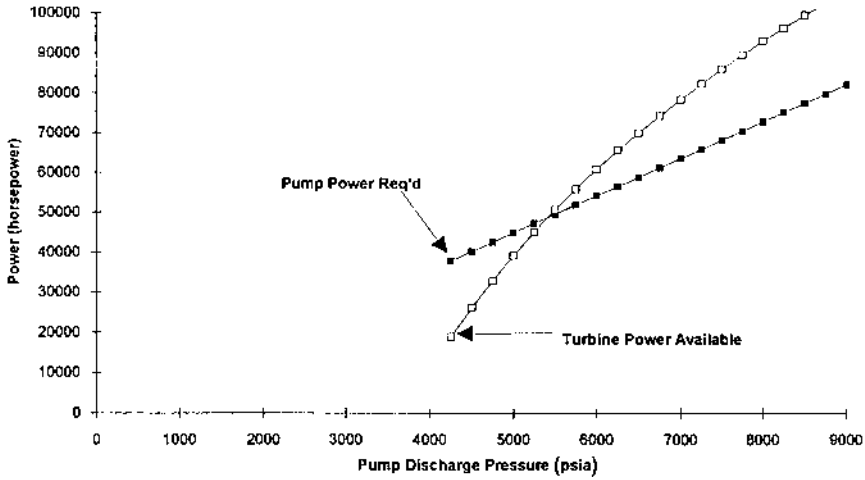

Figure 6 Staged combustion system, turbine power available versus pump power required (pump and turb efficiency = 95%).

strict weight and envelope limitations imposed, the available latitude for this option is quite limited. If blade speed remains constrained to a low value,

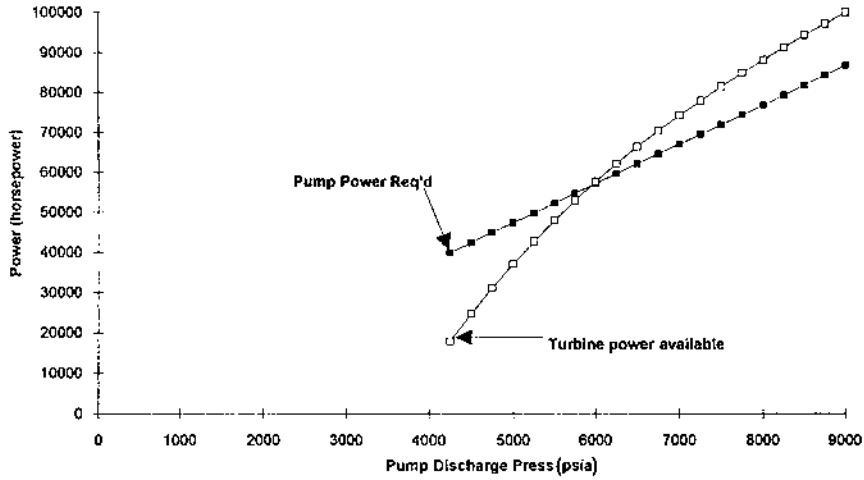

Figure 7 Staged combustion system, turbine power available versus pump power required (pump/turb efficiency = 90%).

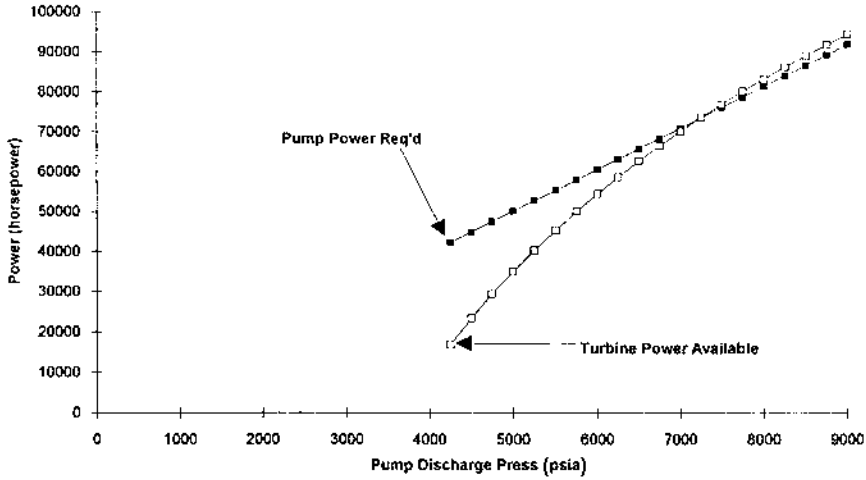

Figure 8 Staged combustion system, turbine power available versus pump power required (pump/turb efficiency = 85%).

and additional turbine performance is needed, other design refinements are employed. These are mentioned later. The mid-1950s, generation of gear-driven turbopumps probably allowed the turbine designer the greatest freedom in setting blade speed, since turbine speed was not directly related to pump speed. The relatively high turbine shaft angular velocities permitted by the gear-driven configuration resulted in a rather compact turbine package delivering relatively high efficiency (somewhat in excess of 60%). The Thor engine turbopump and its descendants are an example of these. It should be noted, however, that this "decoupling" of the turbine from the pump is obtained only at the expense of a large, heavy gearbox. As research efforts increased the suction performance capability of pumps, the increase in attainable pump shaft angular velocity was such that the gear reduction system could be eliminated.

In the engine definition and preliminary design phases, the turbine velocity ratio probably exerts more influence on turbine configuration than any other single quantity. *Velocity ratio* is a term that can be defined either for a single turbine stage or for a group of multiple turbine stages. The usual definition of velocity ratio is U/C_0, where U is the turbine blade tangential velocity (usually taken at the blade midspan for our purposes) when referring to a single stage. When referring to a multistage configuration, U represents the square root of the sum of squares of the tangential velocity of

each stage. The term C_0 represents the gas velocity corresponding to the isentropic enthalpy drop available to the stage (or the turbine). As one can see, increasing blade speed increases velocity ratio. Increasing pressure ratio, increasing inlet temperature, or simply employing a higher-energy working fluid at constant blade speed causes the velocity ratio to decrease. The velocity ratio quantity plays a major role in prediction of thermodynamic efficiency of a turbine as well as in the selection of turbine staging that is to be employed for best performance. As shown in Fig. 9, efficiency of a turbine stage is essentially a linear function of velocity ratio up to the point of maximum efficiency.

Consider the third curve from the left in Fig. 9, "1 row impulse staging." This curve represents, in a somewhat generalized fashion, the maximum efficiency to be expected from a single rotor impulse stage (also known as a DeLaval turbine, for its creator) as a function of the stage velocity ratio. It can be seen that maximum efficiency can be expected from this type of stage at a velocity ratio of 0.40–0.45. Rocket engines operating on the monopropellant and gas generator cycles typically operate with available pressure ratios high enough to drive the gas spouting velocity of a stage into the supersonic regime. As a rule, to obtain optimum stage velocity ratio, gas spouting velocities of this magnitude would require blade speeds that are not reliably attainable. With a single impulse stage, this would lead to depressed turbine stage efficiency. At low velocity ratios, low blade speed

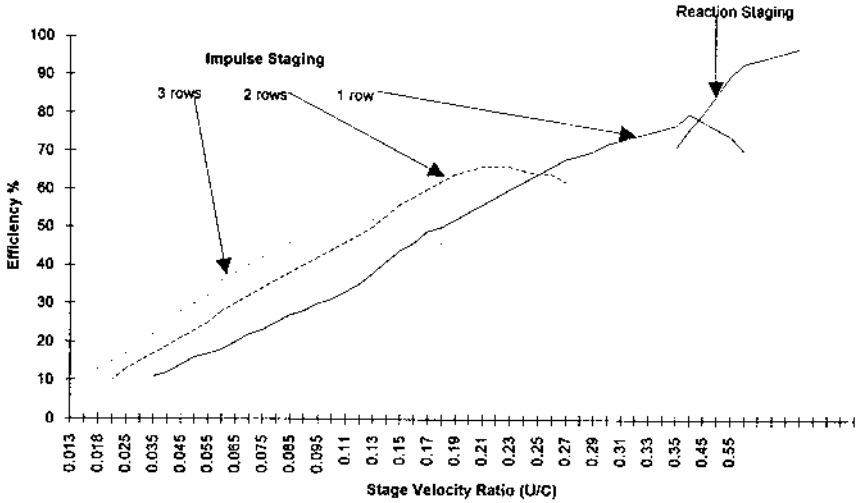

Figure 9 Turbine stage efficiency (total to static) versus stage velocity ratio.

causes low fluid energy extraction, since the magnitude of stage exit velocity is a relatively high fraction of the gas spouting velocity. In certain applications (typically low-power systems) this may be perfectly acceptable. However, if higher performance is required, this problem must be dealt with. A couple of methods exist for improvement of the situation.

The first of these entails the consideration of multistaging. As its name implies, this method consists of satisfying the turbine work requirement with two or more turbine stages coupled together in series. Each stage is designed to contribute a fixed percentage of the total turbine work. First-stage work fractions of 40–60% of total are representative. Each stage can then be analyzed separately. The effect of the reduced stage enthalpy drop will be to lower the C_0-term in the velocity ratio expression. This will raise the stage velocity ratio by an amount inversely proportional to the square root of the stage work fraction. For example, a two-stage design with a 50–50 work split would have a stage velocity ratio equal to $\sqrt{2}$ times the velocity ratio of an equivalent single-stage configuration. This idea could, in theory, be extended to include configurations with three or more stages, the number of stages and work distribution being determined by the target velocity ratio for each stage. In most instances, two turbine stages has proven a practical maximum. This has been due to constraints on size and weight as well as limited benefits to be had by a larger number of stages. In configurations with two turbine stages or less, the turbine mass can generally be overhung on the drive shaft outboard of a bearing. If the overhung mass is increased sufficiently (by the addition of stages), turbine rotor dynamics will be adversely affected, requiring a reduction of shaft angular velocity, and negating the benefit of the multistaging exercise. In that case, another bearing outboard of the turbine (see Fig. 10) would be necessary for satisfactory rotor stability. This bearing would require a separate supporting structure, as well as provisions for lubrication/cooling. Such a configuration would significantly increase the weight, complexity, and cost of the turbine package. Under such conditions, decisions on turbine staging must sometimes be made somewhat subjectively, and with less than complete information. Skill and experience are the key factors in success here. A representative procedure might consist of evaluation of analytically derived turbine performance maps for various staging schemes. The decision on number of stages could be made based on the smallest number of stages that produce a target efficiency. Alternatively, the number of stages could be cut off at a point where significant performance increases are no longer realized. What constitutes ''significant'' would, of course, depend on the application and would probably contain elements of judgment on the part of the designer. Turbines whose performance has been optimized by multistaging include the Thor engine turbine and its descendants, the turbine powering

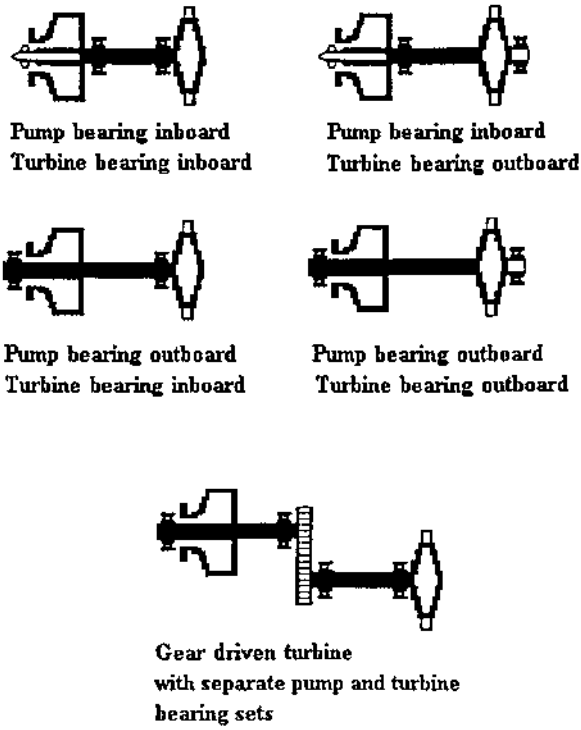

Figure 10 Some representative turbopump rotor bearing support configurations.

the Centaur engine (this is a high-performance expander cycle engine built by Pratt and Whitney), the turbines in the Titan 2, 3, and 4 launch vehicles (built by Aerojet General), as well as the high-pressure turbines in the Space Shuttle main engine.

In some cases, a turbine with a reasonable number of stages may still not be able to yield a stage velocity ratio that is to the designer's liking. A blade speed lower than desired is the usual cause and may be due to a number of factors. Direct-drive turbopumps (machinery with both pump and turbine on a common drive shaft) are the most frequent offenders, as the pump suction performance limitations constrain shaft speed in many cases. Higher-energy turbine working fluids may also play a role here, with increasing gas spouting velocities being available for a given turbine pressure ratio. In these instances, the designer may choose to replace a DeLaval turbine stage with a scheme referred to as a velocity-compounded stage, or a Curtis stage (named for Charles G. Curtis, who patented the

velocity-compounded arrangement in 1896). The fundamental difference between velocity-compounded stages and DeLaval stages can be seen in Fig. 11. The exit flow from the first rotor, still possessing considerable kinetic energy, is turned by a set of stator vanes, although no expansion is intended across these vanes. The flow then impinges on the second rotor, where additional work is extracted. Although additional rotor rows are certainly possible (and may be desirable under some circumstances), two velocity-compounded rows have proven sufficient in production units with which this author is familiar. If we refer to Fig. 9, we can see that at velocity ratios less than approximately 0.25, multiple-row velocity-compounded turbines can offer performance that is superior to that of a single rotor turbine. It should also be noticed that the peak efficiencies offered decrease as the number of rows increases due to higher frictional losses being absorbed by the increasing turbine wetted area. When designing a multiple-row velocity-compounded turbine, an issue of the work split between the rotor rows must be addressed by the designer. The exact work split will depend somewhat on the loading conditions for a particular design. However, it should be

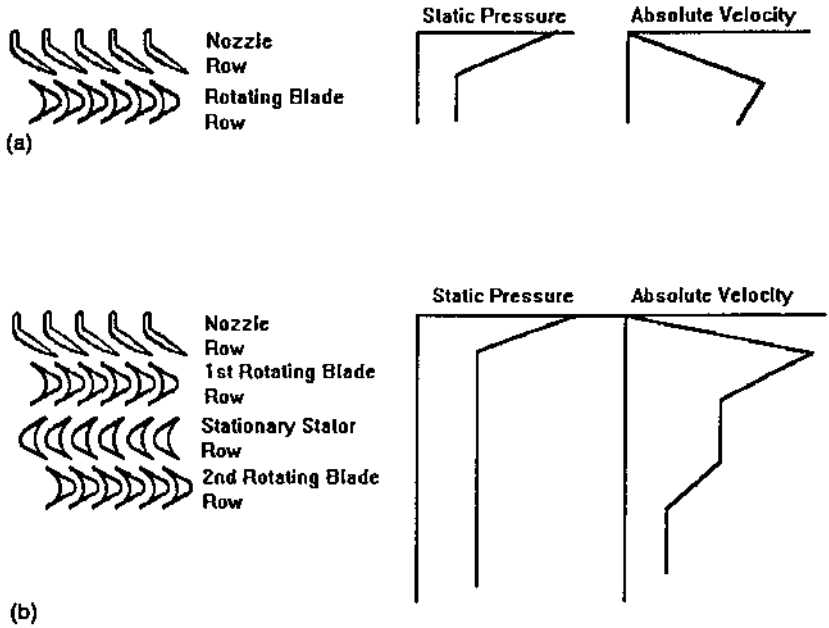

Figure 11 Arrangement of various turbine rotor/stator blade configurations: (a) single-rotor impulse stage, and (b) two-row velocity-compounded stage.

remembered that the second (and any subsequent) rotor rows depend on upstream rotor exit swirl for work-generating capability. Under these conditions, downstream rotor rows will be relatively low work rotors. For example, in a typical two-row velocity-compounded design, a rotor work split of 70–30 or 75–25 might be considered typical.

The staged combustion and expander cycles tend to place greater demands on turbine performance than the monopropellant or gas generator cycles. The performance of the gas generator cycle (a so-called open cycle by virtue of its atmospheric turbine exhaust) is relatively insensitive to turbine efficiency. However, the staged combustion and expander cycles (the so-called closed cycles) involve the turbine package quite intimately in the overall engine system. In this regard, the problems presented by the "closed" rocket engine cycles are not unlike the turbine component matching problem in jet engine design. Not only must the turbine package be capable of sufficient component level efficiency, but it must be "matched" to deliver this efficiency within the range of operation of the rocket engine system.

The first production engine incorporating a closed cycle was the RL-10 engine (also known as the Centaur engine for the stage that it powers) designed and built by the Pratt and Whitney Division of United Technologies. This engine operates on a classic version of the expander cycle and was shown schematically in Fig. 4. Incidentally, this engine has the honor of being the first production liquid-hydrogen-powered rocket engine in the world. As one can see from the figure, LH_2 is discharged from the fuel pump into the cooling circuit for the engine's combustion chamber and nozzle. The flow of heat energy from the chamber's combustion reaction is absorbed by the hydrogen, resulting in a substantial enthalpy increase (as well as a static pressure drop) at the exit from the cooling jacket. Now comes the tricky part. The enthalpy increase across the cooling jacket must be sufficient that the turbine enthalpy drop results in proper turbine performance with a turbine outlet pressure equal to the pressure required in the fuel manifold of the engine's injector. This is probably easier to absorb by looking at the figure than by giving a verbose discussion.

Since we try to minimize required pump discharge pressure in the closed engine cycles, the operating point of a typical expander cycle turbine will tend to be at a considerably higher velocity ratio than that of an open-cycle engine. In the case of the RL-10 (circa 1970), the use of two turbine stages permitted a stage velocity ratio of around 0.35. From Fig. 9, it can be seen that this value is near the optimum for an impulse stage. As a result, a turbine efficiency of almost 75% (total to static efficiency) was obtained. The relevant design conditions were a power output of approximately 660 hp at a shaft speed of 28,670 rpm with a blade pitchline velocity of approximately

740 ft/sec. The turbine pressure ratio at these conditions is approximately 1.4.

Expander cycle engines have been designed, built, and successfully operated by several major rocket engine manufacturers. One of these is (to this author) of particular interest. The engine in question is a prototype built by the Liquid Rocket Division of Aerojet General. This engine is powered by LOX/LH_2 and is in the 3,750-lb thrust class, to be used for an orbital transfer vehicle-type application. To obtain weight savings and reduce complexity in the LOX pump, an extension of the expander cycle known as the dual expander is employed (see Fig. 5). In this concept, the main combustion chamber is constructed separately from the nozzle. These two sections are mechanically joined together. As can be seen in Fig. 5, each section employs a separate regenerative cooling circuit. In this implementation, LOX is heated to a supercritical state in the main combustion chamber cooling circuit, while LH_2 is heated to supercritical conditions in the nozzle jacket. The resulting gaseous oxygen (GOX) (at a temperature of 860 °R) is used for turbine drive in the LOX turbopump, and GH_2 for fuel pump turbine drive. The advantage here is derived from the fact that the oxidizer turbopump is being driven by the same fluid as is being pumped. Whereas in oxidizer pumps being driven by a hot-gas turbine (where the hot gas is generally hot fuel) an elaborate shaft sealing system with inert gas purges is necessary to isolate pump and turbine fluids, the dual expander cycle eliminates this requirement.

The other example of a closed engine cycle that we wish to discuss is the staged combustion cycle. At the time of this writing (January 1993) the only example of this type of engine that is in production in the United States is the Space Shuttle main engine. Japan is in the final stages of development of a staged combustion engine (the LE-7, which is also powered by LOX/LH_2). Actually, it appears (to this author) that the former Soviet Union possesses the greatest experience with this type of engine cycle, having been in production of at least three different models for a period of nearly 30 years.

The staged combustion cycle is shown schematically in Fig. 3. Please note that this cycle, like the expander cycle, places the turbine(s) in series with the main combustion chamber. However, unlike the expander, the staged combustion cycle also places a gas generator (referred to in this cycle as a preburner) between the pump discharge and the turbine package. Also note that two independent preburners may be employed, as is done in the Space Shuttle main engine. Together with LOX throttling valves at the inlets of both preburners, this arrangement gives independent control of both main combustion chamber pressure and engine mixture ratio. When coupled with a high main combustion chamber pressure target, this cycle can place

the greatest demands on turbopump performance of all the classic engine cycles. The ''stacking'' of two or three relatively high-pressure drop items between the pump discharge and the main chamber (throttling valve, preburner injector, and turbine in this instance) gives rise to pump outlet pressure demands that are two to three times the main combustion chamber pressure. However, the mechanics of this cycle can also allow the turbine designer a latitude of design that is lacking in the closed engine cycles. Due to high pump outlet pressure requirements, high turbine blade speeds are generally specified. Also, since the turbine mass flow rates are higher than open-cycle engines (remember, most or all of the fuel is used for turbine drive), the enthalpy drop per pound of working fluid is smaller than in open cycles. The result of these factors is a stage velocity ratio that is generally the highest of the conventional engine cycles. An alternate way of looking at this is through the use of the *speed-work parameter*. This parameter is essentially the ratio of the blade speed squared to the actual enthalpy drop of the stage. As such, it constitutes a sort of energy ratio term, as opposed to the velocity ratio term we have used here.

Regardless of which of these indices is used, the increased available turbine working fluid and the reduced specific work required (compared to an open cycle under the same conditions) result in the opportunity to unload the turbine stage significantly. This manifests itself in higher attainable stage velocity ratios. In the case of the Space Shuttle main engine, for instance, the turbines for both high-pressure turbopumps operate in the velocity ratio range of 0.40–0.50. As one can see from Fig. 9, this is within the range where reaction-type blading can be used to good advantage. Also, this range of operation results in turbine nozzle spouting velocities that generally are subsonic through the machine's operating range. This factor has the effect of reducing the magnitude of the losses in the stage. These losses are due in part to nozzle expansion, blade inlet incidence, and kinetic energy losses traversing the blade row. These losses are proportional to the Mach number of the flow relative to the inlet of the rotating blade row. Lowering the blade inlet Mach number reduces these losses, contributing to higher stage efficiency. Also, subsonic blade inlet conditions permit the use of relatively generous radii on the blade leading edges. In supersonic stages, sharp inlets are generally considered necessary to minimize the effects of shock wave formation at the blade row inlet. These shock waves can restrict flow through the blade row, and adversely affect the stage performance. Larger radii are less sensitive than sharp-edged inlets to the effects of nonzero incidence. As a result, incidence losses can be minimized over a fairly wide flow range with a properly designed subsonic stage.

The turbine that powers the high-pressure fuel turbopump of the SSME employs two reaction stages, with a degree of reaction of

approximately 35% each. Although the turbine efficiency is quoted at approximately 78%, there is evidence from various cold-flow component tests that the actual turbine aerodynamic efficiency is in fact in the mid-80s percent range. The observed efficiency penalty is primarily due to leakage flow through various seals and turbine coolant paths. These are accepted for the sake of improved packaging. Also, the lack of a turbine outlet pressure measurement in the flight hardware configuration makes determination of actual turbine performance very difficult and subject to certain inferences.

In the preceding discussions, it has been assumed that the turbine working fluid enters the rotating blade row around its entire circumference. With the bulk of rocket engine turbines, this is certainly the case. However, some low-power systems may have unique requirements. If the turbine power required is low enough, and the turbine working fluid specific energy is high enough in comparison, then the working fluid flow rate required becomes "small." When this happens, the rotor annulus area becomes small, as determined by the equation of continuity. As a result, turbine blade heights can become quite small. When this occurs, the wetted areas of the hub and tip end walls can increase to the extent that boundary-layer losses on these end walls become a large fraction of total blade row losses. Also, fabrication limitations make it impossible to reduce blade tip-to-housing clearances below a certain absolute value. When blade tip clearances become a significant fraction of the blade height, excessive blade tip leakage can result. These two phenomena can bring about large decreases in turbine performance. In order to keep blade heights reasonable, the turbine inlet manifold can be arranged so as to limit the entry of working fluid to only a portion of the rotor circumference. This portion of the rotor into which drive fluid is entering is known as the *arc of admission*. A turbine operating with an arc of admission of less than 360° is known as a *partial-admission turbine*. It is the task of the turbine designer to adjust both the arc of admission and the rotor diameter such that the best compromise of all design factors is obtained, resulting in minimum losses and maximum efficiency. The design factors we refer to here include normal loss mechanisms, as well as some losses unique to the partial-admission scheme. We attempt to touch on the highlights of these partial-admission unique losses.

It is this author's impression that the losses unique to partial-admission turbines are not quantified particularly thoroughly in the literature, undoubtedly due to the complexity of the mechanisms involved. However, for the purposes of this discussion, these losses can be approximated as falling into two main categories. The first of these is what I refer to as the *fill and drain loss*. When two adjacent turbine blades are moving through an inactive portion of the nozzle arc, the intended

momentum exchange between working fluid and rotor is not taking place, and the blade passage is filled with fluid that may be thought of as stagnant. As the blade passage begins to encounter the active portion of the nozzle, the "high-"energy working fluid entering the passage must displace the "stagnant" fluid before the intended momentum exchange can occur. When the blade passage leaves the active nozzle arc, an analogous process occurs. The "high-energy" fluid that is resident in the blade passage when the passage just leaves the nozzle arc can undergo diffusion while traversing the passage, thus lowering the net momentum exchange. The smaller an individual arc of admission, the larger the role these losses assume as a percentage of the total intended energy exchange. For this reason, the active nozzle arc fraction should be made as large as possible. This could take the form of consolidating several "small" arcs into a single "large" arc. Further enlargement would require a decrease in rotor diameter so that the required annular flow area would be maintained. However, a decrease in rotor diameter lowers the stage velocity ratio, which, as described earlier, tends to reduce stage efficiency. If efficiency is of concern, an iterative design/analysis process would be needed to optimize the rotor diameter/nozzle arc combination. General trends in this situation are illustrated in Fig. 12. This figure illustrates the effects of varying nozzle arc configurations on stage efficiency. Additionally, a single "large" arc is preferable (from a thermo/fluid mechanic standpoint) to several "small" arcs. However, a single arc (or any nonsymmetrical admission) imposes a net bending load on the rotor. The ability of the rotor and bearings to react to this type of load should be checked as part of the design process. If this load is found to be excessive, a more nearly symmetrical nozzle arc may need to be substituted.

The second major type of partial-admission loss is what may be termed a *rotor pumping loss*. As the rotor blades traverse the inactive portion(s) of the nozzle arc, the blade flow passages are immersed in "low-energy" fluid. The rotor blades (and to a lesser extent the turbine disk) behave in this instance like a radial-flow pump, imparting a tangential component of momentum to the fluid. This pumping action absorbs turbine power, detracting from the rate of shaft work generation. This parasitic loss is calculable from basic Euler considerations if the velocity distribution across the disk and blades as a function of radius is known. Unfortunately, the vortex flows associated with fluid adjacent to a rotating disk (the geometry of which is variable) is an extremely complex problem and must be modeled at a very fundamental level to be solved effectively. Consequently, no general forms of "pumping loss" correlations exist to this author's knowledge.

Contemporary examples of partial-admission turbines in rocket engine systems include the turbine in the Agena engine (a highly successful 16,000-

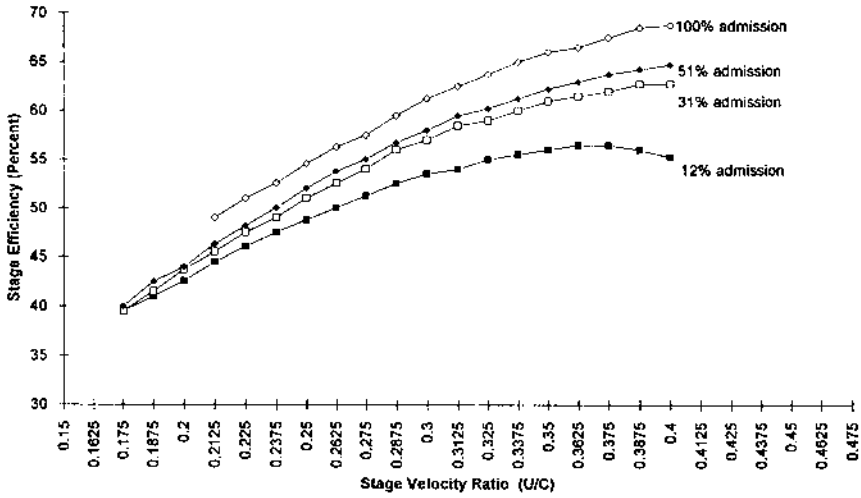

Figure 12 Stage efficiency versus velocity ratio, for a typical turbine stage with four different arcs of admission.

lb thrust engine built by Bell Aerosystems, a division of Textron), the low-pressure-fuel turbopump of the Space Shuttle main engine (built by the Rocketdyne Division of Rockwell International), and the turbine for a version of the XLR-132 (a 3,500-lb thrust orbital transfer vehicle-type engine) also built by Rocketdyne.

Although by no means common in rocket engine applications, another type of turbine that seems to be finding a niche is the hydraulic or liquid-driven turbine. Considering the direction of evolution of system design, hydraulic turbines may become more frequently used in the future.

The place that hydraulic turbines are carving for themselves is as a power source for a small, specialized type of turbopump referred to as a *boost pump* or *low-pressure pump*. These pumps were essentially nonexistent in rocket engines prior to the late 1960s and made their first appearance in a production engine on the Space Shuttle main engine, whose design dates to approximately 1971–1972. Prior to this time, traditional design practice used a single turbopump unit for each propellant. This turbopump ingested its pumped fluid at propellant tank pressure and raised its pressure (in either one or several stages) to the discharge pressure required for engine operation. The advent of the SSME, with its unprecedented turbopump pressure and weight requirements, caused a search for a better method.

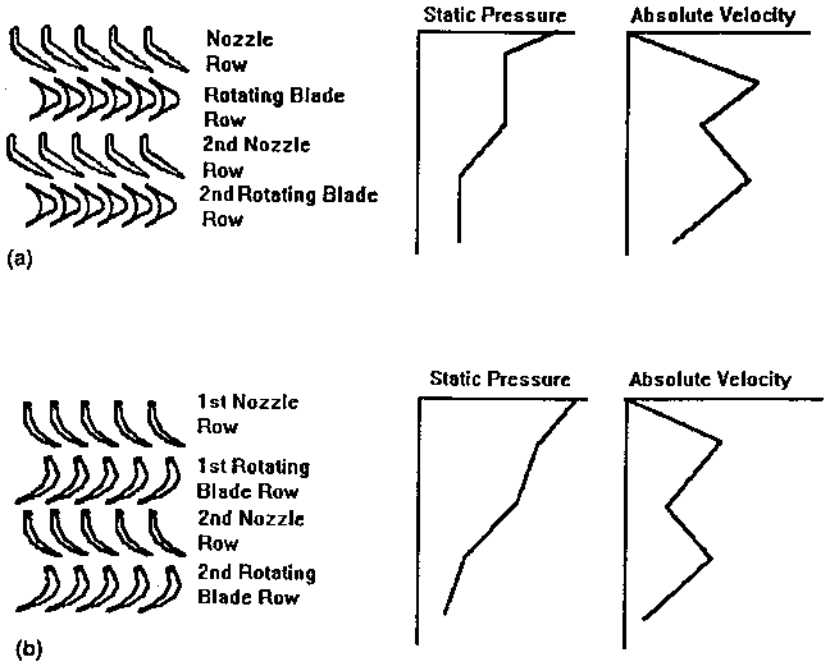

Figure 13 Arrangement of various turbine rotor/stator blade configurations: (a) two-stage pressure-compounded impulse, and (b) two-stage reaction.

Consider the turbopump requirements for a portion of the SSME liquid oxygen system. To support thrust chamber operation, the main pump stage of the high-pressure oxidizer turbopump must maintain a discharge pressure of approximately 4,000 psi at a flow rate of around 900 lb/sec. The liquid oxygen tank pressure at the engine inlet is maintained in the vicinity of 100 psi, with an excursion down to about 20 psi partway through the powered flight. A single liquid oxygen pump capable of supporting inlet pressures as low as 20 psi, and maintaining the needed discharge conditions would result in a machine that is larger, heavier, and less efficient than the engine requirements would allow. Further, it was found that if the LOX pump inlet pressure could be raised to the vicinity of 300 psi, the turbopump design could be optimized for a much more compact machine capable of operating at a much higher speed. Although 300 psi was clearly unreasonable for a propellant tank pressure, it was easily attainable with the use of a small turbopump upstream of the main LOX pump to boost the propellant

pressure from the 20–100-psi level to the 300-psi level. Thus the low-pressure oxidizer turbopump (LPOTP) was born.

The turbine drive concept for the LPOTP is based on the idea that the turbine power for this pump is very low, constituting less than 2% of the total pumping power of the engine system. A hot-gas drive system for the LPOTP turbine would have required an extensive shaft seal system within the pump to prevent comingling of the LOX and fuel-rich hot gas. Additionally, transport of hot gas to the LPOTP turbine drive area would be quite challenging. Since the engine thrust chamber must swivel for steering, and with the LPOTP fixed rigidly to the shuttle orbiter structure, a flexible duct arrangement for LPOTP turbine drive would be necessary. For devices with high power requirements, these challenges would be accepted. However, for the LPOTP turbine, hot-gas drive schemes very quickly overwhelm what should otherwise be a relatively simple task. On the other hand, another source of high-pressure fluid is more readily available—the high-pressure oxidizer turbopump itself. The liquid oxygen exiting the main pump is at a pressure sufficient that a reasonable quantity could provide the work required for the LPOTP function when used to run a suitable liquid-operated turbine. In addition, since the turbine drive fluid and the pumped fluid are the same medium, shaft sealing needs in this application are minimal, being only concerned with preventing gross internal leakage. Also, the prevailing conditions permit the turbine exit pressure to be set at the level of the pump outlet pressure, with the result the both turbine and pump fluids are discharged into the same outlet duct. A simpler arrangement would be very difficult.

A boost pump operated by a hydraulic turbine again found an application in the small dual-expander cycle engine built by Aerojet-General that was mentioned earlier. Due to the small size of the engine and the relatively high LOX pump discharge pressure needed (4,600 psi), it was again found that a dual turbopump arrangement had the potential for better system packaging and performance. In this application, the ''low-pressure'' pump raises the oxidizer pressure by approximately 40 psi to support high-speed operation of the ''high-pressure'' LOX pump. This ''high-pressure'' pump takes the form of a two-stage centrifugal pump, with an inducer upstream of the first-stage impeller. A portion of the inducer discharge flow (approximately 30% of main pump flow) is diverted to the low-pressure pump turbine manifold, where it drives a small hydraulic turbine. This arrangement carries with it all the advantages mentioned in the preceding paragraph.

With these two examples of hydraulic turbine application now clearly proven, this configuration offers a very practical alternative in the problem areas relating to high pump head rise coupled with very low vehicle tank

pressure levels. As long as combustion chamber pressure targets continue to rise, and the desire for lighter vehicle tankage results in decreasing tank pressure budgets, the low-power hydraulic turbine drive concept will continue to be viable, especially for pump applications that involve highly reactive fluids.

I would like to say a word regarding references outside this book for additional reading. The National Aeronautics and Space Administration publishes two documents that should satisfy most readers' needs. The first is a special publication identified as NASA SP-8110 and is titled (appropriately enough) *Liquid Rocket Engine Turbines* 1. Besides touching on a variety of specialized considerations relating to design details, this document also presents a design method that is both simple and successful. The method consists of computing total fluid states at the inlet and exit of nozzle and blade rows, and modifying isentropic computations using lumped parameters known as *loss coefficients*. These loss coefficients account for the major mechanisms of nozzle and blade row losses. Considerable test data exist to substantiate them, and this method has been used to design quite a number of successful turbines for both production and research and development work. This method was introduced by H. D. Emmert. Incidentally, although Emmert's method and data were originally intended for gas turbines, firsthand experience shows that they are also applicable to hydraulic turbines, where the designer substitutes the total liquid head for total enthalpy in the design procedure.

The other reference that I heartily recommend is another NASA special publication. This one is identified as NASA SP-290, titled *Turbine Design and Application* 2. This document is a three-volume set. It is written by the Lewis Research Center and covers all major aspects of turbine technology in considerable detail. Most interesting to this author is the derivation of expressions that are analogous to Emmert's loss coefficients.

ROCKET PROPULSION SYSTEMS—PUMPING ELEMENTS

This section begins our discussion of pumping elements in rocket propulsion systems. In this section, we will discuss the most common types of pumping devices used in rocket systems. These are the centrifugal pump, the axial-flow pump, and the inducer. Our discussions will include areas in which the above three types of pumps are similar, areas in which they differ markedly, and examples of the applicability of each in rocket systems.

Before we discuss the various pumping machinery in detail, a few general remarks regarding the rocket engine system and the pump's role in that system are appropriate.

A liquid rocket engine system (like any complex system) begins its life through a series of trade studies, which progress to ever-finer levels of detail. At some point in the system-level study and design process, a document referred to as a Power Balance Model (or simply an "Engine Balance") is generated. This document is simply a pressure and flow schedule through the various flow paths in the engine system. It incorporates all the agreed-upon engine system boundary conditions (propellant tank pressures in a launch vehicle, for example). In the Power Balance Model, the required propellant flows through each piece of turbomachinery in the engine system are stipulated, along with the total pressure rise of each pump, as well as an efficiency threshold if one is applicable. In the case of an engine system that must be capable of variable thrust, the system pressure and flow schedule at several different operating points is normally published. The performance specifications in the Power Balance Model become the requirements to which the turbomachinery must adhere. When turbomachinery component design has progressed sufficiently to permit its performance characteristics to be approximated, these characteristics are incorporated into the Power Balance Model in order that engine system performance at off-nominal operating points may be computed.

At this point it would be instructive to review one of the fundamental sizing parameters that the pump designer uses for guidance. This is the specific speed, or N_s. N_s is defined as follows:

$$N_s = \frac{NQ^{1/2}}{H^{3/4}} \tag{1}$$

Where

N = pump shaft speed, in revolutions per min.
Q = pump flow rate, in gals per min.
H = pump head rise, in ft-lb_f/lb_m (often abbreviated simply as ft).

When values are assigned for the three variables above, and N_s is computed, the resulting quantity acts more than any other single parameter to fix the geometry of the pump stage and its efficiency potential. Various types of pumping elements (i.e., centrifugal flow, axial flow, Barske, vane pumps, etc.—see Fig. 14) have various ranges of N_s over which they are most applicable. The pump designer's first job is to make a decision regarding the type of pumping element(s) that are most appropriate for a given application. This often necessitates a small trade study of more than one possible configuration. The various alternatives defined from this study are then evaluated for ability to meet the system's requirements, as well as any particular constraints that the system may impose. It is often the case that

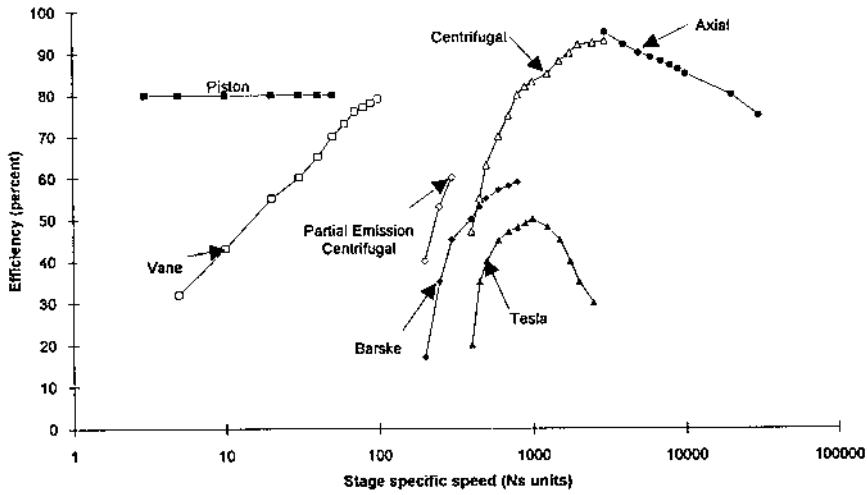

Figure 14 Approxmate values of pump stage efficiency versus stage-specific speed.

one or more candidate configurations will perform more or less equally well, and the choice must then be made according to the skill and experience of the designer.

The reader should note that, of the three variables that fix the N_s parameter, two of them (the pump flow rate Q, and the pump head rise H) are specified by the engine system Power Balance Model, and thus are outside the control of the pump designer. It should now be apparent that the designer's freedom in sizing of a pumping element is very limited, and in many cases barely exists at all. The only input to the pump N_s parameter over which the designer has control is the pump shaft speed [the "N" term in Eq. (1)]. The designer must then use the shaft speed to appropriately set the N_s parameter for a given type of pumping element that is under consideration. Sometimes, the designer may have the freedom to set the pump speed to a value that is at or near the hydrodynamic optimum for a given type of pump configuration. However, more often one or more other items (available pump suction performance, rubbing speed of seals, rotordynamic considerations, etc.) will conspire to limit pump speed such that N_s is set to a value lower than desired.

Although the N_s parameter does not correlate to anything physical in an "explicit" sense, it can give great insight into both the geometry and performance of a pump (or pump stage) if thought of in a "relative" sense. For example, consider a "low" specific speed pump stage. From the terms that make up the N_s-term, we can say the following: a "low" N_s pump

operates at a relatively low volumetric flow rate (particularly in comparison to the head rise imparted). Conversely, the "low" N_s pump operates at a relatively high head rise, in comparison to the flow rate being processed by the pump. Lastly, the "low" N_s pump operates at a relatively low operating speed. Although we have not quantitatively defined what "low" means in each of the above references, it should be thought of as "low" in comparison to the hydrodynamic optimum under the conditions in question.

As with many other generalized design parameters, specificity in the interpretation of N_s is quite important. For example, in a single-stage centrifugal pump, a particular reference to N_s may refer to either the impeller alone, or to the entire pump, and the actual N_s of each of these will be different. Likewise, a very high head multistage pump may have a low N_s for the entire pump (Fig. 15), while having individual stages with quite favorable
N_s-values. When N_s data are being generated, studied, or exchanged, written reference in regard to the point of reference of these data should be considered mandatory.

We shall see in our upcoming detailed discussions that typical liquid rocket engine systems are relatively "low" N_s environments. That is, liquid rocket systems tend to demand relatively low volume flow rates of propellants at relatively high pump head rises. This is true of even large

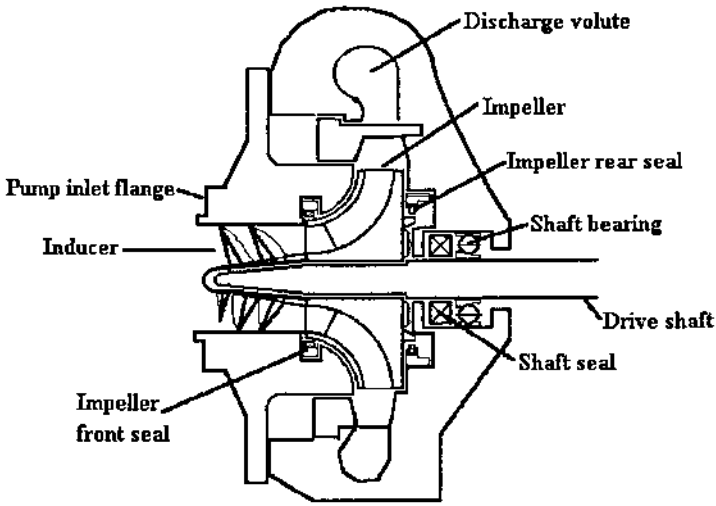

Figure 15 Elements of a typical centrifugal pump. For details see Figs. 15a through 15l.

liquid rocket engine systems, and even more so for smaller engine systems (systems of less than 50,000 pounds thrust, for example).

Both general categories of pumping elements—positive displacement and variable displacement—are, at least in principle, applicable to liquid rocket systems. Which category, and what type within a given category, is a function of the thrust level of the engine system (and therefore its propellant demands) and the system's operating pressure levels.

Positive Displacement Pumping Elements

The category of pumping elements known as "positive displacement" is best recognized as piston pumps, vane pumps, and their derivatives. This type of machinery is commonly encountered in commercial air compressor systems, refrigerant pumps/compressors in air conditioning systems, pumps in hydraulic systems, and other applications. We can note from Fig. 14 that positive displacement pumps occupy the lower-most portion of the specific speed range. In particular, pump specific speed parameters of less than 100 (in rev/min, gal/min, ft units) are best served by positive displacement pumping machinery.

A simplified cross section of a typical positive displacement pump is shown in Fig. 15(a). This pump consists of a piston that reciprocates within a cylinder assembly. The rotating crankshaft and the attached connecting rod provides the reciprocating motion. The pump's interface connections with the fluid system that it services are separate inlet and outlet ports, each connected to the pump cylinder through a check valve. During the intake stroke, the cylinder is filled with a volume of fluid equal to the cross-sectional area of the piston multiplied by the length of stroke of the piston. During the ejection stroke, this same volume of fluid is displaced into the outlet system. This intake–ejection cycle is repeated at the rotational frequency ω of the crankshaft. The result is a mass flow rate from the pump

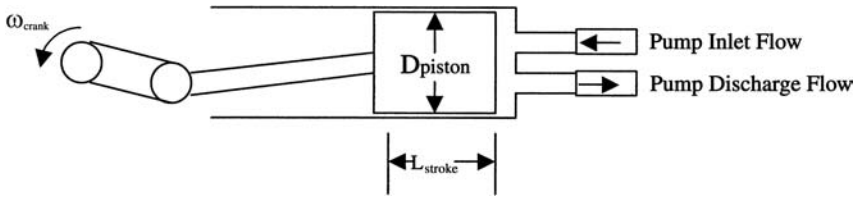

Figure 15a Typical positive displacement pumping element.

that is given by

$$\dot{m} = \rho\pi \frac{D_{\text{piston}}^2}{4} L_{\text{stroke}} \omega_{\text{crank}} \tag{2}$$

Where

ρ = fluid density.
D_{piston} = diameter of piston face.
L_{stroke} = length of piston stroke.
ω_{crank} = crankshaft rotational frequency.

For the sake of completeness, it should be noted that the volume of fluid ingested by the pump on its intake stroke is not quite equal to the cylinder volume, but is decremented somewhat by multiplying by a volumetric efficiency term η_{vol}, which has a value of less than unity. An in-depth explanation of η_{vol} is beyond the scope of this text; however, the value of η_{vol} is chiefly a function of ω_{crank} (in the form of an inverse proportionality) as well as the flow area of the inlet port.

From the standpoint of hydrodynamic performance, we can make the following observations regarding the function of the positive displacement pump in Fig. 15(a):

First, the rate at which mass is processed by the pump is determined only by the rotating speed of the crankshaft, ω_{crank}.

Second, for a given crankshaft rotating speed, ω_{crank}, the pressure at the discharge of the pump is determined uniquely by the pressure–flow characteristic of the system into which the pump discharges. In particular, the pump will generate whatever pressure is required to force the pumped flow rate (determined by ω_{crank}) through the downstream system. This relationship will be satisfied until the pump power required begins to exceed the power available from the prime mover that is operating the pump's crankshaft. After this point is reached, if further increases in discharge pressure are brought about, the crankshaft speed ω_{crank} will adjust itself such that the power available from the prime mover at the new speed will equal the pump power required. The new pump speed, flow rate, and head rise can be solved for quite readily using various iterative techniques.

Third, for a given crankshaft rotating speed, ω_{crank}, changes in the pressure–flow characteristic of the downstream system will not affect the flow rate processed by the pump. The pump discharge pressure will adjust itself so as to match the required pressure for the flow rate being moved through the system. However, mass flow will remain constant up to the point where the power constraint mentioned

above becomes a factor. This statement is sort of a "hybrid" of the above two observations but serves as an alternate way to picture the same process.

An interested reader who researches the marketplace of positive displacement pump products will find variations on the simplified picture of Fig. 15(a) which allow variations in pump flow rate. However, it should be understood that these are modifications of a machine whose basic tendencies are as described in the above paragraphs.

Variable Displacement Pumping Elements

Dominating the specific speed spectrum from a "low" value on the order of 200 (rpm-gpm-ft units) to values in excess of 10,000 is the class of pumping elements broadly known as *variable displacement pumps*. These machines are also referred to as "dynamic" or "rotodynamic pumps." Centrifugal pumps and axial-flow pumps both fall into this general class, as well as a broad range of "in-between" pumps that are neither purely centrifugal or axial. These "in-between" pumps are often referred to as "mixed-flow" or "Francis" pumps.

Shown in Fig. 15(b) is a generalized rotor of a hypothetical variable displacement pump. This rotor has a radius r_1 at its inlet, and a radius r_2 at its outlet. These radii may be equal, or the outlet radius r_2 may be somewhat greater than r_1. The rotor is being turned about the axis of rotation as shown, at an angular velocity ω, requiring a torque T to maintain this velocity. For this example, our rotor is assumed to consist of a single row of moving blades. In the case of multiple moving rows, most real machines intersperse stationary rows between the moving ones. In these cases, the accounting procedure is slightly more involved than that presented here, but not different in generality.

Fluid is flowing steadily through this rotor at a mass rate $\dot{m}$. Fluid enters the rotor in the plane of the radius r_1, with a "bulk" or "through-flow" velocity C_{m1}. This velocity is also referred to as a "meridonal" velocity. In addition to C_{m1}, a component exists in the tangential direction, C_{u1}. The velocity component C_{u1} is often equal to zero. If not equal to zero, C_{u1} is normally in the same direction as rotor rotation and is known as "prewhirl." In cases where prewhirl exists, it is normally generated by the designer for some particular reason. This topic will be discussed in more detail in a subsequent section.

Fluid leaves the rotor in the plane of radius r_2, with a "meridonal" velocity C_{m2} (note that C_{m2} may have a radial component, depending on whether or not the inlet and exit radii are unequal). In addition, a tangential

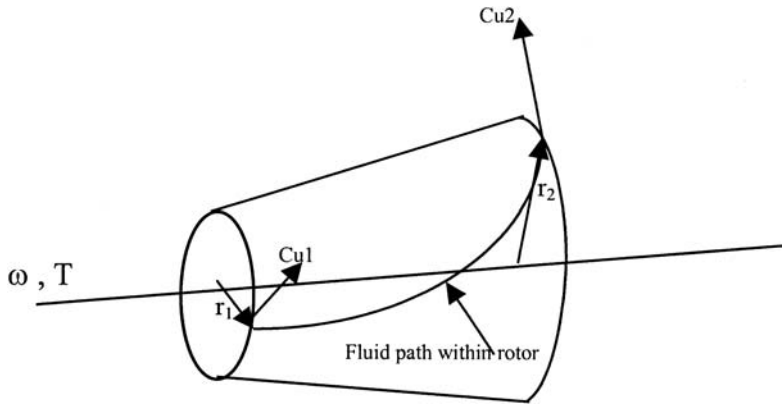

Figure 15b Generalized variable displacement pump rotor.

velocity component C_{u2} exists at the exit. The velocity component C_{u2} is greater than its corresponding component at the rotor inlet (C_{u1}). This fact alone distinguishes the rotor as a pump. (If we were describing a turbine, $C_{u2} < C_{u1}$.)

In the third previous paragraph, it was stated that our rotor requires an applied torque T to maintain its angular velocity ω. For this to be necessary, a resistive torque must be present on the rotor in a direction opposite to the applied torque T. What is the source of this resistive torque? For an answer, we must reexamine the fluid velocity vectors at the rotor's inlet and outlet.

At the rotor inlet station (the plane of radius r_1), the fluid possesses a velocity component C_{u1} in the tangential direction. This means that, with respect to the location of the rotational axis, a unit mass of the fluid possesses an angular momentum (or "moment of momentum") about the rotational axis that is equal to $AM_1 = r_1 C_{u1}$.

At the rotor outlet station (in the plane of radius r_2), the fluid's outlet velocity possesses a component C_{u2} in the tangential direction. At this location, the angular momentum of a unit mass of fluid becomes $AM_2 = r_2 C_{u2}$.

One of Newton's laws can be paraphrased as, "A force applied to a body will produce a change in its linear momentum." If we transform this idea from a "translational" sense to a "rotational" sense, the following adjustments must be made:

1. "Force" becomes "torque."
2. "Linear momentum" becomes "angular momentum."

We can then state (correctly) that, "A torque applied to a body will produce a change in its angular momentum." In the case of steady flow through a control volume that consists of our rotor, this can be written as

$$T = \dot{m}(r_2 C_{u2} - r_1 C_{u1})/g \tag{3}$$

We also know that the applied torque, T, multiplied by the rotational speed ω gives the required power:

$$\mathrm{P} = T\omega = \dot{m}\omega(r_2 C_{u2} - r_1 C_{u1})/g \tag{4}$$

Notice above that the quantities ωr_2 and ωr_1 are the tangential velocities (normally designated as "u") of the rotor at the respective stations.

Substituting the local rotor speeds u_1 and u_2 into Eq. (4) gives us

$$P = \dot{m}(u_2 C_{u2} - u_1 C_{u1}) \tag{5}$$

We should also note that the delivered power P is the rate at which work enters the fluid in its travel through the rotor. More specifically, a suitable statement of the First Law of Thermodynamics says that the rate at which work enters the fluid can be equated to a change in a fluid called *enthalpy*:

$$\frac{P}{\dot{m}} = \Delta_1^2 h_0 \tag{6}$$

where h_0 is the quantity called *stagnation enthalpy*, and the right-hand side of the above equation depicts a change from station 1 (rotor inlet) to station 2 (rotor outlet). For working fluids that are gases, this is a conveniently calculable (from measurements) property. However, for pumps that move liquids, enthalpy changes are not so easily measurable. For this reason, the energy equation is rearranged slightly so as to substitute for enthalpy the sum of internal energy (denoted as u, and not to be confused with rotor speed) and the "pressure energy," or 'head,' denoted as P/ρ where P and ρ represent static pressure and density, respectively. For a liquid pump, if the pumped flow can be approximated as incompressible (as is the case with most rocket pumps to a fair approximation), the change in internal energy between inlet and exit states can be neglected, and h_0 becomes simply the change in stagnation energy, or "head."

If we now combine Eq. (5) and (6), we can write

$$\Delta h_0 = (u_2 C_{u2} - u_1 C_{u1})/g \tag{7}$$

Equation (7) is known as Euler's equation. Unless stated otherwise, this chapter assumes flow to be incompressible, and therefore h_0 is taken to be stagnation "head." It should be pointed out, however, that for any given example this limitation could be relieved by simply interpreting h_0 as

stagnation enthalpy, and using h–S diagrams to illustrate the thermodynamic process of the pump.

If the inlet conditions of a pump rotor are known (the conditions at station 1 in Euler's equation) and the total pump stage head rise requirement is known, the required change in fluid tangential velocity can be computed from Eq. (7) so as to satisfy the pump rotor's total head rise requirement.

Two Ways of Looking at the Work of a Variable Displacement Pump

The computation of the work input to (or done by) a variable displacement pump can be approached in numerous different ways. Since each approach must yield the same result if each approach is correct, equating the two approaches to each other yields some interesting insights.

The Variable Displacement Pump as a Thermodynamic Machine

The preceding development of Euler's equation clearly shows the methodology for describing the variable displacement pump as a thermodynamic machine, or "transfer function." Equations (6) and (7) show that the change in stagnation "head" of a unit fluid mass across the rotor is equal to the work input (this is true no matter what the efficiency of the rotor). In addition, the power expended to drive the rotor is equal to the rate at which unit masses are processed by the rotor, multiplied by the work input to each unit mass, i.e.,

$$\text{Power} = \dot{m}\Delta h_0 \tag{8}$$

Equation (8) is the standard definition for power expended for a pumping device (neglecting inefficiencies).

The Variable Displacement Pump as an Aerodynamic Machine

The other approach we wish to explore for insight into variable displacement pump performance involves the pump (the rotor only, in this discussion) as an aerodynamic machine. Although the following discussion depends somewhat on ideas developed in a subsequent section, the material should not prove painful.

Figure 15(b) shows only the "outside shell" of a typical rotor, along with the inlet and outlet velocity vectors. Figure 15(c) shows a cut-away of the rotor through a plane perpendicular to the rotating axis. From the figure, it is evident that the inside of the rotor contains a cascade of blades. Although eight blades are shown in the figure, this number is notional only.

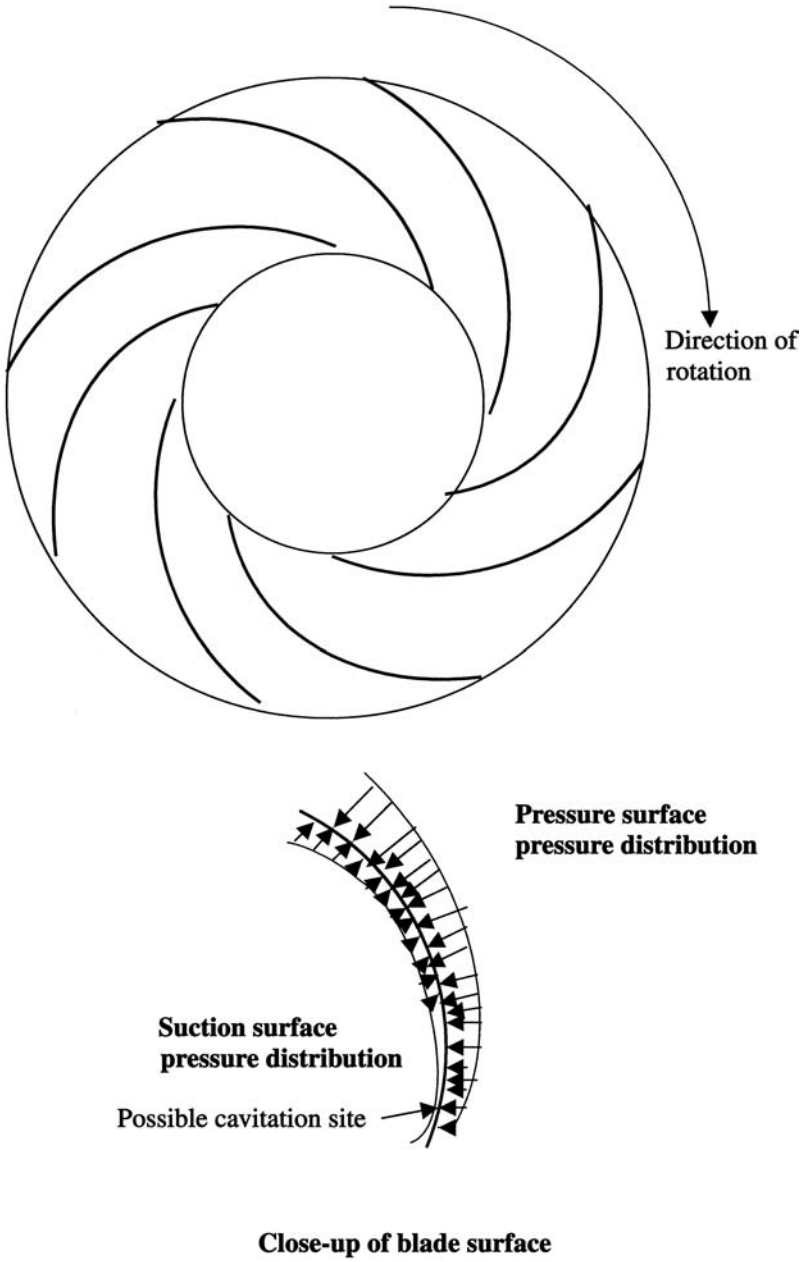

Figure 15c Typical 2-D centrifugal impeller plane view.

Real rotors may contain varying numbers of blades, with the exact number being determined specifically for each rotor application. The blades are designed so that the blade leading edges intersect the incoming flow "smoothly" ("smoothly" is defined in a subsequent section). The blade trailing edges are designed so that the fluid leaves the rotor in a specific direction relative to the rotor, with this direction being defined by the direction of the vector **W**. In addition, the blade section between the inlet and outlet areas is shaped such that the channel formed between adjacent blades guides the flow from inlet to exit conditions with a minimum of energy loss.

In addition to providing minimum energy loss, the blade's shape (in particular, the schedule of the blade angle with the local tangential direction) causes it to act as an aerofoil or hydrofoil under flow conditions. Standard engineering analysis techniques can then be used to infer how the static pressure changes as flow moves over both sides of the blade. On the convex side (the "pressure" surface), the distribution of pressure along the blade length is such that pressure is generally higher than at the same location on the concave side (the "suction" surface). The pressure distribution in the figure is purely notional and is meant only to show the direction of net pressure across a blade.

If the blade camber line is now divided into a large number of sections, then an average pressure force for each "differential" blade section can be arrived at without incurring serious error. The component of this net pressure force in the local tangential direction (the cross product of the local radius vector with the pressure force vector) then yields a torque generated by this blade section that resists the applied rotor torque, T. Integration of this resistive torque over the camber line of all rotor blades must then yield the total resistive torque that is equal and opposite to the applied torque, T. In other words, as the rotor is made to rotate under flow conditions, the pressure difference across the rotor blading generates a force at any particular location that the rotor blading *does work against*. This integrated resistive torque, when multiplied by the rotor operating speed, yields the rate at which work is being expended against that resistive torque.

Although the two approaches outlined above differ substantially in the way they look at the problem, they arrive at the same result for the rate of expenditure of work, or rotor input power.

Basic Hydrodynamic Performance of Variable Displacement Pumps

The hydrodynamic performance of these variable displacement machines is somewhat less deterministic than that of positive displacement pumps. We

have seen that the flow rate through a positive displacement machine is a function only of the volumetric displacement and the operating speed. However, in the case of a variable speed pump, the flow rate processed through the pump also varies with the pressure-flow characteristics of the system that is downstream of the pump.

A number of methods are commonly used to present various performance characteristics of variable displacement pumps. Perhaps the most common of these is the "head-capacity" curve, also referred to as the "head-flow" curve or, simply, the "*H–Q*" curve. An example of such a curve is shown in Fig. 16. The curve's vertical axis denotes the total head rise developed by the pump. The horizontal axis represents the pumped flow rate. Although the units of flow rate are customarily expressed in gal/min, any units are satisfactory as long as consistency is maintained. It can be seen that this curve has a generally negative slope. The pump developed head decreases below the design value for flow rates higher than design flow. At flow rates lower than design, the pump developed head is higher than the design value. It can be seen from the figure that at very low flow rates the *H–Q* characteristic "turns over" and becomes positive-sloped. Most real pumps, particularly those in liquid rocket engine systems, possess this type of characteristic. Some pumps that operate under particularly favorable

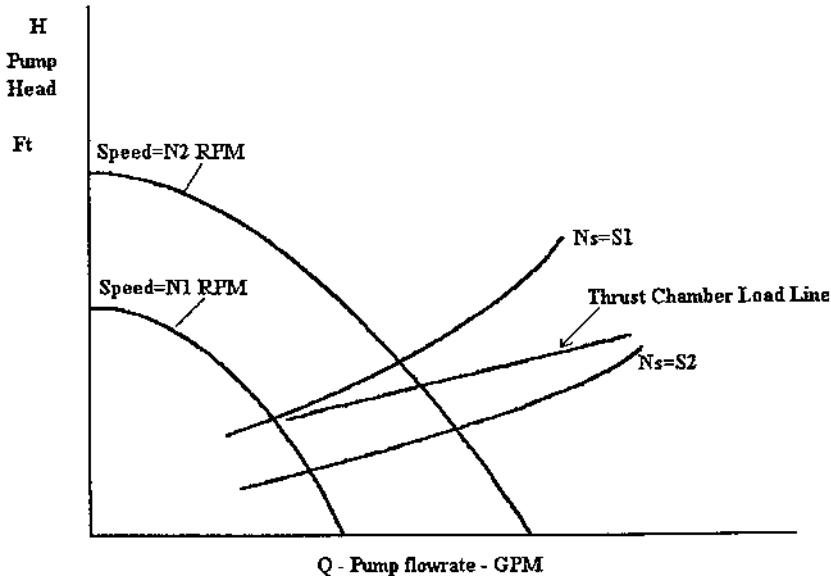

Figure 16 Head-capacity performance curve for an ideal centrifugal pump stage.

circumstances are able to avoid the transition to positive slope and possess a "continuously rising" H–Q characteristic all the way down to zero flow. This characteristic is somewhat rare. Also evident from the figure is that a separate and distinct H–Q curve exists for each operating speed at which a pump is operated.

The general shape of the H–Q characteristic (i.e., the negative slope) can be easily understood by referring to a simplified schematic of the rotor outlet flow. Such a schematic is provided in Fig. 17. From this schematic, three vectors of primary importance can be identified:

1. The vector **U**, which is parallel to the local tangential, direction, and represents the rotor's tangential velocity at the exit.
2. The vector **V**, which represents the exit velocity (in a bulk sense) of the pumped fluid relative to the pump rotor. The magnitude and direction of this vector are a function of the geometry of the rotor blades near the exit, and other elements of the rotor geometry near the exit.
3. The vector **C**, which represents the exit velocity (again, in a bulk sense) of the pumped fluid in an "absolute" frame of reference (relative to the pump's housing). This vector is the sum of vectors **U** and **V**.

The projection of vector **C** in the local tangential direction is represented by C_{u2}. This vector component, along with the vector **U** at the rotor exit, can be substituted into Euler's equation [Eq. (7)] to determine the pump's developed head under the conditions of flow and speed in question. Under conditions of increased flow rate, the magnitude of the vector **W** is increased. When added to a fixed vector **U**, the result is a

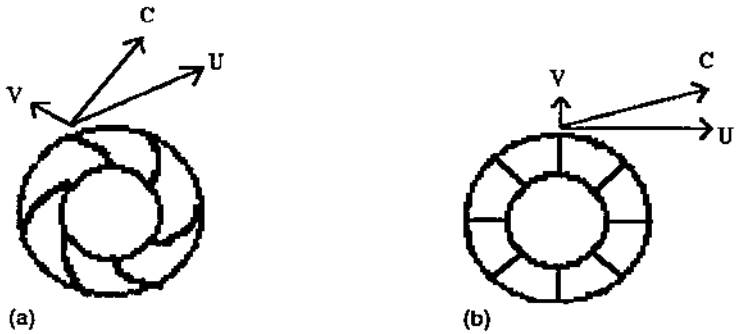

Figure 17 Examples of centrifugal impeller outlet velocity diagrams: (a) typical impeller outlet velocity diagram for "low" head coefficient impeller with backward curved vanes; (b) typical impeller outlet velocity diagram for "high" head coefficient impeller with radial vanes; V, impeller-relative fluid velocity; U, impeller vane velocity; and C, absolute fluid velocity at impeller exit.

somewhat smaller magnitude of vector **C** (as well as a change *in the direction* of vector **C**). (The importance of this will become apparent later.)

An H-Q curve can be derived analytically given knowledge of the pump's geometry by selecting a flow rate; computing the **U**, **W**, and **C** vectors; and computing the head rise from Eq. (7). At flow rates significantly away from the design value, knowledge of various mechanisms of internal energy loss is also required. These will be covered in subsequent sections.

A set of correlations known as *pump affinity laws* is available to enable easy computation of the performance of a pump at any speed of interest if the performance at a given speed is known. These affinity laws relate the flow, developed head, and required power at a new flow rate to that at a reference flow rate. These affinity laws take the following form:

$$\frac{Q_1}{Q_2} = \frac{N_1}{N_2} \tag{9}$$

Where

Q = flow rate of the pumped fluid.
N = pump operating speed.

Subscripts 1 and 2 denote the reference condition, and the other condition of interest, respectively.

$$\frac{H_1}{H_2} = \left(\frac{N_1}{N_2}\right)^2 \tag{10}$$

Where

H = pump developed head, expressed in ft.

$$\frac{P_1}{P_2} = \left(\frac{N_1}{N_2}\right)^3 \tag{11}$$

Where

P is the required pump power.

The Specific speed (N_s) parameter has a companion term that is related to the suction performance requirements (or capabilities) of a rotor or pump stage. This term is known as the suction specific speed (N_{ss}) and is computed

as follows:

$$N_{ss} = \frac{NQ^{1/2}}{\text{NPSH}^{0.75}} \tag{12}$$

Where

N = pump rotating speed, in revolutions per minute.
Q = pump flow rate, in gal/min.
NPSH = net positive suction head, total fluid head above the vapor head.

NPSH is normally defined at the inlet of the pump rotor, as this is where the fluid total pressure comes closest to the vapor pressure.

N_{ss} is used during conceptual and preliminary design as a guide to gauge the sensitivity of a particular pump stage to the effects of cavitation at the rotor inlet. When the N_{ss}-term reaches approximately 8,500 (being careful of the units used in the computation), cavitative effects could be expected to become visible in a pump stage's operation. When the N_{ss}-term reaches approximately 10,000, it could reasonably be expected that the pump's operation will be impeded in a major way by these effects. This is particularly true in liquid rocket engine systems, where the desire to minimize pump weight results in aggressive packaging. An aspect of "aggressive packaging" is the deliberate design of the rotor so as to operate under high hydrodynamic loads. If the rotor's inlet region operates in a highly loaded manner, cavitative behavior will become visible at lower values of N_{ss} than will occur if the inlet hydrodynamic loads are constrained. In the event that high inlet hydrodynamic loads are required, some type of suction performance augmentation is required. This augmentation commonly takes the form of a device called an "inducer", which is discussed in a subsequent section.

The N_{ss}-term for a pump stage could be lowered by decreasing the pump's operating speed [from Eq. (12) the effect of N on N_{ss} is linear] although the effect on stage specific speed *could* result in a decrease in pump efficiency and *will* cause an increase in the required diameter of the pump to produce a given head, which will increase the pump's weight. Likewise, an increase in the inlet NPSH could be used to decrease N_{ss} to a level where satisfactory operation could be maintained. However, in a liquid rocket engine system, an increase in the pump's inlet pressure (which is what is implied by increasing inlet NPSH) is generally not to be counted on, due to the extra weight required in launch vehicle tanks to support the higher-pressure loads. Also, it should be emphasized that N_{ss}, like any other general design parameters, should not be interpreted as anything other than a

general indicator. N_{ss} will give us only a "feel" for the severity of a suction performance problem, but only detailed analyses of candidate designs should be used for specific diagnostic work.

In liquid rocket engine systems, the combination of low pump inlet pressure and cryogenic propellants (which are normally stored quite near their boiling points) generally drive the inlet N_{ss} of a pump stage (or the first stage of a multistage pump) well above the 10,000 mark. In this event, a high suction-performance inducer is generally incorporated into a pump's design from the beginning.

The issue of pump inlet cavitation provokes much discussion, and some details are warranted before we explore centrifugal and axial-pump hardware in more detail. In our previous discussion of Fig. 15(c), we discussed the notion of behavior of the rotor's blade cascade as hydrofoils, and the generation of a resistive torque that opposes the input torque, T. Under these conditions, the concave side (or "suction" side) of the rotor blade experiences a drop in local static pressure. This is followed (as we proceed along the blade camber line) by rotor-relative diffusion (as well as work input due to the radius change), which causes the suction surface static pressure to increase. If the rate of change of the local blade angle is sufficiently high near the leading edge, the region of minimum static pressure can drop below the local vapor pressure. At this point, phase change occurs, with the phenomenon being called "cavitation." Several things should be pointed out relative to this phenomenon:

A survey of the available introductory literature may lead the engineer to believe that cavitation is a "digital" phenomenon, i.e., either cavitation exists or it does not. This is far from the truth. Cavitation can exist to any degree of severity; from so low as to be unnoticeable to so great as to render a pump useless in its intended application. Most high-performance rocket system pumps operate with a significant degree of inlet cavitation. In fact, since most rocket engine system propellant pumps operate on systems that are expendable (a single use only), the required life is sufficiently short that degrees of cavitation are accepted that would be out of the question for a ground-based system.

Although Fig. 15(c) shows the cavitative situation occurring in the context of a centrifugal rotor, the phenomenon occurs in both centrifugal and axial-pump stages.

Although Fig. 15(c) shows the situation occurring due to the natural acceleration on the suction side of a blade, any situation that causes acceleration will produce the same result. For example, providing a

flow stream with insufficient inlet flow area is a common cause of fairly gross inlet cavitation.

Pressure losses at the inlet due to a mismatch between blade angle and flow angle (these are referred to as "incidence losses" and will be discussed in a subsequent section) can contribute to inlet cavitation. For this reason, pumps operating with very low NPSH may not be capable of flow excursions as wide as those with higher inlet pressures.

Before going into our more detailed discussions of centrifugal and axial-flow pump stages, we also wish to introduce the concept of two more hydrodynamic parameters—the *flow coefficient* and the *head coefficient*.

The flow coefficient (expressed as Φ) takes the following form:

$$\Phi = \frac{C_m}{U} \tag{13}$$

Φ can be defined anywhere we choose, although it is most often associated with the inlet and outlet stations of a rotor. When defined at a rotor inlet, C_m represents the "bulk" fluid velocity at the inlet station. U generally represents the rotor tangential velocity at the outermost extent of the inlet station. When discussed at the inlet of a rotor, Φ is relevant for two reasons: first, it defines the tangent of the fluid velocity vector angle at the rotor inlet. The blade angle at the inlet will have to closely approximate the fluid angle in order for the inlet to function properly (if a pump must operate over a range of inlet flows, this match will occur at only one operating point). Second, the value of Φ at the inlet generally defines the range of suction performance capability that can be expected from the pump stage, with lower Φ-values generally being consistent with higher suction performance capability (i.e., the capability to operate at low values of *NPSH*).

When Φ is discussed at the rotor outlet, it defines a quantity referred to as the "outlet swirl parameter." This quantity sets the amount of diffusion required within the rotor and has a significant impact on the shape of the pump's head-capacity curve.

The head coefficient (expressed as Ψ) takes the following form:

$$\Psi = \frac{gH}{U^2} \tag{14}$$

Where

Ψ = head coefficient.
g = acceleration of gravity.
H = rotor (or pump) developed head.

$U =$ rotor tangential velocity.

By inspection, we can see that Eq. (14) relates the square of the rotor speed (and thus, the rotor's specific kinetic energy) to a change in fluid energy. In this way, Ψ can be thought of as an energy ratio—that is, the fraction of rotor kinetic energy that is transferred as energy to the pumped fluid.

As with numerous other design parameters, care and consistency in usage is of great importance. For example, we could refer to the head coefficient of a rotor alone, or of an entire pump stage. While these values would probably be not too different, energy losses between the outlet of a rotor and the outlet of a stage would result in Ψ pump being less than Ψ rotor. Also, when applied to a multistage pumping machine, specificity is required to understand whether Ψ is specified for an entire pump or just one (or possibly more than one) stage.

ROCKET PROPULSION SYSTEMS—CENTRIFUGAL PUMPS

Centrifugal pumps (both single and multistage) dominate the design of propellant pumping elements for liquid rocket engine systems. There are several reasons for this.

First, centrifugal machines are normally fairly simple (both hydrodynamically and otherwise) and rugged. Because of the change in radius through which the pumped fluid is processed, centrifugal stages possess relatively high head coefficients. This normally results in only a single pump stage being required for most cases (with the exception of very high head liquid hydrogen pumps).

The relative hydrodynamic simplicity of centrifugal stages results in a decreased requirement for diffusion within the pump. This makes the centrifugal machine relatively forgiving of changes in the operating point at which it is forced to function. This consideration is particularly important for an engine system that must operate over a range of thrust levels. Since the H–Q characteristic for the rocket engine system and that for the centrifugal pump are not the same shape (see Fig. 19), the pump is forced to operate "off-design" at all operating points except the "design point." Stability of the pump's operation over this range (and often a somewhat larger range) is mandatory for these variable thrust engine systems.

Since the centrifugal pump is capable of delivering relatively high head per stage, these machines generally result in a minimum length of the turbopump rotor assembly. This is important, since long bearing spans often contribute to rotor dynamic difficulties, especially at high operating speeds.

Lastly, although pump isentropic efficiency is seldom an issue for the "open-cycle" rocket engine systems, efficiency thresholds are often introduced by the expander and staged combustion cycle systems. In this case, the pump must demonstrate an efficiency in excess of the threshold value if design chamber pressure is to be achieved. Contemporary centrifugal pumps have repeatedly shown themselves to be capable of meeting these efficiency requirements without major difficulty.

In our previous discussions, we have described the engine balance from which the interface conditions and performance requirements for the propellant pump can be derived. In addition, when a liquid rocket engine system is designed, a maximum weight specification for the system typically exists. This allowable weight is divided between the system's components, and a "weight bogie" for each component is derived. For the propellant pumps, this weight requirement is often the most challenging facet of the pumps's design.

The design process for a propellant pump consists of three essential phases—conceptual design, preliminary design, and detailed design. The conceptual design process for a propellant pump begins with the aid of Eq. (1) and data such as depicted in Fig. 15(d). Using the required pump head

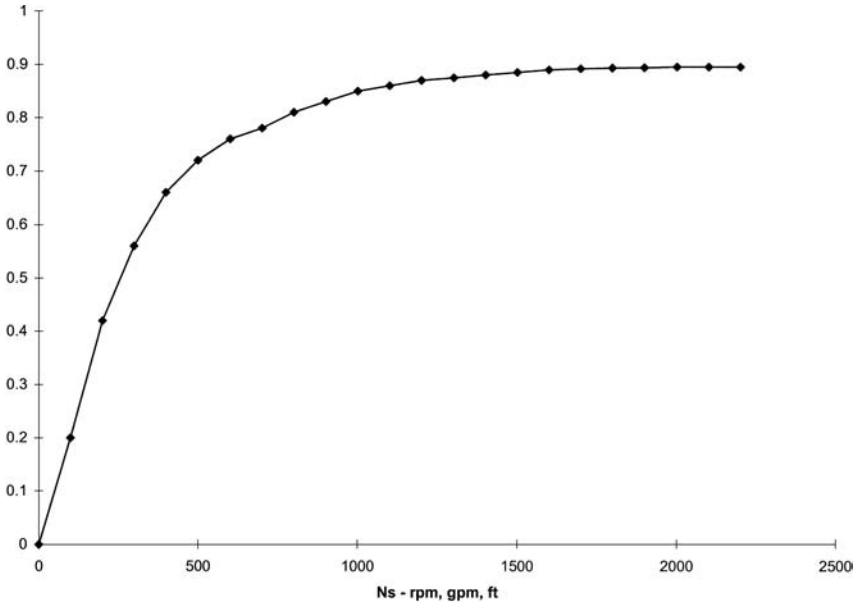

Figure 15d Typical impeller inlet showing blade leading edges and inlet vectors.

and pump flow derived from the engine balance, the pump specific speed can be forced to take on a range of "reasonable" values by solving Eq. (1) for the rotor speed, N. This "reasonable" range of specific speed might vary from 700 to 2,000, in rpm-gpm-ft units.

In a typical application using a dense propellant (i.e., a propellant other than liquid hydrogen), the low end of the examined N_s range will bring about relatively low efficiency, relatively low operating speed, and relatively relaxed suction-performance requirements, as denoted by a relatively low value of suction specific speed [computable using Eq. (12)]. Due to the low operating speed, the impeller tip diameter will be relatively large (to generate a fixed amount of total head), and the impeller exit axial width (the so-called "b2" dimension) will be relatively small to maintain a fixed impeller outlet flow area.

Although challenges regarding suction performance, rotor dynamics, seal durability, etc. can be alleviated by operating at reduced values of N_s, pump weight is adversely affected. Referring to Fig. 15, we can note that as the pump-stage specific speed is decreased, the increasing impeller outside diameter causes the discharge volute to occupy ever-increasing radii (with respect to the pump's rotational axis). This results in the volute's circumference increasing in proportion to its radius. Since the discharge volute must contain the pump's total discharge pressure, the volute's wall thickness (and thus its weight per linear in.) tends to be the greatest of the pump's components. The end result of the decreasing specific speed trend is a propellant pump whose weight quickly exceeds the allowable. In addition, for closed-cycle engines (i.e., expander and staged combustion cycles), especially "small" ones whose propellant flow rates are relatively low, pump specific speed values below approximately 500–700 N_s units may perform at isentropic efficiencies that are below values that may be required by the engine cycles.

Examination of an increasing value of pump specific speed will show the following trends—if we refer to Fig. 15(d) we see that increasing pump N_s will yield an essentially monotonic (though not linear) trend of increasing efficiency. This is due primarily to the progressively more favorable flow passage geometry that increasing N_s provides.

The increasing values of pump N_s also result in decreased impeller diameter due to the higher rotating speeds involved. In all but the largest pumps, this trend tends to bring about decreased impeller weight. In addition, the decreased impeller diameter causes the discharge volute to be "wrapped" around a smaller outer diameter. This decreases volute circumference and can (especially in high-pressure pumps) bring about fairly dramatic decreases in total pump weight.

As we examine the effects of increasing pump N_s, the pump's suction specific speed value (N_{ss}) must be tracked as well. Constraints regarding suction performance are most often the first fundamental constraint that

must be dealt with in attempting to optimize the sizing for a propellant pump. When pump inlet N_{ss}-values exceed approximately 8,000 (rpm-gpm-ft units), an inducer is normally considered beneficial, and mandatory when N_{ss} exceeds approximately 10,000. Inducers are discussed in more detail in a subsequent section. It can be shown that *with normal attempts to optimize engine and turbopump packaging*, liquid rocket engine systems that operate at chamber pressures in excess of approximately 300 psia cannot operate without the benefit of the inducer's added suction performance. In engine systems that incorporate "low-pressure," or "boost" pumps, a criterion for sizing the head rise of the boost pump could be to avoid the use of an inducer in the "high-pressure" pumping element. However, it should be noted that the "low-pressure" pump itself is likely to be essentially a large inducer. It is possible (or likely) that the final selection of propellant pump specific speed will be driven by the maximum suction specific speed at which the pump can operate (i.e., the level of inducer technology available to the pump designer). It is often this constraint that results in the decision to employ the "low-pressure" pumping element.

Referring again to Fig. 15, note the presence and location of the "shaft seal." This seal serves two purposes—first, it prevents gross leakage of the pumped fluid to maintain reasonable pump performance, and in some installations, it (in conjunction with the "impeller rear seal," also in Fig. 15) provides a pressure drop at a specific radial location to set the pump's axial thrust load. In low to moderate chamber pressure engine systems, this seal is often implemented as a spring-loaded face seal that engages a finely finished surface on the rear of the impeller hub. Various materials (bronzes, coated graphites, etc.) have served this seal's purpose. The spring load "P" that is required for effective sealing, together with the seal's radial location (and consequent rubbing velocity, "V") set an effective "power load" term for the seal, denoted as "PV." Depending on the seal material, leakage requirements, and the pumped medium, this "PV"-term is subject to various constraints. The PV constraint for a nonreactive medium (such as Kerosene, or RP-1) might be based on the resulting rate of seal wear, and the seal life required. In a more aggressive medium (liquid oxygen, for example), the maximum achievable PV may be based on avoiding ignition of the seal component in the oxygen-rich atmosphere that exists in its vicinity. Upon reaching a threshold of pump specific speed (the exact value depending on the application), allowable PV values for spring-loaded face seals will be exceeded, and other sealing systems, such as a labyrinth seal, will be required.

Whatever the particulars of a given situation, increasing pump specific speed generally increases the difficulty of the shaft sealing problem and will often present a fundamental constraint that must be dealt with during the sizing and early design processes.

In addition to shaft seals, shaft bearing systems (also shown in Fig. 15) can present problems and constraints in regard to basic specific speed sizing. In particular, rolling element bearings (i.e., ball and roller bearings) are prone to difficulties in the environment presented by a liquid rocket engine system. Attempts to optimize pump specific speed by raising rotating speed typically raise the rotational speed of a rotating element bearing to a point where the internal bearing loading and heat generation become troublesome. In a liquid rocket engine system environment, suitable lubricant fluids are usually absent, and a ball or roller bearing is simply cooled using a metered amount of the pumped fluid. In all cases of which this author is aware, these fluids lack the viscosity required for formation of the typical EHD film that is considered necessary for "lubrication" in the normal sense. In addition, many of these fluids (liquid oxygen, for example) are chemically aggressive. For industrial-grade ball bearings, DN-values in excess of 500,000 (bearing ID in mm multiplied by operating speed in rev/min) degrade life noticeably. When proper lubrication is absent, prediction of results before the fact becomes virtually impossible. Bearing DN-values of 1.6 million have been achieved using liquid oxygen as a coolant. In these cases, bearing lifetimes have proven spurious, unrepeatable, unpredictable, and sometimes less than a single required engine firing.

The dynamics of an operating turbopump rotor may also limit the achievable pump specific speed. Although a detailed discussion of rotor dynamics is beyond the scope of this chapter, it should suffice to say that successful operation of a pump rotor at speeds substantially in excess of 1 or more critical speeds is highly dependent on the availability of adequate damping at bearings and seals to suppress resonances or oscillations at subsynchronous frequencies. This is often a problem in liquid hydrogen turbopumps due to the extremely high head rises involved.

A relatively conservative design philosophy might set a propellant pump's specific speed at 1,500 N_s units as a "first cut" for further evaluation. At this N_s-value, an isentropic efficiency close to the maximum is usually attainable. In addition, suction performance, sealing, and fabrication difficulties are kept to a minimum. In the event that pump weight exceeds that allowable, N_s can be increased in an incremental fashion until the component's weight requirement is met, or until another fundamental constraint becomes evident.

Inlet Sizing

When a workable N_s sizing has been achieved, sizing of the pump inlet is normally the next order of business. A centrifugal pump stage is normally sized to one of two criteria. The first is inlet sizing for maximum efficiency.

Referring to Fig. 15(e), we can see the variables in play. With a "small" inlet area, the fluid inlet meridonal velocity is relatively high, and the impeller blade speed is relatively low, due to its placement on a small radius. With a "large" inlet area, although the fluid inlet meridonal velocity is reduced, the impeller blade speed has been increased due to the placement of impeller blade leading edges on a large radius. Somewhere between these two cases the velocity of the fluid relative to the blade leading edges at the inlet will be minimized. Minimizing this velocity energy (specifically $W_{1t}^2/2g$) acts to minimize the diffusion that must be performed near the impeller inlet, and thus minimizes the energy lost in this process. The process of inlet sizing for minimum impeller diffusion losses fulfills the criteria of sizing for maximum efficiency.

We have seen in previous discussions that propellant pump thermodynamic efficiency is often not a significant problem (within bounds of reason). A much more pressing issue in most cases is the ability of a pump to operate with a very low inlet pressure in relation to the fluid's vapor pressure. This "surplus" of pressure (or head) above the fluid vapor pressure (or head) is referred to as NPSH. The urgency of this issue relates to the weight savings that can be afforded a launch vehicle by a pump's ability to operate at inlet pressures that are consistent with very lightweight propellant tanks (it should be noted here that the larger the launch vehicle, the larger are the available weight savings from a given reduction in pump inlet pressure). For this reason, a more common optimization procedure for inlet sizing of rocket propellant pumps is to minimize the required inlet NPSH. A pump inlet that is sized according to this procedure will invariably be larger than that which would be derived for maximum efficiency. However, it

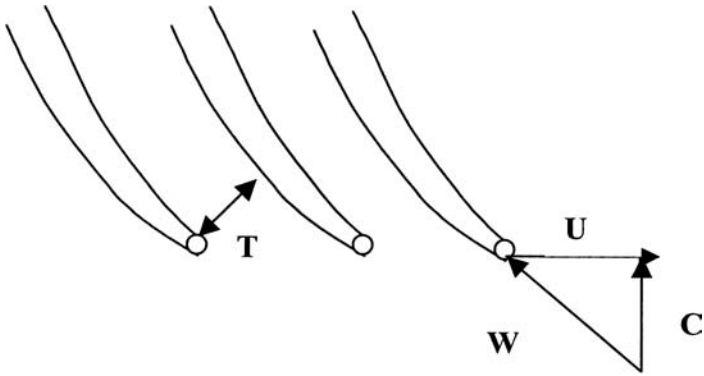

Figure 15e Typical characteristic of pump efficiency versus specific speed.

should be understood that the optimization procedure mentioned above to maximize efficiency neglects the acceleration (and subsequent static pressure drop) experienced by the inlet flow as it accelerates around the blockage presented by the impeller blades. With the low NPSH situations commonly encountered in rocket propellant pumps, this blockage is sufficient to lower the static pressure below the local vapor pressure. This would result in gross cavitation, assuming that equilibrium thermodynamics apply.

In the case of a centrifugal stage that is preceded by a close-coupled inducer (as shown in Fig. 15), sizing of the impeller inlet is actually done to satisfy inducer tip diameter criteria. In particular, industry data (some proprietary, and some public domain) are used to relate a required suction specific speed performance to a necessary inducer inlet flow coefficient. A sample of such data is presented in Fig. 15(f). If we note the definition of the inducer inlet flow coefficient [Eq. (13)], and note that the pump stage's operating speed is already supposed from a candidate specific speed value, then the required inducer tip diameter follows from the inlet flow coefficient needed to meet the suction-performance requirement. The impeller inlet tip dimension is then sized to match the tip diameter of the inducer.

Impeller Sizing

The impeller sizing process begins with the operating speed, N, already determined by the target specific speed. With the impeller speed and

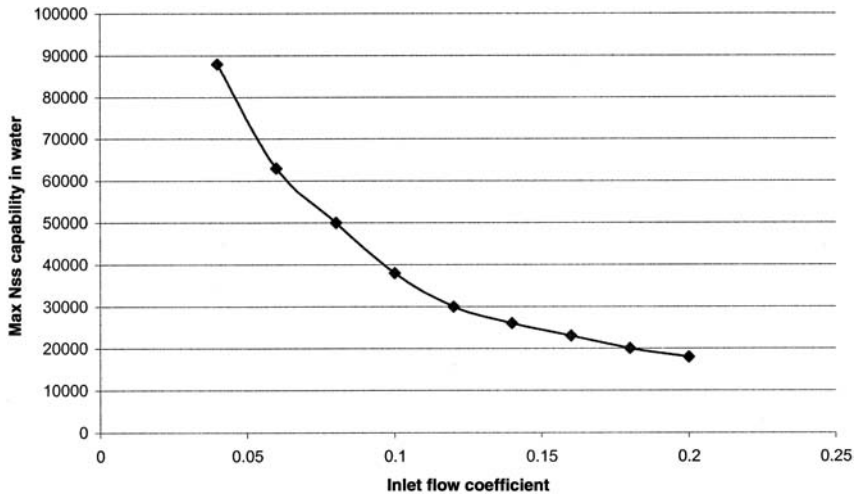

Figure 15f Max N_{ss} capability in water as a function of inlet flow coefficient.

required head (or at least an estimate of it) known, two other major design variables can be determined. These are the impeller diameter and the impeller head coefficient. It should be noted that these two variables are strongly related, as Eq. (14) shows. Given an operating speed, N, the impeller tip speed [U in Eq. (14)] is determined by the diameter. The required head coefficient is then a function of the tip speed and the required impeller head.

An estimate of optimum impeller diameter can be made from another pseudo-dimensionless parameter known as specific diameter, D_s. D_s is defined as

$$D_s = \frac{D_{tip}\Delta H_0^{0.25}}{\sqrt{Q}} \tag{15}$$

Where

D_{tip} = impeller tip diameter in ft.
ΔH_0 = impeller developed head in ft-lb_f/lb_m.
Q = impeller inlet flow, gal/min.

The D_s-value correlates moderately well with a maximum attainable pump efficiency. The D_s-value desired for a centrifugal stage is a function of the stage specific speed and ranges from approximately 0.1 at an N_s of 1,200–1,300 to approximately 0.06 at pump N_s values of around 2,000.

The selected value of D_s determines impeller tip diameter with the help of Eq. (15). Along with the impeller operating speed, N, the impeller tip speed, U, is now determined. From Eq. (14), the target value of the impeller head coefficient, ψ, can now be determined. Appropriate target values of ψ can range from approximately 0.4 at a stage N_s of around 2,000 to values at or above 0.6 at stage N_s-values of around 1,000. It should be noted that the choice of a high target value for the pump head coefficient should be done with caution. Although a relatively high ψ-value can indicate an efficient use of available loading capability, it can also have detrimental effects on the pump's operability in the engine system. For example, a high value of ψ can act to lessen the negative slope of the pump's H–Q curve and can move the point of zero slope to higher flow rates. If an engine system must operate over a significant flow range (the result of thrust control requirements, mixture ratio control requirements, or both), the point of zero slope must be kept away from the pump's intended operating range, or unstable system operation can result. In addition, it should be remembered that the engine start transient must not result in "dwells" at or near points of zero slope of the H–Q characteristic. The amount of energy available to the engine start transient must be sufficient to "boot" the pump to speeds and flows where

stable operation is assured. In some aggressive engine system designs (i.e., those possessing low starting energy to minimize system weight), the effect of the H–Q curve shape (as influenced by head coefficient) should be evaluated for its effect on the system's transient starting performance. Note that while the exactitude of results of these types of analyses is questionable, trends and relative margins can certainly be determined.

The number of blades used in a centrifugal stage impeller can be readily approximated from a number of correlations that are in general use. The number of impeller blades can be expected to vary from 5 or 6 to as many as 24 or 25. However, the combination of high suction-performance requirements and the desire to highly load the pump stage (for weight reduction) leads to the use of impeller blades called "splitters" in many propellant pumps for liquid rocket engine systems. If we refer to Fig. 15(c), we can see that the required number of blades for a particular pump has been determined as eight. However, if all eight blades extend into the impeller eye, the amount of flow area that is "blocked" by the blades causes flow to accelerate to the point where substantial cavitation is encountered. This difficulty is dealt with by placing the leading edges of a number of the blades (perhaps half of them, perhaps more) significantly downstream of the impeller inlet. Of course, these blades extend all the way to the impeller exit, and thus the solidity criterion at the impeller exit for achieving the design head coefficient is met. It should be noted that a uniform criterion for placement of the splitter leading edges does not exist to this author's knowledge. A technique often used to determine this is simply to place the leading edges of the splitters at 50% of the meridonal distance through the impeller flow passage, and then to simulate the resulting flow with any of a number of computer programs available. The results of these simulations can then be used to determine the point in the passage where loading of the full-length blades becomes excessive, requiring the placement of the splitter leading edges somewhat upstream of that point. For propellant pumps that must operate over a significant flow range, these computations should be carried out at the operating point consistent with the highest blade loading.

The angle of the impeller vanes at the impeller inlet can be determined easily from geometry and bulk flow considerations. Referring to Fig. 15(e), flow is approaching the impeller inlet at a velocity C. The impeller blade is moving as shown with a velocity U. The combination of these vectors produces the vector $\mathbf{W}$, or the fluid inlet velocity vector as seen from a point on the impeller. The angle of the blade centerline is normally set to the expected angle of the $\mathbf{W}$ vector, to minimize the losses associated with negotiating the blade leading edge (referred to as *incidence losses*). It should be noted that if the pump must operate over a significant range of inlet flow

coefficient (which defines the tangent of the fluid velocity vector angle at the inlet), then a match will be achieved at one and only one operating point. In this case, determination of the desired blade inlet angle will come from a study of a range of inlet angles, and an optimization to minimize losses over the entire required operating range.

The angle of the impeller vanes at the impeller exit is influenced by a combination of the required impeller head coefficient, the impeller outlet axial width, or the outlet flow coefficient (discussed in a subsequent paragraph) and estimates of the flow situation in the impeller passages just upstream of the impeller exit. In general, if the flow follows the vane angle at the exit, the developed head is easily computed from a combination of the **W** and **U** vectors. However, due to the pressure difference between the blade convex and concave sides, the exit flow "leans" toward the concave side, exiting at an angle that is more nearly tangential than the blade angle. This difference between fluid angle and blade angle at the exit is referred to as *deviation*. In a highly loaded pump stage, the deviation angle can be substantial—perhaps 10 or more degrees. The choice of the proper number of impeller blades at the exit is an important factor in preventing the deviation angle from assuming unreasonable values.

When the impeller inlet and outlet blade angles have been determined, the task of "filling in" the blade between the inlet and outlet confronts us. The procedure for doing so is beyond the scope of this chapter; however, the basic idea is to ramp the local blade angle from the inlet value to the discharge value at a rate (not necessarily a steady one) that keeps blade loading within reasonable ranges on the blade surfaces. It should be noted that velocity gradients on the blade surfaces (particularly the concave, or "suction" surface) are indicators of blade loading and can be computed with any of a number of computer programs available in industry.

The axial width of the impeller outlet (called the "b_2" dimension) is the last of the impeller design parameters to be determined during conceptual and preliminary design. A commonly used technique to size the b_2 dimension is to assume an impeller exit flow coefficient of 0.1. At the impeller exit, the flow coefficient is defined as

$$\phi = \frac{C_{m2}}{U_2} \tag{16}$$

Where

C_{m2} is the radial velocity component at the impeller exit.
U_2 is the tangential velocity (tip speed) at the impeller exit.

From Eq. (16) an impeller radial outlet velocity can be determined—an outlet flow area follows from continuity. The b_2 dimension can then be determined from

$$A_{\text{flow}} = 2\pi r b_2 \tag{17}$$

Where

A_{flow} = outlet flow area computed from continuity.
r = impeller radius.
b_2 = impeller exit axial width.

When b_2 is determined, it is necessary to account for the fact that some flow blockage exists at the impeller exit due to the presence of the blades. In most pumps, this blockage is approximately 10%. If more precise data are available for a particular case, they should be used. During preliminary design, the target value of the outlet flow coefficient can be safely varied from as low as 0.07 to as high as 0.14, and the effect on stage design ascertained. Changes in the outlet flow coefficient will affect the shape of the H–Q curve, the required impeller blade exit angle, and the levels of diffusion inside the impeller. In addition, an unwise choice of the outlet flow coefficient (particularly a choice of one that is too low) can make the design of downstream diffusion systems difficult.

The focus on weight during the design of a propellant pump for a liquid rocket engine system invariably results in a pump that is highly loaded and in particular has high impeller exit velocities. For example, of the total head generated by a typical rocket pump impeller, the fraction that is kinetic energy might be as high as 40%. This high kinetic energy will be lost if it is not converted efficiently into pressure. Therefore, the ability to design and incorporate efficient diffusion systems into rocket turbopumps is extremely important if reasonable performance is to be delivered.

Several early liquid rocket engine systems incorporated turbopumps whose loading was sufficiently light that the required diffusion of the impeller outlet flow could be done in a volute of appropriate design (volutes are covered in more detail in a subsequent paragraph). However, as design practices became more mature and aggressive, impeller exit velocities became high enough that some form of diffusion upstream of the discharge volute was desirable. The two types of diffusers employed fall generally into two categories—vaneless and vaned diffusers.

The vaneless diffuser in a rocket turbopump closely parallels that in a centrifugal compressor with one exception—flow velocities very near the local sonic are not encountered. The vaneless diffuser is just that—a vaneless annular passage outboard of the impeller. In this area, a first approximation

of the flow's behavior can be had by employing the assumption that angular momentum remains constant in the vaneless space, that is,

$$rC_\theta = \text{const} \tag{18}$$

Where

r = distance from impeller rotational axis.
C_θ = tangential component of fluid velocity.

The constant in Eq. (18) can be determined by computing the angular momentum at the impeller exit. The diffusion in the vaneless space comes about with the reduction of C_θ as the pumped fluid moves outboard to increasing radii.

The prime difficulty with the vaneless diffuser comes about as a result of the direction of the impeller outlet velocity in a highly loaded pump stage. It often occurs that the very tight spiral angle (often less than 10° from the tangential) causes flow in the vaneless space to undergo large frictional losses on its way to the discharge volute. For this reason, vaneless diffusers are generally less favored than vaned ones in rocket propellant pumps. This is particularly true if peak pump efficiency must be maintained, as is often the case with closed-cycle engine systems.

The incorporation of vaned diffusers of various kinds into propellant pumps began in earnest in the early 1960s. This was primarily in response to head requirements that were sufficiently high that we could not afford to lose the impeller's exit kinetic energy. Vaned diffusers generally fall into two categories—the so-called vane island, or "wedge" diffuser, and the "cambered vane diffuser." Which type is employed generally depends on the level of sophistication required. Referring to Fig. 18, we can see that the vane island diffuser consists of vanes (or wedges) that form straight, diverging flow passages. Before the advent of computer-controlled machining processes, the vane island diffuser was much easier to fabricate accurately than a vane row that incorporated camber. In addition, the level of diffusion and the general performance of the vane island diffuser are often more amenable to analysis than its cambered counterpart, if for no other reason than that a throat and exit area are more easily identified. It is capable of generally the same level of performance as the cambered vane row. In order to minimize the radial extent of the diffuser, a maximum rate of diffusion might be sought. Past test data for vane island diffusers indicate successful performance with diffuser cone angles of between 7 and 10°, with 8° representing a good design compromise (the *cone angle* represents the angle subtended by the two sides of the diffuser flow passage).

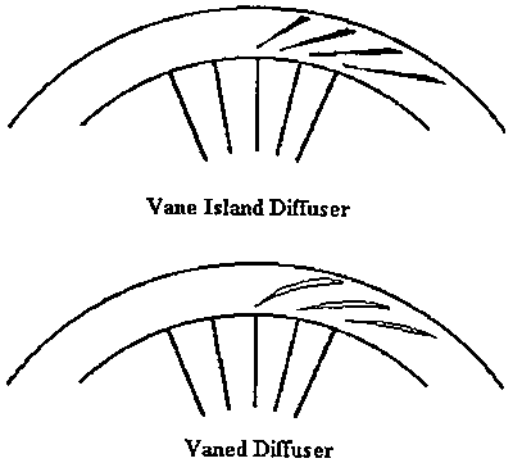

Figure 18 Examples of centrifugal pump stage radial diffuser configurations.

The diffuser incorporating cambered vanes is in common use in rocket turbopumps. In applications where weight is critical (a not uncommon state of affairs), the cambered vane diffuser is often preferred since, due to the vane camber, the radius occupied by the discharge volute can be decreased somewhat over a pump incorporating a vane island diffuser. This attribute will decrease the circumference of the volute (usually the portion of the pump with the thickest walls) and lessen the pump's weight appreciably.

Regardless of the details of the vane geometry employed, both of these "radial diffuser" configurations have essentially the same objective and capabilities. The vane row alters the flow's angular momentum, achieving a given deceleration and static pressure rise over a much-reduced linear distance, and with attendant lower losses.

It should be noted here that analysis of the performance of any vaned diffuser in a centrifugal pump stage is somewhat complicated by the nature of the flow field entering it. The impeller exit flow field is exceedingly complex, with multiple embedded secondary flows. For this reason, care must be used in applying general industrial data from conical diffusers used in piping networks where the nature of the diffuser inlet flow field is very different.

As with virtually any design feature that increases efficiency, options for a vaned diffuser (particularly those incorporating an aggressive amount of diffusion) should be examined carefully before committing to their incorporation. Figure 15(g) shows an example of the efficiency character-

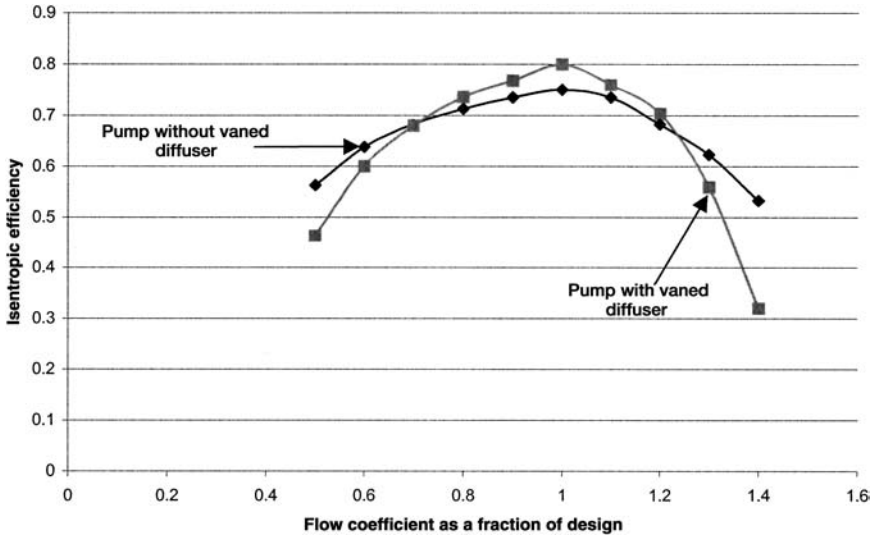

Figure 15g The effect of diffusers on pump efficiency.

istics of typical centrifugal pump stages with and without vaned diffusers. It is clearly evident that stage efficiency is increased in the region of flow coefficient that is in proximity to the "design point." This is the region where the impeller and diffuser are reasonably well matched. The performance increase indicated is the result of the recovery of kinetic energy in the diffuser flow passages. Also evident from the figure is the dropoff in efficiency compared with the nondiffused pump as we move farther from the design flow coefficient. This characteristic is the result of the mismatch of the **C** vector (the absolute fluid outlet velocity from the impeller) with the vane angle of the diffuser's leading edge. This leading edge becomes the source of incidence losses, which continue to increase as we move away from the design flow coefficient, and will eventually lead to separation (or "stall") at the leading edge. This phenomenon often leads to a discontinuity in the pump's H–Q characteristic at this point. When this occurs, a certain hysteresis is normally exhibited, and an increase in flow coefficient beyond the discontinuity is required to recover "attached" flow.

When a vaned diffuser is incorporated into a centrifugal stage, a small vaneless space is normally provided between the impeller exit and the leading edge of the diffuser. This vaneless space provides for mixing of the wakes generated by the impeller blades and allows the diffuser inlet flow to be somewhat more uniform. The clearance between impeller and diffuser generally attempts to balance minimum pressure losses (which are propor-

tional to clearance distance) with diffuser dynamic loads (which are inversely proportional to clearance distance). Pump manufacturers have generally determined the appropriate range of clearance by experiment, and the criteria thus developed are difficult to defend on an analytical basis. However, clearance values of 6 to 10% of the impeller diameter have given good results.

There are also cases where vane rows that carry the name "diffuser" have been incorporated into a centrifugal stage and perform little (if any) diffusion. In very high-pressure rocket propellant pumps, the outboard edge of the discharge volute (which resembles the letter C in cross section) can be subjected to very large bending stresses due to the high pressure immediately outboard of the impeller. The incorporation of a vane row at this location provides a very convenient set of "struts," which react the aforementioned energy as tension in the vane row. Using a "diffuser" in this way is another method of reducing volute (and thus pump) weight.

When the pumped fluid exits the diffuser (if any), it enters the discharge volute. Seen from the outside, the volute resembles a spiral-shaped horn, or scroll. Internally, the volute is a flow passage that is nearly spiral-shaped and with a flow area that gradually increases in the circumferential direction. Figure 15 shows two cross sections of a typical discharge volute.

Discharge volutes are typically designed to one of two possible criteria. Up to the late 1950s, the distribution of flow area in the volute was typically tailored to maintain constant average velocity in the volute. Up to this point, liquid rocket engine systems were typically fixed-thrust systems, and the problems unique to a large, pump-fed variable thrust engines were not yet fully appreciated. As a part of various investigations into pumps that could operate across wider flow ranges, Report 936 of the NACA (by Brown and Bradshaw) showed analytically the advantages of designing a volute with an area distribution designed to conserve angular momentum.

It can be shown that when a volute is designed to conserve average velocity, the angular momentum distribution is nonuniform and monotonically decreasing as we proceed around the volute toward the pump discharge. By applying the moment of momentum equation to the volute bulk flow, and by making an assumption of a free-vortex distribution in the radial direction, an impeller exit pressure distribution can be calculated. When integrated in the circumferential direction, it can be shown that a nonzero net radial load exists on the impeller. This load must be reacted by the shaft-bearing system. This net radial load generally increases at higher-than-design flow coefficients, and numerous component tests of propellant pumps showed bearing distress due to this load during testing.

When the above constant-velocity area distribution is modified so as to conserve angular momentum (i.e., $rC_\theta = \text{constant}$), the volute becomes a diffusion device at and below the design flow coefficient. Moreover, the

integration of impeller exit pressure shows radial loads that are nearly zero (at or near the design flow coefficient), and this result has been substantiated many times in instrumented pump tests.

A point should be made here with regard to the issue of volute sizing. We have shown earlier that since the volute occupies the largest radius in a typical pump, and is subjected to the highest pressures, its weight is a substantial fraction of the total pump weight. As such, it is quite tempting to conserve pump weight by deliberately sizing the volute "small." This design choice increases fluid velocities within the volute for a given mass flow rate. If this is allowed to go to extremes, off-design pump operation may result in extremely high bearing loads and correspondingly short life. It should be pointed out that off-design operation can be induced either by a variable thrust engine system or simply by volute/impeller mismatches due to manufacturing tolerances. If an aggressive volute-packaging scheme is sought, careful attention should be paid to the interactions between the propellant pump and the rest of the engine system. In addition, pump radial loads should be computed for component parts that span the range of allowable manufacturing tolerances.

If excessive radial thrust loads exist due to volute geometry, a number of alternative discharge schemes exist to minimize this problem. Examples of this are shown in Fig. 19. These approaches seek to establish an impeller exit pressure profile that is as symmetric as possible.

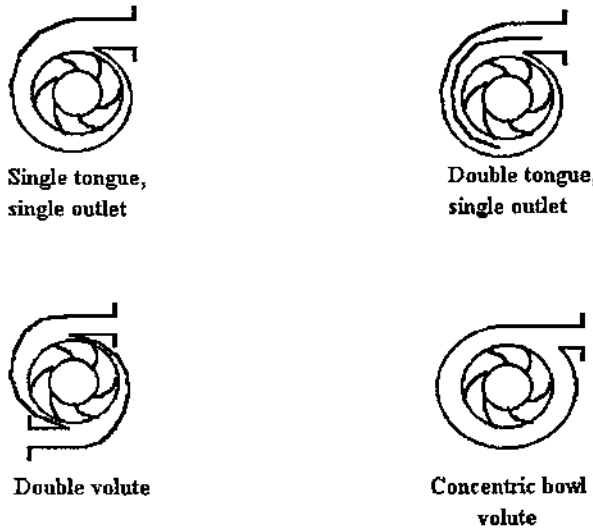

Figure 19 Some examples of centrifugal pump volute configurations.

I would like to conclude this section with a brief discussion of some general aspects of pump hydraulic performance and some of the factors that affect it. Figures 16 and 20 are generic plots of the *H–Q* characteristics of typical centrifugal pump stages. The curves in the *H–Q* plot are typically derived from component-level tests of a propellant pump by a test setup such as that shown in Fig. 21.

The vertical axis of the *H–Q* characteristic represents the head developed by the pump stage and is usually expressed in units of ft (the units are more properly shown as ft-lb_f/lb_m). The horizontal axis represents pump volume flow, usually expressed in gal/min. The two negatively sloped curves in Fig. 19 represent measurements of pump developed head as a function of the pumped flow, while maintaining the pump shaft speed at a constant value—N_1 and N_2 rpm in Fig. 16. It is typical to measure pump performance over a range of speeds in this manner.

Some general observations and cautions about the "constant-speed" *H–Q* curve can be made. First, it can be seen that (for a given operating speed) there exists a maximum flow rate for which the pump develops zero head. The portion of the curve at or near this maximum flow rate is often derived analytically, as opposed to actual testing. The reason for this is

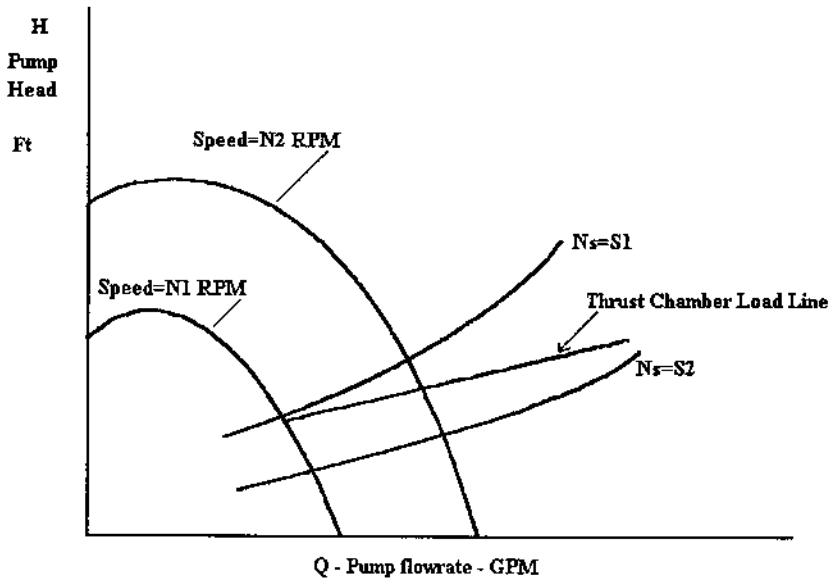

Figure 20 Head-capacity performance curve for a typical centrifugal pump stage.

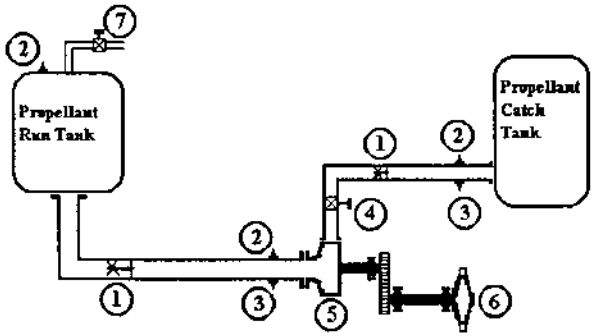

Figure 21 Possible design of centrifugal pump component test stand: 1, propellant flow meter; 2, pressure transducer; 3, temperature transducer; 4, pump discharge throttle valve (may be remotely controlled); 5, pump stage under test; 6, pump stage prime mover; 7, run tank vent valve (may be remotely controlled).

simply that the forces involved in such grossly off-design operation can be destructive to a highly loaded pump.

We can also see that for a flow rate of zero, the pump developed head is a maximum. The head curve increases monotonically between max flow and zero flow and has everywhere a negative slope. This type of H–Q characteristic is called a *continuously rising* characteristic, for obvious reasons. This type of characteristic is sometimes claimed, but rarely (if ever) achieved. Continuously rising H–Q characteristics generally require pump specific speed values that are substantially in excess of those that can be achieved in a liquid rocket propellant pump.

Figure 20 shows an H–Q characteristic that is more indicative of those actually achieved in highly loaded centrifugal pumps. We can see that, at a given operating speed, the flow for maximum head is nonzero and is typically 40–50% of design flow. Below this "maximum head" flow rate, the H–Q characteristic is positively sloped. This means that the pump will respond to a decrease in flow with a decrease in developed head. This is not the behavior that is generally desired for a pump as part of a system, since the normal desire would be for a decrease in system flow to be met with an increase in pump head, to attempt to restore system equilibrium. In the case of a positively sloped H–Q characteristic, it would be (theoretically) possible for a small decrease in flow to bring about the complete collapse of the pump discharge pressure. For this reason H–Q characteristics with a steep negative slope are normally desired. Maximizing the pump's target specific speed best brings this about. High values of pump N_s result in lower target values of pump head coefficient. Lower values of pump head coefficient

generally result in lower pump hydrodynamic loading, which acts to both steepen the H–Q curve and move the point of zero slope to lower flow rates.

Referring again to Fig. 20, the reader will note the two curves labeled "$N_s = S_1$" and "$N_s = S_2$." These curves represent loci of constant values of specific speed [Eq. (1)]. When a pump is tested by operating it against a "constant" load such as a cavitating orifice or throttle valve, changes in the pump operating speed will result in the H–Q data traversing a curve such as this. To say this another way, the pressure versus flow characteristics of a cavitating orifice or valve match the characteristics of a typical pump, with the result that varying the pump speed against the constant load will produce a curve of constant specific speed.

Also shown in Fig. 20 is the H–Q characteristic (or "load line") of a typical liquid rocket engine thrust chamber. Since a rocket chamber essentially represents a "choked" orifice whose working fluid is a perfect gas, the H–Q characteristic of this device is a straight line. It can be seen from this that in order to support operation of a thrust chamber over a given range, the pump must be capable of traversing a corresponding range of specific speed (or flow coefficient) values. In particular, the H–Q characteristic over the required range of pump operation must be stable (negatively sloped). This somewhat complicates the design of a propellant pump that is to power a variable-thrust rocket engine system. The requirement for H–Q stability over a given range often means that the "design operating point" for the propellant pump and that for the engine system as a whole may not be the same point.

Axial-Flow Pumps

In the early 1960s, requirements began to take shape for a generation of liquid rocket engine systems that would use liquid hydrogen (LH_2) in conjunction with liquid oxygen (LOX) as propellants. This new propellant combination would represent the single biggest advance in liquid propulsion since the V-2. When reacted under favorable conditions, LH_2 and LOX deliver a specific impulse performance that is 40–50% higher than the "closest second" propellant combination under similar circumstances. In particular, upper stages powered by LH_2 and LOX could provide sufficiently high performance for a reasonably sized and powered "Advanced Saturn" configuration to lift an Apollo spacecraft to the moon in a single launch.

While the performance characteristics of LH_2 were shown to be very attractive in vehicle-level trade studies, this performance would come at a price. Two attributes of LH_2 would prove troublesome in the development of propellant delivery systems and turbomachinery.

1. First, LH_2's extremely low temperature (36° R to 55° R depending on system operating pressure) results in very high external heat leakage rates into the engine system. These high heating rates would require the engine's fuel system to be insulated in order to preserve the thermodynamic state of the propellant.

2. Second, LH_2's very low density requires that very large work inputs be provided to pump the fluid through a given pressure rise. This would result in a given pump stage being power-limited to a lower pump pressure rise with LH_2 than with other, denser propellants.

Sizing exercises for the Saturn launch vehicle upper stages resulted in baseline engine thrust chamber pressure requirements in the range of 750–1,000 psia. This placed LH_2 turbopump discharge pressures at approximately 1,300 psia, which was at or above the maximum capability for a single centrifugal stage of the day. When this baseline requirement was combined with studies to define a likely amount of "uprating" required over the lifetime of the system, it was clear that a multistage fuel pump would be required.

At the time of these studies, the problems associated with diffusion of high-velocity flow between successive stages of a centrifugal pump had not been addressed satisfactorily. While "industrial" pumps were capable of multistage operation, rocket turbopumps present unique problems. These are related to very high impeller exit fluid velocities and the volume and weight constraints associated with a typical rocket engine system.

For the above reasons, many considered a centrifugal pump to represent an excessive risk for the first generation of LH_2 pump. Requirements were too close to the "edge" of capabilities, and uprating was considered to be a research problem. For the first large LH_2 pump, designers settled instead on an axial-flow pump configuration.

The first successful multistage axial-flow pump designs borrowed heavily from axial-flow compressor technology of the 1950s. Since a great deal of experience already existed with multistage axial-flow compressors, the technical capability to meet any reasonable pump discharge pressure requirement existed merely by adding together a sufficient number of pump stages.

Figure 15(h) shows a cross-section schematic of a typical multistage axial-flow turbopump. Note that this pump contains an inducer (described in a subsequent section) plus seven axial-flow stages. In a typical axial-flow pump, a "stage" consists of a row of rotating blades followed by a row of nonmoving stator blades. The rotor blades accept the outlet flow from the previous stage's stators, perform a given amount of work on the pumped flow, and may or may not diffuse it somewhat in the process. The following

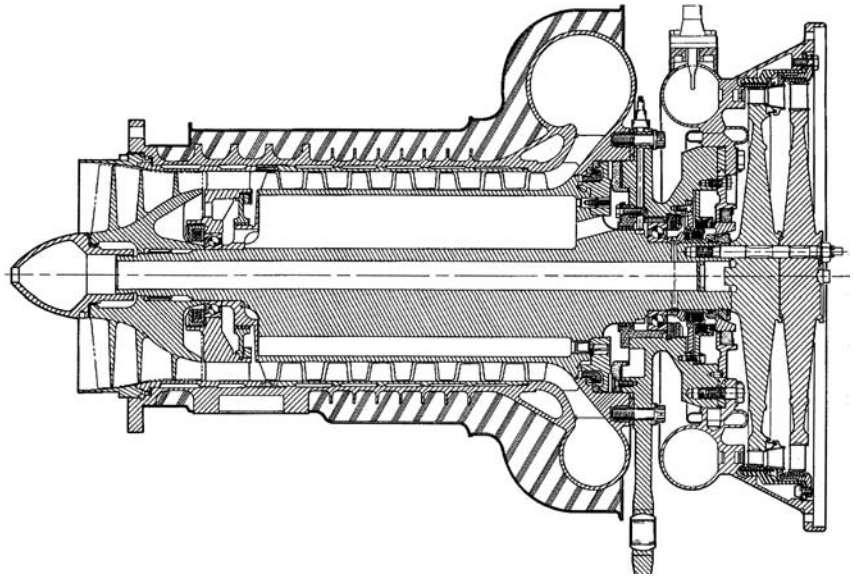

Figure 15h Cross-section of a typical axial flow turbopump.

stator row accepts the rotor's outlet flow, diffuses that flow to convert kinetic energy into static head, and turns the flow field so that its direction matches the inlet direction requirement of the next rotor. Thus, the stator row removes most of the swirl from the rotor outlet flow field, and this swirl energy is converted to static head as efficiently as possible. This pattern is repeated in the subsequent stages of the pump. Although it is not apparent from the figure, each of the seven axial stages is of identical hydrodynamic design. Thus, each stage contributes approximately 1/7 of the total pump head rise (less the inducer head rise). The final axial stage delivers the pumped flow through a radial diffuser and into a discharge volute that are identical in character with those to be found in centrifugal pumps.

The axial-flow pump and centrifugal pump operate on exactly the same physical principles. However, differences in their geometry make them substantially different in their detailed performance characteristics. The remainder of this section will highlight the factors that distinguish axial-flow pumps from their centrifugal-flow cousins.

The most obvious physical difference between the centrifugal and axial configurations can be seen from a study of Fig. 15(h) and 15. It will be noted that, for a given machine overall diameter, the inlet flow area of the axial pump is substantially larger than that of the centrifugal pump. This leads us to a first conclusion that, for a given size class of pump, the flow rates

intended to be processed by an axial-flow machine are noticeably larger than that of the centrifugal-flow machine. By inspection of Eq. (1), we can therefore deduce that the axial-flow machine is to be applied to a higher range of specific speed than the centrifugal machine.

Another very important fundamental difference between the axial and centrifugal pumping elements concerns the details of their respective head generation mechanisms. Figure 15(i) shows a simplified sketch of flow over an axial-flow blade element. The total ideal head rise across this blade element is (like its centrifugal cousin) defined by Euler's equation [Eq. (7)]. However, unlike the centrifugal rotor, for which there is a relatively large change in radius from rotor inlet to exit, flow exits the axial rotor at essentially the same radius at which it entered. To understand the effect of this phenomenon, Eq. (7) could be solved parametrically with "sample" numbers. We might assume that in a typical centrifugal stage, the rotor exit radius is twice that at the inlet (this is a fairly typical situation). For a comparable single-axial stage, the rotor inlet and exit radii are assumed equal (this is the result of an assumption of radial equilibrium). Assuming that all other attributes of both stages are within reasonable ranges,

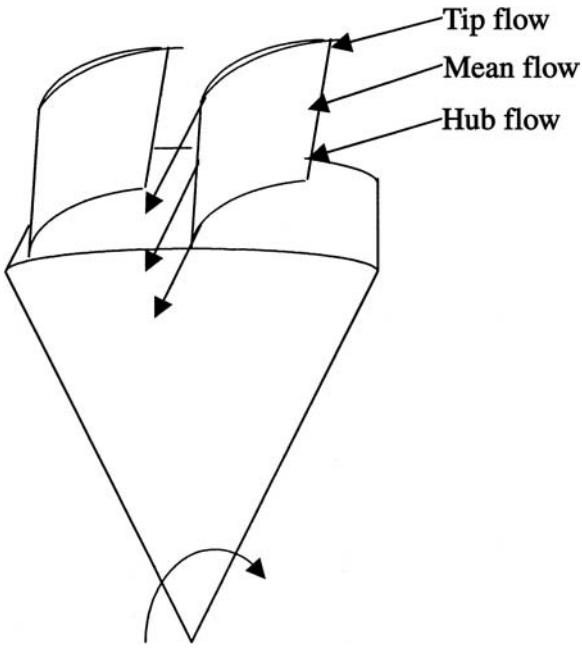

Figure 15i Streamline flow over an axial flow blade.

solutions of Eq. (7) for both stages will yield Euler heads for a centrifugal stage in the range of 2 to 5 times that of an axial stage. This result illustrates the contribution of radius change to head generation in a centrifugal stage versus the axial stage.

For the reasons listed above, design point head coefficients available from axial-flow stages are limited in comparison with typical centrifugal stages. For example, whereas a heavily loaded centrifugal rotor may be capable of head coefficients as high as 0.7, an analogous axial-flow stage may have a peak head coefficient of on the order of 0.4. It should be noted that a stage such as this would have a relatively poor operating range due to the low rotor-relative outlet velocities implied by the vector diagram of such a stage. Achieving this low rotor-relative outlet velocity would require large amounts of diffusion within the rotor, with the attendant problems at flow rates less than design.

In addition to the relatively limited total head per stage in a typical axial pump, it should be understood that kinetic energy constitutes a larger fraction of the total rotor work input than in a centrifugal machine. For this reason, efficient diffusion between the stages of a multistage axial-flow pump is crucial to efficient operation at the design point. In addition, the ability of the interstage diffusion system to perform at off-design flow coefficients may in itself determine the range of the pump's H-Q characteristic over which stable operation is possible.

The characteristics of large inlet flow area (larger than a typical centrifugal stage) combined with relatively low head per stage combine to place axial-flow pump stages at the high end of the specific speed spectrum. It can be seen from Fig. 14 that axial pump stages are generally applicable at stage specific speed values of between 3,000 and 10,000 (rpm-gpm-ft units). It is important to remember that this reference to applicable N_s ranges is for single-pump stages only. As was mentioned previously, differentiating between the N_s-value of an entire pump and that of a single stage is required to prevent nonsensical interpretation of results. For example, an LH_2 pump for a certain large engine operated at an overall pump N_s of approximately 900. The high head implied by this low N_s was split between sufficient axial-flow stages that each pump stage operated at an N_s-value of approximately 4,500.

Figure 15(j) shows a notional rendition of several axial-flow pump stages separated by specific speed. The variation of stage geometry with specific speed is apparent from the figure and is analogous to that of centrifugal stages. In particular, the rotor's radius ratio (hub radius divided by tip radius) varies inversely with specific speed, much as the b_2 dimension of a centrifugal stage varies with specific speed. In addition, the optimum head coefficient varies inversely with specific speed, with the implication

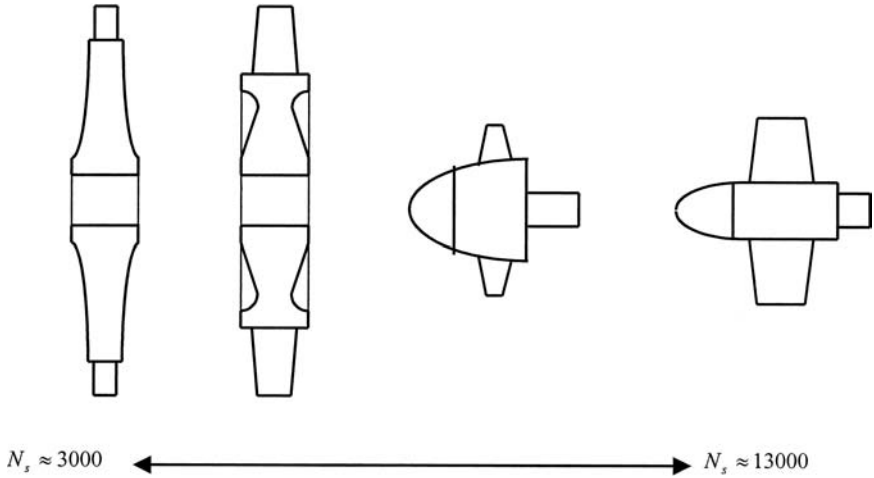

Figure 15j Geometry of typical axial flow pump stages over a range of specific speeds.

that increasing stage N_S will "unload" the stage hydrodynamically. This idea is particularly important with axial-flow stages, where successful diffusion across a range of flow coefficients can be of paramount importance.

Due to its dependence on efficient diffusion between multiple stages, the axial-flow pump is often described as depending on "finesse" for its operation, as opposed to the "brute-force" label of a typical centrifugal stage. One of the consequences of this dependence on efficient diffusion is a fundamental difference in the shape of the *H–Q* characteristic of an axial pump versus that of a centrifugal. Figure 15(k) shows a comparison of typical *H–Q* characteristics for two single-stage centrifugal pumps and a multistage axial-flow pump. We have discussed previously the nature of the centrifugal's *H–Q* characteristic, including the gradual shallowing of the curve to zero slope at decreasing flow rates, followed by a transition to positive slope. In contrast, the axial pump's behavior includes a relatively steep negative-sloped *H–Q* characteristic, with a point discontinuity referred to as the "stall point." The axial pump *H–Q* curve in the figure conveys the notion that the pump's discharge pressure completely collapses at this "stall point." Although this is not universally true, numerous pumps have exhibited this behavior. The rapid decrease in developed head at flow rates lower than "stall flow" is usually caused by hydrodynamic stall (frequently vane leading-edge stall) of one or more diffuser rows within the pump. If the stall condition occurs only in a last-stage diffuser row, the pump's behavior

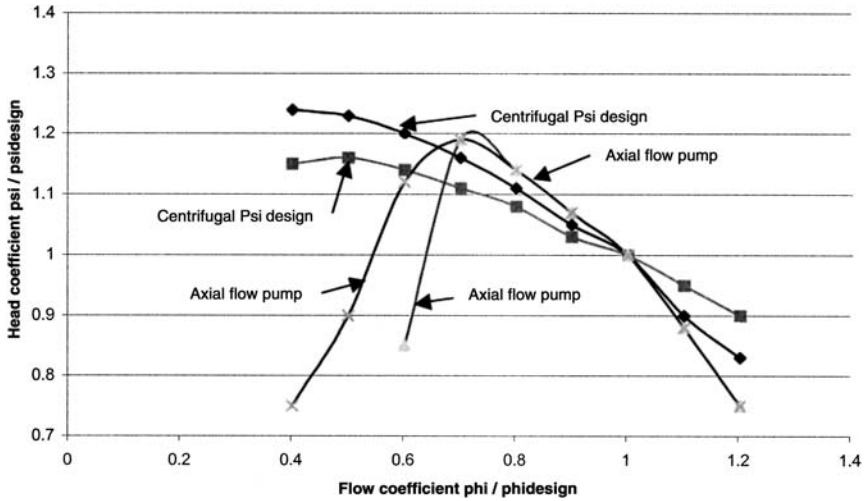

Figure 15k *H–Q* characteristics for several typical pumps.

could fall along the curve labeled "shallow depth of stall" in Fig. 15(k). The principle here is simply that the more diffuser rows continue to operate, the shallower is the depth of stall. On the other hand, if a diffuser in one of the "early" stages of the pump stalls, the velocity diagrams in all subsequent stages are likely to be upset, resulting in a near total collapse of their developed head. The further toward the pump inlet the stall propagates, the steeper is the depth of stall.

The propensity of multistage axial-flow pumps to perform in the manner described above has discouraged their application in modern liquid rocket engine systems. It should also be noted that attempts at "aggressive" packaging for weight savings (i.e., fewer pump stages, more highly loaded stages, etc.) will only aggravate this tendency. It is a fact that axial-flow pumps designed with an effort toward weight conservation have been unable to support significant thrust-level changes of the engine systems and, in one instance, have been unable to support the engine system starting transient. In this last case, elaborate prestart procedures and special control system considerations were necessary to ensure satisfactory engine starts.

Inducers

The continued tendency to optimize launch vehicle design for minimum inert structural weight is well known. Since the propellant tanks of a large liquid propellant launch vehicle are typically the largest pieces of vehicle

structure, the ability to lighten these tanks promises gains in vehicle payload performance that vary from significant to "very large," depending on the size of the launch vehicle. Reducing the weight of these propellant tanks generally requires that internal tank pressures be reduced. The tank pressures needed are normally dictated by the required turbopump inlet pressures of the liquid rocket engine system employed. Therefore, the normal course of launch vehicle design optimization requires a separate optimization of the engine system to enable it to function at turbopump inlet pressures that are as low as possible. In addition, when cryogenic propellants are employed, the propellant storage temperature is typically within a few degrees of its saturation temperature. This results in propellant pump inlet NPSH-values [see Eq. (12)], which are low by most standards.

It has been previously discussed that rocket propellant pumps are normally aggressively packaged in order to reduce weight. A product of this aggressive packaging is a pump stage that is under a high hydrodynamic loading. For a typical centrifugal or axial-flow pump stage, this loading is normally high enough that the low NPSH provided will result in unacceptable cavitation of the stage. In order for these stages to operate satisfactorily, an auxiliary pumping element is required to raise the pumped fluid's pressure such that cavitation of the stage is minimized or prevented. Such a device is called an inducer. Figure 15(l) shows simplified sketches of several types of inducers that have been used in rocket pumps.

It is often said or implied that the rocket turbopump industry has been the major (or only) contributor toward the capability to operate under very low-NPSH conditions. However, advances in this capability have also been driven by the steam turbine power plant industry. The condensers at the outlet of the last turbine stage often cool the water to a temperature just below that of boiling, after which the water is recirculated to the boiler-feed pump inlet. Under these conditions, the boiler-feed pump is operating in a low-NPSH situation. Boiler-feed pump first stages that are equipped with inducers are not uncommon in these situations.

The Redstone battlefield missile (discussed previously) was the first large liquid propellant rocket built in the United States and carried a warhead over a range of 200 miles. The liquid rocket engine system that powered the Redstone was able to operate with noninduced turbopumps. This was due primarily to the missile's limited range and payload and resulting relaxed packaging requirements for the turbomachinery. However, the generation of missile systems immediately following the Redstone represented a fundamental advance, with the requirement that a missile of approximately the same size reach ranges of in excess of 1,000 miles with a heavier payload. Packaging studies for the turbomachinery for these systems indicated the need to operate at a pump inlet suction specific speed of 16,000

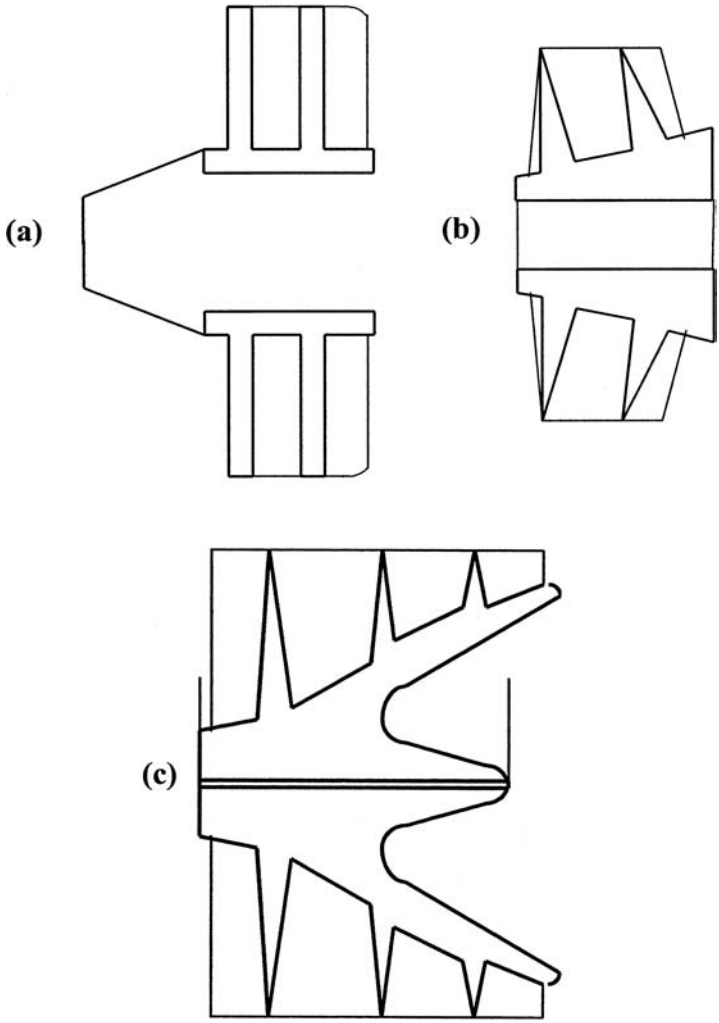

Figure 15l Typical inducer configurations. (a) Cylindrical hub and tip, (b) Cylindrical tip tapered hub, (c) Cylindrical tip tapered hub.

to 18,000 N_{ss} units [see Eq. (12)]. This is in excess of double the 8,000 N_{ss} units that is generally taken to represent the upper end of noninduced pump operation.

The inducer that emerged from design for the above-mentioned engine system is shown in Fig. 15(l)(a). Several characteristics of this inducer are

worth mentioning. First, both the hub and tip are of constant diameter, referred to as a *cylindrical* hub and tip. For this reason, this inducer is truly an axial-flow pumping element. In addition (although this cannot be discerned from the figure), the blading of this inducer is noncambered, or *flat-plate* blading. This implies that the blade exit angle is equal to the blade inlet angle. All flow turning is then done as a result of traversing the leading-edge incidence angle. Attempts to generate increasing head with the flat-plate blading will result in ever-increasing inlet incidence angles, with high losses and large-scale cavitation resulting when inlet incidence becomes excessive. For this reason, head coefficients of these flat-plate inducers are generally limited to values of around 0.08 or less, and best performance is achieved at inlet flow coefficients in the neighborhood of 0.1. Of course, for any given blade inlet and exit angle and inducer speed, the ideal total developed head can still be computed from Euler's equation. The somewhat inflexible nature of the flat-plate blading makes this inducer rather primitive by today's standards. However, the incorporation of this inducer constituted a significant breakthrough in performance and packaging potential. It allowed substantial increases in the pump operating speed at low inlet NPSH. This speed increase allowed reduction in outside diameters of rotating components such that a turbopump of a given physical size could generate over twice the power of that previously possible.

Attempts to generate higher head rises with the inducer in Fig. 15(l)(a) proved to be disappointing. A change from flat-plate to cambered blading enabled some increase in head coefficient capability; however, these attempts were hampered by the need for excessive turning at the inducer hub [blade speeds are slow here, so large hub cambers are required to satisfy Eq. (7) if developed head is to be constant at all radii]. The low rotor-relative outlet velocity that comes about requires very large amounts of diffusion, which result in flow separation at the hub. This phenomenon strictly limits the inducer head coefficients that are attainable with the cylindrical hub design.

The need to provide inducers with head coefficients substantially in excess of 0.1 was answered by the design change shown in Fig. 15(l)(b). While the tip of this inducer is still a cylinder, the inducer hub is tapered. The result is that the flow streamlines adjacent to the hub change radius during the pumping process, reminiscent of a centrifugal pump stage. This feature greatly increases the head rise capability of the inducer. The mechanism behind this increased head capability can be interpreted in either of two ways: if we refer to Eq. (7), and station 2 is taken to be the inducer exit with station 1 at the inducer inlet, we can see by inspection that U_2 is substantially greater than U_1 along the inducer hub. For a given head rise, the required change in fluid tangential velocity (i.e., the amount of blade

camber) is proportionally lower. The other interpretation is: for a given amount of fluid turning at the inducer hub, the hub taper reduces the available flow area, raising the required axial velocity to the point where boundary layers remain well behaved.

A further increase in inducer head rise capability was realized by a transition to the configuration shown in Fig. 15(l)(c). This configuration is often referred to as a *high head inducer* and represents a larger degree of hub taper than previously discussed. Inducer head coefficients of 0.25 are easily achieved with this configuration. The highest suction performance is produced at inducer inlet flow coefficients over a range of 0.07 to 0.1. It should be pointed out that lower inlet flow coefficients would be desirable in theory, but fabrication and structural problems associated with very thin blades normally prevent this. It should also be noted that the hub taper introduces larger blade physical spacing near the inducer discharge, which can reduce the blade solidity in this area to values that are too low to support high blade loading. To deal with this, the type of inducer shown in Fig. 15(l)(c) is often equipped with a row of ''splitter'' blades whose leading edge is placed approximately halfway between the inducer inlet and discharge. This splitter row allows higher blade loading near the inducer discharge by placing the local blade solidities in this area at or near the optimum value.

A modification to the inducer configuration shown in Fig. 15(l)(c) involves extending the inducer in the axial direction and equipping it with a single row of axial-flow blades near the discharge. This single-axial stage is referred to as a ''kicker'' stage. The kicker stage is separate from the inducer itself in order to implement the axial-flow stage at optimum solidity. The combined inducer/kicker rotor is capable of head coefficients of 0.5 or higher. This configuration has found use in ''low-pressure'' or ''boost'' pumps for high-pressure liquid rocket engine systems.

AXIAL THRUST

In the design of turbomachinery, there are a number of individual design issues that arise and must be dealt with to obtain a satisfactorily performing machine. As a rule, the design obstacles that confront conventional turbomachines are magnified in rocket machinery due to the higher operating pressures, energy densities, and smaller allowable envelopes. In this chapter, we have at least hinted at a number of the important issues. I feel that one of these deserves somewhat special mention. This issue concerns rotor axial thrust. The ability to predict axial thrust satisfactorily is an absolute necessity, as we shall see.

As the name implies, *axial thrust* refers to forces acting on the rotor in a direction parallel to the axis of rotation. There are two main contexts for discussion of these forces. In the context of overall rotor design, the term "axial thrust" is generally used to refer to the resultant of all axial forces acting on the rotating assembly. This resultant force is used to determine what type (if any) of axial thrust control devices are necessary. The type of thrust control system used can also depend on the perceived uncertainty of the axial thrust predictions. In some cases, the aerodynamic or hydraulic design of certain turbopump components may have to be altered due to axial thrust considerations. We discuss this later.

The second context for discussion of axial forces concerns the structural design of rotor components when these components are considered as deformable bodies. For example, a turbopump drive shaft may be subjected to a net compressive load due to thrust forces from two opposing rotor components. The structural integrity and/or the stiffness of the drive shaft may be questionable under these conditions. In the case of a built-up rotor (a configuration without a shaft proper and axially retained by a central draw bolt), the distribution of axial loads along the rotor may decide the fundamental orientation of turbopump components. An example of this might be orienting the turbine of a common shaft turbopump such that the tie bolt is subjected to tensile force rather than a compressive force that would be sufficient to relieve the draw bolt preload. Although most of our discussion is oriented toward the first of these contexts, we attempt to carefully distinguish between them when necessary.

The primary generators of axial loads on a turbopump rotor are the power-generating and absorbing components, namely turbine stages, axial and centrifugal pump stages, and pump inducers. We try to provide examples of each.

Refer to Fig. 22. Depicted here is an example of a single-stage turbine rotor. In this example, the turbine rotor is assumed to be supported on its own bearings, independent of any other rotating elements. The rotor shown in the figure represents a classic single-stage impulse turbine. Such an assembly could have been typical of small rocket turbopumps of the 1950s and early 1960s and might be found today in numerous small auxiliary power units. Note the stated flow conditions at various points in the turbine. Since the stage is an impulse stage, we may assume that there is no static pressure drop across the rotor. Therefore, $P_{\text{rotorin}} = P_{\text{rotorout}}$ (actually, a small static pressure drop would exist across the rotor, but we ignore this). Also, note the velocity diagrams showing the absolute and rotor-relative velocity components at the rotor inlet and exit. In a "perfect" rotor, the rotor-relative velocity at the stage outlet (V_2) would equal that at the rotor inlet (V_1). However, in reality, the magnitude of V_2 will be less than V_1. This

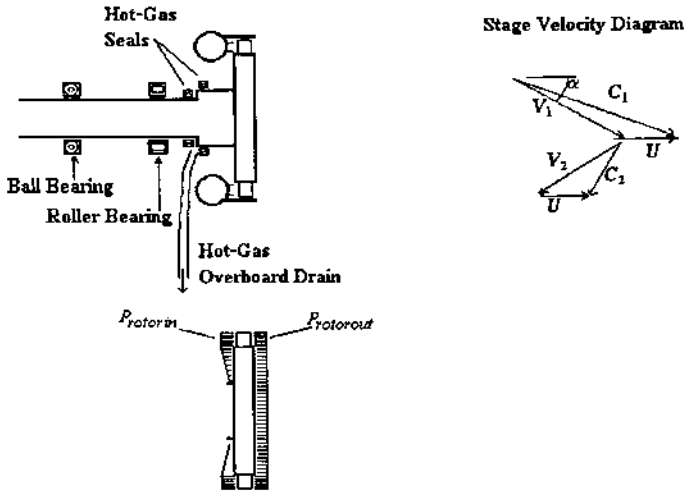

Figure 22 Single-stage impulse turbine.

is due to unrecoverable losses across the blade row, since the flow is nonreversible. Analytical methods exist for quantifying the difference between V_2 and V_1 and are mentioned in the turbine section of this chapter.

With the flow conditions specified, we can set about discussion of the turbine axial force components. The resultant turbine axial force is made up of a summation of two main components. These are a pressure force on the turbine due to a static pressure difference across the rotor, and a momentum force due to a change in fluid axial momentum across the turbine. The turbine pressure force can be thought of (for convenience) as itself consisting of two components. These are a static pressure difference across the blade-row annulus, and the difference of the pressure forces acting across the top and bottom of the turbine disk. For a true impulse-type turbine stage, the blade-row annulus pressure force is obviously zero, since no static pressure difference exists across the blade row. The pressure forces acting on the top and bottom (rotor inlet and rotor outlet) sides of the turbine disk are not so straightforward. If we refer again to Fig. 22, we can see that both turbine disk faces are subjected to vortex-type flow of the turbine working fluid. In the case of the rotor inlet side, the disk (which is moving at a velocity U) is subjected to flow that moves radially inward, beginning at the disk periphery where flow is moving at a velocity $V_1 \cos\alpha$ relative to the disk. Due to interactions between the disk and the layers of fluid adjacent to it, the tangential component of the disk-relative fluid velocity is affected in a

manner similar to that of a vaneless radial pump being run with reverse throughflow. On its way to the center of the disk, the working fluid undergoes an enthalpy increase and a static pressure decrease. The enthalpy change distribution, and thus the pressure change distribution as a function of radius, could be readily computed from Euler's equation if the tangential velocity distribution on the face of the disk were known. This velocity distribution is a strong function of the disk velocity, the geometry of the disk, and the nature of the enclosure in which the disk is rotating. The limiting conditions for this velocity distribution would be a free vortex (in the case where the rotating disk did not influence the fluid's motion) and a forced vortex if the fluid motion matched the disk motion. In reality, for a smooth-surfaced turbine disk, the actual velocity distribution is found to be somewhere between these two limiting cases. A situation similar to that just described exists on the rotor outlet side of the turbine disk. For more specific information as to the calculation of these velocity distributions, see Refs. 9 and 10. H. F. Rue et al. [10] undertook a fairly extensive test program with both water and liquid hydrogen flowing radially inward as well as radially outward over both ribbed and smooth disks. Rib height on the ribbed disks was also varied, as were the clearance between the disks and the housing in which they rotated. Measurements of static pressures on the disk face were obtained at several radii and could be used to deduce velocity distributions across the disk face. The central idea in Rue's effort was that the fluid angular velocity at a given radius was a fraction of the disk angular velocity. The fluid-to-disk velocity ratio is known as K. If this ratio is known across a given radial increment, the difference in static pressure across this increment can be computed from

$$\Delta P = \frac{\rho}{g} K^2 \omega^2 R \Delta R \tag{19}$$

Where

ΔP = change in static pressure across a given radial increment.
ρ = fluid density.
K = fluid-to-disk angular velocity ratio.
ω = disk angular velocity.
R = disk radius.
ΔR = change in disk radius.

If the "delta" terms are reduced to differentials, the pressure force on the entire disk face can be found by integrating radially across the disk. It should be noted here that Stepanoff 11 had previously suggested the idea of

the velocity ratio K, but in somewhat simpler terms. The work of Rue et al. appears to be a significant refinement. For the reader who is interested in further investigation, Ref. 9 is suggested. Authors Daily and Nece approach the problem from the standpoint of classification of the fundamental flow regimes involved. These regimes are related to the range of clearance between the disk and stator, as well as the Reynolds number.

When performing these analyses, it is quite important to use care in the evaluation and assignment of boundary conditions. We discuss two of these in particular that have been the source of problems in the past.

The first of these concerns evaluation of the static pressure at the turbine disk periphery on both the upstream and downstream sides of the disk. The computational methods of Refs. 9 and 10 only address the change in this pressure with radius, so a correct evaluation of this boundary condition is obviously fundamental to obtaining valid pressure distributions on the disk faces. Many turbines (particularly smaller impulse stages) have been designed purely on the basis of gas properties at the flow passage mean section, or blade pitch line. These properties include, of course, the gas static pressure. However, working fluid ejected from a turbine nozzle will in fact tend to follow a free-vortex path, the velocity distribution for which has been defined previously. For this reason, a static pressure gradient will also exist in the radial direction across the flow passage, with the highest pressure existing near the passage outside diameter and the minimum pressure near the nozzle hub. If this gradient is significant, the assignment of a mean line static pressure to the turbine disk periphery will be noticeably in error. This will result in an erroneous pressure distribution being computed across the disk upstream face. At least one large production turbine has suffered axial thrust problems due to omission of the nozzle flow passage static pressure gradient from the disk upstream calculations.

Likewise, on the disk downstream side, the hub static pressure should be considered carefully. In this case, the blade outlet flow again assumes a free-vortex distribution with a radial gradient. Hence, the disk periphery (or hub) downstream static pressure should be computed separately from that on the upstream side.

The second boundary condition issue we wish to mention concerns the effect of the various seals used in turbine stages. If we refer to Fig. 22, we may note the placement of a hot-gas seal package on the upstream side of the turbine disk. This seal is placed where it is in order to prevent hot-gas intrusion into the turbine bearing cavity. These seals are typically of the controlled gap type and seal by means of a drain cavity between the two seal rings that is vented to an area of low pressure, such as atmospheric pressure in a gearbox drain system. The presence of this seal package results in a discontinuity in the pressure distribution across the disk upstream face. If

this discontinuity is neglected in the pressure force computations, erroneous results will be obtained. In the case of Fig. 22, if the stage outlet pressure is substantially above atmospheric, equal disk face static pressures (as might be the case with short blades) would mean that the only unbalanced pressure force would exist axially across the disk at the diameter of the hot-gas seal. From this one could draw the conclusion that the placement and diameter of seal packages could be used as tools for control of pressure force components. This is, in fact, the case and is a fairly common practice in turbomachinery design.

Figure 23 represents the next step up in complexity of the turbine pressure force problem. The turbine depicted here is a two-stage impulse turbine, with interstage leakage minimized through the use of an interstage labyrinth seal. The turbine rotor is independently supported on its own bearings, as before. Although the diameter of the labyrinth seal is normally set so as to minimize interstage leakage, its diameter also influences the turbine disk pressure forces in the manner described earlier.

The turbine momentum force is due (as the name implies) to the change in axial momentum of the working fluid as it traverses the blade row. In an impulse stage, this change in axial momentum is due mainly to blade-row losses that cause deceleration of the fluid in the blade row. The momentum force can be expressed by the conservation of linear momentum:

$$\Sigma F = \frac{\partial}{\partial t}\left(\int_{\mathrm{CV}}\int\int \vec{V}\,\rho\, d\vartheta\right) + \int_{\mathrm{CS}}\int \vec{V}\,\rho\left(\vec{V}\cdot\vec{n}\right)dA$$

Where

CV = integration over an entire control volume.
CS = integration over a control surface.

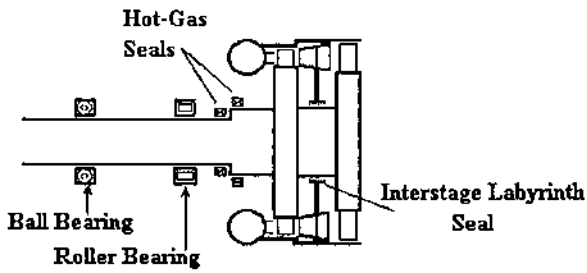

Figure 23 Two-stage pressure-compounded impulse turbine.

$\vec{V}$ and $\vec{n}$ = fluid velocity and control surface normal vectors, respectively.

In this equation, the first term represents the net rate of accumulation of momentum within a control volume. In a "steady-flow" problem such as a turbine blade row, this term vanishes. The second term represents the control volume outlet momentum flux minus the inlet momentum flux. It should also be stressed that the velocity terms in this equation are vector quantities and need to be treated as such.

Through use of these described procedures, the resultant axial force on the turbine rotor can be computed. For a turbine stage as shown in Figs. 22 and 23, where the turbine thrust is reacted by a thrust bearing, the computed value of turbine thrust is used to size and select a suitable thrust bearing.

A simple variant of the above axial thrust problem is shown in Fig. 24. In this instance, the turbine stage shown is a reaction-type stage. As the reader will recall, in a reaction turbine stage a portion of the working fluid static enthalpy drop occurs in the turbine rotor, with a corresponding static pressure drop across the rotor. In this configuration, the axial force component situation is as it was before, with some minor modifications. The blade-row pressure force is now nonzero due to the reaction taking place in the turbine rotor. Also, the rotor momentum thrust term will need to be reexamined due to the effect of the rotor reaction.

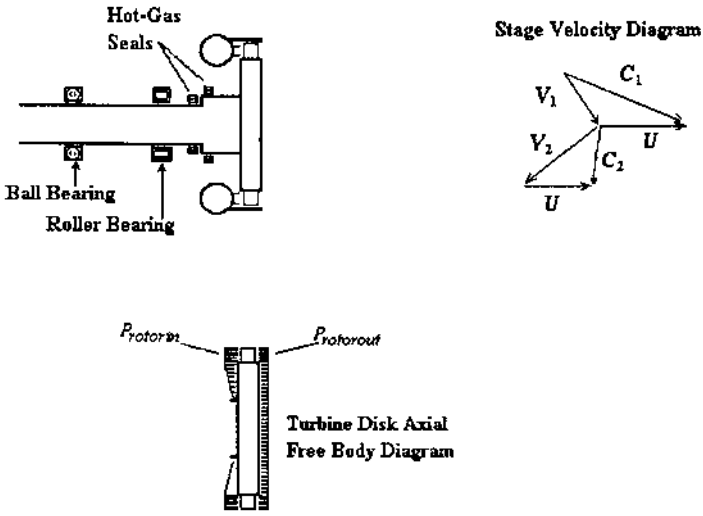

Figure 24 Single-stage reaction turbine.

Pumping elements (i.e., inducers, centrifugal stages, and axial stages) are also generators of axial forces. The fundamental processes that produce axial loads in these elements are exactly the same as those in turbine stages. Consequently, the same analytical techniques used for turbine elements apply also to pumping elements. We discuss an example of each.

Inducers (an example of which is shown in Fig. 25) generate axial loads due to both blade-row pressure forces and fluid momentum thrust. Euler's equation may be written across the blade midspan and the static pressure rise across the blade calculated. This estimate may be functional as a "first cut" for the inducer pressure force. If the inducer has "tall" blades, and if greater accuracy is justified, the blade section may be divided into a series of radial stations. Odd numbers of stations are typically used so that the blade midspan falls inside one of the sections. The blade-row pressure force is then obtained integrating radially across the blade section.

It should be mentioned that thrust analyses of preexisting inducers should be done carefully. The nature of the vortex flow through a typical inducer (particularly a high-performance one) is normally not that of a free vortex, as might be the case with an axial pump rotor row. An inducer blade cross section designed to produce free-vortex flow can easily result in excessive turning and diffusion near the blade trailing edge at the hub. The result of this can be large-scale flow separation in this region. For this reason, high-performance inducers are not usually designed around free-vortex flow.

The other major pressure force term associated with contemporary inducers is that which exists in the cavity inboard of the inducer hub. In many current designs, this cavity is also home to a set of rolling element bearings that support the turbopump rotor. A similar set can usually be found near the turbine end of the machine. This design strategy is shown in

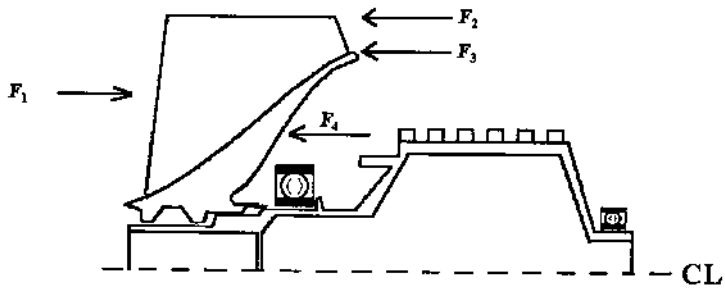

Figure 25 Inducer axial thrust components: F_1, inducer inlet pressure force; F_2, inducer outlet pressure force; F_3, inducer momentum force; F_4 inducer hub cavity pressure force (nonconstant over cavity area).

Fig. 25. The nature of the flow in this cavity is somewhat reminiscent of the distribution over a turbine disk, and load predictions are subject to essentially the same uncertainties as the turbine disk problem. Again, Refs. 9 and 10 can provide us with some useful insight.

The fluid momentum thrust associated with inducers is due mainly to their tapered geometry. Contemporary high-performance inducers generally have tapered hubs, and they may or may not have tapered tips. This results in an increase in the fluid axial momentum across the inducer. This taper is shown clearly in Fig. 25.

Centrifugal pumping elements are easily the most popular pumping elements in use in rocket turbomachinery. As such, their axial thrust characteristics are of great interest. Figure 26 shows a cross section of a "generic" centrifugal pumping element and some of the forces acting on it. As in the case of the elements discussed previously, axial forces are generated due to fluid axial momentum changes as well as pressure forces. Referring to the figure, the pressure force F_1 associated with the impeller inlet area and pressure is readily calculable. The force F_2 is associated with the change in pumped fluid axial momentum. Using the conservation of momentum, this is also calculable, although great care needs to be exercised with regard to the nature of the fluid exit velocity. Although a radial-flow impeller is shown in the figure, this is not the case with many machines. A series of higher specific speed impellers (known as Francis impellers) is commonly used in rocket turbomachines. These impellers expel fluid with a velocity that contains an axial component, and this must be accounted for if axial thrust computations are to be done accurately. The forces shown as F_3 and F_4 are pressure forces exerted on the front and rear shrouds of the impeller, respectively. These pressure forces vary with radius and are due to the recirculating flow that exists between the impeller discharge and its inlet

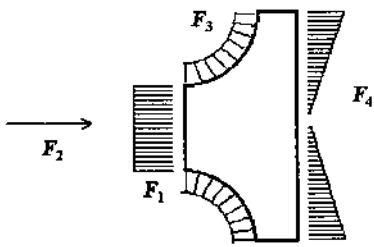

Figure 26 Centrifugal pump stage axial thrust components: F_1, impeller inlet pressure force; F_2, impeller momentum thrust force; F_3, impeller leakage pressure force; F_4, impeller rear face (hub) pressure force.

(in the case of force F_3) and between the discharge and whatever rear impeller seal is present (in the case of force F_4). As mentioned previously, Refs. 9 and 10 provide us with some insight as to the nature of these forces, as well as some methods for predicting them. These forces are subject to the same uncertainties in prediction as those of the turbine disk problem (also mentioned previously). There are, however, two important differences. First, the pressure at the discharge of a centrifugal pump stage is the highest of any point in the system. Together with low impeller inlet pressures, this drives both the highest pressure forces in the system and the sharpest pressure gradients. Second, the pump working fluids tend toward being by far the densest fluids in the system. Therefore, a given enthalpy change (a result of the radial velocity gradients across the hub and shroud) results in a pressure gradient that is "steeper" than for that of a less dense fluid. These differences result in a greater uncertainty in the prediction of centrifugal pump axial thrust than for any other turbopump component.

Efforts to alter the axial thrust generated by a centrifugal impeller are generally confined to the pressure force on the impeller rear face. Two techniques are in common use. The first of these involves the placement of an annual seal (referred to as a wear ring) at a specific diameter on the back face. The area inboard of this seal is most often vented to an area of low pressure, typically the impeller inlet, through pressure-balancing holes drilled in the impeller rear face. With the flow area of the pressure-balancing holes much larger than the flow area of the seal, the seal effectively creates a discontinuity in the pressure distribution across the impeller rear face. Through careful selection of the diameter of the rear seal, the rear-face pressure force can be regulated across a moderate range. Incidentally, although the pressure inboard of the seal is sometimes assumed to be equal to the impeller inlet pressure, various test data tend to indicate that the actual value is somewhat higher (up to approximately 10%) than inlet pressure.

The other common scheme used for control of centrifugal impeller thrust consists of a set of "antivortex" ribs that are integral with the impeller rear face. Through proper design of the ribs and careful attention to rib-to-housing clearance, the pumped fluid in this region can be forced to follow a pattern similar to a forced vortex, resulting in a lower-pressure area than for the smooth face. The selection of the rib diameter is the main design variable here. It should be emphasized that if ribs are used, very close attention must be paid to the axial clearance that exists between the ribs and the pump housing. This tolerance must be tightly controlled if consistent behavior is to be obtained. Also, since the effectiveness of the ribs decreases rapidly with increasing clearance, they may not be suitable for designs where axial shaft motion is required.

Although shrouded centrifugal impellers have been most widely used, the open-faced design bears mention. As its name implies, this type of impeller contains no front shroud, with the result that the entire impeller blade arrangement can be seen. The impellers in the propellant pumps for the Titan launch vehicle have used the open-faced design, as have several experimental high-pressure liquid hydrogen pumps built under government sponsorship. This configuration has the obvious advantage that the entire impeller blade array can be easily accessed, which makes manufacturing relatively simple, especially with the advent of numerically controlled machining. Open-face impellers do, however, have some drawbacks. Perhaps the most serious is the precise control that is required of the clearances between the impeller blades and the front of the pump housing. Pump developed head can fall off rapidly as this clearance increases, due to the increased energy dissipated by recirculation in the area of the gap. This situation can make open-faced impellers impractical in a turbopump where axial shaft motion is required. Incidentally, there have been impellers designed that were both open-faced and using back-face antivortex ribs for axial thrust control. These types of impellers can be particularly troublesome by virtue of the fact that two axial clearances must be closely controlled for the pump to function correctly. The reliable history of pumps of this type bears testimony to the craftsmanship of their builders. The other potential drawback to open-faced impellers is that without a front shroud, the impeller generates a different set of axial thrust forces than a shrouded impeller. Whether this is a problem or not depends, of course, on the design of the turbomachine for which the impeller is intended. It has, however, caused some difficulties in the past.

Before we proceed to some examples of turbopump design configurations, it would be desireable to summarize the axial thrust control devices that are in common use. As stated above, impeller seals or wear rings fall into this category, as do balance ribs or antivortex ribs on the back face of a centrifugal impeller. Rolling element bearings of several types are commonly used in conjunction with seals and ribs and are used to react any residual rotor thrust that may exist. Ball bearings of various kinds, including deep groove balls, angular contact balls, and split inner race balls, have all been used successfully as thrust bearings in production-type machinery. To this author's knowledge, tapered roller bearings have not been used in this capacity. However, current trends in rocket turbomachinery design are (and have been for some time) resulting in machinery that is both physically smaller and operating at higher pressures. This combination has been consistently generating resultant rotor axial forces that are beyond the capability of rolling element bearings to react to for any length of time. To react to these high forces, a device known as a *series flow balance piston* has

been employed. This device as employed in a typical centrifugal pump stage is shown in Fig. 27. The term "series flow" is derived simply from the fact that the flow required to operate the balance piston is tapped off from the pump discharge, in effect being in series with the pump discharge. The pump flow passes first through an annular restriction known as a *high-pressure orifice*. As shown in the figure, the flow area of this restriction varies with the axial position of the rotor. The flow, which is now at an intermediate pressure, moves both tangentially and radially inward toward the rotor axis. The pressure distribution acting over the impeller back face produces an axial direction force, which, with proper design, acts equally and opposite to the unbalanced rotor thrust. At a radius close to the rotor axis, the flow passes through another annular restriction known as a *low-pressure orifice* whose area varies inversely with that of the high-pressure orifice. The area downstream of the low-pressure orifice is vented to some area of lower pressure, such as the pump inlet or a bearing coolant flow circuit. The end product of a properly designed balance piston is an axial force over the impeller rear face that varies with rotor position and tends to counter changes in rotor thrust such that axial equilibrium is maintained. Two points should be noted here. First, the axial force capability of the balance piston is fixed by such factors as the pump discharge pressure, the resistances of the high- and low-pressure orifices, and the radius at which the low-pressure orifice is placed. When the balance piston is designed, these quantities are set (if possible) so as to provide a substantial margin between the maximum anticipated unbalanced rotor thrust and the force capability of the balance piston. Also, it should be understood that the balance piston

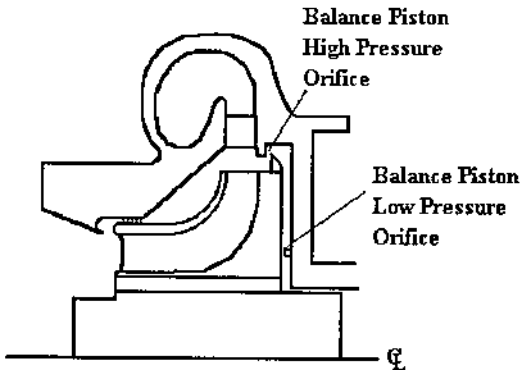

Figure 27 Centrifugal pump stage using a series flow balance piston for control of axial thrust.

is a parasitic device, whose flow requirements have to be added to the pump flow capacity. If the balance piston is included in the initial design, this need not present a problem. However, if the device needs to be added as a retrofit, its flow requirement can penalize both the efficiency and the suction performance of the pump to some degree. There have been past cases where unanticipated high rotor thrust has necessitated the addition of a balance piston. The addition of this device was both difficult and costly. As stated previously, the accurate prediction of axial thrust during design is of the utmost importance.

Using the techniques and references outlined in the preceding paragraphs, it should be possible to compute representative axial thrust forces for any desired turbopump component. The next important design consideration concerns how these components are mechanically integrated to form a complete turbopump.

Axial thrust considerations affect the mechanical design integration of the turbopump in a number of ways. How are the turbine and pump components to be coupled, and what will be their physical arrangement? What types of axial thrust control devices are necessary, and how will they fit into the overall design? If any axial thrust issues remain, can they be resolved by some relatively simple mechanical design change(s)? If not, aero/hydrodynamic modifications to turbine and/or pump elements may prove necessary.

In many instances, the basic coupling and arrangement of turbopump components will be dictated by considerations other than axial thrust, and the designer will have little or no freedom to alter them. For example, in the turbopumps for the Thor and Atlas missiles, the independent shafts for the turbine and the twin pumps were made necessary by the large angular velocity difference between the two. In this case, the turbine axial thrust was reacted to by a suitably sized ball bearing on the turbine shaft. In the case of the pumps, it worked out that the fuel (RP-1) and oxidizer (LOX) pumps exerted axial thrust loads that were similar. In this event, the pumps could be placed in a back-to-back arrangement on the same driveshaft such that the pump thrusts were, for the most part, offset. The unbalanced thrust again was reacted to by a suitable ball bearing. It should be noted here that the ability to react to the steady-state unbalanced thrust with a rolling element bearing was facilitated by the relatively low shaft angular velocity (approximately 6,000 rpm) and the availability of an excellent bearing lubricant in the form of the RP-1 fuel mixed with an extreme-pressure additive. Few contemporary machines will enjoy this luxury.

A simple example of a direct-drive turbopump with thrust reacted to by a rolling element bearing is shown in Fig. 28. In this example, the pumping element is a large (12-in. diameter) inducer, which imparts a head

rise of approximately 700 ft at its design point. Shaft speed at this point is approximately 5,800 rpm. Inducer mass flow rate at the design point is around 1,300 lb/sec. The inducer is driven by a six-stage full-admission hydraulic turbine. Each turbine stage is identical and utilizes a stage reaction of around 30% for good efficiency. The drive fluid for the turbine is LOX at high pressure that is obtained from elsewhere in the engine system. Pressure at the inlet of the turbine is approximately 3,500 psia with a turbine discharge pressure equal to the pump discharge pressure. This allows both pump and turbine fluids to be discharged to a common duct. Leakage of turbine drive fluid into the lower-pressure pump inducer hub cavity is controlled by a labyrinth seal as shown in Fig. 28. The tapered inducer momentum thrust, plus the pressure forces over the inducer inlet, discharge, and rear hub cavity, total an axial thrust force of somewhat in excess of 29,000 lb at the design operating point. The direction of this force is to the left in the figure. It would be desirable to negate as much of this load as possible by tailoring the turbine thrust so as to be equal and opposite the inducer thrust at the design operating point. In this example, the diameter of the rotor labyrinth seal is set such that this goal is achieved. As one can see from the figure, decreasing the seal diameter acts to increase the rotor face area exposed to the turbine inlet pressure. By careful adjustment of this face area, the total turbine thrust is set to the same 29,000 lb as the inducer thrust, but in the opposite direction. Having fulfilled our goal at the design point, attention shifts to the off-design regime. It happens that this turbopump must run satisfactorily down to a pump flow rate of approximately 50% of design. An analysis similar to that for the design point must be conducted for the 50% flow case to determine the rotor axial thrust. For this turbopump, it turns out that the turbine thrust declines more

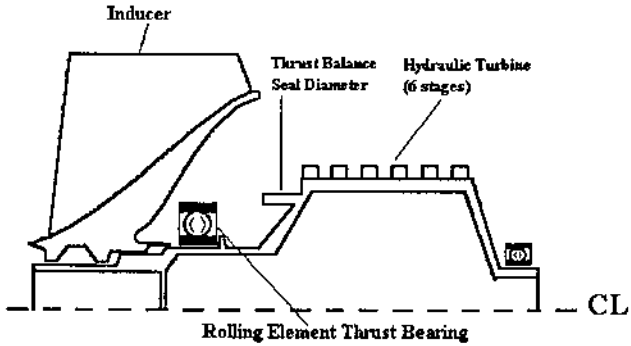

Figure 28 Direct-drive inducer turbopump with rolling element thrust bearing.

rapidly than does the inducer thrust, resulting in a net rotor thrust of approximately 2,500 lb directed toward the pump inlet at the 50% flow condition. At the relatively low shaft speed of this turbopump, a load of this magnitude is easily reacted by a thrust bearing, with a 85-mm-diameter ball bearing being selected.

Figure 29 illustrates a somewhat less straightforward situation. This figure is a schematic representation of the rotor assembly of a contemporary design liquid oxygen turbopump. The rotor illustrated was designed with a two-stage reaction turbine on one end, a large double-suction centrifugal impeller in the middle, and a smaller overhung centrifugal impeller opposite the turbine. The large double-suction impeller theoretically generates no axial thrust due to the symmetry involved. This reduces the problem to one of ensuring that the thrust of the turbine and that of the small overhung impeller are equal and opposite at the machine's design operating point. In the case of the rotor shown in Fig. 29, this balance proved impossible to attain in the first design iteration. The turbine incorporated two stages, each having a degree of reaction of approximately 34%. This pressure distribution was set in the interest of turbine efficiency. However, the nozzle hub outlet pressure of the turbine stages produced turbine disk pressure forces that were too large in comparison to the overhung pump thrust. The discrepancy was too large to be resolved by any allowable

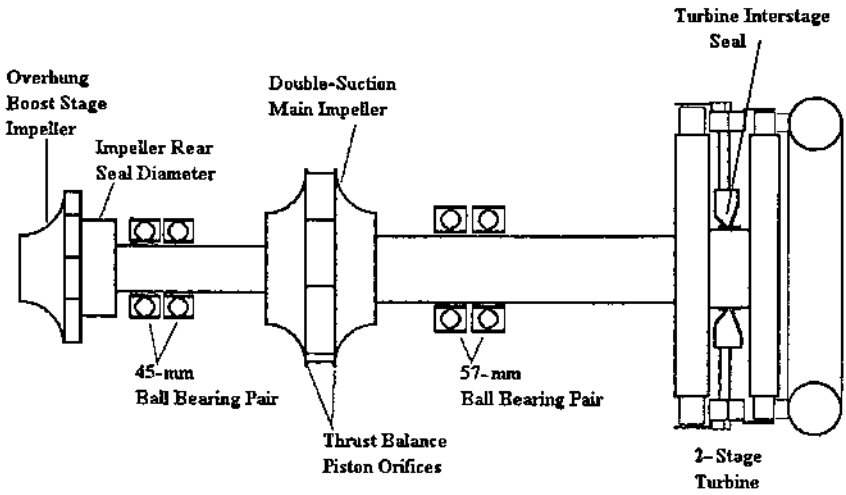

Figure 29 Oxidizer turbopump rotor mechanical arrangement.

modifications to the pump geometry. The only recourse in this situation was reduction in the turbine thrust, which was achieveable only by lowering the nozzle outlet pressure of both turbine stages. This, of course, reduced the degree of reaction in the turbine stages, since the turbine outlet pressure and stage work split were already fixed. The final outcome was the attainment of the design point thrust balance with a sacrifice in turbine efficiency. This turbopump, like that of the previous example, is required to run satisfactorily down to a flow rate of approximately 50% of design. As was also the case in the previous example, the thrust balance obtained at the design point is not applicable in the off-design regime. This requires the use of a thrust control device of some sort. In this example, the unbalanced rotor thrust experienced at off-design conditions is too large to be reacted to steadily by a rolling element bearing. Accordingly, two opposed balance pistons were designed into the large main impeller, using the impeller shrouds as pressure surfaces to develop the axial force. The balance pistons were designed for an axial force capability of approximately 18,000 lb at the minimum turbopump flow conditions, going to approximately 32,000 lb at the pump design point. It should be noted here that in the design of a balance piston for a specified axial force capability, modifications to the impeller inlet and outlet radii may be necessary to meet the target balance piston capacity.

During the start and shutdown transient periods, when the main impeller discharge pressure has not yet developed or has collapsed, an additional thrust reaction device is needed. This is provided by a pair of angular contact ball bearings between the main impeller and the turbine. These rolling element bearings are sufficient to react axial loads during the transient periods, or when the balance piston capacity is otherwise exceeded for short periods.

The final example we cover on this subject is shown in Fig. 30. This figure is a representation of the rotor assembly of a contemporary design liquid hydrogen turbopump. In order to generate the large amount of head required, three consecutive centrifugal stages are employed, with impeller diameters of 12 in. The turbine consists of two reaction stages, each employing a degree of reaction of approximately 35%.

In this design, there exists quite a large disparity between the axial force generated by the turbine and the sum of that generated by the pump stages. At the design operating point, the turbine thrust force amounts to approximately 75,000 lb directed toward the pump end of the machine. On the other hand, the total pump thrust force (that is, the summation of the thrust forces from all three pump stages) amounts to over 600,000 lb in a direction opposite the turbine thrust. To generate the axial force necessary to maintain rotor equilibrium, a balance piston was designed and was made

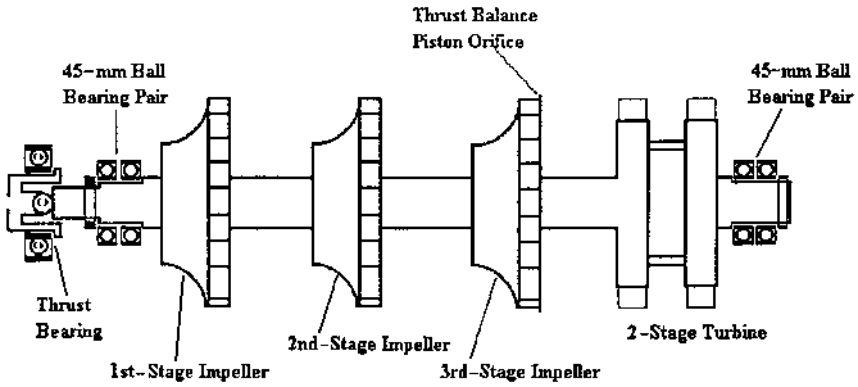

Figure 30 LH_2 turbopump rotor mechanical arrangement.

integral to the third-stage impeller. The axial force generated by the balance piston is such that zero net rotor thrust is maintained while the turbopump is operating. Additionally, the piston's reserve force capacity at the design point is somewhat in excess of 120,000 lb to resist any changes in rotor thrust that may develop.

During start and cutoff transients, when full balance piston capacity is not available, a large rolling element thrust bearing is provided to react to rotor thrust, as shown in the figure. This thrust bearing is particularly useful during the early portion of the pump start sequence, when pump thrust forces have not fully developed. The pump thrust forces lift the rotor off the thrust bearing when the turbopump rotating speed exceeds about 10–15% of its design operating speed.

BEARINGS

The need for bearings in rocket turbomachinery is based on exactly the same principles as in ground-based machinery. Generically speaking, bearings provide the mechanical interface between rotating and stationary hardware, and provide the points (or areas) over which loads are reacted. The forces that must be reacted by bearings can include both radial and axial forces, as well as moment loading or bearing "bending." In addition, a bearing may be required to transmit drive torque from turbine to pump through a drive shaft. This combination of forces imposed on a bearing, as well as the required angular velocity, will determine the required physical configuration

of the bearing. Although rocket turbomachinery and groundbased machinery are similar in the criteria used for bearing selection, unique problem areas exist regarding the operation of rolling element bearings in typical rocket propulsion system applications. We attempt to account for, analyze, and otherwise discuss some of these unique problems.

In our discussions, we focus on bearings of the rolling element type, that is, those bearings that allow relative motion between a shaft and housing by allowing rolling motion between a set of rotating elements (either spherical- or cylindrical-shaped) and a pair of cylindrical rings, or *races*. Although a class of fluid-film bearings (referred to as *hydrostatic* bearings) has undergone a recent resurgence of interest, rolling element bearings continue to constitute the vast majority of bearings in use in rocket propulsion systems. There are several reasons for this. Rolling element bearings are capable of high radial stiffness, with values of 2,000,000 lb/in being reported. Also, to "tune" the critical speeds of a rotor, control of bearing radial stiffness may be required. This is possible with rolling element bearings by providing an axial bearing preload to impart the desired radial stiffness.

The radial stiffness of a rolling element bearing is relatively constant under most reasonable regimes of turbopump operating speeds. The bearing needs no auxiliary equipment to maintain stiffness at low speeds, in contrast to hydrostatic bearings, which require an adequate source of pressurized fluid for operation. If this source is the turbopump itself, a second fluid source may be needed if a hydrostatic bearing is required to operate before adequate pump discharge pressure is available. Also, with few exceptions, a rolling element bearing package of a given load reaction capability tends to occupy less axial space than other bearing types. This can be important in machinery where weight is a strong consideration.

For readers who may be unfamiliar with rolling element bearings and their terminology, a short review might prove constructive. Perhaps the most commonly encountered type is the general purpose Conrad ball bearing. This type of bearing consists of four main components. The *inner race* fits over a shaft, which, in rocket engine turbomachinery applications, is usually in rotation relative to a stationary housing of some kind. The portion of the shaft over which the inner race fits is known as a *journal* and is normally of at least moderate hardness and machined/ground to close tolerances. The inner race inside diameter (known as the *bore*), measured in millimeters, is used to partially identify the bearing. For example, a ball bearing with an inner race diameter of 45 mm is known as a "45-mm ball bearing." For a given bore diameter, several bearing "series" exist, with varying load-carrying capacities and varying outside diameters.

The bearing bore is controlled by bearing manufacturers to very exacting standards of size, uniformity, and surface finish. This allows ready

replacement of a failed bearing with a like part, with high confidence of a proper fit. Several classes of fit (shaft-to-bore) are used, depending on the loads involved and the wishes of the designer. These vary from a light press fit to interference fits that require a shaft-to-bearing temperature difference of several hundred degrees for bearing installation. The outside diameter of the inner race is sometimes termed the *inner raceway*. It contains a circumferential groove of a specific depth and radius of curvature. The balls or "rolling elements" ride in this groove. The groove radius is normally 50–55% of the ball diameter.

The *outer race* fits inside a turbomachine housing, or in some cases fits into a bearing retainer or cartridge, which is itself retained in the machine housing. The outside diameter of the outer race constitutes the outer diameter of the bearing. On the inside diameter of the outer race is the *outer raceway*, which contains a groove similar to that in the inner raceway.

Rolling in the inner and outer raceway grooves is the bearing's complement of rolling elements, which in this example are balls. The balls maintain the proper spacing between the rotating shaft and stationary housing. In this example, the ball bearing is said to be of the Conrad variety. This term makes reference to both the bearing assembly technique and the fact that the number of balls is such that balls are not immediately adjacent to one another. In order to maintain proper spacing of the rolling elements under these conditions another component, the *cage*, is used. The cage, which is a relatively thin webbed piece, contains a "pocket" for each rolling element and many times rides against either the inner or outer raceway. Depending on the nature of the application, cages have been made of many different materials, from various plastics to moderately hard alloy steels, as well as brass, bronze, and fiberglass. Some materials, particularly plastics, may be unsatisfactory by themselves and have been augmented where necessary with metallic sidebands to meet strength requirements. It should be noted here that while it may appear that the cage is not a load-reacting member, this is definitely not the case. While a detailed force analysis is beyond the scope of this chapter, it should be made clear that in many instances the cage is a highly loaded component that requires as much attention to detail as any other bearing component. In those cases where cage structural failure has occurred during operation, catastrophic turbopump failure has resulted.

The current state of the art in rolling element bearings bears witness to the excellence in engineering, manufacturing, and quality control that is prevalent in American industry. A bearing sized appropriately for a piece of machinery, and likely the most highly loaded component in the machine, can be purchased routinely "over the counter" for a price that is normally insignificant compared to the cost of the other machine components. In the

case of our 45-mm ball bearing example, a heavy-duty bearing of this size, capable of supporting combined radial and thrust loads of in excess of 13,000 lb, can be purchased for approximately $150. This bearing, under conditions of proper assembly and lubrication, will react to its rated load continuously for a lifetime measured in hundreds (or thousands) of hours. The uniformity of the product is such that two bearings of the same part number can be interchanged in a turbomachine assembly with no discernible difference in the fit-up between the two bearings. This ability to exchange like parts with no difference in performance demonstrates a level of repeatability in manufacture that is nothing short of superb.

To gain further insight into the level of development of rolling element bearings, it is instructive to examine the tolerances and standards that are maintained routinely in manufacture of the hardware. Let us use the 45-mm bore ball bearing again as an example. The inner race bore, with a nominal maximum of 45 mm, or 1.7717 in., is guaranteed by a typical manufacturer to a tolerance of 0.00045 in. The outer race outside diameter is listed as a nominal maximum of 120 mm, or 4.7244 in. This diameter is guaranteed to a tolerance of 0.0006 in. to ensure interchangeability within machine housing bores. The bearing axial width, with a nominal maximum of 1.1417 in., is maintained to a tolerance of 0.005 in. for a standard single unit. The diameter of the balls in a precision ball bearing is normally held to a range of tolerance of between 10 and 50 microinches, depending on the nature of the bearing application. Uniformity of ball diameter is extremely important, since variations in the orbital velocity of the balls can exert unwanted cage forces, which result in very rapid cage wear and possible structural failure.

The surface finish on the bearing rolling surfaces are, like component diameters, maintained to a uniformity that is excellent. Inner and outer raceway grooves are manufactured to a surface finish of approximately 6 microinches in the circumferential direction, while the average surface finish of a ball can be expected to be on the order of 1 microinch. It is this extreme smoothness of finish of the rolling surfaces that enables modern bearings to operate with remarkable quietness, lack of vibration, and at a coefficient of friction on the order of 0.002–0.007.

Although each bearing application must be considered unique and analyzed carefully, it is possible to use some generalized indicators to mark the trends in bearing performance and capability that have been achieved over the years. The most popular general indicator relating to bearing performance is the DN number. This number is the product of the bearing inner bore diameter in millimeters and the shaft angular velocity in revolutions per minute. Bearing manufacturers generally quote an upper DN limit based on the bearing size, precision class (ABEC 5 or 7 are commonly specified for turbomachinery), and type of lubrication. As we

shall see, contemporary rocket engine turbomachinery generally makes no provision for lubrication of rolling element bearings per se, but rather supplies to the bearing a quantity of the propellant being pumped to act as a coolant. This design practice results in weight reduction due to the omission of both the lubricating fluid supply and the required distribution system, but also a reduced bearing DN capability for a given time period.

The turbopump for the Thor engine system, designed in the early to mid-1950s, incorporates a two-stage impulse turbine similar to that shown in Fig. 23. The turbine shaft is supported by a cylindrical roller bearing for radial load reaction and a ball bearing to react the axial thrust. Both of these bearings are 35-mm bore diameter and operate at approximately 40,000 rpm for a bearing DN number of 1.4×10^6. The twin centrifugal pumps are supported on a common drive shaft by combination of a 70-mm ball bearing and 70-mm cylindrical roller bearing. At a pump shaft speed of 6,800 rpm, a bearing DN number of 476,000 results. The bearings in this turbopump are lubricated by blending the kerosene fuel with an extreme-pressure additive known as Oronite. The mixture of these two fluids results in a quite excellent lubricant.

The F-1 engine employed a direct-drive turbopump that depended on the largest set of rolling element bearings ever used in a production rocket engine system. The large two-rotor turbine (35-in. pitch diameter) was supported by a 170-mm bore cylindrical roller bearing, while a tandem 130-mm bore ball bearing reacted axial thrust. These bearings operated at an angular velocity of 5,500 rpm, with a DN number of 935,000 and 715,000 for the roller and ball bearings, respectively.

The advent of liquid hydrogen as a propellant seemed to mark the general period where cooling/lubrication of a rolling element bearing was no longer performed by either conventional oils or kerosene. There are a number of reasons for this. Among them are the weight savings mentioned earlier, as well as the substantial difficulty of prevention of freezing of the lubricant due to exposure to cryogenic hydrogen. The Pratt and Whitney RL-10 (Centaur) and the Rocketdyne J-2 engine marked the first production use of hydrogen-cooled bearings, the RL-10 using GH_2 as coolant, and the J-2 using hydrogen in the liquid state as coolant. Bearing DN numbers attained in the case of the J-2 engine were 1.6×10^6.

The Space Shuttle main engine makes the greatest demand thus far on rolling element bearings in rocket propulsion systems. The high-pressure fuel turbopump employs two pairs of 45-mm bore ball bearings at a shaft speed of 37,000 rpm at maximum thrust, for a bearing DN number of 1.7×10^6. Likewise, the high-pressure oxygen turbopump employs two 45-mm bore ball bearings in concert with two 57-mm bore ball bearings. These bearings are cooled by a supply of liquid oxygen obtained from the pump,

amounting to about 17 lb/sec for all four bearings. At maximum thrust, the turbopump shaft speed is approximately 31,000 rpm, resulting in a maximum bearing DN number of 1.8×10^6. The bearing DN numbers of the SSME high-pressure turbopumps are considered to represent the current maximum for propellant-cooled service and are not likely to be exceeded by an operational system in the near future.

The materials used in the construction of modern rolling element bearings are the product of several decades of research, development, and evolution. Significant advances in materials science have often been made by the developers of bearings. Given the perpetual desire for better bearing performance, higher attainable speed, longer life, and more "forgiving" bearing operation, this should come as no surprise. In fact, some of the "premier" bearing manufacturers themselves make the stock material from which their products are ultimately fabricated. This is done in the interest of maintaining the ultimate in material quality control. The required emphasis on homogeneity of the bearing material can hardly be overstated, as this controls both the uniformity of distribution of alloying elements as well as the occurrence of impurity inclusions, which may act as sites for preferential initiation of failure. In addition to sufficient uniformity, the proper material physical characteristics are quite crucial to good bearing performance. In order to maintain the intended clearances between internal machine components, and to run without undue vibration, the rolling elements and raceways must be extremely hard and smooth. However, these elements must not be brittle, to avoid fracture under conditions of sudden load change. In order to endure highly loaded conditions (especially in ball bearings) the materials must possess great mechanical strength. To obtain long bearing life, the material's fatigue endurance properties must be quite favorable.

A number of materials have been developed (or adopted) to meet all of these requirements and are in widespread use in both the commercial bearing industry and the aerospace industry. Probably the most commonly used bearing material in commercial use today is an alloy known as AISI 52100. This is a high-carbon (0.95–1.10%), moderate-chromium (1.30–1.60%) alloy that is readily through-hardenable. Ultimate strengths of 500,000 psi are attainable in the heat-treated condition. Corresponding material hardness is normally in the range of 61–65 on the Rockwell C scale. AISI 52100 is used for both balls and raceways and exhibits one of the best fatigue lives of all bearing materials when used under the proper conditions. AISI 52100 has been used in several successful rocket engine turbomachinery systems.

Special bearings fabricated from materials that represent an improvement over the basic 52100 have been developed to meet the more demanding

needs of the aircraft gas turbine and aerospace industries. These materials have been selected specifically to exhibit improved fatigue life under conditions of elevated temperature. Many of these materials are actually adaptations of tool steels such as T1, M1, and M2. An example of a material of this class in production use today is M50, another type of tool steel. The gear-driven turbopump of the Atlas and Thor engines uses a roller bearing fabricated from M50 to support the overhung mass of the two-stage turbine. Although hot-gas intrusion into the bearing cavity is theoretically prevented by a hot-gas seal package (see Fig. 23), heating effects on this roller bearing have been observed. Instrumentation sensing bearing outer race temperature has detected values in the 800°F range. Nevertheless, very good fatigue performance is achieved under these conditions with M50.

Like AISI 52100, the M50 alloy is intended to be through-hardened. However, under some conditions (principally higher bearing speed and consequently higher centrifugal loading), the fracture toughness of the basic M50 alloy has been found to be marginal. To augment fracture toughness, a case-hardening version of M50 has been developed, known as M50-Nil.

In the case of rocket turbomachinery systems, the most common bearing material in current use is a material known as 440C. 440C is a martensitic, through-hardening stainless steel with a high carbon (1.1% nominal) and chromium (17% nominal) content. It is through-hardenable to the same general degree as AISI 52100 and exhibits excellent performance as a bearing material. Although its fatigue life characteristics are not quite as good as those of 52100, 440C's corrosion resistance makes it a very convenient material for use in machinery where the chemical environment may be adverse, such as in rocket systems. Whereas materials such as 52100 must be protected from corrosion by grease or other preservatives, 440C has no such requirement. If excessive operating temperatures can be avoided (440C's corrosion resistance diminishes with increasing temperature), superior bearing performance under comparatively hostile conditions can be achieved. As far as rocket engine turbomachinery systems are concerned, 440C is generally considered to be the best compromise between corrosion resistance, fatigue life potential, and other material properties. It has been used as the bearing material in most production cryogenic turbopumps, especially those involved in moving liquid hydrogen. The fuel and oxidizer turbopumps of the J-2 engine both used 440C as bearing material, as do all four turbopumps for the Space Shuttle main engine.

In recent years, the increasing demands placed on bearing performance (particularly by the aerospace industry) have spurred interest in the use of more exotic materials for bearing components, especially the rolling elements. Considerable effort has been expended since the 1970s involving research into the use of certain sintered ceramic-type materials for bearing

components. Of these, one seems to show particular promise. This is silicon nitride. It has a number of properties that make it attractive for use in rolling element bearings. For instance, relatively high-use temperatures have essentially no effect on the material's hardness. Incidentally, silicon nitride has a hardness of approximately 90 on the Rockwell C scale. Silicon nitride can be used with confidence at temperatures twice that recommended for general use of the best bearing steels. Also, due to its relatively low density (less than half that of typical bearing steels), internal bearing loading due to high operating speeds is reduced.

Other properties of silicon nitride can create some justifiable concern to its application as a bearing material. For instance, although the compressive strength of the material is quite high, its corresponding strength in tension is approximately one third that of a typical bearing steel. Also, the material's tolerance to surface defects is somewhat adverse and unpredictable. Whereas a steel rolling element can generally tolerate a surface defect such as spalling and continue to provide satisfactory service, "spalling" of a silicon nitride rolling element's surface can lead to rapid catastrophic failure of the rolling element. In addition, many of the normal nondestructive test methods used for steel bearing components rely on the magnetic and conductivity properties of steels that are not present in ceramics.

Like rolling elements, bearing cages have similarly been the object of quite a bit of development work. In the area of commercial bearings, a large number of materials have been found suitable. Probably the most frequently used material (by volume) is low-carbon mild steel. For general purpose ball bearings a cage is assembled from two halves, both of which are stamped from steel sheet or strips. On assembly, the halves are riveted together to surround the balls. When somewhat higher strength is required, alloy steels such as 4130 and/or 4340 have been used and have been heat-treated to moderate hardness. Brass-type materials are also frequently found both in angular contact ball bearings and roller bearing cages.

As was mentioned previously, plastics of various kinds have also been used for bearing cages. In this application, plastics have some unique advantages. They are quite easy to machine or otherwise form to relatively complex shapes, they tend not to retain detrimental debris, and many possess their own lubricity. Although they may be lacking structurally by themselves, this has been rectified to an extent by augmenting them with metallic sidebands. In rocket turbopump systems, plastic cages have seen widespread use. For instance, in the turbine package of the Thor and Atlas turbopumps, the turbine shaft ball bearing that is used to react axial thrust was at one point equipped with a phenolic cage. This cage was equipped with aluminum sidebands for structural strength. When the bearing load

was increased due to engine uprating, it was necessary to replace the phenolic cage with a one-piece bronze cage. A plastic cage material that is particularly popular for propellant-cooled service in cryogenic turbopumps is known by the trade name Armalon. It consists of a glass-fiber structural portion heavily filled with PTFE. Its favorable features include sufficient strength and stiffness to be used without additional structural support, adequate material properties at cryogenic temperatures, and sufficient chemical inertness to be used in service with reactive oxidizers.

As was previously mentioned, the usage of rolling element bearings in rocket turbomachinery systems is thought by many to be at a plateau that is not likely to be exceeded with conventional materials and design practices. Through care and attention to detail, bearings in rocket turbomachinery regularly show capability that is considerably in excess of that quoted by manufacturers and is attained under quite hostile conditions. For some time, attention has been turning to methods for eliminating the comparatively short life expectations of high-DN propellant-cooled rolling element bearings, as well as eliminating the fundamental shaft speed limitations (DN limit) that they impose. At the time of this writing, the most promising of these is considered by many to be the hydrostatic bearing. Although first installed in prototype turbopumps in the 1960s, a true systematic capability for hydrostatic bearing design had to await the arrival of appropriate numerical techniques for solutions of Reynolds' equations, which govern the hydrostatic flow problem. Over a number of years, techniques were perfected for design of a hydrostatic bearing with specified properties. With these techniques available, the hydrostatic bearing is being considered as a design alternative for the next generation of rocket propulsion systems. The bearing DN constraint imposed by rolling element bearings can be eliminated in this manner.

Elimination of the DN constraint will enable the design of higher performing systems, as well as ridding us of the time-consuming bearing inspection and replacement procedures that represent a significant portion of the maintenance cost of a reusable propulsion system.

ACKNOWLEDGMENTS

I would like to thank three individuals for their contributions to the preparation of this chapter. They are (in alphabetical order) Mr. Jim Boynton, Mr. Richard Carlson, and Mr. Tony Eastland, all of the Rocketdyne Division of Rockwell International. I owe Mr. Boynton and Mr. Eastland a great debt of gratitude for their continued long-distance support and encouragement during the research and writing of the text. The

combination of their humbling degree of expertise and their unending graciousness ensured my survival during this period. Through Mr. Carlson, I have found that classes and texts only begin the training of an engineer. Not many people know it, but both the Apollo and Space Shuttle programs survived on more than one occasion only due to his quick thinking and extreme competence.

I would also like to thank the staff of NASA Lewis Research Center for permission to publish Figs 9, 11, 14, 15, 16, and 27 from their various design criteria texts. Also, my thanks to Dr. Gene Jackson of Rocketdyne for his permission to reprint Fig. 10 from his own work.

REFERENCES

1. National Aeronautics and Space Administration, *Liquid Rocket Engine Turbines*, NASA SP-8110 (1974).
2. National Aeronautics and Space Administration, *Turbine Design and Application*, NASA SP-290 (1972).
3. T. Katsanis and W. D. McNally, *FORTRAN Program for Calculating Velocities and Streamlines on the Hub-Shroud Mid-Channel Flow Surface of an Axial or Mixed Flow Turbomachine Part I—User's Manual*, NASA TN D-7343 (1973).
4. T. Katsanis and W. D. McNally, *FORTRAN Program for Calculating Velocities and Streamlines on the Hub-Shroud Mid-Channel Flow Surface of an Axial or Mixed Flow Turbomachine Part II—Programmer's Manual*, NASA TN D-7344 (1974).
5. T. Katsanis and W. D. McNally, *FORTRAN Program for Calculating Velocities and Streamlines on a Blade-to-Blade Stream Surface of a Tandem Blade Turbomachine*, NASA TN D-5044 (1969).
6. T. Katsanis and W. D. McNally, *FORTRAN Program for Calculating Velocities in a Magnified Region on a Blade-to-Blade Stream Surface of a Turbomachine*, NASA TN D-5091 (1969).
7. B. Eckert and E. Schnell, *Axial und Radial Kompressoren*, Springer-Verlag, Berlin (1961).
8. National Aeronautics and Space Administration, *Liquid Rocket Engine Turbopump Rotating Shaft Seals*, NASA SP-8121 (1978).
9. J. W. Daily and R. E. Nece, *Trans. ASME J. Basic Eng.*, March (1960).
10. H. F. Rue, *Trans. ASME J. Eng. Power*, April (1966).
11. A. J. Stepanoff, *Centrifugal and Axial Flow Pumps*, John Wiley and Sons, New York (1957).
12. National Aeronautics and Space Administration, *Liquid Rocket Engine Turbopump Bearings*, NASA SP-8048 (1971).
13. National Aeronautics and Space Administration, *Liquid Rocket Engine Centrifugal Flow Turbopumps*, NASA SP-8109 (1973).

12

Turbomachinery Performance Testing

Nathan G. Adams
The Boeing Company, Mesa, Arizona, U.S.A.

AERODYNAMIC PERFORMANCE TESTING

Chapter Objective

Gas turbine propulsion system development traditionally proceeds from design conceptualization to analysis to individual component/stage performance testing before the complete engine is assembled and run. The objective of this chapter is to introduce methodologies, techniques, and suggested procedures for turbomachinery component aerodynamic performance testing. Turbomachinery component testing reduces design and development risks while verifying engineering analysis and performance estimates. Inlets, fans, compressors, combustors, turbines, and exhaust nozzle components are all traditionally tested individually as part of the gas turbine development process. Even after an engine has been assembled and tested, component tests are often used to support performance improvements and diagnostic testing.

Materials presented in this chapter are focused on fan, compressor, and turbine-stage aerodynamic performance testing. The component of

interest may be a single rotor and stator assembly or a combination of several individual rotor/stator vane blade rows operating together as, for example, a multistage axial compressor. Fundamental test concepts that are used to quantify individual turbomachinery stage performance characteristics are presented. Test concepts described are essentially applicable to fan, compressor, and turbine stages. Newcomers to the turbomachinery test field will find this chapter useful in developing an understanding for what is required to plan for and conduct a successful test activity.

Chapter Outline

The intent of this chapter is not that of presenting all possible test and measurement techniques that are used throughout the industry and at research laboratories, nor is it to recommend or specify any particular testing approach. Rather, the materials presented reflect what the author feels to be important in the definition, planning, and conducting turbomachinery test activities.

The first section discusses turbomachine component performance testing and the impact of different system operational characteristics on performance. The second section presents test methodologies, the third test hardware, and the fourth instrumentation design considerations. Test procedures and data presentation considerations are presented in the last two sections.

Turbomachinery mechanical test procedures and requirements are not covered in this chapter. However, this does not diminish the importance of mechanical testing to verify vibration, stress, and fatigue life characteristics in the development of gas turbine equipment.

Component Performance Testing

The validity and applicability of individual turbomachinery component performance testing are based on the premise that actual engine environmental conditions are accurately simulated with the test rig. With an accurate simulation, component performance measured with the test rig will be equivalent to that of the same component operating in the gas turbine engine.

Gas turbine cycle analyses traditionally utilize performance maps in describing the steady-state aerothermodynamic performance characteristics of each turbomachine component over its complete operating range. The principal objective of individual component testing is to define the respective component performance maps. Sufficient test rig instrumentation must be utilized to accurately measure and compute stage performance character-

istics. The more accurate the performance maps, the more accurate will be the overall gas turbine cycle performance predictions. In addition, instrumentation is also often included on the test rig for flow diagnostic evaluation of the individual blade rows and localized areas of interest.

For steady-state operation (engine and flight operating conditions changing very slowly with time), the component maps describe several performance features. Typical compressor and turbine maps are shown in Figs. 1 and 2. Performance maps are characterized with stage total pressure ratios plotted as a function of corrected flow rate at different corrected rotational speeds. As seen, each speed line has a distinctive locus of performance data. Also included on performance maps are constant efficiency islands as is shown in Fig. 1. See the final section for a definition of corrected flow parameters.

Compressor and fan maps also include a stall line. The stall line identifies the locus of unstable operating conditions with stable operation to the right of the stall line. The operating regions that include choked flow through the blade passages are recognized by the vertical speed line performance characteristics. Referring to the performance map examples, we see a weak dependence of turbine performance on wheel speed, contrasted with a relatively strong dependence shown by compressors and fans.

Each turbomachine component performance map is associated with a specific configuration and flow-path geometry. Blading differences, flow-path geometric changes, running tip clearance changes, different gaps,

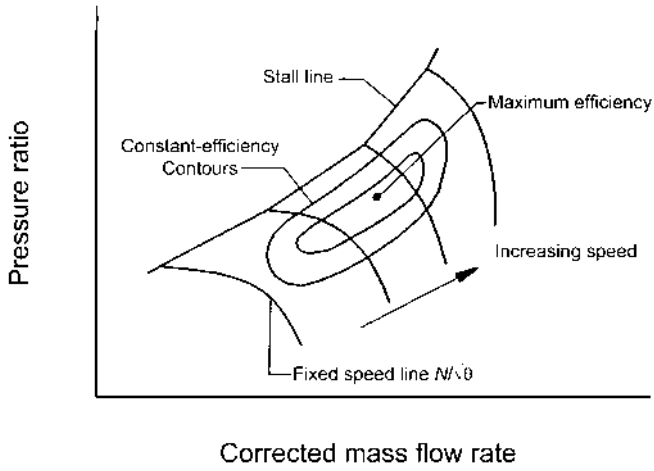

Figure 1 Typical compressor map.

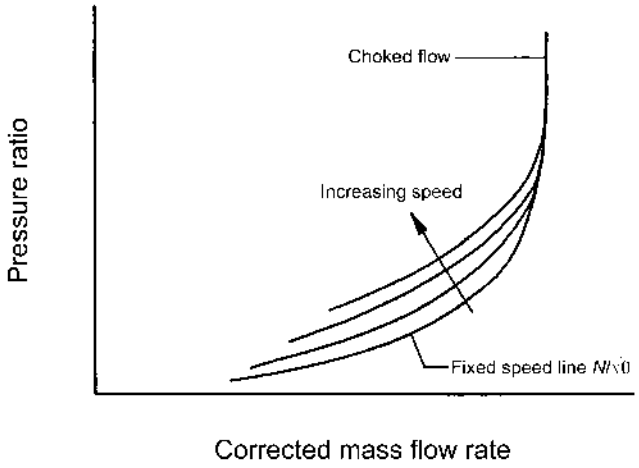

Figure 2 Typical turbine map.

cracks, and seals, and leakage flow rates throughout the stage flow path can impact overall performance. Separate performance maps are normally required for each geometric configuration. Often performance scalars are defined to quantify stage performance differences due to small geometric variations.

Normally, full-scale component test rigs are used to experimentally define performance maps. Meaningful performance measurements are made when actual flow paths, blading, and rotor speeds are faithfully reproduced. In addition, inlet and outlet velocities, pressures, and temperature distributions must also simulate accurately those in the gas turbine engine installation. Specialized hardware and instrumentation are also used to support design development and diagnostic testing.

Operational Characteristics' Impact on Performance

It is important to recognize that specific performance numbers defined by component maps are dependent on several different stage operational characteristics. These include nonuniform inlet flows, commonly referred to as inlet distortion, Reynolds number effects, changes in gas thermodynamic properties, and transient operations. There is no generalized methodology to account for the impact of these characteristics on steady-state performance. For a given stage, different operational characteristics can result in different performance maps.

Inlet Distortion

Most turbomachinery stages are designed assuming uniform pressure, temperature, and velocity profiles at the stage inlet plane. However, integration of the individual stages into the gas turbine engine and its resultant installation into the vehicle of interest often leads to nonuniform inlet flow characteristics. In particular, fan and compressor stages, due to their close proximity to the inlet, are typically subjected to distorted inlet flows. Inlet flow distortion includes both steady-state and time-variant total pressures, static pressures, swirl, and total temperatures at the stage inlet plane.

Nonuniform fan and compressor inlet flows can be generated from several different sources. Typical sources include extreme vehicle maneuvering and the resultant flow separation from the inlet lip, inlet duct boundary layers and separated flows, hot-gas ingestion during armament firing, shock–boundary-layer interactions, and "S-shaped" ducts that result in local flow curvature. Nonuniform inlet conditions can lead to both circumferential and radial distortion characteristics.

Usually inlet disturbances are attenuated in both magnitude and spatial extent as they pass through a turbomachine stage. Test rig inlet distortion testing often includes special instrumentation at the stage exit to measure exit plane flow distortion characteristics.

The effects of inlet distortion are generally detrimental to turbomachinery performance. Direct effects include a degradation of total stage pressure rise, flow, and efficiency. In addition, there is often a decrease in stall margin, resulting in a reduced range of stable operation.

Typically, stage performance with inlet distortion is determined experimentally as part of the test program. For these tests, inlet flow distortion characteristics are simulated in the test rig. As an example, total pressure distortion patterns are typically generated with wire mesh screens mounted in the upstream flow path. The shape and solidity of the patterns are tailored to generate specific total pressure profiles. Vehicle inlet total pressure surveys can be used to define the desired total pressure profiles. Reference [1] presents the methodologies required to define wire mesh patterns that will simulate specific pressure profiles for fan and compressor distortion testing.

Figure 3 shows an example of classical wire mesh shapes that are used for fan and compressor total pressure inlet distortion testing. Performance maps are generated for different inlet distortion patterns. Performance scalars, that is, ratios of flow rates, pressures, and efficiencies that relate distorted with undistorted performance, are then calculated for each of the distortion patterns. Methodologies to equate distortion shapes and

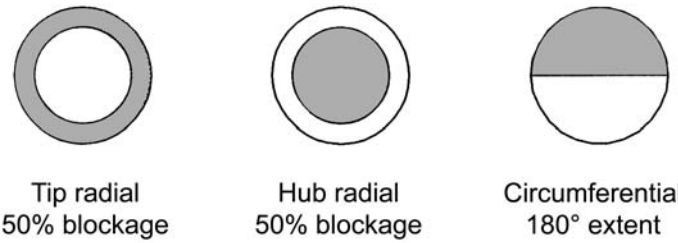

Figure 3 Classical distortion screen shapes.

magnitudes to stage performance characteristics are described in Ref. [2]. In addition, Refs. [3–8] are several of many papers that describe inlet distortion effects on gas turbine performance.

Unsteady inlet flow properties can also be a source of unwanted mechanical excitation of stage blading and ducting hardware. Mechanical design considerations must ensure that blade natural frequencies do not coincide with those anticipated from unsteady inlet flows.

Reynolds Number

The impact of Reynolds number on performance is more often associated with smaller turbomachines operating at extreme altitudes where the air density is much less than at sea level. Under these high-altitude ambient conditions, the stage Reynolds number (based on blade chord as the characteristic length and mean stream fluid properties) will be much less than at sea level. Fans, front ends of compressor stages, and the last turbine stages are most susceptible to Reynolds number effects. For most larger engines, Reynolds number effects are minimal. An empirical rule of thumb suggests that for stage Reynolds numbers greater than 2×10^5, Reynolds number impact on stage performance is relatively unimportant.

Blade boundary-layer behavior is a very strong function of Reynolds number. In an axial compressor, for example, the smaller Reynolds number due to extreme altitude operation can result in a transition delay from a laminar to a turbulent boundary layer. A laminar boundary layer is more likely to separate, which can result in blade stalling much earlier than at the higher Reynolds numbers. Flow separation not only deteriorates local stage performance but can also impact downstream stage performance.

For small gas turbine engines with high-altitude operating conditions, design applications normally require larger blade chords (increased characteristic length) to minimize Reynolds number effects.

Gas Thermodynamic Properties

Turbomachinery performance is also very dependent on the working fluid gas properties, including molecular weight and specific heat ratios. Several operational situations that can impact gas thermodynamic properties include the reingestion of hot exhaust gases, gun gas ingestion rocket exhaust ingestion, and operations in a high-humidity environment. Performance consequences include changes in specific heat ratios that can readily impact compressible flow properties, which include the local speed of sound.

Transient Operations

Typical turbomachinery performance maps do not include transient operating characteristics. Performance maps are generated assuming steady flow conditions with the mechanical hardware in thermal equilibrium.

TEST METHODOLOGY

Testing Approach

An approach that one might follow in defining and planning for a turbomachine component test is briefly described. The first step in test planning is that of defining the performance parameters that must be measured to satisfy the test objectives. Specific instrumentation required to record performance should also be specified.

In addition, one must specify both the speed and flow ranges required for the test. The engineer must select a facility that both meets geometric interface requirements and is capable of operating over the flow and speed ranges required for the performance test. Once the test facility has been selected and the required performance data specified, the test rig design can be accomplished. Normally, test rigs are designed using full-scale hardware with the rotor turning at the design speed and with full-scale flow rates.

However, successful testing can be accomplished with scaled test rigs. Scaling requirements include maintaining flow similarity between the full and scaled hardware. Reynolds number, Mach number, and characteristic geometric relationships must be maintained. The operating conditions within the stage must be dynamically similar, with the respective blade velocity triangles preserved. Classical scaling parameters for turbomachinery blading are defined in Ref. [9].

Required Performance Data

Test data required to produce turbomachine component performance maps include rotational speeds, flow rates, pressure ratios, and measurements that can be used for component efficiency calculations. In addition, the aerodynamicist will want to know test parameters such as total pressure and temperature radial distributions, static pressures on both the hub and outer casing flow paths, dynamic measurements including running tip clearances, dynamic pressures to quantify rotor blade shocks, when present, and unsteady flow characteristics, and wake rakes to quantify pressure and temperature profiles behind the stator assemblies.

Required Measurements

The selection of proper instrumentation is one of the most important aspects of turbomachinery testing. The amount of instrumentation utilized on a test rig is related directly to the information and data required. A more detailed description of each of the measurement sensors is presented in a later section.

Figure 4 shows a test rig cross-section schematic with typical instrumentation that is utilized in classical aerodynamic performance testing. Included are radial immersion total pressure and total temperature rakes, numerous static pressure taps, selected radial surveys and wake rakes, and dynamic response instrumentation. Not shown but of equal importance are flow rate and speed measurements, in addition to ambient test condition measurements. Stage performance is defined from total pressure, temperature, flow rate, and shaft speed measurements. The total or stagnation state of the fluid is defined as that state that would be achieved if the fluid were

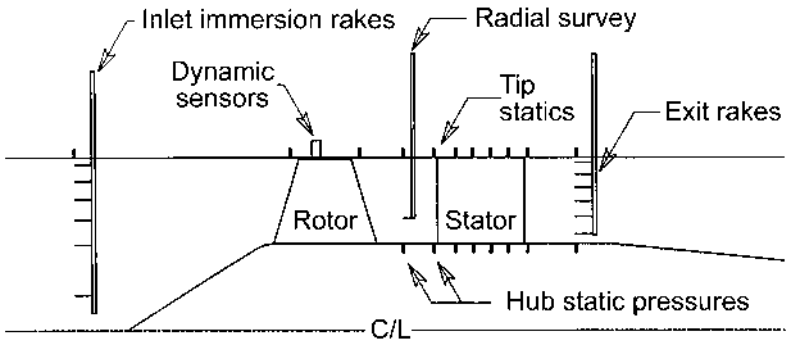

Figure 4 Test rig instrumentation setup.

brought to rest isentropically. Total pressure and temperature measurements are made with sensors that stagnate the flow at the point of interest in the flow field. Very accurate total pressure and temperature measurements can be made with well-designed sensors. Other instrumentation illustrated in Fig. 4 is used to support flow-field definition and performance diagnostic analysis.

Even though the flow paths and blading characteristics are considerably different for single and multistage fans, axial and cetrifugal compressors, and turbines, the performance measurement requirements and techniques are essentially the same for each of these turbomachine components.

The total pressure increase/decrease across the stage of interest is measured using total pressure sensors located at specific streamwise stations relative to the blading. An accurate measurement requires that both inlet and exit total pressures be recorded. As seen in Fig. 4, inlet total pressures are recorded with radial immersion rakes located just upstream of the stage of interest. This normally includes multiple individual rakes, which are equally spaced around the circumference.

Stage exit total pressures are also measured with multiple radial immersion rakes located downstream of the stage exit plane. Total temperatures across the stage are measured with thermocouple temperature sensors mounted on radial immersion rakes. The change in total temperature across the stage coupled with the stage pressure ratio can be used to calculate stage adiabatic efficiency and aerodynamic power requirements.

Static pressure taps, mounted flush to both the inner and outer flow path walls, are installed throughout the test rig. Typical locations are seen in Fig. 4. Static pressures measured in conjunction with total pressures and temperatures can be used to calculate local flow velocities. In addition, static pressure taps can be located at rotor and stator leading and trailing edges on both the hub and shroud, completely around the flow-path circumference. Circumferential static pressure distributions are a good indication of flow velocity uniformity. Uniform static pressures suggest uniform velocities, whereas nonuniform static pressures indicate nonuniform velocities.

A row of static pressure taps is often placed at midpassage between two of the stator blades along both the hub and tip shrouds. These measurements provide a quantitative assessment of the static pressure changes across the stator assembly. Other static pressure taps are located at stationary and traversing measurement planes.

In addition to instrumentation requirements for performance measurements, the engineer will often instrument the test rig to acquire specific test data that can be used for blade-row performance diagnostic purposes.

These measurements include radial surveys directly behind the rotor, wake rake measurements behind fixed blades and struts, boundary-layer probes to measure profiles in the boundary layer, dynamic pressure sensors located near the rotor for stall/surge indications, and tip clearance probes to measure in real time the running blade-tip clearance.

Total pressure, temperature, and yaw (circumferential) and pitch (radial) absolute flow angles at the rotor exit plane can be measured with yaw-nulling probes, which are traversed radially across the flow path. Wake rakes consist of a series of pressure taps mounted on a fixture such that a circumferential spatial pressure distribution is measured across the flow path at a fixed radius. Wake rakes can be mounted on radial survey mechanisms so that wake profiles can be recorded across the flow path.

High-response pressure transducers flush mounted in the vicinity of the rotor blade tip are used to measure unsteady static pressures on the flow duct outer casing. These data can be monitored to identify flow separation and shock waves on the rotor blade tip.

Rotor blade-tip clearance differences can impact stage performance, especially in compressors and fans. Typically, stage pressure rise and efficiency decreases with increased blade-tip–shroud clearance [10]. Test rigs usually include dynamic proximity sensors to measure rotor tip clearances during testing. Sensors are mounted circumferentially over the blade tips, flush to the outer flow path.

Not shown in Fig. 4 but equally important is the instrumentation required for flow rate and test rig speed measurements. Often a torque meter is used to measure test rig power consumption or generation.

Instrumentation also required but not discussed in this chapter includes that required to monitor in real time the mechanical health of the test rig and test facility during test rig operations.

Instrumentation Planning and Layout

The previous section identified the measurements required for turbomachinery aerodynamic performance testing. In this section we discuss the methodologies for placing and locating the instrumentation on the test rig.

Total Pressure Measurements

Stage pressure ratios are calculated using averaged pressures measured from both the inlet and discharge total pressure rakes. An understanding of where the inlet and discharge total pressure rakes are located in the test rig relative to the stage blading is important in the total system performance analysis of gas turbine machines. Unless corrected for, the measured stage pressures

include not only the pressure change across the turbomachine blading of interest but also the pressure losses due to flow-path ducting from the inlet pressure measurement plane to the stage of interest and from the blading exit plane to the discharge measurement station.

A careful accounting of both stage pressure ratio characteristics and flow-path total pressure losses must be made. Often flow-path duct losses are ''doubled-dipped'' because the analyst fails to recognize that flow-path duct losses are included in the stage performance map because of the way the test rig was instrumented. Likewise, losses may be missed should the analyst not include duct losses that were thought to be included, but were not, in the stage performance map pressure characteristics.

Radial immersion rakes, similar to the rake configuration seen in Fig. 5, are used to measure turbomachine stage inlet and exit pressures. Total pressures are measured with impact or kiel sensors mounted on rakes that are immersed into the flow path. The individual impact sensor tube axes should be aligned parallel to the incoming flow direction. A choice must be made by the engineer to select the number of rakes such that the flow field is adequately defined but the flow path is not blocked nor significantly altered by the installed rakes.

A generally accepted practice is to install inlet rakes at least a duct diameter upstream of the test stage. This separation distance minimizes flow and mechanical interactions due to the rake's wake on the test blading, while

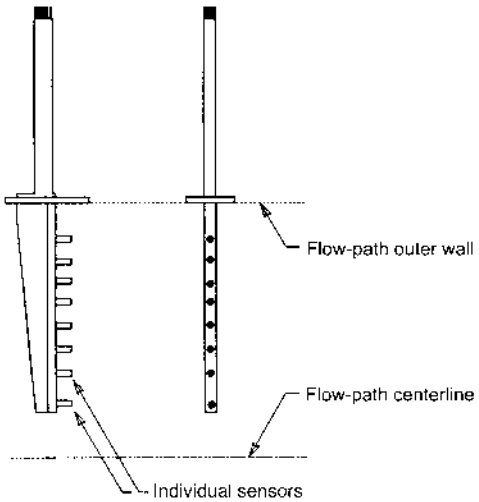

Figure 5 Radial immersion rake.

still being sufficiently close to measure representative inlet pressures. Multiple inlet rakes are typically spaced uniformly around the duct circumference. Typically, three to four rakes are installed for the inlet measurement, as illustrated in Fig. 6. Provisions must be made should there be obstacles such as structural members, struts, and cross shafting in the inlet flow path. Inlet rakes should not be installed near or directly behind these objects.

Test-cell ambient conditions can be used as inlet flow conditions if the test rig includes a well-designed and fabricated inlet bellmouth that is coupled to the test stage with a "short," clean, axisymmetric duct. A test rig configured in this manner does not require inlet rake instrumentation. The assumption is that there are no significant sources of pressure loss through the bellmouth and ducting into the test rig and that the bellmouth inlet flow is uniform. Uniform inlet flow can be assumed if the bellmouth lip is located at least one diameter above the test cell floor and one diameter away from any obstructions in front of the bellmouth. In this case the ambient pressure is the test rig inlet pressure, with the ambient temperature being the inlet total temperature.

Stage discharge total pressure radial immersion rakes are normally located as close as possible to the test stage exit plane. Using the trailing blade-row chord as a measure, the rakes are normally located less than a chord length downstream of the trailing edge. The actual placement of the rakes in the test rig may depend on many factors, including accessibility and structure/struts in the flow path.

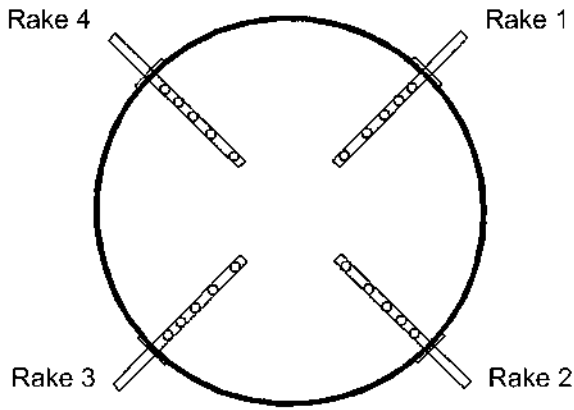

Figure 6 Typical inlet rake orientation.

The circumferential placement of the exit rakes must be carefully selected. The flow field immediately downstream of a stator vane blade row is characterized by periodic blade wakes that mix out while propagating downstream. If the measurement rakes are placed far enough downstream, the wakes are essentially mixed and the flow is relatively uniform. Should this be the case, the circumferential placement of the rakes is not critical.

For most test applications, the rakes are placed relatively close to the stage exit. Here the flow is nonuniform because of the wakes generated by the test stage blading. Should all the sensing elements be located in wake-free flow-field regions, the integrated pressures will be high. Likewise, should all the sensors be located in the wake, the integrated pressures will be low. In order to get a more representative pressure average, the positions of the individual rakes are indexed equally across the blade passage so that the different wake flow properties are equally measured.

An example of how this might be done is illustrated in Fig. 7. Here we have arbitrarily selected a stage exit plane that includes 11 stator blades spaced 32.7° apart and 4 individual immersion rakes to measure the total pressure. As seen, the four rakes have been located approximately 90° apart. Rake positioning is accomplished by indexing each rake a specific circumferential distance from a fixed reference point such as a stator blade

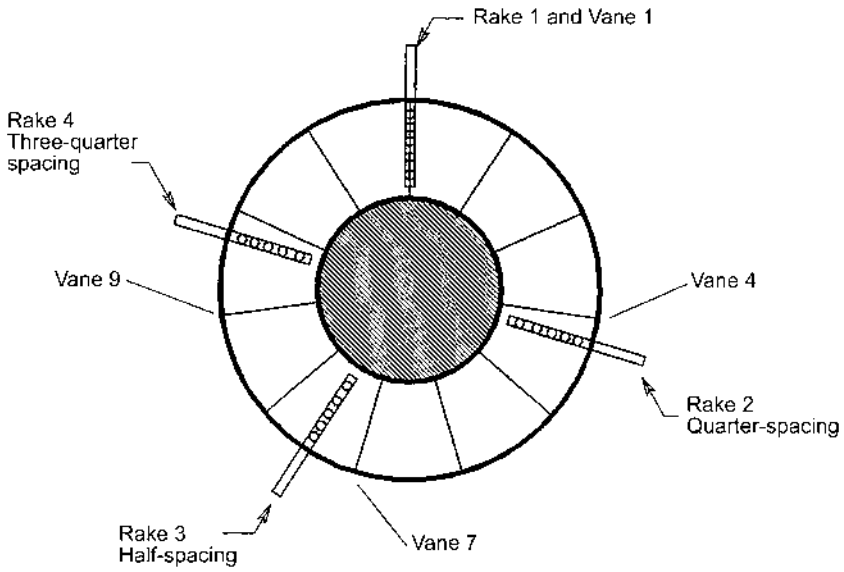

Figure 7 Exit rake placement.

trailing edge. For convenience, we have positioned the first rake directly behind one of the blade trailing edges, in this case the stator blade at top dead center. Since we have chosen to use four rakes, the 32.7° blade spacing is divided into four equal segments of 8.2° each. The second rake is then positioned 8.2° past the trailing edge of blade number 4. Likewise, rake 3 is positioned 16.4° past the trailing edge of blade number 7, with rake 4 positioned 24.6° past blade number 9. In this manner, each discrete part of the nonuniform pressure flow field is measured. Should three rakes be used, each rake would be indexed across a third of the blade passage, and so on for any number of rakes in the measurement plane.

Similar care must be exercised in determining the radial position of the sensors on the rake. Typical rakes will include between five and eight individual pressure sensors per rake. Each sensor should be positioned at the centroid of a constant-area ring. This is illustrated in Fig. 8. For this example we have specified that a five-element rake be installed in the flow field. In order to locate the position of the individual pressure sensors on the rake the flow-path area is divided into five equal area rings as seen in Fig. 8. The sensors are then located at the centroid of each equal-area ring. By installing the sensors in this manner, each pressure tap "sees" equal-flow areas. As a result, area-averaged data reduction can be accomplished by

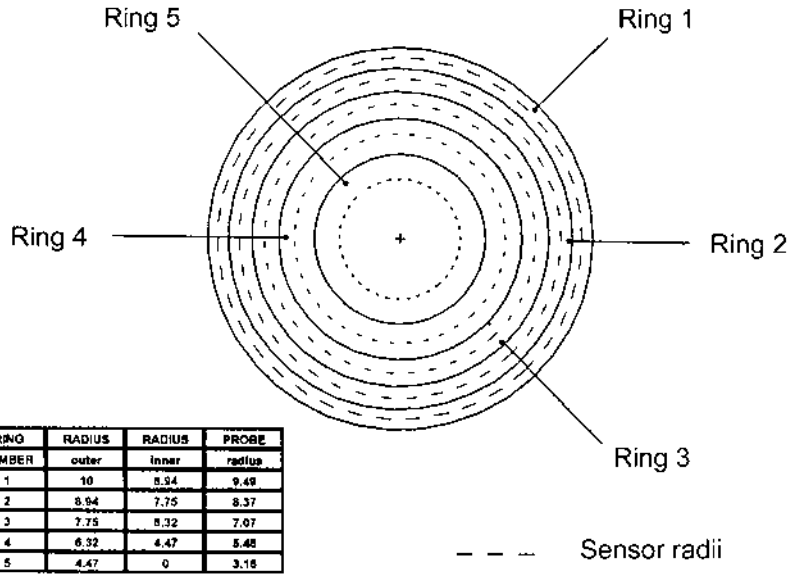

RING NUMBER	RADIUS outer	RADIUS inner	PROBE radius
1	10	8.94	9.49
2	8.94	7.75	8.37
3	7.75	6.32	7.07
4	6.32	4.47	5.48
5	4.47	0	3.16

Figure 8 Radial sensor distribution.

simply arithmetically averaging the several measurements in the measurement plane.

Individual pressure probes inserted into the flow path can also be used in performance testing. These sensors are usually used in flow-path regions where it is impractical to install rakes, where flow-path blockage must be minimized, or at locations in the flow path where isolated measurements are required.

As an alternative to radial immersion rakes, two-dimensional traversing actuators, usually controlled by preprogrammed microprocessors, have been developed to survey the flow path with single-element sensors. The probe is traversed both radially and tangentially to preselected positions. Once the probe is in place, data are recorded before the probe moves to the next position. Measurement locations can be tailored to maximize measurements in areas of interest (such as a wake behind a strut or blade) while minimizing measurements in areas of uniform flow. Advantages of this type of measurement system include minimizing flow-field blockage, minimizing instrumentation-induced flow disturbances, and eliminating probe-to-probe measurement variations.

Disadvantages include the amount of time required to complete a two-dimensional survey. Each measurement requires time for the probe to be positioned and data to be recorded. In addition, a large amount of data can be acquired that requires complicated data reduction and analysis schemes. The use of two-dimensional traversing mechanisms can also be complicated by available real estate on the test rig. In some cases, special test hardware must be designed and integrated onto the test rig to accommodate these traversing systems.

Static Pressure Measurements

Static pressures are normally measured with flush-mounted taps located on outer and inner flow paths. Static pressures coupled with measured total pressures can be used to calculate local flow velocities. In order to do this, static pressure taps are normally located in the same measurement plane as the total pressure sensing elements as illustrated in Fig. 9. Typically, static pressure taps are equally spaced around the circumference on both the inner and outer flow paths. As shown in Fig. 9, the static taps are located equidistant between each of the rakes. This is done so that the rake installations will have minimum impact on the static pressure measurements.

Pitot-static pressure probes can be used to measure both total and static pressures at the same point in the flow field. A typical Pitot-static probe configuration is seen in Fig. 10. Most Pitot-static probe applications

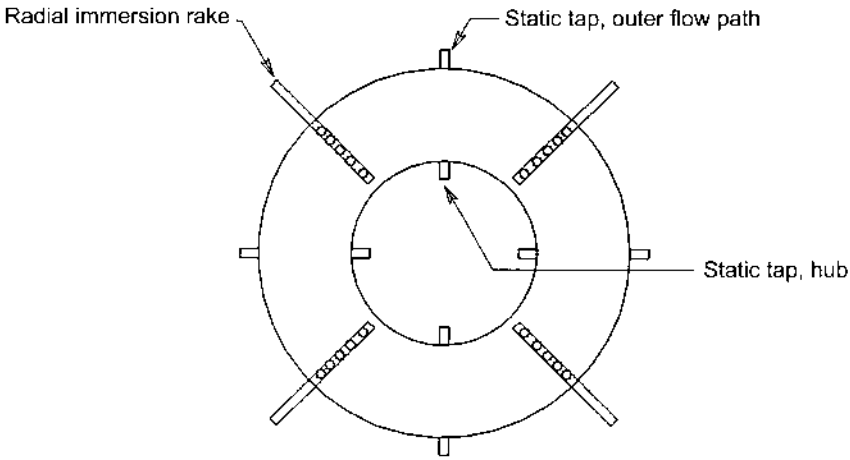

Figure 9 Immersion rake–static pressure tap positioning.

are found with inlet flow measurements where the flow is relatively uniform. Significant measurement errors will occur if the probe is not properly aligned with the flow. In addition, the probes have relatively long sensing heads to minimize sensitivities to flow Mach numbers.

Total Temperature Measurements

Total temperature measurements are used to calculate stage adiabatic efficiencies. In addition, radial survey temperature data can be used to calculate rotor work distributions across the flow path. Turbomachinery flow-field total temperatures are recorded using thermocouple sensors,

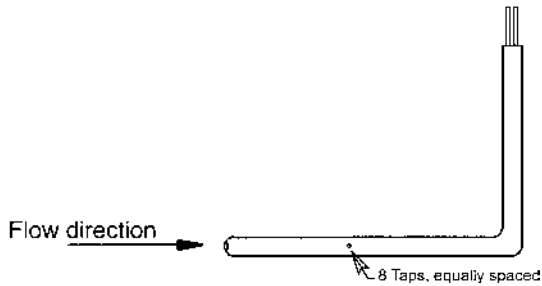

Figure 10 Pitot-static tube configuration.

usually mounted in radial immersion rakes similar to the total pressure rakes discussed earlier. Often temperature and pressures sensors will be installed on the same rakes. Rake design considerations for total pressure sensors also apply to total temperature sensors. Individual temperature sensors can also be placed throughout the flow field as required and used in the two-dimensional surveys as described earlier.

Care must be exercised in using temperature measurements to calculate stage efficiencies for low-pressure-ratio machines. Small temperature-measuring errors, including that of the thermocouple wire, can impact the accuracy of the small temperature difference measurements across low-pressure-ratio turbomachinery. To illustrate, Fig. 11 shows the sensitivity of 1, 2, and 4 °F measurement errors on stage efficiency calculations for a range of pressure ratios. For a fan/compressor that generates a 1.65 pressure ratio, a 1 °F temperature measurement error results in an error of approximately 1% in calculated efficiency. For low-pressure ratios (<1.3), it is recommended that a torque meter be used to measure stage power consumption and efficiencies, rather than calculating efficiencies from temperature rise measurements.

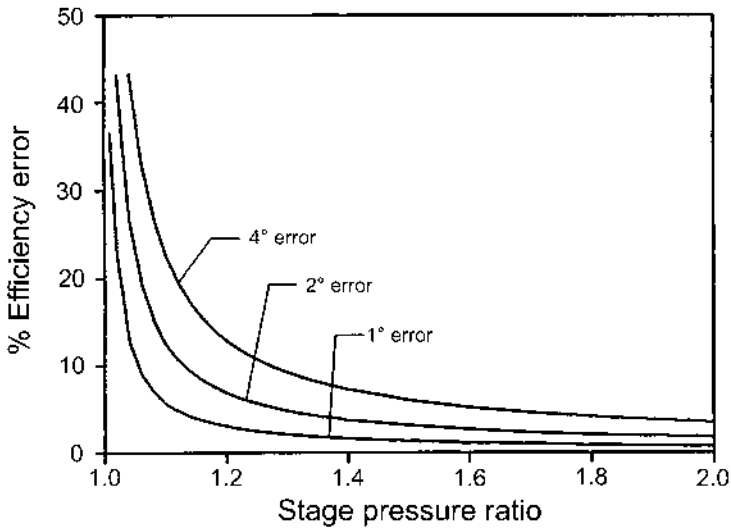

Figure 11 Efficiency sensitivity.

Radial Surveys

One of the principal techniques for turbomachine performance diagnostics is the radial survey. This measurement technique is normally used at blade-row exit planes, in particular behind rotor blades. Using an actuator, a single probe is traversed radially across the flow path. The radial survey can be used where there is no room to mount immersion rakes, where probe blockage and flow interference must be minimized, and where the flow field has nonuniform swirl. Most radial actuator mechanisms will null the sensing element into the flow direction. Performance characteristics of individual blade rows from hub to tip can be quantified by measuring total pressures, temperatures, and flow angles as a function of radius across the flow path. These measurements can be used to calculate tangential, radial, and axial-flow angles and pressure and temperature distributions. Figure 12 shows typical measured flow angles and total pressure radial profiles behind a fan rotor. It is interesting to note that the flow-field properties are not uniform but vary significantly from hub to tip.

An important characteristic of the radial survey is an ability to null the sensing element into the flow direction. By doing so, the local flow swirl angle is defined in the absolute reference frame. In addition, pressure- and temperature-sensing elements on the nulled probe are aligned with the flow direction, which typically reduces measurement errors. A well-accepted technique used to null the sensing element is to include a "cobra" probe as

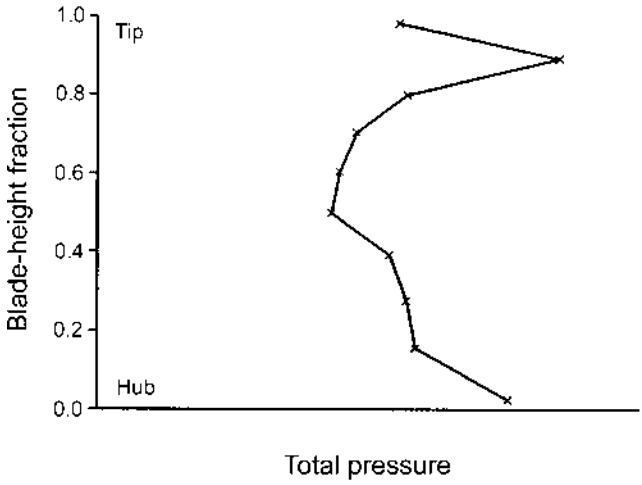

Figure 12(a) Radial pressure profile.

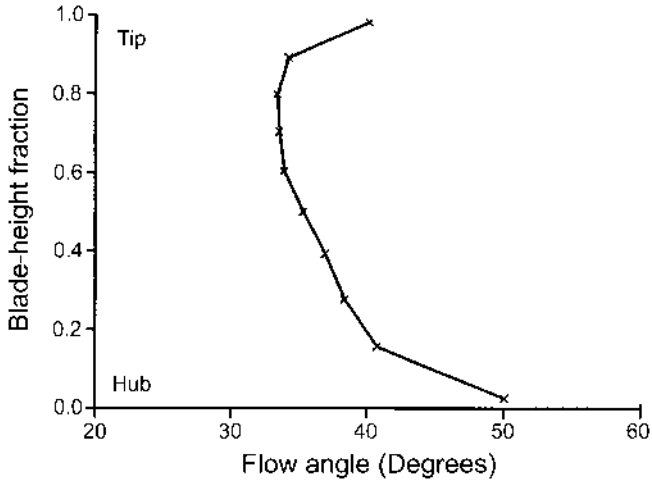

Figure 12(b) Radial flow angle profile.

part of the measurement probe. An illustrative cobra probe configuration is seen in Fig. 13.

Cobra probes are designed to measure flow angles in a plane perpendicular to the probe axis. The pressure-sensing elements consist of two tubes whose inlets are angled into the flow direction. A center tube can be used to measure total pressures or temperatures, depending on what is required. The cobra probe is nulled into the flow by rotating the probe around its axis until the two outer direction-sensing pressures are balanced. Feedback control loops required for probe nulling are typically integrated directly into the radial survey control units. Often radial surveys are accomplished in pairs. One probe is used to determine flow angle, which in turn is used to orient a performance probe on the second system directly into the flow.

Test procedures using radial surveys could include a slow continuous traverse across the flow field to identify areas of interest. The engineer can then position the probe at radii where more detailed measurements are required.

Wake Rakes

Wake rakes are normally utilized to measure localized flow-field characteristics behind objects in the flow path, such as struts and stator vanes. A

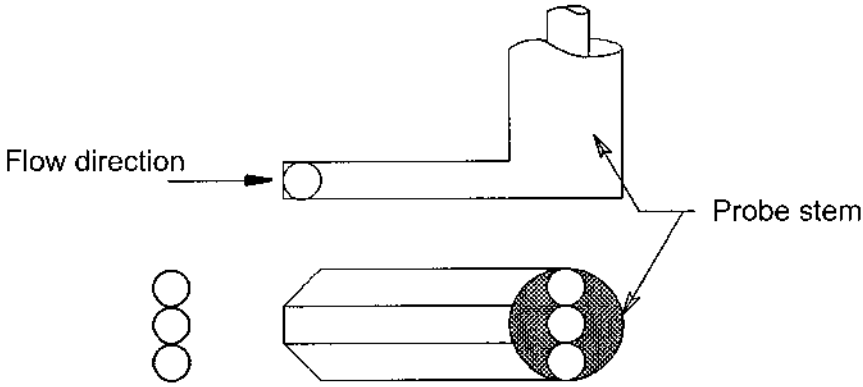

Figure 13 Cobra probe configuration.

typical wake rake configuration is seen in Fig. 14. This particular rake has been designed to measure the total pressure distribution behind a fan stator blade. The rake has been sized to measure the area equivalent to a complete blade-to-blade passage width.

A typical wake rake total pressure profile measured behind a fan stator is seen in Fig. 15. As can be seen, considerable flow-field detail is available in

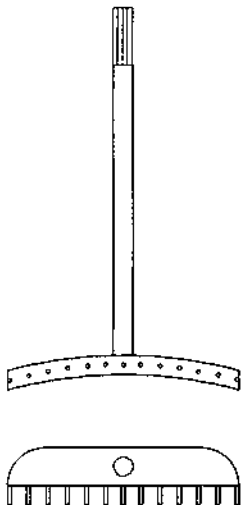

Figure 14 Wake rake configuration.

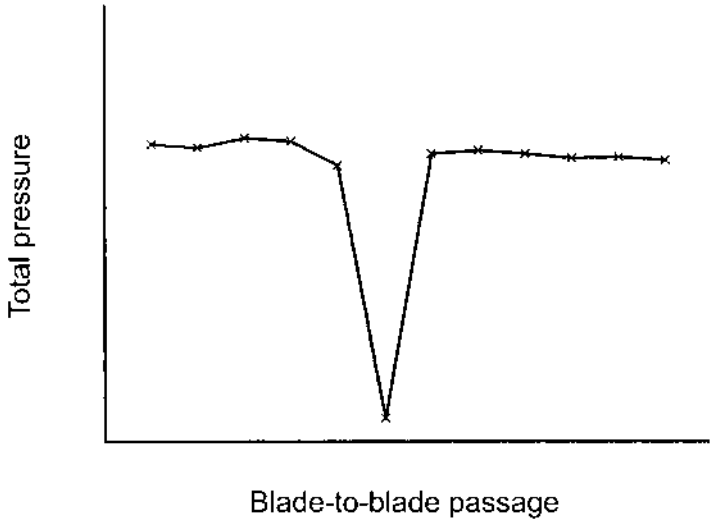

Figure 15 Wake rake total pressure profile.

this measurement. In addition, the profiles can be integrated to give very accurate flow-field properties at the measurement plane.

Rotor Wheel Speeds

Test rig rotor stage rotational speeds must be accurately determined at each operating point during the test. Rotational speed can be measured with a magnetic pulse generator or a photoelectric sensor in conjunction with a geared tooth mounted on the drive shaft. Data are normally transmitted to a frequency counter calibrated to read rpm directly.

Torque Measurements

A torque meter can be used to measure the power required to drive the test rig or, in the case of a turbine rig, the power generated. Included in the torque meter measurement are both stage aerodynamic power and the mechanical power required to overcome drive system losses from bearings and windage. The power utilization due to aerodynamic work must be separated from the mechanical power losses for accurate performance measurements. The torque meter typically includes a calibrated strain gauge element bonded to the drive shaft. The measured torque and shaft rotational speed are used to calculate power.

Mass Flow Rate Measurements

Accurate test rig flow measurements are required in the generation of performance maps. Flow rates are normally measured with hardware that is either a part of or installed directly into the flow path. This includes inlet bellmouths, venturi meters, flow nozzles, and square-edged orifice plates. Flow measurements are typically made either well upstream or downstream of the test hardware where fluid properties are relatively uniform. Pressure measurements coupled with known geometric parameters and calibration flow coefficients are used to calculate resultant flow rates.

Another technique that can be used to calculate flow rates is to integrate radial total pressure profiles across the flow path. These data coupled with wall static pressures and temperature measurements are used to calculate flow rates.

Fan test rigs that split the flow into core and bypass require additional flow measurements so that bypass ratios can be accurately calculated. Typically the total inlet flow and either the core or bypass flows are measured. Additional flow rate measurements are required for bleed flows and turbine cooling air-flow measurements.

Dynamic Measurements

Even though turbomachine performance testing is accomplished during steady-state operating conditions, rotor blade running tip clearance and unsteady static pressure at the rotor blade tips are usually monitored throughout the test.

Rotor blade-tip clearances can impact stage efficiencies, especially in compressors and fans. Test rigs normally include dynamic proximity sensors to measure rotor tip clearances in real time during rig testing. Sensors are typically mounted circumferentially over the blade tips, flush to the outer flow path.

Unsteady pressure measurements can be used to determine when the rotor is getting near a stall operating condition. Typical high-response pressure transducer output traces are seen in Figs. 16 and 17. Here we see the blade passage static pressure rise from the suction to the pressure side of the rotor as it passes beneath the pressure transducer. These data can be used to monitor rotor blade flow quality. The periodic, smooth, uniform pressure rise characteristic as seen in Fig. 16 implies the absence of flow separation in the blade passage. On the other hand, the nonuniform, ''ragged'' pressure rise characteristics as seen in Fig. 17 show blade passage flow separation and unsteadiness. The flattened portion of the pressure trace is an indication of separated flow. The apparent random pressure fluctuations are indicative of unsteady flows incident on the rotor. Some

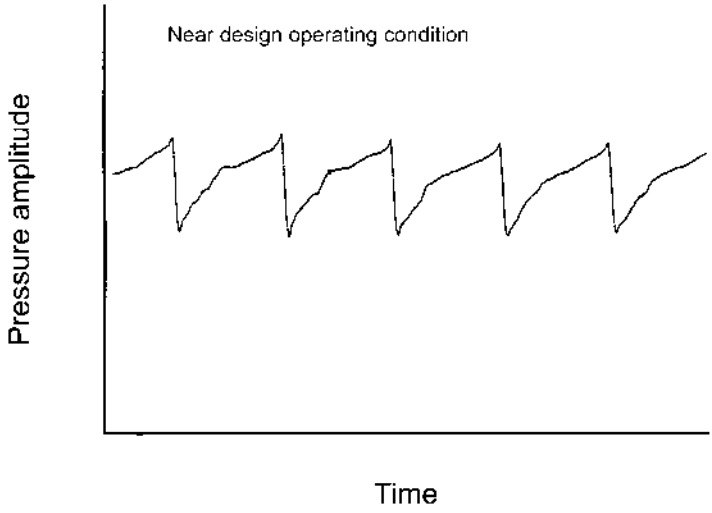

Figure 16 Blade-tip pressure traces.

localized flow fluctuations are generated by the presence of rotating stall cells in the rotor blading.

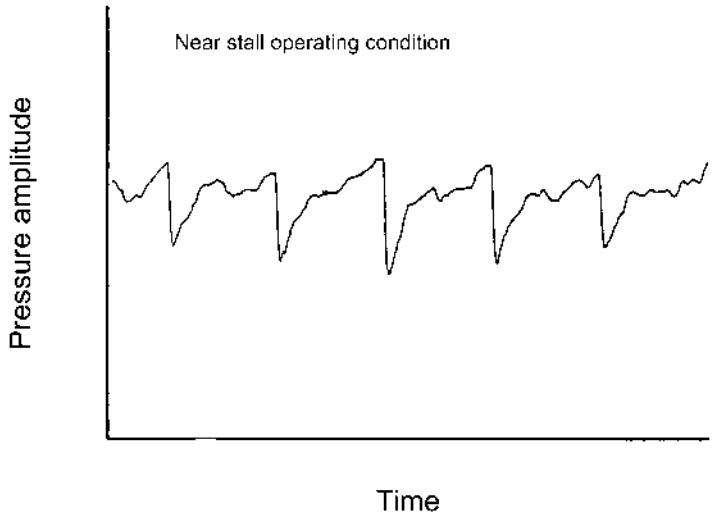

Figure 17 Blade-tip unsteady pressure traces.

Ambient Conditions

In addition to test rig instrumentation and measurements, an accurate measurement of the local ambient conditions must be made during the test activity. These measurements include barometric pressure, ambient temperature, relative humidity, and wind speed and direction if testing is accomplished outside in an unprotected area. If the test rig is installed inside a closed test cell, test-cell static pressure should be recorded.

TEST HARDWARE

Test hardware, commonly referred to as "test rigs," is designed to simulate flow and operating conditions found in the turbomachine stage of interest. Great care must be taken to duplicate the flow path and blading as close as possible to the stage that is being simulated. Test rigs are normally designed so that a complete range of performance data can be measured. This implies that the rotor blade speeds be variable and that the stage pressure ratios be controlled with a type of flow resistance such as a throttle valve.

The test facility must have the power capacity and speed range to operate the test rig over the operating conditions required for performance testing. In addition, the test hardware must be designed to accommodate the instrumentation required for the test activity. Test stage flow properties must be duplicated as closely as possible to those of the component of interest in the gas turbine.

A schematic of a typical test rig for fan and compressor test activities is seen in Fig. 18. Test rig components include a variable-speed drive system, inlet and discharge ducting, a control valve, flow-measuring hardware, and the test stage of interest.

Normally an aerodynamically contoured bellmouth is used for the test rig air inlet. The bellmouth shape should have a large radius to minimize localized high-velocity areas and to produce a uniform inlet flow. The bellmouth can also be used as an accurate flow-measuring device. Other flow-measuring devices typically used in rig testing are venturi meters, flow nozzles, and sharp-edge orifice plates. Flow-measuring devices must be sized for given flow ranges to ensure that measurement accuracies are maintained. Because of the broad range of air flows required for most performance testing, it is often necessary to change the size of the flow-measuring device so that it will be operating at its most sensitive flow range for that part of the test.

Some test rigs include an inlet plenum chamber upstream of the test rig inlet plane. The chamber is normally several diameters larger than the flow

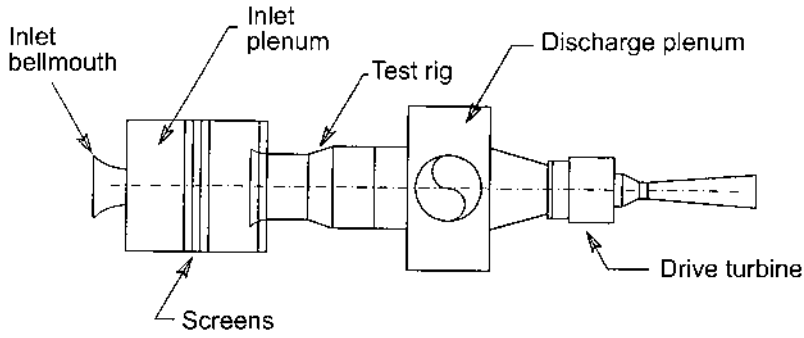

Figure 18 Typical test rig schematic.

ducting. Screens and honeycomb flow straightening sections are used to remove swirl and total pressure distortion, hence ensuring a uniform inlet flow into the test rig. The plenum is also a low-velocity region in which pressure and temperature can accurately be measured. The flow transitions from the plenum to the test rig with a bellmouth.

Fan and compressor stage operating points are determined by matching the stage pressure rise to the pressure loss of the test rig discharge system. The downstream pressure losses are modulated with a variable-flow resistance generator such as a throttle valve or variable solidity screens placed over the discharge duct. As the resistance increases, the system pressure drop increases, forcing the compressor stage to match, and consequently to operate at a higher pressure ratio.

The variation in downstream system loss with flow rate can be seen by plotting the pressure loss characteristics on a performance map as shown in Fig. 19. The pressure loss varies as the square of downstream flow velocity and consequently the square of flow rate. Different valve settings or screen solidities result in different loss coefficients, hence defining different loss characteristics. It is important to realize that the pressure characteristic that represents the "open" throttle valve or the "no-screen" configuration is the lowest pressure limit at which the test rig will operate. Should the performance map require lower pressure ratios at high flows, the test rig discharge ducting must be tailored to reduce pressure losses.

Constant-speed performance characteristics seen on performance maps are generated by setting the desired test rig speed with minimum downstream resistance and recording the performance test data. The test rig must have the capability to hold fixed speeds very closely, especially for fan

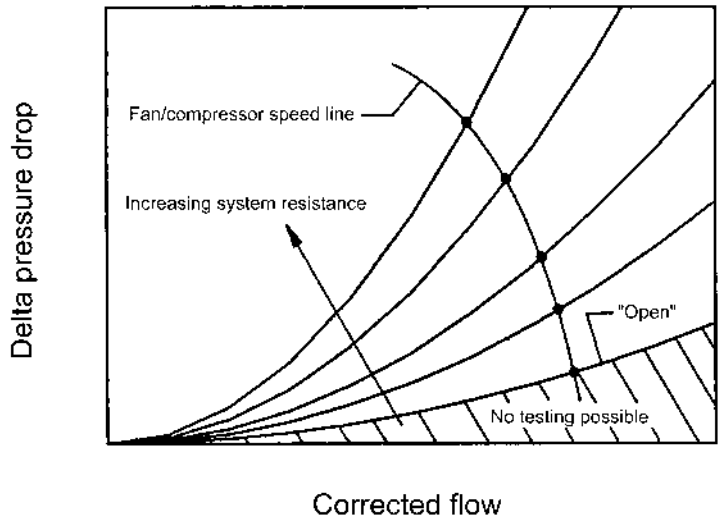

Figure 19 Downstream resistance.

and compressor rigs where the performance is so sensitive to rotor blade speed. Downstream resistance is then increased by closing a throttle valve or partially blocking the discharge with screens. The test stage responds by pumping at a higher pressure to match the increased downstream losses. The performance data are once again recorded.

This process is continuously repeated until stall or surge is detected. Safety dictates that test rigs not be operated in a surge or stall operating condition. The stall line is defined by recording a performance point as close to stall as possible without stall actually occurring. At all operating conditions, data points should not be recorded until the test rig has achieved thermal equilibrium. The complete process is repeated for different rotor blade speeds until the desired performance map has been generated.

Turbine test rigs require a high-temperature and -pressure air supply to drive the stage. The resultant turbine power is absorbed by a dynamometer coupled directly to the drive shaft. Turbine stage loading is varied by increasing or decreasing the resistance offered by the dynamometer.

INSTRUMENTATION DESIGN CONSIDERATIONS

This section presents a brief overview of the design of instrumentation sensors utilized in gas turbine testing. Volumes of information are available to the test engineer to support sensor selection and design.

Instrumentation Requirements

Selection of proper instrumentation is one of the most important aspects in turbomachinery component testing. Of equal importance are the design and integration of the sensors into the test rig. Obviously, one would desire instrumentation that does not influence or disturb the flow while recording data. Several test facilities are developing and using nonintrusive measurement techniques such as laser doppler velocimetry for turbomachinery testing. However, most turbomachine development test programs still use pressure and temperature sensors installed on probes and rakes to measure flow-field performance properties in the test stage.

Instrumentation sensors should be designed to minimize flow disturbances. Local stream blockage due to probes and rakes should be minimized by aerodynamically shaping the rake assemblies and probe stems along with the sensing end of the probe assembly. A small frontal area with a low drag coefficient is desired.

One must also consider the mechanical design of the sensing element. The assembly must be mechanically stiff so that it will not "flap in the breeze" or fatigue. The probe should be designed such that its natural frequency does not coincide with frequencies inherent on the test rig. Often, strain gauges and even miniature accelerometers are installed on the probe stems to monitor the mechanical health of the probe. Probe breakage during testing can have catastrophic consequences on high-speed turbomachine blading, flow ducting, and downstream instrumentation.

Rake and probe assemblies are typically installed in the test rig through openings in the outer flow path. Easy instrumentation accessibility for inspection, cleaning, and recalibration during the test activity is important. Individual probes must be able to pass through small openings. Normally this will be a small circular hole, often not more than a quarter inch in diameter. The hole must be large enough to allow the probe stem to move freely but not so large that it becomes a major leak source during the test.

Another important consideration in the design and installation of sensing elements is its ability to be washed and cleaned during the course of the test. Under normal circumstances the sensing elements are clean when flow checked and calibrated. However, during testing a considerable amount

of small debris (oils, lubricants, fine dirt, sand, etc.) can impinge and attach to the sensing elements. As the material builds up, the aerodynamic and consequently performance characteristics of the sensing elements will deteriorate. Often sensors will become completely plugged if not periodically cleaned.

Performance Instrumentation

Pressure Measurements

Static Pressure. Static pressure is the actual fluid pressure. It is normally measured by a small tap inserted perpendicular to and flush with the flow boundary. In addition, local flow stream static pressures can be measured with Pitot-static probes as described earlier. The preferred static pressure measurement technique for gas turbine testing is that of flush-mounted taps.

Typically, static pressure taps are installed in constant-area ducts away from abrupt bends and area changes. A typical static pressure tap installation is shown in Fig. 20. The pressure taps must be drilled perpendicular to the flow boundary with the hole square-edged. In addition, great care must be exercised to ensure that the tap is burr-free [11,12]. It is good test practice to inspect and clean the static pressure taps after prolonged test rig operations.

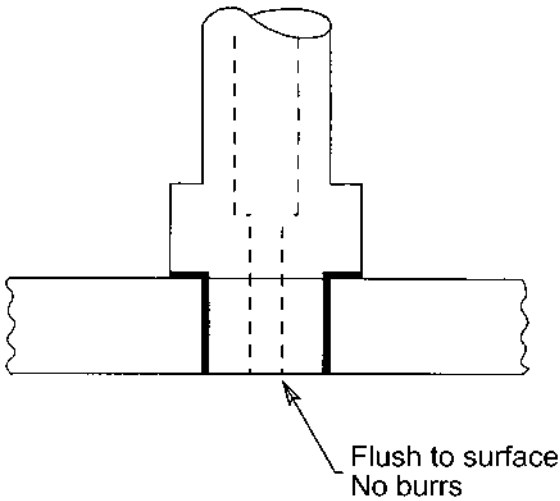

Figure 20 Wall static pressure tap.

Dynamic Pressure. Dynamic pressure is associated with the kinetic energy of the fluid. It cannot be measured directly but is calculated from local fluid velocity and density properties.

Total Pressure. Total pressure, often referred to as stagnation pressure, is the sum of both the static and dynamic pressures. It can be measured by a probe that is at rest with respect to the test rig system boundaries. The probe can be designed such that the fluid is isentropically stagnated at the point of interest. An important consideration in the selection of a total pressure sensor configuration is its relative insensitivity to flow angle changes, especially if the sensor will be fixed in the flow stream.

Sensor measurement quality is quantified by its recovery factor. The recovery factor is the ratio of measured pressure to actual pressure. Recovery factors are normally determined over the expected range of flow Mach numbers and flow angles by flow testing in a calibration facility. Recovery factors are utilized in the data reduction process to correct measured pressure values to actual pressures.

The impact tube and kiel probe are most often used to measure total pressures in gas turbine testing. Either sensing element can be mounted on a radial immersion rake or single element probe.

The impact total pressure sensor consists of a relatively small cylindrical tube with its axis aligned in the flow direction. A cylindrical tube with a square leading edge can have flow angle insensitivities up to $\pm 10^\circ$ in subsonic flows. Flow angle insensitivity can be increased up to 20° by beveling the internal wall as seen in Fig. 21. These sensors are typically manufactured from stainless steel tubing and are relatively simple to fabricate. Impact sensors are often used on radial immersion rakes where the flow field is relatively uniform.

The cross section of a kiel pressure sensor is seen in Fig. 22. The kiel probe is insensitive to flow angles up to $\pm 45^\circ$. It is also insensitive to Reynolds number effects and turbulence errors over a wide range of flow velocities. The kiel sensor seems to be the total pressure sensor of choice for turbomachinery testing because of its extraordinary flow angle insensitivities. However, it is more complicated to fabricate. Individual kiel probes are commercially available, typically with flow and calibration characteristics included.

In supersonic flows the pressure sensors do not indicate local total pressure because of the shock wave that is formed in front of the sensing element. The local total pressure can be calculated from the measured pressure using normal shock pressure drop relationships.

Total pressure sensor operating characteristics and design considerations as well as flow calibration procedures and recovery factor calculations

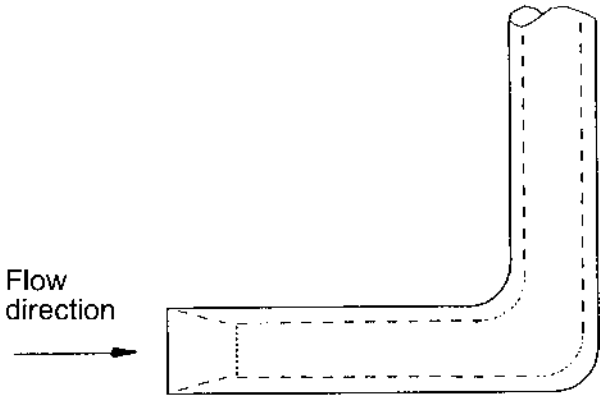

Figure 21 Pressure impact probe configuration.

are well documented in the measurement and instrumentation design literature [11,12].

Temperature Measurements

There are no practical methods to measure static temperatures in a gas turbine test rig. Typically, total temperatures are measured, with static temperatures calculated as part of the data reduction process. Temperature sensing in turbomachine testing is accomplished almost exclusively with

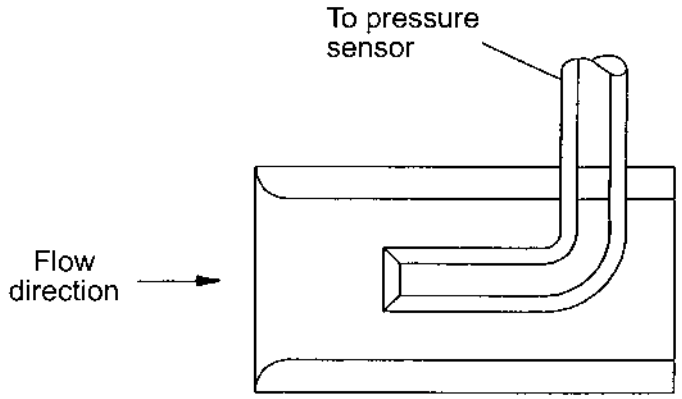

Figure 22 Total pressure kiel sensor.

thermocouples. With care in construction and calibration, thermocouple temperature measurements can be made accurate to less than a degree in measurement error. A temperature measurement technique for a broad range of flow velocities and flow angles is to imbed the thermocouple junction inside a sensor configuration similar to a pressure impact tube.

The effects of thermal equilibrium must be considered in the design and use of temperature probes. Thermal energy can be transferred from the measurement point both by heat conduction down the probe stem or rake body and by radiation to surrounding surfaces. This reduces the sensed temperature from the actual local total temperature. Radiation heat-transfer losses can be minimized by placing a shield over the thermocouple. In addition, a small vent at the rear of the probe can be used to balance the heat loss with thermal energy from the fluid by convective heat transfer.

Two principal thermocouple sensor designs are typically used in turbomachine testing. These include bare-bead thermocouples and shielded sensor configurations. Figure 23 illustrates the basic differences between the two configurations. The bare-bead thermocouple sensor has a relatively simple design and is easy to fabricate. Fast response is the primary advantage of this design. However, the bare-bead thermocouple is subject to radiation losses and to Mach number and Reynolds number effects. In

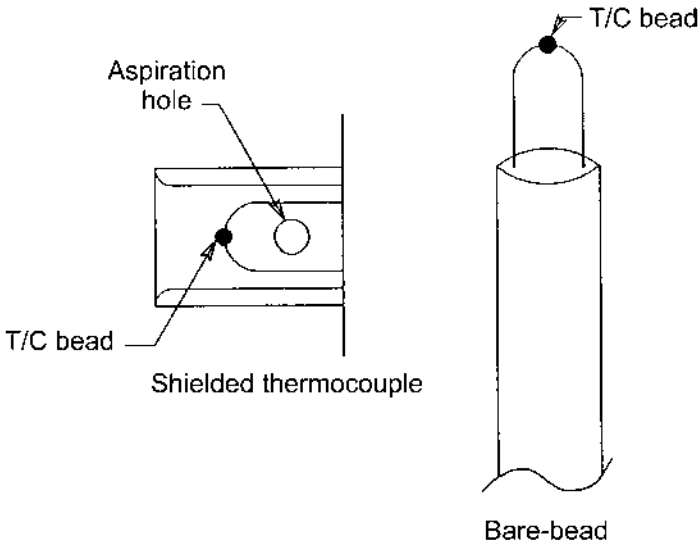

Figure 23 Temperature sensor configurations.

addition, the sensors can be easily damaged by handling and by any foreign object damage (FOD) that is present in the flow.

Shielded thermocouple sensors are insensitive to radiation losses and Mach and Reynolds number effects. In steady-state flow conditions, the shielded thermocouple sensors provide higher recovery factors. These sensors are insensitive to flow angle and also provide FOD protection. Care must be taken throughout the test activity to ensure that both the sensing tube and the aspiration vent hole do not get plugged up.

The recovery characteristics of the probe are primarily a function of velocity over the thermocouple junction. Shielded probes reduce free-stream velocity, resulting in a higher recovery. Temperature recovery factors that relate the indicated to actual temperatures are determined by a flow calibration process.

As with pressure measurements, temperature measurement techniques and sensing element designs are well documented in the literature. Many sensor configurations are also available commercially at a modest cost.

Flow Angle Measurements

The local flow angle can be determined either by nulling a sensor into the flow and recording the resulting angle or by using fixed sensors. The fixed sensors have installed on the sensing head a series of pressure elements that have fixed geometric relationships to each other. The most sensitive design will generate a large pressure gradient between two points on the probe for very small flow angle differences.

Two-dimensional probes are used to measure flow angles in one direction only. Typical two-dimensional sensors include three-claw, three-hole, wedge, and cobra probes. These configurations are illustrated in Fig. 24.

Three-dimensional probes are used to measure both yaw and pitch angles. These sensors include five-claw, four-hole, spherical, and pyramid probes. A typical pyramid probe configuration is seen in Fig. 25. The three-dimensional probes are not only used to measure flow angles but can also sense total and static pressures. This is accomplished by using a series of flow calibrations where each of the individual sensor pressures is recorded as a function of fixed yaw and pitch angle for a range of flow Mach numbers. References [13] and [14] present both design criteria and the required calibration techniques and resultant data reduction processes to process the data from three-dimensional flow angle probes. Numerous flow direction probe configurations are available commercially. These sensors are typically flow checked and calibrated by the manufacturer.

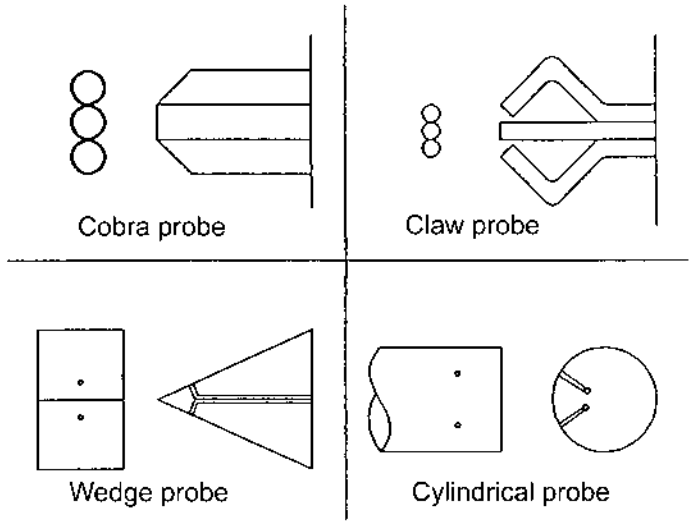

Figure 24 Typical two-dimensional flow direction sensors.

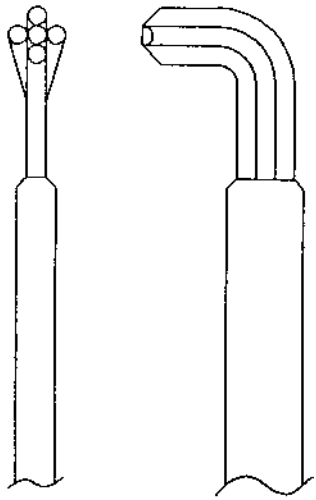

Figure 25 Pyramid probe configuration.

TEST PROCEDURES AND DATA COLLECTION

While preparing for a test program there are several recommended pretest activities that should be accomplished to help ensure a successful test program. Many times testing has been accomplished only to find out after the fact that critical instrumentation was not functioning or data were not recorded properly. Troubleshooting instrumentation and measurement problems and errors during the test can impact cost and schedules. The following, which is by no means comprehensive, includes several recommended activities that should be performed to minimize measurement problems during the test activity.

Pretest

Prior to test rig installation into the test cell, a careful inspection of the hardware should be made. During the inspection, the following types of questions should be addressed: Are the flow ducts properly aligned to avoid steps in the flow path? Are the flow-path ducts free from oil and debris? Are the measurement sensors facing into the flow direction? Are the sensors free from machining burrs, dirt, and grime? Have protective caps been removed from the sensors? Are the lines running from the individual sensors labeled properly so that they will be hooked up to the correct data channels? Do survey actuators fit and traverse without obstructions? Are sensors that are located over the rotor blade row flush-mounted so that they will not get clipped by the rotor blade during testing? Has each of the instrumentation sensors been flow checked to ensure that calibration tolerances are satisfied?

Daily Before Testing

Simple checkout procedures before each day's testing can also minimize instrumentation problems. Before testing starts, it is recommended that the test rig be leak checked. This can be done by sealing and pressurizing the test rig slightly above ambient. Once the test rig is pressurized, several data scans can be recorded. Pressure data channels with readings less than rig pressure indicate that a leak may be present. Sources of leaks can include poor connections and broken lines.

A second recommended check is a "zero-data scan" to record ambient temperatures and pressures of all measurements prior to the start of testing. This is one of the best instrumentation diagnostics that can be performed. During the data scan all readings should indicate ambient conditions. When individual sensors do not read ambient values, it is a good indication that there is a potential problem with that sensor and/or data channel.

Thermocouple lead wires should be inspected periodically. Improperly wired or damaged thermocouple circuits can result in temperatures being sensed outside the test rig instead of at the instrument sensor. A good check for thermocouple operation is to immerse temperature rakes and probes in a hot bath. Any thermocouple channel that reads less than the bath temperature should be checked out for potential problems.

During Testing

Several simple things can be done throughout the test to minimize measurement errors and questions about the test data. These include asking questions like: Are the temperature reference junctions at the right temperature? If an ice bath is being used, is ice in the bath? If at all possible, reference pressures and temperatures should be monitored throughout the test to ensure high data quality. The test engineer should have a good feel before the test starts for the magnitudes of the several data parameters being recorded. Unexpected data values can indicate malfunctioning and deteriorated instrumentation performance. This can trigger a quick check of the instrumentation systems before testing continues.

Test Procedures

The ultimate goal of performance testing is to record performance data. Performance map speed lines are acquired by setting the rotor speed at different fixed rpm values. Since testing is normally accomplished at different times and ambient air temperatures, the physical speed is set using the corrected speed relationship. This is determined by multiplying the desired rig speed by the square root of the actual to reference temperature ratio. The next section discusses corrected speed calculations.

Time should be allowed for the test rig to achieve thermal equilibrium before performance data are acquired. Hardware expansion due to thermal gradients and blade growth due to centrifugal forces occur as different operating conditions are set. Equilibrium is often determined by monitoring a small group of select thermocouple readings. Once all readings have "leveled out" to a predetermined setting (e.g., less than 1 °F change per minute), the data can be recorded. It is recommended that at least two and preferably three or four continuous data scans be recorded at each operating point. Once the data scans have been recorded, the throttling device can then be activated to modulate the downstream resistance pressure to set a new performance point. Once the new operating condition is set, time must once again be allowed for the test rig to achieve thermal equilibrium before the data point is recorded.

This procedure is repeated while moving up the speed line until stall or surge is encountered. It is strongly recommended that the test rig not be operated knowingly in stall and surge. Monitoring dynamic pressures over the rotor blade tip can give a good indication of an impending stall/surge. A test rig fan or compressor stage in surge can experience violent flow fluctuations and high mechanical vibrations and loads. Test hardware has been known to break during hard surges and during continuous operation in stall.

The stall condition at each speed line is determined by operating the test rig as close to stall as possible without the machine actually stalling during the data acquisition process.

DATA PRESENTATION

Data Reduction and Analysis

Following the test activity, a large amount of time and effort is often expended in reducing and analyzing test measurements. Included in this process is the conversion of measured/recorded data to test data in engineering units. This is normally accomplished using pre- and posttest calibrations combined with data acquisition system sensitivity ranges. Once the data are in engineering units, data "calculations and manipulations" are accomplished for analysis and presentation.

Calculations that are normally performed include mass flow rates, rotor speeds, measurement plane average pressures and temperatures, and stage efficiencies. Once the absolute performance parameters are calculated, corrected values and data required for performance map generation are produced.

Flow rates and rotor speeds are corrected to a reference set of operating conditions. Using corrected parameters, performance test data recorded at different ambient pressure and temperature operating conditions can be compared on the same performance map. Typically, reference operating conditions are ambient pressure and temperature for a standard day at sea level (59 °F, 14.696 psia). The data correction factors are nondimensional pressure and temperature ratios. These ratios are calculated by dividing the measured absolute stage inlet total pressure with the reference pressure and stage inlet absolute total temperature with the absolute reference temperature [15].

Corrected Flow

The flow rates used for performance map presentation are corrected using the following expressions:

$$\dot{m}_{\text{corr}} = \frac{\dot{m}\sqrt{\theta}}{\delta}$$

$$\theta = \frac{T_{\text{T in}}}{T_{\text{ref}}} \qquad \delta = \frac{P_{\text{T in}}}{P_{\text{ref}}}$$

where $\dot{m}$ is the measured flow rate and θ and δ are, respectively, the temperature and pressure ratios discussed earlier. Corrected mass flow rate can be equated to the stage inlet Mach number.

Corrected Speed

Rotor blade speeds are corrected to standard conditions using this equation:

$$N_{\text{corr}} = \frac{N}{\sqrt{\theta}}$$

where N is the physical speed. The corrected speed is related to the rotor blade tip Mach number.

Performance Parameters

The following expressions are typical of those used to calculate turbomachine performance parameters. These expressions can be tailored to meet individual test and data presentation requirements.

Bellmouth Flow Rate. Bellmouth measurements provide an accurate flow measurement technique without obstructing the flow-like venturi meters, flow nozzles, or orifice plates. Bellmouth flow rates can be calculated with the following expression:

$$\dot{m} = (\text{Cd})A\sqrt{\frac{\gamma}{R}}\frac{P_{\text{T}}}{\sqrt{T_T}}\sqrt{\frac{2}{\gamma-1}\left[\left(\frac{P}{P_{\text{T}}}\right)^{2/\gamma} - \left(\frac{P}{P_{\text{T}}}\right)^{(\gamma+1)/\gamma}\right]^{1/2}}$$

In this equation the static pressure is that measured downstream of the bellmouth, the total properties are either ambient test-cell properties or those measured in the flow path, and Cd is the discharge loss coefficient for the bellmouth. The area used for calculations is that of the duct cross section at the static pressure measurement plane. The static pressure taps are typically installed in a constant-area duct approximately one duct diameter downstream from the bellmouth.

Pressure Ratios. Stage pressure ratios are calculated by dividing the average stage exit total pressure by the average inlet total pressure. The pressure ratios are calculated using absolute pressure values:

$$P_{\mathrm{R}} = \frac{P_{\mathrm{T\ exit}}}{P_{\mathrm{T\ in}}}$$

For turbine stages, the pressure ratio is normally calculated by dividing the inlet average pressure by the exit average pressure.

Temperature Ratios. Stage temperature ratios are calculated by dividing average exit temperatures with average inlet temperatures. The temperatures must be in absolute units for this calculation:

$$T_{\mathrm{R}} = \frac{T_{\mathrm{T\ exit}}}{T_{\mathrm{T\ in}}}$$

Fan and Compressor Power. The aerodynamic turbomachine stage horsepower requirements can be calculated as follows:

$$\text{power} = \frac{C_{\mathrm{p}} T_{\mathrm{T\ in}} \dot{m}}{0.707\eta} \left[P_{\mathrm{R}}^{(\gamma-1)/\gamma} - 1 \right]$$

The temperature used in this calculation is that of the air at the stage inlet plane, with the pressure ratio and efficiency being those across the stage of interest.

Power from torque meter measurements can be calculated with the following:

$$\text{power} = \frac{N(\mathrm{Tor})}{K}$$

In this expression, the value of the constant K is $1000/2\pi$ when torque (Tor) is in Newton-meters, power in kilowatts, and speed in rps. It is equal to 63,030 for torque in inch-pounds, power in horsepower, and speed in rpm [9].

Stage Efficiency. Fan and compressor stage efficiency is defined as the ratio of ideal work of compression to actual work of compression at a given

pressure ratio [15]. It can be calculated directly from stage pressure and temperature measurements:

$$\eta = \frac{P_R^{(\gamma-1)/\gamma} - 1}{T_R - 1}$$

Likewise, for uncooled turbine stages, the efficiency is defined as the ratio of actual work to the ideal work at a given pressure ratio:

$$\eta = \frac{1 - T_R}{1 - P_R^{(\gamma-1)/\gamma}}$$

Local Mach Number. Local flow Mach numbers can be calculated at any position in the flow path where the total and static pressures and temperatures are known. This can be done using the isentropic flow relations:

$$M = \sqrt{\frac{2}{\gamma - 1}\left[P_R^{(\gamma-1)/\gamma} - 1\right]}$$

The specific heat ratio is a function of temperature.

Data Presentation

Performance Maps

The customary method of presentation for turbomachine stage performance characteristics are the maps described in the first section. Two sets of data are normally presented, which completely describe the stage aerodynamic performance. These include a family of corrected constant-speed lines with stagnation pressure and temperature ratios plotted as a function of corrected flows. Stage adiabatic efficiency is calculated as a function of measured pressure and temperature ratios or from torque meter measurements.

Stall Margin Definitions

A measure of great interest to turbomachine designers is the fan and compressor stall margin. It is a measure of performance margin between a stage operating point and the stall line. Often, stage performance specifications will include a stall margin requirement. There are at least two well-accepted definitions for stall margin, constant-speed line stall margin and constant-flow stall margin.

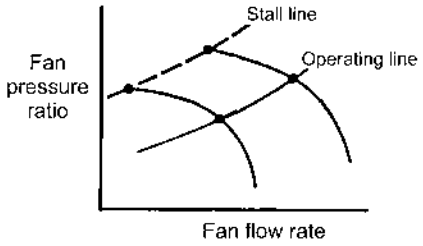

$$\text{Stall margin} = \left\{ \frac{\left[\frac{m\sqrt{\theta}/\delta}{PR} \right]_{oper}}{\left[\frac{m\sqrt{\theta}/\delta}{PR} \right]_{stall}} - 1.0 \right\} \times 100$$

Figure 26 Constant-speed stall margin.

Figure 26 illustrates the definition of the constant-speed stall margin, whereas Fig. 27 defines constant-flow stall margin. Both definitions are widely used in the industry.

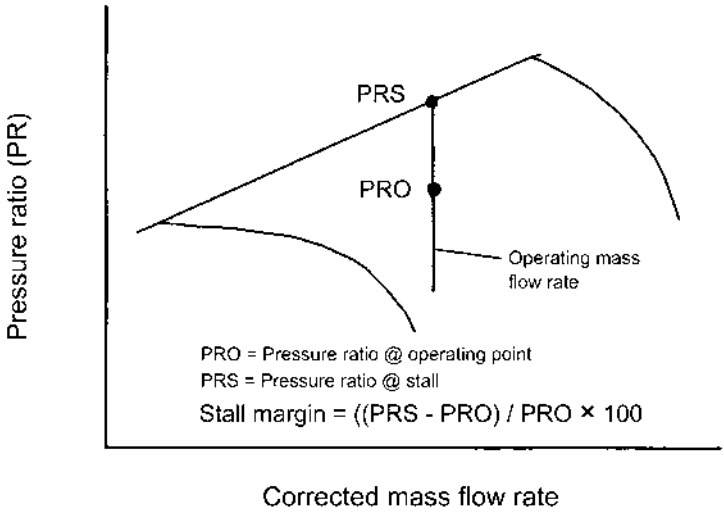

Figure 27 Constant-flow stall margin.

SYMBOLS

A	Cross-section area
Cd	Discharge coefficient
C_p	Constant-pressure specific heat of air
K	Torque meter unit conversion constant
M	Mach number
$\dot{m}$	Mass flow rate
$\dot{m}_{corr}$	Corrected mass flow rate
N	Rotor wheel speed
N_{corr}	Corrected speed
P	Static pressure
Power	Stage power
P_R	Pressure ratio
PRI	Pressure ratio at stall line
PRO	Pressure ratio at operating point
P_T	Total pressure
R	Gas constant
SM	Stall margin
Tor	Torque
T_R	Temperature ratio
T_T	Total temperature
γ	Ratio of specific heats
δ	Pressure ratio, measured to reference
η	Adiabatic stage efficiency
θ	Temperature ratio, measured to reference
( )in	Stage inlet properties
( )exit	Stage exit properties

REFERENCES

1. B. W. Overall, "A Procedure for the Design of Complex Distortion Screen Patterns for Producing Specified Steady-State Total Pressure Profiles at the Inlet of Turbine Engines," AEDC-TR-72-10, Arnold Engineering Development Center, Arnold Air Force Station, Tennessee, January (1972).
2. "Gas Turbine Engine Inlet Flow Distortion Guidelines," ARP 1420, Society of Automotive Engineers, Warrendale, PA (1978).
3. C. Reid, "The Response of Axial Flow Compressors to Intake Flow Distortion," ASME 69-GT-29, The American Society of Mechanical Engineers, New York, March (1969).
4. F. Roberts, G. A. Plourde, and F. Smakula, "Insights Into Axial Compressor Response to Distortion," AIAA 68–565, AIAA 4th Propulsion Joint Specialist Conference, Cleveland, OH, June (1968).

5. G. A. Plourde and A. H. Stenning, "The Attenuation of Circumferential Distortion in Multi-Stage Axial Compressors," AIAA 67–415, AIAA 3rd Propulsion Joint Specialist Conference, Washington DC, July (1967).
6. R. H. Soeder and G. A. Bobula, "Effect of Steady-State Pressure Distortion on Inlet Flow to a High-Bypass-Ratio Turbofan Engine," NASA TM 82964, Lewis Research Center, Cleveland, OH, October (1982).
7. W. M. Braithwaite, E. J. Graber Jr., and C. M. Mehalic, "The Effect of Inlet Temperature and Pressure Distortion on Turbojet Performance," AIAA 73–1316, AIAA/SAE 9th Propulsion Conference, Las Vegas, NV, November (1973).
8. J. Mace and D. Sedlock, "A Perspective on Developing New Inlet Distortion Measurement and Predictive Methods," AIAA 81–1589, AIAA/SAE/ASME 17th Joint Propulsion Conference, Colorado Springs, CO, July (1981).
9. Robert Jorgensen, ed. *Fan Engineering* 8th ed. Buffalo Forge Company, Buffalo, NY (1983).
10. I. N. Moyle, "Analysis of Efficiency Sensitivity Associated with Tip Clearance in Axial Flow Compressors," ASME 88-GT-316, The American Society of Mechanical Engineers, New York, NY (1988).
11. R. P. Benedict, *Fundamentals of Temperature, Pressure, and Flow Measurements*, John Wiley & Sons, New York (1977).
12. R. C. Dean, *Aerodynamic Measurements*, Gas Turbine Laboratory, Massachusetts Institute of Technology, Cambridge (1953).
13. G. E. Glawe, L. N. Krause, and T. J. Dudzinski, "A Small Combination Sensing Probe for Measurement of Temperature, Pressure, and Flow Direction," NASA TN D-4816, Lewis Research Center, Cleveland, OH, October (1968).
14. T. J. Dudzinski and L. N. Krause, "Flow Direction Measurement with Fixed-Position Probes," NASA TM X-1904, Lewis Research Center, Cleveland, OH, October (1969).
15. J. L. Kerrebrock, *Aircraft Engines and Gas Turbines*, MIT Press, Cambridge, MA (1977).

13

Automotive Superchargers and Turbochargers

William D. Siuru, Jr.*

U.S. Air Force, Colorado Springs, Colorado, U.S.A.

INTRODUCTION

Supercharging uses a mechanically driven "air pump" to artificially supply the engine cylinders with a greater amount of air/fuel mixture than would be taken in under normal atmospheric conditions. The basic concept in most supercharging devices is to increase the outlet pressure over the inlet pressure and therefore the density of the air delivered to an engine above ambient atmospheric conditions. This in turn increases the mass of air drawn into the cylinders during each intake stroke. Then, if the optimum air-to-fuel ratio is still maintained, more fuel can be combusted to produce more power output.

A supercharged engine of a given displacement size can produce significantly more power and torque compared to the same engine when normally aspirated, that is, not supercharged. Conversely, a smaller and

* Retired

lighter supercharged engine can produce the same power as a larger and heavier normally aspirated engine (Fig. 1). The smaller engine (1) consumes less fuel under idle conditions, (2) has less mass and inertial loading, (3) has lower frictional and partial-load pumping losses, and (4) produces less emissions under partial-load conditions. Smaller supercharged engines in turn allow smaller, more compact vehicles without sacrificing performance. Supercharging can compensate for the power loss that occurs with the less dense air available as a vehicle climbs in altitude.

A supercharger typically consists of a compressor to increase the pressure of the air inflow, which is usually driven off the engine crankshaft either by belts or gears (Fig. 2). A turbo supercharger, or simply a turbocharger, consists of a centrifugal compressor that is driven directly by a gas turbine, which in turn is driven by engine exhaust gases. It should be noted that a turbocharger is a form of supercharger. However, common terminology will be used here. A mechanically driven compressor will be called a supercharger, while an exhaust-driven turbine/centrifugal compressor combination is a turbocharger (Fig. 3).

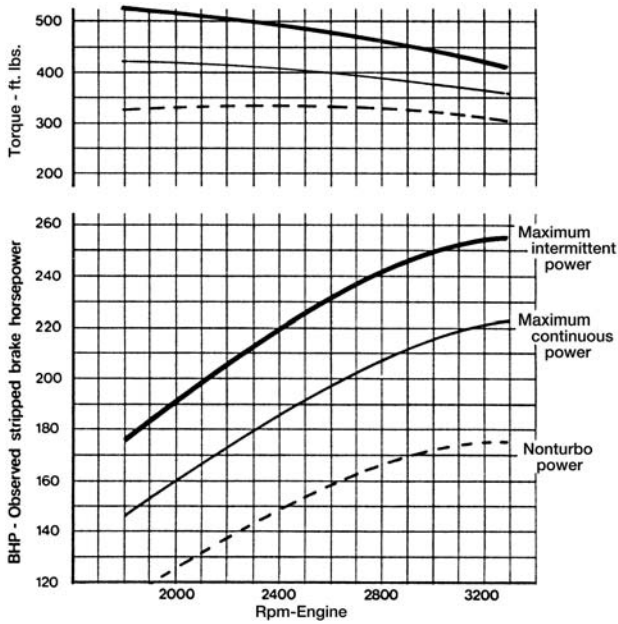

Figure 1 Comparison of the performance between a turbo supercharged (turbocharged) diesel V-8 engine and a naturally aspirated engine (nonsuper charged). (Courtesy Hypermax Engineering, Inc.)

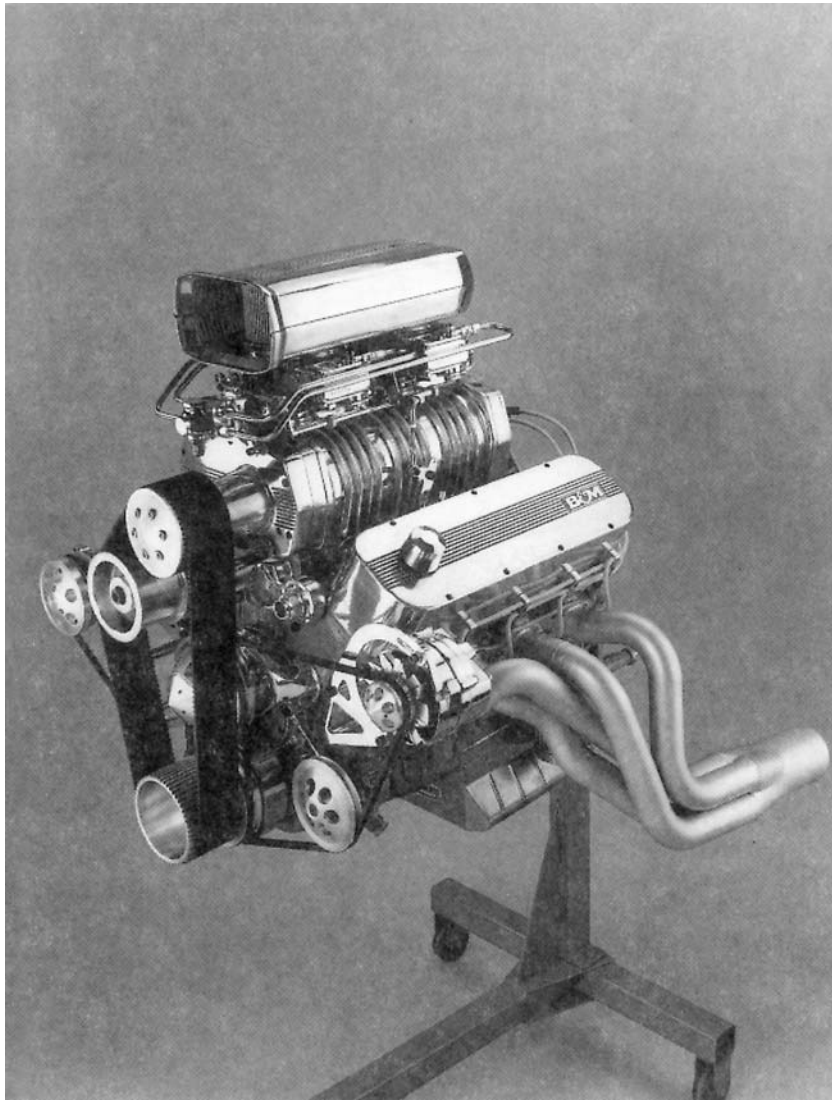

Figure 2 A Roots-type supercharger driven off the crankshaft by a belt drive. (Courtesy B&M Automotive Products.)

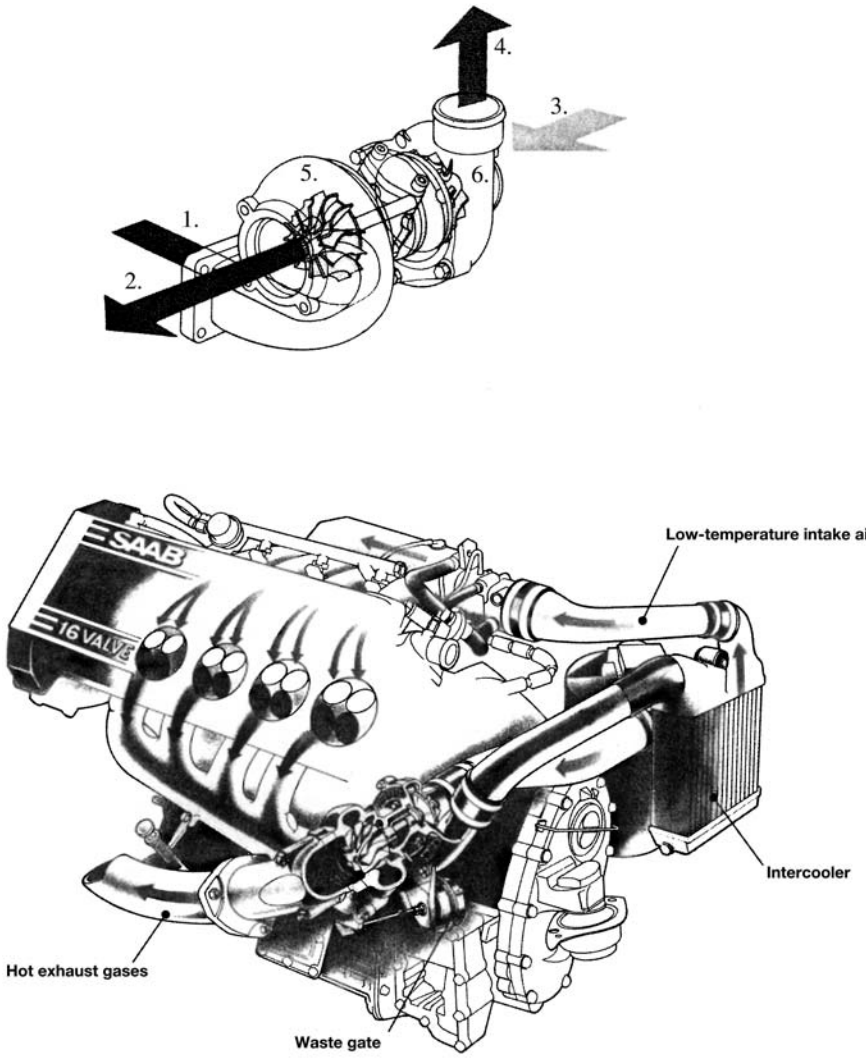

Figure 3 Typical turbocharger installation on a spark ignition engine. After the air has been compressed in the turbocharger, it is cooled as it flows through the intercooler. The wastegate is a valve that controls the boost pressure. (Courtesy Saab Automobile AB.)

The supercharger was in routine use many years before the turbocharger, primarily because it took longer to develop the materials needed for the turbochargers, which operate at very high speeds and temperatures. Many of the materials that allowed mass-produced turbochargers were developed for aircraft gas turbine engines.

Superchargers driven directly off the engine rather than by exhaust gases are extremely responsive in providing an instantaneous increase in power. In contrast, the turbocharger's rotating parts, the turbine and compressor, take a finite time to be spun up to operating speed after the throttle is opened. This time is commonly referred to as turbo lag (Fig. 4). Turbo lag is a result of incompatibility in matching the engine, a volume machine, with a speed machine, the turbocharger. Engineers have done a commendable job in reducing turbo lag, but it has not been entirely eliminated.

Being mechanically driven, usually off the crankshaft via belts or gears, the supercharger can be a complex piece of machinery. Therefore, it is usually more expensive to manufacture than a turbocharger. It often is more difficult to find space for superchargers in the engine compartment. By operating at very high speeds, turbochargers are very compact and require

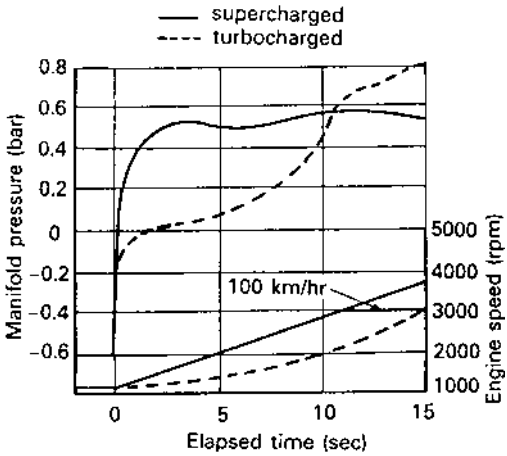

Figure 4 Comparison of a 2.5-L engine fitted with a Roots-type supercharger versus the same engine fitted with a turbocharger. Note that the supercharger provides a high manifold (boost) pressure almost instantaneously. The turbocharger takes longer to reach maximum boost pressure because of "turbo lag." Therefore, engine speed rises faster with the supercharger compared to the turbocharger. (Courtesy Porsche AG.)

significantly less space in the engine compartment. However, supercharger concepts, such as belt-driven centifugal compressors and pressure-wave superchargers, can rival turbochargers in the space they consume.

The supercharger is usually less efficient, drawing off more power from the engine and adding to fuel consumption. At first, it may seem that you are getting something for nothing with a turbocharger, since it is powered by the energy of the exhaust gases, which normally would be wasted out of exhaust pipe. However, closer examination shows the turbine in the turbocharger does increase to back pressure in the exhaust manifold, which in turn results in reduced engine power output. Fortunately, this loss of power in driving the turbine is relatively small in relation to the power increase obtained at the flywheel. Also, there are frictional losses, mainly in turbine and compressor shaft bearings, though again these are relatively small. A supercharger is more likely to be noisier, often with a characteristic whine, than a carefully designed and maintained turbocharger. The two are compared in Table 1.

A BRIEF HISTORY OF SUPERCHARGING AND TURBOCHARGING

Supercharging is almost as old as the internal combustion engine itself. Rudolf Diesel produced his first supercharger design in 1896, only about 20 years after Dr. Nickolaus August Otto had invented his four-stroke engine. In 1901, Sir Dugald Clark found that an engine produced more power when the volume of air entering a cylinder was increased artificially. Around the turn of the century, Rateau in France developed the centrifugal compressor, and in 1902 Louis Renault patented a system using a centrifugal fan to blow air into the carburetor inlet.

In 1907, American Lee Chadwick with J. T. Nicholls used a single-stage centrifugal compressor to put the carburetor under pressure to increase volumetric efficiency. This concept was extended to a three-stage, belt-driven centrifugal compressor that supplied the carburetor with pressurized air. In 1908, Chadwick's car equipped with a blower won the Great Despair hill climb in Pennsylvania. In the next 2 years, the car won more races, and the replicas produced were the first 100-mph cars sold to the public. In 1905, Swiss Alfred Buchi developed the first successful modern turbocharger driven by engine exhaust gases.

Supercharger technology advanced rapidly during World War I to allow fighters and bombers to fly at higher altitudes. The supercharger compressed the thin air of high altitudes so the engines could get sufficient air for proper combustion. Besides increasing the amount of air supplied to

Table 1 Superchargers Versus Turbochargers

Parameter	Supercharger	Turbocharger
Performance	30–40% Power increase over naturally aspirated engine Increased low-RPM torque No turbo lag—dramatic improvement in startup and passing acceleration, particularly with automatic transmission	30–40% Power increase over naturally aspirated engine
Temperatures		Increased underhood temperatures may require component upgrading
Efficiency loss	Mechanical friction	Increased engine back pressure
Packaging	Fairly simple if belt-driven	Major revisions required to package new exhaust system
Lubrication system	Self-contained	Uses engine oil and coolant
System noise	Pressure pulsation and gear noise	High-frequency whine and wastegate

Note. Based on information supplied by Eaton Corporation.

the engine at high altitudes, supercharging provided extra power for takeoffs and climbs. Initially, developments centered around the Roots-type positive displacement blower, but were superceded by more efficient centrifugal compressors.

Supercharging was pursued between the wars, first for military aircraft and then for commercial airliners like the Boeing 247 and Douglas DC-3 that could fly above most adverse weather. The Boeing 307 Stratoliner also had a pressurized cabin achieved by as a byproduct of supercharging. While most engine makers concentrated on superchargers driven via gears off to the engine crankshaft, General Electric had developed a successful aircraft turbo supercharger or turbocharger by 1925.

Meanwhile, supercharging was picked up by auto racers by the early 1920s. In 1921, a six-cylinder Mercedes 28/95 using a Roots-type blower won the Coppa Florio. In 1923, Fiat was the first to supercharge a Grand Prix race car, first using a Wittig vane-type supercharger, but switching to a Roots-type blower. The latter used a charge air cooler before the carburetor.

The Alfa Romeo P2's supercharged straight eight delivered a then-impressive 140 hp at 5,500 rpm. Mercedes entered a supercharged car in the 1923 Indianapolis, and a Duesenberg with a supercharged engine first won the Indy 500 in 1924. The Duesenberg used a centrifugal compressor and was the first supercharging system to suck air through the carburetor. Now the latent heat of vaporization of the fuel could be used to cool the blower and the fuel/air mixture. This resulted in a greater mass of mixture being forced into the engine. Incidently, Fred and Augie Duesenberg and Harry Miller were major forces in developing supercharged cars in the United States. Between 1925 and 1938, most Grand Prix cars including Alfa Romeos, Auto-Unions, Bugattis, Delages, and Mercedes were supercharged. In 1937–1939, Grand Prix racing was completely dominated by the enormously powerful Mercedes and Auto Union supercharged cars. The Auto Unions with 6-L, 16-cylinder engines developed as much as 520 hp and the Mercedes W 125 produced 646 hp, both with two-stage Roots-type blowers. With the exception of Mercedes, who persisted in downstream carburetor positioning until 1937, the practice of mounting the carburetor in front of the supercharger became normal. The W 125's straight eight's power output would not be matched until the turbocharged Indianapolis, CanAm, and Grand Prix race cars of the 1970s and 1980s. Supercharging was also available on top-of-the-line road cars of the 1930s in both Europe and the United States. Automakers like Alfa Romeo, Auburn, Bentley, Buggati, Cord, Delage, Duesenberg, Mercedes Benz, and a few more had supercharged models in their catalogs.

Aviation supercharging again moved ahead during World War II, and turbochargers proved themselves in aircraft like the B-17 Flying Fortress, B-24 Liberators, P-38 Lightning, and P-47 Thunderbolt. By the early 1950s, the piston engine had reached its zenith with the Wright Turbo-Compound, an 18-cylinder engine that could produce up to 3,700 hp and allowed airliners like the Douglas DC-7 and Lockheed Super Constellation to fly across the continent or the Atlantic Ocean nonstop. Supercharger and turbocharger technology was also used to improve the power/weight ratios and obtain maximum power from large diesel engines for ships and for electrical power generation. Turbocharged diesel engines for trucks were introduced in the mid-1950s.

There was a brief return of supercharged race cars in Europe right after World War II, However, by 1950–1951 unsupercharged Ferraris dominated racing and the use of supercharged cars declined, abetted by a change in Grand Prix rules in 1952 limiting supercharged cars to 500 cm^3. Turbocharging would appear in this racing venue in about 23 years. In 1951, a turbocharged Cummins Diesel Special appeared in the Indianapolis 500, and turbocharged Offenhausers made their debut here in 1966. By the mid-

1960s, turbocharging was used by USAC racers, and of course supercharging and turbocharging were used and improved by drag racers.

Kaiser was the first U.S. automaker in 1954 and 1955 to market a supercharged engined car after the war. It used McCulloch superchargers to boost the output of its 226.2-cubic-inch displacement (cid) six-cylinder engines from 118 to 140 hp. Studebaker-Packard also used McCulloch/Packard superchargers on the 289-cid V-8 used in the 1957 and 1958 Packards and Studebakers as well in the 1963–1964 Studebaker Avanti. For 1957 only, Ford offered a McCulloch/Paxton supercharger on its 312-cid V-8 that was conservatively rated at 300 hp. There was also a NASCAR version of the engine that developed 340 hp for stock-car racing.

The 1962–1963 Oldsmobile Jetfire was the first production car to use a turbocharger. Oldsmobile engineers added an AiResearch turbocharger to the Buick-built 215 V-8. The Turbo-Rocket engine produced 215 hp compared to 155 hp for the normally aspirated version of the engine. The Turbo-Rocket engine also had an ultrahigh compression ratio of 10.25:1. Indeed, combining turbocharging with a high compression ratio was the Jetfire's downfall because it led to severe denotation problems. To cure this problem, Oldsmobile used a specially formulated Turbo-Rocket fluid, really a mixture of water and alcohol, which was injected into the engine. Chevrolet offered a TRW turbocharger for its 1962–1966 Corvairs with their rear-mounted air-cooled six-cylinder engines with more success.

By the mid- to late 1970s, turbocharging became a commonly used means to boost the power of small-displacement engines that were being used to achieve better fuel economy. Porsches, BMWs, Saabs, Buicks, and many others were available with turbocharged engines.

Finally, in the late 1950s, General Motors investigated "air-injection supercharging" (Fig. 5) as an alternative to a mechanically driven supercharger or exhaust-driven turbocharger. Air was stored at very high pressures in air bottles that were pressurized by a couple of engine-driven air compressors. The high-pressure air was injected directly into the cylinder through a separately actuated poppet valve in the cylinder head during the compression stroke after the intake valve was closed. Additional fuel was also added through the carburetor. Tests on a 2.7-L, six-cylinder engine showed that air-injection supercharging increased horsepower output about 2.5 times. Additionally, direct air injection reduced both temperatures in the cylinder and increased the turbulence, both allowing higher cylinder pressures without knocking. While the concept looked good on paper and in tests, there were several drawbacks. The air bottles took up almost all the trunk space, even they though there was only sufficient air for a couple of minutes of supercharging. The system was quite complex and costly, and it

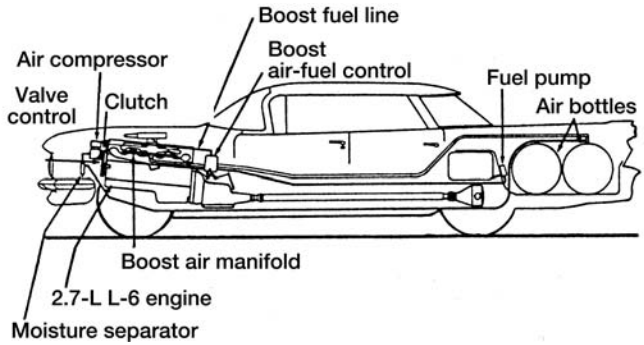

Figure 5 Schematic of the "air-injection supercharging" system tested by General Motors in the late 1950s.

took at least a half hour to bring the tanks up to full charge using the engine-driven compressors. The 3,000-psi air bottles could also become "bombs" in a crash.

SUPERCHARGERS

There are basically two distinct categories, classified according to compressor type, of mechanically driven superchargers that have been used with production gasoline engines. First there are the positive-displacement types, which are characterized by the Roots, rotary piston, or vane-type superchargers. During each revolution, the positive-displacement supercharger pushes the air charge into a zone of higher pressure.

The second type is a dynamic or kinetic supercharger that uses a mechanically drive radial- or axial-flow compressor. These turbomachines convert the mechanical energy into kinetic energy by accelerating the air charge. This increased kinetic energy is converted to increased pressure by using of a diffuser. Incidentally, the turbocharger is a kinetic turbomachine except the drive energy comes from an exhaust-driven turbine rather than being mechanically driven by the engine crankshaft via belt or gears. Indeed, it is also called a turbosupercharger.

Roots Blower

The Roots-type blower was invented and originally marketed by P. H. & F. M. Roots of Connersville, Indiana, in 1866. This positive-displacement supercharger is probably the best known and at one time the most widely used mechanically driven supercharger for automotive applications.

The basic Roots blower uses two counterrotating lobed rotors that mesh together. Air entering the intake port is trapped between a rotor lobe and the casing while it is carried around to the discharge port. The two rotors do not actually touch, because they are driven in proper phase by externally mounted gears (Fig. 6).

The Roots-type supercharger is more correctly called a blower rather than a compressor because the volume of air trapped by a lobe does not change while being transferred from the inlet to discharge port at constant pressure. Compression does not occur internally in the supercharger, but in the downstream restriction through area reduction. When the air charge is exposed to the outlet port, part of this higher-pressure air flows back into the supercharger to equalize the local pressure. The meshing rotors seal the pressurized volume as they rotate back to the inlet port.

The volume of air pumped during each revolution is a function of the length and diameter of the rotor. These dimensions, along with the lobe profile and port shape, control the flow rate pattern over the rpm operating range. While the basic design will work with two lobes per rotor, three- and four-lobe versions have been used.

Advantages of the Roots-type blower include a balanced rotating system and a relatively low operating temperature. Disadvantages include somewhat reduced reliability at high rotational speeds. Also, the tight tolerances require precise engineering and manufacturing, leading to

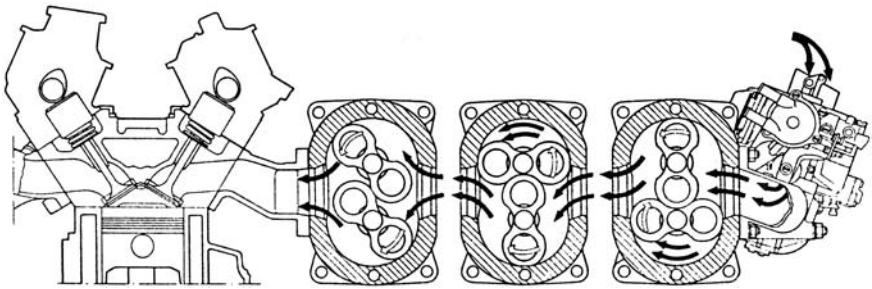

Figure 6 Operation of a twin-rotor Roots blower. The air is trapped between the lobes and the casing while it is carried from inlet to outlet. Note the area reduction after the discharge port that provides the pressure boost. (Courtesy Fiat/Lancia.)

relatively high unit costs. Frictional losses are relatively low with Roots blowers because the only rotating contact is between the synchronizing gears, which usually run in their own lubrication chamber. However, because of compression difficulties, the overall efficiency of Roots blowers can be below 50%. Low friction and a design that eliminates out-of-balance forces allow the Roots-type blower to run at speeds up to 10,000 rpm. Speed limitations result from rotor flexing that can cause rotor lobes to clash or due to excessive thrust loading can cause the rotors to operate out of phase or bearings to spin in their housings (Fig. 7).

High noise level has been a long-time disadvantage of Roots-type superchargers, which produce a very distinctive noise, especially at low

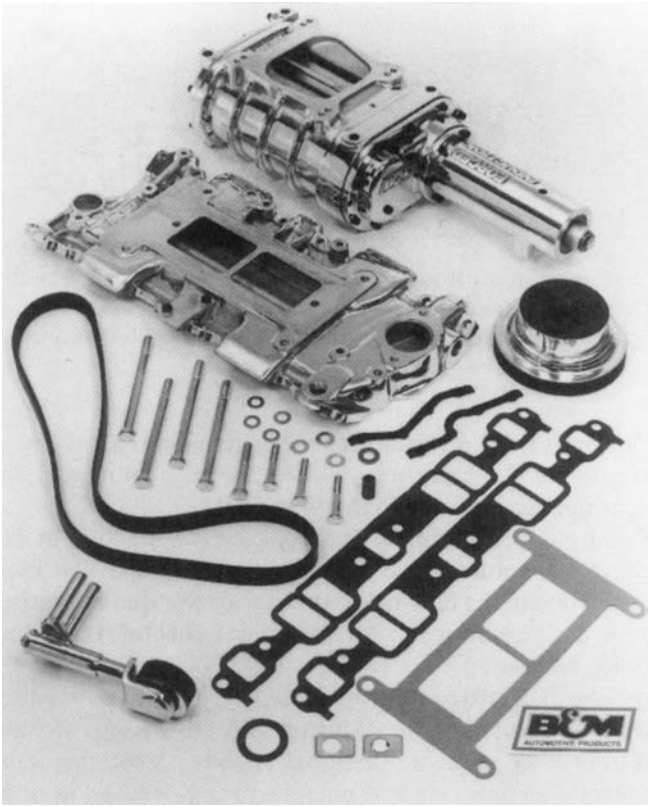

Figure 7 The Roots-type blower is a rather complex piece of machinery. The twin rotor lobes can be seen in the actual supercharger in the upper portion of the picture. (Courtesy B&M Automotive Products.)

speeds. The sound is caused by the surging or pulsing intake and discharge at both the inlet and discharge manifolds, repectively, as the lobes pass the delivery port. This noise can be reduced substantially by using three or more lobe rotors. Another, more satisfactory approach uses rotors with a helically shaped rotor. The helix layout is along the longitudinal axis. This configuration reduces the noise pulsations because the air delivery is smoother with less pressure spikes. The twisted rotor design provides nearly constant inlet and outlet volumes and pressures while minimizing losses in volumetric efficiency. In addition to twisted rotors, attention must be paid to the shape of the inlet and outlet ports to obtain optimum noise reduction. Besides reducing noise, twisted designs can also have higher efficiency.

The volumetric efficiency of a naturally aspirated engine is defined as the ratio of the actual volume of air drawn into the cylinder during one induction stroke to the geometric or theoretical swept volume of the cylinder. Losses in volumetric efficiency can be attributed to filters, carburetor or throttle valves, manifold ducting, port and valve restrictions, plus residual exhaust gases left from the previous cycle. Supercharging and turbocharging can improve volumetric efficiency, even above 100% in some cases.

Normally, boost pressure in mechanical superchargers such as the Roots-type blower is controlled through use of a clutch that can be disengaged or has controlled slippage. A bypass valve can also be used to relieve excessive pressures. The disadvantage of the latter technique is that it dissipates some of the energy that went into moving the air, representing a loss in efficiency and a waste of fuel. However, proper valve design can minimize this loss.

Rotary Piston Compressors

Rotary piston machines are generally true compressors in which the volume of a chamber changes between inlet and outlet resulting in an internal pressure rise. Many rotary piston compressors have been proposed, usually with an intersecting axis rotary piston configuration where the axis of the moving elements and the housing are not parallel and may operate with an oscillating motion. However, very few have been used in automotive applications to any extent, mainly because they are usually quite complex and require precise machining, leading to high manufacturing cost. Providing continual sealing during the complete operation cycle is one of the main design challenges.

Probably the most successful rotary piston design is the Kuhnle, Kopp & Kausch Ro-charger (Fig. 8). The design uses a twin-lobed piston that rotates eccentrically with respect to the unit's main axis of rotation. A three-

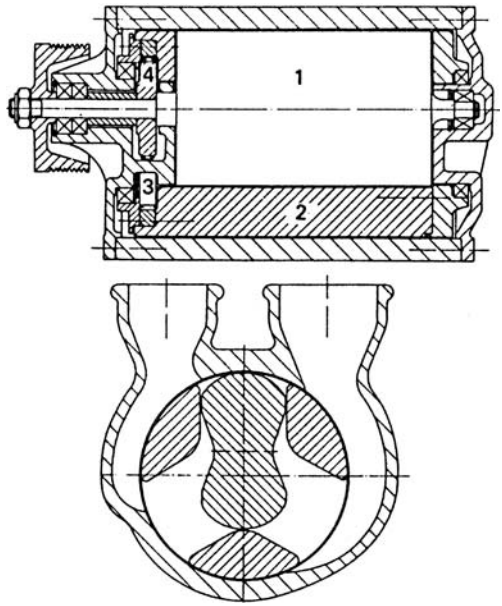

Figure 8a Layout of the Ro-charger rotary piston supercharger: 1, twin-lobe rotating position; 2, triple-chamber rotating cylinder; 3, ring gear that drives cylinder; 4, sprocket gear, which meshes with ring gear to drive piston drive shaft. (Courtesy Kuhnle, Kopp & Kausch AG.)

chamber cylinder with three inlet/outlet ports rotates on the main axis inside the Ro-charger housing. A ring gear and sprocket drive the outer cylinder and inner piston, using a 3:2 ratio to synchronize these elements. The Ro-charger is belt-driven by the engine crankshaft.

There are three compressions per cycle. Looking at one compression cycle, the cycle starts when the inlet port is open to the intake manifold. Here the chamber has its maximum volume as air enters it. As the cylinder rotates, a piston lobe rotates into the chamber and the internal volume decreases, increasing the air pressure. By the time the rotating cylinder reaches the outlet port, the volume is at a minimum and the delivery pressure is maximized. Future rotation forces the air from the chamber through the outlet port and the process repeats itself.

Positive sealing is not possible with the Ro-charger, so pressure losses are mininized by accurate machining of the components. This results in

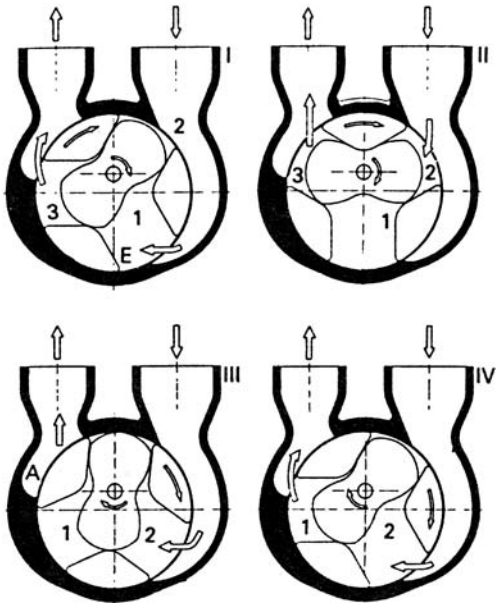

Figure 8b How the Ro-charger operates: Phase I, the cylinder is positioned so chamber 1 is fully opened to the intake port and air is drawn in. Phase II, chamber 1 is at maximum volume. Phase III, piston moves into chamber 1 to compress the air charge. Phase IV, chamber 1 is positioned to it is opened to the outlet port and air is discharged to the intake manifold. The cycle repeats itself as chamber 2 is now opened to the intake port.

minimum leakage between the various elements. The Ro-charger is a very compact unit relative to the volume of air handled.

Vane-Type Compressors

Vane-type compressors are closely related to piston types, but they have been used somewhat more frequently in practical automotive applications. A common feature of vane-type compressors is that they use a number of sliding vanes. These vanes divide the housing into compartments whose volume changes as the vanes rotate. The volume change occurs since the vanes are attached to a rotor or other device that rotates with an eccentric motion. At the beginning of the cycle, the compartment is open to the inlet manifold and the resulting vacuum draws in the air charge. As the device

rotates, the compartment volume decreases in size to compress the charge. As the chamber volume reaches a minimum, it is opened to the discharge port and therefore the intake manifold [Fig. 9(a)].

One important advantage of piston and vane-type compressors over Roots-type blowers is that the compression occurs within the compressor itself. Internal compression increases the density and thus the weight of the air charge delivered during each revolution. The temperature rise for a given weight of charge air is also reduced. The pressure differential between the discharge port and the inlet manifold is reduced, improving the pumping efficiency. This means less power is required to drive the supercharger to achieve a given pressure increase.

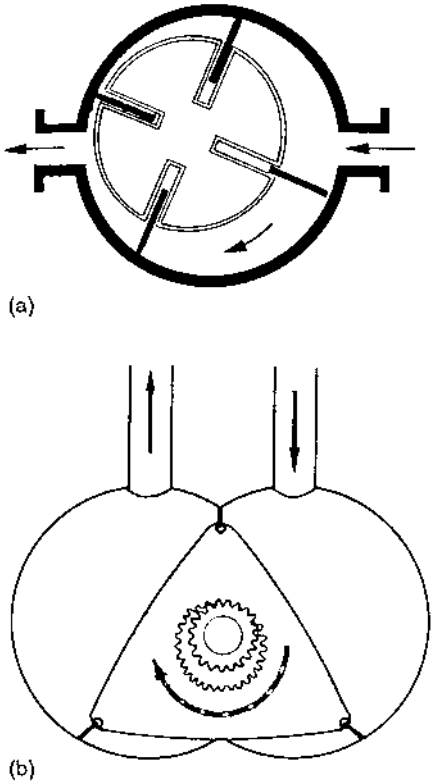

Figure 9 (a) Operating principles of a sliding vane-type supercharger. (b) A sliding vane-type supercharger that operates on the same principle as a Wankel rotor engine.

The vanes in many designs are prevented from actually touching the housing walls, so there is a very small clearance to reduce friction and eliminate vane tip wear. One of the problems with some vane-type compressors is the requirement to actively lubricate the sliding vane, adding to the complexity and resulting in possible oil contamination of the air charge. New materials can eliminate the need for lubrication. One successful design uses the same operating principles as the Wankel rotary automotive engine [Fig. 9(b)].

Screw-Type Compressors

The concept of using one or more helices within an enclosure for compression dates back to the 1800s. One of the more successful was the Lysholm screw compressor (Fig. 10). In this device, the twin helical rotors, one with four helixes, the other with six, rotate at different speeds, actually a 6:4 ratio, so they mesh as they rotate. The clearance volume between the two screws decreases along their length to perform the compression. The Lysholm screw compressor is quite compact and provides a pulse-less discharge. However, it does require close-tolerance machining and assembly, since positive sealing is not possible. Both actively lubricated and dry-running designs have been used, the latter in automotive applications.

G-Laders

The G-lader mechanical supercharger was developed in the 1980s by Volkswagen as an economical competitor to the highly popular turbo-chargers (Fig. 11). The design was originally patented by Frenchman L. Creux in 1905. The design gets its name from the G-shaped spiral blower element that is moved eccentrically within another similar but fixed spiral. The blower spiral is rocked by another eccentric control shaft in such a manner that inlet and outlet ports are uncovered at the appropriate time as the volume of space between the spirals decreases. There is a duplicate chamber, operating out of phase to give a smoother as well as a higher volume of air charge.

Centrifugal Superchargers

The centrifugal supercharger, a kinetic turbomachine, uses a centrifugal compressor like that used by the turbocharger, except it is mechanically driven. Therefore, many of the features and characteristics covered in detail

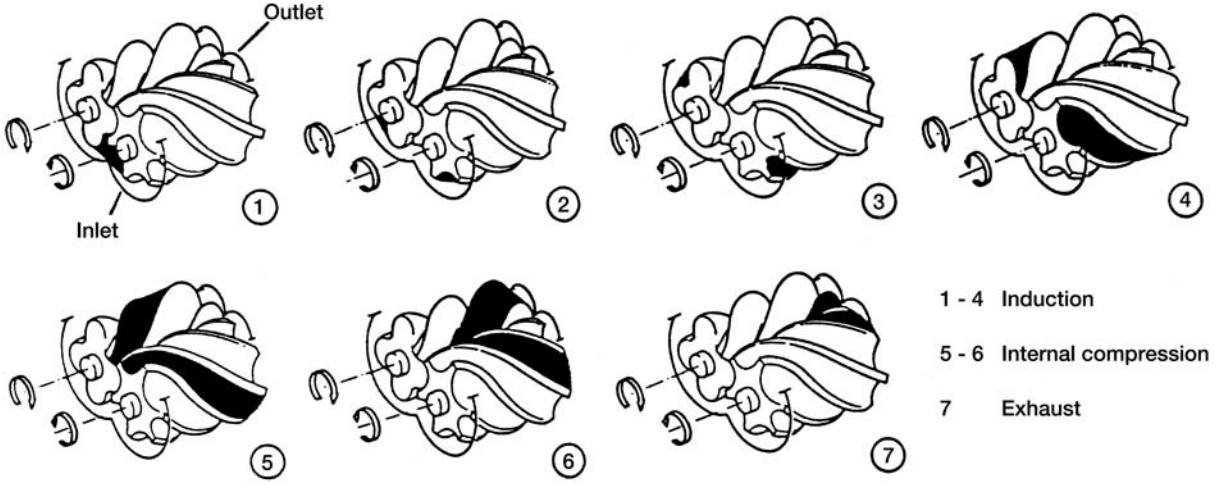

Figure 10 The Lysholm screw compressor uses two screw-type rotors with a different number of helices and turning at different speeds. Because of these differences, the volume of air trapped between the screws is decreased along their length to perform the compression. (Courtesy Fleming Thermodynamics, Ltd.)

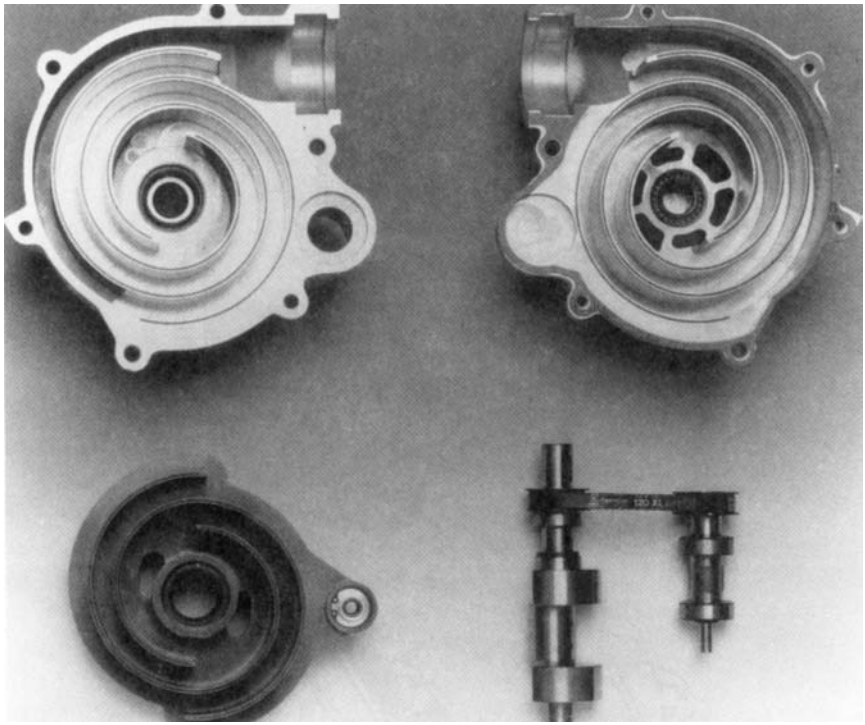

Figure 11a Key components of the G-lader supercharger. At the top are the two halves of the housing with the fixed G-shaped spiral chambers. In the lower left is the G-shaped rotating element that mates with the spiral in the housing. The shaft element that provides the oscillating motion is shown in the right corner. (Courtesy Volkswagen AG.)

in the next section on turbochargers apply to the mechanically driven compressor as well.

While a single-stage radial-flow compressor can provide a high pressure ratio, very high rotational speeds are required if the compressor is to be kept to a reasonable size. Unlike positive-displacement-type compressors, kinetic devices do not displace the same volume of air during each revolution. Therefore, in a centrifugal compressor, output pressure is proportional to the square of the rotational speed. Compressor speeds of up to 25,000 rpm may be needed before any noticeable positive boost pressure above atmospheric pressure is achieved. Since the input speed to the

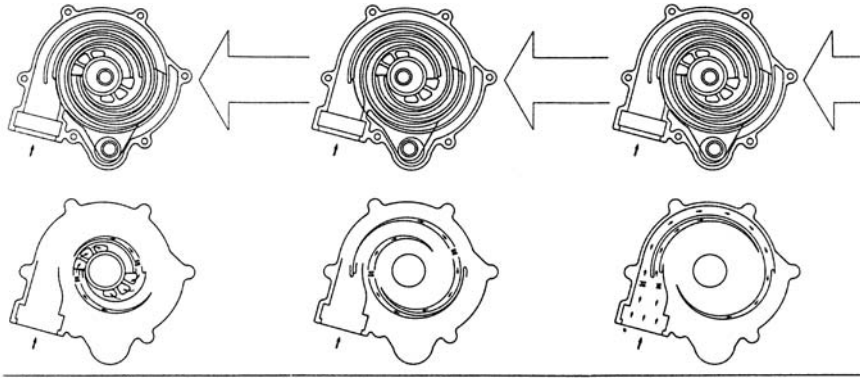

Figure 11b Principle of operation of the G-lader supercharger. Air brought in through the inlet port is compressed by the oscillation of the fixed and movable G-spirals before it exits the centrally outlet port at higher pressure. (Courtesy Volkswagen AG.)

supercharger is that of the engine crankshaft, roughly between 2,000 to 6,000 rpm, a high-ratio step-up in speed is required to reach maximum compressor speeds of up to 100,000 rpm or higher, as well as providing boost at low engine speeds.

The air volume required by a reciprocating engine is proportional to the speed of the engine. Thus there must be a matching of a proportional requirement with a squared air supply, which can become a problem. The usual solution to the matching challenge is to use a variable-speed drive. For instance, the venerable and still popular Paxton supercharger uses a gearless, planetary ball drive to provide smooth speed multiplication. The ZF-TURMAT centrifugal supercharger uses a combination of a variable-speed belt drive drive and 1:15 ratio planetary step-up gearing. In addition, the ZF-TURMAT can be turned off and on via an electromagnetic friction clutch on the input side of the supercharger.

Centrifugal superchargers are a popular alternative to turbochargers because they too are very compact relative to the volume of air handled. They also are relatively inexpensive to manufacture, are easy to install, and require minimum space in the engine compartment. The installation of a centrifugal supercharger does not require modification of the exhaust system like a turbocharger. However, the belt drive system used to drive the alternator, water pump, air conditioner compressor, and power steering pump may require revision (Fig. 12).

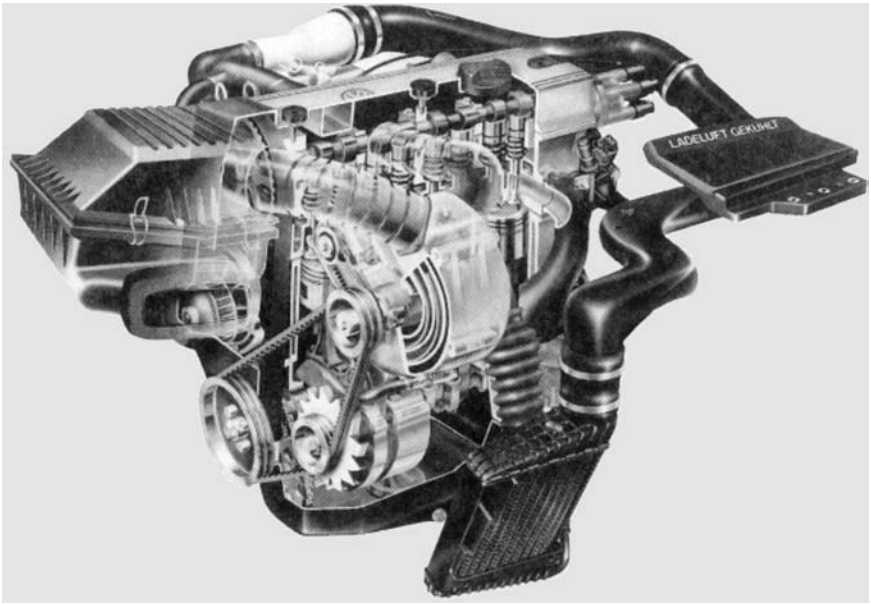

Figure 11c G-Lader supercharger is driven by the engine's crankshaft via a toothed belt drive. Air is taken in at the top of the supercharger. The compressed air leaving the central port passes through the air-to-air intercooler in the lower center of the picture. (Courtesy Volkswagen AG.)

Because the centrifugal supercharger runs cooler than an exhaust-driven turbocharger, an intercooler may not be needed. Also, heat shields and other thermal protection provisions associated with the installation of a turbocharger are not required. Most important, the centrifugal compressor provides virtually a near-instant boost without turbo lag. Finally, unlike many positive-displacement superchargers, the centrifugal supercharger is immune to backfire problems.

Maximum Compression Ratios

The boost pressure resulting from supercharging or turbocharging effectively increases the pressure in the cylinders. This has the same effect as increasing the compression ratio. There is a maximum compression ratio for spark ignition engines because excessive combustion chamber pressure can lead to denotation and potential engine damage (Fig. 13). This problem

Figure 12a Installation of a centrifugal supercharger requires some revision of the belt drive system so it can be driven off the crankshaft pulley. (Courtesy Paxton Superchargers.)

can be alleviated by using a fuel with a higher octane rating or by decreasing the effective compression ratio. The latter can be done by using a thicker head gasket or a decompression plate. More satisfactory solutions include removing metal from cylinder head to increase the volume of the combustion chamber, or better yet replacing pistons with ones that result in a lower compression ratio. Water injection into the cylinder can also help.

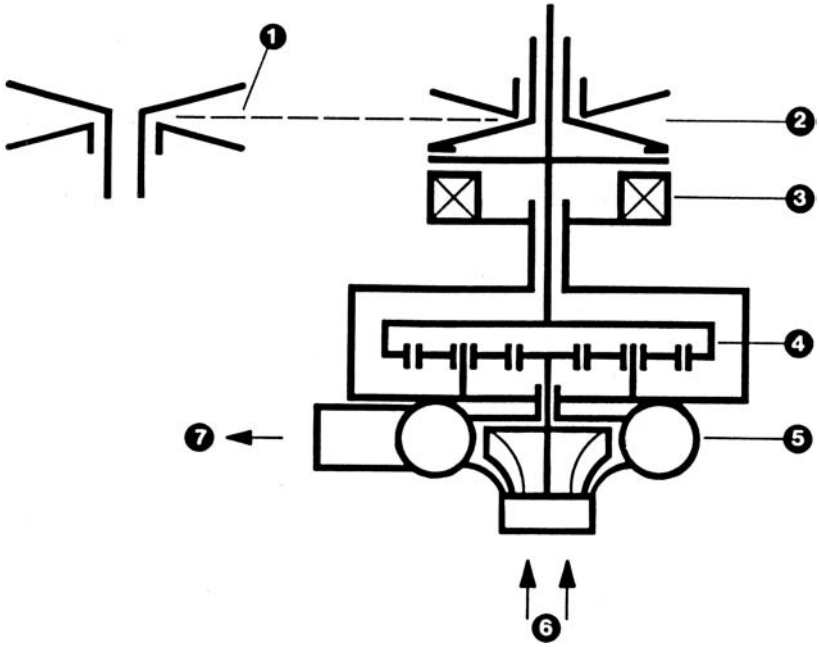

Figure 12b Schematic of centrifugal supercharger installation: 1, primary pulley for V-belt drive on engine crankshaft; 2, secondary pulley on turbocharger; 3, electromagnetic clutch; 4, planetary step-up gears; 5, centrifugal compressor; 6, air inlet; 7, air discharge. (Courtesy Zahnradfabrik Friedrichshafen AG.)

TURBOCHARGERS

Although there are several significantly different types of mechanical superchargers, exhaust-driven turbochargers used in automotive applications use the same basic design layout with differences in component design.

Turbochargers consist of a centrifugal compressor with radial outflow through either a vaneless or vaned diffuser housing (Fig. 14). The diffuser housing usually has a tapered constant-velocity volute collector that leads to a diffusing outlet duct that routes the higher-pressure air to the engine cylinders. The turbocharger turbine uses a centripetal radial-inflow exhaust-gas turbine, surrounded by a vaneless or vaned turbine housing connected to the exhaust manifold. The compressor and turbine wheels are mounted on a

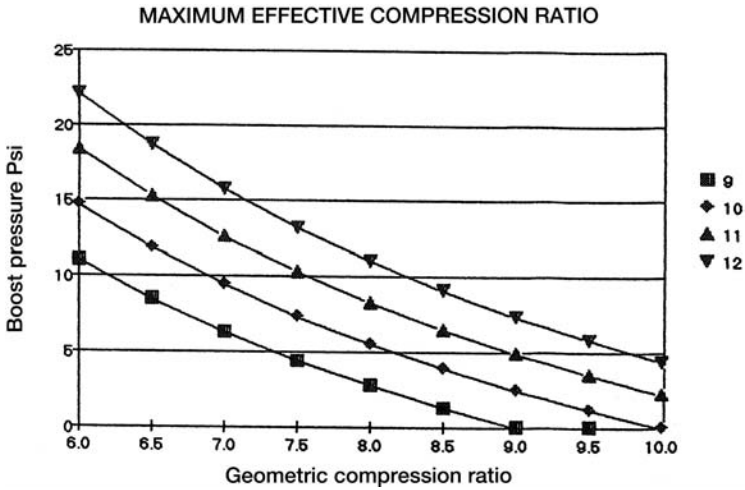

Figure 13 The geometric compression ratio is the ratio for a normally aspirated engine. The four maximum effective compression ratios—9, 10, 11, and 12 shown here—are the values where denotation could occur. This ratio depends heavily on the octane ratio of the fuel used.

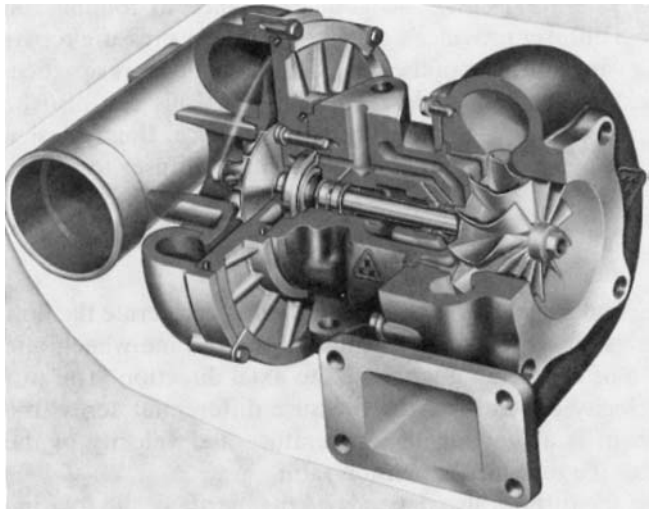

Figure 14a Example of a turbocharger for a spark ignition engine. (Courtesy Kuhnle, Kopp & Kausch AG.)

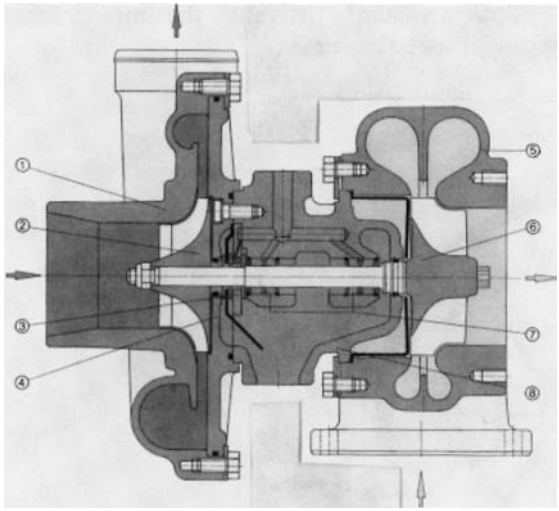

Figure 14b Components of the typical turbocharger: 1, compressor housing; 2, compressor wheel; 3, thrust bearing; 4, compressor backplate; 5, turbine housing; 6, turbine wheel; 7, bearings; 8, bearing housing. (Courtesy Kuhnle, Kopp & Kausch AG.)

common shaft and rotate at the same radial velocity. The shaft runs on bearings and usually uses thrust rings and has oil seals at both ends. Because of the high speeds involved, the unit requires very precise balancing.

In a radial-flow turbocharger, the gas flow nearest the hub will be parallel with the rotation axis and the flow will be at right angles to the hub at the perimeter of the compressor or turbine wheel. For the compressor, inlet air flows parallel to the hub and exits at right angles to the hub. For the turbine, the exhaust gases enter the turbine at the outer perimeter at right angles and are turned so they exist parallel to the hub. Some turbochargers use a mixed-flow design where flow at the wheel perimeter is less than at right angles to the hub axis, so that it is a combination of axial and centrifugal flow, that is, ''mixed.''

In axial-flow turbomachines, the direction of flow of the working gases remains essentially parallel to the axis of rotation. While used in very large engine applications, they are rarely, if ever, used in automobiles or trucks. Therefore, axial-flow turbochargers are not discussed further.

Compressor Design

The compressor impeller spins at very high speeds so that centrifugal forces accelerate the air to very high velocities so they attain a high level of kinetic energy. This high kinetic energy is then converted to an increase in static pressure in the diffuser section, which has a gradually increasing cross-sectional area. As pressure increases, the air velocity is significantly reduced. A collector or volute then collects the air flow around the perimeter of the diffuser and delivers it to the exit duct, where it flows to the engine cylinders.

There are several compressor designs in use. The simplest uses straight blades, which are easy and inexpensive to manufacture. However, straight blades result in relatively low compressor efficiencies because the shock waves are produced at the blade tips. Shock loss can be reduced by using curved inducer blades. Here the angle of curvature at the leading edge is chosen so it has exactly the same angle as the air entering the compressor. Finally, backward-curved inducer blades can be used. Here the blades are curved backward from the direction of rotation. For a given pressure rise, backward-curved blading requires a higher tip speed but the exiting velocity is lower. This means a greater percentage of the overall pressure rise takes place within the impeller and less occurs in the diffuser. Curved blades are more difficult to produce and are subjected to greater bending stress at the blade roots. Currently, backward-curved blades offer the highest peak compressor efficiency. Shrouded impellers have been used because they reduce air-flow recirculation within the blade, leading to maximum efficiency. They are now rarely used because they are difficult to manufacture, tend to be weaker, and are subject to dirt accumulation.

Early compressor diffusers used a series of divergent nozzles to convert kinetic energy to pressure rise via volume expansion. Nozzles have been replaced in current turbochargers by a ring of angled vanes that provide the required divergent passages. Vaned diffusers are usually used with compressor impellers with radial blades. The simplest, and now the most popular, design uses a vaneless diffuser usually with parallel walls. The volume of space between the walls increases with increasing radial distance from the impeller tip. The vaneless diffuser allows a broad operating range, low manufacturing cost, and good resistance to fouling and erosion. The vaneless diffuser provides a significantly lower-pressure recovery compared with a vaned diffuser of the same diameter and works particularly well with backward-curved blades. The diffuser walls can also be designed with a nonlinear area increase with radial distance. In any design it is important to ensure smooth internal surfaces in the diffuser to reduce frictional losses.

Turbine Design

The turbine housing and wheel together are designed to accelerate the flow of exhaust gases, transfer their energy to rotating the turbine wheel, and change the direction of flow from a tangential to axial direction. The turbine's rotational velocity depends on the pressure differential across the turbine, which in turn is a function of the temperature and velocity of the exhaust gas as well as the turbine's expansion ratio.

The velocity of the turbine also depends on the inertia of the rotating parts, namely, the turbine and compressor wheel, and the A/R ratio of the turbine housing. The A/R ratio is the area of the turbine inlet measured at its narrowest point, or throat, divided by the distance from this point to the turbine's rotational axis (Fig. 15). A large A/R ratio means the exhaust gases impinge on the turbine wheel at a shallow angle, resulting in a relatively low rotational speed. With a smaller A/R ratio, the impingement angle is increased so the rotational speed increases.

If the turbine housing entry has a circular cross section, calculation of the A/R ratio is quite straightforward. Otherwise the A/R ratio can be calculated using both conservation of mass and angular momentum principles. The latter results in the requirement that turbine housing volute provide a free vortex flow field at the tip of the turbine wheel, meaning the tangential velocity must vary from its magnitude at the inlet throat of the housing to the velocity needed to match the turbine wheel tip speed. The calculations assume two-dimensional flow and neglects both friction and

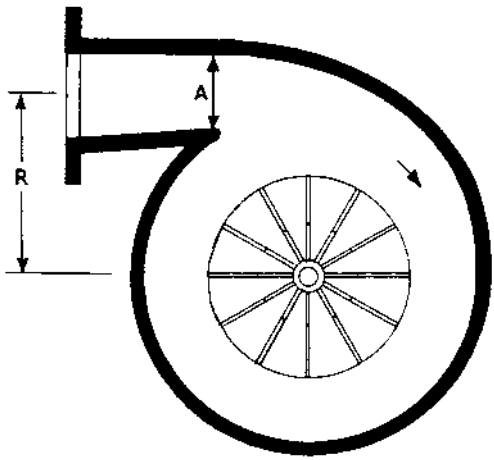

Figure 15 Definition of A/R ratio parameters (circular cross section).

compressibility effects. Referring to Fig. 16:

$$A/R = Q/K$$

Where

Q = flow rate of exhaust gases = AV_t.
A = cross-sectional area of the volute at the tongue.
V = tangential velocity component at the tongue.
$K = 2\pi R_w^2 N_w$.
R_w = wheel tip radius.
N_w = wheel tip velocity.

Finally, R_{DC} is defined as the dynamic center and determines the location that divides the area of the scroll into two areas, each supplying half the flow volume:

$$R_{DC} = A/(A/R)$$

Normally, the turbine freely turns at least 25,000 rpm under cruise conditions. Then when the throttle is opened wider, the carburetor or fuel injection system supplies more fuel, which is combusted, producing more exhaust gases. This additional thermal energy accelerates the turbine and compressor wheels so the compressor supplies more pressurized air to the combustion chambers. The rate of acceleration of the wheels depends on the moment of inertia of the rotating components, the A/R ratio of the turbine housing, and the amount of thermal energy available in the exhaust gases. Turbo, turbine, or throttle lag is the time delay while the turbocharger's rotating parts accelerate in response to increased gas flow that results from increased throttle opening. This lag results in a delay of full power delivery. The lag time depends on the amount of engine load and speed as well as the

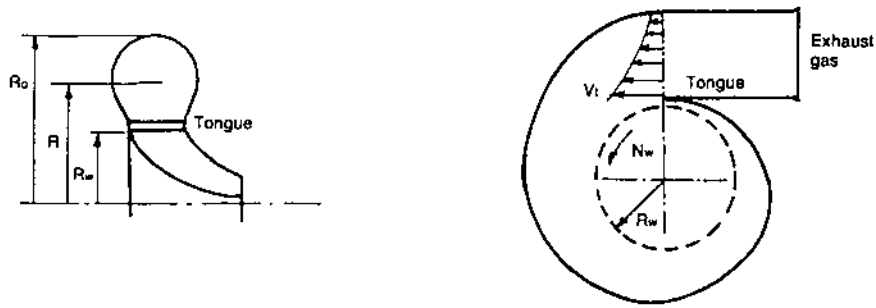

Figure 16 Definition of A/R ratio parameters (general configuration).

inertia of the wheel assembly. Minimum lag results with small-diameter turbine wheels that have a minimum of mass located near the wheel's perimeter.

In order to increase the response of small turbochargers, multiple entry passages, usually two, are sometimes used. The multiple entry design improves the low-speed turbine response by taking advantage of the natural exhaust gas pulse energy created when the exhaust valves open.

The earliest turbochargers used radial blades in the gas turbine, which led to rather larger turbine wheel diameters that were also heavy and had high inertia. Both installation-size constraints and performance response dictate small, lightweight turbines with low intertia. Turbine design has tended toward achieving more axial flow in the turbine.

A turbine with nozzles is the equivalent of the vaned diffuser in a compressor. Its main purpose is to add a swirling motion to the exhaust gases before they enter the turbine wheel. While the gas velocity increases as the gases pass through the nozzle vanes, in practice with small cross-sectional turbine inlet ports and those with multiple entry ports, the inlet velocities are already very high so only a small amount of further acceleration takes place within the nozzle vanes. Actually it is possible to dispense with the nozzle vanes entirely. Then the turbine housing has to be shaped so it produces the required initial swirling motion. Like vaneless compressors, nozzleless turbines are now very common because they are less expensive to manufacture and are very reliable while still providing acceptable efficiencies.

One desirable option is the variable-nozzle turbine such as the VNT (Variable Nozzle Turbocharger) developed by Chrysler for its four-cylinder engines (Fig. 17). Here the nozzle vanes pivot to vary the area between vanes, which changes the power output characteristics of the turbine. In the VNT, 12 aerodynamic vanes pivot individually on a nozzle ring. The vanes are moved by the unison ring to adjust the flow of exhaust gases to the turbine wheel in response to control inputs from the system computer. At idle or while cruising when turbo boost is not needed, the vanes are held at the 40–50% open position, resulting in minimum exhaust restriction. When the throttle is opened, the vanes are momentarily positioned to restrict flow to increase exhaust gas velocity to rapidly accelerate the turbine to increase boost at low rpm for greater transient low-speed torque and better response. As engine and power speed increase, the exhaust flow increases and the vanes are reopened to obtain higher flow for maximum boost and power.

The disadvantages of variable nozzles include their greater complexity, and thus added expense, and need to provide linkages or other techniques to move the nozzles. The latter is complicated because power servos are needed

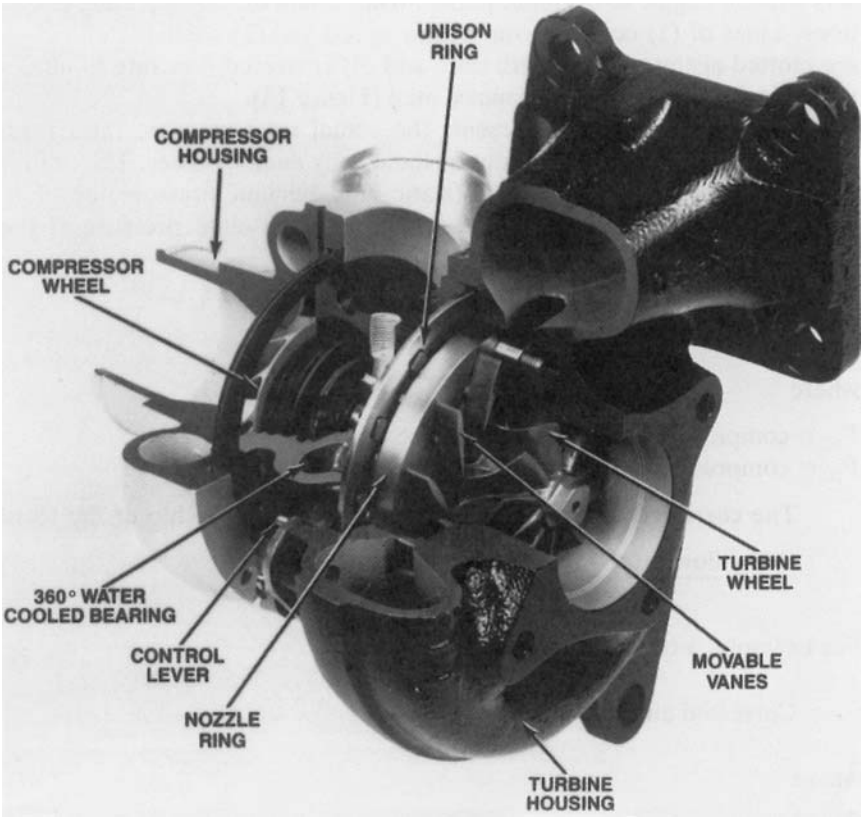

Figure 17 Variable nozzle turbocharger. (Courtesy Chrysler Corporation.)

to move vanes under high gas pressure forces, and mechanical parts must operate reliably in a very-high-temperature environment without lubrication.

Compressor Performance Maps

Compressor performance maps are used to describe the performance of particular centrifugal compressors. They are also used to match compressors with an engine to optimize performance under actual operating conditions. Lines of (1) constant compressor speed and (2) adiabatic efficiency are plotted against (3) pressure ratio and (4) corrected flow rate to obtain the typical compressor performance map (Fig. 18).

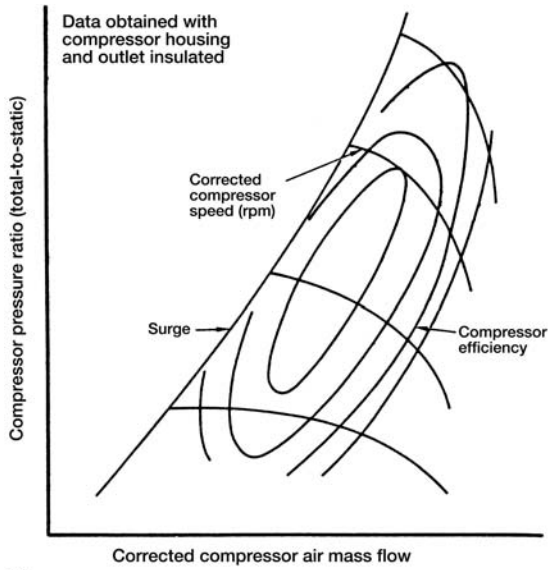

(a)

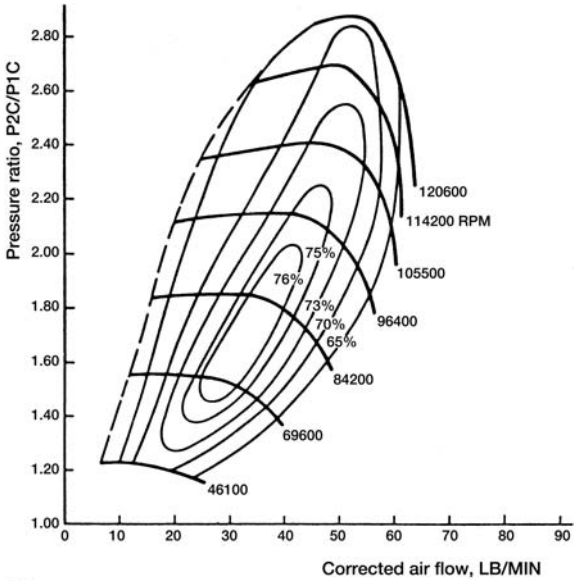

(b)

Figure 18 (a) Turbocharger compressor map, (b) typical compressor map. (Courtesy Turbonetics, Inc.)

The pressure ratio represents the actual total pressure ratio from compressor inlet to outlet without including any ducting losses. The ratio is determined by dividing the total (static plus dynamic pressure) absolute pressure at the compressor outlet by the total absolute pressure at the compressor inlet:

$$\text{pressure ratio} = \frac{P_{2C}}{P_{1C}}$$

Where

P_{1C} = compressor inlet air total pressure (in. Hg abs.).
P_{2C} = compressor discharge air total passage (in. Hg abs.).

The corrected air flow is corrected using a relationship of the form

$$\frac{(\text{mass flow rate}) \times (\text{absolute temperature})^{1/2}}{(\text{pressure})}$$

For example, a typical correction is

$$\text{corrected air flow} = \frac{W_a (T_{1C}/545)^{1/2}}{P_{1C/28.4}}$$

Where

T_{1C} = compressor inlet air total temperature (degrees R).
W_a = compressor discharge air flow (lb/min).

Likewise, the compressor speed is corrected using a a correction of the form

$$\frac{(\text{compressor speed})}{(\text{temperature})^{1/2}}$$

A typical correction is

$$\text{corrected compressor speed} = \frac{N}{(T_{1C}/545)^{1/2}}$$

where N is the compressor speed (rpm).

The basis for the adiabatic compression efficiency is an adiabatic compression in which the pressure increases without any thermal loss or gain. However, the temperature increases with increased pressure. This ideal temperature is compared with the actual higher temperature obtained in practice due to energy losses to determine the adiabatic efficiency.

Theoretically this efficiency is:

$$\text{compressor efficiency} = \frac{\text{isentropic enthalpy rise across compressor stage through compressor pressure ratio}}{\text{actual enthalpy rise across compressor stage}}$$

or

$$\text{compressor adiabatic efficiency} = \frac{T_{1C}\,Y}{T_{2C} - T_{1C}}$$

Where

T_{2C} = compressor outlet air total temperature (degrees R).
$Y = (P_{2C}/P_{1C})^{0.283} - 1$.

There are three main areas on the centrifugal compressor map. The central area is the stable operating zone. The surge line in the low flow rate area at the left of Fig. 18(a) defines an area of pressure and flow rate where compressor operation is unstable. Surging occurs when the mass flow rate through the compressor is reduced while maintaining a constant pressure ratio until a point is reached where local flow reversal occurs in the boundary layers. If the flow rate is further reduced, complete reversal occurs. This will relieve the adverse pressure gradient until a new flow regime is established at a lower pressure ratio. The flow rate will again build up to the initial condition, and this flow instability will continue at a fixed frequency and in some cases can become quite violent.

The compressor map shows a tradeoff in compressor design. The narrower the operating range of the compressor, the sharper the surge. However, the broader the range, the lower the peak efficiency.

Turbine Performance Map

The performance map for the turbine shows the lines of constant corrected speed, corrected exhaust gas flow, and overall turbine efficiency plotted against turbine pressure ratio (Fig. 19). The total-to-static pressure ratio is used here since the actual exit conditions cannot be predicted for a particular installation.

$$\text{pressure ratio (expansion ratio)} = \frac{P_{1T}}{P_{2T}}$$

Where

P_{1T} = inlet gas total absolute pressure (in. Hg).

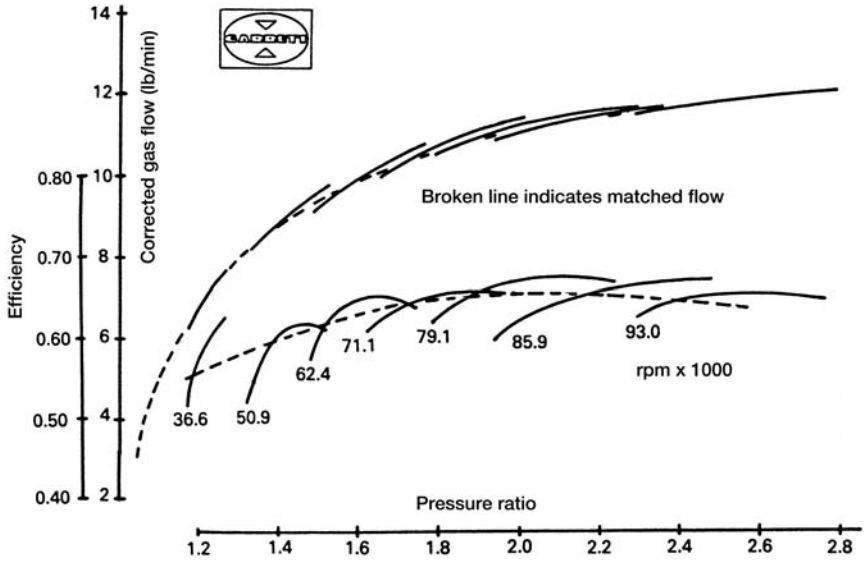

Figure 19 Typical turbine performance map. Because the gas flow versus pressure ratio is hardly different at different turbine speeds, it can be quite accurately approximated by a single curve. (Courtesy Allied Signal/Garrett Turbocharger Division.)

P_{2T} = outlet gas static absolute pressure (in. Hg).

The turbine gas flow is

$$\text{corrected gas flow} = \frac{W_g (T_{1T})^{1/2}}{P_{1T}}$$

Where

T_{1T} = turbine inlet gas total pressure (degrees R).
W_g = turbine gas flow (lb/min).

The corrected turbine speed is

$$\text{corrected turbine speed} = \frac{N}{(T_{1T})^{1/2}}$$

where N is the turbine speed (rpm).

The overall turbine efficiency includes both the turbine efficiency and the mechanical efficiency, which includes bearing losses.

$$\text{combined efficiency} = \frac{\text{actual enthalpy rise across compressor}}{\text{isentropic enthalpy drop through turbine expansion ratio}}$$

Altitude Effects

The turbine and compressor speed depends on the pressure differential between the turbine inlet and outlet. The greater this pressure differential between the exhaust manifold and atmospheric pressure, the higher the turbine and compressor speed. Since the manifold pressure remains relatively constant, as atmospheric pressure decreases, such as when climbing in altitude, the increase in speed will cause the compressor to increase boost pressure. Thus a turbocharger is largely self-compensating with respect to altitude.

Boost Control

It is necessary to limit the maximum boost pressure provided by a turbocharger. For example, the typical turbocharger used on conventional automobiles and light trucks is designed to provide a maximum boost pressure of 5–10 psi. By comparison, turbochargers for motorsports competition (road racing, hill climbing, rallying, oval track, etc.) use boost pressure up to 25 psi, while short-duration events like drag racing and tractor pulling can tolerate boost pressures in the 20–75 psi range.

There are three reasons for controlling boost pressure in turbocharged systems. First, excessive boost pressures can lead to preignition and denotation in the combustion chamber, leading to severe engine damage. Second, turbocharger speeds have to be limited to prevent self-destruction. Finally, speeds have to be controlled so that the turbocharger can be matched to the engine to obtain the desired performance characteristics over the wide operating range found in automotive applications.

The earliest boost controls consisted of fixed restrictions in the inlet or exhaust ducting, or even both. Incidentally, even the air filter or carburetor choke can provide a measure of boost control. Fixed restrictions provide progressive control that varies as the square of the exhaust flow. For example, when the restriction limits the maximum boost pressure, there is also a corresponding restriction at lower rpm, resulting in less efficient engine performance and poorer throttle response.

Currently, the most common method of controlling turbocharger boost is through the use of a wastegate. An externally mounted wastegate is

mounted on or near the exhaust manifold or turbine housing. The wastegate provides a flow path through which exhaust gases can bypass the turbine, going directly to the discharge exhaust pipe. A common form of wastegate uses a poppet valve connected to a diaphragm (Fig. 20). The chamber in front of the diaphragm is connected by a pressure feed line that senses boost pressure downstream of the compressor housing in the intake manifold. When the boost pressure exceeds a threshold value, the pressure on the diaphragm begans to overcome the pressure exerted by the spring on the otherside of the diaphragm, thus compressing the spring and opening the poppet valve. This lets an increasing percentage of the exhaust gas travel to the turbine exhaust pipe without passing through the turbine, halting the acceleration of the turbine and the subsequent increase in boost pressure. The amount of boost pressure is determined by the strength of the spring, sometimes referred to as the cracking pressure. Springs can be changed to vary boost pressure. Some more expensive wastegates have the capability to

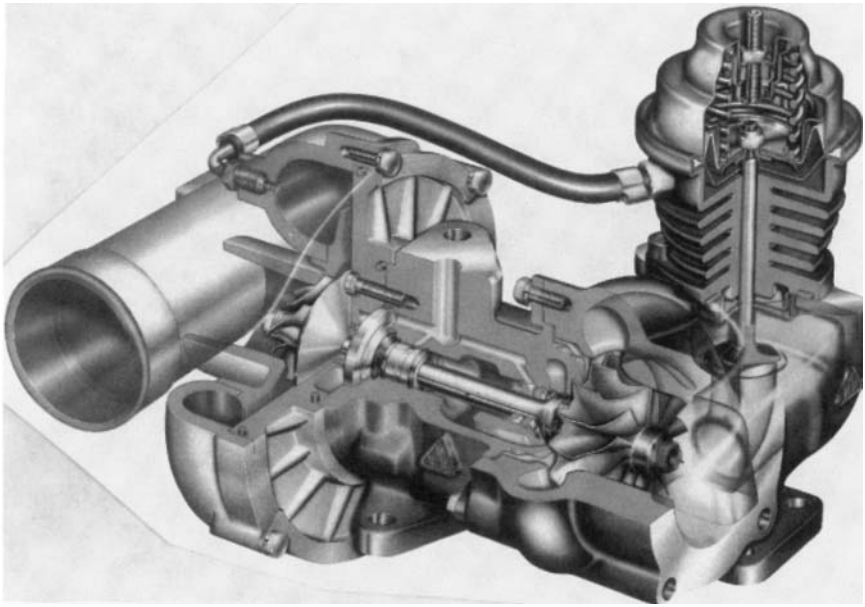

Figure 20 Turbocharger fitted with an integral boost pressure control valve. Boost pressure sensed in the discharge outlet from the compressor is transmitted via the tubing to the diaphragm side of the control valve. When boost pressure exceeds the spring force, the poppet valve is opened so a portion of the exhaust gas bypasses the turbine. (Courtesy Kuhnle, Kopp & Kausch AG.)

adjust the spring force to vary the boost pressure that will open the valve. Using a wastegate reduces overall fuel consumption efficiency because as the title implies, energy is "wasted" when exhaust gases bypass the turbine.

There are several alternate wastegate designs. For example, a swinging arm-type valve can be used (Fig. 21). In smaller engine applications, the wastegate is integrated into the turbine housing, thus eliminating the need for external high-temperature exhaust-line joints that can lead to problems.

The other class of boost control devices involves a variable-geometry turbine that effectively changes the A/R ratio and thus the turbine wheel speed and in turn the boost pressure. The simplest of these devices uses a turbine housing scroll with twin inlet passages, one of which can be closed

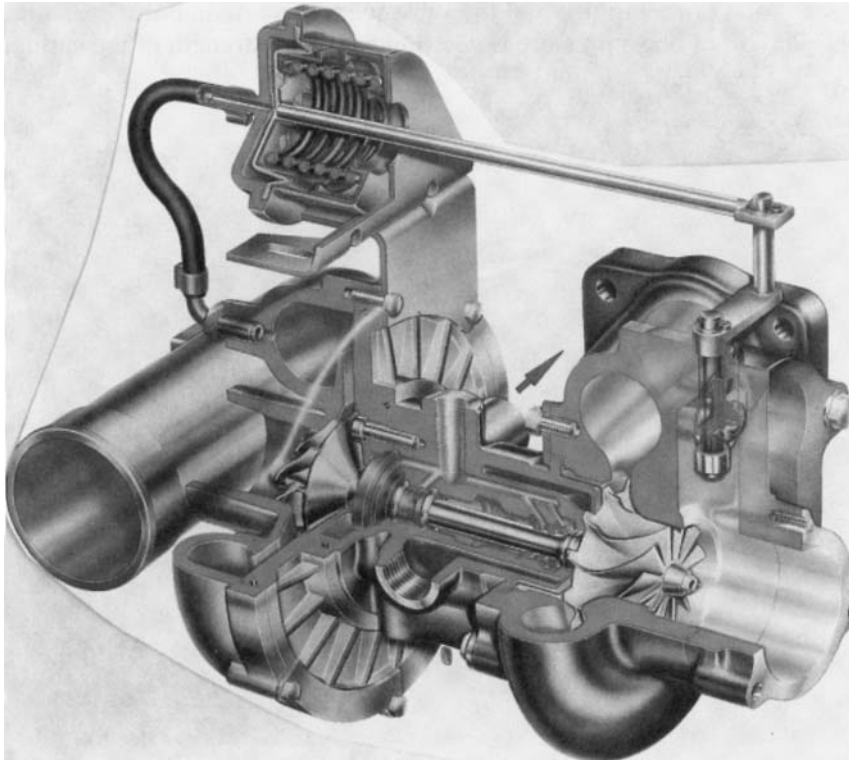

Figure 21 Turbocharger fitted with swinging arm-type valve. Boost pressure sensed in the discharge outlet from the compressor is transmitted via the tubing to the diaphragm side of the control valve. When boost pressure exceeds the spring force, the shaft opens the swing valve so a portion of the exhaust gas bypasses the turbine.

off by a selector valve. This design has only two modes of operation, exhaust gas flow with one or both passages open, and therefore only two A/R ratios are available. Disadvantages of this approach include reduced turbine efficiency caused by wake loss and additional surface friction, plus high-temperature stresses on the thin dividing wall. An alternate version of this concept uses a horizontally sliding gate that closes off part of the turbine housing volute at low speeds.

One more flexible variable-nozzle boost control concept uses a single movable vane placed at the turbine inlet (Fig. 22). This device changes the A/R ratio by changing the effective throat area over a relatively large range. The design is potentially quite reliable because of the limited number of moving parts and offers a relatively large operating range. There is a reduction in efficiency because of gas leakage through the side gap between the vane and housing, wake loss, and a nonuniform velocity distribution.

A more complex variable-geometry design uses multiple nozzle vanes located on the perimeter of the turbine housing. (The VNT design previously mentioned is one example.) The individual vanes are linked together so they mechanically move in unison. Changing the passage area between the vanes is used to control the turbine speed. While more complex, more costly to manufacture, and somewhat less reliable, the design provides excellent efficiency and a very wide operating range. A larger turbine

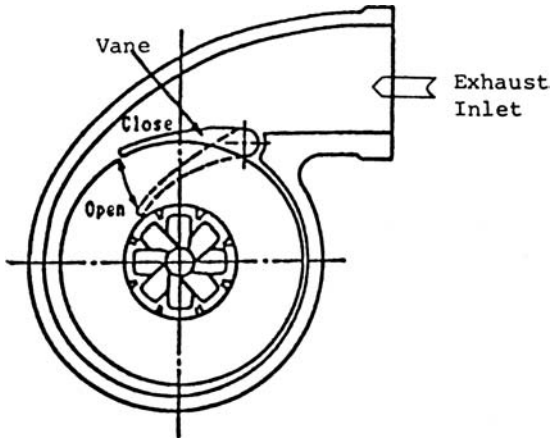

Figure 22a Single vane used to control exhaust gas velocity supplied to turbine wheel is a simple means of controlling boost pressure. (Courtesy Mitsubishi Heavy Industries America, Inc.)

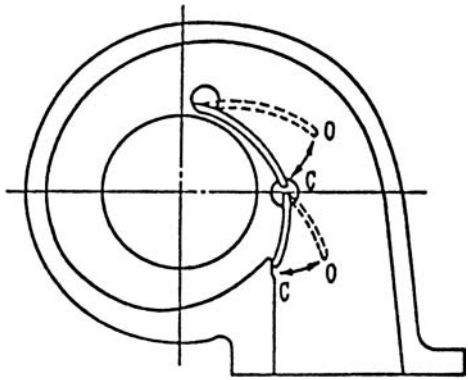

Figure 22b Two vanes are used to provide a form of variable inlet turbine. (Courtesy Mitsubishi Heavy Industries America, Inc.)

housing is also needed to house the vanes, and the substantial exhaust gas forces on the vanes require a heavy-duty servo system to move them. While variable-geometry designs provide boost control, they are often used with wastegates in order to match the requirements for boost control over the speed ranges found in passenger-car applications.

Bearing Design

There are several possible designs for bearing location. Early turbocharger designs often used a straddle design where bearings were located at the end of the common shaft for the turbine and compressor wheels. The design allows sufficient space for sealing and is conducive to water cooling of the bearings. An alternative, older design uses a single overhung layout where bearings are only located on one side, usually on the cooler compressor side. The large bending moment resulting from the cantilever design leads to significant bending stresses on the shaft.

Most current automotive turbochargers use a double overhung layout where bearings are located between the two wheels. The design results in a low-cost, lightweight, compact configuration. Bearing sealing and temperature differential problems are quite solvable. Most of these small-size turbochargers use sleeve-type bearings that are both cooled and lubricated by oil from the engine lubrication system.

Intercoolers

As the compressor increases boost pressure and charge density, the temperature of the air also increases. This increase in temperature results in an increase in air volume, thus decreasing the charge density a bit. However, a bigger problem is that higher air temperatures can cause excessive thermal stress on engine componentry and produce conditions that can lead to denotation and preignition. The solution now often used is the installation of an intercooler.

The temperature increase in the compressor (Fig. 23) can be estimated by the relationship

$$T_2 = T_1(P_2/P_1)^{0.286}$$

Where

T_1 = absolute temperature of air entering compressor.
T_2 = absolute temperature of air leaving compressor.
P_1 = absolute pressure on inlet side of compressor.
P_2 = absolute pressure on outlet side of compressor.

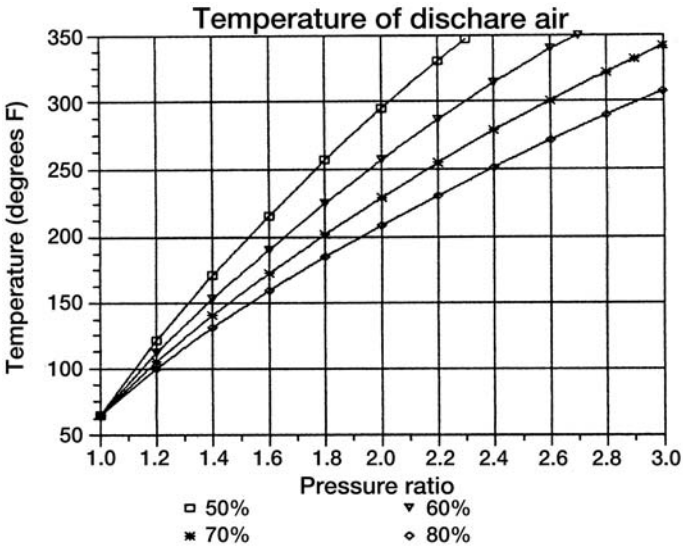

Figure 23 Increase in air discharge temperature as a function of boost pressure ratio for various turbocharger efficiencies.

However, the temperature has to be modified by the adiabatic efficiency of the compressor. Therefore, the actual temperature increase is

$$\Delta T = \frac{(T_2 - T_1)}{n_{ab}}$$

where n_{ab} is the compressor's adiabatic efficiency.

Intercooling, aftercooling, and charge air cooling are all terms used to describe the method of cooling the air inlet charge by installing a heat exchanger in the inlet manifolding between the compressor discharge and the engine. The intercooler is used to cool the charge air to increase the density of the charge and therefore its mass flow into the engine. The greater mass flow of air allows a greater quantity of fuel/air mixture converted to power. Intercooling also reduces the thermal loading on engine parts like valves and pistons. Reducing charge air temperature also reduces the problem of preignition and denotation in spark ignition engines.

Intercooler heat exchangers are usually of the air-to-charge-air or water-to-air type. Unlike a radiator, the core through which air flows should offer as little restriction as possible, and at the same time it must present the maximum surface area with cooling medium. There are several cooler configurations for automotive applications. Most common systems use an air-to-air heat exchanger located in front of the main radiator, or alternately at any convenient location at the front of the vehicle where it can take best advantage of the airstream. Since turbocharging is used normally when the vehicle is moving, the ram-air effect should be sufficient, eliminating the need for a fan. Plastic or rubber ducting can be used to bring air from the compressor and deliver it to the engine after being cooled by passing through the intercooler.

In more rarely used air-to-water intercooler designs, the cooling water can be simply normal engine coolant that is circulated through the intercooler. More complex air-to-water designs use a separate cooling circuit. Besides the intercooler for cooling the air charge, there are another water-to-air radiator to reject this heat and a pump to circulate the coolant.

Intercooling does result in some disadvantages. When air flows through the heat exchanger, there is a pressure drop offsetting some of the density increase resulting from cooling. Also, space must be provided in the engine compartment for the heat exchanger and associated plumbing. Excessive cooling can lead to condensation in the inlet manifold. Finally, intercoolers add to the expense of the vehicle.

TURBOCHARGING DIESEL ENGINES

Turbochargers are widely used on compression ignition (diesel) engines in both automobiles and trucks. Although operating on the same principles, there are some differences compared to turbocharging a spark ignition (gasoline) engine. Automotive diesel engines can be supercharged, but the practice is rare in production applications. The performance improvements gained by turbocharging a diesel engine are so dramatic that today most automobile and light-truck diesels are turbocharged, as are virtually all heavy-duty, over-the-road truck engines.

In the diesel engine, only air is drawn into the cylinder. The air is compressed, increasing its temperature above the point needed to ignite the separately injected fuel. Combustion occurs relatively slowly as the fuel mixes with the high-temperature air. The power output is controlled by varying the amount of fuel injected. Unlike a spark ignition engine where the air/fuel mixture ratio is nearly constant at or very near the stoichiometric value, in a diesel engine it is only necessary to have sufficient air to assure complete combustion of the fuel injected. Excess air is always acceptable, and indeed desirable, in a diesel engine. The power output of a diesel engine is dependent on the amount of fuel combusted, and the engine's maximum power output at any speed is determined by the amount of air available to burn the fuel efficiently. Insufficient intake air for a given load condition will result in a rapid decrease in efficiency. The maximum air mass flow for a normally aspirated diesel engine is limited by engine cylinder displacement. To increase power output, either the engine speed or displacement has to be increased.

A turbocharger can substantially increase air mass flow and density. When additional fuel is added to the increased air mass, the resultant power increase is limited basically only by the mechanical and thermal capabilities of the engine. A turbocharger for an automotive diesel should allow engine operation over a relatively wide speed range for the desired flexibility needed for highway use. The turbocharger should provide boost from as low an engine speed as possible, for example, 1,200 rpm, without causing excessive back pressure in the exhaust manifold. High back pressures can be reflected back to the engine, causing high cylinder pressures and an increase in fuel consumption.

The excess air supplied by a turbocharger can reduce combustion chamber and exhaust temperatures, providing higher power output without the need for very high-temperature-resistant, and thus more expensive, materials. Also, the fuel control system can be simplified when the engine is supplied with excess air. Excess air can scavenge the cylinders at the end of the exhaust stroke to remove the last traces of exhaust gases. Finally, excess

air can reduce carbon monoxide and unburned hydrocarbon emissions. The lower combustion temperatures that result with excess air lead to a reduction in nitrogen oxide emissions.

Operating a diesel's engine's turbocharger continuously to provide boost under full-load conditions can result in excessive thermal loads on the engine, leading to reduced engine life. An intercooler can be used to reduce this damaging heat load. Unlike intercoolers on turbocharged or supercharged gasoline engines, which are added to extract more power by eliminating denotation, the diesel's intercooler only helps reduce operating temperatures for durability and reliability.

The absence of denotation problems allows much higher boost pressures even when diesels normally operate at much higher compression ratios. Currently, maximum pressures are limited by the mechanical strength of engine components as well as by the maximum injection pressures that can be provided by an efficient and reliable fuel pump that must work against the high combustion chamber pressures.

One technique that can be used to extract more energy from a turbocharger is to make use of the high-pressure, high-velocity exhaust pulses generated each time an exhaust valve opens. This peak pulse pressure can be many times higher than the average exhaust manifold pressure. To utilize these pressure pulses, the exhaust system must be designed so that the high-pressure peaks are not canceled out by the low pressures, as is the case when only a single-inlet turbine housing is used. The pulse pressure technique requires from each cylinder head a separate exhaust connection that delivers the exhaust gases to a special divided inlet housing.

Turbocompounding

Additional energy can be extracted from the exhaust by using turbocompounding. While this can be done in several ways, one successful turbocompound diesel truck engine is marketed by Saab Scandia (Fig. 24). Here a second power turbine is located downstream from a conventional turbocharger in the gas stream to extract the additional thermal energy before it is exhausted out the exhaust pipe. This second turbine is mechanically connected to the crankshaft to utilize the power extracted. Because this second turbine can run at speeds of up to 65,000 rpm, gearing can present serious engineering challenges, since high turbine speeds must be matched to relatively low crankshaft speeds with the flexibility to match the instantaneous engine rpm needed for changing road speeds. Therefore, Saab Scandia uses a fluid coupling to provide both the speed and flexibility required. According to Saab Scandia, turbocompounding

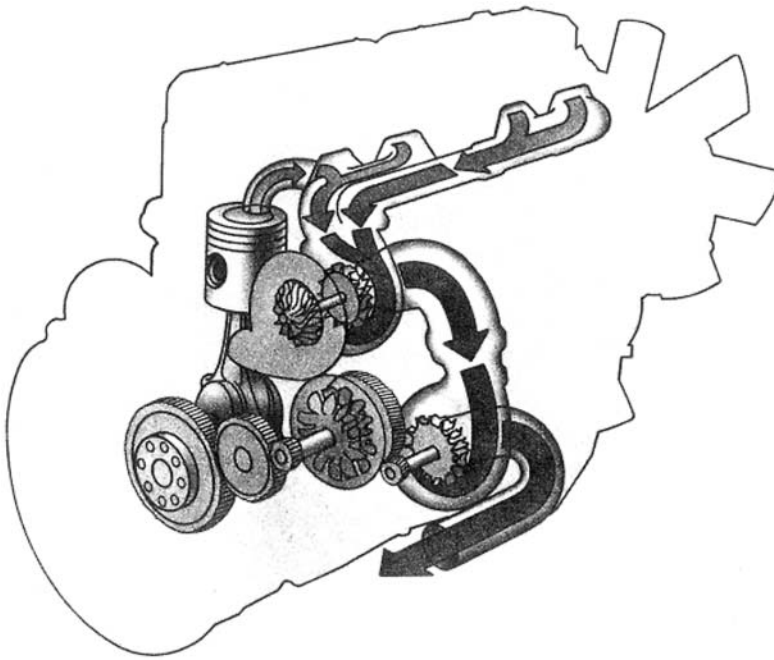

Figure 24 Turbocompound diesel engine. The exhaust gas first drives a normal turbocharger. Then the exhaust gases drive a second turbine, which is attached to a gear drive so it can rotate a fluid coupling. The fluid coupling transfers energy to the crankshaft through additional gearing. (Courtesy Saab Scandia.)

increases the efficiency of its already intercooled turbocharged diesel truck engine by an additional 2%, for a total efficiency of 46%.

Pressure-Wave Supercharging

Pressure-wave supercharging can combine the advantages of both a mechanically driven supercharger and an exhaust-driven turbocharger. Burghard conceived a pressure-wave machine in 1910, Brown Boveri of Switzerland began working on the concept as early as 1909, and by 1940/1942 Claude Seippel had invented the COMPREX design (Fig. 25). The COMPREX supercharger is a simple machine; the underlying thermodynamic processes involved are very complex. Therefore, while much development work was done and prototypes built, a successful pressure-wave supercharger for an automotive diesel engine had to wait for the

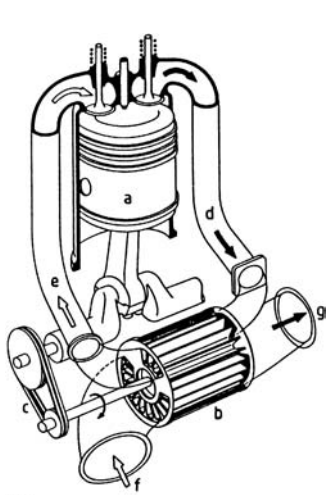

(a)

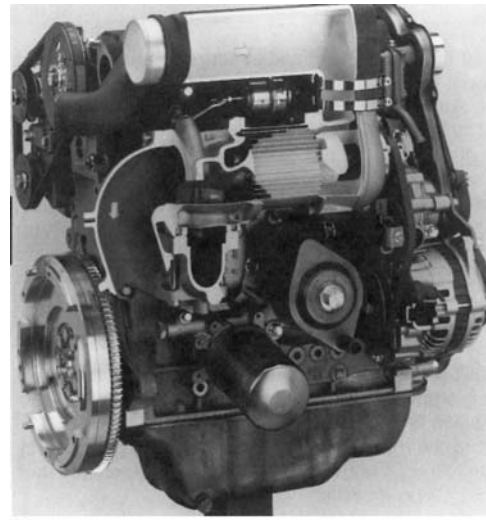

(b)

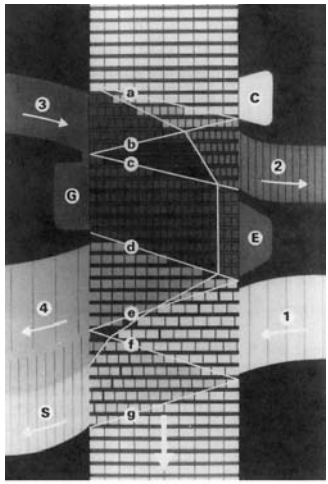

(c)

Figure 25 (a) Schematic of the COMPREX supercharger: a, combustion chamber; b, rotor with cells; c, belt drive to drive rotor; d, exhaust gas from combustion chamber; e, high-pressure air charge; f, ambient air pressure; g, exhaust gases delivered to exhaust system. (b) COMPREX installed on a small diesel engine. (c) Pressure-wave (a–g) process in the COMPREX supercharger: 1, suction air entering COMPREX rotor for next cycle; 2, compressed air charge to engine; 3, exhaust gases from engine acting on air charge; 4, exhaust gases discharged; S, Scavenging air; C, compression pocket; E, expansion pocket; G, gas pocket. (Courtesy COMPREX AG.)

advent of high-speed digital computers to perform the huge number of computations and complex modeling needed to optimize the design. COMPREX AG, a Swiss company, now builds the pressure-wave superchargers that have been on Japanese Mazda 626 Capella models since 1987.

Like a supercharger, the COMPREX is driven off the engine crankshaft at a speed proportional to engine speed. Typically, the COMPREX runs at about 30,000 rpm using a toothed belt drive system that increases the speed five to eight times. Unlike a normal supercharger, no energy is transferred from the crankshaft except to overcome friction and inertia. Only about 1% of the engine output is required to overcome friction and windage losses.

The COMPREX consists of an engine-driven rotor located between two end casings connected to intake and outlet ducts for the charge air and exhaust gases, respectively. The inlet and outlet ports for air are located at one end and the exhaust inlet and outlet ports are at the other end. The rotor has axial vanes that form passages called cells, which are opened at both ends. Ambient air enters the cells through the inlet port and is carried around by the vanes until it is opposite the exhaust gas port. At this point, the high-pressure exhaust gases rush into the chamber to compress the air charge, which is pushed toward the opposite end and forced through the high-pressure air duct in the air casing to the engine. During this process the exhaust gases are reflected back out of the exhaust port and the inlet charge is directed to the engine. The pressure wave created by the exit of the exhaust gas through the exhaust port allows a fresh inlet charge to enter the inlet port, and so the cycles continues. There is no contact between the casings and rotor faces, but the gap is very small to minimize leakage.

Before the exhaust gas penetrates the rotor to the extent that it would flow out with the compressed air, the rotor cells are brought into connection with the outlet duct in the gas casing by the rotation of the rotor. The exhaust gas flows out of the rotor, expands, and the suction produced by the powerful flow is able to draw in fresh air through the low-pressure duct of the air casing and into the rotor cells.

Because of the very short period that the inlet charge and exhaust gas are in contact without any physical barrier, there is no contamination of air by the hot exhaust and heat is not transferred. The concept takes advantage of the physical fact that when two gases with different pressures are brought into direct contact, equalization of pressure occurs faster than the mixing of the gases. This is especially true if the gases are guided in narrow channels or cells.

Since energy transfer is accomplished by pressure waves traveling at the speed of sound, the COMPREX provides instantaneous response. With

this plus the fact that the exhaust gas does not have to drive any machinery, there is essentially no turbo lag.

FURTHER READING

A. Allard, *Turbocharging and Supercharging*, Patrick Stephens, Wellingborough, England (1986).

C. A. Amann, "Air-Injection Supercharging—A Page from History," SAE Paper No. 920843 (1992).

M. C. Brands, J. R. Werner, J. L. Hoehne, and S. Kramer, "Vehicle Testing of the Cummins Turbocompound Diesel Engine," SAE Paper No. 810073 (1981).

P. Conlan and R. Fleck, "An Experimental Investigation to Optimise the Performance of Supercharged, Two-Stroke Engine," SAE Paper No. 930980 (1993).

T. Curless, *Turbochargers: Theory, Installation, Maintenance, and Repair*, Motorbooks International, Osceola, WS (1985).

J. Davis and G. Wallace, *B&M Superchargers Technical Manual*, B&M Automotive Products, Chatworth, CA.

A. Hishikawa, Y. Okazaki, and P. Busch, "Developments of Variable Turbine for Small Turbochargers," SAE Paper No. 880120 (1988).

M. Hitomi, Y. Yuzuriha, and K. Tanaka, "The Characteristics of Pressure Wave Supercharged Small Diesel Engine," SAE Paper No. 89054 (1989).

J. D. Humphries, *Automotive Supercharging and Turbocharging*, Motorbooks International, Osceola, WS. (1992).

T. Kollbruner, "Comprex (tm) Supercharging for Passenger Diesel Car Engine," SAE Paper No. 800884 (1980).

J. H. Lewis, G. Burrel, and F. W. Ball, "The Oldsmobile F-85 Jetfire Turbo Rocket Engine," Society of Automotive Engineers, June (1962).

R. R. Lundstrom and J. M. Gall, "A Comparison of Transient Vehicle Performance Using a Fixed Geometry, Wastegate Turbocharger and a Variable Geometry Turbocharger," SAE Paper No. 860104, February (1986).

H. MacInnes, *Turbochargers*, H P Books, Tucson, AZ. (1984).

A. Mayer, E. Pauli, and J. Gygax, "Comprex (tm) Supercharging and Emissions Reduction in Vehicular Diesel Engines," SAE Paper No. 900881 (1990).

H. Mezger, "Turbocharging Engines for Racing and Passenger Cars," SAE Paper No. 780718, August (1978).

Y. Okazaki, E. Matsuo, N. Matsudaira, and P. Busch, "Development of a Variable Area Radial Turbine for Small Turbocharger," ASME Paper No. 88-GT-102 (1988).

M. L. Schorr, *Turbocharging: The Complete Guide*, Motorbooks International, Osceola, WS (1979).

G. Schruf and A. Mayer, "Fuel Economy for Diesel Cars by Supercharging," SAE Paper No. 810343 (1981).

"Turbocharger Nomenclature and Terminology," SAE J922, SAE Recommended Practice, July (1988).
G. Zehnder and A. Mayer, "Supercharging with Comprex (tm) to Improve the Transient Behavior of Passenger Car Diesel Engines," SAE Paper No. 860450 (1986).

14

Tesla Turbomachinery

Warren Rice
Arizona State University, Tempe, Arizona, U.S.A.

Tesla-type turbomachinery is distinguished by the fact that the rotor is composed of flat parallel corotating disks, spaced along a shaft. A throughflow of fluid between the disks results in momentum exchange between the fluid and the disks and hence shaft torque and power. Tesla designed, built, and tested such machines but was not able to achieve industrial applications of them.

In the subsequent years, many investigations have been carried out to determine the performance and efficiency of this type of turbomachinery. These have been both analytical and experimental. Most of the investigations have had a certain limited application as the objective, with regard to size and speed as well as the nature of the operating fluid. However, some of the investigations have tried to establish the generalized performance of Tesla-type turbomachines. In general, it has been found that the efficiency of the rotor can be very high, at least equal to that achieved by conventional rotors. But it has proved very difficult to achieve efficient nozzles in the case of turbines. For pumps and compressors, efficient diffusion after the rotor has proven difficult to achieve. As a result, only modest machine efficiencies have been demonstrated. Principally for these reasons the Tesla-type

turbomachinery has had little utilization. There is, however, a widespread belief that it will find applications in the future, at least in situations in which conventional turbomachinery is not adequate. This includes the use with very viscous fluids, fluids containing abrasive particles, and two-phase fluids.

The flow in the rotor may be either laminar or turbulent, with certain advantages and disadvantages in each of the regimes. It is necessary to carefully distinguish which type of flow is considered in reports by the various investigators.

Herein, the principles of the Tesla-type turbomachinery are reviewed and the problems with nozzles and diffusers (which limit the machine efficiency) are discussed. The analytical methods that have been found useful in modeling and calculating the flow in the rotor are reviewed, and the experimental results obtained by some investigators are described. An extensive list of references is presented, and summaries are made of the main results and conclusions that have been reported.

Nomenclature

h	Spacing between disks
r	General radial coordinate in space between disks
r_i	Inner radius of disk
r_o	Outer radius of disk
Q	Volume flow rate between two disks
$\bar{u}$	Average (disk-to-disk) radical component of velocity
$\bar{v}_o$	Average (disk-to-disk) tangential component of velocity, at outer radius of disk
ν	Kinematic viscosity of fluid
μ	Viscosity of fluid
Ω	Angular velocity of pair of disks
ρ	Density of fluid

INTRODUCTION

Tesla is most widely recognized for his outstanding contributions in the fields of generation, transmission, and utilization of electrical power. However, he was also the inventor of a unique type of turbomachinery that can be applied as liquid pumps, liquid or vapor or gas turbines, and gas compressors [1]. The Tesla turbine was widely discussed in the semitechnical

press at the time of the invention [2–7]. The Tesla turbomachinery is distinguished by the fact that the rotor is composed of flat parallel corotating disks spaced along a shaft. A throughflow of fluid between the disks results in momentum exchange between the fluid and the disks and hence shaft torque and power. Tesla designed, built, and tested such machines but was not able to achieve significant industrial application of them. Figures 1 and 2 are schematic diagrams of a Tesla-type pump and turbine.

As a turbine, the multiple-disk rotor is contained in a housing provided with nozzles to supply high-speed fluid approximately tangential to the rotor. The fluid flows spirally inward and finally exhausts from the rotor through holes or slots in the disks near the shaft. As a pump or compressor, fluid enters the rotor through holes near the shaft, flows spirally outward, and exhausts from the rotor into a diffuser such as a volute scroll. Shaft power is delivered by the turbine, and shaft power must be supplied to the pump or compressor. The performance and efficiency of the rotor of such machines are dependent on the combination of shaft speed, disk inner and outer diameters, spacing between the disks and the fluid properties, and flow rate. The performance of the overall turbine is strongly dependent also on the efficiency of the nozzles and the nozzle–rotor interaction. The performance of the pump is also strongly dependent on the interaction of fluid leaving the rotor with that in the volute and on the efficiency of diffusion in the volute. In general, flow in the rotor may be laminar or turbulent or mixed.

There was little activity concerning the Tesla turbomachinery until a revival of interest began in the 1950s [8–17]. Research was widespread after that, particularly in the area of analytical modeling of the flow in the space between two disks in a rotor, and continues at present. References [18–79] are representative. Many attempts have been made to commercialize Tesla-

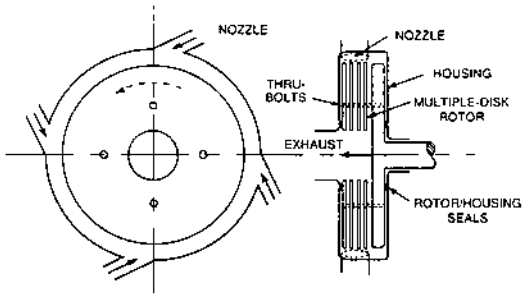

Figure 1 Schematic diagram of a Tesla-type turbine.

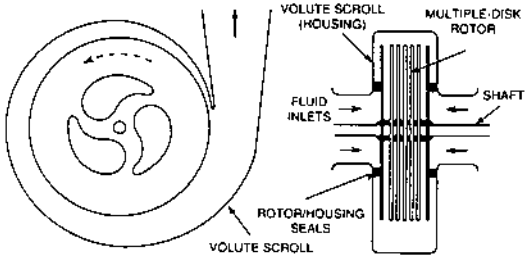

Figure 2 Schematic diagram of a Tesla-type pump.

type turbomachines, especially as pumps, but no widespread applications are apparent. While rotor efficiencies can be very high in this type of turbomachine, there are inherent losses in the fluid flows entering and exiting the rotor. As a turbine, the nozzles are necessarily long and inefficient. As a pump or compressor, the diffuser or volute must handle flow with a very small entering angle, which causes the volute to be very inefficient. For these and other reasons, actual Tesla turbomachines have efficiencies much less than might be expected from consideration of the flow in the rotor. There is little or no literature devoted to the flows that cause the main losses in Tesla-type turbomachinery. Tesla-type turbomachinery is variously referred to in the literature as multiple-disk or friction or shear force (or, nonsensically, boundary-layer) turbomachinery.

MULTIPLE-DISK ROTORS HAVING LAMINAR FLOW

A way of analytically modeling the flow in a multiple-disk rotor known as bulk-parameter analysis was used by early investigators [7, 9–11, 16, 17, 21, 24, 49]. It is usable for both laminar and turbulent flow. In this method of analysis, the frictional interaction between the fluid and the disks is represented in terms of an empirical fluid friction factor. This results in ordinary differential equations, which, together with simple boundary and entrance conditions, constitute a problem easily solved using computer-implemented stepwise calculations. The method is limited in usefulness by the inadequacy of the friction factor concept.

In the case of laminar flow, much better analytical modeling can be achieved. Partial differential equations can be established rather simply together with appropriate boundary and inlet conditions. Because the flow path is long compared with the disk spacing, order-of-magnitude arguments

can be made to simplify the equations somewhat and reduce them to pseudo-parabolic form. The problem can then be solved by any one of several available means.

Some investigators have used truncated series substitution methodology to make solutions [23, 25, 29, 32], but the method has accuracy limitations. A much more widely used method is to solve the problem using computer-implemented finite-difference methods; Refs. [19] and [33] are typical examples. Integral methods have also been used, mainly to shorten the computer execution time required for solution [38]. Most of the literature has considered the fluid to be incompressible, although some investigators have calculated laminar compressible flows [48, 53, 65, 71].

Wu [78], in 1986, made detailed comparisons of results from all of the available literature. It was found that when the results of investigations using similar solution means were compared there was close agreement, within accuracy limitations. It was also concluded that the finite-difference solutions all obtained good accuracy and produced essentially the same results, and such solutions are recommended to be used.

It is also clear from the literature that the calculated results for laminar flows between corotating disks are in excellent agreement with experimental results for such flows [35, 44]. While future efforts may lead to increased accuracy or shorter computer execution time, present published methodology and results are sufficient for use in the design of laminar-flow multiple-disk rotors for pumps, compressors, and turbines. Some generalized information for such rotors has been presented [45, 46].

The results of a solution of a flow consist of detailed knowledge of the distribution of the velocity and pressure throughout the flow between the disks. From this, the relationship between the mass flow rate and the pressure change from inlet to exit become known and allow determination of design facts such as the number of disks required for an application of interest. The solutions are parameterized using the following or equivalent parameters: for outward flows (pumps), Reynolds number $(\rho\Omega h^2/\mu)$, flow-rate number $(Q/2\pi r_i^2\Omega h)$, and radius ratio (r_o/r_i); for inward flows (turbines) the additional parameter $(\bar{v}_o/\Omega r_o)$ is required. The results can be arranged to provide values of dimensionless torque, dimensionless pressure, dimensionless power, rotor efficiency, etc.

With proper use of the analytical results, the rotor efficiency using laminar flow can be very high, even above 95%. However, in order to attain high rotor efficiency, the flow-rate number must be made small, which means high rotor efficiency is achieved at the expense of using a large number of disks and hence a physically large rotor. For each value of flow-rate number there is an optimum value of Reynolds number for maximum efficiency. With common fluids, the required disk spacing is dismayingly

small, causing laminar-flow rotors to tend to be large and heavy for a prescribed throughflow rate.

Extensive investigations have been made of Tesla-type liquid pumps using laminar-flow rotors [64]. It was found that overall pump efficiency was low even when rotor efficiency was high because of the losses occurring at the rotor entrance and exit mentioned earlier.

CRITERIA FOR THE OCCURRENCE OF LAMINAR AND OF TURBULENT FLOW IN MULTIPLE-DISK ROTORS

It is established that a wide range of types (or regimes) of flow can occur between corotating disks including wholly laminar flow, laminar flow with regions of recirculation, wholly turbulent flow, laminar flow proceeding through transition to turbulent flow, and turbulent flow proceeding through "reverse transition" or "relaminarization" to laminar flow. There is experimental evidence concerning these flows [26, 27, 31, 35, 42, 44], and the hydrodynamic stability of laminar flows between corotating disks has been investigated [31, 66]. Wu [78], considering all available experimental and analytical evidence, concluded that the viscogeometric number α proposed by Nendl [42, 55] most adequately characterizes the flow regime, where $\alpha = \bar{u}h^2/vr$. While the data of the various investigators are somewhat contradictory, a reliable guide appears to be that flow is laminar for $\alpha < 10$, in transition for $10 \leqslant \alpha < 20$, and turbulent for $\alpha \geqslant 20$. The various investigators introduce rather pragmatic and differing definitions of "laminar" and "turbulent," which further complicates the matter. It is desirable that it be explored further both experimentally and by additional hydrodynamic stability analysis.

MULTIPLE-DISK ROTORS HAVING TURBULENT FLOW

The bulk-parameter (friction factor) type of analysis of flow in a multiple-disk type of rotor was referenced in the foregoing discussion of laminar flows. It has been used extensively to calculate turbulent flows but with mostly unknown degrees of adequacy. The transition criteria presented are not applicable for bulk-parameter use, the hydraulic diameter concept is required, and the assumption must be made that pipe-flow frictional correlations are valid for flows between corotating disks. Nevertheless, such analyses have been the only analytical prediction method available until relatively recently, and methods now becoming available are not yet well established. Wu [78] gives an extended

comparison of the results of various bulk-parameter methods of analysis with several sources of experimental data for turbulent flows between corotating disks.

Momentum integral equation methods have been and continue to be used to calculate the subject turbulent flows [26, 34, 36]. In these methods, ordinary differential equations describing the flow are written based on assumed distribution forms for the velocity and on empirical expressions for the stresses in the flow. Some of these rely on experience and/or specialized experimental results and are found not to be universal. Within carefully noted bounds, however, these methods can be very successfully used by an experienced investigator and have yielded strong insights into and design information for the turbulent flows of interest.

In principle, the set of partial differential equations applicable for turbulent flow can be written, provided with appropriate boundary and entrance conditions, and then solved in some manner using computer implemented calculations. In practice, there are several aspects of the process that cannot be executed with confidence that the calculated results will agree with reality. Principal among these is that a model or mechanism describing the turbulent transport of linear momentum must be prescribed. Furthermore, the partial differential equations are much more complicated for turbulent than for laminar flow. In the entrance region, the equations must be solved in elliptical form before changing over to simplified pseudo-parabolic equations to continue the calculations.

Truman [73] carried out calculations for turbulent flow between corotating disks using eddy-viscosity/mixing-length turbulence (stress) modeling, and using a finite-difference method for solving the partial differential equations. Wu [78] used a slightly modified version of the computer-implemented calculations provided by Truman, to compare calculated results with experimental data for turbulent flow due to Bakke [26] and Köhler [34]. In general, agreement was good but with some qualifications and reservations discussed in detail by Wu [78]. It was noted that at high rotor angular speeds the calculations indicated recirculation in the turbulent flow that could not be detailed since the pseudo-parabolic equations are not applicable for recirculating flows.

Truman et al. [76] have also calculated similar flows using an anisotropic two-equation turbulence model. More analytical study and much more experimental investigation of the turbulent flow between corotating disks are needed to establish the most applicable methods for calculating the flows with confidence and for the results to be useful in the design of turbomachines. Wu [78] has outlined an experimental apparatus and procedure that might provide the next needed insights for progress in this area.

ACTUAL TESLA-TYPE TURBOMACHINERY

Many individuals and groups attempting to commercialize Tesla-type turbomachines have designed, constructed, and operated them. Pumps have received the most interest, but compressors and turbines have also been built and operated. While much useful test data have no doubt been recorded, very little has been published or otherwise made known because of a perceived need for keeping information proprietary. Thus, this large body of information is not available to most investigators.

Most Tesla-type turbines and pumps have been designed using intuition and simple calculations or empirical experience and "rules of thumb." This has almost always led to the use of large spaces between the disks corresponding to turbulent flow between the disks.

There is published information concerning actual Tesla-type pumps [17, 18, 20, 21, 28, 34, 37, 47, 49, 50, 54, 59, 64, 67]. All the information presented shows lower efficiency than was desired. In general, the pumps designed with little prior calculated rotor design information showed efficiencies below 40%. Adequate calculated rotor design information resulted in higher efficiency but still in the range of 40–60%. All things considered, it seems probable that Tesla-type pumps of reasonable size, operating with common fluids, will not exceed an efficiency of 65% at best, with careful attention to volute/rotor matching. Many Tesla-type pumps intended to be commercially competitive have not been provided with a volute or any other type of diffuser.

A number of Tesla-type turbines have been constructed for use with steam, gas, and water. Very few data have been published concerning them. There are references with published information concerning experimental turbines [2–6, 8–11, 13, 16, 24, 51, 63]. As with pumps, the turbine efficiencies have been low and the machine sizes large per unit of power delivered. All of the turbines reported probably operated with turbulent flow in the rotor.

Most recent pumps and turbines of the Tesla type have used rotors composed of disks with a central hole, rather than the spoke construction used by Tesla. The disks are carried on throughbolts extending from a thicker master disk fastened to the shaft; thus, the rotor is overhung. Although most machines have used thick disks, there seems to be little reason to do so since the disks have only small forces acting on them and are not required to be perfectly flat.

Many design questions remain unanswered at this time. Whether the disks should be rough or smooth, for best performance, is controversial, as is the question concerning appropriate rotor-to-housing seals. There are some ideas concerning ways to improve volute or nozzle performances that remain undemonstrated. An early idea of improving performance of rotors

by composing them of nested cones rather than flat disks has been shown to produce no performance advantages and to introduce structural handicaps [20, 79].

CONCLUSION

Tesla-type turbomachinery probably cannot prove competitive in an application in which more conventional machines have adequate efficiency and performance. Thus, it cannot be expected to displace conventional water pumps or conventional water turbines or gas turbines. Tesla-type turbomachinery should be considered in applications in which conventional machines are inadequate. This includes applications for small shaft power, or the use of very viscous fluid or non-Newtonian fluids. There is some reason to believe that multiple-disk turbomachines can operate with abrasive two-phase flow mixtures with less erosion of material from the rotor. For that reason, they should be further investigated for applications to produce power from geothermal steam and particle-laden industrial gas flows. There may also be unique applications possible using ceramic disks. There is considerable evidence that multiple-disk turbomachinery can be quieter in operation than is conventional machinery and that the noise produced is more nearly "white" noise without a prevailing sound signature. Multiple-disk pumps are well known to resist cavitation [20, 49]. It is the only type of turbomachinery that can be easily constructed in a relatively primitive machine shop.

ACKNOWLEDGMENT

This review was presented earlier, in Rice [80].

REFERENCES

1. V. Popović, R. Horvat, and N. Nikolić, "Nikola Tesla, 1856–1943, Lectures, Patents, Articles," Nikola Tesla Museum, Belgrade, Yugoslavia (1956).
2. "Tesla's New Method of and Apparatus for Fluid Propulsion," *Electrical Rev.*, Sept. 9: 515–517 (1911).
3. "The Tesla Turbine," *Electrical Rev.*, Sept. 30: 637 (1911).
4. "Bladeless Turbines," *Engineering*, *92*: 637 (1911).
5. "The Tesla Steam Turbine," *Eng. News*, *66*: 448–449 (1911).
6. "The Tesla Steam Turbine," *Sci. Am.*, Sept. 30: 296–297 (1911).

7. E. Merigeault, "Les Turbines a Frottements ou Turbines Tesla," *Rev. Mecan.*, Juin: 534–544 (1914).
8. R. K. Warner, "The Design, Construction, and Testing of a Tesla Turbine," M.S. Thesis, University of Maryland (1949).
9. H. B. Schroeder, "An Investigation of Viscosity Force in Air by Means of a Viscosity Turbine," BAE Thesis, Rensselaer Polytechnic Institute, January (1950).
10. J. H. Armstrong, "An Investigation of the Performance of a Modified Tesla Turbine," M.S. Thesis, Georgia Institute of Technology, June (1952).
11. R. C. North, "An Investigation of the Tesla Turbine," Ph.D. Dissertation, University of Maryland (1969).
12. T. V. Vannérous, "Rotierende Scheiben für Luftvorwärmer mit Gebläsewirkung," *Allg. Wärme-technik*, *6*: 257–262 (1955).
13. S. K. P. Young, "The Investigation and Analysis of the Tesla Turbine," M.S. Thesis, University of Illinois (1957).
14. E. M. Gol'din, "Hydrodynamic Flow Between Separator Plates," Izv. an SSSR., OTN, No. 7, pp. 80–88 (1957).
15. G. A. Tirskii, "Nonstationary Flow with Heat Transfer in a Viscous Incompressible Fluid Between Two Revolving Discs Accompanied by Fluid Influx," *Doklady Akad. Nauk., SSR*, *119*: 226–228 (1958).
16. E. L. Gruber, Jr., "An Investigation of a Turbine with a Multiple Disk Rotor," M.S. Thesis, Department of Mechanical Engineering, Arizona State University, May (1960).
17. F. J. Smith, "An Investigation of a Disc Type Pump," M.S. Thesis, Department of Engineering Science, Arizona State University, May (1960).
18. D. O. Chrismer, "An Investigation of a Disk Type Blower," M.S. Thesis, Department of Mechanical Engineering, University of Houston, August (1960).
19. M. C. Breiter and K. Pohlhausen, "Laminar Flow Between Two Parallel Rotating Disks," ARL 62–318, Aeronautical Research Laboratory, OSR, USAF, Wright-Patterson AFB, March (1962).
20. S. H. Hasinger and L. G. Kehrt, "Investigation of a Shear-Force Pump," *ASME Trans. J. Eng. Power*, *85*(3): 201–207 (1963).
21. W. Rice, "An Analytical and Experimental Investigation of Multiple Disk Pumps and Compressors," *ASME Trans. J. Eng. Power*, *85*: 191–198 (1963).
22. R. C. Perel'man and V. I. Polikovskii, "Theory of Disc-Type Pumps," *Izvestiya Acad. Sc. USSR OTH Energetika i Transport*, *1*: 101–112 (1963).
23. J.-L. Peube, "Sur l'Ecoulement Radial Permanent d'un Fluide Visqueux Incompressible Entre Deux Plans Paralléles Fixes," *J. Mecanique*, *II*: 377–395 (1963).
24. W. Rice, "An Analytical and Experimental Investigation of Multiple Disk Turbines," *ASME Trans. J. Eng. Power*, *87*: 29–36 (1965).
25. F. Kreith and J.-L. Peube, "Écoulement Entre Deux Disques Paralléles en Rotation," *C. R. Acad. Sci. Paris*, *260*: 5184–5187 (1965).

26. E. Bakke, "Theoretical and Experimental Investigation of the Flow Phenomena Between Two Co-Rotating Parallel Disks with Source Flow," Ph.D. Thesis, University of Colorado (1965).
27. F. Kreith, "Reverse Transition in Radial Source Flow Between Two Parallel Planes," *Phys. Fluids*, *8*: 1189–1190 (1965).
28. S. H. Hasinger, L. G. Kehrt, and O. T. Goksel, "Cavitation Tests with a High Efficiency Shear Force Pump," *ASME Proc.*, Symposium on Cavitation in Fluid Machinery, Chicago, Nov. 7–11, pp. 132–147 (1965).
29. J.-L. Peube and F. Kreith, "Écoulement Permanent d'un Fluide Visqueux Incompressible Entre Deux Disques Paralléles en Rotation," *J. Mecanique*, *5*(2): 261–286 (1966).
30. D. Nendl, "Eine theoretische Betrachtung der Reibungsturbo-maschinen von Nikola Tesla," Doktor-Ingenieurs Dissertation, Technischen Hochschule Aachen, July 12 (1966).
31. E. M. Gol'din, "Flow Stability Between Separator Plates," Izv. an SSSR, *Mekhanika Zhidkostei i Gasov*, *1*(2): 152–155 (1966).
32. L. Matsch and W. Rice, "An Asymptotic Solution for Laminar Flow of an Incompressible Fluid Between Rotating Disks," *ASME Trans. J. Appl. Mechanics*, *35*(1): 155–1559 (1968).
33. K. E. Boyd and W. Rice, "Laminar Inward Flow of an Incompressible Fluid Between Rotating Disks, with Full Peripheral Admission," *ASME Trans. J. Appl. Mechanics, 35*(2): 229–237 (1968).
34. M. Köhler, "Die Strömung durch das Spaltelement einer Reibungs-pumpe," Doktor-Ingenieurs Dissertation, University of Karlsruhe, July 9 (1969).
35. R. G. Adams and W. Rice, "Experimental Investigation of the Flow Between Corotating Disks," *ASME Trans. J. Appl. Mechanics*, *37*(3): 844–849 (1970).
36. M. Köhler, "Die Strömung durch das Spaltelement einer Reibungs-pumpe," *Strömungsmechanik und Strömungamaschinen*, *9*: 24–45 (1971).
37. M. Köhler, "Die Strömung swischen zwei parallelen rotierenden Scheiben," *Acta Mechan.*, *12*: 33–51 (1971).
38. B. E. Boyack and W. Rice, "Integral Method for Flow Between Corotating Disks," *ASME Trans. L. Basic Eng.*, *93*: 350–354 (1971).
39. V. I. Misiura and L. D. Dronov, "Comparison of the Experimental Characteristics of Disk-type and Rotodynamic Centrifugal Pumps," *Aviatsionnaia Tekhnika*, *15*(1): 146–149 (1972).
40. V. I. Misyura, "Laminar Flow of an Incompressible Liquid Between Two Rotating Discs," *Izv. Akad. Nauk SSSR, Mekhanika Zhid. Gaza*, *5*: 178–183 (1972).
41. D. Nendl, "Eine Theoretische Betrachtung der Tesla-Reibungs-pumpe," VDI-Forsch.-Heft 527, pp. 29–36 (n.d.).
42. D. Nendl, "Reibungsturbine," VDI-Berichte Nr. 193, pp. 287–293 (1973).
43. G. Dibeluis and D. Nendl, "Reibungsturbomaschinen," Nr. 2348, Lehrstuhl und Institut für Dampf-und Gasturbinen der Rhein.-Westf. Techn. Hochschule Aachen (1973).

44. L. L. Pater, E. Crowther, and W. Rice, "Flow Regime Definition for Flow Between Corotating Disks," *ASME Trans. J. Fluids Eng.*, *96*: 29–34 (1974).
45. M. E. Crawford and W. Rice, "Calculated Design Data for the Multiple-Disk Pump Using Incompressible Fluid," *ASME Trans. J. Eng. Power*, *96*: 274–282 (1974).
46. M. J. Lawn and W. Rice, "Calculated Design Data for the Multiple-Disk Turbine Using Incompressible Fluid," *ASME Trans. J. Fluids Eng.*, *96*: 252–258 (1974).
47. A. M. Grabovskii, "Use of Disc Pumps for Handling Viscous Liquids," *Izv. Vyssh. Ucheb Zaved, Stroi i Arkhit*, *2*: 117–121 (1974).
48. C. E. Basset, Jr., "An Integral Solution for Compressible Flow Through Disc Turbines," 10th Intersociety Energy Conversion and Engineering Conference, Newark, DE, Aug. 18–22 (1975).
49. U. M. Barske, "Investigations on the Pumping Effect of Rotating Discs," *Proc. 1975, Inst. Mech. Engineers*, *189*: 36/75.
50. S. Murata, M. Yutaka, and I. Yoshiyuki, "A Study on a Disk Friction Pump," *Bull. JSME*, *19*: 168–178 (1976).
51. R. Steidel and H. Weiss, "Performance Test of a Bladeless Turbine for Geothermal Applications," Lawrence Livermore Laboratory, Report No. UCID-17068, March 24 (1976).
52. W. Rice, D. F. Jankowski, and C. R. Truman, "Bulk-Parameter Analysis for Two-Phase Through-flow Between Parallel Corotating Disks," *Proceedings*, 1976 Heat Transfer and Fluid Mechanics Institute, University of California, Davis, June 21–23 (1976).
53. P. W. Garrison, D. W. Harvey, and I. Catton, "Laminar Compressible Flow Between Rotating Disks," *ASME J. Fluids Eng.*, September: 382–389 (1976).
54. S. Murata, M. Yutaka, and I. Yoshiyiki, et al., "A Study on Disk Friction Pump. Part 2, Experiments on Flow Through Corotating Disks and Pump Performance," *Bull. JSME*, *19*: 1160–1171 (1976).
55. D. Nendl, "Dreidimensionale laminare Instabilitäten bei ebenen Wänden," *Z. Ange w. Math. Mech.*, *56*: T211–213 (1976).
56. E. Bakke and F. Kreith, "Disk Pump Performance in Turbulent Flow," *ASME J. Fluids Eng.*, ASME Paper No. 77-WA/FE-26.
57. C. R. Truman, W. Rice, and D. F. Jankowski, "Laminar Throughflow of Varying-Quality Steam Between Corotating Disks," *ASME Trans. J. Fluids Eng., 100*: 194–200 (1978).
58. Von G. A. Euteneuer and M. Piesche, "Betriebsverhalten einer Reibungsturbine bei turbulentem Stromfeld und viskosem, inkompressiblem Medium im Spaltelement," *Forsch. Ing.-Wes.*, *44*: 79–84 (1978).
59. V. I. Misyura, "Determination of Hydraulic Losses in a Disc Pump," *Izv. VUZ., Aviat. Tekh.*, *22*: 39–43 (1979).
60. C. R. Truman, W. Rice, and D. F. Jankowski, "Laminar Throughflow of a Fluid Containing Particles Between Corotating Disks," *ASME Trans. J. Fluids Eng.*, *101*: 87–92 (1979).

61. M. Piesche, "Investigation of the Flow and Temperature Field of a Viscous Fluid in an Element of a Shear-Force Pump," 6th Conference on Fluid Machinery, Budapest, pp. 836–846 (1979).
62. K.-O. Felsch and M. Piesche, "Zum Betriebsverhalten einer Reibungsturbine und deren Einsatz als Wärmetauscher," *Strömungs-mech. Strömungs-maschin.*, *27*: 1–19 (1979).
63. A. B. Davydov and A. N. Sherstyuk, "Experimental Research on a Disc Microturbine," *Russ. Eng. J.*, *60*: 26–28 (1980).
64. J. H. Morris, "Performance of Multiple-Disk-Rotor Pumps with Varied Interdisk Spacings," David W. Taylor Naval Ship R and D Center, Bethesda, MD, U.S. Navy Report Number DTNSRDC-80/008, August (1980).
65. M. Piesche, "Berechnung der kompressiblen, laminaren Unter schallströmung in einer Tesla-Turbine," *Strömungsmech. Strömungsmachin.*, *28*: 25–31 (1980).
66. A. Gusev and F. H. Bark, "Stability of Rotation-Modified Plane Poiseuille Flow," *Phys. Fluids*, *23*: 2171–2177 (1980).
67. M. Piesche and U. Müller, "Uber den Wärmetransport im Spatelement einer Reibungspumpe," *Acta Mech.*, *35*: 173–186 (1980).
68. M. Ravindran and K. Arasu, "Some Performance Studies on a Multiple Disk Pump," *Proceedings* Tenth Natl. Conf. on Fluid Mechanics and Fluid Power, Jamshedpur, India, Dec. 27–29, Paper A3, pp. 43–49 (1981).
69. K. O. Felsch and M. Piesche, "Ein Beitrag zur Berechnung der Strömung in einer Tesla-Trubine bei temperaturabhängiger Zähigkeit des Fördermediums," *Ing. Arch.*, *50*: 121–129 (1981).
70. K. O. Felsch and M. Piesche, "Berechnung der Spaltströmung in einer Reibungspumpe bei temperatureabhängiger Viskosität zur Förderung hochviskoser Flüssigkeiten," *Acta Mech.*, *38*: 19–30 (1981).
71. M. Piesche and K. O. Felsch, "Kompressible Unterschall-strömungen in Reibungsverdichtern," *Acta Mech.*, *41*: 99–107 (1981).
72. M. Piesche, "Betriebseigen-schaften konventioneller laufradgit-ter radialer Baurt im Vergleich mit Spaltelementen von Reibungs-pumpen," *Strömungsmech. Strömungsmaschin.*, *31*: 1–21 (1982).
73. C. R. Truman, "Turbulent Source Flow Between Stationary and Rotating Disks," Ph.D. Dissertation, Department of Mechanical and Aerospace Engineering, Arizona State University, August (1983).
74. Z. Tadmor, P. S. Mehta, L. N. Valsamis, and J.-C. Yang, "Corotating Disk Pumps for Viscous Liquids," *Ind. Eng. Chem. Proc. Des. Dev.*, *24*: 311–320 (1985).
75. J. W. Chew, "Computation of Flow and Heat Transfer in Rotating Disc Systems," 2nd ASME-JSME Thermal Engineering Conference, Hawaii, March (1987).
76. C. R. Truman and S. A. Shirazi, "Prediction of Turbulent Source Flow Between Corotating Disks with an Anisotropic Two-Equation Turbulence Model," ASME International Gas Turbine Conference, Anaheim, CA, May 31–June 4 (1987).

77. A. K. Chattopadhyay, D. N. Roy, and G. Biswas, "Radial Flow of a Viscous Fluid Between Two Coaxially Rotating Discs," *Indian J. Technol.*, *29*: 221–227 (1991).
78. P.-S. Wu, "Evaluation of Analytical Models for Multiple-Disk Pump Rotor Calculation," M.S. Thesis, Department of Mechanical and Aerospace Engineering, Arizona State University, May (1986).
79. K. W. McAlister and W. Rice, "Laminar Through Flow of Newtonian Fluid Between Co-Axial Rotating Cones," *ASME Trans. J. Appl. Mech.*, *37*: 210–212 (1970).
80. W. Rice, "Tesla Turbomachinery," *Proceedings, IV International Tesla Symposium*, September 22–25, Serbian Academy of Sciences and Arts, Belgrade, Yugoslavia, pp. 117–125 (1991).

15

Hydraulic Turbines

V. Dakshina Murty
University of Portland, Portland, Oregon, U.S.A

The word *turbomachine* is derived from the Latin word *turbo*, which means whirl or something that spins. Such a term includes various types of machines involving pressure head, such as compressors, pumps, blowers, turbines, and so forth. The common feature of all these machines is that they all have a rotating shaft on which are mounted a number of vanes, which move because the working fluid comes into contact with them. Such contact produces a change of momentum, and this change in momentum for the working fluid results in motion of the vanes. A turbomachine can be defined as a device in which energy transfer occurs between a fluid in motion and a rotating shaft due to dynamic action, which results in changes in pressure and fluid momentum. These are different from positive-displacement machines such as a reciprocating piston cylinder, because in such machines the work input or output is primarily due to moving boundaries.

Turbomachines can be classified in several different ways. One method of classification is based on whether they are power-producing or power-absorbing. Examples include the Francis turbine, Kaplan turbine, and steam and gas turbines for the former and centrifugal pump, compressors, fans, and blowers for the latter. Another method of

classification is based on the direction of the flowing fluid in the runner. Based on this criterion, a turbomachine could be classified as an axial-flow, radial-flow, or mixed-flow machine. Examples of axial-flow machines are Kaplan turbines and axial-flow fans or blowers. A centrifugal pump and Francis turbine are examples of radial-flow machines. It should be noted that due to the complex flow passage of a turbomachine, there is no clear delineation between the types of machines in terms of direction of flow. Although the Kaplan turbine is classified as an axial-flow turbine, the fluid does have some radial velocity in it. The same comment applies to other machines, too. Thus, when one refers to an axial-flow machine, the implication is that the flow is predominantly in the axial direction. Yet another way of classifying turbomachines is based on the nature of the working fluid, whether it is compressible or incompressible. Examples of the former are various types of steam and gas turbines, compressors, and so forth, while all types of hydraulic turbines, pumps, low-speed blowers, and fans belong to the latter category.

This chapter deals with hydraulic turbines, their common features, their operating characteristics, design features, differences, and so forth. Before these aspects are discussed in detail, the underlying unifying features of turbomachines like dimensional analysis, performance characteristics, and Euler turbine equations must be studied. In the rest of the chapter the various nondimensional groups of hydraulic machines are derived followed by the Euler turbine equation derivation, and the performance of different hydraulic turbines is discussed in detail. It should be pointed out that among the pertinent features in the discussion of hydraulic turbines and their mechanical characteristics are cost estimates, availability and use of water resources, and selection of various units. These are not discussed in this chapter, and the reader is referred to excellent references on such subjects by Fritz [1], Walters and Bates [2], and Warnick et al. [3].

DIMENSIONAL ANALYSIS OF HYDRAULIC TURBINES

For any hydraulic machine, it is of interest to obtain a relationship between head (specific energy or pressure), flow rate, power, torque, and so on with size, speed, and fluid properties. Some of the important variables are the flow rate Q, specific energy E, power P, speed N, a characteristic dimension D for size, density ρ, and viscosity μ. The dimensions of the variables are given in Table 1.

Table 1 Variables of Interest in Turbomachines with Their Dimensions

Flow rate	Q	L^3t^{-1}
Specific energy	E	L^2t^{-2}
Power	P	ML^2t^{-3}
Rotational speed	N	t^{-1}
Size	D	L
Density	ρ	ML^{-3}
Viscosity	μ	$ML^{-1}t^{-1}$

Using Buckingham's pi theorem (see Streeter and Wylie [4]), these variables can be combined into the following dimensionless groups:

$$\pi_1 = \frac{Q}{ND^3} \qquad \pi_2 = \frac{E}{N^2D^2}$$
$$\pi_3 = \frac{P}{\rho N^3 D^5} \qquad \pi_4 = \frac{\mu}{\rho N D^2} \tag{1}$$

The groups π_1 and π_3 are called the capacity (or flow) coefficient and power coefficient, respectively. The group π_4 has the form of reciprocal of Reynolds number and therefore represents the importance of viscous effects of the fluid. If it is recognized that the product ND represents the peripheral velocity of the rotor u, then π_4 indeed is the reciprocal of Reynolds number. Finally, π_2 is called the head coefficient. If E, the specific energy of the fluid, is replaced by its dimensional equivalent gH, then the equation for π_2 can be replaced by

$$\pi_2 = \frac{gH}{N^2D^2} \tag{2}$$

When dealing with hydraulic machines, whether they are power-producing or power-absorbing, it a is very common practice to refer to the head H on the machine. Centrifugal pumps often are used to pump fluids in reservoirs located H units above the location of the pump. Similarly, all hydraulic turbines utilize the stored potential energy of the fluid to convert into mechanical shaft power. Such potential energy is available either in the form of natural reservoirs or artificially created on rivers through dams. Hence the total specific energy available to the fluid is equivalent to gH (less the losses). Thus it is quite appropriate to replace E by gH while dealing with hydraulic machines.

The head and power coefficients can be combined by eliminating D from them. The resulting variable is called the *specific speed* (or sometimes

the *turbine specific speed*). The resulting equation can be written as

$$n'_s = \frac{N\sqrt{P}}{\sqrt{\varrho}(gH)^{5/4}} \tag{3a}$$

An alternate but perhaps more useful form of Eq. (3) can be obtained by combining the head and flow coefficients and eliminating D from them. The result is then

$$n_s = \frac{N\sqrt{Q}}{(gH)^{3/4}} \tag{3b}$$

The variable n_s is sometimes called the *pump specific speed*. A close look at Eqs. (3) and (3a) would immediately reveal that they are both equivalent, since P, Q, and H are related by the expression

$$P = \rho g Q H \tag{4}$$

In writing Eq. (4), care must be exercised to distinguish whether H represents the gross or net head. Here it is assumed that H is the net head. Otherwise the hydraulic efficiency η needs to be introduced, which for most hydraulic turbines operating at the design point is close to 90%.

The variable specific speed defined in Eq. (3a) or (3b) is one of the most useful practical factors in sizing hydraulic machines. For turbines or pumps handling large discharges at low heads, a high specific speed is indicated; for high heads and low discharges the specific speed is low. It is interesting to observe that the type (axial, radial, or mixed) of the machine in question is strongly influenced by the specific speed. For high specific speeds, which are due to high discharges (and/or low heads), a large flow area is required to accommodate these high flow rates. An axial-flow machine would best accomplish this since for such machines the flow area is proportional to D^2 (in fact, $\sim\pi D^2$ less the area occupied by the hub). Kaplan turbines and axial-flow fans fall into this category. These are designed for best efficiency when operating at low heads and high discharges. On the other hand, for low specific speed machines, which require low discharges and correspondingly high heads, centrifugal or radial-flow type machines are best suited. In such machines, since the flow is radial the flow area is proportional to the circumference, and therefore D, thus producing relatively low discharges. Also, since the flow moves radially, the change in centrifugal head produces high pressure changes. Examples of such machines are the centrifugal pump and Francis turbine. Thus as the specific speed increases, the shape of the impeller changes from purely centrifugal, to mixed, to purely axial. These are shown pictorially in Fig. 1.

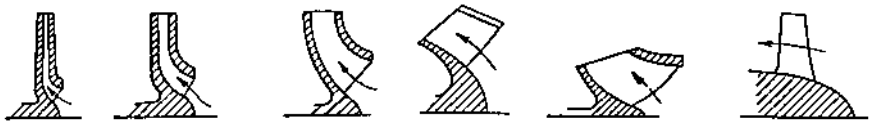

Figure 1 Variation of impeller shapes with N_s.

It is also possible to use the specific speed to select the type of machine appropriate for given requirements. Listed in Table 2 are the ranges of specific speeds corresponding to each type of hydraulic machine. Thus the numerical value of the specific speed gives a useful guideline as to the type of hydraulic machine that needs to be used. It also turns out that specific speed is directly related to the most efficient hydraulic turbine. One final comment needs to be made in connection with specific speeds. The variables n_s and n'_s as defined in Eqs. (3a) and (3b) are dimensionless. However, practicing engineers use a slightly different form. Since the values of ρ and g are constant, they are removed from the definitions. Thus, new expressions for specific speed can be written as

$$N'_s = \frac{N\sqrt{P}}{(H)^{5/4}} \qquad N_s = \frac{N\sqrt{Q}}{(H)^{3/4}} \tag{5}$$

Where

N is in rpm.
Q is in gallons per minute.
H is in feet.
P is in horsepower.

Table 2 Specific Speeds for Various Hydraulic Machines (Logan [5])

Turbomachine	Specific speed range
Pelton wheel	0.03–0.3
Francis turbine	0.3–2.0
Kaplan turbine	2.0–5.0
Centrifugal pumps	0.2–2.5
Axial-flow pumps	2.5–5.5

Unlike n_s and n'_s, the values of N_s and N'_s given by Eq. (5) are not dimensionless. They are related by the following expressions:

$$N'_s = 273.3n'_s \qquad N_s = 17,182n_s \tag{6}$$

EULER TURBINE EQUATION

In order to analyze the kinematic and dynamic factors in the design of turbomachines, it is necessary to relate the fluid velocities and the rotor velocity to the forces of interaction due to the momentum changes of the fluid inside the rotor. This can be very conveniently performed using the angular momentum principle applied to finite control volumes, which states that

$$\vec{M} = \frac{\partial}{\partial t}\int \vec{r}\times\vec{V}\rho dv + \int \vec{r}\times\vec{V}\rho\vec{V}\,dA \tag{6a}$$

For steady flows, the first term becomes zero. As shown in Fig. 2, a fixed control volume is chosen that encloses the turbomachine rotor. A fixed coordinate system is chosen such that the z-axis is aligned with the axis of rotation. The fluid enters the rotor at a radius r_1 with velocity $\vec{V}_1$; the fluid leaves the rotor at a radius r_2 and with velocity $\vec{V}_2$. The term of $\rho\vec{V}dA$ in the surface integral is the mass flow rate into and out of the control volume. For steady flow, flow rate in should be equal to flow out of the control volume. The velocity vector $\vec{V}$ at any point on the rotor can be conveniently represented by its components V_z, V_r, and V_u, which stand for the axial, radial, and tangential components, respectively. The fluid enters the rotor at a radius r_1 and leaves at a radius r_2. The forces on the rotor are caused by the changes in the absolute velocity of the fluid at the rotor inlet and exit. The change in the axial velocity (or axial momentum) causes the axial thrust, while the change in the radial velocity produce bending forces on the rotor. Neither of these forces gives rise to torque to cause rotation of the shaft. Thus the torque (moment along the axis) causing rotation of the rotor can be written as

$$M_z = \begin{vmatrix} 0 & 0 & 1 \\ r & 0 & z \\ V_r & V_u & V_z \end{vmatrix} \tag{6b}$$

Denoting the constant mass flow rate at inlet and outlet by $\dot{m}$, the torque can

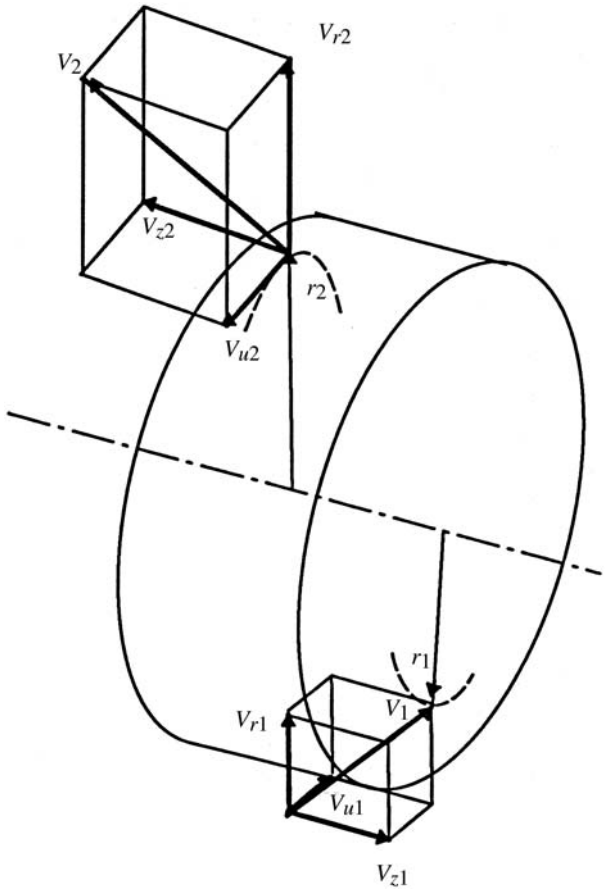

Figure 2 Flow and velocity components through a rotor.

then be written as

$$T = \dot{m}(r_2 V_{u2} - r_1 V_{u1}) \tag{7}$$

and power is given by the product of torque and rotational speed ω. The resulting equation can be conveniently written as

$$P = \dot{m}(u_2 V_{u2} - u_1 V_{u1}) \tag{8}$$

where the product of radius and the angular velocity has been replaced by the tangential speed of the rotor. There are two other forms in which Eq. (8)

can be expressed. The first form is obtained by dividing Eq. (8) by $\dot{m}$. Thus,

$$E = (u_2 V_{u2} - u_1 V_{u1}) \tag{8a}$$

The other form is obtained by dividing Eq. (8a) by g, and thus,

$$H = \frac{(u_2 V_{u2} - u_1 V_{u1})}{g} \tag{8b}$$

Equation (8) [or alternately Eq. (8a) or (8b)] is called Euler's turbine equation and is of utmost importance in the analysis of all types of turbomachinery.

Impulse Turbines

An impuse turbine is one in which the total pressure drop of the fluid occurs inside one or more nozzles and there is no drop in pressure as the fluid flows through the rotor. This statement is particularly true when the working fluid is water. Such turbines are most useful when water is available with large potential energy. When such large heads are available, the potential energy is first converted into kinetic energy by letting the fluid flow through large pipes called penstock, and the high kinetic energy fluid then impinges on vanes or buckets. Thus kinetic energy is converged into force, which results in torque on the shaft. A small part of kinetic energy is lost in fluid friction on the wheels, and another small part is lost as kinetic energy of the fluid leaving the vanes. A hydraulic impulse turbine is a called Pelton wheel, which is by far the most important machine among hydraulic turbines and has evolved from the development of earliest hydraulic turbines, frequently called water wheels. It is named after Lester A. Pelton (1829–1908), who patented it in 1880. The basic features of the Pelton wheel are shown in Fig. 3. It consists of a rotor on which ellipsoidal or hemispherical buckets are mounted along the circumference, one or several nozzles that direct the high-kinetic-energy fluid onto the buckets, and a flow-controlling mechanism in the nozzles, usually in the form of a spear whose movement is hydraulically controlled. The spear controls the amount of flow and at the same time provides smooth flow with minimal losses. An important feature of Pelton wheels is that all available potential energy of the fluid is converted into kinetic energy outside the rotor (in this case inside the penstock and nozzles). Thus the pressure all over the bucket is essentially atmospheric and the energy transfer occurs purely through impulse action. The rotor is not enclosed, and the water leaving the turbine goes to the tail race.

The velocity diagrams are shown in Fig. 4. At the inlet the jet is almost aligned with the blade and the inlet velocity degenerates to a straight line. At

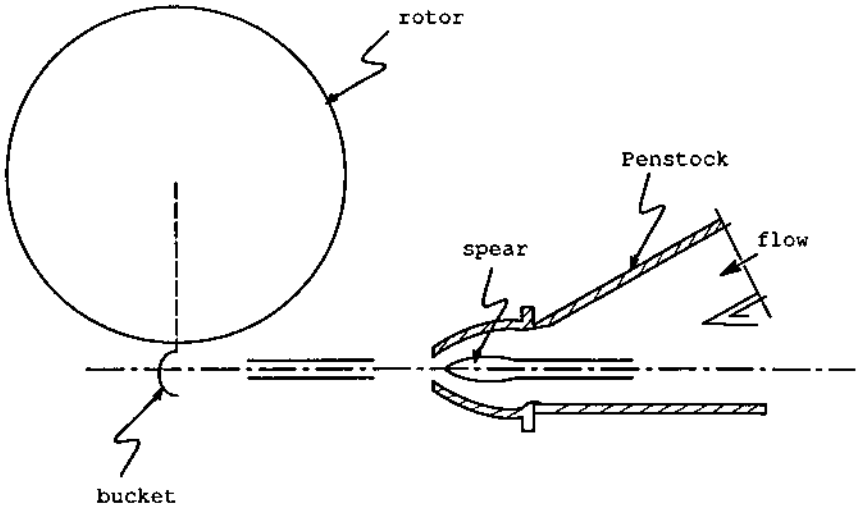

Figure 3 Schematic diagram of Pelton wheel.

the outlet the fluid leaves with a relative velocity w_2, making an angle of β_2 with the blade speed. The specific energy is given by the following

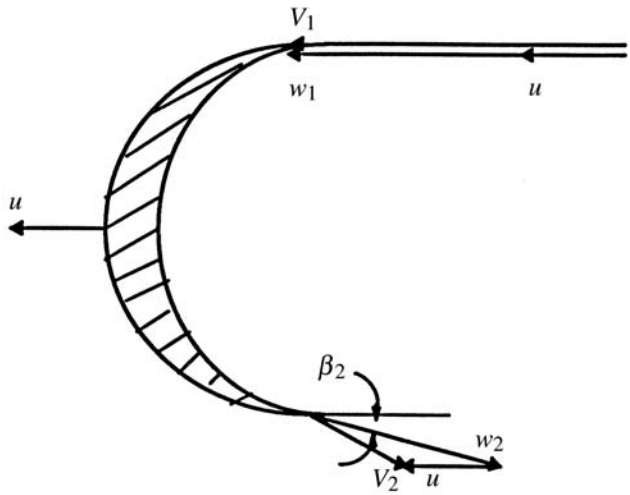

Figure 4 Velocity triangles for Pelton wheel.

expression:

$$E = u(V_1 - u)(1 + \cos\beta_2) \tag{9}$$

Where

$u =$ blade speed.
$V_1 =$ jet speed.
$\beta_2 =$ blade angle at the exit.

The maximum power is obtained when β_2 is zero. However, when the blade angle is zero, water exiting from one bucket would strike the back of the succeeding bucket, so that the overall efficiency of the turbine would be reduced. Hence, the value of β_2 is normally set to 10–15°.

The bucket of a typical Pelton wheel is shown in Fig. 5. For reasons of symmetry, the jet emerging from the nozzle is split into two parts and the fluid is equally distributed in the hemispherical buckets. Theoretically the centerline of the bucket, called the splitter, should be shaped like a cusp, with the two hemispheres meeting at the center, making the angle of contact of the two surfaces zero. However, this is not possible due to two reasons: first because of the difficulty in manufacturing such an intersection, and second because of the entrained sand and other abrasive particles in the jet, which invariably erode the splitter surface. Typical dimensions of the bucket

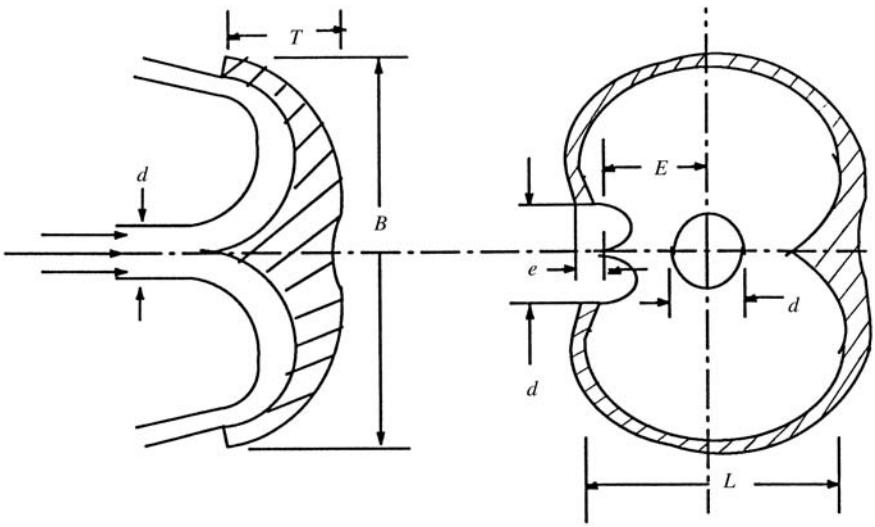

Figure 5 Typical Pelton wheel dimensions.

shown in Fig. 5 (see Kadambi and Prasad [6] and Shepherd [7]) are $B/d = 3$; $e/d = 0.35$; $T/d = 0.8$–0.95; $L/d = 2.5$–2.8; and $E/d = 0.85$.

The mechanical shaft power generated by the Pelton wheel is converted into electrical power by means of the electric generator, which is mounted on the same shaft of as the turbine. The generator must run at a constant speed, since the electric power generated must have a constant frequency. Hence the turbine must operate at a constant speed. This is most likely when the water to the turbine is supplied at a constant rate and under a constant head. Any changes in the electrical power requirements would result in corresponding changes in the load on the turbine, and the turbine would have to modify its power output accordingly. The power output from the Pelton wheel can be changed by changing the head on the turbine or the flow rate through it. It is generally not feasible to change the power delivered by changing the head. Hence, it is necessary to regulate the water supply to the turbine. This is accomplished by equipping the nozzle with a movable, conical, spear-shaped needle as indicated in Fig. 6. The longitudinal motion of the spear controls the annular area available for flow and thus controls the flow rate. The needle itself is carefully designed so as to allow a uniform jet of water at all times to impinge the buckets, thereby minimizing turbulence losses. Thus the principal advantage of flow control using a needle in the nozzle is that the velocity of the jet is nearly constant irrespective of the position of the needle. However, the needle mechanism has a disadvantage when the load on the turbine is suddenly reduced. Pelton

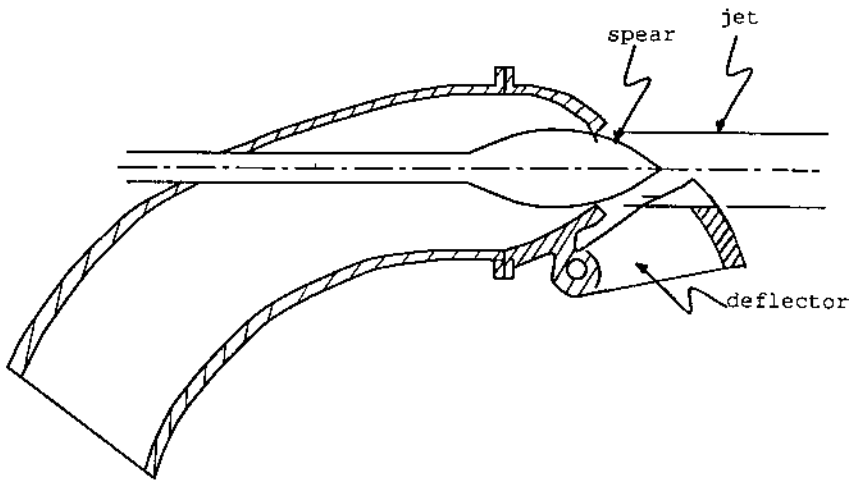

Figure 6 Needle assembly for flow control in a Pelton wheel.

wheels operate under high heads. This necessitates a long penstock, and a sudden closing of the nozzle in response to a sudden drop of demand results in water hammer in the penstock. Thus water control using needle movement is suitable only when the penstock is relatively short. Otherwise, suitable precautions must be taken to avoid water hammer. This is accomplished using the jet deflector as shown in Fig. 6. If the load on the turbine is reduced suddenly, the jet deflector is first moved into its position to deflect a portion of the water from impinging on the turbine until the needle can be moved slowly to the proper position. It is reported that the movement of the deflector can be accomplished in as little as 3 sec while the movement of the needle may take a few minutes (see Brown and Whippen [8]). Nozzles have been developed empirically for several years, and some typical dimensions are shown in Fig. 7. The proportions as recommended by Shepherd [6] can be summarized as follows: $d_1/d = 1.2–1.4$; $d_2/d = 3–4$; $d_3/d = 1.25–1.5$; $\alpha = 60–90^\circ$; and $\beta = 40–60^\circ$.

Reaction Turbines

A reaction turbine is one in which a significant portion of the pressure drop takes place in the rotor. Hence these are designed so that the fluid fills the rotor completely. Also, any such machine must have the rotor enclosed so that the decrease in pressure of the fluid takes place in the runner passages, and not freely in all directions. The water exiting the turbine has a considerable amount of kinetic energy and also pressure. Hence it is essential that this type of turbine is completely enclosed. The most common example of a reaction turbine is the lawn sprinkler. Reaction turbines are

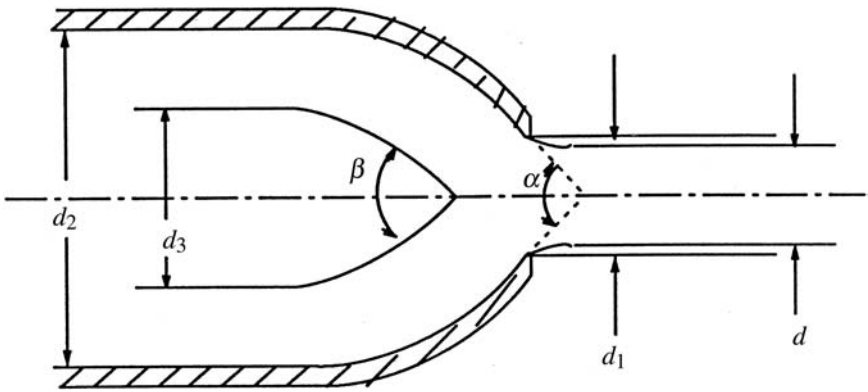

Figure 7 Typical dimensions of a Pelton wheel nozzle.

classified according to the direction of flow of water in the runner. If the direction of flow is predominantly in the radial direction, then the turbine is called a radial-flow turbine; if the direction is mainly in the axial direction, then it is called an axial turbine. Two of the most common examples of these turbines are the Francis and Kaplan turbines, respectively.

Francis Turbine

The first well-designed Francis turbine was built in 1849 by a hydraulic engineer named James B. Francis. As originally conceived, it was a purely radial machine. It should be mentioned that all inward flow reaction hydraulic turbines are called Francis turbines. Modern designs of Francis turbines have some mixed-flow characteristics in them. A schematic diagram of a Francis turbine is shown in Fig. 8. It consists of a spiral casing, a runner, a set of guide vanes, and a draft tube. The inlet of the spiral casing is connected to the penstock. Water is uniformly distributed around the circumference of the runner by using the spiral casing. In order to distribute

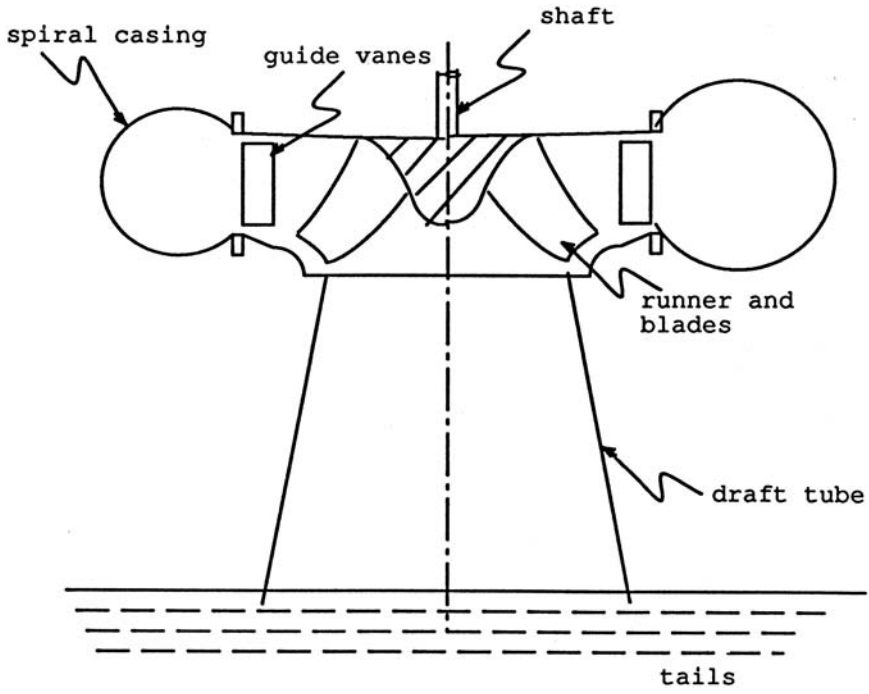

Figure 8 Schematic diagram of a Francis turbine.

the water uniformly around the circumference, it is necessary to reduce the area available for flow. Thus the casing takes the shape of a spiral, which gives the maximum area at the entrance and almost zero at the tip, hence the name spiral casing. Water from the spiral casing is guided onto the runner by a set of guide vanes, which are sometimes called wicket gates, placed circumferentially. These can be set to any angle desired and their shape is designed so that the water passes over them with minimum friction losses. The water then passes through the runner and then discharges into a draft tube.

As already mentioned, the flow in the runner of modern Francis turbines is not purely radial, but a combination of radial and axial flows. The width of the runner depends on the specific speed. The higher the specific speed, the higher the width of the runner, since higher specific speeds necessarily mean larger flows and correspondingly larger flow areas. The runners can typically be classified as slow, medium or normal, and fast runners, with their specific speed (N_s) ranges being 60–120, 120–180, and 180–300, respectively. These are pictorially shown in Fig. 9.

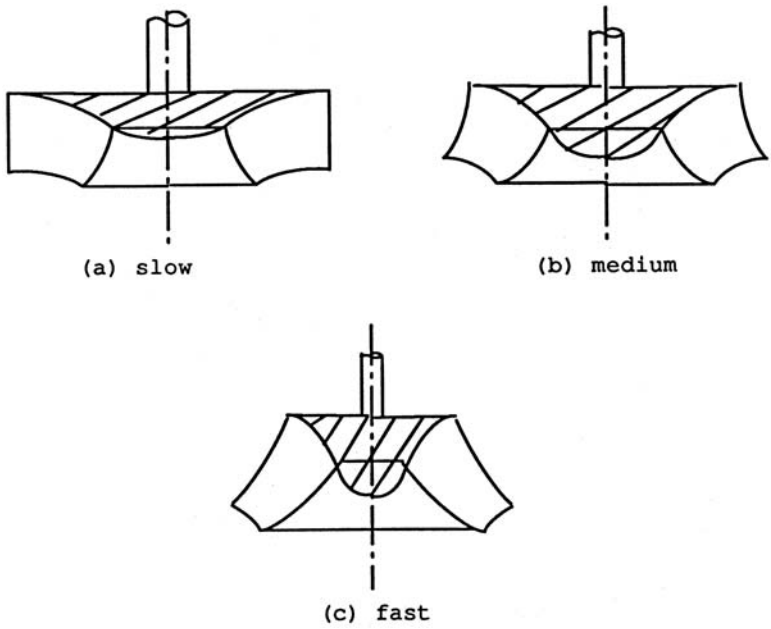

Figure 9 Variation of Francis turbine runners.

The manufacturers of hydraulic turbines over the years have developed several techniques for estimating the various parameters and dimensions of different parts of turbines. These techniques are based on experience gained over the years and on a thorough knowledge of the principles of theory of turbines. Since the variables are many, and all design practices are not standardized, it is quite likely to experience differences in the design of turbines from different companies. It is therefore highly desirable for an engineer to compare several designs and combine them with his or her experience before the final selection is made. The reader would thus find large variations in the design process based on the source. The procedures mentioned in this chapter are based on the recommendations of Brown and Whippen [8].

In a typical design of the Francis turbine, the input variables are the head under which the turbine would operate, the required speed of the runner, and the required power output. The output variables that need to be determined are then the diameter of the runner, the number of stay vanes, the number of buckets on the runner, and the height of the runner.

A reasonable estimate of the flow rate through the turbine can be made from the expression for power as follows:

$$P = \eta\gamma QH \tag{10}$$

where η and γ are the hydraulic efficiency and specific weight, respectively. At the design point the efficiency of hydraulic turbines is between 0.88 and 0.94 (see Shepherd [7]). Once the flow rate Q is known, the specific speed can be computed. This fixes the most suitable type of turbine that can be selected. The velocity of the fluid entering a reaction turbine cannot be accurately determined using the orifice formula, since the pressure at the turbine inlet is greater than atmospheric. However, the orifice formula can be suitably modified to get an estimate for the inlet velocity. Thus,

$$V_1 = c(2gh)^{1/2} \tag{11}$$

where c is a coefficient between the values of 0.8 and 0.6 for specific speeds ranging from 25 to 85. Other values can be obtained by interpolation. The water from the wicket gates makes an angle α_1 with the circumference of the rotor. This angle ranges from 15 to 35° when the specific speed, N_s, ranges from 25 to 85, with intermediate values obtained from interpolation. The number of wicket gates and the number of stay vanes for reaction turbines are equal and are selected somewhat arbitrarily. These are usually multiples of 4 and range from 12 to 28, depending on the size of the runner, with the higher number used for larger diameters.

The blade velocity u_1 is determined by using the speed ratio ϕ, which is defined as the ratio of blade velocity to fluid velocity V_1:

$$\phi = u_1/V_1 \tag{12}$$

Its values range from 0.6 to 0.9 for N_s ranging from 25 to 85. The knowledge of the blade velocity can be used in computing the runner diameter. The next step in the design process is to size the gates and the runner. The most important dimension in this regard is the height of the gates, which in a sense also determines the height of the runner. This can be easily done since the flow rate, the velocity of water at entrance, and the angle α_1 are known. Thus, the height of the gates B is given by

$$B = Q/(V_1 \pi C D \sin \alpha_1) \tag{13}$$

In this above equation, C is a coefficient that allows for the thickness of the gates. The value of C is usually about 0.95. The relative velocity can now be computed using the law of cosines as follows (see Fig. 10):

$$w_1 = (u_1^2 + V_1^2 - 2u_1 V_1 \cos \alpha_1)^{1/2} \tag{14}$$

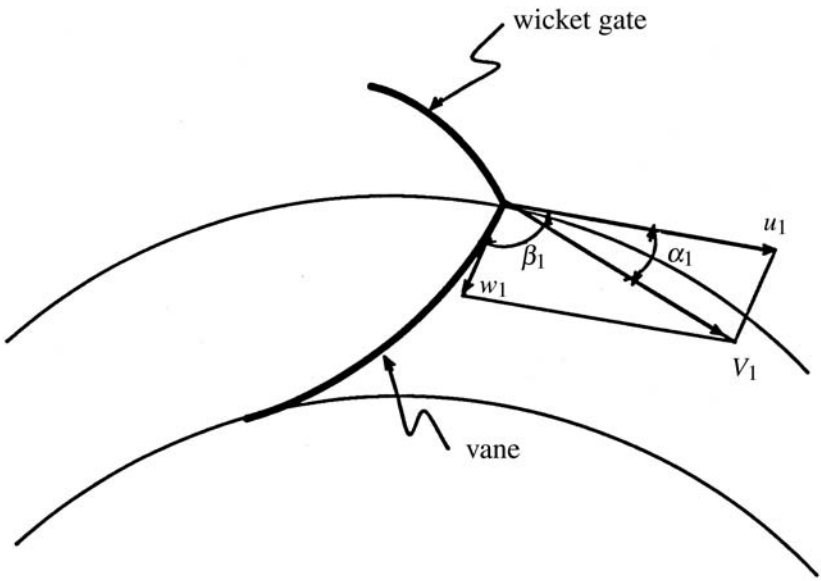

Figure 10 Velocity triangle at entrance of Francis runner.

The direction of the relative velocity can be calculated from the relationship

$$\sin(180 - \beta_1) = (V_1/w_1)\sin\alpha_1 \tag{15}$$

The blade angle β_1 typically is greater than 90°, with the maximum value being 135°.

In most theoretical analysis, it is assumed that the water leaving the turbine runner is purely in the axial direction. This condition results in the greatest efficiency for the Francis turbine, since all the inlet momentum of the fluid would have been converted into torque. However, this is seldom achieved in practice since the water exiting the turbine will still have a nonzero, but small, radial velocity. The common practice is to ignore this component and assume that the exit velocity from the runner is the same as the inlet velocity of the draft tube. In order that the water from the runner enters the draft tube properly, the blades should be nearly tangent to the circle through the exit edges of the buckets. The blade angle at the exit of the buckets is typically between 15 and 30°.

The final design variable is the number and shape of the buckets. The standard practice in the turbine industry is to use 15 buckets. Some modern turbines have 13, 17, or 19 buckets, with the larger number of buckets being used when the specific speed is low. The blade angles at the inlet and outlet are selected within the broad guidelines already mentioned. The contour of the intermediate portion of the bucket is formed so that there is a gradual change in the direction of the relative velocity and the area available for flow.

Kaplan Turbines

In situations where large volumes of water are available with low heads, it is essential to provide large flow areas, which can be easily accomplished using axial-flow machines. A propeller turbine is such a machine. It is a reaction turbine that operates under heads of 15 to 250 ft when specific speed N_s ranges from 300 to 1,000. It is primarily an axial-flow type of device. A propeller turbine with adjustable blades is called a Kaplan turbine, named after the German Professor Victor Kaplan who developed such a turbine between 1910 and 1924. A schematic diagram for a Kaplan turbine is shown in Fig. 11.

Water passes over stay vanes and passes through wicket gates before coming into contact with the blades. The space between the wicket gates and the blades is used to turn the direction of flow from radial to nearly axial. After passing over the blades, the water flows through a draft tube. Typical efficiencies of Kaplan turbines are in the range of 90–93% at the design point.

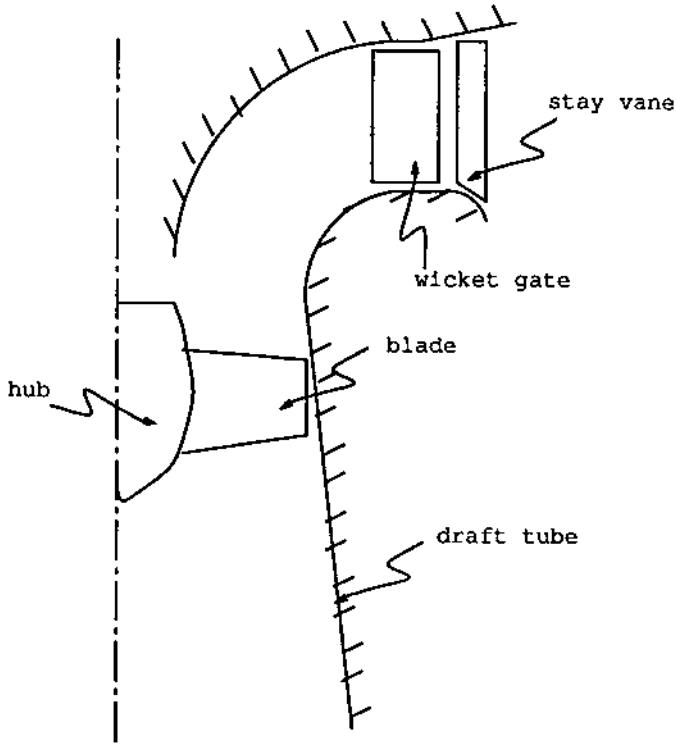

Figure 11 Schematic diagram of Kaplan turbine.

The design methodology for propeller turbines proceeds along the same lines as a Francis turbine. There are, however, some important differences, the most important being the value of ϕ, the speed ratio. While this value was low for Francis turbines, it can be as high as 1.5–2.5 for propeller turbines. The ratio of hub diameter to blade diameter, d/D, is a very important parameter in propeller turbines. Some variations of head, specific speeds, d/D, and number of blades for axial-flow turbines are shown in Table 3.

The volumetric flow of water is given by the expression

$$Q = \pi(D^2 - d^2)V_{ax}/4 = (\pi/4)(D^2 - d^2)\psi(2gH)^{1/2} \tag{16}$$

with the flow ratio ψ being in the range 0.35–0.75.

An important feature of axial-flow turbines is that the blade speed varies along the blade, and hence the blade angle β also varies from point to

Table 3 Variation of Some Quantities for Kaplan Turbines (see Kadambi and Prasad [6])

	Head					
	5 m	20 m	40 m	50 m	60 m	70 m
Number of blades	3	4	5	6	8	10
d/D	0.3	0.4	0.5	0.55	0.6	0.7
Approx. N_s	1,000	800	600	400	350	300

point. However, the blade speeds at inlet and outlet are equal. If the diameters at the tip and hub are known, blade speeds can be determined, and vice versa. By assuming that the axial velocity is constant, the inlet and exit velocity triangles can be drawn at the hub and tip. From these, the blade angles β_1 and β_2 can be determined. The typical number of blades in Kaplan turbines is between 5 and 8. The highest number of blades is 10.

Draft Tubes

As pointed out in the previous sections, a Pelton wheel operates at high heads (and low specific speeds). By their very design, such turbines are essentially open to the atmosphere. Also, the kinetic energy of the fluid leaving the runner is a very small percentage of the total available head (typically a few percent). This is in direct contrast with reaction turbines, in which a considerable portion of kinetic energy is available at the exit of the runner, which would be wasted if the turbine is placed just above the tails, and the outgoing water just exhausted to the atmosphere. Since reaction turbines operate under small heads, the exit kinetic energy constitutes a significant portion of the total head. It has been reported by Jagdish Lal [9] that the exit kinetic energy could range from 15 to 45% of the net head for Francis and Kaplan turbines, respectively. Hence any efforts to recover this energy would greatly improve the overall efficiency. A draft tube primarily serves this purpose. If the turbine is placed at some distance above the tails, leading the outgoing water to the tails through a tube, two things happen. First, the pressure immediately outside the runner (i.e., the inlet of the draft tube) becomes less than atmospheric and the water reaches atmospheric pressure only at the tail race. This improves both the output and efficiency of the turbine. Second, by letting the tube from the turbine to the tails be slightly divergent, a part of the exit kinetic energy can be converted into

pressure. This improves the turbine output further. Such a tube is called the draft tube. It should be pointed out that the addition of a draft tube is neither feasible nor desirable in the case of an impulse turbine such as the Pelton wheel, since as already mentioned the exit kinetic energy is very low and Pelton wheel runners are not confined as reaction turbines. A schematic diagram of the draft tube is shown in Fig. 12.

An approximate analysis of the draft tube can be performed by considering only the meridional velocity components. If the subscripts e and t represent the conditions at the exit of the turbine (nearly the same as inlet of the draft tube) and at the tails, the pressures and velocities are related by the following expression:

$$p_e/\gamma + V_e^2/2g + H_s = p_a/\gamma + V_t^2/2g + h_f \tag{16}$$

where H_s and h_f are respectively the height of exit of turbine above the tails and losses. It has been assumed that the pressure at the exit of the draft tube (inside) is nearly atmospheric. Thus rearranging Eq. (16), we get

$$p_e/\gamma = p_a/\gamma - (V_e^2 - V_t^2)/2g + (h_f - H_s) \tag{17}$$

Notice that even in the absence of diffusion effects, the value of p_e is lower than than p_a. Thus the addition of draft tube creates a partial vacuum at the turbine exit, thereby increasing the net head under which the turbine operates. Notice also that the second term on the right-hand side of Eq. (17) is the gain in the velocity head due to diffusion effects only, which can be

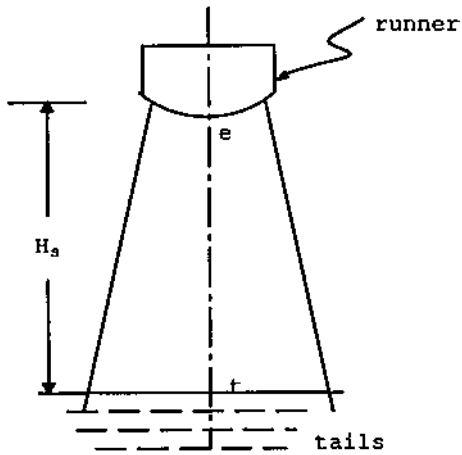

Figure 12 Schematic diagram of draft tube.

denoted by h_d. Thus the efficiency of the draft tube can be defined as the ratio of real diffusion effects versus ideal diffusion effects, that is,

$$\eta_d = (h_d - h_f)/h_d = 1 - h_f/[V_e^2 - V_t^2)/2g] \tag{18}$$

Draft tubes are broadly classified into four categories. These are shown in Fig. 13. The first type is shaped like the frustum of a cone and is simply called the straight divergent tube. It has an efficiency of about 85% and is useful for low specific speed vertical-shaft Francis turbines. The

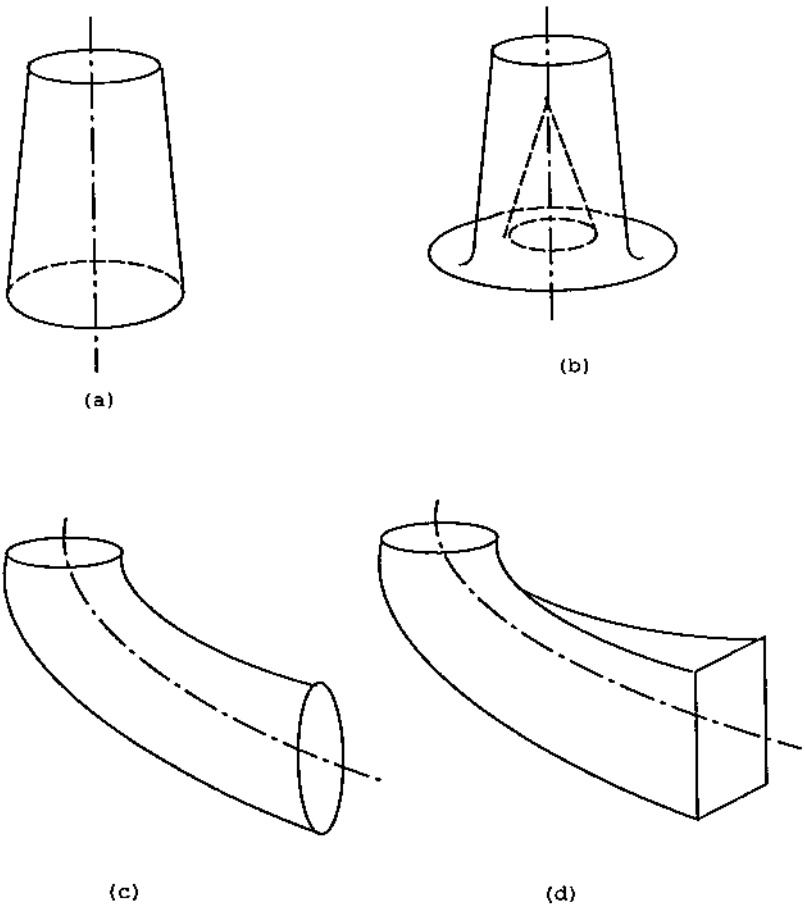

Figure 13 Types of draft tubes: (a) straight divergent type, (b) hydracone, (c,d) elbow type.

second type is called Moody's spreading tube or the hydracone. This is also a straight tube except it is bell-shaped with a solid conical core in the central portion of the tube. This type has the advantage that it can allow flow with a whirl component of velocity with minimal losses. This type of draft tube also has an efficiency of about 85% (see Jagdish Lal [9]). The third type is called the simple elbow tube and can be used when there are space limitations. The efficiency is usually much lower, of the order of about 60%. The last type is similar to the third except that the exit from the draft tube is rectangular in shape rather than circular.

The geometrical parameters of draft tubes, like the length and included angle, are governed by two factors. First, the length of the tube should not be so long as to cause cavitation at the inlet of the draft tube. Second, the diffuser angle should be small enough so that separation does not occur. The latter is achieved by keeping the diffuser angle less than 10°.

Cavitation in Turbines

According to Bernoulli's theorem (see Wilson [10]), an increase in velocity in a fluid is accompanied by a decrease in pressure. For any liquid there is a lower limit beyond which the absolute pressure cannot decrease. This value is called the vapor pressure and depends on the nature of the liquid and local temperature. If at any point liquid flows into a region where the pressure is reduced to vapor pressure, the liquid boils locally and vapor pockets are formed. The vapor bubbles are carried along with the liquid, and when they reach regions of higher pressure, they suddenly collapse. This process is called *cavitation*. The collapsing action produces high-pressure pulses, often of the order of gigapascals. When such collapse takes place adjacent to solid walls continually and at high frequency, the material in that zone gets damaged. This is called pitting of solid surfaces. Cavitation is also accompanied by noise, vibration, and drop in efficiency, since the turbine is operating at an off-design point, and can be observed to happen in draft tubes, trailing edges of turbine blades, and so forth. In order to avoid cavitation, it is necessary that the absolute pressure at every point be above vapor pressure. A simplified analysis of cavitation can be performed as follows. Consider the draft tube shown in Fig. 14. By applying the energy equation between the exit of the turbine and the tails, the following equation is obtained.

$$p_e/\gamma + V_e^2/2g + H_s = p_a/\gamma + h_f \tag{19}$$

where the subscript e refers to the exit of the turbine, which is nearly the

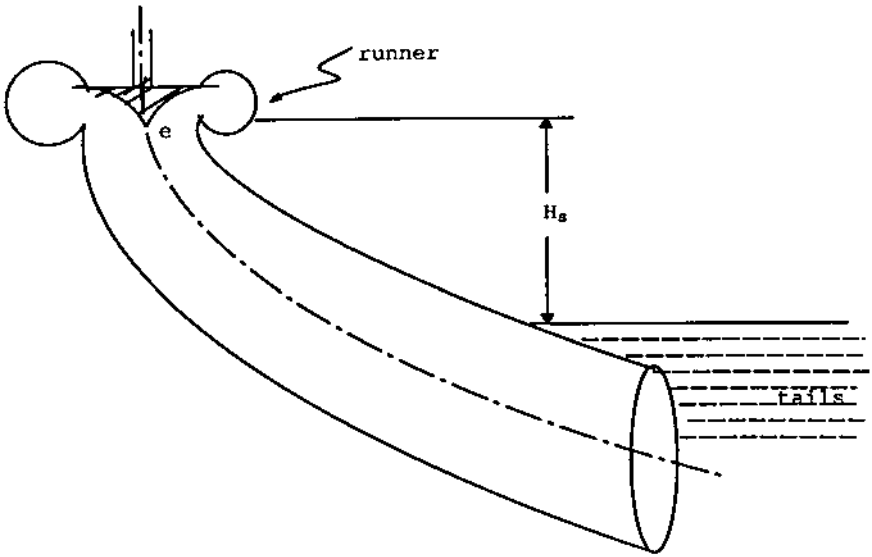

Figure 14 Draft tube setting.

same as the inlet of the draft tube. Thus

$$V_e^2/2g = (p_a - p_e)/\gamma - (H_s - h_f) \tag{20}$$

Cavitation occurs when the value of p_e becomes equal to the vapor pressure of the fluid at the local temperature. The cavitation parameter σ can be defined as the ratio of exit velocity head and head on the machine. Thus,

$$\sigma = (V_e^2/2g)/H = [(p_a - p_v)/\gamma - (H_s - h_f)]/H \tag{21}$$

where p_e has been replaced by the vapor pressure p_v. Usually, the head loss h_f is small and is dropped from the equation. Thus a number called the *Thoma cavitation coefficient*, named after the German engineer Dietrich Thoma (1881–1943), can be defined as

$$\sigma = [(p_a - p_v)/\gamma - H_s]/H \tag{22}$$

In order to avoid cavitation, it is necessary that $\sigma > \sigma_c$, where σ_c is called the *critical cavitation coefficient*. The values of σ_c are determined experimentally by plotting σ versus efficiency. For large values of σ, efficiency is nearly constant. When σ falls below σ_c, however, the efficiency rapidly drops off. This is also accompanied by increased noise and vibration. Typical values of σ_c are given in Table 4.

Table 4 Typical Values of Critical Cavitation Coefficients for Francis and Propeller Turbines [11]

	Turbine Type							
	Francis	Francis	Francis	Francis	Francis	Kaplan	Kaplan	Kaplan
N_s	20	40	60	80	100	100	150	200
σ_c	0.025	0.1	0.23	0.4	0.64	0.43	0.73	1.5

NOMENCLATURE

A = surface area.
D = diameter of the rotor (characteristic dimension).
E = specific energy.
g = acceleration due to gravity.
H = head on the machine.
$\dot{m}$ = mass flow rate.
N = rotational speed of the rotor (rpm).
N_s = dimensional specific speed.
n_s = dimensionless specific speed.
P = power.
Q = volumetric flow rate.
T = torque.
$\vec{V}$ = absolute velocity of fluid.
V_u = tangential velocity component.
V_z = axial velocity component.
V_f = radial velocity component.
v = volume.

Greek Symbols

α = angle made by wicket gates.
β = blade angle.
μ = viscosity of the fluid.
ϕ = speed ratio = u/V.
ρ = density.
π_i = dimensionless groups.
ω = angular velocity of rotor = $2\pi N/60$.

REFERENCES

1. J. J. Fritz, *Small and Mini Hydropower Systems*, McGraw-Hill, New York (1984).
2. R. N. Walters and C. G. Bates, Selecting Hydraulic Reaction Turbines, Engineering Monograph No. 20, Bureau of Reclamation, U.S. Department of the Interior (1976).
3. C. C. Warnick in collaboration with H. A. Mayo, J. L. Carson, and L. H. Sheldon, *Hydropower Engineering*, Prentice-Hall, Englewood Cliffs, NJ (1984).
4. V. L. Streeter and E. B. Wylie, *Fluid Mechanics*, 8th ed., McGraw-Hill, New York (1985).
5. Logan, Earl Jr., *Turbomachinery Basic Theory and Applications*, Marcel Dekker, Inc., New York, 1981.
6. V. Kadambi and M. Prasad, *An Introduction to Energy Conversion, Vol. III, Turbomachinery*, Wiley Eastern, New Delhi (1977).
7. D. G. Shepherd, *Principles of Turbomachinery*, Macmillan, New York (1956).
8. L. P. Brown and W. E. Whippen, *Hydraulic Turbines*, Parts I–III, International Correspondence Schools, Scranton, PA (1976).
9. J. Lal, *Hydraulic Turbines*, 6th ed., Metropolitan, New Delhi (1986).
10. D. G. Wilson, *The Design of High Efficiency Turbomachinery and Gas Turbines*, MIT Press, Cambridge, MA (1984).
11. R. L. Dougherty, J. B. Franzini, and E. J. Finnemore, *Fluid Mechanics with Engineering Applications*, 8th ed., McGraw-Hill, New York (1985).